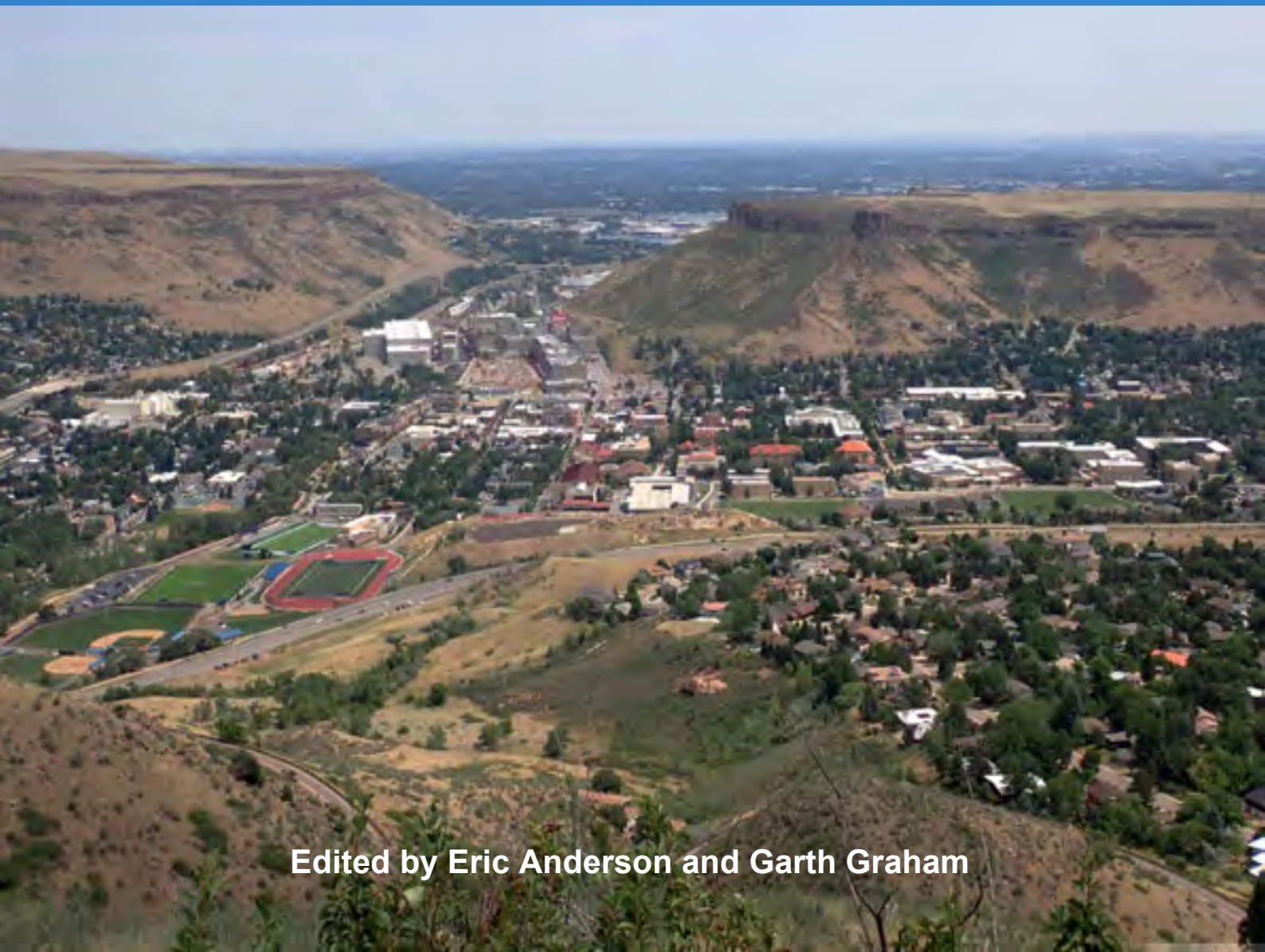
18TH SGA Biennial Meeting

2025 Colorado School of Mines Golden, Colorado USA

August 3-7, 2025

PROCEEDINGS VOLUME 2



Edited by Eric Anderson and Garth Graham

ISBN 979-8-90030-540-0



The theme of the 18th SGA Biennial Meeting - the 60th Anniversary of Society of Geology Applied to Mineral Deposits (SGA) is “Mineral Resources for Our Ever-Changing World”

Suggested citation for the entire proceedings:

Anderson ED and Graham GE eds. (2025) Mineral Resources for Our Ever-Changing World. Proceedings of the 18th SGA Biennial Meeting, August 3-7, Golden, Colorado, USA, 1246 pp.

Suggested citation for an individual paper:

Pfaff K, Kasprowicz F, Caine JS, Benzel WM, Lowers HA (2025) Combining Scanning Electron Microscopy, X-Ray Diffraction, and X-Ray Fluorescence to Characterize Shear Zones at the Pogo Gold Deposit, Alaska. In: Proceedings of the 18th SGA Biennial Meeting, August 3-7 2025, 3: 1157-1160.

Volume 1

Symposium: Metallogenic evolution of North America
Plate tectonics, earth evolution and the secular distribution of mineral systems
Evolution of sedimentary basins and ore formation: Special session to honor the career of David Leach
Targeting mineral deposits in metamorphic terranes
Structural geology in ore deposit genesis: Mechanisms, models, and mineralization

Volume 2

Ore deposits associated with magmatic systems: Porphyry/epithermal deposits
Ore deposits associated with magmatic systems: Magmatic Ni-Cu-PGE and Fe-Ti-P deposits
Ore deposits associated with magmatic systems: Alkaline magmatism and carbonatites
Ore deposits associated with magmatic systems: Volcanogenic massive sulfides: in honor of Jim Franklin
Ore deposits associated with magmatic systems: Tin-tungsten and rare metal deposits

Volume 3

Critical Mineral Resources: Opportunities and challenges
Geochemical processes in ore deposition (SGA-SEG co-sponsored)
New frontiers in analytical techniques for the explorationist
Discovery through geophysics, remote sensing, and hyperspectral techniques

This publication cannot be reproduced in whole or in part without the permission of The Society for Geology Applied to Mineral Deposits (SGA).

A digital version of this Proceedings is available from the SGA website www.e-sga.org

Welcome to the 60th Anniversary of SGA!

Welcome to Golden and the 18th Biennial meeting of Society for Geology Applied to Mineral Deposits. Once again, the SGA Biennial has attracted delegates from around the world (>40 countries), and across academia and industry, to take part in the first ever SGA meeting held in the United States. The meeting is hosted by the Colorado School of Mines, which was founded in 1874 and is the oldest university in Colorado. The Local Organizing Committee presents an exciting Scientific Program over the four days of presentations. We thank all of you who submitted an abstract for a talk or a poster for your efforts. We also have 4 Plenary and 22 Keynote talks that are dispersed throughout the meeting. Short Courses and Field Trips that round out our program are sure to be the most rewarding ways to begin and end this biennial SGA event. SGA is also celebrating its 60th anniversary since the organization's founding in Heidelberg, Germany in 1965.

This conference would not have been possible without our many sponsors, and we thank everyone.

Welcome to Golden – and welcome to the 18th Biennial meeting of the SGA!

Karen Kelley

Conference Chair, SGA Golden 2025

Committee Members

Karen D. Kelley, USGS, Conference Chair
Rich Goldfarb, Colorado School of Mines, Technical Program Chair
Mary Carr, Colorado School of Mines, Logistics and Advisory Chair
Erik Tharalson, United States Geological Survey, Field Trips Co-Chair
Mary Doherty, Geological Consultant, Field Trips Co-Chair
Lew Kleinhans, Consultant, Field Trips Co-Chair
Katharina Pfaff, United States Geological Survey, Short Courses Co-Chair
Simon Kocher, Colorado School of Mines, Short Courses Co-Chair
Ben Frieman, Colorado School of Mines, Social Program Chair
Quinton Hennigh, San Cristobal Mining, Sponsorships & Exhibits Co-Chair
Lauren Terry, Colorado School of Mines, Sponsorships & Exhibits Co-Chair
Eric Anderson, United States Geological Survey, Abstract Volume Editor
Garth Graham, United States Geological Survey, Abstract Volume Editor

SPONSORS

Patron Sponsor

BHP

Diamond Sponsor

FREEPORT
FOREMOST IN COPPER

Platinum Sponsor

Teck

Gold Sponsors

RioTinto
CODELCO
GLENCORE
SAN CRISTOBAL MINING
BARRICK
eldorado gold
USGS
science for a changing world

Silver Sponsors

AGNICO EAGLE
minsur
Newmont
FLEET

Copper Sponsors

PORTABLE ppb
MINERSAI

We thank all convenors of SGA 2025

Session Convenors

Symposium: Metallogenic provinces of North America
Rich Goldfarb – Colorado School of Mines
Craig Hart – Consultant
Elizabeth Holley – Colorado School of Mines
Steve Piercey – Memorial University

Plate tectonics, earth evolution and the secular distribution of mineral systems
David Huston – Australian National University
Hartwig Frimmel – University of Würzburg
Yang Li – Peking University

Critical Mineral Resources: Opportunities and Challenges
Simon Jowitt – University of Nevada, Reno
Zhaoshan Chang – Colorado School of Mines
Matthieu Harlaux – BRGM
Phil Verplanck – U.S. Geological Survey

New Frontiers in Analytical Techniques for the Explorationist
Garth Graham – U.S. Geological Survey
Mary Doherty – Consultant
Anna Vymazalova – Czech Geological Survey

Structural Geology in Ore Deposit Genesis: Mechanisms, Models, and Mineralization
Nicolas Thébaud – University of Western Australia
Amanda Hughes – University of Arizona
Yvette Kuiper – Colorado School of Mines
David Rhys – Panterra Resources

Evolution of Sedimentary Basins and Ore Formation: Special Session to Honor the Career of David Leach
Karen Kelley – U.S. Geological Survey
Salah Bouhlel – University of Tunisia
Lluis Fontboté – University of Geneva
Jan Pašava – Czech Geological Survey
Yucai Song – Chinese Academy of Geological Sciences
Sam Spinks – Teck

Targeting Mineral Deposits in Metamorphic Terranes
Patrick Mercier-Langevin – Agnico Eagle
Anne-Sylvie André-Mayer – University of Lorraine
Paolo Garofalo – University of Bologna
Steffen Hagemann – University of Western Australia
Jochen Kolb – Karlsruhe Institute of Technology
Iain Pitcairn – Stockholm University

SGA-SEG Session: Geochemical Processes in Ore Deposition
Crystal Laflamme – Laval University
Jeff Hedenquist – University of Ottawa
Gleb Pokrovski – University of Toulouse
Stuart Simmons – Consultant

Discovery through Geophysics, Remote Sensing, and Hyperspectral Techniques
Eric Anderson – U.S. Geological Survey
James Austin – CSIRO Mineral Resources

Ore Deposits associated with Magmatic Systems:

- **Alkaline Magmatism and Carbonatites**
  Nolwenn Coint – Geological Survey of Norway
  Sophie Decrée – Geological Survey of Belgium
  Danielle Klinger – U.S. Geological Survey
- **Magmatic Ni-Cu-PGE and Fe-Ti-P Deposits**
  Chris Jenkens – U.S. Geological Survey
  Chusi Li – Indiana University
- **Porphyry/Epithermal Deposits**
  Gülcan Bozkaya – Pumukkale University
  Paola Chadwick – Eldorado Gold Corporation
  Tony Christie – GNS Science
  David Cooke – CODES, University of Tasmania
  Doug Kirwin – Consultant
  Zhiming Yang – Chinese Academy of Geological Sciences
- **Volcanogenic Massive Sulfides: In Remembrance of Jim Franklin**
  Mark Hannington – University of Ottawa
  Jorge Relvas – University of Lisbon
- **Tin-Tungsten and Rare Metal Deposits**
  Bernd Lehmann – Technical University Clausthal
  Jingwen Mao – Chinese Academy of Geological Sciences

Ore deposits associated with magmatic systems: Porphyry/epithermal deposits

Efemçukuru Intermediate Sulfidation Epithermal Gold Deposit, Türkiye: Evidence for a Magmatic-Hydrothermal Origin 348
Tim Baker, Caglar Acimaz, Omer Ilgin, Kaleb Boucher, Peter Lewis, David Rhys, Alfredo Camacho, and David Selby

A Multi-scale Study of Gold Deportment in the Goldstorm Porphyry Cu-Au Deposit, Northwest British Columbia, Canada 352
Jessica Baldwin, Kate Rubingh, Nikola Denisova Shaun Barker

Ages and trace element fertility of porphyry-related mineralization in the Philipsburg polymetallic district, Montana, with a comparison to Butte. 356
Celine M.E. Beaucamp, Christopher H. Gammons, Jay M. Thompson, Holly J. Stein

The Huntoon Copper Project, Mineral County, Nevada – Unravelling a dismembered magmatic-hydrothermal system 360
James H.S. Blight and Lawrence C. Carter

Ferropyrosmalite-bearing fluid inclusions in the porphyry Cu-Mo deposits: A record of regional metasomatism in NW Turkiye 364
Gülcan Bozkaya, Ömer Bozkaya, Alfons van den Kerkhof, Graciela Sosa, David A. Banks

Distribution of mineralization in different lithologies of the Ochtiná – Rochovce W-Mo porphyry deposit (Western Carphatians, Slovakia). 367
Jana Brčeková, Peter Koděra, Rastislav Vojtko, Diego Delgado Yanez, František Bakos

The Porphyry to Epithermal Transition: A 2025 Explorer's Perspective Toward Improving Discovery Rates 371
Vertrees 'Mac' Canby

Multi-million-year magmatic maturation preceding the formation of the supergiant Llurimagua porphyry Cu-Mo deposit (Western Cordillera, Ecuador) 373
Hugo Carrasco, Massimo Chiaradia, Alexey Ulianov, Maria Ovtcharova, Carlos Urrutia, Sergio Cubelli, Carolina Rodríguez, Angelo Aguilar, Juan Jaramillo, Hugo Narvaez, Yorki Patiño, Sergio Pichott

Reassessing the Schultze Granite, Arizona, USA: A New Temporal Framework for the Globe-Miami Magmatic- Hydrothermal System 377
Lawrence C. Carter, Robert G. Lee, Adam Gorecki, Dan Condon, David Selby, Holly J. Stein, Robert Creaser, Simon Chenery, Matthew Power, Benjamin Buse, Ester M. Jolis

Chronological framework for the magmatic- hydrothermal transition and mineralisation in the Yerington porphyry system, Nevada: A re-evaluation 381
Lawrence C. Carter, Simon R. Tapster, David Selby, Ben J. Williamson, Gavyn K. Rollinson

Exploring the apparent dominance of low Ti zircon in porphyry Cu deposits and its implications on the origin of zircon: perspective matters 385
Maria Paula Castellanos-Melendez, Michael Schirra, Marcel Guillong and Olivier Bachmann

Alunite characterization of high sulfidation epithermal deposits in the Vicuña District, Argentina-Chile 389
Leticia González Castellote, Elizabeth Holley

Taca Taca Bajo: An Early Halo-Type Porphyry Copper Deposit in Salta, Argentina. 393
Federico Cernuschi, Santiago Gigola, Raymond Rivera, Guillermo Almandoz, David Arribasplata, Tim Ireland, Paula Gonnet, Ezequiel Iglesias, Rocío Gil, Juan Burlando, Steve Andersson

Skarn geometry and sectors, and their applications in exploration 397
Zhaoshan Chang Qihai Shu

Skarn-Porphyry Transition: Understanding and Applications in Exploration 401
Zhaoshan Chang Shiqiang Huang James Cannell

Magmatic Input in the Formation of Epithermal Au-Ag Deposits of the Hauraki Goldfield, New Zealand 405
Anthony B Christie, Mark P Simpson, Robert L Brathwaite

Porphyry Cu-Au Related Hydrothermal Alteration in the Radersburg District, Elkhorn Mountains, Montana 409
Joseph J. Clevenger, John H. Dilles, Kyle Eastman, Eric D. Anderson

Relationships of lithocaps to porphyry and epithermal deposits – an example from the Baguio district, Philippines 413
David R. Cooke, Lejun Zhang, Zhaoshan Chang, Noel C. White, Pete Hollings, Michael Baker, and Cari Deyell

Trace and critical elements in UV-fluorescent and non- fluorescent sphalerite from the Butte porphyry-lode deposit, Montana, USA....415
Kyle A. Eastman, Christopher H. Gammons, Celine Beaucamp, Jay M. Thompson, Heather A. Lowers

The epithermal-skarn transition at the La Colorada deposit, Zacatecas, Mexico....419
Joshua Ebner, Zhaoshan Chang, Pedro Francisco, Dante Juarez, Patricio Perez, Chris Emerson, Shiqiang Huang, Sidney Hemming, Richard Wendlandt

Porphyry ore-deposit potential of northeast Australia – New insights from early-Paleozoic tectonic models 423
Alexander Edgar, Ioan Sanislav, Paul Dirks and Carl Spandler

Mineralogy, Paragenesis, and Geochemistry of the Zgounder Ag-Hg Deposit (Central Anti-Atlas, Morocco): Insights into Ore Genesis....427
Atiq El majid, Belkacim Said, Anne-Sylvie André-Mayer, Abdelhakim El bahat, Lahcen Maasou, Abdelhay Ben-Tami

Skarn Zoning Patterns of the Large Zn-Pb-Ag La Colorada Deposit, Chalchihuites District, Zacate- cas, Mexico....431
Pedro Francisco, Zhaoshan Chang, Chris Emerson, Dante Juarez, Patricio Perez

Role of Magmas in Forming a Large Skarn Sys- tem: A case study from La Colorada Deposit (Za- catecas, Mexico)....435
Pedro Francisco, Zhaoshan Chang, Shiqiang Huang, Chris Emerson, Dante Juarez, Patricio Pe- rez, Robert Creaser

Geology, Mineral Alteration and Mineralization of the Santa Cecilia Porphyry Au-Cu Deposit, Maricunga Belt, Northern Chile....439
José Franco, Luciano Bocanegra, Piotr Paleczek, Antonio Arribas

Exploring the role of volcanic activity in porphyry copper systems in Yerington, NV....443
Anna Ellen Freudenstein, Dawid Szymanowski, Lorenzo Tavazzani, John Dilles, Cyril Chelle-Michou

Tracing fluid evolution during batholith and deposit formation: In-situ and bulk rock Mo isotopes from the Questa porphyry Mo deposit, New Mexico, USA....447
Sean P. Gaynor, Nicolas D. Greber, Qasid Ahmad, Pia Künzi, Ingo Horn, Stefan Weyer

Te and Au mobility at the porphyry-epithermal transition: Insights from experiments and numerical simulations....451
Nicole C. Hurtig, Jonathan R. Adams, Louvel Marion, Aneta Slodczyk, Alexander P. Gysi, Artas A. Migdisov

The epithermal deposits of Chatkal-Kurama (Uzbekistan): micro-nanomineralogy of gold, silver, and associated elements....455
Rustam Khalmatov, Anna Gioncada, Danis I. Filimon

Geochemical and C-O signatures in carbonates around the Basin porphyry, Utah, USA....459
Michael J. Kirschbaum, Zhaoshan Chang Jeff Nicholes, Adam Pacey

Genesis of stibnite mineralisation in epithermal deposits based on coupled Sb and S isotopic composition of stibnite....463
Peter Koděra, Ryan Mathur, Degao Zhai, Rastislav Milovský, Pavel Bačo, Juraj Majzlan

Understanding Overlapping Mineralizing Systems of the Ruby Hill Project, Eureka, NV....467
Alyssa Lindsey, Simon M. Jowitt

Comparing magmatism and hydrothermal alteration using magnetic modelling and stable isotopes at the Clementine porphyry copper prospect, Montana, USA....471
Benjamin P. Magnin, Julia A. McIntosh, George H. Brimhall

Effects of hydrothermal alteration on K-feldspar of the syenite-hosted Quemaldero porphyry Cu prospect in Cordon, Isabela, Philippines....475
Pearlyn Manalo, Akira Yaginuma, Jillian Aira Gabo-Ratio, Akira Imai, Kalin Kouzmanov, Ryohei Takahashi, Hinako Sato, Andrea Agangi, Graciano Yumul Jr.

Skarn-Hosted Cu Mineralization at the Thompson Knolls Discovery, Utah, USA....479
Chad Mann, Sergei Diakov, Quinton Hennigh, Zhaoshan Chang, Shiqiang Huang, Mathias Burisch

Distribution of indium and tellurium in the HS to IS Pefka epithermal deposit: Insights from LA-ICP-MS analyses of sulfides and sulfosalts....483
M. Melfou, P. Voudouris, R. Klemd, M. Keith, V. Melfos, A. Tarantola, L. Papadopoulou, N. Kantiranis

Magmatic evolution and related Cu-Mo(-W) porphyry ore mineralization in the light of isotopic geochronology and geochemistry – a case study from Variscan orogenic belt in Poland....487
Stanislaw Z. Mikulski, Holly J. Stein, Ian S. Williams, Marek Markowiak, Ewa Krzemińska

Geology, alteration and mineralization of the La Virgen high-sulfidation epithermal-porphyry district, Peru ..491
Raul Montesinos, Zhaoshan Chang, Juan Carlos Castelli, Shiqiang Huang, Willis Hames, Robert A. Creaser

Role of Oligocene Volcanism in the geological setting of Ag-Au-Pb-Zn-Cu mineralization at the Plomosas District, San Marcial Area, Western Sierra Madre Occidental -Sinaloa Mexico.....495
Paula Montoya-Lopera, Gilles Levresse, Marcio Fonseca, Luis Coto, Marlen Salgado, Javier Villegas, Miguel Díaz, Daniel Schrader

Skarn-related epithermal Pb-Zn mineralization: a new model for the Laki ore field (Central Rhodope, Bulgaria) 499
Lison Moynier, Yannick Branquet, Nathan Cogné, Pierre Gautier, Boris Ivanov, Ianko Gerdjikov

Trace elements in sulfides (pyrite, chalcopyrite, molybdenite) from the porphyry Mo-Cu-W Myszków deposit (Poland): petrogenetic significance, prospecting application, and importance for the raw materials challenges 503
Beata Naglik, Magdalena Dumańska-Słowik, Tomasz Toboła, Ryszard Habryn, Artur Sosnal

Fluid inclusion data provide new insights into the origin and evolution of the Epithermal Ag-Au mineralization at Galim-Legalgorou, Cameroon volcanic line (CVL)_Edited 507
Terence Cho Ngang, Thomas Wagner, Cheo Emmanuel Suh

Lithology, hydrothermal alteration and mineralization characteristics of the Apollo Porphyry Breccia Complex, Middle Cauca Belt, Marmato, Caldas, Colombia.....511
Jonathan Orozco-Rios, David Londoño Vanegas, Richard M. Tosdal, David Reading, Carlos D. Rios, Oscar J. Pinilla

Mineralogy, Galena Pb isotopes and Nd isotopes of the associated dikes from Ag-Hg Imiter deposit, Anti-Atlas, Morocco: implications for metal sources 515
Mehdi Ousbih, Brian Cousens, Askkour Fatiha, Yves Geraud, Alexiane Favier, Hafida El Bilali, Mohamed Ezzghoudy, Abdelaziz Gaouzi, Oubaassine Hassane, Richard Ernst, Moha Ikenne

Aolunhua: A porphyry Mo deposit associated with adakite-like magmas in an intra-continental extensional setting, northeastern China 519
Hegen Ouyang

A porphyry ore deposit in the making: unique insights into magmatic processes leading to ore fertility through the Taapaca volcano 523
Iván Mateo Espinel Pachón, Zoltan Zajacz, Cristóbal González Rodríguez, Michael Schirra, Alexandra Tsay and Mara Miranda

Copper Creek, Arizona: Laramide, Early Halo Style Porphyry, Cupola and Breccia Hosted Mineralization.....527
Dante Padilla, Benedek Gal, Matias Sanchez, Thomas Bissig, Paul Harbidge

Ore deposits and prospects in the Bolnisi mining district: general overview and future exploration prospectivity, Lesser Caucasus, Georgia 531
Nino Popkhadze, Shota Tagviashvili, Malkhaz Natsvlishvili, Joni Shubitidze, Giorgi Ugrekhelidze, Badri Gogia, Şafak Utku Sönmez, Robert Moritz

New lithological approach for the 3D geological modeling of the Upper Cretaceous Sakdrisi gold copper epithermal deposit, Bolnisi District, Georgia.....535
Nino Popkhadze, Badri Gogia, Shota Tagviashvili, Giorgi Ugrekhelidze, Malkhaz Natsvlishvili, Joni Shubitidze, Safak Somenz, Robert Moritz

Camp Creek Copper-Molybdenum-(Gold) Porphyry Alteration-Mineralogy and Intrusive Classification: Exploring for Blind Copper Mineralization in Northern British Columbia, Canada.....539
Maxwell L. Porter, Shaun L. Barker, Farhad Bouzari, Maria A. Rodriguez-Mustafa, Robert G. Lee, K B. Riedell

Magmatic fluids in the Chuquicamata porphyry copper deposit, revealed by fluid inclusions analyses 543
Isaac Rodríguez, Ivan Farías, Kalin Kouzmanov, Alexandra Tsay, Zoltan Zajacz and Eduardo Campos

Aranzazu Skarn: Zoning Patterns and Geological Controls.....547
Oscar Solis, Zhaoshan Chang

Episodic Epithermal Ore Formation During Late Cretaceous Rifting and Felsic Magmatism in the Cu-Au Bolnisi Mining District, SW Georgia.....551
Şafak Utku Sönmez, Robert Moritz, Nino Popkhadze, Alexey Ulianov, Malkhaz Natsvlishvili

Revisiting the classic Tonopah Ag-Au district, Nevada 555
Cristy Stoian, Thomas Monecke, William Howald, Christopher Leslie, Peter Vikre, Mathias Burisch

Igneous Amphibole and Apatite from the Grasberg Porphyry Cu-Au Deposit, Indonesia: Insights into the magmatic degassing of volatiles.....559
Adi Sulaksono, Shogo Aoki, Takuya Echigo, Yasushi Watanabe, Antonio Arribas

Paleosurfaces and hydrodynamics of a diatreme complex during formation of the Sunnyside porphyry Cu-Mo-Ag system, Arizona 563
Peter G. Vikre, Frederick T. Graybeal, Robert J. Kamilli, and Robert J. Fleck

Structural and Hydrothermal Controls on Mineralization of the Bronson Slope Porphyry Cu-Au-Mo Deposit, British Columbia: Implications for Exploration Targeting. 567
Luis Jacobo Yagual, Marcus Adam, William Threlkeld, Antonio Arribas

Ore deposits associated with magmatic systems: Magmatic Ni-Cu-PGE and Fe-Ti-P deposits

Mafic underplating as a possible source for iron oxide- apatite deposits in Norrbotten, Sweden 571
Tobias E Bauer, Maxim Y Smirnov, Ervin Veress, Thorkild M Rasmussen, Oskar Rydman, Leslie A Logan, Joel BH Andersson, Jochen Kamm, Graham Hill, Fernando Tornos

New Perspectives on Fe-Ti±V Mineralization in the Ślęża- Kunów Area, SW Poland: Findings from the SEMACRET Project.....575
Tomasz Bieńko, Olga Rosowiecka, Stanisław Mikulski, Marcin Olkowicz

Mantle Oxidation and its impact in sulfur speciation: Insights from the Cretaceous Komatiites in Gorgona island.....579
Camilo Andrés Conde Carvajal, Iván Mateo Espinel Pachón, Ana Elena Concha Perdomo

Understanding lower crustal sulfide ore systems: Insights from ultramafic pipes in the Ivrea-Verbano Zone, Italy 583
Shelby Clark, Marek Locmelis, Marilena Moroni, Gianluca Sessa, Mattia Pistone, Sara Elliott

Preliminary LA-ICP-MS trace element data for ilmenite and apatite from Fedorivka, Stremyhorod and Nosachiv Ti-P deposits in the Ukrainian Shield.....587
Krzysztof Foltyn, Władysław Zygo, Adam Piestrzyński, Leonid Shumlyanskyy

Petrogenesis and ore-forming processes of the ultramafic Kylmäkoski Ni-Cu-(Co) magmatic sulfide deposit, SW Finland 591
Patrick Hehn, Karsten Haase, Manuel Keith, Reiner Klemd, Christoph Beier, Harald Strauss, Martin Kutzschbach

The Mineral System Approach Applied to Magmatic Ni- Cu-PGE Sulfide Deposits: Sink Processes Revisited by Recent Experimental Studies 595
Giada IACONO-MARZIANO, Ville J. VIRTANEN, Shenghong YANG

Magmatic and Metasomatic Controls on PGE Mineralization in Chromitites of the Tróia-Pedra Branca Mafic-Ultramafic Complex, Borborema Province, Brazil 599
Adriana V Jacomini, Juliana C Marques, Rafael S Diniz, Thiago B Diniz

Origin of the high Pd/Pt ratio of the J-M Reef Stillwater Complex Montana USA.....603
M. Christopher Jenkins and William D. Smith

Age and Isotopic Data from Mafic/Ultramafic Intrusions in the Karasjok Greenstone Belt, Northern Fennoscandia; Implications for Ni-Cu-PGE Prospectivity.....607
Trond Slagstad, Alf Andre Orvik, Eduardo Mansur, Harald Hansen, Grace Howe, Peter Dodds

The role of alteration to Ni-Cu mineralization at the Great Dyke of Zimbabwe 611
Ema Vokic, Sibila Borojevic Sostaric

Petrogenesis and mineralization potential of the Bradley Peak komatiitic basalts, Wyoming Province.....615
Lisa Zieman, M. Christopher Jenkins, Michael Zientek, Jacob Poletti, Alan D. Rooney

Ore deposits associated with magmatic systems: Alkaline magmatism and carbonatites

The Role of Alkali Bicarbonate-sulfate Brines in the Genesis of Carbonatite REE Resources at the Bear Lodge Alkaline Complex, Wyoming.....619
Allen K. Andersen, Danielle A. Olinger, Mitchell M. Bennett

Stable Isotope Composition and Geochemistry of Calcite and Dolomite in the Mountain Pass carbonatite: A lens into petrogenesis.....623
Erin K. Benson, Kathryn E. Watts, Jay M. Thompson, Heather A. Lowers

The 3D structure and evolution of a REE-rich carbonatite: insights from the Chilwa Alkaline Province.....627
Sam Broom-Fendley, Kathryn Goodenough, Michael Marks, Paul Armitage, and the REEDRILL Science Team.

The rare earth element and fluorite deposit at Monte Muambe, Northwest Mozambique.....631
A. Jamie Church, Sam Broom-Fendley, Cédric Simonet, Frances Wall

Crystallization Age and Evolution of Calcite Melteigite- Calcium Carbonatite: a Study of Zircon Systematics from the Fen Complex, Southern Norway 635
Nolwenn Coint, Trond Slagstad, Magdalena Huyskens, Kristian Drivenes and Ana Carolina Rodrigues Miranda

Niobium-rich Minerals from the Sheep Creek Carbonatite-Related Deposits, Montana, USA 639
Christopher H. Gammons, Heather A. Lowers, Jay M. Thompson

New Perspectives on Hydrothermal Mobilization of Rare Earth Elements (REE) in Carbonatites − Alkaline Systems in New Mexico, USA 643
Alexander Gysi, Nicole Hurtig, Daniel Harlov, Jay M. Thompson, Katharina Pfaff

Fingerprinting magmatic REE deposit sources with zircon petrochronology 647
Ian W. Hillenbrand, Erin K. Benson, Kathryn Watts, and Jay Thompson

Scandium-rich Mineralization at the Crystal Mountain Fluorspar Mine, Montana, USA 651
Natalie Kilanowski-Doroh, Gary Wyss, and Christopher H. Gammons

Zr-U-Th-Phases in Clinohumite-Spinel-Bearing Marbles as Potential Tracers of HFSE-Fertile Granitic Rocks 655
Šárka Kučerová, Martin Kubeš, Milan Novák, Michal Poňavič, Anna Vymazalová, Jaromír Leichmann

Mineralogical and Geochemical Variation of Porphyritic Dikes within the North Stock Gold Prospect, Rattlesnake Hills Alkaline Complex, Central Wyoming, USA 659
Brandi Lawler

Rare Earth Element Redistribution in Ultramafic Lamprophyres of Western Kentucky: Insights from Petrography and Geochemistry 663
Georgina Lukoczki, Kyle Dayton, Zachary Walton, Esteban Gazel

Characterization of REE-bearing Syenites in the Semarule Igneous Complex (SIC), Southeast Botswana .667
Rita Ngwanaotsile, Akira Imai, Kotaro Yonezu, Akane Ito, Zibisani Bagai

Hydrothermal Veining and Fenitization as Vectors for Hydrothermal REE Mobilization in the Lemitar Mountains Carbonatite, New Mexico 671
Willa Obringer, Alexander Gysi, Nicole Hurtig

Distribution and Genesis of REE-Nb-Ta Deposits Associated with Carbonatites and Alkaline Complexes in Canada 675
Anne-Aurélie Sappin, Michel G. Houlé, Wouter Bleeker

The early magmatic history of the Cripple Creek complex, Colorado, USA: Insights from olivine-hosted melt inclusions and implications for ore formation 679
Michael Schirra, Zoltan Zajacz

Hyperspectral Cathodoluminescence of Bastnäsite at the Mountain Pass Mine, USA: Implications for REE Mineralisation and Mining 683
Paul Slezak, Siri L. Simonsen, Chloe L. Tolbert, Travis McLing

Cambro-Ordovician Alkaline Intrusions in Idaho: Examining a Segment of North America's Western Interior Alkaline REE belt. 687
Cody J. Steven, Reed S. Lewis, Liam Knudsen

Fluorite as a vector for hydrothermal REE mineralization in the Gallinas Mountains deposit, New Mexico...691
Aadish Velmani, Alexander Gysi, Nicole Hurtig

Formation of the Mount Weld rare earth deposit, Western Australia: geochronology constraints..... 695
Philip L. Verplanck, Cameron M. Mercer, Jay M. Thompson, Martin Danišík, Ganesh Bhat, and Heather A. Lowers

The Geochemistry of Magnetite from Bayan Obo Fe-REE- Nb Deposit, China: Implications for Ore Genesis 699
Lan Yang, Yang Li, Yan Yu, Xian-Hua Li

Hydrothermal Metasomatism Controlled REE Mineralization at Bayan Obo Revealed by Zircon Petrochronology 703
Yan Yu, Yang Li, Lan Yang, Li-Guang Wu, Xian-Hua Li

Ore deposits associated with magmatic systems: Volcanogenic massive sulfides: in honor of Jim Franklin

---

Multi-scale hydrothermal mobilization of Ca, Al and Cu during serpentinization: new insights from the Ronda Massif (Spain) 707
Bastien Audran, Marc Ulrich, Yannick Branquet, Guillaume Barré, Georges Beaudoin, Philippe Boulvais

The Hambok volcanic-associated massive sulfide deposit, Bisha VMS District, Eritrea: discovery, geology and mineralogy 711
C. Tucker Barrie, Ingrid Kjarsgaard, and Demetrius Pohl

Polymetallic quartz veins at the Hod Maden Cu-Au deposit, Turkey 715
Bader Bilgin, Thomas Monecke, T. James Reynolds

James Franklin and ore deposits in the 1970s 719
Lawrence M. Cathles

Insights on the formation of tin ores in the Neves Corvo Cu-Zn-Pb(-Sn) deposit, from in situ trace element analysis and O-isotopes of cassiterite 721
Marta S. Codeço, Sarah A. Gleeson, Jorge M.R.S. Relvas, Vitor Barrote, Maria R. Scicchitano, Franziska, D.H. Wilke

New geochemical and Sr-Nd data from Lower Cryogenian arc volcanic rocks of Tichibanine Ben- Lagrad Group (Bou-Azzer, Central Anti-Atlas, Morocco): Constraints on petrogenesis and geodynamic context 725
Ali El-masoudy, Abdeslam Toummite, Moha Ikenne, Said Ilmen, Yassine Lmahfoudi, Laurent Sapor, Lhou Maacha, Mohamed Zouhair, Yassine Lmahfoudi, Marieme Jabbour, Stanislav Zverev

The mid-Cretaceous VMS belt in the Peruvian coast. 729
Lluís Fontboté, Massimo Chiaradia, Jorge E. Spangenberg, Irena Peytcheva

Lithogeochemistry of the La Mina VMS deposit in the Macuchi Unit (Western Cordillera, Ecuador): metalogenetic implications 733
Darío Fuentes, Fabián Villares, Luis López, Joaquín A Proenza, Álvaro Perez, Santiago Almagor, Xandé López

Mineralization Processes at Escanaba Trough 737
Amy Gartman, Jaycee Favela, Katlin Adamczyk, John Jamieson, Rob Zierenberg, Isobel Yeo

The volcanic-hosted massive sulfide mineral system in space and in time – a tribute to Jim Franklin 740
David L Huston

Relationship between Fe-Cu and polyelement Co-Ni-Pb- Bi-Sb-As-S mineralization at the Tisová deposit (Bohemian Massif) 744
Jan Kamenský, Jan Pašava, Anna Vymazalová, Irina Andronikova, Petr Rojík

Zircon petrochronology of Paleoproterozoic VMS deposits in the Penokean Orogen, Wisconsin, USA 748
Robert Lodge, Aidan Kwiatkowski, and Evan Weber

Hydrothermal alteration overprinted by contact metamorphism: Balducho VMS prospect, central Peru 752
Emily Mora, Lluís Fontboté, Silvia Rosas Lizárraga, Victor García, Thed Mena, Edgar Pichardo

Geologic setting of the Pueblo Viejo Au-Ag-(Cu-Zn) mining district, Dominican Republic – links to volcanogenic massive sulphide (VMS) mineralization 756
Carl Nelson, Hugo Dominguez, Rene Leonardo A., Jose Polanco, Carlos Carrasco C.

Mineral and geochemical zonation at the Åkulla Au-Te deposit, Skellefte VMS district, Sweden. 760
Paulina Nordfeldt, Iain K. Pitcairn, Scott Halley, Rodney L. Allen and Harold L. Gibson

Definition of Besshi-type VMS deposits based on their geological, geochronological features and tectonic settings 764
Tatsuo Nozaki, Ken Nakayama and Yasuhiro Kato

In-situ sulfur isotope analysis of pyrite in the c. 1.88Ga Rävliden North VMS deposit, Skellefte district, Sweden 768
Jonathan Rincon, Nils F. Jansson, Helen Thomas, Majka C. Kaiser, Mac F. Persson, Heejin Jeon, and Christina Wanhainen

Petrogenesis and VMS Prospectivity of 1.8 Ga Magmatism within the Archean Marshfield Terrane, Penokean Orogen, USA 772
Lyndsie Vickers, Robert Lodge, and Evan Weber

Ore deposits associated with magmatic systems: Tin-tungsten and rare metal deposits

---

Unraveling the genesis of critical minerals: Petrogenetic and hydrothermal controls on cassiterite mineralization in the Mayo-Darlé region, Cameroon 776
Jonas Didero Takodjou Wambo, Sylvestre Ganno, Kumbong Terence Chiandeh, Jean Paul Nzenti, Paul D. Asimow

Ore minerals on the flanks of the Deputatskiy Sn-Ag cluster – Bulatskoye, Jubileyniy and Kaleo Ag-Au-Zn-Pb ore occurrences, Republic of Sakha (Yakutia), Russia 780
Polina N. Leibham, Nikolay V. Bondarenko, Valentina N. Gerasimova, Mikhail V. Bereznev

Precipitation mechanisms of wolframite and scheelite from hydrothermal fluids 784
Xiang-Chong Liu

Magmatic Hydrothermal vs. Metamorphic Hydrothermal Fluids: Scheelite Trace Element Signatures 788
Kairan Liu, Zhaoshan Chang, Shiqiang Huang

Timing of meteoric-water incursion controls tin mineralization scale 792
Peng Liu, Bernd Lehmann, Francois Holtz, Stefan Weyer, Nigel J. Cook, Maria Rosa Scicchitano, Christopher L. Kirkland, Xiaoyan Li, Zhian Bao, Zexian Cui, Franziska D.H. Wilke, Honglin Yuan, Jingwen Mao

Metal source evolution of Carboniferous molybdenum- tungsten (Mo-W) mineralization during incremental growth of a granite batholith (Late Variscan Aar Massif, Switzerland) 795
N.J. Saintilan, N.D. Greber, R.A. Creaser, M. Ovtcharova, D. Selby, M. Wiederkehr, U. Schaltegger

Zircon and cassiterite U-Pb dating of the Taucane Project: New horizons for tin exploration in Peru.....799
Pablo Valverde, Lisard Torró, Daniel Alayza, Diego Benites, Sava Markovic, Lorenzo Tavazzani, Dawid Szymanowski, Cyril Chelle-Michou, Matthieu Harlaux, Miroslav Kalinaj

Quantitative Prediction Methods and Applications of Digital Ore Deposit Models.....803
Keyan Xiao

Can Sn^{4+} be transported in hydrothermal fluids?.....807
Shun-Da Yuan, Jia-Xin Wang, Xue-Ni Zhang, Ying Yang, Liu-Lin Xu, Pan-Lao Zhao

Efemçukuru Intermediate Sulfidation Epithermal Gold Deposit, Türkiye: Evidence for a Magmatic-Hydrothermal Origin

Tim Baker[1], Caglar Acimaz[2], Omer Ilgin[2], Kaleb Boucher[3], Peter Lewis[1], David Rhys[4], Alfredo Camacho[5], and David Selby[6]
[1]Eldorado Gold Corporation, 11th Floor, 550 Burrard Street, Vancouver BC Canada
[2]Tüprag Efemçukuru Altın Madeni, 35470 Menderes/İzmir, Türkiye
[3]Mineral Deposit Research Unit, University of British Columbia, BC, Canada; now Teck Resources, Vancouver, Canada
[4]Panterra Geoservices Inc., Vancouver, BC, Canada
[5]Clayton H. Riddell Faculty of Environment, Earth, and Resources, University of Manitoba, Winnipeg, Manitoba, Canada
[6]Department of Earth Sciences, University of Durham, Durham, UK

Abstract. Efemçukuru is one of the most significant intermediate sulfidation (IS) epithermal gold deposits in the West Tethyan orogen. The deposit is in the Miocene belt of Western Anatolia, Türkiye, and has produced over 1.2 Moz of gold since mining started in 2011. Key IS characteristics include manganese-rich vein assemblages (rhodonite and rhodochrosite) and base metal-rich ore. Detailed mapping has delineated over 40 km of epithermal veins that are hosted within a dominantly normal extensional fault-vein network. The fault architecture also controls the distribution of rhyolite dykes and hornfels (calc-silicate alteration) that at depth hosts molybdenite-bearing quartz-feldspar-amphibole veins. Detailed geochronology supports cross-cutting field relationships with early rhyolite dykes (13.17±0.25 Ma; U-Pb zircon) and calc-silicate alteration (12.97±0.74 Ma; Re-Os molybdenite) pre-dating the epithermal vein event (12.3±0.1 Ma; Ar-Ar, adularia). Carbon and oxygen isotope data support a mixed meteoric-magmatic fluid source with evidence of boiling and cooling of magmatic fluids in zones of the highest gold-grades. The spatial and temporal relationships and fluid characteristics indicate Efemçukuru formed from an evolving magmatic-hydrothermal system.

1 Introduction

The Efemçukuru gold mine in Western Anatolia, Türkiye, has produced over 1.2 Moz of gold since the underground operation opened in 2011, and has a remaining measured and indicated resource of 5.4 Mt @ 6.6 g/t for 1.2 Moz. Consequently, the deposit is one of the most significant intermediate sulfidation (IS) epithermal systems in the West Tethyan belt (Baker, 2019). Here we describe the geology of the deposit which includes the compilation of over a decade of detailed geological mapping to determine the epithermal vein distribution, in addition to complementary geochronological and stable isotope studies in order to establish the temporal and spatial evolution of the system. The combined field relationships and isotopic data support a magmatic-hydrothermal origin for the epithermal deposit.

2 Deposit Geology

Western Anatolia, Türkiye, is host to several major Miocene porphyry and epithermal gold systems including the Kişladağ gold-only porphyry deposit, Ovaçik low sulfidation epithermal gold deposit and Efemçukuru (Baker, 2019). The gold-rich region is part of the Western Tethyan orogen that is defined by a series of Cretaceous through Cenozoic magmatic belts with a strike length of over 3,500 km from Slovakia to Iran which continues to the east through the Central and Eastern Tethyan orogen (Richards, 2014). The magmatic belts in Türkiye broadly young from north to south with Cretaceous to Paleogene subduction-related arc magmatism in the Pontides transitioning to post-collision, extension-related Oligocene-Miocene magmatism in central and western Anatolia formed during slab-roll back (Jolivet et al., 2015).

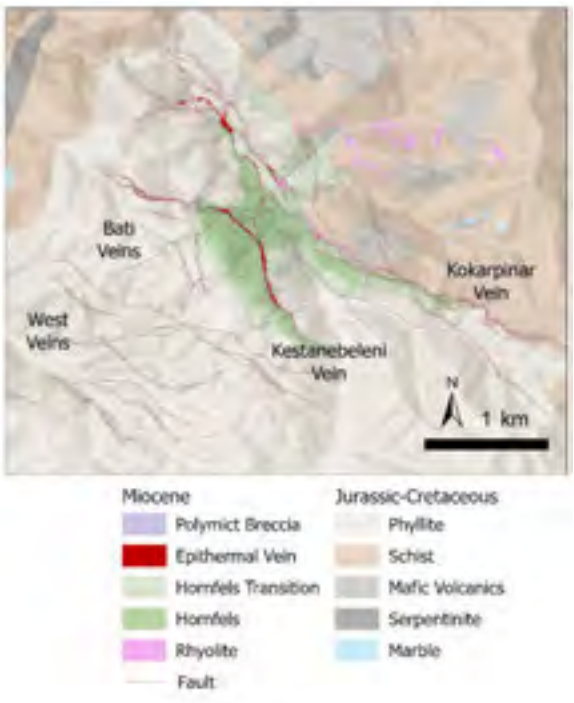


Figure 1. Geological map of the Efemçukuru deposit showing the distribution of epithermal veins, hornfels (calc-silicate alteration) and rhyolite dykes hosted by the Bornovo Flysch.

The Efemçukuru deposit is hosted in the center of a NE-SW trending horst known as the Seferihisar Horst, which regionally exposes Upper Jurassic to Lower Cretaceous basement rocks of the Bornova Flysch. The flysch comprises lower greenschist

facies schist, mafic volcanics and serpentinite, and interbedded marble (Okay and Altiner, 2007). The metamorphic rocks are host to an extensive (~ 12 km^2) fault network that controls the distribution of rhyolite dykes, hornfels (calc-silicate alteration) and epithermal veins (Fig. 1).

Detailed mapping has delineated over 40 km of epithermal veins including the two main NW-SE striking fault-vein systems, Kestanebeleni and Kokarpinar. The thickest and economically most significant areas of vein development occur in the Kestanebeleni vein system on NNW-trending, steeply dipping segments. In the footwall to the Kestanebeleni vein is the similarly oriented Bati veins and further to the southwest is the West vein system with a dominantly NW-SE strike. East-side down displacement of hornfels and schist contacts across the Kestanebeleni and Kokarpinar veins combined with internal vein textures suggests that the veins formed during late movement on the host fault systems. Lithological displacement, the sigmoidal shape to the vein system, and the geometry of extensional veins and splays suggest the vein systems formed during ENE-WSW extension that controlled oblique normal > dextral (right lateral) displacement on EW- to WNW trending vein segments, and dip slip with greatest dilatancy on NNW trending segments.

Epithermal veins cut rhyolite dikes and the early calc-silicate alteration (Stage I). The latter is characterized by veins and breccia, that locally cements cataclasite and consists of a mineral assemblage of quartz-chlorite-epidote-actinolite. At depth (> 600 m) this stage is characterized by quartz, K-feldspar, hornblende and biotite alteration and veins with molybdenite. Primary, coeval, fluid inclusions in these veins comprise brine (multi-solid halite-bearing inclusions) and vapor-rich inclusions.

The main epithermal stage commenced with vein and breccia fill of fine-grained quartz and rhodonite (pyroxmangite), rhodochrosite, minor pyrite, and rare adularia (stages II and III). The main quartz-sulfide stages (IV and V) consist of veins of quartz and minor rhodonite, axinite, rhodochrosite, and calcite that are disseminated and banded with fine-grained pyrite, galena, and sphalerite. Rhodonite and rhodochrosite are less common in this stage and quartz is the dominant gangue mineral. The last vein stage (VI) includes thin veinlets of quartz, calcite, and rare rhodochrosite.

The Kestanebelini vein has well defined ore shoots named South (SOS), Middle (MOS) and North (NOS) ore shoots which exhibit a mineralogical zonation. The vein is dominated by rhodonite and rhodochrosite in the upper portions of the SOS, whereas the sulfide content of the MOS and NOS, particularly at depth, is much higher. The increased sulfide content coincides with an increase in Pb and Zn in the MOS and NOS. The Ag/Au ratio is typically higher at depth and on the periphery of the veins.

3 Geochronology

The temporal evolution of the Efemçukuru system has been constrained via age dating of zircon in the pre-mineral rhyolite dykes, molybdenite hosted within the calc-silicate veins and alteration, and adularia in the epithermal veins (Fig. 2).

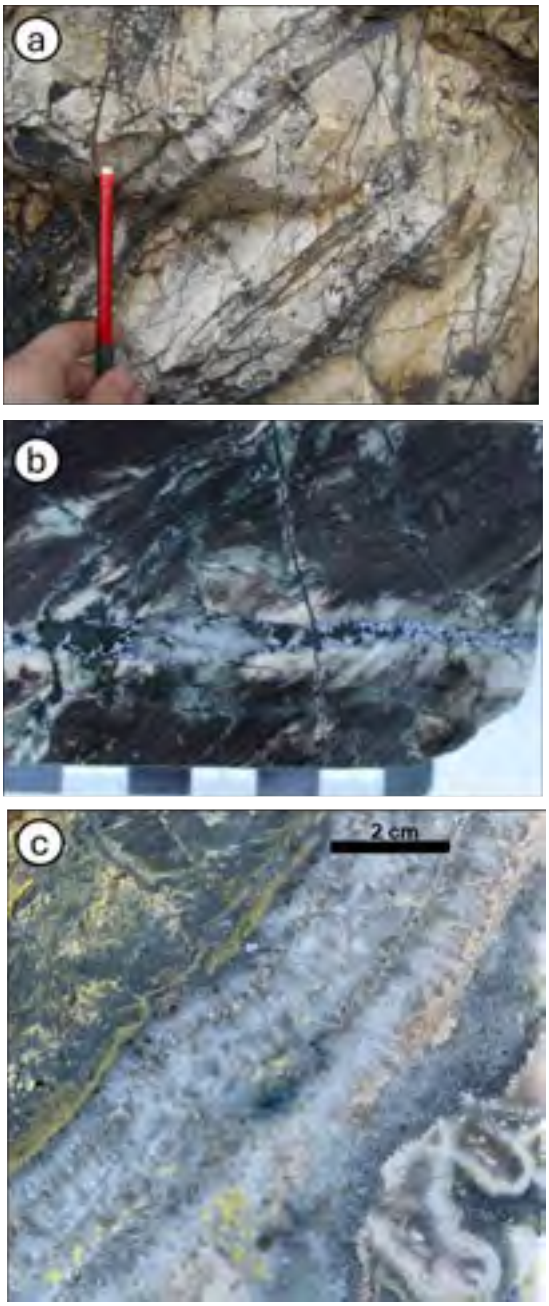


Figure 2. (a) Pre-mineral rhyolite (13.17 ± 0.25 Ma U-Pb zircon) cut by epithermal veins; (b) Calc-silicate hosted quartz-amphibole-albite-molybdenite vein (12.97 ± 0.74 Ma, Re-Os molybdenite; KV591-1028.3m); (c) Adularia (stained yellow) in Bati epithermal vein (12.3 ± 0.1 Ma, Ar-Ar; BTD-024 274.8m, 6.5 g/t Au).

Zircon geochronology was carried at the Pacific Center for Isotope and Geochemical Research (PCIGR) at the University of British Columbia, Canada, using laser ablation inductively coupled plasma mass spectrometry (see Lee et al., 2021 for

methodology). Molybdenite was dated following the Re-Os methodology described by Selby and Creaser (2004), at the University of Durham, UK, and adularia dated using the Ar-Ar technique at the University of Manitoba, Canada. Age dates are consistent with cross-cutting field relationships with pre-mineral rhyolite dated at 13.17±0.25 Ma, molybdenite in calc-silicate alteration dated at 12.97±0.74 Ma, and gold-bearing epithermal vein hosted adularia dated at 12.3±0.1 Ma.

4 Stable Isotopes

Carbonate bearing vein and host rock samples were analyzed for ^{13}C and ^{18}O isotopes at the University of British Columbia utilizing the Mineral Deposit Research Unit's Mineral Isotope Analyzer and following the methodology of Barker et al. (2011). Ten samples were selected from host calcareous flysch (n=2), phyllite (n=6), and marble (n=2) rocks, and 196 vein samples from all stages of the paragenesis. Samples from the host rocks range in $\delta^{13}C_{VPDB}$ from -0.47 to +2.20‰ and in $\delta^{18}O_{VSMOW}$ from +8.28 to +21.33‰. Vein calcite comprised 51 of the samples, while rhodochrosite accounted for the remaining 145 samples, however, there is no obvious isotopic difference between rhodochrosite and calcite samples. Values of $\delta^{13}C_{VPDB}$ range from -4.39 to +2.09‰ in Stage I veins (n=6); -9.51 to -2.71‰ in Stage II veins (n=4); -13.03 to +0.71‰ in Stage III veins (n=62); -11.76 to +2.15‰ in Stage IV veins (n=75); -10.46 to +1.80‰ in Stage V veins (n=27); and -14.19 to +0.91‰ in Stage VI veins (n=22). Oxygen isotope composition ($\delta^{18}O_{VSMOW}$) ranges from +3.78 to +15.93‰ in Stage I veins; +12.53 to +18.59‰ in Stage II veins; +1.03 to +26.20‰ in Stage III veins; +2.45 to +25.39‰ in Stage IV veins; +3.09 to +22.59‰ in Stage V veins; and +1.93 to +22.64‰ in Stage VI veins.

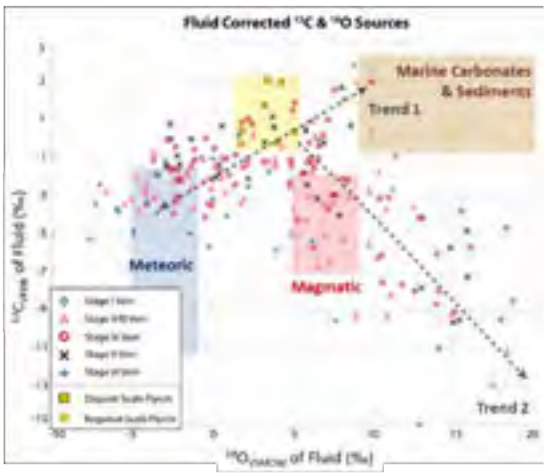


Figure 3. Plot of $\delta 13_{CPDB}$ versus $\delta 18O_{SMOW}$ (fluid corrected values) for carbonate-bearing vein and wall rock samples.

To assess the effects of fluid-rock or fluid-fluid interaction on the carbon and oxygen isotopic variation on vein carbonates, all carbonate samples were calculated to a fluid composition using carbonate fractionation factors (see Boucher, 2016 for details) and temperatures constrained from fluid inclusions in quartz and sphalerite (185 - 328°C, Oyman et al., 2003).

Two distinct trends are recognized which are likely related to distinct fluid processes (Fig. 3). Samples forming Trend 1 are best explained as a result of mixing of paleo-meteoric waters from Miocene Anatolia (blue box) and typical Tethyan Marine carbonates and sedimentary rocks (brown box). Flysch within 1 km of epithermal veins show a depleted isotope signature (yellow box), suggesting they were isotopically equilibrated with the hydrothermal fluids. Trend 2 is best explained by degassing (boiling) and cooling of a fluid with initial isotope conditions consistent with magmatic fluids (pink box). Samples which fall on Trend 2 correspond to samples with the highest gold grades in both the Kestanebelini and Kokarpınar veins suggesting boiling was a key process in high grade gold precipitation. This is consistent with vein textures indicative of boiling.

4 Conclusions

The Efemçukuru gold deposit can be classified as an intermediate sulfidation epithermal vein deposit due to its high-base metal content and the Mn-rich nature of the vein mineralogy, analogous to intermediate-sulfidation epithermal veins of Mexico (Simmons et al., 2005) and southern Peru (Chavet et al., 2006). The dominantly NE-dipping Efemçukuru veins formed during the latest stages of displacement within faults that had east side down, normal > dextral shear sense, with greatest dilation along NNW-trending, dilational segments. The faults also controlled the distribution of pre-mineral rhyolite dikes and calc-silicate alteration. At depth the latter alteration manifest as quartz, alkali feldspar, hornblende and biotite alteration and veins with molybdenite. The presence of coeval high salinity brine and vapor-rich inclusions suggest a deep magmatic source to the high temperature calc-silicate event. A magmatic contribution is further supported by the results of detailed carbon and oxygen isotope analysis of vein carbonates. The isotope data support mixing between meteoric and magmatic fluids. Furthermore fluid process modelling suggest boiling and cooling of magmatic fluids was critical in the generation of the high grade gold shoots within the epithermal veins.

Acknowledgements

Eldorado Gold Corp. are thanked for their permission to publish. Jeff Hamilton is thanked for his work on the figures.

References

Baker T (2019) Gold ± copper endowment and deposit diversity in the West Tethyan magmatic belt, southeast Europe: Implications for exploration. Econ Geol 114: 1237–1250.

Barker SLL, Dipple GM, Dong F, Baer DS (2011) Use of laser spectroscopy to measure the 13C/12C and 18O/16O compositions of carbonate mienrals. Analytical Chem 83:2220-2226.

Boucher KS (2016) The structural and fluid evolution of the Efemçukuru epithermal gold deposit, western Turkey. M.Sc. thesis, Vancouver, University of British Columbia, 190 p.

Chauvet A, Bailly L, Andre AS, Monie P, Cassard D, Tajada FL, Vargas JR, Tuduri J (2006) Internal vein texture and evolution of the epithermal Shila-Paula district, southern Peru. Min Deposita 41: 387-410.

Drayson D, Camacho A, Sanborn-Barrie M, Regis D, Larson K, Osinchuk A, (2022) Deformation history and tectonic significance of the Sanagak Lake shear zone, Boothia Peninsula, Nunavut. Can J of Earth Sci, 59:1031-1052.

Jolivet L, Menant A, Sternai P, Rabillard A, Arbaret L, Augier R, Laurent V, Beaudoin A, Grasemann B, Huet B (2015) The geological signature of a slab tear below the Aegean. Tectonophysics 659: 166-182.

Lee RG, Byrne K, D'Angelo M, Hart CJR, Hollings P, Gleeson SA, Alfaro M, (2021) Using zircon trace element composition to assess porphyry copper potential of the Guichon Creek batholith and Highland Valley Copper deposit, south-central British Columbia. Min Deposita 56: 215–238.

Okay AI, Altiner D (2007) A condensed Mesozoic succession North of Lzmir: A fragment of the Anatolide-Tauride Platform in the Bornova Flysch Zone. Turk J of Earth Sci 16: 257-279.

Oyman T, Minareci F, Piskin Ö (2003) Efemçukuru B-rich epithermal gold deposit (Izmir, Turkey). Ore Geol Rev 23: 35–53.

Richards J (2014) Tectonic, magmatic, and metallogenic evolution of the Tethyan orogen: From subduction to collision. Ore Geol Rev 70: 323–345.

Selby D, Creaser RA (2004) Macroscale NTIMS and microscale LA-MC-ICP-MS Re-Os isotopic analysis of molybdenite: Testing spatial restrictions for reliable Re-Os age determinations, and implications for the decoupling of Re and Os within molybdenite. Geochim et Cosmoch Acta 68: 3897–3908.

Simmons SF, White NC, John DA (2005) Geological characteristics of epithermal precious and base metal deposits. Econ Geol 100th Anniversary Volume: 485–522.

A Multi-scale Study of Gold Deportment in the Goldstorm Porphyry Cu-Au Deposit, Northwest British Columbia, Canada

Jessica Baldwin[1], Kate Rubingh[1], Nikola Denisova[1] Shaun Barker[1]
[1]Mineral Deposit Research Unit (MDRU), Department of Earth, Ocean and Atmospheric Sciences, University of British Columbia, Vancouver, Canada

Abstract. A workflow to understand the hydrothermal alteration and associated gold deportment was applied to the Goldstorm porphyry copper gold deposit, a recently discovered system in northwest British Columbia's Golden Triangle. The deposit consists of a gold and copper mineralized diorite intrusion surrounded by gold and silver mineralization hosted in volcaniclastic rocks. The highest-grade gold mineralization is associated with quartz, quart-carbonate-pyrite, and quartz-chalcopyrite-pyrite veins. Vein density logs of these vein types were calculated over assayed interval lengths. A deposit wide alteration model was developed using shortwave infra-red and 4-acid geochemical data. Gold mineralization was found predominantly in three alteration-lithology domains; i) potassic altered diorite, ii) potassic altered volcaniclastic rocks, and iii) quartz-sericite-pyrite altered volcaniclastic rocks. The results of this modelling were used to group data for input into principal component analysis to determine mineralogical associations with gold. The outcomes of this statistical analysis were tested by petrographic and SEM studies. The study shows that gold deportment varies in each domain, reflecting the evolution from neutral, high temperature potassic alteration, in which gold is found with chalcopyrite, to a lower temperature potassic alteration, where gold is found in with pyrite; overprinted by a later epithermal event.

1 Introduction

Northwest British Columbia's 'Golden Triangle' is a well-endowed mineral region in the Stikine arc terrane. It hosts many economic mineral deposits ranging from volcanic massive sulfide (VMS) to porphyry – epithermal in nature. Much of this mineralization is associated with Late Triassic to Middle Jurassic period volcanism (Alldrick, 2004).

The Goldstorm porphyry Cu-Au deposit is located at the northern end of the Sulphurets fault trend, which is host to the Seabridge Gold Kerr-Sulphurets-Mitchell porphyry copper deposits (KSM) (Campbell 2016). A tabular, Lower Jurassic (U/Pb crystallization age 193.58±0.83Ma, CODES 2023 [unpublished]) porphyritic diorite is emplaced into Jurassic intermediate volcaniclastic rocks of the Lower Hazelton Group, Betty Creek Formation. The deposit is bound by two major thrust faults, which truncate mineralization.

The 2024 Mineral Resource reported a 21.7Moz Au @ 0.92g/t, 2.87Blb Cu @ 0.18%, and 128.7Moz Ag @ 5.48g/t (Tudor Gold 2024). Typical for gold rich porphyry deposits, Goldstorm is deficient in molybdenum (Sillitoe 2000). The majority of the copper is present as chalcopyrite within the diorite intrusion. The gold is hosted within the diorite intrusion and in the surrounding volcaniclastic host rocks. Gold is typically very fine grained (<40 µm) and is associated with vein hosted chalcopyrite, bornite, and pyrite, and as free gold within quartz and calcite veins.

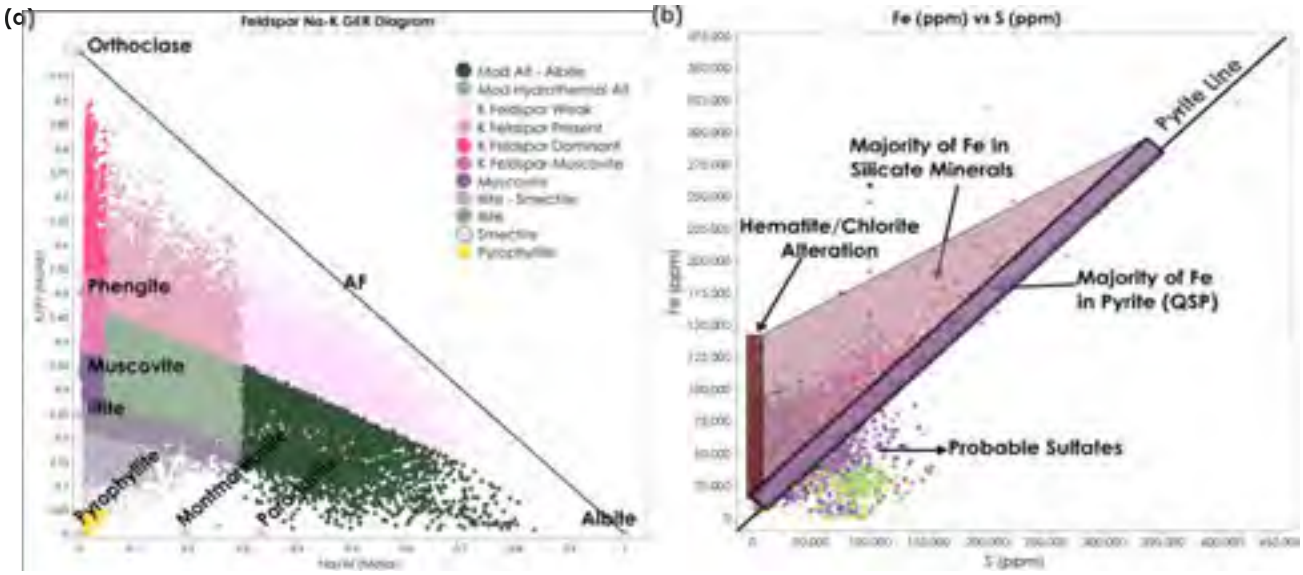


Figure 1 4-acid geochemical plots used in the generation of the alteration model. (a) data classified by observations from Na/Al and K/Al feldspar control diagram to determine dominant mineral assemblage (b) Fe vs S diagram to establish dominance of sulfide vs sulfate vs mafic minerals

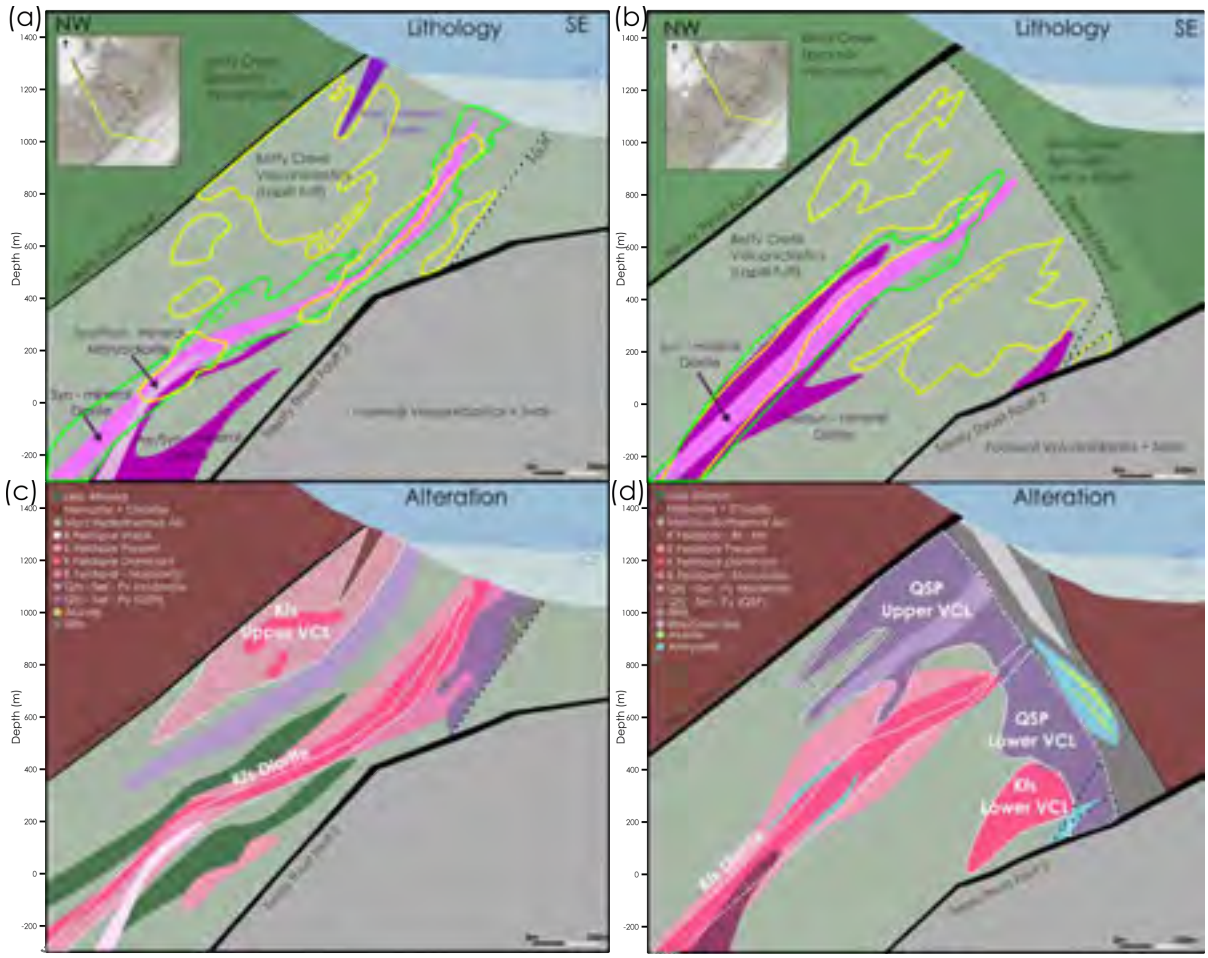


Figure 2 Cross sections looking NE through Goldstorm deposit. (a) South section: lithology model with Cu and Au cutoffs highlighted; (b) South section: alteration model; (c) North section: lithology model with Cu and Au cutoffs; (d) North section: alteration. VCL (volcaniclastic rocks), Kfs (potassic alteration), QSP (quartz-sericite-pyrite alteration)

The purpose of this study is to develop a deposit wide alteration model using downhole shortwave infra-red (SWIR) and 4-acid geochemical data to assess the variation in mineralogical associations with gold mineralization using Principal Component Analysis (PCA). Reflected and transmitted light petrography, scanning electron microscopy (SEM), and μ-X-ray fluorescence (μXRF) mapping were used to evaluate samples selected from the Goldstorm deposit.

2 Samples and Methods

2.1 Data Collection

Shortwave infra-red data was collected at 5-10m intervals on half-core samples from nine drillholes. Drillholes were selected to capture variations in lithology, alteration, and grade. Half core samples were collected from the same drillholes for further analysis, including whole rock geochemical analysis, thin sections, and geochronology. Tudor Gold Corp. provided 4-acid geochemical data for all drillholes from the 2021 and 2022 drilling season.

2.2 Data Collection

Additional SWIR data was collected using a TerraSpec spectrometer on half-core samples that were cleaned and dried. The spectra were processed using 'The Spectral Geologist (TSG™)' software and the results were used in conjunction with 4-acid geochemical data to domain the alteration. The alteration model was derived through the evaluation of multiple geochemical assessments, including the feldspar control diagram, K/Rb and Fe/S ratios, and the Ca-Fe-S ternary diagram (Fig. 1). Based on immobile element characterization, the rocks share similar intermediate primary geochemical compositions, suggesting that changes in major mobile element composition generally reflect hydrothermal alteration.

The derived alteration domains were further divided based on relative position to the host diorite into upper volcaniclastic host rocks, lower volcaniclastic host rocks, and diorite, and used to group the data set for input into Principal Component Analysis (PCA). Thirteen elements associated with porphyry and epithermal style mineralization (Fig. 3) were selected (Halley 2015). Data was normalized using centered log ratio normalization (CLR) to reduce the impact of the

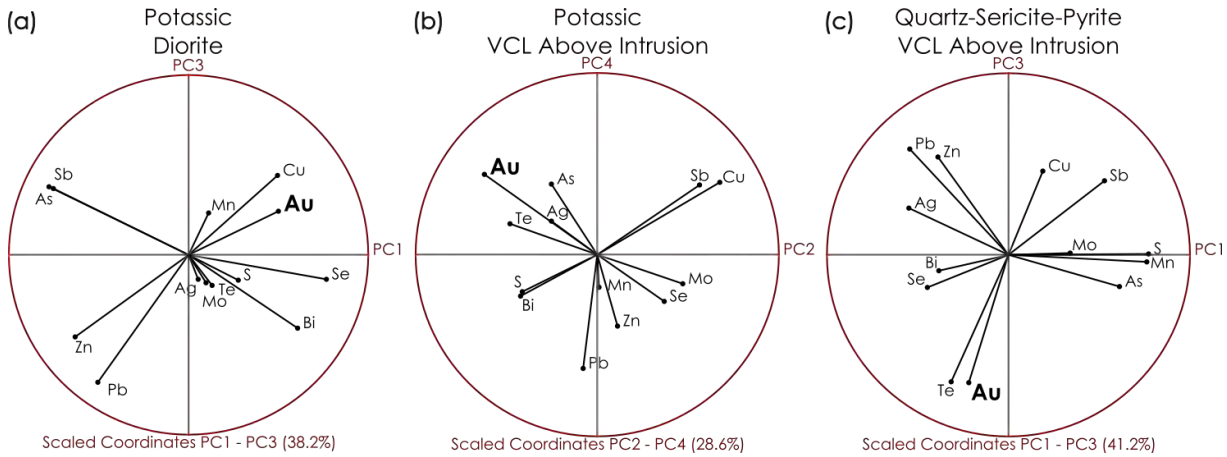


Figure 3 Graphical representations of results of PCA. (a) Kfs altered diorite; (b) Kfs altered upper volcaniclastic rocks; (c) QSP altered upper volcaniclastic rocks. (VCL) volcaniclastic rocks

range of magnitudes. Principal components with eigen values >1 and the highest loadings for Au were selected for assessment. Vein density logs were constructed over assay sample intervals from logging and core photos, and these were identified as being related to elevated gold grades. A total of 44 drill core samples were selected for polished thin sections. The samples were mapped using a Bruker M4 Tornado µ-XRF before and after thin section preparation. The thin sections were examined using a petrographic microscope and 14 representative sections were chosen for SEM analysis to further characterize gold deportment.

3 Results and Discussion

3.1 Results

Alteration modelling (Fig. 2 a, c) defined five primary mineralized lithology–alteration domains: 1) quartz-sericite-pyrite (QSP) altered upper volcaniclastic rocks, 2) potassic (Kfs) altered upper volcaniclastic rocks, 3) QSP altered lower volcaniclastic rocks, 4) Kfs altered lower volcaniclastic rocks, and 5) Kfs altered diorite. The diorite and upper volcaniclastic rock hosted domains are the focus of this paper.

The logged vein types each display a strong spatial correlation to a different alteration domain. Quartz-chalcopyrite-pyrite veins are restricted to the potassic altered diorite, coarse grained, carbonate-quartz-pyrite veins are associated with potassic altered volcaniclastic rocks, and the banded quartz-gold veins are associated with strongly QSP altered volcaniclastic rocks.

The results of the PCA (Fig. 3) illustrate that the elemental associations with gold vary with alteration and lithology. In the potassic altered diorite, Au displays the strongest covariance with Cu. In the Kfs altered upper volcaniclastic rocks, Au has high covariance with Ag, followed by As and Te. In the QSP altered upper volcaniclastic rocks, Au has high covariance with Te.

Petrographic and SEM analyses supported the variability and derived elemental associations found in the PCA. In the potassic altered diorite, Au is present as inclusions of electrum in chalcopyrite and

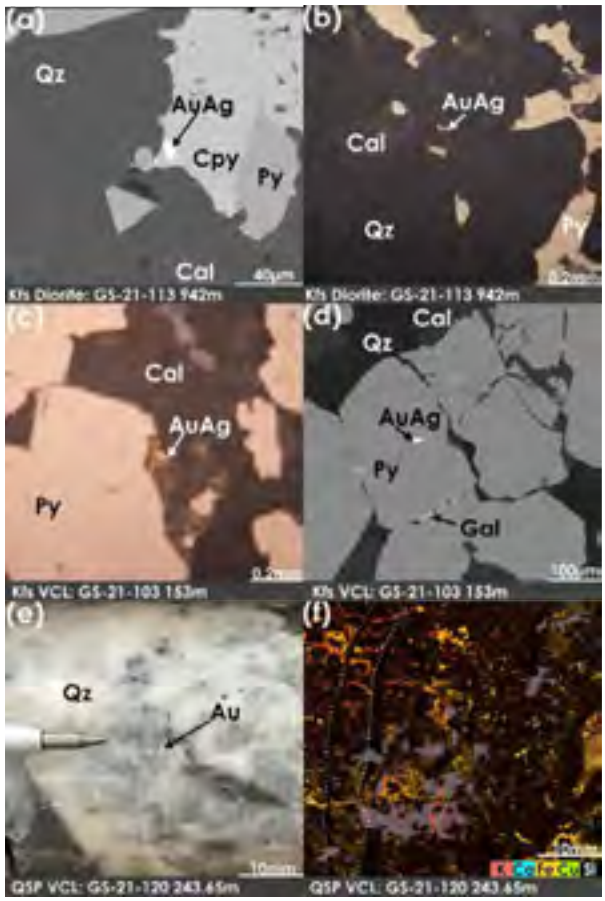


Figure 4 Images of gold mineralization. (a) electrum (AuAg) inclusion in chalcopyrite (Cpy); (b) electrum in quartz (Qz) calcite (Cal) vein; (c) electrum on edge of pyrite (Py) grain in carbonate vein; (d) electrum as inclusion in pyrite; (e) Gold (Au) in banded quartz vein; (f) µXRF image of quartz vein showing subtle banding

in the vein matrix (Fig. 4 a, b). In the potassic altered upper volcaniclastic rocks, Au is present as inclusions in pyrite and in the vein matrix (Fig. 4 c, d). In the QSP altered, upper volcaniclastic rocks, Au is present as visible gold hosted in epithermal style quartz veins (Fig. 4 e, f). In samples containing no veins, with Au >1ppm, no gold was observed in as free gold or refractory gold.

3.2 Discussion

In magmatic-hydrothermal mineral deposits, sulfide and alteration mineral assemblages reflect the physiochemical conditions present during formation. Variations in alteration and sulfide mineralogy at the Goldstorm deposit capture the evolution of an early high-temperature, high-pressure, near-neutral hydrothermal fluid into a later lower-temperature, lower-pH fluid. There is evidence of additional hydrothermal events, which resulted in the overprinting of intermediate epithermal style mineralization over the earlier porphyry style mineralization.

The diorite intrusion displays broad potassic alteration, consisting predominantly of potassium feldspar and minor biotite. Gold in porphyry copper deposits is commonly thought to be deposited primarily during high temperature potassic alteration, forming as inclusions within copper sulfides (bornite, chalcopyrite) (Kesler et al. 2002), which are observed in Goldstorm.

Gold in the upper volcaniclastic rocks is distributed in two different alteration domains. Gold mineralization in the south occurs within carbonate-quartz-pyrite veins hosted by volcaniclastic rocks which have undergone potassic alteration. Gold is present as electrum inclusions within pyrite and disseminated within the vein matrix. The decrease in copper present in these veins, relative to the quartz-sulfide veins within the diorite, suggests that this stage occurred after or contemporaneously with the intrusion hosted gold, as the fluid evolved to decreased salinity, reducing its ability to transport copper as chlorides, while gold remained soluble as a bisulfide complex (Seward 1991).

Alteration mapping in the north indicates that QSP alteration overprints pre-existing potassic alteration within the volcaniclastic rocks. This assemblage indicates a decrease in fluid temperature and pH. Linear trends of the strongest QSP alteration mapped in the north suggest its development was likely influenced by structures subparallel to the bounding faults (Fig. 2). SEM analysis of pyrite revealed no discernible gold, implying that if present, it exists as very fine-grained inclusions or within the crystal lattice.

The banded, silica-gold veins contain clasts of strongly QSP altered host rocks, suggesting that they formed during a later hydrothermal event. The spatial correlation of these veins to zones of strong QSP alteration suggests that the structural pathways which focused the QSP alteration were reactivated and used as conduits for this epithermal event.

4 Conclusions

The Goldstorm porphyry deposit hosts abundant Cu, Au and Ag mineralization, the deportment of which varies predictably with magmatic-hydrothermal alteration. Five prominent mineralized alteration-lithology domains were identified, each characterized by a unique alteration and sulfide mineral assemblage, reflecting the temporal evolution of the hydrothermal system. The proposed ore paragenesis of the deposit is comprised of three main stages: 1) early high-temperature potassic alteration associated with diorite emplacement, hosting Au primarily within chalcopyrite and pyrite; 2) QSP alteration along pre-existing structures, potentially remobilizing gold and resulting in further pyrite formation; and 3) late-stage formation of banded, silica-gold veins, as the product of a later hydrothermal event which reactivated the structures that channelled QSP alteration.

The proximity of the epithermal quartz vein hosted mineralization to porphyry style alteration and mineralization implies the potential for shallow emplacement of the initial mineralized intrusive event. The neighbouring KSM deposits are generally analogous in age and geochemistry but are hosted in the deeper Stuhini sediments and lack the abundant epithermal gold overprinting (Campbell 2016).

The detailed understanding of mineralized domain evolution is crucial for optimizing exploration and resource extraction. By delineating the spatial distribution of these domains and characterizing the gold deportment within each, we can improve resource estimation, guide exploration efforts towards high-grade zones, and provide a framework for targeted metallurgical sampling.

Acknowledgements

We would like to thank the team at MDRU for their guidance and Tudor Gold Corp. for supporting this consortium and providing the data for this study.

References

Alldrick DJ (1993) Geology and metallogeny of the Stewart mining camp, northwestern British Columbia. British Columbia Geological Survey Bulletin 85:105.

Alldrick DJ, Nelson JL & Barresi T (2004) Geology and mineral occurrences of the Upper Iskut River area: tracking the Eskay Rift through northern British Columbia (Telegraph Creek NTS 104G/1, 2; Iskut River NTS 104B/9, 10, 15, 16).

Campbell ME “Magmatic History of the Kerr-Sulphurets-Mitchell Copper-Gold Porphyry District, Northwestern British Columbia (NTS 104B),” 2016, 12.

Halley S (2015) Footprints: hydrothermal alteration and geochemical dispersion around porphyry copper deposits. SEG Newsletter 100: 11-17.

Kesler SE, Chryssoulis SL, Simon G (2002) Gold in porphyry copper deposits: Its abundance and fate. Ore Geology Reviews 21(1-2): 103-124. doi:10.1016/S0169-1368(02)00084-7

Sillitoe RH (2000) Gold-rich porphyry copper deposits: Descriptive and genetic models and their role in exploration and discovery. Reviews in Economic Geology 13: 315-344.

Stanley CR, Madeisky HE (1996) Lithogeochemical exploration for metasomatic zones associated with hydrothermal mineral deposits using Pearce element ratio analysis. Short course notes on Pearce element ratio analysis.

Ages and trace element fertility of porphyry-related mineralization in the Philipsburg polymetallic district, Montana, with a comparison to Butte

Celine M.E. Beaucamp[1], Christopher H. Gammons[1], Jay M. Thompson[2], Holly J. Stein[3]
[1] Montana Technological University, Butte, MT, USA
[2] U.S. Geological Survey, Denver, CO, USA
[3] AIRIE Program, Fort Collins, CO, USA

Abstract. The Philipsburg mining district is a Mo-Cu porphyry system with associated Cordilleran polymetallic veins. Geochronology was employed to date the porphyry (~66 Ma, U/Pb in zircon) and molybdenite mineralization from the veins (~76 Ma, Re-Os). Age results suggest that the two-mineralization events model proposed by Lund et al. (2018) for the Butte district can be applied to the Philipsburg deposit. Furthermore, common fertility indicators from zircon trace elements were analyzed with variable success to characterize the existing Mo-Cu mineralization of the Philipsburg porphyry. This raises concerns about the benefits of this method and/or the importance of sampling, which could impact exploration for similar porphyry deposits.

1 Introduction

The Philipsburg mining district is Montana's second most productive polymetallic deposit. It produced over 24M oz of Ag, 83,000 oz of Au, 36M kg of Zn, 10M kg of Pb, 1.8M kg of Cu, and 295k metric tons of Mn between 1864 and the 1980s (Prinz 1967). Multiple quartz-feldspar porphyry intrusions and associated skarn crop out north of the veins. They were investigated during two exploration campaigns in the 1960s and 1980s. Significant Mo-Cu mineralization was found but never produced. In this study, dates were obtained on zircons (U/Pb) and molybdenite (Re-Os) from the porphyry and the vein area, respectively, to determine the sequence of mineralizing events that produced the Philipsburg deposits. In addition, titanium-in-zircon temperatures and porphyry mineralization indicators were applied based on the zircon's trace element content for magma fertility estimation and were compared to data from the Butte porphyry deposit.

2 Geologic background

The Philipsburg mining district overlies the Paleoproterozoic Great Falls tectonic zone in the basement and lies south of the Lewis and Clark fault zone and west of the late Cretaceous Helena salient of the Mesoproterozoic Belt basin. Numerous N-S striking Mesozoic thrust faults (Sevier orogeny) cross the area. Cenozoic extension is recorded by normal faults and two important detachment zones marking the east and west borders of the tectonic block hosting the district.

The district is underlain by a folded series of Mesoproterozoic to Mesozoic sedimentary rocks (Fig. 2). The sedimentary rocks were intruded by the

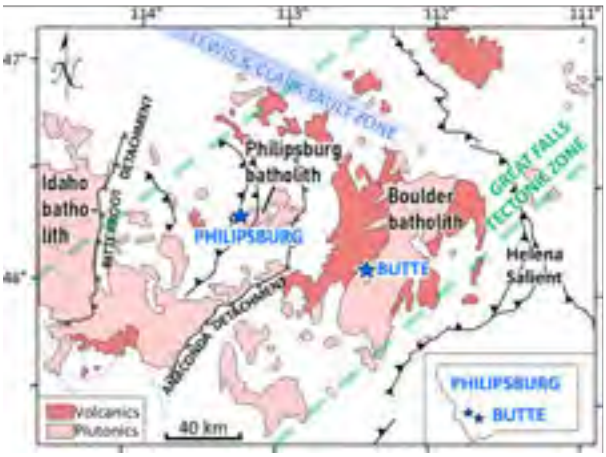
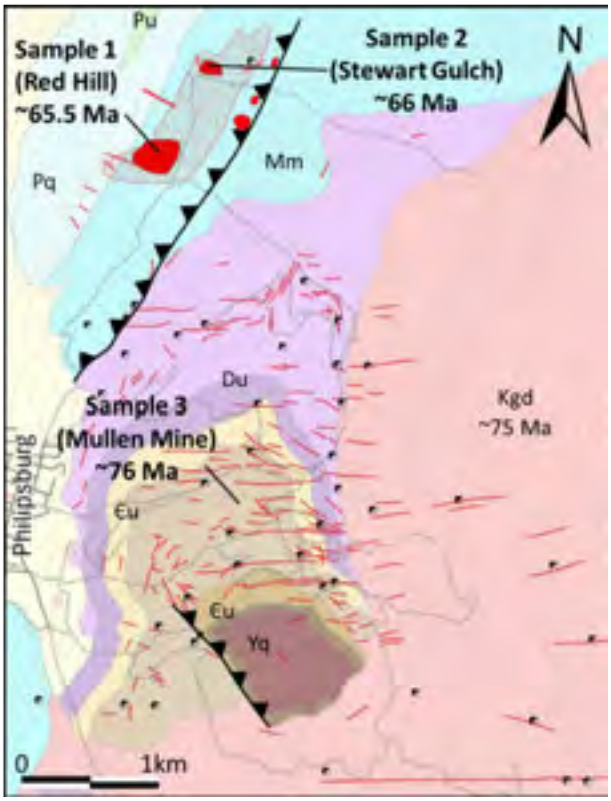


Figure 1. Regional geologic context of the Philipsburg mining district in relationship to tectonics and igneous rocks of southwest Montana.

75 Ma Philipsburg batholith (Naibert et al 2010). Minor quartz-feldspar porphyritic intrusions crop out on the district's northern end. They are associated with a mineralized garnet-actinolite skarn, a dyke with Unidirectional Solidification Textures (USTs), highly silicified material and gossan, and marble from the host Mississippian limestone. South of the porphyry system, mineralized veins generally strike E-W and are hosted by both the sedimentary rocks and the batholith. Two main categories of veins are recognized: steeply south-dipping quartz veins mined principally for Ag, Zn, and Pb, and quartz veins along bedding mined for Ag (Prinz 1967). The Philipsburg district fits the model of zoned Cordilleran polymetallic vein deposits (also called "Butte-type") associated with a porphyry system (Beaucamp et al 2024).

3 Results

Analyzed zircons were collected from two quartz-feldspar porphyry samples from the district's north end (Fig. 2). The first sample is of a quartz-feldspar porphyritic intrusion from Red Hill (Fig. 2 and 3), with highly sericitized feldspars, and containing accessory minerals zircon, monazite, and rutile. The second sample is from Stewart Gulch with mm-sized, equigranular quartz bands displaying USTs in a matrix of feldspar containing the same accessory minerals as above. The zircons were processed using standard gravimetric and magnetic separation techniques at the Montana Bureau of Mines and Geology in Butte, MT. One hundred grains for each



Mining structures (adit, shaft, stockpile, dump)
Polymetallic veins
TKi: Tertiary-Cretaceous Cu-Mo porphyritic intrusion and associated skarn
Kgd: Cretaceous granitic batholith
Pq: Pennsylvanian Quadrant Fm.
Mm: Mississippian Madison Fm.
Du: Devonian undifferentiated
Eu: Cambrian undifferentiated
Yq: Quartzite of the Mesoproterozoic Belt Supergroup

Figure 2. Geology of the Philipsburg mining district and sample locations.

sample were mounted in polished, 1" diameter epoxy pucks that were examined by cathodoluminescence using an FE-SEM at Montana Technological University. The samples were then sent to the USGS-LTRACE laboratory in Denver, CO, where 43 of the mounted zircons were analyzed with LA-ICP-MS for Al, Ce, Dy, Er, Eu, Fe, Gd, Hf, Ho, La, Lu, Nb, Nd, P, Pb, Pr, Sm, Ta, Tb, Th, Ti, Tm, U, Y, Yb, and Zr. The following ratios were measured: $^{238}U/^{206}Pb$, $^{207}Pb/^{206}Pb$, $^{206}Pb/^{238}U$, and $^{208}Pb/^{232}Th$ and the following ratio was calculated: $^{207}Pb/^{235}U$. Finally, the temperature of the magma was determined using the titanium-in-zircon method (Ferry and Watson 2007).

The third sample is a specimen of altered wallrock from the Mullen mine dump. The sample matrix consists of K-feldspar cut by cm-scale actinolite veins containing disseminated molybdenite, scheelite, pyrite, and chalcopyrite. This sample was sent for Re-Os age determination at the AIRIE laboratory in Fort Collins, CO. Seven molybdenite crystals were drilled, resulting in 17.9 mg of ~70% molybdenite powder.

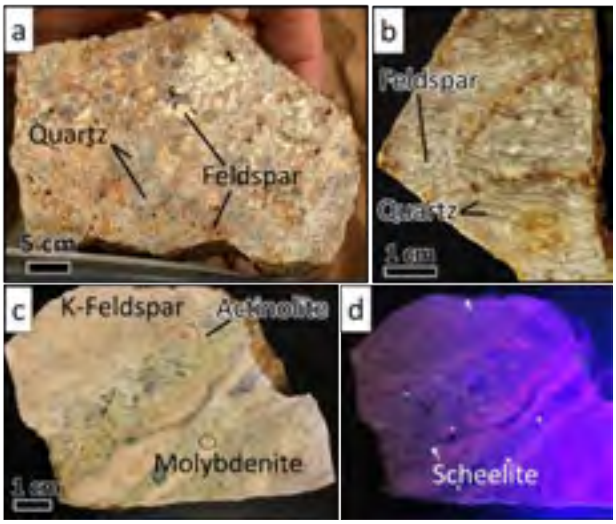


Figure 3. Samples analyzed in this study. a) Sample 1 from Red Hill; b) Sample 2 from Stewart Gulch; c) & d) Sample 3 from the Mullen mine under visible light and short-wave UV light (bright specks: scheelite).

3.1 Age data

Zircons from samples 1 & 2 yielded ^{207}Pb-corrected $^{206}Pb/^{238}U$ ages of 65.55 ± 0.41 Ma and 66.26 ± 0.73 Ma, respectively (Fig. 4). The two ages are indistinguishable within their two-sigma analytical uncertainty. The mean square of weighted deviation (MSWD) for sample 1 is satisfactory (<1), while the higher MSWD for sample 2 (2.4) possibly reflects some additional complexity during Late Cretaceous crystallization. The common Pb composition of $^{207}Pb/^{206}Pb$ = 0.84 ± 0.01 was used, resulting in a correction of <0.1% of the $^{206}Pb/^{238}U$ ages. These uncertainties do not include the decay constant errors of 0.11%. Both samples show late Paleoproterozoic to Neoproterozoic and Late Cretaceous inheritance.

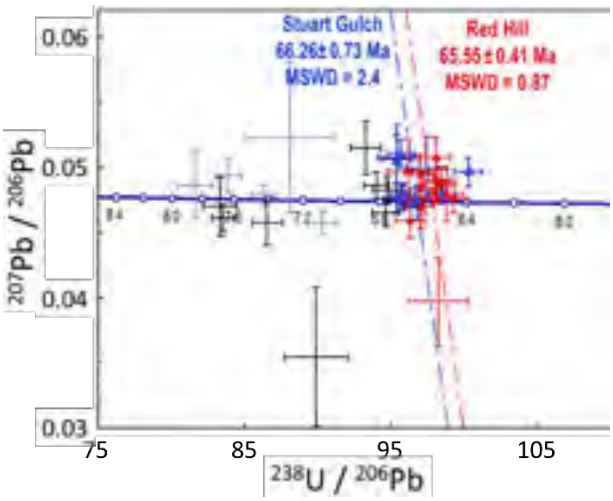


Figure 4. Zircon ages from samples 1 and 2. Sample 1: Red Hill is in red (included in the age determination) and black (omitted); Sample 2: Stuart Gulch is in blue (included) and light blue (omitted).

The Re, ^{187}Os, and common Os contents of molybdenite from sample 3 are reported in Table 1. The sample yields an age of 75.76 ± 0.35 Ma.

Table I. Re-Os age from sample 3 (Molybdenite – Mullen mine). Abs = absolute error. w/λ = age uncertainty inclusive of the ^{187}Re decay constant uncertainty.

Re (ppm)	Re	30.52
	Abs error	0.052
^{187}Os (ppb)	^{187}Os	24.23
	Abs error	0.072
Common Os (ppb)	Os	0.29
	Abs error	0.032
Age (Ma)		75.76
Abs error w/λ		0.35

3.2 Trace-element data

Plots for rare earth elements normalized to chondrite (Boynton 1985) show a strong (+) Ce anomaly for all age groupings, a weak (-) Eu anomaly for the Late Cretaceous zircons, and a strong (-) Eu anomaly for the Proterozoic zircons (Fig. 5). Zircons in the 63-70 Ma range the inferred age of the porphyry events) have higher light and middle REE contents.

Figure 6 shows selected fertility indicators for Philipsburg and several porphyritic dikes at Butte (Dilles et al 2015). Magmatic conditions necessary to form a Cu-porphyry deposit require an oxidized magma state and a higher degree of magmatic fractionation, indicated by specific proxy elements or element ratios. Pizarro et al (2020) extensively explained the reasoning behind the above-listed characteristics for magma oxidation state and fractionation, as well as the fertility thresholds used in this study. Plot 5a shows the temperature from 63-70 Ma magma (related to porphyry mineralization) ranging from 550 to 800 °C; it is notable that ages and temperatures are similar to those from the porphyry mineralization at Butte. Plots 5b to 5e show fertility windows based on selected indicators. The graphs show that some ratios from the Philipsburg district fall better into the fertility windows than others: Eu_N/Eu^*, 10 000 x $(Eu_N/Eu^*)/Y$, Hf, and Th/U. Others do not appear to be reliable fertility indicators for this district, the least reliable being (Ce/Nd)/Y. Data from the Butte porphyry deposits have an even poorer correlation with most indicators. The Porphyry Indicator Zircon concept (PIZ), following conventions from Pizarro et al (2020) and using zircons for age determination of the porphyry (~66 Ma), resulted in a 33% positive correlation from Philipsburg's sample 1 (Red Hill) and 0% from sample 2 (Stewart Gulch). In Butte, 0% of the porphyry-age zircons met the PIZ criteria.

4 Discussion

4.1 Ages

The mainstream model for the timing of mineralization in the Butte district puts the formation of the polymetallic veins shortly after the emplacement of a deeper but genetically related porphyry system (Reed et al 2013). However, a recent paper (Lund et al 2018) has proposed a two-event model in which 1) a set of Ag-Pb-Zn veins formed during the cooling of the 75 Ma Boulder batholith, and 2) metals were remobilized and replaced by high-grade Cu-sulfides when the porphyry Cu-Mo system intruded some ten m.y. later. The ages presented in this study also suggest two stages of mineralization for the Philipsburg district. However, the paragenetic relationship between the molybdenite sample from the Mullen Mine and the surrounding quartz veins is unclear.

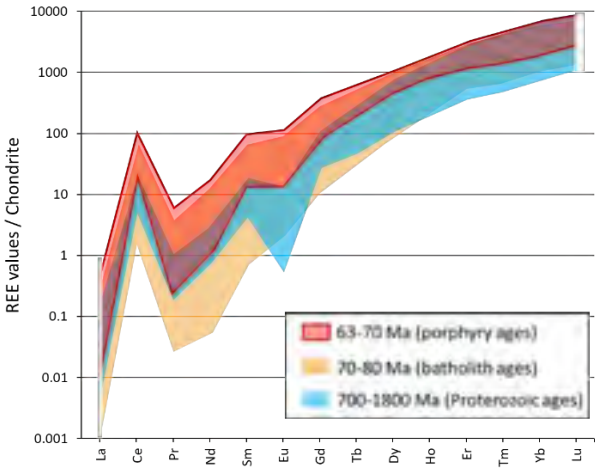


Figure 5. Chondrite-normalized REE patterns for zircons from both porphyry samples from Philipsburg organized by age.

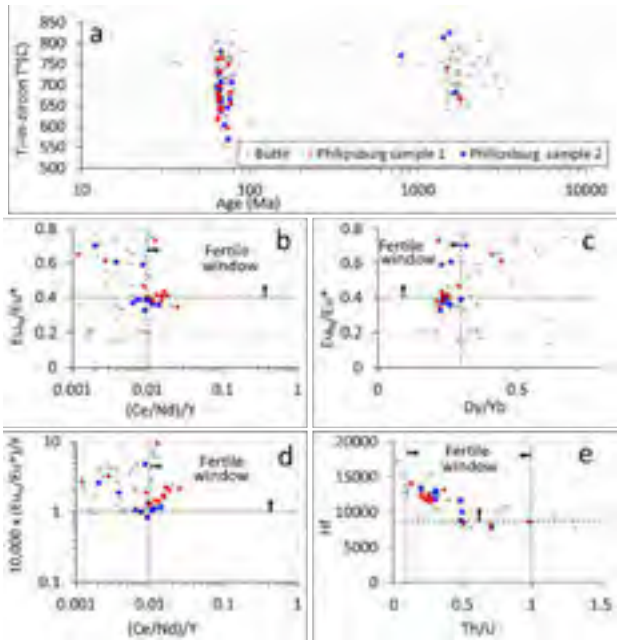


Figure 6. Additional zircon plots for Philipsburg (this study) and Butte (Dilles et al 2015). a) Crystallization temperature vs. calculated age; b,c,d,e) fertility cross-plots for zircon analyses used in the age determinations (dashed lines represent boundaries of fertility windows).

4.2 Magma fertility indicators from the porphyry system

Butte and Philipsburg are very similar deposits: ~65 Ma Cu/Mo porphyries with associated Cordilleran polymetallic lode deposits, spatially associated with a ~75 Ma batholith. Both have been leading producers of Cu, Ag, Zn, and Mn in Montana and are in the same general tectonic region.

Porphyries from both districts are known to be mineralized. Yet, plots of the trace element content of their zircons do not always fall into the fertility windows of the indicators recommended in the literature. Pizarro et al (2020) suggest that 54% or more of zircons with PIZ characteristics reflect a potential for porphyry deposits. Our data from Philipsburg and the data of Dilles et al (2015) from Butte show that Butte's and Philipsburg's zircons hardly reach that threshold. Other authors also have mentioned the variable effectiveness of the fertility indicators. This study demonstrates that either 1) some fertility indicators may be more universally applicable than others or 2) the samples selected were from outcrops that were not as linked to mineralization as others. The first possibility implies that fertility indicators in use, in fact, may not well predict magma fertility. This can be due to the reset of U-Pb but not of trace elements by the high temperature during residence in magma. The second explanation raises the concern of sampling selection accuracy, which could lead to false negatives and missed opportunities when applying this method for Cu/Mo porphyry exploration. In either case, this study reports a failure of fertility indicators in characterizing known economic systems.

5 Conclusions

The Philipsburg district contains a Mo-Cu porphyry system with associated Cordilleran polymetallic veins. It shares many geologic and geochronologic characteristics with its close neighbor, the famous Butte mining district. The Philipsburg porphyry system was dated at ~66 Ma (U/Pb in zircon), about ten m.y. younger than the neighboring Philipsburg batholith. Furthermore, molybdenite several km south of the porphyry system was dated at ~76Ma (Re-Os), raising the question of the existence of pre-porphyry mineralization, as was determined in the Butte district.

Zircon trace elements from Philipsburg's porphyry were also analyzed as fertility indicators. Although some zircon fertility indicators accurately document the mineralization potential of the Philipsburg porphyry outcrops, others are moderately useful. (Ce/Nd, Th/U, and Dy/Yb), (Ce/Nd)/Y did not indicate fertility. Multiple drilling campaigns have documented significant Mo-rich skarn mineralization associated with the ~ 65 Ma porphyry event at the north end of the Philipsburg district. Therefore, either the fertility indicators approach is not universally reliable, or the zircons analyzed in this study from Philipsburg and by Dilles et al (2015) from Butte were not genetically related to the spatially associated mineralization.

Acknowledgments

This study was sparked by an unpublished zircon geochronologic datum on the Stewart Gulch porphyry obtained by the late Dr. Frank Dudas, which he communicated at the beginning of the author's doctorate. The author would like to thank the Antonioli family for providing access to their property and archives. This study was funded by the National Science Foundation (Award 2327676). The author also thanks the Society of Mining and Metallurgical Engineers, the Geological Society of America, the Montana Geological Society, the American Federation of Mineralogical Society, and the Tobacco Root Geological Society for financial support.

These data are preliminary or provisional and are subject to revision. They are being provided to meet the need for timely best science. The data have not received final approval by the U.S. Geological Survey (USGS) and are provided on the condition that neither the USGS nor the U.S. Government shall be held liable for any damages resulting from the authorized or unauthorized use of the data.

References

Beaucamp CM, Gammons CH, Thompson JM, Lowers HA (2024) Fluorescent sphalerite rich in tungsten, copper, gallium, silver, and other elements from the Cordilleran-style, polymetallic veins of Philipsburg, Montana. Ore Geology Reviews 173:106267

Boynton WV (1985) Cosmochemistry of the rare earth elements: meteorite studies. In Developments in geochemistry. Elsevier 2:63-114

Dilles JH, Kent AJ, Wooden JL, Tosdal RM, Koleszar A, Lee RG, Farmer LP (2015) Zircon compositional evidence for sulfur-degassing from ore-forming arc magmas. Economic Geology 110(1):241-251.

Ferry JM, Watson EB (2007) New thermodynamic models and revised calibrations for the Ti-in-zircon and Zr-in-rutile thermometers. Contributions to Mineralogy and Petrology 154(4):429-437.

Lund K, McAleer RJ, Aleinikoff JN, Cosca MA, Kunk MJ (2018) Two-event lode-ore deposition at Butte, USA: 40Ar/39Ar and U-Pb documentation of Ag-Au-polymetallic lodes overprinted by younger stockwork Cu-Mo ores and penecontemporaneous Cu lodes. Ore Geology Reviews 102:666-700.

Naibert TJ, Geissman JW, Heizler MT (2010) Magnetic fabric, paleomagnetic, and 40 Ar/ 39 Ar geo chronologic data bearing on the emplacement of the Late Cretaceous Philipsburg Batholith, SW Montana fold-and-thrust belt. Lithosphere, 2(5): 303–327

Pizarro H, Campos E, Bouzari F, Rousse S, Bissig T, Gregoire M, Riquelme R (2020) Porphyry indicator zircons (PIZs): Application to exploration of porphyry copper deposits. Ore Geology Reviews 126:103771.

Prinz, W. C. (1967). Geology and ore deposits of the Philipsburg district, Granite County, Montana (No. 1237). US Govt. Print. Off.

Reed M, Rusk B, Palandri J (2013) The Butte magmatic-hydrothermal system: One fluid yields all alteration and veins. Economic Geology 108(6):1379–1396.

The Huntoon Copper Project, Mineral County, Nevada – Unravelling a dismembered magmatic-hydrothermal system

James H.S. Blight[1] and Lawrence C. Carter[2,3]
[1]Great Western Mining Corporation PLC, Dublin, Ireland.
[2]LC Geoscience Ltd, Cornwall, UK [3]Camborne School of Mines, Cornwall, UK.

Abstract. The Huntoon Copper Project (HCP) is Great Western Mining's flagship project in Mineral County, Nevada, USA. It comprises five distinct but potentially related copper prospects within a 6 km radius, in a relatively remote area. The host rocks are situated in the Mina Deflection, a zone of sinistral transtension within the broader dextral Walker Lane, and the setting is therefore structurally complex; Cenozoic extension, shearing and likely tilting have dismembered the Cretaceous intrusive-hydrothermal system. The HCP includes skarn mineralisation at M2, breccia mineralisation at M4, porphyry and epithermal mineralisation at West Huntoon, along with various other prospects and showings (e.g. Smith Mine, M5). Geochemical and geophysical anomalies correlate with the prospects and indicate the potential for future extension. A substantial amount of the ground is obscured by post mineral cover and the HCP is under-explored as a consequence. From recent exploration drives, here we provide a first geological, geochemical and geochronological framework for the district seeking to link activity across the multiple levels of the magmatic-hydrothermal system exposed in various fault blocks across the Huntoon Valley.

1 Introduction

The Huntoon Copper Project (HCP) comprises five granite-related prospects arrayed around the margins of the Huntoon Valley, a perched tectonic basin in the Walker Lane of western Nevada (Figures 1 & 2). The Huntoon Valley is situated in Mineral County, approximately 15 km northeast of the border with California.



Figure 1. Map of Mineral County Nevada.

The HCP includes: M2, an established skarn copper resource (4.3 Mt at 0.45% Cu); M4 and West Huntoon, advanced exploration projects with initial drill intercepts in a mineralised breccia zone and copper baring host rocks to a granite cupola zone, respectively; Smith Mine, an early stage prospect featuring an outcropping felsic dyke intruding carbonate horizons with abundant copper oxides; and M5, a polymetallic prospect with a large gold & copper in soils anomaly, and sulphide stringers outcropping at surface.

2 Methods

Field observations and sampling of intrusive phases, magmatic-hydrothermal features and soils. All soil samples were analysed at Paragon Geochemical Laboratories, Reno, Nevada. Soil samples were screened to -80 mesh and analysed by method FSAU-25; aqua regia digest with ICP-MS finish for a 51-element suite. Grab samples were analysed at ALS in Reno, Nevada using the complete characterisation method CCP-PKG05, for whole rock analysis, analysing trace elements by fusion, with aqua regia digestion for the volatile trace elements; carbon and sulphur by combustion analysis; and base metals via four-acid digestion. Samples from the HVGD, WFG and CPG underwent zircon separation at Zircon LLC, Tuscon, USA. Zircons were handpicked and prepared as polished blocks before imaging by SEM-CL and analysis by LA-ICP-MS at Washington State University.

2 Geology

The geology of the Huntoon Valley can be divided into three broad parts; host rocks; intrusions and related mineralisation; and post mineralisation cover (Figure 2).

The host rocks, exposed in the hills surrounding the valley, are Permian to Jurassic meta-sediments and volcanics, with associated mafic porphyry intrusions, the latter notably exposed to the northeast of West Huntoon prospect. Carbonate horizons within these host rocks are associated with mineralisation at a number of localities.

Granitoid intrusions make up a significant majority of the outcrops to the north and northeast of the valley, and major units include the Huntoon Valley Granodiorite [HVGD], and the Whiskey Flat Granite [WFG] (Stewart et al. 1984). One area of

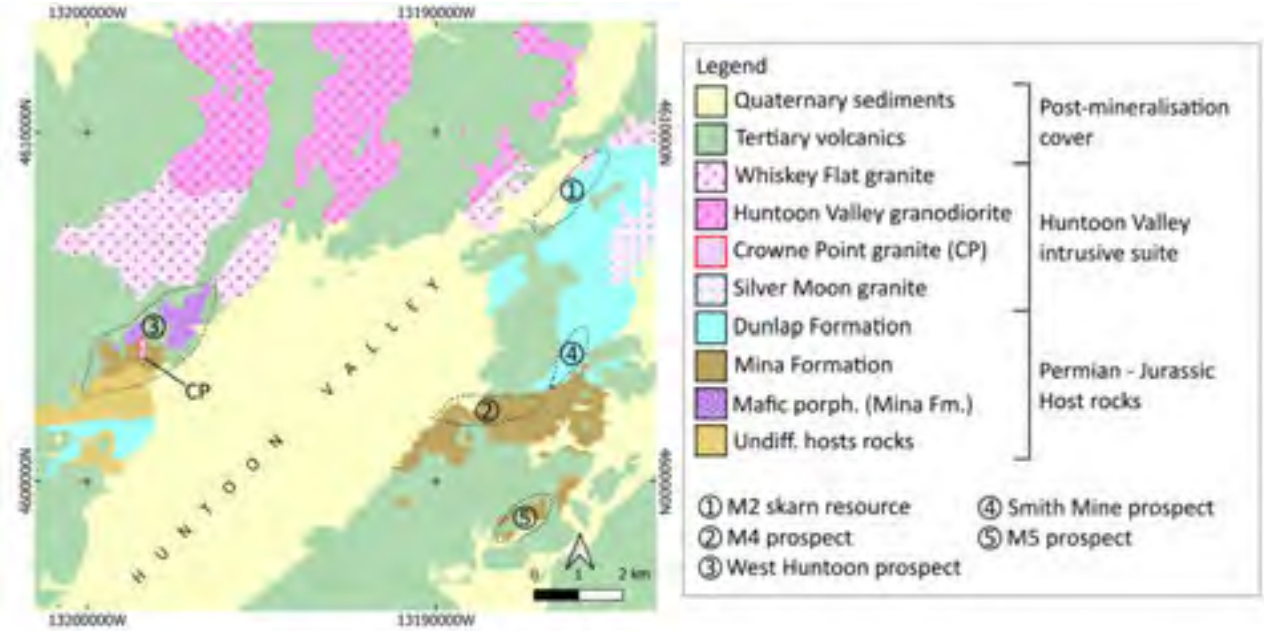


Figure 2. Geology map of the Huntoon Valley and surrounds, simplified after Stewart et al. (1984). Boundaries of prospects based on combinations of geological mapping and geochemical & geophysical anomalies. Several prospects are constrained where anomalies are obscured by cover.

granite outcrop, the Crowne Point Granite [CPG], was unmapped prior to late 2023, and this unit contains several key magmatic-hydrothermal textures (Figure 3) described in Section 4 below.

Post mineralisation cover includes an extensive Tertiary volcanic succession exposed on the hills, and recent unconsolidated sediments in the valley floor area.

3 Structure

Like other large-scale magmatic hydrothermal systems in the Basin and Range (Yerington, Proffett 1977; Robinson, Bauer et al. 1960), HCP has been dismembered and tilted by various younger faults. The structural setting in the Huntoon Valley is particularly complicated by its location with the Mina Deflection (Nagorsen-Rinke et al., 2013) of the Walker Lane (Faulds et al., 2008), an oblique-sinistral transtension system of faults, resulting in left lateral displacement of various portions of the system, along with typical block tilting and resultant differential preservation.

4 Magmatic-hydrothermal features

During fieldwork in 2023-24 multiple lines of evidence for a widespread magmatic-hydrothermal system in the Huntoon Valley were identified including geochemical (Loucks 2014), textural (Carter and Williamson 2022), and on the basis of spatial relationships between alteration and mineralisation of different types (Corbett 2009):

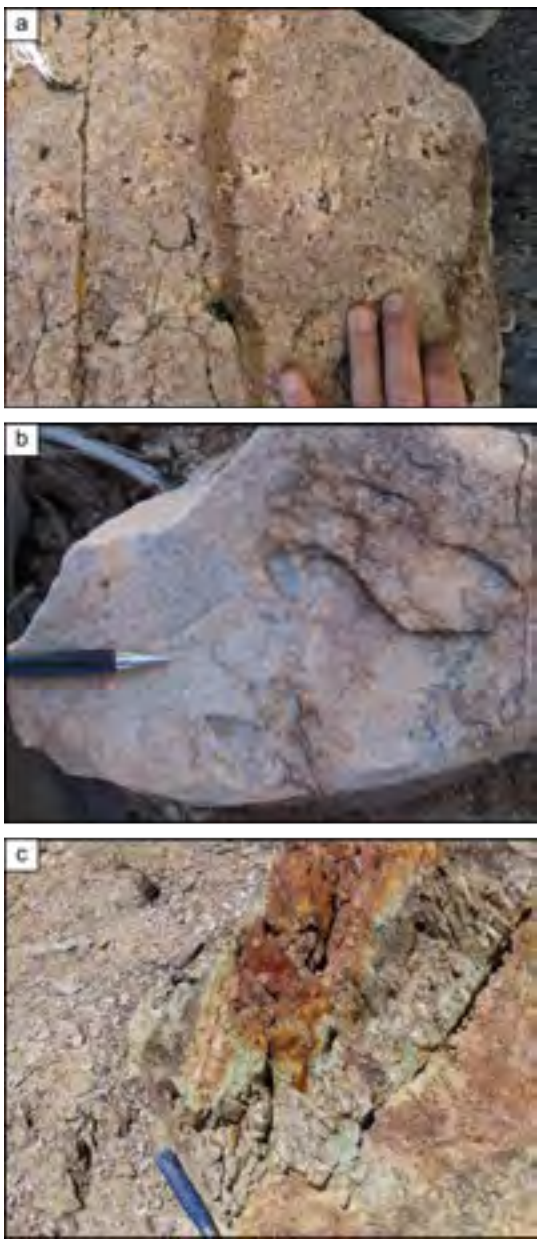


Figure 3 (right) a) quartz lined miarolitic cavities (undoubted evidence for magmatic fluid exsolution; Candela 1997); b) Aplitic granite cupola zone with quartz feldspar USTs growing from internal contact; c) phyllic alteration and copper shows in an aplitic granitic cupola zone.

- Large geochemically fertile coarse-grained plutons (WFG and HVGD).
- Finer-grained phases of the WFG cut by aplitic porphyry.
- Wall rocks featuring intense Na-Ca to propylitic alteration and M-type veins.
- An aplitic cupola zone (CPG) containing abundant pegmatite pods, quartz eyes, miarolitic cavities (Figure 3a), quartz unidirectional solidification textures (USTs; Figure 3b), and locally intense stockworks of deep, A, and B-type quartz veins, associated with copper shows in the granite (Figure 3c).
- A shear zone in host rocks to the CPG with apparently remobilised Cu mineralisation.
- Epithermal style veins, with exceptionally high grades of Au and Ag. A mineralised breccia pipe (in drill core from the M4 prospect).
- Several examples of mineralised hypabyssal granitic/aplitic intrusions with associated skarn mineralisation.

5 Geochemistry

Soil and whole-rock geochemistry results delineate a 3km^2 area of copper anomalism at West Huntoon (Figure 4) with local patchy gold anomalism throughout (n=284, median 121 ppm Cu, 14 ppb Au, maximum 4267 ppm Cu, 1,940 ppb Au). Anomalies also occur at the other prospects of variable intensity and areal extent (e.g. M2, 0.3 km^2; n=102, median 131 ppm Cu, 3 ppb Au, maximum 2,598 ppm Cu, 87 ppb Au).

Whole-rock geochemical fingerprinting of exposed portions of the likely dismembered Huntoon Valley igneous suite characterises different units within a weakly peraluminous and weakly adakitic I-type granitic system which, in part, has undergone high degrees of magmatic evolution (Richards, 2011). Whilst the recently mapped Crowne Point granite's highly evolved nature means it does not conform to all geochemical 'fertility' indicators for porphyry deposits (e.g. Sr/Y), it appears geochemically to be an evolved relation to the weakly adakitic Whisky Flat granite (which does plot within the 'fertile' domain on Al_2O_3/TiO_2, Sr/Y, Zr/Y etc diagrams; Loucks, 2014). These most evolved granites are likely the most prospective for associated magmatic-hydrothermal mineralisation.

6 Zircon Analyses

Zircons were extracted from a suite of three samples from the intrusions of the Huntoon Valley, including the Huntoon Valley Granodiorite, the Whiskey Flat Granite and the Crowne Point Granite. Samples underwent mineral separation at Zirchron LLC, Tuscon, Arizona. Zircons were handpicked and prepared as polished blocks before imaging by SEM-CL and analysis by LA-ICP-MS at Washington State University.

6.1 U-Pb Geochronology

The HG (110.7 ± 1.2 Ma) and the WFG (110.5 ± 1.3 Ma) are unresolvable from each other. The ~110 Ma age temporally overlaps with formation of the Sierra Nevada batholith to the west, but other local comparisons are hard given the paucity of U-Pb geochronological data. Biotite and hornblende K-Ar ages of ~86 Ma and ~100 Ma respectively have been reported from the Huntoon Valley (Evernden and Kistler, 1970), but these ages should be treated with caution as the K-Ar isotopic system can be reset by metamorphism or hydrothermal alteration. These zircon ages agree with the whole-rock geochemistry that suggests the HG and the WFG share an evolutionary path, with a common magmatic source zone.

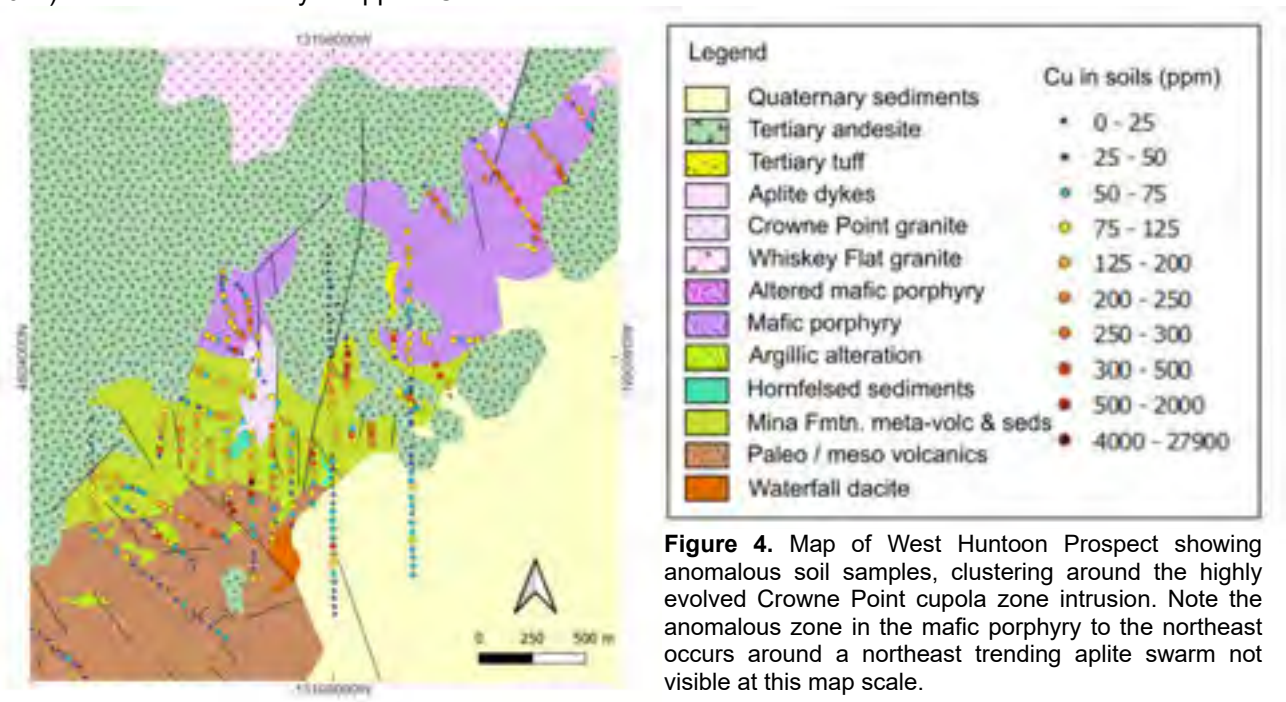


Figure 4. Map of West Huntoon Prospect showing anomalous soil samples, clustering around the highly evolved Crowne Point cupola zone intrusion. Note the anomalous zone in the mafic porphyry to the northeast occurs around a northeast trending aplite swarm not visible at this map scale.

The Crowne Point granite yields a surprising age of 257.7 ± 3 Ma. However, the crystal habits displayed under cathodoluminescence (CL) by zircons from Crowne Point, were notably poor, largely lacking oscillatory zoning, suggesting they may be inherited. Furthermore, all the zircons from this sample have high U contents, which is known to cause Pb loss. Radiation damage from the high U concentrations could also explain the lack of oscillatory zoning in CL. Pb loss is known to cause under-estimation of ages, however non concordant zircons were excluded from MSWD age calculations. If the ~257 Ma age is correct, this would indicate that the CPG is entirely unrelated to the Whiskey Flat system and place it temporally long before the beginnings of the Sierra Nevada arc (~220 Ma; Evernden and Kistler, 1970; Barth et al., 2011). Field relations and whole rock geochemistry suggest the CPG is an evolved phase of the WFG (Carter, 2023). It is therefore considered more likely that these zircons are inherited from the Permian wall rocks.

6.2 Zircon Geochemistry

Compared to the global reference suite of barren vs porphyry Cu-Mo-Au bearing systems presented in Lu et al. (2019), the WFG and HG sit within the porphyry 'fertile' domains. Signatures include having Eu/Eu* values of >0.3 and (Ce/Nd)/Y values of > 0.002, Ce/Nd values typically >10 and Dy/Yb values of <0.3. Zircons from the WFG and HG mostly overlap in geochemistry, in agreement with their unresolvable U-Pb ages, although the Dy/Yb effectively separates the two geochemically with the HG having lower values of <~0.17 compared to ~0.26-0.15 for the WFG. The WFG and HG zircons, however, do overlap in Hf concentration, typically thought to reflect melt evolution (e.g. Claiborne et al., 2006). Some WFG zircons appear to have higher Th/U ratios than HG zircons. In summary, these geochemical signatures are encouraging for the potential for porphyry systems in the Huntoon Valley; they suggest the presence of water-rich magmatic systems which underwent amphibole-dominated melt evolution with suppression of plagioclase; a key ingredient in fertile systems (e.g. Richards, 2012; Nathwani et al., 2024).

Conclusions

A previously unrecognised, widespread, structurally dismembered and geochemically fertile intrusive-hydrothermal complex is present in and around the Huntoon Valley. Evidence for fluid release from high level, evolved intrusions is extensive. This system was likely emplaced at or shortly after 110 Ma. Several instances of copper mineralisation and related alteration occur associated with this system, and due to the paucity of modern exploration and the extent of post-mineralisation cover it is likely that further mineralisation remains to be discovered in the Huntoon Valley.

Acknowledgements

We would like to express our gratitude to Robert O'Connell, Operations Director at Great Western Mining, for his invaluable logistical support. Additionally, we thank Andy Goetz for his work in the field, and Viktor Valencia for zircon analysis and U-Pb age interpretation.

References

Barth AP, Walker JD, Wooden JL, Riggs NR, Schweickert R (2011). Birth of the Sierra Nevada magmatic arc: Early Mesozoic plutonism and volcanism in the east-central Sierra Nevada of California. Geosphere 7 (4):877–897. https://doi.org/10.1130/GES00661.1

Bauer Jr HL, Cooper JJ, Breitrick RA (1960) Porphyry Copper Deposits in the Robinson Mining District White Pine County, Nevada. Book:220-228.

Carter LC, Williamson BJ (2022) Textural indicators of mineralisation potential in porphyry magmatic systems – A framework from the archetypal Yerington District, Nevada. Ore Geology Reviews 143, 104783. https://doi.org/10.1016/j.oregeorev.2022.104783

Carter L (2023) Reconnaissance Level Geochemical Fingerprinting – Huntoon Valley, Nevada. GWM commissioned report

Corbett G (2009) Anatomy of porphyry-related Au-Cu-Ag-Mo mineralised systems: Some exploration implications. Australian Institute of Geoscientists North Queensland Exploration Conference.

Claiborne LL et al (2006) Tracking magmatic processes through Zr/Hf rations in rocks and Hf and Ti zoning in zircons: An example from the Spirit Mountain batholith, Nevada. Mineralogical Magazine 70:517–543

Evernden JF, Kistler RW (1970). Chronology of emplacement of Mesozoic batholithic complexes in California and western Nevada. USGS Professional Paper 623. https://doi.org/10.3133/pp623

Faulds JE, Henry CD, Spencer JE, Titley SR (2008) Tectonic influences on the spatial and temporal evolution of the Walker Lane: An incipient transform fault along the evolving Pacific–North American plate boundary. Ores and orogenesis: Circum-Pacific tectonics, geologic evolution, and ore deposits: Arizona Geological Society Digest. 22:437-70

Loucks RR (2014) Distinctive composition of copper-ore-forming arc magmas. Australian Journal of Earth Sciences 61: 5–16. https://doi.org/10.1080/08120099.2013.865676

Lu YJ, Loucks RR, Fiorentini ML, McCuaig TC, Evans NJ, Yang ZM, Hou ZQ, Kirkland CL, Parra-Avila LA, Kobussen A (2016) Zircon compositions as a pathfinder for porphyry Cu ± Mo ± Au mineral deposits. Society of Economic Geologists Special Publication No. 19

Nagorsen-Rinke S, Lee J, Calvert A (2013) Pliocene sinistral slip across the Adobe Hills, eastern California–western Nevada: Kinematics of fault slip transfer across the Mina deflection. Geosphere 9(1):37-53

Nathwani C, Blundy J, Large SJE et al., 2024. A zircon case for super-wet arc magmas. Nature Communications 15: 8982. https://doi.org/10.1038/s41467-024-52786-5

Proffett JM (1977) Cenozoic geology of the Yerington District, Nevada, and implications for the nature and origin of Basin and Range faulting. Geological Society of America Bulletin 88 (2):247-266.

Richards JP (2011) High Sr/Y arc magmas and porphyry Cu±Mo±Au deposits: Just add water. Econ Geol 106 (7): 2075-1081. https://doi.org/10.2113/econgeo.106.7.1075

Stewart JH, Kleinhampl FJ, Speed RC and Johannesen DC (1984) Geologic map of the Little Huntoon Valley quadrangle, Mineral County, Nevada No. 84-503

Ferropyrosmalite-bearing fluid inclusions in the porphyry Cu-Mo deposits: A record of regional metasomatism in NW Turkiye

Gülcan Bozkaya[1], Ömer Bozkaya[1], Alfons van den Kerkhof[2], Graciela Sosa[2], David A. Banks[3]

1 Department of Geological Engineering, Pamukkale University, TR-20160, Denizli, Türkiye (gbozkaya@pau.edu.tr)
2 Geoscience Center, Georg-August-Universität Göttingen, Goldschmidtstrasse 3, D-37077 Göttingen, Germany
3 School of Earth and Environment, University of Leeds, LS2 9JT Leeds, United Kingdom

Abstract. Quartz segregations in paragneisses from the Biga Porphyry belt contain highly saline multiphase fluid inclusions with the rare daughter mineral ferropyrosmalite detected by Raman analysis, besides halite, sylvite, hematite, and/or magnetite. The amphibole-forming reaction from ferropyrosmalite and brine in the heated fluid inclusions is reported in the Biga Peninsula for the first time. The mineralizations is hosted within the local Permo-Triassic metamorphic/sedimentary rocks and Oligocene-Early Miocene granitoids in the Tepeoba Cu-Mo deposit. Ore-bearing veins and stockworks are developed within brecciated host rocks, consisting of quartz, chalcopyrite, pyrite, molybdenite, sphalerite, pyrrhotite and gold, with the later development of supergene goethite/limonite, malachite and azurite. Cathodoluminescence of quartz veins show multi-stage vein filling associated with the mineralization.

1.Introduction

Biga Peninsula, situated in Western Anatolia, shares a similar tectonic evolution with the broader region. It has undergone significant tectonic transformations from the Late Cretaceous to Early Miocene period. Following the Miocene, this compressional regime transitioned into an extensional tectonic regime, still oriented NS, leading to the development of several graben structures, including the Edremit, Kalkım, and Bayramiç grabens (Fig. 1).

Pre-Jurassic basement rocks of the region are subdivided into three principal units: Pre-Karakaya Complex, Kazdağ Group, and Karakaya Complex.

Pre-Karakaya Complex comprises low-grade metamorphosed metasedimentary rocks, represented primarily by the Kalabak Formation, along with intrusive igneous rocks. These lithologies are exposed north of Edremit and Havran. The metasedimentary assemblage is predominantly composed of phyllites and quartz-feldspar schists. These units are intruded by the Late Triassic Çamlık metagranodiorite in the eastern sector and by the Oligocene–Miocene Eybek granodiorite in the west.

Kazdağ Group constitutes a structurally complex anticlinorium and is composed mainly of various metamorphic rocks, including gneiss, amphibolite, and marble. These rocks have been intruded by Late Tertiary granitoids.

Karakaya Complex, also referred to as the Karakaya Formation, consists of a Lower Triassic, low-grade metamorphosed suite of diverse lithologies. These include metaconglomerate, arkosic metasandstone, quartzite, metasiltstone, slate, radiolarite, metamudstone, metaspilite, basic volcanic rocks, and diabase.

Porphyry Cu-Mo, porphyry Cu-Au, porphyry Au and porphyry Mo present in the Western Anatolian Province form distinct belts that are, from oldest to youngest and northernmost to southernmost, Tavşanlı, Biga, and Afyon-Konya porphyry belts. Porphyry Cu-Mo systems are the most common within the Tavşanlı porphyry belt where the oldest (pulse 1) plutonic rocks are exposed, while porphyry Cu-Au and porphyry Mo systems characterize the Biga porphyry belt where the second and third pulses are recorded.



Figure 1. The mineralization is hosted within the local Permo-Triassic metamorphic/sedimentary rocks and Oligocene-Early Miocene granitoids.

Ferropyrosmalite, the Fe-rich endmember of the pyrosmalite series [$(Fe,Mn)_8Si_6O_{15}(OH,Cl)_{10}$] (Yang et al. 2012), is a relatively rare phyllosilicate that occurs in different metal-bearing ore deposits and is intimately associated with metasomatic processes, mostly attributed to the presence of hypersaline hydrothermal fluids (Li and Naldrett 1993; Pan et al.1993; Borrok et al. 1998; Tazava et al. 1999; Hanley and Mungall 2003; Cepedal et al. 2003; Koděra et al. 2003; Wanhainen et al. 2012). Though commonly associated with actinolite, sulfides, chlorides, and iron oxides (Vaughan 1986; Pan et al.

1993; Dong and Pollard 1997; Koděra et al. 1998; Tazava et al. 1999; Hanley and Mungall 2003), robust constraints on ferropyrosmalite genetic conditions are still scarce. In this context, Koděra et al. (2003) proposed a retrograde reaction of clinopyroxene to ferropyrosmalite in saline fluid inclusions from altered granodiorites associated with a Fe-skarn deposit. Since the reaction between both minerals occurs at ca. 450°C, clinopyroxene might have been originally present as a daughter mineral but was subsequently replaced by ferropyrosmalite as part of a low-temperature equilibrium assemblage (Koděra et al. 2003).

2 Mineralization

Tepeoba Cu-Mo-Au deposit occurs at the southern side of the Eybek granodiorite complex of Miocene age. The area in which the deposit is located is characterized by Pb-Zn-Cu geochemical anomalies and by alternation of metasandstone, metamudstone and leucogranite, occurring at the southern margin of Eybek granodiorite. Microdiorite and aplite intruded the granite, granodiorite and sedimentary rocks (Fig. 2). Sedimentary rocks near the granite underwent contact metamorphism, represented by andalusite and biotite.



Figure 2: Aplitic vein cut through sulfide-bearing sillimanite (sil)-hornfels in alteration zone.

The deposit consists of hydrothermal breccia, including fragments of andalusite-biotite schist in a matrix of biotite. The deposit extends for 280 m southward with the maximum thickness of 80 m. The deposit was overturned with its top to the south during Miocene normal faulting, resulting in a full exposure of the hydrothermal alteration zones associated with the granodiorite-granite complex on the present surface. The ore veins contain mainly pyrite, chalcopyrite, molybdenite, sphalerite, pyrrhotite, rare native gold (Fig.3).

The alteration sequence in order of increasing proximity to mineralized breccia is a propylitic zone, which is characterized by small amounts of chlorite and pyrite, but by lack of distinct pyrite shell and K-silicate zone. This zone also contains biotite with chalcopyrite disseminations and quartz veins. Quartz veins associated with the K-silicate alteration contain halite or sylvite saturated polyphase inclusions. A muscovite zone occurs in the biotite schist above the breccia zone. Muscovite associated quartz veins also occur in the granite, overprinting on the K-silicate alteration.

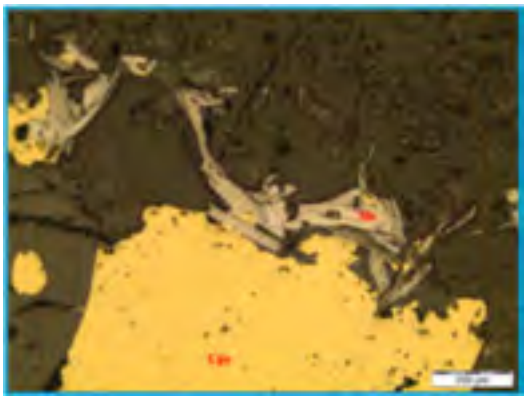


Figure 3. The ore veins contain mainly pyrite, chalcopyrite, molybdenite, sphalerite, pyrrhotite, rare native gold

3 Methodology

A detailed study of fluid inclusions from metamorphic quartz segregations of high- to medium-grade metasedimentary rocks was performed, combining fluid inclusion petrography, cathodoluminescence, microthermometry, and Raman spectroscopy (Pamukkale (Turkey) and Gottingen (Germany) Univ.). LA-ICP-MS and EBSD analyses were performed at Leeds University (UK).Sulfur isotopic compositions were measured on a Finnigan MAT-251 isotope mass spectrometer at the ACMELabs (Canada). Both the hydrogen and oxygen isotope analyses were performed on a MAT-253 EM spectrometer at the ACMELabs (Canada).

4 Results

Fluid inclusion assemblages hosted in quartz can be classified as liquid-rich (c.70 vol%), vapor rich (>70 vol%) and as containing multiphase inclusions. Halite and sylvite are common daughter phases together with several other solids, i.e., ferro-pyrosmalite, hematite, magnetite, pyrite, chalcopyrite and calcite, identified by Raman spectroscopy (Fig. 4). All the solid bearing inclusions have the same crystals in them. Phase transitions during microthermometry indicates an NaCl+ KCl+CaCl2 brine composition. Th of vapor-rich inclusions (CO2 and H2S) are ~370°C with a salinity of ~1 wt.% NaCl-equiv. salinity. Th for the V-phase disappearance ~300°C with salinity of ~9 wt. % NaCl-equiv. Halite dissolution temperature up to ~500°C and for hematite-bearing inclusions >600ºC,

with salinities of ~35 wt.% NaCl-equiv. LA-ICP-MS and EBSD analyses of solids in open inclusions, indicate the major components in the fluid are Na, K, Ca, and Fe, with significant, but lower concentrations of Cu, Au, Ag. The δ34S values of sulfides ranges from 2.3 to 2.7‰, consistent with a magmatic source of sulfur. Also δD, from -69 to -61‰ and $\delta^{18}O$ from 8.2 to 8.6‰ of fluid inclusions and quartz indicate a magmatic fluid source.

Re-Os ages of molybdenite are 25.03- 25.11 ± 0.14 Ma for the veins and 25.62 ± 0.09 Ma for the breccia, consistent with the age of the granite (Watanebe et al., 2003).

The combined data suggests that Tepeoba represents an extended porphyry-copper mineralization event at the Biga porphyry belt. The magmatic fluids produced both prograde and retrograde alteration of the host calcareous rocks and the development of a skarn-type deposits in the Biga Peninsula (NW Turkey).

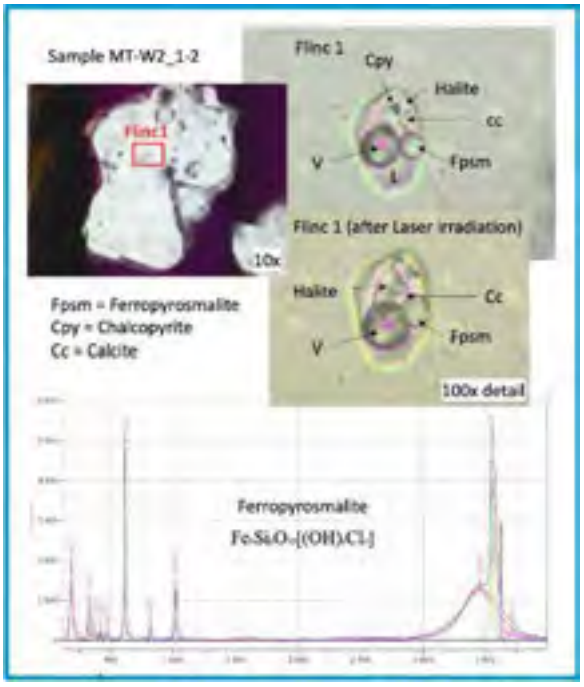


Figure 4: Multiphase fluid inclusion containing L+V, Fe-pyrosmalite (Fpsm), chalcopyrite (Cpy), calcite (Cc) and halite (H) identified by Raman spectroscopy

Acknowledgements

The authors would like to thank the Doğu Biga mining company (Balıkesir) for their permission to investigate.

References

Altree-Williams A, Pring A, Ngothai Y, and Brugger J (2015) Textural and compositional complexities
resulting from coupled dissolution-reprecipitation reactions in geomaterials. Earth-Science Rev 150, 628–651.

Apopei AI & Buzgar N (2010) The Raman study of amphiboles. Analele Ştiinţifice de Universităţii Al. I. Cuza Iaşi Geologie, 56, 57–83.

Aragón E, Castro A, Díaz-Alvarado J, and Liu D-Y (2011) The North Patagonian batholith at Paso
Puyehue (Argentina-Chile). SHRIMP ages and compositional features. Journal of South American Earth Sciences, 32, 547–554.

Assarsson GO (1950) The quaternary system CaCl2-
KCl-NaCl-H2O. Journal of the American Chemical Society, 72, 1433–1436.

Bakker RJ (2017) Re-equilibration processes in fluid inclusion assemblages. Minerals, 7, 117.

Banaszak M (2014) Differentiation regimes in the Central Andean magma systems:Case studies of Taapaca and Parinacota volcanoes, Northern Chile, 238 p. Ph.D. thesis, University of Göttingen, Göttingen.

Bechis F, Encinas A, Concheyro A, Litvak VD, Aguirre-Urreta B, and Ramos VA (2014) New age constraints for the Cenozoic marine transgressions of northwestern Patagonia, Argentina (41°–43° S): Paleogeographic and tectonic implications. Journal of South American Earth Sciences, 52, 72–93.

Behr H-J, and Frentzel-Beyme K (1987) Permeability and paleoporosity in crystalline bedrocks of the Central European Basement—Studies of cathodoluminescence. In H.J. Behr and C.B. Raleigh, Eds., Exploration of the Deep Continental Crust, 2, p. 477–497. Springer.

Bodnar RJ (2003) Introduction to aqueous electrolyte fluid inclusions. In I. Samson, A. Anderson, and D. Marshall, Eds., Fluid Inclusions: Analysis and Interpretation, 32, p. 81–100. Mineralogical Association of Canada, Vancouver.

Watanabe Y, Murakami H, Cengiz İ, Sarı R, Küçükefe Ş, Yıldırım S (2003) Study on Hydrothermal Deposits and Metallogeny in Western Turkey, Progress Report-1, MTA Report Archive Nr: 10614, 70 pp.

Distribution of mineralization in different lithologies of the Ochtiná – Rochovce W-Mo porphyry deposit (Western Carphatians, Slovakia).

Jana Brčeková[1], Peter Koděra[1], Rastislav Vojtko[2], Diego Delgado Yanez[1], František Bakos[3]
[1]*Department of Mineralogy, Petrology and Economic Geology, Faculty of Natural Sciences, Comenius University in Bratislava, Slovakia.*
[2]*Department of Geology and Paleontology, Faculty of Natural Sciences, Comenius University in Bratislava, Slovakia.*
[3]*Green View, s.r.o., Slovakia*

Abstract. Ochtiná-Rochovce W-Mo deposit occurs in the contact zone of Veporicum and Gemericum superunits in the Western Carpathians. Since 2015, the deposit is the subject of exploration activity, which provided data for our research. Based on a detailed mineralogical and geochemical study, criteria for the correct recognition of main rock types and the reinterpretation of inaccurate lithological data in the database were established. Subsequent statistical evaluation of the data and a new 3D deposit model indicate that phyllite and basic metavolcanics of the Ochtiná Formation usually have much higher W contents than sandstones of the Rimava Fm. There is no significant difference in W content between phyllite and metavolcanics. A significant variation of ore grades and the W/Mo ratio was observed in holes in N-S direction, while the central part of the deposit is the richest in both elements. In several holes there is a significantly elevated W content in their oxidised parts, especially if the oxidation zone is sufficiently thick (> ~20 m) and all sulphur is completely removed. Molybdenum becomes to be elevated only rarely.

1 Introduction

Ochtiná-Rochovce W-Mo deposit is the only known deposit of its kind in the Western Carpathians. This deposit was discovered in the 1980s by a government-funded drilling campaign, followed by a detailed exploration (Václav et al. 1988; Lörincz et al. 1993). Exploration found and calculated non-economic resources of 50.9 Mt of Mo ore and 7.4 Mt of W ore with 0.097 % Mo and 0.113 % W (Lörincz et al., 1993). Since 2015, the company Green View, s.r.o. continued in exploration of the upper part of the deposit. In total, 20 new drill holes (OV-1 – OV-20; Fig. 1 A) were drilled to a maximum depth 150 m. In contrast to the earlier drilling, these holes were inclined and mostly oriented to NW to intersect the Lubeník-Margecany line (LML). Exploration resulted in economic resources of 5.0 Mt of Mo ore and 2.4 Mt of W ore at a grade of 0.22 % for both metals (Bakos et al. 2016).

The deposit is located in the contact zone of Veporicum and Gemericum superunits, genetically linked to a Late Cretaceous monzodiorite to granodiorite intrusive complex

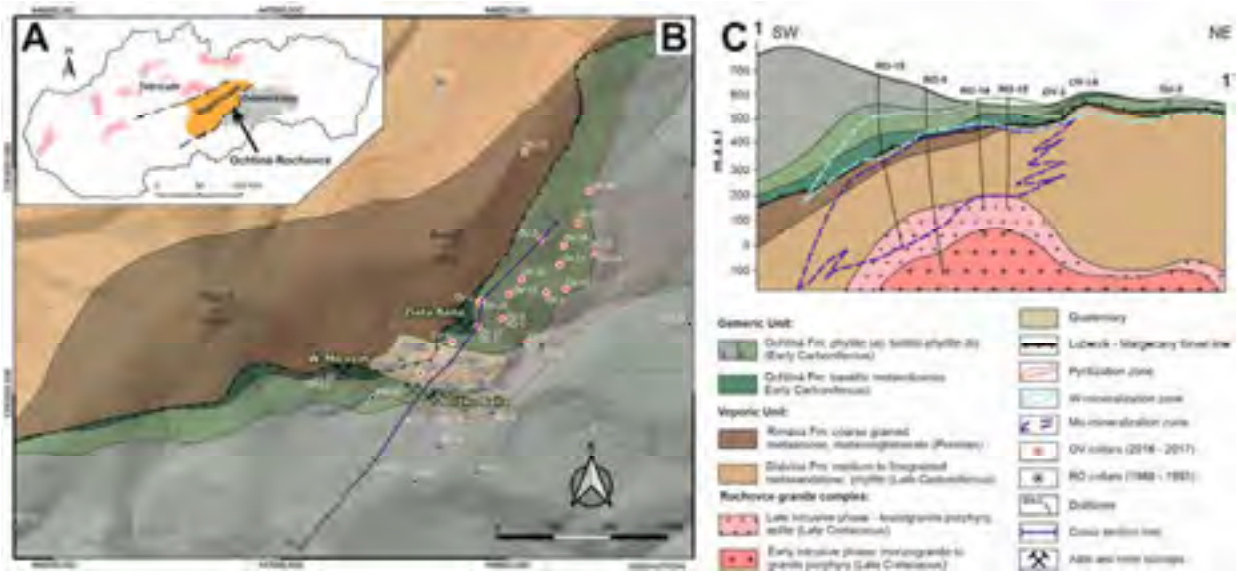


Fig. 1 Geological setting of the Ochtiná-Rochovce deposit (modified from Lörincz et al. 1993 using the data of GreenView, s.r.o). A. Main tectonic units of the Inner Carpathians in Slovakia with the position of the study area. B. Simplified geological map of the deposit. C. Simplified cross section of the deposit.

emplaced in the Lubeník-Margecany suture line in 3.7 to 7.5 km depth (Václav et al., 1988; Kohút et al., 2013; Fig. 1). According to SHRIMP U-Pb data on zircons from monzogranite and Re-Os dating of molybdenite, both are similar age (81.5 ± 0.7 and 81.4 ± 0.3 Ma, respectively; Kohút et al., 2013). The Gemeric Unit is represented by Lower Carboniferous mylonitized schists with intercalated conglomerates and frequent metamorphosed basalts and basaltic pyroclastics (Ochtiná Fm). The Veporic Unit comprises Permian metasandstone (Rimava Fm) and underlying Carboniferous metamorphosed sandstone/ graywacke and phyllite (Slatviná Fm). The deposit consists of two zones, which are partly overlapping (Fig. 1c). The lower Mo zone is ~400 m thick and occurs in 200 to 600 m depth, hosted partly by the endocontact of the granitoids, but mainly by the overlying Veporic unit. It is represented by molybdenite hosted by a stockwork of quartz veinlets. The upper W zone is ~100 m thick and reaches from surface to depths down to 300 m. It is represented by disseminated-stockwork and less frequent quartz veins in the Veporic and Gemeric units. Principal ore minerals are scheelite and less common wolframite in a quartz gangue (Lörincz et al. 1993).

The aim of this study is to provide reliable geochemical, mineralogical and textural criteria to recognise the main types of rocks, and to evaluate the distribution of mineralisation in individual lithologies in shallow part of the deposit.

2 Methods

Most of the samples used in this work come from the drilling survey of the company Green View, s.r.o., which also provided its survey database, containing standard drilling documentation, as well as 1700 semi-quantitative chemical analyses from 1 m or, more rarely, 2 m intervals of drill core (ALS laboratory, analytical codes ME-MS41 and W-ICP85). However, lithological documentation was often unreliable or missing due to difficult macroscopic identification of the rocks.

Detailed research was carried out on representative samples from boreholes, vein outcrops on the surface and in the Zlatá Baňa adit. Selected samples of fresh and variably hydrothermally altered rock were further evaluated by quantitative powder X-ray diffraction (XRD) and microcrobe analyses (WDS, EDS, SEM, BSE; ŠGÚDŠ, ÚVZ SAV, Friedrich-Schiller University Jena, Geozentrum Nordbayern). Semiquantitative chemical analyses provided by Green View, s.r.o. were complemented by more precise ICP-MS whole-rock analyses in Bureau Veritas labs (analytical code LF202).

Data provided by Green View were reinterpreted by results from mineralogical and geochemical research. Data from earlier exploration drilling (RO-1 – RO-19) were digitized from archive reports of Václav et al. (1988) and Lörincz et al. (1993).

The resulting database containing data from old explorations (Lörincz et al., 1993) and new drilling exploration (provided by Green View, s.r.o.) was used to create a 3D geological model of the deposit and refinement of the geological map in the vicinity of the LML (Fig. 1). A digital model of the relief in the form of a LiDAR (www.skgeodesy.sk) was used to define a surface boundary of the 3D model. GIS and 3D modeling were done using QGIS software and Leapfrog Geo software. Implicit RBF methodology was applied to 3D modelling of main lithologies, LML thrust fault and distribution of mineralization. The RBF algorithm employs interpolation functions to estimate values from known data and then geological surfaces are constructed as a part of the model-building process.

2 Results

2.1 Characteristics of the main lithological types

Phyllite of the Ochtiná Fm. (grey-green colour) is the most ubiquitous lithology in the studied holes, but mineral composition varies probably due to the primary variation from phyllite to biotitic phyllite and/or due to a variable incorporation of basic metavolcanics and products of hydrothermal alteration in the vicinity of veinlets. According to XRD analyses, unaltered phyllite is characterised by a well-developed foliation and by alternating layers rich in quartz and mica (muscovite and/or biotite). According to XRD analyses, variably altered phyllite contains quartz and muscovite accompanied by chlorite, K-feldspar, pyrite and minor amount of biotite and plagioclase.

Basic metavolcanics (dark green colour) are represented by metabasalts, basaltic tuffs and tuffites, intercalated with biotitic phyllite and rare lenses of metamorphosed ultrabasic rocks. Based on XRD analyses main minerals are amphibole, biotite, plagioclase, and quartz. In minor amounts, muscovite, illite-smectite,

pyrite, chlorite, pyroxene, titanite, epidote, and kaolinite are present.

Metasandstones of the Rimava Formation are of light gray to gray-green color, and are dominated by quartz, accompanied by less common muscovite, plagioclase, chlorite and biotite.

2.2 Reinterpretation of lithological logging

Characterization of main lithologies in the holes, combined with the database of semiquantitative chemical analyses of the holes, were used for reinterpretation of the original lithological logging by GreenView. Our precise ICPMS chemical and mineralogical data from individual lithological units were compared to the less precise analyses from the corresponding 1 or 2 m intervals in the holes, as well as to analyses from all intervals in all holes having similar chemistry and similar macroscopic appearance. Only three main lithologies, i.e. phyllite and basic metavolcanics of the Ochtiná Fm. and metasandstones of the Rimava Fm., were used for statistical processing of data. In some individual analyses or short intervals in the holes the affiliation was not entirely clear, such as phyllites with some metavolcanic component, therefore such intervals were filtered out, together with oxidized and transitional intervals between oxidized and unoxidized rocks, to avoid bias in the statistical processing. The statistical comparison showed that despite absolute concentrations of most elements in the semiquantitative analyses are significantly undervalued, their relative concentrations in individual lithologies are still sufficiently different and follow the same trend of relative enrichment or depletion as seen in the ICPMS data obtained in this work. It follows that the semiquantitative chemical analyses combined with their textural features enable to reliably recognize and differentiate the main lithologies at the deposit for most intervals in the holes. For example, basic metavolcanics can be distinguished from phyllites by significantly increased values of Al, Ca, Fe, Mg, Ti, Sr and V. Metasandstones, on the other hand, have very low contents of all analyzed elements. At this scale, hydrothermal alteration of rocks does not matter as it occurs just in the close vicinity of veinlets.

2.3 GIS and 3D modelling

The created 3D model of the deposit provides spatial representation of the subsurface lithological boundaries, LML surface and distribution of mineralization (Fig 2 A).

The model shows the course of the LML fault thrust, that dips of ~43° and an azimuth is ~132°. Compared to the earlier geological map of Lörincz et al. (1993), the surface projection of 3D lithological contacts enabled to recognize a shift of lithological boundaries as well as the main fault at the surface towards the north-west, especially in the north-eastern part of the deposit. This result was included in the modiefied geological map and cross section of the deposit (Fig. 1).

The model also enabled to visualize the distribution of W and Mo within individual lithological units in the shallow and deeper part of the deposit and their relationship to the position along to the LML fault.

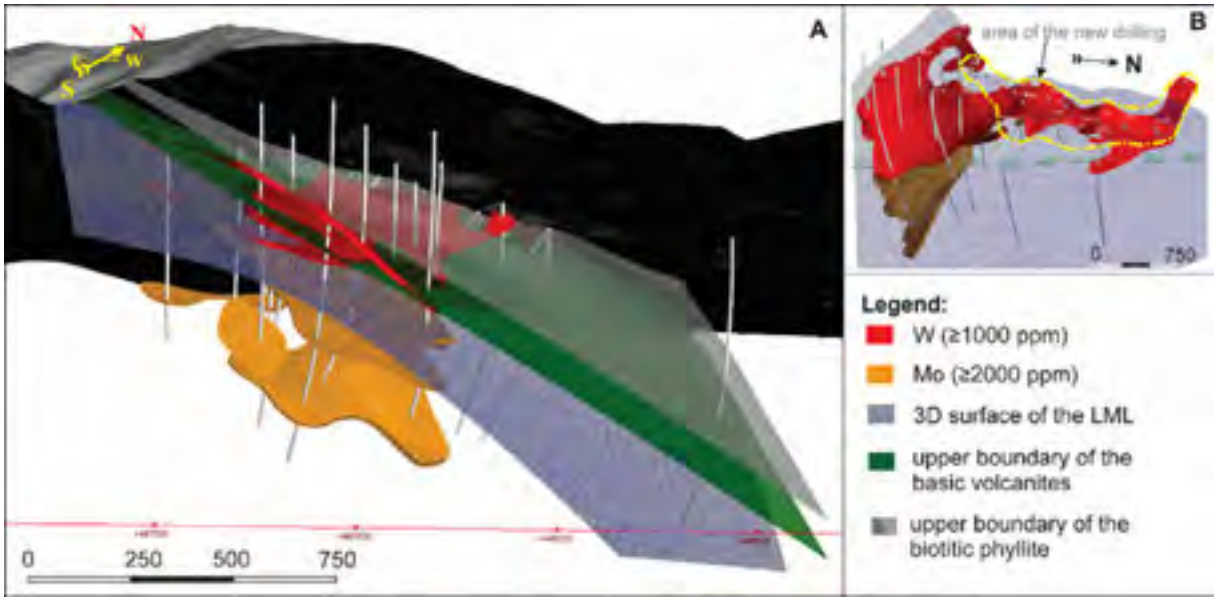


Fig. 2 3D model showing the location of W-Mo mineralization within lithological units (A) and along the surface of the Lubeník-Margecany thrust line (B, downer view to the west).

3 Distribution of mineralization

The corrected lithological logging of drill holes was also used for a reliable evaluation of distribution of ore mineralization and associated features within the different lithologies (Fig. 3). In general, phyllite and basic metavolcanics of the Ochtiná Fm. usually have much higher W content than metasandstones of the Rimava Fm. However, there is no significant difference in W content between phyllite and metavolcanics, although metavolcanics are richer in pyrite.

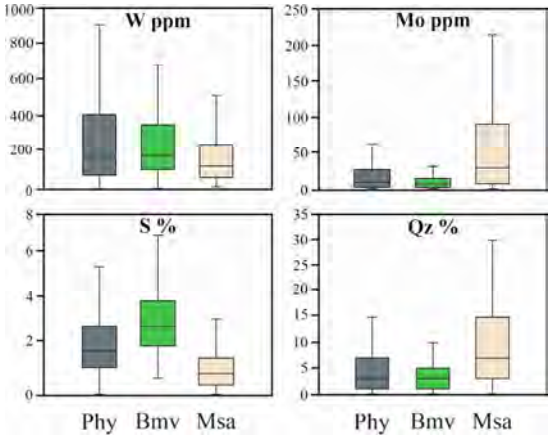


Fig. 2 Box-and-whisker plots showing distribution of W, Mo, S and quartz in the main lithologies: phyllites (Phy) of the Ochtiná Fm., basic metavolcanics (Bmv) of the Ochtiná Fm., and metasandstones (Msa) of the Rimava Fm. The edges of the boxes correspond to lower and upper quartile, the line within the box is median. The ranges of the data are shown by the whiskers.

In contrast, metasandstones usually have significantly higher Mo concentrations together with a high quartz content due to the common presence of quartz veins and accompanying silicification in these rocks. Nevertheless, pyrite (sulphur) content in metasandstones is significantly lower than in the other two main lithologies. The LML is not preferentially mineralized, although in some of the holes there is a significantly increased amount of pyrite and quartz veining.

In terms of spatial distribution of Mo and W around the LML, it was observed that the northmost holes usually have very low Mo contents in all lithologies even if W contents are elevated. In the central part of the area Mo is typically elevated in all lithologies and these holes are also usually the richest in W. The southernmost holes have high Mo content just in the metasandstones of the Rimava Fm and variable W contents in all lithologies.

In several holes there is a significantly elevated W content in their oxidised parts (sometimes up to several thousand ppm), especially if the oxidation zone is sufficiently thick (> ~20 m) and all sulphur is completely removed (e.g., OV-1a, 2, 5).

Molybdenum becomes to be elevated only rarely (OV-1a, 14, 18), sometimes it is even depleted in the oxidation zone (OV-7, 8, 12). However, the weathering profiles in some holes in the central part of the deposit were disturbed by a likely ancient landslide (Quaternary in Fig. 1b), thus the corresponding W and Mo analyses should be interpreted in this part with a caution. The landslide was recognized in both sets of drill holes by a sudden local increase in thickness of Quaternary debris, reaching up to 43 m.

Acknowledgements

Acknowledgement: This work was supported by the grant APVV-22-0134.

References

Bakos F, Jánošík M, & Sýkora M (2016) Final report with reserves calculations - Ochtiná W, Mo, Re mineralisation. GreenView report. (in Slovak)

Kohút M, Stein H, Uher P, Aimmerman A, Hraško L (2013) Re-Os and U-Th-Pb dating of the Rochovce granite and its mineralization (Western Carpathians, Slovakia). Geologica Carpathica, 64(1): 71–79.

Lörincz L, Švantnerová E, Bachňák M (1993) Final report: Ochtiná-Rochovce Mo, W, exploration survey, status at 30.9.1993. Geofond Bratislava, 225 p. (in Slovak)

Václav, J., et al., 1988: Prognostic evaluation of Mo-W mineralization south of Rochovice. Final report, Geofond Bratislava, 386 p. (in Slovak)

The Porphyry to Epithermal Transition: A 2025 Explorer's Perspective Toward Improving Discovery Rates

Vertrees 'Mac' Canby[1]
[1]*Senior Vice President Exploration, Freeport McMoRan Exploration Corporation, Denver, USA*

Abstract. Remarkable advances continue in expanding the empirical, genetic, and predictive links between porphyry deposits and spatially-related epithermal systems. Despite these advances and the continuing discovery of geologically 'blind' Cu-Au-Mo deposits within linked epithermal environments, rate of discovery of the economically-viable subset in this search-space struggles to keep pace with predicted increases in demand for porphyry-hosted metals, particularly Cu. Societal pressures against new large surface mines also continue to push exploration toward deeper environments. These trends underscore the importance of finding better predictive features for porphyry deposits, specifically the subset of high-grade end members. Rapidly improving, highly sensitive mass-analytical techniques and supporting data analytics, a widening range of concealment environments defined by new discoveries, and ability to digitalize and view data from historically-documented epithermal districts define three pillars with potential to transform our discovery rates. Making this transformation requires adaptation in our geologic workflows, exploration risk tolerance, willingness to collaborate across institutions and most importantly, our ability to attract motivated, collaborative, lateral-thinkers to industry and applied research.

1 The Challenge of Economic Discovery in the Porphyry-Epithermal Environment

Search for 'blind' porphyry deposits – those where ore is completely concealed by pre-ore rock - is increasingly important considering exploration maturity of the near-surface search space as well as mounting pressure against development of new large surface mines. Exploration focus on deposits in deeper, concealed geologic environments makes understanding of the porphyry-epithermal transition vital. Reliable criteria for identifying targets and assigning a probability of discovery, as well as the probability of ultimate economic viability of a discovery remain challenging. Explorationists and investors face a daunting statistic: economically-viable porphyry deposits - those that can support the massive initial capital requirements of standalone bulk underground mining operations - must be of exceptional grade. Such deposits comprise perhaps the top ~5% of the deposit class. Despite over six decades of exploration and actual discovery of immense metal endowments within blind porphyry systems, only a few percent of some fifty such discoveries have reached production as standalone/start-up underground operations that may increasingly typify the smaller-footprint mines of the future. These fifty or so blind discoveries themselves represent a subset of a much larger drill-tested population of targets. As the deeper portions of the known inventory of epithermal (particularly high-sulfidation) systems are rapidly being recognized and tested for their porphyry potential, we need both improved targeting tools and a widening range of target concepts to expand the physical and psychological search space beyond the obvious. A similar urgency exists for lowering the cost of bulk underground mining to bring a larger proportion of these discoveries into viability.

2 Emerging Tools for Transforming Discovery Rates

The growing inventory of blind porphyry discoveries as well as the explosion in analytical capability for geologic materials and related data analytics define a new era with potential to improve discovery rate. Three mutually-supporting pillars that will better define the porphyry-epithermal transition space are emerging: new detailed analytical methods and data-analytics applied at mass scale; a continually-widening range of concealment environments revealed by new discoveries; and ability to digitalize and assimilate large amounts of conventional historical data from long-recognized deposits and prospects worldwide.

Commercially-available, mass-scale analysis of geologic material via LIBS, XRF, XRD, spectral reflectance etc. has transformed what were once boutique, restricted analyses on limited sample volumes into exhaustive sets of uniformly-collected multi-variate data in three dimensions, and at wide ranges of granularity. Mines and advanced projects are increasingly generating large geochemical, mineralogical and rock-property data for ore- and waste-characterization. Application into greenfield environments will be most effective as large, three-dimensional arrays of key parameters accumulate in a growing number of ore deposits as well as from failed prospects. Second, learnings from several newly-discovered deposits – including some giants - demonstrate environments of remarkably abrupt transition between very weakly altered rock and adjacent large, high-grade porphyry systems. These give confidence that the search-space for blind porphyry deposits at shallow, economically-

reachable depths may be wider than currently recognized. Such examples provide guidance for future research in the linked epithermal-porphyry environment. Finally, the growing ability to digitalize conventional geo-data from historically- documented porphyry-epithermal occurrences provides a much sounder context for establishing empirical relationships between porphyry systems and their epithermal neighbors, even where genetic ties are still uncertain. Parameters as simple as the type and scale of metal endowments in related porphyry and epithermal systems may be critical to establish targeting criteria. Combining these three components has potential to transform our future discovery rate of economically-viable blind porphyry deposits.

Several focus areas are already evident which may best leverage these growing data sets and tools. Our concepts of a 'transition' between epithermal and porphyry deposits imply a genetic link and a continuity of time, space, and chemistry. Establishing better certainty of these links is a priority, so that genuinely diagnostic components can be distinguished from spatially coincident, geologically similar, but genetically-unrelated features – which the author believes are likely a major source of distraction of limited exploration resources. The 'open plumbing' of major porphyry metal districts commonly results in multiple and overlapping hydrothermal events, many of them barren yet ostensibly indistinguishable from – and often incorrectly attributed to - their productive neighbors. Intermediate-sulfidation systems, despite their widespread distribution around porphyry deposits, have received much less focus that high-sulfidation epithermal systems as proxies for adjacent porphyry deposits, and warrant more research at all scales. Increasingly sensitive geochronology will continue to be a major contributor to distinguishing productive pulses; detailed geochemical fingerprinting may continue to help distinguish and vector within distal 'escape features' back to their productive porphyry sources. To leverage these massive new data sets toward better discovery rates, strong collaboration and attracting a wider range of challenge-driven talent are key.

This talk reviews the parallel histories of porphyry-epithermal deposit discovery and research milestones, and some key recent takeaways; current key economic parameters determining viability of concealed porphyry deposits; emerging tools and a perspective on how to improve our discovery rates within the emerging knowledge-potential of the porphyry-epithermal transition .

Multi-million-year magmatic maturation preceding the formation of the supergiant Llurimagua porphyry Cu-Mo deposit (Western Cordillera, Ecuador)

Hugo Carrasco[1], Massimo Chiaradia[1], Alexey Ulianov[2], Maria Ovtcharova[1], Carlos Urrutia[3], Sergio Cubelli[3], Carolina Rodríguez[3], Angelo Aguilar[3], Juan Jaramillo[3], Hugo Narvaez[3], Yorki Patiño[3], Sergio Pichott[3]
[1]Department of Earth Sciences, University of Geneva, 1205 Geneva, Switzerland.
[2]Institute of Earth Sciences, University of Lausanne, 1015 Lausanne, Switzerland
[3]Corporación Nacional del Cobre de Chile (Codelco), Huérfanos 1270, Santiago, Chile.

Abstract. The Llurimagua Cu-Mo porphyry deposit (>10 Mt Cu) is hosted within the Miocene Apuela Batholith, the largest composite intrusive body in the Western Cordillera of northwestern Ecuador. LA-ICP-MS U-Pb zircon ages indicate a northward younging trend from ~24 to ~15 Ma. Younger magmatic pulses occurred following a period of compression (~15–13 Ma) associated with the impingement of the Carnegie Ridge at the trench. These pulses correspond to the emplacement of intermediate-composition plutons at ~12–13 Ma at Cuellaje and porphyries at ~8–9 Ma at Llurimagua. These intrusions predated the emplacement of the main felsic porphyry unit that hosts mineralization at ~7.5 to 7.0 Ma. The temporal evolution between ~17 and ~7 Ma is characterized by a progressive increase in whole-rock Sr/Y and Zr/Y fertility indicators over time, along with a gradual depletion of HREEs. This trend suggests prolonged lower crustal maturation driven by compression ± crustal thickening before the formation of Llurimagua.

1 Introduction

Cu-rich porphyry Cu deposits are the world's largest source of copper and a significant source of molybdenum and rhenium. These deposits form in syn-subduction settings associated with arc magmatism in thick continental crust (Richards 2009; Chiaradia 2020, 2022).

Supergiant porphyry Cu deposits (>10 Mt Cu) are often preceded by a prolonged increase in fertility indicators, a key characteristic of these systems (Chiaradia et al. 2009; Stern et al. 2011; Nathwani et al. 2021; Large et al. 2024). Understanding the temporal evolution of fertile magmatic systems from precursor intrusions (barren batholiths) to pre-, syn-, and post-mineralization porphyry pulses is critical for both exploration strategies and deciphering the controls on deposit size.

This study investigates the timescales and petrogenetic evolution of precursor and syn-mineral magmatism at the Llurimagua supergiant porphyry Cu deposit in the northern Western Cordillera of Ecuador, sampled from drillcores. To achieve this, we integrate LA-ICP-MS and ID-TIMS U-Pb zircon geochronology with whole-rock geochemistry, focusing on fertility indicators and REE patterns to assess their temporal evolution.

2 Geological settings

The Ecuadorian Andean margin is shaped by the subduction of the Nazca Plate beneath the thick continental lithosphere of the South American Plate (Fig. 1a). A key feature of this process is the subduction of major topographic asperities, such as the aseismic Carnegie Ridge and the Grijalva Fracture Zone (Gutscher et al. 1999).

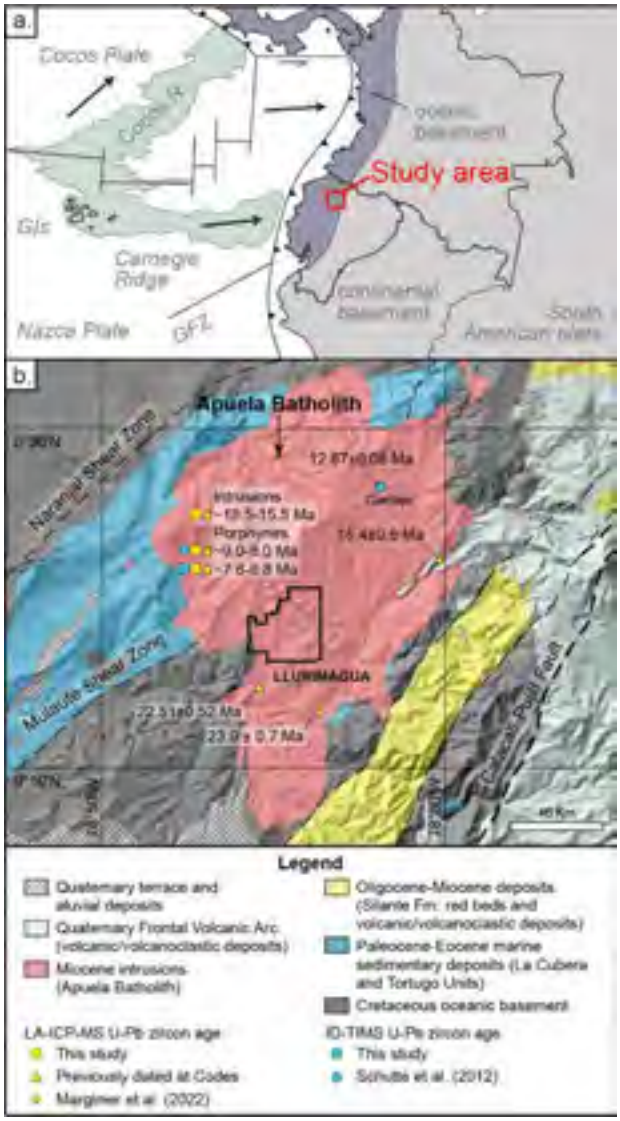


Figure 1. a. Geological setting of northwestern South America, highlighting the accreted oceanic basement in the northern Andes and the ongoing subduction of the Carnegie Ridge beneath the Ecuadorian continental margin (Gutscher et al. 1999). **b.** Simplified geology of the Apuela Batholith and the Llurimagua porphyry Cu deposit in the Western Cordillera of Ecuador (geology adapted from Boland et al. 2000), showing the available geochronological data.

The Apuela Batholith and Llurimagua porphyry Cu deposit are located in the northern part of the Western Cordillera of Ecuador (Fig. 1b). The Apuela Batholith is the largest intrusive body in this region, approximately 50 km long and 10–30 km wide. These units are exposed in a tectonic block bounded by the Calacalí-Pujilí Fault to the east and the Naranjal Shear Zone to the west (Boland et al. 2000). The basement of the Western Cordillera comprises allochthonous Cretaceous oceanic plateau rocks of the Pallatanga Formation, part of the Caribbean Large Igneous Province, which accreted onto the Ecuadorian margin during the Late Cretaceous (Goossens and Rose 1973; Vallejo et al. 2009; Spikings et al. 2024).

Locally, the Apuela Batholith crosscuts the Mulaute Shear Zone and intrudes Cretaceous marine sedimentary deposits of the Mulaute and Pilatón Units to the east, as well as Paleocene–Eocene marine sedimentary deposits of the La Cubera and Tortugo Units to the west (Fig. 1b). The southeastern margin of the batholith is tectonically juxtaposed against red beds, volcanic, and volcaniclastic deposits of the Oligocene–Miocene Silante Formation (Boland et al. 2000). Quaternary arc volcanoes, part of the Ecuadorian Frontal Arc, are located ~10–20 km west of the Apuela Batholith (Chiaradia et al. 2020). Granodiorites at Cuellaje and porphyry intrusions at Llurimagua crosscut the batholith, yielding ages of 12.87 ± 0.08 Ma and 9.01 ± 0.06 Ma, respectively (Schütte et al. 2010a).

3 Petrography of the intrusive units at Llurimagua

The freshest intrusive rocks of the Apuela Batholith, sampled from drill cores at Llurimagua, are tonalites composed primarily of plagioclase, quartz, and mafic minerals (Fig. 2a). Minor fine-grained interstitial albite is also present. However, quartzdioritic and granodioritic compositions have also been reported at different locations within the batholith (van Thournout et al. 1990; Boland et al. 2000; Schütte et al. 2010a). Three igneous units were identified based on texture, ranging from medium- to coarse-grained and varying in the proportions of hornblende and biotite. Sharp intrusive contacts were observed between distinct equigranular intrusive units. These units are locally crosscut by minor aplitic dykes.

The porphyry units within the deposit are highly hydrothermally altered, and intrusive contacts were not observed in the drill cores. The largest porphyry unit corresponds to a quartz-plagioclase porphyry, characterized by coarse- to medium-grained phenocrysts within a fine-grained aplitic groundmass (Fig. 2b). In thin sections, magmatic textures are preserved in samples that show albitization of plagioclase (Fig. 2b).

Two porphyry intrusions, namely, a coarse-grained quartz porphyry and a medium- to fine-grained porphyry, are texturally distinct from the main porphyry unit and yield older U-Pb zircon dates as outlined below. The coarse-grained quartz porphyry is locally crosscut by a mafic dyke that has been altered to secondary biotite.

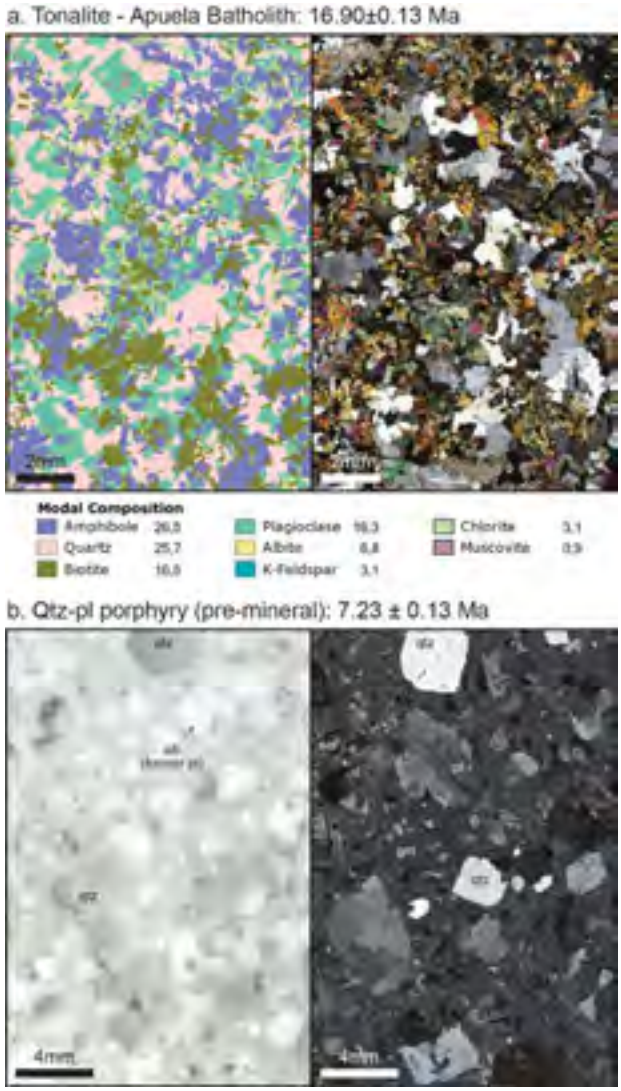


Figure 2. Photographs of representative rock samples. **a.** Tonalite LL8714, with a QEMSCAN false-colour mineralogical map on the left and an XPL micrograph on the right. **b**. porphyry LL1703, with a PPL micrograph on the left and an XPL micrograph on the right. Abbreviations: ab, albite; gm, groundmass; pl, plagioclase; qtz, quartz; ser, sericite.

4 Geochronology and geochemistry

LA-ICP-MS U-Pb ages of the Apuela Batholith from this study, unpublished data generated at CODES Analytical Laboratories, University of Tasmania, for Codelco, and previously published data (Margirier et al. 2023) indicate older ages of ~24 Ma in the south, ~18.5–15.5 Ma in central part (Llurimagua), and ~15.5 Ma at the northeastern margin of the batholith (Fig. 1b, Fig. 3a). Additionally, an ID-TIMS U-Pb zircon age of 12.87 ± 0.08 Ma from a granodiorite (Schütte et al. 2010a) at Cuellaje, in the north part of the batholith (Cuellaje), represents a younger magmatic pulse that intruded the batholith. This geochronological data suggests that magmatism within the batholith followed a northeastward

younging trend from ~24 to ~12 Ma, preceding the emplacement of pre-mineral porphyry units at ~8–9 Ma and ~7–7.5 Ma, which are spatially and temporally related to the formation of Llurimagua (Fig. 3b). Furthermore, ID-TIMS zircon ages, though more precise, overlap with LA-ICP-MS data (Fig. 3b). Two weighted mean ages were calculated from the same sample, the older age yielded ~7.6 Ma showing a deep zircon negative Eu-anomaly, while the younger one ~7.2 Ma lacks it, likely reflecting different magmatic conditions.

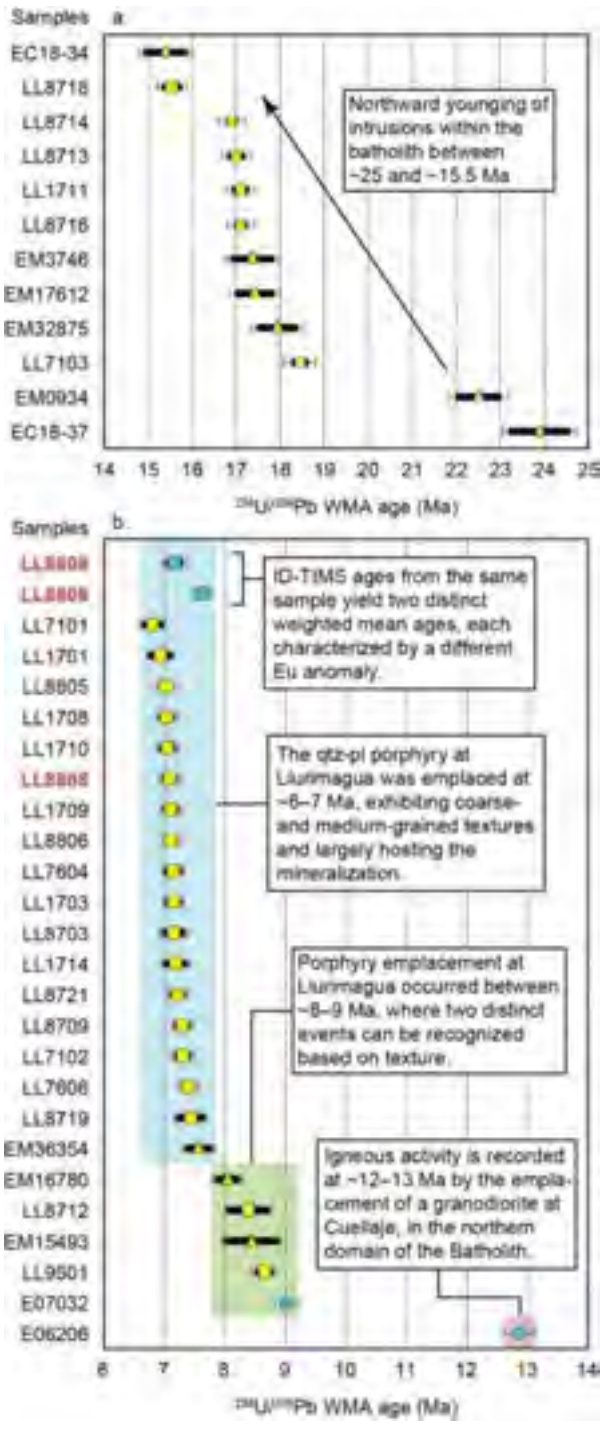


Figure 3a-b. LA-ICP-MS U-Pb zircon ages of the Miocene igneous units of the Apuela Batholith and Llurimagua.

To evaluate the chemical temporal evolution, we used whole-rock analyses from this study and compiled data from Schütte et al. (2010b), excluding samples with a loss on ignition (LOI) >2 wt.%. Immobile elements indicate that units from the Apuela Batholith, intrusions at ~12 Ma, and porphyry intrusions at ~8–9 Ma primarily have andesitic compositions, while the ~7–7.5 Ma porphyry intrusions are more evolved, exhibiting dacitic compositions (Fig. 4a; Winchester and Floyd 1977). Chondrite-normalized rare earth element plots (Fig. 4b-c; McDonough and Sun 1995) show LREE enrichment and variable MREE and HREE depletion, except in the ~7–7.5 Ma porphyry units, likely reflecting hydrothermal alteration effects on the REE spectra. A negative Eu anomaly is absent in all units except for the intrusions of the Apuela Batholith. An altered mafic rock (LOI = 3.32) that crosscut a ~8.6 Ma porphyry exhibits a basaltic-andesitic composition and a small negative Eu anomaly.

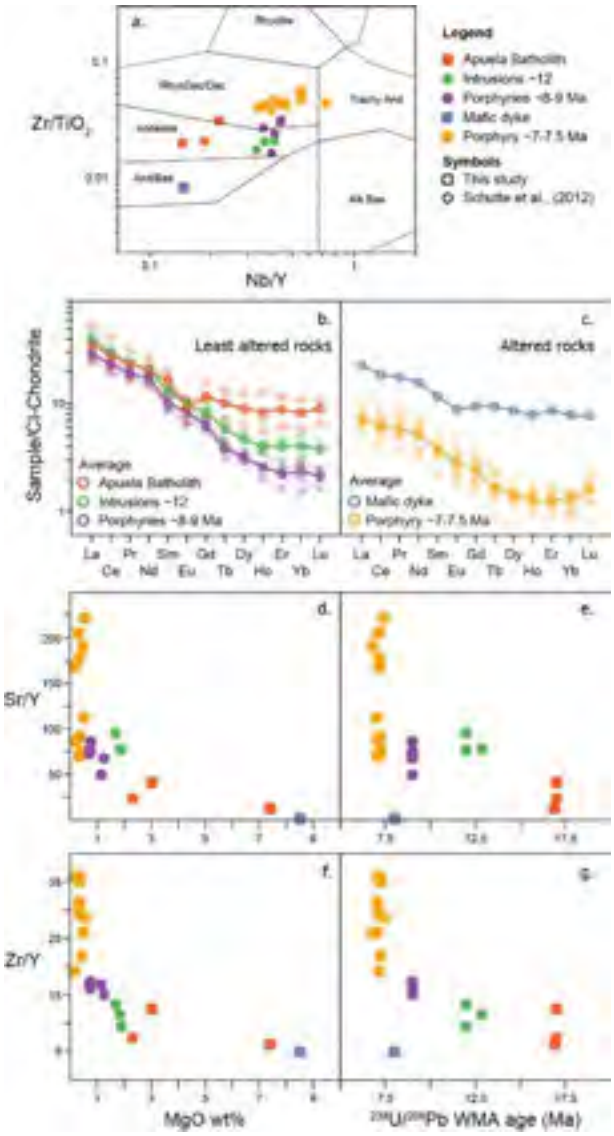


Figure 4. Whole rock geochemistry plots **a.** Discrimination plot of igneous rocks (Winchester and Floyd 1977). **b-c.** REE concentrations normalized to the CI-chondrite (McDonough and Sun 1995). **d-g.** Geochemical fertility proxies against MgO and U-Pb zircon ages

All these units define typical geochemical differentiation trends, with MgO positively correlating with FeO_T, TiO2, V, Sc, Y, and HREE (e.g. Dy and Yb). Furthermore, fertility proxies such as Sr/Y and Zr/Y increase as MgO decreases (Fig. 4d, f). Combining the geochemical and geochronological data reveals a temporal trend of increasing geochemical fertility proxies over time, showing a ramp-up in fertility indicator values over at least ~10 Ma, preceding the formation of the Llurimagua porphyry Cu deposits.

A temporal trend is also reflected in the REE compositions, where the Apuela Batholith exhibits the flattest REE spectra, followed by a progressive depletion of MREE and HREE with the emplacement of subsequent equigranular and porphyry intrusions.

This evolving magmatic system suggests prolonged lower crustal maturation, potentially linked to compressional tectonics ± crustal thickening associated with the subduction of the Carnegie Ridge. This interaction likely facilitated fractionation processes at deeper crustal levels, which stabilized garnet in addition to amphibole under high hydrous conditions.

4 Conclusions

The temporal and geochemical evolution of the Apuela Batholith and its associated porphyry intrusions during the Miocene suggests a protracted and progressively deeper magmatic maturation driven by compression ± crustal thickening, which ultimately led to the formation of the Llurimagua porphyry Cu-Mo deposit. The interplay of compression ± crustal thickening and prolonged magma maturation over millions of years is a key factor in the formation of porphyry Cu deposits.

Acknowledgements

We are grateful to CODELCO (National Copper Corporation of Chile) for funding this project. We also appreciate the collaboration and insightful discussions with the exploration teams at CODELCO and EMSAEC (Exploraciones Mineras Andinas Ecuador).

References

Boland M, Pilatasig L, Ibadango E, et al (2000) Geology of the Cordillera Occidental of Ecuador between 0°00′ and 1°00′ N. CODIGEM - British Geological Survey

Chiaradia M (2020) Gold endowments of porphyry deposits controlled by precipitation efficiency. Nature Communications 2020 11:1 11:1–10. https://doi.org/10.1038/s41467-019-14113-1

Chiaradia M (2022) Distinct magma evolution processes control the formation of porphyry Cu–Au deposits in thin and thick arcs. Earth and Planetary Science Letters 599:117864. https://doi.org/10.1016/J.EPSL.2022.117864

Chiaradia M, Merino D, Spikings R (2009) Rapid transition to long-lived deep crustal magmatic maturation and the formation of giant porphyry-related mineralization (Yanacocha, Peru). Earth and Planetary Science Letters 288:505–515. https://doi.org/10.1016/J.EPSL.2009.10.012

Chiaradia M, Müntener O, Beate B (2020) Effects of aseismic ridge subduction on the geochemistry of frontal arc magmas. Earth and Planetary Science Letters 531:115984. https://doi.org/10.1016/J.EPSL.2019.115984

Goossens P, Rose W (1973) Chemical Composition and Age Determination of Tholeiitic Rocks in the Basic Igneous Complex, Ecuador. GSA Bulletin 84:1043–1052. https://doi.org/10.1130/0016-7606(1973)84<1043:CCAADO>2.0.CO;2

Gutscher M-A, Malavieille J, Lallemand S, Collot J-Y (1999) Tectonic segmentation of the North Andean margin: impact of the Carnegie Ridge collision. Earth and Planetary Science Letters 168:255–270. https://doi.org/10.1016/S0012-821X(99)00060-6

Large SJE, Nathwani CL, Wilkinson JJ, et al (2024) Tectonic and crustal processes drive multi-million year arc magma evolution leading up to porphyry copper deposit formation in Central Chile. Journal of Petrology 65:. https://doi.org/10.1093/PETROLOGY/EGAE023

Margirier A, Strecker MR, Reiners PW, et al (2023) Late Miocene exhumation of the Western Cordillera, Ecuador, driven by increased coupling between the subducting Carnegie Ridge and the South American continent. Tectonics 42:e2022TC007344. https://doi.org/10.1029/2022TC007344

McDonough WF, Sun S s (1995) The composition of the Earth. Chemical Geology 120:223–253. https://doi.org/10.1016/0009-2541(94)00140-4

Nathwani CL, Simmons AT, Large SJE, et al (2021) From long-lived batholith construction to giant porphyry copper deposit formation: petrological and zircon chemical evolution of the Quellaveco District, Southern Peru. Contributions to Mineralogy and Petrology 2021 176:2 176:1–21. https://doi.org/10.1007/S00410-020-01766-1

Richards JP (2009) Postsubduction porphyry Cu-Au and epithermal Au deposits: Products of remelting of subduction-modified lithosphere. Geology 37:247–250. https://doi.org/10.1130/G25451A.1

Schütte P, Chiaradia M, Beate B (2010a) Geodynamic controls on Tertiary arc magmatism in Ecuador: Constraints from U–Pb zircon geochronology of Oligocene–Miocene intrusions and regional age distribution trends. Tectonophysics 489:159–176. https://doi.org/10.1016/J.TECTO.2010.04.015

Schütte P, Chiaradia M, Beate B (2010b) Petrogenetic evolution of arc magmatism associated with Late Oligocene to Late Miocene porphyry-related ore deposits in Ecuador. Economic Geology 105:1243–1270. https://doi.org/10.2113/ECONGEO.105.7.1243

Spikings R, Betancur S, Vallejo C, et al (2024) New constraints on the tectonic history of the basement of the Western Cordillera and coastal forearc of Ecuador. Lithos 488–489:107821. https://doi.org/10.1016/J.LITHOS.2024.107821

Stern CR, Skewes MA, Arévalo A (2011) Magmatic evolution of the giant El Teniente Cu–Mo deposit, Central Chile. Journal of Petrology 52:1591–1617. https://doi.org/10.1093/PETROLOGY/EGQ029

Vallejo C, Winkler W, Spikings RA, et al (2009) Mode and timing of terrane accretion in the forearc of the Andes in Ecuador. In: Kay SM, Ramos VA, Dickinson WR (eds) Backbone of the Americas: Shallow Subduction, Plateau Uplift, and Ridge and Terrane Collision. Geological Society of America, p 0

van Thournout, F, Quevedo, L, Pasteels, P, Boven, A (1990) Radiometric ages of igneous from northwestern Ecuador. Bulletin van de Belgische Vereniging voor Geologie

Winchester JA, Floyd PA (1977) Geochemical discrimination of different magma series and their differentiation products using immobile elements. Chemical Geology 20:325–343. https://doi.org/10.1016/0009-2541(77)90057-2

Reassessing the Schultze Granite, Arizona, USA: A New Temporal Framework for the Globe-Miami Magmatic-Hydrothermal System

Lawrence C. Carter[1,2], Robert G. Lee[3], Adam Gorecki[3], Dan Condon[4], David Selby[5], Holly J. Stein[6,7], Robert Creaser[8], Simon Chenery[4], Matthew Power[9], Benjamin Buse[10], Ester M. Jolis[11]
[1]LC Geoscience Ltd, Cornwall, UK
[2]Camborne School of Mines, Cornwall, UK
[3]BHP, Tuscon, Arizona, USA
[4]British Geological Survey, Keyworth, UK
[5]Durham University, UK
[6]University of Oslo, Norway
[7]AIRIE, Fort Collins, USA
[8]University of Alberta, Canada
[9]Vidence Inc., Burnaby, Canada
[10]University of Bristol, UK
[11]Geological Survey of Finland, Espoo, Finland

Abstract
Understanding of porphyry systems is fragmentary due to a paucity of exposed magmatic root-zones. Questions remain on how sufficient volumes of mineralizing fluids are focused, and over what timescales. To address this, we integrate results of field, micro-textural, geochemical and geochronological studies into a self-consistent 4-D framework for the Schultze Granite – previously interpreted as the exposed root-zone of the Globe-Miami porphyry district, Arizona. We show that mineralization within related deposits (Resolution, Pinto Valley and Copper Cities) occurred over a period of ~1.3 Myrs (~65.1-63.8 Ma), coincident with the age of a porphyry dyke at Pinto Valley (~64.5 Ma), but significantly pre-dates (by ~1-2 Myrs) emplacement of the Schultze Granite, which occurred rapidly (in <~600 kyrs, from ~62.6 Ma). The Schultze Granite did not therefore contribute to the formation of these deposits. Instead, the magma which formed it evolved and injected aplitic-porphyry dykes which underwent syn-emplacement first-type boiling and fluid exsolution to produce quartz USTs, miarolitic cavities and DQ & A-type quartz veins. Cu mineralization only occurred where and once these fluids cooled below ~600 °C. The aplitic-porphyry dykes served as fluid conduits for at least 400 kyrs, feeding ~1 Myrs (~62.5-61.5 Ma) of hydrothermal mineralization in the Ocelot-Old Dominion system.

1 Introduction

Even though porphyry deposits are amongst the most intensively studied of all mineralization types (Richards 2018), our understanding of their genesis is limited due a paucity of exposure, particularly of their deeper root-zones (Seedorff et al. 2008), and fragmented information on their timescales of formation. Consequently, it is unclear how sufficient quantities of magmatic-hydrothermal fluids are sourced and transported upwards into the ore-forming environment, and over what timescales.

We aim to provide fundamental constraints from our studies of the Schultze Granite which is temporally located within the Globe-Miami porphyry district in the Southwest United States. Detailed characterization of the granitic intrusion and its relation to porphyry-style mineralization will aid in the development of more reliable conceptual and exploration models.

The multiphase Schultze Granite (Figure 1) is located in the root-zone of the structurally dismembered Globe-Miami porphyry district, with both partly exposed due to tectonic tilting (e.g. Creasey 1980; Maher 2008; Seedorff et al. 2008). The granite was previously thought to have been the source of mineralizing fluids to the overlying porphyry deposits (e.g. Creasey 1980; Seedorff et al. 2008; Briggs 2022).

The root-zone has previously been characterised at a reconnaissance level, including the mapping of early “E” and main “M-J” phases of the granite as well as numerous phases of dyke intrusion and hydrothermal alteration (Figure 1; e.g. Creasey 1980; Stavast 2006; Maher 2008; Seedorff et al. 2008; Runyon et al. 2019). However, previous geochronological studies (Rb-Sr, K-Ar, and zircon LA-ICP-MS U-Pb) have been unable to adequately differentiate the sequence and timing of intrusion through the multiphase Laramide system, and did not directly address the timing of mineralization (Creasey 1980; Loader 2017; Seedorff et al. 2019).

The granite stock, dykes and associated veining therefore offers the opportunity to build a self-consistent geological, geochemical and geochronological framework detailing the nature and timing of the magmatic-hydrothermal transition, the exsolution and flow of mineralizing fluids, and to assess the timescales of hypogene mineralization.

2 Methods

The fundamental first-order controls for this study are from field observations, including cr0ss-cutting

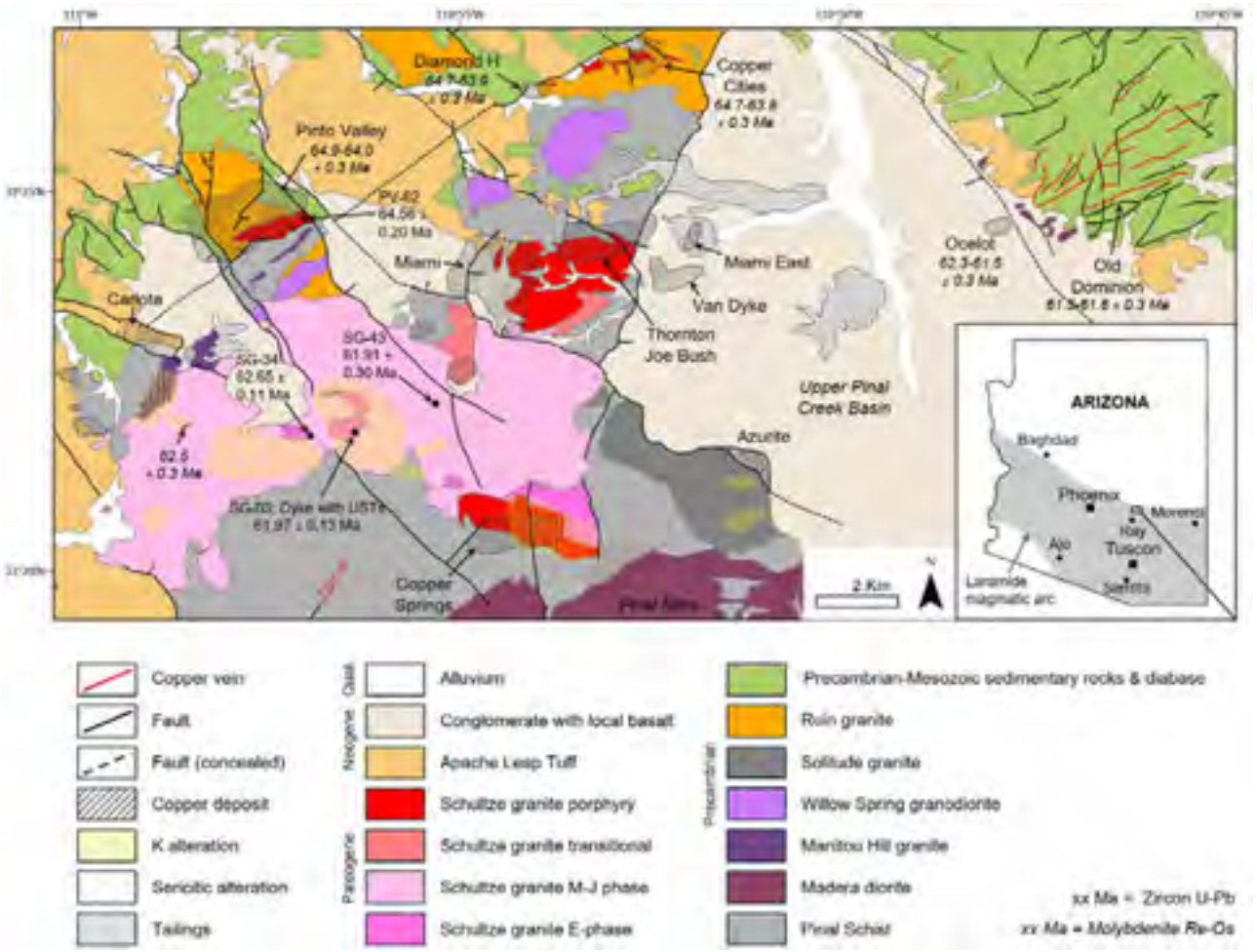


Figure 1. Simplified geological maps of the Globe-Miami district and the Schultze Granite, with major porphyry deposits highlighted. Geology from Creasey (1980), Stavast (2006) and Briggs (2022), alteration from Stavast (2006). Zircon U-Pb CA-ID-TIMS and molybdenite Re-Os ID-NTIMS age determinations are marked (2σ uncertainties). Named copper deposits denote historic and active mining as well as areas of known mineralization.

relationships, disequilibrium phenomena, textures indicative of fluid exsolution, and mineralization and alteration in outcrop across the Globe-Miami District, as well as from drill core from the Pinto Valley, Copper Cities and Ocelot porphyry copper deposits.

Based on these observations, key samples exhibiting magmatic-hydrothermal textures and mineralized quartz veins were chosen for micro-XRF mapping at the GTK and/or preparation as 30 µm thick polished sections. Following petrographic study, select samples were mapped using automated mineralogy at Vidence Inc., Canada, and micro-textures studied by SEM-EDS-CL at the University of Plymouth and University of Bristol, UK. The SEM-EDS-CL and mineralogical maps guided EPMA analysis at the University of Bristol to determine Ti and Al concentrations in different generations of quartz. The Ti-in-quartz geothermometer of Wark and Waston (2006) was used to estimate quartz crystallisation temperatures for select quartz grains, using quartz reference material detailed in Audétat et al. (2014) to determine analytical uncertainties.

Samples of different phases of the Schultze Granite as well as dykes that host magmatic-hydrothermal textures underwent whole-rock geochemical analysis at ALS (CCP-PKG05) and zircon separation at Zirchron Llc. The zircons were then hand-picked, prepared as polished blocks and imaged using a cold cathode CL microscope at Camborne School of Mines before being analysed by LA-ICP-MS at the British Geological Survey. Select zircon grains were then picked for high precision U-Pb CA-ID-TIMS geochronology at the British Geological Survey. Molybdenite samples from Pinto Valley, Diamond H, Copper Cities, Ocelot drill core and outcropping in the Schultze granite were analysed for Re-Os geochronology by ID-NTIMS at Durham University, the AIRIE program and the University of Alberta.

3 Key findings

Since complete cross-sections through the root zones of porphyry systems are rare (e.g. Seedorff et al., 2008), our new geological, geochemical and geochronological framework for the Globe-Miami porphyry district provides significant constraints for our understanding of magmatic-hydrothermal systems worldwide. Key findings include:

1) The Schultze Granite represents a batholith scale mid to upper-crustal magma chamber

through which porphyritic to aplitic dykes were emplaced into the upper crust releasing magmatic-hydrothermal fluids which produced porphyry copper deposits.

2) There is significant textural evidence (miarolitic cavities, quartz USTs, DQ and A-type quartz veins; nomenclature after Cernuschi et al. 2023 and Gustafson and Hunt 1975) (Figure 2) for the fluid-rich nature of the magmas which formed the aplitic porphyry dykes, and that these exsolved large volumes of mineralizing fluids. Upward fluid flow was at least partly via inter-crystal permeability in mush dykes (see Carter et al. 2021, Carter and Williamson 2024) which led to their funneling into narrow zones of high-grade porphyry mineralization.
3) Paragenetic study of magmatic-hydrothermal textures and mineralized quartz veins by SEM-EDS-CL and EPMA show that Cu sulfides are only associated with moderate and dull CL quartz with TitaniQ of crystallisation temperatures of <~600°C (Figure 3). This indicates that Cu sulfide precipitation did not occur until fluids cooled below ~600°C and/or redox conditions permitted (Sillitoe 2010; Cernuschi et al. 2023).
4) Whole rock geochemistry as a geochemical exploration indicator should be correlated with petrography and field sampling programs as variance can occur over meters depending on magmatic conditions at time of crystallization. With this approach, causative mush dyke generations which display evidence for exsolving and acting as conduits for magmatic-hydrothermal fluids can be geochemically differentiated from earlier intrusive phases.
5) New ages provide a higher precision temporal framework for the emplacement of the Schultze Granite and formation of porphyry copper deposits within the Globe-Miami district in Southwestern United States. Specifically, ~1.3 Myrs (~65.1 – 63.8 Ma) of mineralization at Resolution, Pinto Valley, Diamond H and Copper Cities is coincident with ~64.5 Ma porphyry dyke emplacement at Pinto Valley and pre-dates emplacement of the Schultze system, by 1-2 Myrs. The Schultze Granite forming melts were rapidly emplaced (<600 kyrs from ~62.6 Ma), with ~1 Myrs (~62.5-61.5 Ma) of associated hydrothermal mineralization at Ocelot and Old Dominion.

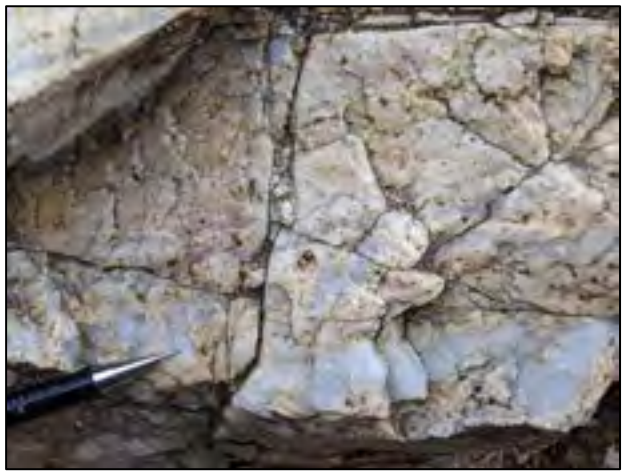


Figure 2 Quartz USTs in an aplitic porphyry dyke that cuts the Schultze Granite.

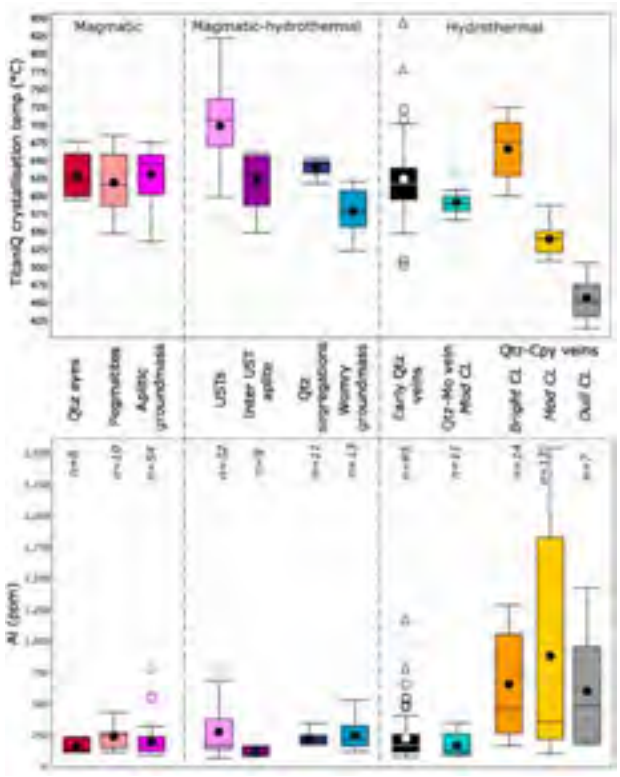


Figure 3. Box and whisker plots of TitaniQ thermometry and Al concentration determined EPMA analysis of quartz in magmatic, magmatic-hydrothermal and hydrothermal textures from across the system.

Acknowledgements

BHP is thanked for funding and supporting this research. L. Mahoney and G. Small are thanked for field support. T. Nahnybida, P. Devries and Capstone Copper are thanked for providing access to Pinto Valley. R. Leadbitter is thanked for thin section preparation and V. Valencia is thanked for zircon separation. Micro-XRF was supported by the Academy of Finland via RAMI infrastructure project (#337560). J. Berry is thanked for SEM support at University of Plymouth. A. Audétat is thanked for the piece of quartz reference material for EPMA analysis. C. Ottley and G. Nowell are thanked for laboratory support at Durham University. N. Caciagli, G. Cobenas, N. Januszczak, P. Lhotka, A. Rust, R. Loucks and J. Wilkinson are thanked for detailed discussions at various points of the project.

References

Audétat A et al. (2014) Characterisation of a natural quartz crystal as a reference material for microanalytical determination of Ti, Al, Li, Fe, Mn, Ga and Ge. Geostandards and Geoanalytical Research 39(2): 171–184. Doi: 10.1111/j.1751-908X.2014.00309.x

Briggs DF (2022) Geology and History of the Globe-Miami Mining Region, Gila and Pinal Counties, Arizona: Arizona Geological Survey Contributed Report CR-22-B, 243 p.

Carter LC and Williamson BJ (2024) Migration and focusing of porphyry deposit-forming fluids through aplitic mush of the Saginaw Hill cupola, Arizona, United States. Frontiers Earth Science 12, 1426111. Doi: 10.3389/feart.2024.1426111

Carter LC et al. (2021) Crystal mush dykes as conduits for mineralising fluids in the Yerington porphyry copper district, Nevada. Communications Earth & Environment 2, 59. Doi: 10.1038/s43247-021-00128-4

Cernuschi F et al. (2023). A Reevaluation of the Timing and Temperature of Copper and Molybdenum Precipitation in Porphyry Deposits. Econ Geol 118(5): 902-931. Doi: 10.5382/econgeo.5032

Creasey SC (1980) The Schultze granite, the Tea Cup granodiorite, and the Granite Basin porphyry: A geochemical comparison of mineralized and unmineralized stocks in southern Arizona. USGS Professional Paper 1303. doi: 10.3133/pp1303

Gustafson LB and Hunt JP (1975) The porphyry copper deposit at El Salvador, Chile. Econ Geol 70: 857–912. doi:10.2113/gsecongeo.70.5.857

Loader, M.A., 2017. Mineral indicators of porphyry Cu fertility. PhD thesis, Imperial College London.

Maher DJ (2008) Reconstruction of Middle Tertiary extension and Laramide porphyry copper systems, east-central Arizona. PhD thesis, University of Arizona.

Richards JP (2018) A Shake-Up in the Porphyry World? Econ Geol 113 (6): 1125-1233. Doi: 10.5382/econgeo.2018.4589

Runyon SE et al. (2019) Coarse muscovite veins and alteration in porphyry systems. Ore Geol Rev 113: 103045. Doi: 10.1016/j.oregeorev.2019.103045

Seedorff E et al. (2008) Root Zones of Porphyry Systems: Extending the Porphyry Model to Depth. Econ Geol 103: 939-956.

Seedorff et al. (2019) Temporal Evolution of the Laramide Arc: U-Pb Geochronology of Plutons Associated with Porphyry Copper Mineralisation in East-Central Arizona, *in* Geologic Excursions in Southwestern North America: Pearthree P. A., *ed.*, Geological Society of America Field Trip Guide 55: 369-400.

Stavast WJA (2006) Three-dimensional evolution of magmatic hydrothermal systems, Schultze granite and Ruby Star granodiorite, Arizona. PhD thesis, University of Arizona.

Wark DA and Watson EB (2006) TitaniQ: a titanium-in-quartz geothermometer. Contrib Mineral and Petrol 152 (6): 743–754.

Chronological framework for the magmatic-hydrothermal transition and mineralisation in the Yerington porphyry system, Nevada: A re-evaluation

Lawrence C. Carter[1,2], Simon R. Tapster[3], David Selby[4], Ben J. Williamson[2,5], Gavyn K. Rollinson[2]
[1]LC Geoscience Ltd, Cornwall, UK
[2]Camborne School of Mines, Cornwall, UK
[3]British Geological Survey, Keyworth, UK
[4]Durham University, UK
[5]University of Bristol, UK

Abstract
The timescales of extraction and focussing of sufficient volumes of mineralising fluids to form porphyry Cu(-Au-Mo) deposits remains unclear. Here, we provide fundamental constraints from detailed field, mineralogical, geochemical and geochronological studies of the classic Yerington porphyry-district of Nevada. Porphyry-type deposits are exposed in an exceptionally well preserved, ca. 8 km palaeodepth section which is now near horizonal due to Cenozoic extension and tilting. From high precision zircon U-Pb age determinations, the Luhr Hill granite cupola of the Yerington batholith and multiple generations of aplitic- and porphyry dykes, on which the porphyry-type deposits are centred, were emplaced within only a few 100 kyrs. Cu mineralisation within miarolitic cavities and USTs in the dykes, and associated quartz veins, was paragenetically late, not occurring until the fluids responsible had cooled below ~600 °C. From molybdenite Re-Os age determinations, hydrothermal mineralisation in the Bear and Ann Mason deposits was coeval with and much longer lived (>1 Myrs) than magma emplacement. We suggest that the early, high temperature fluids probably travelled up into the epithermal environment and possibly out of the system, and it was fluids from deeper, which had cooled over time, which moved up through highly permeable, partially crystallised 'mush' dykes which caused the hypogene mineralisation.

1 Introduction

Most models for porphyry deposit formation require direct release of mineralising fluids from magmas in stocks, cupolas, and/or dykes in the upper parts of magmatic systems (e.g. Dilles 1987; Cloos 2001; Richards 2005; Sillitoe 2010; Heinrich 2024). It is however difficult to reconcile how the vast volumes of fluids required to form porphyry deposits and associated alteration could be supplied from such small bodies of magma (Seedorff et al. 2005; Sillitoe 2010). Alternatively, they are suggested to be derived from a larger underlying magma chamber (e.g. Dilles 1987; Large et al. 2021), but the timescales during which they migrate and are focused into adequately narrow zones of mineralisation remains poorly understood. What has been established, from recent micro-textural (Carter et al. 2021; Cernuschi et al. 2023; Carter et al. 2024;), geochronological (e.g.; Chang et al. 2017; Li et al. 2017; Carter et al. 2022; Virmond et al. 2024) and numerical modelling studies (Chiaradia and Caricchi 2017; Gruzdeva et al. 2024), is that magmatic-hydrothermal mineralisation was much longer lived, and generally relatively late, compared with the interval of magmatism.

To address the current uncertainties, we study the classic Yerington Cu(-Mo-Au) porphyry district, Nevada, where Cenozoic extensional faulting and tilting has exposed a near horizontal, ca. 8 km palaeodepth, cross-section through the porphyry system, from volcanics down through a number of porphyry centres to their plutonic root zones (Proffett and Dilles 1984; Dilles 1987) (Figure 1). Evidence is preserved for the multiple emplacements of genetically associated plutons, generation of at least four porphyry deposits, the magmatic-hydrothermal transition, fluid pathways through aplitic porphyry dykes and subsequent hydrothermal mineralisation (Dilles 1987; Carter et al. 2021; Carter et al. 2022; Castellanos-Melendez et al. 2024).

Recent geochronological investigations have detailed the episodic assembly of the Yerington batholith (Carter et al., 2022; Castellanos-Melendez et al., 2024), but the timeline and duration of porphyry-style mineralisation remain poorly defined, leaving key aspects of the temporal framework unresolved. We integrate field and micro-scale textural observations, geochemical data, high precision zircon U-Pb CA-ID-TIMS ages for the plutons and dykes, and molybdenite Re-Os ID-NTIMS dates for molybdenite-bearing veins to assess the relative timing and duration of magmatism and porphyry-style mineralisation across the system.

2 Methods

Field observations and sampling of mineralised miarolitic cavities, unidirectional solidification textures (USTs) and quartz veins were undertaken across the Yerington District and several kilometres of drill core from the Ann Mason, Yerington, Bear and Ann Mason porphyry deposits. A subset of samples were prepared as polished thin sections for optical microscopy, QEMSCAN automated mineralogy, SEM-EDS-CL imaging and EPMA analysis at Camborne School of Mines, University of Exeter, UK. EPMA was undertaken to measure Ti concentrations in quartz, from which crystallisation temperatures were calculated using the TitaniQ geothermometer of Wark and Watson (2006). We assumed an $_{a}TiO_2$ of 0.7 given the common occurrence of titanite in the assemblage. To

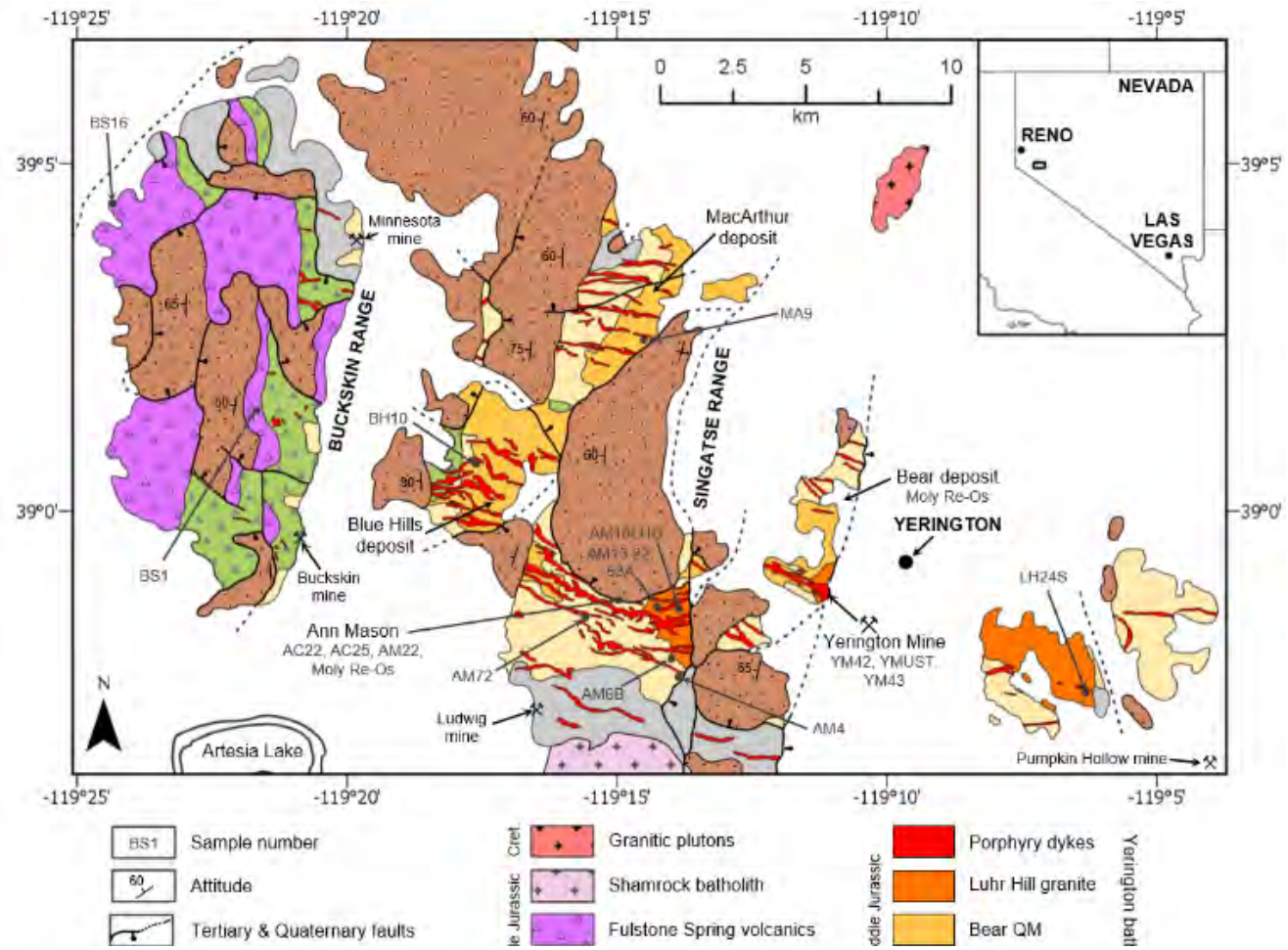


Figure 1. Simplified geological map of the Yerington District, Nevada, showing known major mineral deposits and localities sampled for zircon U-Pb CA-ID-TIMS and molybdenite Re-Os geochronology. Geology from Hudson & Oriel (1979), Proffett & Dilles (1984, and references therein) and Dilles & Wright (1988). QM = quartz monzonite, QMD =

supplement the recent geochronological data provided by Carter et al. (2022) and Castellanos-Melendez et al. (2024), selected porphyry dykes from the Ann Mason and Yerington deposits were chosen for high precision zircon CA-ID-TIMS geochronology at the Geochronology and Tracers Facility, British Geological Survey. Molybdenite in quartz veins and from fracture fills were sampled from drill core from the Bear deposit for molybdenite Re-Os ID-NTIMS age determination at Durham University, UK.

3 Results and Discussion

3.1 Emplacement of the magmatic system

Based on zircon U-Pb dates, emplacement of the Luhr Hill granite cupola and the aplitic- and porphyry dyke generations was extremely rapid. The timescale between cupola emplacement and early porphyry dyke emplacement is seemingly unresolvable by zircon CA-ID-TIMS geochronology (i.e. < ~100 kyrs). The age of subsequent aplitic- and porphyry dyke intrusions are resolvable but show multiple generations were emplaced within a few 100 kyrs. This extremely short timescale agrees with recent numerical simulations that illustrate the ascent of volatile-rich, porphyry mineralising, felsic magmas from the deep to shallow crustal levels (~30 to <10 km depth) can occur in just hours to days (Abdullin et al., 2024), almost instantaneously in geological time.

The extremely rapid rates of emplacement are also consistent with the magmatic-hydrothermal textures observed within the dykes, such as quartz USTs, that likely indicate intense undercooling as well as rapid pressure fluctuations within a dynamic environment (e.g. Kirwin 2005; Carter and Williamson 2002; Muller et al. 2023). In addition, from TitaniQ thermometry on quartz from the USTs, the temperatures of crystallisation are comparable with those of quartz phenocrysts in the Luhr Hill granite (Carter et al. 2021), and the host aplitic- and porphyry dykes, suggesting that these textures formed at or shortly after dyke emplacement.

3.2 Relative timing of hypogene mineralisation

From paragenetic studies of hypogene Cu mineralisation at Mason Pass, Ann Mason the Yerington mine, it occurred relatively late in the genesis of the Yerington magmatic-hydrothermal system. This is evidenced from mineralised miarolitic cavities, quartz USTs, and the aplitic groundmass

around these textures all containing bright CL quartz, which crystallised at magmatic temperatures (~700°C). Chalcopyrite is only associated with relatively late and cooler (<~600°C) dull CL quartz. This quartz forms networks around the bright CL quartz and healing micro fractures. Molybdenite appears both early and late in the hypogene assemblage, being associated with both bright and dull CL quartz. The likely cause of sulphide precipitation was a decrease in fluid (and therefore quartz crystallisation) temperature, although a change in redox and pH due to fluid mixing and/or wall-rock reaction cannot be ruled out (Sillitoe 2010; Cernuschi et al. 2023), hence a lack of mineralisation in the early/hotter magmatic-hydrothermal features. Cu-Fe sulphides only tend to precipitate where/once fluid temperature drops below ~600°C.

3.3 Re-Os constraints on timescales of mineralisation

Molybdenite Re-Os dates for quartz-chalcopyrite-molybdenite and quartz-molybdenite veins and molybdenite fracture coatings provide direct age constraints on the timing of hypogene mineralisation in the Bear deposit. The molybdenite Re-Os dates agree with those from Ann Mason (Carter et al. 2022) and are consistent with multiple hydrothermal events over a period of more than 1.8 Myrs, from 167.78 ± 0.08 Ma to 165.65 ± 0.37 Ma.

Molybdenite Re-Os dates from Bear and Ann Mason agree with zircon U-Pb dates combined with field constraints to place the onset of mineralisation in the Yerington batholith at ~167.5 Ma. Molybdenite Re-Os dates are also suggestive of multiple pulses of hydrothermal activity, but over longer timescales than granite and dyke emplacement. They overlap with the eruption of the Fulstone volcanics, around 1.5 Myrs after emplacement of the Luhr Hill granite cupola (Carter et al. 2022). That chalcopyrite-molybdenite mineralised quartz UST texture in an aplitic dyke yield relatively young molybdenite dates compared to quartz-molybdenite veins and molybdenite fracture fills at Ann Mason is further suggestive of multiple magmatic-hydrothermal events after emplacement of the Luhr Hill granite cupola. These findings align with other geochronological studies and numerical models of porphyry deposit formation which suggest that magmatic-hydrothermal mineralisation was much longer lived and generally relatively late compared with magmatism in the parts of the systems, occurring over periods in excess of 1.5 Myrs after emplacement of host magmatic rocks (e.g. Romero et al. 2010; Stein 2014; Spencer et al. 2015; Chang et al. 2017; Chiaradia and Caricchi 2017; Li et al. 2017; Carter et al. 2022; Gruzdeva et al. 2024; Virmond et al. 2024).

4 Implications of a long-lived magmatic-hydrothermal system

These observations and age determinations are suggestive of sustained fluid release and flow after the initial, rapid period of pluton and dyke intrusion. This relatively long episode of hydrothermal activity can be explained by ongoing processes focusing fluids from deeper, longer-lived portions of an open magmatic-system, probably involving percolative reactive flow (Blundy 2022) via supersolidus permeability in fluid-crystal mush (Carter et al. 2021; Carter and Williamson 2024). This allows for much larger volumes of fluids to be involved in mineralisation, and over much longer time periods, than assumed for closed systems.

The molybdenite Re-Os dates also confirm that mineralisation at Ann Mason and Bear was coeval. Given the petrographic, geochemical and geochronological consistencies between dykes from Ann Mason, Bear, Yerington and MacArthur (Dilles 1987; Carter et al. 2022; Castellanos-Melendez et al. 2024), it is most likely that mineralisation also occurred at the same time at Yerington and MacArthur. This suggests that mineralisation across all of the Yerington batholith's porphyry centres occurred within the same time frame, a key factor to be incorporated into any future numerical models for magmatic-hydrothermal fluid flow.

We suggest that these processes should be considered in all new genetic, exploration and numerical models for porphyry and similar types of magmatic-hydrothermal systems.

Acknowledgements

This work was supported by a NERC Isotope Geosciences Facilities grant [IP-1876-1118] and LC Geoscience Ltd, and was allied to the NERC Highlight Topic award 'From Arc Magmas to Ores (FAMOS): A Mineral Systems Approach' [NE/P017452/1]. We are thankful for field support and drill core access from T. Bonsall of Lion Copper Gold and M. Cunningham of Hudbay Resources (previously Mason Resources). S. Zahony is thanked for donating the UST sample from the Yerington Mine, reportedly collected by H. Ware in the 1970s. J. C. Andersen and S. Broom-Fendley (Camborne School Mines, University of Exeter) are thanked for EPMA support. A. Audétat is thanked for the piece of quartz reference material for EPMA analysis. SelFrag AG are thanked for use of their EPF device. A. Wood (British Geological Survey, Keyworth) is thanked for sample preparation. G. Nowell and C. Ottley (Durham University) are acknowledged for their analytical support.

References

Abdullin R et al. (2024) Ascent of volatile-rich felsic magma in dykes: a numerical model applied to deep-sourced porphyry intrusions. Geophysical Journal International 236(3): 1863-1876. Doi: 10.1093/gji/ggae027

Blundy J (2022) Chemical differentiation by mineralogical buffering in crustal hot zones. J Petrol 63: 1–36. Doi: 10.1093/petrology/egac054

Carter LC and Williamson BJ (2022) Textural indicators of mineralisation potential in porphyry magmatic systems - a framework from the archetypal Yerington District, Nevada. Ore Geol Rev 143, 104783. Doi: 10.1016/j.oregeorev.2022.104783

Carter LC and Williamson BJ (2024) Migration and focusing of porphyry deposit-forming fluids through aplitic mush of the Saginaw Hill cupola, Arizona, United States. Frontiers Earth Science 12, 1426111. Doi: 10.3389/feart.2024.1426111

Carter LC et al. (2021) Crystal mush dykes as conduits for mineralising fluids in the Yerington porphyry copper district, Nevada. Communications Earth & Environment 2, 59. Doi: 10.1038/s43247-021-00128-4

Carter LC et al. (2022) A rapid change in magma plumbing taps porphyry copper deposit-forming magmas. Sci Rep 12, 17272. Doi: 10.1038/s41598-022-20158-y

Castellanos-Melendez M.P. et al. (2024) From birth to death: The role of upper-crustal thermal maturation and volcanism in porphyry ore formation revealed in the Yerington district. EPSL 647, 119053. Doi: 10.1016/j.epsl.2024.119053

Cernuschi F et al. (2023). A Reevaluation of the Timing and Temperature of Copper and Molybdenum Precipitation in Porphyry Deposits. Econ Geol 118(5): 902-931. Doi: 10.5382/econgeo.5032

Chang J et al. (2017) Geological and chronological constraints on the long-lived Eocene Yulong porphyry Cu-Mo deposit, Eastern Tibet: implications for the lifespan of giant porphyry Cu deposits. Econ Geol 112(7): 1719–1746. Doi: 10.5382/econgeo.2017.4527

Chiaradia M and Caricchi L (2017) Stochastic modelling of deep magmatic controls on porphyry copper deposit endowment. Sci Rep 7: 44523. Doi: 10.1038/srep44523

Cloos M (2001) Bubbling magma chambers, cupolas, and porphyry copper deposits. International Geology Review 43: 285–311.

Dilles JH (1987) Petrology of the Yerington Batholith, Nevada: evidence for evolution of porphyry copper ore fluids. Econ Geol 82: 1750–1789.

Dilles JH and Wright JE (1988) The chronology of early Mesozoic arc magmatism in the Yerington District of western Nevada and its regional implications. GSA Bull 100(5): 644-652.

Gruzdeva Y, Weis P and Andersen C (2024) Timing of Volatile Degassing From Hydrous Upper-Crustal Magma Reservoirs With Implications for Porphyry Copper Deposits. Journal of Geophysical Research: Solid Earth 129: e2023JB028433. Doi: 10.1029/2023JB028433

Heinrich CA (2024) The Chain of Processes Forming Porphyry Copper Deposits—An Invited Paper. Econ Geol 119(4): 741–769. Doi: 10.5382/econgeo.5069

Hudson DM and Oriel WM (1979) Geologic map of the Buckskin Range, Nevada: Nevada Bureau of Mines and Geology, map 64.

Kirwin DJ (2005) Unidirectional solidification textures associated with intrusion related Mongolian mineral deposits, *in* Seltmann, R., Gerel, O. and Kirwin, D.J., eds., Geodynamics and metallogeny of Mongolia with special emphasis on copper and gold deposits: Society of Economic Geologists-International Association for the Genesis of Ore Deposits field trip, 2005: IAGOD guidebook series 11. London. (Centre for Russian and Central EurAsian Mineral Studies, Natural History Museum): 63–84.

Large SJE et al. (2021) Copper-mineralised porphyries sample the evolution of a large-volume silicic magma reservoir from rapid assembly to solidification. EPSL 563: 116877. Doi: 10.1016/j.epsl.2021.116877

Li Y et al. (2017) Cyclic magmatic hydrothermal evolution in porphyry systems: high-precision U-Pb and Re-Os geochronology constraints on the Tibetan qulong porphyry Cu-Mo deposit. Econ Geol 112(6): 1419–1440. Doi: 10.5382/econgeo.2017.4515

Müller A, Kirwin D and Seltmann R (2023) Textural characterization of unidirectional solidification textures related to Cu–Au deposits and their implication for metallogenesis and exploration: Mineralium Deposita 58: 1211–1235. Doi: 10.1007/s00126-023-01175-x

Proffett JM and Dilles JH (1984). Geological map of the Yerington District, Nevada: Nevada Bureau of Mines and Geology, map 77.

Richards JP (2005) Cumulative factors in the generation of giant calc-alkaline porphyry Cu deposits, *in* Porter, T.M., ed., Super porphyry copper and gold deposits: A global perspective, v. 1: Adelaide, PGC Publishing: 7−25.

Romero B et al. (2010) Molybdenite mineralisation and Re-Os geochronology of the Escondida and Escondida Norte porphyry deposits, Northern Chile. Resource Geology 61(1): 91-100. Doi: 10.1111/j.1751-3928.2010.00150.x

Seedorff E et al. (2005) Porphyry Deposits: Characteristics an Origin of hypogene Features. Econ Geol 100: 251-298.

Sillitoe RH (2010) Porphyry Copper Systems. Econ Geol 105: 3-41.

Spencer ET et al. (2015) The distribution and timing of molybdenite mineralisation at the El Teniente Cu-Mo porphyry deposit, Chile. Econ Geol 110(2): 387–421. Doi: 10.2113/econgeo.110.2.387

Stein HJ (2014) Dating and Tracing the History of Ore Formation, *in* Holland H.D. and Turekian K.K., eds., Treatise on Geochemistry, Second Edition, v. 13, Oxford, Elsevier: 87-118.

Virmond AL et al. (2024) Multi-million-year magmatic and hydrothermal activity is key to the formation of supergiant to behemothian porphyry copper deposits: Contrib Mineral Petrol 179: 88. Doi: 10.1007/s00410-024-02167-4

Wark DA and Watson EB (2006) TitaniQ: a titanium-in-quartz geothermometer. Contrib Mineral Petrol 152 (6): 743–754.

Exploring the apparent dominance of low Ti zircon in porphyry Cu deposits and its implications on the origin of zircon: perspective matters

Maria Paula Castellanos-Melendez[1], Michael Schirra[2], Marcel Guillong[1] and Olivier Bachmann[1]
[1]Department of Earth and Planetary Sciences, ETH Zurich, Switzerland
[2]Department of Geoscience, University of Nevada, Las Vegas, USA

Abstract. Zircon, considered a late accessory mineral in intermediate-felsic arc magmatism, is a common petrochronological tool in porphyry Cu deposits due to its resistance to hydrothermal activity. However, the depth and timing of zircon crystallization and its reliability as recorder of upper-crustal magmatic processes is currently debated. The apparent prevalence of low Ti zircon in porphyry dikes associated with Cu mineralization has led to suggest that extremely water-rich melts stored at mid- to lower-crustal depths are the source of the porphyry dikes and their zircon cargo. We explore the apparent dominance of low Ti zircon in porphyry systems and compile zircon geochemical data from porphyry Cu districts where the precursor magmatism is available. We show that when considering a larger portion of the magmatic system, zircon geochemistry could reflect an upper-crustal magmatic evolution that culminates in low Ti, low Th/U, high Hf and high Yb/Gd zircon in porphyry dikes. Since the occurrence of low Ti zircon in porphyry systems can be explained by fractional crystallization of an upper-crustal reservoir, the proposed deep origin of zircon and the resulting need for extraordinarily water-rich melts involved in porphyry Cu deposit formation are subject to further debate and should be considered with caution.

1 Introduction

Zircon in porphyry Cu deposits (PCDs) has been widely used as a pathfinder for fertile systems (Lu et al. 2016; Wilkinson et al. 2017) due to its robustness under hydrothermal alteration. Recently, geochemical modelling of Ti contents in zircon has been used to propose that the common low Ti zircon from porphyry dikes could be used as fingerprint of extraordinarily wet melts that saturate zircon at deep crustal levels (Nathwani et al. 2024), challenging the upper-crustal origin of zircon and with it the occurrence of long-lived upper-crustal magmatic reservoirs.

However, low Ti zircon is also common in plutonic and volcanic systems where zircon likely crystallizes at upper-crustal conditions (e.g., Wielicki et al. 2012; Troch et al. 2018; Castellanos-Melendez et al. 2024). Additionally, zircon trace element geochemistry in PCDs has been interpreted to record the upper-crustal evolution of the magmatic system that culminates in the felsic and low temperature melts of the porphyritic dikes (Large et al. 2021; Castellanos-Melendez et al. 2024). Considering these and further observations explored below that seem to contradict a deep origin of zircon in PCDs and, importantly, the limited sample suites in porphyry districts where the plutonic roots of porphyry dikes are inaccessible, we consider critical to re-visit the apparent prevalence of low Ti zircon in PCDs using available zircon geochemical data from districts where the precursor magmatism is accessible.

Our observations show that porphyry dikes record an ample range of zircon Ti contents with a significant overlap between the zircon in porphyry dikes and in the precursor plutons. Moreover, zircon geochemistry could reflect the upper-crustal magmatic evolution of a long-lived system from which late and low temperature melts, that form low Ti zircon, feed porphyry intrusions.

2 Materials and methods

Zircon trace element contents were compiled from available datasets from porphyry systems where a genetic connection between the PCDs and the surrounding plutons or batholiths has been established. Since the magmatic roots of PCDs are rarely accessible, only few districts display the desired scenario: Yerington, Bingham Canyon, Ok Tedi, Quevalleco and Rio Blanco – Los Bronces. Kernel density plots of Ti contents in zircon were obtained using IsoplotR (Vermeesch 2012) for zircon from both porphyry dikes and associated plutons. Generally, all units that post-date Cu mineralization were excluded. Additionally, Ti maps were obtained by LA-ICP-MS from zircon grains in porphyry dikes from the Yerington district. Titanium mapping was conducted using an ASI RESOlution excimer ArF (193 nm) laser ablation system coupled to a Thermo Fisher Element XR sector field ICP-MS by rastering a rectangular area with a slit size of 7x7µm, repetition rate of 20 Hz and sample fluence of 2 J/cm^2. The software Iolite4 (Hellstrom et al. 2008; Paton et al. 2011) was used for raw data processing, map construction and profile extraction using 15.2 wt% Si content in zircon as internal standard for Ti quantification.

3 Geological setting

When PCDs are found at the Earth's surface, the feeding magmatic system usually lies few kilometres beneath the mineralized stocks, at inaccessible depths (Sillitoe 2010). However, in few cases, PCDs are found surrounded by plutons genetically linked to the magmatic system that produced the mineralization. Five porphyry Cu districts were selected based on the availability of

zircon geochemical data from both, porphyry dikes and plutons or batholiths genetically linked to the hypabyssal units and are briefly introduced below.

The Yerington district, Nevada, USA, comprises a composite Jurassic batholith that has been tilted exposing up to 8 km paleodepth (Dilles 1987). The Jurassic magmatism initiated with the emplacement of the McLeod Hill quartz-monzodiorite, followed by the emplacement of the Bear and Luhr Hill plutons, of which the latter sourced the porphyritic dikes (Dilles 1987).

At *Bingham Canyon*, Utah, USA, an early equigranular monzonite represents most of the exposed intrusive phase and is shortly succeeded by four porphyritic dikes: a quartz-monzonite porphyry, a latite porphyry, a biotite porphyry and a quartz-latite porphyry. The main Cu mineralization is associated with the first two whereas the latter one is linked to the main Mo mineralization (Large et al. 2021 and references therein).

At *Ok Tedi*, Papua New Guinea, the geology of the intrusive units remains unclear. However, at the mine scale, two main intrusions (the Sydney and the biotite monzodiorite) are in direct association with the Fubilan monzonite porphyry. More distally, the Anju andesite intrusive phase is also associated with the Ok Tedi intrusive complex (Large et al. 2018 and references therein).

The *Quevalleco* deposit, southern Peru, is one of the three PCDs genetically linked to the composite Yarabamba batholith and locally to the Quevalleco granodiorite intrusive phase. Several porphyry dikes are identified in association with the Cu mineralization: an early granodiorite porphyry, two inter-mineral porphyries and a late porphyry that postdates most of the Cu (Nathwani et al. 2021 and references therein).

Finally, *Rio Blanco – Los Bronces* is the largest known Cu mining district and is hosted in stocks of the San Francisco Batholith. Various porphyry intrusions related to the Cu mineralization are distinguished as well as a post-mineralization porphyry intrusion (Deckart et al. 2012). Here, we use the terminology and zircon data reported in Nathwani et al. (2024).

4 Results and discussion

Available zircon geochemical data from porphyry dikes and the associated plutonic bodies in the reviewed districts show that Ti content in zircon vary from few ppm to up to 20 ppm Ti in porphyry dikes and up to 35 ppm Ti in the associated plutons with a significant overlap between the two groups and bimodal or complex distributions (Fig. 1). Importantly, the volume of data available from porphyry dikes and associated plutons is not directly comparable, resulting in distributions of Ti contents in zircon biased towards the porphyry dike population, which commonly represents the most voluminous dataset. In the case of Bingham Canyon, the more noticeable difference between the plutonic unit and the porphyry dikes could therefore be related to the scarcity of zircon data from plutons compared to porphyry dikes.

Trace element ratios in zircon like Th/U show a general decrease with decreasing Ti, used as a proxy for temperature (Watson et al. 2006), and increasing Hf. A singular general trend is present in all five districts and is built by a continuum between the zircon in plutons and the zircon in porphyry dikes. The zircons from the plutonic precursor magmatism reach higher Th/U ratios, lower Hf and higher Ti contents, whereas zircons in porphyry dikes extend to the lowest Th/U ratios, highest Hf and lowest Ti contents, with a significant overlap between the two groups (Fig. 2).

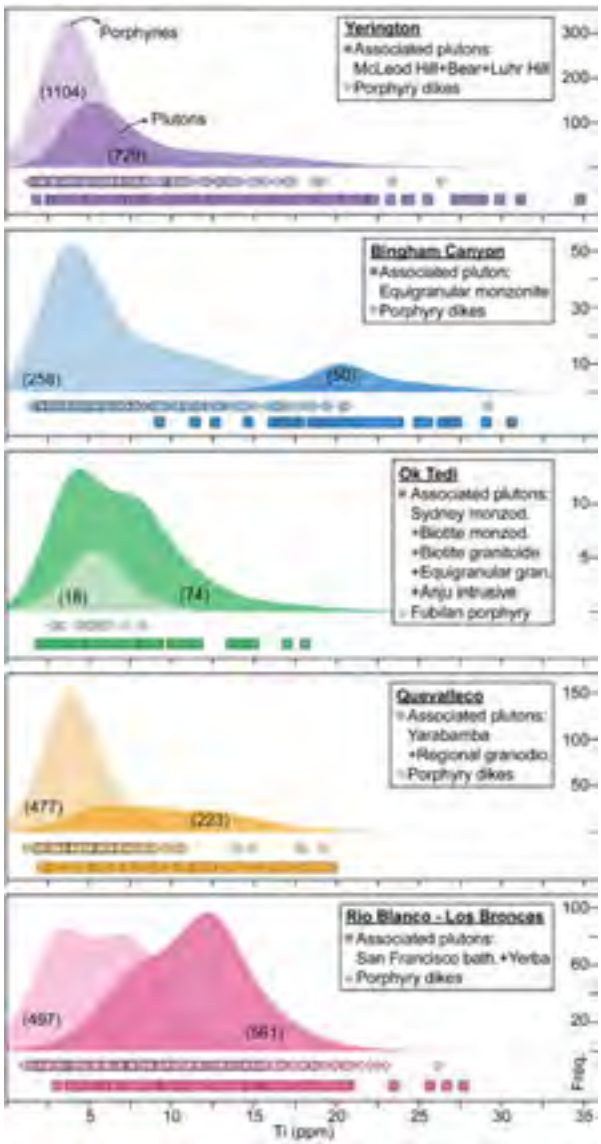


Figure 1. Kernel density curves of Ti content (ppm) in zircon from plutons and porphyry dikes from Yerington, Bingham Canyon, Ok Tedi, Quevalleco and Rio Blanco – Los Bronces. Data extracted from Castellanos-Melendez et al. (2024), Large et al. (2018, 2021); Nathwani et al. (2021, 2024), respectively. Individual data points are shown below the curves. Note the significant overlap between the Ti content in zircon from plutons associated to the porphyry Cu systems and the Ti content in zircon from the porphyry dikes.

The observed decrease in Th/U with decreasing Ti and increasing Hf content are indicative of zircon crystallization from a cooling and differentiating melt (Claiborne et al. 2010). Importantly, the strong overlap between the zircon from the precursor magmatism and the porphyritic dikes along a similar cooling trend suggests that the two zircon populations are part of a continuum in a magmatic system that evolved through time.

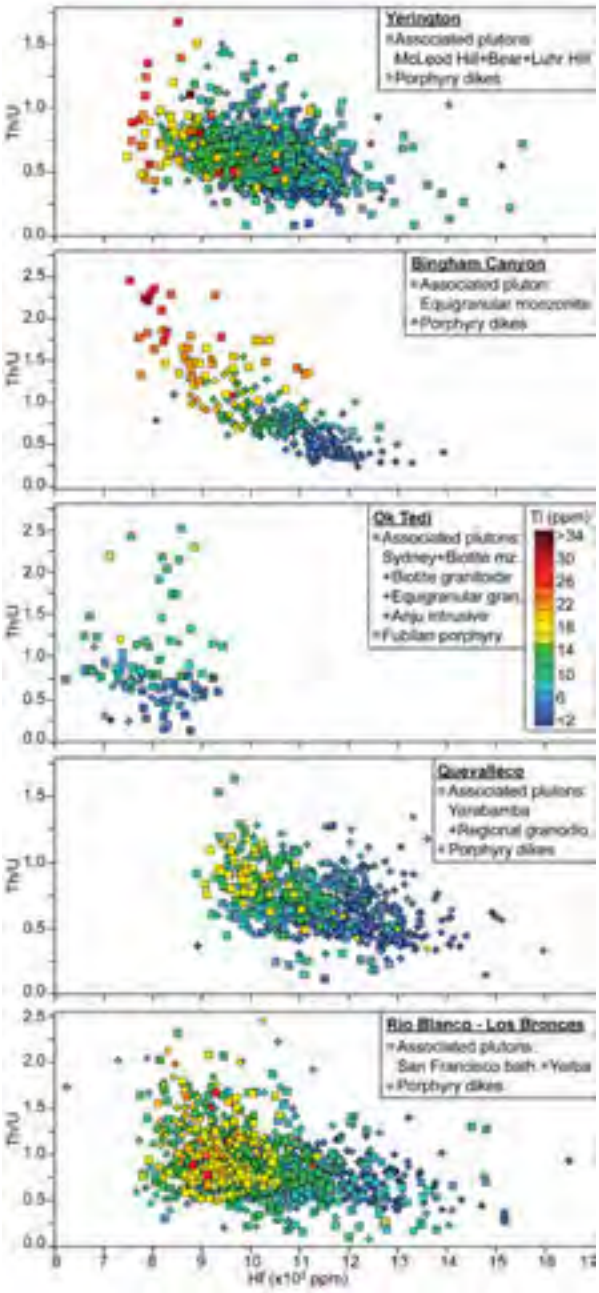


Figure 2. Th/U ratio versus Hf content in zircon from plutons and porphyry dikes from Yerington, Bingham Canyon, Ok Tedi, Quevalleco and Rio Blanco – Los Bronces. Symbols are colored based on their Ti content. Note the general trend of decreasing Th/U with decreasing Ti and increasing Hf content in each district. Data extracted from Castellanos-Melendez et al. (2024), Large et al. (2021, 2018); Nathwani et al. (2021, 2024).

Moreover, an increase in Yb/Gd ratio with decreasing Th/U and Ti content is also present in all districts and characteristic of an evolving magma that fractionates amphibole and titanite (Olson et al. 2017). The co-crystallization of zircon and titanite in the porphyry related magmas has been established at various porphyry Cu systems, for example, at Bingham Canyon and Yerington, where titanite is described as a late, low temperature mineral phase (Dilles 1987; Large et al. 2021; Castellanos-Melendez et al. 2024). These observations are in line with zircon being part of an upper-crustal fractionating assemblage.

Although thermal constraints have questioned the longevity of upper-crustal magmatic reservoirs, thermal modelling has suggested that after a thermal anomaly has been created due to the frequent injection of melt in the crust, long-lived upper-crustal magmatic reservoirs can be sustained (Karakas et al. 2017). Similar models for Bingham Canyon further support the establishment of an evolving upper-crustal magma reservoir that feeds porphyritic dikes (Large et al. 2021). Rare reverse zoning in Ti content in zircon from porphyry dikes (e.g., Large et al. 2021; Castellanos-Melendez et al. 2024) further supports the injection of hotter melts into the magmatic reservoir prior to porphyry dike extraction, which are needed to sustain a low crystallinity melt over long time periods (Bindeman et al. 2023).

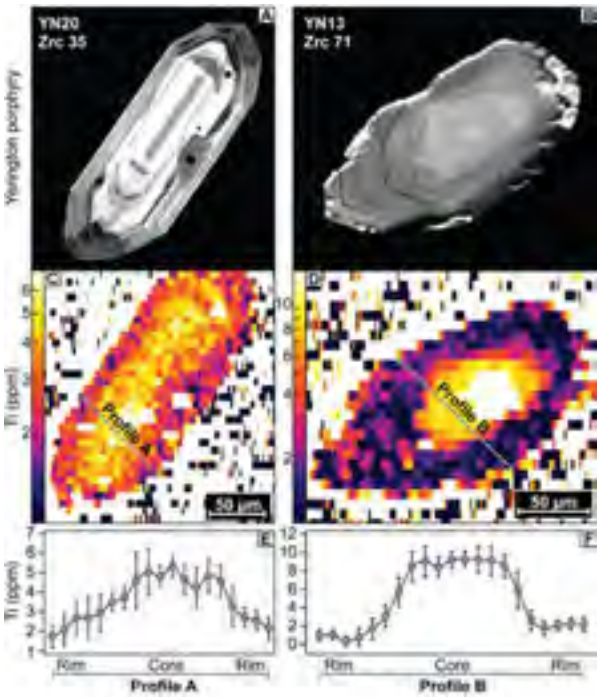


Figure 3. A and B) Cathodoluminescence image of zircon grains from porphyry dikes from the Yerington Cu district (Reported in Castellanos-Melendez et al. (2024)). C and D) LA-ICP-MS of Ti content (ppm) in zircon. Laser slit size of 7x7 µm. Note the decrease in Ti content towards the rim. E-F) Profile of Ti content across zircon grains extracted from the LA-ICP-MS. Final Ti content in zircon are expected to be ca. 10% higher that the reported values after applying the suggested correction on Ti concentrations of Szymanowski et al. (2018).

At the grain scale, changes in Ti content in zircon are preliminarily visualized here with Ti mapping by LA-ICP-MS of zircon grains from porphyry dikes from the Yerington district. Titanium maps show the general decrease in Ti content towards the rim expected during cooling (Fig. 3). Additionally, they exemplify the common variations in Ti within single zircon grains, contradicting the suggested dominance of homogeneous low Ti contents in zircon from porphyry dikes (Nathwani et al. 2024). Internal variations in Ti content in porphyry zircons have also been reported for systems like Ok Tedi and Bingham Canyon (Large et al. 2018, 2021).

The data reviewed here, and the Ti maps obtained from porphyry-dike zircon grains suggest that the zircon population in porphyry systems records the thermal history of the upper-crustal magmatic reservoir and the late stages of magma evolution and cooling. Since the porphyritic stocks are assumed to be extracted from highly evolved melts in an underlying magmatic reservoir (Sillitoe 2010), it is expected that the zircon record in porphyry dikes alone is biased towards the low temperature and evolved geochemical signatures. When the precursor magmatism is considered, however, it becomes more noticeable that the zircon cargo in porphyry dikes is part of a single fractionating trend that can characterize an evolving upper-crustal magmatic reservoir.

Based on our observations, we suggest that the proposed genetic link between low Ti zircon in PCDs and deep extraordinarily water-rich melts should be considered with caution. Instead, we favor an upper-crustal magmatic evolution as the simplest explanation to the available zircon geochemical data from porphyry Cu districts. This implies that super-wet melts may not play a first order control on PCD formation, in line with the more “normal” ~2-6 wt% H_2O contents suggested by Chiaradia (2020).

References

Bindeman IN, Melnik OE, Guillong M, Utkin IS, Wotzlaw JF, Schmitt AK & Stern RA (2023) Age of the magma chamber and its physicochemical state under Elbrus Greater Caucasus, Russia using zircon petrochronology and modeling insights. Sci Rep, 13:9733.

Castellanos-Melendez MP Dilles J, Guillong M, Bachmann O & Chelle-Michou C (2024) From birth to death: The role of upper-crustal thermal maturation and volcanism in porphyry ore formation revealed in the Yerington district. Earth Planet Sci Lett, 647:119053.

Chiaradia M (2020) How much water in basaltic melts parental to porphyry copper deposits? Front Earth Sci, 8:138.

Claiborne LL, Miller CF & Wooden JL (2010) Trace element composition of igneous zircon: a thermal and compositional record of the accumulation and evolution of a large silicic batholith, Spirit Mountain, Nevada. Contrib Mineral Petrol, 160:511-531.

Deckart K, Clark AH, Cuadra P & Fanning M (2013) Refinement of the time-space evolution of the giant Mio-Pliocene Río Blanco-Los Bronces porphyry Cu–Mo cluster, Central Chile: new U–Pb (SHRIMP II) and Re–Os geochronology and 40 Ar/39 Ar thermochronology data. Miner Depos, 48:57-79.

Dilles JH (1987). Petrology of the Yerington Batholith, Nevada; evidence for evolution of porphyry copper ore fluids. Econ Geol, 82:1750-1789.

Hellstrom J, Paton C, Woodhead J & Hergt J (2008) Iolite: software for spatially resolved LA-(quad and MC) ICPMS analysis. Mineralogical Association of Canada short course series, 40:343-348.

Karakas O, Degruyter W, Bachmann O & Dufek J (2017) Lifetime and size of shallow magma bodies controlled by crustal-scale magmatism. Nat Geosci, 10:446-450.

Large SJ, von Quadt A, Wotzlaw JF, Guillong M & Heinrich CA (2018) Magma evolution leading to porphyry Au-Cu mineralization at the Ok Tedi deposit, Papua New Guinea: Trace element geochemistry and high-precision geochronology of igneous zircon. Econ Geol, 113:39-61.

Large SJ, Buret Y, Wotzlaw JF, Karakas O, Guillong M, von Quadt A & Heinrich, CA (2021) Copper-mineralised porphyries sample the evolution of a large-volume silicic magma reservoir from rapid assembly to solidification. Earth Planet Sci Lett, 563:116877.

Lu YJ, Loucks RR, Fiorentini M, McCuaig TC, Evans NJ, Yang ZM et al. (2016) Zircon compositions as a pathfinder for porphyry Cu±Mo±Au deposits. In: Richards JP (ed) Tectonics and Metallogeny of the Tethyan Orogenic Belt, 1st edn. Society of Economic Geologist, Wyoming, pp 329-348

Nathwani CL, Simmons AT, Large SJ, Wilkinson JJ, Buret Y & Ihlenfeld, C (2021) From long-lived batholith construction to giant porphyry copper deposit formation: petrological and zircon chemical evolution of the Quellaveco District, Southern Peru. Contrib Mineral Petrol, 176:1-21.

Nathwani C, Blundy J, Large SJ, Wilkinson JJ, Buret Y, Loader MA et al. (2024) A zircon case for super-wet arc magmas. Nat Commun, 15:8982.

Olson NH, Dilles JH, Kent AJ & Lang, JR (2017) Geochemistry of the Cretaceous Kaskanak batholith and genesis of the Pebble porphyry Cu-Au-Mo deposit, southwest Alaska. Am Min, 102:1597-1621.

Paton C, Hellstrom J, Paul B, Woodhead J & Hergt, J (2011) Iolite: Freeware for the visualisation and processing of mass spectrometric data. J Anal At Spectrom, 26:2508-2518.

Sillitoe RH (2010) Porphyry copper systems. Econ Geol, 105:3-41.

Szymanowski D, Fehr MA, Guillong M, Coble MA, Wotzlaw JF, Nasdala L et al. (2018) Isotope-dilution anchoring of zircon reference materials for accurate Ti-in-zircon thermometry. Chem Geol, 481:146-154.

Troch J, Ellis BS, Schmitt AK, Bouvier AS & Bachmann, O (2018) The dark side of zircon: textural, age, oxygen isotopic and trace element evidence of fluid saturation in the subvolcanic reservoir of the Island Park-Mount Jackson Rhyolite, Yellowstone (USA). Contrib Mineral Petrol 173:1-17.

Vermeesch P (2012) On the visualisation of detrital age distributions. Chem Geol, 312, 190-194.

Watson EB, Wark DA & Thomas, JB (2006) Crystallization thermometers for zircon and rutile. Contrib Mineral Petrol, 151:413-433.

Wielicki MM, Harrison TM & Schmitt, AK (2012) Geochemical signatures and magmatic stability of terrestrial impact produced zircon. Earth Planet Sci Lett, 321:20-31.

Wilkinson JJ, Cooke DR, Baker MJ, Chang Z, Wilkinson CC, Chen H et al. (2017) Porphyry indicator minerals and their mineral chemistry as vectoring and fertility tools. GSC.

Alunite characterization of high sulfidation epithermal deposits in the Vicuña District, Argentina-Chile

Leticia González Castellote[1], Elizabeth Holley[1]
[1]Center to Advance the Science of Exploration to Reclamation in Mining, Department of Geology and Geological Engineering, Colorado School of Mines, 1516 Illinois Street, Golden, Colorado 80401, USA

Abstract: The Vicuña District is located along the Argentina-Chile international border, within the metallogenic belt of the same name, connecting the Maricunga belt in the north and El Indio belt in the south. This study focuses on the Filo del Sol (FDS) and Lunahuasi (LN) Cu-Au-Ag projects, hosted in high sulfidation epithermal and porphyry environments. Both projects occur along a NNE structural-alteration trend that extends over 13 km, share similar host-rock and alteration pattern, but differ on main mineralization styles. In general, at FDS, chalcocite, covellite, enargite, pyrite and, chalcopyrite with Au and Ag mineralization is disseminated. Conversely, at LN the mineralization forms massive veins with pyrite and enargite plus Au and Ag. Multiple occurrences of alunite are documented along the NNE structurally controlled trend. Alunite morphology and geochemistry have been attributed to different formation environments, including hydrothermal and supergene. At depth some alunite is associated with high sulfidation state sulfides, whereas other alunite preceded the mineralization. This ongoing study documents mineralogical, geochemical and geochronological features of alunite occurrences at FDS and LN. These observations provide initial clues to understand the relationship between mineralization and alteration patterns that later might vector mineral exploration in the district.

1 Introduction

The Filo del Sol and Lunahuasi Cu-Au-Ag deposits (latitude 28°29´24´´ and longitude 69°39´36´´) are part of a NNE corridor of porphyry and high sulfidation epithermal deposits and prospects, informally named Filo del Sol-Los Helados Corridor, that runs along the international border between Argentina (San Juan and La Rioja provinces), and Chile (Atacama region), at elevations between 4,000 m and 5,500 m.

These deposits belong to the Vicuña District or the Vicuña Belt (Perelló et al. 2023). The Vicuña Belt extends 40 km north-south and 10 km east-west. Geochronologic results indicate that the Vicuña Belt ranges in age from Late Oligocene to Middle Miocene, linking the Maricunga belt (23 – 12 Ma) in the north and El Indio belt (12 – 4 Ma) in the south (Fig. 1).

Within the Vicuña Belt, principal deposits discovered to date are Filo del Sol, Los Helados, Josemaría, Caserones and the recently added Lunahuasi deposit. Numerous other prospects and exploration targets with varying degrees of geologic understanding are also present in the belt.

This area corresponds to a region characterized by the inversion of extensional faults defining the uplift of blocks from the Permo-Triassic basement. The main thrust responsible for this tilting is the El Potro fault (in the west), causing the uplift of the horst where El Potro-Toro is located. The other main structural corridor is located to the east of the



Figure 1. Location of the Vicuña District, and Filo del Sol and Lunahuasi projects. a) Vicuña metallogenic belt, between the Maricunga and the El Indio belt with location of mineral deposits. b) Detailed geology of Filo del Sol and Lunahuasi area. Modified from Sillitoe et al. (2019)

district, defined as the Mogotes-Angosturas system fault. These main structures control a system of NNE regional faults in the district (Los Helados, Ventanas, Portezuelo and other faults) related to a belt of Miocene intrusive and hydrothermal events (Los Helados porphyry ~13 Ma, Portones porphyry ~13 Ma, Josemaría porphyry ~25 Ma). Filo del Sol and Lunahuasi intrusion were emplaced between ~18 to ~12 Ma (internal company report, unpublished).

Filo del Sol and Lunahuasi share similar alteration styles, with strong advanced argillic alteration. The main assemblages includes residual quartz, alunite, pyrophyllite, dickite, kaolinite, and minor zunyite and topaz. The mineral association is variable across the different targets of the deposit, as well as the alteration intensity, depending on the original host rock.

The advanced argillic and argillic alteration correlates with the high sulfidation mineralization,

represented by chalcocite, covellite, enargite, pyrite and chalcopyrite with associated Au and Ag.

Different types of alunite have been identified in the advanced argillic alteration throughout the district. These can be classified based on their mineral paragenesis, crystal habit, grain size, color, spectral curve, and stable isotope values. Furthermore, Ar/Ar and K/Ar dating analysis on alunite in the district revealed a decreasing age trend from south to north, from ~15 Ma to ~ 8 Ma (internal company report, unpublished).

This ongoing study aims to characterize the alunite (age, composition, texture, relation to mineralization), with the objective of distinguishing pre-mineralization alunite, mineralization-related alunite, and post-ore or late-stage alunite (Deyell et al. 2005; Holley et al. 2016), in order to provide insight useful for continuing exploration.

2 Regional geology

The Vicuña district is in the Andean Cordillera between 28°11´ to 28°32´ south latitude. This belt is part of a north trending Late Oligocene to Middle Miocene magmatic arc that is the northern boundary of the present-day Chilean-Pampean flat-slab segment (~27° - 33° S). The Maricunga belt in the north contains many porphyry Au, porphyry Cu-Au and high sulfidation epithermal Ag-Au deposits (Vila and Sillitoe 1991). To the south, the El Indio belt is dominated by high sulfidation epithermal Au-Ag deposits (Bissig et al. 2001; Charchaflié et al. 2007; Holley et al. 2016).

The regional geology of the district is dominated by fault-bounded blocks of Permo-Triassic volcano-plutonic rocks. The igneous rocks, mostly granitic and monzogranitic composition, are assigned to the Choiyoi group, a large igneous province that extends from northern Chile through the Cordillera Frontal of Argentina and Chile and southwards as far as Argentinian Patagonia (Sato et al. 2015).

The Permo-Triassic basement features an unconformity, overlain by a Mesozoic to Tertiary volcano-sedimentary sequence, including volcaniclastic breccias and conglomerates, with variable composition, grain size and angularity of the clasts. Continental volcanic rocks and associate terrigenous strata of Late Eocene to Early Miocene are preserved only locally on the Chilean side of the frontier, but are more widespread farther east in Argentina, where they occupy structurally defined basins (Panteleyev and Cravero 2001; Sillitoe et al. 2019).

Various Oligocene to Miocene intrusions are present throughout the Vicuña belt, as well as isolated intrusions of Eocene age.

3 Deposit geology: Filo del Sol and Lunahuasi

The Permo-Triassic units of the Choiyoi group, both intrusive and extrusive facies, represent the oldest rocks at Filo del Sol and Lunahuasi deposits. The intrusive facies is typically coarse-grained monzogranite, granodiorite to diorite. The volcanic facies of the Choiyoi group are mostly rhyolite, tuff, lapilli tuffs, banded rhyolites and volcanic breccias. These rocks exhibit two main textures: fragmental and porphyritic, while aphanitic and ignimbrite rhyolites are observed locally. Some zones with pyroclastic textures showing fluidal features, consistent with extrusion (internal company report, unpublished).

Above the Permo-Triassic basement unconformity, the volcano-sedimentary sequence comprises conglomerates, volcanic breccias, and irregular andesite, with a likely Late Cretaceous age. Ash-flow tuffs of dacitic to rhyolitic composition are also present.

At Filo del Sol, mafic bodies, including stocks, dikes, sills, and minor intrusives, of pre-Miocene age (Perelló et al. 2023), intrude the volcano-sedimentary sequence. At Lunahuasi, stocks and dikes of diorite to quartz diorite composition also intruded the volcano-sedimentary sequence (internal company report, unpublished).

Igneous intrusions are grouped by composition (dacitic and andesitic) and age and are related to the main mineralization in the Filo del Sol area. This aspect for Lunahuasi is not defined yet.

Regarding the alteration, Filo del Sol exhibits a high sulfidation overprint on preexisting porphyry-style alteration. Perelló et al. (2023) defined two principal alteration types: early, deep potassic alteration and shallow advanced argillic alteration. Intervening zones of white micas overprint the shallow portion of potassic alteration at Filo del Sol.

At Lunahuasi, the alteration represents a typical vein-hosted high sulfidation system, with alteration halos that gradually transition outwards from the veins: massive sulfides and fine quartz in the nucleus of the vein, dickite – alunite and vuggy quartz or fine grain quartz, illite – smectite and kaolinite; and outward to chlorite – epidote – pyrite.

The mineralization style differs in these two deposits: at Filo del Sol, alteration is related to multiple events of high sulfidation epithermal Cu-Au-Ag that overprinted a Cu-Au porphyry deposit, followed by supergene processes and enrichment. The main mineralization is disseminated with, chalcocite, covellite, enargite, pyrite, chalcopyrite, bornite, Ag-As-Sb sulfosalts and a variety of Ag-bearing sulfides.

At Lunahuasi, the mineralization is hosted by veins that follow structures which are subvertical and strike north-south to north-northeast, with well defined features, typical of a high sulfidation system. The sulfides are characterized by a massive to semi-massive nature with minor dissemination, principally pyrite and enargite, and subordinant chalcocite and covellite. Locally tennantite (replacing enargite) and chalcopyrite occur, indicating an intermediate sulfidation evolution (NGEx Minerals Ltd, NI 43-101 report).

4 Results

This study is primarily focused on characterization of alunite. Fieldwork consisted of surface and drill core sampling of multiple targets along the trend, followed by SWIR (Short Wave Infrared) analysis using an ASD-Terraspec device to ensure the purity of the alunite. Associated minerals and the alunite composition was determined (the latter from the 1480 nm absorption feature for Na – K – Ca). Most of the alunites in this study have a potassic composition; with a few samples dominated by a sodic composition.

Polished sections of the collected samples were analyzed under a transmitted light microscope, allowing the classification of alunites into two main groups: massive and disseminated alunite. These groups can be subdivided based on the grain size: massive fine alunite, massive coarse + fine alunite, disseminate fine alunite and disseminated coarse alunite (Fig. 2).

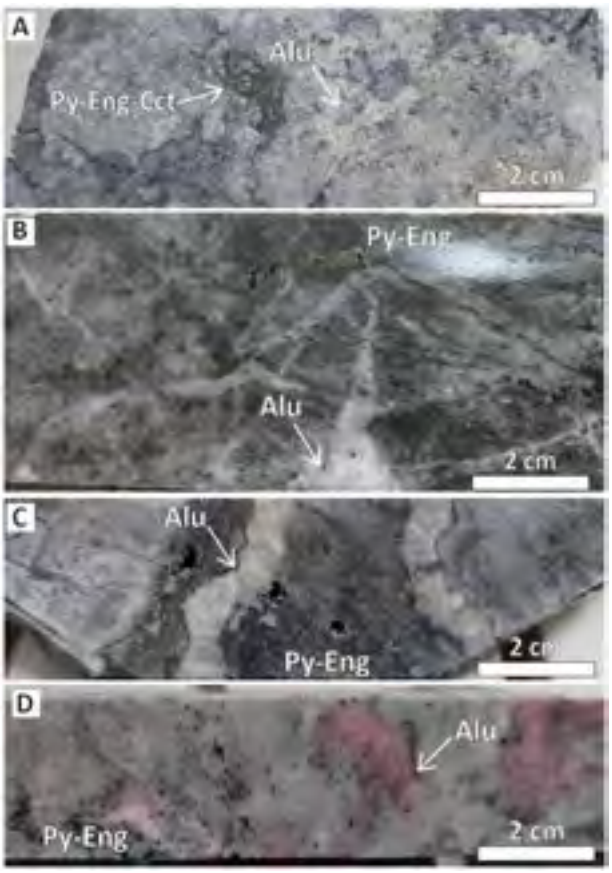


Figure 2. Different types of alunites defined under the microscope. a) Disseminated fine alunite (LGCV-031-FDS drill core). b) Disseminated coarse alunite (LGCV-036-LN drill core). c) Massive coarse + fine alunite (LGCV-024-FDS drill core). d) Massive fine alunite (LGCV-021-LN drill core). Abbreviations: Alu = alunite, Cct = chalcocite, Eng = enargite.

Polished sections were also analyzed by reflected light microscopy to identify the opaque minerals and their relationship with the alunite crystals. Pyrite deposition is coeval or closely related to the alunite deposition, as evidenced by pyrite crystals occurring along the edges of alunite crystals or following cleavage lines. In other samples, sulfide deposition occurred after alunite deposition, as sulfides fill spaces or cavities. Reflected light microscopy reveals alternating bands of pyrite and enargite, tennantite-tetrahedrite replacing enargite, enargite as inclusion in pyrite and vice versa; covellite replacing enargite, and covellite and bornite replacing pyrite in quartz veinlets and in alunite veins; and chalcopyrite disseminated and in veinlets with other sulfides (Fig. 3).

The Ar/Ar and K/Ar ages used in this study are analyses conducted by the company.

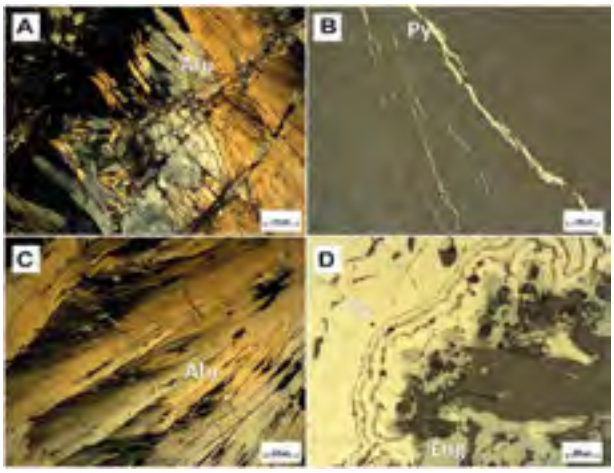


Figure 3. Photomicrographs in transmitted and reflected light. a) Transmitted light, massive alunite coarse + fine grained (LGCV-049-FDS drill core). b) Same sample, reflected light, pyrite along the edges of alunite crystals. c) Transmitted light, massive coarse + fine alunite (LGCV-048- FDS drill core). d) Different view of the same sample in reflected light, alternating bands of pyrite and enargite. Scale bar: 500 µm.

5 Discussion and conclusions

There are different styles of alunite in the samples collected for this study, initially classified based on crystal habit, grain size, and composition. They can also be categorized according to their mineral paragenesis, as some thin sections reveal a close relationship between sulfide and alunite deposition, while others suggest that sulfides may have been deposited at a later stage.

The samples from the Lunahuasi deposit are predominantly composed of pyrite-enargite, and minor covellite, indicating a high-sulfidation mineralization event, with minor tetrahedrite-tennantite and local chalcopyrite, suggesting evolution to an intermediate sulfidation state. In contrast, the mineral paragenesis at Filo del Sol appears more complex, with pyrite-enargite present but also a high content of covellite, chalcocite, chalcopyrite, and some bornite, highlighting the overprinting of high-sulfidation mineralization onto the porphyry system.

There are two groups of alunites. The first group consists of massive-habit alunites, where pyrite deposition appears to be contemporaneous or

closely related to alunite formation. The second group includes alunites in which the relationship with sulfides is not coeval, and we are unable to define if this alunite is pre-mineralization or post-mineralization.

The Ar/Ar dating results in this ongoing study will provide a framework to distinguish different types of alunite in both deposits, define the relationship between alunite types and mineral paragenesis, and evaluating potential variations in the samples along the north-south structural-alteration trend. In addition, S isotope analyses will help to indicate the origin of alunite samples, in the context of mineral assemblage, texture and occurrence, and will potentially provide information on zonation.

Acknowledgements

This study is supported by NGEx Minerals through its membership in CASERM. We would like to thank the geology and technical team from NGEx Minerals and Vicuña Corp for support of fieldwork at the project site. We thank Julian Forestier and Aylén Tremea for their continuous assistance in providing project related information and geology discussions. A special acknowledgment to Diego Charchaflié, Bob Carmichael and Wojtek Wodzicki for their valuable support throughout the development of this project. Finally, we deeply appreciate the contribution of Jeff Hedenquist, whose interested and support encouraged us to complete this abstract; his corrections were highly valuable.

References

Bissig T, Lee JKW, Clark AH, Heather KB (2001) The Cenozoic history of volcanism and hydrothermal alteration in the Central Andean Flat-Slab Region: New ^{40}Ar-^{39}Ar constrains from the El Indio-Pascua Au (-Ag, Cu) belt, 29°20´-30°30´S. International Geology Review 43:312-340

Charchaflié D, Tosdal RM, Mortensen JK (2007) Geologic Framework of the Veladero high-sulfidation epithermal deposit area, Cordillera Frontal, Argentina. Economic Geology 102(2):171-192. https://doi.org/10.2113/gsecongeo.102.2.171

Deyell CL, Rye RO, Landis GP, Bissig T (2005) Alunite and the role of magmatic fluids in the Tambo high-sulfidation deposit, El Indio-Pascua belt, Chile. Chemical Geology 215(1-4):185-218. https://doi.org/10.1016/j.chemgeo.2004.06.038

Holley EA, Bissig T, Monecke T (2016) The Veladero high-sulfidation epithermal gold deposit, El Indio-Pascual Belt, Argentina: Geochronology of alunite and jarosite. Economic Geology 111(2):311-330. https://doi.org/10.2113/econgeo.111.2.311

Panteleyev A, Cravero O (2001) Faja del Potro and Cordón de La Brea ore deposits, La Rioja and San Juan: Radiometric dating, analytical results and sample documentation. Servicio Geológico Minero Argentino (SEGEMAR), Serie Contribuciones Técnicas, Recursos Minerales 11, 56 p

Perelló J, Sillitoe RH, Rossello J, Forestier J, Merino G, Charchaflié D (2023) Geology of porphyry Cu-Au and epithermal Cu-Au-Ag mineralization at Filo del Sol, Argentina-Chile: Extreme Telescoping During Andean Uplift. Economic Geology 118(6):1261 – 1290. https://doi.org/10.5382/econgeo.5029

Sato AM, Llambías EJ, Basei MAS, Castro CE, (2015) Three stages in the Late Paleozoic to Triassic magmatism of southwestern Gondwana, and the relationships with the volcanogenic events in coeval basins. Journal of South American Earth Sciences 63:48-69 https://doi.org/10.1016/j.jsames.2015.07.005

Sillitoe RH, Devine FAM, Sanguinetti MI, Friedman RM (2019) Geology of the Josemaría porphyry copper-gold deposit, Argentina: Formation, exhumation, and burial in two million years. Economic Geology 114(3):407-426. https://doi.org/10.5382/econgeo.4645

Vila T, Sillitoe RH (1991) Gold-rich porphyry systems in the Maricunga Belt, northern Chile. Economic Geology 86(6):1238-1260. https://doi.org/10.2113/gsecongeo.86.6.1238

Taca Taca Bajo: An Early Halo-Type Porphyry Copper Deposit in Salta, Argentina

Federico Cernuschi [1,2], Santiago Gigola [3,2], Raymond Rivera [2], Guillermo Almandoz [3], David Arribasplata [2], Tim Ireland [2], Paula Gonnet [2], Ezequiel Iglesias [2], Rocío Gil [2], Juan Burlando [2], Steve Andersson [2].

[1]Eclectic Rock, Punta del Este, Uruguay
[2]First Quantum Minerals, Salta, Argentina
[3]Independent Consultant, Mendoza, Argentina

Abstract. Taca Taca Bajo is a Cu-Mo-Au porphyry deposit located in Salta, Argentina. Mineralization is related to a large and central rhyodacitic stock emplaced during the Oligocene. The Cu-mineralization at Taca Taca Bajo is hosted by chalcopyrite-rich early halo alteration selvages, mainly of the Green-Gray Sericite subtype that overprint K-silicate alteration and are dominantly hosted in an Ordovician granite wall rock. The low Fe content of this wall rock results in the formation of these early halos with a high muscovite/biotite ratio. As the system evolves, the early halo fluid's increasing acidity and the wall rock's decreased buffering capacity result in the formation of white sericite alteration selvages and patches. This alteration overprints the Green-Gray early halos, and the chalcopyrite they contain is locally transformed into higher sulfidation assemblages with chalcocite and pyrite, but without increasing the Cu-grade. The Mo-mineralization is related to banded molybdenite quartz veins and associated Mo-rich quartz vein subtypes, formed close in time and space with the Cu-rich early halos. A shallow and central Au-rich zone is thought to be initially related to bornite-rich early halos, now obliterated by the formation of the leached cap where limonite now hosts the Au. This process also resulted in the development of a chalcocite supergene enrichment blanket below the leached cap together with associated exotic Cu.

1 Introduction

Taca Taca Bajo (TTB) is an Oligocene Cu-Mo-Au porphyry deposit located within the Puna region of NW Argentina (Ar/Ar biotite-muscovite and Re/Os molybdenite: ~ 29 to 28 Ma; Ince, 2024). TTB is genetically related and centered on at least three rhyodacitic to dacitic porphyry dikes and a large central stock (U/Pb zircons: ~30 to 29 Ma; Ince, 2024). These TTB porphyries intruded the back arc of Chile's extensive and economically significant Eocene to Oligocene porphyry Cu belt (~ 130 km E).

Measured and indicated resources are 2,200 Mt @ 0.43 % Cu, 0.012 % Mo, and 0.09 g/t Au (0.13 CuEQ % cut-off, Gray *et al.*, 2021).

2 Methods

This work summarizes the cumulative work done by many geologists and data generated from several companies that previously explored and developed the project, including BHP, Corriente, Rio Tinto, and Lumina. Extensive and detailed mapping and cross-sections were done over the years (*e.g.* Almandoz, 2015). The new interpretations and conceptual model result from re-logging campaigns and geochemical and mineralogical studies by First Quantum Minerals, including observations throughout several of the 473 diamond holes drilled at TTB and supporting whole-rock assay data, spot SWIR spectral data, and optical and TIMA petrography. A key NW-SE cross-section was constructed and presented here (Figure 1).

3 Lithology

The Oligocene rhyodacitic and dacitic porphyritic intrusions at the center of TTB were previously inferred as discrete and discontinuous dikes based on mapping partial outcrops. However, a central body has been reinterpreted as a large porphyry stock of ~ 500 m diameter (Figure 1). This coarse-grained and crowded porphyry stock is inferred to predate the bulk of the magmatic-hydrothermal porphyry system and, therefore, can be considered immediately pre-mineral. At least a couple of generations of thin inter-mineral porphyry dikes cross-cut the stock and were intruded close in time with mineralization (Figure 1).

The TTB stock is low grade, particularly at depth, and most of the Cu-mineralization is hosted on its peripheral wall rock, a coarse-grained Ordovician granite with abundant leucocratic aplitic sills (Figure 1, U/Pb in zircons: ~459 to 441 Ma; Gray *et al.*, 2021; Ince, 2024). This granite was emplaced in a lower Ordovician (or older) metasedimentary sequence that crops out 1 km west of the deposit and is observed in drill hole core as garnet-magnetite-epidote skarn xenoliths.

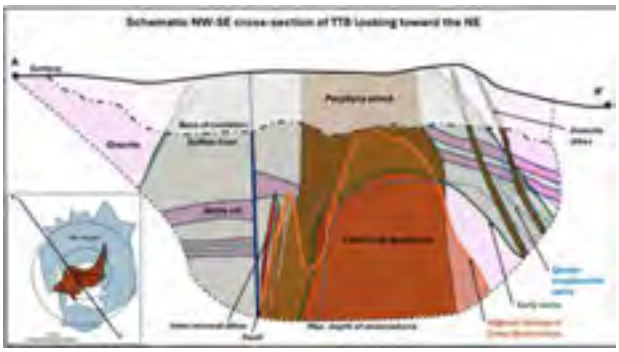


Figure 1. Schematic NW-SE cross-section across the TTB porphyry deposit, south of the main supergene enrichment blanket. The insert shows a plan view.

Dolerite sub-vertical dikes, of presumable late Ordovician age, cross-cut the granite with a dominant NS strike. Younger Permian sub-vertical rhyolitic dikes and coeval volcanic units crosscut

and overlay (respectively) the Ordovician batholith and its wall rock (Choiyoi Group, U/Pb zircons range from ~271 to 253 Ma; Gray *et al.*, 2021; Ince, 2024).

3 Hydrothermal alteration and veining

Muscovite-rich alteration is the most voluminous alteration at shallow depth at TTB and is intimately related to Cu-mineralization. This alteration overprints older K-silicate alteration, observed as hydrothermal biotite with less K-feldspar, which continues at depth without overprints.

Previously, the muscovite alteration was interpreted as two Sericitic (Phyllic) alteration events: 1) an early sericitic alteration event comprised of light green alteration selvages that host most of the Cu-mineralization, followed by 2) a sericitic event comprised of white alteration selvages and patches that largely postdate the Cu-mineralization. The muscovite-rich alteration was considered a rare variation of D-type veins without sulfide centerlines but with well-developed sericitic halos. These events overprint older K-silicate alteration above a deeper and central zone with barren quartz veins, interpreted as barren A veins, noting significant differences like milky color, coarse grain, and lack of aplitic texture.

In this way, the formation of the TTB porphyry deposit was considered an oddity: K-silicate alteration and A veins were maybe too hot to precipitate Cu, and therefore, Cu-sulfides precipitated above it with the earlier stages of sericitic (phyllic) alteration resulting in Cu-rich, green sericitic halos lacking central D-veins.

3.1 Early halos:

Based on vein/halo cross-cutting relationships and mineralogic observations, we have re-interpreted the early (light green) muscovite-rich alteration as Cu-bearing early halo alteration, mainly of the Green-Gray Sericite sub-type (Figure 2A, GGS, Cernuschi *et al.,* 2023). These halos are composed of shreddy muscovite (phengite, Benavides, 2017), K-feldspar, and traces of biotite, andalusite, corundum, chalcopyrite, pyrite, and rare bornite (Cornejo, 2015; Cernuschi *et al.,* 2019). Other subtypes of early halos, typically observed in porphyry deposits elsewhere, are sporadic at TTB, like Pale-Green Sericite (PGS, Figure 2B), or virtually absent, like Early Dark Micaceous (EDM). This is due to the granitic wall-rock low Fe content, which favors muscovite's formation over biotite and, hence, the characteristic light green color (Cernuschi *et al.,* 2019 & 2023). Zones of TTB with abundant early halos correlate well with the hypogene Cu mineralization with an average of ~ 0.4 Cu %. These zones also include low-density quartz veins with chalcopyrite globally referred to as AB due to the scarcity of cross-cutting relationships and various morphological variabilities between A and B being the most common. These veins are formed close in time with the early halos, possibly before them, and in stability with K-silicate alteration.

3.2 White sericite:

The occurrence of white sericite alteration can be divided into two zones: an inner zone where they overlap the GGS early halos and the Cu-mineralization, and an outer zone where the white sericite halos are barren, have pyrite and extend for approximately 500 m outwards of the Cu-mineralization.

White sericite alteration selvages in the inner zone remain not fully understood. They lack the pyrite center line characteristic of most D-veins in deposits elsewhere (Figure 2C). These alteration selvages are irregular and discontinuous, forming in cases alteration patches, rather than the more straight-walled sericitic halos to D-veins. Despite being white and muscovite-rich, they are morphologically more reminiscent of early halos than sericitic halos to pyrite D-veins. Where timing relationships can be observed, the white sericite halos cross-cut the GGS early halos and, in some cases, pervasively overprint them, replacing K-feldspar, phengite, and biotite with pure muscovite. In other areas, GGS early halos are hosted in the granite wall rock and change into white sericite halos across contacts into aplitic sills, indicating identical timing and wall rock control on the mineralogy. Cross-cutting relationships with B and C veins cannot be established, as these veins are rare at TTB. These observations suggest that white sericite alteration is likely mainly formed immediately later than GGS early halos but may also be formed at identical times but with different mineralogy controlled by Fe availability in the wall rock.

As previously reported, in the inner zone, the distribution of both GGS early halos and white sericite selvages and patches is impossible to deconvolute and map independently. This overprint sometimes results in a higher sulfidation assemblage with chalcocite, pyrite, and rare traces of bornite that replace the chalcopyrite-rich assemblage in GGS early halos with changes in sericite color and Cu-sulfide mineralogy occurring over just a few tens of centimeters. The Cu grade, however, is not high-graded and Au content decreases slightly in zones with white sericite overprint. We consider that the white sericite event likely expresses the continued up-flow of the early halo fluid. At some stage, after the bulk of the Cu-Fe-sulfides are precipitated with the GGS early halos and the wall rock has lost buffering capacity due to the extensive formation of phengite after magmatic feldspar, new batches of fluid up-flow resulted in the formation of more pure muscovite and local high sulfidation conditions.

In this interpretation, neither the GGS early halos nor the white sericite halos are related to typical Sericitic (Phyllic) alteration in the inner zone. These halos result from early halo fluid alteration,

which is formed close in time to K-silicate alteration. Fluid-to-wall-rock ratios, buffering capacity, and Fe availability control the mineralogy of the halos.

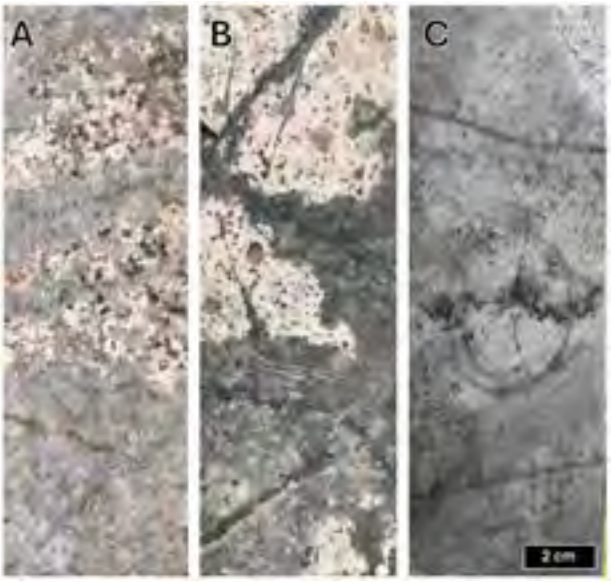


Figure 2. Early halos host the chalcopyrite ore at TTB: A) Green-Gray Sericite (TTBJ11-18-433m), B) Pale Green Sericite (TTBJ11-18-207m), C) White Sericite patches with hypogene chalcocite (TTBJ22-162-420m).

3.3 K-silicate alteration and AB quartz veins

Early halos and AB quartz veins are contained within a broader zone of older K-silicate alteration. This alteration is observed as hydrothermal (shreddy) biotite that replaces magmatic hornblende. TIMA mineralogy revealed hydrothermal K-feldspar replacing magmatic feldspar is more abundant than previously thought based on optical petrography and hand lens observations. Contrastingly, the cross-cutting early halo alteration results in K-feldspar, muscovite, and biotite replacing magmatic feldspar and overprinting the previous shreddy biotite after hornblende. Hydrothermal magnetite is absent in both K-silicate and early halo alteration, as in most early halo-type porphyry deposits elsewhere (Cernuschi *et al.,* 2023).

3.4 Mo-rich and barren quartz veins

Banded molybdenite quartz (BMQ, Cernuschi *et al.,* 2023) veins and associated morphologies of Mo-rich quartz veins are stable with K-silicate alteration. They are responsible for the high-grade Mo-mineralization at TTB (Figure 3A). There are no cross-cutting observations concerning GGS early halos and the AB quartz veins.

Early halos, AB veins, and BMQ veins cross-cut older barren deep quartz veins (DQ, Figure 3B, C), which are most abundant at the low Cu-grade core of the system. K-silicate alteration is the most intense there, and overprinting early halo alteration is absent. The DQ veins are composed of massive quartz, K-feldspar, and anhydrite. Anhydrite veins with minor quartz, biotite-only veinlets, and narrow aplite dikes are also observed and may have been formed closely in time with DQ veins.

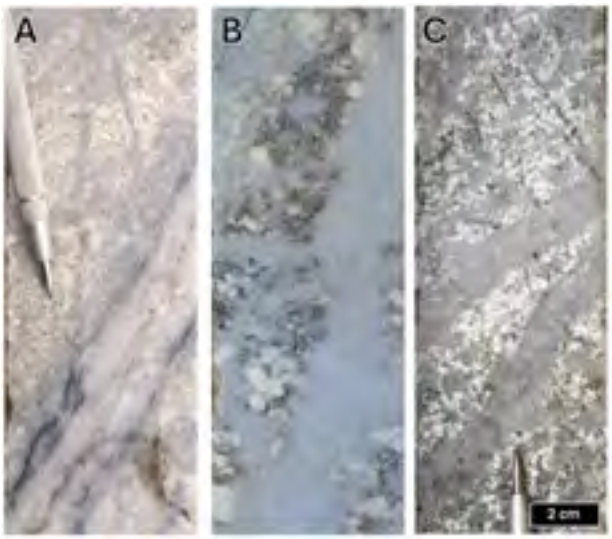


Figure 3. A) Banded Molybdenite-Quartz vein (BMQ, TTBJ12-80-387m), B) thick deep quartz (DQ) vein (TK-18-302m), DQ vein with white K-feldspar (TTBJ12-80-259m).

3.5 The Cu-Mo-Au mineralization

Early halos and associated AB veins are most abundant at the upper parts of the TTB stock and its immediate granite wall rock and wrap into deep flanks around the low Cu-grade core, resulting in an inverted cup-shaped Cu-mineralization zone (Figure 1). This Cu-mineralization zone partially coincides with a similarly distributed zone with BMQ veins, resulting in a similarly shaped Mo-mineralization zone. The Cu-mineralization is asymmetrically distributed, with more mineralization on the NW flank and significantly less on the SE flank. Nonetheless, in plan view the mineralization forms a roughly symmetrical annular zone surrounding the low Cu-grade core. This symmetry is best recognized by observing the distribution of Mo-mineralization on the surface since Mo is not affected by supergene remobilization (insert in Figure 1).

Gold mineralization is related to Cu-sulfides in early halos, and the richest Au zone lays above the low Cu-grade core, where bornite is inferred to have been abundant, as observed in other early halo-type and hybrid deposits elsewhere (*e.g.,* Bingham: Landtwing *et al.,* 2010). This shallow zone is now intensely oxidized, and Au is likely hosted in limonites; therefore, the higher bornite content cannot be confirmed.

3.6 Other vein and alteration types

Pyrite veinlets of the D-type, with and without sericitic halos, are rare and only observed locally at the system's periphery.

Propylitic alteration, composed of chlorite and less abundant and variable epidote, pyrite, specularite, and magnetite, has been observed in the outermost, barren zones of TTB.

Advanced Argillic alteration is virtually absent. Nonetheless, TIMA mineralogy has detected trace amounts of woodhousite, alunite, and pyrophyllite. These locally observed minerals (reported from only one drill hole) may relate to the *Planicie Norte* veins that cross-cut TTB towards the system's north. These are Au-rich pyrite-quartz veins likely meso- to epithermal in origin. The lack of distinct epithermal textures is reminiscent of cordilleran lodes as the Main Stage veins at Butte, Montana.

4 Supergene oxidation

Supergene smectites, gypsum, and alunite are abundant in the TTB leached cap and immediately beneath it. The leached cap reaches up to 300 m over the central parts of the deposit, where it stripped most of the hypogene Cu mineralization. A significant portion of this Cu has been precipitated underneath as supergene chalcocite, forming an enrichment blanket (mainly under the northern half of the deposit) and laterally as exotic chalcocite (K-Ar ages in alunite range from ~24 to 21 Ma). The leached cap preserves most hypogene Mo and Au mineralization as these elements are relatively immobile. Nonetheless, molybdenite cannot be recognized with hand lens in the leached cap, with Mo probably incorporated into limonites. As discussed above, Au was probably hosted in bornite and is now mixed with the limonites.

5 Structure and Preservation

TTB is exposed close to the top of the hypogene Cu-Mo-Au mineralization, with a central depleted zone where the barren core is close to surface. The leached cap and the underlying blanket of higher grade supergene chalcocite have overprinted the hypogene mineralization. The plan view asymmetry in the distribution of the copper mineralization with respect to the low Cu-grade core has yet to be fully understood. NW-striking post-mineral faults bound at least three blocks through the TTB deposit: north, central, and south. Differential uplift, down drop, and tilting may have resulted in less preservation of the Cu-Mo-Au ore zone at the SE than at the NW, as suggested by Orts (2008). These and other faults and fractures also control some, narrow but deep supergene mineralized zones that locally extend down to > 800 m from the current surface.

3 Discussion

Taca Taca Bajo shares several characteristics with early halo-type deposits elsewhere (Cernuschi *et al.,* 2023): 1) the Cu-Mo-mineralization is related to a central and pre-mineral stock and hosted in its wall rock, rather than in early-mineral porphyry dikes, 2) the barren core has abundant DQ veins and lacks voluminous late- and post-mineral intrusions, 3) the Cu mineralization is related to early halos rather than quartz A veins, 4) the light color of the early halos is due to the low content of biotite and abundance of phengite, 5) this mineralogy and relatively low Cu-grade is related to the low Fe-content of the granite wall rock, 6) D-veins with sericitic halos are volumetrically minor, and 7) BMQ and related veins are common and host most of the Mo-mineralization.

The abundance of typical GGS early halos and rare but likely related white sericite alteration selvages and patches requires more study. The mineralogy and timing of the TTB halos are reminiscent of sericitic halo types described at Copper Cliff (Montana, Uribe-Mogollon *et al.,* 2018).

The outcropping occurrence of a deeply-formed early halo-type deposit in the Oligocene back arc of Argentina is likely related to the strong compression, crustal shortening and thickening, and consequent uplift and erosion that took place over the Oligocene and Miocene periods. This process resulted in the formation of the Altiplano (base altitude of ~3,500 masl) that extends into Bolivia, northern Chile, and southern Peru.

Acknowledgments

We thank FQML for supporting this investigation and sharing the findings, particularly those of Mike Christie, Markku Lappalainen, and Cecilia Artica.

References

Almandoz G (2015) Taca Taca Project Presentation. Corriente Argentina.

Benavides S (2017) Characterisation of sericitic alteration at the Taca Taca Bajo porphyry Cu deposit, Argentina: Unpublished M.S. thesis, Tasmania, Australia, University of Tasmania, 162 p.

Cernuschi F, Dilles JH, Osorio J, Proffett JM & Kouzmanov K (2023) A reevaluation of the timing and temperature of copper and molybdenum precipitation in porphyry deposits. Econ Geol 118:931–965.

Cernuschi F, Rivera R, Dilles JH, Benavides S & Kouzmanov K (2019) Mineralogical variations in early halo alteration selvages of porphyry deposits from North and South America [abs.]: Society of Economic Geologists, SEG 2019: South American Metallogeny: Sierra to Craton, Santiago, Chile, October 7–10, 2019, Proceedings.

Cornejo P (2015) Petrographic report, internal for FQM.

Gray D., Lawlor, M. & Briggs, A. 2021. Taca Taca Project, Sata Province, Argentina. Amended and Restated NI 43-1010 Technical Report.

Ince M (2024) The genesis and evolution of retro-arc porphyry systems: Insights from the Taca Taca Bajo Cu-Mo-(Au) and Bajo de la Alumbrera Cu-Au deposits of NW Argentina. Unpublished thesis. The University of Western Australia. 221 pp.

Landtwing MR, Furrer C, Redmond PB, Pettke T, Guillong M & Heinrich CA (2010) The Bingham Canyon porphyry Cu-Mo-Au deposit. III. Zoned copper-gold ore deposition by magmatic vapor expansion: Economic Geology, v. 105, p. 91–118.

Orts S (2008) Taca Taca Bajo Structural Interpretation. Internal report for Rio Tinto.

Sim R, Davis B & Larsden D (2013) Taca Taca Property. NI 43-101 Technical Report.

Uribe-Mogollon C & Maher K (2018) White mica geochemistry of the Copper Cliff porphyry Cu deposit: Insights from a vectoring tool applied to exploration: Econ Geol 113:1269–1295.

Skarn geometry and sectors, and their applications in exploration

Zhaoshan Chang[1] Qihai Shu[2]
[1]Department of Geology and Geological Engineering, Colorado School of Mines, Golden, CO 80401, USA
[2]China University of Geosciences, Beijing

Abstract. To better estimate a skarn zone's distance to the causative intrusion to help exploration, skarn geometry needs to be considered. Based on geometry, skarns are grouped into contact skarns wrapping around a main causative intrusion in the contact zone (mostly <400-500 m thick), and branch skarns that extend outwards for kilometers away from the intrusion (up to 4,500 m drill tested). Branch skarns may occur along apophyses from the main causative intrusion, faults, lithology boundary, favorable carbonate layers, or the contact of older intrusions. Combining skarn geometry and zoning patterns, sectors are defined as packages of traditional zones. Six sectors are defined to better estimate the distance from the main causative intrusion. Sector 1 is the contact skarn. Sector 2 is around apophyses from the main intrusion. Sectors 3-6 are along other fluid channels not in direct contact with causative intrusions, with Sectors 3-4 being distal skarns and Sectors 5-6 CRDs (Carbonate Replacement Deposits). Sector 3 features brown pyroxene, Sector 4 rhodonite, Sector 5 Fe carbonates, and Sector 6 Mn-carbonates.

1 Introduction

Skarn zonation (Meinert 1997; Chang and Meinert 2008) is one of the most effective tools for the exploration of skarns and linked deposits including porphyry, greisen, CRD (carbonate replacement deposits; quartz-carbonate-sulfides), intermediate sulfidation epithermal (IS), and Carlin and Carlin-like types of deposits (e.g., Meinert et al. 2005; Chang et al. 2019; Ebner et al. 2023). The current description of skarn zoning is mostly relative, e.g., proximal and distal. However, the needs in exploration is more than the relative position. A commonly asked exploration question is how far a zone is to the intrusive source. To address this question, we found that skarn geometry is an important factor, because the same skarn zone may be at significantly different distance in skarns of different shape or control. For example, the green garnet zone is <330 m from the intrusion at Antamina, Peru (Mrozek et al. 2020) whereas green garnet at Jiama, China, occurs up to ~2,000 m away (Shu et al. 2024). Skarn geometry is also critical for resources modelling. In this study, we summarize the skarn geometry, attempt to define sectors that is related to skarn geometry, for better estimation of a skarn occurrence' distance to the causative intrusion. This is an initial step to build a quantitative skarn zoning model.

2 Known zoning patterns of calcic skarns

Metalliferous skarns are mostly related to magmas, although there are a few metamorphic hydrothermal skarns (e.g., Poblete et al. 2021, 2024). Skarns are best developed in carbonates, with minor cases in basalt and basaltic andesite (Lawrence et al. 2017; Chang et al. 2018). The causative intrusion of a calcic skarn replacing mostly limestones typically has red garnet-bearing endoskarns, as veins or patches that may transition to porphyry style veins inward (e.g., Chang et al. 2015), and to massive endoskarn at the intrusion contact. Zoning patterns in exoskarns include, from proximal to distal locations and assuming the causative intrusion is oxidized and the wall rocks reduced: 1) garnet/pyroxene ratio decreases; 2) garnet color becomes lighter, e.g., from red to brown then to yellow/green; 3) pyroxene color changes from light green to dark green and locally to brown. Rhodonite may occur farther outwards; 4) Mn content increases in pyroxene and garnet (to a lesser degree); 5) locally a wollastonite zone at the marble front (Fig. 1). Beyond the exoskarn, there is a white marble zone that may or may not host CRD, which grades out to grey marble then limestone. Fluid escape structures/veins may occur in the marble and limestone (Fig. 1).

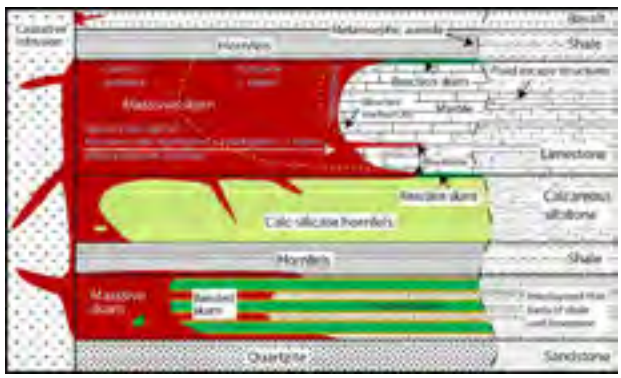


Figure 1. Typical skarn zonation in various types of wall rocks (modified from Chang et al. 2019)

Calcareous shale and siltstone will be metamorphosed to calc-silicate hornfels that is impermeable. Later hydrothermal skarn may cut it as veins, or cement fragments of it close to the intrusion (Fig. 1). Reaction skarns also form during contact metamorphism, at the boundary between limestone and shale/siltstone. In a package with interlayered thin beds of shale and limestone, the shale beds may be converted to pyroxene-rich layers, sandwiched by garnet layers and then marble. During later hydrothermal alteration, the

marble layers are replaced by hydrothermal garnet, and at the intrusion contact, the reaction skarn may be brecciated and cemented by hydrothermal skarn (Fig. 1). Basalt or the equivalents do not change during contact metamorphism, but may be altered by hydrothermal skarns (Fig. 1).

At a larger district scale, a proximal skarn may transition to a porphyry or greisen deposit inside the causative intrusion, depending on how felsic it is. Distal skarns may transition to CRDs that zone from massive texture closer to skarns to vein texture outwards. Farther out, Carlin type or Carlin-like (with native gold; otherwise similar to Carlin) deposits may occur. Where volcanic rocks overlie carbonates, the CRD transitions upwards to IS veins in the volcanic rocks (e.g., at La Colorada, Mexico; Ebner et al., 2023; Fig. 2).

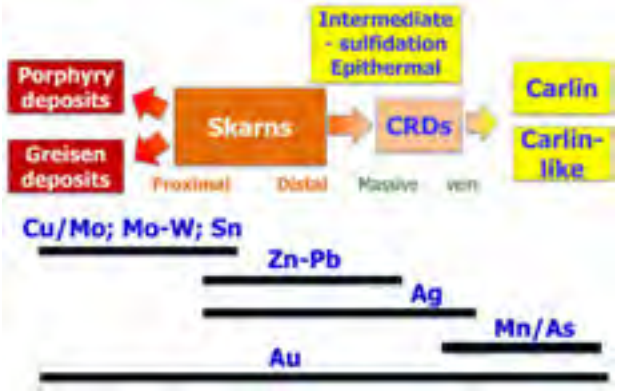


Figure 2. District scale zoning of a skarn system

The metals in the causative intrusion and proximal skarn could be Cu, Au, Mo, W, Sn or Fe, depending on the redox state and fractionation degree of the magma (Chang et al. 2019). Note that the strongest Mo mineralization is at the intrusion margin whereas the Cu peak is some distances away. The outer limit of Fe oxides (magnetite, mushketovite, specular hematite) is closer to the causative intrusion than that of the sulfides. Distal skarns and CRDs may contain Zn-Pb-Ag mineralization. Silver can occur at proximal locations but the grades are typically lower there (e.g., <15 g/t). The Ag grade increases outwards and reaches the highest grades (e.g., >600 ppm; locally >3000 ppm) in far CRDs (e.g., at Yumpag, Peru; Ligarda et al. 2023; Table 1). Farther out from Ag is Mn (e.g., Uchucchacua and Yumpag, Peru; Ligarda et al. 2023) or As (e.g., at Balya, Turkey). Gold may occur at any locations in the system, from intrusions to skarns, CRDs, IS veins, and Carlin/Carlin like deposits (Fig. 2). Gold can be produced by both oxidized and reduced magmas, although the magmas are typically less felsic.

3 Skarn geometry and geological locations

Magmatic hydrothermal skarns occur wrapping around the causative intrusions in the contact zone (contact skarn). Some extend farther outwards as branches for long distance along some elements. They are defined here as branch skarns. They may or may not transition to CRDs. Contact skarns are typically <400-500 m wide, whereas branch skarns-CRDs can be much longer, up to 4,500 m drill tested (e.g., at Bajiazi, China; Table 1).

Contact skarns of some of the largest skarns are only ~25 – 380 m wide, e.g., ~330 m at Antamina, Peru (26 Mt Cu, 23 Mt Zn+Pb, 32,648 t Ag; Mrozek et al., 2020), ~380 m at Ertsberg East, Indonesia (1,483 t Au, 18 Mt Cu; Leyes et al. 2012), ~80 m at Zhuxi, China (2.7 Mt W; Yang et al. 2025), and ~25 m at Laochang, China (1.22 Mt Sn; Cheng et al. 2013; Table 1). In contrast, branch skarns can be a few km long, e.g., ~4.5 km at Bajiazi (Zhao et al. 2003) and Chitudian (Duan et al. 2011), ~3 km at Beiya-Luping (Asia Now Resources, 2012; Mao et al. 2017), >2.1 km at Jiama (Shu et al. 2024), China, and >2.4 km at Uchucchacua, Peru (Ligarda et al. 2023; Table 1). Most of the large skarns have branch skarns.

Table 1. Maximum width/thickness of contact skarns and lengths of branch skarns of some skarn systems

Deposit	Resources	Contact SK (m)	Branch SK (m)	Branch SK loc.
Antamina, Peru	26 Mt Cu, 23 Mt Zn, 32,648 t Ag @ 11 g/t, 0.59 Mt Mo	~330	0	NA
Ertsberg East, Indonesia	18 Mt Cu, 1,483 t Au, 9,837 t Ag @ 3.3 g/t	~380	0	NA
Ferrobamba, Peru	12 Mt Cu, 86 t Au, 4,875 t Ag @ 2.3 g/t	~200	0	NA
Jiama, China	7.4 Mt Cu, 208 t Au, 11,163 t Ag @ 6 g/t; 0.62 Mt Mo, 1.70 Mt Zn+Pb	~80	>2,100	5
Toromocho, Peru	7.0 Mt Cu, 0.25 Mt Mo, 9,743 t Ag @ 7.1 g/t	~250	~2,100	3, 4, 5
Big Gossan, Indonesia	2.3 Mt Cu, 125 t Au, 1,560 t Ag @ 5.7 g/t	~30	~1,100	4
Beiya - Luping, China	370 t Au, 200 Mt Fe ore, 0.8 Mt Cu, 2.08 Mt Pb+Zn, 8,250 t Ag @ 51.9 g/t	~70	~3,000	4, 5
Zhuxi, China	2.7 Mt W, 0.11 Mt Cu, 1,165 t Ag	~80	~1,600	3, 4, 5
Laochang, China	1.22 Mt Sn	~25	~1,400	3, 5
Uchucchacua, Peru	14,000 t Ag @368 g/t	Unk	>2,400	3
Yumpag, Peru	3,670 t Ag @ 700 g/t	Unk	>1,800	3+5
Baiyinnuo'er, China	2.4 Mt Zn+Pb, 1,027 t Ag @ 31.4 g/t	~100	~650	3, 4, 6
Chitudian, China	1.9 Mt Zn+Pb, 2,450 t Ag	<10	~5,200	3
Bajiazi, China	0.37 Mt Zn+Pb; 1,647 t Ag @ 186 g/t	~10	~4,500	3

Contact skarns occur around the main intrusion (Location #1; Fig. 3), whereas branch skarns may occur along apophyses from the main intrusion (#2), along faults (#3), along the lithology boundaries between carbonates and other sedimentary rocks such as shale-siltstone, chert layer, or volcanic rocks (#4), along certain favourable carbonate beds among a thick carbonate package (#5), or along the contact of older intrusions (#6; Fig. 3). Some examples are listed in Table 1. Location #6 could be confusing and poses challenges to the way of

identifying causative intrusions by the proximity to intrusion. An example is at the Baiyinnuo'er Zn-Pb skarn, China, where ~139 Ma skarns occur along the contact of ~245 Ma intrusions (Shu et al. 2017).

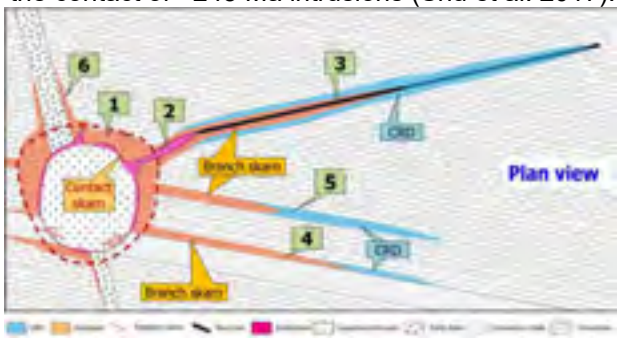
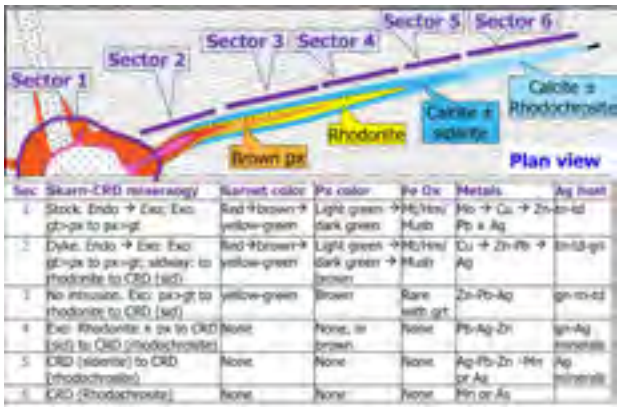


Figure 3. Skarn geometry and geological locations.

4 Sectors

Figure 4 shows a conceptual skarn system from the causative intrusion outwards, using Locations #1 and #2-3 to represent an intrusive source and fluid channels. The skarn system is divided into six sectors. There is zonation in each sector, i.e., sectors are packages of traditional zones. In general, Sector 1 is around the main causative intrusion and has most of zones in Fig. 1. Sector 2 is around an apophysis from the main intrusion and features brown pyroxene. Sectors 3-6 do not have intrusions. In the fluid channels, Sector 3 features brown pyroxene, Sector 4 rhodonite, Sectors 5 and 6 are CRD-only. Sector 5 features Fe-carbonates and Sector 6 Mn-carbonates.



Sec	Skarn-CRD mineralogy	Garnet color	Px color	Fe Ox	Metals	Ag host
1	Stock: Endo → Exo; Exo: gt>px to px>gt	Red→brown→ yellow-green	Light green → dark green	Mt/Hm/ Mush	Mo → Cu → Zn-Pb + Ag	tn-td
2	Dyke: Endo → Exo; Exo: gt>px to px>gt; sidway: to rhodonite to CRD (sid)	Red→brown→ yellow-green	Light green → dark green → brown	Mt/Hm/ Mush	Cu → Zn-Pb → Ag	tn-td-gn
3	No intrusion. Exo: px>gt to rhodonite to CRD (sid)	yellow-green	Brown	Rare with gt	Zn-Pb-Ag	gn-sp-td
4	Exo: Rhodonite + px to CRD (sid) to CRD (rhodochrosite)	None	None, to brown	None	Pb-Ag-Zn	gn-Ag minerals
5	CRD (siderite) to CRD (rhodochrosite)	None	None	None	Ag-Pb-Zn ±Mn or Au	Ag minerals
6	CRD (Rhodochrosite)	None	None	None	Mn or As	

Figure 4. Sectors around an oxidized intrusion with reduced wall rocks. Endo: endoskarn; Exo: exoskarn; gt: garnet; px: pyroxene; sid: siderite; Mt: magnetite; hm: specular hematite; mush: mushketovite; tn: tennantite; td: tetrahedrite

In detail, Sector 1 is the contact skarn with the typical zoning patterns in Figure 1 (garnet/pyroxene ratio, garnet color, pyroxene color, and Mn in garnet / pyroxene, etc.; Fig. 4), but the pyroxene is typically green. It also lacks significant rhodonite and CRDs. Sector 2 occurs around and beyond the tip of a fertile dyke or sill. The apophysis may have endoskarn throughout. The Sector 2 zoning is similar to that of Sector 1 but the pyroxene can reach brown color, and on the sides close to the end of the apophyses, there may be rhodonite before the skarn transitions to a narrow CRD zone. Sectors 3-6 are along fluid channels. In the fluid channel of Sector 3, the skarn is dominated by the pyroxene>garnet zone (Fig. 4), or it may be green/yellow garnet if the magma is very oxidized and/or the wall rock is not reduced. The pyroxene is brown. On the side(s), rhodonite may occur and then the distal skarn transitions to CRD. Sector 4 is the most distal skarn featuring rhodonite, ± wollastonite and/or brown pyroxene in the fluid channel. On the sides, it transitions to CRD. Sectors 5 and 6 are CRDs. Calcite is ubiquitous; the part closer to the skarn, Sector 5, may contain also Fe-carbonates (siderite or ankerite), whereas the distal CRD (Sector 6) contains Mn carbonates (manganoan calcite to rhodochrosite) at the end of a CRD. Where an apophysis does not have a fluid channel beyond its end, Sectors 3-6 may be compacted,e.g., at Groundhog, USA(Meinert 1987).

Metal zonation in the sectors is also summarized in Fig. 4, similar to the description in Section 2. Fe oxides are typically in Sector 2 but occasionally reaches Sector 3. Silver mineralogy changes from mainly tennantite-tetrahedrite in Sector 1, to additional galena in Sector 2, mainly galena in Section 3, additional Ag minerals in Sector 4, and mainly Ag minerals (proustite-pyrargyrite, acanthite, native Ag) in Sectors 5-6. Locations #4, #5, and #6 have similar sectors.

5 Discussion

The skarn geometry and locations are strongly controlled by rock permeability and fluid channels. Around the main causative intrusion (Location #1) and their apophyses (Location #2), the permeability is caused by the explosive water release from the magma chambers (Burnham 1979) that generates fracture arrays and local breccias. In carbonate wall rocks, these greatly facilitates the dissolution of carbonates by the weakly acidic magmatic hydrothermal fluids, providing Ca and space for massive skarns. This permeability is greater than pre-existing permeability therefore the skarns are centered around the causative intrusion. Other branch skarns are controlled by fluid channels with various types of permeability. Faults are good channels (Location #3). Location #4 is at lithology boundaries, and features stratabound skarns-CRDs. This is controlled by bedding parallel slip fault that is produced during folding due to its position at a rheology contrast (soft carbonates vs harder shale/siltstone, chert, or volcanic layers). Certain carbonate layers (Location #5) may also be fluid channels due to higher primary permeability. For example, fossiliferous limestones (e.g., at Yumpag, Peru; Ligarda et al 2023) and clastic carbonates may be more permeable than pure chemical precipitation carbonates in which calcite grains are fine and interlocked. If a carbonate contains impurities such as clay, quartz or feldspars, secondary permeability may be generated during thermal metamorphism through reactions such as

quartz + calcite = wollastonite + CO_2 gas. The loss of mass (CO_2) pervasively generates small but interconnected open spaces which increases the rock permeability. Location #6, the contact of an older intrusion, could also be a channel for later fluids, where secondary permeability can be produced during contact metamorphism if wall rocks are dirty limestones. The availability of a channel for fluids to leave the contact zone strongly affects how far a skarn zone may occur, e.g., a pyroxene>garnet zone may be only tens to a few hundred meters away in a contact skarn, whereas the same zone can be >1 km away in a branch skarn.

Skarn zoning is related to temperature decrease (e.g., main intrusion to apophysis; skarn to CRD; increasing Mn in minerals; magnetite to sulfides) or a redox gradient (e.g., garnet/pyroxene ratio; lighter to darker green pyroxene color), whereas local conditions, e.g., Mg, Al, and organic matter contents of wall rocks, depth, and magma temperatures may complicate the trends (e.g., Chang and Meinert, 2008). In branch skarns, the thermal gradient along a fluid channel is much smaller than that perpendicular to the channel, which may disturb the proximal vs distal indications, e.g., the pyroxene zone is more proximal than a CRD in a contact skarn, but a CRD on the side(s) of a channel may actually be closer than a pyroxene skarn in the channel in branch skarn (Fig. 4).

Given the above complexities, sectors better estimate the distance of a skarn to the causative intrusion than traditional zones. The distance estimation of a sector is still a range, but will be a smaller range than that of a zone.

Acknowledgements

We benefited from the discussions with Larry Meinert and Noel White.

References

Asia Now Resources Corp. (2012) Technical report on the Beiya Project, Yunnan Province, China. 139p.

Burnham CY (1979) Magmas and hydrothermal fluids. In: Barnes HL (ed.) Geochemistry of Hydrothermal Ore Deposits 2nd ed, Wiley, New York: 71-136.

Chang Z, Meinert LD (2008) Zonation in skarns—complexities and controlling factors. In: Proceedings of AusIMM PACRIM Congress, 24-26 Nov 2008, Gold Coast, Australia: 303–306

Chang Z, Meinert L, Lawrence D, Mrozek S, Zhang L (2018) Skarns replacing igneous rocks: Symposium Proceedings, 15th Quadrennial IAGOD Symposium, Salta, Argentina. 28-31 August 2018: 207-208.

Chang Z, Mrozek S, Meinert LD, Windle S (2015) Skarn-porphyry transition: an example from the Antamina skarn, Peru. In: Proceedings of AusIMM PACRIM Congress, 18-21 March 2015, Hong Kong, China: 409-413.

Chang Z, Shu Q, Meinert LD (2019) Skarn Deposits of China, in: Chang Z, Goldfarb RJ (Eds.), Mineral Deposits of China, Society of Econ Geol Special Pub 22: 189-234.

Cheng Y, Mao J, Chang Z (2013) The origin of the world class tin-polymetallic deposits in the Gejiu district, SW China: Constraints from metal zonation characteristics and ^{40}Ar-^{39}Ar geochronology. Ore Geol Rev 53:50-62

Duan S, Xue C, Chi G, Liu G, Yan C, Feng Q, Song Y (2011) Ore geology, fluid inclusion, and S- and Pb-isotopic constraints on the genesis of the Chitdian Zn-Pb deposit, southern margin of the north China Craton. Resour Geol 61:224-240

Ebner J, Chang Z, Francisco P, Juarez D, Perez P, Emerson C, Hemming S, Wendlandt R (2023) The Epithermal-Skarn Transition at the La Colorada Deposit, Chalchihuites District, Zacatecas, Mexico. SEG conference 2023 abstract, London, UK

Lawrence DM, Allibone AH, Chang Z, Meffre S, Lambert-Smith JS, Treloar PJ (2017) The Tongon Au deposit: Northern Cote d'Ivoire: An example of Paleoproterozoic Au skarn mineralization. Econ Geol 112:1571-1593

Leys CA, Cloos M, New BTE, MacDonald GD (2012) Copper-gold±molybdenum deposits of the Ertsberg-Grasberg District, Papua, Indonesia. Soc Econ Geol Spec Pub 16:215-235

Ligarda R., Aquino JL, Munoz JC, Salazar JC, Arias E, Ventura M (2023) Redescubrimiento del distrito minero de Uchucchacua: de gran productor de plato a productor de zinc-plomo-(cobre) en el future. XXI Congres Peruano de Geologia.

Mao J, Zhou Y, Liu H, Zhang C, Fu D, Liu B (2017) Metallogenic setting and ore genetic model for the Beiya porphyry-skarn polymetallic Au orefield, western Yunnan, China. Ore Geo Rev 86:21-34

Meinert LD (1987) Skarn zonation and fluid evolution in the Groundhog mine, Central mining district, New Mexico. Economic Geology 82: 523-545.

Meinert LD (1997) Application of skarn deposit zonation models to mineral exploration: Exploration and Mining Geology 6: 185–208.

Meinert LD, Dipple GM, Nicolescu S (2005) World Skarn Deposits, In: Hedenquist JW, Thompson JFH, Goldfarb RJ, Richards JP (Eds.), Economic Geology 100th Anniversary Volume: 299-336.

Mrozek S, Chang Z, Spandler C, Windle S, Raraz C, Paz A (2020) Using whole rock geochemistry to optimize skarn classification and evaluate element mobility during skarn formation: An example from the Antamina deposit, Peru. Econ Geol 115:177-188

Poblete JA, Dirks PHGM, Chang Z, Huizenga J-M, Griessman M, Hall C (2021) The Watershed tungsten deposit, NE Queensland, Australia: Permian metamorphic tungsten mineralization overprinting Carboniferous magmatic tungsten. Econ Geol 116:427-451

Poblete JA, Huizenga J-M, Chang Z, Dirks P (2024) The Permian Watershed tungsten deposit (northeast Queensland, Australia): Fluid inclusion and stable isotope constraints. Aust J Earth Sci 71:1183-1202

Shu Q, Chang Z, Hammerli J, Lai Y, Huizenga J-M (2017) Composition and evolution of fluids forming the Baiyinnuo'er Zn-Pb skarn deposit, NE China: insights from laser ablation ICP-MS study of fluid inclusions. Econ Geol 112:1441-1460

Shu Q, Deng J, Chang Z, Wang Q, Niu X, Xing K, Sun X, Zhang Z, Zeng Q, Zhao H, Yu F (2024) Skarn zonation of the giant Jiama Cu-Mo-Au deposit in southern Tibet, SW China. Econ Geol 119:1-22

Shu Q, Lai Y, Sun Y, Wang C, Meng S. (2013) Ore genesis and hydrothermal evolution of the Baiyinnuo'er zinc-lead skarn deposit, northeast China: Evidence from isotopes (S, Pb) and fluid inclusions. Econ Geol 108:835–860

Yang Y, Pan X, Liu B, Dong J (2025) Newly discovered veinlet-disseminated type scheelite mineralization in the deep-seated biotite monzogranite from the giant Zhuxi deposit: Implications for source and evolution of ore-forming fluids. Ore Geol Rev 177: 106451.

Zhao Y, Dong Y, Li D, Bi C (2023) Geology, mineralogy, geochemistry, and zonation of the Bajiazi dolostone-hosted Zn-Pb-Ag skarn deposit, Liaoning Province, China. Ore Geol Rev 23:153-182

Skarn-Porphyry Transition: Understanding and Applications in Exploration

Zhaoshan Chang[1] Shiqiang Huang[1] James Cannell[2]
[1]Department of Geology and Geological Engineering, Colorado School of Mines, Golden, CO 80401, USA
[2]Minera Las Bambas, Peru

Abstract. This study attempts to address the industry need of using skarns to find porphyry deposits, by examining the skarn-porphyry transition. The transition occurs inside fertile intrusions hosted in carbonates, starting from massive to semi-massive endoskarn at the intrusion margin that grades to endoskarn veins inward, then a zone with mixed endoskarn and porphyry-style veins with K-alteration halos, and eventually to only high temperature porphyry veins in the interior of the intrusion. This transition is controlled by the supply of Ca, mainly from the dissolution of carbonate wall rocks by weakly acidic magmatic hydrothermal fluids, and high temperatures. Implications to exploration is discussed based on the understanding.

1 Introduction

Porphyry deposits are the major source of copper and a significant source of Au and Mo. They are the exploration targets of many mineral companies. A common question from explorers working in a carbonate-bearing terrane (including a volcanic terrane with minor carbonate beds) is how to find porphyry deposits using skarns. This study attempts to address this question by examining the skarn-porphyry transition. The features of skarns related to porphyry deposits were studied in the early 1980s (e.g., Einaudi, 1982A, 1982B), and the research became much less afterwards (e.g., Franchini et al. 2000). The direct transition between skarn and porphyry has not been well studied systematically.

2 Skarn-Porphyry Proportion in a Deposit

Skarn and porphyry deposits have the same fluid source, fertile magmas. The major difference in the environments is the wall rock types, carbonate vs non-carbonates (Meinert et al. 2005; Sillitoe 2010; Cooke et al. 2014; Chang et al. 2019; Yang and Cooke 2019). Skarns rarely develop in non-carbonate environments, except in some relatively mafic volcanic rocks with a basaltic to basaltic andesite composition (e.g., Lawrence et al. 2017; Chang et al. 2018). In carbonate terranes, the skarn/porphyry proportion can range from ~100% to ~0% (Table 1). Where there are significant of both (>~20%), the grades in skarns are typically higher than that in the porphyry ores (e.g., Einaudi, 1982B).

3 Skarn-Porphyry Transition

The skarn-porphyry transition occurs inside a causative intrusion emplaced in carbonates, between endoskarn and porphyry style veins. Outside of the intrusion, the carbonates are altered to massive exoskarn. Some examples are summarized below.

Table 1. Skarn proportion of skarn-porphyry deposits

Deposit	Resources	Skarn proportion
Morelos, Mexico	195 t Au, 1,327 t Ag, and 0.5 Mt Cu	~100%
Antamina, Peru	26 Mt Cu, 23 Mt Zn, 32,648 t Ag @ 11 g/t, 0.59 Mt Mo	>95%
OK Tedi, PNG	1.9 Mt Cu, 239 t Au Au	80%
Twin Buttes, AZ, USA	~4 Mt Cu	80%
Mission, AZ, USA	~4 Mt Cu	80%
Bisbee, AZ, USA	3.8 Mt Cu	65%
Grasberg-Ertsberg district, Indonesia	58 Mt Cu, 4,788 t Au, 22,674 t Ag, 0.53 Mt Mo (0.5% Cu cutoff)	54% Cu, 47% Au, 73% Ag, 44% Mo
Toromocho, Peru	7.0 Mt Cu, 0.25 Mt Mo, 9,743 t Ag	~50%
Santa Rita, NM, USA	3.2 Mt Cu	20%
Ely, Nevada	3.3 Mt Cu	20%
Bingham, Utah, USA	32 Mt Cu, 1,635 t Au, 25,602 t Ag, 1.31 Mt Mo, 3 Mt Zn+Pb	24% Cu, 23% Au, 4% Mo, 60% Ag, 100% Zn+Pb
Cananea, Mexico	~41 Mt Cu, 0.63 Mt Mo	~5%
Cerro Corona, Peru	0.88 Mt Cu, 157 t Au	~0%

Antamina, Peru: Antamina contains 26 Mt Cu metal, 23 Mt Zn, 32,648 t Ag, and 0.59 Mt Mo (Mrozek et al. 2020). It is the largest Zn-Pb and Ag and second largest Cu single body skarn in the world. There are multiple fertile intrusions (Mrozek et al. 2015). At the contact of the earliest intrusion, a quartz monzonite porphyry (P1A), the endoskarn is massive red garnet with only local residual patches of the intrusion (Fig. 1E). Where such patches are not present, the massive endoskarn is identified using whole rock geochemistry (Mrozek et al. 2020). Inward, the endoskarn becomes densely disseminated green pyroxene with minor red garnet (Fig. 1D). Farther inward is a zone with multiple vein relationships: some veins contain both green pyroxene and granular quartz; some green pyroxene veins cut across granular quartz veins; and some granular quartz veins cut across green pyroxene veins (Figs. 1B-C). These different vein relationships occur mixed in the same interval, therefore, the green pyroxene (endoskarn) and the granular quartz (early porphyry vein) are interpreted to have formed in a short period of time, e.g., of the same high-temperature stage, despite there are contradicting relationships at the individual vein level. Farther inward, endoskarn minerals disappear

and the veins become purely of porphyry style, as granular quartz veins with secondary biotite halos and the vein density is locally up to ~40% (Fig. 1A; Chang et al. 2015).

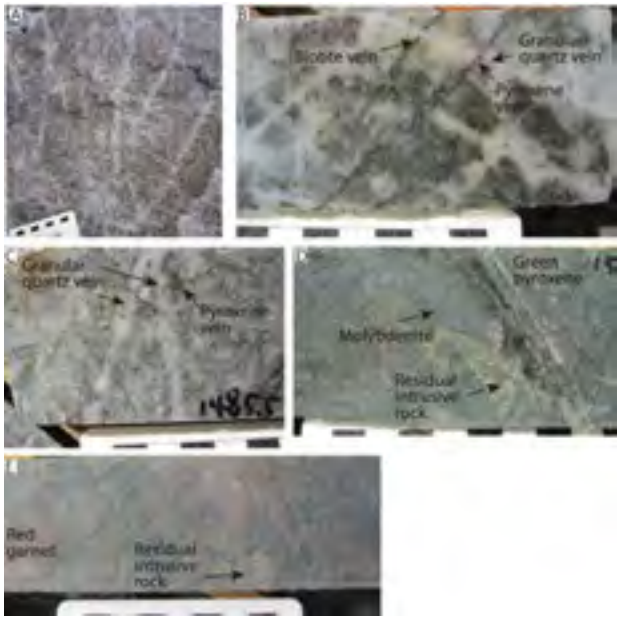


Figure 1. Endoskarn-porphyry transition at Antamina, Peru (modified from Chang et al. 2015)

Morelos Au skarn, Mexico: The Morelos skarn contains 195 t Au, 1,327 t Ag, and 0.5 Mt Cu (Torex Gold 2022; Burish et al. 2023). The skarn consists of mainly the El Limon-Guajes section and the Media Luna section. At El Limon, the causative intrusion is a reduced granodiorite. The endoskarn features massive red garnet endoskarn at the intrusion margin that becomes red garnet veins inward with halos of densely disseminated green pyroxene. Farther inward, the green pyroxene domain becomes confined in vein-shape domains that is surrounded by a white-tan colored domain (Fig. 2B-C) characterized by disseminated wollastonite, titanite and light green pyroxene in the intrusive rock. Farther inward, the endoskarn disappear and the fresh rock contains only sparse veinlets of quartz with K-feldspar halos (Fig. 2A).

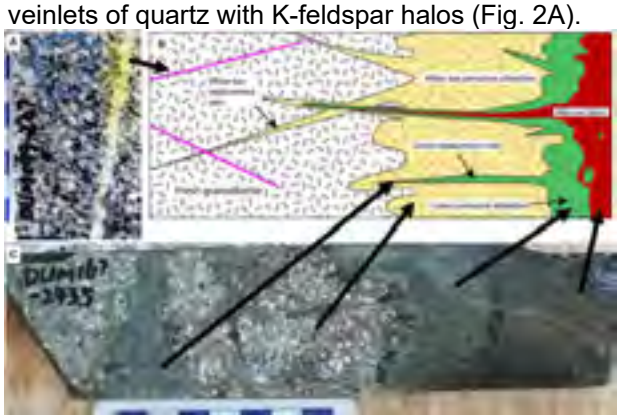


Figure 2. Endoskarn-porphyry transition at El Limon, Morelos Au skarn, Mexico. A: K-feldspar halo of a quartz veinlet confirmed by staining. B: Endoskarn-porphyry transition model; C: A core illustrating the zonation. Sparse endoskarn veins occur locally >300 m inward from the intrusion margin.

Ferrobamba Cu-Au skarn, Peru: The Ferrobamba skarn, one of the major skarns in the Las Bambas district, contains 6.5 Mt Cu metal, 45.6 t Au, and 2,744 t Ag (remaining resources as of June 2024; MMG 2024). There are six equigranular-porphyritic diorite - monzonite - quartz diorite - quartz monzodiorite intrusions (MZB, MBF, MZM, MZH, MZD, and MZQ) and a post-mineralization lamprophyre dyke. Most of the mineralization is related to MZH (Cannell et al. 2019). The margin of MZH has been altered to massive endoskarn (Fig. 3A), as identified through geochemistry studies following the method of Mrozek et al. (2020). Inwards, there is a zone with coexisting disseminated red garnet + green pyroxene endoskarn (or red garnet vein with pyroxene halos) and porphyry quartz vein with K-feldspar halos (Fig. 3B). Farther inward, endoskarn disappears and there are only porphyry style veins including quartz veinlets with K-feldspar halos and slightly later quartz-biotite-anhydrite veins (Fig. 3C).

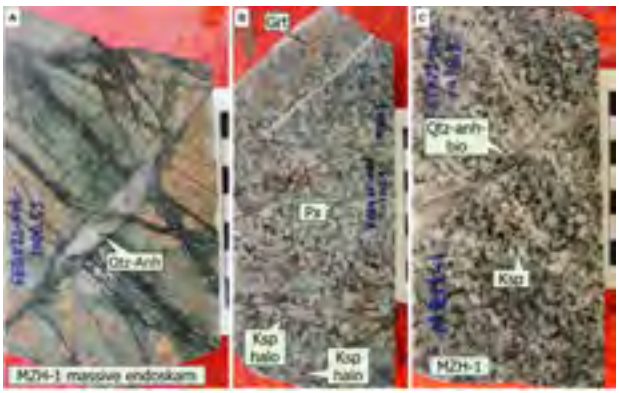


Figure 3. Endoskarn-porphyry transition at Ferrobamba, Peru

Sombrero skarn project, Peru: No resources have been defined yet, but the syn-skarn crystal-crowed monzonite / monzodiorite porphyry contains abundant red garnet endoskarn veins. The endoskarn volume is >50% closer to the intrusion margin, and <50% inwards. Locally, the red garnet in veins transitions to quartz in the same vein with K-feldspar halos (Fig. 4).



Figure 4. Skarn-porphyry transition at Ccascabamba area, Sombrero project, Peru.

In summary, the skarn-porphyry transition starts from massive to semi-massive, red-garnet bearing endoskarn at the intrusion margin. It changes inwards to endoskarn veins with less endoskarn

minerals, then to a transitional zone with co-existing endoskarn (disseminated or veins with halo) and early stage porphyry-style quartz vein typically with K alteration (K-feldspar and/or secondary biotite) halos. Farther inward, only porphyry-style veins occur and endoskarns disappear (Fig. 5).

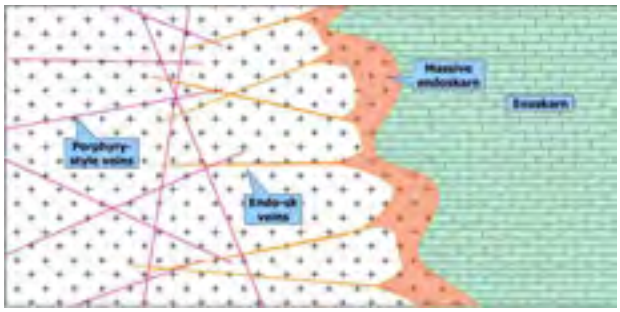


Figure 5. Skarn-porphyry transition model

4 Discussions

The skarn-porphyry transition from the margin of a causative intrusion to its interior is characterized by the decreasing of skarn minerals including garnet, pyroxene and less common wollastonite. These minerals are Ca-rich silicates, therefore the mineralogical change from endoskarn to porphyry-style quartz veins is driven by the decreasing supply of Ca. The Ca is likely from the dissolution of wall rock carbonates by magmatic hydrothermal fluids that is typically weakly acidic with HCl, H_2SO_4, plus other acids in special cases (e.g., HF, H_2CO_3; Burnham, 1979). The carbonate dissolution provides Ca for the formation of prograde skarn minerals, and the space for the exoskarn minerals to grow. The magmatic hydrothermal fluids flow outwards from the intrusion, but Ca may have diffused inward from high concentration locations (outside of the intrusion) to low concentration locations (inside the intrusion). The magmatic hydrothermal fluids are likely nearly saturated with SiO_2 as they are in equilibrium with high SiO_2 (>50%) magmas. They may likely be abundant in Fe, as demonstrated by the compositions of single fluid inclusions in quartz phenocrysts, e.g., up to ~21.6 wt% Fe in quartz in the Mole granite in Australia (Audetat et al. 2000), and by Fe-Cl daughter minerals in fluid inclusions in quartz phenocrysts of the granite porphyry related to the Empire skarn, Idaho (Chang and Meinert, 2004). With these components, andradite garnet forms through a reaction: $3Ca^{2+}_{(aq)} + 3SiO_{2(aq)} + 2Fe^{3+}_{(aq)} + 6H_2O \rightarrow Ca_3Fe^{3+}_2Si_3O_{12}$ (andradite) + $12H^+$. And wollastonite forms via reaction: $Ca^{2+}(aq) + SiO_2(aq) + H_2O \rightarrow CaSiO_3$ (wollastonite) + $2H^+$.

Another important condition for the skarn formation is high temperature. For example, at X_{CO2}=0.5 and P_{fluid} = 0.5 kbar, quartz and calcite will not occur together but will react to form wollastonite, based on the phase diagram in Meinert et al (2005). In other words, if there are Ca in high temperature fluids containing Ca and Fe, quartz will not form but the Si, Ca and Fe will react to form garnet and/or pyroxene (depending on the redox state and therefore the proportion of Fe^{3+} and Fe^{2+}), plus wollastonite if the Fe runs out. Early porphyry veins with K-alteration halos typically form at high temperatures (e.g., >550 °C; Sillitoe, 2010), therefore, the quartz vein without skarn minerals in the interior of the system described indicates the lack of Ca.

The Ca supply issue explains the lack of skarns around fertile intrusions that have produced porphyry mineralization but little skarns in carbonate wall rocks, such as Cerro Corona, Peru, and Grasberg, Indonesia. At Cerro Corona, the later intrusions all intruded into the earlier barren pluton (Gold Fields, 2016, pers comm), therefore the fluids did not interact with carbonate wall rocks therefore there was no supply of Ca. Grasberg has a similar situation. The fertile Main Grasberg intrusion was emplaced in the middle of a complex composed of Dalam Andesite, Dalam Diorite, Dalam Fragmental, and Dalam Volcanics (Leys et al. 2012), therefore its magmatic fluids were blocked from encountering the carbonate wall rocks to dissolve them to supply Ca. Bingham, Utah, and Ely, Nevada, USA, has only ~20-24% of the Cu-Au in skarns, probably because the wall rocks are dominated by sandstone and shale, with only minor carbonate beds (Einaudi 1982B).

5 Implications to exploration

As the supply of Ca has a strong control on whether the product is a skarn or a porphyry system, if the target is a porphyry deposit and a skarn is only to be used as a tool, a first step should be examining the host rock stratigraphy. A package dominated by siliciclastic sedimentary rocks (e.g., at Bingham, Utah) or volcanic rocks (e.g., Batu Hijau, Indonesia) has more potential to host a porphyry deposit. If the stratigraphy is dominated by carbonates, there may be porphyry style alteration if the intrusion is large enough, but the grades in porphyry may be lower than that of the skarn, or be sub-economic (Einaudi 1982B). If the host stratigraphy is determined to be favourable, then use the skarn zoning patterns (e.g., Meinert 1997; Chang and Meinert 2008; Shu et al 2024; Chang and Shu 2025) to find the causative intrusion of the skarn, which has a good chance to be a porphyry deposit.

Even if a stratigraphy package is dominated by carbonate, there is still hope if a later fertile magma intruded into an earlier intrusion, which blocked the magmatic hydrothermal fluids from encountering the carbonate wall rocks. Magma fertility indicators coupled with intrusive sequence studies may be applied on skarn-lacking intrusions hosted in carbonates to evaluate whether it is possible to find a porphyry deposit.

What if a fertile magma intrudes a pre-existing skarn, e.g., at Antamina (Mrozek et al. 2015)? Because the Ca has already been consumed to form the earlier skarn, and calc-silicates cannot be readily destroyed to release the Ca, there is a

shortage of Ca. Quartz veins of porphyry style will likely form and the older skarn will just be a host rock. The addition of porphyry veins in the older skarn will like increase the grades of the latter, as noticed in Einaudi (1982B) for skarns related to porphyry Cu plutons.

There is some hydrothermal calcite in the low temperature retrograde alteration of skarns, typically filing interstices of garnet, pyroxene and/or wollastonite, or in late veins. Such calcite may react with the later fluids to form a new generation of skarn, but its quantity is likely small due to the limited supply of Ca.

The endoskarn-porphyry transition vein package also helps to identify causative intrusions, in addition to the skarn zoning patterns that point to the causative intrusions. The red garnet in endoskarn and the K-alteration halo of the porphyry veins indicate high temperatures, therefore the source of the fluid is likely nearby and being the progressively downward solidifying intrusion itself. Note that the red color of garnet is critical, as lower temperature green garnet veins may form inside earlier rocks including volcanic rocks; they are not indicative of causative intrusions.

Acknowledgements

We appreciate the discussions with Sugeng Widodo on the Grasberg-Ertsberg district, and Coppernico for the permission to use the Sombrero photo.

References

Audetat A, Gunther D, Heinrich CA (2000) Causes for large-scale metal zonation around mineralized plutons: Fluid inclusion LA-ICP-MS evidence from the Mole Granite, Australia. Econ Geol 95:1563-1581

Burish M, Bussey SD, Landon N, Nasi C, Kakarieka A, Gerdes A, Albert R, Stein HJ, Gabites JA, Friedman RM, Meinert LD (2023) Timing of magmatism and skarn formation at the Limon, Guajes, and Media Luna gold ± copper skarn deposits at Morelos, Guerrero State, Mexico. Econ Geol 118: 695-718

Burnham CY (1979) Magmas and hydrothermal fluids. In: Barnes HL (ed.) Geochemistry of Hydrothermal Ore Deposits 2nd ed, Wiley, New York:71-136

Cannell J, Wise J, Crawford A, Smith Q, Garay A (2019) Geochronology and igneous geochemistry of the Ferrobamba porphyry-skarn deposit, Las Bambas, southern Peru: Abs vol Soc Econ Geol annual meeting, Santiago, Chile. October 7-10, 2019.

Chang Z, Meinert L, Lawrence D, Mrozek S, Zhang L (2018) Skarns replacing igneous rocks: Symposium Proceedings, 15th Quadrennial IAGOD International Association on the Genesis of Ore Deposits Symposium, Salta, Argentina. 28-31 August 2018: 207-208.

Chang Z, Meinert LD (2004) The magmatic-hydrothermal transition - Evidence from quartz phenocryst textures and endoskarn abundance in Cu-Zn skarns at the Empire Mine, Idaho, USA. Chem Geol 210:149-171

Chang Z, Meinert LD (2008) Zonation in skarns—complexities and controlling factors: PACRIM Congress 2008, Australasian Institute of Mining and Metallurgy (AusIMM), Gold Coast, Queensland, Australia, November 24–26, 2008, Extended Abstracts:303–306

Chang Z, Mrozek S, Meinert LD, Windle S (2015) Skarn-porphyry transition: an example from the Antamina skarn, Peru. In: Proceedings of AusIMM PACRIM Congress, 18-21 March 2015, Hong Kong, China: 409-413

Chang Z, Shu Q (2025) Skarn geometry and sectors, and their applications in exploration. In: Proceedings of the 18th SGA meeting, 3-7 August 2025, Golden, Colorado, USA: this volume.

Chang Z, Shu Q, Meinert LD (2019) Skarn Deposits of China, in: Chang Z, Goldfarb RJ (Eds.), Mineral Deposits of China, Soc Econ Geol Spec Pub 22:189-234

Cooke DR, Hollings P, Wilkinson JJ, Tosdal RM, Turekian HDHK (2014) Geochemistry of porphyry deposits. Treatise on Geochem 13: 357-381

Einaudi ET (1982A) Description of skarns associated with porphyry copper plutons. In: Titley SR (Ed) Advances in Geology of the Porphyry Copper Deposits, Southwestern North America, The University of Arizona Press, Tucson, Arizona, USA: 139-183

Einaudi ET (1982B) General features and origin of skarns associated with porphyry copper plutons. In: Titley SR (Ed) Advances in Geology of the Porphyry Copper Deposits, Southwestern North America, The University of Arizona Press, Tucson, Arizona, USA: 185-209

Franchini MB, Meinert LD, Montenecro TF (2000) Skarns related to porphyry-style mineralization at Caicayen Hill, Neuquen, Argentina: Composition and evolution of hydrothermal fluids. Econ Geol 95:1197-1213

Lawrence DM, Allibone AH, Chang Z, Meffre S, Lambert-Smith JS, Treloar PJ (2017) The Tongon Au deposit: Northern Cote d'Ivoire: An example of Paleoproterozoic Au skarn mineralization. Econ Geol 112:1571-1593

Leys CA, Cloos M, New BTE, MacDonald GD (2012) Copper-gold±molybdenum deposits of the Ertsberg-Grasberg District, Papua, Indonesia. Soc of Econ Geol Spec Pub 16:215-235

Meinert LD (1997) Application of skarn deposit zonation models to mineral exploration: Explor Mining Geol 6:185–208

Meinert LD, Dipple GM, Nicolescu S (2005) World Skarn Deposits, In: Hedenquist JW, Thompson JFH, Goldfarb RJ, Richards JP (Eds.), Economic Geology 100th Anniversary Volume: 299-336.

MMG Limited (2024) Mineral resources and ore reserves statement as at 30 June 2024. 309p.

Mrozek S, Chang Z, Meinert LD (2015) A model for the intrusive sequence and Cu-Zn skarn formation at the Antamina deposit, Peru. In: Proceedings of AusIMM PACRIM Congress, 18-21 March 2015, Hong Kong, China: 423-429

Mrozek S, Chang Z, Spandler C, Windle S, Raraz C, Paz A (2020) Using whole rock geochemistry to optimize skarn classification and evaluate element mobility during skarn formation: An example from the Antamina deposit, Peru. Econ Geol 115:177-188.

Shu Q, Deng J, Chang Z, Wang Q, Niu X, Xing K, Sun X, Zhang Z, Zeng Q, Zhao H, Yu F (2024) Skarn zonation of the giant Jiama Cu-Mo-Au deposit in southern Tibet, SW China. Econ Geol 119:1-22

Sillitoe RH (2010) Porphyry copper systems. Econ Geol 105:3-41

Torex Gold Resources Inc (2022) NI 43-101 Technical Report. 658p.

Yang Z, Cooke DR (2019) Porphyry copper deposits in China. In: Chang Z, Goldfarb RJ (Eds) Mineral Deposits of China. Soc Econ Geol Special Pub 22:133-187

Magmatic Input in the Formation of Epithermal Au-Ag Deposits of the Hauraki Goldfield, New Zealand

Anthony B Christie[1], Mark P Simpson[2], Robert L Brathwaite[3]
[1]Emeritus Scientist, GNS Science, Lower Hutt, New Zealand. Email: t.christie@gns.cri.nz
[2]Senior Scientist, GNS Science, Wairakei, New Zealand. Email: m.simpson@gns.cri.nz
[3]Emeritus Scientist, GNS Science, Lower Hutt, New Zealand, Email. b.brathwaite@gns.cri.nz

Abstract. The extent of magmatic input in the formation of epithermal Au-Ag deposits may influence the metal budget and, if recognizable, may provide an indicator of prospectivity in exploration. Possible indicators of magmatic input in the formation of epithermal vein deposits of the Hauraki Goldfield may include: 1) close spatial and temporal association with porphyry Cu style mineralization (Thames Au-Ag quartz veins with the Ohio Creek porphyry Cu prospect); 2) high salinity fluid inclusions in vein minerals (e.g. Waihi, Wharekirauponga and Tui sphalerite); 3) an ore mineralogy with telluride-bearing minerals, especially bismuth tellurides (Thames and Tui); 4) the abundance of metals deposited (Thames, Golden Cross, Karangahake and Waihi); 5) sulfur isotope values for sulfides of near 0 per mil; 6) radiogenic lead isotope values of galena (Paritu, Coromandel and Tui); and 7) positive gravity anomalies (Waihi). None of these criteria are definitive, each having possible alternative interpretations. However, the high salinity fluid inclusions in sphalerite at Waihi, Wharekirauponga and Tui are the most convincing for a magmatic fluid contribution during mineralization. When the various factors are considered cumulatively, we suggest that magmatic fluids have contributed to the mineralization of many of the Hauraki Goldfield Au-Ag deposits.

1 Introduction

The c. 50 epithermal quartz vein Au-Ag deposits in the Hauraki Goldfield have produced more than 12 Moz of gold and 62 Moz of silver (Christie et al. 2007). The deposits were formed from hydrothermal fluids associated with volcanism from ca.18 to ca. 2 million years ago (Mauk et al. 2011). The active geothermal systems of the Taupō Volcanic Zone to the south are considered modern analogues, with deeply circulating meteoric water heated by magma bodies at depth (Rowland and Simmons 2012). The resulting hydrothermal fluid reacts with wall rocks on ascent to the surface and can at shallower levels deposit gold, silver and other metals in open channels (veins) from boiling and/or mixing with groundwater. In addition to heat and minor fluid, the magma may also supply CO_2, H_2S and other constituents including metals. The extent of magmatic supply may influence the metal budget (Simmons and Browne 2000, 2007) and, if recognizable, may provide an indicator of prospectivity in exploration of epithermal Au-Ag deposits. We discuss seven possible indicators of magmatic fluid input.

2 Geology

The geological sequence in the goldfield begins with a basement of Jurassic greywacke, overlain by Miocene to Pliocene volcanic rocks starting around 18 Ma, initially with andesites and dacites (Fig. 1). Around 12 million years ago, rhyolite volcanism commenced on the eastern side of the goldfield. The sequence is capped by late andesite <3 Ma. Volcanism finished between 2 and 1.5 million years ago, when it shifted south to the Taupō Volcanic Zone.

Importantly, for sourcing magmatic hydrothermal fluids, the volcanic rocks are intruded by igneous intrusive bodies ranging in size from the Paritu pluton to small stocks and dikes.

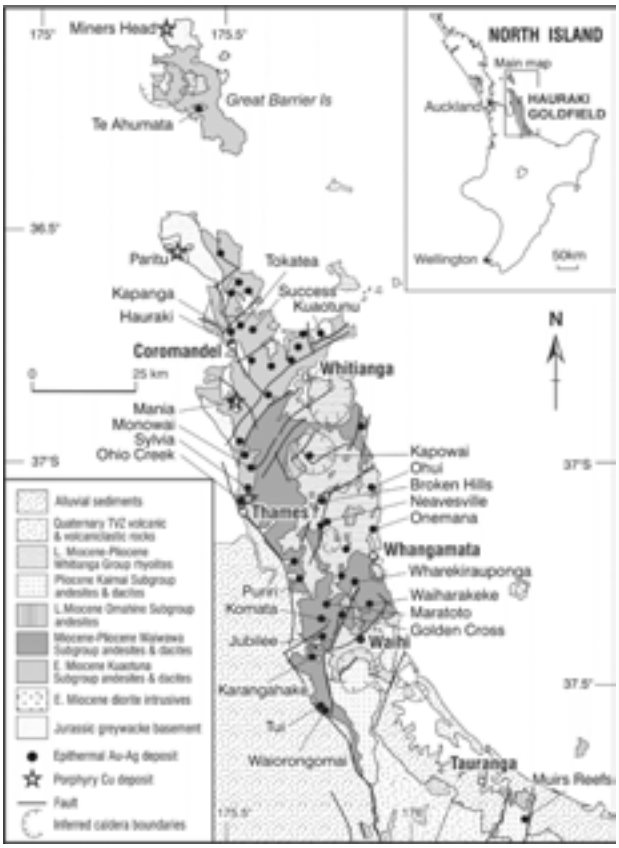


Figure 1. Regional geology and mineral deposits of the Hauraki Goldfield (modified after Christie et al. 2007).

3 Mineral deposits

The goldfield contains a few porphyry Cu type deposits and about 50 epithermal Au-Ag quartz vein deposits (Fig. 1). The total production from the 1850s to date is more than 12 Moz of Au and 60 Moz of Ag plus small quantities of Zn-Pb-Cu concentrate from Tui (Christie et al. 2007; Torckler et al. 2016). The

epithermal deposits are volcanic-related and classified as low sulfidation. However, some deposits grade from Au-Ag mineralization into Zn-Pb-Cu-Ag-Au mineralization with depth (e.g. Waihi and Karangahake) and Tui is predominantly Zn-Pb-Cu style mineralization with only local Au-Ag minerals, suggesting that the Zn-Pb-Cu parts of these deposits have more affinity with intermediate sulfidation deposits. The Waihi deposit is World Class, having produced more than 8.5 Moz of gold and production continues from underground mining. Modern exploration has had some major success with new vein discoveries and definition of mineable resources at Waihi, Karangahake, Golden Cross and Wharekirauponga.

3 Porphyry Cu association

Northeast of the Thames Goldfield, the Kaiser and Sylvia epithermal quartz veins, have a close spatial and temporal relationship to intrusive rocks of the Ohio Creek porphyry Cu deposit and its advanced argillic alteration lithocap at Lookout Rocks (Figure 2; Brathwaite et al. 2001). This intrusion was likely the source of heat, some fluid and metals resulting in high temperature base metal rich mineralization in the epithermal veins as described by Merchant (1978, 1986).

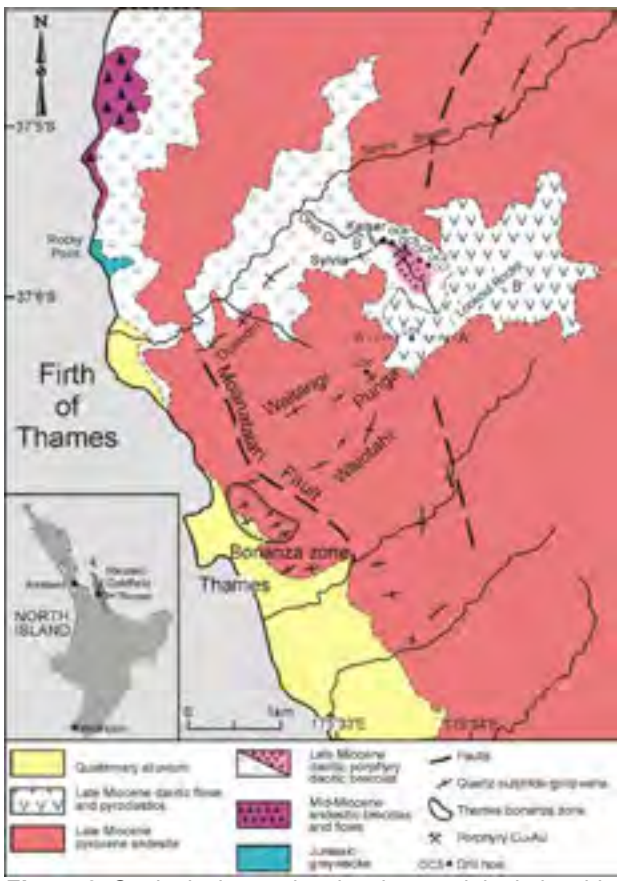


Figure 2. Geological map showing the special relationship of the Kaiser and Sylvia epithermal veins to the Ohio Creek porphyry deposit (locations of drillholes OC1, 2, 4, 5 and 6) (modified after Brathwaite et al. 2001).

4 Fluid inclusions

Measurements of fluid inclusion ice-melting temperatures (T_m) in epithermal vein minerals of the goldfield suggest most of the hydrothermal fluids had apparent salinities of between 0.5 and 2 weight percent equivalent NaCl (Christie et al. 2007), However, much higher concentrations have been measured from fluid inclusions in sphalerite at Waihi Wharekirauponga and Tui, ranging up to 6.8 (Fyfe 2014), 7.6 (Hudson 2022) and 11.9 weight percent equivalent NaCl (Figure 3; Simpson 2017), respectively. These high salinities suggest a significant magmatic fluid component in the epithermal hydrothermal fluids.

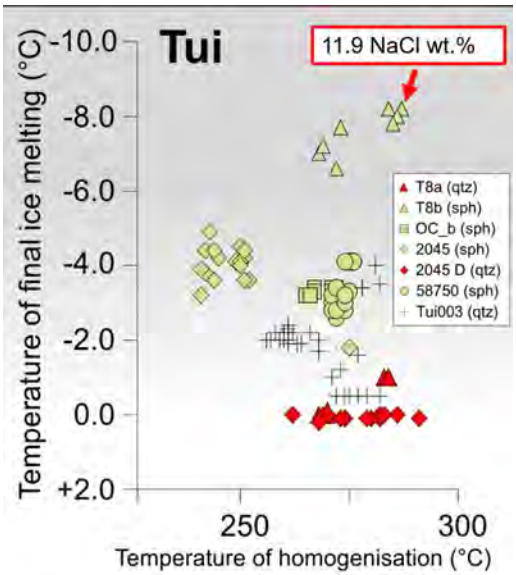


Figure 3. Fluid inclusions in sphalerite from Tui with final ice melting temperatures suggesting a maximum salinity of 11.9 wt% eq. NaCl (modified after Simpson 2017); qtz = quartz, sph = sphalerite.

5 Ore mineralogy

A few of the epithermal veins in the goldfield have minerals that are indicative of deposition from high temperature fluids possibly related to pulses of magmatic fluids. These include the sulfides bismuthinite at Thames and Tui, primary bornite at Tui, and molybdenite at Thames, Neavesville and Waihi.

Telluride minerals have been suggested in some other studies as indicating a magmatic input in geothermal and epithermal hydrothermal fluids (e.g. Simmons and Browne 2000, 2007; Rowland and Simmons 2012). Bismuth telluride minerals formed at high temperature include tetradymite found at Thames and Tui, and altaite and tellurobismutite also found at Thames (Merchant 1978; Christie 1982; Christie et al. 2007). Thames stands out in having an unusually large number and quantity of telluride minerals compared to other deposits in the goldfield.

6 Abundance of metals deposited

The large amount of Au and Ag at Thames, Golden Cross, Karangahake, Wharekirauponga and Waihi compared to other deposits (e.g. Tokatea, Kuaotunu, Kapowai, Broken Hills, Jubilee and Waiorongomai) may reflect a greater flux (larger reservoir) of metals. The greater Au-Ag endowment could indicate a more significant magmatic contribution in the form of a long-lived heat supply and also a likely supply of metals.

7 Sulfur isotopes

Analyses of sulfur isotopes in sulfide minerals from the Hauraki epithermal deposits lie between -3.1 and +4.6 per mil δS^{34}_{CDT} (Fig. 4A; Christie and Robinson 1992). Much of this spread of values is due to the different fractionation factors of the various sulfide minerals (Fig. 4B). Christie and Robinson (1992) suggested these data indicated a fluid composition of +2 per mil, consistent with magmatic sulfur at 0 per mil, possibly with some minor crustal contamination.

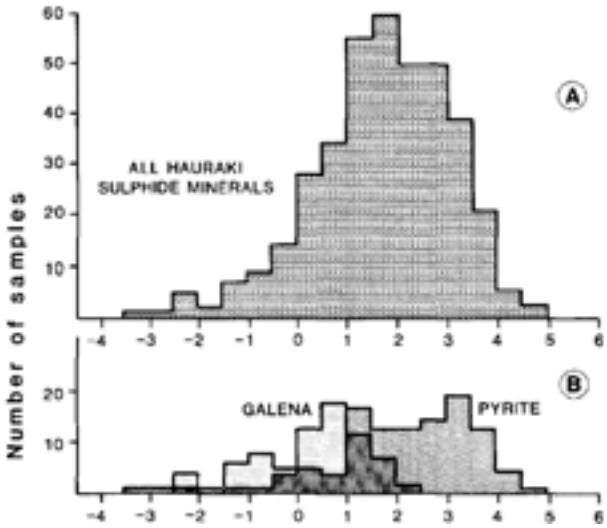


Figure 4. A. Collective δS^{34}_{CDT} values for pyrite, sphalerite, chalcopyrite and galena (n=394) from 20 vein deposits of the Hauraki Goldfield (Christie and Robinson 1992). B. Separation of minerals because of different fractionation factors (chalcopyrite and sphalerite histograms would be between galena and pyrite – the dark area is the overlap in values of galena and pyrite).

8 Lead isotopes

Following earlier work by Cooper and Richards (1969) and Robinson (1974), Gabites and Christie (1994) measured lead isotopes in galena from 30 different vein deposits and on whole rock samples of greywacke, andesite, and rhyolite. The galena data show a separation of deposits on different trend lines on plots of $^{208}Pb/^{204}Pb$ vs $^{206}Pb/^{204}Pb$ (Fig. 5) and $^{207}Pb/^{204}Pb$ vs $^{206}Pb/^{204}Pb$, suggesting different lead batches or mixtures of different sources. From most to least radiogenic (i,e. decreasing $^{208}Pb/^{204}Pb$ and $^{207}Pb/^{204}Pb$ ratios) these are:

- **Paritu area** (Doctors Creek and Sorry Mary Stream veins)
- **Coromandel area** (Tokatea, Preeces Point, Petote Stream and Tiki Stream veins)
- **Tui**
- **Waiorongomai**
- **Waihi** (Martha) - **Karangahake** (Talisman) – **Waitekauri areas**
- **Thames area** (Monowai, Zeehan, Comstock, Sylvia, Watchmans, Australian, Karaka Creek and May Queen veins)

Based on comparison with the analyses of greywacke, andesite and rhyolite, there is no simple match of galena to a specific rock type, partly because of overlaps in ranges between greywacke, andesite and rhyolite (cf. Robinson 1974; Booden et al. 2012 Fig. 10b). A variable mix of sedimentary and igneous sources is likely between the different deposits as proposed for the lead in geothermal systems in the nearby Taupδ Volcanic Zone (Hedenquist and Gulson 1992). More work is required to understand these relationships, especially to define the magmatic signature, however it appears that there is at least a partial magmatic source of lead in many of the deposits. There is insufficient detail to quantify the extent.

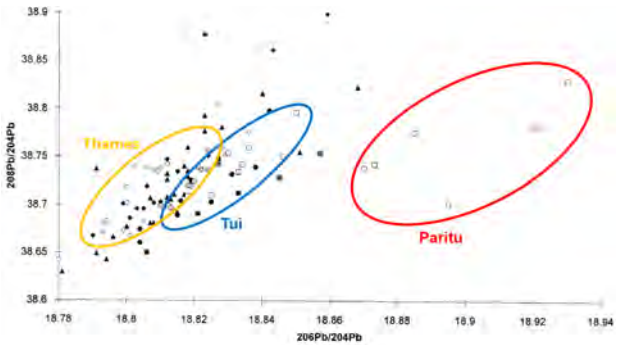


Figure 5. Lead isotope analyses of galena samples from 30 epithermal vein deposits of the Hauraki Goldfield (Gabites and Christie 1994).

9 Positive gravity anomalies

Morell et al. (2011) identified two positive gravity anomalies at Waihi and suggested that they represented magmatic intrusions that were sources of heat and hydrothermal fluid beneath Waihi (Figure 6). Detailed gravity surveys are required at other deposits to further test this hypothesis.

10 Conclusions

None of the seven suggested criteria are definitive of a magmatic contribution with each having possible alternative interpretations. However, the high salinity fluid inclusions in sphalerite at Tui, Wharekirauponga and Waihi are the most convincing for a magmatic fluid contribution during mineralization. When the various factors are considered cumulatively, we

suggest that magmatic fluids have contributed to the mineralization of many of the Au-Ag deposits of the goldfield. Further research is required to quantify the input for individual deposits.

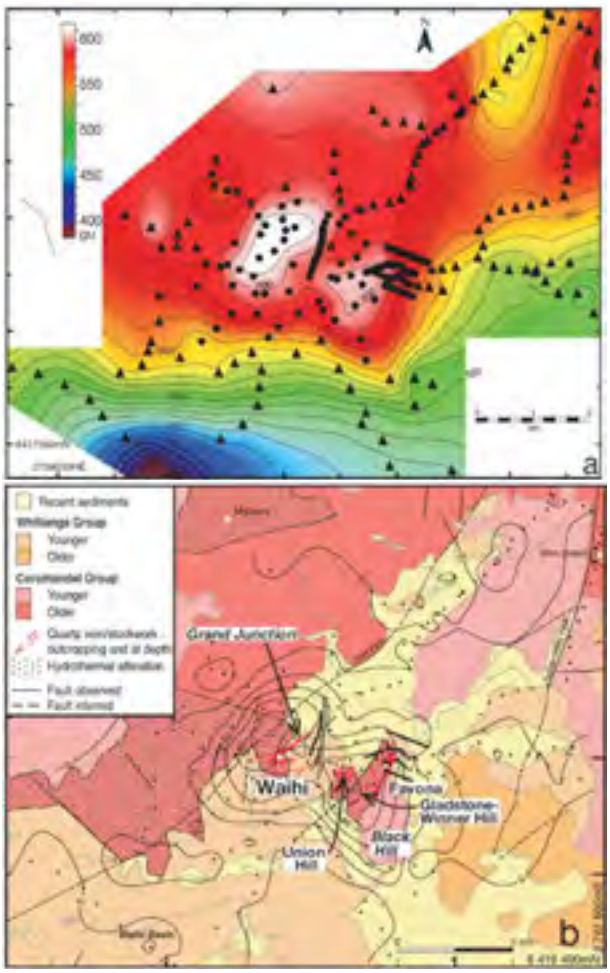


Figure 6. Gravity maps of the Waihi area after Morell et al (2011) showing separate positive gravity anomalies, potentially related to twin intrusions, under the Martha vein system (Waihi label) and the Favona vein. a. Bouguer gravity anomaly map, and b. Geology and residual gravity anomaly map. Both maps have a contour interval of 10 gu.

.

Acknowledgements

Funding for the author's research contributing to this study was provided by the New Zealand Government.

References

Booden M, Smith IEM, Mauk JL, Black PM (2012) Geochemical and isotopic development of the Coromandel Volcanic Zone, northern New Zealand, since 18 Ma. Jour Volcan Geotherm Res 219-220:15-32

Brathwaite RL, Simpson MP, Faure K, Skinner DNB (2001) Telescoped porphyry Cu-Mo-Au, advanced argillic alteration and polymetallic quartz-sulfide-gold-anhydrite veins in the Thames District, New Zealand. Mineral Deposita 36:623-640

Christie AB (1982) Fluid inclusions, stable isotopes and geochemistry of porphyry copper and epithermal vein deposits of the Hauraki gold-silver province, New Zealand: Unpublished PhD thesis, Victoria University of Wellington, New Zealand. 769 p

Christie AB, Robinson BW (1992) Regional sulfur isotope studies of epithermal Au-Ag-Pb-Zn-Cu deposits in the Hauraki goldfield, South Auckland. NZ Jour Geol Geophys 35:145-150

Christie AB, Simpson MP, Brathwaite RL, Mauk JL, Simmons SF (2007) Epithermal Au-Ag and related deposits of the Hauraki Goldfield, Coromandel Volcanic Zone, New Zealand. Econ Geol 102:785–816

Cooper JA, Richards JR (1969) Lead isotope measurements on volcanic and associated galenas from the Coromandel-Te Aroha region, New Zealand. Geochem Jour 3:1-14

Fyfe S (2014) Variable ore mineralogy in the Waihi vein system, Hauraki Goldfield, Waihi, New Zealand. Unpublished MSc thesis, The University of Auckland, New Zealand, 218 p

Gabites JE, Christie AB (1994) Lead isotopic studies of mineral deposits in the Coromandel Volcanic Zone, North Island, New Zealand. Geological Society of America 1994 annual meeting, abstracts with programs: A-498 (poster)

Hedenquist JW, Gulson BL (1992) Intrusive and basement rock sources of lead in hydrothermal systems of the Taupð Volcanic Zone, New Zealand. Geochim Cosmochim Acta 56:2821-2829

Hudson SA (2022) Geochemical and vein textural investigation of the Wharekirauponga epithermal Au-Ag deposit, Hauraki Goldfield, New Zealand. Unpublished MSc thesis, The University of Auckland, New Zealand. 155 p

Mauk JL, Hall CM, Chesley JT, Barra F (2011) Punctuated evolution of a large epithermal province: the Hauraki Goldfield, New Zealand. Econ Geol 106:921-943

Merchant RJ (1978) Metallogenesis in the Thames - Tapu area Coromandel Peninsula, New Zealand: Unpublished PhD thesis, The University of Auckland, New Zealand. 363 p

Merchant RJ (1986) Mineralization in the Thames district - Coromandel. In: Henley RW, Hedenquist JW, Roberts PJ eds, Guide to the active epithermal (geothermal) systems and precious metal deposits of New Zealand. Monograph Series on Mineral Deposits 26:147-163. Berlin, Gebruder & Borntraeger

Morrell AE, Locke CA, Cassidy J, Mauk JL (2011) Geophysical characteristics of adularia-sericite epithermal gold-silver deposits in the Waihi-Waitekauri region, New Zealand. Econ Geol 106:1031-1041

Robinson BW (1974) The origin of mineralization at the Tui mine, Te Aroha, New Zealand, in the light of stable isotope studies. Econ Geol 69:910-925

Rowland JV, Simmons SF (2012) Hydrologic, magmatic and tectonic controls on hydrothermal flow, Taupō Volcanic Zone, New Zealand: implications for the formation of epithermal vein deposits. Econ Geol 107:427-457

Simmons SF; Browne PRL (2000) Hydrothermal minerals and precious metals in the Broadlands-Ohaaki Geothermal System; implications for understanding low-sulfidation epithermal environments. Econ Geol 95:971-999

Simmons SF, Browne PRL (2007) The flux of gold and related metals through a volcanic arc, Taupō Volcanic Zone, New Zealand. Geology 35:1099–1102

Simpson MP (2017) Microthermometry of deep veins from the Waihi, Karangahake and Tui epithermal vein deposits, southern Hauraki Goldfield. Proceedings of the AusIMM New Zealand Branch 50th annual conference, pp 284-293

Torckler L, Hobbins JM, Christie AB (2016) Mining and exploration of the epithermal gold-silver deposits at Waihi, Hauraki Goldfield. In: Mineral Deposits of New Zealand – Exploration and Research, Christie AB (ed), AusIMM Monograph 31:303-312

Porphyry Cu-Au Related Hydrothermal Alteration in the Radersburg District, Elkhorn Mountains, Montana

Clevenger, Joseph J.[1], Dilles, John H.[1], Eastman, Kyle[2], Anderson, Eric[3],
[1] College of Earth Ocean and Atmospheric Sciences, department of geology and Geophysics, Oregon State University, Corvallis, Oregon, USA
[2]Montana Bureau of Mines and Geology, Butte, Montana, USA
[3]U.S. Geological Survey, Denver Federal Center, Denver, Colorado, USA

Abstract., West of the town of Radersburg, among satellite plutons of the Boulder Batholith, Exxon drillholes reaching 800m depth encountered modest Cu-Au grades (0.1-0.2wt%Cu) in zones of quartz-chalcopyrite-pyrite±magnetite veins, associated with high temperature biotite and K-feldspar wall-rock alteration. This apparent porphyry copper deposit lies less than a km south of two historic auriferous pyrite deposits; the Keating and Ohio-Keating veins. Here we present preliminary data recording hydrothermal alteration in surface exposures and select subsurface samples. Above and outboard from the central potassic zone, the district is characterized by abundant feldspar destructive white mica alteration overprinting a central k-feldspar-carbonate>sericite-albite±chlorite feature that suggests low temperature primary hydrothermal fluids. Pervasive potassium addition is recorded through multiple spectroscopic methods. Sulfides are zoned outwards from chalcopyrite-pyrite, to proximal pyrite, to distal pyrrhotite>pyrite. This occurs concomitant with a shift in muscovite Al-OH SWIR feature position from >2205 (more phengite component) proximally to <2205 (more muscovite component) distally. The early addition of K-feldspar and CO_2 (carbonate) likely buffered later, lower temperature acid fluids, maintaining near neutral conditions and thereby producing the phengitic mica observed. Pyrrhotite>pyrite mineralization zones reflect lithology and potentially distance from fluid source while subsurface alteration mineralogy indicates multiple stages of fluid overprinting.

1 Introduction

The Cedar Plains or Radersburg Mining district of southwestern Montana lies roughly 70km east-northeast of the town of Butte, within the rising limb of a regional north to south trending syncline of the Laramide-Sevier fold-thrust belt. Within the Radersburg 7.5' quadrangle, hydrothermal base and precious metal mineralization occur as carbonate replacement, skarn, vein type, and porphyry type deposits related to a series of local intrusive dikes and stocks that post-date Laramide-Sevier deformation and intrude Paleozoic sedimentary suites, the Late Cretaceous Elkhorn Mountains Volcanics (EMVs, middle member is ~83.3±1.8 Ma and the lower member ~84.9±1.6 Ma (Lund 2022)) and an older suite of felsic (andesitic) plutons collectively termed the Rattlesnake mass (Klepper et al. 1971). Sills and stocks related to the Rattlesnake mass are frequently cut by mineralized veins.

In the late 1970's Exxon Minerals Co. identified a low-grade porphyry copper center in the Eastern Elkhorn Mountains just west of the town of Radersburg. Here, Exxon drilled to a depth of 750m encountering a series of granodiorite porphyry dikes that intrude Elkhorn Mountain Volcanics and Slim Sam Formation country rocks with characteristic high temperature potassium feldspar and biotite alteration associated with minor and low-grade copper (0.1-0.2wt%Cu) and gold mineralization at depth (PA Mitchell, written commun. 1981). Two roughly north trending, <2m thick quartz (Qtz)-calcite (Calc)-auriferous pyrite (Py)-chalcopyrite (Ccp) veins were mined for gold during the period of 1866-1947 and were the leading Montanan producers of the commodity for many years. These were the Keating (~N5^{0}E/70^{0}W) and the Ohio-Keating (~N15^{0}W/80^{0}W) vein systems (Klepper et al. 1971). Ar-Ar dating of hornblende and mica in the Rattlesnake intrusion combined with similar analyses in lamprophyre dikes which crosscut, and therefore post-date, mineralized veins, bracket the timing of mineralization and suggest that emplacement of the Ohio-Keating vein occurred between 78.2±0.1 Ma and 78.0±0.1 Ma (Dilles et al. 2024). However, regionally, intrusions related to mineralization such as the Congress mine granodiorite porphyry, Diamond Hill granodiorite porphyry, and the Vosberg granodiorite porphyry, give ages of 75.9±0.7Ma, 77.1±1.6 Ma, and 70.5±0.4Ma respectively, suggesting mineralization primarily occurred during a younger phase of magmatism (Dilles et al. 2024). Al-in-hornblende barometry indicates most plutons were emplaced at ~1.3-2.0 Kbar pressure which is equivalent to ~5-8km depth (Dilles et al. 2024).

Notably, the primary commodity of this porphyry related magmatic-hydrothermal deposit, historically, has been not copper, but gold and contains little copper, even in the highest temperature zones probed via diamond drill core. Few porphyry deposits feature gold as the primary commodity and the temporally and genetically related (by the Boulder Batholith) Butte deposit lacks significant gold (Reed and Dilles 2021). The root cause of this difference in metal endowment is likely magmatic in nature (Olson 2022) but close observation of the chemical footprint of alteration might reveal a correlative link. Additionally, gold is easily scavenged and remobilized by high temperature vapors containing H_2S and low temperature acid fluids respectively (Kesler et al. 2002).

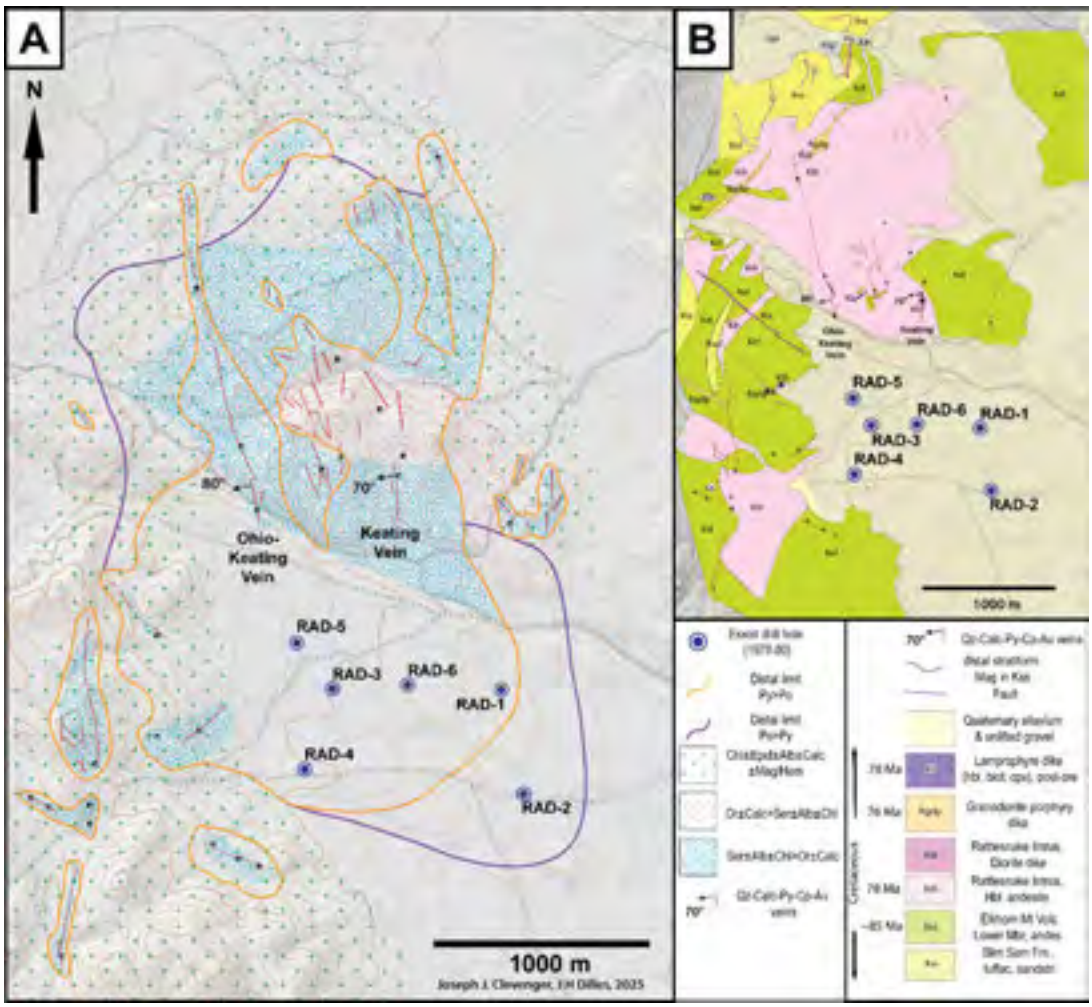


Figure 1. Hydrothermal alteration (left) and geology (right) of the Radersburg district.

Understanding the distribution and character of alteration features in Radersburg could help to guide exploration of the resource as well as answer questions as to the link between magmatic volatile phases and metal zonation at the deposit scale.

2 Methods

Geology, alteration mineralogy, and mineralization were mapped at 1:12,000 scale in a roughly 3x5km region centered on the Keating and Ohio-Keating veins. Alteration minerals were identified in outcrop and hand sample via hand lens and recorded along with veins and faults using an altered Anaconda system utilizing mylar overlays atop satellite image basemaps (Einaudi, 1997). Chip samples were systematically sampled at the intersection of ten northings and eastings in a roughly 200m by 200m grid across this same region. The hydrous mineralogy of the chips were analysed via Short Wave Infrared (SWIR, 900-2500nm wavelength) spectroscopy using an ARCoptix FT-IR spectrometer and selected samples were analysed via X-ray diffraction (XRD) for identification of anhydrous silicate phases. Additionally, samples were analysed for major and trace elements via portable x-ray fluorescence spectrometer.

3 Results and Discussion

Exxon drilled core (holes RAD-3 and RAD-5) evidence three distinct stages of alteration at depth: 1) Primary high-T K-feldspar-biotite alteration of magmatic phases , 2) hydrolytic feldspar destructive muscovite/sericite alteration, and 3) late low-T and near-neutral pH clay alteration. Host rock not overprinted by low-T clay species is pervasively altered to mixtures of Qtz-Ms-k-feldspar. The former alteration style is associated with sparse near vertical, aplitic sucritic Qtz+fine-grained k-feldspar A-veins that are cut by abundant cm scale sheeted poorly mineralized Qtz-Ccp-Py-Mag B-veins. The later often feature distinct mm scale K-feldspar selvages and, more rarely, patchy Mag-Py selvages. These are all crosscut by thin mm scale subvertical quartz veinlets, which are themselves cut by thin mm scale brittle fracture filling pyrite veinlets. Many B-veins appear re-opened, with limpid quartz girded by K-feldspar or Mag-Py selvages surrounding fluid inclusion-rich murky quartz. These murky quartz veins, which appear as “mineral water” peaks in SWIR can be seen crosscutting vertical B-veins at subvertical angles and often contain central illite pods and illite or illite-smectite selvages. These relationships are most apparent in Hole 3, where illite or smectite selvages occur along subvertical fluid-inclusion-rich

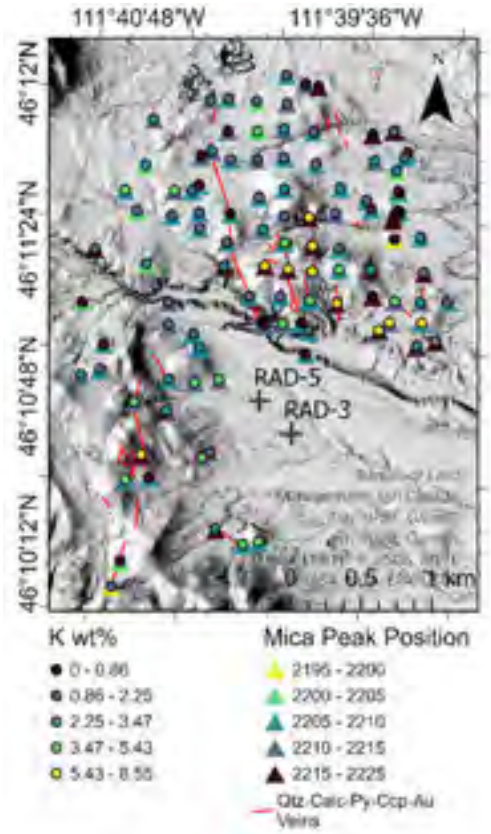


Figure 2. Wt% K values (circles) measured via pXRF and the position of the mica Al-OH feature in the SWIR spectral range (triangles) of chip samples across the Radersburg district. Warmer colors indicate higher K concentrations and muscovitic mica compositions while cooler colors indicate low K values and phengitic mica compositions. Qz-Calc-Py-Au-Cu veins are mapped in red.

often feature void filling carbonate and are locally associated with chlorite and diffuse smectite (mapped as montmorillonite) pervasively altering groundmass feldspars. In hand sample, plagioclase phenocrysts can be seen partially altered to a pale lime-green-colored clay that is likely montmorillonite.

Within vein quartz can be seen late, secondary vapor-rich and liquid-rich (small vapor bubble e.g. 5-10%vol) fluid inclusion trails that cut across or are not associated with growth zones. These inclusions likely reflect a boiling assemblage for a dilute fluid at T<374°C and P<220 bars (Bodnar et al. 1985). Assuming the liquid-like fluid has a density of ~0.7g/cc, this would correspond to depths of 2.4-3km under hydrostatic conditions. The addition of salt allows for higher T and P. Sheeted, 100% quartz veins in RAD 3 and 5 exhibit ductile recrystallization textures suggesting temperatures of >350-400^{0}C (Tullis and Yund 1977). Undeformed quartz growth zones associated with vein chalcopyrite and calcite contain liquid-rich high salinity fluid inclusions with small vapor bubbles (~10 vol%), halite, and locally oxides. Some vapor-rich inclusions are also observed. The high salinity inclusions must form by brine-vapor unmixing, suggesting a max P of 1.4 kbar based on the apex of the brine-vapor solvus at ~700°C (but could be considerably less if the bulk parental fluid is on the low salinity side of the solvus) (Bodnar et al. 1985). At lithostatic pressures, the depths would therefore be <4-5 km.

In contrast to drill holes 3 and 5, surface expressions of alteration lack hydrothermal biotite-K-feldspar and Qtz-Ccp vein evidence for high- T porphyry magmatic-hydrothermal fluids (Fig. 1). To the north of Keating Gulch, the topographic high, here called Keating Hill, exhibits elevated K and Th values in airborne and ground-based GRS measurements (Anderson et al. 2025), which are corroborated here by pXRF analyses in addition to ICP-OES bulk rock geochemical analyses (Fig. 2). In this ~0.5km by 1 km zone north of the Exxon drill holes, K values are elevated relative to unaltered andesite (<2.3 wt%K) to as much as 8.5-12 wt%K (Fig.1-2). Here, granodioritic plutonic and andesitic volcanic country rocks are altered to mixtures of Qtz-K-feldspar-Ser-Calc±Alb±Chl±Po-Py with additional supergene clays and limonite after sulfides. XRD, petrography, and SEM analyses further suggest that these assemblages are dominated by K-feldspar with only minor sericite. Amphibole sites in the granodioritic country rocks (Rattlesnake intrusion) are altered to chlorite group minerals (clinochlore+trace phases) although XRD analyses reveal trace amount of relict unaltered hornblende. No biotite alteration is indicated. The alteration of primary plagioclase (andesine to oligoclase compositions are indicated from bulk rock geochemical data) to K-feldspar without biotite alteration of hornblende suggests hydrothermal fluids at the depth now exposed as the modern surface did not reach T>450^{0}C and, based on these phase relationships, might have been carbonate-rich and at circum-neutral pH (Beane 1974). At temperatures <450°C, biotite in the presence of muscovite would break down to form chlorite+K-feldspar (Dilles and John 2020).

All analytical data indicate that sericite present here is muscovite-phengite, which is generally stabilized at log(aK^+/aH^+) between ~3-4, corresponding to maximum temperatures of ~550^{0}C at 1Kbar pressure (Seedorff et al. 2005). Decreasing temperatures broadens the stability field to increased aK^+/aH^+ values. Within this space, muscovite characteristically varies in crystallinity and composition, with smaller less uniformly stacked crystallites with Al and K deficiencies (relative to end-member muscovite) forming at lower temperatures (<300^{0}C, muscovite series members of this kind being designated illite (Grim 1962; Bailey 1984; Reyes 1990)), more Fe and Mg rich — phengitic— compositions forming at higher aK^+/aH^+, and muscovitic compositions at lower aK^+/aH^+ (Halley 2015). The latter variation in composition is controlled by a coupled Tschermak-type substitution of (Fe^{2+},Mg^{2+})+Si^{4+} for Al^+ and can be tracked via a characteristic shift of the Al-OH feature position in the short-wavelength infrared (SWIR) spectrum from 2195nm at muscovite/muscovite-paragonite compositions to 2220nm at phengite (Halley 2015).

Fourier-transform near-infrared (FT-IR SWIR) spectroscopy analyses of samples collected from where alteration assemblages generally reflect Or±Calc>Ser±Alb are strictly >2215nm, indicating phengitic mica compositions, and suggesting host rock feldspars effectively buffered the magmatic-hydrothermal fluids to near neutral pH (and elevated $\log(m_{KCl+K}/m_{HCl+H})$) (Sepp 2022).

Surrounding this narrow band of Or±Calc>Ser±Alb±Chl alteration is a broader region of propylitic alteration characterized by Chl-Alb±Epid±Calc with sparse disseminated sulfide or no sulfide but cut by Qz-Calc-Py-Au-Cu vein localized alteration typified by short wavelength sericite in excess of K-feldspar (Fig. 1-2). Higher K concentrations generally correspond to these local alteration aureoles with K values otherwise dropping to ≤3wt%K (Fig. 2). Within this region, a distal band of low pH alteration north of Keating Hill and wrapping around to the west-southwest, is indicated by samples featuring white micas with Al-OH features ranging from 2195-2205nm. This trend likely reflects evolving fluid chemistry upon cooling and depressurization during upward and outward movement away from the hydrothermal center.

Surface mineralization consists of two primary zones of sulfide addition. A lobe of pyrrhotite>pyrite which wraps around the eastern side of Keating hill and a larger region of pyrite>pyrrhotite which covers Keating Hill itself and extends ~2500m to the north. The latter mineralization style characterizes the Keating and Ohio-Keating veins and can be seen in surface exposures to the south of the Ohio-Keating mine. More distal expressions occur locally and correspond to ore veins such as those uncovered at the Black Friday and Gopher mines. Zones of pyrrhotite>pyrite likely correspond to Fe-rich lithologies that induced fluid compositions with high aFe but low fS and thus the precipitation of pyrrhotite in preference to pyrite. The general zoning consists of early Py-Ccp±Mag in high T K-feldspar biotite altered regions giving way upwards and outwards to Po±Py with Or±Calc>Ser±Alb±Chl alteration and distal weak propylitic alteration beyond. Qz-Calc-Py-Au-Cu veins such as the Keating and Ohio-Keating cut all three zones and are associated with overprinting Ser±Alb±Chl>Or±Calc and feature muscovite with Al-OH features <2210nm. This relationship implies that the latter veins and alteration are late forming relative to other alteration and mineralization types.

In general, despite the character of the ore, alteration in this district is more characteristic of a porphyry system than an epithermal environment. The lack of significant silica alteration and the dominance of pyrite in veins, absence of significant argillic and steam-heated alteration, as well as the lack of phreatic brecciation precludes the classification of the system as an epithermal deposit. Further, pressure and depth estimates from petrographic analyses of fluid inclusions, hornblende barometry, and regional geology indicate the system formed below the epithermal environment.

Acknowledgements

We thank SCOUT Discoveries Corp. in Coeur d'Alene, Idaho for the use of their core scanning facilities, Eurasian Minerals for providing us the historic Exxon core, Peter Mitchell for his advice and preservation of Exxon materials, the USGS for providing bulk geochemical analyses, and many others for their support of this project.

References

Anderson et al. (2025) Airborne radiometric data map alteration of porphyry copper systems in the Elkhorn district, MT. Proceedings of the 18th Biennial SGA Meeting, August 2025, Golden, CO, USA.

Bailey S (1984) Micas. Reviews in Mineralogy and Geochemistry 46(1). Mineralogical Society of America

Beane RE (1974) Biotite stability in the porphyry copper environment. Economic Geology 69(2):241-256

Bodnar et al (1985) Synthetic fluid inclusions in natural quartz. III. Determination of phase equilibrium properties in the system H_2O-NaCl to 1000^0C and 1500 bars. Geochimica et Cosmochimica Acta 49(9):1861-1873

Dilles et al. (2024) Zircon Age and Geochemistry of Granites Related to Porphyry and Polymetallic Mineral Deposits of the Eastern Elkhorn Mountains and Boulder Batholith, Montana. In: Geological Society of America Abstracts Vol. 56, pp 399546).

Dilles JH and John D (2021) Porphyry and epithermal mineral deposits. In: Encyclopedia of Geology, 2nd edn. Academic Press 2021, pp 847-866

Einaudi MT (1997) Mapping altered and mineralized rocks. An introduction to the "Anaconda Method". Short-course notes Stanford University, USA.

Grim RE (1962) Applied clay mineralogy. McGraw Hill, New York

Halley S et al. (2015) Footprints: Hydrothermal alteration and geochemical dispersion around porphyry copper deposits. Society of Economic Geologists newsletter 100:1-17

Kesler SE, Chryssoulis SL, Simon G (2002) Gold in porphyry copper deposits: its abundance and fate. Ore Geology Reviews 21(1-2): 103-124.

Klepper M, Robinson GD, Smedes HW (1971) On the nature of the Boulder batholith of Montana. Geological Society of America Bulletin 82(6):1563-1580

Lund K, Aleinikoff JN (2022) Temporal relations between the Boulder Batholith and Elkhorn Mountains Volcanics, western Montana: "The Nature of Batholiths" revised. In: Proceedings of the Montana Mining and Mineral Symposium 2021: Montana Bureau of Mines and Geology Special Publication 123:89-97

Olson N (2022) Petrologic Investigations into the Magmatic Processes That lead to Au, Ag, and Base Metal Fertility: Insights from Pebble, Alaska and the Emigrant Pass Volcanic Field, Nevada. Dissertation, Oregon State University.

Reyes AG (1990) Petrology of Philippine geothermal systems and the application of alteration mineralogy to their assessment. Journal of Volcanology and Geothermal Research 43:279–309

Sepp M (2022) What lies Beneath? Origin and Transition from the Shallow Epithermal Au-Ag Lithocap to Deeper Porphyry Cu Environment: Insights from the Magmatic Hydrothermal Deposits at Yerington, Nevada, and Summitville, Colorado. Dissertation, Oregon State University

Tullis J and Yund RA (1977) Experimental deformation of dry Westerly granite. Journal of geophysical research 82(36):5705-5718.

Relationships of lithocaps to porphyry and epithermal deposits – an example from the Baguio district, Philippines

David R. Cooke[1], Lejun Zhang[1], Zhaoshan Chang[1,2], Noel C. White[1,3], Pete Hollings[4], Michael Baker[1], and Cari Deyell[6]

[1] CODES, Centre for Ore Deposit and Earth Sciences, University of Tasmania, Private Bag 79, Hobart, Tasmania, 7001, Australia

[2] Department of Geology and Geological Engineering, Colorado School of Mines, Golden, Colorado 80401, USA

[3] Ore Deposit and Exploration Centre, School of Resource and Environmental Engineering, Hefei University of Technology, Hefei, Anhui 230009, China

[4] Department of Geology, Lakehead University, 955 Oliver Road, Thunder Bay, ON, P7B 5E16, Canada

[5] Veracio, Montreal, QC, Canada

Abstract. The Baguio lithocap, Philippines, is associated spatially with Pliocene to Pleistocene porphyry Cu-Au, intermediate- and high-sulfidation state epithermal vein systems, and Cu-Au and Au-Pb-Zn skarns. It is dominated by advanced argillic alteration (quartz-alunite) with pyrohylllite-dickite muscovite alteration exposed at lower elevations. The lithocap is densely populated, causing access issues for exploration. Surface sampling of weathered and fresh samples provided the basis for detailed whole rock geochemical, SWIR and alunite mineral chemistry analyses that highlight two upflow zones for the Baguio lithocap, at its north-eastern and south-eastern ends, implying that the lithocap is a composite alteration domain sourced from at least two magmatic-hydrothermal centers. There is potential for discovery of porphyry Cu-Au mineralization beneath the NE and SE upflow zones adjacent to the lithocap.

1 Introduction

The Baguio district, Philippines, contains porphyry Cu-Au deposits, intermediate and high sulfidation epithermal veins, and skarns (Fig. 1), which all formed during the last 3 Myr (Waters et al., 2011; Cooke et al., 2011). The district also contains the Baguio lithocap, a large domain of silicic, advanced argillic and argillic altered rocks that mostly crops out at high elevation on the northwest side of the district (UNDP, 1987; Aokli et al., 1993). The lithocap is more than 7 km long, up to 3 km wide and over 300 m thick and is flanked by porphyry and epithermal deposits at lower elevations to the south, east and north. The lithocap is densely populated in places, meaning that it is underexplored; it is unclear as to whether it is genetically related to one or more of the known porphyry deposits, or if there is potential for the discovery of additional porphyry and/or epithermal resources beneath or within the lithocap. It is also unclear whether the lithocap is a simple or composite lithocap – i.e., is it the outflow zone for acidic fluids derived from a single system, or were fluids derived from more than one fluid source, producing a complex zone of overprinting of multiple advanced argillic and silicic assemblages?.

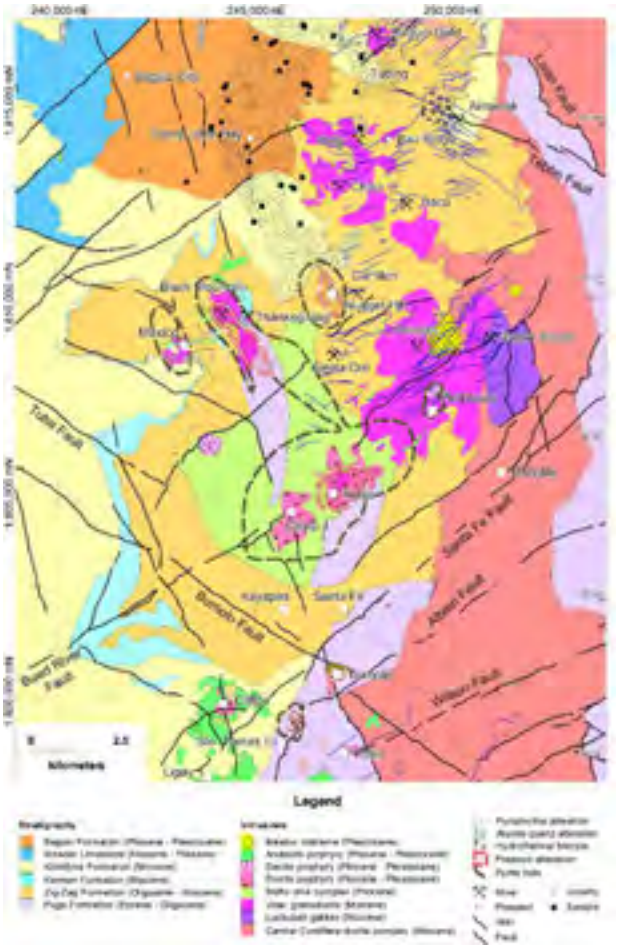


Figure 1. Geologic map of the Baguio district, modified after Waters et al. (2011). Abbreviation: Sto = Santo.

2 Alteration mineralogy and geochemistry

The lithocap is dominated by quartz-alunite and massive quartz alteration, with pyrite common in some exposures and limonites (hematite, goethite, minor jarosite) abundant in weathered outcrops. Shortwave infrared (SWIR) analyses highlight a large range in results for the 1,480 nm absorption feature, from 1,479 (alunite) to 1,494 nm (natroalunite), with higher values defining two coherent anomalies at the northeastern and

southeastern ends of the lithocap. Despite intense weathering locally, whole-rock analyses are dominated by hypogene alteration compositions and are consistent with SWIR data. Significant and widespread Bi, Te, Se, and Sn anomalies and more limited Mo and Au anomalies correlate with the SWIR results. This suite of anomalous pathfinder elements is consistent with a deeper level of exposure of the lithocap, as also implied by the presence of high temperature advanced argillic and white mica alteration minerals; approximately 500 – 1,000 m of erosion is estimated since lithocap formation.

3 Conclusions

By applying a combination of geological, mineralogical, geochemical, and spectral data, two potential upflow zones have been identified for acidic magmatic-hydrothermal fluids that formed the Baguio lithocap. There is potential for additional porphyry deposits to be discovered below and/or adjacent to the northeastern and/or southeastern flanks of the lithocap, where the lithocap upflow zones are located.

Acknowledgements

Thank you to all sponsors and research team members from AMIRA P765 and 765A, and AMIRA project manager Alan Goode. Thanks to Jeff Hedenquist and Dave Braxton who were involved in the sampling programs, and to Paddy Waters and the team of exploration geologists and support staff at Anglo American (including Rene Gonzales, Norman Tamayo, Ferdie Banez, Andrew C. Cabrera, Reynaldo Estacio, Ian U. Furigay, Gabriel Ogad and Melodie Pascual) - their support was critical to our field sampling campaign.

References

Aoki M, Comsti EC, Lazo FB, Matsuhisha Y (1993) Advanced argillic alteration and geochemistry of alunite in an evolving hydrothermal system at Baguio, northern Luzon, Philippines. Resource Geology 43:155–164.

Cooke DR, Deyell C, Waters PJ, Gonzales RI, Zaw K (2011) Evidence for magmatic-hydrothermal fluids and ore-forming processes in epithermal and porphyry deposits of the Baguio district, Philippines. Econ Geol 106:1399–1424.

United Nations Development Programme (1987) Geology and mineralization in the Baguio area, Northern Luzon: United Nations Development Programme, Bureau of Mines and Geo-Sciences, Department of Environment and Natural Resources, Technical Report 5, 82 p.

Waters PJ, Cooke DR, Gonzales RI, Phillips D (2011) Porphyry and epithermal deposits and $^{40}Ar/^{39}Ar$ geochronology of the Baguio district, Philippines. Econ Geol, 106:1335–1363.

Trace and critical elements in UV-fluorescent and non-fluorescent sphalerite from the Butte porphyry-lode deposit, Montana, USA

Kyle A. Eastman[1,2], Christopher H. Gammons[1], Celine Beaucamp[1], Jay M. Thompson[3], Heather A. Lowers[3]
[1]Department of Geological Engineering, Montana Technological University, Butte, MT, USA
[2]Montana Bureau of Mines and Geology, Butte, MT, USA
[3]U.S. Geological Survey, LTrace Laboratory, Denver, CO, USA

Abstract. Sphalerite from the Butte District displays variable ultraviolet fluorescence, with intensely red and yellow fluorescent sphalerite occurring in the central, high-sulfidation state part of the district, and non-fluorescent sphalerite in distal veins. Coupled substitution of Cu, Ag, W, In, Ga, Ge, As, Sb, and Bi occurs in fluorescent Butte sphalerite; non-fluorescent sphalerite is Fe-rich with lower trace element contents and common finely distributed chalcopyrite inclusions ("chalcopyrite disease"). Fluorescence, combined with mineral associations and textures, provides a useful and easily-applied vector towards the high-sulfidation central zones of porphyry-epithermal districts and distinguishes sphalerite with potentially important critical or by-product element contents.

1 Introduction

Sphalerite is an isometric zinc sulfide, with simple and coupled substitution of Fe and other elements yielding variation in visible light color and UV fluorescence color. Sphalerite is a primary ore of zinc, and an important source of the critical elements Ga, In, Ge, and Cd (Frenzel and others, 2016); it occurs in a variety of deposit types, including porphyry-epithermal-skarn systems, Mississippi-Valley-Type (MVT) carbonate replacements, and sediment-hosted base metal deposits (SEDEX-type).

The Butte porphyry-lode district is hosted within the 76 Ma Butte Granite phase of the Boulder Batholith (Figure 1), with mineralization ages ranging from 74-62 Ma (Lund et al. 2018). At Butte, sphalerite-bearing intermediate and high-sulfidation state Main Stage veins cut earlier domes of porphyry-style Cu-Mo mineralization. Butte is classified as a "supergiant" porphyry Cu deposit based on contained Cu (Cooke et al. 2005) but has also been an important historic producer of Mo, Ag, Pb, Au, and the critical commodities Mn, Zn, Cd, Bi, As, Se, and Te (Anaconda Geological Dept. 1971). In 1930, the Anaconda Copper Company patented a process to remove Ge from Zn sulfate solutions (US Patent US1848264A) and later developed a Ge extraction circuit. As of 2024, China has prohibited exports of Ga, Ge, and Sb to the United States, further focusing efforts to understand the deportment of these elements in domestic sources.

Main Stage veins at Butte are conjugate sets of steeply-dipping and generally E-W striking structures, which can be over 2km in strike length and exceed 5m in width (Houston and Dilles 2013). These veins are mineralogically zoned around the center of the district, near the Leonard Mine shaft and Berkeley Pit. Central Zone Main Stage veins are characterized by higher sulfidation state minerals such as enargite, chalcocite, bornite, and covellite, surrounded by an Intermediate Zone with increased sphalerite content. In the Peripheral zone, the Mn minerals rhodochrosite and rhodonite appear, along with Ag minerals and abundant sphalerite and galena. General geochemical zonation in the Main Stage veins shows central Cu-As(Ag) trending outward to Cu-Zn(Ag) and distal Zn-Mn-Ag (Pb, Cu).

This study uses historic sample collections along with more recent drilling and sampling to investigate the trace and critical element content of sphalerite from Butte, relate the mineral chemistry to UV fluorescence, develop vectoring tools, and compare Butte sphalerite with other occurrences in the region – notably the Philipsburg District (Figure 1; Beaucamp et al. 2024).

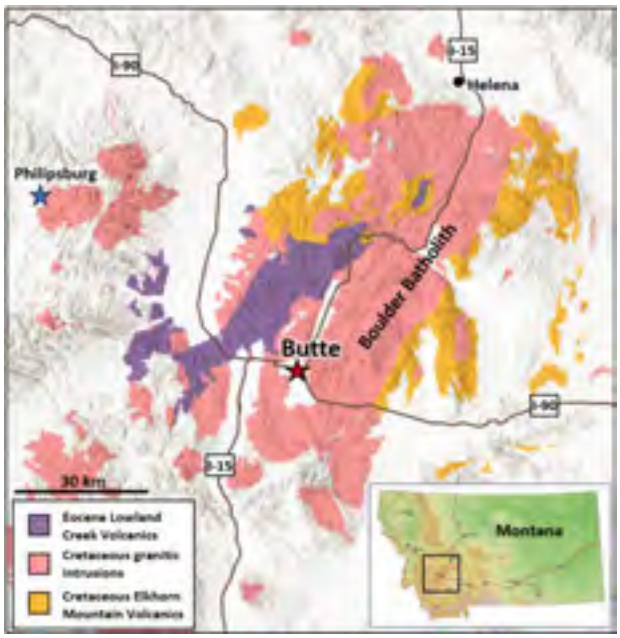


Figure 1. Simplified geologic map of southwestern Montana showing the Butte and Philipsburg mining districts. Geologic map data from Vuke et al. 2007.

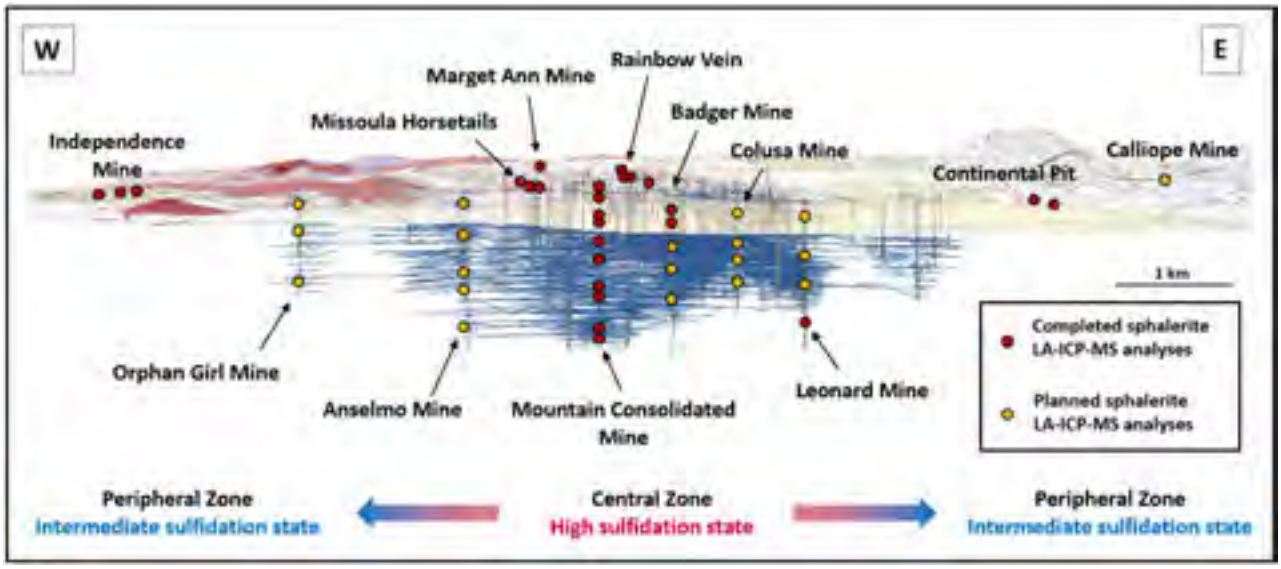


Figure 2. Locations of sphalerite samples with the historic Butte mine workings, looking north. Sampled mines are labeled, with completed analyses in red and planned analyses in yellow. Geologic map surface layer from Houston and Dilles (2013).

2 Methodology

Sphalerite samples from the now-flooded underground mines in the Butte District were selected from the historic Anaconda Research Collection (ARC), housed at the Montana Bureau of Mines and Geology. Drill core made available by Silver Bow Mining Corp provided additional samples from the northern part of the district, and the authors' personal sampling of mine dumps (2015-2024) provided coverage for some distal veins.

Polished mounts were prepared and imaged in both reflected light and 365nm ("long-wave") UV light. Hyperspectral cathodoluminescence (HCL) imaging and LA-ICP-MS analyses were conducted at the USGS Denver Microbeam Laboratory. False-color HCL images were used to guide selection of LA-ICP-MS point and map analysis areas, with 51 isotopes measured; ^{7}Li, ^{23}Na, ^{24}Mg, ^{27}Al, ^{29}Si, ^{31}P, ^{34}S, ^{39}K, ^{44}Ca, ^{47}Ti, ^{51}V, ^{53}Cr, ^{55}Mn, ^{57}Fe, ^{59}Co, ^{60}Ni, ^{63}Cu, ^{66}Zn, ^{71}Ga, ^{73}Ge, ^{74}Ge, ^{75}As, ^{77}Se, ^{85}Rb, ^{88}Sr, ^{89}Y, ^{90}Zr, ^{93}Nb, ^{95}Mo, ^{109}Ag, ^{111}Cd, ^{115}In, ^{118}Sn, ^{121}Sb, ^{125}Te, ^{137}Ba, ^{139}La, ^{140}Ce, ^{172}Yb, ^{182}W, ^{185}Re, ^{195}Pt, ^{197}Au, ^{202}Hg, ^{205}Tl, ^{206}Pb, ^{207}Pb, ^{208}Pb, ^{209}Bi, ^{232}Th, and ^{238}U. A 30µm beam size was used for point analyses, and a 20µm beam size was used for element mapping.

3 Results

UV fluorescence and HCL imaging show brightly-colored and detailed banding and sector zonation in Butte sphalerite (Figure 3). With a few exceptions, the most intensely fluorescent sphalerite occurs in the Central and Intermediate zones of the Main Stage Veins, with high-Fe non-fluorescent sphalerite ("blackjack") becoming dominant in the Peripheral zone.

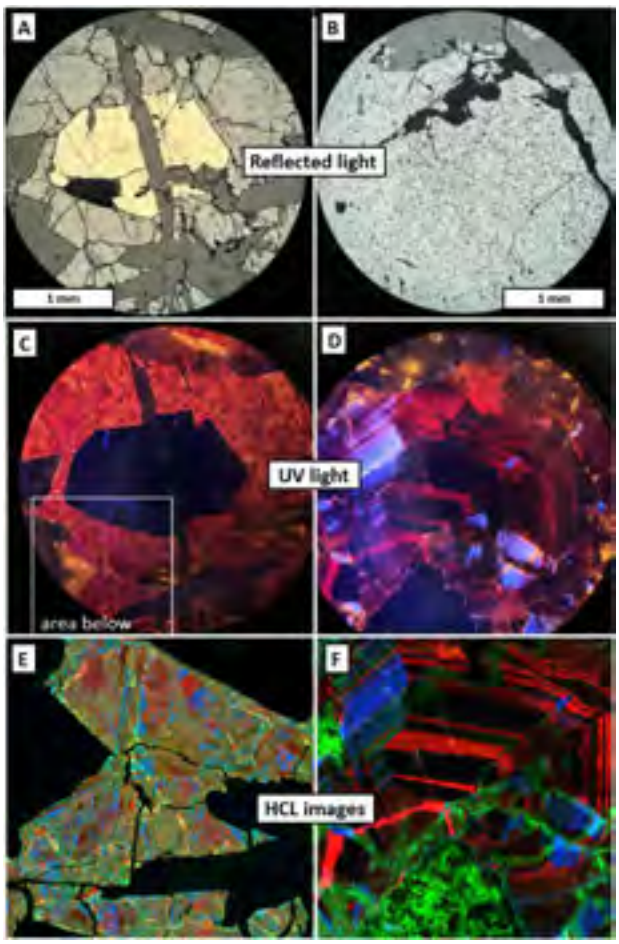


Figure 3. Reflected-light (A, B), UV light (C, D), and false-color HCL images (E, F) of fluorescent sphalerite from the Mountain Consolidated Mine, Butte.

LA-ICP-MS data on Butte sphalerite indicates the amount of Fe required to suppress UV fluorescence is ~500ppm. Data from fluorescent Butte sphalerite (Figure 3) show elevated Cu, Ga, Ge, In, and W – similar to Butte sphalerite data from Ortelli (2015), and Philipsburg UV-fluorescent sphalerite data (Beaucamp et al. 2024).

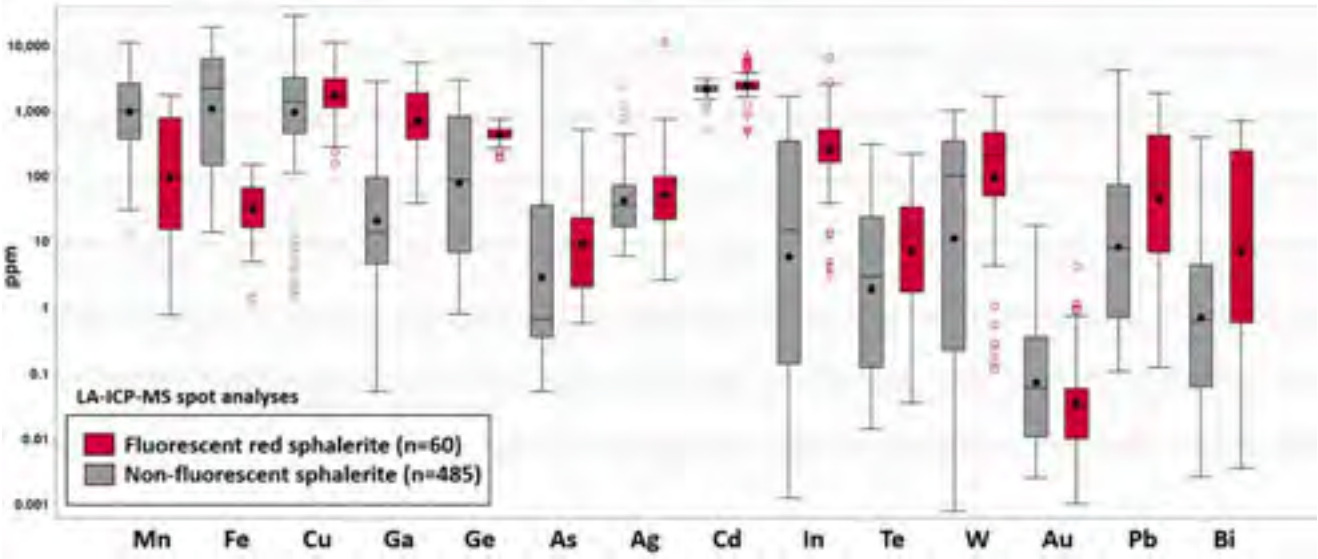


Figure 4. LA-ICP-MS spot analyses of fluorescent red sphalerite compared to non-fluorescent sphalerite. Box = middle 50%, line in the box = median, circle = mean, whiskers = 5th and 95th percentile, outliers at top and bottom.

Ortelli (2015) did not analyse for W, and Philipsburg sphalerite analyses by Beaucamp and others (2024) is the first documented occurrence of high W in sphalerite (>10 ppm). A limited range of Cd content in sphalerite (~1200 ppm) suggests that the Zn/Cd ratio in the ore-forming fluid is constant and that competition with other minerals is not occurring.

Trace element-rich sphalerite in the Central Zone of the Butte District (i.e., Mountain Consolidated and Badger mines) is commonly fluorescent red, although complicated textures with orange, yellow, green, blue and other colors are common. Red fluorescence appears to be associated with W, In, Ga, and Cu content (Figures 4 and 5). Coupled substitution of these and other elements is believed to be stoichiometric, as shown in the following equations (modified from Beaucamp et al. 2024):

Simple substitution

$ZnS + \mathbf{M}^{2+} \leftrightarrow \mathbf{M}S + Zn^{2+}$

(**M** = Fe, Mn, Cd, Hg, Pb)

Coupled substitution, trivalent

$\mathbf{A}^{+} + \mathbf{M}^{3+} \leftrightarrow 2Zn^{2+}$

(**M** = Ga, In, As, Sb, Bi; **A** = Cu, Ag)

Coupled substitution, tetravalent

$2\mathbf{A}^{+} + \mathbf{M}^{4+} \leftrightarrow 3Zn^{2+}$

(**M** = Ge; **A** = Cu, Ag)

Coupled substitution, hexavalent

$4\mathbf{A}^{+} + \mathbf{M}^{6+} \leftrightarrow 5Zn^{2+}$

(**M** = W; **A** = Cu, Ag)

LA-ICP-MS element mapping of a sample from the Badger Mine (AMC 20422) is shown in Figure 5; a Principal Component Analysis was conducted on log-transformed sphalerite data in this map area (Figure 5A).

This analysis identified two main groupings of sphalerite composition; W-Cu-Ga-In and Ge-Ag-As (+/-Sb), although some mixing occurs. These two groups appear as alternating bands in the map area (Figure 5B), suggesting cyclic changes in fluid chemistry. The W-Cu-Ga-In group broadly aligns with strong red fluorescence (Figure 5C), and the Ge-Ag-As group displays yellow or yellow-brown fluorescence and occasional non-fluorescence.

Figure 5D shows a coupled substitution plot in atomic ppm units (ppma) for the same data in the LA-ICP-MS element map area; the W-Cu-Ga-In population follows the 1:1 line closely, which supports the coupled substitution model. The Ge-Ag-As group deviates from the 1:1 line into the excess Cu-Ag field. This could be explained by one or more of the following: 1) abundant, sub-microscopic inclusions of a Cu-Ag rich phase; 2) substitution of Cu^{2+} instead of the expected Cu^{+}; 3) sulfur site vacancies.

Chalcopyrite disease (fine chalcopyrite inclusions in sphalerite) is a common feature of high-Fe and non-fluorescent sphalerite from the Peripheral Zone veins at Butte. High Cu in LA-ICP-MS spot data on this non-fluorescent sphalerite can commonly be attributed to chalcopyrite disease. Most strongly fluorescent sphalerite, including in sample AMC 20422 (Figure 5), has high Cu (to >1000 ppm) and low Fe, and lacks chalcopyrite disease; in this case Cu appears to participate in coupled substitution. Low Fe sphalerite which may be strongly fluorescent requires higher sulfidation state conditions, and this relationship is also present at the Philipsburg district (Barton and Skinner 1979; Beaucamp et al. 2024).

Tennantite-(Zn) is an important intermediate sulfidation state phase that occurs with fluorescent sphalerite at Butte in the transition between the Central and Intermediate zones (i.e., Badger Mine), and this aligns with the outer edge of the Cu-rich veins at Butte.

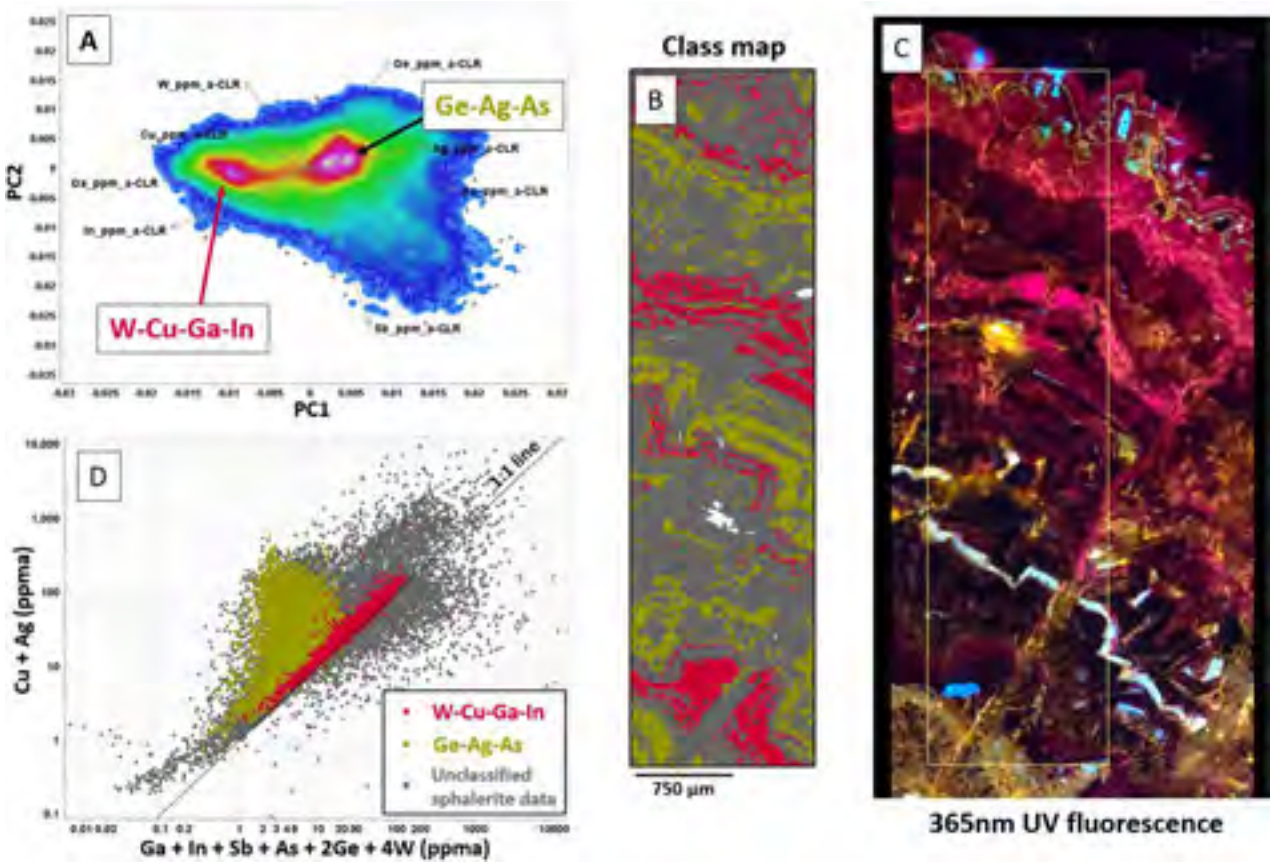


Figure 5. (A) PCA biplot of LA-ICP-MS map data for sample AMC 20422, Badger Mine. **(B)** Class map showing W-Cu-Ga-In (red) and Ge-Ag-As (yellow) populations. **(C)** UV fluorescence with map area. **(D)** Coupled substitution plot with data in atomic ppm (ppma), PCA classes shown.

4 Conclusions

UV-fluorescent sphalerite at Butte occurs in the Central and Intermediate zones of Main Stage veins in the district, and is associated with higher sulfidation state mineralogy, like at Philipsburg. Fluorescence, along with reflected light microscopy of ore mineralogy and textures such as chalcopyrite disease, provides a useful and easily applied vector towards the high sulfidation central zones of porphyry-epithermal districts, and possible high-grade deep ore zones. Substitution of trace elements into sphalerite is associated with varying fluorescent colors and is useful for distinguishing sphalerite that may host important critical and by-product commodities. Ongoing work attempts to link specific elements with fluorescent colors and HCL response; hydrothermal experiments to synthesize sphalerite with known metal contents is a key component of this research.

Acknowledgements

This research was supported by NSF Grant 2327676 to CHG. We thank Michael Peet, Nick Risedorf, and Robert Hogan at Silver Bow Mining Corp, and Connie Thomson, Denise Herman, and Daniel Buckley at the MBMG.

References

Anaconda Company Geological Department (1971) Total Butte, Montana, metal production, 1880-1970; 1p.

Barton PB, and Skinner BJ, (1979) Sulfide mineral stabilities, *in* Barnes, H.L. (ed) 1979, Geochemistry of hydrothermal ore deposits vo. 2; John Wiley Inc., 798p.

Beaucamp-Stout C, Gammons CH, Thompson JA, and Lowers HA (2024) Fluorescent sphalerite rich in tungsten, copper, gallium, silver and other elements from the Cordilleran-style, polymetallic veins of Philipsburg, Montana; Ore Geol Rev, 173, 106267. https://doi.org/10.1016/j.oregeorev.2024.106267

Cooke DR, Hollings P, and Walshe JL (2005) Giant Porphyry Deposits: Characteristics, Distribution, and Tectonic Controls. Econ Geol; 100 (5): 801–818. https://doi.org/10.2113/gsecongeo.100.5.801

Frenzel M, Hirsch T, and Gutzmer J, (2016) Gallium, germanium, indium, and other trace and minor elements in sphalerite as a function of deposit type - a meta-analysis. Ore Geol Rev 76, 52–78. https://doi.org/10.1016/j.oregeorev.2015.12.017

Houston RA, and Dilles JH (2013) Structural geologic evolution of the Butte District, Montana; Econ. Geol. 108, p.1397–1424. https://doi.org/10.2113/econgeo.108.6.1397

Lund K, McAleer RJ, Aleinikoff JN, Cosca MA, and Kunk MJ (2018) Two-event lode-ore deposition at Butte, USA: 40Ar/39Ar and U-Pb documentation of Ag-Au-polymetallic lodes overprinted by younger stockwork Cu-Mo ores and penecontemporaneous Cu lodes: Ore Geol Rev, 102, p. 666–700.https://doi.org/10.1016/j.oregeorev.2018.05.018

Ortelli M (2015) Polymetallic main stage vein formation at Butte, Montana (USA): Combining trace element geochemistry and fluid inclusion study in coexisting ore and gangue minerals, Ph.D. thesis, Universite de Geneve.

Vuke SM, Porter KW, Lonn JD, and Lopez DA (2007) Geologic Map of Montana: MBMG Map 62-A, scale 1:500,000.

The epithermal-skarn transition at the La Colorada deposit, Zacatecas, Mexico

Joshua Ebner[1*], Zhaoshan Chang[1], Pedro Francisco[1], Dante Juarez[2], Patricio Perez[2], Chris Emerson[2], Shiqiang Huang[1], Sidney Hemming[3], Richard Wendlandt[1]

[1] Geology and Geological Engineering Department, Colorado School of Mines, Colorado, USA
[2] Pan American Silver, Zacatecas, Mexico
[3] Lamont-Doherty Earth Observatory, Columbia University, New York, USA
** Currently at Freeport-McMoRan Inc., Arizona, USA*

Abstract. The La Colorada deposit in the Chalchihuites District of Zacatecas, Mexico, features intermediate sulfidation (IS) epithermal, carbonate replacement (CRD), skarn, and porphyry mineral deposit types. Volcanic-hosted IS veins are observed to transition downward into CRD veins in carbonates in underground workings, with the same mineral assemblage, but more calcite. Illite crystallinities, a temperature proxy, of hydrothermally altered volcanic rocks next to IS veins range from 0.6 (~245 ℃) to 1.9 (~300 ℃). Fluid inclusion homogenization temperatures in sphalerite and quartz from IS and CRD veins range from 234 ℃ to 325 ℃. The two data sets indicate two heat and fluid sources that coincide with two syn-skarn intrusive centers. K-Ar dating of 0.2-1 µm illite reveals a minimum age of ~55 Ma for the IS veins. The host rocks are dated at 67-68 Ma, skarn and porphyry mineralization at ~60-64 Ma, and post-mineralization dykes at ~41 Ma. The above observations and data suggest that the skarn, CRD, and IS veins at La Colorada are transitional. This finding opens new exploration potential in IS districts where there are carbonates below volcanic rocks. Exploring below the volcanic-hosted IS veins may lead to related CRD-skarn-porphyry mineralization in the underlying carbonates.

1 Introduction

At La Colorada, intermediate sulfidation (IS) epithermal veins have been mined intermittently for almost 100 years (Moller et al. 2001). Starting in 2018, Pan American Silver has drilled beneath the IS veins and found a large skarn-carbonate replacement (CRD) deposit with lesser porphyry mineralization. As of June 30th, 2024, the skarn resources are 327 Mt averaging 2.79% Zn, 1.29% Pb, and 35 g/t Ag, containing 9.13 Mt Zn, 4.23 Mt Pb, and 367 Moz Ag metals, much larger than the veins (23.9 Mt @ 2.40% Zn, 1.38% Pb and 254 g/t Ag containing 0.6 Mt Zn, 0.3 Mz Pb, and 195 Moz Ag). It is now the second largest Zn-Pb skarn in the world in our skarn database with >1700 deposits. This discovery triggered great interest to look for skarn-porphyry ores below IS veins elsewhere. But is the coexistence of epithermal and skarn ores at La Colorada only a coincidence or are they genetically linked? If so, exploring for skarn in carbonates beneath IS veins is a reasonable strategy. This study addresses this question by examining the epithermal-skarn relationship at La Colorada.

Most mineralized skarns and all IS deposits are genetically related to magmas (Einaudi et al. 1981; Hedenquist et al. 2000). IS veins are generally hosted in volcanic rocks and rarely in siliciclastic rocks, and mostly occur at shallow depths (<1 km; Hedenquist et al. 2000). In mineral deposit models, they are above and laterally offset from associated porphyry deposits, whereas high-sulfidation epithermal deposits are envisioned directly above a porphyry deposit (Sillitoe 2010; Chang et al. 2011). IS veins are believed to be the distal and shallow parts of porphyry deposits (Hedenquist et al. 2000; Sillitoe 2010). By contrast, skarns mostly occur in carbonates and calcareous rocks at deeper levels, and can be associated with porphyry deposits, with distal CRD mineralization (Einaudi et al. 1981; Meinert et al. 2005; Chang et al. 2019).

2 Deposit Geology

The stratigraphy comprises of, from oldest to youngest, Early Cretaceous Fresnillo Formation (Fm) calcareous mudstone and limestone, Cuesta del Cura Fm limestone and calcareous mudstone, Late Cretaceous Indidura Fm siltstones with interlayered limestone and mudstone, Ahuichila Conglomerate, Late Cretaceous to Early Paleocene Lower Volcanic Complex dacitic volcanic and intrusive rocks, Upper Volcanic Supergroup rhyolitic pyroclastic rocks, and Quaternary conglomerate (Fig. 1; Albinson 1988; Moller et al. 2001).

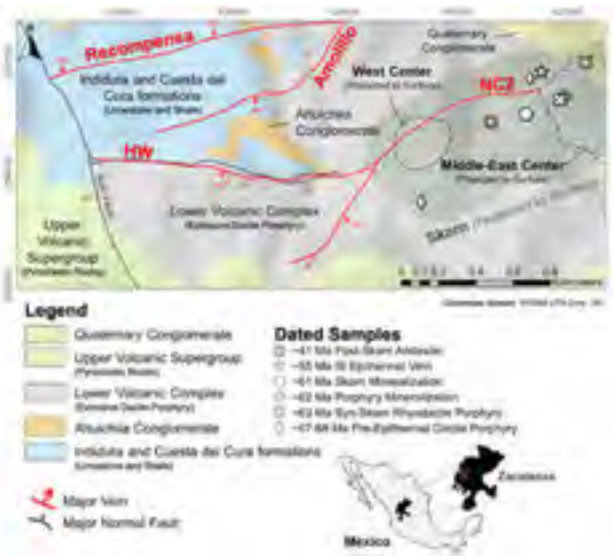


Figure 1. Surface geologic map of La Colorada. Samples dated in this study were collected underground and are projected from depth. The middle-east and west center intrusive centers, and skarn are projected from depth. Geology modified after Wafforn et al. (2019)

Two intrusion clusters are concealed below the surface: a west center and a middle-east center (Fig. 1). The middle-east center comprises pre-skarn andesite porphyry (AP) and rhyodacite porphyry (RDP), syn-skarn RDP (main stock; ~600 m diameter) and pre-epithermal dacite porphyry (DP; minor), late-skarn DP and RDP, and post-skarn andesite (AD) dykes. The west center has syn-skarn AP and RDP, late-skarn DP, and post-skarn AD (Francisco et al. 2024).

Regional compression created fold networks in the basement comprising the Fresnillo, Indidura, and Cuesta del Cura formations. The folds were locally thrusted and overturned in the early Eocene (Moller et al. 2001). Northwest-striking normal faults propagated during Oligocene-Eocene basin and range extension; these faults have since been offset by normal faults, such as the Azul Fault (Fig. 1; Wafforn et al. 2019).

2.1 The IS Epithermal Veins

There are three main veins: NC2-HW, Amolillo, and Recompensa. The NC2-HW vein is the largest at ~2.9 km long and ~1.9 m wide, and dips to the SE. The Amolillo vein is ~1.4 km long and ~2.2 m wide, and also dips to the SE. The Recompensa vein is ~0.9 km long and ~1.7 m wide and dips to the NW. All major veins dip 60-85°. Traditionally, all veins from the surface (~2,400-2,550 m elevation) to the bottom of the mine (~1,870 m elevation) were termed epithermal, regardless of whether the host rock is dacitic volcanic rocks or limestone. The veins do not extend up into the Upper Volcanic Supergroup (Albinson 1988). In this study, “IS veins” only refer to veins hosted in volcanic rocks.

The veins are composed of quartz, calcite, sulfides (mainly sphalerite, galena, pyrite, and minor acanthite), lesser sulfosalts (tennantite- tetrahedrite, fahlore, polybasite-pearcerite), and local native silver (Chutas and Sack 2004). Veins are multigenerational with brecciation of veins and earlier breccias. Vein and vein fragments exhibit local banding/crustiform textures, but most are simple veins without internal textures. Vein halos are dominated by illite alteration with minor chlorite and disseminated sulfides. The vein features are typical of intermediate-sulfidation epithermal veins (Hedenequist et al. 2000).

2.2 The Skarn – CRD – Porphyry Mineralization

Skarns occur around the west and middle-east intrusive centers. The west center contains only dikes (<100 m wide), whereas the middle-east center is a large stock (~600 m diameter) with apophyses. Red-garnet endoskarn veins occur at the margins of syn- and late-skarn intrusions at both centers. The endoskarn veins in the larger middle-east intrusion transition inwards to porphyry-style quartz stockwork veins. The skarns exhibit zoning away from the syn-skarn intrusions including: decreasing garnet/pyroxene ratios, lightening of garnet color, and color change of pyroxene from green to brown with the appearance of rhodonite just before the skarn transitions to CRD (Francisco et al. 2024), that are typical of skarns (e.g. Chang and Meinert 2008). CRD-style mineralization (quartz-carbonate-sulfides-sulfosalts) occurs outward of the skarn. Massive CRD close to the skarn transitions to distal vein-style CRD (Fig. 2). The distal vein-style CRD is identical to carbonate-hosted veins traditionally termed epithermal (e.g. the western part of Amolillo and Recompensa veins in Fig. 1).

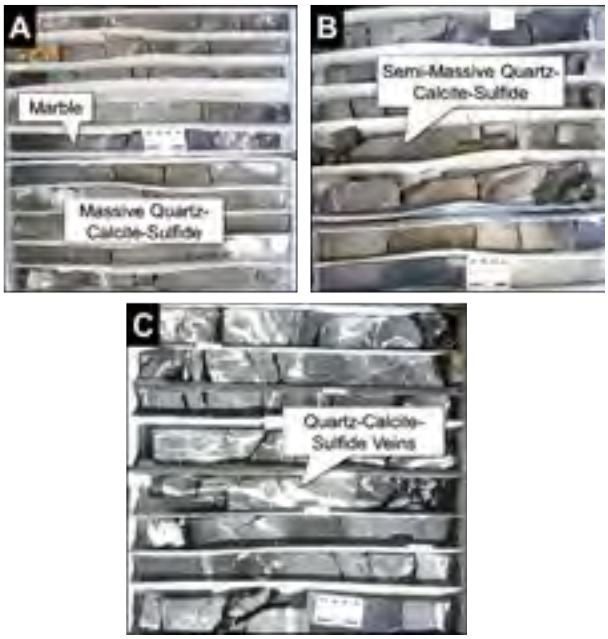


Figure 2. Transition from massive CRD to distal vein-type CRD. A) Massive; B) Semi-massive or wide veins; C) Narrow veins. Core box length is 1 m

3 The Epithermal-CRD/Skarn Transition

At the volcanic-carbonate contact, IS and CRD veins comprise segments of the same vein, suggesting a transitional relationship between IS and CRD mineralization (Fig. 3). The mineralogy of IS and CRD veins is the same (quartz-calcite-sulfides), but with more calcite in the CRD veins. This difference is attributed to the capacity of the host rock to provide Ca and CO_3^{2-} to form calcite, which are more abundant in calcareous rather than volcanic wallrocks.

Homogenization temperatures (T_h) of primary fluid inclusion assemblages (FIA) from IS and CRD veins vary from 225-318 °C in sphalerite and from 192-325 °C in quartz. Within a fluid inclusion assemblage, the range of homogenization temperatures is less than 5 °C, with an average standard deviation of 2.3 °C. The first ice melting temperatures (eutectic temperatures, T_e) fall into two groups: -28.0 to -27.9 °C and -22.0 to -20.8 °C, which are consistent with the NaCl-H_2O system (metastable and true T_e; Pattrick et al. 1985).

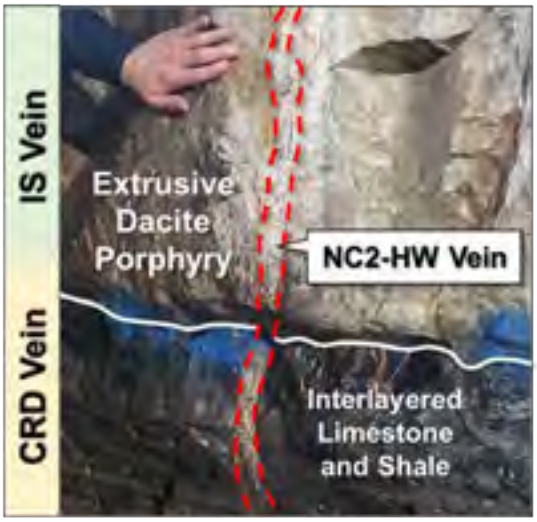


Figure 3. 3 cm-wide NC2-HW vein crossing the volcanic-carbonate contact

Illite crystallinity values measured by short wavelength infrared (SWIR) spectrometers, IC-SWIR, range from 0.6 (~245 ℃) to 1.9 (~300 ℃). IC-SWIR is mainly affected by illite formation temperature (e.g. Calder et al. 2022). The T_h of FIAs strongly positively correlate with the IC-SWIR values of the same samples (R^2 = 0.93; n = 3). Together, IC-SWIR and T_h reveal two high temperature zones along the NC2-HW vein (Fig. 4). The first is near the midpoint of the vein, where T_h increases from 265 °C to 325 °C laterally over ~250 m. The second is near the east-end of the vein, where IC-SWIR increases from 1.1-1.4 (~265-280 ℃) to 1.4-1.9 (280-300 ℃) laterally over ~550 m to the NE. The two high temperature zones indicate two fluid sources for the NC2-HW vein, coinciding with the west and middle-east syn-skarn intrusive centers. A separate high temperature zone is to the NW along the Recompensa vein, where a surface sample has a high T_h between 310-325 °C (Fig. 4A). This sample also contains rhodonite, a mineral common at the outer limit of distal skarns that forms at temperatures >350 °C (Maresch and Mottana 1976). The Recompensa vein may overlie another, yet undiscovered, intrusive center.

Two pre-epithermal dacite porphyries are dated at 67.1±1.0 Ma and 67.6±1.9 Ma in this study using LA-ICP-MS U-Pb zircon dating. All uncertainties in this contribution are at a 95% confidence level. Skarn and porphyry samples from the middle-east center yielded dates of 62.5±1.0 Ma (syn-skarn RDP; U-Pb zircon), 61.1±2.4 Ma (exoskarn; U-Pb garnet), and 62.0±0.2 Ma (porphyry mineralization; Re-Os molybdenite), indicating a date of ~62 Ma for the porphyry-skarn mineralization (Francisco et al. 2024). The NC2-HW IS vein is dated at 54.8±3.4 Ma (K-Ar illite; 0.2-1 µm) in this study. However, a maximum T_h of 280 °C was measured in a vein near the sample. This may exceed the closure temperature of <2 µm illite, which is 240-280 °C (Hunziker et al. 1986) or 260-317 °C (Garduño-Martínez et al. 2015). The true age of the IS veins could be older than the K-Ar illite date. We also dated two fresh andesite dykes that cut the epithermal veins; they are 40.7±0.5 Ma and 40.9±0.4 Ma (zircon U-Pb). La Colorada is one of two >50 Ma IS deposits among the 35 in Mexico; the rest are in the ranges of 39-27 Ma or 24-18 Ma (Camprubi and Albinson 2007).

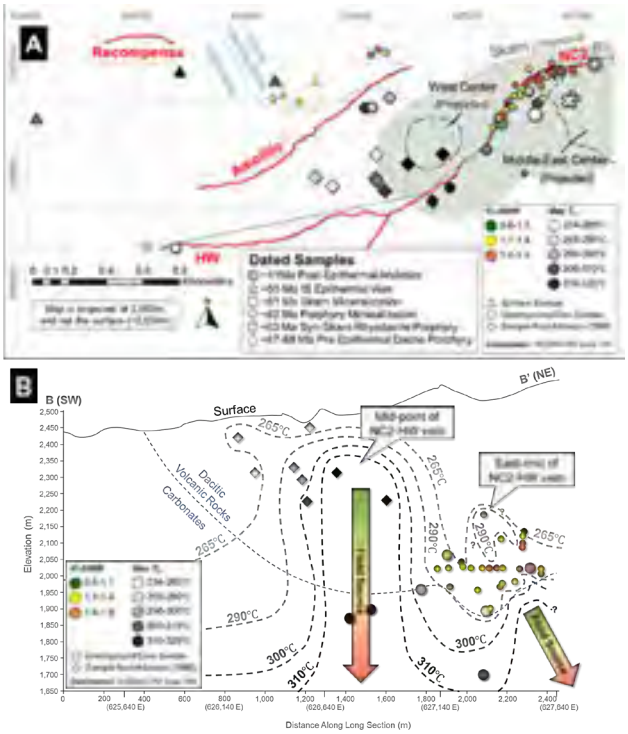


Figure 4. A) Plan view of the IC-SWIR and maximum T_h (max T_h) datasets. IC-SWIR is measured from the hanging wall (<1 m) of IS veins. The max T_h include measurements from Albinson (1988). Samples dated in this study are projected onto the map. B) Long section (B-B') along the strike of NC2-HW. Temperature contours are drawn from max T_h and IC-SWIR measurements. Possible fluid sources are indicated

4 Discussions and Conclusions

Field observations reveal a clear transition from IS veins down into CRD veins and then to skarn-porphyry mineralization. Temperature gradients revealed by illite crystallinity and fluid inclusion thermometric data show two heat centers that spatially coincide with the west and middle-east skarn-porphyry centers. This suggests a transitional relationship between the IS veins in volcanic rocks and CRD-skarn-porphyry mineralization in the underlying carbonates. Geochronology confines the epithermal age between ca. 67 and 55 Ma, which is compatible with the ~62 Ma age of the skarns and porphyry. This study concludes that the shallow epithermal veins and deeper skarn at La Colorada are genetically linked; their co-location is not a coincidence.

The findings of this study are applicable to any IS district globally where volcanic rocks overlie carbonates. Exploration below the IS veins into carbonate rocks may reveal CRD-skarn-porphyry

mineralization. IC-SWIR can be used to quickly and cheaply vector towards CRD-skarn-porphyry mineralization from the shallow epithermal environment (Fig. 5). Clusters of high IC-SWIR and/or T_h values may indicate proximity to a fluid source, and therefore proximity to the related CRD-skarn.

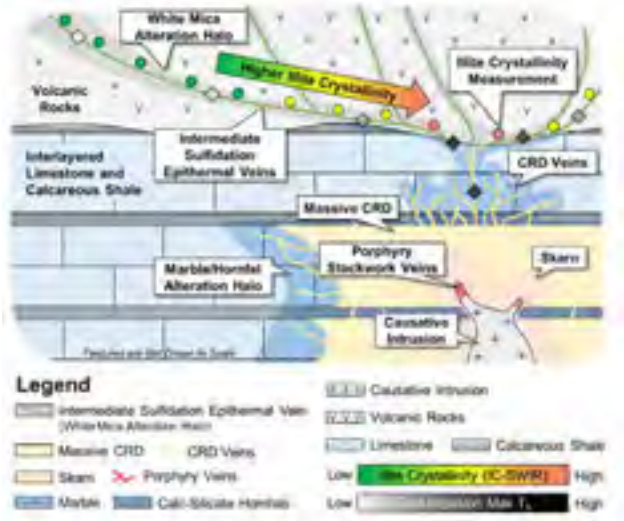


Figure 5. The transitional relationship between IS and CRD-skarn mineralization at La Colorada. IC-SWIR and fluid inclusion T_h are complimentary vectors for locating related CRD-skarn from shallow IS veins

Acknowledgements

We thank the Colorado School of Mines, Pan American Silver, and the Society of Economic Geologists for generous funding and support.

References

Albinson T (1988) Geologic reconstruction of paleosurfaces in the Sombrerete, Colorada, and Fresnillo districts, Zacatecas State, Mexico. Econ Geol 83:1647–1667. https://doi.org/10.2113/gsecongeo.83.8.1647

Calder M, Chang Z, Arribas A, Gaibor A, Dunkley P, Pastoral J, Kouzmanov K, Spandler C, Hedenquist J (2022) High-grade copper and gold deposited during postpotassic chlorite-white mica-albite stage in the Far Southeast Porphyry deposit, Philippines. Econ Geol 117:1573-1596

Camprubí A, Albinson T (2007) Epithermal deposits in México—update of current knowledge and an empirical reclassification. In: Alaniz-Álvarez SA, Nieto-Samaniego ÁF, eds., Geology of México: Celebrating the Centenary of the Geological Society of México: Geol Soc Am Bull Special Paper 422:377–415. https://doi.org/10.1130/2007.2422(14)

Chang Z, Hedenquist JW, White NC, Cooke, DR, Roach M, Deyell CL, Garcia J, Gemmell JB, McKnight S, Cuison AL (2011) Exploration tools for linked porphyry and epithermal deposits: example from the Mankayan intrusion-centered Cu-Au district, Luzon, Philippines. Econ Geol 106:1365-1398. https://doi.org/10.2113/econgeo.106.8.1365

Chang Z, Meinert LD (2008) Zonation in skarns: complexities and controlling factors. In: Proceedings of the PACRIM Congress 11:303-306

Chang Z, Shu Q, Meinert LD (2019) Skarn Deposits of China. Society of Economic Geologists Special Publication 22: 1-12. https://doi.org/10.5382/SP22.01

Chutas N, Sack R (2004) Ore Genesis at La Colorada Ag-Zn-Pb seposit in Zacatecas, Mexico. Mineral Mag 6:923-937 https://doi.org/10.1180/0026461046860231

Einaudi TM, Meinert LD, Newberry RJ (1981) Skarn deposits. Econ Geol 75th Anniversary Volume, Skinner BJ (Ed.)

Francisco P, Chang Z, Huang S, Emerson C, Juarez D, Perez P, Creaser RA (2024) The role of magmas in forming a big skarn system: a case study from La Colorada deposit (Zacatecas, Mexico). Abstract volume of the SEG 2024 Conference, 27-30 September 2024, Windhoek, Namibia

Garduño-Martínez DE, Puig TP, Solé J, Martini M, Alcalá-Martínez JR (2015) K-Ar illite-mica age constraints on the formation and reactivation history of the El Doctor fault zone, Central Mexico. Revista Mexicana de Cincias Geológicas 32:306-322. https://www.scielo.org.mx/pdf/rmcg/v32n2/2007-2902-rmcg-32-02-00306

Hedenquist JW, Arribas AR Jr, Gonzalez-Urien E (2000) Exploration for epithermal gold deposits. Rev in Econ Geol 13:245-277. https://doi.org/10.5382/Rev.13.07

Hunziker JC, Frey M, Clauer N, Dallmeyer RD, Friedrichsen H, Flehmig W, Hochstrasser K, Roggwiler P, Schwander H (1986) The evolution of illite to muscovite: mineralogical and isotopic data from the Glarus Alps, Switzerland. Contrib Mineral Petrol 92:157-180. https://doi.org/10.1007/BF00375291

Maresch WV, Mottana A (1976) The pyroxmangite-rhodonite transformation for the $MnSiO_3$ composition. Contrib Mineral Petrol 55: 69-79. https://doi.org/10.1007/BF00372755

Meinert LD, Dipple GM, Nicolescu S (2005) World Skarn Deposits, In: Hedenquist JW, Thompson JFH, Goldfarb RJ, Richards JP (Eds.), Econ Geol 100th Anniversary Volume

Moller SA, Islas J, Davila RT (2001) New discoveries in the La Colorada district, Zacatecas State, Mexico. New mines and discoveries in Mexico and Central America. Special Publication in Econ Geol 8:95-105. https://doi.org/10.5382/SP.08.07

Pattrick R, Shepherd TJ, Rankin AH, Alderton, DHM (1985) A practical guide to fluid inclusion studies. Mineral Mag 50:352-353. https://doi.org/10.1180/minmag.1986.050.356.32

Sillitoe RH (2010) Porphyry copper systems. Econ Geol 105:3-41 https://doi.org/10.2113/gsecongeo.105.1.3.

Wafforn M, Emerson C, Delgado A (2019) Technical report for the La Colorada property, Zacatecas, Mexico. https://www.panamericansilver.com/wp-content/uploads/2024/02/Pan-American-Silver-La-Colorada-NI-43-101-2024.pdf. Accessed 20 February 2022

Porphyry ore-deposit potential of northeast Australia – New insights from early-Paleozoic tectonic models

Alexander Edgar [1*] Ioan Sanislav [2], Paul Dirks [2] and Carl Spandler [3]

[1] Centre for Exploration Targeting (CET) University of Western Australia, Perth, Australia
[2] Economic Geology Research Unit (EGRU) James Cook University, Townsville, Australia
[3] School of Physics, Chemistry and Earth Sciences, The University of Adelaide, Adelaide, Australia

Abstract. Metamorphic garnet grains from the early-Paleozoic Running River Metamorphics in northeastern Queensland record evidence of diamond-facies, ultra-high-pressure (UHP) metamorphism. Peak metamorphic conditions are constrained to at least 3.5 GPa and ~ 850 ºC. We interpret the Clarke River Fault as a Paleozoic suture zone which has recorded the accretion of continental and oceanic fragments to the paleo-continental margin. The Running River Metamorphics have been later intruded by a series of syn-tectonic, adakite-like, felsic plutons with geochemical signatures that reflect a fertile melt source conducive to the formation of porphyry ore deposits. These plutons were emplaced at too great a depth to have formed typical porphyry ore deposits. However, the northern Charters Towers Province shares many geological similarities to the proximal Greenvale Province, where the erosional level may be shallower, and the potential for porphyry deposit formation and preservation may be greater.

1 Introduction

The Tasmanides of eastern Australia host a number of world class Cu-Au porphyry ore deposits such as the the Cadia-Ridgeway ore bodies (~ 50MOz Au, ~9.5Mt Cu; Harris et al. (2020)) Currently, world-class porphyry ore deposits are limited in distribution to the Ordovician-Silurian Macquarie Arc of the Lachlan Orogen, NSW. Similarities in the geology of the Macquarie Arc have been reported throughout the northernly Thomson and Mossman Orogens (Dirks et al., 2021; Henderson et al., 2011), however, the northern Tasmanides have received comparatively little exploration attention and major deposits have yet to be discovered.

Neoproterozoic to early-Paleozoic tectonic models generally position the northern Tasmanides within a back-arc setting, which developed atop of a Neoproterozoic oceanic passive margin in response to an outboard, west-dipping subduction complex. In north Queensland, such interpretations are supported by widespread, age-correlative stratigraphy and mineralisation styles including several significant VMS deposits (Thalanga, Balcooma). However, documentation of several ophiolite complexes of island-arc and oceanic affinities tectonically emplaced along major domain-bounding structures has challenged longstanding models (Edgar et al., 2022a; Edgar et al., 2023).

The Clarke River Fault in north Queensland is a major tectonic boundary which extends east-west along the contact between the Thomson and Mossman Orogens (Dirks et al., 2021; Edgar et al., 2023; Edgar et al., 2022b). In this study, we describe rocks from the Running River Metamorphics which preserve evidence of ultrahigh pressure metamorphism to diamond facies. Such conditions are commonly attributed to collisional orogens, and suggest that early-Paleozoic terrane accretion played a significant role in continent growth within the northern Tasmanides. Syn-collisional felsic plutons yield geochemical signatures consistent with fertile, Cu-Au porphyry forming melts, which together with the geodynamic regime, position the northern Tasmanides as a frontier region for porphyry exploration.

2 Geological Setting

The geology of eastern Australia dominantly records the Neoproterozoic-Paleozoic evolution of the Tasmanides accretionary system (Cawood et al., 2011; Cawood, 2005; Cawood et al., 2009). The Tasmanides comprise a collage of five orogenic belts, namely the Delamarian, Thomson, Lachlan, Mossman and New England Orogens, which broadly display younging trends from west to east. These orogenic belts have been widely interpreted to record the eastward retreat of a long lasting, west-dipping, subduction system, which encompassed the northeastern margin of the Gondwana supercontinent during the Neoproterozoic-Paleozoic times. In north Queensland, the early evolution of this system is best recorded by exposures of basement rocks from the Charters Towers Province within the Thomson Orogen, and Broken River Province within the Mossman Orogen.

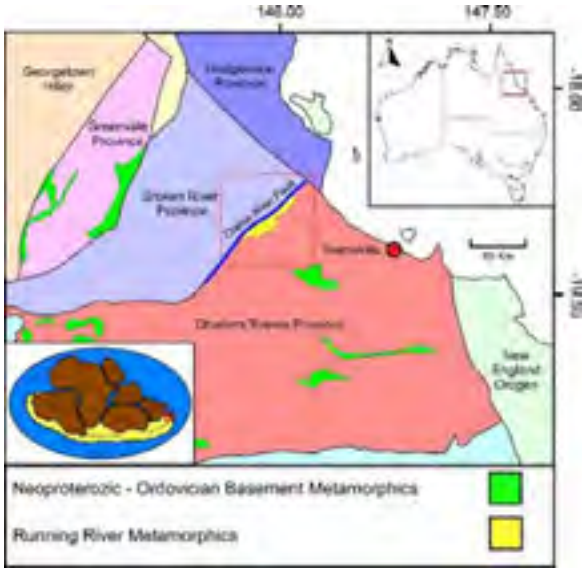


Figure 1. Regional setting of the Running River Metamorphics, north Queensland, Australia. From Edgar et al. (2022b).

Exposures of Neoproterozoic-early Paleozoic basement generally lie proximal to domain-bounding structural lineaments. One such basement inlier is the Running River Metamorphics, positioned along the Clarke River Fault which extends along the northern contact of the Charters Towers Province, and southern contact of the Broken River Province. The Running River Metamorphics consist of Ordovician, amphibolite-facies metaigneous and metasedimentary rocks which were interpreted by Dirks et al. (2021) to record accretion of a seamount during the late stages of the Delemarian Orogeny. The sequence was intruded by the post peak-metamorphic, ~456 Ma Falls Creek Tonalite.

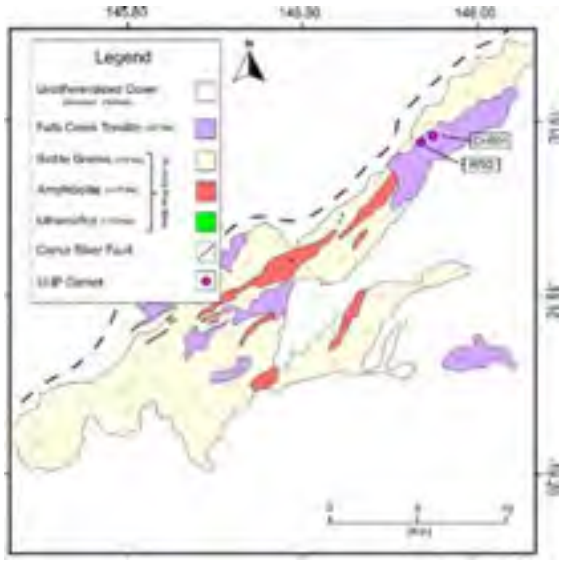


Figure 2. Local geological map of the Running River Metamorphics. From Edgar et al. (2022b).

The metasedimentary-metaigneous package consist of a garnet-bearing quartzite unit, which is generally exposed as rafts along the Falls Creek Tonalite margins, and as intercalations within broader amphibolite (meta-basalt) units. Garnet grains from garnet-rich domains within this quartzite unit are often heavily fractured and boudinaged, with larger grains displaying undulose extinction in crossed polarized light microscopy. The garnets, which are metamorphic in origin, contain inclusions and exsolution of quartz, rutile, apatite, amphibole, carbonate, graphite, and diamond.

3 Petrography

Garnet grains contain a suite of high-pressure and high-temperature inclusions and exsolution features. Metamorphic microdiamond grains, confirmed by raman spectroscopy, commonly occur within the cores or mantle zones of large garnet grains. The diamond grains are closely associated with cubic graphite, various carbonate species, and C-rich fluid inclusions. Radial fracture sets developed around quartz grains record the phase transition from coesite to quartz, in which a significant volume increase results in fracturing of the surrounding host mineral (garnet). Crystallographically oriented needles and rods of rutile, apatite, quartz, and silicate minerals reflect Ti, P, Si and possibly Na destabilisation and exsolution from garnet during retrograde metamorphism.

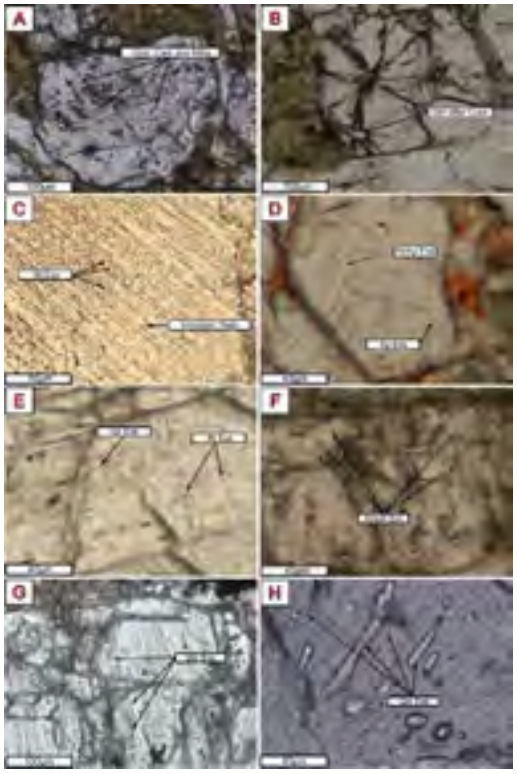


Figure 3. Petrographic evidence for ultra-high pressure metamorphism. From Edgar et al. (2022b).

4 P-T Constraints

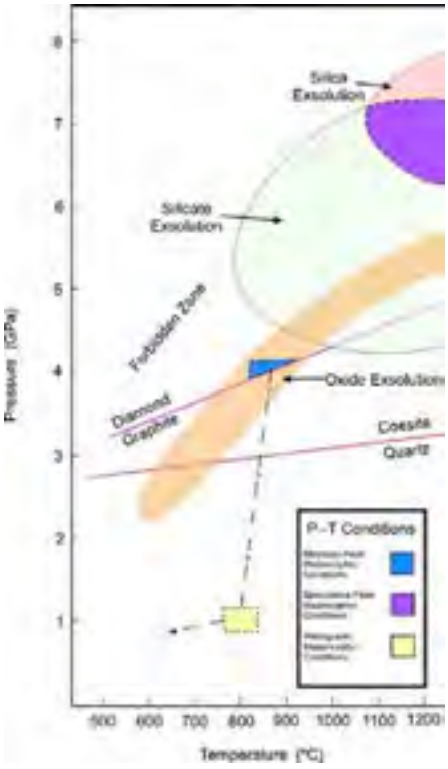


Figure 4. Minimum P-T conditions (blue triangle) recorded by the Running River Metamorphics based on inclusion and exsolution mineralogy. From Edgar et al. (2022b).

The presence of metamorphic microdiamond inclusions indicate that the Running River Metamorphics were metamorphosed under conditions of at least ~3.5 GPa and ~850 °C (Fig. 4). This estimation is consistent with Zr-in-rutile thermometry analyses collected from rutile inclusions within the same garnet grains. These data reflect the highest-pressure conditions for regional metamorphism recorded in Australia. Although speculative, amphibole and silica exsolution within garnet cores may indicate extreme P-T conditions > 5 GPa and > 1000 °C (Keller and Ague, 2020).

5 Magma Fertility

Samples of the late-syn-tectonic Falls Creek Tonalite yield geochemical signatures consistent with derivation from hydrous, oxidized arc magmas (Fig. 5). Samples contain high Sr/Y ratios and Low Zr concentrations, reflecting plagioclase suppression and Sr enrichment, prolonged amphibole fractionation resulting in Y depletion, and early titanite fractionation resulting in Zr depletion (Loucks, 2014; Wells et al., 2021). The hydrous nature of the magmas is further supported by a pronounced, positive Eu anomaly, consistent with plagioclase suppression under hydrous conditions. Such magmas have the potential to produce porphyry Cu-Au deposits.

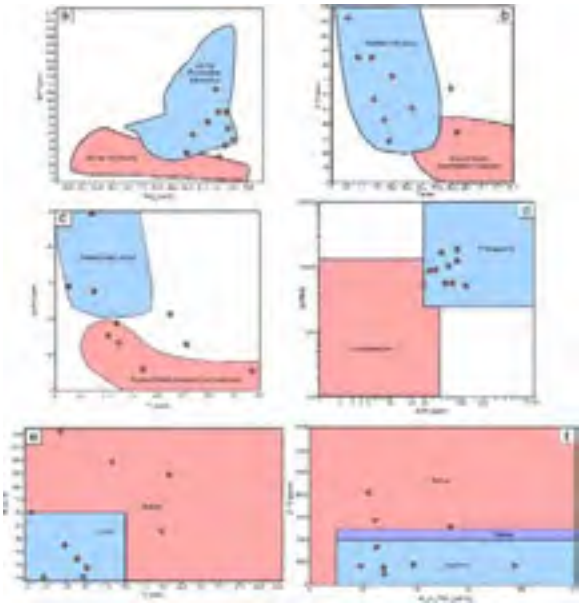


Figure 5. Major and trace element magma fertility discrimination plots with data points from the post peak-metamorphic Falls Creek Tonalite. From Edgar et al. (2023).

6 Discussion

Diamond-facies, UHP metamorphism is typically described within arc-continent or continent-continent collisional settings (Brown, 2007; Ernst and Liou, 1999; Liou et al., 2004). Documentation of UHP metamorphism from the Running River Metamorphics indicates that Wilson-cycle processes, such as ocean closure and terrane collision, were active across the northern Tasmanides during the early-Paleozoic.

Syntectonic, felsic, arc-plutons associated with these collisional events yield geochemical signatures consistent with derivation from hydrous arc magmas with the potential to generate porphyry Cu-Au ore deposits. However, the Falls Creek Tonalite underwent ductile deformation during the D_4 contractional event as described by Dirks et al. (2021) under mid-crustal conditions. This indicates that the Falls Creek Tonalite has been emplaced at too great a depth for typical porphyry-style mineralisation (Sillitoe, 2010). However, synchronous volcanic rocks and subvolcanic porphyry intrusions within the Greenvale province indicate preservation of the early-Paleozoic paleo-surface across the province (Withnall et al., 1991). The similarities in lithology, structural style and metamorphic facies between the Greenvale Province and Running River Metamorphics, combined with preservation of the upper crust, make the Greenvale Province a compelling exploration target for early Paleozoic porphyry deposits.

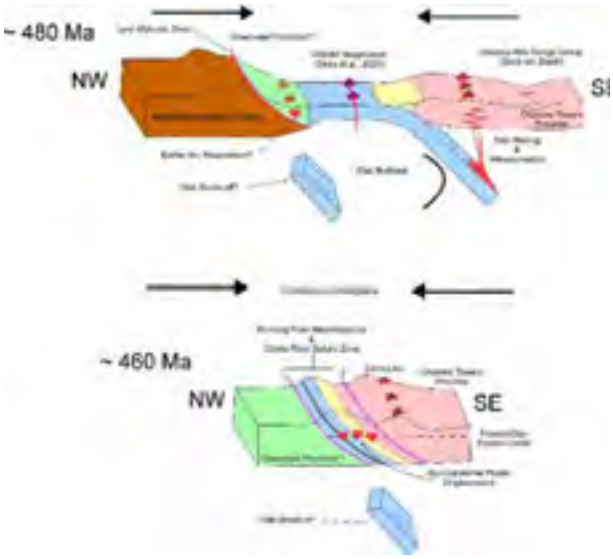


Figure 6. Early-Paleozoic tectonic setting of the northern Tasmanides during emplacement of fertile, felsic plutons. From Edgar et al. (2023).

References

Brown M (2007) Metamorphic conditions in orogenic belts: a record of secular change: International Geol Rev 49:193-234.

Cawood P, Leitch E, Merle RE, and Nemchin A (2011) Orogenesis without collision: Stabilizing the Terra Australis accretionary orogen, eastern Australia: Bulletin, v. 123, no. 11-12, p. 2240-2255.

Cawood PA (2005) Terra Australis Orogen: Rodinia breakup and development of the Pacific and Iapetus margins of Gondwana during the Neoproterozoic and Paleozoic: Earth-Science Rev 69:249-279.

Cawood PA, Kroner A, Collins W J, Kusky TM, Mooney W D, and Windley BF (2009) Accretionary orogens through Earth history: Geological Society, London, Special Publications, v. 318, p. 1-36.

Dirks HN, Sanislav IV, and Abu Sharib ASAA (2021) Continuous convergence along the paleo-Pacific margin of Australia during the Early Paleozoic: Insights from the Running River Metamorphics, NE Queensland: Lithos 398-399.

Edgar A, Sanislav I, and Dirks P (2022a) Tectonic setting and mineralisation potential of the Cowley Ophiolite Complex, north Queensland: Australian Jour Earth Sci 69:1-17.

Edgar A, Sanislav I, and Dirks P (2023) The origin of mafic–ultramafic rocks and felsic plutons along the Clarke River suture zone: implications for porphyry exploration in the northern Tasmanides: Australian Jour Earth Sci 70:1123-1138.

Edgar A, Sanislav IV, Dirks PH, and Spandler C (2022b) Metamorphic diamond from the northeastern margin of Gondwana: Paradigm shifting implications for one of Earth's largest orogens: Science Advances 8:eabo2811.

Ernst WG, and Liou JG (1999) Overview of UHP Metamorphism and Tectonics in Well-Studied Collisional Orogens: International Geol Rev 41:477-493.

Harris AC, Cooke DR, Cuison ALG, Groome M, Wilson AJ, Fox N, Holliday J, and Tosdal R (2020) Geologic Evolution of Late Ordovician to Early Silurian Alkalic Porphyry Au-Cu Deposits at Cadia, New South Wales, Australia.

Henderson R, Innes B, Fergusson CL, Crawford A, and Withnall I (2011) Collisional accretion of a Late Ordovician oceanic island arc, northern Tasman Orogenic Zone, Australia: Australian Jour Earth Sci 58:1-19.

Keller DS & Ague JJ (2020) Quartz, mica, and amphibole exsolution from majoritic garnet reveals ultra-deep sediment subduction, Appalachian orogen: Science Advances 6.

Liou JG, Tsujimori T, Zhang RY, Katayama I, and Maruyama S (2004) Global UHP Metamorphism and Continental Subduction/Collision: The Himalayan Model: International Geol Rev 46:1-27.

Loucks R (2014) Distinctive composition of copper-ore-forming arcmagmas: Australian Jour Earth Sci 61:5-16.

Sillitoe RH (2010) Porphyry copper systems: Econ Geol 105:3-41.

Wells T, Meffre S, Cooke DR, Steadman J, and Hoye J (2021) Assessment of magmatic fertility using pXRF on altered rocks from the Ordovician Macquarie Arc, New South Wales: Australian Jour Earth Sci 68:397-409.

Withnall I, Black L, and Harvey K (1991) Geology and geochronology of the Balcooma area: part of an Early Palaeozoic magmatic belt in North Queensland: Australian Jour Earth Sci 38:15-29.

Mineralogy, Paragenesis, and Geochemistry of the Zgounder Ag-Hg Deposit (Central Anti-Atlas, Morocco): Insights into Ore Genesis

Atiq El majid[1,2], Belkacim Said[1,3], Anne-Sylvie ANDRÉ-MAYER[2], Abdelhakim El bahat[4], Lahcen Maasou[4], Abdelhay Ben-Tami[1,4]

[1]*University of Ibn Zohr –LAGAGE Laboratory, Faculty of Sciences, Agadir, Morocco.*
[2]*University of Lorraine –GeoRessources research Center, Nancy, France.*
[3]*University of Quebec in Abitibi-Timiskaming, Mining and Environmental Research Institute, Canada.*
[4]*Aya Gold & Silver, Casablanca, Morocco.*

Abstract. The Ag-Hg mineralization at the Zgounder deposit (Siroua massif, central Anti-Atlas), is hosted primarily in the Saghro Group rocks (630-600 Ma). The orebodies form structurally controlled lenses (~60 m in length) along the Bou Salda (600-580 Ma)-Imghi contact. High-grade Ag ore is mainly concentrated at the intersections of NNW-SSE and NE-SW with E-W fault system, and occurs as sulfosalts and native silver within quartz-chlorite veins, crackle breccias, and disseminated in metasediments and a dolerite dyke. The ore mineral assemblages present hydrothermal features that may be related to an intermediate-sulfidation (IS) epithermal system. Sulphide geochemistry and chlorite geothermometry reveal a cooling from ~386°C to 268°C during the early stages of Ag-deposition, reaching 106°C during the jalpaite-bearing later stage. The mineralogical evolution, thermal trends, and absence of boiling-related textures suggest Ag ore precipitation from fluid dilution and/or mixing, with significant REE mobilization leading to the formation of an Allanite-(La) enriched stage.

1 Introduction and Geological setting

The Zgounder Ag-Hg mine, dates back to the 10th century, and is currently operated by Aya Gold & Silver. This Ag-Hg deposit remains poorly studied compared to its counterpart deposits in the Eastern Anti-Atlas. Early studies (e.g, (Petruk 1975; Essarraj et al. 1998) provided geological insights, but key aspects of ore genesis-fluid origins, heat and metal sources, as well as deposition mechanisms-remain still uncertain. This study aims to refine the features of the hydrothermal Ag-Hg mineralization (geometry, textures, mineral footprints and fingerprints), to better discuss both the epithermal signature of this Ag-Hg deposit, and the related hydrothermal ore formation processes.

The Zgounder deposit is located on the western Precambrian flank of the Siroua Inlier, within a structurally complex Ediacaran terrain. The oldest rocks unit in the region is the clastic Imghi formation of Saghro Group (630–600 Ma) (Fig. 1). It consists of weakly metamorphosed sediments striking E-W, steeply dipping southward. The Imghi Formation is intruded by several magmatic bodies, classified into: (i) The Bou Salda Group (600-580 Ma) and (ii) The Ouarzazate Group (580–538 Ma) (Thomas et al. 2004). The whole is crosscut with a dense fracture network, dominated by NE-SW, E-W and N-S faults, including the major Zgounder Fault (ZF) (Fig. 1), which offsets the earlier NE-SW and E-W strike-slip faults. The Zgounder deposit is mainly hosted in the Imghi Fm. The Ag-Hg orebodies form steeply south-dipping, structurally controlled lenses, reaching up to 60 m in length. High-grade silver is concentrated at the intersection of NNW-SSE and NE-SW with (E-W) fault system, but the grade decreases northward beyond the lithological contact (Imghi-Bou Salda) and westward past the Zgounder Fault.

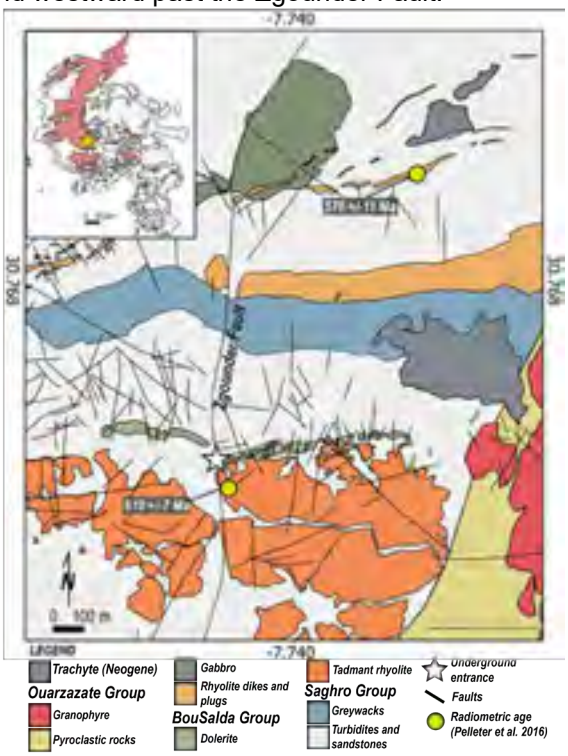


Figure 1. Geological Map of Zgounder region with radiometric ages obtained from (Pelleter et al. 2016).

2 Sampling and Analytical methods

A total of 30 mineralized specimens was collected from underground mining tunnels at depths going from -2125 m to -1950 m. Microscopic studies of the mineral assemblages as well as crystallochemical characterization were conducted at GeoResources research Center (Nancy, France). Mineral identification were supported by scanning electron microscopy (SEM) with high-resolution back-scattered electron (BSE) images (10 µm at 25 kV)

carried out on a TESCAN VEGA3 LM equipped with a 30mm^2 Bruker XFlash6 EDS. Ten thin sections were selected for µXRF analyses using a Bruker TORNADO M4. The µXRF maps were collected at 15 keV with an accelerating voltage of 50kV and a current of 300µA. Major and minor elements were measured with CAMECA SX-100 electron probe micro-analyzer (EPMA) equipped with five WDS spectrometers. The analytical condition for the electron beam are an accelerating voltage of 15 to 25 kV, a beam current and diameter of 10 nA and 1-3 µm respectively.

3 Results

3.1 Alteration and ore-forming stages

The Zgounder deposit exhibits four distinct hydrothermal alteration assemblages. i) Vein-type propylitic alteration, defined by epidote-chlorite-calcite-albite ± pyrite, predominates in the surrounding volcanic rocks (Fig. 2A, B). This assemblage transitions into ii) argillic alteration (Quartz-Chlorite-Sericite-smectite) iii) Albite-Quartz+/-Sericite primarily developed along the fringes of mineralized veins within metasediments. A localized iv) allanite (La)-quartz assemblage, occurring exclusively with Ag mineralization and postdating the argillic alteration (Fig. 2C, D).

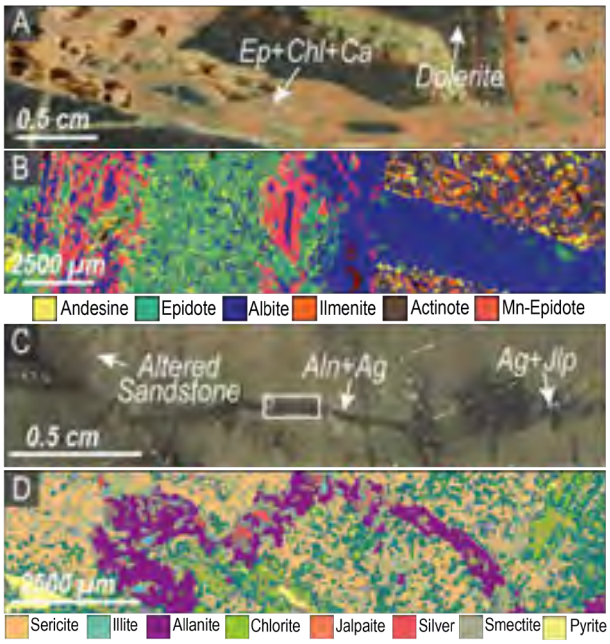


Figure 2. A.B) Hand specimen and elemental µXRF map of a propylitic altered dolerite. C) Specimen of an Ag mineralized sandstone; D) Mineral µXRF map showing the argillic and allanite (La)-quartz alteration associated with silver ore. (Ep: Epidote; Chl: Chlorite; Ca: Calcite; Aln: Allanite; Ag: Silver; Jlp: Jalpaite).

Based on field and textural observations, the Zgounder deposit is characterized with 4 successive hydrothermal stages as follows:

i) The Fe-As stage is represented essentially with pyrite and minor occurrence of arsenopyrite. The pyrite is omnipresent and texturally identified as PyI and PyII. PyI is present as disseminated nodular aggregates within metasediments, dolerite dykes, and rhyolites, occasionally forming linear pyritic arrays parallel to bedding (S_0). In some samples the Py I shows a compositional zoning in Co and Ni. PyII occurs in centimeter-scale quartz-chlorite veins that crosscut PyI.

ii) The Co-Ni sulfarsenide stage is characterized by cobaltite-gersdorffite replacing Py I and forming atoll-like structures around Py II. Py I shows a porous texture, with sulfarsenides infilling its core and fractures (Fig. 3A), suggesting a dissolution-precipitation process.

iii) The Base Metal Sulphide (BMS) Stage is primarily dominated by sphalerite and is divided into two substages. The first substage (iiia) consists of dark brown sphalerite (Sph I) and honey-brown zoned sphalerite (Sph II), associated with galena (Gn) and minor chalcopyrite (Cpy) (Fig. 3B, C).

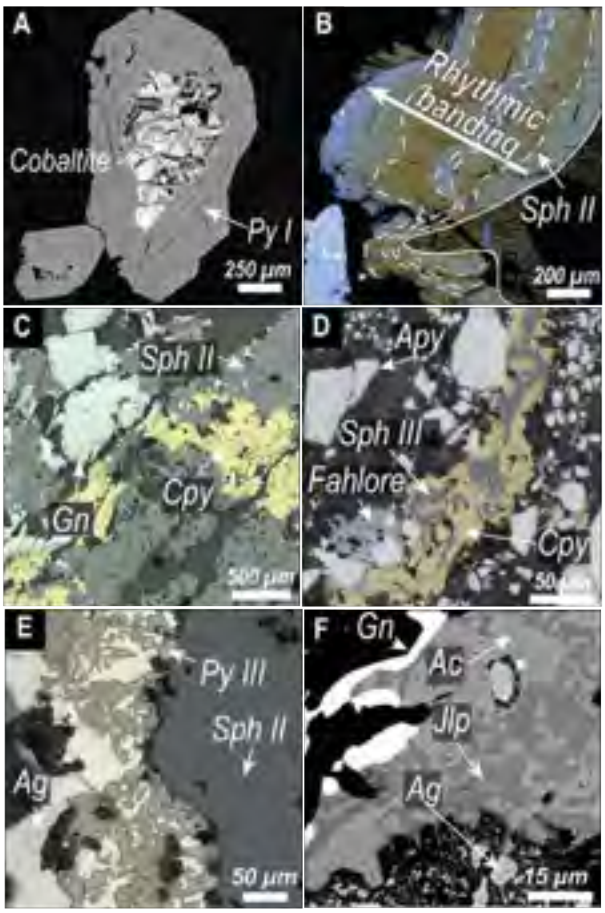


Figure 3. A. BSE image of Pyrite I showing replacement with Cobaltite. B. Transmitted light image of Growth Zoning in Sphalerite II. C. Reflected light image of BMS subtype iiia stage. D. Reflected light image of BMS subtype iiib stage. E. Reflected light image of Pyrite III and Silver worm-like symplectic texture. F. BSE image of Jalpaite-Acanthite in replacement of Native silver. (Jlp: Jalpaite; Ag:Silver; Sph: Sphalerite; Py; Pyrite; Gn: Galena; Cpy: Chalcopyrite; Apy: Arsenopyrite; Ac: Acanthite; Fahlore: Ag tetrahedrite/Tennantite).

The second substage (iiib) is characterized by the co-precipitation of silver-bearing sulfosalts

(tetrahedrite, tennantite, kenoargentotetrahedrite) with colourless sphalerite (Sph III), which crosscuts both Sph I and Sph II (Fig. 3D). iv) the Ag-Hg stage is found disseminated, in quartz-chlorite veins associated to BMS stage, solely filling fractures and intergrowth with Py III patches (Fig. 3E).

In some samples, the Ag is associated to Allanite (La) veins crosscutting the quartz-chlorite-BMS-Ag veins. Acanthite is the primary Ag sulphide, often forming symplectic worm-like textures with Jalpaite (Ag_3CuS_2) as it replaces the earlier Ag-Hg ores (Fig. 3F). A post-ore supergene stage is characterized by cinnabar and secondary Cu-sulphides (chalcocite, bornite).

3.2 Sphalerite composition

Sphalerite is the second most abundant sulfide in the Zgounder deposit. Sphalerite composition presents helpful insight on hydrothermal fluids evolution as well as identifying the deposits typology (Cook et al. 2009). EPMA results reveal distinct compositional variations across three generations of sphalerite. Sph I is characterized by the highest Fe (5.61 wt%) and Mn (0.04 wt%) averages but the lowest Zn (60.4 wt%). In conjunction with the obtained linear trends the $Zn^{2+} \leftrightarrow (Fe, Mn)^{2+}$ direct substitution is the most dominant in Sph I and Sph II (Fig. 4A), implying that the replacement of Zn by Fe may partly promote the replacement of Mn, which explains the variation in color within rhythmic bands of Sph II. In contrast, Sph III exhibits significantly lower Fe (0.5 wt%) and Mn (0.01 wt%) averages, indicating direct Cd incorporation into the sphalerite lattice via $Zn^{2+} \leftrightarrow Cd^{2+}$ substitution. This substitution process is evidenced by a strong negative Zn-Cd correlation (R = -0.86) (Fig. 4D).

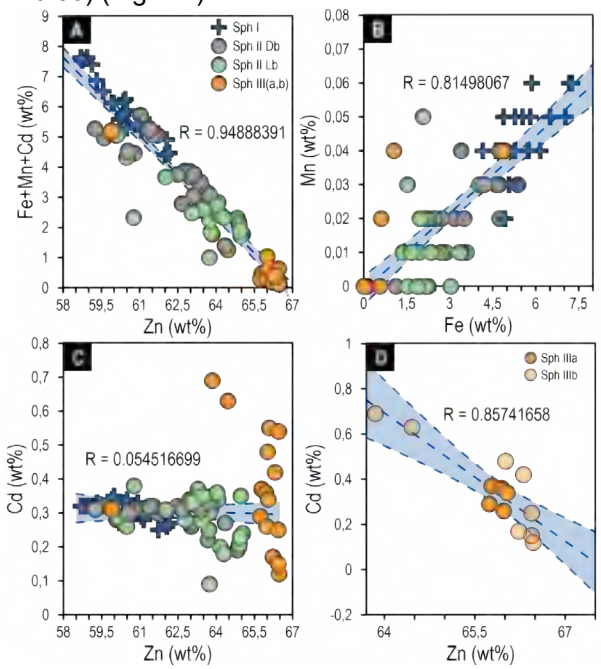


Figure 4. Binary plots for selected elements for the three sphalerite types based from EPMA. (Sph= Sphalerite; Sph II Db; Sph II Lb= Dark bands and light-color bands respectively in zoned sphalerite II; Sph III (a,b) = colorless Sphalerite III in Albite veins and chlorite-Quartz veins respectively).

3.3 Chlorite geothermometry

The studied chlorites are primarily Type I trioctahedral and spanning from Fe-chlorite “Chamosite” (Chl I, II and III) to Mg-chlorite “Clinochlore" (Chl IV). The temperature evolution trend of ore stages was characterized using chlorite crystallization temperatures calculated from two empirical formulas (TC88, Cathelineau 1988; TJ91 - Jowett 1991) and two semi-empirical formulas (TB13 - Bourdelle et al. 2013; IN18 - Inoue et al. 2018). The results are summarized in a box-and-whisker plot (Fig. 5). Temperatures derived from TC88 and TJ91 range from 232–385°C and 228–395°C, respectively (Fig. 5). This ±10°C variations suggests that XFe^{2+} has minimal impact on empirical calculations.

The results indicate a clear temperature decrease from Chl I (Py I stage, averaging 381°C) and Chl II (Py II stage, averaging 386°C) to Chlorite IIa (Co-Ni sulfarsenide stage, averaging 360°C). These values align with fluid-inclusion homogenization temperatures for the As-Co stage (340–480°C; Essarraj et al. 1998). The lowest recorded temperatures correspond to Chl IV (Sph III + Ag fahlore stage), averaging 268°C (Fig. 5). The semi-empirical methods yield lower temperature estimates: TB13 gives an average of 300°C, while IN18 ranges from 188–346°C, with a mean of 283°C. Both methods confirm a consistent cooling trend, with IN18 typically yielding values up to 50°C lower than TB13.

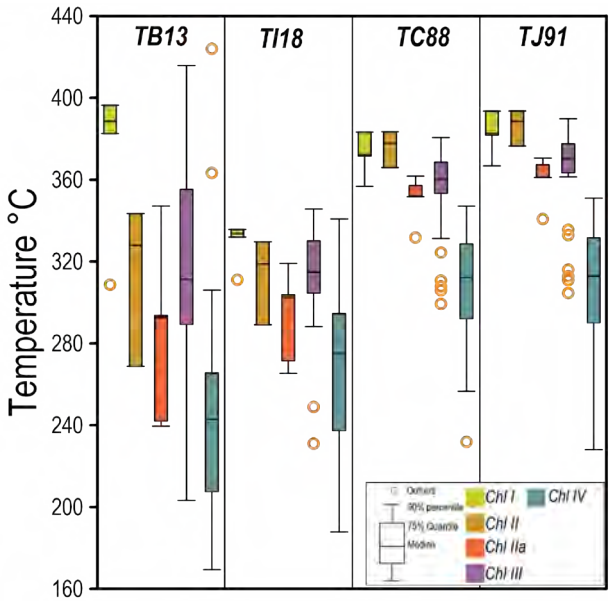


Figure 5. Box-and-whisker plot comparing between semi-empirical and empirical thermometers used for temperature estimation of the different chlorite generations.

4 Discussion and conclusion

Acknowledgements

This work was partially supported by the “PHC Toubkal” programme N° TBK/24/196, funded by the French Ministry for Europe and Foreign Affairs, the French Ministry for Higher Education and Research, and the Moroccan Ministry for Higher Education, Scientific Research and Innovation (MESRSI). The authors also express their gratitude to Aya Gold & Silver for their valuable support.

References

Bourdelle F, Parra T, Chopin C, Beyssac O (2013) A new chlorite geothermometer for diagenetic to low-grade metamorphic conditions. Contrib Mineral Petrol 165:723–735. https://doi.org/10.1007/s00410-012-0832-7

Cathelineau M (1988) Cation site occupancy in chlorites and illites as a function of temperature. Clay Minerals 23:471–485. https://doi.org/10.1180/claymin.1988.023.4.13

Cook NJ, Ciobanu CL, Pring A, et al (2009) Trace and minor elements in sphalerite: A LA-ICPMS study. Geochimica et Cosmochimica Acta 73:4761–4791. https://doi.org/10.1016/j.gca.2009.05.045

Einaudi M, Hedenquist J, Inan E (2003) Sulfidation State of Fluids in Active and Extinct Hydrothermal Systems: Transitions from Porphyry to Epithermal Environments. In: Society of Economic Geologists Special Publication. pp 285–313

Essarraj S, Boiron M-C, Cathelineau M, et al (1998) Brines related to Ag deposition in the Zgounder silver deposit (Anti-Atlas, Morocco). European Journal of Mineralogy 10:1201–1214

Fan M-S, Ni P, Pan J-Y, et al (2023) Rare disperse elements in epithermal deposit: Insights from LA–ICP–MS study of sphalerite at Dalingkou, South China. Journal of Geochemical Exploration 244:107124. https://doi.org/10.1016/j.gexplo.2022.107124

Gamarra-Urrunaga JE, Castroviejo R, Bernhardt H-J (2013) Preliminary mineralogy and ore petrology of the intermediate-sulfidation Pallancata Deposit, Ayacucho, Peru. The Canadian Mineralogist 51:67–91. https://doi.org/10.3749/canmin.51.1.67

Inoue A, Inoué S, Utada M (2018) Application of chlorite thermometry to estimation of formation temperature and redox conditions. Clay Minerals 53:143–158. https://doi.org/10.1180/clm.2018.10

Jowett EC (1991) Fitting Iron and Magnesium into the Hydrothermal Chlorite Geothermometer. In Proceedings of the GAC/MAC/SEG Joint Annual Meeting, Toronto, ON, Canada, 27–29 May 1991

Marcoux É, Wadjinny A (2005) Le gisement AgHg de Zgounder (Jebel Siroua, Anti-Atlas, Maroc) : un épithermal néoprotérozoïque de type Imiter. Comptes Rendus Geoscience 337:1439–1446. https://doi.org/10.1016/j.crte.2005.09.005

Nutt CJ (1989) Chloritization and associated alteration at the Jabiluka unconformity-type uranium deposit, Northern Territory, Australia. Canadian Mineralogist 27 pt 1:41–58

Pelleter E, Cheilletz A, Gasquet D, et al (2016) U/Pb Ages of Magmatism in the Zgounder Epithermal Ag–Hg Deposit, Sirwa Window, Anti-Atlas, Morocco. In: Bouabdellah M, Slack JF (eds) Mineral Deposits of North Africa. Springer International Publishing, Cham, pp 143–165

Petruk W (1975) Mineralogy and geology of the Zgounder silver deposit in Morocco. The Canadian Mineralogist 13:43–54

Sillitoe R, Hedenquist J (2003) Linkages between volcanotectonic settings, ore-fluid compositions, and epithermal precious-metal deposits. Society of Economic Geologists Special Publications, No. 10, 315-343.

Skinner BJ (1966) The system Cu-Ag-S. Economic Geology 61:1–26. https://doi.org/10.2113/gsecongeo.61.1.1

Thomas RJ, Fekkak A, Ennih N, et al (2004) A new lithostratigraphic framework for the Anti-Atlas Orogen, Morocco. Journal of African Earth Sciences 39:217–226. https://doi.org/10.1016/j.jafrearsci.2004.07.046

Ye L, Cook NJ, Ciobanu CL, et al (2011) Trace and minor elements in sphalerite from base metal deposits in South China: A LA-ICPMS study. Ore Geology Reviews 39:188–217. https://doi.org/10.1016/j.oregeorev.2011.03.001

Zhuang L, Song Y, Liu Y, et al (2019) Major and trace elements and sulfur isotopes in two stages of sphalerite from the world-class Angouran Zn–Pb deposit, Iran: Implications for mineralization conditions and type. Ore Geology Reviews 109:184–200. https://doi.org/10.1016/j.oregeorev.2019.04.009

Skarn Zoning Patterns of the Large Zn-Pb-Ag La Colorada Deposit, Chalchihuites District, Zacatecas, Mexico

Pedro Francisco[1], Zhaoshan Chang[1], Chris Emerson[2], Dante Juarez[2], Patricio Perez[2]
[1]Colorado School of Mines, USA
[2]Pan American Silver, Mexico

Abstract. The La Colorada deposit in Zacatecas, Mexico, includes genetically linked intermediate sulfidation epithermal (IS), carbonate replacement (CRD), skarn, and porphyry styles of mineralization, and is the 2nd largest Zn-Pb skarn in the world. This research focus on the identification and application of skarn zoning patterns to assist exploration and understand the deposits' genesis. For this, two cross-sections were built, which revealed the following field identifiable skarn zoning patterns from causative intrusions outwards: 1) red garnet endoskarns; 2) decreasing garnet:pyroxene ratio, 3) pyroxene color changing from green to brown then most of the cases rhodonite appears at the most distal locations, 3) garnet color becoming lighter (red to brown to yellow-green), and 4) magnetite disappears. In addition, microprobe analysis shows Mn increasing in pyroxene from 0.1 to 30.6 wt%, and in garnet, from 0.1 to 1.9 wt%. Metal zonation features the highest Mo(-Cu) inside the porphyry, Cu in the porphyry and proximal skarn, Zn-Pb in distal skarn-CRD and Ag in the IS epithermal veins, although the low grades of the metals have significant spatial overlaps. The skarn zoning patterns, and Mn trends reveal two distinct mineralization centers at La Colorada.

1. Introduction

The Zn-Pb-Ag La Colorada deposit in the Chalchihuites district of the Zacatecas state, Mexico, features a spectrum of mineralization styles including intermediate sulfidation epithermal (IS), carbonate replacement (CRD), skarn, and porphyry. Current mining operations focus on the IS veins in the overlying volcanic cover that transition downwards to CRD in the underlying carbonate-rich sedimentary rocks (Ebner et al, 2022). Much more Zn-Pb-Ag skarn-CRD with lesser porphyry Mo(-Cu) mineralization has been discovered below the eastern part of the IS vein zone by Pan American Silver from extensive drilling since 2018. As of June 30, 2024, the skarn resources are 327 Mt averaging 2.79% Zn, 1.29% Pb, and 35 g/t Ag, containing 9.13 Mt Zn, 4.23 Mt Pb, and 367 Moz Ag metals, much bigger than the veins (23.9 Mt @ 2.40% Zn, 1.38% Pb and 254 g/t Ag containing 0.6 Mt Zn, 0.3 Mt Pb, and 195 Moz Ag; Pan American Silver, 2024). It is now the second largest Zn-Pb skarn in the world in our skarn database with >1700 skarns. The porphyry Mo(-Cu) mineralization exists at depth and surrounded by skarns, > 1.2 km below the current surface. The deposit remains open towards depth and laterally.

Zoning patterns are vectors essential for exploration targeting, for identifying causative intrusion(s) among the typically multiple generations of intrusions in a skarn-porphyry deposit, delineating fluid flow paths, and understanding the genesis and controls of skarns (Zharikov 1970; Einaudi et al. 1981; Meinert 1997; Meinert et al. 2005; Chang and Meinert 2008; Chang et al. 2019). In this study, we aim to identify the skarn zoning patterns that are useful to skarn exploration elsewhere. Furthermore, due to its vertical extension that preserves the roots and tops of a large magmatic-hydrothermal system, the research will help decipher connections between different styles of mineralization and can be used as an exploration model in similar systems, especially where only the tops or the causative intrusions have been discovered.

2. La Colorada Deposit Geology

La Colorada's stratigraphic column features an Early to Late Cretaceous thick sequence of interbedded limestones, calcareous-shale and occasional chert of the Fresnillo, Cuesta del Cura and Indidura Formations (Fig. 1). The package is unconformably overlain by Late Cretaceous to Early Paleocene colluvial sediments of the Ahuichila Conglomerate. A major unconformity exists between the sedimentary sequence and the overlying dacitic volcanic rocks of the Late Cretaceous-Eocene Lower Volcanic Complex (LVC) that comprises much of the volcanic cover at La Colorada. Tertiary pyroclastic rocks, rhyolitic tuffs, and ignimbrites of the Upper Volcanic Supergroup (UVS) unconformably overlie the LVC locally (Albinson 1988; Moller et al. 2001), followed by Quaternary sediments (Fig. 1). Intrusions are all concealed below the surface, clustered at the

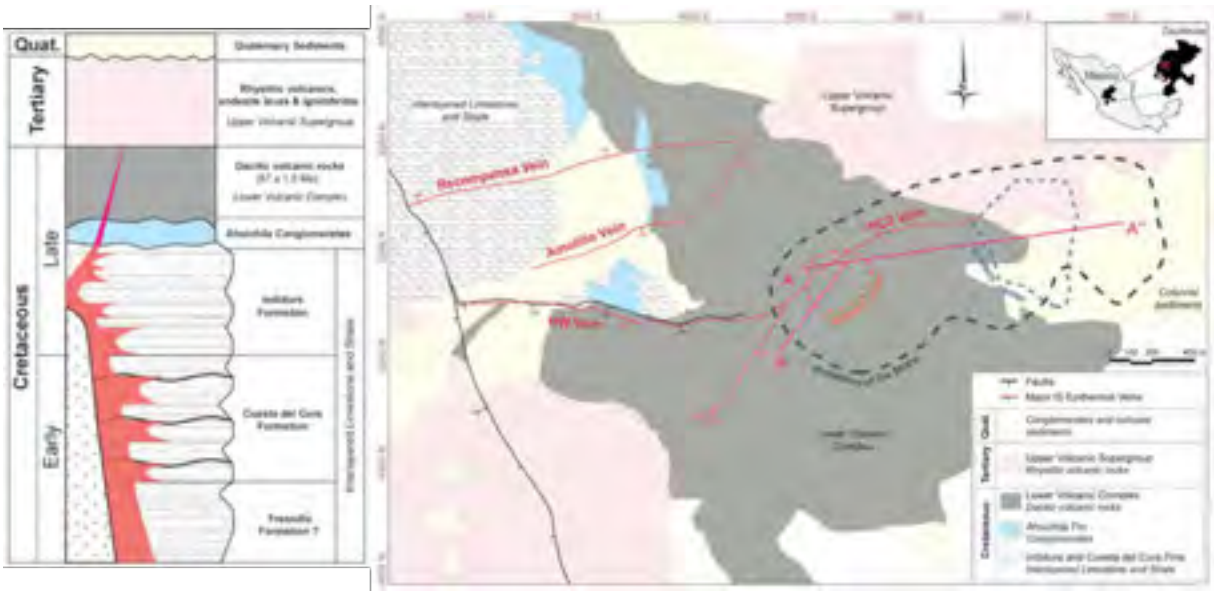


Figure 1. Left - Stratigraphic column of La Colorada deposit's mining area including IS epithermal (pink), skarn-CRD (red) and porphyry styles of mineralization. Right - La Colorada mining district surface geology map with the projections of skarn mineralization (green dashed line), the western center (orange dashed line) and the eastern center (blue dashed line).

western center and eastern center (Figs. 1 and 2). The eastern center comprises pre-skarn andesite porphyry (AP) and rhyodacite porphyry (RDP), syn-skarn RDP (main stock) and minor late-skarn dacite porphyry (DP) and RDP, and post-skarn andesite (AD) dykes. The western center has syn-skarn AP and RDP, late-skarn DP, and post-skarn AD; all narrow dykes (Fig. 2; Francisco et al. 2024).

3. The skarn

The La Colorada skarn formed in five stages at both centers. The Stage 1 contact metamorphism produced marble, some containing Al-dominant garnet patches and thin bands (reaction skarns), and calc-silicate hornfels. Stage 2 prograde skarn is mainly comprised of garnet, pyroxene, local wollastonite, and minor rhodonite. Garnet is mainly andraditic and comprises 60 to 70% of the skarn. Pyroxene compositions vary between diopside, hedenbergite and johannsenite. Stage 3 early retrograde skarn consists of epidote, amphibole, vesuvianite, quartz, magnetite, and local specular hematite. Stage 4 late retrograde skarn encompasses the economic assemblages with sphalerite, galena, chalcopyrite, and tennantite-tetrahedrite that are accompanied by quartz, calcite, and lesser manganoan calcite, and anhydrite. Minor Stage 5 barren calcite veins cut across all earlier assemblages. Red garnet-dominant endoskarn veins occur at the margins of all causative intrusions. They transition inwards to quartz stockworks containing molybdenite, pyrite and scarce chalcopyrite in the larger eastern rhyodacite porphyry stock (~600 m diameter; Figs. 1 and 2) but not in the narrow dykes (<100 m) in the west center. The skarns wrap around the main stock and also along the apophyses from it (Fig. 2).

4. Skarn Zoning Patterns

To determine La Colorada skarn zoning patterns, two cross-sections A-A' (NE-SW) and A'-A'' (E-W) were logged. Each field identifiable zoning pattern is based on the mineralogy of the same paragenesis stages, and they are shown in the two sections (Fig. 2). From proximal to distal, the exoskarn zones include: A) garnet/pyroxene > 1 (the three garnet zones) to garnet/pyroxene < 1 (the two pyroxene zones), to a zone with mixed skarn-marble, then to a locally massive CRD zone (Stage 4 assemblage but no residual Stage 2-3 minerals), and farther to vein CRD (not shown in Fig. 2 but roughly along the 25 ppm Ag contour in marbles). The vein CRD extends upwards into the volcanic cover and becomes IS veins with higher Ag grades (e.g., >100 ppm Ag shell in Fig. 2; Ebner et al. 2023). B) garnet color becomes lighter, from red to brown and yellow-green (Figure 2). C) pyroxene color from green (mostly) to brown starting ~300-400 m away from the main intrusion, and the brown pyroxene zone may be up to 200 m long along dykes

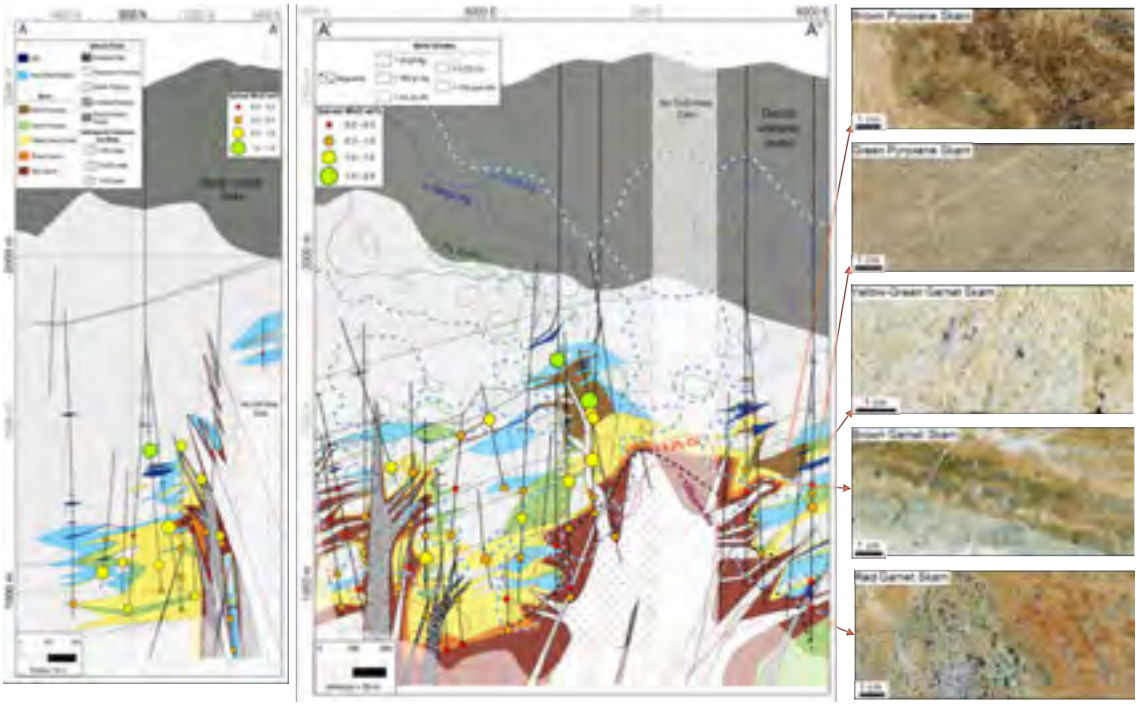


Figure 2. Left – Cross-section A-A' (NE-SW) showing skarn zoning patterns and garnet MnO wt% concentrations in the western center skarn. Middle – Cross-section A'-A'' (E-W) showing skarn zoning patterns, garnet MnO wt% concentration, and metal zonation in the western and eastern centers. Right – skarn samples collected in each of the defined skarn zones.

(Fig. 2). Lesser pink rhodonite occurs in the most distal skarn before it transitions to CRD. D) Magnetite occurs closer to the main middle-east stock, for a few meters from the stock margin at the stock's top to ~250 m at deeper positions (~500 m deeper); farther along some deep apophyses.

EPMA (Electron Micro-Probe Analysis) analyses show that Mn in garnet and pyroxene increases away from the causative intrusions. The concentration of MnO in garnet increases from 0.1 to 1.2 in section A-A' and from 0.1 to 2.0 in section A'-A'' (Fig. 2), and in pyroxene, it increases from 0.1 to 3.7 wt% in section A-A' and 0.1 to 31 wt% in section A'-A''.

Metal zonation based on all drill-hole assay data and the derived Leapfrog model is shown in Fig. 2, cross section A'-A''. The relatively higher grades of Mo (>100 ppm; not ore grade) only occurs in the more felsic RDP eastern center, and are inside the stock or shortly outwards. The >0.2% Cu grades are mostly slightly away from the intrusion margin but still in proximal skarns. The >5% Zn+Pb shell is outwards from the >0.2% Cu contours and extends farther upwards, up to the base of the volcanic cover along some channels. The major channels are shown by the 25 ppm Ag shell. Two channels are above the eastern center, with one roughly along the longest dyke originated from the stock. One is above the western center. The higher grades of Ag (>100 ppm) are dominantly in the shallower part, in the volcanic cover (IS veins) and shortly below its base (vein CRD; Fig. 2). The transition from IS vein to CRD mineralization, in particular close to the volcanics-carbonates' contact, is marked by decreasing Ag and increasing Zn-Pb.

Silver mineralogy also varies systematically. In the proximal low Ag zone, Ag is mostly in galena and tennantite-tetrahedrite. In the distal high Ag zone (mainly IS veins), Ag is mostly in Ag sulfosalts, acanthite, and native silver (Chutas and Sack 2004).

5. Discussion and Conclusions

The La Colorada skarn zoning patterns verify the existence of two distinct intrusive centers: the western dykes and the eastern stock (larger; Fig. 2). The two centers are about 550 m apart and both produced skarn-CRD mineralization. So far, the western center lacks porphyry-style mineralization probably because the dykes are smaller (<100 m wide) than the eastern stock (~600 m across). It also lacks Mo mineralization likely because the syn-skarn intrusion is mainly andesite porphyry, more mafic than the eastern stock that is

mainly composed of a rhyodacite porphyry. Considering that the dykes originated from the eastern stock similarly contain red garnet endoskarn veins but lack porphyry veins, as the western dykes, it is inferred that the narrow western dykes may sit on top of a deeper and larger intrusion that hasn't been drilled into yet.

The La Colorada skarn vertical zoning is well developed in the eastern center. In the western center, the skarn itself is less developed whereas the CRD with Ag is still present. The lack of skarn is probably due to the tops of the narrow dykes running out of heat and ore fluids, similar to the longest upward RDP dyke at the eastern center; skarns are also missing at its top tip. The lateral zoning follows the same zoning patterns as the vertical zoning. In the western center, the skarn extends ~450 m laterally to the SW from the causative dykes (Fig. 2, A-A'). The absence of brown pyroxene skarn in the western center (Fig. 2) indicates a steeper thermal gradient and therefore a hotter intrusion, which is consistent with the more mafic composition (andesitic), and the lower Mn content of the garnet and pyroxene compared with the eastern RDP stock.

The recognition of zoning patterns of the large La Colorada skarn system helps predict fluid flow paths, establish the connection between distinct styles of mineralization and reconstruct the genesis of the deposit. The zoning patterns also assist the ongoing near-mine exploration and have led to the recent discovery of additional skarn-CRD mineralization, IS epithermal veins and intrusions (Pan American Silver 2024). Given La Colorada's size, unique preservation and diversity of mineralization, the skarn zoning patterns here presented are an excellent exploration tool for deposits in similar geological contexts, especially where only IS epithermal, CRD, and/or skarn mineralization has been found. For instance, the NW-trending Mexican Silver Belt (Spurr 1923) hosting La Colorada extends for >2000 km from southwestern United States to south of Mexico (Guerrero state), which also includes many major Au-Ag and Ag-Zn-Pb deposits with IS epithermal veins in the same stratigraphic position as La Colorada veins. In such cases, if the presence of carbonate-rich sequences below the IS vein-bearing volcanic rocks is verified, the potential for skarn-CRD and even deeper porphyry mineralization is vast.

Acknowledgements

We thank Pan American Silver Corp. for all the financial, logistical and field support throughout this research project. We are also grateful to Heather Lowers and Miguel Gaspar for discussions and assistance with EPMA work, and Peter Megaw for discussions.

References

Albinson T (1988) Geologic Reconstruction of Paleosurfaces in the Sombrerete, Colorada, and Fresnillo Districts, Zacatecas State, Mexico. Econ Geol 83:1647–1667.

Chutas N, Sack R (2004) Ore Genesis at La Colorada Ag-Zn-Pb Deposit in Zacatecas, Mexico. Mineral Mag 68:923-937.

Chang Z, Meinert LD (2008) Zonation in Skarns: Complexities and Controlling Factors. In: Proceedings of the PACRIM Congress 11, pp 303-306.

Chang Z, Shu Q, Meinert LD (2019) Skarn Deposits of China. In: Chang Z and Goldfarb RJ (Eds.), Mineral Deposits of China, SEG Spec Pub 22: 189-234.

Ebner J, Chang Z, Francisco P, Juarez D, Perez P, Emerson C, Hemming S, Wendlandt R (2023) The Epithermal-Skarn Transition at the La Colorada Deposit, Chalchihuites District, Zacatecas, Mexico. SEG Conference 2023 abstract and poster.

Einaudi MT, Meinert LD, Newberry RJ (1981) Skarn deposits: Econ Geol 75th Anniversary Volume, pp 317–391.

Francisco P, Chang Z, Huang S, Emerson C, Juarez, D, Perez P, Creaser RA (2024) The role of magmas in forming a big skarn system: A case study from La Colorada deposit (Zacatecas, Mexico). Abstract volume of the SEG 2024 Conference, 27-30 September 2024, Windhoek, Namibia.

Meinert LD (1997) Application of skarn deposit zonation models to mineral exploration. Explor Min Geol 6:185-208.

Meinert LD, Dipple GM, Nicolescu S (2005) World Skarn Deposits. In: Hedenquist JW, Thompson JFH, Goldfarb RJ, Richards JP (Eds.), Econ Geol 100th Anniversary Volume, pp 299-336.

Moller SA, Islas J, Davila RT (2001) New Discoveries in the La Colorada District, Zacatecas State, Mexico. SEG Spec Pub 8:95-105.

Pan American Silver (2024) Pan American Silver Reports Mineral Reserves and Mineral Resources as at June 30, 2024. https://panamericansilver.com/operations/silver-segment/la-colorada-skarn/. Accessed 18 February 2025.

Spurr JE (1923) The Ore Magmas: Volume Two. New York, McGraw Hill.

Zharikov VA (1970) Skarns. Int Geol Rev 12:541–559, 619–647, and 760–775.

Role of Magmas in Forming a Large Skarn System: A case study from La Colorada Deposit (Zacatecas, Mexico)

Pedro Francisco[1], Zhaoshan Chang[1], Shiqiang Huang[1], Chris Emerson[2], Dante Juarez[2], Patricio Perez[2], Robert Creaser[3]
[1]Colorado School of Mines, USA
[2]Pan American Silver, Mexico
[3]University of Alberta,Canada

Abstract. The La Colorada deposit in Mexico is a large skarn system, containing 367 Moz Ag, 9.13 Mt Zn, and 4.23 Mt Pb. It is the 2nd largest Zn-Pb skarn in the world. The deposit also features linked intermediate-sulfidation epithermal, carbonate replacement, and porphyry styles of mineralization. The ores are around and above a western center and an eastern center ~550 m apart, each has intrusions of pre-, syn-, late-, and post-skarn timing, based on cross-cutting relationships, skarn zoning patterns, and the alteration of the intrusions. The western center is composed of syn-skarn andesite porphyry (AP) and rhyodacite porphyry (RDP) dykes, late-skarn dacite porphyry (DP) dykes, and post-skarn andesite dykes (AD), the largest ~100 m wide. The eastern center consists of pre-skarn AP and RDP dykes, syn-skarn RDP stock (~600 m across), late-skarn DP and RDP, and post-skarn AD dykes. Molybdenite Re-Os (n=3), zircon U-Pb (26) dating, and skarn garnet U-Pb (9) dating reveals mineralization ages of ~63 Ma in the western and ~62 Ma in the eastern center, and late-skarn ages of ~60 Ma, indicating mineralization over a period of ~3 myrs. The large size of La Colorada is likely related to the multiple fertile intrusions emplaced at separate locations.

1. Introduction

The Zn-Pb-Ag La Colorada deposit in the Chalchihuites district of the Zacatecas state, Mexico, features linked intermediate-sulfidation epithermal (IS), carbonate replacement (CRD), skarn, and porphyry styles of mineralization (Ebner et al. 2022; Francisco et al. 2024). Abundant Zn-Pb-Ag skarn-CRD with lesser porphyry Mo(-Cu) mineralization was discovered below the eastern part of the IS vein zone by Pan American Silver from extensive drilling in 2018. As of June 30, 2024, the skarn resources are 327 Mt averaging 2.79% Zn, 1.29% Pb, and 35 g/t Ag, containing 9.13 Mt Zn, 4.23 Mt Pb, and 367 Moz Ag metals, much bigger than the veins (23.9 Mt @ 2.40% Zn, 1.38% Pb and 254 g/t Ag containing 0.6 Mt Zn, 0.3 Mt Pb, and 195 Moz Ag; Pan American Silver, 2024). It is currently the second largest Zn-Pb skarn in the world in our skarn database with >1700 skarns. The deposit is still open and exploration on-going. The large size is attractive to the minerals industry. In this study, we investigate the magmatic contribution to its large size, through investigating the intrusive sequence, determining their relationship with skarns, and followed by dating.

2. La Colorada Deposit Geology

La Colorada's stratigraphy features an Early to Late Cretaceous thick sequence of interbedded limestones, calcareous-shale and occasional chert of the Fresnillo, Cuesta del Cura and Indidura Formations (Fig. 1). The carbonate-rich sedimentary package is unconformably overlain by Late Cretaceous to Early Paleocene colluvial sediments of the Ahuichila Conglomerate. Farther up is a major unconformity and then the dacitic volcanic rocks of the Late Cretaceous-Eocene Lower Volcanic Complex (LVC), dated at ~67 Ma (Fig. 2; Ebner et al. 2022). Tertiary pyroclastic rocks, rhyolitic tuffs, and ignimbrites of the Upper Volcanic Supergroup (UVS) unconformably overlie the LVC (Albinson 1988; Moller et al. 2001). The youngest unit is the Quaternary sediments (Fig. 1).



Figure 1. La Colorada surface geology map with the surface projections of skarns (green dashed line) and the two intrusive centers, western and eastern.

2.1 Intrusions at La Colorada

There are multiple intrusions concealed and only intersected in drill holes at depths. They

are andesitic, dacitic and rhyodacitic. Most of the intrusive rocks are porphritic with aphanetic groundmass. The porphyritic intrusions are mainly distinguished according to the proportion of quartz phenocrysts. Andesite porphyries (AP) contain non- to scarce visible quartz (<1%), abundant plagioclase (10-15%), minor K-feldspar (<2%), biotite (2-5%) and amphibole (<2%) phenocrysts. Dacite porphyries (DP) contain little quartz (1-5%), abundant plagioclase (15-20%), some K-feldspar (<4%), and minor biotite (<1%) phenocrysts. In rhyodacite porphyries (RDP), the proportion of plagioclase and biotite phenocrysts is similar to DP but contains significantly more quartz (>5%) and K-feldspar (4-10%) phenocrysts. K-feldspar phenocrysts are large, euhedral and commonly have rapakivi textures. Andesite dykes (AD) are aphanitic with local amygdales but no phenocrysts, composed of pyroxene and/or amphibole, biotite, and plagioclase. All the intrusions contain accessory magnetite, indicating that they are oxidized.

The intrusions occur in two clusters, the east and west centers that are ~550 m apart (Figs. 1 and 2). The intrusions in the western center are dykes; the largest one is ~100 m wide. The eastern center include a ~600 m wide stock and >1.2 km below the surface (Figure 2), plus several narrow dykes.

3. Intrusive Sequence

The intrusive sequence at La Colorada is determined by one or more of the following cross-cutting relationships: A) Later intrusion truncating veins and/or phenocrysts of an earlier intrusion; B) Later intrusion exhibiting chilled margins against an earlier intrusion; C) Later intrusion containing clasts of earlier intrusions; D) Later intrusions containing clasts of skarns produced by earlier intrusions.

The sequence in the western center is AP-W, RDP-W, and then DP-W. The AP-W is cut across by RDP-W (Fig. 3A) and DP (Figs. 3B and C). The DP-W is later than RDP-W, as the former contains RDP-W xenoliths. In the eastern center, AP-E and RDP-E1 dykes are determined to be the earliest because they are pre-skarn, with only a low-temperature alteration assemblage. The ~600 m wide RDP-E2 stock is crosscut by narrow DP-E, RDP-E3 and RDP-E4 dykes (Fig. 3D and E). Minor AD dykes cut across all other intrusions and mineralization at both centers.

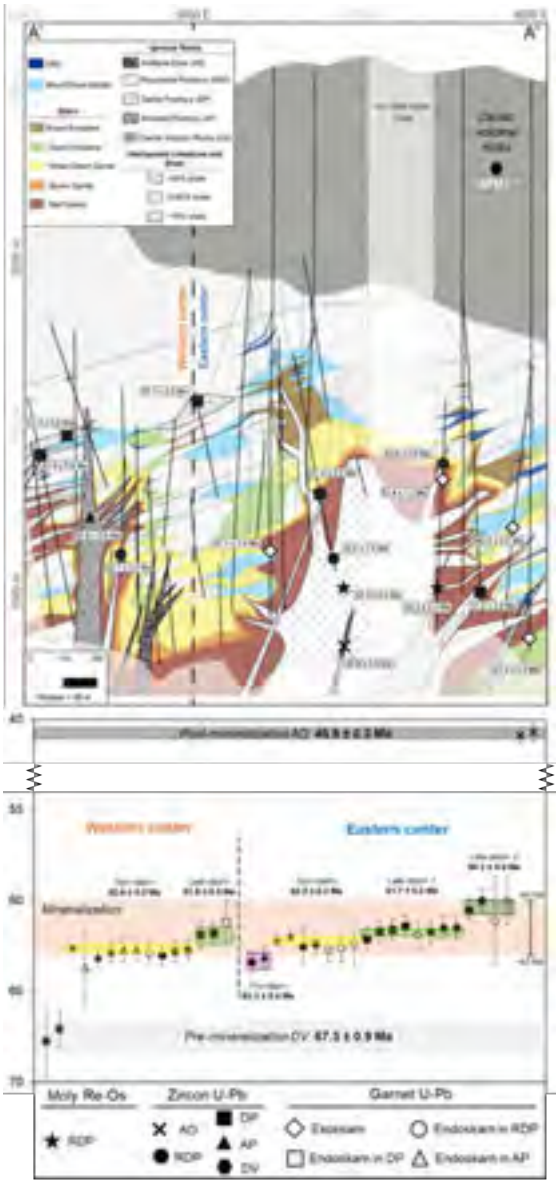


Figure 2. Top: Cross-section A'-A' displaying exoskarn zoning patterns and the two intrusive centers. Some dating results are included in the section. Bottom: All La Colorada dating results including weighted mean for pre-, syn- and late-skarn in the western center and eastern center (separated by a dashed line), pre-mineralization DV and post-mineralization AD.

4. Intrusion-Skarn Timing

The timing of intrusions relative to skarns can be pre-, syn-, late-, and post-skarn. This is determined by zoning patterns of the exoskarns and the alteration of the intrusions, supplemented by geochronology. Dating itself can reject a genetic relationship, but is insufficient to establish a relationship, because the dating uncertainties (95% confidence internal) are typically bigger than the time it takes to form a skarn (<0.04 myrs; Pollard et al. 2021).

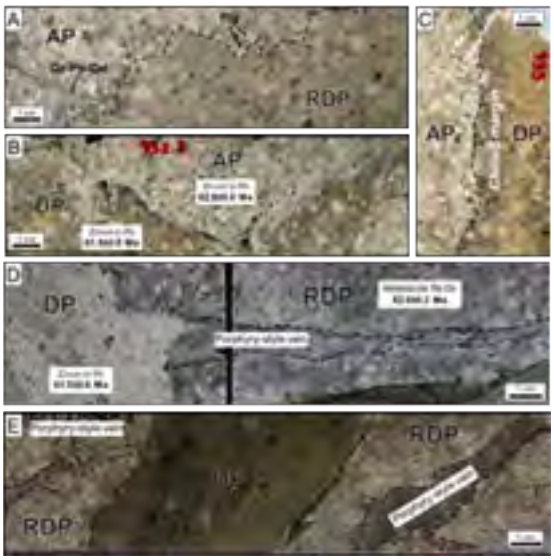


Figure 3. A: RDP-W cuts across AP-W and truncates its plagioclase phenocrysts & a quartz-pyrite-calcite veinlet in it. B: DP-W containing clasts of AP-W. C. DP-W has chilled margin against AP-W. D & E: syn-skarn RDP-E2 is cut across by DP-E. The DP-E truncates porphyry-style veins in RDP-E2.

Skarn zoning patterns (Meinert 1997; Chang and Meinert 2008A; Chang et al. 2019) is the most reliable way to identify the causative/syn-skarn intrusion. Skarn occur at both centers at La Colorada. The exoskarn zoning patterns include, from the causative intrusions outwards: A) garnet:pyroxene ratio decreases; B) garnet color becomes lighter, from proximal red to brown then distal yellow-green; C) pyroxene color changes from green to brown. Lesser pink rhodonite occurs in the most distal skarn before it transitions to CRD. D) massive CRD or mixed marble-green garnet zone (Fig. 2); and E) vein-style CRD in >25 ppm Ag plumes extending upwards from the distal skarns or massive CRDs at the two centers in marble and into the volcanic cover.

At La Colorada, pre-skarn intrusions do not have zoned exoskarns, and are cut by only low temperature vein, mainly of quartz-carbonate-sulfide (Fig. 4A), with alteration haloes of illite, smectite and/or chlorite. Syn-skarn intrusions are identified by being at the proximal end of zoned exoskarns (typically containing red garnet), and the occurrence of red-garnet endoskarn veins (Fig. 4B). The endoskarn veins may transition to porphyry-style veins inwards in larger causative intrusions (e.g., RDP-E2 stock; Fig. 2C). Post-skarn intrusions are fresh and cut across all type of mineralization. These intrusions may also contain xenoliths of skarn, and/or earlier intrusions. Late-skarn intrusions have syn-skarn characteristics, usually red garnet endoskarn veins (Fig. 4E), but are smaller with lesser mineralization.

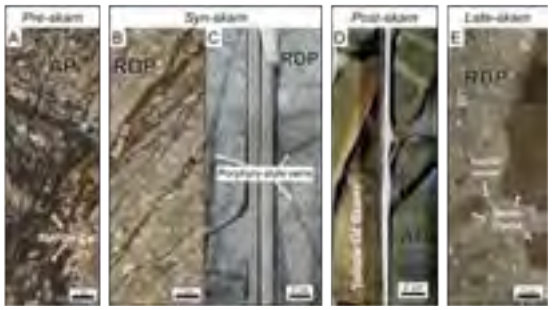


Figure 4. A: Pre-skarn AP-E cut by low temperature quartz-calcite-sulfide veins with illite alteration. B: Syn-skarn RDP-E2 with high-temperature red garnet endoskarn veins. C. Syn-skarn RDP-E2 with a stockwork of porphyry-style quartz-molybdenite-pyrite veins. D: Post-skarn AD crosscuts skarn mineralization. E: Late-skarn RDP-E3 with red garnet endoskarn veinlets and skarn clasts of a prior mineralization event.

Based on the above criteria, the western center features syn-skarn AP-W and RDP-W, late-skarn DP-W, and post-skarn AD-W dykes. The eastern center consists of pre-skarn AP-E and RDP-E1 dykes, syn-skarn RDP-E2 stock, late-skarn DP-E, RDP-E3, and RDP-E4 dykes, and post-skarn AD dykes (Fig. 2).

5. Geochronology

The intrusions at La Colorada are dated using zircon U-Pb method (n=26), the skarns with garnet U-Pb (n=9) method, both at the Colorado School of Mines LA-ICP-MS/MS lab, and the mineralization by molybdenite Re-Os at University of Alberta, Canada (n=3). Ages of pre-, syn-, late-, and post-skarn events of both centers are the weighted means of the individual dates of all types of the same event (Fig. 2).

In the western center, the syn-skarn event has an age of 62.6 ± 0.2 Ma. The late-skarn is slightly younger, 61.8 Ma ± 0.5 Ma. In the eastern center, the pre-skarn event is at 63.3 ± 0.4 Ma, and the syn-skarn event 62.2 ± 0.2 Ma. There are two late-skarn events, one at 61.7 ± 0.2 Ma, and the other one younger, at 60.3 ± 0.4 Ma. The post-skarn AD dykes are much younger at 40.8 ± 0.3 Ma.

6. Discussion and Conclusions

The large size of La Colorada may have significant contribution from the magmatism, including the multiple fertile intrusions and their layout. A typical skarn and porphyry deposit

typically has only one or two causative intrusions (e.g., Cooke et al. 2005; Meinert et al. 2005; Chang and Meinert 2008B; Sillitoe 2010; Calder et al. 2022). Having multiple fertile intrusions likely increases the supply of fluids and metals e.g., at Antamina, Peru, the largest skarn in the world (Chang et al. 2015; Mrozek et al. 2015, 2021). La Colorada has three syn-skarn intrusions (RDP-E2, AP-W, and RDP-W), and four late-skarn intrusions (DP-E, RDP-E3, RDP-E4, and DP-W), and they lasted for ~3 myrs from ~63 to 60 Ma (Fig. 2), which contributes to the large size.

The fertile intrusions are in two centers ~550 m apart. This enables more fertile intrusions to contact carbonates to generate more skarn-CRDs and have an efficient metal deposition mechanism due to pH buffering by carbonates (e.g., Shu et al., 2017), which also contributes to the large size. If a fertile intrusion intrudes an earlier intrusion or skarn, there is no more supplies of carbonates therefore there will be little new skarns, and the metal deposition is not as effective as in a skarn environment.

Geochronology at La Colorada reveals that the fertile intrusions and mineralization become younger from west to east, despite that the eastern center has older intrusions (pre-skarn). The syn-skarn event of the western center is 62.6±0.2 Ma while the counterpart in the east is 62.2±0.2 Ma. The late-skarn intrusions and skarns are at 61.8±0.5 Ma in the west, while the late-skarn events in the east are at 61.7±0.2 Ma and 60.3±0.4 Ma. Magmas evolved from andesitic to rhyodacitic in both centers. The eastern center has shallow dykes that goes down to a larger stock (Fig. 2), based on which it is inferred that the dykes in the west center may also lead to a larger fertile stock downwards.

Acknowledgements

We thank Pan American Silver Corp. for all the financial, logistical and field support.

References

Albinson T (1988) Geologic Reconstruction of Paleosurfaces in the Sombrerete, Colorada, and Fresnillo Districts, Zacatecas State, Mexico. Econ Geol 83:1647-1667.

Calder M, Chang Z, Arribas A, Gaibor A, Dunkley P, Pastoral J, Kouzmanov K, Spandler C, Hedenquist J. (2022) High-Grade Copper and Gold Deposited During Postpotassic Chlorite-White Mica-Albite Stage in the Far Southeast Porphyry Deposit, Philippines. Econ Geol 117:1573-1596.

Chang Z, Meinert LD (2008A) Zonation in Skarns: Complexities and Controlling Factors. In: Proceedings of the PACRIM Congress 11, pp 303-306.

Chang Z, Meinert LD (2008B) The Empire Cu-Zn Mine, Idaho, USA: Exploration implications of unusual skarn features related to high fluorine activity. Econ Geol 103:909-938.

Chang Z, Mrozek S, Meinert LD, Windle, S (2015) Skarn-porphyry transition: an example from the Antamina skarn, Peru. In: Proceedings of PACRIM 2015, pp 409-413.

Chang Z, Shu Q, Meinert LD (2019) Skarn Deposits of China. In: Chang Z and Goldfarb RJ (Eds.), Mineral Deposits of China, SEG Spec Pub 22:189-234.

Cooke DR, Hollings P, Walshie JL (2005) Giant porphyry deposits: Characteristics, distribution, and tectonic controls. Econ Geol 100 (5):801–818.

Ebner J, Chang Z, Francisco P, Juarez D, Perez P, Emerson C, Hemming S, Wendlandt R (2023) The Epithermal-Skarn Transition at the La Colorada Deposit, Chalchihuites District, Zacatecas, Mexico. SEG Conference 2023 abstract and poster.

Francisco P, Chang Z, Huang S, Emerson C, Juarez D, Perez P, Creaser RA (2024) The role of magmas in forming a big skarn system: A case study from La Colorada deposit (Zacatecas, Mexico). Abstract volume of the SEG 2024 Conference.

Meinert LD (1997) Application of skarn deposit zonation models to mineral exploration. Explor Min Geol 6:185-208.

Meinert LD, Dipple GM, Nicolescu S (2005) World Skarn Deposits. In: Hedenquist JW, Thompson JFH, Goldfarb RJ, Richards JP (Eds.), Econ Geol 100th Anniversary Volume, pp 299-336.

Moller SA, Islas J, Davila RT (2001) New Discoveries in the La Colorada District, Zacatecas State, Mexico, New Mines and Discoveries in Mexico and Central America. SEG Spec Pub 8:95-105.

Mrozek S, Chang Z, Meinert LD (2015) A model for the intrusive sequence and Cu-Zn skarn formation at the Antamina deposit, Peru. In: Proceedings of PACRIM 2015, pp 423-429.

Mrozek S, Chang Z, Spandler C, Windle S, Raraz C, Paz A (2020) Using whole rock geochemistry to optimize skarn classification and evaluate element mobility during skarn formation: An example from the Antamina deposit, Peru. Econ Geol 115:177-188.

Pan American Silver (2024). Pan American Silver Reports Mineral Reserves and Mineral Resources as at June 30, 2024. https://panamericansilver.com/operations/silver-segment/la-colorada-skarn/. Accessed 18 February 2025.

Pollard PJ, Jongens R, Stein H, Fanning M, Smille R (2021) Rapid Formation of porphyry and skarn copper-gold mineralization in a postdubduction environment: Re-Os and U-Pb geochronology of the Ok Tedi mine, Papua New Guinea. Econ Geol 116:533-558.

Shu Q, Chang Z, Hammerli J, Lai Y, Huizenga JM (2017) Composition and evolution of fluids forming the Baiyinnuo'er Zn-Pb skarn deposit, NE China: insights from laser ablation ICP-MS study of fluid inclusions. Econ Geol 112:1441-1460.

Sillitoe RH (2010) Porphyry Copper Systems. Econ Geol 105:3-41.

Geology, Mineral Alteration and Mineralization of the Santa Cecilia Porphyry Au-Cu Deposit, Maricunga Belt, Northern Chile

José Franco[1], Luciano Bocanegra[2], Piotr Paleczek[2], Antonio Arribas[1]
[1]The University of Texas at El Paso, Department of Earth, Environmental and Resource Sciences, USA
[2]Torq Resources, Vancouver, British Columbia, Canada

Abstract. The Santa Cecilia porphyry Au-Cu deposit, located in the Maricunga Belt of northern Chile, exhibits a complete porphyry copper system alteration column, ranging from deep potassic alteration to shallow advanced argillic and silicic assemblages. This study aims to refine ore distribution within the alteration zones, primarily in the Cerro del Medio sector, while ongoing studies continue in the Pircas and Gemelos sectors. Santa Cecilia lies adjacent to the Caspiche deposit (1,091 Mt @ 0.55 g/t Au), separated by a 250-m-wide valley, and formed during the latest Oligocene (~25 Ma). The results define four main alteration zones at Cerro del Medio starting with potassic (biotite-magnetite), chlorite-white mica (chlorite-muscovite-albite), white mica (quartz-muscovite-albite), and a lithocap (quartz-pyrophyllite, quartz-alunite, vuggy residual quartz). Copper-gold mineralization at Cerro del Medio is genetically linked to porphyry intrusions and the Quebrada Seca formation, with hydrothermal alteration dated around 25 Ma. The system displays a vertically zoned alteration pattern typical of porphyry deposits, transitioning from deep potassic to shallow advanced argillic assemblages. Three mineralization stages are recognized, with the highest copper grades associated with early magnetite-chalcopyrite veinlets in the biotite-magnetite zone. Geological similarities with the Caspiche deposit suggest a shared magmatic origin.

1 Introduction

The Santa Cecilia porphyry gold-copper project is located in the Maricunga metallogenic belt between latitudes 26° and 28°S in the high Andes of the Atacama Region, northern Chile. The Maricunga Belt is rich in gold-silver-copper epithermal and porphyry deposits of Miocene to Oligocene age, such as La Coipa, Refugio, Caspiche and Cerro Casale. South of it, the Vicuña Belt hosts deposits like Los Helados and Josemaria, and farther south, the El Indio Belt contains the Pascua-Lama and El Indio epithermal deposits of Miocene age (Fig. 1).

The history of exploration in the Santa Cecilia district spans decades, marked by various efforts to uncover its mineral potential. In the 1980s, aerial surveys and geological exploration were conducted and by 1982 exploration in the Maricunga Belt identified key areas, including Santa Cecilia.

In 1983, the Santa Cecilia property was secured, leading to geological reconnaissance and sampling between 1984 and 1985. An option agreement was later signed, and from 1986 to 1990, access roads were developed, and 47 holes (14,012 m) were drilled. However, the option was relinquished in 1990. Subsequent exploration efforts continued with the discovery of the Caspiche deposit in 2010 and later surveys and drilling campaigns. In 2021, Torq resources acquired an option on the project and started drilling in 2023. In January 2025, Torq Resources announced a joint venture transaction with Gold Fields to continue exploring the district for economic mineralization.



Figure 1. Chile's most significant mineral deposits along metallogenic belts (mod. from kuraminerals.com).

This study presents the first geologic and mineralogical documentation of the Cerro del Medio deposit in the Santa Cecilia property, focusing on lithology, stratigraphy, hydrothermal alteration, and metallic mineralization based on surface and drill hole samples. The research aims to enhance the understanding of Santa Cecilia's formation and its possible connection to the adjacent Caspiche deposit (Sillitoe et al., 1991; Sillitoe et al., 2013). Previously identified as a porphyry copper system with limited details, this study seeks to provide a comprehensive geological framework by examining host lithologies, deposit age, hydrothermal evolution, and mineralization processes. Particular

attention is given to the key alteration and mineralization events responsible for copper, gold, and molybdenum enrichment, offering insights relevant to mineral exploration within the Santa Cecilia-Caspiche district and similar geological settings.

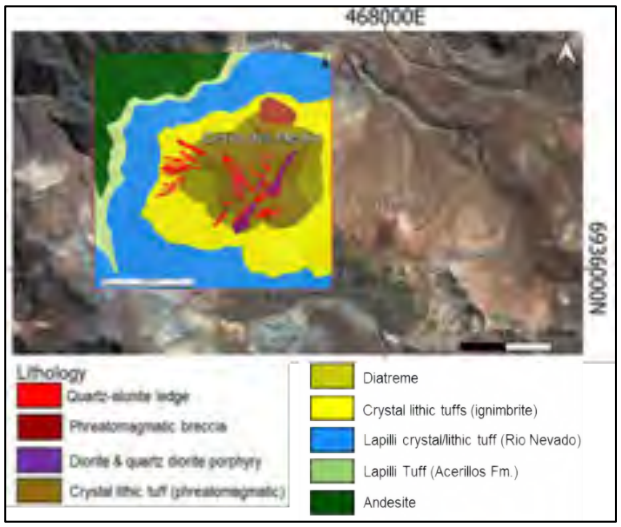


Figure 2. Geological map of the Cerro del Medio within the Santa Cecilia project area (mod. from Torq Resources Inc. 2023).

The geology of the Santa Cecilia district consists of several stratigraphic units spanning from the Paleocene to the Holocene (Fig. 2). The Quebrada Seca Formation (early Paleocene) at the bottom of the sequence comprises andesite, while the Estratos de Quebrada Acerillo Formation (late Paleocene) includes pyroclastic and volcano-sedimentary units. The Estratos de Rio Nevado Formation (Oligocene) features pyroclastic and sedimentary deposits with zircon U-Pb ages between 28.8±0.9 Ma and 26.7±0.4 Ma and Late Oligocene rhyolite domes, hydrothermally altered, with a U-Pb age of 25.7±0.6 Ma. Younger units include Miocene volcanic complexes (16–13 Ma) and late Miocene dacitic to rhyolitic lava and tuff (8.4±0.4 Ma to 5.9±0.6 Ma). The youngest units in the district are Pleistocene-Holocene mass-wasting deposits, including gravitational collapse deposits and colluvium. These geological units collectively characterize the Santa Cecilia geologic district system (Mpodozis et al., 2018; Kay et al., 1994).

The objectives are to identify mineral assemblages and the timing of hydrothermal alteration, evaluate Cu-Au grades across alteration stages, and examine relationships between alteration and mineralization centers.

2 Methods

For this study, sixty-nine samples were collected and analyzed from outcrops and drill core, selected to represent different lithologies, alteration assemblages, and metal concentrations within the Santa Cecilia porphyry system. Three main analytical techniques were used: micro-X-ray fluorescence spectrometry (μXRF), X-ray diffraction (XRD), and scanning electron microscopy with energy-dispersive X-ray detection (SEM-EDAX). μXRF provided qualitative elemental distribution maps, though gold content was undetectable. XRD identified mineral phases, while SEM-EDAX was used to study alunite crystal habits and composition. Geochemical data from the 2023–2024 drilling campaign aided in sample selection and mineralization distribution analysis. Additionally, new Ar-Ar geochronological data were obtained from three samples (two biotite and one alunite) to constrain the timing of alteration and mineralization at Cerro del Medio. Radiometric dating, performed at Auburn University, involved standard mineral separation, irradiation at Oregon State University, and analysis using a GLM-110 mass spectrometer.

3 Results and Discussion

3.1 General Geology

The Cerro del Medio area consists of six primary lithological units: volcanic rocks, pyroclastic rocks, diatreme breccia, porphyritic intrusions, limited hydrothermal breccia, and quartz-alunite ledges (Figs. 2 and 4). Mapped in chronological order, these units provide a framework for understanding the geological system. Volcanic rocks, part of the Quebrada Seca Formation, exhibit biotite-magnetite alteration and a hornfelsic texture due to contact metamorphism. Pyroclastic rocks, including lapilli tuff and lapilli-crystalline tuff, belong to the Río Nevado and Quebrada Acerillos formations. A substantial diatreme breccia body crosscuts earlier lithologies and is polymictic, containing clasts of various compositions. Two major porphyritic intrusions, diorite and dacite porphyries, exhibit different textures and mineral compositions. They are cut by a stockwork system, as described below.

3.2 Mineralization and Hydrothermal History

The mineralization and hydrothermal history of Cerro del Medio are reconstructed using various geochronological techniques to establish the temporal relationship between igneous activity and alteration/mineralization. ^{40}K-^{39}Ar dating by Sillitoe et al. (1991) indicates alteration events between 24.1 ± 0.8 Ma (alunite) and 24.3 ± 0.7 Ma (muscovite). Additional zircon ^{238}U-^{206}Pb dating from Torq (2023) suggests two distinct igneous events: the earliest volcanic breccia at 26 ± 0.4 Ma, followed by a diorite porphyry at 25.1 ± 0.5 Ma. This sequence suggests that the breccia predates the diorite porphyry, which may have contributed to the thermal and chemical conditions necessary for later mineralization.

The mineralization stage, as dated by ^{187}Re-^{187}Os in molybdenite (Torq, 2023), falls between 25.2 Ma and 24.7 Ma, representing the maximum and minimum errors, respectively (Fig. 3). This timeline overlaps with the alteration ages, reinforcing the idea that hydrothermal fluids remained active shortly after or during igneous emplacement. The presence of overlapping dates implies a direct genetic link between the magmatic and mineralizing processes. However, it remains uncertain whether the diorite porphyry itself is responsible for mineralization or if an earlier, still undiscovered, intrusion played a role.

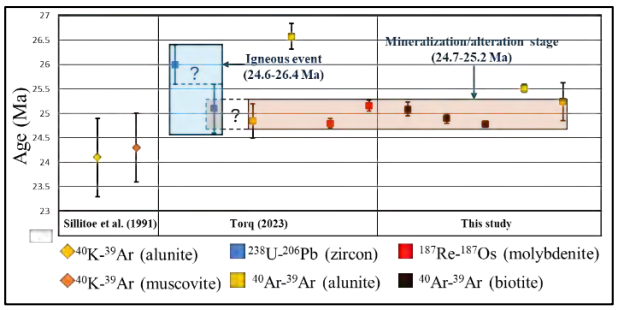


Figure 3. Summary of radiometric age data from Santa Cecilia (Cerro del Medio sector).

Comparing Cerro del Medio with other deposits in the Maricunga Belt, such as Santa Cecilia, Caspiche, Maricunga Mine, and La Coipa, indicates that they share a similar age range (~20–25 Ma) (Lohmeier et al., 2022). This supports the broader metallogenic context of Cerro del Medio within the Maricunga belt's porphyry-epithermal systems.

3.3 Alteration Zonation

Cerro del Medio exhibits a well-developed alteration zonation characterized by four primary alteration types: biotite-magnetite (potassic), chlorite-white mica, white mica, and aluminosilicate. These alteration types form distinct halos, with the deeper biotite-magnetite alteration at ~700 m below the highest elevation in Santa Cecilia (~4,500 m.a.s.l), transitioning upward to chlorite-white mica (~400–850 m depth), then white mica (~800–50 m depth), and finally aluminosilicate at surface to ~300 m depth (Fig. 4).

The aluminosilicate alteration consists of alunite-quartz ledges with orientations of E-W and NW-SE, transitioning to NNE-SSW near the diorite porphyry. These ledges display vuggy quartz textures indicative of extreme acidic conditions (pH <1.5) transitioning to a less acidic environment (pH 2–4) at ~300 m depth, where minerals such as pyrophyllite, diaspore, dickite, and kaolinite are found. These conditions align with hypogene advanced argillic alteration as described by Hedenquist & Arribas (2022).

The alteration pattern is consistent with classic porphyry Cu (±Au) systems (Sillitoe, 2010), with a well-developed lithocap overlaying the deeper potassic alteration. The lithological and alteration model (Fig. 4) suggests that mineralization is hosted in volcanic deposits intruded by diorite and dacite porphyry units, with hydrothermal activity forming an inverted cone-like alteration structure, indicating promising drilling targets near the structural center and further east.

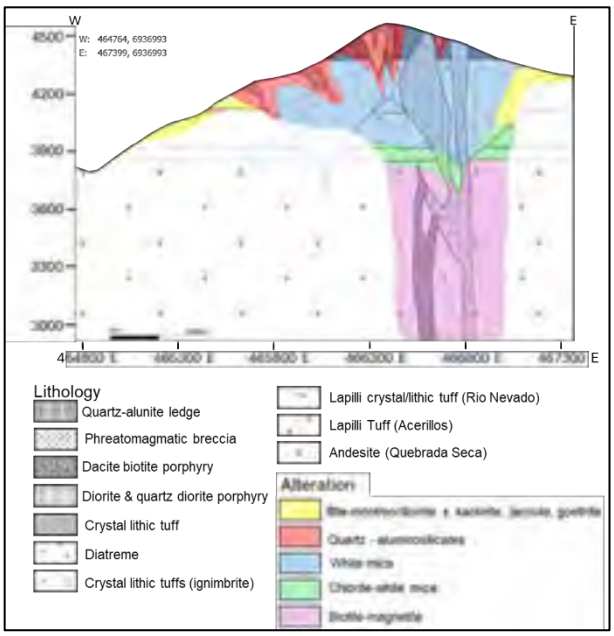


Figure 4. Cross-section of the schematic lithologic and alteration model of the Cerro del Medio.

3.4 Mineralization Stages

The mineralization at Cerro del Medio can be divided into three distinct stages, each associated with specific alteration and veinlet types (Fig. 5).

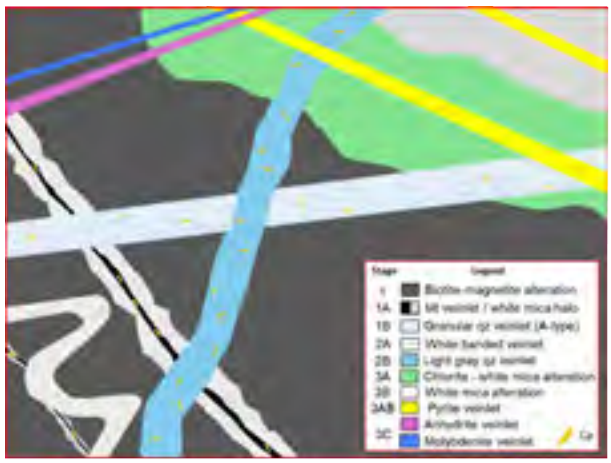


Figure 5. Summary schematic illustration of the paragenetic relations between hydrothermal alteration and mineralization/veining at Cerro del Medio. Crosscutting relationships indicate timing, which can be simplified as follows: Stage 1: magnetite-quartz stage; Stage 2: quartz-rich stage; Stage 3: sulfide-sulfate stage. Mt: magnetite, qz: quartz, Cp: chalcopyrite.

Firstly, the magnetite-quartz stage produced biotite-magnetite alteration and magnetite veinlets with granular quartz (A-type). These veinlets are

commonly associated with chalcopyrite and hematite, but later pyrite overprints have locally modified their mineralogy. Notably, banded quartz veinlets, common in Maricunga porphyry gold deposits, are present but not abundant in Cerro del Medio, suggesting potential gold-copper enrichment in neighboring sectors at Pircas and Gemelos.

Secondly, the quartz-rich stage is characterized by white-banded and light-gray quartz veinlets, that locally contain disseminated chalcopyrite. These features resemble those found in the Caspiche deposit (Sillitoe et al., 2013), where high copper grades correlate with magnetite and quartz veinlets. At Cerro del Medio, these veinlets are most abundant within the biotite-magnetite alteration zone, supporting a link between this alteration type and copper enrichment.

Finally, the sulfide-sulfate stage produced pyrite, anhydrite, and molybdenite mineralization. Pyrite is particularly abundant in the biotite-magnetite alteration zone, extending into white mica alteration and alunite-quartz veins. The presence of sulfate (anhydrite) suggests late-stage hydrothermal fluid evolution, potentially remobilizing and redistributing copper ore.

These observations highlight the multi-stage evolution of mineralization at Cerro del Medio, where early-stage magnetite-quartz and quartz-rich veinlets host copper, while later sulfide-sulfate overprinting modifies the ore distribution.

3.5 Cerro del Medio and Caspiche

Given their proximity (~3 km apart) and similar geological settings, Cerro del Medio and Caspiche exhibit comparable mineralization characteristics. Both systems formed in the late Oligocene, with Caspiche mineralization dated at 25.4±0.09 Ma (Gold Fields 2009, in Sillitoe et al. 2013), nearly contemporaneous with Cerro del Medio (24.7–25.2 Ma).

Alteration patterns also share similarities. Caspiche exhibits potassic, propylitic, potassic-calcic, chlorite-white mica, and advanced argillic alteration. These broadly correlate with Cerro del Medio's biotite-magnetite (potassic), chlorite-white mica, white mica, and aluminosilicate alteration types. Notably, potassic alteration at Caspiche includes K-feldspar and albite, while Cerro del Medio's potassic alteration is dominated by biotite and magnetite, potentially due to differences in host rock lithology.

4 Conclusions

Copper-gold mineralization at Cerro del Medio is closely linked to porphyry intrusions and the Quebrada Seca formation, with hydrothermal alteration occurring around 25 Ma, shortly after the emplacement of subvolcanic diorite porphyry. The deposit exhibits a vertically zoned alteration pattern typical of porphyry copper systems, transitioning from deep biotite-magnetite (potassic) alteration to intermediate chlorite-white mica and white mica zones, and finally to a shallow aluminosilicate (advanced argillic) lithocap very similar to model from Sillitoe (2010).

Three mineralization stages were identified: (1) magnetite-quartz, (2) quartz-rich, and (3) sulfide-sulfate. The highest copper grades are found in the biotite-magnetite zone, associated with magnetite veinlets and chalcopyrite mineralization, while later sulfide-sulfate overprinting appears to cause dilution. Gold distribution is less variable across stages. The biotite-magnetite zone, located between 730 and 990 meters below the surface, represents the primary target for high-grade copper mineralization, with the exposed lithocap serving as a surface indicator.

Cerro del Medio shares significant similarities with the Caspiche deposit, including alteration zonation and mineralization stages, suggesting a genetic link and a common deep-seated magma source for both porphyry systems.

Acknowledgements

Faculty at UTEP is acknowledged for their support, with special thanks to external donors Mr. Lewis Teal and Ms. Marisa de la Vega for their generosity in facilitating participation in fieldwork and key conferences. Logistical support provided by Torq Resources Inc. during fieldwork providing access to samples and data and permission to present this abstract.

References

Hedenquist JW & Arribas A (2022) Exploration implications of multiple formation environments of advanced argillic minerals. Econ Geol 117(3):609–643. https://doi.org/10.5382/econgeo.4880.

Kay SM, Mpodozis C, Tittler A & Cornejo P (1994) Tertiary magmatic evolution of the Maricunga mineral belt in Chile. Inter Geol Rev 36:1079–1112.

Lohmeier S, Lehmann B, Schneider A, Hodgkin A, Burgess R (2022) Ore mineralogy, geochemistry, and dating (Re-Os, Ar-Ar) of the El Volcán porphyry/epithermal system, Maricunga Gold Belt, Northern Chile. Economic Geology; 117 (1): 25–55. doi: https://doi.org/10.5382/econgeo.4856.

Sillitoe RH (1991) Reconnaissance K-Ar geochronology of the Maricunga gold-silver belt, northern Chile. Econ Geol 86: 1261–1270.

Sillitoe RH (2010) Porphyry copper systems. Econ Geol 105(1):3-41.

Sillitoe RH, Tolman J & Kerkvoort GV (2013) Geology of the Caspiche porphyry gold-copper deposit, Maricunga Belt, Northern Chile. Econ Geol 108(4):585–604. https://doi.org/10.2113/econgeo.108.4.585.

Mpodozis M, Constantino Clavero R, Jorge Quiroga C, Rodrigo, Droguett, V, Bárbara & Arcos R (2018) Geología del área de Cerro Cadillal-Cerro Jotabeche, Región de Atacama [en línea]. Santiago: SERNAGEOMIN. Carta Geológica de Chile, Serie Geología Básica nº200.

Exploring the role of volcanic activity in porphyry copper systems in Yerington, NV

Anna Ellen Freudenstein[1], Dawid Szymanowski[1], Lorenzo Tavazzani[1], John Dilles[2], Cyril Chelle-Michou[1]
[1]Department of Earth and Planetary Sciences, ETH Zürich, CH
[2]College of Earth, Ocean and Atmospheric Sciences, Oregon State University, USA

Abstract. The development of volcanic activity in a magmatic system is thought to hinder the formation of porphyry copper deposits (PCDs). Although PCD formation is by now well-understood, there are a limited number of known porphyry systems with extant coeval volcanic units that can be used to test this hypothesis. The Jurassic Yerington district, USA, is an exception, with tilting exposing a nearly continuous section across the volcanic units, deposits, and batholith. We investigate the relationship between PCDs and volcanic activity through the lens of zircon petrochronology in effusive and explosive volcanic units associated with the Yerington batholith, using both in-situ LA-ICP-MS and high-precision CA-ID-TIMS U-Pb methods. Geochronological data shows that these volcanics erupted both pre- and post-mineralisation but show a <1 Myr gap coinciding with the emplacement of porphyry dikes associated with the copper mineralisation. These results further confirm the incompatibility of PCD formation with sustained volcanic activity in the same magmatic system.

1 Introduction

Porphyry copper deposits (PCDs) are the most significant global supplier of copper (Cu), as well as being an important source for gold (Au), molybdenum (Mo) and rhenium (Re) (Sillitoe 2010). As demand for Cu increases to support our escalating energy production and transport requirements, it becomes increasingly important to deepen our understanding of the magmatic systems that generate economic porphyry copper deposits.

An open question is the role of volcanic activity in the formation and termination of mineralising systems. Porphyry copper formation requires a large volume of magma in the shallow crust which degasses metal-bearing fluids. It has therefore been proposed that any coeval or sub-coeval large-scale volcanic activity would be incompatible with PCD formation, as the required volatiles and metals would be vented to the atmosphere (Pasteris 1996; Sillitoe 2010; Richards 2018; Chiaradia and Caricchi 2022).

Constructing this model is complicated by the rarity of volcanic units associated with known porphyry Cu deposits. Generally, by the time a deposit is exposed at the surface, the overlying volcanics have been eroded. However, exceptions can be found where volcanic units are displaced through tilting or are preserved distally to the deposit. The latter is the case in the Bajo de la Alumbrera deposit (Argentina), where local volcanic deposits have been dated to within 20 ka of the termination of mineralisation (Buret et al. 2017). To confirm and generalize the observations at Bajo de la Alumbrera, studies of other coeval volcanics porphyry copper systems are required.

Coeval volcanic and porphyry intrusions are also found in Yerington, USA, where the upper 10 km of a Jurassic magmatic system with associated copper mineralisation has been displaced and tilted 60-90° W during Tertiary extension (Proffett 1977; Proffett and Dilles 1984). The unique exposure at Yerington means that the petrology and chronology of the porphyries, mineralising dikes, and individual intrusive units of the batholith have been comprehensively characterized (Proffett 1977; Proffett and Dilles 1984; Dilles 1987; Dilles et al. 2000; Schöpa et al. 2017; Carter et al. 2022; Castellanos-Melendez et al. 2024). Despite this, the temporal relationship between the volcanics and mineralising porphyries at Yerington is not well understood. These factors make it an excellent location to continue the investigation of the role that volcanic activity may have played in the initiation and termination of porphyry copper mineralisation.

This work aims to explore the detailed petrochronology of zircon from coeval volcanic units at the porphyry copper system in Yerington to reveal the dynamics of porphyry emplacement and eruptive activity in PCD-forming magmatic systems.

2 Geological Background

The Yerington magmatic system formed in the Middle Jurassic, and consists of a composite pluton which is associated with four known centres of porphyry copper deposition (Dilles 1987), as well as associated porphyry dikes and volcanic units. The pluton consists of three distinct sequentially emplaced units: the McLeod Hill quartz monzodiorite, the Bear intrusion, and the Luhr Hill intrusion, becoming increasingly more silicic and decreasing in volume with each intrusive phase. High-precision U-Pb in zircon geochronology place the emplacement ages of each unit at 168.6 – 167.5 Ma, 167.5 – 167.3 Ma, and 167.4 – 166.6 Ma (Castellanos-Melendez et al. 2024), although field relations show there was likely no overlap in the emplacement of the Bear and Luhr Hill intrusions.

The emplacement of several ore-forming granite porphyry dike swarms is interpreted to have occurred over ~0.9 Myr (167.3 – 166.4 Ma). These dike swarms are sourced from the Luhr Hill intrusion (Dilles 1987).

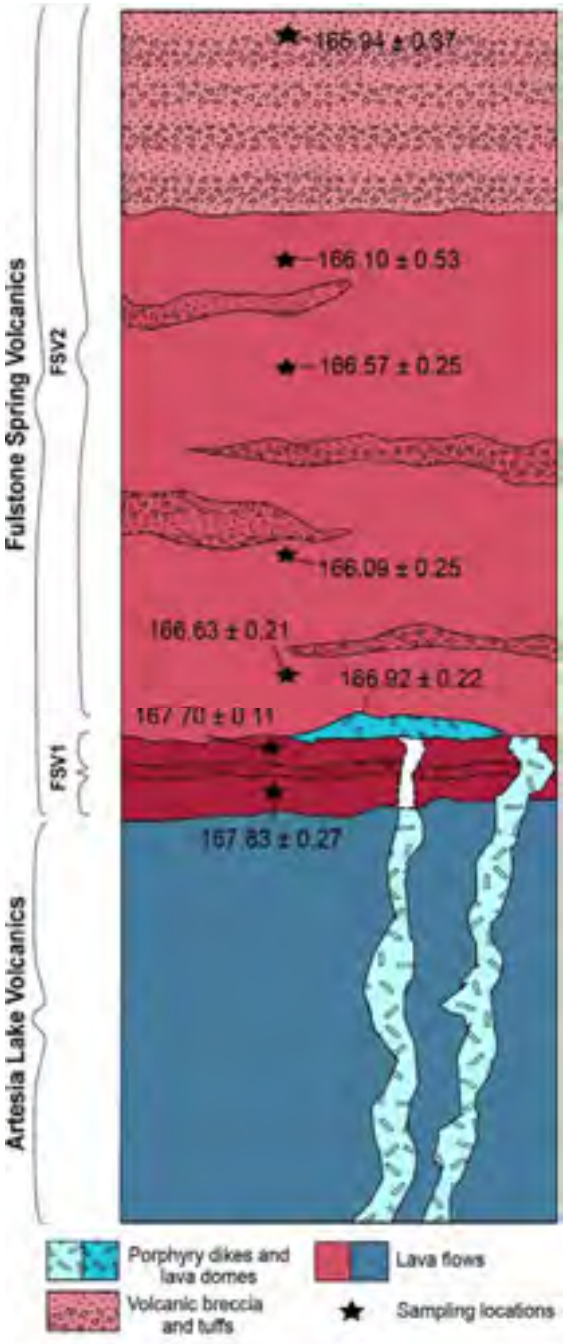


Figure 1. Schematic stratigraphic column with sampled volcanic units in the Buckskin Range. Modified after Dilles and Wright 1988. Ages are Bayesian eruption age estimates based on data from this study (see Methods; Keller et al. 2018).

The Middle Jurassic volcanic units in Yerington are exposed in the Buckskin Range, 1 – 2 km to the west of the known porphyry copper deposits and much of the batholith. The current exposure is related to the lateral displacement of the volcanic cover during Tertiary extension. The volcanic deposits consist of two distinct units: the Artesia Lake volcanics (ALV) and Fulstone Spring volcanics (FSV) (Fig. 1; Salas 1971; Proffett and Dilles 2008). ALV consists of andesitic and dacitic flows and domes, as well as ignimbrites, volcaniclastic sandstones, and breccias (Proffett and Dilles 2008). This volcanic package is thought to be sub-coeval with the McLeod Hill pluton, the earliest of the three intrusive units that make up the Yerington batholith, which intrudes ALV at the base, and overlaps in age (Dilles 1987). ALV hosts the lithocap environment above the mineralising system, and is pervasively hydrothermally altered (Proffett and Dilles 2008). Samples from lava and volcaniclastic units near the top of the ALV section provide an eruption age estimate around 168.3 Ma (Carter et al. 2022; Castellanos-Melendez et al. 2024).

FSV unconformably overlies ALV, with a likely erosive loss of up to 800 m of the ALV unit prior to deposition of FSV (Dilles 1987). FSV is bounded at the base by two lava units divided by a distinct, conglomeratic volcaniclastic layer. Above these, the bulk of FSV units consist of trachytic to dacitic lava flows and domes intercalated with volcaniclastic layers (Proffett and Dilles 2008). Interpretation of the bulk of the FSV stratigraphy is complicated by the extensive tectonic reworking experienced by the Buckskin sector. The uppermost bound of FSV is the Willow Springs Tuff, a dacitic ash-flow tuff (Proffett and Dilles 2008). Previous work has dated the main units (i.e. trachytic to dacitic flows and domes) of FSV to approximately 166.4 – 166.6 Ma (Dilles and Wright 1988; Carter et al. 2022; Castellanos-Melendez et al. 2024).

3 Methods

3.1 Sampling

Samples were taken from multiple stratigraphic sections of FSV across the central to northern Buckskin Range. All major FSV subunits were sampled to create a comprehensive geochronological overview of pre-, syn- and post-mineralisation volcanic activity in Yerington.

3.2 Zircon Petrochronology: LA-ICP-MS and TIMS

Zircon grains were separated from rock samples from the base of the Fulstone Spring Volcanics at ETH Zürich using conventional heavy mineral separation methods. The grains were mounted on epoxy discs and cathodoluminescence (CL) images were obtained using a Deben Centaurus panchromatic cathodoluminescence detector coupled to a JEOL JSM-6390LA Scanning Electron Microscope (SEM). In-situ U-Pb dates and trace element data were obtained by LA-ICP-MS using an ASI RESOlution excimer ArF (193 nm) laser ablation system coupled to a Thermo Fisher Element XR sector field ICP-MS. Based on LA-ICP-MS results and CL imaging, 5 – 15 zircons per sample were selected for high-precision geochronology using chemical abrasion

isotope dilution thermal ionization mass spectrometry (CA-ID-TIMS) on a Thermo Triton Plus TIMS instrument at ETH Zürich following methods as described in Castellanos-Melendez et al. (2024). Eruption ages for the volcanics and emplacement ages of the porphyry dikes are estimated using a likelihood-based Bayesian eruption age estimation algorithm drawing on a synthetic zircon dataset based on the MELTS volcanic zircon distribution as a prior. (Keller et al. 2018; Keller 2018). All dates are reported with analytical uncertainties at the 95% confidence level.

4 Results and preliminary discussion

Preliminary data indicate two phases of volcanic activity in the geochronological record (see Fig. 2). The first comprises the two lowest lava units in FSV, (FSV1 Fig. 1). These units have been previously classified as FSV based on their lithological similarities to the main FSV units (Proffett and Dilles 2008), but zircon geochronology and alteration mineralogy place them as transitional between FSV and ALV. Bayesian eruption age modelling places the eruption of these units very close in time, at 167.83 ± 0.27 Ma and 167.70 ± 0.11 Ma, respectively. They are followed by an approx. 0.8 Myr hiatus, after which we see the beginning of the second eruptive phase, characterized by the near-continuous emplacement of the remaining FSV units.

The hiatus in volcanic activity corresponds to the emplacement interval of the mineralising porphyries (Fig. 2), between 167.2 and 166.7 Ma (Castellanos-Melendez et al. 2024) with some overlap between the end of porphyry dike emplacement and the beginning of the second eruptive phase. The oldest volcanic unit (166.92 ± 0.22 Ma) of the second phase overlaps in age with porphyry dike emplacement. It consists of a volumetrically minor trachytic lava which is more porphyritic than other FSV lava units. It has been suggested that this unit is a lava dome that may have been extruded from the late porphyry dikes (Proffett, pers. commun, 2006). Its' position in the geochronological record between the emplacement of FSV1 and FSV2 indicates that the hiatus is likely not attributable to erosion and is instead due to a cessation or reduction in major volcanic activity during this period.

All other overlying FSV units have estimated eruption ages of 166.6 – 165.9 Ma (Fig. 2). These units make up the bulk of the erupted magma volume in the FSV unit. Known volcanic activity in the Yerington magmatic system terminates with the emplacement of the Willow Springs Tuff (WST; Fig. 2), with an eruption age of 165.94 ± 0.37 Ma, approx. 0.5 Myr after the emplacement of the Luhr Hill granite and the termination of porphyry dike emplacement.

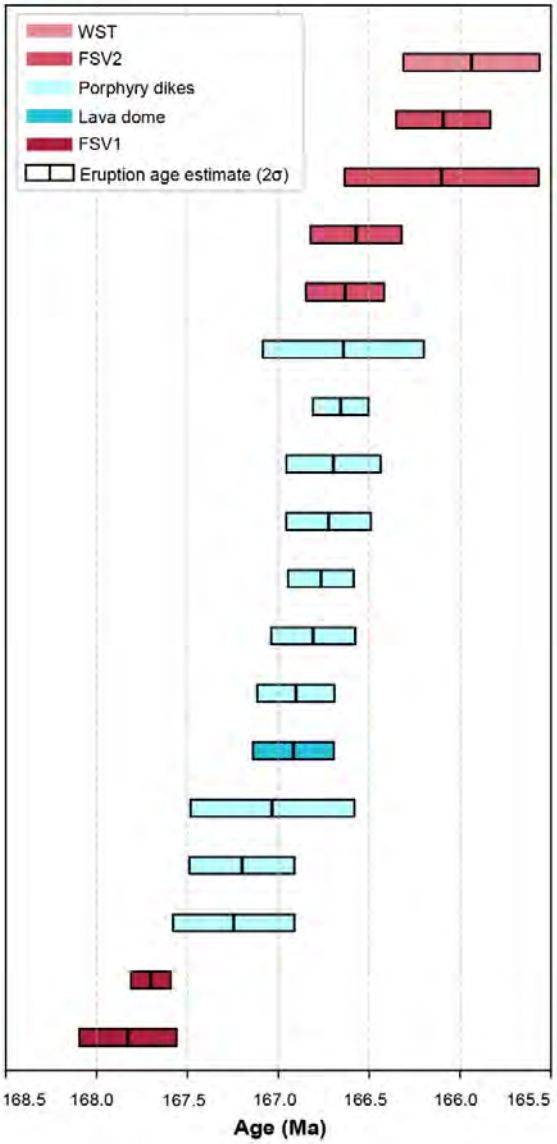


Figure 2. Ranked age plot showing Bayesian eruption/emplacement age estimates for the Fulstone Spring Volcanics and for mineralising porphyry dikes from the Yerington magmatic system. Porphyry dike data from Castellanos-Melendez et al. (2024). WST – Willow Springs Tuff. All ages reported with 95% uncertainty.

5 Conclusion

Our initial geochronological results allow improved assessment of the relative timing of volcanic activity and mineralising porphyry dike emplacement at the Yerington porphyry copper system. These results suggest that the Fulstone Spring Volcanics were emplaced in two pulses, separated by a hiatus of approx. 0.8 Myr, during which the mineralising dikes that formed the PCDs at Yerington were emplaced. These results align with previous research on the geochronology of PCD adjacent volcanism at Bajo de la Alumbrera, lending strength to the hypothesis that major volcanism and the emplacement of mineralising

porphyry dikes (and subsequent PCD formation) are incompatible processes.

Acknowledgements

The authors acknowledge the generous funding through the grant SNSF 200021_212892.

References

Buret Y, Wotzlaw J-F, Roozen S, et al (2017) Zircon petrochronological evidence for a plutonic-volcanic connection in porphyry copper deposits. Geology 45:623–626. https://doi.org/10.1130/G38994.1

Carter LC, Tapster SR, Williamson BJ, et al (2022) A rapid change in magma plumbing taps porphyry copper deposit-forming magmas. Sci Rep 12:17272. https://doi.org/10.1038/s41598-022-20158-y

Castellanos-Melendez MP, Dilles J, Guillong M, et al (2024) From birth to death: The role of upper-crustal thermal maturation and volcanism in porphyry ore formation revealed in the Yerington district. Earth Planet Sci Lett 647:119053. https://doi.org/10.1016/j.epsl.2024.119053

Chiaradia M, Caricchi L (2022) Supergiant porphyry copper deposits are failed large eruptions. Commun Earth Environ 3:1–9. https://doi.org/10.1038/s43247-022-00440-7

Dilles JH (1987) Petrology of the Yerington Batholith, Nevada: Evidence for evolution of porphyry copper ore fluids. Econ Geol 82:1750–1789. https://doi.org/10.2113/gsecongeo.82.7.1750

Dilles JH, Einaudi MT, Proffett JM, Barton MD (2000) Overview of the Yerington porphyry copper district: Magmatic to nonmagmatic sources of hydrothermal fluids: Their flow paths and alteration effects on rocks and Cu-Mo-Fe-Au ores. Soc Econ Geol Guideb Ser 32:55–66

Dilles JH, Wright JE (1988) The chronology of early Mesozoic arc magmatism in the Yerington district of western Nevada and its regional implications. GSA Bull 100:644–652. https://doi.org/10.1130/0016-7606(1988)100<0644:TCOEMA>2.3.CO;2

Keller CB (2018) Chron.jl: A Bayesian framework for integrated eruption age and age-depth modelling. https://doi.org/10.17605/OSF.IO/TQX3F

Keller CB, Schoene B, Samperton KM (2018) A stochastic sampling approach to zircon eruption age interpretation. Geochem Perspect Lett 31–35. https://doi.org/10.7185/geochemlet.1826

Pasteris JD (1996) Mount Pinatubo volcano and “negative” porphyry copper deposits. Geology 24:1075–1078. https://doi.org/10.1130/0091-7613(1996)024<1075:MPVANP>2.3.CO;2

Proffett JM (1977) Cenozoic geology of the Yerington district, Nevada, and implications for the nature and origin of Basin and Range faulting. GSA Bull 88:247–266. https://doi.org/10.1130/0016-7606(1977)88<247:CGOTYD>2.0.CO;2

Proffett JM, Dilles JH (1984) Geologic map of the Yerington district, Nevada

Proffett JM, Dilles JH (2008) Lower Mesozoic sedimentary and volcanic rocks of the Yerington region, Nevada, and their regional context. In: Wright JE, Shervais JW (eds) Ophiolites, Arcs, and Batholiths: A Tribute to Cliff Hopson. Geological Society of America, p 0

Richards JP (2018) A Shake-Up in the Porphyry World? Econ Geol 113:1225–1233. https://doi.org/10.5382/econgeo.2018.4589

Salas G (1971) Geology and exploration possibilities of the eastern Buckskin Range, Douglas County, Nevada. American Heritage Museum, Laramie, Wyoming

Schöpa A, Annen C, Dilles JH, et al (2017) Magma Emplacement Rates and Porphyry Copper Deposits: Thermal Modeling of the Yerington Batholith, Nevada. Econ Geol 112:1653–1672. https://doi.org/10.5382/econgeo.2017.4525

Sillitoe RH (2010) Porphyry Copper Systems. Econ Geol 105:3–41. https://doi.org/10.2113/gsecongeo.105.1.3

Tracing fluid evolution during batholith and deposit formation: In-situ and bulk rock Mo isotopes from the Questa porphyry Mo deposit, New Mexico, USA

Sean P. Gaynor[1], Nicolas D. Greber[2,3], Qasid Ahmad[3,4], Pia Künzi[3], Ingo Horn[5], Stefan Weyer[5]
[1]U.S. Geological Survey, Geology, Geophysics, and Geochemistry Science Center, Denver 80225, USA
[2]Muséum d'historie naturelle de Genève, Genève, Switzerland
[3]Insititut für Geologie, Universität Bern, Bern, Switzerland
[4]Centre de Recherches Pétrographiques et Géochimiques, Université de Lorraine - CNRS, Nancy, France
[5]Insititut für Mineralogie, Leibniz University Hannover, Hannover, Germany

Abstract. The Oligocene Questa porphyry Mo deposit, located in New Mexico, USA, is a well-characterized system that formed over 400 kyr, punctuating the 8 Myr formation of the Questa-Latir batholith. Detailed sampling of the intrusions and minerals associated with magmatic-hydrothermal mineralization, as well as bookending barren intrusions, allows for examination of the Mo isotope record of the deposit and its host batholith. Through this established chronologic framework, such data can yield insights into the metallogenesis of deposit formation and long-term magma genesis evolution for upper crustal magmatism. The Mo isotopic compositions of barren intrusions yield a younging trend towards lighter δ^{98}Mo. However, intrusions associated with Mo deposit formation yield heavier δ^{98}Mo relative to barren magmatism, by up to 2.0‰. This indicates that they were affected by an isotopically heavy and Mo-rich fluid. The in-situ data from molybdenite covers the range observed in mineralized bulk rocks. However, individual samples consistently yield Mo isotopic variations of 0.4‰ to 0.5‰. The consistency of the δ^{98}Mo variation in in-situ analyses of molybdenite within hand samples and individual mineral grains is likely the result of MoS_2 crystallization in a closed system and reflects an almost complete precipitation of Mo.

1 Introduction

Molybdenum (Mo) behaves extremely incompatibly in silicate environments and is only present in trace concentrations in the upper crust. As a result, the formation of porphyry Mo deposits represent extreme evolutionary events in crustal geochemistry, and therefore likely represent the coincidence of rare periods of evolution from magmas that are potentially derived from uncommon magma reservoirs. Variations in molybdenum isotopes in magmatic (±hydrothermal) environments can be due to changes in magma sources (i.e., open-system behavior) or evolutionary processes of the system (i.e., closed-system). Deciphering between these variations could be beneficial, because Mo fractionates towards increasingly heavier compositions through progressive magmatic and hydrothermal processes. Therefore, the composition of molybdenite crystals may telescope away from parental magmas and could be serve as a vectoring tool during mineral exploration. However, this type of campaign-style measurements is currently stymied by the constraints of digestive chemistry; novel analytical approaches are needed for this style of work. Furthermore, identification of closed-system Mo fractionation requires a parallel assessment of potential influences from open system behavior. For example, analyzing barren intrusions unaffected by hydrothermal processes may reveal shifts in magma genesis and inform how long-term batholith formation effects crustal differentiation.

The Oligocene Questa porphyry Mo deposit, located in northern New Mexico, USA, is an excellent location to further assess the temporal and spatial distribution of Mo isotope compositions, and evaluate the potential of using these compositions as a tool to either determine the location of unexplored ore deposits or understand how shifting magma genesis parallels potential shifts in metallogenesis. Due to exploratory drilling, access to underground workings and exposures of bookending non-mineralizing magmatism, it is possible to analyze the Mo isotope composition of both rocks and minerals associated with mineralization, as well as barren intrusive rocks temporally associated the deposit formation. Due to extensive recent study of these rocks, there is a published high-precision geochronological framework for these rocks, complete model for deposit formation and published radiogenic isotope geochemical compositions, allowing for a detailed evaluation of the significance and utility of Mo isotopes in batholith and deposit formation.

2 Geological Setting

The Latir magmatic center, which hosts the Questa porphyry Mo deposit, had a prolonged history of magmatism (>10 Myr) and was punctuated by periods of magmatic-hydrothermal mineralization (Figs. 1; Lipman and Reed, 1989; Gaynor et al. 2019a; Gaynor et al., 2019b; Gaynor et al., 2023). The volcanic-plutonic complex is exposed over approximately 1,200 km^2, and the regional sedimentary record suggests a substantial volume of volcanic rocks has been removed by erosion (Lipman et al., 1986). The first igneous rocks preserved within the Latir magmatic center are 28.5 Ma andesites and the oldest exposed intrusive rocks were emplaced at approximately 27.0 Ma (e.g., Lipman et al., 1986). Volcanism culminated with the eruption of the ~500 km^3 peralkaline Amalia Tuff at 25.52 Ma and subsequent collapse of the Questa caldera.

Following the eruption of the Amalia Tuff, the majority of exposed plutonic rocks at Questa intruded over a period of at least 6.2 Myr (25.29 – 19.88 Ma; Gaynor et al., 2019b). Exposed plutonic rocks become younger and structurally deeper towards the south and are broadly grouped into three categories: resurgent plutons, caldera rim plutons, and southern plutons (Lipman et al., 1986). The first phase of intrusions is preserved as granitic resurgent plutons are the northernmost intrusions, and closest in age to the 25.52 Ma Amalia Tuff, and followed by the caldera rim plutons, exposed south of the resurgent plutons (Rosera et al., 2013; Gaynor et al., 2019a; Gaynor et al., 2019b). Caldera rim plutons are also spatially and genetically associated with varying degrees of hydrothermal alteration and mineralization, including fracture- and vein-hosted Cu-Au-Ag±Mo mineralization and the Questa porphyry Mo deposit. The final period of plutonic assembly within the Questa batholith was the southern plutons, which are not related with mineralization (Gaynor et al., 2019b; Gaynor et al., 2023).

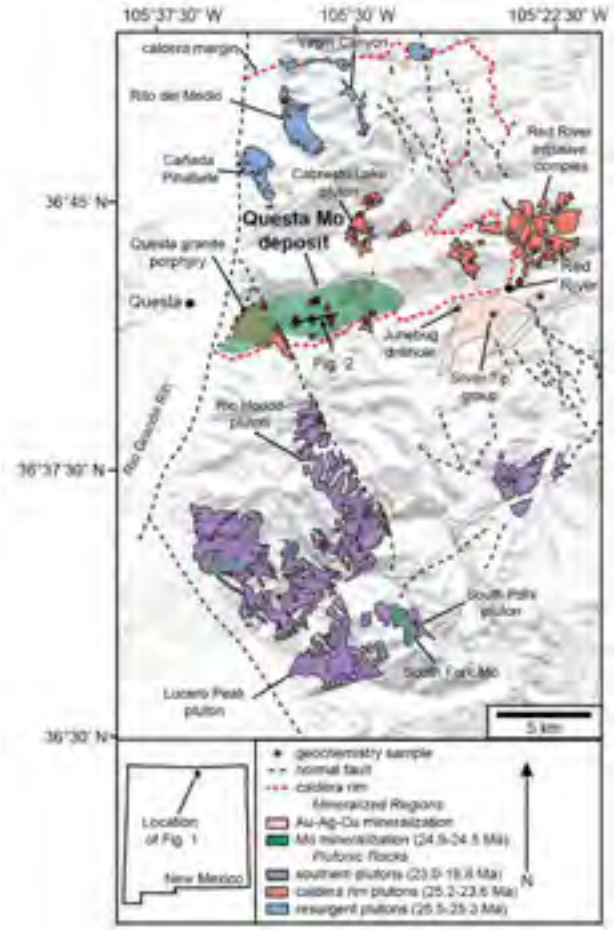


Figure 1. Simplified geologic map of the Latir magmatic center, showing the sample locations for this study (modified from Gaynor et al., 2023).

The Questa porphyry Mo deposit is the largest ore deposit within the Questa batholith, and formed from episodic, F-rich porphyritic intrusions and their magmatic-hydrothermal mineralizing fluids (e.g., Rosera et al., 2013; Gaynor et al., 2019a). Detailed U-Pb zircon geochronology of intrusive rocks, Re-Os molybdenite geochronology from throughout the deposit, and 3-dimensional structural study of the magmatic-hydrothermal complex demonstrate that the Questa Mo deposit was assembled incrementally by at least five cross-cutting, discrete intrusive units between approximately 25.0 and 24.5 Ma and combine to a total volume of approximately 0.62 km^3 (Fig. 2; Gaynor et al., 2019a). These intrusions are spatially, temporally and genetically linked to high-grade zones of Mo mineralization (MoS_2 > 0.2 wt.%). Their genetic relationship to Mo mineralization is based on cross-cutting relationships, the orientation of mineralized veins emanating from intrusive roof contacts, unidirectional solidification textures underlying high-grade zones of Mo mineralization, widespread aplitic textures, zonation of hydrothermal alteration away from intrusive contacts, the presence of narrow auto-brecciated bands along intrusive contacts, spatial proximity to mineralization and potassic alteration, and coeval high-precision U-Pb zircon and Re-Os molybdenite geochronology.

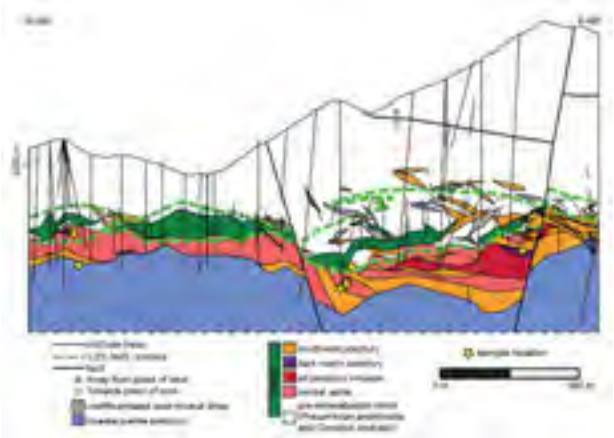


Figure 2. Simplified geologic cross section from the Questa porphyry Mo deposit, highlighting the subeconomic Questa granite porphyry intrusion underlying a series of small-volume Mo-mineralizing intrusions. All subsurface sample locations shown on this figure are projected into section. Major faults are shown as the bold, black lines. Drill core traces are only shown within a 60-m window of this section. No vertical exaggeration. Modified from Gaynor et al. (2019a).

3 Methods

To assess the temporal evolution of the Latir magmatic center, geologic units were organized by relative and absolute ages, and published relationships between intrusions and mineralization. Samples from the Latir magmatic center were collected from surface outcrops, underground exposures and drill core from the Questa mine and surrounding region, including samples characterized by previous studies (e.g., Gaynor et al., 2023). Whole rock samples were analyzed for Mo isotope compositions at the University of Bern using double spike and chromatographic separation. Purified samples were measured on a Neptune Plus MC-ICP-MS and standardized relative to the δ^{98}Mo composition of NIST SRM

3134. Detailed methods are presented in Ahmad et al. (2021).

In-situ measurements of Mo isotopes were made of molybdenite crystals from drill core at Leibniz University using a Neptune Plus MC-ICP-MS coupled to a femtosecond laser ablation system. Instrumentation mass bias was calculated and corrected by simultaneously measuring a Zr solution and measurement of unknowns was bracketed by measurements of a molybdenite crystal with a known isotopic composition and recalculated to NIST SRM 3134.

4 Results

In-situ measurements of molybdenite from the Questa porphyry Mo deposit range from -0.4‰ to 1.1‰, with compositional variations within individual samples between 0.4‰ to 0.5‰ (Fig. 3). Whole rock δ^{98}Mo compositions from the Latir magmatic center range from -0.6‰ to 2.1‰, with the compositions of intrusions not associated with the Questa porphyry Mo deposit span a smaller range, from -0.5‰ to 0.3‰.

5 Discussion

5.1 Efficacy of In-Situ Molybdenite Mo Isotope Measurements

In-situ Mo isotope geochemistry allows for greater spatial resolution of compositional variations and the ability to assess in the context of sample petrography; however, it is necessary to evaluate if the technique is precise and accurate. The precision of in-situ δ^{98}Mo data is approximately ±0.1‰ (2SD), which allows for resolving previously published compositional variations found in molybdenite (e.g., Greber et al., 2014). New in-situ data from molybdenite associated with the Questa deposit have compositional variations similar to the those previously found both in molybdenite samples from the Questa deposit (Fig 3; Greber et al., 2014), as well as those observed in molybdenite samples from other localities (e.g., Greber et al., 2011). Furthermore, molybdenite sample material first characterized for Mo isotopes using LA-ICPMS was subsequently removed from the sample mounts and analyzed again using traditional solution measurement techniques, yielding overlapping compositions, confirming the accuracy of this technique. As a result, in-situ measurements of molybdenite for Mo isotope compositions represents a far simplified workflow relative to traditional solution measurements and allow for isotopic information from samples with petrographic context, and is a crucial way to test if open-system or closed system processes dominant during mineral precipitation.

5.2 Potential of Molybdenum Isotopes as a Vectoring Tool

Molybdenum isotopes have been interpreted to fractionate by both magmatic evolution and hydrothermal processes, both causing Mo to shift towards heavier compositions. During hydrothermal processes, fractionation occurs due to Rayleigh distillation, where light isotopes are progressively incorporated into molybdenite, leaving the remaining fluid isotopically heavier (e.g., Hannah et al., 2007; Greber et al., 2014). Therefore, molybdenite that crystallized distal from its parental magma should be isotopically heavier than that which precipitated in an earlier, more proximal setting. Based on this behavior, the composition of molybdenite has potential as a vectoring tool, with heavier compositions indicative of distance to source intrusions and higher-grade mineralization. Furthermore, this relationship should also cause a negative correlation between δ^{98}Mo composition and the concentration of Mo in rocks associated with porphyry Mo deposits, as majority of molybdenite is deposited proximal to parental magmas in Climax-type deposits (e.g., Carten et al. 1988).

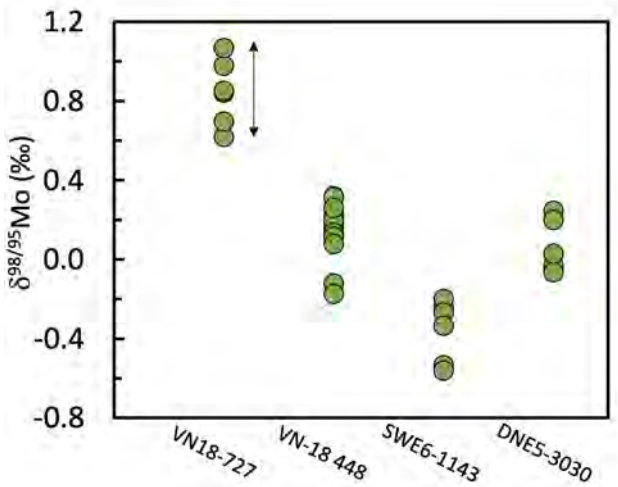


Figure 3. Molybdenite in-situ LA-ICPMS Mo isotope geochemical data from four samples from the Questa porphyry Mo deposit, highlighting the isotope heterogeneities found within samples, and compositional variations across the deposit.

However, there is not a correlation between distance of mineralized materials relative to causative intrusions δ^{98}Mo compositions at Questa, nor is there a correlation between δ^{98}Mo compositions and [Mo] for mineralized intrusions. Further, there is considerable isotope composition heterogeneities within individual molybdenite veins. These relationships indicate that δ^{98}Mo compositions for the Questa porphyry Mo deposit are likely the result of both isotope fractionation within individual pulses of mineralization and the aggregate result of multiple pulses of mineralization, causing mixing of compositions during progressive Mo enrichment to ore grades. This interpretation matches previous observations ore zones within Climax-type porphyry Mo deposits, with cyclical, episodic magmatic-hydrothermal processes responsible for mineralization (e.g., Carten et al. 1988; Rosera et al. 2013; Gaynor et al. 2019a). In

this model, the composition of whole rock samples associated with the ore deposit are a function of volumetric mixing of molybdenite that precipitated from compositionally variable pulses, which is further confirmed as the composition of molybdenite analyzed here and in Greber et al. (2014) share a similar distribution of compositions as the whole rock data from this work.

5.3 Myr-Scale Evolution of Crustal Reservoirs Recorded in Incremental Batholith Growth

Mantle sources are interpreted to have values of ~-0.2‰ δ^{98}Mo, with variations in that composition requiring subduction modification or hydrothermal alteration (e.g., Willbold and Elliott, 2023). The mean composition of molybdenite and whole rock data from the Questa deposit is approximately -0.2 ‰ δ^{98}Mo. Given that fluid exsolution fractionates δ^{98}Mo >1‰ between fluid and minerals (e.g., Kaufmann et al. 2021), the recorded compositions indicate that deposit was formed from an initial composition heavier than the mantle (Fig. 4). We interpret this reflects genesis for this deposit was from hydrothermally altered lower crust or subcontinental lithospheric mantle, likely by tectonic events in the 1 Gyr preceding deposit, which may have also enriched magma sources in Mo. This aligns with radiogenic isotope geochemistry for porphyry Mo-type systems, which indicate ancient lower crust contributed to its magma genesis (Gaynor et al. 2023; Rosera et al. 2023).

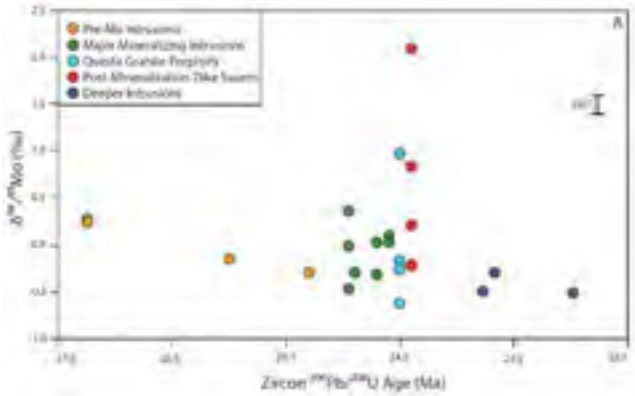


Figure 4. Temporal progression of δ^{98}Mo compositions within the Questa-Latir magmatic center, highlighting the long-term trend to lighter compositions in the barren rocks. Geochronology from Gaynor et al. (2019b).

Intrusions from barren intrusions bookending deposit formation are unlikely to be as modified by heavy isotope contributions from fluid fractionation and mineralization, and instead represent a secular record through batholith formation. Within these samples, there is a younging trend to lighter isotope compositions. This long wavelength shift in Mo isotope composition parallels similar changes in radiogenic isotopes for the same whole rock samples (Gaynor et al., 2023), indicating that this change in Mo isotope compositions is a function of changes in magma genesis, rather than a decrease in magma evolution associated with isotope fractionation. This indicates that deposit formation within magmatic centers with lifespans over millions of years is likely the result of the alignment of multiple factors within a discrete period of time, including a period of unique source(s) for magma genesis.

Acknowledgements

This project would not have been possible without the cooperation from Chevron Mining Inc., who provided access to mine property and drill core. Any use of trade, firm, or product names is for descriptive purposes only and does not imply endorsement by the U.S. Government.

References

Ahmad Q, Wille M, König S, Rosca C, Hensel A, Pettke T, Hermann J (2021) The molybdenum isotope subduction recycling conundrum: A case study from the Tongan subduction zone, Western Alps and Alpine Corsica. Chem Geo 576:120231. Doi:10.1016/j.chemgeo.2021.120231.

Carten RB, Geraghty EP, Walker BM, Shannon JR (1988) Cyclic development of igneous features and their relationship to high-temperature hydrothermal features in the Henderson porphyry molybdenum deposit, Colorado. Econ Geol 83:266-296. doi:10.2113/gsecongeo.83.2.266.

Gaynor SP, Rosera JM, Coleman DS (2019a) Intrusive history of the Oligocene Questa porphyry molybdenum deposit, New Mexico. Geosphere 15:548-575. doi:10.1130/GES01675.1.

Gaynor SP, Coleman DS, Rosera JM, Tappa MJ (2019b) Geochronology of a Bouguer gravity low. JGR SE 124:2457-2468. Doi:10.1029/2018JB015923.

Gaynor SP, Rosera JM, Coleman DS (2023) Genesis of the Questa Mo porphyry deposit and nearby mineralization, New Mexico, USA. Econ Geol 118. 1319-1339. doi:10.5382/econgeo.5011.

Greber ND, Hofmann BA, Voegelin AR, Villa IM, Nägler TF (2011) Mo isotope composition in Mo-rich high- and low-T hydrothermal systems from the Swiss Alps. GCA 75:6600-6609. Doi:10.1016/j.gca.2011.08.034.

Greber ND, Pettke T, Nagler TF (2014) Magmatic-hydrothermal molybdenum isotope fractionation and its relevance to the igneous crustal signature. Lithos 190-191:104-110. doi:10.1016/j.lithos.2013.11.006.

Kaufmann AKC, Pettke T, Wille M (2021) Molybdenum isotope fractionation at upper-crustal magmatic-hydrothermal conditions. Chem Geo 578:120319. doi:10.1016/j.chegeo.2021.120319.

Lipman PW, Mehnert HH, Naeser C (1986) Evolution of the Latir volcanic field, northern New Mexico, and its relation to the Rio Grande rift, as indicated by potassium-argon and fission track dating. JGR 91:6329-6345. doi:10.1029/JB091iB06p06329.

Rosera JM, Coleman DS, Stein, HJ (2013) Re-evaluating genetic models for porphyry Mo mineralization at Questa New Mexico: Implications for ore deposition following silicic ignimbrite eruption. G-cubed 14:787-805. doi:10.1002/ggge.20048.

Rosera JM, Frazer RE, Mills RD, Jacob K, Gaynor SP, Coleman DS, Farmer, GL (2023) Fluorine-rich mafic lower crust in the southern Rocky Mountains: The role of pre-enrichment in generating fluorine-rich silicic magmas and porphyry Mo deposits. Am Min 108:1573-1596. doi:10.2138/am-2022-8503.

Willbold M, Elliott T (2023) Molybdenum isotope evidence for subduction-modified, recycled mafic oceanic crust in the mantle sources of ocean island basalts from La Palma and Hawaii. EPSL 621:118399. doi:10.1016/j.epsl.2023.118399.

Te and Au mobility at the porphyry-epithermal transition: Insights from experiments and numerical simulations

Nicole C. Hurtig[1], Jonathan R. Adams[1], Louvel Marion[2], Aneta Slodczyk[2], Alexander P. Gysi[1,3], Artas A. Migdisov[4]
[1] Dept. of Earth and Environmental Science, New Mexico Tech, Socorro, NM, 87801, USA
[2] Institut des Sciences de la Terre d'Orléans, CNRS/BRGM/UnivOrleans, Orléans, F-450171, France
[3] New Mexico Bureau of Mineral Resources, New Mexico Tech, Socorro, NM, 87801, USA
[4]Earth and Environmental Division, Los Alamos National Laboratory, Los Alamos, NM 87545, USA

Abstract. Tellurium is an important critical element used in thin-film solar cells and is mined from Cu porphyry and Au-Ag epithermal deposits. Ore forming fluids commonly transition from intermediate-density fluids exsolving from the melt at high temperature and pressure into the 2-phase region with co-existing brine and vapor in the porphyry environment. As a result of cooling and decompression fluids evolve along a vapor-dominated path to form high-sulfidation or along a liquid-dominated paths to form intermediate-sulfidation deposits at the surface. Here, we investigate the mobility of Te and Au in aqueous fluids with different phase states, e.g. vapor, brine, liquid and supercritical fluids. In the porphyry environment, Te shows greater mobility compared to Au at high temperature. Redox plays an important role in controlling Au-Te ratios. Modeling predictions indicate that hydrated Te species dominate at high logf_{O2}, whereas experimental results indicate that hydrated Te species are more soluble than hydrated Au species across all redox conditions. In liquid hydrothermal fluids, Au is ~6 orders of magnitude more soluble than Te in fluids equilibrated with sulfides and phonolite.

1 Introduction

In natural systems, Te is enriched in magmatic-hydrothermal systems where hydrothermal fluids generally play a crucial role in ore forming processes (Williams-Jones and Heinrich, 2005; Hurtig and Williams-Jones, 2015). Tellurium often occurs as a trace element in Cu-Fe sulfides and sulfosalts or as a minor phase e.g. tellurides, which makes it challenging to understand its distribution and enrichment mechanisms. Our capability to predict the mobility of Te in hydrothermal fluids is limited by the availability of thermodynamic data for individual aqueous and/or gaseous species, in particular, at elevated temperature and pressure relevant to ore genesis.

The role of water as a solvent is key to understanding metal transport in aqueous fluids, which can be decompressed from a liquid-like to a vapor-like fluid density above the critical point of water without crossing phase boundaries (Hurtig et al., 2021). The region of supercritical fluids further elevates current challenges in predicting and understanding metal transport in magmatic-hydrothermal systems, highlighting the need for new equations of state and thermodynamic models.

Here, we present new experimental data from solubility and spectroscopic Raman studies of Te in vapor, brine and supercritical fluid. Thermodynamic data are derived from experiments and implemented into the GEM-Selektor code package (https://gems.web.psi.ch/) to simulate Te and Au mobility in porphyry and epithermal fluids.

2 Methods

2.1 Solubility Experiments

Batch-type experiments were conducted using Ti autoclaves from Parr Instruments following a similar method to previous studies (Hurtig and Williams-Jones, 2014; Migdisov et al., 2014). Solid TeO_2 was interacted with water vapor at 250, 300 and 320 °C and water vapor pressures of 10 bar to saturation pressure, P_{sat} (Adams, 2023). The oxygen fugacity was buffered by MoO_2-MoO_3, WO_2-WO_3 and Ni-NiO. After quenching, the experimental solutions were analysed using ICP-MS to determine the Te content and solids were analysed using XRD and Raman spectroscopy. Logarithmic fugacity of water is fitted to logf_{Te} using a power function, which is integrated at integer numbers to extra logarithmic equilibrium constants (logK_y) for $TeO_2(H_2O)_y$ species with y = 1-5. The logK_y were fitted to temperature (K) using a polynomial function (Fig. 1a) and implemented into the GEM-Selektor code package. Predicted logf_{Te} values are shown in Figure 1b and compared to experimental data from Glemser et al. (1965) at 418 °C.

2.2 Raman Spectroscopy

Raman spectroscopy was conducted at ISTO-CNRS in Orléans, France using a Planex IHPV reactor equipped with sapphire cells (Louvel et al., 2015). Solutions are prepared by dissolving a known amount of $TeCl_4$ solid into solutions with pH 1 and 10; the pH is adjusted by adding NaOH or HCl. LiCl was added to increase the salinity to very high concentrations for stabilization of Te chloride complexes and Na_2SO_4 was used to spike solutions with SO_4^{2-} for internal calibration. Solutions were loaded into a sapphire cell, which was then placed into the IHPV reactor, where it was pressurized to experimental pressures (500 and 700 bar) at room temperature and then heated up to 600 °C. Highly saline fluids undergo phase separation above 450 °C, whereas moderately saline fluids remain in a single-phase with an intermediate density at supercritical conditions (Fig. 2).

A 355 nm UV laser was used at 90 mW power, a grating of 2400 grooves/mm and spectra were collected for 1-60 s with 2-3 acquisitions depending

on the signal intensity. Spectra shown in Figure 2 were normalized to total intensity for the interval 240-1600 cm^{-1} and the background was subtracted using the Fityk software package.

2.3 Numerical Simulations

Geochemical simulations were carried out using the GEM-Selektor code package (Kulik et al., 2013) and the MINES thermodynamic database (Gysi et al., 2023) for minerals, aqueous species and gases. Thermodynamic properties for aqueous Te species were updated in Hurtig et al. (2023) and gaseous Te species were taken from Adams (2023).

We carried out simulations of Au and Te mobility in vapor-like and intermediate density fluids which include the following models: 1) cooling and decompression models at a fluid density of 100 and 300 kg/m^3; 2) redox titration model at 250 °C investigating Te and Au speciation and mineral buffering. The mobility of Te, Au, Ag and base metals (Cu, Zn, Pb) in aqueous liquid-like fluids was simulated during equilibration of a 5 wt% NaCl fluid with a typical phonolite rock from the Cripple Creek Au-Te deposit in CO. Simulation of fluid-rock interaction was conducted using a rock titration model, where 0.01 to 800 g of phonolite is added to 1000 g of solution. In addition to phonolite this fluid was equilibrated with calaverite, hessite, chalcopyrite, sphalerite, galena, pyrite, fluorite and calcite to ensure saturation with respect to ore forming minerals.

3 Results and Discussion

3.1 Solubility experiments: Te transport in vapor-like fluids

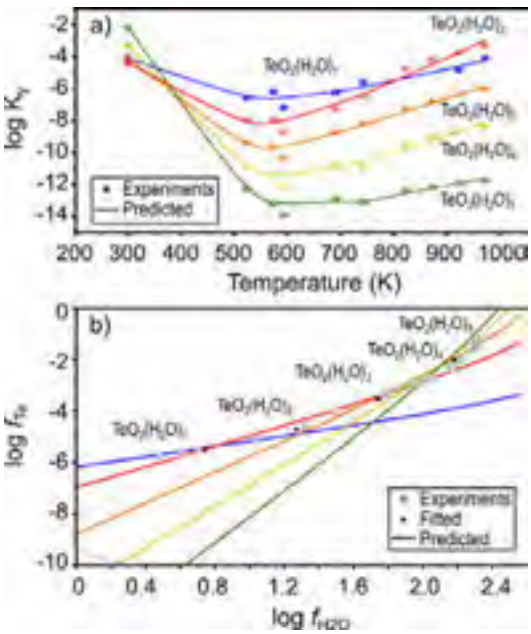


Figure 1. a) Logarithmic equilibrium constants logK_y for hydration step 1-5 for gaseous TeO_2. b) Comparison of predicted Te fugacity using experimentally derived logK_y and experimental data from Glemser et al. (1965) at 418 °C (black squares) and the fitted power function used for extracting integer hydration steps (red circles).

Experiments conducted at low water vapor pressure <1 bar (Glemser and Haeseler, 1960) show a linear relationship between logf_{Te} and logf_{H2O} with a slope of 1 or 2. This relationship indicates the stability of $TeO_2(H_2O)_1$ and $TeO_2(H_2O)_2$. At higher water vapor fugacity (logf_{H2O}), Te fugacity increases exponentially with increasing f_{H2O} (Glemser et al., 1965; Adams, 2023). This increase of logf_{Te} with increasing logf_{H2O} can be fitted using a power function and indicates the presence of higher hydration numbers similar to $AuCl(H_2O)_y$ (Hurtig and Williams-Jones, 2014).The enthalpy of hydration after hydration step ~2 becomes similar to that of adding water molecules to water clusters (Velizhanin et al., 2020; Hurtig et al., 2021). The logK_y of $TeO_2(H_2O)_{1\text{-}5}$ were extracted from experiments at 250-320 °C (Adams, 2023) and 400-700 °C (Glemser and Haeseler, 1960; Glemser et al., 1965) and fitted to $\log K_y = a_0 + a_1T + a_2T^{-1} + a_3\ln T$ (Fig. 1a). Uncertainty is generally better than 0.2 log units and predicted Te fugacity using experimentally derived thermodynamic properties for hydrated tellurate species fits well with experimental data (Fig. 1b).

3.2 Raman Spectroscopy: Te speciation in vapor, brine and supercritical fluids

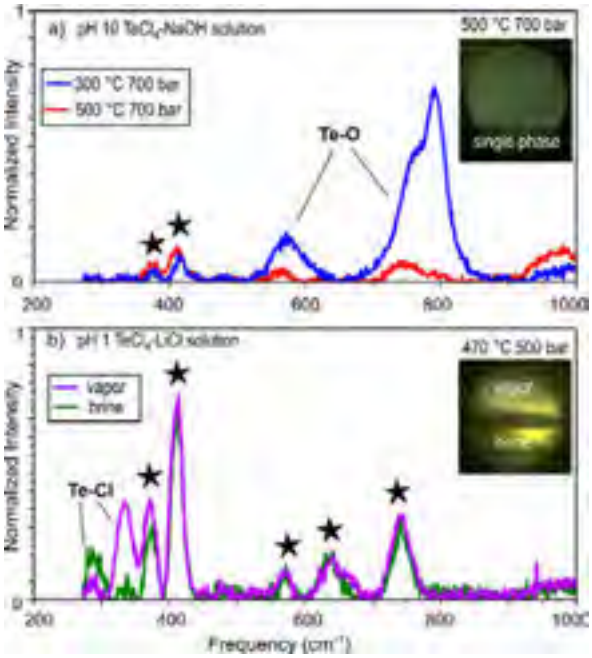


Figure 2. Raman spectra of $TeCl_4$-bearing solutions at high temperature and pressure showing a) Te-O bands at pH 10 and b) Te-Cl bands at pH 1. The black stars indicate spectra of the sapphire cell.

Raman spectroscopy of $TeCl_4$-bearing solutions between 25-600 °C reveals a peak at ~618 cm^{-1} and a peak group at 690-795 cm^{-1} in alkaline (pH 10) solutions with ~0.2 mol/kg dissolved $TeCl_4$ (Fig. 2a). These peaks overlap with Te-O vibrational bands of TeO_2 solid at 646 cm^{-1} indicating that they represent tellurate species (e.g., $H_2TeO_3^0$, $HTeO_3^-$, TeO_3^{2-}). Scattering intensity drastically decreases at supercritical conditions as is shown by normalized

intensity spectra collected at 300 and 500 °C and 700 bar (Fig. 2a).

In highly saline acidic fluids (pH 1), a peak at ~287 and at 335 cm^{-1} occur, which are interpreted to represent $TeCl_4^0$ and other Te chloride species. There is a switch over in peak intensity between 287 cm^{-1}, which is higher in the brine and 335 cm^{-1}, which is higher in the vapor indicating a possible change in speciation between brines and vapors (Fig. 2b).

3.3 Applications to porphyry systems: Te and Au in intermediate- and low-density fluids

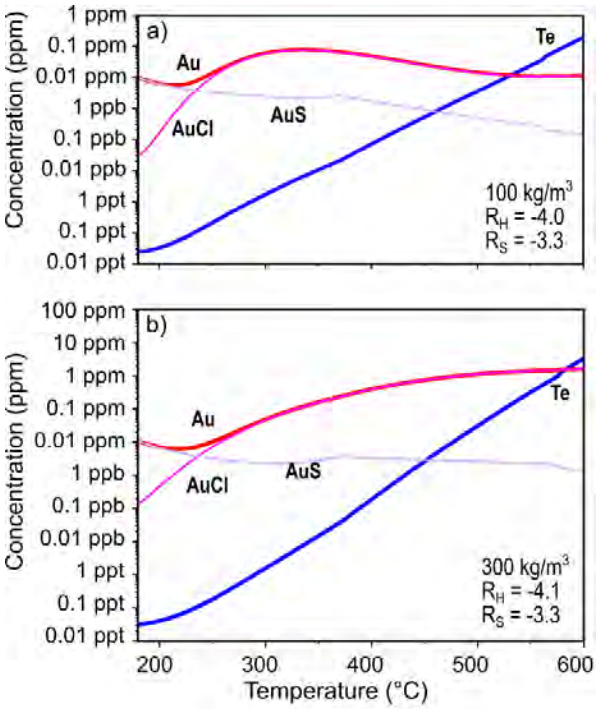


Figure 3. Gold and Te concentrations in a) vapor-like fluids with density of 100 kg/m^3 and b) and intermediate-density fluids a density of 300 kg/m^3 during isochoric cooling from 600 to 180 °C.

Magmatic-hydrothermal fluids responsible for metal transport in porphyry systems are supercritical, moderately saline (2-8 wt% NaCl eq.) and exsolve at high temperatures 600-800 ºC from a silicate melt (Williams-Jones and Heinrich, 2005). As a result of cooling and decompression, fluids undergo phase separation forming a low-density vapor and a hypersaline brine (30-60 wt.% NaCl eq.). Isochoric cooling models with a starting density of 100 and 300 kg/m^3 at 600 °C follow the water vapor saturation pressure below the critical point of water. The redox potential R_H, log(f_{H2}/f_{H2O}), is 4.0-4.1 which is typical for porphyry systems and corresponds to a buffering mineral assemblage of magnetite, anhydrite, rutile and silicate minerals (quartz, biotite, K-feldspar) at high temperature (Hurtig et al., 2021).

At high temperature and low density, Te fugacity is ~1 order of magnitude higher compared to Au fugacity. However, Te fugacity decreases with decreasing temperature whereas Au shows a solubility maximum at ~320 °C at 100 kg/m^3 and at ~510 °C at 300 kg/m^3. These simulations suggest that Au is more readily mobilized out of the porphyry environment and Te shows a similar behavior to other redox sensitive elements such as Mo and would more likely be retained at depth unless a highly oxidizing fluid remobilizes Te.

3.4 Applications to epithermal systems: Te and Au mobility as a function of redox and fluid rock reaction

The control of redox is evaluated using a redox titration model where water vapor is equilibrated with a mineral assemblage of tellurite, hematite and gold and $H_{2(g)}$ is added until the mineral assemblage changes to calaverite, pyrrhotite and gold (Fig. 4). On the right side of the diagram, logf_{O2} is highly oxidizing and equivalent of a vapor with atmospheric oxygen contents, whereas on the left side of the diagram, logf_{O2} is highly reducing and equivalent to Ni-NiO buffered conditions.

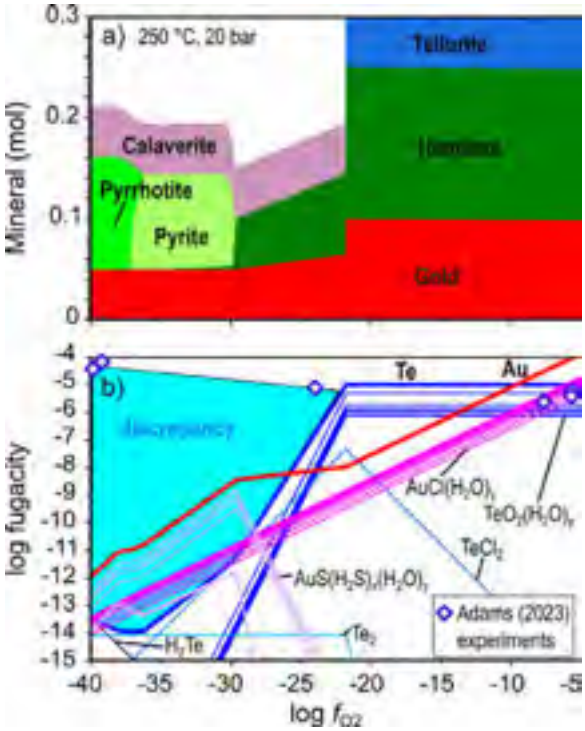


Figure 4. Redox titration model showing a) mineralogy equilibrated with the vapor and b) logarithmic fugacity of total Au (bold red) and Te (bold blue) and hydrated AuCl (magenta), AuS (pink), TeO_2 (blue) and other Te species (light blue, black). The blue shaded area shows the discrepancy between predicted Te speciation and experimentally observed total Te fugacity from Adams (2023).

Gold fugacity decreases with decreasing logf_{O2}, whereas Te fugacity is constant at oxidizing conditions, and decreases ~10 orders of magnitude between logf_{O2} -25 to -35. Finally, Te fugacity increases again slightly due to the presence of reduced Te species such as $H_2Te_{(g)}$ and $Te_{2(g)}$. Importantly, there is a discrepancy of ~10 orders of magnitude between predicted and experimentally measured Te fugacity indicating the presence of hydrated reduced Te species. Additional

experiments are needed to derive thermodynamic properties for the reducing hydrated Te species.

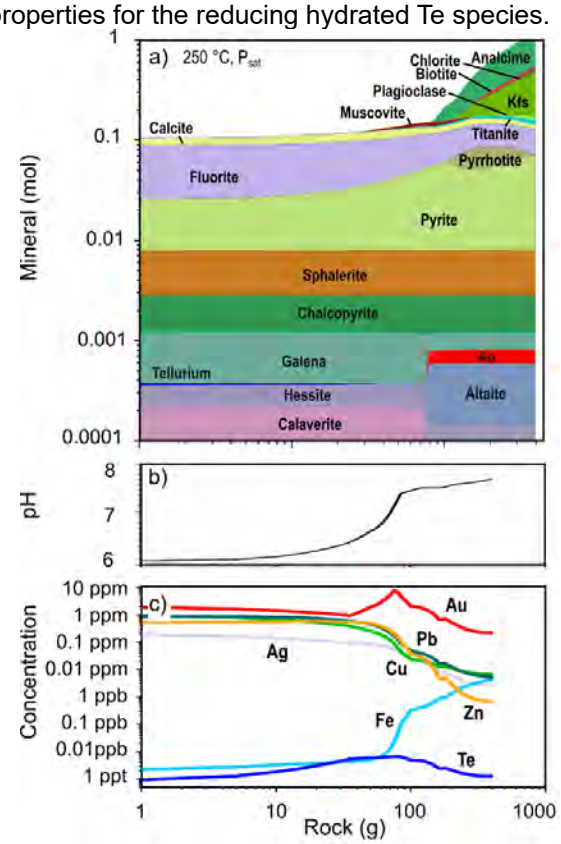


Figure 5. Phonolite titration model showing a) mineralogy, b) pH and c) fluid composition as a function of rock added to 1 kg of 5 wt% NaCl fluid equilibrated with sulfides and tellurides at 250 °C and P_{sat}.

In liquid-like fluids equilibrated with typical Cripple Creek phonolite, Te mobility is very low (Fig. 5) and Au concentrations are ~6 orders of magnitude higher compared to Te. Similar to the vapor models, thermodynamic properties of reduced aqueous Te species are unknown at hydrothermal conditions therefore leaving open questions with regard to the true mobility of Te in hydrothermal fluids. Importantly, Au and Te mobility increase ~1 order of magnitude at a fluid to rock ratio of 10 and a pH of ~7. In Au-Te window, the concentrations of Ag, Cu, Pb and Zn decrease drastically promoting Te and Au mobility and suppressing the mobility of base metals and Ag.

4 Conclusions

Simulations using the hydration model indicate that metal mobility in vapor-like and intermediate-density fluids strongly depends on pressure and temperature. As a result, these fluids can deposit large amounts of metals without undergoing phase separation upon decompression. The efficiency of mineral precipitation from low and intermediate-density fluids therefore diverges from that of liquid-like fluids, for which cooling and/or fluid-rock reaction (pH) is driving mechanism for mineral precipitation.

Acknowledgements

Funding support for this study was provided by New Mexico Tech through startup funding to NH and travel stipend through the university of Orléans for a research stay at ISTO in 2023. JA also received support through the Yardley fellowship at NMT and the McKinstry Grant through SEG. We thank B. Frey and D. Baca for support with ICP-MS analyses at the New Mexico Bureau of Geology.

References

Adams JR (2023) The solubility of TeO_2 and tellurium gas speciation in water vapor at 250-320°C, MSc thesis: New Mexico Institute of Mining and Technology: 1–60 p.

Glemser O and Haeseler R (1960) Über gasförmiges $TeO(OH)_2$-Gasförmige Hydroxyde III: Die Naturwissenschaften, v. 47, no. 20, p. 467–468.

Glemser O, Müller A, and Schwarzkopf H (1965) Über die Reaktion von TeO_2 mit Wasserdampf bei höheren Drucken und Temperaturen: Die Naturwissenschaften, v. 52, no. 6, p. 129–130.

Gysi AP, Hurtig NC, Ruiguang P, Miron GD, and Kulik DA (2023) MINES thermodynamic database:

Hurtig NC & Williams-Jones AE (2014) An experimental study of the transport of gold through hydration of AuCl in aqueous vapour and vapour-like fluids: Geochimica et Cosmochimica Acta, v. 127, p. 305–325.

Hurtig NC & Williams-Jones AE (2015) Porphyry-epithermal Au-Ag-Mo ore formation by vapor-like fluids: New insights from geochemical modeling: Geology, v. 43, no. 7, p. 587–590.

Hurtig NC, Migdisov AA and Williams-Jones AE (2021) Are vapor-like fluids viable ore fluids for Cu-Au-Mo porphyry ore formation? Economic Geology, v. 116, no. 7, p. 1599–1624.

Hurtig NC, Gysi AP, Monecke T, Petersen S, and Hannington, MD (2023) Tellurium Transport and Enrichment in Volcanogenic Massive Sulfide Deposits: Numerical Simulations of Vent Fluids and Comparison to Modern Sea-Floor Sulfides: Economic Geology, v. submitted.

Kulik DA, Wagner T, Dmytrieva SV, Kosakowski G, Hingerl FF, Chudnenko KV, and Berner UR (2013) GEM-Selektor geochemical modeling package: Revised algorithm and GEMS3K numerical kernel for coupled simulation codes: Computational Geosciences, v. 17, no. 1, p. 1–24.

Louvel M, Bordage A, Da Silva-Cadoux C, Testemale D, Lahera E, Del Net W, Geaymond O, Dubessy J, Argoud R, and Hazemann JL (2015) A high-pressure high-temperature setup for in situ Raman spectroscopy of supercritical fluids: Journal of Molecular Liquids, v. 205, p. 54–60.

Migdisov AA, Bychkov AY, Williams-Jones AE, and van Hinsberg VJ (2014) A predictive model for the transport of copper by HCl-bearing water vapour in ore-forming magmatic-hydrothermal systems: Implications for copper porphyry ore formation: Geochimica et Cosmochimica Acta, v. 129, p. 33–53.

Velizhanin KA, Alcorn CD, Migdisov AA, and Currier RP (2020) Rigorous analysis of non-ideal solubility of sodium and copper chlorides in water vapor using Pitzer-Pabalan model: Fluid Phase Equilibria, v. 522, p. 112731.

Williams-Jones AE & Heinrich CA (2005) Vapor transport of metals and the formation of magmatic-hydrothermal ore deposits: Economic Geology, v. 100, no. 7, p. 1287–1312.

The epithermal deposits of Chatkal-Kurama (Uzbekistan): micro-nanomineralogy of gold, silver, and associated elements

Rustam Khalmatov[1,2], Anna Gioncada[3], Danis I. Filimon[3]
[1] *Institute Geology and Geophysics, University of Geological Science, Tashkent, Uzbekistan*
[2] *Center for Advanced Technologies, Tashkent, Uzbekistan*
[3] *Department of Earth Sciences, University of Pisa, Pisa, Italy*

Abstract We examined the nature of the distribution of gold and other elements in the epithermal ores of the Chatkal-Kurama region of Uzbekistan. Our analyses of the primary ore-forming minerals revealed the presence of minerals (> 100 μm) and invisible structural forms of gold, primarily in arsenopyrite, chalcopyrite, and As-bearing pyrite. Micromineral (10 μm to 100 μm) and nanomineral (10 μm to 0.n μm) were also identified, including Bi, Te, Se nanominerals. The variation in the mineral assemblages is discussed in relation to depth.

1 Introduction

The methodology of micro- and nanomineralogy, which is based on studying mineral inclusions ranging in size from 100 μm to 100 nm, is particularly important in the study of precious metal deposits. The complex geochemistry of epithermal deposits in Chatkal-Kurama region (Uzbekistan), with anomalies of Au, Ag, Te, Se, Cu, Sb, Pb and Bi, is reflected in a complex mineralogy with sulfides (e.g. pyrite, chalcopyrite), sulfosalts (e.g. tetrahedrite-tennantite, freibergite), tellurides (e.g. petzite, hessite, altaite, calaverite) and selenides (e.g. aguilarite, naumannite). Previous research on this topic in Uzbekistan has highlighted the complex study of nanomineralogy associated with ore minerals in different ore deposits (Khalmatov 2009; Koneev et al. 2010; Khalmatov and Koneev 2015; Khalmatov et al. 2019) Based on these foundations, this research contributes with new micro-nanomineralogy studies to increasing the knowledge of gold-silver and gold-tellurium epithermal deposits in the Chatkal-Kurama region.

2 Methods

The study of micro-nanomineralogical composition of ore deposits was conducted using a Carl Zeiss scanning electron microscope with an Oxford Instrument Microanalysis System EDS detector and SX-50 Cameca microanalyzer at the Natural History Museum in London. This instrument provides detailed analysis of the microstructures of ore samples with high resolution and the ability to observe at the nanoparticle level. The energy dispersive analysis (EDS) system allows the chemical composition of materials to be determined with high accuracy, which is important for identifying the distribution of rare elements in the ore.

3 Geological settings of the deposit

The Kurama region is the Eastern end of the Valeriano-Beltau-Kurama volcano-plutonic arc (Dolgopolova et al. 2017). Andesitic volcanism and granitoid plutonism are widely manifested in the region. The age of super-subduction magmatism is 320–289 Ma (U-Pb, SHRIMP), and the age of epithermal pyrite mineralization is 298 Ma (Os-Re) (Dolgopolova et al. 2017). For comparative studies, two reference representatives of epithermal deposits were selected: the Au-Te type Kochbulak ore field (including, e.g., Nishbash, Uzun, Kalta, Chetgi; Fig 1, A) and the Au-Ag type Kyzylalmasay ore field (Severo-Vostochnyy, Kyzyl'alma, Mezhdurech'ye, Samarchuk Chumauk I, II; Fig 1, B). The Kochbulak ore bodies are represented by steeply dipping veins, interfacial vein-metasomatic deposits, explosive breccia pipes with gold content up to 20,000 g/t. They are hosted in berezitized and argilized dacites and andesites (C_2), along SW-NE and NW-SE trending faults (Fig. 1, A). At Kyzylalmasay, ore bodies are represented by veins and interformational deposits in argillized and berezitized andesites, syenite-diorites (C_2), and granites (S_2-D_1). The ore-enclosing structure is 10 km-long. The main ore-bearing zone was formed by the Kyzylalmasay and Karabausky fractures (Fig. 1, B).

4 Micro-nanomineralogy of ores

The form in which each element occurs depends on the physicochemical conditions and its physical state. For example, gold, in its classical representation, is a noble metal that does not interact with other substances. However, when in the form of nanoparticles, gold can form various compounds under different conditions and deposit types, such as Au_3Ni, Au_2Bi, AuCu, $AuPb_2$, $AuTe_2$, $AuSb_2$, Au_2Hg, AgAuS, and Ag_3AuSe (Koneev et al. 2010).

Based on the principle that specific compounds are associated with certain conditions, the distribution of mineral forms of elements across the deposit cross-sections was analyzed.

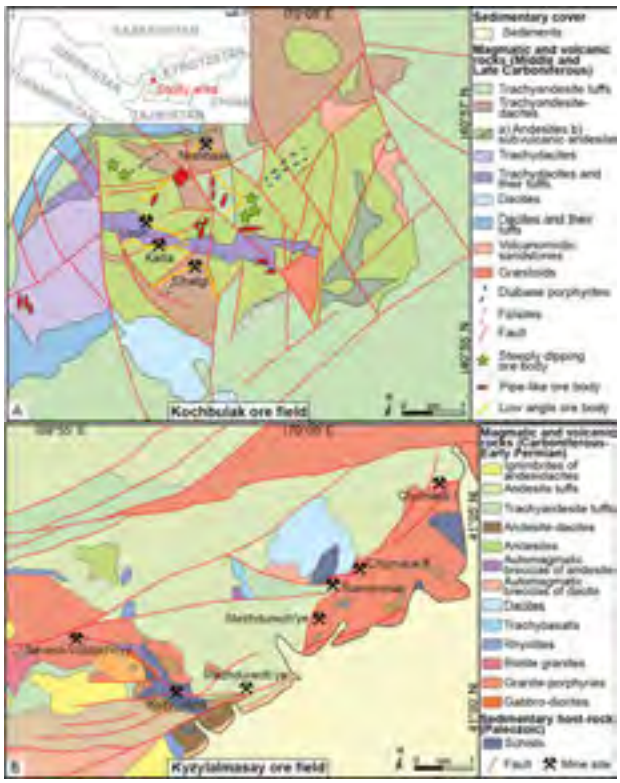


Figure 1. Geological map of Kochbulak (A) and Kyzylalmasay (B) ore fields (Anon 2001)

4.1 Gold-silver type (Kyzylalmasay)

The gold studied from the Kyzylalmasay deposit exhibits a distinct feature. At greater depths (500 m), a significant amount of tellurides were encountered (Table 1). The gold's fineness increased by approximately 200‰ (from 660 to 860‰), while the overall amount of kustelite decreased.

The dominant Au-Ag telluride mineral is petzite ($AuAg_3Te_2$). Minerals characteristic of Au-Ag mineralization—naumannite, aguilarite, and polybasite—contain tellurium concentration of up to 7-10%. In the microparageneses of gold, lead-bismuth sulfosalts (gustavite-lillianite), their selenides (naumannite, aguilarite), and tellurides (tetradymite, tellurobismuthite, aleksite), as well as other minerals (zinkenite, cervelleite and other, Au-Ag-Sb-Te phases), may also be present.

Petzite remains stable at temperatures above 210°C and, along with hessite and bogdanovichite, is characteristic of the relatively upper zones of Au-Te mineralization.

Figure 3 shows nanominerals closely intergrown with gold. In chalcopyrite, nanogold with lead and bismuth selenides forms a microparagenesis (an assemblage of minerals formed together). This could suggest that it originated either from the breakdown of a complex compound or through the diffusion of impurity elements into a diffusion trap (Bortnikov et al. 1987).

Gold exhibits two main types of occurrences: 1.) syngenetic, where gold is deposited within mineral crystals along with paragenetic microminerals and 2. Epigenetic, where gold cuts through other minerals along fractures.

Table 1. Micro- and nanominerals of gold-silver type ores in the Kyzylalmasay deposits

Connection type	Mineral	Formula
Native, intermetallics	Silver	Ag
	Kustelite	$AuAg_3$
	Electrum	AuAg
	Animikite	(Ag,Sb)
	Allargentum	Ag_6Sb
Sulfides	Acanthite	Ag_2S
Sulfosalts	Freibergite	$(Ag,Cu,Fe,Bi)_{12}Sb_4S_{13}$
	Se-polybasite	$Ag_{16}Sb_2(Se,S)_{11}$
	Se-stephanite	$AgFe_2S_3$
	Sternbergite	$AgFeS_2$
	Gustavite	$PbAgBi_3S_6$
	Argentopyrite	Ag_3SbS_3
	Wittichenite	$Cu_2(Zn,Fe)SnS_4$
Selenides, sulfoselenides	Naumannite	$Ag_2(Te,Se)$
	Aguilarite	$Ag_2(Te,Se,S)$
	Berzelianite	Cu_2Se
Tellurides, sulfotellurides	Hessite	Ag_2Te
	Stutzite	Ag_5Te_3
	Petzite	Ag_3AuTe_2
	Sylvanite	Ag_3AuTe_4
	Calaverite	$AuTe_2$
	Cervellite	Ag_4TeS
	Tsnigriite	$Ag_9SbTe_3S_3$
	Volynskite	$AgBiTe_2$
	Tellurobismuthite	Bi_2Te_3
	Tetradymite	$Bi_{14}Te_{13}S_8$
	Alexite	$PbBi_2Te_2S_2$

Analyzing the obtained images, clear nanoinclusions of both gold and other minerals are visible. However, gold particles larger than 1–10 μm are more frequently observed. Thus, nano-assemblies or nanocomposites are noted. In other instances, these accumulations appear as aggregates formed after the breakdown of a solid solution or as secondary gold formed after earlier sulfides.

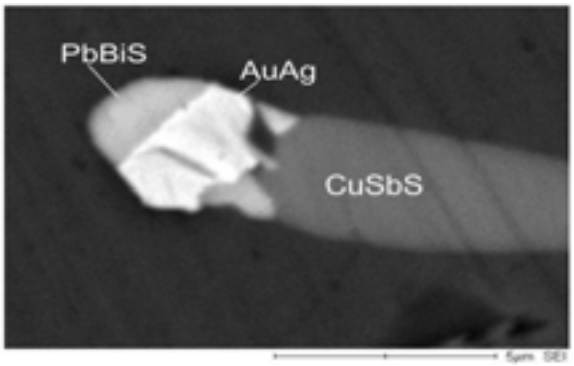


Figure. 3. The microparagenesis of gold with lead sulfo-bismuthite and tetrahedrite

Silver is represented by nearly all ore classes of minerals: native silver, intermetallics (allargentum), simple sulfides (acanthite), sulfosalts (gustavite, freibergite, polybasite), selenides (naumannite, aguilarite), and tellurides (hessite, cervelleite). Most of the minerals in the gold-silver type deposit are

effectively new for the Kyzylalmasay deposit, as all identified phases are tellurium-bearing varieties, particularly naumannite and aguilarite. Tellurium content can reach 7–10%. It is also notable that many silver minerals contain gold, especially in selenides with tellurium and in silver tellurides. Silver mineralization consistently accompanies gold, ranging from 1,200 meters (surface) to 747 meters depth. Evidently, as the depth of the "Razvedochnaya" shaft increases, silver mineralization decreases, giving way to Bi-Se phases and eventually Bi-Te phases.

Based on the observed changes in the forms of elements with depth, the following developments can be predicted:

- Fineness will increase.
- The size of native gold will decrease.
- The quantity of gold tellurides (sylvanite, calaverite), as well as Sb, Pb tellurides (tellurantimony, altaite), and subsequently Bi tellurides (tetradymite, tellurobismuthite) will increase.
- The number of selenides will decrease, initially silver selenides (naumannite, aguilarite) and later bismuth selenides (bogdanovichite, laitakarite).
- The diversity of antimony minerals will reduce, transitioning from silver intermetallics to polybasite, freibergite, tetrahedrite, and miargyrite.
- Arsenic will transition from arsenian pyrite to intermediate sulfosalt forms (tetrahedrite-tennantite-goldfieldite-annivite), and subsequently to arsenopyrite.

The study of micro- and nanomineral forms of element occurrence indicates that at a horizon of +700 meters, the upper part of a transitional zone between electrum-silver and gold-tellurium mineralization has been exposed. With increasing depth, gold-tellurium mineralization becomes dominant. Correspondingly, the geochemical association of gold with Ag, Sb, Se, and likely Hg decreases, while associations with Te, Bi, Pb, S, and As increase.

4.2 Gold-tellurium type (Kochbulak)

Epithermal gold-tellurium deposits (Kochbulak) are associated with volcanic activity. There is also noted increased sulfidation, with a predominance of minerals such as Cu, Pb, Bi, and a wide distribution of tellurides in micro- and nanomineral forms (Table 2).

Native gold is distributed very unevenly. It occurs in intergrowths with quartz, tetrahedrite-tennantite , sulfides, and tellurides. The gold is predominantly very fine and fine (0.0n mm - 0.1-0.2 mm), with larger particles up to 1-2 mm occurring less frequently. The forms of native gold include lumpy, spongy, platy, and xenomorphic. The fineness of gold ranges from 780 to 995‰, with a decrease in the amount of electrum compared to the gold-silver type (Table 2). The highest fineness is observed in gold from earlier generations. Lower-fineness gold is associated with tetrahedrite-tennantite , chalcopyrite, and hessite. Electrum is associated with Ag-(Cu)-Pb-Bi-sulfosalts, hessite, and tin minerals.

The main gold telluride minerals are petzite, calaverite, montbretite, and costovite. Hessite is the most widespread (Fig. 5). At temperatures below 155°C, cubic hessite transforms into monoclinic; along with stützite, it forms during the breakdown of solid solution below 120°C. Empressite remains stable below 170-210°C; above this, it decomposes into stützite and tellurium. The relationship between hessite and petzite is more complex. Some researchers consider petzite as a gold-bearing hessite. According to other data, at 250°C, hessite and petzite form solid solutions, and it is noted that hessite rarely occurs in nature without petzite, forming fine-disperse aggregates. Bortnikov et al. (1987) established that the association of petzite with gold, hessite, and calaverite is stable only below 313°C, with a stable microparagenesis of calaverite + hessite + gold above this temperature. Sylvanite, krennerite, and petzite are stable in the temperature range of 120-280°C.

Another widespread group is bismuth tellurides (Table 2), with tetradymite and tellurobismuthite being the most common. Tetradymite is more widespread. The typomorphic minerals of the productive complexes in gold ore formation deposits are gold and silver tellurides, including minerals from the tetradymite group, especially the joesite group, which are characterized by a high degree of sulfur replacement with tellurium, as well as petzite in the form of microinclusions in pyrite (G.A. Yurgeson pers. comm.).

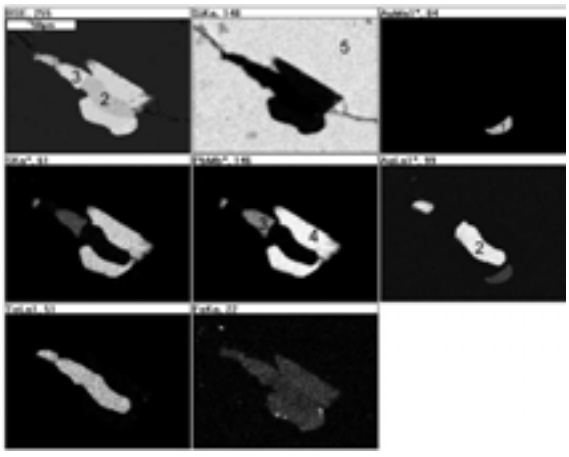


Figure 5. Native gold, lead and silver tellurides.
1-native gold; 2-hessite; 3-tellurium-containing galena; 4-galena; 5-quartz

Table 2. Micro- and nanominerals of gold-telluride type in the Kochbulak deposits

Connection type	Mineral	Formula
Native, intermetallics	Gold Electrum Tellurium Bismuth Copper	Ag AuAg Te Bi Cu

Sulfides, sulfosalts	Yutenobogardtite-petrovskaite	Ag_3AuS_2 - AgAuS
	Galenobismuthite	$PbBi_2S_3$
	Pavonit	$AgBi_3S_5$
	Cupropavonite	$Cu_2AgPbBi_5S_{10}$
	Halkostibit	$CuSbS_2$
	Emplectitis	$CuBiS_2$
	Enargite	Cu_3AsS_4
	Tennatite	$Cu_{12}As_4S_{13}$
	Tetrahedrite	$(Cu,Fe)_{12}Sb_4S_{13}$
	Bi-tetrahedrite	$(Cu,Fe)_{12}(Bi,Sb)_4S_{13}$
Sulfostannates	Kesterite	$Cu_2(Zn,Fe)SnS_4$
	Stannine	Cu_2FeSnS_4
	Stannoidite	$Cu_8(Fe,Zn)_3Sn_2S_{12}$
Tellurides, sulfotellurides	Hessite	Ag_2Te
	Stutzite	Ag_5Te_3
	Petzite	Ag_3AuTe_2
	Kawatzulite	Bi_2Te_2Se
	Tetradymite	Bi_2Te_2S
	Empressite	AgTe
	Calaverite	$AuTe_2$
	Krennerite	Au_3AgTe_8
	Montbreyite	Au_2Te_3
	Sylvanite	Ag_3AuTe_4
	Tellurobismuthite	Bi_2Te_3
	Volynskite	$AgBiTe_2$
	Coloradoite	HgTe
	Altaite	PbTe
	Tellurantimony	Sb_2Te_3
	Bi-tellurantimony	$(Bi,Sb)_2Te_3$

5 Conclusions

In the studied deposits of Kyzylalmasay and Kochbulak, the ratio between tellurides of different compositions is quite complex. These ores contain gold and gold-silver tellurides, as well as tellurides of metals such as Hg, Pb, Sb, Cu, Fe, and Ni-coloradoite, altaite, tellurantimony, freibergite, melonite, weissite, and rickardite. Bismuth tellurides are widespread. Furthermore, in high-temperature deposits, bismuth tellurides are more commonly represented by minerals containing less tellurium—tetradymite. This is explained by the fact that bismuth, a much more abundant element in high- and medium-temperature deposits than in low-temperature ones, has a larger mass, atomic volume, and electron configuration in higher energy sublevels compared to gold and other elements. As a result, bismuth "takes" tellurium from gold and other elements (Ciobanu et al…….. Additionally, tellurium itself is less abundant in these deposits than in near-surface, epithermal ones. In the gold-silver type, there are typically high concentrations of selenium, but only in the form of selenides, sulfoselenides, and sulfoselenotellurides of bismuth.

The prevalence of micro- and nanomineral forms with depth serves, first, as an indicator of the scale of mineralization— the larger and more diverse the mineral composition, the greater the extent of mineralization. Second, experimental studies of sulfide-telluride-selenide systems allow the reconstruction of the temperature regime of ore formation. Thus, the temperature regime of mineral associations in the Chatkal-Kurama region deposits changes with depth from early to late associations, ranging from 500 to 100°C.

Acknowledgements

The research was supported by OT-F8-01 grants of the Ministry of Higher Education, Science and Innovation of the Republic of Uzbekistan. Thanks to Prof. R. Seltmann for conducting analyses.

References

Anon (2001) Ore Deposits of Uzbekistan. Tashkent GIDROINGEO, 100 pp

Bortnikov NS, Genkin AD, Kovalenker VA (1987) Mineralogical and geochemical indicators of hydrothermal ore formation conditions. In: Endogenous Ore Regions and Deposits. Moscow, Nauka, pp. 40-59

Dolgopolova A, Seltmann R, Konopelko D, Biske Yu S, Shatov V, Armstrong R, Belousova E, Pankhurst R, Koneev R, Divaev F (2017) Geodynamic evolution of the western Tien Shan, Uzbekistan: Insights from U-Pb SHRIMP geochronology and Sr-Nd-Pb-Hf isotope mapping of granitoids. Gondwana Research 47:76-109. DOI 10.1016/j.gr.2016.10.022

Khalmatov R (2009) The Kyzylalmasay gold-silver deposit (Uzbekistan): micromineralogy and geochemistry of ores from deep horizons. 10th SGA Biennial Meeting. Townswill, Australia.1:117-119

Khalmatov RA, Koneev R, Kim M (2019) Au-Ag-Te and Au-Ag-Se mineralizations as indicators of high-low sulfidation types of epithermal deposits of the Kurama volcanic-plutonic region (Uzbekistan). 15th SGA Biennial Meeting, Glasgow, Scotland. 3:1035-1037

Khalmatov RA, Koneev RI (2015) Epithermal gold mineralization of the Kurama volcanic region of the Western Tien Shan (Uzbekistan). 13th SGA Biennial Meeting. Nancy, France. 1:307-308

Koneev RI, Khalmatov RA, Mun Yu S (2010) Nanomineralogy and nanochemistry of ores from gold deposits of Uzbekistan. Geology of Ore Deposits 52(8):755-766

Geochemical and C-O signatures in carbonates around the Basin porphyry, Utah, USA

Michael J. Kirschbaum[1], Zhaoshan Chang[1] Jeff Nicholes[2], Adam Pacey[3]
[1]Depart of Geology and Geological Engineering, Colorado School of Mines, Golden, CO 80401, USA
[2]Jeff Nicholes LLC, Elko, Nevada, USA
[3]Rio Tinto Exploration, Bundoora, Victoria, Australia

Abstract. We investigate the signatures around the sub-economic Basin porphyry deposit in Utah, to compare the results with those from well-mineralized systems to help better understand the processes and identify the conditions for fertile systems. Samples were collected from the lowermost carbonate horizons; Tatow dolomite, and Howell and Dome limestone. The boundary between the lowest Tatow and the underlying quartzite is inferred to be a slip fault. Bulk rock samples have elevated Cu and Mo to ~2 km from the Basin porphyry, Au, Ag, Co, Ni, and Te to ~1 km, and Fe and S to ~0.5 km. Tatow samples show depletions of Mg and Mn within ~0.5 km of the intrusion. All bulk rock O isotope composition show water involvement for ~3.5 km in the uppermost Dome unit ($\delta^{18}O$ <20.1‰ VSMOW), and for >7.5 km in the Howell and Dome units. The hydrothermal signature in bulk rock $\delta^{13}C$ values (<-2.25‰ VPDB) extends only ~0.5 km from the Basin porphyry. Vein carbonate isotope signatures are more sensitive. The C isotopes show a hydrothermal halo of ~1.5 km. The O isotopes of all three units are hydrothermal for >7.5 km, and with other depletions ~4.5 and ~6.5 km to the south.

1 Introduction

Porphyry deposits are the major source of Cu and an important source of Au and Mo, and are the main target of many major companies. To increase the exploration success rate, distal signatures and vectors of porphyry deposits in volcanic rocks have been studied (e.g., Chang et al. 2011; Cooke et al. 2014, 2020; Wilkinson et al. 2015). Similar studies on signals and vectors in carbonates started later (e.g., Barker and Dipple, 2019; Beinlich et al. 2019; Piurkowski et al. 2022; Kirschbaum et al. 2022) and they focused on large deposits. In this study, we investigate the signatures and vectors in carbonates around the sub-economic Basin porphyry, Utah, USA, as a comparator to help better understand the processes and identify the conditions for fertile systems. The Basin porphyry has been explored since the late 1800s including drilling in the recent years but no significant porphyry-skarn mineralization has been found (Krahulec 2018).

2 Deposit Geology

The stratigraphy in the Drum district includes, from old to young, Cambrian Prospect Mountain Quartzite, Pioche Formation (Fm) with a Lower member (Mbr) phyllite and an Upper Tatow Mbr dolomite, Howell Limestone, Chisholm Fm shale, Dome Limestone, Whirlwind Fm shale-limestone, Sawsey Limestone, Wheeler shale, Pierson Cove Fm mudstone, Lower Trippe Limestone, Fish Springs Limestone, and Lower Lamb Dolomite, covered by Tertiary andesite (Hintze and Davis 2003). The boundary between Tataw dolomite and the underlying quartzite is inferred to be a bedding-parallel slip fault. The strata are displaced for short distances by pre-mineralization E- and NE-trending tear faults and some minor NW faults (Fig. 1).

The Basin porphyry (~1.5 x 0.8 km) intruded the strata from Prospect Mountain Quartzite on the east, to Pierson Cove Fm on the west (Fig. 1). The intrusion is composed of fine grained equigranular diorite and diorite porphyry. The syn-mineralization quartz monzonite porphyry hosts quartz-molybdenite B-veins with pyrite center lines and secondary biotite halos. The pre-mineralization diorite has secondary biotite and disseminated pyrite-chlorite alteration. The porphyry is dated at 36.6 ± 0.4 Ma and the diorite 36.5 ± 0.4 Ma (2 s; LA-ICP-MS zircon U-Pb). Next to the porphyry, alternating thin layers of shale and carbonate have been converted to reaction skarns during contact metamorphism. Marble occurs up to ~1 km away although Tatow is mostly marble for >7.5 km. The hydrothermal skarn is narrow, <10 m. The garnet is dated at 36 ± 7 Ma (2 s; LA-ICP-MS U-Pb).

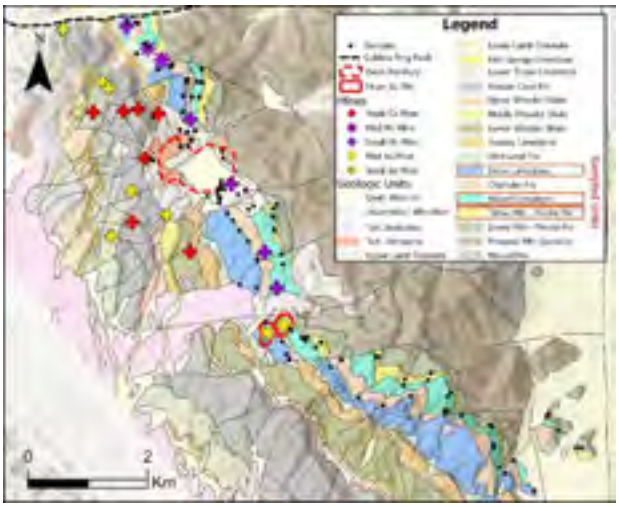


Figure 1. Geologic map of the Drum Mountain mining district (modified from Dommer 1980 and unpublished map by Adair 1969)

The intrusion has an alteration halo ~100-600 m including hydrothermal skarns and lower temperature alterations. Some small Cu and Au deposits occur from 100 to 2,500 m from the intrusion boundary, as intermediate-sulfidation epithermal veins and CRD veins, with silicification halos (jasperoid; Fig. 1). Grab sample grades are up

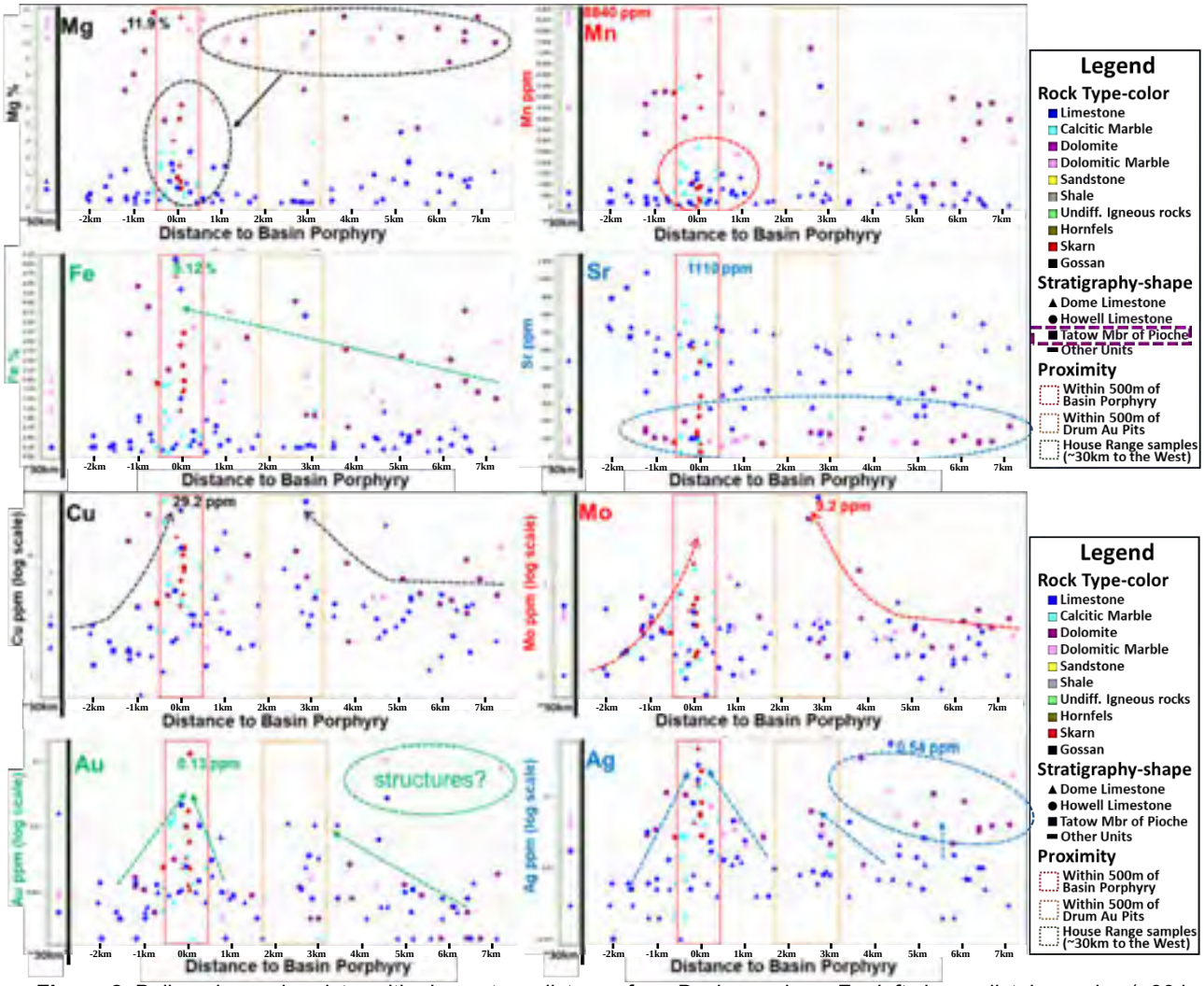


Figure 2. Bulk rock geochemistry with element vs. distance from Basin porphyry. Far left shows distal samples (~30 km).

to 100 ppm. Pebble dikes occur north and south of the intrusion for >3 km; fragments include quartzite, limestone, and intrusive rocks (porphyries). Some pebble dikes contain Au (up to 20 ppm in grab samples). Pebble dikes are typically around where there is elevated Au. Mn deposits occur in the Tatow Mbr along strike, up to 2 km north and south of the Basin porphyry (Fig. 1). Ore minerals include rhodochrosite, Mn-calcite and Mn-dolomite. The Mn deposits contain minor Au (locally 0.3-0.6 ppm), Ag (locally 0.4-3.1ppm), little Zn (~0.02%), As (~0.31%), and trace Pb (Crittenden 1961). The two Drum Au open-pits 3 km SE of the Basin porphyry are classified as a “distal disseminated” type with production of 0.074 Moz Au (Krahulec 2011, 2018). 143 carbonate vein-bearing samples were collected from Tatow, Howell, and Dome of all outcrops, ~2 km to the NE and ~7.5 km to the SE of the Basin porphyry (Fig. 1).

3 Bulk Rock Geochemistry

Bulk rock data excluding a few Mn ore/gossan samples are plotted in Fig. 2. Tatow samples have high Mg (~7-12%) in the whole area, with elevated Fe (~1-4%), and Mn (~0.2-0.4%; Fig. 1). Four samples of regional Tatow Mbr ~28 km away from the Basin porphyry, far away from any known mineralization, have similar Mg, Fe, and Mn compositions, therefore it is inferred that such high values are sedimentary. Within 0.5 km of the Basin porphyry, the Tatow Mbr shows Mg and Mn depletion (excluding Mn ores) and Fe enrichment (up to 5.12%). All units show enrichment of Cu and Mo to ~2 km, Co, Ni, Te, Au and Ag up to ~1 km, and S to ~0.5 km from the Basin porphyry. Strong Be, Ce, Ta, and Se anomalies extend ~1.2 km from the Basin porphyry. Note that there are also weak anomalies of Cu, Mo, Co, Ni, Te, Be, Ce, Se, & Ta near the Drum Au pits (~2.5-3 km from Basin) and erratic anomalies around the 4.5 km, 6-6.5 km and 7-7.5 km distances from the Basin porphyry (Fig. 2).

4 C-O Isotope Signatures – Bulk Rock

The bulk rock O isotope compositions show that all the Howell and Tatow samples have $\delta^{18}O$(VSMOW) values <20.1‰, below the Cambrian marine carbonate range of 20.1-24.5‰ (Fig. 3; Veizer et al. 1999), indicating the interaction with water. The Dome samples have sedimentary signatures >3.5 km away from the Basin porphyry (Fig. 3).

The O isotope signatures of all the samples show an overall decreasing trend toward the Basin

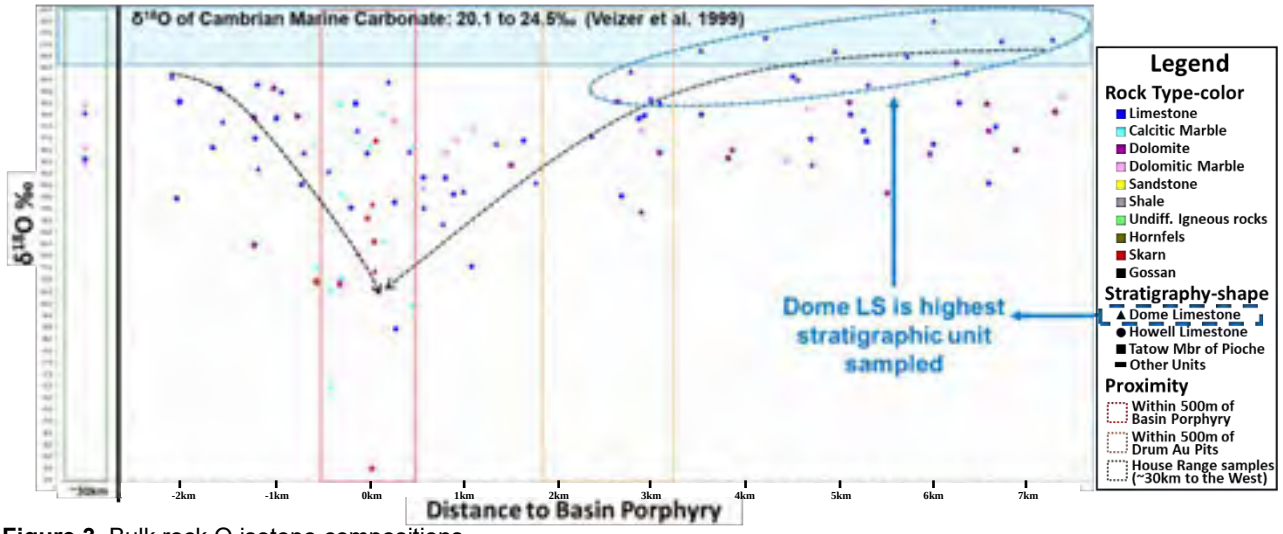


Figure 3. Bulk rock O isotope compositions

porphyry, down to ~10.5‰, with a few down to ~3‰ next to the porphyry (Fig. 3). This implies that the Basin porphyry is a source of the fluids that the carbonates have interacted with. The Dome samples (highest stratigraphic position) show the strongest trend, continuing to increase for ~7.5 km away from the Basin porphyry, whereas the samples of Tatow and Howell trends flatten at ~3.5 km, despite that the samples beyond 3.5 km still show hydrothermal signatures (Fig. 3).

The C isotope compositions of most of the samples show marine sedimentary signature, above -2.25‰ (Fig. 4; Veizer et al. 1999). Only some samples close to the intrusion (<1.2 km) have lower values and show signs of interaction with water. A decreasing trend appears within 0.5 km of the Basin porphyry, where the $\delta^{13}C$(VPDB) decreases to -6.3 to -5.5‰ next to the intrusion (Fig. 4). The C isotopes are less sensitive to hydrothermal interactions than O isotopes, as have been found in previous studies (e.g., Vazquez et al. 1998).

5 C-O Isotope Signatures – carbonate veins

Paragenesis of carbonate veins in rocks were characterized based on visual observations and ultraviolet (UV) imaging, then drilled out for C-O isotope analysis. Carbonate vein samples have been found to record more distal and subtle C-O isotope signals, e.g, at Cinco de Mayo, Mexico (Beinlich et al., 2019) and at Bingham, Utah (Kirschbaum et al. 2023).

At the Basin porphyry, the majority of the samples show a hydrothermal signature in their vein carbonate O isotope compositions, including the Dome samples (Fig. 5). There is a decreasing trend towards the Basin porphyry, with the $\delta^{18}O$(VSMOW) values down to ~0.5‰ next to the intrusion, and the data also show other centers at ~4.5 km and ~6.5 km SE of the intrusion (Fig. 5). The vein C isotopes around the Basin porphyry similarly show the intrusion as a fluid center, but the halo size is ~1.5 km (Fig. 6), bigger than that of bulk rock (~0.5 km).

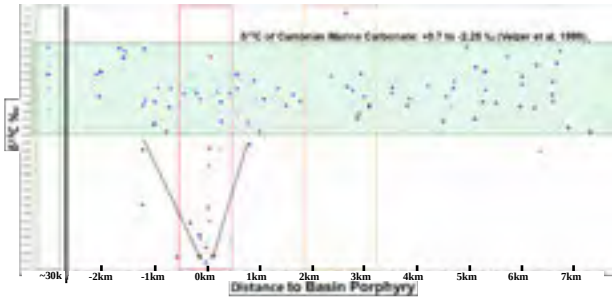


Figure 4. Bulk rock C isotope compositions

6 Discussions and Conclusions

Bulk rock geochemistry shows a halo of 0.5-2.0 km around the Basin porphyry, much shorter than that around the Bingham porphyry (5-6 km; Kirschbaum et al. 2022). This is consistent with the Basin porphyry resources being much smaller than that of Bingham. Both the bulk rock and vein carbonate C-O isotope compositions show a trend around the Basin porphyry, similar to other hydrothermal deposits hosted in carbonates, and the vein carbonate C-O isotope compositions can detect a larger halo than that of the bulk rock. The O isotope signals are >7.5 km wide, comparable with that of Bingham (Kirschbaum et al 2023), possibly because of the slip faults between carbonates and siliciclastic layers, and/or the Basin porphyry did release large amount of water but was short of metals.

There is some disturbance of the trends around the Basin porphyry, especially in the more sensitive parameters such as vein carbonate C-O isotope compositions. The disturbance might be related to other hydrothermal events, possibly before the Basin porphyry, but the detailed mechanism is yet to be revealed.

Acknowledgements

We thank Rio Tinto and CASERM for the sponsorship, and Alderan Resources (now Hawk Resources) for the access and field support.

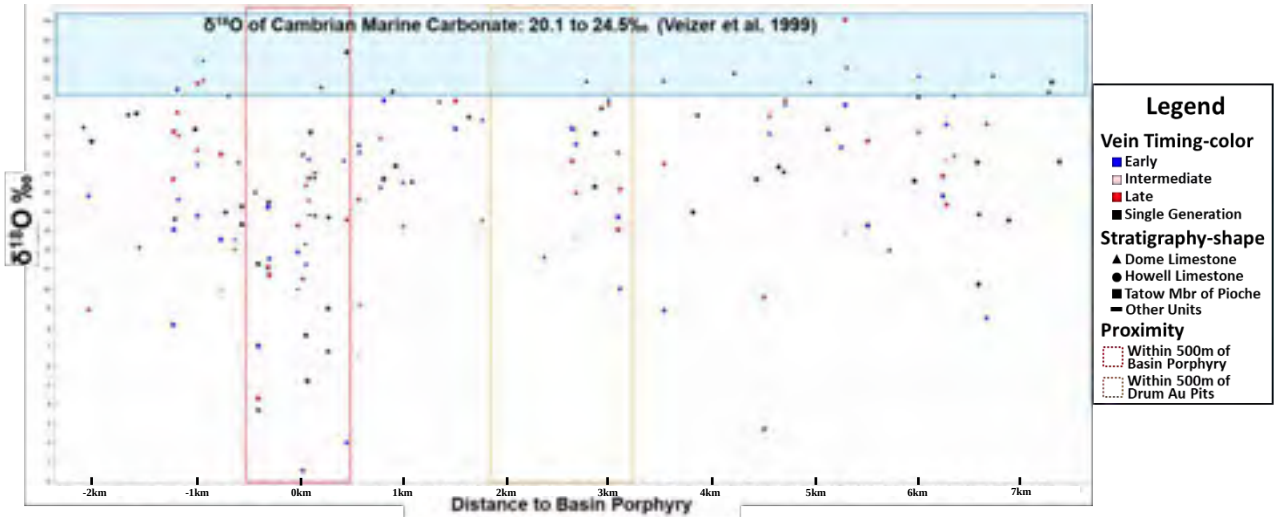


Figure 5. Vein carbonate O isotope compositions

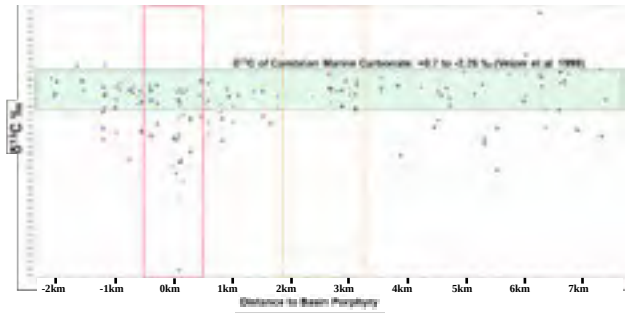


Figure 6. Vein carbonate C isotope compositions

References

Barker SL, Dipple GM (2019) Exploring for carbonate-hosted ore deposits using carbon and oxygen isotopes. in: Cecree S and Robb L (Eds) Ore Deposits: Origin, Exploration, and Exploitation:185-207

Beinlich A, Barker SLL, Dipple GM, Hansen LD, Megaw PKM (2019) Large-scale stable isotope alteration around the hydrothermal carbonate-replacement Cinco de Mayo Zn-Ag deposit, Mexico. Econ Geol 114:375-396

Chang Z, Hedenquist JW, White NC, Cooke DR, Roach M, Deyell CL, Garcia J Jr, Gemmell JB, McKnight S, Cuison AL (2011) Exploration tools for linked porphyry and epithermal deposits: Example from the Mankayan intrusion-centered Cu-Au district, Luzon, Philippines. Econ Geol 106:1365-1398

Cooke DR, Baker M, Hollings P, Sweet G, Chang Z, Danyushevsky L, Gillbert S, Zhou TF, White N, Gemmell JB, Inglis S (2014) New advances in detecting the distal geochemical footprints of porphyry systems – epidote mineral chemistry as a tool for vectoring and fertility assessments. Soc of Econ Geol Special Pub 18:127-152

Cooke DR, Wilkinson JJ, Baker M, Agnew P, Phillips J, Chang Z, Chen H, Wilkinson CC, Inglis S, Hollings P, Zhang L, Gemmell JB, White NC, Danyushevsky L, Martin H (2020) Using mineral chemistry to aid exploration – a case study from the Resolution porphyry Cu-Mo deposit, Arizona. Econ Geol 115:813-840

Crittenden MD, Jr, Straczek JA, Roberts RJ (1961) Manganese deposits in the Drum Mountains, Juab and Millard counties, Utah. USGS Bull 1082-H:493-544

Dommer ML (1980) Geology of the Drum Mountains, Millard and Juab counties, Utah. BYU Geol Stud 27, Part 3:55-72

Hintze LF, Davis FD, (2003), Geology of Millard County, Utah. UGS Bull 133

Kirschbaum M, Chang Z, Agnew P, Pacey A, Nickerson P, Sasso A, Schroeder K, Gundy K (2023) Far field geochemistry and C-O isotope signatures of the Bingham porphyry Cu-Au-Mo deposit in carbonate wallrocks. SEG 2023 Conference, 26-29 August 2023, London, UK.

Kirschbaum MJ, Chang Z, Agnew P, Pacey A, Nickerson P, Sasso A, Schroeder K, Gundy K (2022), Distal signatures of the Bingham porphyry Cu-Au-Mo mineralization in carbonate wallrock., in: The critical role of minerals in the carbon-neutral future, Proceedings of the 16th SGA meeting, 28-31 March 2022, Rotorua, New Zealand 2:95

Krahulec K (2011) Sedimentary rock-hosted gold and silver deposits of the Northeastern Basin and Range, Utah. Great Basin evolution and metallogeny, GSN Symposium 1;31-62

Krahulec K (2018) Utah Mining Districts. UGS OFR 695

Lindsey DA (1982) Tertiary volcanic rocks and uranium in the Thomas Range and northern Drum Mountains, Juab County, Utah. USGS Prof Paper 1221

Lovering TG, McCarthy JH Jr (1978) Detroit mining district, in Lovering TG and McCarthy JH Jr, Eds, Conceptual models in exploration geochemistry, the Basin and Range Province of the western United States and northern Mexico. J of Geochem Expl, V 9, N 2-3:168–174

Nutt CJ, Thorman CH (1992), Pre-late Eocene structures and their control of gold ore at the Drum Mine, west-central Utah. USGS Bull 2012:F1-F7

Nutt CJ, Thorman CH, Snee LW, Hintze LF (1996) Eocene or older attenuation faults in the eastern Great Basin. In: Coyner AR, Fahey PL (Eds) Geology and ore deposits of the American Cordillera. April 1995: Reno/Sparks, Geol Soc of Nevada Symp Proc:609-623

Piurkowsky S, Chang Z., Brunetto P (2022) Geochemical zoning patterns in carbonate wallrocks of the Candelaria Cu-Au district, Chile. in: The Critical Role of Minerals in the Carbon-Neutral Future, Proceedings of the 16th biennial SGA meeting, 28-31 March 2022, Rotorua, New Zealand, V 2:142

Vazquez R, Vennemann TW, Kesler SE, Russell N (1998) Carbon and oxygen isotope halos in the host limestone, El Mochito Zn-Pb-(Ag) skarn massive sulfide-oxide deposit, Honduras, Econ Geol 93(1):15-31

Veizer J, Ala D, Azmy K, Bruckschen P, Buhl D, Bruhn F, Carden GAF, Diener A, Ebneth S, Godderis Y, Jasper T, Korte C, Pawellek F, Podlaha O, Strauss H (1999) $^{87}Sr/^{86}Sr$, $\delta^{13}C$ and $\delta^{18}O$ evolution of Phanerozoic seawater. Chem Geol 161:59–88

Wilkinson JJ, Chang Z, Cooke DR, Baker MJ, Wilkinson CC, Inglis S, Chen H, Gemmell JB (2015) The chlorite proximitor: A new tool for detecting porphyry ore deposits. J Geochem Expl 152:10-26

Genesis of stibnite mineralisation in epithermal deposits based on coupled Sb and S isotopic composition of stibnite

Peter Koděra[1], Ryan Mathur[2], Degao Zhai[3], Rastislav Milovský[4], Pavel Bačo[5], Juraj Majzlan[6]
[1]Department of Mineralogy, Petrology and Economic Geology, Faculty of Natural Sciences, Comenius University in Bratislava, Slovakia
[2]Department of Geology, Juniata College, Huntingdon, USA
[3]State Key Laboratory of geological processes and mineral resources, China University of Geosciences, Beijing, China
[4]Earth Science Institute, Slovak Academy of Sciences, Slovakia
[5]State Geological Institute of Dionýz Štúr, Slovakia
[6]Institut für Geowissenschaften, Mineralogie, Friedrich-Schiller-Universität Jena, Germany

Abstract. The famous Kremnica and Zlatá Baňa epithermal deposits are hosted in two different Neogene volcanic fields in the Western Carpathians, Slovakia. In both deposits, stibnite-rich veins occur outside of major vein structures, accompanied by illite, illite/smectite, and kaolinite alteration, and affiliated to late-stage fluids (< 2 wt% NaCl eq., < 150 °C). Sulfur isotopic composition of stibnite and sulfides is different at both deposits, likely due to a different magmatic-hydrothermal evolution of the parental magmatic chambers in both Volcanic Fields. The Sb isotopes ($\delta^{123}Sb$), however, show similar values and trends of gradual simultaneous increase with $\delta^{34}S$ values, explained by a progressive precipitation of stibnite and its fractionation with the fluid. The data were modeled by two coupled Rayleigh fractionation models, (for Sb and for S), assuming a predominant Sb transport in $HSb_2S_4^-$ with a variable amount of S species. At both deposits, the heaviest $\delta^{123}Sb$ values are accompanied by a decrease in the $\delta^{34}S$ values probably due to the commencement of pyrite/marcasite precipitation. According to the models, stibnite precipitation was triggered by temperature decrease accompanied by mixing with a mildly acidic fluid (pH 4–5) of a steam-heated CO_2-rich condensate on margins and in the final stages of epithermal systems.

1 Introduction

Stibnite mineralizations in epithermal systems are relatively common, but rarely form economic accumulations. They commonly occur relatively close to the surface in areas with high geothermal gradients in peripheral parts of epithermal systems (e.g. above Au-Ag mineralization), or in the central parts they are superimposed on Au-Ag mineralization at depth. However, reasons for such distribution are not yet well understood. In the Carpathian Neogene volcanics, stibnite in epithermal veins is found in Romania (e.g. Baia Sprie, Capnik), Hungary (Gyöngyösoroszi) and Slovakia (Kremnica, Zlatá Baňa), and has been mined at several locations. In this contribution, we present the results of study of Sb and S isotopes in the two Slovakian epithermal deposits, as well as the results of modeling that allowed us to reproduce the behaviour of Sb and S isotopes and clarify the transport and precipitation mechanisms related to stibnite crystallization in epithermal systems in general. Details of this work can be found in the publication of Koděra et al. (2024).

2 Stibnite at the Kremnica deposit

The Kremnica low-sulfidation Au-Ag deposit is located in the northern part of the Central Slovak Volcanic Field in the Kremnické Vrchy Mts. More than 120 veins occur mostly in andesite of the pre-graben stage of the volcano and are grouped into two main vein systems. The first consists of veins located on a first-order lystric fault structure, accompanied by low-angle second-order vein structures closer to the surface, and complementary antithetic veins. The second vein system is located in the hanging wall of the main lystric fault beneath the town of Kremnica. Two main ore stages are represented here, the Au-Ag stage and the Sb-Hg stage, including 6 substages (Böhmer 1966).

The Sb-Hg stage followed intensive intermineralization tectonics and comprises 2 substages. In the older quartz-carbonate substage, carbonates (Fe-dolomite to ankerite) predominate, especially in the upper and most distant parts of the veins, accompanied by rare quartz and occasional sulfides, sulfosalts and electrum. The stibnite substage with abundant stibnite, pyrite, marcasite in the quartz-chalcedony vein is best developed on the underlying structures of the Schrämen vein, mainly in the Šturec area. It forms veins, metasomatic bodies and veinlets with abundant stibnite, pyrite and marcasite. Towards depth, the Sb content decreases and stibnite is replaced by marcasite. The veins are about 300 m long, 0.5 to 2 m thick. On average, they contained 3% Sb and in 1971-1972, 25.8 kt of Sb ore was extracted from them. In the 2nd vein system, stibnite crystals occur in cavities of older precious metal mineralization, accompanied by dark opal. Less significant stibnite mineralization is also present in the northern (Hlavná and Kirchberg veins) as well as in the southern parts of the vein system (Horná Ves, Bartošova Lehôtka) (Böhmer 1966).

Extensive wall-rock alteration include adularia, quartz, illite, with variably occurring pyrite and carbonates. Kaolinite occurs mainly in the rock and veins at depths of up to 100-200 m and indicates the presence of extensive areas of steam-heated, low-pH waters that accompanied the veins at a level close to the paleosurface. Based on the study of

fluid inclusions and isotopic geothermometry, stibnite veins formed above the level of boiling of fluids at temperatures of ~90-130 °C (Böhmer 1966; Koděra et al. 2014).

3 Stibnite at the Zlatá Baňa deposit

The Zlatá Baňa intermediate-sulfidation Pb-Zn-Au-Ag-Sb deposit is located in the northern part of the Eastern Slovak Neogene Volcanic Filed in the Slanské Vrchy Mts. in the central zone of the Zlatá Baňa andesite stratovolcano. In the central part of this zone, predominantly Pb-Zn-Au±Cu-Ag veins and veinlets are present, while younger Sb±Au-Ag and Sb±Hg mineralization occurs in its marginal parts (Štohl et al. 1994). Veins with Sb-Au-Ag mineralization were mined from the 17th century until the beginning of the 20th century.

Stibnite is a part of the youngest stages of mineralization, which were preceded by Au-Ag mineralization and base metal mineralization. There are three stibnite veins on the northern edge of the deposit (Gašpar and Jozef with Sb±Au-Ag mineralization), one vein is in the southern margin of the central zone (Nozger with Sb±Hg mineralization) and rarely stibnite also occurs in base metal veins in the central part of the ore field, where the Sb mineralization is younger. Stibnite is found on veins, lenses and hydrothermal breccias in silicified and pyritized zones with a thickness of up to 5 m, but individual veins are only 0.1 m thick. The vein filling consists of quartz, carbonates (mainly dolomite) and chalcedony (in subsurface parts). Usually coarse-grained stibnite forms irregular, often monomineralic veins. It is associated with quartz, pyrite and rare arsenopyrite. In the central part of the ore field, various Ag-Pb-Sb sulfosalts are associated with stibnite (Ďuďa 1992).

Mineralization and hydrothermal breccias are accompanied by illitization, which has a regional distribution in the central part of the field, passing towards margins into smectite alteration and into the most external propylitization. The surrounding alteration locally overlaps with advanced argillization, related to intrusions of diorite porphyry in the ore fields (Štohl et al. 1994). According to Jeleň and Kovalenker (1995) Sb±Au-Ag mineralization crystallized from fluids at 200-150 °C.

4 Methodology

The studied samples come from historical collections archived at the Comenius University in Bratislava and at the Geological Institute of D. Štúr, including 17 stibnites, 5 sphalerites and 2 pyrites from different parts of both deposits. Samples of pure sulfides were fragmented, sieved and hand-picked under a binocular microscope to confirm mineral purity. Sulfur isotopes were measured on a MAT 253 mass spectrometer connected to a Flash2000HT Plus elemental analyzer via a ConFlo IV continuous flow interface (at the Slovak Academy of Sciences in Banská Bystrica). Sulfide samples (150-400 µg) were mixed with an equal amount of V_2O_5, packed in tin capsules and burned with oxygen in a quartz tube filled with WO3 and electrolytic copper at 1000 °C. The accuracy of the measurements is 0.21 ‰. The isotopic composition of antimony was measured on a Neptune Plus mass spectrometer at the Washington State University. Approximately 50 mg of samples were dissolved in 4 ml of heated, ultrapure aqua regia. The solutions were measured in low resolution mode and in dry plasma. The analytical uncertainty for all samples is 0.02 ‰. Further analytical details can be found in Koděra et al. (2024).

The obtained sulfur isotope data were complemented by an archived set of unpublished $\delta^{34}S_{CDT}$ data from both deposits, obtained in the years 1983 to 1986 at the D. Štúr Institute of Geology in Slovakia.

5 Sb and S isotope fractionation models

The measured $\delta^{123}Sb$ values of stibnite range from –0.15 to +1.28 ‰ in Kremnica and from +0.12 to +1.54 ‰ in Zlatá Baňa. The corresponding sulfur isotope ($\delta^{34}S$) analyses of stibnite range from +0.04 to +2.34 ‰ in Kremnica and from –3.88 to –2.11 ‰ in Zlatá Baňa. These data were supplemented by sulfur isotope analyses that are not accompanied by Sb isotope data. For Kremnica, they include two stibnites (+2.73 and +2.84 ‰ $\delta^{34}S$) and two pyrites (–0.56 and +0.82 ‰ $\delta^{34}S$). From Zlatá Bana, six sphalerite samples gave a range from –1.42 to +0.55 ‰ $\delta^{34}S$.

Both investigated isotopic systems show the same evolution pattern in the $\delta^{123}Sb$ versus $\delta^{34}S$ diagram (Fig. 1). This pattern, at least for $\delta^{123}Sb$ values, is comparable to the recent studies of Zhai et al. (2021) and Kaufmann et al. (2024). These authors determined that within a single mineralization stage, $\delta^{123}Sb$ values in the mineralizing system evolve in a monotonous fashion and increase with the progressive precipitation of Sb minerals. Zhai et al. (2021) used this trend in $\delta^{123}Sb$ values to determine the direction of fluid flow and estimated the Sb isotope fractionation factor between stibnite and fluid: $\alpha_{fluid\text{-}stibnite} = 0.9994$, but the dependence of the fractionation on temperature or Sb speciation in the fluid is not yet known. Assuming that the gradual increase in $\delta^{123}Sb$ values corresponds to the precipitation process in the hydrothermal system, its consequence could be a correlation with $\delta^{34}S$ values (Fig. 1). The observed trend can be interpreted as an initial increase in $\delta^{34}S$ values by about 2‰, but a decrease occurred in the youngest stibnite. The trend is similar for both studied deposits, although $\delta^{34}S$ values in Kremnica are systematically higher than in Zlatá Baňa. Changes in $\delta^{123}Sb$ and $\delta^{34}S$ values indicate that the S pool in the fluid was not significantly larger than the Sb pool. This implies that the fluids carried a small amount of Sb complexes (mainly in the form of the $H_2Sb_2S_4(aq)$ complex or its deprotonated

forms), but also a small amount of S complexes other than Sb-S complexes (H_2S(aq) and HS^-).

To model the changes in sulfur isotopic composition associated with stibnite precipitation from low-temperature hydrothermal fluid, we constructed a Rayleigh fractionation model, which is graphically represented by the green curves in Figure 1. For this model, we assume a Sb isotope fractionation factor $\Delta_{fluid\text{-}stibnite}$ = 0.9994 (Zhai et al. 2021) and a S isotope fractionation factor $\alpha_{stibnite\text{-}H2S}$ = 0.9958, which was calculated from the S isotope fractionation between stibnite and H_2S $\Delta_{stibnite\text{-}H2S}$ = –4.2 ‰ at 150 °C (Ohmoto and Rye 1979). These two coupled Rayleigh models assume that stibnite is the only crystallizing solid that acquires Sb and S from the fluid. It can be seen from Figure 1 that the models reproduce well the increase in $\delta^{34}S$ values of stibnite, which is accompanied by a gradual increase in $\delta^{123}Sb$ values. The slope of the data points for the Zlatá Baňa samples can be well described by a fluid with a m_S/m_{Sb} ratio of ~ 2. The Kremnica data are better described by a fluid with a higher sulfur content, with a m_S/m_{Sb} ratio of ~ 3-4.

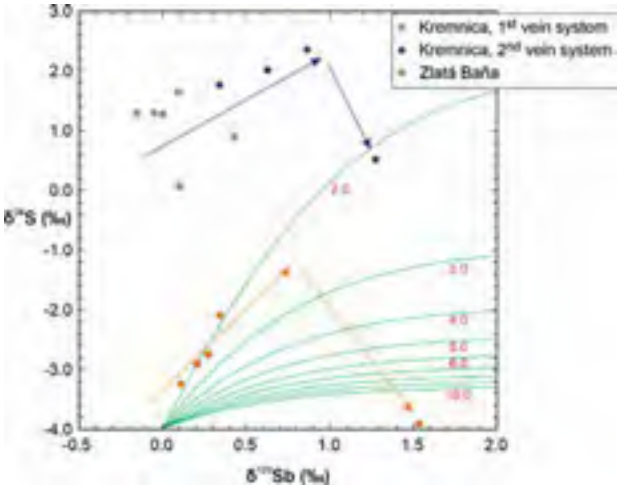


Figure 1. Isotopic composition of stibnite samples from Zlatá Baňa (orange) and Kremnica (1st vein system – grey, 2nd vein system – blue). Blue and orange arrows show the assumed evolution of Sb-S isotopic values. Green curves show the simultaneous Rayleigh fractionation of Sb and S isotopes upon stibnite crystallization, and they show the isotopic composition of the instantaneous product, i.e., stibnite. The curves are marked with the molar ratios m_S/m_{Sb} in the fluid (red numbers). The starting fluid for the samples from Zlatá Baňa has a composition of 0.6 ‰ $\delta^{123}Sb$ and 0.4 ‰ $\delta^{34}S$ and the $\alpha_{stibnite\text{-}H2S}$ fractionation factor was calculated for 150 °C. The very first stibnite crystal has a composition of 0.0 ‰ $\delta^{123}Sb$ and –4.0 ‰ $\delta^{34}S$. Note that the starting composition can be arbitrarily chosen, resulting simply in the translation of the calculated (green) curves. For the Kremnica samples, the starting point should be chosen with a higher $\delta^{34}S$ than for the Zlatá Baňa samples.

In both deposits, the highest $\delta^{123}Sb$ values are accompanied by a sudden decrease in $\delta^{34}S$ values, probably due to the onset of sulfide or sulfate precipitation. The mineralogical and textural data from both deposits indicate that stibnite crystallization was accompanied or followed by pyrite or marcasite crystallization, or anhydrite or barite crystallization, respectively. Since the fractionation of these sulfides is $\Delta_{pyrite\text{-}H2S}$ = +1.8 (at 200 °C) or +2.9 ‰ (extrapolated to 100 °C; Ohmoto and Rye 1979), precipitation of pyrite or marcasite depletes the fluid of the heavier isotope (^{34}S) and leads to a decrease in the $\delta^{34}S$ values of the subsequently precipitated sulfide minerals. A similar effect, with a much larger fractionation, is associated with the oxidation of sulfide to sulfate, with a value of $\Delta_{sulfate\text{-}H2S}$ = +29.5 (at 200 °C) or +43.8 ‰ (extrapolated to 100 °C; Ohmoto and Rye 1979). The onset of precipitation of these minerals therefore gradually leads to a lighter sulfur isotopic composition in them, but also in associated minerals including stibnite.

The sulfur isotopic composition of the Kremnica stibnites is about 4.4‰ heavier than the stibnites from Zlatá Baňa. A similar difference in $\delta^{34}S$ is also visible in other sulfides from these two deposits, including sulfides from earlier stages with higher temperatures. This difference is probably related to the different isotopic composition of the parental hydrothermal fluids and not to the specific conditions of stibnite crystallization in the studied deposits. The sulfur isotopic composition of calc-alkaline hydrothermal systems can be influenced by several factors, such as crustal assimilation, degassing processes, or contamination of the source mantle magmas by the subducted slab. We assume that the difference in the sulfur isotopic composition of the studied deposits could be related to the different magmatic-hydrothermal evolution and lithospheric processes in the Central and Eastern Slovak Volcanic Fields. This is probably also related to regional metallogenesis, as the Central Slovak Volcanic Field is much richer in ore deposits than the Eastern one.

6 Genesis of epithermal stibnites

In hydrothermal fluids, Sb mobility depends on temperature, pH and sulfur fugacity, which also corresponds to observations from active geothermal areas with stibnite precipitation in boreholes (Wilson et al. 2007). In hydrothermal Sb deposits, stibnite is abundant in late mineralization stages and generally precipitates from moderately saline fluids (3.5–6.5 wt% NaCl eq.) and at low temperature (<200 °C) (Wiliams-Jones and Normand 1997). In low-sulfidation epithermal systems, fluids have lower salinity because they have a significant proportion of meteoric water. The low stibnite crystallization temperature here is probably caused by the low total Sb concentration in the fluids, which results in Sb supersaturation occurring only at lower temperatures. A decrease in temperature is considered to be the main mechanism of stibnite precipitation, especially if Sb is transported in the form of neutral hydroxyl complexes. A sharp drop in pH can also be a significant cause of stibnite precipitation (Williams-Jones and Normand 1997).

At Kremnica and Zlatá Baňa, both types of stibnite precipitation mechanisms could have operated (Fig. 2). Since stibnite crystallization occurred only in the final stages of hydrothermal activity, fluid cooling was certainly an important factor. However, fluid acidification was probably also significant, since Sb transport occurred mainly in the form of the $HSb_2S_4^-$ complex, the stability of which is sensitive to cooling and acidification. Fluid acidification is indicated by the presence of illite-kaolinite ± smectite alteration in the vicinity of the veins. According to Hedenquist and Arribas (2022), such an association of alteration minerals is a consequence of the presence of steam-heated condensate enriched in CO_2 and H_2S, which is commonly present at the margins and at the end of the activity of epithermal systems and originates from the boiling of the fluid flowing from deeper parts of the system. The condensate is represented by an electrolyte-free solution with a temperature of ~120-170 °C, present at a depth of several hundred meters. The formation of sulfates in the condensate is minor, since below the groundwater level there is only a low content of dissolved oxygen in the meteoric water. In contrast, the steam-heated zone above the groundwater level is affected by acid leaching due to H_2S oxidation. In late stages, the sufficiently cooled and almost neutral Sb-containing fluid can mix with the steam-heated, slightly acidic, CO_2-rich condensate (Fig. 2). The combination of both processes thus makes stibnite precipitation more efficient, even if the fluid contains only sub-ppm concentrations of Sb. This interpretation is also supported by the typical location of stibnite veins at the edges of both studied epithermal deposits, since in low- and intermediate-sulfidation epithermal systems, CO_2-rich condensate occurs just in their marginal parts (Hedenquist and Arribas 2022).

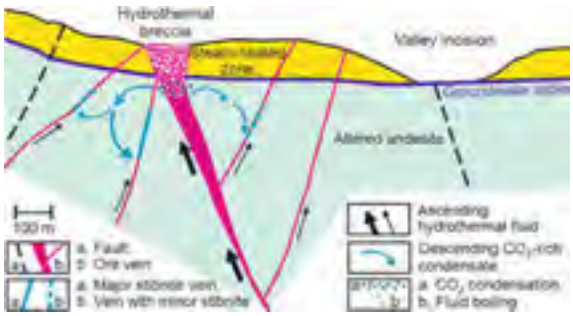


Figure 2. Schematic model of the formation of stibnite veins in late stages and on margins of low- to intermediate-sulfidation sulfidation systems. Effective crystallization of stibnite is associated with cooling of ascending hydrothermal fluids and is further enhanced by mixing with mildly acidic CO_2-rich condensate. The model was created using the schemes in Sillitoe (2015) and Hedenquist and Arribas (2022).

Acknowledgements

The research was supported by grants APVV-22-0134 and VEGA 1/0313/20. J. Majzlan was financially supported by a Deutsche Forschungsgemeinschaft grant MA 3927/43-1. R. Mathur acknowledges NSF EAR grant no. 2233426.

References

Böhmer M (1966) Geology and mineral associations of gold-bearing veins in the central part of the Kremnica ore field. Acta Geol Geogr Univ Comenianea, Geologica 11:5-123 (in Slovak)

Hedenquist JW, Arribas A (2022) Exploration implications of multiple formation environments of advanced argillic minerals. Econ Geol 117:609–643

Jeleň S, Kovalenker VA (1995) Thermodynamic conditions for the formation of Au-Ag base metal mineralization at the Zlatá Baňa deposit. Proceedings of the conference Third geological days of Ján Slávik, Geologický ústav D. Štúra, Bratislava, pp 71–74 (in Slovak)

Kaufmann A, Lazarov M, Weyer S, Števko M, Kiefer S, Majzlan J (2024) Changes in antimony isotopic composition as a tracer of hydrothermal fluid evolution at the Sb deposits in Pezinok (Slovakia). Miner Depos 59, 559-575

Koděra P, Lexa J, Fallick AE, Wälle M, Biroň A (2014) Hydrothermal fluids in epithermal and porphyry Au deposits in the Central Slovakia Volcanic Field. In: Garofalo PS, Ridley JR (eds) Gold-transporting Hydrothermal Fluids in the Earth's Crust. Geol Soc Lond Spec Publ 402:177–206

Koděra P, Mathur R, Zhai D, Milovský R, Bačo P, Majzlan J (2024) Coupled antimony and sulfur isotopic composition of stibnite as a window to the origin of Sb mineralization in epithermal systems (examples from the Kremnica and Zlatá Baňa deposits, Slovakia). Miner Depos. https://doi.org/10.1007/s00126-024-01333-9

Molnár F, Nagymarosy A, Jeleň S, Bačo P (2010) Minerals and wines: Tokaj Mts., Hungary and Slanské vrchy Mts., Slovakia. Acta Mineralogica-Petrographica, Field Guide Series 15

Ohmoto H, Rye RO (1979) Isotopes of sulfur and carbon. In: Barnes HL (ed.) Geochemistry of hydrothermal ore deposits. John Whiley & Sons, pp 509–561

Sillitoe RH (2015) Epithermal paleosurfaces. Miner Depos 50, 767–793

Štohl J, Lexa J, Kaličiak M, Bacsó Z (1994) Metallogeny of stockwork base metal mineralizations in Neogene volcanics of Western Carpathians. Mineralia Slovaca 26:75–117 (in Slovak with English summary)

Wilson N, Webster-Brown J, Brown K (2007) Controls on stibnite precipitation at two New Zealand geothermal power stations: Geothermic 36:330–347

William-Jones AR, Normand C (1997) Controls of mineral parageneses in the system Fe-Sb-S-O. Econ Geol 92:308–324

Zhai D, Mathur R, Liu SA, Liu J, Godfrey L, Wang K, Vervoort J (2021) Antimony isotope fractionation in hydrothermal systems. Geochim Cosmochim Acta 306:84–97.

Understanding Overlapping Mineralizing Systems of the Ruby Hill Project, Eureka, NV

Alyssa Lindsey[1], Simon M. Jowitt[1]
[1]Ralph J. Roberts Center for Research in Economic Geology, Nevada Bureau of Mines and Geology, University of Nevada, Reno, USA

Abstract. The historic Eureka district outside Eureka, NV, hosts gold, silver, base metal, and critical mineral deposits. This study focuses primarily on the northern extent of the Eureka Mining District, the historic Ruby Hill property. Mineralization styles in the project area includes zinc skarn, carbonate replacement deposit (CRD), distal disseminated Ag-Au, and Carlin-type. Samples and data from drilling provide a guide to determine the spatial, temporal and genetic relationships between skarn, CRD, distal-disseminated, and Carlin-type deposits. Preliminary analysis of core and petrographic sections have identified complex overlapping events with evidence of repeated paragenesis and mineralogical variation between zones. Initial interpretation of geochemical data for the intrusions in the Ruby Hill project area suggests that units likely belong to a single, cogenetic magmatic suite with a similar fractionation history. Ongoing work aims to establish complete paragenetic sequences and geochemical zonation for each deposit, alongside characterization of alteration styles and zoning within the Cretaceous intrusions. These analyses will be complemented by U-Pb dating of zircon, garnet, and calcite to constrain the timing of magmatic and hydrothermal events.

1 Introduction

The Ruby Hill project is part of the Eureka Mining District, located west of the town of Eureka in central Nevada. Mining history began in 1862 with the discovery of an oxidized Pb-Zn-Au-Ag ore body at surface (Curtis 1884). The scope of this study is limited to the northern region of the district, the Ruby Hill property, which hosts zinc skarn, carbonate replacement deposits (CRD), distal disseminated Au-Ag, and Carlin-type occurrences (Fig. 1). These are all important mineralization styles that can be sources of precious metals, base metals, and critical metals (e.g. In, Ge, Ga, Te). In a model system, one would see a gradation from relatively higher temperature zinc skarn to distal CRD extending to distal-disseminated mineralization (Sillitoe 2010). At Ruby Hill however, some of the different mineralization styles appear to overlap. To understand the complex relationships that this system exhibits, a multidisciplinary approach is needed.

Research conducted for this project includes detailed petrographic analysis and geochemical analysis to characterize the mineralized zones and intrusive units. The characterization will be complemented with U-Pb radiometric dating on zircons, calcite, and garnets. These techniques will provide a foundation for understanding the spatial, temporal, and genetic relationships between mineralized zones.



Figure 1. Map of study area with white stars depicting locations of mineralized zones discussed in this research.

2 Geologic Background and Mineralization

2.1 Regional Geology

The Eureka Mining district lies at the southeastern end of the Battle Mountain-Eureka Carlin-type mineralization trend. The district's sedimentary sequence, which hosts mineralization, was deposited along a passive continental margin from the Cambrian to Ordovician and consists primarily of limestone, dolomite, and quartzite with minor siltstone and shale. The region was tectonically active during the early Cretaceous (100-120 Ma), as part of the Central Nevada fold and thrust belt that formed during the Sevier orogeny (50-155 Ma), characterized by regional thrust faults and the formation of the Eureka culmination—an anticline formed as a fault bend fold from the Ratto Canyon thrust sheet (Long et al. 2014).

The compressional regime was accompanied by magmatism in the late Cretaceous, evidenced by the intrusion of the Ruby Hill Stock and Graveyard Flats Stock, dated between 105 and 107 Ma (Vikre 1998). Mid-Cretaceous base-metal mineralization includes zinc skarn, CRD, and distal-disseminated gold-silver occurrences (Fig. 2A-E). Although mineralization has not been directly dated, the spatial relationship with Cretaceous intrusive units and post-mineral offset on Basin and Range extensional faults provide evidence for a Cretaceous age (Vikre 1998). In addition, recent Re-Os dating by i-80 Gold Corp. on molybdenite from the Ruby Hill Stock yields an age of 108.4 ± 0.5 Ma.

Post-Cretaceous tectonics transitioned from compression to extension, reactivating many former

compressional structures as extensional features. This period formed significant district-scale NW-SE and NE-SW normal faults, notably the Jackson-Holly fault system, which is believed to be a regional conduit for Carlin-type deposits (Hoge et al. 2015). Eocene magmatic activity involved the emplacement of andesite dikes and associated andesite to rhyolite volcanic flows, aligning with regional tectonic trends across the Basin and Range (Long et al. 2014).

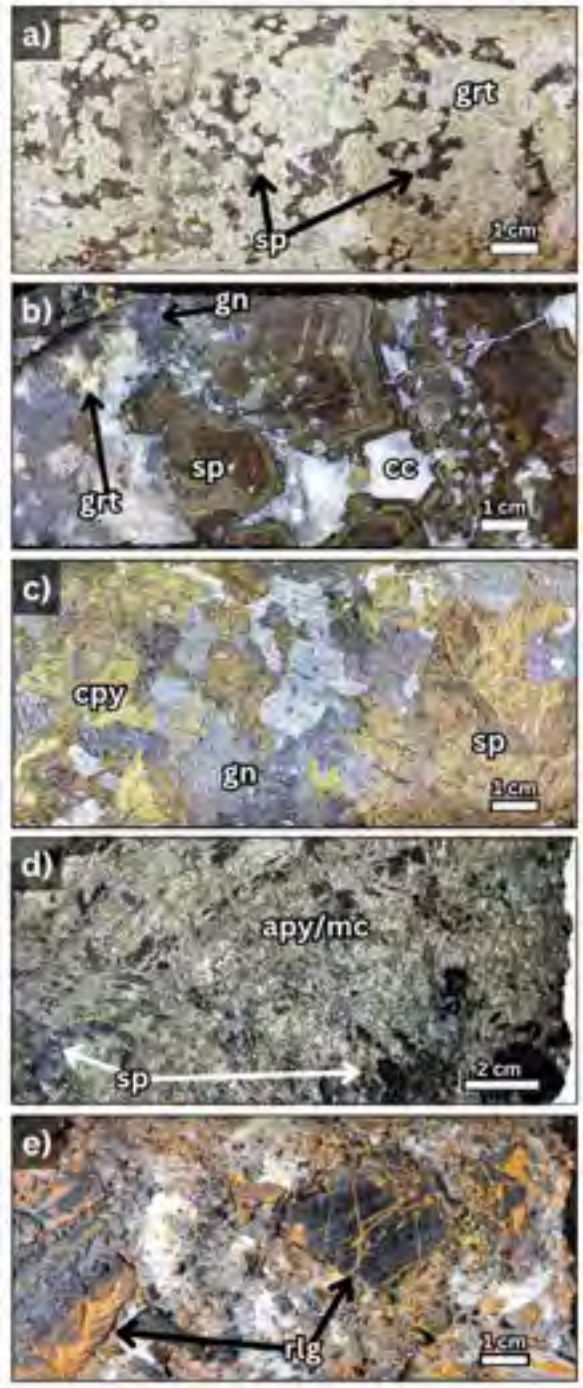


Figure 2. Core photos depicting mineralization styles. A) Zinc skarn mineralization with brown sphalerite (sp) filling in space between green garnets (grt). B) Zinc skarn mineralization with garnet, galena (gn), calcite (cc), pyrite (py), and large, well-formed banded sphalerite. C) Hilltop CRD mineralization with sphalerite, galena, chalcopyrite (cpy), and calcite. D) CRD sample from Fad exhibiting well-formed marcasite (mc) crystals coated with arsenopyrite (apy) and sphalerite. E) Carlin-type mineralization hosted in silicified and brecciated silty limestone with abundant realgar (rlg) from the Ruby Deeps Zone

3 Methods and Data

Samples from 166 drillholes in the northern extent of the district were collected and analyzed. A total of 16,607 sample assays from 86 drillholes were provided by i-80 Gold Corp; these were analyzed by 4-acid digest with AES finish for a 35-element suite. Further analysis of 66 whole rock bulk intrusive samples was conducted at ALS.

From the 108 samples collected, 89 polished petrographic sections were prepared representing mineralized zones and intrusive units. The polished sections were examined with an Olympus binocular petrographic microscope in reflected and transmitted light. Samples from the distal-disseminated Mineral Point deposit have not been available for this project and historic assay data is limited.

4 Initial Results

4.1 Carlin-Type Mineralization

The youngest recognized mineralization style in the district is assumed to be Eocene Carlin-type gold mineralization located throughout the Eureka mining District. The mineralization timing and characterization are inferred based on typical Carlin-type mineralogy, alteration, geochemical signatures, relation to Eocene structures, and apatite fission track analysis (Hastings et al. 2008).

The Carlin-type Ruby Deeps refractory deposit and 426 oxide deposit has a total indicated resource of 1,791,000 tonnes with 436,000 ounces Au at 7.6 g/t and 92,000 ounces Ag at 1.6 g/t. The total inferred resource is 4,188,000 tonnes with 988,000 ounces Au at 7.3 g/t and 286,000 ounces Ag at 2.1 g/t. The refractory deposit is characterized by arsenian-pyrite rims around pre-existing pyrite grains, an abundance of orpiment and realgar, and the absence of base metal sulfides. Brecciation is common and typical alteration is comprised of decarbonatization and silicification (Fig. 2e). The 426 oxide deposit is similar, but strongly oxidized and mineralization is hosted in breccias, gouge, and surrounding limestone units.

4.2 Zinc Skarn Mineralization

The Blackjack zinc skarn is located on the margin of the Graveyard Flats stock in the Goodwin limestone formation. A key intercept from drilling undertaken by i-80 includes 116.3 m at 10.1% Zn, 0.6% Pb, 37.0 g/t Ag, and 0.3 g/t Au. The contact between the strongly altered stock and limestone is irregular and mineralization extends into the stock as endoskarn and as replacement of xenoliths. The Blackjack occurrence is characterized by semi-massive to massive sulfides-primarily sphalerite with lesser

galena, chalcopyrite, pyrite, marcasite, pyrrhotite, arsenopyrite, and tennantite/tetrahedrite. Mineralization is associated with prograde skarn minerals, predominantly garnet with minor pyroxene, and wollastonite (Fig. 2a). In many samples, sulfides replace the earlier garnet phase (Fig. 3a). Early pyrrhotite is also partially to fully replaced by pyrite, marcasite, and sphalerite (Fig. 3c).

Previous research describes two distinct phases of sphalerite, the first is fine-grained sphalerite and the second is finely banded sphalerite (Vikre 1998). The fine-grained sphalerite appears homogenous in color, often dark red-brown, and is present as smaller mm-scale crystals (Fig. 2a). The finely banded sphalerite is well-zoned, light brown to dark brown in color and coarser grained, up to a maximum of 10 cm in diameter (Fig. 2b- c). Both sphalerite types occur in the zinc skarn; and preliminary analysis corroborates the previous determination that the finely banded sphalerite is younger than the fine-grained sphalerite.

4.3 CRD Mineralization

CRD occurrences extend across the entire Eureka Mining District and are hosted in a variety of limestone and dolomite units. The Hilltop occurrence is located proximal to the Blackjack zinc skarn and the Fad deposit is 2 km south of Hilltop (Fig. 1)

The Hilltop occurrence is characterized by massive sulphide replacement bodies composed primarily of sphalerite, galena, pyrite, and chalcopyrite (Fig. 2h). Hilltop petrography has revealed an early euhedral pyrite phase followed by multiple phases of sphalerite, galena, chalcopyrite, and tetrahedrite (Fig 3e). Assays released by i-80 Gold Corp. include 3.1 m at 4.2 g/t Au, 433.6 g/t Ag, 20.7 % Zn, 12.4 % Pb, and 0.6 % Cu.

The Fad deposit has a historic resource of 3,540,173 tons at 5.14 g/t Au, 196.46 g/t Ag, 8.0% Zn, and 3.8% Pb. Mineralization is composed primarily of sphalerite, galena, bornite, pyrite, marcasite, and arsenopyrite (Fig. 3e-g). A diverse assemblage of accessory minerals is present, including proustite, pyrargyrite, bournonite, covellite, tetrahedrite, and electrum. Fad samples appear heavily fractured, likely due to post-mineral faulting. Based on cross-cutting relationships and mineral assemblages, arsenopyrite appears to have formed first, followed by marcasite (Fig. 3e). Subsequently, sphalerite and galena formed. Bornite is the last major mineral phase and appears to preferentially replace marcasite and arsenopyrite (Fig. 3g).

Both Hilltop and Fad contain oxidized zones that are characterized by cerussite ($PbCO_3$), anglesite ($PbSO_4$), smithsonite ($ZnCO_3$), and concentration of Au due to weathering processes. Assays released from i-80 in 2023 highlight the elevated gold values with an intercept of 60.2 g/t Au, 908.7 g/t Ag, 1.1% Zn, and 15.7% Pb over 10 m.

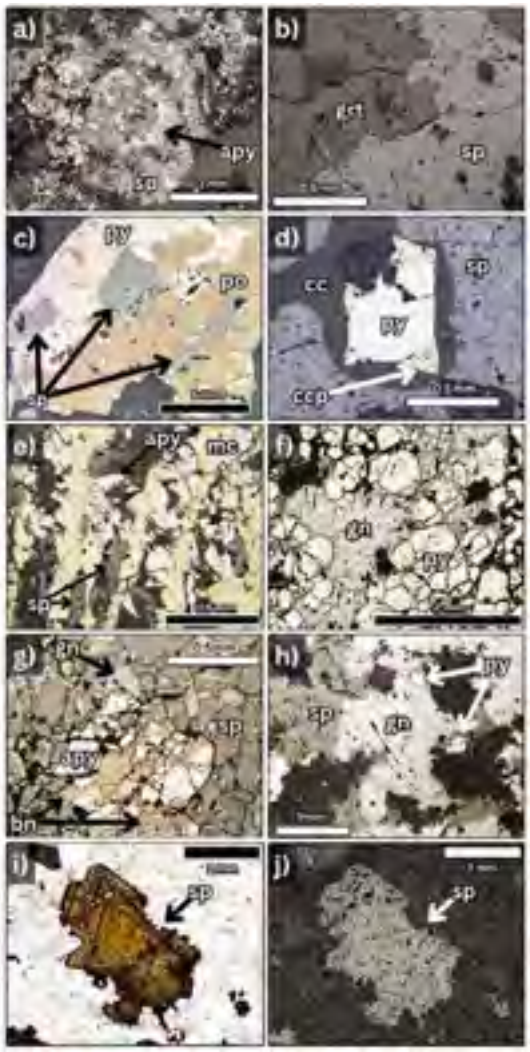


Figure 3. Photomicrographs of skarn and CRD samples. A) Skarn sample with relict garnet replaced by sphalerite (sp) and arsenopyrite (apy). B) Skarn sample with sphalerite surrounding garnet (grt). C) Skarn sample exhibiting pyrrhotite (po) largely replaced by pyrite (py) with sphalerite. D) Skarn sample with euhedral pyrite partially replaced by chalcopyrite (ccp), sphalerite, and calcite (cc). E) CRD sample with intergrown arsenopyrite and marcasite (mc). F) CRD sample with pyrite and galena. G) Brecciated CRD sample, sphalerite and galena with bornite (bn) and arsenopyrite. H) CRD sample with early pyrite, galena and sphalerite with chalcopyrite disease. I) Zoned sphalerite crystal in calcite matrix (transmitted light). J) Sample (I) in reflected light. Sphalerite in B), D) and I)-J) exhibits chalcopyrite disease

4.4 Intrusive Geochemistry

Previous work has identified 3 Cretaceous units: The Ruby Hill Stock, The Graveyard Flats Stock, and the Bullwhacker Sill. These units are calc-alkaline with intermediate composition (Fig. 4). Multi-element spidergrams (Thompson, 1982; McDonough and Sun, 1995) show consistent trends across all samples, with negative anomalies in Ta and Nb. These features are typical of arc-related magmatism and align with Cretaceous intrusive trends across the Great Basin (Barton, 1990). These patterns suggest that the intrusive units likely belong to a single, cogenetic magmatic suite.

Observational differences can likely be attributed to variable alteration; early petrographic and core observations indicate that the intrusions are overprinted by potassic, phyllic, and argillic alteration with varying intensity. Ongoing work aims to classify this alteration and assess the spatial distribution of these assemblages to determine if alteration zoning is present.

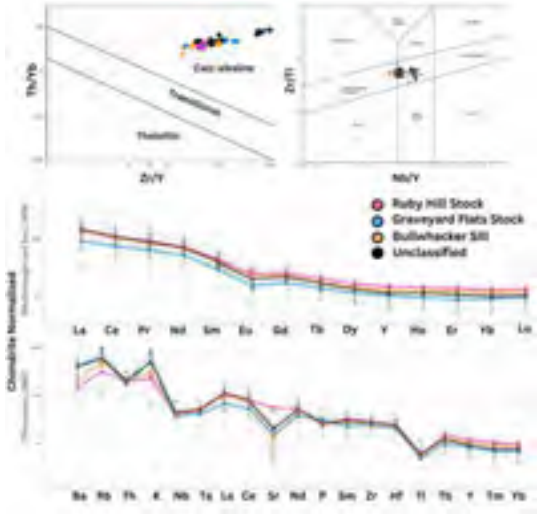


Figure 3. Geochemical classification and multi-element diagrams for Cretaceous intrusive rocks from the Ruby Hill property. The Zr/Y vs. Th/Yb diagram (top left) indicates calc-alkaline affinity (Ross et al. 2009). The Nb/Y vs. Zr/Ti classification diagram (top right) suggests samples are intermediate in composition (Pearce, 1996). Chondrite- and primitive mantle-normalized multi-element variation diagrams (bottom) highlight consistent fractionation patterns (Thompson 1982; McDonough and Sun, 1995). Colors represent logged intrusive units: Ruby Hill Stock (pink), Graveyard Flats Stock (blue), Bullwhacker Sill (orange), and unclassified intrusions (black).

5 Future Work

Future work will focus on detailed petrographic analysis using transmitted, reflected, and fluorescent light to establish paragenetic sequences for each mineralized zone. These observations will be complemented by scanning electron microscope (SEM) analysis to obtain electron dispersive spectra (EDS) and backscattered electron images. Further geochemical and petrographic analysis of intrusive data will characterize alteration in the intrusive units and assess potential alteration zoning. While analysis of assay data will aid in identifying major and minor element zonation patterns within the system. These analyses will be integrated with U-Pb radiometric dating of zircon, calcite, and garnet to constrain the timing of intrusive emplacement and mineralization events.

6 Conclusions

Initial results reveal the complex and overlapping mineralization styles present at the Ruby Hill project evidenced by overlapping assemblages, repeated paragenesis, and replacement textures. In addition, Cretaceous intrusive units likely represent a single magmatic suite with varying degrees of alteration; however, further work is necessary to provide a complete characterization of the system.

Acknowledgements

This work is part of a master's thesis with expected completion in January 2026. We thank i-80 Gold Corp for access to data and drill core for this research. We also appreciate the support and guidance provided during our research by the University of Nevada, Reno, the Nevada Bureau of Mines and Geology, and Ralph J. Roberts Center for Research in Economic Geology.

References

Barton MD (1990) Cretaceous magmatism, metamorphism, and metallogeny in the east-central Great Basin. In: Wernicke BP (ed) Basin and Range extensional tectonics near the latitude of Las Vegas, Nevada. Geol Soc Am Mem 174:283–302

Curtis JS (1884) Silver-lead deposits of Eureka, Nevada. US Geol Surv Monogr 7:1–200

Hastings MH (2008) Relationship of base-metal skarn mineralization to Carlin-type gold mineralization at the Archimedes gold deposit, Eureka, Nevada. MSc thesis, University of Nevada, Reno, 111 pp

Hoge J, Pennell WM, Garside LJ (2015) The Jackson-Lawton-Bowman normal fault system and its relationship to Carlin-type gold mineralization, Eureka district, Nevada. In: Pennell WM, Garside LJ (eds) New Concepts and Discoveries: Geological Society of Nevada Symposium Proceedings, May 2015, Sparks, Nevada. Vol 2, pp 967–1000

Long SP, Henry CD, Muntean JL, Edmundo GP, Cassel EJ (2014) Early Cretaceous construction of a structural culmination, Eureka, Nevada, U.S.A.: Implications for out-of-sequence deformation in the Sevier hinterland. Geosphere 10:564–584. https://doi.org/10.1130/GES00997.1

McDonough WF, Sun S-s (1995) The composition of the Earth. Chem Geol 120:223–253

Pearce JA (1996) A user's guide to basalt discrimination diagrams. In: Wyman DA (ed) Trace element geochemistry of volcanic rocks: applications for massive sulphide exploration. Geol Assoc Can Short Course Notes 12:79–113

Ross PS, Bédard JH (2009) Magmatic affinity of modern and ancient subalkaline volcanic rocks determined from trace-element discriminant diagrams. Can J Earth Sci 46:823–839. https://doi.org/10.1139/E09-054

Sillitoe RH (2010) Porphyry copper systems. Econ Geol 105:3–41. https://doi.org/10.2113/gsecongeo.105.1.3

Thompson RN (1982) Magmatism of the British Tertiary Volcanic Province. Scott J Geol 18:49–107. https://doi.org/10.1144/sjg18010049

Vikre PG (1998) Intrusion-related, polymetallic carbonate replacement deposits in the Eureka district, Eureka County, Nevada. Nev Bur Mines Geol Bull 111:1–58

Comparing magmatism and hydrothermal alteration using magnetic modelling and stable isotopes at the Clementine porphyry copper prospect, Montana, USA

Benjamin P. Magnin[1], Julia A. McIntosh[1], George H. Brimhall [2]
[1] U.S. Geological Survey, Denver, USA
[2] Clementine Exploration LLC, Wise River, USA

Abstract. Recent mapping of the underexplored Clementine prospect in southwestern Montana has revealed evidence of hydrothermal alteration and mineralized breccia vein gossan interpreted to represent the upper expression of a Cretaceous, sediment-hosted copper porphyry system. The prospect is at the nexus of several Cretaceous granites, including the pre-mineralization Butte Granite and Big Hole Canyon plutons and local pre- to post-mineralization granite intrusions. Here, 3D magnetic inversions and stable isotope data are used to evaluate the spatial and genetic relationship of mineralization and Cretaceous magmatism. Magnetic inversions reveal a zone of high magnetic susceptibility beneath the prospect that is related to an exposure of unaltered, likely post-mineralization granite. The granite appears to connect to the Big Hole Canyon pluton at depth, suggesting it is a late-stage differentiate of the cooling, pre-mineralization pluton that may have been one of several potential heat sources for the mineral system at Clementine. This is supported by carbon isotope values of graphite that indicate organic material in shale of the Cretaceous Kootenai Formation was subject to metamorphism. Preliminary light hydrogen isotope values of actinolite hydrothermal orbs suggest formation following magmatic outgassing during thermal advection from an underlying intrusion.

1 Introduction

The Clementine prospect of southwestern Montana, ~30 km southwest of the porphyry and vein deposits at Butte (Fig. 1A), has received little attention for mineral exploration due to its rough topography, dense vegetation, and limited road access. Recent geologic mapping has uncovered evidence of hydrothermal alteration and local Cu-W-As-Sb breccia vein gossan spatially associated with the Cretaceous Big Hole Canyon pluton (BHCp) and Butte Granite of the Boulder Batholith (Fig. 1B; Brimhall, 2018). The main alteration assemblage observed at the prospect are spherical actinolite-titanite-calcite orbs and disseminated chalcopyrite (Brimhall and Fanning 2019). Similar orbicular alteration was documented in skarn from the Carr Fork area at Bingham, UT and is associated with a contact metamorphism aureole (Atkinson and Einaudi 1978). At Clementine, these alteration zones are distal to the breccia vein gossan, and they are interpreted to represent the alteration halo of a sediment-hosted porphyry copper system (Brimhall 2023). Based on U-Pb dating of hydrothermal titanite, the age of mineralization is interpreted to be ca. 72.7–70.7 Ma (Brimhall and Fanning 2019; Brimhall 2023), which is younger than both the Butte Granite (U-Pb zircon of 76.9–74.7 Ma; du Bray et al. 2012) and the southern phase of the BHCp (Ar-Ar biotite of 85.7–74.7 Ma; Zinter et al. 1983). The northern phase of the BHCp has not been dated. Neither pluton is hypothesized as the source of metals nor fluids of the mineral system. Instead, a younger intrusion is inferred at depth (Brimhall, 2023).

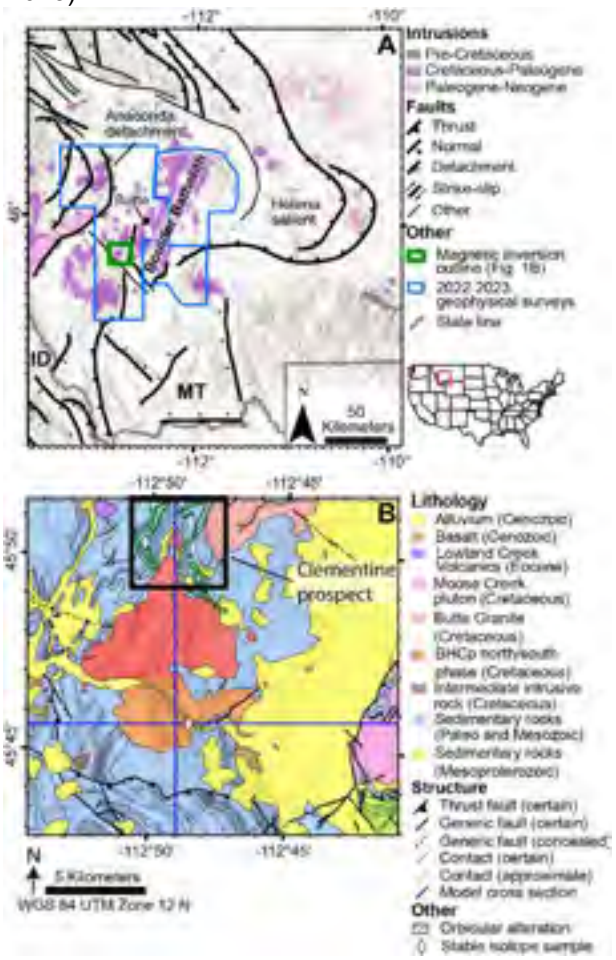


Figure 1. (A) Map of regional structures and magmatism in SW Montana. Geology from Horton (2017). (B) Geologic map of Clementine prospect used for near-surface magnetic susceptibility model. Internal contacts illustrate structure of sedimentary units. Geology from Hespenheide (2003) and McDonald et al. (2012). Orbicular alteration from Brimhall and Fanning (2019).

As part of the Earth Mapping Resources Initiative (Earth MRI), the USGS collected airborne magnetic

data at a 200m line spacing and 80m nominal height to better understand the mineral systems surrounding the Boulder Batholith (Fig. 1A; USGS 2023). This study presents new magnetic modelling of Earth MRI data supplemented by stable isotope measurements of magmatic and hydrothermally formed minerals to better understand Cretaceous magmatism, hydrothermal fluids, and ore formation at the Clementine prospect.

2 Methods

2.1 3D magnetic inversion

Aeromagnetic data were inverted using Mag3D software (Li and Oldenburg 1996) to investigate the subsurface geometry of Cretaceous plutons adjacent to the Clementine prospect, and to evaluate the validity of the interpreted source intrusion beneath mapped altered and mineralized zones (Fig. 1B). The model consists of an orthogonal mesh of contiguous cells that are 150m wide and 75m thick for ¼ the model length, and 150m thick down to ½ the model length. The inversion volume was expanded in the ±x, ±y, and -z direction by three cells (150, 225, and 337.5m wide) to reduce edge effects. Anomalous magnetic field data were decimated so that an average of 2 observations occur over each cell. The magnetic observation height was determined by adding the helicopter's laser altimeter to a 10m digital elevation model (DEM). The same DEM was used to constrain the topography.

A near surface magnetic susceptibility model (≤300m) was created to constrain the inversion and produce geologically realistic results. The model is based on 1:100,000 scale surface geologic mapping (McDonald et al. 2012), topography, estimated unit thicknesses, and magnetic susceptibility measurements collected in the field using an SM-30 magnetic susceptibility meter (Table 1). Additional magnetic susceptibility measurements of the BHCp were incorporated from Hespenheide (2003). Unit thicknesses are based on geology reports (McDonald et al. 2012), and the model assumes vertical lithologic contacts. Maximum, minimum, and average magnetic susceptibility values were assigned to each unit in the model (Table 1). Outside the near-surface model, a constant maximum (0.2 SI), minimum (0 SI) and reference susceptibility (0.001 SI) were assigned. The final model acts as an upper and lower bound, as well as a reference and initial model to constrain the inversion results.

2.2 Stable isotope analytical techniques

Rock samples were collected from outcrops at the Clementine prospect and the southern phase of the BHCp (Fig. 1B). Samples were disaggregated and picked for graphite (treated with 3N HCl to remove calcite) and hydrous minerals including biotite, actinolite, and chlorite.

Graphite (0.8 mg) was loaded into Sn capsules and pyrolyzed in a Thermo Flash 2000 Elemental Analyzer. Carbon isotopic analyses were completed using Thermo Scientific Delta V gas source isotope ratio mass spectrometer (IRMS) at the USGS in Denver (method of Johnson et al. 2018).

Hydrous minerals (1 mg) were loaded into Ag capsules and decomposed in a Thermo Temperature Conversion Elemental Analyzer. Evolved H_2 gas was purified by gas chromatography and analyzed for hydrogen isotopes using a Thermo Scientific Delta V gas source IRMS at the USGS in Denver (method adapted from Sharp et al. 2001).

Carbon and hydrogen isotope ratios are reported in conventional delta notation in units of per mil (‰), as follows: $\delta R = ((R_{sample}/R_{standard}) - 1) \times 1000$, where R is the atomic abundance ratio of $^{13}C/^{12}C$ or $^{2}H/^{1}H$ in the sample and the standards Vienna Pee Dee Belemnite (VPDB) for C and Vienna Standard Mean Ocean Water (VSMOW) for H. Analytical error was ±0.2‰ for $\delta^{13}C$ and ±1‰ for $\delta^{2}H$.

Table 1. Magnetic susceptibility and thickness values for the geologic model. Data from this study and Hespenheide (2003). N–number of measurements, LCV–Lowland Creek Volcanics, MCp–Moose Creek pluton, BHCp–Big Hole Canyon pluton, Inter.–intermediate, and sed.–sedimentary.

Unit	Thickness (m)	Upper Bound (SI)	Lower Bound (SI)	Reference (SI)	N
Alluvium	75	0.000000	0.000000	0.000000	0
LCV	75	0.000759	0.000122	0.000249	32
Basalt	75	0.007440	0.001320	0.002945	16
Inter. intrusions	300	0.085300	0.000714	0.001000	0
Butte Granite	300	0.029400	0.011800	0.021896	48
MCp	300	0.008800	0.000714	0.005262	48
BHCp north	300	0.058200	0.000718	0.037100	21
BHCp south	300	0.132000	0.018500	0.068000	36
Phanerozoic sed. rocks	300	0.000603	0.000000	0.000105	287
Meso-proterozoic sed. rocks	300	0.004960	0.000002	0.000209	80

3 Geophysical aspects of the BHCp

Magnetic susceptibility models were obtained through a series of inversions with differing data misfit values (i.e., closely fitting the observed data). A preferred model was chosen that reproduced all observed anomalies (Fig. 2A), had a low data misfit, and yielded results consistent with known geology. A 3D view of the preferred model shows three zones of high susceptibility. Zone 1 is a subvertical body that underlies the southern phase of the BHCp (Fig.

1B), has the highest susceptibility values in the model (Fig. 2B and C), and corresponds with the most magnetite-rich rocks at the surface (Hespenheide, 2003).

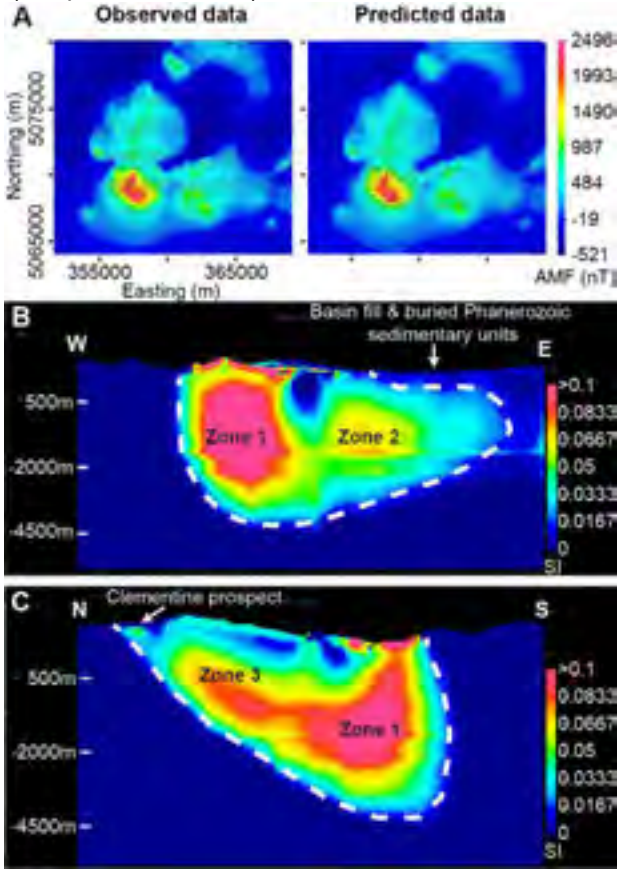


Figure 2. Preferred magnetic susceptibility model from geophysical inversion. (A) Predicted magnetic response compared to observed data. Magnetic maps match extent of Figure 1B. (B) E-W and (C) N-S cross-sections. See Figure 1B for section lines.

The second zone of high susceptibility extends to the east under Cenozoic unconsolidated sediment and Phanerozoic siliciclastic and carbonate units inferred at depth (Figs. 1B, 2B). This magnetic volume corresponds with isolated exposures of granodiorite (McDonald et al. 2012) and is likely a buried pluton that may be related to the BHCp. Although the economic potential of this buried feature is unknown, it is spatially associated with Paleozoic and Mesozoic carbonate-bearing units at or near the surface that contain W-bearing skarn prospects (Andersen et al. 2023).

The third high-susceptibility zone extends and thins to the north, corresponding with the northern phase of the exposed BHCp (Figs. 1B, 2C; Hespenheide, 2003). A south-plunging magnetic protrusion extends off the northern margin of the buried BHCp and outcrops in the axis of a plunging anticline, inside mapped zones of orbicular alteration (Figs. 1B, 2C). A recent 1:30,000 scale map reveals that this northern exposure consists of two separate granite intrusions (Brimhall 2018). The northernmost intrusion is altered, with a crystallization age of 76.92±0.52 Ma (U-Pb zircon) and an alteration age of 72.7±1 Ma (U-Pb titanite; Brimhall 2023). The southern, undated granite intrudes baren hydrothermal breccia and is unaltered, suggesting it was emplaced post-mineralization. Due to the likely magnetite destruction from hydrothermal alteration in the northern intrusion, the southern intrusion is interpreted to represent the shallow magnetic feature in the model. Its subsurface connection to, and slightly lower magnetic susceptibility than the greater BHCp (i.e., less iron; Fig. 2C) suggest that the granite may be an evolved, late-stage differentiate that protruded from the BHCp, indicating that the BHCp was still cooling during hydrothermal activity and may have been one of several potential heat sources. No other high-susceptibility feature that may represent a buried syn-mineralization intrusion, as suggested by Brimhall (2023), is indicated from geophysical modelling. Although not recognized in the model, such an intrusion may still exist if it is not magnetic or any pre-existing magnetite was subsequently destroyed by oxidizing fluids.

4 Understanding metamorphism and orbicular alteration using stable isotopes

Biotite and chlorite from the BHCp gave δ^2H_{VSMOW} values of -61 to -53‰, with a biotite outlier of -101‰ (Fig. 3A). The stable isotope values of biotite and chlorite from the BHCp are consistent with a pristine magmatic origin. However, one biotite sample from the BHCp is negatively shifted in hydrogen isotope value. Since there is no petrographic evidence of recrystallization, this data suggests alteration by a fluid composed primarily of meteoric water.

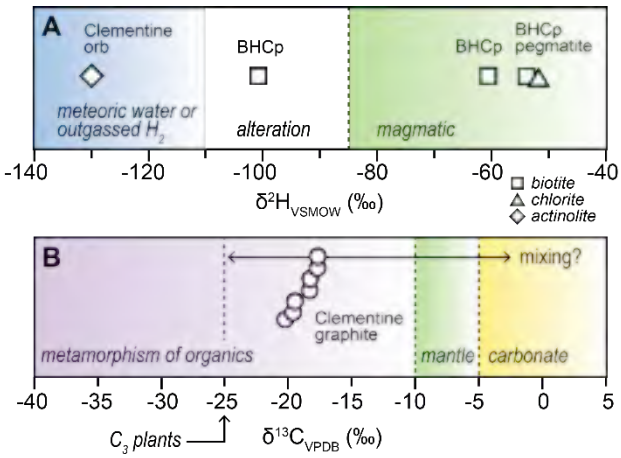


Figure 3. Stable isotope compositions of minerals from the BHCp and the Clementine prospect. (A) δ^2H_{VSMOW} of hydrous minerals relative to possible H sources (Sheppard et al. 1969). (B) $\delta^{13}C_{VPDB}$ of graphite relative to possible C sources (Luque et al. 2012).

Graphite from the Clementine prospect gave $\delta^{13}C_{VPDB}$ values of -20.2 to -17.7‰ (Fig. 3B). Carbon

isotope values suggest graphite formed following metamorphism of organic material in shales of the parent Cretaceous Kootenai Formation. To shift the carbon isotope values more positively than organic carbon (-25‰) and promote graphitization ~1 km from the igneous contact (cf. Wada et al. 1994), carbonate carbon was likely contributed from Kootenai Formation limestones.

Actinolite from the Clementine prospect orbs gave an average δ^2H_{VSMOW} value of -131‰. This preliminary negative hydrogen isotope value is consistent with precipitation from a meteoric fluid or from H_2 outgassed from a magma during advection. The former suggests that meteoric water entered fractures in the shallow system that was heated conductively by an intrusion. However, the latter is more likely as it is supported by proximity of graphite to the orb zone. This is because thermodynamic models of redox equilibria in porphyry copper deposits by Brimhall (2023) indicate that graphite is stable in the actinolite-titanite-calcite orb stability field.

5 Conclusions

Inversion of aeromagnetic data reveals a volume of high magnetic susceptibility material immediately south of mineralized breccia vein gossan, underlying zones of orbicular alteration. The magnetic volume is interpreted to represent a post-mineralization, cogenetic late-stage differentiate of the pre-mineralization BHCp. If true, this relationship indicates that the BHCp was actively cooling during hydrothermal activity at Clementine and may have been one of several potential heat sources. This is supported by metamorphism inferred from graphite C isotope values in orbicular alteration zones. Preliminary light hydrogen isotope values of hydrothermal orb actinolite suggests formation with a meteoric-hydrothermal fluid or outgassed H_2 from magma incorporated into an advective magmatic-hydrothermal fluid. The latter is more likely as thermodynamic models support the formation of graphite proximal to actinolite-titanite-calcite orbicular alteration. Although magnetic modelling did not detect a syn-mineralization intrusion at depth, such an intrusion may have low magnetic susceptibility, or its magnetite was destroyed by oxidizing hydrothermal fluids.

Acknowledgments

This research was supported by the USGS Mineral Resources Program and Earth Mapping Resources Initiative. Any use of trade, firm, or product names is for descriptive purposes only and does not imply endorsement by the U.S. Government.

References

Andersen AK, Goldman, MA, Bennett MM, Dicken CL, Brown PJ, Parks HL (2023) Tungsten resources of the northern Rocky Mountains, Montana and Idaho—a synthesis and quantitative assessment of skarn-hosted resources. USGS Sci Investig Rep 2023-5012

Atkinson WW, Einaudi MT (1978) Skarn formation and mineralization in the contact aureole at Carr Fork, Bingham, Utah. Econ Geol 73:1326–1365. https://doi.org/10.2113/gsecongeo.73.7.1326

Brimhall G (2018) Orbicular Alteration at the Clementine Porphyry Copper Prospect of Southwest Montana: Defining the Edges of Advective Flow in the Porphyry Copper Paradigm. In Scarberry KC, Barth S (eds) Proceedings, Montana mining and mineral symposium. MBMG Special Publication 120, pp 71–84.

Brimhall G (2023) An operative porphyry copper model based on thermochemical evidence of convective gaseous hydrogen transport and mega-stratovolcanic eruptions containing anhydrite. In Van Rythoven A, Barth S (eds) Proceedings, Montana Mining and Mineral Symposium. MBMG Special Publication 124, pp 11–32.

Brimhall G, Fanning M (2019) Supporting the Transition to Deep Porphyry Copper Exploration: SHRIMP U/Pb Radiometric Dating of Titanite ($CaTiSiO_5$) in the Distal and Superajacent Orbicular Alteration Zone of the Clementine Prospect, Southwest Montana. In Scarberry KC, Barth S (eds) Proceedings of the Montana mining and mineral symposium. MBMG Special Publication 121, pp 117–132.

du Bray EA, Aleinikoff JN, Lund K (2012) Synthesis of Petrographic, Geochemical, and Isotopic Data for the Boulder Batholith, Southwest Montana. USGS Professional Paper 1793.

Hespenheide MA (2003) Emplacement mechanisms of the Big Hole Canyon pluton, southwest Montana. Thesis, University of Wyoming.

Horton JD (2017) The State Geologic Map Compilation (SGMC) geodatabase of the conterminous United States. USGS data release. https://doi.org/10.5066/F7WH2N65

Johnson CA, Stricker CA, Gulbransen CA, Emmons MP (2018) Determination of $\delta^{13}C$, $\delta^{15}N$, or $\delta^{34}S$ by Isotope-Ratio-Monitoring Mass Spectrometry Using an Elemental Analyzer. USGS Techniques and Methods 5-D4. https://doi.org/10.3133/tm5D4

Li, Y, Oldenburg, DW (1996) 3-D inversion of magnetic data. Geophys 61 (2):394–408. https://doi.org/10.1190/1.1443968

Luque FJ, Crespo-Feo E, Barrenechea JF, Ortega L (2012) Carbon isotopes of graphite: Implications on fluid history. Geosci Front 3(2):197–207. https://doi.org/10.1016/j.gsf.2011.11.006

McDonald C, Elliott CG, Vuke, SM, Lonn JD, Berg RB (2012) Geologic map of the Butte South 30' x 60' quadrangle, southwestern Montana. MBMG Open-File Rep 622, 1 sheet, scale 1:100,000.

Sharp ZD, Atudorei V, Durakiewicz T (2001) A rapid method for determination of hydrogen and oxygen isotope ratios from water and hydrous minerals. Chem Geol 178:197–210-. https://doi.org/10.1016/S0009-2541(01)00262-5

Sheppard SMF, Nielsen RL, Taylor HP (1969) Oxygen and hydrogen isotope ratios of clay minerals from porphyry copper deposits. Econ Geol 64(7):755–777. https://doi.org/10.2113/gsecongeo.64.7.755

USGS (2023) Porphyry Copper Systems of the Boulder batholith, Montana. USGS. https://www.usgs.gov/centers/gggsc/science/porphyry-copper-systems-boulder-batholith-montana#overview. Accessed 15 January 2025

Wada H, Tomita T, Matsuura K, et al (1994) Graphitization of carbonaceous matter during metamorphism with references to carbonate and pelitic rocks of contact and regional metamorphisms, Japan. Contr Mineral and Petrol 118:217–228. https://doi.org/10.1007/BF00306643

Zinter GG, Snee LW, Sutter JF (1983) Geology, petrology, and age of emplacement of the Big Hole Canyon intrusion near Dewey, southwest Montana. Geol Soc Am Abstr Progr 15(5):412.

Effects of hydrothermal alteration on K-feldspar of the syenite-hosted Quemaldero porphyry Cu prospect in Cordon, Isabela, Philippines

Pearlyn Manalo[1], Akira Yaginuma[1], Jillian Aira Gabo-Ratio[2], Akira Imai[3], Kalin Kouzmanov[4], Ryohei Takahashi[1], Hinako Sato[1], Andrea Agangi[1], Graciano Yumul Jr. [5]

[1]Graduate School of International Resource Sciences, Akita University, Akita, Japan
[2]National Institute of Geological Sciences, University of the Philippines, Diliman, Quezon City, Philippines
[3]Faculty of Engineering, Kyushu University, Fukuoka, Japan
[4]Department of Earth Sciences, University of Geneva, Geneva, Switzerland
[5]Cordillera Exploration Company, Inc., Taguig City, Philippines

Abstract. Alkalic intrusion-hosted porphyry Cu deposits are an interesting type of ore deposits because of its rare known distribution but significant metallic endowment. To further our understanding of ore-forming processes in alkalic rocks in island arcs, we characterized the Quemaldero porphyry Cu prospect in Cordon, Isabela, Philippines. Detailed investigations of mineralogy, textures, cathodoluminescence (CL), mineral chemistry and oxygen isotopes of feldspars that occur both as primary rock-forming minerals and as products of hydrothermal activity have revealed important insights into magmatic-hydrothermal activity in this alkalic porphyry prospect.

K-feldspar from weakly altered syenite in Quemaldero has blue cathodoluminescence and low K content compared to the pervasively altered syenite, which has light blue luminescence. The blue luminescent K-feldspar is enriched in light rare earth elements (REEs) and depleted in heavy REEs, with a sharp positive Eu anomaly, typical of magmatic feldspars. The light blue luminescent hydrothermal K-feldspar has a flat REE pattern with variable positive Eu anomalies. Furthermore, $\delta^{18}O$ values of the primary K-feldspar is within the range of magmatic values (+3 to +15‰), while those of the secondary K-feldspar are near 0‰. These results highlight geochemical differences between the magmatic and hydrothermal K-feldspars, providing novel insights into the evolution of hydrothermal mineralization at the Quemaldero prospect.

1 Introduction

The Philippines is well-known for having large epithermal and porphyry-type deposits associated with calc-alkaline magmatism (e.g. Sillitoe and Gappe, 1984; Imai, 2000; Yumul et al., 2003). Gold and copper mineralization associated with alkalic rocks in the Philippines is rare, and comparatively few studies have been completed (e.g., Wolfe and Cooke, 2011). Alkalic porphyry deposits are best known from Canada and Australia (e.g. Lang et al., 1995; Cooke et al., 2007). Although comparatively uncommon, alkalic-hosted deposits can contain significant amounts of copper and gold. Understanding styles of mineralization and alteration of these types of deposits would be helpful in future exploration.

One challenge in the exploration for alkalic-hosted porphyry Cu deposit is recognizing subtle alteration zones. In syenite-hosted deposits, the host rocks are essentially composed of igneous alkali feldspar that has commonly been altered to secondary alkali feldspars. Distinguishing differences between igneous and secondary alkali feldspars is therefore necessary to delineate sodic and calc-potassic alteration zones. In this study, we looked at petrographic, cathodoluminescence, mineral chemistry, and oxygen isotopic signatures of feldspars from Quemaldero to characterize magmatic and hydrothermal events that led to the mineralization.

2 Geological Background

The Quemaldero porphyry Cu prospect is in Cordon, Isabela, northern Luzon Island. It is located on the northern flank of the Caraballo Mountain, which bounds the Cagayan Basin to the south (Fig. 1). It is part of the Marian project area currently being explored by the Cordillera Exploration Co., Inc. Gold was previously mined at the Marian Gold Mine (Fig. 1) from the 1970s to 1980s.

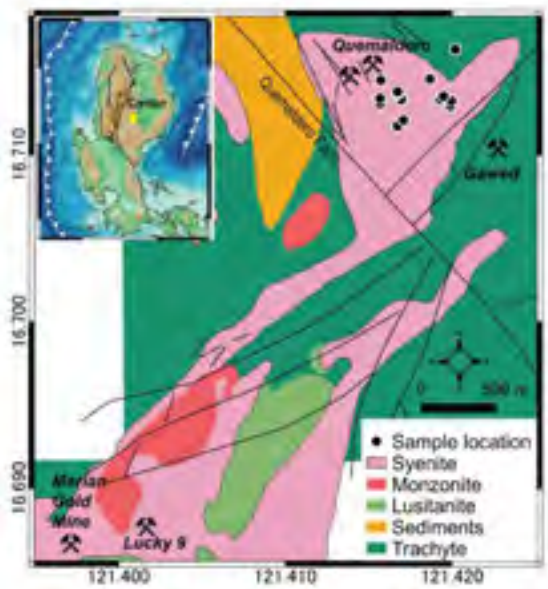


Figure 1. Geologic map of the Quemaldero prospect and surrounding areas in the Marian Mine, Cordon, Isabela, Philippines (modified from Cordillera Exploration Co., Inc., unpublished)

The host rocks of the prospect belong to the Cordon Syenite Complex, which intruded co-magmatic tephritic phonolites at 23.1 ± 3.0 Ma (Knittel, 1983). The Cordon Syenite Complex is

composed of medium- to coarse-grained alkalic rocks that vary in texture from equigranular to porphyritic, as well as in composition, from alkali feldspar syenite, syenite, and monzonite to lusitanite.

3 Methods

Rock samples were collected in Cordon, Isabela. Petrographic observations of thin sections and polished mounts were conducted using a Nikon LV100N POL polarizing microscope attached to a Nikon D5600 camera at Akita University. Automated quantitative mineralogical analysis was conducted using a QEMSCAN Quanta 650F at the University of Geneva. Optical cathodoluminescence (CL) imaging of polished thin sections was carried out using a NewTec Scientific optical-CL stage attached to an Olympus BX41 petrographic microscope at the University of Geneva. Scanning electron microscope cathodoluminescence (SEM-CL) images and CL spectra were obtained using a Gatan MonoCL4 attached to a JEOL JSM-IT300 SEM at Akita University. Major and minor element chemistry analysis of feldspar was conducted using a JEOL JXA-8230 electron probe microanalyzer (EPMA), and trace element contents were measured using an Elemental Scientific Laser NWR193 laser ablation system coupled with an Agilent 8900 ICPMS-QQQ at Akita University. Oxygen isotopic composition of the feldspars from weakly altered and pervasively altered rocks were analysed in Activation Laboratories, Ltd., Ontario, Canada.

4 Results

4.1 Mineralogy

Weakly-altered samples of porphyritic syenite are composed of medium-grained dark groundmass surrounding tabular K-feldspar phenocrysts up to 2 cm in length (Fig. 2A). Copper mineralization occurs as discontinuous sulfide veinlets within pervasively altered and highly oxidized syenite (Fig. 2B).

Petrographically, K-feldspar phenocrysts typically display a plagioclase core that has been partially altered to albite (Fig. 3A and 3B). The groundmass is composed of K-feldspar, biotite and pyroxene, which has been altered to calcite, secondary biotite, chlorite and hematite. Accessory apatite is also common.

Sulfide veinlets are dominantly composed of bornite and chalcopyrite. Secondary covellite and chalcocite occur along rims of the bornite. Sulfide veinlets are surrounded by an albite alteration envelope.

4.2 Cathodoluminescence

K-feldspar of the weakly altered syenite shows strong blue luminescence, whereas the plagioclase cores vary from being red luminescent to non-luminescent (Fig. 4), depending on the degree of alteration to albite and calcite. K-feldspar of the pervasively altered syenite shows a relatively weak blue luminescence, whereas albite appears dark brown (Fig. 5).

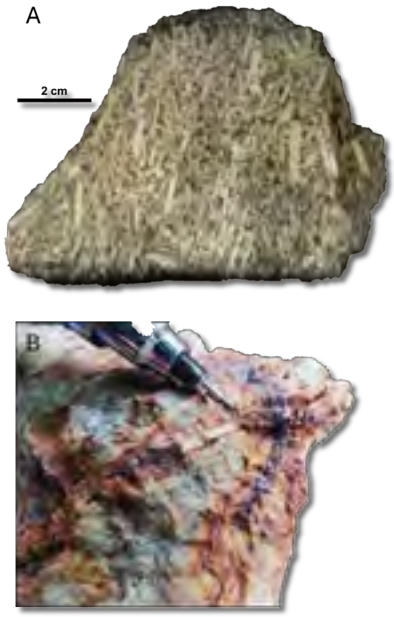


Figure 2. A) A weakly-altered porphyritic syenite from the Quemaldero porphyry Cu prospect, Cordon, Isabela. B) A pervasively altered syenite cut by discontinuous sulfide veinlets.

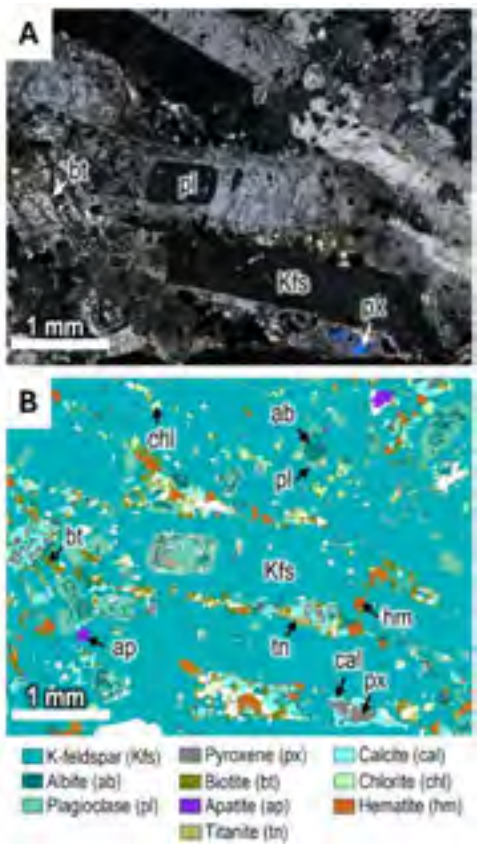


Figure 3. A) Crossed-polar transmitted-light photomicrograph and B) QEMSCAN map of the weakly-altered porphyritic syenite of the Quemaldero prospect. Abbreviations for minerals in A) is same as in B).

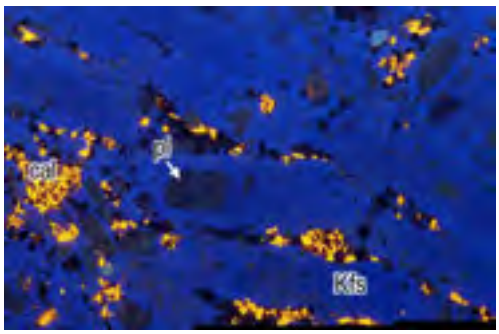


Figure 4. Optical cathodoluminescence of a weakly-altered porphyritic syenite of the Quemaldero prospect. K-feldspar phenocrysts show blue luminescence. Albitized plagioclase appears darker. The field of view is similar to that of Figure 3. Abbreviations: cal = calcite, Kfs = K-feldspar, pl = plagioclase.

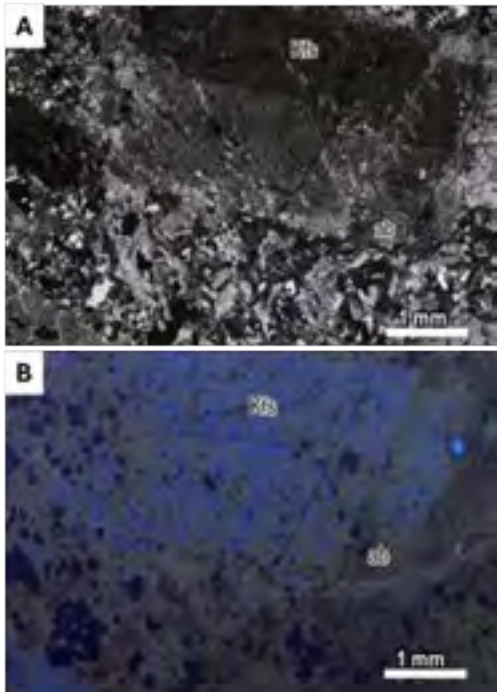


Figure 5. A) Crossed-polar transmitted light photomicrograph and B) optical cathodoluminescence image of the pervasively altered syenite of the Quemaldero prospect. K-feldspar phenocrysts show blue luminescence. Kfs = K-feldspar, pl = plagioclase

Cathodoluminescence spectral analysis of the K-feldspar from the weakly altered syenite revealed a high intensity peak at 420 to 450 nm and a subordinate peak at ~720 nm. K-feldspar from the pervasively altered syenite has lower peak intensities at the same wavelengths.

Plagioclase (An < 60) from the weakly altered syenite has a high peak intensity at 750 nm and subordinate peak at ~450 nm. Albite from the pervasively altered syenite shows the same intensity at 450 nm, but the peak in the red region is slightly shifted to 720 nm.

4.3 Mineral Chemistry

The earliest feldspar is plagioclase with anorthite content ranging from 30 to 60 mol%. It is overgrown by the strongly blue luminescent K-feldspar with 60-70 mol% orthoclase content (Fig. 6). The lighter blue-luminescent K-feldspar in the pervasively altered syenite has higher orthoclase content (> 70 mol%). Hydrothermal albite has negligible Ca and K contents (Fig. 6).

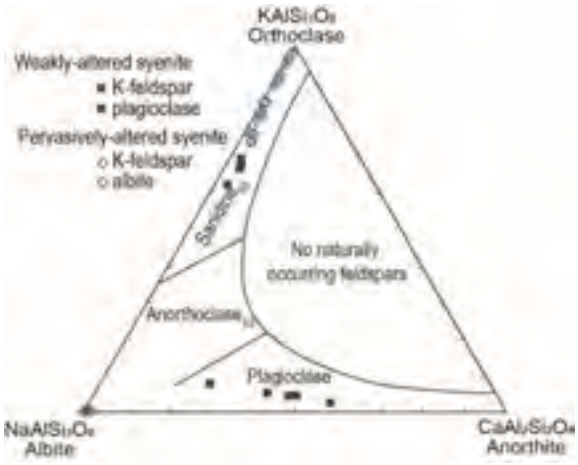


Figure 6. Ternary diagram showing the compositions of feldspar (after Deer et al., 2013) in the weakly altered and pervasively altered syenite of the Quemaldero prospect.

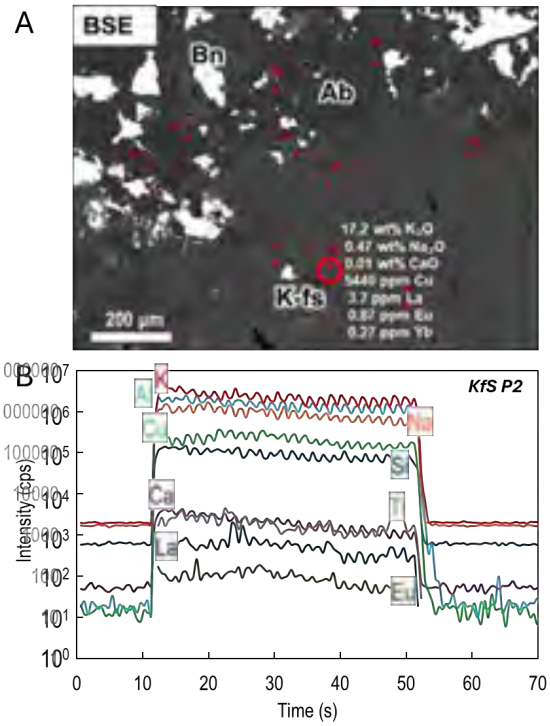


Figure 7. A) Backscattered electron image of K-feldspar and albite in the pervasively altered syenite. B) Time-resolved plot of laser ablation ICP-MS analysis on K-feldspar. The equivalent composition is shown in A. K-fs = K-feldspar, Ab = albite, Bn = bornite.

Laser ablation ICP-MS analyses revealed that the K-feldspar of the weakly altered syenite has Cu contents below 100 ppm, whereas secondary K-feldspar from the pervasively altered syenite contains up to 5,000 ppm Cu (Fig. 7A). Time-resolved laser ablation ICP-MS plot shows a generally flat pattern of Cu intensity, similar to K, Al, Na and Si (Fig. 7B), which precludes the possibility that Cu occurs as mineral inclusions in the feldspar.

Chondrite-normalized REE patterns (normalizing values after Boynton, 1984) show that the K-feldspar from the weakly altered syenite is enriched in light REEs and depleted in heavy REEs, with strong positive Eu anomaly (Fig. 8). K-feldspar from the pervasively altered syenite has a relatively wide range of REE concentrations and generally higher heavy REE contents (Fig. 8).

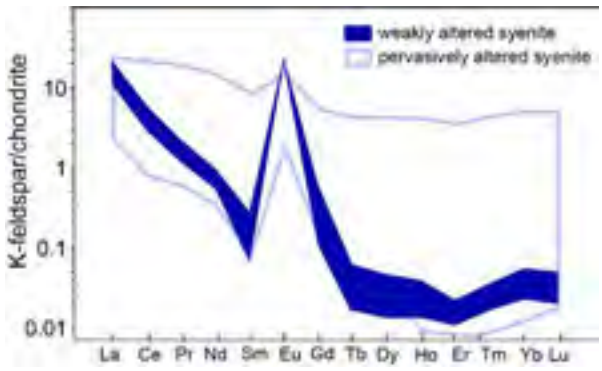


Figure 8. Chondrite-normalized rare earth element patterns of K-feldspar from weakly altered and pervasively altered syenite of the Quemaldero prospect. Chondrite-normalizing values are from Boynton (1984).

4.4 Oxygen Isotopes

Oxygen isotopic ratios ($\delta^{18}O_{SMOW}$) of the blue luminescent K-feldspar from the weakly altered syenite are positive, ranging from +3 to +15 ‰. These are generally higher than those of the light blue luminescent K-feldspar of the pervasively altered syenite, which range from -3 to 0 ‰.

5 Discussion

Igneous and hydrothermal K-feldspars at Quemaldero have distinct characteristics in terms of mineral chemistry, O-isotopes, and cathodoluminescence.

The strong blue luminescent K-feldspar in the weakly altered syenite has REE patterns typical of magmatic feldspars. The K-feldspar with lighter blue luminescence has REE patterns that are flatter and more scattered, indicative of variable mobility. The $\delta^{18}O_{SMOW}$ values are lower, possibly indicating lower temperatures of formation. The decrease in the cathodoluminescence intensity of the secondary K-feldspar at 450 nm could be attributed to the stabilization of Lowenstein bridges (Al-O-Al) during recrystallization at lower temperatures (Finch and Klein, 1999).

Potassium enrichment of the secondary K-feldspar potentially reflects the decreasing temperature in the system. As temperature decrease, Na could have preferentially partitioned to the aqueous fluid, while K partitioned to the rock. The secondary K-feldspar contain significantly higher amounts of Cu than the magmatic feldspar, potentially indicating Cu enrichment during potassic alteration.

6 Conclusions

Copper mineralization at the Quemaldero porphyry Cu prospect was accompanied by albite and K-feldspar alteration. Magmatic K-feldspar has distinct chemistry and cathodoluminescence from the hydrothermal K-feldspar. The combination of petrography, CL imagery and O isotopes potentially provide a new tool for distinguishing alteration effects in alkalic porphyry Cu systems.

Acknowledgements

We are grateful to Cordillera Exploration Co., Inc. (CExCI) and the members of Economic Geology Lab of Akita University for the assistance and valuable discussions. This work was financially supported by JSPS KAKENHI grants 21K04960, 21KK0089, 22K14633 and 22KK0246.

References

Boynton W (1984) Cosmochemistry of the rare earth elements; meteorite studies. In Henderson P (Eds) Rare earth element geochemistry. Elsevier, Amsterdam.

Cooke DR, Wilson AJ, House MJ, Wolfe RC, Walshe JL, Lickfold V, Crawford AJ (2007) Alkalic porphyry Au–Cu deposits and associated mineral deposits of the Ordovician to early Silurian Macquarie Arc, New South Wales. Australian Journal of Earth Sciences 54: 455–463.

Deer W, Howie R, Zussman J (2013) An Introduction to Rock-Forming Minerals. Min Soc Great Britain and Ireland, 498 pp.

Finch A, Klein J (1999) The causes and petrological significance of cathodoluminescence emissions from alkali feldspars. Contrib Mineral Petrol 135: 234-243.

Holliday JR, Cooke DR (2007) Advances in geological models and exploration methods for copper ± gold porphyry deposits. In Milkereit, B (Ed) Proceedings of Exploration 07: 5th Decennial International Conference on Mineral Exploration: Toronto, Prospectors and Developers Association of Canada, p. 791−809.

Imai A (2000) Mineral paragenesis, fluid inclusions and sulfur isotope systematics of the Lepanto Far Southeast porphyry Cu-Au deposit, Mankayan, Philippines. Res Geol 50: 151-168.

Knittel U (1983) Age of the Cordon Syenite Complex and its implication on the mid-Tertiary history of North Luzon. Phil Geol 37: 22-31.

Lang JR, Lueck B, Mortensen JK, Russell JK, Stanley CR, Thompson JFH (1995) Triassic-Jurassic silica-undersaturated and silica-saturated alkalic intrusions in the Cordillera of British Columbia: Implications for arc magmatism: Geology 23: 451–454.

Sillitoe R (2010) Porphyry copper systems. Econ Geol 105: 3-41.

Sillitoe RH, Gappe IM, Jr (1984) Philippine Porphyry Copper Deposits: Geologic Setting and Characteristics. UNDP Technical Support for Regional Offshore Prospecting in East Asia, Thailand: CCOP Project Office, (RAS/81/120), 89pp.

Wolfe RC, Cooke DR (2011) Geology of the Didipio region and genesis of the Dinkidi alkalic porphyry Cu-Au deposit and related pegmatite, northern Luzon, Philippines. Econ Geol 106: 1279-1315.

Yumul G Jr, Dimalanta C, Maglambayan V, Tamayo R Jr (2003) Mineralization controls in island arc settings: Insights from Philippine metallic deposits. Gond Res 6: 767-776.

Skarn-Hosted Cu Mineralization at the Thompson Knolls Discovery, Utah, USA

Chad Mann[1], Sergei Diakov[2], Quinton Hennigh[3], Zhaoshan Chang[1], Shiqiang Huang[1], Mathias Burisch[1]
[1] Geology & Geological Engineering, Colorado School of Mines, Golden, USA
[2] BCM Resources, Vancouver BC, Canada
[3]Crescat Capital, Denver, USA

Abstract. This is a first description of the recently discovered Cu mineralization at Thompson Knolls, UT Including petrographic observations, geochemical whole rock data and LA-ICP-MS U-Pb ages of skarn-related garnet. Disseminated chalcopyrite is mainly hosted by exoskarn and minor endoskarn zones. Exoskarn is invariably magnesian with mainly pyroxene, tremolite, talc, calcite, chlorite and serpentine. Endoskarn altered dikes comprise mainly pyroxene and garnet. Chalcopyrite is the main host of Cu and is intimately intergrown with retrograde talc, chlorite, and serpentine. A total of six garnet samples were collected from TK6, TK8, and TK14 and were dated successfully. The four ages of samples from TK14 range from 155 ± 2 Ma to 160 ± 4 Ma.

Skarn characteristics imply a relatively shallow formation environment in an intermediate to distal distance to the causative source intrusion. The recognition of a systematic geochemical and mineralogical zoning across the intersected skarn zones, may provide useful criteria for exploration targeting.

1 Introduction

The Thomspon Knolls discovery in Millard County, western Utah (Fig. 1), is a greenfields exploration project 100% owned by BCM Resources investigating Cu-Mo-(Au)-mineralization related to a skarn-porphyry system. Located in the greater west-central Great Basin of Utah, Thompson Knolls is one of several magmatic-hydrothermal copper deposits, such as Bingham Canyon, the Yerington District, Robinson Mine, and the Notch Peak Intrusive.

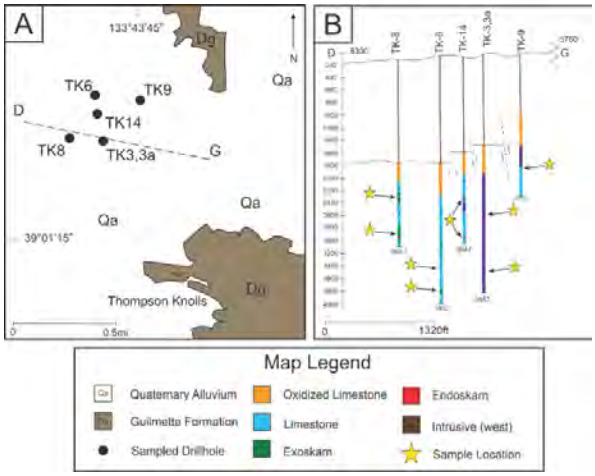


Figure 1. A) Sampled boreholes (plan view) with D-G cross section and regional geology. B) Cross-section along D-G of sampled boreholes showing general sampling locations and intersected geology.

The Thompson Knolls project lies within what was previously called the King's Canyon district now proposed to be called Thompson Knolls District, where a 1972 USGS aeromagnetic survey observed a large positive magnetic anomaly.

The Confusion Range, located directly north and west of the Thomspon Knolls discovery site, is the only significant outcropping geology in the area. The sedimentary rocks exposed in the range are folded sequences of the mid-Palaeozoic aged Pennsylvanian Ely Limestone and the Permian Arcturus. Directly west of the discovery, several smaller outcrops of the Devonian Guilmette formation and the Simonson dolomite. The Guilmette formation is a dolomite rich unit with intercalations of limestone and minor sandstone.

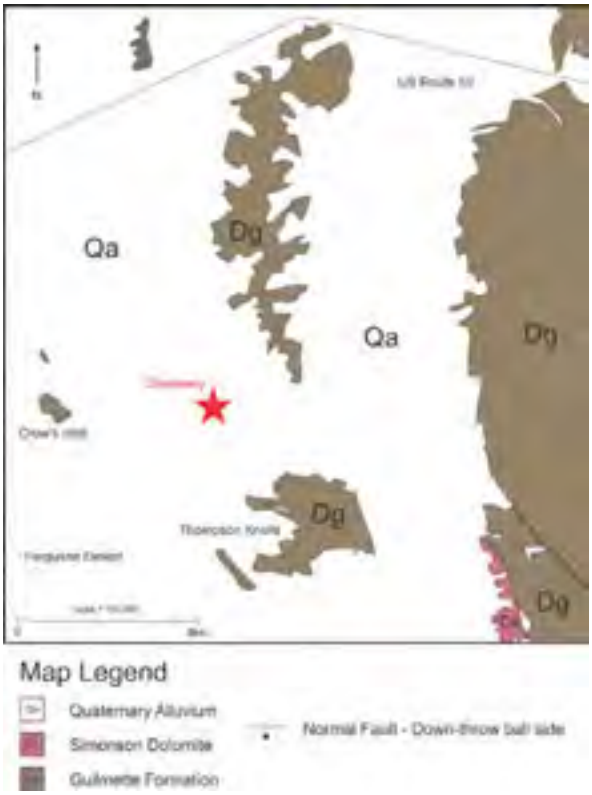


Figure 2. Thompson Knolls location (Au, Ag) in Millard County, Utah. Geology modified from Hintze and Davis (2002) and Hintze (1974).

There is no skarn alteration or other evidence for magmatic-hydrothermal overprint recognized in those outcrops. The discovery itself is overlain by a vast alluvium cover typical of the basins in the Great Basin region (Fig. 2).

Cu-Au-Ag-Mo mineralization was intersected in seven boreholes and is hosted by skarn and phyllic alteration. Here we present the first geological description of this Cu mineralization and employ LA-ICP-MS U-Pb garnet dating to constrain the timing of alteration within its regional metallogenic context.

2 Samples and Methods

2.1 Samples

The samples taken from the discovery drilling efforts were limited in size to quarter-core, three-inch-long segments. These samples primarily came from the boreholes that indicated skarn mineralization, copper sulphide mineralization, or both. A total of 38 representative samples from boreholes TK3, 3a, TK6, TK8, TK9, and TK14 were collected for lithological classification (Fig. 1). Alongside the core sampling, the bulk geochemical assay data was made readily available by BCM Resources, thus no samples were collected to conduct bulk geochemistry. 32 thin section samples at 30-micron thickness were acquired from BCM Resources and the University of Arizona from boreholes TK1, TK2, TK3,3a, and TK6.

2.2 Methods

Thirty-eight samples of boreholes TK3,3a, TK8, TK9, and TK14 were collected from which 17 thin sections and 4 1-inch round mounts were produced for further analyses. Transmitted light and reflected light petrography were conducted on thin sections and round mounts for mineralogical classification. Additionally, round mounts were used for SEM/EDS imaging and semi-quantitative data collection.

LA-ICP-MS U-Pb dating of garnet was carried out using a Resolution-SE 193 nm ArF excimer laser ablation system with an S-155 sample chamber, and an Agilent 8900 ICP-MS/MS, with the two connected via a signal smoothing SQUID device following a similar approach as described in Burisch et al. (2023).

3 Results and Discussion

3.1 Intrusive units and phyllic alteration

Two intrusive units were intersected in the boreholes (Fig. 3). The East intrusive has a biotite-bearing quartz-monzonite composition with a porphyritic texture. The East intrusive is intercepted in TK1 and TK2. The East intrusion is partially overprinted by phyllic alteration but does not host significant mineralization. Locally, minor disseminated molybdenite is recognized.

The West intrusive is intercepted in borehole TK3 and 3a and is of granitic to granodioritic composition with a porphyritic texture. Additionally, several dikes intersected in TK6, 8 and 14 have similar igneous compositions (Fig. 3).

The intrusion is pervasively altered and hosts abundant disseminated molybdenite and veins with quartz and molybdenite. The most abundant alteration mineral is muscovite accompanied by minor epidote and K-feldspar.

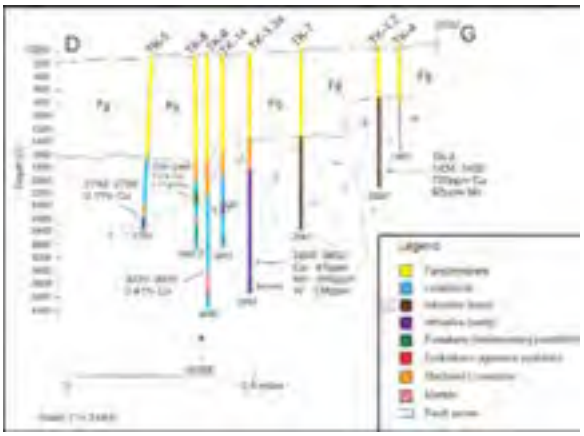


Figure 3. Cross-section of the Thompson Knolls discovery drilling along DG (Fig. 1) running northwest to southeast. TK6, TK14, and TK14 are projected from the north, and TK7 is projected from the south.

3.2 Skarn characteristics and Cu mineralization

Skarn alteration is observed as discontinuous sub-horizontal zones which range from 0.5 to 15 m apparent thickness in borehole intercepts (Fig. 3). Most skarn presents as exoskarn with only minor endoskarn overprinting porphyritic dikes. Most of the intercepted skarn is exoskarn that is primarily composed of pale green pyroxene and rare garnet, which are overprinted by retrograde tremolite, talc, serpentine and undefined Mn-oxyhydroxides. The prograde endoskarn mainly comprises green enstatite pyroxene and a pale red to green-brown andradite garnet with a garnet/pyroxene ratio of about 0.5 to 1 (Fig. 4). The igneous texture is commonly well preserved. Retrograde minerals are mainly epidote and amphibole.

Copper mineralization is associated with retrograde skarn alteration. The main opaque minerals are chalcopyrite, pyrite, pyrrhotite, molybdenite, magnetite, and Mn-oxyhydroxides. Chalcopyrite and pyrrhotite are typically intimately intergrown and occur mainly as dissemination in talc and serpentine-rich retrograde skarn. Locally, mineralization may also occur as vein-infill or stockwork zones (Fig. 4).

3.3 Geochronology

A total of six garnet samples were collected from TK6, TK8, and TK14 and were dated by LA-ICP-MS U-Pb dating technique. Four ages of skarn samples from TK14 range from 155 ± 2 Ma to 164 ± 3 Ma (Fig. 5). One sample from TK8.1 has an age of 159 ± 2 Ma, and one sample from TK6.1 is dated to 162 ± 2 Ma. As a group, all the garnet ages overlap within uncertainty, suggesting that skarn alteration is

related to one magmatic-hydrothermal event that occurred during the Late Jurassic (Fig. 5).

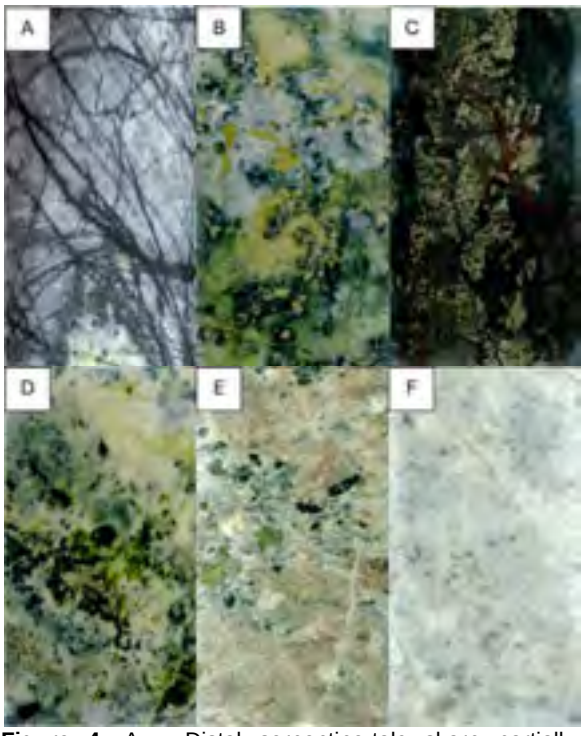


Figure 4. A – Distal serpentine-talc skarn partially replacing dolostone protolith. B – Exoskarn with mainly pyroxene replaced by serpentine and sulfide C – Retrograde exoskarn with Pyrite + Chalcopyrite + Iron Oxides + Pyrrhotite. D – pyroxene replaced by talc, serpentine and sulphides. E – Endoskarn with red garnet and pale green pyroxene F – Porphyry intrusive overprinted by phyllic alteration

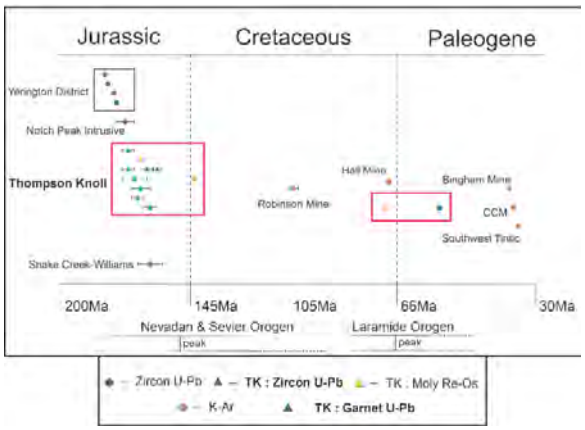


Figure 5. A regional scale deposit-age plot from available geochronology data. Thompson Knolls is highlighted with a red box. Brief tectonic history at the bottom of the figure provides brief information on the tectonic history.

The new age data and previously available geochronological data are compiled in Figure 5 to provide a regional framework. The compiled data suggests that three metallogenic periods are regionally important for ore formation that occurred in the Jurassic, Cretaceous, and Paleogene, respectively. Skarn-hosted Cu mineralization at Thompson Knolls is related to the oldest of these metallogenetic periods.

3.2 Skarn Environment and Implications for Exploration

The magnesian mineralogy of exoskarn is related to Mg-rich dolostones as the main protolith. The only exceptions are minor endoskarn zones that have a calcic composition. Magnesian skarns do not show typical mineralogical zoning that is recognized in calcic skarn systems (Meinert et al. 2005: Burisch et al. 2023). The discontinuous nature of skarn zones and the high abundance of tremolite, talc and Mn-oxyhydroxides imply an intermediate to distal position of the intersected skarn zones relative to their causative source intrusion (Fig. 3 and 6).

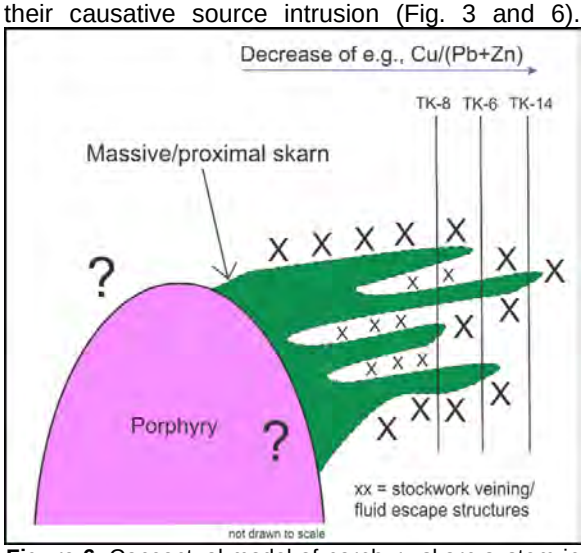


Figure 6. Conceptual model of porphyry skarn system in relation to skarn borehole intercepts; TK8, TK6, and TK14.

This assumption is furthermore supported by relatively low skarn bulk rock Cu/(Zn+Pb) values of about 50 to 5. Moreover, the Cu/(Zn+Pb) ratios change systematically across the boreholes from TK8 (50), to TK6 (23), to TK14 (9), to TK9 (4) (Fig. 6). This decrease in Cu/(Zn/Pb) is interpreted as a systematic geochemical gradient along the fluid flow path, which may provide useful information to vector towards the “yolk” of the system.

4 Conclusions

The Thompson Knolls discovery is a magnesian skarn hosted copper mineralization that likely formed in an intermediate to distal position relative to its yet undiscovered causative source intrusion.

Six garnet-bearing skarn samples were dated and constrained the timing of skarn alteration to the late Jurassic (˜155-160 Ma). The geochemical and mineralogical data implies systematic zoning across the intersected skarn zones, which may provide useful criteria for exploration targeting in deeply buried magmatic-hydrothermal systems.

Acknowledgements

We thank BCM Resources, specifically Octavio Urbina, Jon Schloderer, and Rick Redfern for access to drill core material, geophysical, geochemical, and petrographical data.

References

Armstrong RL (1972) Low-Angle (Denudation) Faults, Hinterland of the Sevier Orogenic Belt, Eastern Nevada and Western Utah: Geol Soc Amer Bull 83:1729–1754.

BCM Resources Corp (2025) Thompson Kolls, accessed 12 February 2025, https://bcmresources.com/projects/thompson-knolls-3/

Burisch M, Bussey SD, Landon N, Nasi C, Kakarieka A, Gerdes A, Albert R, Stein HJ, Gabites JA, Friedman R M, Meinert LD (2023) Timing of Magmatism and Skarn Formation at the Limon, Guajes, and Media Luna Gold ± Copper Skarn Deposits at Morelos, Guerrero State, Mexico: Econ Geol 118:695–718.

Bon RL (1996) Summary of mineral activity in Utah 1996, Utah Geological Survey Circular 98, Utah Geological Survey, 12 p.

Dickinson WR (2004) Evolution of the North American Cordillera: Annual Review of Earth and Planetary Sciences 32:13–45.

Dickinson WR (2006) Geotectonic evolution of the Great Basin: Geosphere 2:353–368.

Einaudi MT, Meinert LD and Newberry RJ (1981) Skarn deposits: Economic Geology 75th Anniversary Volume, p. 317–391.

Greene DC (2014) The Confusion Range, west-central Utah: Fold-thrust deformation and a western Utah thrust belt in the Sevier hinterland: Geosphere, v. 10, p. 148–169.

Hose RK, Blake MC Jr, (1976) Geology and mineral resources of White Pine County, Nevada: Nevada Bureau of Mines and Geology, Bulletin 85, p. 1–32.

Hose RK (1977) Structural geology of the Confusion Range, west-central Utah: Geosphere, v. 10, p. 101–115.

Hintze LF, Davis DF (2002) Geologic map of the Tule Valley 30 × 60 Quadrangle and parts of the Ely, Fish Springs, and Kern Mountains 30 × 60 Quadrangles, northwest Millard County, Utah: Utah Geological Survey, Map 186.2.

Lee J (1989) Geology of the Mount Moriah Quadrangle, Nevada: Geosphere, v. 12, p. 100–115.

Meinert LD (1992) Skarns and Skarn Deposits: Geoscience Canada 19:145–162.

Meinert LD (2000) Gold in skarns related to epizonal intrusions: SEG Reviews 13:347–375.

Meinert LD, Dipple GM, and Nicolescu S (2005) World skarn deposits: Economic Geology 100th Anniversary Volume, p. 299–336.

U.S. Geological Survey (1972) Aeromagnetic map of parts of the Delta and Richfield 1° by 2° quadrangles, Utah, Open-File Report 72-387, U.S. Geol Surv 1 plate.

U.S. Geological Survey (2024) Geologic map of the Tule Valley 30' x 60' quadrangle and parts of the Ely, Fish Springs, and Kern Mountains 30' x 60' quadrangles, northwest Millard County, Utah, U.S. Geol Surv 1 map.

Wyld SJ (2000) Triassic evolution of the arc and backarc of northwestern Nevada, and evidence for extensional tectonism: Geological Society of America Special Paper 347:185–207.

Wyld SJ (2002) Structural evolution of a Mesozoic backarc fold-and-thrust belt in the U.S. Cordillera: New evidence from northern Nevada: Geological Society of America Bulletin, v. 114, p. 1452–1468.

Zimmerman JE (2009) Gold mineralization at Kings Canyon, Millard County, Utah: Utah Geological Association Publication 38, p. 187–196.

Distribution of indium and tellurium in the HS to IS Pefka epithermal deposit: Insights from LA-ICP-MS analyses of sulfides and sulfosalts

M. Melfou[1], P. Voudouris[2], R. Klemd[3], M. Keith[3], V. Melfos[1], A. Tarantola[4], L. Papadopoulou[1], N. Kantiranis[1]

[1]Faculty of Geology, Aristotle University of Thessaloniki, Greece
[2]Faculty of Geology and Geoenvironment, National and Kapodistrian University of Athens, Greece
[3]GeoZentrum Nordbayern of Friedrich-Alexander-Universität (FAU) Erlangen-Nürnberg, Germany
[4]Université de Lorraine, CNRS, GeoRessources Laboratory, France

Abstract. The Pefka high- to intermediate-sulfidation deposit hosts the highest In and Te grades in rock chips in Greece. This study aims to investigate mineralogical and geochemical controls on In and Te enrichment in sulfides and sulfosalts. Detailed petrography and LA-ICP-MS analyses reveal distinct mineralization stages, with key In and Te carriers including roquesite, tennantite-(In), colusite, luzonite, and tellurides. Pyrite geochemistry provides insights into fluid evolution. The results contribute to understanding epithermal enrichment processes for In and Te in numerous mineral phases at the Pefka deposit.

1 Introduction

Indium and tellurium are critical metals for renewable energy primarily sourced as by-products of base-metal mining (Müller et al. 2025). Understanding their geological occurrences is crucial for enabling more targeted exploration and efficient extraction (Müller et al. 2025). The Pefka high- (HS) to intermediate-sulfidation (IS) deposit hosts exceptional In (1160 ppm) and Te (>1000 ppm) grades in rock chips, making it an ideal case to study the enrichment processes of these metals in an epithermal environment (Voudouris et al. 2022; Melfou et al. 2023).

Studies on the distribution of elements such as In and Te in multi-mineral assemblages are rare and are needed as stated by Cook and Ciobanu (2015). The Pefka deposit provides an ideal case study, with its diverse ore mineralogy and the rarity of sphalerite, allowing the partitioning of In to be examined in other minerals (Cook and Ciobanu 2015). Thus, the objective of this study is to investigate the capacity of minerals to incorporate In and Te at various stages of mineralization and the processes that control their enrichment. Furthermore, the study aims to assess pyrite as an indicator of ore-forming conditions within a deposit characterized by a complex paragenetic sequence with numerous mineral phases.

2 Geological background

The Rhodope metallogenic province in Greece (Fig. 1a), within the broader Western Tethyan metallogenic belt, hosts numerous epithermal deposits in Oligocene-Miocene volcanic rocks (Melfos and Voudouris 2017). The Pefka-Loutros area, as part of the supra-detachment northern Hellenic Thrace basin, is associated with both sedimentary and calc-alkaline to high-K and locally shoshonitic volcanic rocks, linked to the Tertiary syn- to late-orogenic extensional processes in the Rhodope province (Kilias et al. 2013). Many HS and IS epithermal deposits are hosted in hydrothermally altered volcanic rocks and tuffs and exhibit intermediate argillic to sericitic-argillic (Fig. 1b) and locally adularia alteration.

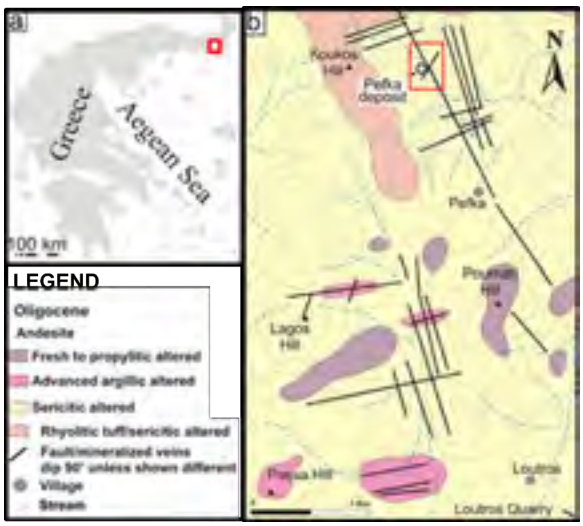


Figure 1. (a) Sketch map of Greece. (b) Alteration map of the Pefka-Loutros area. Modified after Voudouris et al. (2022). The location of the Pefka deposit is highlighted with the red rectangle in both images.

The HS to IS Pefka deposit, located within this area, is the most significant deposit, is structurally controlled, and is characterized by multistage NNW- and NE-trending quartz and quartz-carbonate veins and breccias. The mineralization is enriched in base, rare, and critical metals (e.g., Cu, Fe, Au, Ag, Pb, Zn, Bi, Sn, Ge, Ga, In, Mo, V, As, Hg, Te, and Se), exhibiting an exceptional ore mineralogy that includes a wide variety of sulfosalts (e.g., enargite, luzonite, tennantite), sulfides (e.g., pyrite, chalcopyrite, galena), and tellurides (e.g., hessite, altaite, coloradoite), and native metals (Voudouris 2006; Melfos and Voudouris 2012; Repstock et al. 2015; Voudouris et al. 2022). Bulk ore concentrations in rock chips reach up to 2300 ppm Se, 1160 ppm In, >1000 ppm Te, 390 ppm Ag, 345 ppm Au, and 250 ppm Bi, making the deposit the richest one in Te and In grades in Greece (Melfou et al. 2023).

3 Methods

Ore samples were collected from outcrops of the vein systems in the Pefka deposit and from piles outside abandoned galleries and were analyzed using Electron Microprobe Analysis (EMPA) and Laser Ablation Inductively Coupled Plasma Mass Spectrometry (LA-ICP-MS), at the GeoZentrum Nordbayern, Germany, to determine the major and minor element composition of various sulfide and sulfosalt minerals.

4 Results

4.1 Petrography with focus on analyzed sulfides and sulfosalts

This section focuses on the petrography of the most abundant minerals analyzed using LA-ICP-MS to link the petrographic and geochemical observations. The mineralization was divided into three main stages: (1) Pb-Se, (2a-b) Cu-As-Au-In-V-Sn, and (3) Zn-Te-Sb stages (Fig. 2a-f). Stage 1 is characterized by massive 1-2 cm thick galena veins (Fig. 2a). Stage 2a is related to quartz veins with luzonite and enargite (Fig. 2b) that are typical for HS environments, while stage 2b fahlores marks the transition from HS to IS conditions (Voudouris et al. 2022). Stage 3 is characterized by carbonate-quartz vein system with sulfides and sulfosalts that are associated with IS environments (Voudouris 2006; Repstock et al. 2015; Voudouris et al. 2022).

Microscopically, galena (Fig. 2c) commonly hosts enargite and tetrahedrite-(Cd) inclusions in stage 1, and is accompanied by gangue quartz. Roquesite forms at the edges of the galena (Fig. 2c), suggesting their close genetic relation. The galena is crosscut by stage 2a-b enargite, bournonite, tennantite-(In), tennantite-(Fe), and tennantite-(Cu) (Fig. 2c). The stage 2a mineralization predominantly consists of luzonite (Fig. 2b) or enargite, often associated with pyrite. Pyrite of stage 2a occurs in two varieties, including py_{1a} that is bright in back scatter electron (BSE) images and inclusion-rich py_{1b} that is darker in BSE imaging. $Pyrite_{1a}$ forms thin semi-massive veins (up to 0.5 cm) and microscopically consists of anhedral grains that usually host large luzonite inclusions and/or are surrounded by tennantite-(Cu) (Fig. 2d). $Pyrite_{1b}$ is found as disseminations in quartz veins related to sericite or barite, while sometimes it surrounds py_{1a} (Fig. 2d). Chalcopyrite (ccp_1) accompanies enargite in this stage. Stage 2b includes gray quartz containing native gold grains associated with subhedral py_2, goldfieldite, or tennantite-(Fe) (Fig. 2e). Other sulfosalts, such as colusite and watanabeite, hosting metals such as V and Sn, are part of the sulfosalt assemblage in this stage. Quartz veins from Stages 2a and 2b are associated with sericite and minor APS (aluminum phosphate-sulfate) minerals, including svanbergite ($SrAl_3(PO_4)(SO_4)(OH)_6$). Stage 3 represents the IS stage, characterized by quartz and carbonate veins (Fig. 2e) comprising chalcopyrite, tetrahedrite-(Zn) and -(Fe), tellurides and minor sphalerite. These are associated with euhedral pyrite (py_3), which contains numerous mineral inclusions (Fig. 2f). This stage is also accompanied by sericite and barite.

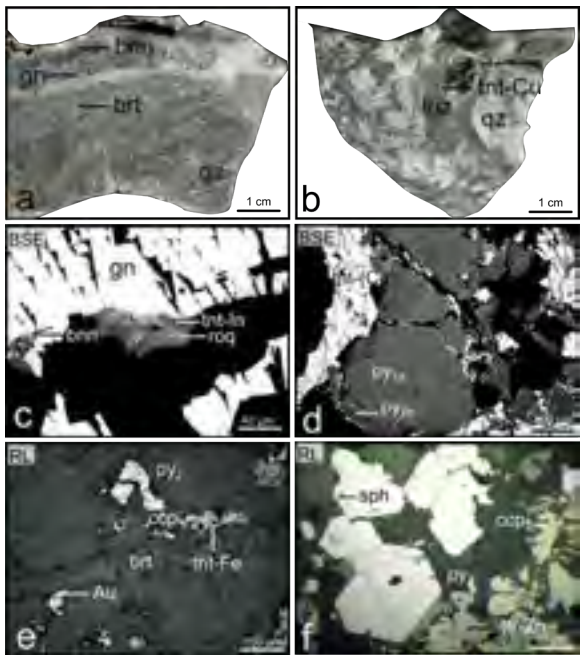


Figure 2. Macroscopic (a-b), BSE microscopic (c-d), and reflected light (RL) microscopic (e-f) images of the high-grade ore at the Pefka deposit. (a) Galena (gn)-quartz (qz) vein of stage I, replaced by bournonite (bnn) and crosscut by an Au-rich quartz vein with barite (brt) grains. (b) Quartz vein with massive luzonite (luz), surrounded by tennantite-(Cu) (tnt-Cu). (c) Galena replaced by bournonite, tennantite-(In) (tnt-In), and roquesite (roq). Remnants of galena are observed between roquesite and tennantite-(In) (d) Anhedral, bright inclusion-poor py_{1a} and darker, inclusion-rich py_{1b} at the rims, surrounded by tennantite-(Cu). (e) Native Au at the rims of a barite grain, accompanied by subhedral py_2 and tennantite-(Fe) (tnt-Fe) than includes chalcopyrite (ccp_1) inclusions. (f) Euhedral py_3 hosting sphalerite (sph) and tetrahedrite-(Zn) (ttr-Zn) inclusions in contact with chalcopyrite (ccp_2) and tetrahedrite-(Zn).

4.2 Geochemistry of sulfides and sulfosalts from the Pefka deposit

In this study, we examined the elemental composition of pyrite, which provides insights into the conditions under which the ore was formed, and the composition of the other analyzed sulfides and sulfosalts, with particular emphasis on In and Te. Pyrite shows enrichment in Se and Te concentrations that have high median values of 113 ppm and 2 ppm respectively in py_2, while Ge is higher in py_1, with a median at 1 ppm. Silver concentrations are elevated in py_1, with median values at 5 ppm, while Co is elevated in py_2, with median values at 2 ppm reaching 150 ppm.

Indium and Te concentrations obtained from LA-ICP-MS analyses vary among the sulfide groups, including pyrite (py_1–py_3), chalcopyrite (ccp_1-ccp_2), and galena (Fig. 3a). In pyrite, In and Te reach up to

0.5 ppm and 22 ppm, respectively, while in galena, they are up to 30 ppm and 20 ppm, and in chalcopyrite ccp_2, up to 500 ppm and 100 ppm, respectively (Fig. 3a).

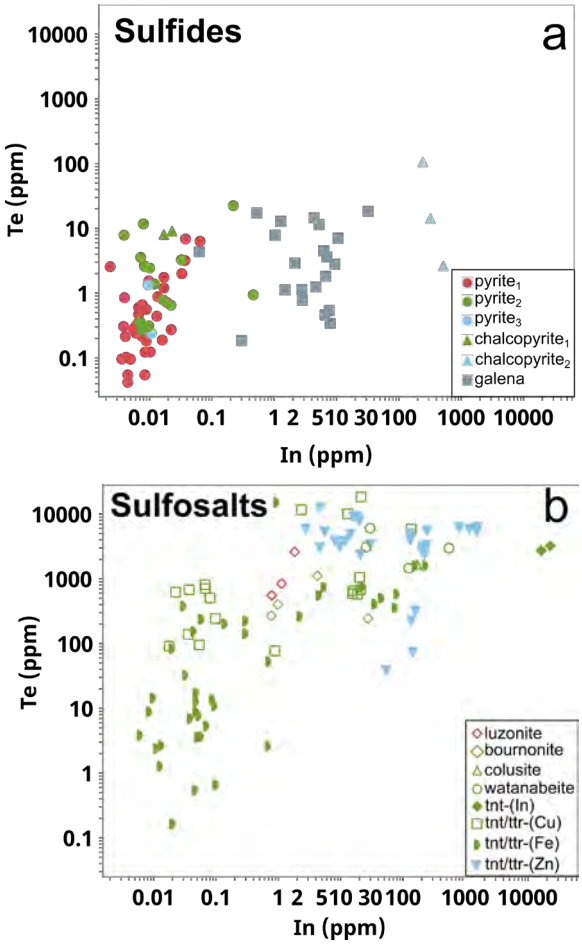


Figure 3. Geochemical variations analyzed with LA-ICP-MS from the Pefka deposit across different stages of sulfides (a) and sulfosalts (b). (a) Indium versus Te contents in different types of pyrite, chalcopyrite, and galena. (b) Indium versus Te contents in sulfosalts (luzonite, bournonite, colusite, watanabeite, and tennantite/tetrahedrite varieties). Colors are indicative of the different stages: Stage 1 is grey, 2a is red, 2b is green and 3 is pale blue.

LA-ICP-MS analyses of sulfosalts included luzonite from stage 2a and bournonite, colusite and watanabeite from stage 2b. Luzonite exhibits high Te contents of up to 3000 ppm. Luzonite is In-depleted, while bournonite of stage 2b hosts up to 30 ppm In. Colusite and watanabeite contain up to 550 ppm In and 7000 ppm Te (Fig. 3b). Indium in tennantite reaches up to 2 wt% in the analyzed data, while previous research noted up to 6 wt% In in the tennantite-(In) (Voudouris et al. 2022; 2023). The tennantite-(In) also hosts Zn up to 1.4 wt%. Stage 2b tennantite/tetrahedrite-(Cu) and -(Fe) ranges from In- and Te-poor to In- and Te-rich, with tennantite/tetrahedrite-(Zn) reaching up to 1500 ppm In and 0.9 wt% Te (Fig. 3b). A slight positive correlation between In and Te contents ($R^2 = 0.5$) is observed in these minerals.

5 Discussion

5.1 Physicochemical conditions of ore-formation from pyrite geochemistry

Pyrite and its elemental ratios serve as indicators of ore-forming processes such as cooling, fluid mixing, and boiling (Keith et al. 2022; Falkenberg et al. 2024). The Se/Te ratio reflects temperature changes, with py_{1a} suggesting higher formation temperatures (median Se/Te ~1000) and py_3 lower (~1), while py_{1b} (~100) and py_2 (~10) fall in between (Fig. 4a). The Se/Ge ratio points towards ore fluids with a mixed magmatic and meteoric fluid component, with py_{1a} and py_2 falling within the magmatic fluid field, whereas py_{1b} and py_3 suggest a mixed magmatic-meteoric component (Fig. 4b). It is notable that the high-In stage 2b shows elevated Se/Ge ratios, suggesting an important contribution of magmatic fluids at the In-rich stage. The Ag/Co ratio (>1) (Fig. 4c) in all Pefka pyrites suggests boiling (Román et al. 2019; Schaarschmidt et al. 2021), supported by mineralogy (Voudouris et al. 2022).

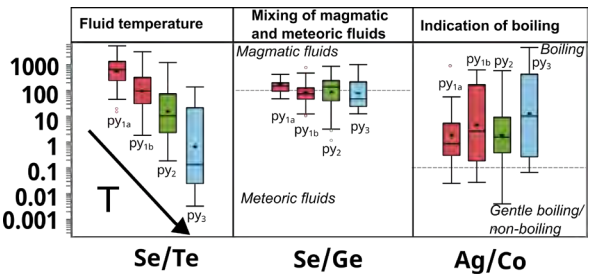


Figure 4. Boxplots from ratios derived from in-situ LA-ICP-MS data in pyrite from the Pefka deposit, used to infer physicochemical parameters of the ore-forming conditions. (a) The Se/Te ratio, which indicates cooling of the fluid temperature (Keith et al. 2022; Falkenberg et al. 2024). (b) The Se/Ge ratio, which reflects the mixing of magmatic and meteoric fluids (Keith et al. 2022; Falkenberg et al. 2024). (c) The Ag/Co ratio reflects boiling or non-boiling conditions (Román et al. 2019; Schaarschmidt et al. 2021). Colors are indicative of the different stages: stage 2a is red, 2b is green and 3 is pale blue.

5.2 Distribution of In and Te in sulfides and sulfosalts from the Pefka deposit

The Pefka deposit hosts, to our knowledge, the most In and Te rich mineralization in Greece with the presence of these two metals in a variety of minerals. The main carriers of In are roquesite that hosts 48 wt% In and tennantite-(In) that hosts up to 6 wt% In (Voudouris et al. 2022; 2023). Both minerals belong to stage 2, while roquesite also appears at the end of stage 1. Indium is also present in sphalerite of stage 3 (up to 0.31 wt%; Voudouris et al. 2022). The main carriers of Te are stage 2b goldfieldite that host up to 12 wt% Te and stage 3 tellurides (e.g., hessite, petzite, coloradoite, native Te, etc.), in which Te is the main constituent of the minerals. The tellurides also occur in minor amounts in stage 2b in association with goldfieldite.

However, the in-situ LA-ICP-MS analyses revealed the ability of sulfides, including pyrite, galena, and chalcopyrite, as well as sulfosalts such as tennantite-tetrahedrite, enargite, colusite, bournonite, and watanabeite to host In and Te in their structure or in the form of micro-inclusions. Galena of stage 1 shows a moderate enrichment of In, but as revealed by the LA-ICP-MS spectra, this is related to the presence of micro-inclusions, probably of roquesite. The rest of the analyzed minerals show flat LA-ICP-MS patterns for In and Te, suggesting their possible presence in the structure of the minerals. Stage 2a minerals such as luzonite show no enrichment in In (up to 2 ppm) and a moderate enrichment in Te (up to 3000 ppm) (Fig. 3b). The sulfosalts of stage 2b, excluding the main carriers (i.e. roquesite and tennantite-(In)), host up to 550 ppm In and 1.9 wt% Te. Stage 3 sulfosalts and specifically tetrahedrite-(Zn) host up to 1500 ppm of In and 0.9 wt% of Te, highlighting that in the absence of sphalerite In can be incorporated in other minerals rich in Zn. Chalcopyrite is also a carrier of In and Te in the last IS stage.

Magmatic fluids, evidenced by high Se/Ge ratios in pyrite (Fig. 4b), contributed significantly during the In-rich stage 2b, and fluid phase separation (boiling indicators) further concentrated In and Te. In-rich minerals are closely associated with Sn-bearing phases, underscoring a geochemical affinity between In and Sn found in other epithermal deposits, as higher grades of In have been detected in Sn-rich polymetallic systems (Mejías et al. 2023 and references therein).

5 Conclusion

The distribution of In and Te in the Pefka deposit is related to different mineral assemblages and processes. A systematic decrease in the Se/Te ratio of pyrite indicates progressive cooling of the ore-forming fluids while the Se/Ge ratio suggests that high In grades are related to the contribution of magmatic fluids. Additionally, Ag/Co ratios in pyrite suggest boiling conditions during both the HS and IS stages. The LA-ICP-MS analyses reveal that sulfides and sulfosalts play a critical role in hosting In and Te, from the HS stage, through the transition, to the final IS stage. Early-stage galena shows moderate enrichment, with In and Te concentrations ranging up to 30 ppm and 20 ppm, respectively, possibly because of the presence of inclusions. In contrast, later-stage tennantite-tetrahedrite varieties exhibit significantly higher concentrations, with up to 6 wt% In and 1.9 wt% Te. Minerals such as colusite, watanabeite and chalcopyrite act as significant carriers, with In and Te present possibly in the structure of the minerals, as evidenced from the flat LA-ICP-MS spectra. These findings highlight the importance of sulfides and sulfosalts not only as repositories of critical metals but also as proxies for reconstructing the physicochemical processes that governed ore deposition in the Pefka deposit.

Acknowledgements

Dr H Brätz is thanked for her assistance during the LA-ICP-MS analyses and processing. Boliden Mineral AB is gratefully acknowledged for providing financial support to the ongoing PhD thesis of M Melfou related to critical and rare metals enrichment in the epithermal systems of the Pefka-Loutros area.

References

Cook NJ, Ciobanu CL (2015) Mineral hosts for critical metals in hydrothermal ores. In Mineral Resources in a Sustainable World, Proceeding of the 13th Biennial SGA Meeting, 24-27 August 2015, Nancy, France. 2:707-710

Falkenberg JJ, Keith M, Melfos V, et al.(2024) Insights into fluid evolution and Re enrichment by mineral micro-analysis and fluid inclusion constraints: Evidence from the Maronia Cu-Mo ± Re ± Au porphyry system in NE Greece. Miner Deposita 59(7): 1407-1431

Keith M, Haase KM, Chivas AR, Klemd R (2022) Phase separation and fluid mixing revealed by trace element signatures in pyrite from porphyry systems. Geochim Cosmochim Acta 329:185-205

Kilias A, Falalakis G, Sfeikos A, Papadimitriou E, Vamvaka A, Gkarlaouni C (2013) The Thrace basin in the Rhodope province of NE Greece — A tertiary supradetachment basin and its geodynamic implications. Tectonophysics 595:90-105

Mejías O, Parbhakar-Fox A, Jackson L, Valenta R, Townley B (2023) Indium in ore deposits and mine waste environments: Geochemistry, mineralogy, and opportunities for recovery. J Geochem Explor 255:107312

Melfos V, Voudouris P (2012) Geological, Mineralogical and Geochemical Aspects for Critical and Rare Metals in Greece. Minerals 2:300-317

Melfos V, Voudouris P (2017) Cenozoic metallogeny of Greece and potential for precious, critical and rare metals exploration. Ore Geo Rev 89:1030-1057

Melfou M, Voudouris P, Klemd R, Keith M, Melfos V, Kantiranis N (2023) In-situ trace element analyses of pyrite from the Pefka epithermal Cu-Au-Te-In-Se deposit, Rhodope, Northern Greece. In Proceedings of the 17th SGA Biennial Meeting, 28 August - 1 September 2023, Zurich, Switzerland. 1:163-166

Müller D, Groves DI, Santosh M, Yang CX (2025) Critical metals: Their applications with emphasis on the clean energy transition. Geosyst Geoenviron 4:100310

Repstock A, Voudouris P, Kolitsch U (2015) New occurrences of watanabeite, colusite, “arsenosulvanite” and “Cu-excess” tetrahedrite-tennantite at the Pefka high-sulfidation epithermal deposit, northeastern Greece. J Min Geochem 192:135-149

Román N, Reich M, Leisen M, Morata D, Barra F, Deditius AP (2019) Geochemical and micro-textural fingerprints of boiling in pyrite. Geochim Cosmochim Acta 246:60-85

Schaarschmidt A, Haase KM, Klemd R, et al. (2021) Boiling effects on trace element and sulfur isotope compositions of sulfides in shallow-marine hydrothermal systems: Evidence from Milos Island, Greece. Chem Geol 583:120457

Voudouris P (2006) A comparative mineralogical study of Te-rich magmatic-hydrothermal systems in northeastern Greece. Miner Petrol 87:241-275

Voudouris P, Repstock A, Spry P, et al. (2022) Physicochemical constraints on indium-, tin-, germanium-, gallium-, gold-, and tellurium-bearing mineralizations in the Pefka and St Philippos polymetallic vein- and breccia-type deposits, Greece. Ore Geol Rev 140:104348

Voudouris P, Biagioni C, Sejkora J, Musetti S (2023) Tennantite-(In), IMA 2023-011. In: CNMNC Newsletter, 73. Eur J Miner. 35:397-402

Magmatic evolution and related Cu-Mo(-W) porphyry ore mineralization in the light of isotopic geochronology and geochemistry – a case study from Variscan orogenic belt in Poland

Stanislaw Z. Mikulski[1], Holly J. Stein[2,3], Ian S. Williams[4], Marek Markowiak[5], Ewa Krzemińska[1]
[1]Polish Geological Institute-National Research Institute, 4 Rakowiecka Street, 00-975 Warszawa, Poland
[2]AIRIE Program, Innosphere Ventures, 320 East Vine Drive, Suite 203, Fort Collins, CO 80524 USA
[3]Department of Geosciences, University of Oslo, 0316 Oslo, Norway
[4]The Research School of Earth Sciences, The Australian National University, Canberra, ACT 2601, Australia
[5]Polish Geological Institute-National Research Institute,ul. Królowej Jadwigi 1, 41-200 Sosnowiec, Poland

Abstract. SHRIMP U-Pb dating of zircon from igneous rocks and Re-Os isotopic studies of molybdenite from the Kraków-Lubliniec tectonic zone (KLFZ), indicate that porphyry-type Mo-Cu(-W) ore mineralization is closely related to the felsic Carboniferous-Permian magmatism in space and time. Our U-Pb isotopic studies show that felsic magmatism in the area was a relatively short-lived event (303.8 ± 2.2 to 294.7 ± 2.3 Ma).This range is consistent with Re-Os isotopic ages of molybdenite (300 ± 2 to 296 ± 2 Ma) from the Myszków Mo-Cu(-W) porphyry deposit and other Cu-Mo prospects in the KLFZ and most probably along other regional NW-trending major shear zones developed in the foreland of the Variscan orogenic belt in central Europe. The Cu-Mo prospects along the KLFZ occur over 60 km from Mysłów to the Będkowska Valley.
The results of oxygen isotope studies of zircon in igneous rock samples from KLFZ indicate the mixing of mantle [$\delta^{18}O$ ~5.3 ± 0.3‰] and crustal [$\delta^{18}O$ >6‰] melts, however with insignificant contamination from sediments. A systematic record of the influence of hydrothermal processes on the O isotopic composition of igneous zircon is widely visible [$\delta^{18}O$ <4‰] in Cu-Mo mineralized zones.

1 Geologic background of Cu-Mo(-W) porphyry-style ore mineralization

The study area is located in southern Poland along the regional Kraków-Lubliniec Fault Zone (KLFZ) which separates the Upper Silesia Block (part of the Brunovistulian composite Terrane) and Małopolska Block (a thinned marginal part of Baltica), and constitutes the foreland of the Variscan orogenic belt in the central part of Europe (Żelaźniewicz et al. 2016). The KLFZ runs parallel to the Trans-European Suture Zone (TESZ), one of the most important composite suture zones in Europe (Figure 1, upper insert). The KLFZ, were active as part of mega-shear zones which resulted from the clockwise rotation of the African plate with respect to the European plate (Ziegler 1986; Żaba 1999). Here, extensive plutonic and volcanic activity resulted from the amalgamation of the Małopolska and Brunovistulian terranes during the Carboniferous-Permian. The eastern part of the European Variscides was the site of rapid continental extension, uplift and deep fracturing (Żelaźniewicz et al. 2016). The transition from a post-collisional to a within-plate setting was favourable for the formation of porphyry and epithermal types of ore mineralization in uplifted areas (Mikulski, Williams 2014). However, subsequent Mesozoic and Cenozoic tectonics strongly influenced the rate of erosion, and thus the exhumation or deeper burial of small, individual porphyry systems (Mikulski et al. 2019).

In the KLFZ under Mesozoic-Cenozoic platform cover, the Myszków Cu-Mo(-W) porphyry type deposit and several very prospective areas for other porphyry-, skarn-contact metasomatic and vein type deposits have been recognized (Harańczyk 1980; Piekarski 1995; Podemski, ed. 2001; Lasoń 2003; Oszczepalski et al. 2010). All are genetically related to Variscan felsic magmatism and hosted by Ediacaran-Palaeozoic sediments and igneous rocks.

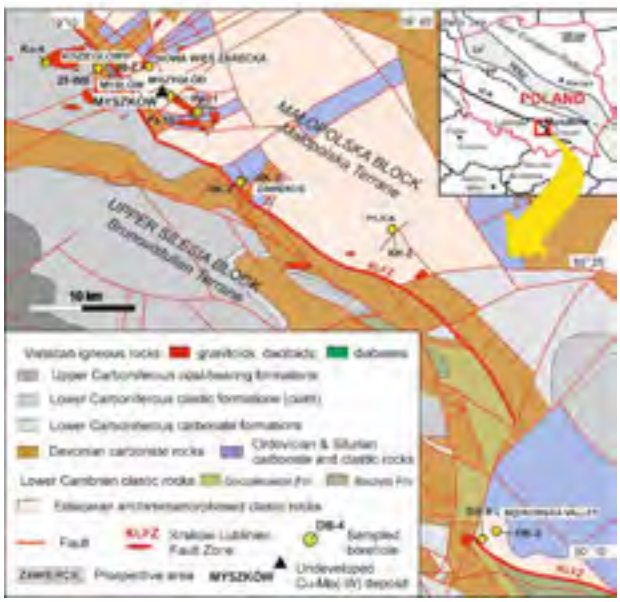


Figure 1. Geological sketch without Mesozoic and Cenozoic sediments in the southern Poland (after Buła et al. 2002) with the location of the selected boreholes being the subject of U–Pb, O and Re-Os isotope studies (modified after Mikulski et al. 2019). *CF* Caledonian Front, *H–K* Hamburg–Kraków Tectonic Zone, *KLFZ* Kraków–Lubliniec Fault Zone, *TESZ* Trans-European Suture Zone (Teisseyre–Tornquist Zone), *VF* Variscan Front

The dominant igneous rocks in the KLFZ are those of felsic composition; granodiorites and dacitoids. Rocks of intermediate to mafic composition, represented by dykes of lamprophyre and/or diabase, are less abundant (Słaby et 2010; Wolska 2012). In the Myszków Cu-Mo(-W) deposit anticipated economic resources down to a depth of 1,000 m are estimated at >550 Mt sulfide ores, with 0.295 Mt of Mo, 0.238 Mt of W and 0.8 Mt of Cu, with anticipated sub-economic resources at 0.298 Mt of Mo, 0.212 Mt of W and 0.771 Mt of Cu.

Geochemically, the felsic rocks (granitoids and dacitoids) are peraluminous, calc-alkaline, and medium-K to high-K with moderate #Mg (0.39-0.46). The granitoids are classified as I-*type* magmatic rocks, and were emplaced in a post-collisional environment (Mikulski et al., 2019).

Ore-hosting rocks are often strongly altered to varying degrees, mainly by sericitization, silicification, feldspathization, argillitization and sulfidization (Koszowska, Wolska 2000; Markowiak 2015).

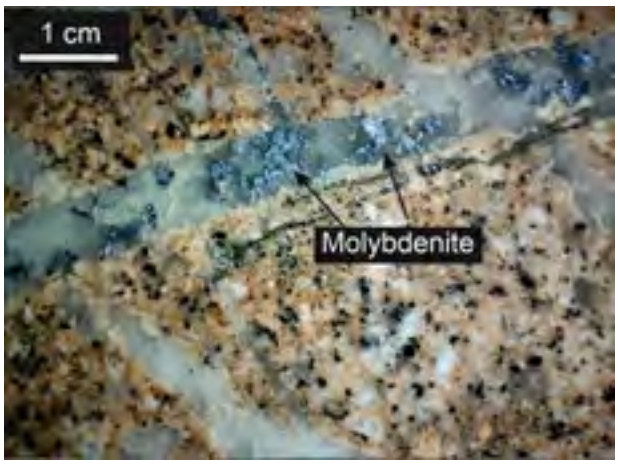


Figure 2. Quartz veinlet with molybdenite mineralization hosted by granite at the Myszków Cu-Mo(-W) deposit in Poland; Pz-26 borehole, 1009.3m depth

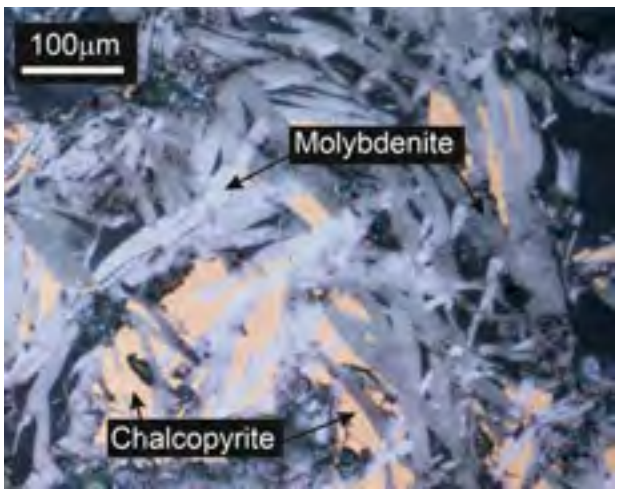


Figure 3. Characteristic forms of molybdenite occurrence in association with chalcopyrite at the Myszków undeveloped Cu-Mo(-W) deposit; Pz-14 borehole, 899.5m depth

Some intervals are more intensely mineralized with numerous generations of quartz veinlets with molybdenite, pyrite and chalcopyrite as well as locally with Pb-Zn-Fe, Au-Ag, and Bi-Te and/or younger REE mineralization (Mikulski et al. 2019).

2 Samples and Methods

Re and Os isotopic data for 17 samples of molybdenite from the Myszków deposit and prospective areas in KLFZ were determined by the AIRIE Program, Colorado State University (Stein et al. 2005; Mikulski, Stein 2010).

Geochronology for igneous rocks from the KLFZ is sparse using modern U-Pb SHRIMP methods. For U-Pb isotopic study magmatic zircon was selected from 20 different igneous rock samples from the archive boreholes located in mineralized areas in the KLFZ (Figure 1). The sensitive high-resolution ion microprobe (SHRIMP) analyses were made at the Research School of Earth Sciences, Australian National University.

Oxygen isotope analyses of zircon from the 20 samples previously subject to U-Pb studies at the ANU were performed by the SHRIMP IIe/MC at the Polish Geological Institute-National Research Institute in Warsaw. To date, about 600 oxygen isotope analyses have been performed in igneous rocks from areas prospective for Cu-Mo(-W) mineralization in the KLFZ zone. Each sample is most often represented by 25–30 point analyses.

3 Results and discussion of isotopic investigations of magmatic zircon by SHRIMP U-Pb and O, and molybdenite by Re-Os

Zircon U-Pb isotopic measurements of felsic igneous rocks yielded ages from 303.8 ± 2.2 to 294.7 ± 2.3 Ma. Molybdenite from different localities in the KLFZ, including the Myszków deposit, crystallized during the time interval 300 ± 2 to 296 ± 2 Ma. The majority of molybdenites have moderate Re concentrations ranging from ca. 30 to 90 ppm. A distinctive feature of zircon is the presence of characteristic magmatic oscillatory zoning and minor inherited zircon cores with a wide range of isotopic ages (Paleoproterozoic-Neoproterozoic). Most of the felsic igneous zircon from the magmatic rocks shows concentric zoning and intermediate Th/U in rims (0.30–0.65).

Isotopic results show that igneous and hydrothermal activity in the KLFZ was restricted to a short interval of time, ca. 10 Ma, coinciding with the Carboniferous-Permian transition.

The compilation of zircon oxygen isotope ratios from samples from the KLFZ reveals variable magmatic $\delta^{18}O$ values, interpreted as mixing of mantle ($\delta^{18}O$ ~5.3 ± 0.3 ‰) and crustal melts $\delta^{18}O$ > 6 ‰, with no contamination by sediments (i.e. $\delta^{18}O$ >10‰). There is also a systematic record of the influence of hydrothermal processes with $\delta^{18}O$

values <4 ‰, which remains an independed indicator of temporal an genetic relation between magmatism and (hydrotermal) mineralization (Figure 4). Mineralized porphyry systems, and other types of Cu-Mo(-W) ores within the KLFZ, are closely related to the felsic magmatism in space and time. As an example, molybdenite from different generations of quartz veinlets in the Myszków Mo-Cu(-W) deposit crystallized during the time interval 300 ± 2 to 296 ± 2 Ma (Figure 5).

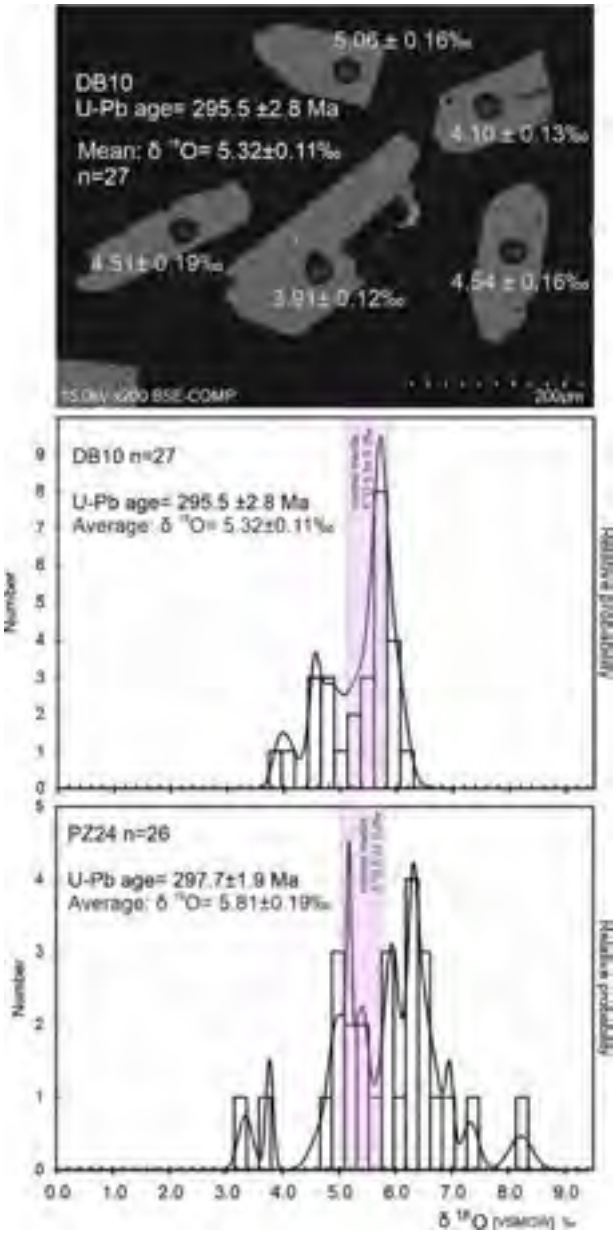


Figure 4. Post-analysis inspection of oxygen SHRIMP analysis pits via electron microscope (BSE) imaging showing analysis location and δ ^{18}O value for sample DB10 (Cu-Mo-W prospective) with multimodal distribution of δ ^{18}O data presented on histogram /probability plot diagram compared with data of coeval sample Pz24 (Myszków Cu-Mo-W Deposit). Zircons that have low ^{18}O (<5 ‰) suggest influence of the paleohydrothermal system on the host rocks.

Similarly, molybdenite from quartz veins that cut dacite and granitoid north of Myszków, yields Re-Os ages of 300.0 ± 2.0 and 299.0 ± 2.1 Ma, respectively. These are indistinguishable from the zircon U-Pb age for granodiorite from the same borehole, 300.2 ± 3.6 Ma, and zircon ages of 301.0 ± 2.1 – 295.9 ± 2.9 Ma, respectively, from the Myszków-Mrzygłód region. The same is true of Cu-Mo mineralization elsewhere in the KLFZ.

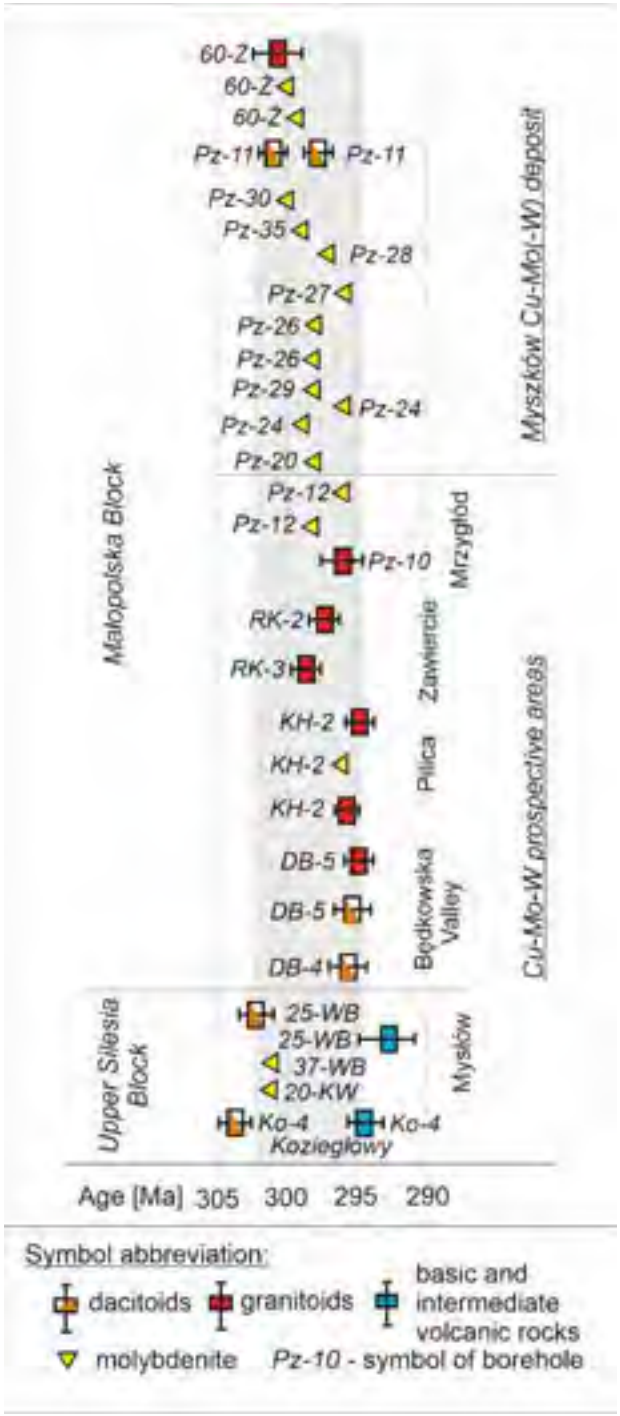


Figure 5. Comparison of SHRIMP zircon U–Pb ages with molybdenite Re–Os ages from the Kraków–Lubliniec Fault Zone in Poland (after Stein et al. 2005; Mikulski and Stein 2012; Mikulski et al. 2019).

The zircon ages of granodiorites from the Pilica region are 295.6 ± 1.9 Ma. Molybdenite from the same region gives an age of 296.3 ± 1.4 Ma. These ages are also consistent with those measured on

dacite zircon from the Będkowska Valley. Moreover, Re-Os ages of molybdenite (301 ± 2 Ma) from quartz veinlets cutting rhyolite and Palaeozoic metamudstone in two boreholes near Mysłów are consistent with the zircon U-Pb ages measured here on dacitoids.

5 Conclusions

The results of our isotopic (U-Pb, O and Re-Os) investigation show that Carboniferous-Permian felsic magmatism was important to the development of Cu-Mo(-W) porphyry type ore mineralization in different places beyond the Myszków deposit in the KLFZ, and most probably along other regional NW-trending major shear zones developed in the foreland of the Variscan orogenic belt in central Europe.

The Mo-Cu(-W) mineralization noted in the KLFZ area is spatially and genetically related to the hydrothermal alteration zones occurring within and around the porphyry intrusions. The relationships between mineralization, Variscan magmatism, intensity and nature of alteration, and the age of molybdenite clearly indicate a post-magmatic hydrothermal origin of the discussed mineralization.

References

Buła Z (ed), Habryn R, Krieger W, Kurek S, Markowiak M, Woźniak P (2002) The Geological Atlas of the Paleozoic (without Permian) rocks contacts between the Upper Silesian and Małopolska Blocks. Państwowy Instytut Geologiczny, Warszawa

Guzik K., Galos K., Kot-Niewiadomska A., Eerola T., Eilu P., Carvalho J., Fernandez-Naranjo F.J., Arvidsson R., Arvanitidis N., Raaness A. (2021) Potential benefits and constraints of development of critical raw materials' production in the EU: Analysis of selected case studies. Resources, 10 (7): 67. https://doi.org/10.3390/resources 10070067

Karwowski Ł (1988) Evolution of the mineralizing fluids of the Variscan copper-molybdenum formation of Cracowides on the example of the Myszków-Mrzygłód region. Prace Nauk Uniw Śląsk w Katowicach 929:89 (in Polish with English summary)

Koszowska E, Wolska A (2000) Mineralogical and geochemical study of thermally altered country rocks of granodioritic intrusion in the Będkowska Valley near Kraków (S Poland). Annales Societatis Geologorum Poloniae, 70:261–280

Lasoń K (2003) Geochemistry of the molybdenum–tungsten porphyry deposit Myszków. Biul Państ Inst Geol 405:87–108 (in Polish with English summary)

Harańczyk C (1980) Palaeozoic porphyry copper deposits in Poland. SGA Spec Publ 1:89–95

Markowiak M (2015) Description of ore mineralization against the background of thermal-metasomatic alterations of rocks in the Żarki-Kotowice area. Prace Państ Inst Geol 203:74 (in Polish with English summary)

Mikulski SZ, Stein HJ (2012) The age of molybdenites in Poland in the light of Re–Os isotopic studies. Biul Państ Inst Geol 452:199–216 (in Polish with English summary)

Mikulski SZ, Oszczepalski S, Markowiak M (2012) The occurrence and prospective resources of molybdenum and tungsten ores in Poland. Biul Państ Inst Geol 448(2):297–314 (in Polish with English summary)

Mikulski SZ, Williams IS. (2014) Zircon U-Pb dating of igneous rocks in the Radzimowice and Wielisław Złotoryjski auriferous polymetallic deposits, Sudetes, SW Poland. Annales Societatis Geologorum Poloniae, 84: 213–233.

Mikulski SZ, Williams IS, Markowiak M (2019) Carboniferous–Permian magmatism and Mo–Cu (W) mineralization in the contact zone between the Małopolska and Upper Silesia Blocks (south Poland): an echo of the Baltica–Gondwana collision International Journal of Earth Sciences (2019) 108:1467–1492. https://doi.org/10.1007/s00531-019-01715-9

Naglik B, Toboła T, Dumańska-Słowik M, Dimitrova D, Derkowski P, Zieliński G, Habryn R, Nadłonek W (2022) Multi-stage ore forming history of the Variscan porphyry Mo-Cu-W Myszków deposit (Poland): Evidence from trace elements of pyrite. Ore Geology Reviews, 150, 105185. https://doi.org/10.1016/j.oregeorev.2022.105185

Oszczepalski S, Markowiak M, Mikulski SZ., Lasoń K, Buła Z, Habryn R (2010) Porphyry Mo–Cu–W mineralization within Precambrian–Paleozoic rocks – prospectivity analysis of the border zone of the Upper Silesia and Małopolska blocks. Biul Państ Inst Geol 439: 339–354.

Piekarski K (1995) Geologic setting and ore mineralizations characteristics of the Myszków area (Poland). Geol Quarterly 39(1):31–42

Podemski M (ed), Buła Z, Chaffee MA, Cieśla E, Eppinger R, Habryn, R, Karwowski Ł, Lasoń K, Markiewicz J, Markowiak M, Snee LW, Ślósarz J, Truszel M, Wybraniec S, Żaba J (2001) Palaeozoic porphyry molybdenum-tungsten deposit in the Myszków area, southern Poland. Polish Geol Inst Spec Pap 6:87

Słaby E, Breitkreuz C, Żaba J, Domańska-Siuda J, Gajdzik K, Falenty K, Falenty A (2010) Magma generation in an alternating transtensional–transpressional regime, the Kraków–Lubliniec Fault Zone,Poland. Lithos 119:251–268. https://doi.org/10.1016/j.lithos.2010.07.003

Stein H, Markowiak M, Mikulski SZ (2005) Metamorphic to magmatic transition captured at the Myszków Mo–W deposit, southern Poland. In: Mao J, Bierlein FP (eds) Mineral deposit research:meeting the global challenge. Springer, Berlin, pp 833–836

Wolska A (2012) Petrology and geochemistry of granitoids and their mafic microgranular enclaves (MME) in marginal part of the Małopolska Block (S Poland). Mineralogia 43(1–2):3–127

Żaba J (1999) The structural evolution of Lower Palaeozoic succession in the Upper Silesia and Małopolska block border zone (Southern Poland). Prace Państ Inst Geol 166:162 (in Polish with English summary)

Żelaźniewicz A, Obec-Dziedzic T, Fanning CM, Protas A, Muszyński A (2016) Late Carboniferous-Early Permian events in the Trans-European Suture Zone: tectonic and acid magmatic evidence from Poland. Tectonophysics 675:227–243. https://doi.org/10.1016/j.tecto.2016.02.040

Ziegler PA (1986) Geodynamic model for the Palaeozoic crustal consolidation of Western and Central Europe. Tectonophysics 126:303–328. https://doi.org/10.1016/0040-1951(86)90236-2

Geology, alteration and mineralization of the La Virgen high-sulfidation epithermal-porphyry district, Peru

Raul Montesinos[1], Zhaoshan Chang[1], Juan Carlos Castelli[2], Shiqiang Huang[1], Willis Hames[3], Robert A. Creaser[4]
[1] Department of Geology and Geological Engineering, Colorado School of Mines, Golden, Colorado 80401, USA,
[2] Mappex Consulting, Santiago de Chile
[3] Auburn University, Alabama, USA
[4] University of Alberta, Edmonton, Alberta, Canada

Abstract. This study seeks to enrich our knowledge and understanding of high-sulfidation (HS) ore-forming processes in siliciclastic rocks, and guide exploration in siliciclastic terranes, by studying the La Virgen district in northern Peru. The La Virgen district is 17 km east of the giant Lagunas Norte HS epithermal deposit, in which the HS mineralization is mostly hosted in the sandstone of the Chimu Formation and other siliciclastic rocks. In addition, this study reveals that in siliciclastic rocks, advanced argillic (AA) alteration is cryptic, commonly filling microfractures, quartz interstices and replacing some feldspar grains, requiring SWIR detection. Pyrophyllite, typical in clay-rich units, is not a reliable vector toward porphyry systems in these settings. Additionally, discovered porphyry style mineralization in the eastern part of the district, and it has its own associated AA alteration and HS mineralization that is significantly older than the HS system in the western side, based on mapping, geochronology, SWIR (Short Wavelength Infra-Red) spectral analysis, petrography, LA-ICP-MS trace element analysis and mapping, and whole rock geochemistry.

1 Introduction

Most of the major high-sulfidation epithermal (HS) deposits are hosted in igneous rocks, including: Yanacocha, Peru (>70 Moz Au; Pilco and McCann 2021); Pascua Lama, Chile-Argentina (>21 Moz Au; Chouinard et al. 2005); Pueblo Viejo, Dominican Republic (>41.7 Moz Au; Vaughan et al. 2021); Lepanto, Philippines (Hedenquist et al. 1998; Chang et al. 2011; Calder et al. 2022); Mt Carlton, Australia (Sahlstorm et al. 2018, 2020), hosted in volcanic rocks, and Zijinshan, China, hosted in granite (Chen et al. 2019). However, the giant Lagunas Norte HS deposit in northern Peru (~14 Moz Au) is mainly hosted in quartz sandstones (~80%; with the rest in volcanic rocks; Cerpa et al. 2013). This discovery indicates that HS deposits may form in siliciclastic rocks, which opens large tracts of land of siliciclastic rocks for HS deposit exploration. This study focuses on La Virgen, another HS district mainly hosted in sandstones, to 1.) help reveal how siliciclastic rocks react with hydrothermal fluids, especially with acid fluids, 2.) describe how the HS mineralization occurs in sandstones, and 3.) identify features, patterns and vectors that can be used to explore in siliciclastic terrains. Additionally, we report new findings through detailed 1:2000 mapping in this district that was traditionally regarded as hosting a single HS epithermal deposit.

2 La Virgen District (LVD) Geology

2.1 Lithology

The sedimentary rocks of the LVD are Lower Cretaceous siliciclastic rocks, listing from oldest to youngest: Chimú Formation (Fm) quartz sandstones with coal seams, Santa Fm black shale, siltstone, and limestone, Carhuaz Fm sandstones and mudstone, Farrat Fm sandstones, Inca Fm grey shale and black limestone, and Chulec Fm limestone and calcareous siltstone. The strata are covered by the Tertiary Calipuy Group volcaniclastic rocks. The sedimentary rocks were folded at least twice and chopped up by many faults of various timing. The faults had multiple movements; some of them generated tectonic breccias that were later altered and cemented by hydrothermal fluids (tectonic-hydrothermal breccias). The sedimentary rocks were intruded by andesite porphyry, feldspar porphyry, and phreatomagmatic breccias of ~22-21 Ma (dated in zircons by U-Pb method), and later dacite porphyries and their related phreatomagmatic breccias of ~17 Ma (dated in zircons by U-Pb method; Figs.1-2).

2.2 Structures

The sedimentary rocks in the LVD were strongly affected by intense Eocene folding (Mégard 1984) and thrust faulting associated with the Inca II orogeny (Noble et al.1979). Mineralization in the LVD was localized by both Inca folds and thrust-related structures and by later N-S, NW, and E-W trending faults. The major faults such as Alumbre, Suro, Tres Rios, Escalerilla, Cerro Blanco and Cuypampa are those controlling the mineralization and alteration, whereas the minor faults such as Cerro Blanco, F1-F4, E1, E2 and C1 are intensively fractured zones and local faults. Minor faults also control the distribution of alteration and mineralization (Fig.1).

2.3 Alteration

The alteration and mineralization occurred in two events and two domains: ~22-21 Ma porphyry-HS mineralization in the eastern Escalerilla-Cuypampa Domain with the source being the feldspar porphyry in its Cuypampa block, and the ~18-17 Ma HS mineralization in the La Virgen Domain, with its

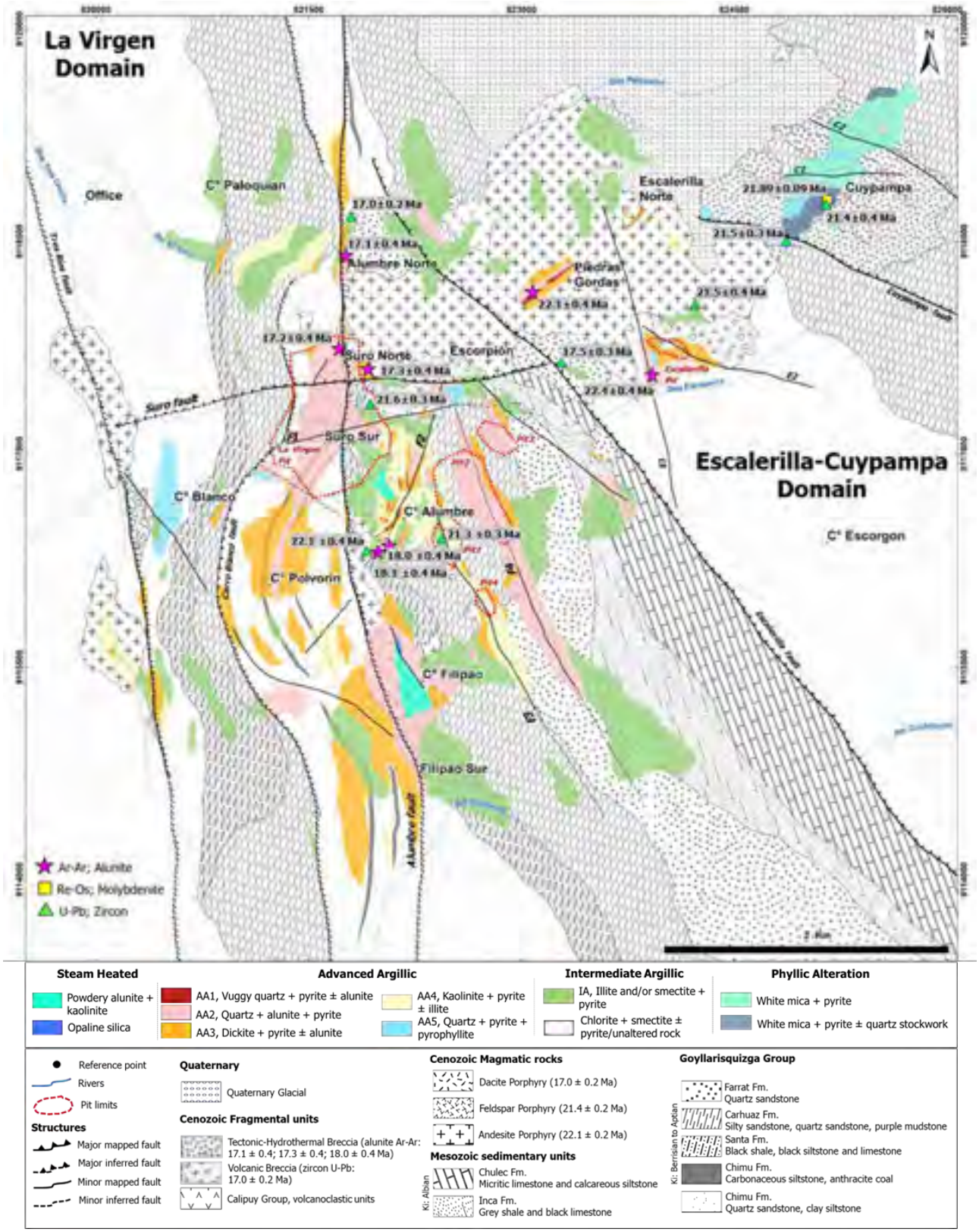


Figure 1. Simplified geology map, based on the 1:2000 mapping of this study. The La Virgen Domain is on the left side of the map and the Escalerilla-Cuypampa on the right, divided by the Escalerilla fault. Dating results are shown in the geology-alteration map, including seven alunite Ar-Ar dates, eight zircon U-Pb dates, and one molybdenite Re-Os date

magmatic center possibly below Cerro Alumbre. Hydrothermal alteration includes five types of advanced argillic alteration (AA1 vuggy quartz + pyrite ± alunite, AA2 quartz + alunite + pyrite, AA3 dickite + pyrite ± alunite, AA4 kaolinite + pyrite ± illite, and AA5 quartz + pyrite + pyrophyllite), intermediate argillic alteration (IA ± pyrite) in the HS deposits, and K-feldspar alteration and slightly later phyllic alteration (quartz-sericite-pyrite) associated with the porphyry-style mineralization. The alteration is structurally and lithology controlled. The AA and IA alterations are typically zoned. The highly

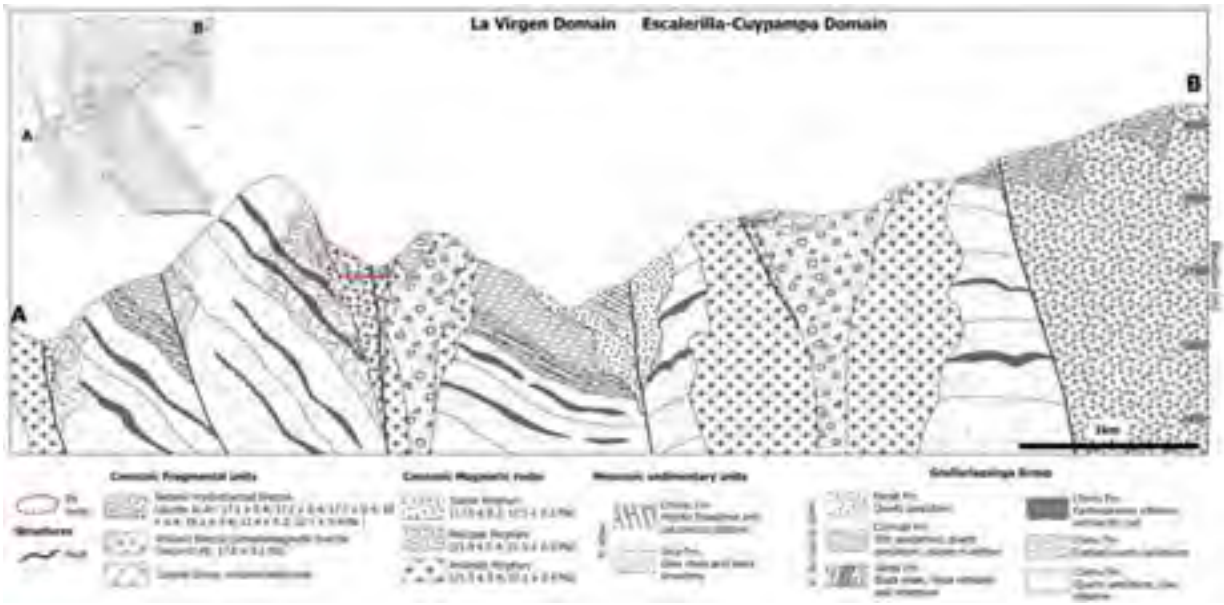


Figure 2. Generalized geological section of the La Virgen District, based on the 1:2000 mapping in this project

fractured and brecciated Chimu sandstones are altered by AA alterations in which alunite, dickite, pyrophyllite, and quartz fill the interstitial open spaces between the resistant quartz grains, fill microfractures, and replace minor feldspar grains. The alteration is cryptic, with the altered sandstone appearing fresh. The alteration minerals also cement and alter clasts of tectonic-hydrothermal breccias (Fig.1).

2.4 Mineralization

The Cu-Au HS mineralization consists of pyrite, enargite, and minor famatinite, luzonite, covellite, digenite, sphalerite, galena, tennantite, tetrahedrite, and visible gold. Gold also occurs in pyrite2, pyrite3, and enargite, as revealed by LA-ICP-MS mapping. HS mineralization is accompanied by silicification that occurs partly as blackish silica with fine-grained pyrite and partly as creamy silica. The silicification also fills interstitial open spaces between grains of the sandstone, fractures in sandstones, and as cement of breccias. The porphyry style mineralization consists of pyrite, molybdenite and chalcopyrite.

3 Geochronology

We used zircon LA-ICP-MS U-Pb dating to date igneous rocks, the alunite Ar-Ar method to date alteration, and the molybdenite Re-Os method to date porphyry mineralization. Dating uncertainties are all reported at 95% confidence level in this study and incorporate all uncertainties (e.g., decay constant uncertainties).

The intrusive rocks on both sides of the Escalerilla Fault are found to be of similar ages. For the andesite porphyry, 21.5 ± 0.5 Ma on the eastern side, vs 22.1 ± 0.4 Ma and 21.6 ± 0.3 Ma (related volcanic breccia) on the western side. The slightly younger feldspar porphyry on the eastern side is dated at 21.4 ± 0.4 Ma and 21.5 ± 0.3 Ma. The youngest dacite porphyry is dated at 17.5 ± 0.3 Ma (east) and 17.0 ± 0.2 Ma (west; Fig. 1).

East of the Escalerilla Fault, molybdenite from the porphyry-style veins is dated at 21.89 ± 0.09 Ma; it overlaps with the age of the host feldspar porphyry (21.4 ± 0.4 Ma). Alunite samples from two AA patches in the east are dated at 22.1 ± 0.4 Ma and 22.4 ± 0.4 Ma, statistically the same, and they are also very similar to the molybdenite Re-Os date and the date of their host rock, andesite porphyry (21.5 ± 0.4 Ma; Fig. 1).

West of the Escalerilla Fault, five alunite samples are collected over a long distance of ~2.2 km, from SW of Cerro Alumbre to the La Virgen pit, then to Alumbre Norte (Fig. 1). The Ar-Ar dates are all younger than the alunite and molybdenite dates east of the Escalerilla Fault, that are similar to each other, but with a slight younging trend from south to north. The two samples SW of Cerro Alumbre are dated at 18.1 ± 0.4 Ma and 18.0 ± 0.4 Ma, younger than the host rock andesite porphyry (22.1 ± 0.4 Ma). Around the La Virgen pit to the north, the two samples are dated at 17.3 ± 0.4 Ma and 17.2 ± 0.4 Ma. The northern most sample is dated at 17.1 ± 0.4 Ma. It is not clear whether there is a minor resetting by the 17.0± 0.2 Ma dacite porphyry at the north end of the 5 samples (Fig. 1).

4 Discussions and Conclusions

4.1 AA alteration in siliciclastic rocks

The advanced argillic (AA) alteration in siliciclastic rocks at LVD is largely cryptic to the naked eye. The rocks, especially sandstones, with AA alteration appear the same as fresh sandstones, mainly due to the lack vuggy texture, the low abundance of alunite, dickite and pyrophyllite, and the small grain sizes, as such minerals could only grow in the tiny interstices between sandy grains. To detect and identify the alteration types, SWIR

spectral analysis is required, whereas for quick mapping of large areas with such alteration, airborne hyperspectral, ASTER, and another remote sensing techniques will be helpful for camp-district scale. One of the major lessons from this study is that SWIR analysis should be widely applied in siliciclastic terrains to identify cryptic clay minerals in reconnaissance exploration, even if the rocks look fresh.

4.2 Two domains in the LVD: La Virgen and Escalerilla-Cuypampa

The LVD has only been explored, recognized, and mined under the concept of a single high-sulfidation mineralization system since its discovery (Noble and Mckee 1999). This study found that it is composed of two domains, based on mapping and radiometric dating of alunite and molybdenite. Although both the La Virgen Domain and the Escalerilla block of the Escalerilla-Cuypampa Domain have HS mineralization and related AA-IA alteration, they formed in two different events (ca. 18-17 Ma vs. ca. 22-21 Ma, respectively) and are unrelated. The HS alteration-mineralization in the Escalerilla block has a similar age as the porphyry-style mineralization in the Cuypampa block, therefore, it is inferred that the Escalerilla HS is related to the Cuypampa porphyry (ca. 22-21 Ma). The HS mineralization-alteration in the La Virgen domain, was developed later at ca. 18-17 Ma (Fig.1).

4.3 Exploration implications of the findings

The findings of this research show that HS-porphyry systems can occur in siliciclastic terrains, which opens large tracts of land for the exploration of such deposits. For example, in northern Peru, where there is over ~45,500 Km^2 Lower Cretaceous siliciclastic rock, the potential for discovering new deposits is quite high. Other siliciclastic districts worldwide should also be explored for such deposits. For the exploration techniques, this study demonstrated that SWIR analysis is necessary on seemingly fresh sandstones, because the advanced argillic alteration in them may be cryptic to the naked eye.

Traditionally, pyrophyllite is used to indicate a higher temperature and deeper position than alunite (e.g., Chang et al. 2011; Calder et al. 2022). This study shows that this vector should be used more carefully in siliciclastic terranes, because pyrophyllite may preferably replace clay-rich lithologies, therefore there is an additional lithological control in addition to temperature/depth/acidity control.

Acknowledgements

We thank Mochica Resources and the geological team, Katharina Pfaff, Moises Mera, and Kelsey Livingston for the financial and technical supports.

References

Calder MF, Chang Z, Arribas A, Gaibor A, Dunkley P, Pastoral J, Kouzmanov K, Spandler C, Hedenquist JW (2022) High-grade copper and gold deposited during post-potassic chlorite-white mica-albite stage in the Far Southeast porphyry deposit, Philippines. Econ Geol 117:1573-1596

Cerpa LM, Bissig T, Kyser K, McEwan C, Macassi A, Rios HW (2013) Lithologic controls on mineralization at the Lagunas Norte high-sulfidation epithermal gold deposit, northern Peru. Minera Depos 48:653–673

Chang Z, Hedenquist JW, White NC, Cooke DR, Roach M, Deyell CL, Garcia J, Gemmell JB, Mcknight S, Cuison AL (2011) Exploration Tools for Linked Porphyry and Epithermal Deposits: Example from the Mankayan Intrusion-Centered Cu-Au District, Luzon, Philippines. Econ Geol 106:1365–1398

Jing Chen, David R. Cooke, José Piquer, David Selley, Lejun Zhang, Noel C. White; Hydrothermal Alteration, Mineralization, and Structural Geology of the Zijinshan High-Sulfidation Au-Cu Deposit, Fujian Province, Southeast China. Econ Geol 114: 639–666

Chouinard A, William-Jones A, Leonardson RW, Hodgson CJ, Silva P, Tellez C, Vega J, Rohas F (2005) Geology and genesis of the multistage high-sulfidation epithermal Pascua Au-Ag-Cu deposit, Chile and Argentina. Econ Geol 100:463-490

Hedenquist JW, Arribas A Jr, Reynolds TJ (1998) Evolution of an intrusion-centered hydrothermal system; Far Southeast-Lepanto porphyry and epithermal Cu-Au deposits, Philippines. Econ Geol 93:373−404

Mégard, F. (1984) The Andean orogenic period and its major structures in central and northern Peru. J. Geol. Soc. Lond., 1, 893–900.

Noble, D., Farrar, E., Cobbing, E. 1979. The Nazca Group of south‐central Peru: Age, source, and regional volcanic and tectonic significance. Earth and Planetary Science Letters, v. 45, p. 80‐86

Donald C. Noble, Edwin H. McKee, 1999. "The Miocene Metallogenic Belt of Central and Northern Perú", Geology and Ore Deposits of the Central Andes, Brian J. Skinner

Pilco R, McCann S (2021) Gold Deposits of the Yanacocha District, Cajamarca, Peru. Society of Economic Geologists Special Publication 23:451–465

Sahlstrom F, Chang Z, Arribas A, Dirks P, Johnson CA, Huizenga JJ, Corral I (2020) Reconstruction of an early Permian, sub-lacustrine 1 magmatic-hydrothermal system: Mt Carlton epithermal Au-Ag-Cu deposit, northeastern Australia. Econ Geol 115:139-152

Sahlstrom F, Dirks P, Chang Z, Arribas A, Corral I, Obiri-Yeboah M, Hall C (2018) The Palaeozoic Mt Carlton Deposit, Bowen Basin, NE Australia: Shallow High-Sulfidation Epithermal Au-Ag-Cu Mineralization Formed during Rifting. Econ Geol 113:1733-1767

Vaughan J, Nelson CE, Garrido G, Polanco J, Garcia V., Macassi A (2021) The Pueblo Viejo Au-Ag-Cu-(Zn) deposit, Dominic Republic. Society of Economic Geologists Special Publication 23:451–465

Role of Oligocene Volcanism in the geological setting of Ag-Au-Pb-Zn-Cu mineralization at the Plomosas District, San Marcial Area, Western Sierra Madre Occidental -Sinaloa Mexico

Paula Montoya-Lopera[1*], Gilles Levresse[2], Marcio Fonseca[3], Luis Coto[3], Marlen Salgado[3], Javier Villegas[3], Miguel Díaz[3], Daniel Schrader[3]
[1]Centre for Ore Deposit and Earth Science (CODES), University of Tasmania, Hobart, Australia
[2]Instituto de Geociencias, Universidad Nacional Autónoma de México, Querétaro, México
[3]GR Silver Mining Ltd. Vancouver, Canada
**paula.montoyalopera@utas.edu.au*

Abstract. The Plomosas District and San Marcial Area (PDSMA) host multiple Ag-Au-Pb-Zn-Cu mineralization events, from early Cretaceous Cu porphyry geological setting to Eocene high sulphidation Ag epithermal veins and Oligocene high-grade Ag-Cu-Pb-Zn-Au tectono hydrothermal breccias, located at the southern end of the Sierra Madre Occidental (SMOc) in Sinaloa, Mexico. Recent field observations, detailed petrography, U/Pb and ^{39}Ar-^{40}Ar age dating of the entire stratigraphic sequence were used to characterize the evolution of multiple mineralization styles and obtain new insights into the evolution of the southern extension of the SMOc. The PDSMA doesn't have a typical SMOc stratigraphic column. The local basement is composed of non-deformed Late Jurassic volcanoclastic units and coeval felsic intrusions, crosscut by the root of Laramide intrusive. Early to late Oligocene silicic ignimbrites, intermediate lava flows, and occasional basalt flows directly overly the Jurassic basement and Laramide intrusive, separated by an angular discordance. Several Oligocene coarse intermediate porphyry bodies and a few Miocene rhyolitic domes intrude the PDSMA stratigraphy. Within the Oligocene volcanic sequence an angular discordance separates an early and a late period. The recent studies presented here highlight the importance of overprint explosive volcanism in the genesis of the multiple mineralization episodes in the PDSMA and in the southern SMOc.

1 Introduction

The Sierra Madre Occidental (SMOc) is a physiographic province which extends from Sonora to Nayarit states. It constitutes one of the largest silicic igneous provinces on Earth, and it is known for hosting numerous important porphyry and epithermal deposits (Camprubí and Albinson 2007; Valencia-Moreno et al. 2017; Montoya-Lopera et al. 2019, 2020(a), (b), 2024). The stratigraphy of the entire Sierra Madre Occidental has been described by several authors (Gastil 1975; McDowell and Keizer 1977; Henry et al. 2003; Ferrari et al. 2007, 2018; Montoya-Lopera et al. 2019, 2024, Valencia-Moreno et al. 2021;) as metamorphosed Jurassic volcanoclastic basement, superposed by the Cretaceous-Eocene Laramide Arc. In a markedly angular discordance, bimodal magmatism was emplaced of large volume silicic ignimbrites and minor basaltic lavas (Ferrari et al. 2018; UVS; McDowell and Keitzer 1977) which were formed in two flare up episodes ~35–29 Ma along the entire province and at ~24–20 Ma in the southern SMO (Ferrari et al. 2007, 2018; McDowell and McIntosh 2012; Montoya-Lopera et al. 2019, 2024) (Fig. 1).

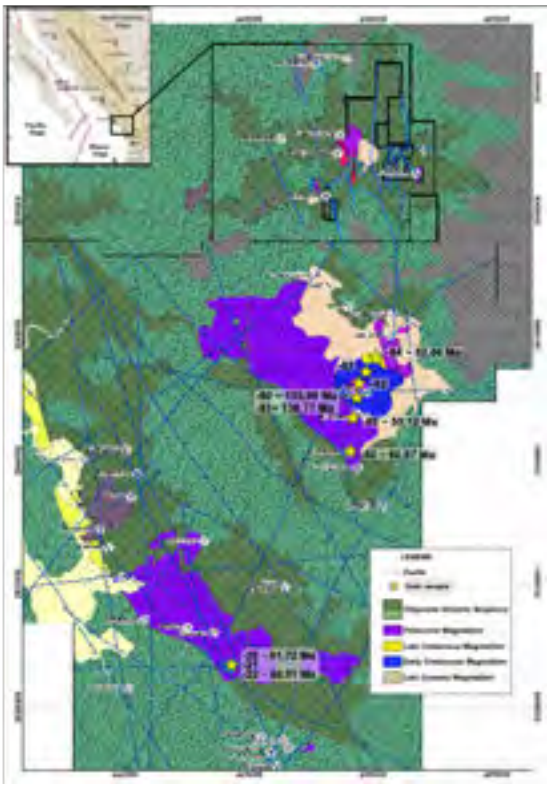


Figure 1. Regional geology map of the southwestern Sierra Madre Occidental with location of Plomosas District and-San Marcial Area (PDSMA)

2 Mining history, local geology and mineralization

Earliest record of mining at Plomosas District - San Marcial Area dates at 18th century. Since then, artisanal and major mining activity was conducted intermittently. Historical production has been estimated in 2.5 million tons averaging 190 g/t Ag, 0.92 g/t Au, 2.02% Zn and 2.38% Pb.

The local geology was poorly understood until recently. However, despite that SMO is a large and continues igneous province, the district displays a stratigraphy column different from other areas to the north depending on its structural controlled, horst and grabens. In the Plomosas graben, located to the

north of the San Marcial Area, the basement is composed of non-deformed Late Jurassic volcaniclastic units and coeval felsic intrusions, early Oligocene sequences of silicic ignimbrites, intermediate lava flows directly overly the Jurassic basement in an erosional unconformity both tilting West. The succession is covered by an angular unconformity to East by bimodal ignimbrite package, several Oligocene intermediate porphyry bodies and rhyolitic domes crosscut the stratigraphic column (Montoya-Lopera et al. 2024) (Fig. 1, 2)

Plomosas District and San Marcial Area mineralization has been described as a series Ag-Cu-Pb-Zn hydrothermal breccias, that striking NNW and dipping 45-60 W or East and have been recognized for a length of more than a kilometre (Gonzalez-Partida et al. 2006, Montoya-Lopera et al. 2024). Multiple mineralized zones have been defined with an initial wide geometry 150m long strike and 300m down dip on average structurally controlled by N-S low and high angle fault breccias. The mineralization consists of a sequence of overlapping events, the earlier Pb-Zn rich event crosscutting by high grade Ag breccia, both cut by younger epithermal Au low sulphidation system.

Previous fluid inclusion studies considered the Pb-Zn mineralization as a single low sulphidation epithermal event showing an evolution between two hydrothermal stages, from an early deep intermediate sulfidation stage, with salinities ranging from 7 to 12 wt.% NaCl equiv., rich in base metal sulphides, to a late shallow low sulfidation stage, with salinities ranging from 0.2 to 3.5 wt.% NaCl equiv., rich in silver sulphides and sulfosalts (Gonzalez-Partida et al. 2006). This two-stages behaviour can be seen in other deposits in the SMO (e.g., El Barqueño district, Camprubí et al. 2016; San Dimas, Montoya-Lopera et al. 2020(a), (b)), which coincides with the relationship described by Nelson (2001) between the salinity and the type of metal in the deposit.

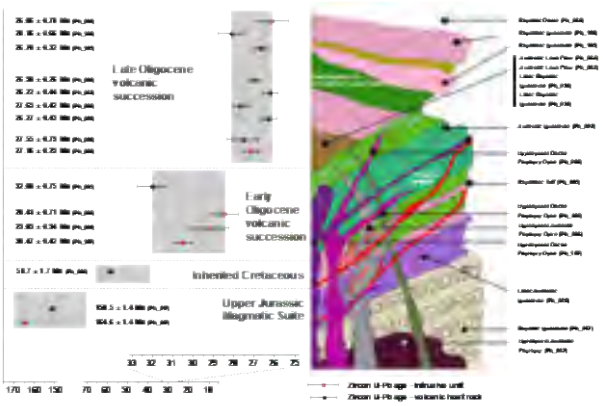


Figure 2. Historic Plomosas Mine area stratigraphy and geochronology taken from Montoya-Lopera et al. (2024)

2.1 New geochronology dates and revision of the local San Marcial Area stratigraphy and mineralization events

Our detail revision of the entire stratigraphy integrates the results of mapping, new advance petrography, geochronology and previous studies. The San Marcial Area stratigraphy can be summarized by undeformed Late Jurassic volcanoclastic sequences, intruded by Early Cretaceous and Paleocene intrusive and hypabyssal bodies unconformity covered by the two sequences of early and late Oligocene intermediate to felsic lavas an ignimbrite (Fig. 1, 9).

San Marcial Area mineralization comprises, i) Laramide Cu-Mo porphyries (Fig. 1, 3, 9 La Tigra intrusive in blue), Late Cretaceous thick Ag deformed veins hosted on Guayabo intrusive (Fig. 1, 9 dark purple bottom left), and Paleocene Ag epithermal veins hosted in Tecuan bodies (Fig. 1, 9 dark purple body); ii) Oligocene hematite tectonic hydrothermal breccias, earliest high grade Pb-Zn > Ag-Cu > Au at Plomosas District (Fig. 4, 5, 6); and high grade Ag > Pb-Zn > Cu at San Marcial. Plomosas mineralization is hosted on early Oligocene volcanic sequence tilting West Fig. 2), meanwhile San Marcial is hosted at the discordance between Jurassic volcanoclastic sequences and Early Oligocene volcanic packages tilting deeply to East (Fig. 1, 3 breccia in green-red).

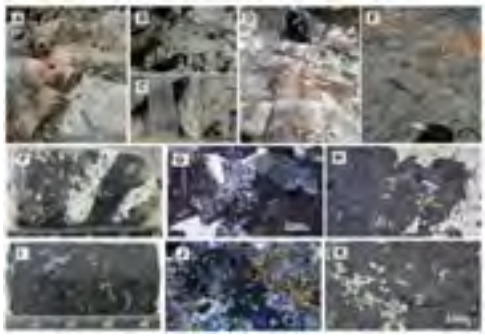


Figure 3. Laramide Cu porphyry mineralization at La Tigra

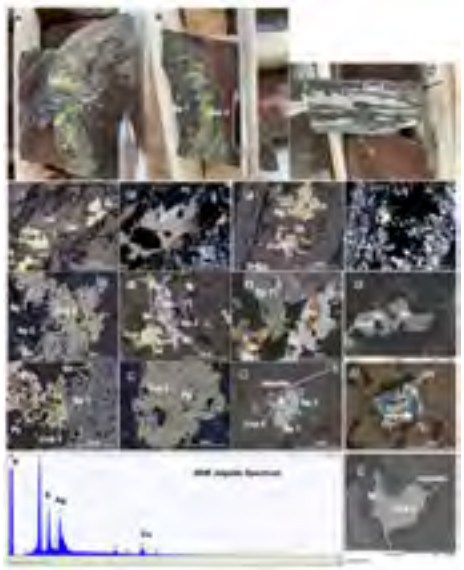


Figure 4. Oligocene Pb-Zn > Ag-Cu > Au mineralization at Plomosas District

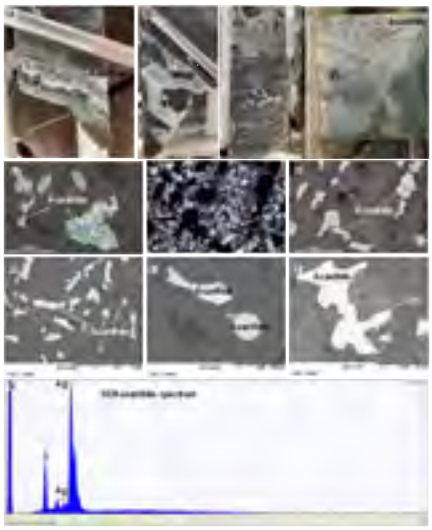


Figure 5. Oligocene high grade Ag low temperature epithermal veins at the top of Plomosas District

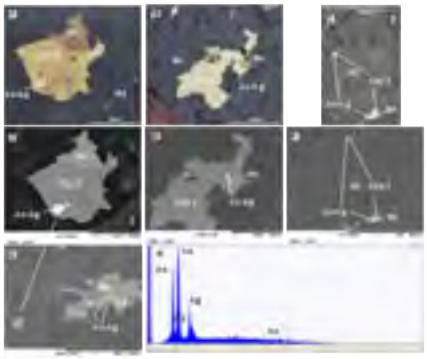


Figure 6. Oligocene Au low sulphidation epithermal system at Plomosas District

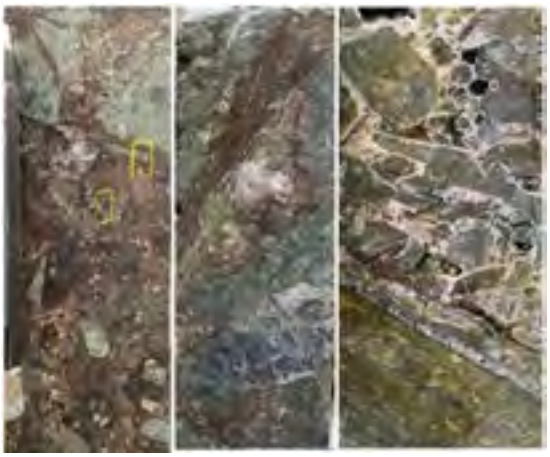


Figure 8. San Marcial high grade Ag > Pb-Zn > Cu hematite tectonic hydrothermal breccia. From left to right, pre ore hematite bx, high grade ore hematite breccia, hydrothermal Qz breccia. Ag sulphides can be on clast, matrix or thin veins

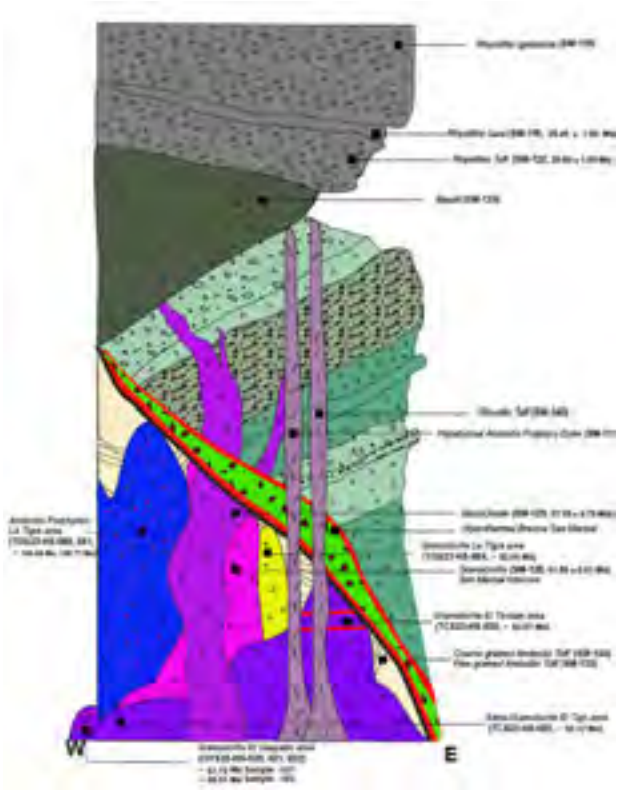


Figure 9. San Marcial Area stratigraphy and new geochronology data

3. New insights into the geological and metallogeny evolution of overprint mineralization episodes at PDSMA

Based on recent zircon trace element geochemistry of the entire stratigraphy and considering the cross-cutting relationship of the multiples mineralization events, we could better describe the metallogeny evolution of the multiple mineralization events in the district. Figure 5. presents the comparison of zircon chemistry with that of the San Dimas district and previous studies at Plomosas (Montoya-Lopera et al. 2019, 2024). As we show in this study, even though the stratigraphy of the three areas has slightly differences, Jurassic magmatism is not observed at San Dimas, whereas the Laramide magmatism of is poorly represented in Plomosas District; at San Marcial Area horst and surrounding extensional areas, the roots of this Laramide arc is well preserved but not the volcanic counterpart that is in San Dimas. Similar as San Dimas, at PDSMA, the magma fertility increases during the formation of Sinaloa batholith in the Eocene, however intense tectonic uplift overlapped by the extension of the Opening of California Gulf lead an angular discordance that put in contact Jurassic rocks against Oligocene volcanic sequences in PDSMA.

At PDSMA, a hydrated and oxidized event can be inferred at the beginning of Paleocene, 10 Ma younger than that determined in the San Dimas. Paleocene and Eocene are reduced and hydrated at PDSMA, whereas they are highly oxidized in San Dimas. The Oligocene event shows a comparable

hydration grade, but oxidation is much higher than in San Dimas, peaking at 27Ma. This peak of the magma conditions corresponds at the end of tilting of the Oligocene volcanic sequence and PDSMA high grade Ag-Pb-Zn-Cu hematite tectonic hydrothermal breccia development. On the other hand, the lack of LVC volcanic counterpart at PDSMA and the xenocrysts found in the Oligocene volcanic sequences indicates that magmas were at least partly produce by melting of intrusive rocks in the upper crust, suggesting that magma recycling in the upper crust had an important role in the generation of telescoping high-grade Ag-Pb-Zn-Cu hematite tectonic hydrothermal breccias.

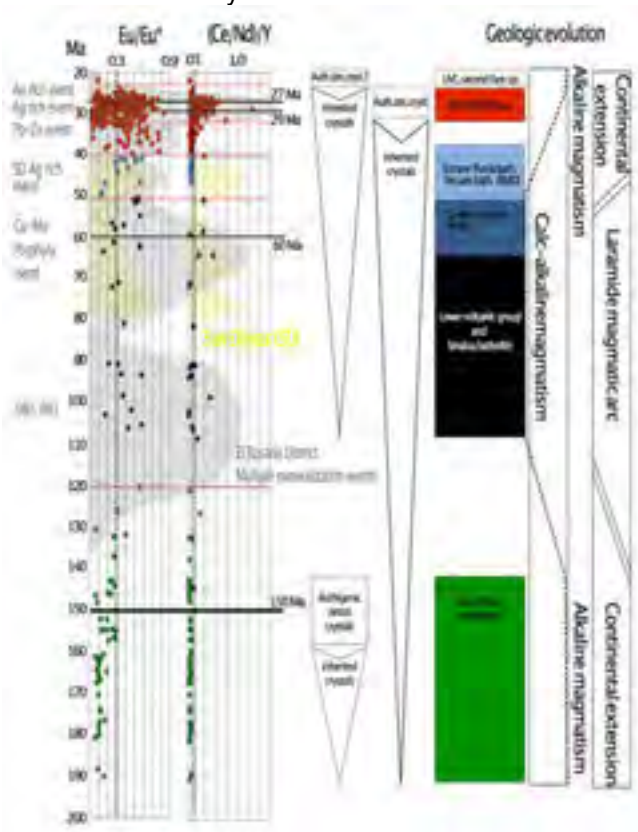


Figure 10. Geochronology and zircon trace element geochemistry from San Marcial Areas

Acknowledgements

We thank GR Silver Mining Ltda, and geology staff for their contribution to this study, we also thank Dr Marina Vega for her assistant at Cortical Fluid Laboratory, Dr Carlos Ortega and Dr Carlos Carrasco for U/Pb analysis, Juan Tomas Vazquez and Alexander Cuison for elaboration of thin sections at IGEO, UNAM and CODES, UTAS, we also thanks to CSL Laboratories at UTAS for MLA-AMICS analysis.

Funding

This research was founded through San Marcial project by University of Tasmania, CODES and sponsorship by GR Silver Mining Ltda.

References

Camprubí A, Albinson T (2007) Epithermal deposits in México—Update of current knowledge, and an empirical reclassification. Geology of Mexico: Celebrating the centenary of the Geological Society of Mexico 422: 377.

Camprubí A, Iriondo A, López-Martínez M, Ramos-Rosique A (2016) Geochronology of Mexican mineral deposits. IV: the Cinco Minas epithermal deposit, Jalisco. Boletín de la Sociedad Geológica Mexicana 68(2): 357-364.

Ferrari L, Orozco-Esquivel T, Bryan S, López-Martínez M, Silva-Fragoso A (2018) Cenozoic magmatism and extension in western Mexico: Linking the Sierra Madre Occidental silicic large igneous province and the Comondú Group with the Gulf of California rift. Earth-Science Reviews 183: 115-152.

Ferrari L, Valencia-Moreno M, Bryan S (2007) Geology of the western Mexican volcanic belt and adjacent Sierra Madre Occidental and Jalisco block. Geological Society of America Special Paper 334: 65-83.

Gastil P (1975) Plutonic zones in the Peninsular Ranges of southern California and northern Baja California: Geology 3: 361–363.

González-Partida E, Camprubí A, González-Sánchez F, Sánchez-Torres J (2006) Fluid inclusion study of the Plomositas–Los Arcos polymetallic epithermal vein tract, Plomosas district, Sinaloa, Mexico. Journal of Geochemical Exploration 89 (1-3): 143-148.

Henry C, McDowell F, Silver L (2003) Geology and geochronology of granitic batholithic complex, Sinaloa, México: Implications for Cordilleran magmatism and tectonics. Geological Society of America Special Paper 374: 237-273.

McDowell F, McIntosh W (2012) Timing of intense magmatic episodes in the northern and central Sierra Madre Occidental, western. Geosphere 8: 1505-1526.

McDowell FW, Keizer RP (1977) Timing of mid-Tertiary volcanism in the Sierra Madre Occidental between Durango city and Mazatlán, México. Geol Soc America Bull 88: 1479-1487.

Montoya-Lopera P, Ferrari L, Levresse G, Abdullin F, Mata L (2019) New insights into the geology and tectonics of the San Dimas mining district, Sierra Madre Occidental, Mexico. Ore Geol Rev 105: 273-294.

Montoya-Lopera P, Levresse G, Ferrari L, Orozco-Esquivel T, Hernández-Quebedo G, Abdullin F, Mata L (2020) a, New geological, geochronological and geochemical characterization of the San Dimas mineral system: Evidence for a telescoped Eocene-Oligocene Ag/Au deposit in the Sierra Madre Occidental, Mexico. Ore Geol Rev 118: 1-15.

Montoya-Lopera P, Levresse G, Ferrari L, Rizzo AL, Urquiza S, Mata L (2020) b Genesis of the telescoped Eocene silver and Oligocene gold San Dimas deposits, Sierra Madre Occidental, Mexico: Constraints from fluid inclusions, oxygen-deuterium and noble gases isotopes. Ore Geol Rev 120: 103427.

Montoya-Lopera P, Levresse G, Ferrari L, Catchpole H, Coto L, Mar F, Castro-Cardenas A (2024) Oligocene magmato-tectonic events influential in the development of Pb, ag and Au mineralization at the Plomosas deposit, southwestern Sierra Madre Occidental, Mexico. International Geol Rev 67: 103-119.

Valencia-Moreno M, López-Martínez M, Orozco-Esquivel T, Ferrari L, Calmus T, Noury M, Mendívil-Quijada H (2021) The Cretaceous-Eocene Mexican Magmatic Arc: Conceptual framework from geochemical and geochronological data of plutonic rocks 220: 103721.

Valencia-Moreno M, Camprubi A, Ochoa Landin L, Calmus T, Mendivil-Quijada H (2017) Latest Cretaceous-early Paleogene “boom” of porphyry Cu mineralization associated with the Laramide magmatic arc of Mexico. Ore Geol Rev 81: 1113–1124.

Skarn-related epithermal Pb-Zn mineralization: a new model for the Laki ore field (Central Rhodope, Bulgaria)

Lison Moynier[1], Yannick Branquet[1], Nathan Cogné[1], Pierre Gautier[1], Boris Ivanov[2], Ianko Gerdjikov[2]
[1] Geosciences Rennes, UMR 6118, University of Rennes, 35042 Rennes, France
[2] Dpt. of Geology, Sofia University "St. Kliment Ohridski", 1504 Sofia, Bulgaria

Abstract. Skarns are calc-silicate assemblages resulting from magmato-hydrothermal processes. Occasionally, they are enriched in sulphides. Among them, the Pb-Zn ore skarns are frequently formed at some distance from the causative magmatic intrusion. During their transport along regional scale faults the fluids can be enriched in Mn and Fe, which results in distal Pb-Zn skarns often associated with Mn-rich calc-silicates. Thus, identifying the tectonic context of the fluid draining faults and the magmatic activity enabling the fluid circulation are of first interest for ore prospection.
This study combines structural, petrological and geochronological data on the Pb-Zn mineralization of the Laki district (Central Rhodope, Bulgaria). We describe a sulphide-poor Mn-skarn that we date at 32.4 ± 1.8 Ma (U-Pb on epidote) and a sulphide-rich carbonate replacement ore body (CROB) previously dated at ca. 30-29 Ma. We interpret them as reflecting different fluid pulses of the same hydrothermal event. The Mn-skarn marks the peak of the regional volcanic activity (cf. the nearby Borovitza caldera), whereas the CROB marks its end. Structural data show that the fluids were drained along a system of conjugate strike-slip faults accommodating N-S horizontal shortening.

1 Introduction

Skarns are calc-silicate assemblages resulting from metasomatic reactions during magmato-hydrothermal processes. If the percolating fluids are metal-rich, the assemblage acts as a precursor for sulphide mineralization during or following the skarn retrograde stage, with base and/or precious metals endowment (Einaudi et al. 1981; Meinert et al. 2005). Among these skarn-related mineralized systems, some are referred to as "distal" because they are formed at some distance from the causative magmatic intrusion and are usually controlled by large faults acting as fluid drains (e.g. Meinert 1987). In epithermal environments, Mn-rich distal skarns are common and frequently host a Pb-Zn mineralization (e.g. Einaudi et al., 1981, Abrecht 1985). In the course of their transport, the magmatic fluids are enriched in Mn and Fe (Einaudi et al. 1981), leading to the crystallisation of Mn-rich gangue minerals (Meinert et al. 2005). If temperatures are too low to trigger the crystallization of prograde Mn-rich calc-silicates, carbonate horizons may be directly replaced by sulphides, forming carbonate replacement ore bodies (CROB) commonly found adjacent to the fluid draining faults (Megaw et al., 1988). A challenge for mineralized Mn-rich distal skarns and CROB exploration is (i) to characterize the favourable faults and assess the tectonic environment that was able to activate them at the time of metal-rich fluid flow, and (ii) to identify the causative intrusive complex(es), which potentially host richer ore systems.

In Bulgaria, the Central Rhodope Region (CRR) hosts important Pb-Zn ore deposits corresponding to CROB spatially associated with Mn-rich skarns (e.g., Vassileva et al. 2009) (Fig. 1). Here, we provide new structural, petrological, and geochronological data based on observations and samples from the two currently active mines of the Laki district (Govedarnika and Dzhurkovo; Fig. 1).

2 Geological and metallogenic setting

2.1 The Central Rhodope Region

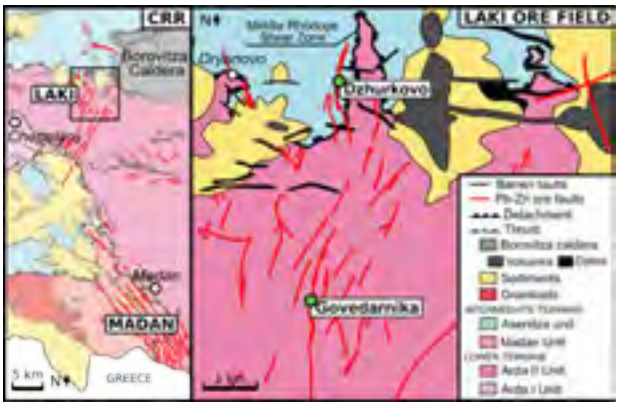


Figure 1. Simplified tectonic map of the Central Rhodope with the main Pb-Zn ore veins (modified after Ivanov et al. 2000 and Kounov et al. 2020).

The CRR essentially consists of high-grade metamorphic rocks shaped by a series of syn-metamorphic thrusts and extensional detachments related to the Alpine orogen (e.g., Ivanov et al. 2000; Kounov et al. 2020).

In the area of Laki, the main Alpine structure is the north-dipping Middle Rhodope Shear Zone interpreted as either a post-orogenic (Ivanov et al. 2000; Kaiser-Rohrmeier et al. 2013; Kounov et al. 2020) or a syn-orogenic (Gerdjikov et al. 2010) detachment. Its footwall, which hosts almost all the Pb-Zn deposits of the district, consists of migmatitic gneisses with subordinate marble layers and metabasic lenses. In this unit, top-to-north shearing along the low-dipping detachment produced a sequence of ductile-then-brittle fault rocks crosscut by steeper north-dipping normal faults. Syn-shearing emplacement of pegmatites related to

near-peak metamorphic conditions is dated at 39.9 ± 2.3 Ma at Govedarnika (U-Pb on titanite (Ttn); Georgieva et al. 2022). Ongoing shearing under decreasing temperatures occurred at ~34-36 Ma (Kaiser-Rohrmeier et al. 2004, 2013; Gerdjikov et al. 2010).

Sedimentary and volcanic rocks cover the metamorphic series and seal the detachment (Fig. 1). The volcanites emanate from the nearby Borovitza caldera which was active between ~33.5 and 31 Ma (Marchev et al. 2013).

2.2 The Central Rhodope Pb-Zn metallogenic background

The Laki and Madan ore fields are the main Pb-Zn districts of the CRR. In both districts, the base metal deposits occur as polymetallic sub-vertical fault-related bodies and low-dipping stratoid bodies replacing marble layers (e.g., Vassileva et al. 2009).

In the Madan district, which was the topic of most previous studies, ore faults are described as part of a system of conjugate strike-slip faults with dominant dextral NNW-striking faults and subordinate sinistral NNE-striking faults (e.g. Atanassov et al. 1972; Manev 1975). No detailed structural analysis has been carried out in the Laki district. There, ore faults are vertical and dominantly NNE-striking (Ivanov et al. 1986; Buret 2012). Kaiser-Rohrmeier et al. (2013) suggested that the Laki ore faults were formed in a post-orogenic extensional setting.

The paragenetic sequences of both the ore faults and the stratoid CROB are characterized by galena (Ga), sphalerite (Sp), pyrite (Py), and chalcopyrite (Cpy) (plus arsenopyrite in Madan), in a Quartz (Qz)-carbonate gangue with additional chlorite (Chl), epidote (Ep), muscovite (Ms), and hematite (Hem). Buret (2012) distinguished three polymetallic phases for the Dzhurkovo veins.

Sulphide-poor skarn assemblages are also documented in close spatial relation with the economic Pb-Zn deposits. In Laki, they are described as pre-ore skarn composed of prograde calc-silicates including johannsenite (Jhn) followed by retrograde amphiboles (Amp) and iron oxides (Buret 2012). Garnet (Gt) from the prograde skarn assemblage yielded U-Pb ages of ca. 39 Ma (Vassileva et al. 2020). In Madan, equivalent rocks correspond to a distal Mn-skarn composed of prograde Jhn, rhodonite (Rdn), and Ep. However, they differ from the Laki skarns because the retrograde phase contains disseminated sulphides (Ga, Sp and Py) together with Mn-Amp. Therefore, although not economic, the Madan Mn-skarns are considered as syn-ore (e.g. Vassileva et al. 2009; Hantsche et al. 2021).

The age of ore deposition at Laki is constrained by ^{40}Ar-^{39}Ar ages on Ms and K-feldspar at ~29-32 Ma (Kaiser-Rohrmeier et al. 2004; Buret et al. 2013). Isotopic studies argue for a mineralizing fluid primarily coming from a magmatic source and subsequently modified during flowing through the metamorphic series (e.g. Marchev and Moritz 2006).

3 Results

3.1 Petrological study

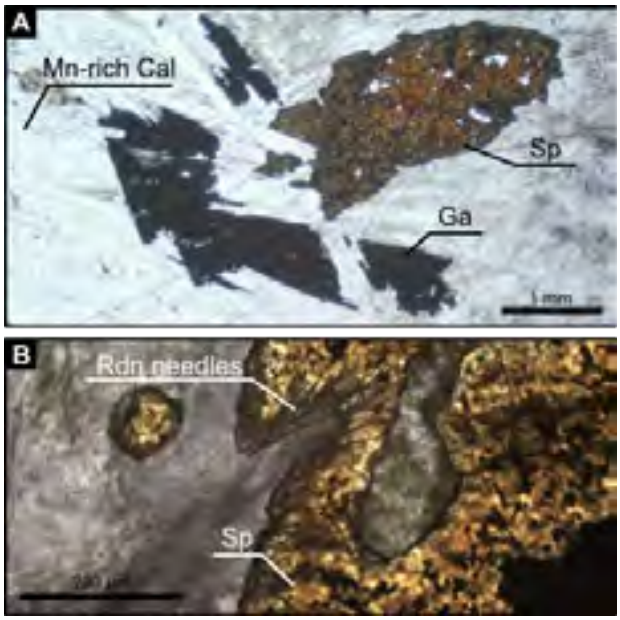


Figure 2. Photomicrographs in polarized light of sulphides formed together with Mn-skarn. A) Sp and Ga grown along Mn-rich Cal cleavages and B) Rdn needles inside Sp.

In the Laki mines we identified two sulphide-bearing assemblages and a barren skarn.

The first assemblage is partly comparable to the Mn-rich skarns described at Madan (Hanstche et al. 2021). It consists of sub-synchronous Mn-rich mineral fronts replacing marbles. The fronts are composed of Rdn needles, acicular Jhn, Mn-rich calcite (Cal), starry Ep, Hem, and Qz in variable proportions. In contrast to the case at Madan, no evidence of retrograde phases such as the alteration of Rdn and Jhn into Amp is observed. Moreover, textural evidence shows that some sulphides grew synchronously with Mn-rich Cal and Rdn needles (Fig. 2).

The second assemblage is a Pb-Zn CROB that contains enough sulphides to be of economic interest. Its gangue is composed of prismatic Qz with minor Chl, Ep, Hem, and Ms, plus late Cal and siderite that grown in geodic cavities.

The third mineral assemblage corresponds to a thin (up to ~15 cm thick) non-mineralized and Mn-depleted skarn observed at the contact between marbles and felsic rocks (pegmatites, gneisses). It is characterized by a prograde assemblage made of diopside, Gt, clinozoïsite, Ttn, apatite (Ap), and Ep, and a retrograde assemblage made of Amp, Cal, Chl, magnetite, and Hem.

3.2 Structural analysis

As long ago recognized, the CROB occur in sites where steep ore-bearing faults, which are of economic interest and petrographically described by Buret (2012), intersect low-dipping marble layers (e.g., Vassileva et al. 2009). Our structural analysis of ore faults in the Laki mines shows that they were active as strike-slip faults at the time of ore deposition. Kinematic criteria such as en échelon patterns of extensional veins indicate that the NNE-striking faults are sinistral while a subordinate set of NNW-striking faults is dextral. The north-dipping normal faults are barren and crosscut by the ore faults.

Mine observations show that the Mn-skarn was formed due to fluid circulation within localized drains such as lithological contacts and fractures. In contrast, CROB result from fluid flow within larger damage zones and/or dilatant sites along the strike-slip faults, enabling larger fluid volumes to circulate.

3.3 U-Pb dating of Mn-skarn and barren skarn

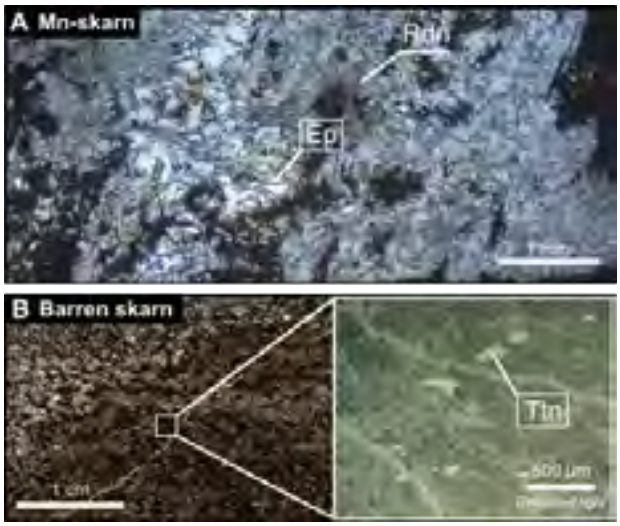


Figure 3. Textural position of the investigated minerals (LA-ICPMS U-Pb dating). A) Ep associated with Mn-rich minerals (Rdn, Jhn) of the Mn-skarn. U-Pb dating on Ep yields 32.4 ± 1.8 Ma (n = 30, MSWD = 0.8). B) Ttn grown synchronously with the barren skarn minerals and aligned within the metamorphic foliation. U-Pb dating on Ttn yields 41.7 ± 0.9 Ma (n = 26, MSWD = 1.1) and 41.7 ± 1.4 Ma (n = 30, MSWD = 1.2)

We performed U-Pb dating on the starry Ep aggregates from the Mn-skarn sampled in the Govedarnika mine (Fig. 3A). It yields an age of 32.4 ± 1.8 Ma that we interpret as dating both to the Ep crystallization and the Mn-skarn formation.

We dated prograde Ttn from two barren skarns from the Dzhurkovo mine and surface outcrop (Fig. 3B). We interpret the ages of ca. 42 Ma as dating both the Ttn crystallization and the prograde stage of the barren skarn.

4. Interpretation and discussion

4.1 Pre-ore syn-migmatitic barren skarn

The ca. 42 Ma age obtained here for the barren skarn is ≥ 10 Ma older than the ages of sulphide deposition at ca. 29-32 Ma (Kaiser-Rohrmeier et al. 2004; Buret et al. 2013; this study). Therefore, the barren skarn is disconnected from the Pb-Zn mineralizing event. In contrast, its age is undistinguishable from both the ca. 39 Ma ages obtained on Gt from prograde skarn assemblages (Vassileva et al. 2020) and the ca. 40 Ma age obtained on pegmatites that represent melts extracted from anatectic levels (Georgieva et al. 2022). Hence, we interpret the barren skarns as the result of metasomatic exchanges between marble layers and gneisses or syn-migmatitic pegmatite injections.

4.2 Syn-caldera multi-pulse hydrothermalism

The data suggest that the two sulphide-bearing assemblages of the Laki ore field (i.e. Mn-skarn and CROB) reflect distinct fluid circulations. Their fluids flew through different drains and their gangues are made of different minerals. Moreover, the ca. 32 Ma age obtained here for the Mn-skarn suggests that it was formed during the peak of the volcanic activity recorded in the Borovitza caldera (cf. Marchev et al. 2013) whereas the CROB was formed in the aftermath of its end (30-29 Ma, Kaiser-Rohrmeier et al. 2004). This suggests that Pb-Zn sulphide deposition was polyphased and reflects a multi-pulse hydrothermal system controlled by the same magmatic source. This is consistent with a magmatic origin of the CROB fluids (e.g. Marchev and Moritz 2006). This type of system has been described by Mariko et al (1996) for the Kamioka Pb-Zn skarn deposits (Japan), where five mineral assemblages, all containing sulphides, are linked to the same magmatic event.

4.3 Structural control on Pb-Zn deposits

Our structural analysis of the ore faults in the Laki district shows that they belong to a system of conjugate strike-slip faults that is consistent with the one documented in the Madan district (e.g. Manev, 1975). The main difference is that the NNE-striking sinistral faults vs. the NNW-striking dextral faults are dominant in the Laki vs. the Madan district, respectively (Fig. 1). On the scale of the CRR, this fault pattern documents a regime of N-S horizontal shortening at the time of ore deposition. The network of steep strike-slip faults, formed after extension, enabled a far-distant transport of the hydrothermal fluids. During N-S shortening, the north-dipping normal faults associated with the detachment remained closed and impermeable to fluid circulations, preventing mineralization along them.

The synchronism between Pb-Zn hydrothermalism and the volcanic activity in the Borovitza caldera suggests that the latter was formed under the same N-S shortening regime. While it might be intuitive that calderas are formed

preferentially in extensional settings, the data rather suggest that the Borovitza caldera opened as a pluri-kilometric pull-apart. In agreement with this view, Dhont et al (2008) described the eastern margin of the caldera as being controlled by a major NNW-striking dextral fault.

5. Conclusion

The Laki Pb-Zn deposits post-date extensional shearing on the Middle Rhodope Shear Zone and were formed under a regime of N-S horizontal shortening. Consequently, the Pb-Zn mineralization precipitated within conjugate strike-slip faults and by replacement of marble levels (Mn-skarn and CROB) while the detachment remained barren.

The Pb-Zn multi-pulse hydrothermal activity took place between ca. 32 and 29 Ma and was coeval with the volcanic activity recorded in the Borovitza caldera. We identified two sulphide-bearing assemblages. The first, formed at ca. 32 Ma, is a non-economic distal Mn-skarn in which sulphides are intergrown with Mn-rich calc-silicates. No retrograde stage was associated with sulphide deposition, at variance with what is reported at Madan and elsewhere (e.g. Einaudi et al. 1981; Meinert et al. 2005; Hanstche et al. 2021). The second assemblage involved larger volumes of fluids. It corresponds to a massive sulphide CROB (cf. Megaw et al. 1988) formed at ca. 30-29 Ma, in the aftermath of the end of magmatism in the Borovitza caldera.

Acknowledgements

This project was funded by the RILA program (PHC France-Bulgaria, project 51273PB), the OSUR (AO 2023, Axe Ressources Naturelles), and the University of Rennes (AAP Défis scientifiques 2024). We thank Laki Invest-Dzhurkovo EOOD for giving access to the mines and Philippe Boulvais who helped during the first stages of the project.

References

Abrecht J (1985) Manganiferous pyroxenes and pyroxenoids from three Pb-Zn-Cu skarn deposits. Contrib Mineral Petrol 89: 379 – 393.

Atanassov A, Kolkovski B, Dobrev D, Iliev Z (1972) Movements and mineralization along Spoluka-Laikov Chukar Fault, Madan District. Annuaire Univ Sofia, 1,, Geol. 65: 137-155. (in Bulgarian)

Buret Y (2012) Polymetallic mineralisation of the Djurkovo deposit, Laki mining district, southern Bulgaria: Paragenesis and fluid evolution. MSc Thesis Univ Geneva, 151 p.

Buret Y, Kouzmanov K, Spikings R, Gerdjikov I. (2013) Timing of polymetallic Pb-Zn mineralisation in the Laki district, southern Bulgaria – constraints from $^{40}Ar/^{39}Ar$ dates. 11th Swiss Geoscience Meeting, Lausanne, Abstract Vol: 103-104.

Dhont D, Yanev Y, Bardintzeff JM, Chorowicz J (2008) Evolution and relationships between volcanism and tectonics in the central-eastern part of the Oligocene Borovitsa caldera (Eastern Rhodopes, Bulgaria). J Volc Geotherm Res 171: 269-286.

Einaudi MT, Meinert LD, Newberry RJ (1981) Skarn deposits. Econ Geol 75th Anniv Vol: 317-391.

Georgieva Y, Milenkov G, Vassileva R, Georgieva S (2022) Trace-element signatures of pegmatite and post-pegmatite minerals from the Govedarnika Pb-Zn deposit, Laki district, Central Rhodopes. Rev Bulg Geol Soc 83: 89-92.

Gerdjikov I, Gautier P, Cherneva Z, Bosse V, Ruffet G (2010) Late Eocene synmetamorphic thrusting and syn-orogenic extension across the metamorphic pile of the Bulgarian Central Rhodope. Geologica Balcanica 39: 132-133.

Hantsche AL, Kouzmanov K, Milenkov G, Vezzoni S, Vassileva R, Dini A, Sheldrake T, Laurent O, Guillong M (2021) Metasomatism and cyclic skarn growth along lithological contacts: Physical and geochemical evidence from a distal Pb-Zn skarn. Lithos 400-401: 106408

Ivanov Z, Dimov D, Sarov S (2000) Structure of the Central Rhodopes, In: Ivanov Z (ed), Structure, Alpine evolution and mineralizations of the Central Rhodopes area (South Bulgaria), Guide to excursion B, ABCD-GEODE Workshop: 6-20.

Kaiser-Rohrmeier M, Handler R, von Quadt A, Heinrich C (2004) Hydrothermal Pb–Zn ore formation in the Central Rhodopian Dome, south Bulgaria: Review and new time constraints from Ar–Ar geochronology. Schweizer Mineral Petrogr Mitteil 84: 37–58.

Kaiser-Rohrmeier M, von Quadt A, Driesner T, Heinrich C, Handler R, Ovtcharova M, Ivanov Z, Petrov P, Sarov S, Peytcheva I (2013) Post-orogenic extension and hydrothermal ore formation: high-precision geochronology of the Central Rhodopian Metamorphic Core Complex (Bulgaria-Greece). Econ Geol 108: 691–718.

Kounov A, Seward D, Burg JP, Stockli D, Wüthrich E (2020) Cenozoic thermal evolution of the Central Rhodope Metamorphic Complex (Southern Bulgaria). Int J Earth Sci 109: 1589–1611.

Manev D (1975) Structure-formation stages in the Madan ore field. Ore-Forming Processes and Mineral Deposits 1: 20-28. (in Bulgarian)

Marchev P, Moritz R (2006) Isotopic composition of Sr and Pb in the Central Rhodopean ore fields: Inferences for the genesis of the base-metal deposits. Geologica Balcanica 35: 49-61.

Marchev P, Harkovska A, Pecskay Z, Panteva V, Popov M (2013) Geology, petrology and K-Ar geochronology of Topolovo-Pilashevo dyke swarm (TPDS) and lavas from the NW Borovitsa volcano (Eastern Rhodopes, Bulgaria). Acta Vulcanologica 25: 99–110.

Mariko T, Kawada M, Miura M, Ono S (1996) Ore formation processes of the Mozumi skarn-type Pb-Zn-Ag deposit in the Kamioka Mine, Gifu Prefecture, Central Japan - A mineral chemistry and fluid inclusion study. Resource Geology 46: 337-354.

Megaw PKM, Ruiz J, Titley SR (1988) High-temperature, carbonate-hosted Ag-Pb-Zn(Cu) deposits of northern Mexico. Econ Geol 83: 1856-1885.

Meinert LD (1987) Skarn zonation and fluid evolution in the Groundhog Mine, Central mining district, New Mexico. Econ Geol 82: 523-545.

Meinert LD, Dipple GM, Nicolescu S (2005) World skarn deposits. Econ Geol 100th Anniv Vol: 299-336.

Vassileva RD, Atanassova R, Bonev IK (2009) A review of the morphological varieties of ore bodies in the Madan Pb-Zn deposits, Central Rhodopes, Bulgaria. Geochemistry, Mineralogy and Petrology 47: 31-49.

Vassileva RD, Grozdev V, Peytcheva I, von Quadt A, Salnikova E (2020) Andradite from Pb-Zn Djurkovo deposit, Central Rhodopes: chemical composition and U/Pb dating. Rev Bulg Geol Soc 81: 58–60.

Trace elements in sulfides (pyrite, chalcopyrite, molybdenite) from the porphyry Mo-Cu-W Myszków deposit (Poland): petrogenetic significance, prospecting application, and importance for the raw materials challenges

Beata Naglik[1], Magdalena Dumańska-Słowik[2], Tomasz Toboła[2], Ryszard Habryn[1], Artur Sosnal[1]
[1]Polish Geological Institute-National Research Institute, Upper Silesian Branch, Sosnowiec, Poland
[2]AGH University of Krakow, Poland

Abstract. Recent studies employing mineralogical, geochemical, and isotope analyses of the most common sulfides (pyrite, chalcopyrite, molybdenite) from the porphyry Myszków Mo-Cu-W deposit (Poland) have revealed their potential to preserve key-petrogenetic information on the mechanisms of metal enrichment and physicochemical conditions prevailing at the time of their crystallization. Moreover, systematic variations in the geochemical and isotopic signatures of pyrite revealed its potential as another exploration tool targeting the centers of porphyry-type mineralization. Finally, the ability of sulfides to incorporate trace elements, including critical raw materials, was comprehensively analyzed, critically evaluated, and discussed here.

1 Introduction

A growing number of studies targeting the geochemical characteristics of ore minerals *via* laser ablation combined with inductively coupled plasma mass spectrometry (LA-ICP-MS) have contributed to our knowledge on metallogenesis processes, the physicochemical properties of mineralizing fluids, the variation of fluids composition along with time and their effect on the ore minerals distribution, as well as possible injection of magma of different composition during long-lived magmatic-hydrothermal activity (e.g. introduction of metals and/or triggering the volatile release). Porphyry Cu deposits (and associated epithermal Au deposits) provide an excellent opportunity to study systematic variations of geochemical signatures of ore phases as these systems are usually characterized by mineralogical zonality, and possess several distinctive ore-forming events to compare by means of fluids physicochemical conditions (Sillitoe 2010).

Geochemical studies conducted so far in the porphyry Myszków Mo-Cu-W deposit have mainly concerned the whole rocks – both mineralized and those constituting their cover (see Podemski 2001; and the literature therein). Such an approach has its practical consequences: firstly, it leads to an underestimation of the content of elements occurring in low concentrations (by averaging the results of analyses on samples containing both ores and gangue minerals), and secondly, it does not provide information on the affinity of selected elements, including the critical raw materials, to specific sulfides and their preferential incorporation into their structure (e.g. Velásquez et al. 2020). However, knowledge of the preferential mineralogical host for trace elements is essential for identifying opportunities and developing strategies for their recovery.

This work is a summary of the results of mineralogical and geochemical studies of ore mineralization from the porphyry Myszków Mo-Cu-W deposit (the Kraków-Lubliniec Fault Zone, Poland), including LA-ICP-MS analyses of the three most common sulfides (pyrite, chalcopyrite, and molybdenite) and isotope studies of pyrite (SHRIMP IIe/MC), conducted in 2019-2024. The aim of the research was to better understand the metallogenesis of the porphyry Myszków Mo-Cu-W deposit (petrogenetic objective), to propose new geochemical exploration proxies (prospecting objective), and finally, to define interesting, from the economic point of view, trace elements impurities in selected sulfides (raw material objective).

2 Geological settings

The polymetallic Mo-Cu-W Myszków deposit (unexploited yet) is located at the Kraków-Lubliniec Fault Zone (KLFZ) and features porphyry-style mineralization within metamorphic surroundings (tectonically deformed Ediacaran flysh-like rocks), intruded by Late-Carboniferous granitoids (see Podemski 2001; and the literature therein) (Fig.1) The KLFZ marks the boundary between two distinctive tectonic units: (1) the Upper Silesian Block (USB) and (2) the Małopolska Block (MB), which have been considered as terranes of Gondwana and Baltica affinity, respectively (Mikulski et al. 2019).

The deposit has four distinct types of hypogene alterations, i.e., potassic, propylitic, argillic, and phyllic, providing key guides for exploration in this area. The ore mineralization resulted from both contact metamorphism (early, skarn-type mineralization) and post-magmatic, hydrothermal activity (main hydrothermal mineralization). The sulfides are mainly represented by pyrite, chalcopyrite, and molybdenites, accompanied by sphalerite and galena (Ślósarz 2001).

The precipitation of ores occurred in a series of pulses controlled by different fissure systems and was characterized by diverse paragenetic sequences (Ślósarz 2001). Generally, three periods of mineralization have been defined at the Myszków deposit: (1) early, skarn-forming (period I), (2) main, hydrothermal (period II), and (3) late, post-ore (period III). Period I is represented by magnetite-sulfide mineralization found in hornfelses, skarns, and metasomatites. Within period II, different stages of ore deposition have been distinguished: (1) feldspar-molybdenite veins with biotite, (2) quartz-feldspathic, pegmatitic veins, (3) quartz veins with molybdenite and scheelite (stockwork system), (4) black quartz veins with molybdenite, and (5) quartz-polymetallic veins (without molybdenite). Finally, period III produced mainly ankerite-barite-fluorite mineralization and the youngest carbonate veins with sphalerite and galena.

The Myszków Mo-Cu-W deposit was recognized as a result of an intensive drilling program (over 30 km of drilling) carried out by PGI-NRI in the years 1975-1992 and covering an area of 0.54 km^2 and down to the depth of 1300 m (Piekarski et al. 1993). It remains the only European porphyry-style deposit of the Variscan age (297.5 +/- 0.5 Ma) still undergoing active exploration (Guzik et al. 2021). Molybdenum, Cu, and W occur as major valuable metals, while Ag, Au, and Re have the potential to be by-products.

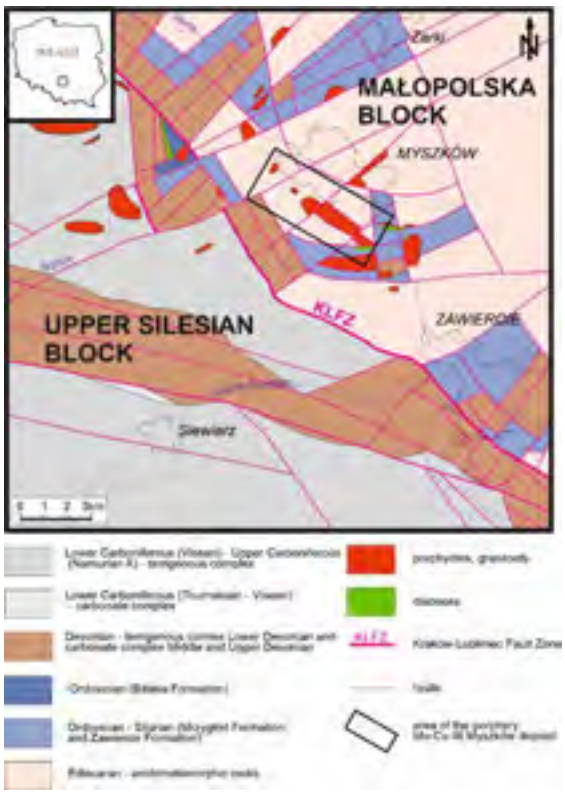


Figure 1. Geological map of the porphyry Mo-Cu-W Myszków deposit (modified after Buła et al. 2008).

3 Pyrite

Pyrite, one of the main components of the Myszków Mo-Cu-W ore mineralization, is associated with different fissure systems. The geochemistry of pyrite from the various generations of veins differentiates fluids composition during the evolution of this porphyry system (Naglik et al. 2022). For example, the Se/Te ratio was found to decrease along with the temperature drop as a result of the mixing of magmatic fluids with meteoric waters (Naglik et al. 2022). Moreover, the non-homogeneous distribution of cobalt and nickel, together with microtextural features of pyrite was attributed to phase separation (i.e., boiling conditions), which is probably the most effective ore depositional process in both high-temperature porphyry Cu deposits and their epithermal counterparts.

In addition to being an excellent petrogenetic indicator, pyrite has been also considered as a vectoring mineral towards the mineralization center (see Holiday & Cook 2007; and the literature therein). For the porphyry Myszków Mo-Cu-W deposit the key pyrite-hosted elements, which make predictions about likely distance and direction to ore include Ag, As, Bi, Co, Sb, Te, and their elemental ratios (Sb/Te, Co/Bi, Ag/Ni, Co/As) (Fig.2). Additionally, there was a gradual decrease in $\delta^{34}S$ of late-stage pyrite outwards from the deposit core to the peripheral zone, extending laterally for a distance of up to 3 km, and hence providing another tool to assist future drilling programs in the KLFZ, which represents a multi-commodity (Mo, Cu, W, Ag, Au, Re, Co, Bi) prospect to meet the growing demand for critical and base metals.

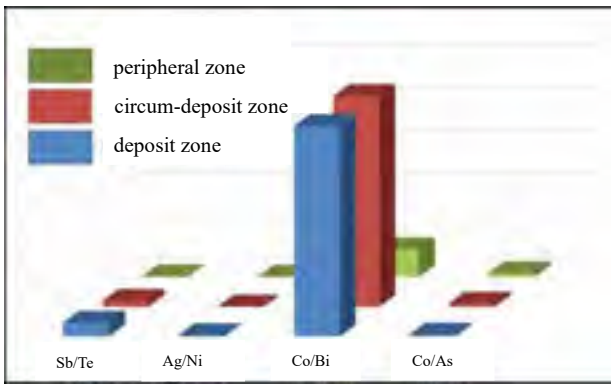


Figure 2. Average trace element ratios of Sb/Te, Ag/Ni, Co/Bi, and Co/As in late-stage pyrite from the Myszków Mo-Cu-W porphyry deposit as a function of distance-to-center.

Quite recently, porphyry-type pyrite has also attracted economic interest as an alternative source of supply for critical metals due to the new recovery techniques proposed, especially for Co (e.g. Velásquez et al. 2020). The pyrite from Myszków is effective in scavenging some trace elements, including Co, Te, and Ce (the last one hosted by monazite-(Ce) inclusions; Naglik et al. 2021, 2022). Hence, an economic assessment should be done including an estimation of Co tonnage and a

feasibility study of the additional unit operations related to its recovery.

4 Chalcopyrite

Chalcopyrite is the principal ore mineral of copper; however, its ability to host trace elements remains poorly understood. The porphyry Myszków Mo-Cu-W deposit is characterized by the common presence of chalcopyrite that occurs as fine-grained crystals disseminated in the potassic, phyllic, and pyritic halos, and filling several generations of veins formed under different physicochemical conditions. It often forms intergrowths with pyrite, sometimes sphalerite, bornite, and galena, and locally with chalcocite.

Chalcopyrite is generally considered a poor carrier for trace elements, especially in the presence of co-crystallized common sulfides, like sphalerite or galena (e.g. George et al. 2018). The incorporation of elements into the chalcopyrite studied here is facilitated by elevated temperature and pressure. The high-temperature chalcopyrite related to skarn- and main-hydrothermal stage of mineralization shows the highest concentrations of Ag (up to 55.80 ppm), Bi (up to 50.10 ppm), Ga (up to 4.01 ppm), In (up to 29.20 ppm), Pb (up to 11.50 ppm), and Sn (up to 312.90 ppm) (Fig.3). In contrast, As (up to 12.81 ppm), Cd (up to 30.00 ppm), and Sb (up to 9.49 ppm) exhibit a clear affinity to chalcopyrite accompanying the youngest carbonate veins.

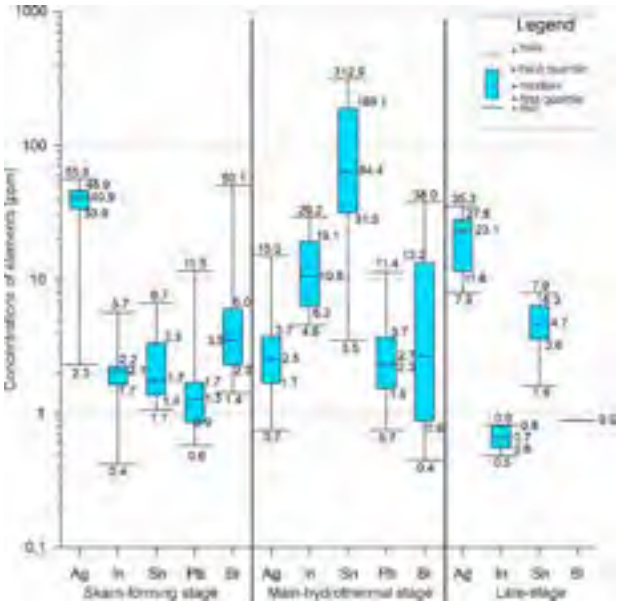


Figure 3. Boxplot of the elemental data obtained with LA-ICP-MS for chalcopyrite.

In the context of literature data on chalcopyrite from porphyry deposits worldwide, the main-stage specimens from the Myszków Mo-Cu-W deposit are distinguished by a relatively high content of In and Sn, which substitute for Fe in the structure of the sulfide. The significant concentration of Sn in stockwork chalcopyrite seems to confirm the hypothesis of the influx of fluids of a more reducing nature at this stage of the evolution of the system (Huston et al. 1995). It could be also supported by the elevated concentrations of Te in main-stage pyrite (Naglik et al. 2022) and the presence of pyrite-hosted cassiterite inclusions (Naglik et al. 2021).

Co-precipitation of chalcopyrite and pyrite deduced from textural relationships makes it possible to discuss the trace elements fractionation between these two, the most common sulfides at the deposit scale. The general partitioning trends could be identified for Ag, As, Cd, Co, In, Ni, Sb, and Sn. Arsenic, cobalt, and nickel preferentially partition into pyrite, while Ag, Cd, In, Sb, and Sn are primarily concentrated in chalcopyrite, and those relationships occur irrespective of the stage of mineralization, type of veins, and host rocks.

From an economic point of view, elevated concentrations are noted for Ag, In, and Sn. Silver is a well-established by-product within porphyry deposits where it is recovered from gold-silver alloy; although Ag might be also hosted by tellurides and galena as well. In some cases, however, chalcopyrite turns out to be a very important Ag carrier (e.g. Eskdale et al. 2022). Indium does not form distinct minerals, but is commonly extracted from sphalerite; however, In-bearing chalcopyrite is also known from some hydrothermal ore systems of different origins (e.g. Kieft and Damman 1990). Tin is generally found in uneconomic concentrations in porphyry Cu deposits with some exceptions, e.g. the Climax mine, where it was recovered as a by-product from cassiterite (e.g. John and Taylor 2016).

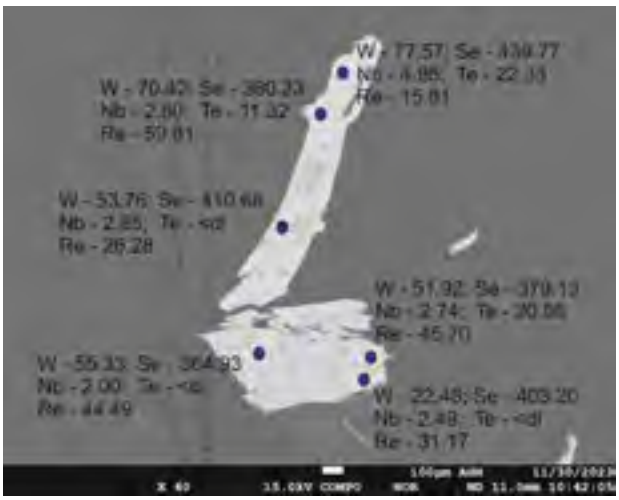
5 Molybdenite

Similarly to pyrite and chalcopyrite, molybdenite precipitated during several different mineralization stages; however, it is the most common within the main hydrothermal veins. In turn, unlike pyrite and chalcopyrite, molybdenite practically does not occur in low-temperature veins of the late mineralization stage.

Molybdenite from the porphyry Myszków Mo-Cu-W deposit was dated using the Re-Os method and is characterized by a relatively narrow crystallisation range of 300 ± 1 million to 296 ± 1 million years (Mikulski and Stein 2012). It is the main carrier of rhenium – an element that, like indium, does not form its own minerals, but it is recovered as a by-product. The molybdenite crystals studied here are characterized by the Re content of several dozen ppm (below 100 ppm), which is a typical feature of porphyry deposits (Mo subtype). Moreover, it is believed that the content of rhenium in molybdenite depends on the geotectonic conditions of the deposit and indicates the origin of the metals (Stein et al. 2001). In the case of the porphyry Myszków Mo-Cu-W deposit, the average Re content not exceeding 100 ppm may suggest a mixed, i.e. mantle-crust genesis of the magmas for the formation of the parent intrusion (Słaby et al. 2010).

Molybdenite from the porphyry Myszków Mo-Cu-W deposit also hosts significant traces of Nb, Se, Te, and W, which occur as structurally-bonded elements (Fig.4). Enrichment of molybdenite in these metals has been previously reported from deposits of hydrothermal origin (e.g. Pašava et al. 2016).

Acknowledgments



The research was financially supported by the Polish Geological Institute-National Research Institute statutory funds (Projects Nos. 62.9012.2317.00.0 and 61.7305.2400.00.0 for B.N.), the National Science Centre, Poland (Project No. 2020/04/X/ST10/00572 for B.N.), the program „Excellence initiative – Research University" for the AGH University of Krakow (No. 6353 for M.D-S.), and AGH grant No. 16.16.140.315. We thank the reviewer very much for the constructive comments.

References

Buła Z, Byś I, Florek R, Habryn R, Jachowicz M, Kwarciński J, Laskowicz R, Liszka B, Madej K, Maksym A, Markowiak M (2008) Atlas Geologiczno-Strukturalny Paleozoicznego Podłoża Karpat Zewnętrznych i Zapadliska Przedkarpackiego: Warsaw, Polish Geological Institute (in Polish).

Eskdale AE, Smith DJ, Ene VV, Negulici M, Onescu D (2022) Economic By-Products in copper Porphyries: Silver in the Ascutita Cu-Porphyry, Romania. Ore Geol Rev 150: 105135.

George LL, Cook NJ, Ciobanu CL (2016) Partitioning of trace elements in co-crystallized sphalerite–galena–chalcopyrite hydrothermal ores. Ore Geol Rev 77: 97-116.

Guzik K, Galos K, Kot-Niewiadomska A, Eerola T, Eilu P, Carvalho J, Fernandez-Naranjo FJ, Arvidsson R, Arvanitidis N, Raaness A (2021) Potential benefits and constraints of development of critical raw materials' production in the EU: Analysis of selected case studies. Resources 10(7): 67.

Holliday JR, Cooke DR (2007) Advances in geological models and exploration methods for copper±gold porphyry deposits. In: Proceedings of exploration 7: 791-809.

John DA, Taylor RD (2016) By-products of porphyry copper and molybdenum deposits. https://doi.org/10.5382/REV.

Kieft K, Damman AH (1990) Indium-bearing chalcopyrite and sphalerite from the Gåsborn area, West Bergslagen, central Sweden. Mineral Mag 54(374): 109-112.

Mikulski SZ, Stein HJ (2012) The age of molybdenites in Poland in the light of Re-Os isotopic studies. Biuletyn Państwowego Instytutu Geologicznego 452: 199-216.

Mikulski SZ, Williams IS, Markowiak M (2019) Carboniferous-Permian magmatism and Mo-Cu (W) mineralization in the contact zone between the Małopolska and Upper Silesia Blocks (south Poland): An echo of the Baltica-Gondwana collision. Int J Earth Sci 108(5): 1467-1492.

Naglik B, Dumańska-Słowik M, Toboła T, Derkowski P, Habryn R, Markowiak M (2021) Diversity of Pyrite-Hosted Solid Inclusions and Their Metallogenic Implications — A Case Study from the Myszków Mo-Cu-W porphyry deposit (the Kraków-Lubliniec Fault Zone, Poland). Minerals 11: 1426.

Naglik B, Toboła T, Dumanska-Slowik M, Dimitrova D, Derkowski P, Zielinski G, Habryn R, Nadlonek W (2022) Multi-stage ore forming history of the Variscan porphyry Mo-Cu-W Myszków deposit (Poland): evidence from trace elements of pyrite. Ore Geol Rev 105185.

Pašava J, Svojtka M, Veselovský F, Ďurišová J, Ackerman L, Pour O, Drábek M, Halodová P., Haluzová E (2016) Laser ablation ICPMS study of trace element chemistry in molybdenite coupled with scanning electron microscopy (SEM) - an important tool for identification of different types of mineralization. Ore Geol.Rev. 72: 874-895.

Piekarski K, Gajowiec B, Siemiński A, Truszel M, Habryn R., Markowiak M, Kurbiel H, Karwasiecka M, Łuszczkiewicz A, Stępniewski M (1993) Geological Report on Myszków Mo-W-Cu Ores Deposit, in C2 Category in Myszków, Myszków Commune, Częstochowa Province: State Geological Institute, National Geological Archive, Warsaw, Poland.

Plotinskaya OY, Abramova VD, Groznova EO, Tessalina SG, Seltmann R, Spratt J (2018) Trace-element geochemistry of molybdenite from porphyry Cu deposits of the Birgilda-Tomino ore cluster (South Urals, Russia). Mineral Mag 82(S1): S281-S306.

Podemski M (2001) Palaeozoic porphyry molybdenum-tungsten deposit in the Myszków area, Southern Poland. Warsaw.

Sillitoe RH (2010) Porphyry Copper Systems. Econ Geol 105: 3-41. https://doi.org/10.2113/gsecongeo.105.1.3.

Słaby E, Breitkreuz C, Żaba J, Domańska-Siuda J, Gaidzik K, Falenty K, Falenty A (2010) Magma generation in an alternating transtensional–transpressional regime, the Kraków–Lubliniec Fault Zone, Poland. Lithos 119(3-4): 251-268.

Stein HJ, Markey RJ, Morgan JW, Hannah J., Scherstén A (2001) The remarkable Re–Os chronometer in molybdenite: how and why it works. Terra Nova 13(6): 479-486.

Ślósarz J (2001) Mineralogical characteristics of the mineralization. In: Podemski M. (ed) Palaeozoic Porphyry Molybdenum-Ungsten Deposit in the Myszków Area, Southern Poland. Polish Geological Institute, Special papers, Warsaw, pp. 43-53.

Velásquez G., Carrizo D., Salvi S., Vela I., Pablo M., Pérez A. (2020) Tracking cobalt, REE and gold from a porphyry-type deposit by LA-ICP-MS: A geological approach towards metal-selective mining in tailings. Minerals 10(2): 109.

Fluid inclusion data provide new insights into the origin and evolution of the Epithermal Ag-Au mineralization at Galim-Legalgorou, Cameroon volcanic line (CVL)_Edited

Terence Cho Ngang[1,2], Thomas Wagner[2], Cheo Emmanuel Suh[1]
[1]Department of Geology, Mining and Environmental Science, Faculty of Science, The University of Bamenda, P.O. Box 39, Bambili, North West Region, Cameroon,
[2]Institute of Mineralogy and Economic Geology, RWTH Aachen University Wullner Strasse 2, 52062, Aachen, Germany.

Abstract. Galim-Legalgorou, located on the Cameroon volcanic line, is now known to host significant epithermal Au-Ag mineralization, likely of the low sulfidation type. Although ore mineralogy and microchemistry of electrum and sphalerite have largely demonstrated this claim, questions regarding the fluid sources and physico-chemical conditions at mineralization remained unanswered. This study presents the major fluid inclusion features (petrography, microthermometry, composition) and attempts an explanation of their bearing on the origin and evolution of the mineralization. Secondary assemblages with co-existing liquid and vapor inclusions suggest that a vapor phase existed at mineralization, and may have been triggered by hydrothermal explosions leading to hydrofracturing and brecciation. All fluid inclusions are two-phase aqueous solutions with low average salinities (2.2 wt% $NaCl_{eqv}$), and homogenization temperatures ranging from 176 – 303 ^{0}C (av. 263 ^{0}C), typical of conditions in epithermal systems. A negative correlation is observed between homogenization temperatures and fluid salinities indicating a volatile-free fluid boiling process that excludes fluid mixing as a principal trigger of mineralization. Inclusion composition shows that Na and K are the dominant ions in solution, suggesting that the fluid was in equilibrium with Na- and K-rich rocks and minerals. These data further support the claim of an epithermal mineralization at Galim-Legalgorou.

1 Introduction

Galim-Legalgorou in northern Cameroon is now known to potentially host significant Au-Ag mineralization of the low sulfidation epithermal type associated with rocks of the Cameroon volcanic line (CVL), an intracontinental rift system, in a region, only previously known for orogenic Au deposits (Ngang et al. 2024).

The characteristics of the hydrothermal fluids that drive a mineral system can be directly measured from fluid inclusions trapped in minerals such as quartz and calcite, precipitated directly from the ensuing fluid. Data from fluid inclusion petrography, microthermometry experiments and bulk inclusion analyses, when used in combination with field relations can provide highly valuable genetic constraints to a given mineral deposit (Bodnar et al. 1985; Pudack et al. 2009; Zhai et al. 2009). The often-low salinity (<10 wt% NaCl) and low temperature (150-300 ^{0}C) fluids associated with epithermal mineral systems, are typically of mixed meteoric/magmatic origin and dominated by liquid water and vapor. Boiling, fluid-mixing and near-surface vapor condensation have been recognized as the main mechanisms of mineral deposition in epithermal systems (Hedenquist et al. 2000; Puddack et al. 2009). Although the field relations, ore minerology and microchemistry of electrum and Fe-rich sphalerite largely suggest an epithermal low-sulfidation origin for the Galim-Legalgorou deposit, questions on the fluid sources and exact physico-chemical conditions that accompanied the mineralization remained unanswered. This paper therefore highlights the fluid inclusion features of quartz veins associated with the mineralization and how these may have contributed to the evolution of the deposit.

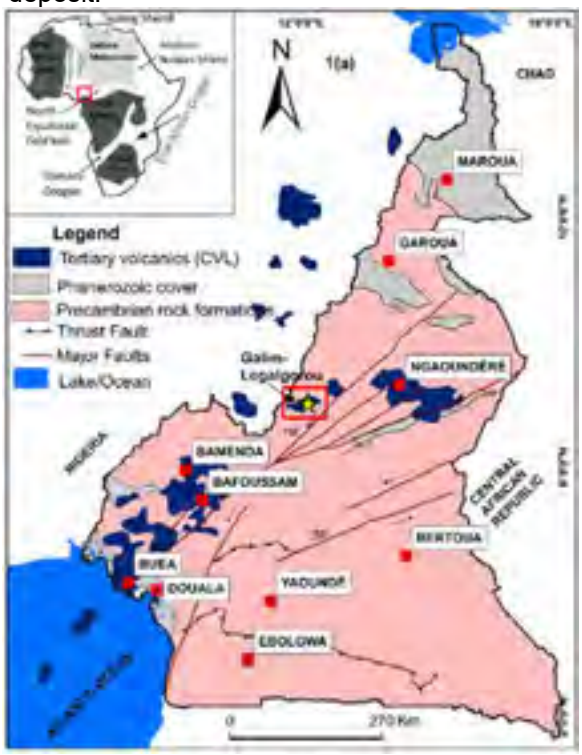


Figure 1. Geology map of Cameroon with focus on the study area within the Cameroon volcanic line (CVL)

The Galim-Legalgorou Ag–Au mineralization is located in one of the major blocks of the north-western branch of the Cameroon Volcanic Line (CVL) on latitude 7° 16′ 20″ N and longitude 12° 18′ 32″ E (Fig. 1)

The main features of the Galim-Legalgorou Au-Ag deposit have been captured for the first time by Ngang et al. (2024). The gold mineralization is hosted within ore jogs in felsic volcanic rocks that

commonly show significant hydrothermal alteration including kaolinite, dickite, smectite and chlorite. Gold occurs as electrum and generally associated with pyrite, Fe-rich sphalerite and acanthite.

Although the field relations, ore minerology and microchemistry of electrum and Fe-rich sphalerite largely suggest an epithermal origin for the Galim-Legalgorou deposit, questions regarding the exact fluid sources and the physico-chemical conditions that may have accompanied the mineralization remained unanswered. This paper therefore highlights fluid inclusion data of quartz veins associated with the mineralization and how these may have contributed to the evolution of the deposit.

2 Samples and methods

2.1 Samples

Quartz occurs both as quartz veins and within fractures in the brecciated host rock fabric where it portrays characteristic dog-tooth and honey-comb textures. Quartz exists as chalcedony and amethyst (Fig. 2 a-d), with chalcedony being clearly of two generations - an early generation (Qz-1) that is crossed-cut by a late generation (Qz-2). On the field, gold mineralization is however more closely linked to amethyst than chalcedony. Chalcedony also generally lacks inclusions of adequate sizes that can reliably be measured. This study therefore considers only fluid inclusions in amethyst.

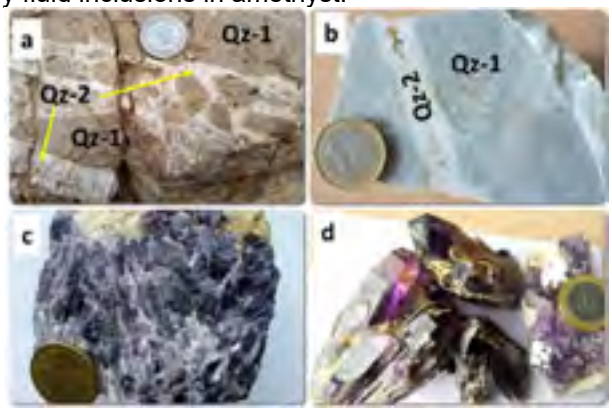


Figure 2. Hand specimens of Chalcedonian quartz (a-b) and amethyst (c-d) from veins and ore jogs from Galim-Legalgorou.

2.2 Methods

Fluid inclusion study was completed at the Institute of Applied Mineralogy and Economic Geology (IML) of the RWTH Aachen University, Germany. Fluid inclusion sections were prepared in the same way as normal thin sections except that they were polished on both sides and are also made to be relatively thicker (150-250 µm). Fluid inclusion assemblages (FIA) were identified and studied on the LEICA-DM4500-P polarizing microscope.

To better understand and classify fluid inclusion assemblages (FIAs), the textural characteristics of the fluid inclusions-bearing quartz were investigated using CL8200 Mk5-2 Optical Cathodoluminescence imaging. This was done to define discrete quartz generations, which could subsequently be used for a better understanding of the relationships between the inclusions and the quartz growth.

Microthermometry experiments were conducted on carefully selected fluid inclusions on the heating/freezing stage attached to a Leica-DM 2700-P polarizing microscope, using liquid nitrogen as the freezing agent. A total of 186 fluid inclusions were analysed in amethyst associated with Au-Ag mineralization by freezing-heating experiments. Fluid salinities were determined from freezing point depressions of ice for all measured fluid inclusion sub-types using the program HOKIEFLINCS (Steele-MacInnis et al. 2012) built with data from Bodner (1993).

Composition data for six fluid inclusions was obtained by LA-ICP-MS following standard procedures.

3 Results and discussion

3.1 Results

All inclusions are aqueous in nature (H_2O-NaCl + vapor bubble) with only trace amounts of other gases (N_2) and sometimes solids. Four sub-types of fluid inclusions (s-type 1, s-type II, s-type III and s-type IV) were identified in amethysts, based on their shapes and L-V filling ratios only (Fig. 3 a-i).

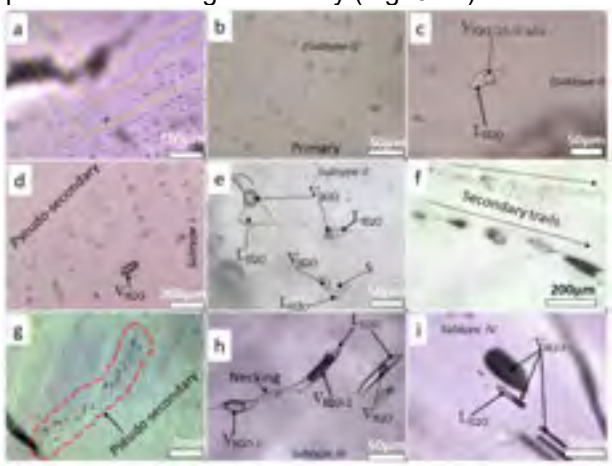


Figure 3. Transmitted light images showing fluid inclusion sub-types in amethyst. Most inclusions are two-phase aqueous solutions.

Some secondary assemblages show coexisting fluid inclusions with volume ratios of between 0-100% gas and 0-100% liquid (Fig 4). Some of these assemblages are almost entirely vapor rich (>90% of the assemblage inclusions) inclusions, indicating the existence of a vapor phase during fluid evolution in the system.

The distribution of homogenization temperatures (T_h) and salinity for the different sub-types are shown in Figure 5 (a-b). All sub-type I inclusions recorded initial ice melting temperatures-$iTm_{(ice)}$ (where observable) between -29 to -21.4 ^{0}C (average -25.2 ^{0}C), final ice melting temperatures ($Tm_{(ice)}$) between

-1.4 and -0.5 0C (average -1.1 ^{0}C) and homogenized (T_h) into the liquid phase between 267 and 303 ^{0}C (average 286.2 ^{0}C).

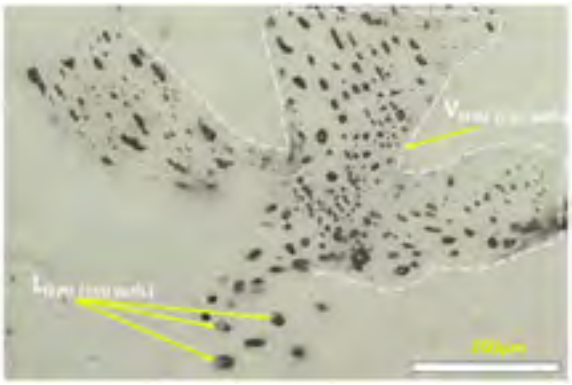


Figure 4. Secondary FIA with coexisting liquid rich and vapor-rich inclusions, a majority being entirely vapor rich

The salinity of type I inclusions was estimated to range from 0.9 to 2.4 wt% NaCl equiv (average 1.8 wt% NaCl equiv).

Sub-type II (n = 10) and III inclusions (n = 15) freeze between -37.5 and -28.5 ^{0}C (average -30.4 ^{0}C), start melting ($iTm_{(ice)}$) between -24.5 and -21 ^{0}C (average -23.4) with final melting temperatures from -1.8 to -0.8 ^{0}C and yielding salinities from 1.4 to 3.1 wt% NaCl equiv. The solid phase observed in some sub-type II inclusions did not homogenize to liquid, even at temperatures above 360 ^{0}C although the inclusions themselves homogenize (V-L) between 287.6 and 291.5 ^{0}C (av. 290.4 ^{0}C). Subtype-III inclusions homogenize between 215 and 261.5 ^{0}C (av. 236.3 ^{0}C), in the liquid phase.

Most sub-type IV inclusions (n = 16) freeze at -23.5 to -22.6 ^{0}C, and $Tm_{(ice)}$ occurred at -1.5 to -1.3 ^{0}C, corresponding to salinities of 2.1 to 2.4 wt% NaCl equiv. A majority of these inclusions became permanently dark after heating to about above ~240-245 ^{0}C. This could be due to leakage or decrepitation of the inclusion. However, some of these inclusions (n = 10) still nucleated a bubble in a liquid on cooling below 150 ^{0}C, implying the inclusion homogenizes in the vapor phase (~180-245 ^{0}C), despite being a liquid-rich inclusion at room temperature.

Secondary inclusions along trails (n=24), with co-existing vapor-rich and liquid-rich inclusions, mostly freeze between -44.5 and -46 ^{0}C with final ice melting temperature between -2.9 and -2.4 ^{0}C, corresponding to a slightly higher salinity of 4.2-4.8 wt% NaCl equiv, relative all other sub-types. These inclusions recorded the widest homogenization temperature range (180-360 ^{0}C) likely due to the masking effect of post-entrapment modification of some of the inclusions (Chi et al. 2021). These highly erratic T_{hs} have not been considered in our analyses of data in this work because of the known low reliability index of measurements of T_{hs} for these kinds of FIAs (Chi et al. 2021).

The six inclusions analysed by LA-ICP-MS show similar chemical compositions with significant concentrations of Na, K, Cl, Li, B, Fe, As, Rb and Sb. Na^+ (average 7280 ppm) and K^+ (average 1803 ppm) are the dominant cations in solution, while Cl- (14251 ppm) is the dominating anion. The data suggest that the fluid was probably in equilibrium with Na- and K-rich rocks and minerals.

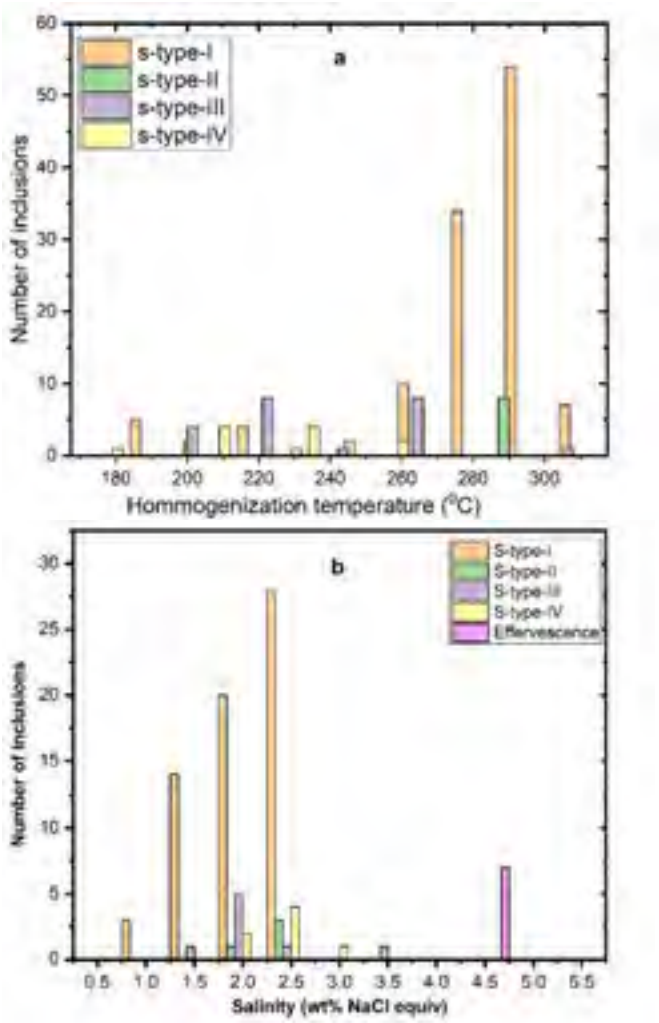


Figure 5. Bar charts showing the distribution of (a) homogenization temperatures and (b) sanity of fluid inclusions measured in amethyst

The observation of FIAs with co-existing vapor-rich and liquid-rich inclusions leads to the conclusion that boiling played an important role in the deposition of ore. It is clear from the assemblage in Fig. 4, that at least, a separate vapor phase existed in the system that may have triggered boiling and hydrothermal brecciation of the overlying rock, leading to mineral deposition (Loucks 2000).

Furthermore, a negative correlation is observed between homogenization temperatures and fluid salinities (Fig 6). This is consistent with a volatile-free fluid boiling process that excludes fluid mixing as a principal role of mineralization (Zhai et al. 2009).

To confirm the environment of deposition, we plotted the T_h data vs. the salinity data (Fig 7), in compositional fields of porphyry, skarn, Sn-W, epithermal, Irish type, Missisippi valley-type (MVT), and lode gold deposit types (Wilkenson 2001).

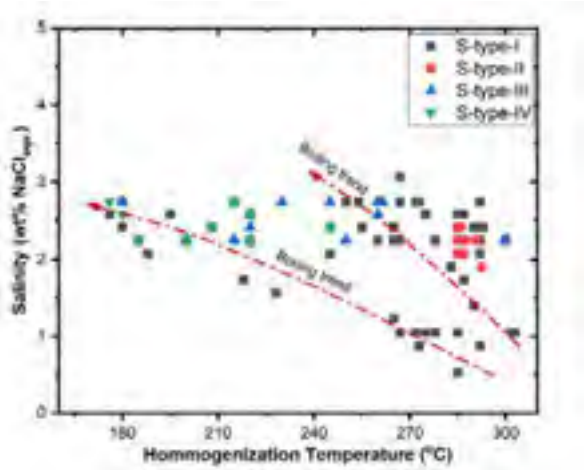


Figure 6. Plot of T_h vs Salinity of measured inclusions, showing a negative slope, indicative of boiling trend.

The data from this study plots in the epithermal field, with only a small overlap into the lode gold field. Considering that field relations, petrographic and geochemical studies show that the mineralization is hosted within felsic volcanic rocks, it is safe to conclude that this plot reinforces an epithermal origin for the mineralization.

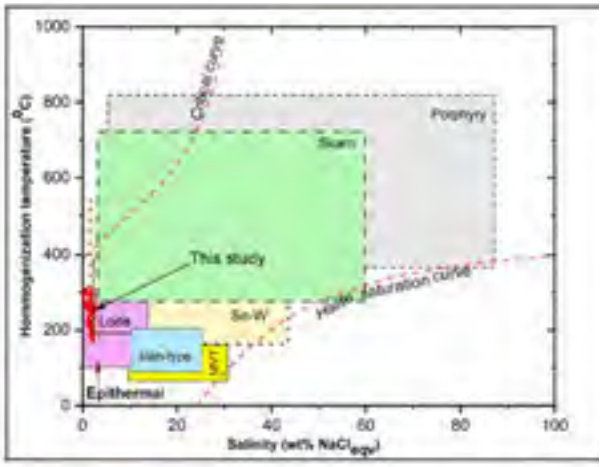


Figure 7. Summary T_h vs. salinity diagram illustrating typical ranges for inclusions from different deposit types. Most inclusions in this study plot in the Epithermal field. Figure modified from Wilkinson (2001).

4 Conclusions

The data presented in this work, seeks to complement earlier studies of the ore mineral associations, mineral chemistry of electrum and sphalerite and hydrothermal alteration signatures, which already demonstrated, to some extent, that the mineralization at Galim-Legalgorou is of an Epithermal low sulfidation type. Fluid inclusion petrography, microthermometry and composition suggest that the mineralization formed in a minimum of two stages at typical epithermal temperatures (176 ^{0}C to 303 ^{0}C) and underwent transient periods of hydrostatic fluid pressure, with boiling as an important mechanism of ore deposition during the late stages of fluid evolution.

Acknowledgements

This abstract is part of the PhD thesis of the first author. Funding for research stay in Germany was provided by the German Academic Exchange Service (DAAD) within the framework of the bi-nationally supervised doctorate scholarship program, in collaboration with the Universities of Bamenda (Cameroon) and the Geofluids laboratory of the Institute of Mineralogy and Economic Geology (RWTH Aachen University), Germany. This study was also supported by the German Research Foundation (DFG), infrastructure grant INST222/1401-1.

References

Bodnar RJ, Reynolds TJ, Kuehn CA (1985) Fluid inclusion systematics in epithermal systems, in Berger, B.R., and Bethke, P.M., eds., Geology and Geochemistry of Epithermal Systems. Reviews in Economic Geology, 1985/01/01; pp. 73-97.

Bodnar RJ (1993) Revised Equation and Table for Determining the Freezing Point Depression of H2O-NaCl Solutions. Geochimica et Cosmochimica Acta, 57, 683-684. https://doi.org/10.1016/0016-7037(93)90378-A

Canet C, Franco SI, Prol-Ledesma R.M, González-Partida E, Villanueva-Estrada RE (2011) A model of boiling for fluid inclusion studies: Application to the Bolaños Ag–Au–Pb–Zn epithermal deposit, Western Mexico, Journal of Geochemical Exploration, Volume 110, Issue 2, 2011, Pages 118-125, ISSN 0375-6742, https://doi.org/10.1016/j.gexplo.2011.04.005.All references have a hanging indent so that the first author stands out.

Chi G, Diamond LW, Lu H, Lai J & Chu H (2021) Common Problems and Pitfalls in Fluid Inclusion Study: A Review and Discussion. Minerals, 11(1), 7. https://doi.org/10.3390/min11010007

Hedenquist JW, Arribas A & Gonzalez-Urien E (2000) Epithermal gold deposits: Styles, characteristics and exploration. Economic Geology and the Bulletin of the Society of Economic Geologists, 95(3), 451-484.

Loucks RR (2000) Precise geothermometry on fluid inclusion populations that trapped mixtures of immiscible fluids. American Journal of Science 300(1):23-59, January 2000. doi:10.2475/ajs.300.1.23

Ngang TC, Suh CE, Wagner T, Bafon TG, Fusswinkel T, Vishiti A (2024) Epithermal Ag–Au mineralization at Galim Legalgorou, Cameroon Volcanic Line: insights from alteration mineralogy and mineral chemistry of electrum and sphalerite. International Journal of Earth Sciences (2024) 113:1285–1301; https://doi.org/10.1007/s00531-024-02427-5

Pudack C, Halter WE, Heinrich CA, Pettke T (2009) Evolution of Magmatic Vapor to Gold-Rich Epithermal Liquid: The Porphyry to Epithermal Transition at Nevados de Famatina, Northwest Argentina. Economic Geology 2009; 104 (4): 449–477. doi: https://doi.org/10.2113/gsecongeo.104.4.449

Steele-MacInnis N, Lecumberri-Sanchez P, Bodnar RJ (2012) HOKIEFLINCS_H2O-NACL: A Microsoft Excel spreadsheet for interpreting microthermometric data from fluid inclusions based on the PVTX properties of H2O–NaCl. Computers & Geosciences 49 (2012) 334–337. doi: 10.1016/j.cageo.2012.01.022

Wilkinson JJ (2001) Fluid inclusions in hydrothermal ore deposits. Lithos 55 (2001) 229–272.

Zhai W, Sun X, Sun W, Su L, He X, Wu Y (2009) Geology, geochemistry, and genesis of Axi: A Paleozoic low-sulfidation type epithermal gold deposit in Xinjiang, China, Ore Geology Reviews, Volume 36, Issue 4, 2009, Pages 265-281, ISSN 0169-1368

Lithology, hydrothermal alteration and mineralization characteristics of the Apollo Porphyry Breccia Complex, Middle Cauca Belt, Marmato, Caldas, Colombia

Jonathan Orozco-Rios[1], David Londoño Vanegas[1], Richard M. Tosdal[2,3,] David Reading[3], Carlos D. Rios[3], Oscar J. Pinilla[3]
[1]Universidad de Caldas, Manizales, Colombia
[2]PicachoEx LLC, Folly Beach, U.S.A.
[3]Collective Mining Ltd, Toronto, Canada

Abstract. Porphyry copper deposits, the world's primary source of copper and associated precious metals, commonly contain magmatic-hydrothermal breccias that are pre-, syn- or post mineral. The Apollo porphyry breccia complex (APBC) in Colombia's Middle Cauca Belt comprises diorite porphyry rocks and breccias, composing part of the Miocene Combia Volcanic Province (CVP). The APBC is a polyphase intrusive complex composed of six phases, with five being pre-breccia and one post breccia. Three breccia facies are identified: crackle, angular, and fluidized breccia. The breccia was emplaced into a porphyry stockwork vein system and overprinted by potassic and chlorite – sericite alteration assemblages. Sulfide minerals consisting of chalcopyrite-pyrite-pyrrhotite-sphalerite- galena with local scheelite are zoned within the breccia.

1 Introduction

Porphyry copper deposits, the world's primary source of copper and associated precious metals (Seedorff et al. 2005), are intricately linked to the development of stockwork veins and magmatic-hydrothermal breccias. The breccias where present play a crucial role in mineralizing processes (Sillitoe 1985; Corbett and Leach 1998; Davies 2002). The APBC is located in the Middle Cauca Belt of Colombia (Fig. 1), it offers a case study for understanding these complex geological phenomena.

The APBC is situated in the Caldas department, approximately 130 km south of Medellin. This late Miocene complex comprising polyphase diorite porphyry overprinted by breccia was emplaced into the low-grade metamorphic rocks of the Mesozoic Arquía Complex (Weber et al. 2020). The APBC is part of the regional Miocene CVP, which represents the magmatic arc formed by the ongoing subduction of the Nazca plate beneath the South American plate since the Oligocene (Marín-Cerón et al. 2019; Weber et al. 2020).

The Apollo Au-Ag-Cu-W breccia that occurs within the APBC is a syn-mineralization hydrothermal breccia hosted in a low-grade Au-Cu porphyry stockwork. This deposit showcases a multi-stage mineralized complex, featuring both a porphyry Cu-Au stockwork and an intermineralization Au-Ag-Cu-W high-temperature polymetallic breccia.

To unravel the complexities of the APBC and its associated mineralization, we conducted detailed drill core logging to produce deposit-scale north to south cross sections exhibiting lithology, hydrothermal alteration assemblages and mineralization patterns.

2 Regional geology

The Northern Andean Block (NAB) has undergone a complex tectono-magmatic evolution since the Oligocene, influenced by interactions among the Farallon/Nazca, South American, Caribbean plates, and the Panamá Chocó arc (León et al. 2018; Montes et al. 2019; Gonzales et al. 2023). The fragmentation of the Farallon Plate into the Nazca and Cocos plates at ~23 Ma (Lonsdale 2005) and the Panamá-Chocó arc collision with South America drove significant orogenesis and magmatism (Montes et al. 2019; León et al. 2018).

The NAB magmatic evolution from late Oligocene to Pliocene is marked by eastward arc migration and increased magmatic activity (Leon et al. 2018; Montes et al. 2019). Initial magmatism (26-18 Ma) in the Western Cordillera (Marín-Cerón et al. 2019; Gonzales et al. 2023) was followed by middle Miocene eastward migration with increased deformation and crustal thickening (Leon et al. 2018; Montes et al. 2019; Weber et al. 2020). The CVP was controlled by fault systems (Marín-Cerón et al. 2019; Villalba et al. 2023) and represents middle Miocene magmatism (11.8-4.7 Ma) with calc-alkaline compositions (Leal-Mejía et al. 2017; Bissig et al. 2017; Jaramillo et al. 2019; Santacruz et al. 2021; Weber et al. 2020). Magmatism continued in the Middle Cauca Valley since ~6 Ma (Echeverri et al. 2024), with Pliocene (~4 Ma) activity shifting eastward to the modern arc (Wagner et al. 2017). Many of the porphyry and epithermal deposits within the larger NAB are associated with the CVP including the Middle Cauca Belt (MCB), which includes the APBC (Shaw et al. 2019).

The APBC is located on the eastern flank of the Western Cordillera close to the Marmato district (Santacruz et al. 2021; Fig. 1). The APBC deposit is associated with late Miocene intrusive rocks hosted within an angular breccia facies and porphyry stockwork, with late, gold-silver bearing sheeted carbonate base metal veins (CBM; Redwood 2022).

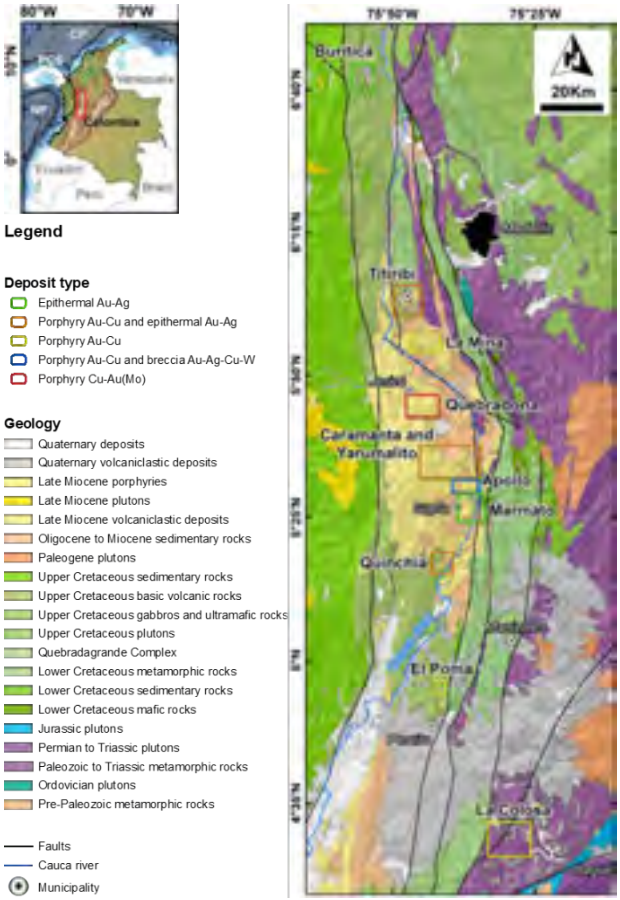


Figure 1. MCB regional geology map. Location and type of main deposits including the APBC.

3 Samples and Methods

Detailed relogging focused on lithology, silicate hydrothermal alteration assemblages and mineralization utilized 16 diamond drill holes (6,455 metres) along a N-S section through a small part of the breccia.

4 Results and Discussion

The polyphase porphyry complex is dominated by diorites and quartz diorites divided into six distinct phases separated by chilled intrusive contacts. The intrusions are medium to fine grained and porphyritic textures.

The primary mineralogy consists principally of plagioclase, quartz, minor biotite, and hornblende, along with trace apatite and zircon in a fine-grained, interlocking quartz-feldspar groundmass. Of the six phases, five are brecciated and constitute the main body of the APBC (Fig. 2). Alteration occurrences are variable, including secondary biotite, chlorite-sericite, carbonate-rich chlorite-sericite, chlorite-epidote and intermediate argillic assemblages (Fig. 5). The sulfides are present in all six lithologies and correspond to disseminated sulfides, mainly pyrite, pyrrhotite, chalcopyrite, and carbonate base metal veins with sphalerite and galena (Fig. 4). scheelite is also present locally in the upper parts of the breccia.

4.1 Porphyry suite

The multi-phase intrusions in the APBC demonstrate an evolutionary sequence from oldest to youngest. A north-to-south deposit-scale section shows the distribution of the six distinct porphyry phases, with P10 to P50 representing pre-breccia intrusions and P60 constituting a post-breccia event (Fig. 2). P10 and P20 are medium-grained, porphyritic precursor intrusions. P30 is a medium-grained early phase exhibiting equigranular to porphyritic texture. This porphyry is crosscut by the P40 intrusion, a quartz diorite that represents the most volumetrically significant porphyry body. P50 is an intermineralization, fine-grained porphyritic quartz diorite intrusion. The youngest phase, P60, comprises coarse-grained porphyritic diorite dikes that crosscut the entire system and are only locally altered to chlorite – epidote.

The groundmass of the porphyries is consistently fine-grained (<0.1mm) and composed primarily of plagioclase and quartz. The phenocryst to groundmass ratio is approximately 7:3 throughout the intrusive suite.

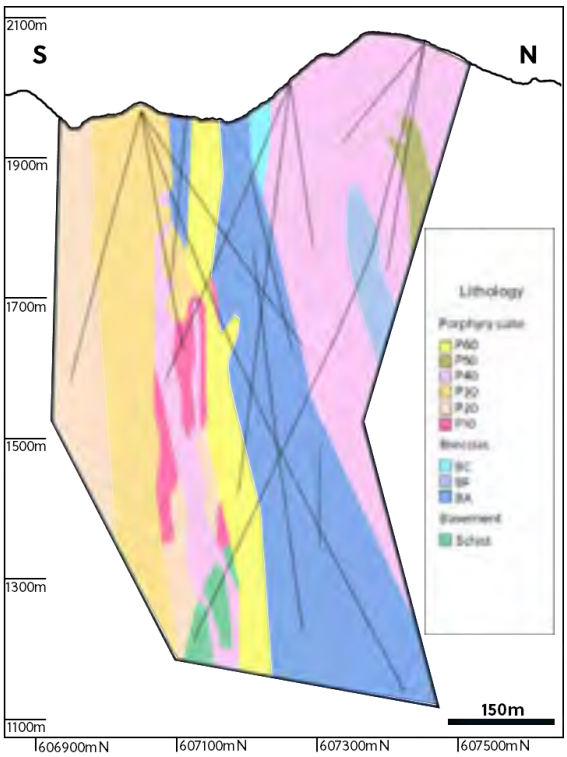


Figure 2. Interpreted lithology section through the APBC. Breccia legend comprises BC: crackle breccia, BF: fluidized breccia and BA: angular breccia.

4.2 Brecciated porphyry facies

Three main breccia facies have been described: crackle breccia, fluidized breccia, and angular breccia (Fig.3). Gradational contacts between all facies reflect units that are consistently definable through core-scale observations. The crackle breccia contains slightly rotated angular fragments that display minimal displacement, with the matrix confined to fractures less than 2 mm thick. The

crackle breccia is localized on the margins of the angular breccia. The angular breccia is predominantly a polymictic, angular breccia with transported clasts. It is cement-rich and clast-supported, with a diverse alteration mineralogy characterized by sericite and chlorite, along with hydrothermal biotite at depth. This facies was overprinted by most of the sulfides. The fluidized breccia has a milled matrix composing more than 30% of the rock, together with rounded clasts that are poorly sorted to chaotic and matrix-supported. The fluidized breccia has similar textures to angular breccia but lacks significant mineralization. It formed mainly in P40 and P30 in the northeastern upper part of the deposit.

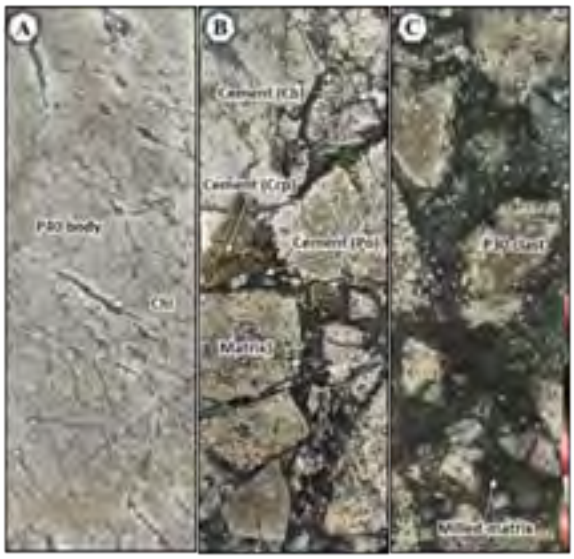


Figure 3. Representative core photographs of the breccia facies A) Typical monomict crackle breccia. B). Sulfide-bearing angular breccia. C) Fluidized breccia with subrounded-rounded clast morphology. Cb-Carbonate, Po-Pyrrhotite, Ccp-Chalcopyrite, Chl-Chlorite.

4.3 Silicate hydrothermal alteration assemblages

Characteristic features for each alteration type and their distribution are shown in Figs. 4 and 5. Secondary biotite alteration occurs mainly in P10, P20, and P30 porphyries, concentrating in deeper parts of the APBC, mainly towards the south of the deposit. Chlorite-sericite alteration of secondary biotite is widespread in the APBC. Within the angular porphyry breccia, the chlorite-sericite assemblage contains abundant carbonate.

A chlorite-epidote alteration assemblage surrounds the APBC, extending north and south, predominantly in P40 and P60 porphyries. Intermediate argillic alteration overprints earlier silicate assemblages and is associated with late-stage carbonate base metal veins and faulted rocks.

4.4 Sulfide mineral assemblages

The main sulfide assemblages that occur in Apollo are chalcopyrite-pyrite-pyrrhotite and the CBM veins. The upper breccia is dominated by a chalcopyrite-pyrite assemblage distributed within the angular breccia body, grading towards a pyrite-dominated zone to the north and a pyrrhotite-dominated zone to the south (Fig. 6). CBM veins overprint older sulfide events and all units throughout the APBC. Characteristic macroscopic features of the main mineralization assemblages are shown in (Fig. 4). Scheelite is concentrated in the upper part of the angular breccia, grading downwards to the chalcopyrite zone.

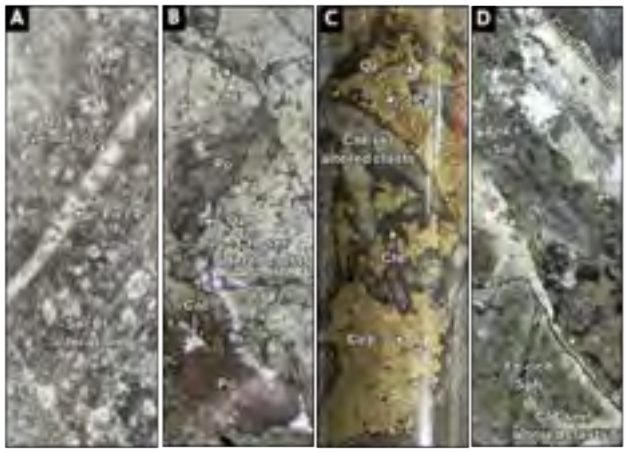


Figure 4. A) P30 porphyry with secondary biotite and a quartz veinlet with pyrrhotite and pyrite. B) Pyrrhotite within angular breccia with chlorite, calcite, quartz and minor sericite. Quartz diorite clasts with chlorite-sericite alteration. C) Chalcopyrite-pyrite cement in the angular breccia. D) Intermediate argillic assemblage forming a halo around a CBM vein. Yellowish carbonates are associated with Fe-rich sphalerite, galena and pyrite.

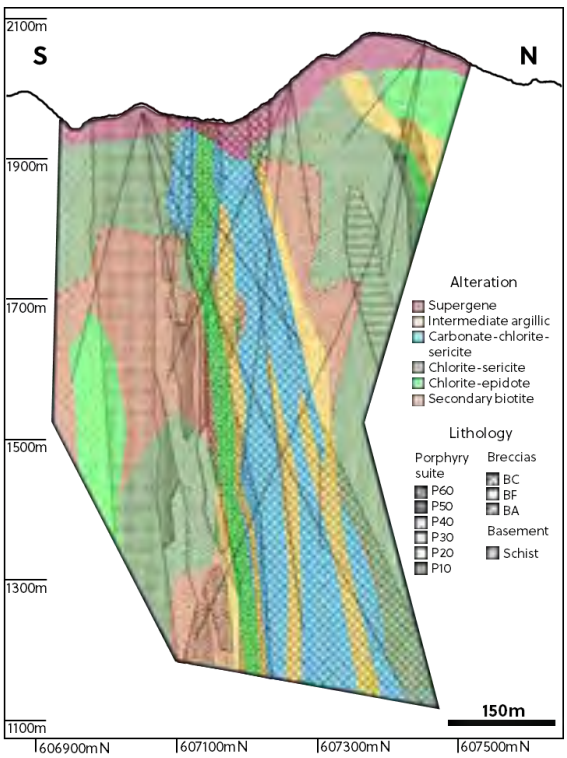


Figure 5. North to south Apollo cross section showing alteration assemblages with background lithology.

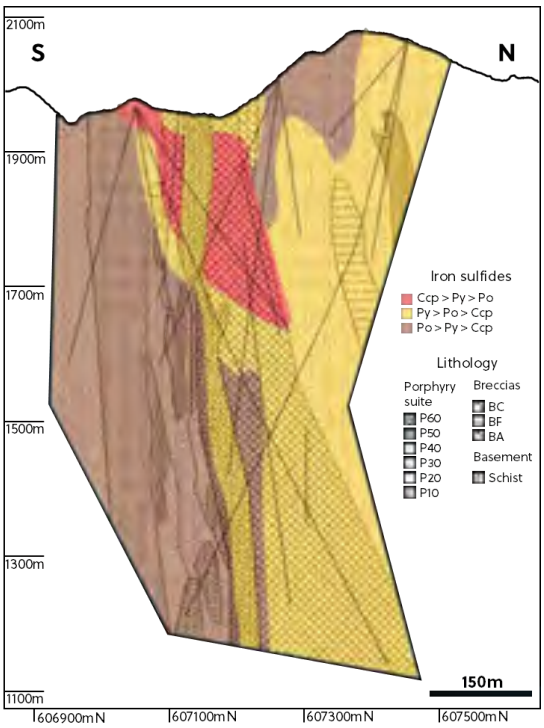


Figure 6. Interpreted distribution of Cu-Fe sulfides with background lithology. Po-Pyrrhotite, Ccp-Chalcopyrite, Py-pyrite.

5 Conclusions

The APBC showcases a multi-stage Au-Ag-Cu-W hydrothermal system within the Middle Cauca Belt. The deposit is characterized by six porphyry phases, three distinct breccia facies, and a complex series of hydrothermal minerals ranging from secondary biotite and chlorite-epidote to chlorite-sericite and intermediate argillic assemblages. The chalcopyrite-pyrite-pyrrhotite assemblage was overprinted by CBM veins, and a scheelite-rich zone formed in the upper portions of the breccia. The APBC formed due to several intrusive, brecciation, alteration, and mineralization events, and its characterization has contributed to the broader understanding of porphyry-breccia systems in the highly prospective Middle Cauca Belt.

Acknowledgements

This research was supported by Collective Mining Ltd, who provided access to proprietary databases and financial support. The views expressed are those of the authors and do not necessarily represent the company's official policies or endorsements.

References

Bissig T et al (2017) High Sr/Y magma petrogenesis and the link to porphyry mineralization as revealed by garnet-bearing I type granodiorite porphyries of the middle Cauca Au-Cu belt, Colombia. Econ Geol 112: 551–568. https://doi.org/10.2113/econgeo.112.3.551

Corbett GJ, and Leach TM (1998) Southwest Pacific gold-copper systems: Structure, alteration, and mineralization: Econ Geol: 238.

Davies AG (2002) Geology and genesis of the Kelian gold deposit, east Kalimantan, Indonesia: Doctoral dissertation, Uni of Tasmania, Australia, 405p.

Echeverri S, Murcia H et al (2024) Late Miocene – Pliocene eastward magmatic arc migration record in the Northern Andes at 5°N latitude, west-central Colombia, Intern Geol Review 67: 3773-3802 https://doi.org/10.1080/00206814.2024.2444583

González R et al (2023) Kinematics and convergent tectonics of the Northwestern South American plate during the Cenozoic. Geochemistry, Geophysics, Geosystems 24: 1–32. https://doi.org/10.1029/2022GC010827.

Jaramillo JS et al (2019) Petrogenesis of the late Miocene Combia Volcanic complex, northwestern Colombian Andes: Tectonic implication of short term and compositionally heterogeneous arc magmatism. Lithos 330: 194–210. https://doi.org/10.1016/j.lithos.2019.02.017.

Leal-Mejía H et al (2017) The Late Miocene Middle Cauca Au-Cu porphyry belt, Colombia: time-space distribution of magmatism and controls on Au mineralization: Mineral Resources to Discover - 14th SGA Biennial Meeting 2017 1:1–5.

León S et al (2018) Transition from collisional to subduction-related regimes: An example from Neogene Panama-Nazca- South America interactions: Tectonics 37: 119–139. https://doi.org/10.1002/2017TC004785.

Lonsdale P (2005) Creation of the Cocos and Nazca plates by fission of the Farallon plate: Tectonophysics 404 (3-4): 237–264. https://doi.org/10.1016/j.tecto.2005.05.011.

Marín-Cerón MI et al (2019) Late Cenozoic to Modern-Day Volcanism in the Northern Andes: A Geochronological, Petrographical, and Geochemical Review. In: Cediel F, Shaw RP (ed) Geol and Tectonics of Northwestern South America. Springer Cham, Switzerland: 603–648.

Montes C et al (2019) Continental margin response to multiple arc-continent collisions: The northern Andes-Caribbean margin: Earth-Scie Rev 198: 1-19. https://doi.org/10.1016/j.earscirev.2019.102903

Redwood S (2022) NI 43-101 technical report for the Guayabales gold-silver-copper project, department of Caldas, Colombia. Collective Mining Ltd. https://www.sedarplus.ca/csa-party/records/document.html?id=531d45ef960a18a792387d451371c424ebcd5cd6b68afa135fe89edfa915dd20

Santacruz L et al (2021) The age and petrogenesis of reduced to weakly oxidized porphyry intrusions at the Marmato gold deposit, Colombia, Ore Geology Reviews, 131, 103953. https://doi.org/10.1016/j.oregeorev.2020.103953

Seedorff E et al (2005) Porphyry deposits: Characteristics and origin of hypogene features. In: Hedenquist JW et al. (ed) SEG 100th Anniversary Volume, pp 251-298. https://doi.org/10.5382/AV100.10

Shaw RP et al (2019) Phanerozoic metallogeny in the Colombian Andes: A tectono-magmatic analysis in space and time. In: Cediel F, Shaw RP (ed) Geol and Tectonics of Northwestern South America. Springer Cham. https://doi.org/10.1007/978-3-319-76132-9_6

Sillitoe RH (1985) Ore-related breccias in volcanoplutonic arcs: Econ Geol 80: 1467–1514. https://doi.org/10.1007/BF00202933

Villalba et al (2023) Compositional and geothermobarometric analysis of the Upper Miocene tholeiitic volcanic products in the northern Andes at 5-6° N latitude: The Combia Volcanic Province: Andean Geology: 50 (2): 181-200. doi: 10.5027/andgeoV50n2-3503

Wagner et al (2017) Transient slab flattening beneath Colombia. Geophysical Research Letters 44 (13): 6616-6623.

Weber et al (2020) The Combia Volcanic Province: Miocene Post-Collisional Magmatism in the Northern Andes. The Geology of Colombia 3: 355–394. https://doi.org/10.32685/pub.esp.37.2019.12

Mineralogy, Galena Pb isotopes and Nd isotopes of the associated dikes from Ag-Hg Imiter deposit, Anti-Atlas, Morocco: implications for metal sources

Mehdi Ousbih[1], Brian Cousens[2], Askkour Fatiha[3], Yves Geraud[4], Alexiane Favier[4], Hafida El Bilali[2], Mohamed Ezzghoudy[3], Abdelaziz Gaouzi[5], Oubaassine Hassane[6], Richard Ernst[2,7], Moha Ikenne[1]

[1]Laboratory of Applied Geology, Faculty of Sciences and Techniques, Moulay Ismaïl University of Meknes, Errachidia, Morocco.
[2]Isotope Geochemistry and Geochronology Research Centre, Department of Earth Sciences, Carleton University, Ottawa, Canada.
[3]Department of Geology, Faculty of Sciences, Ibn Zohr University, Agadir, Morocco.
[4]University of Lorraine-CNRS-GeoRessources, Nancy, France.
[5]Managem Group, Casablanca, Morocco.
[6]Department of Geology, Faculty of Sciences, Cadi Ayyad University,Marrakech, Morocco.
[7]Department of Geology and Geography, National Research Tomsk State University, Russian Federation.

Abstract. The Imiter deposit is a significant silver-rich base metal deposit. The deposit is primarily composed of sub-horizontal ore bodies located at the contact between the Saghro Group (SG) shales and Ouarzazate Group (OG) volcaniclastics. Silver mineralization occurs as steeply dipping north-trending veins, gently south-dipping veins, and stockwork ore within conglomerates, tuffs, and andesites. The ore mineralogy includes Ag-Hg amalgam, argentite, polybasite, tetrahedrite-tennantite, proustite-pyrargyrite, acanthite, chalcopyrite, arsenopyrite, pyrite, sphalerite, and galena. Lead isotopic data from galena reveal two distinct groups, indicating two origins for mineralizing fluids: one crustal and one mantle-derived. The silver deposits are closely associated with a swarm of mafic to felsic dikes with varying orientations: NE to N70 in the SG and N-S to N10 in the OG. The first group of dikes is characterized by initial $^{143}Nd/^{144}Nd$ ratios of 0.511787–0.511970, moderately negative εNd values (-0.15 to -2.78), and older Nd model ages (1.3–1.7 Ga), suggesting a locally enriched mantle source or enhanced crustal contamination. The second group exhibits initial $^{143}Nd/^{144}Nd$ ratios of 0.511885–0.512075, Nd model ages of 1.00–1.29 Ga, and positive εNd values (0.02–2.84), indicative of a juvenile source.

1 Introduction

Primary silver (Ag) ore deposits are predominantly hydrothermal in origin and include diverse genetic types such as epithermal systems (low-, intermediate-, and high-sulfidation), volcanogenic massive sulfide (VMS) deposits, sedimentary-exhalative (SEDEX) mineralization, sediment-hosted Ag–Cu systems, carbonate replacement and skarn assemblages, porphyry Cu systems, mesothermal Ag–Pb–Zn deposits, and Ag–Co–Ni–As vein systems (Kesler and Simon, 2015). The Imiter deposit, located in the Anti-Atlas of Morocco, stands out as a world-class Ag–Hg district, both economically significant and geologically representative of Neoproterozoic–Cambrian metallogenic processes.

Previous studies have largely focused on the structural, stratigraphic, and hydrothermal evolution of the Imiter district, yet the origin of the metal source particularly the potential involvement of mantle-derived components remains debated. While some regional investigations have suggested crustal sources or recycling of older basement materials (Levresse et al., 2004; Ikenne et al., 2007, 2020), the role of mantle input has not been thoroughly addressed or directly tested using isotopic data. This study aims to evaluate the potential contribution of mantle-derived magmatism to metal sourcing at Imiter by integrating Pb isotopes from galena and Nd isotopes from spatially associated dikes.

Although the Nd isotopic data are not obtained from the mineralized material itself, they offer a proxy for the magmatic input and crustal assimilation processes within the district. We acknowledge the limitations of indirect sampling and aim to critically assess the strength of isotopic evidence in light of these constraints. By examining the genetic link between mineralization, magmatic source regions, and broader geodynamic evolution of the Anti-Atlas, this work seeks to contribute new insight into the debated mantle-crust interactions underlying metal enrichment in one of North Africa's most important silver districts.

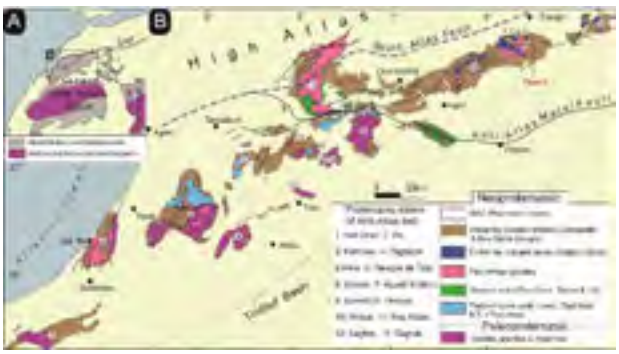


Figure 1. a. The location of the Anti-Atlas belt along the northwestern margin of the West African Craton. **b**. Simplified map of the Anti-Atlas belt, showing the main

Precambrian inliers, with the location of the Imiter mine area (modified from Gasquet et al. 2005).

The Imiter Silver Deposit (IAD), ranked as the tenth-largest global silver producer, has been exploited since the 8th century (Levresse et al., 2004). The deposit's ore bodies are structurally controlled by a major fault contact between lower Ediacaran turbiditic sequences and Late Ediacaran volcanic-sedimentary rocks, subvolcanic intrusions, and plutonic units (Fig. 2). Silver mineralization predominantly manifests as steeply dipping, north-trending veins and shallow south-dipping veins within sandstones, spatially linked to the Imiter fault system. Secondary mineralization occurs as stockwork ore hosted in conglomerates, tuffs, and andesites. The IAD comprises four principal mining sectors: Imiter I, Imiter II, Imiter South, and Igoudrane. Mineralization exhibits diverse textural features, including brecciated, ribbon, and disseminated textures, with quartz and carbonates dominating the gangue assemblage. Silver enrichment is closely associated with intermediate to mafic dikes that intrude both the Saghro Group (SG) basement and Ouarzazate Group (OG) cover sequences.

Despite its economic significance, the genetic model of the IAD remains contentious in the Anti-Atlas region. Although numerous geochemical studies have been conducted, key uncertainties persist regarding the origin(s) of ore-forming fluids, metal sources, thermal drivers, depositional mechanisms, and the absolute timing of mineralization.

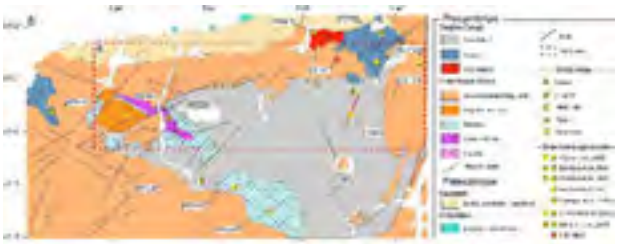


Figure 2. Geological map of the Imiter mine area showing the location of the mining sectors.

2 Methodology

Field investigations, including geological mapping, stratigraphic logging, sample collection, and facies analysis, were conducted across three representative sections during two field campaigns. Doubly polished thin sections were prepared for advanced microanalytical techniques: scanning electron microscopy (SEM), backscattered electron (BSE) imaging, and electron probe microanalysis (EPMA). Twelve samples were systematically selected for Pb isotope analysis, prioritizing variability in elevation, host rock lithology, vein geometry (orientation and dip), mineralization texture, mineral paragenesis, and silver grade. Additionally, twenty dike and sill samples were collected from surface exposures and underground workings proximal to the deposit for Nd isotope analysis.

3 Mineral chemistry

Silver mineralization in the Imiter deposit is associated with distinct paragenetic stages, including Ag-Hg amalgam in hydrothermal sulfides and epithermal Ag-rich assemblages. Key mineral phases identified include galena, pyrite, arsenopyrite, sphalerite, freibergite, and löllingite. Microprobe analyses reveal that galena exhibits significant compositional variability, with elevated Zn, Fe, Cu, and Sb concentrations inversely correlated with Pb content. Notably, Hg was undetected in galena, excluding the presence of micro-inclusions of Ag-Hg amalgam within this phase. However, Hg was identified in coexisting base-metal sulfides, confirming its abundance and supersaturation in the hydrothermal system.

The absence of Hg in galena is interpreted as a consequence of abrupt physicochemical changes (e.g., temperature, pH, salinity) during ore formation. These fluctuations promoted the preferential incorporation of Zn, Fe, Cu, and minor Sb, Bi, and Mn into galena, while Hg partitioned into other sulfides or remained in the fluid phase (Baroudi et al., 2001; Levresse et al., 2004)

4 Pb isotope composition

The Pb isotopic compositions of the analyzed samples were compared with regional Anti-Atlas ore deposits using conventional covariation diagrams ($^{207}Pb/^{204}Pb$ vs. $^{206}Pb/^{204}Pb$ and $^{208}Pb/^{204}Pb$ vs. $^{206}Pb/^{204}Pb$). Despite a scattered distribution, two distinct isotopic groups were identified. The first group (IGD-LN, R4, SS1) exhibits elevated $Pb^{206}Pb/^{204}Pb$ ratios (18.1727–18.5397), plotting between the crustal evolution curves of Stacey and Kramers (1975) and the orogenic model of Doe and Zartman (1979), indicative of a dominant crustal Pb contribution. In contrast, the second group (SS2, Igd-S, LN, N5, R6, F1S, SNN1, F0) displays markedly lower $^{206}Pb/^{204}Pb$ values (18.1012–18.1382), falling below both reference curves. This deviation suggests either a depleted mantle-derived component or interaction with a distinct, less radiogenic crustal reservoir during ore formation. The contrasting isotopic signatures highlight the complex interplay of crustal and potential mantle sources in the metallogenesis of the Anti-Atlas region.

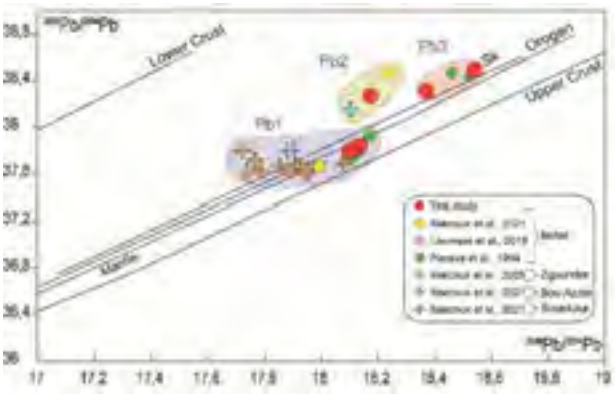


Figure 3. Plots of 207Pb/204Pb versus 207Pb/204Pb (a) and $^{208}Pb/^{204}Pb$ versus $^{206}Pb/^{204}Pb$ (b) from Imiter mine and other Anti Atlas ores mine (Zartman and Doe 1981).

5 Nd isotopes of dyke

This study focuses on the geochemical and Nd isotopic composition of the Imiter Mine Dikes (IMD) in the Imiter silver district. The analyzed dikes, which include basalt, basaltic-andesite, dacite, microdiorite, and keratophyre, were sampled from unaltered outcrops in surface and subsurface exposures. Structural analysis reveals contrasting orientations for the IMD: NE–ENE trends dominate within the lower Ediacaran sequences, while N–S to NNE orientations are prevalent in the Late Ediacaran series, with limited intrusions cross-cutting the overlying Paleozoic cover. Nd isotopic data distinguish two geochemically distinct groups (Fig. 4). Group 1 (IMD 1) is characterized by initial $^{143}Nd/^{144}Nd$ ratios of 0.511787–0.511970, moderately negative εNd values (-0.15 to -2.78), and Paleoproterozoic Nd model ages (1.3–1.7 Ga), consistent with derivation from an enriched lithospheric mantle or crustally contaminated magmas. In contrast, Group 2 (IMD 2) exhibits higher initial $^{143}Nd/^{144}Nd$ ratios (0.511885–0.512075), positive εNd values (+0.02 to +2.84), and younger Mesoproterozoic model ages (1.00–1.29 Ga), indicative of a juvenile mantle source with minimal crustal interaction. Notably, Group 2 displays a negative correlation between εNd values and SiO_2 content, suggesting progressive crustal assimilation during magmatic evolution or mixing between mantle-derived melts and older crustal components. These findings highlight the interplay of heterogeneous mantle sources and crustal processes in the genesis of the IMD.

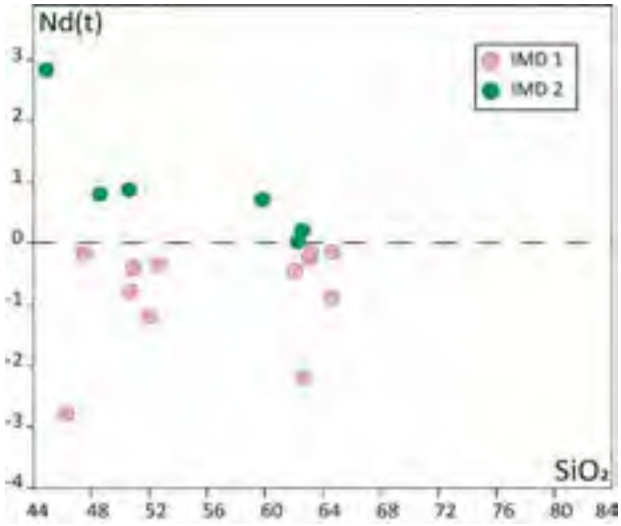


Figure 4. εNd values exhibit a negative correlation with SiO_2.

6 Conclusion

Pb isotopic data from the Imiter Ag deposit indicate at least three hydrothermal events involving two distinct Pb sources (Pb1 and Pb2), and a mixed signature (Pb3). Nd isotopic analyses of associated dikes reveal two magmatic groups: one reflecting enriched mantle and crustal contamination (Group 1), and the other a juvenile mantle source (Group 2). The εNd–SiO_2 relationship suggests varying degrees of crustal assimilation. While the data support a hybrid metal source involving both mantle and crustal inputs, the interpretation remains indirect due to the lack of isotopic data from mineralized rocks themselves. These findings highlight the metallogenic complexity of the Imiter district and point to a potential, though not yet fully constrained, mantle contribution to Ag–Hg mineralization

References

Ikenne M, Ennaciri A, Ouguir H, Cousens B, Ziyadi R, Mouhagir M, El-Gaouzi A (2007) Geochemical signature and geodynamic significance of an ag-hg mineralized dyke swarm in the neoproterozoic inlier of imiter - Anti-Atlas (Morocco). Ofioliti 32 (2): 109-18. https://doi.org/10.4454/ofioliti.v32i2.351.

Ikenne M, Souhassou M, Saintilan N. J, Karfal A, Hassani A. E, Moundi Y, Ousbih M, Ezzghoudi M, Zouhir M, Maacha L (2021) Cobalt–nickel–copper arsenide, sulfarsenide and sulfide mineralization in the Bou Azzer window, Anti-Atlas, Morocco: one century of multi-disciplinary and geological investigations, mineral exploration and mining. Geological Society, London, Special Publications 502(1): 45-66. https://doi.org/10.1144/SP502-2019-132.

Levresse G, Cheilletz A, Gasquet D, Reisberg L, Deloule E, Marty B, Kyser K (2004) Osmium, sulphur, and helium isotopic results from the giant Neoproterozoic epithermal Imiter silver deposit, Morocco: evidence for a mantle source. Chemical geology 207(1-2): 59-79. https://doi.org/10.1016/j.chemgeo.2004.02.004.

Kesler S, Simon (2015) Mineral Resources, Economics and the Environment (2nd ed.). Cambridge University Press, Cambridge. https://doi.org/10.1017/CBO9781139871426.
Stacey J.S, Kramers J.D (1975) Approximation of terrestrial lead isotope evolution by a two-stage model. Earth Planet. Sci. Letters 26:207–221. https://doi.org/10.1016/0012-821X(75)90088-6.

Aolunhua: A porphyry Mo deposit associated with adakite-like magmas in an intra-continental extensional setting, northeastern China

Hegen Ouyang[1]
[1]*Institute of Mineral Resources, Chinese Academy of Geological Sciences, Beijing, 100037, China*

Abstract. The Aolunhua porphyry Mo deposit is located in northeastern China in an intra-continental extensional setting. This deposit is intimately associated with differentiated adakite-like rocks and comprises at least seven phases of Mo-related intrusions, emplaced during and near the end of alteration and mineralization events. The majority of the ore is found in quartz-molybdenite ± pyrite and molybdenite veins hosted primarily in the monzogranite porphyry. LA-ICP-MS U-Pb zircon geochronology indicates that magmatism and mineralization at Aolunhua occurred between 131.6 ± 1.4 Ma and 124.4 ± 0.8 Ma, during the exhumation of metamorphic core complexes in the Central Asian Orogenic Belt. The syn-mineralization monzogranite porphyry at Aolunhua exhibits adakite-like characteristics with depleted mantle- or juvenile crust-derived isotopic signatures and high magmatic oxygen fugacity (FMQ +2.05 ± 0.30). The oxidized nature of the magmatic-hydrothermal system at Aolunhua is also supported by the presence of hematite and anhydrite daughter minerals in fluid inclusions. The Aolunhua deposit shows similarities to porphyry Cu-Mo deposits but is distinguished by its Cl-poor magmatic-hydrothermal signature, leading to enrichment in Mo and deficiency in Cu. Magmatic apatite Cl contents may therefore differentiate porphyry Mo-related intrusions from those associated with porphyry Cu-Mo systems.

1 Introduction

Intra-continental extensional settings related to foundering of shallowly subducted slab and subsequent melting of metasomatized subcontinental lithosphere in accretionary orogens (Rosera et al., 2024; Farmer et al., 2024) or delamination of thickened continental crust in collisional orogens (e.g., Chen et al., 2017) are favourable sites for the development of porphyry Mo deposits. These deposits are commonly associated with high silica intrusions ($SiO_2 \geq 70$ wt.%) that are characterized by high F (up to 1.0 wt.%), Rb (up to 1137 ppm), and Nb (up to 150 ppm) contents (Audétat, 2015; Chen et al., 2017), and negative $\varepsilon_{Nd}(t)$ and $\varepsilon_{Hf}(t)$ isotopic compositions (i.e., ancient crust- or enriched mantle-derived magma source; Chen et al., 2017; Gaynor et al., 2023). In addition, porphyry Cu-Mo deposits are commonly associated with adakite-like intermediate to felsic intrusions that have distinctive chemical compositions, such as high Sr/Y and La/Yb (both>20; Richards, 2011), minimal Eu anomaly ($Eu/Eu^* \approx 1$), and positive $\varepsilon_{Nd}(t)$ and $\varepsilon_{Hf}(t)$ isotopic compositions (i.e., depleted mantle- or juvenile crust-derived magma source; Hou et al., 2015; Carter et al., 2022).

This study systematically reports a distinctive porphyry Mo deposit at Aolunhua, Great Xing'an Range, northeastern China. Aolunhua formed in an intra-continental extensional setting (Wang et al., 2006). Its cogenetic intrusions are depleted mantle- or juvenile crust-derived adakite-like rocks, which can produce Cu-Mo mineralization (Ma et al., 2009). However, Aolunhua contains 0.09 Mt of Mo but no recoverable Cu. The selective enrichment of metals at Aolunhua poses an obvious question: what are the key factors responsible for determining Cu-Mo or Mo mineralization in porphyry systems? This is an important question to address as it is vital for a more accurate understanding of the formation of porphyry deposits and classification of porphyry Mo deposits. Additionally, it may provide clues (i.e., ore fertility indices) pertinent to the identification of areas hosting porphyry Cu-Mo or Mo deposits.

Aolunhua has been extensively studied (e.g., Ma et al., 2009; Shu et al., 2009). Previous studies have primarily focused on the anatomy of the deposit. Nevertheless, the reason why depleted mantle- or juvenile crust-sourced magmas with high Sr/Y exclusively triggered porphyry Mo mineralization at Aolunhua has not been adequately considered. This study re-examines relationships among rock types, hydrothermal alteration, and mineralization by integrating field observations, zircon U-Pb geochronology, and detailed petrological and mineral chemistry studies and aims to (1) constrain the sequence of magmatic and mineralization events, (2) document the distribution of alteration and mineralization, and (3) elucidate the conditions and processes responsible for Mo rich, Cu poor endowment at Aolunhua. The results highlight the presence of a potentially new class of porphyry Mo deposit in intra-continental extensional settings and indicate that the availability of Cl is an important factor in determining the Cu/Mo of oxidized porphyry systems.

2 Results and Discussion

2.1 Field and geochronological constraints on magmatic-hydrothermal events at Aolunhua

Syn-mineralization monzogranite porphyry, diorite, granodiorite porphyry and aplite, together with the post-mineralization quartz porphyry, have been dated. The new LA-ICP-MS zircon U-Pb $^{206}Pb/^{238}U$ data show that the intrusion age of the syn-mineralization monzogranite porphyry is 131.6 ± 1.4 Ma. This age falls within 2σ uncertainty of the

molybdenite Re-Os model ages for molybdenite hosted in the monzogranite porphyry, which range from 133.9 ± 2.1 Ma to 131.1 ± 1.8 Ma (Ma et al., 2009; Shu et al., 2009). These ages provide permissive evidence for the cogenetic relationship between the monzogranite porphyry and Mo mineralization at Aolunhua. The LA-ICP-MS zircon U-Pb weighted mean $^{206}Pb/^{238}U$ age of the syn-mineralization granodiorite porphyry obtained in this study is 129.3 ± 0.9 Ma. This date overlaps with the weighted mean $^{206}Pb/^{238}U$ ages of the syn-mineralization diorite and aplite of 128.5 ± 2.4Ma and 127.3 ± 1.3 Ma, respectively. These three new ages constrain the intrusion ages of the other three syn-mineralization intrusions at Aolunhua within a temporally unresolvable range between 129.3 ± 0.9 Ma and 127.3 ± 1.3 Ma. The LA-ICP-MS zircon U-Pb weighted mean $^{206}Pb/^{238}U$ age of the post-mineralization quartz porphyry is 124.4 ± 0.8 Ma. The new geochronology data constrain magmatism and mineralization between 131.6 ± 1.4 Ma and 124.4 ± 0.8 Ma.

2.2 Aolunhua: an unusual porphyry Mo deposit related to intra-continental extension

New geochronology data show that the timing of magmatism and mineralization in the Aolunhua deposit is coeval with the timing of exhumation of metamorphic core complexes, and development of graben basins and large-scale normal faults/detachments throughout the eastern segment of the Central Asian Orogenic Belt (e.g., Meng, 2003; Wu et al., 2011; Ouyang et al., 2015), indicating that Aolunhua was formed in an intra-continental extensional setting. Compared to typical porphyry Mo deposits in intra-continental extensional settings, however, the syn-mineralization monzogranite porphyry at Aolunhua is significantly less evolved with SiO_2 contents of 68.2 to 70.2 wt.%. In addition, the syn-mineralization monzogranite porphyry is characterized by high Sr/Y (57-82), a negligible Eu anomaly (Eu/Eu*=0.9-1.0), and a depleted mantle- or juvenile crust-derived Sr-Nd-Hf isotopic signature [$^{87}Sr/^{86}Sr_i$=0.7049-0.7052, $\varepsilon_{Nd}(t)$=0.5-1.4, $\varepsilon_{Hf}(t)$=3.2-5.4]. Such characteristics are at odds with those of intrusions associated with porphyry Mo deposits in intra-continental extensional settings worldwide. Moreover, most known porphyry Mo deposits in intra-continental extensional settings commonly contain fluorite. Examples include the Shangfanggou-Nannihu-Sandaozhuang, Donggou, Shapinggou, and Caosiyao deposits in the northern and southern margins of the NCC, as well as the Chalukou and Hashitu deposits in the Great Xing'an Range, and the Climax, Urad-Henderson, and Questa deposits in the Colorado Mineral Belt. However, the Aolunhua deposit stands out as fluorite-free. The evidence presented above indicates that Aolunahua probably formed in an intra-continental extensional setting, associated with fluorine-poor, depleted mantle- or juvenile crust-derived adakite-like magmas.

2.3 Mo-enrichment and Cu-deficiency at Aolunhua

As discussed above, geochemical data show that the syn-mineralization monzogranite porphyry at Aolunhua is adakite-like, with isotopic signatures of depleted mantle- or juvenile crust-derived magma. Such geochemical characteristics are broadly comparable to those of porphyry Cu-Mo related intrusions. Paradoxically, Aolunhua is enriched in Mo but overall lacks Cu enrichment. The question remains: why adakite-like magmas with depleted mantle- or juvenile crust-derived isotopic signatures at Aolunhua are only fertile for Mo and not for Cu mineralization?

The studies of Černý et al. (2005) showed that porphyry Mo-related intrusions are generally less-oxidized than those hosting Cu-Mo deposits. Our results show that the fO_2 of the syn-mineralization intrusions at Aolunhua (FMQ+1.81 ± 0.30 to FMQ+2.13 ± 0.13) are comparable to those of porphyry Cu-Mo related intrusions, indicating that the oxidation state of the ore-related intrusions may not be a dominant factor in the development of Cu-poor, Mo-rich deposits such as Aolunhua. The elevated redox state of the system is also consistent with the presence of hematite and anhydrite daughter minerals in fluid inclusions hosted within the quartz phenocrysts of the Aolunhua monzogranite porphyry.

In addition to fO_2, magma volatile content affects the capacity of magmas to transport metals from deep to shallow crustal levels and the partitioning of metals into exsolving magmatic-hydrothermal fluids (e.g., Grondahl and Zajacz, 2022). Apatite is commonly found in igneous rocks and can incorporate several volatile species into its crystal structure (Webster and Piccoli, 2015). As such, it can represent an excellent recorder of magma volatile budgets (e.g., Li and Costa, 2020). The SO_3 contents of the syn-mineralization magmatic apatite grains are highly variable (ranging from below detection limit to 0.41 wt.%), whereas their Cl concentrations are systematically low (<0.10 wt.%; Fig. 1). The large variation in magmatic apatite SO_3 content may be controlled by the different timing of apatite crystallization relative to fluid saturation. Although the data are scattered, two general groups can be discerned, one characterized by low apatite Cl and SO_3 contents (both <0.10 wt.%), and a second comprising low apatite Cl (<0.10 wt.%) with elevated SO_3 (0.10 to 0.41 wt.%) concentrations. The low apatite Cl and SO_3 contents may be controlled by magma degassing and/or fluid exsolution processes (Cline and Bodnar, 1994), as Cl and S preferentially partition into aqueous fluids and/or vapour phases in shallow silicic systems (Edmonds and Wallace 2017). Considering S is significantly less soluble in the melt phase than Cl at shallow crustal depths (Zajacz et al. 2012), the low Cl, high SO_3 apatite contents (decoupling) most likely reflects low Cl ore-forming magmas at Aolunhua rather than volatile loss.

Available experimental and fluid inclusion data show that Mo mineralization is less dependent on Cl content than Cu dominated systems (e.g., Keppler and Wyllie, 1991), as Mo can be transported as molybdic acid species (H_2MoO_4; Keppler and Wyllie, 1991), as Mo-oxo-chloride complexes (MoO_2Cl^+, MoO_2Cl_2, or MoO_2Cl^{3-}; Ulrich and Mavrogenes, 2008), or as ion pairs ($NaHMoO_4$, $KHMoO_4$, Na_2MoO_4, K_2MoO_4; Ulrich and Mavrogenes, 2008) in ore-forming fluids. Conversely, Cu is dominantly transported as an aqueous chloride complex (e.g., $CuCl^0$ and $CuCl^{2-}$) (e.g., Williams-Jones and Migdisov, 2014). The enrichment of Mo and deficiency of Cu at Aolunhua most likely relates to the Cl poor nature of the magmatic-hydrothermal system, resulting in low efficiency scavenging of Cu from the oxidized adakite-like magma during fluid exsolution, ultimately decreasing Cu mineralization potential. This conclusion is in good agreement with the systematic Cl poor nature of magmatic apatites from intrusions associated with porphyry Mo-only deposits worldwide.

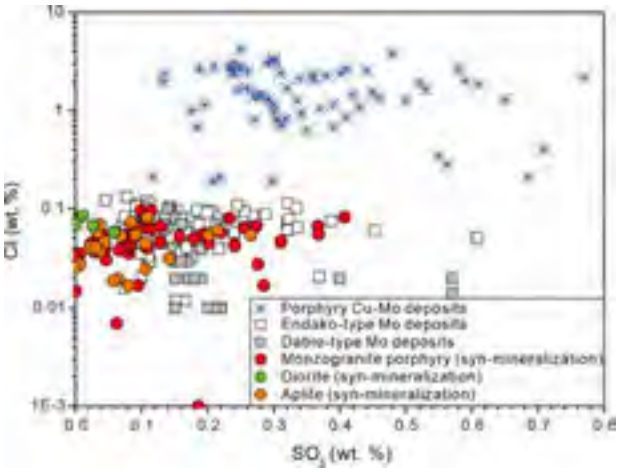
2.4 Implications for porphyry formation and exploration

Porphyry Cu-Mo deposits commonly form from oxidized adakite-like magmas derived from depleted mantle or juvenile crust (e.g., Richards, 2011; Hou et al., 2015; Carter et al., 2022). These sources provide the essential metals necessary for the formation of porphyry Cu-Mo deposits (Hou et al., 2015). The oxidized adakite-like magmas can stabilize Cu and Mo as soluble species, enhancing the mobility of theses metals and leading to the generation of metal-rich magmas (Carter et al., 2022). This process facilitates the formation of hydrothermal systems as the magma ascends to the upper crust, where porphyry Cu-Mo deposits develop (Richards, 2011). Consequently, it has been traditionally proposed that oxidized adakite-like magmas derived from depleted mantle or juvenile crust play a crucial role in the concentration of Cu and Mo within porphyry Cu-Mo systems (e.g., Richards, 2011; Hou et al., 2015). Conversely, porphyry Mo systems are commonly thought to be associated with oxidized normal rhyolite magmas derived from enriched mantle or ancient crust (e.g., Pettke et al., 2010; Chen et al., 2017). The research results from Aolunhua indicates that porphyry Mo deposits may also be genetically related to depleted mantle- or juvenile crust-derived oxidized adakite-like magmas. This finding suggests that the primary distinction between porphyry Cu-Mo and porphyry Mo deposits may not stem from the source region (i.e., depleted mantle or juvenile crust source vs. enriched mantle or ancient crust source) of the magma or the processes it undergoes during evolution (i.e., these parameters are not critical in producing variations in Cu/Mo in oxidized porphyry systems).

In comparison to porphyry Cu-Mo related intrusions, apatite grains from the Aolunhua porphyry Mo-related intrusions are characterized by distinctly lower Cl concentrations, while SO_3 concentrations remain comparable. Given that S is significantly less soluble in the melt phase than Cl at shallow crustal depths, the Cl-poor nature of the Aolunhua apatite likely reflects the presence of low Cl ore-forming magmas rather than volatile loss. This inference is further supported by the absence of any systematic difference in Cl content among apatite hosted in biotite and plagioclase and groundmass-hosted crystals. Consequently, it is propose that the availability of Cl in magmatic-hydrothermal systems may be pivotal in determining the relative endowment of Cu vs. Mo in oxidized porphyry systems, rather than the characteristics of magma source regions or magma evolution processes. Magmas originating from Cl-depleted source regions or those that do not release significant amounts of Cl during partial melting are more likely to form porphyry Mo deposits, even if they stem from depleted mantle or juvenile crust. Conversely, if enriched mantle or ancient crust contains elevated Cl levels, magmas derived from these sources are more inclined to forming porphyry Cu-Mo deposits.

The uniform whole-rock major, trace element and isotopic compositions, and oxygen fugacity among global porphyry Cu-Mo and the Aolunhua porphyry Mo related intrusions makes it challenging to distinguish Cu-Mo from Mo only mineralizing magmas based on whole-rock elemental (e.g., Sr/Y), isotopic (e.g., Sr-Nd-Hf), or oxygen fugacity criteria alone. Accordingly, developing a means to discriminate between porphyry Cu-Mo and Mo deposits could potentially prove useful for guiding more efficient mineral exploration. The magmatic apatite data show that compared to porphyry Cu-Mo related intrusions, apatite grains from the Aolunhua porphyry Mo-related intrusions are characterized by distinctly lower Cl concentration (<0.10 wt.% vs. up to 4.30 wt.% Cl). Similarly, Cl-poor magmatic apatites are also observed in Endako- and Climax-type porphyry Mo related intrusions. This suggests that apatite Cl content has the potential to discriminate between porphyry Cu-Mo related intrusions and those associated with porphyry Mo deposits (Fig. 1). Even in multi-intrusive magmatic-hydrothermal systems, magmatic apatite serves as a robust geochemical proxy, as demonstrated in the case of Aolunhua. Apatite with anomalously low Cl content (<0.10 wt.%) appears diagnostic in indicating a higher potential for porphyry Mo rather than porphyry Cu-Mo mineralization. Hence, routine major element analysis of apatite from intrusions or stream sediments may be a useful approach for refining potential targets for porphyry Cu-Mo or porphyry Mo mineralization on district- or regional-scales.

Figure 1. Covariation of Cl and SO_3 for magmatic apatites from the Aolunhua syn-mineralization monzogranite porphyry, diorite and aplite, compared to a compilation of several porphyry Cu-Mo related intrusions, and Endako- and Dabie-type porphyry Mo related intrusions.



Acknowledgements

This research is supported by the Scientific Research Fund of the China Central Non-Commercial Institute (KK2203) and the National Science Foundation of China (42372096).

References

Audétat A (2015) Compositional evolution and formation conditions of magmas and fluids related to porphyry Mo mineralization at Climax, Colorado. Journal of Petrology 56:1519–1546.

Carter LC, Tapster SR, Williamson BJ, Buret Y, Selby D, Rollinson G K, Millar L, Parvaz, DB (2022) A rapid change in magma plumbing taps porphyry copper deposit-forming magmas. Scientific Reports 12:17272.

Černý P, Blevin PL, Cuney M, London D (2005) Granite-related ore deposits. Economic Geology 100th Anniversary Volume: 337-370.

Chen YJ, Wang P, Li N, Yang YF, Pirajno F (2017) The collision-type porphyry Mo deposits in Dabie Shan, China. Ore Geology Reviews 81: 405–430.

Cline JS, Bodnar RJ (1994) Direct evolution of brine from a crystallizing silicic melt at the Questa, New Mexico, molybdenum deposit. Economic Geology 89:1780-1802.

Edmonds M, Wallace PJ (2017) Volatiles and exsolved vapor in volcanic systems. Elements 13:29-34.

Farmer GL, Morgan L, Cosca M, Mize J, Bailley T, Turner K, Mercer C, Ellison E, Bell A (2024) Mantle melting in regions of thick continental lithosphere: Examples from Late Cretaceous and younger volcanic rocks, Southern Rocky Mountains, Colorado (USA). Geosphere 20:1411-1440.

Gaynor SP, Rosera JM, Coleman DS (2023) Genesis of the Questa Mo porphyry deposit and nearby polymetallic mineralization, New Mexico, USA. Economic Geology 118:1319-1339.

Grondahl C, Zajacz Z (2022) Sulfur and chlorine budgets control the ore fertility of arc magmas. Nature Communications 13:4218.

Hou ZQ, Duan LF, Lu YJ, Zheng YC, Zhu DC, Yang ZM, Yang ZS, Wang BD, Pei YR, Zhao ZD, McCuaig TC (2015) Lithospheric architecture of the Lhasa terrane and its control on ore deposits in the Himalayan-Tibetan orogeny. Economic Geology 110:1541-1575.

Keppler H, Wyllie PJ (1991) Partitioning of Cu, Sn, Mo, W, U, and Th between melt and aqueous fluid in the systems halplogranite-H_2O HCl and halplogranite-H_2O HF. Contributions to Mineralogy and Petrology 109:139-150.

Li WR, Costa F (2020) A thermodynamic model for F-Cl-OH partitioning between silicate melts and apatite including non-ideal mixing with application to constraining melt volatile budgets. Geochimica et Cosmochimica Acta 269:203–222.

Ma XH, Chen B, Lai Y, Lu YH (2009) Petrogenesis and mineralization chronology study on the Aolunhua porphyry Mo deposit, Inner Mongolia, and its geological implications. Acta Petrologica Sinica 25:2939-2950 (in Chinese with English Abstract).

Meng QR (2003) What drove late Mesozoic extension of the northern China-Mongolia tract? Tectonophysics 369:155-174.

Ouyang HG, Mao JW, Zhou ZH, Su HM (2015) Late Mesozoic metallogeny and intracontinental magmatism, southern Great Xing'an Range, northeastern China. Gondwana Research 27:1153-1172.

Pettke T, Oberli F, Heinrich CA (2010) The magma and metal source of giant porphyry-type ore deposits, based on lead isotope microanalysis of individual fluid inclusions. Earth and Planetary Science Letters 296:267-277.

Richards JP (2011) High Sr/Y arc magmas and porphyry Cu±Mo±Au deposits: Just add water. Economic Geology 106:1075-1081.

Rosera JM, Gaynor SP, Ulianov A, Schaltegger U (2024) Using stochastic point pattern analysis to track regional orientations of magmatism during the transition to Cenozoic extension and Rio Grande Rifting, Southern Rocky Mountains. Tectonics 43:e2023TC007902.

Shu QH, Jiang L, Lai Y, Lu YH (2009) Geochronology and fluid inclusion study of the Aolunhua porphyry Cu-Mo deposit in Arhorqin area, Inner Mongolia. Acta Petrologica Sinica 25:2601-2614 (in Chinese with English Abstract).

Ulrich T, Mavrogenes J (2008) An experimental study of the solubility of molybdenum in H_2O and KCl–H_2O solutions from 500 °C to 800 °C, and 150 to 300 MPa. Geochimica et Cosmochimica Acta 72:2316-2330.

Wang F, Zhou XH, Zhang LC, Ying JF, Zhang YT, Wu FY, Zhu, RX (2006) Late Mesozoic volcanism in the Great Xing'an Range (NE China): timing and implications for the dynamic setting of NE Asia. Earth and Planetary Science Letters 251:179-198.

Webster JD, Piccoli PM (2015) Magmatic apatite: A powerful, yet deceptive, mineral. Elements 11:177–182.

Wu FY, Sun DY, Ge WC, Zhang YB, Grant ML, Wilde SA, Jahn BM (2011) Geochronology of the Phanerozoic granitoids in northeastern China. Journal of Asian Earth Sciences 41:1-30.

Williams-Jones AE, Migdisov AA (2014) Experimental constraints on the transport and deposition of metals in ore-forming hydrothermal systems. Special Publications of the Society of Economic Geologists, https://doi.org/10.5382/SP.18.05.

Zajacz Z, Candela PA, Piccoli PM, Sanchez-Valle C (2012) The partitioning of sulfur and chlorine between andesite melts and magmatic volatiles and the exchange coefficients of major cations. Geochimica et Cosmochimica Acta 89:81-101.

A porphyry ore deposit in the making: unique insights into magmatic processes leading to ore fertility through the Taapaca volcano

Iván Mateo Espinel Pachón[1], Zoltan Zajacz[1], Cristóbal González Rodríguez[2], Michael Schirra[1], Alexandra Tsay[1] and Mara Miranda[1]
[1]University of Geneva, Switzerland
[2]Millenium Institute on Volcanic Risk Research- Ckelar Volcanoes, Chile

Abstract. The site(s) of magma storage and differentiation, the origin of the enrichment of ore-forming constituents, as well as the crustal depth at which the main stage of fluid exsolution occurs in magmatic systems associated with major porphyry type Cu – (Mo-Au) deposits is a hotly debated subject. To obtain key information on these processes, we studied the Taapaca volcano in the Central Volcanic Zone of the Andes, which produced voluminous dacites with major and trace element compositions closely resembling those of porphyry stocks associated with world-class porphyry Cu - (Mo-Au) deposits. We analyzed igneous phenocrysts and silicate melt inclusions within them from several eruptive untis of Taapaca. We show that the dacites form by the efficient mixing of rhyolitic melts stored at various crustal levels (~20 – 3 km depth) with oxidized, mafic mantle-derived melts donating both ore-forming constituents and adakitic trace element signature. The results highlight the importance of upper mid-crustal magma storage, mixing and hybridization in the generation of porphyry ore-fertile magmatic systems and indicate that recent models may underestimate the direct role of primary mantle-derived component in the generation of magmatic-hydrothermal ore fertility.

1. Introduction

Porphyry copper deposits are genetically linked to arc magmatism, yet the processes controlling the fertility of magmatic systems remain incompletely understood because of the general absence of well-preserved records of magmatic history in mineralized systems due to the erosion and extensive hydrothermal alteration of associated volcanic / sub- volcanic lithologies. Numerous studies have traditionally focused on metal sequestration and fluid exsolution processes within upper crustal magma reservoirs. However, the influence of deep crustal processes on ore fertility has gained significant attention over the past 1-2 decades (Audétat 2010, 2015; Chiaradia et al. 2012; Matjuschkin et al. 2016; Grondahl and Zajacz 2017, 2022; Chiaradia 2022; Chiaradia and Caricchi 2022; Schirra et al. 2024). This study highlights the Taapaca Volcano as a particularly well-suited setting to investigate these processes. Taapaca represents a long-lived magmatic system developed under low magma flux conditions, which produced a well-preserved volcanic sequence with the majority of rocks showing textures and major and trace element geochemistry closely resembling those of porphyry stocks associated with world-class porphyry Cu – (Mo-Au) systems. These geochemical signatures include fertility indicators such as elevated Sr/Y and La/Yb ratios, as well as low Zr concentrations. In addition, an active hydrothermal system is associated with the volcano, which may very well be forming economic mineralization at depth. At the same time Taapaca provides an extensive unaltered volcanic rock record, thus it is an ideally suited system to study magmatic processes leading to fertility for hydrothermal ore genesis.

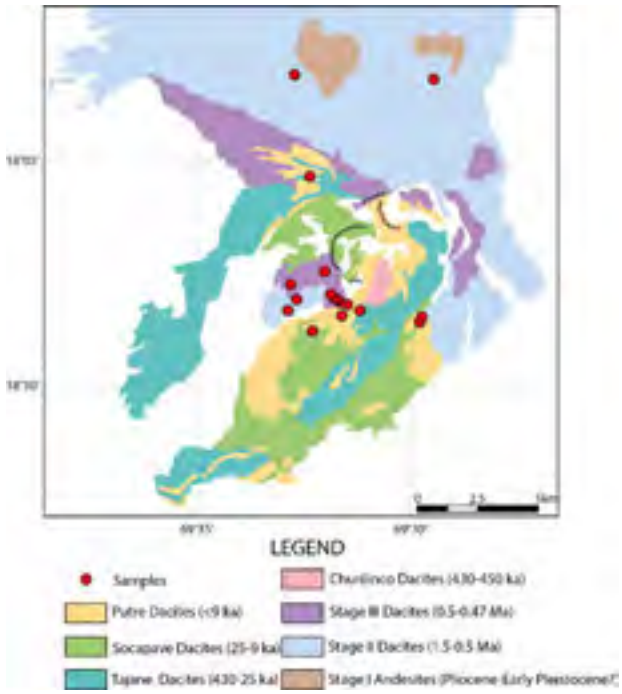


Figure 1. Simplified Geological map of Taapaca volcano in the Central Andes of Northern Chile (18°S) adapted from (Clavero et al. 2004). Sampling sites are shown.

Taapaca is located in the Central Volcanic Zone (CVZ) of the Andes in Chile, near the Bolivian border. It is a large dacitic complex (~35 km³) that has been active for at least 1.5 Ma. It erupted compositionally homogeneous dacites (62–67 wt% SiO_2) on one of the thickest continental crusts on Earth, ~70 km thick (Prezzi et al. 2009).

The oldest unit, Stage I (Pliocene–Early Pleistocene?), consists of clinopyroxene-rich andesitic lava flows, which are only exposed on the northern flank of the volcano. Between 1.5 and 0.5 Ma, the northern and eastern flanks of the volcano developed extensively, forming Stage II, which is characterized by dacitic lavas, domes, block-and-ash flows, and lahar deposits. These rocks contain phenocrysts of plagioclase, biotite, quartz, and

amphibole, as well as centimetric megacrysts of sanidine and mafic enclaves (~54 SiO_2 wt%) (<1 vol%) with oval shapes. Following this, Stage III dacites formed, producing lavas, domes, and block-and-ash flow deposits. These rocks contain higher proportions of sanidine megacrysts and mafic enclaves (<3 vol%) than Stage II. The most recent activity, Stage IV, began around 0.45 Ma and continues to the present, generating domes and associated deposits. These rocks share mineralogical similarities with Stages II and III but contain a greater abundance of mafic enclaves (<6 vol%) and sanidine megacrysts reaching up to 12 cm in size. This stage has been subdivided into four subunits based on stratigraphic and radiometric constraints: Churilinco (430–450 ka), Tajane (430–25 ka), Socapave (25–9 ka), and Putre (<9 ka; Clavero et al. 2004).

2. Samples and Methods

Fresh volcanic rocks from all major eruptive units of Taapaca Volcano (Fig. 1) were collected during a field campaign. Eighteen of the 39 samples collected were selected for detailed analysis. First, petrographic thick sections (~300 µm thickness) were prepared, revealing well-preserved, fresh phenocrysts. Seventy-five amphibole crystals from all eruptive events were analyzed along core to rim profiles for major and minor element compositions using a JEOL JXA-iHP200F hyperprobe (EPMA), equipped with 4 Wavelength Dispersive X-ray Spectroscopy (WDS) detectors at the University of Geneva. Furthermore, Laser Ablation Inductively Coupled Plasma Mass Spectrometry (LA-ICP-MS) analysis were performed on the same phenocrysts to obtain trace element compositions, and bulk major and trace element analysis of the groundmass surrounding the amphibole crystals were also conducted by LA-ICP-MS by using large beams that facilitated representative sampling.

Silicate melt inclusions were analyzed using LA-ICP-MS following the methodology of Halter et al. (2002). This approach involves ablating the entire inclusion with its host mineral, followed by deconvolution of their respective signals. A key advantage of this method is that it allows analysis without reheating the inclusion, which may induce leakage and volatile loss. Additionally, it enables simultaneous quantification of sulfur (S) and chlorine (Cl) alongside major and trace elements, minimizing the risk of unrepresentative results due to volatile loss into the vapor bubble (Venugopal et al. 2020; Grondahl and Zajacz 2022). The analyses were conducted at the University of Geneva using an NWR 193 HE laser ablation system coupled with an Agilent 8900 triple quadrupole ICP-MS. A custom-built ablation cell and gas purification system were employed to enhance the accuracy of S and Cl measurements along with a comprehensive suite of major and trace elements.

3. Results

3.1. Mineral Chemistry, thermobarometry and oxybarometry

Olivine containing Cr-rich spinels occurs exclusively in the Socapave unit. It has a magnesium number (#Mg) of ~78 and Ni concentrations ranging from 1200-2500 ppm.

Clinopyroxene is present in Stage I and in mafic enclaves within Tajane. In Stage I clinopyroxene, Cr_2O_3 concentrations are approximately 0.03 wt%, while they range from 0.10 to 0.75 wt% in the Tajane enclaves. Similarly, the #Mg in Stage I clinopyroxene varies from 0.67 to 0.80, while in Tajane enclaves, it remains relatively constant at around 0.80. Machine learning thermobarometry for clinopyroxene-bearing magmas (Ágreda-López et al. 2024) provide temperatures for Stage I ranging from 1020 up to 1070 °C and pressures ranging from 100-400 MPa. In contrast, Tajane enclave temperatures range from 1050 to 1100°C, and the pressures from 500 up to 850MPa.

Plagioclase is present in all the eruptive events. In Stage I, it is characterized by FeO contents ranging from 0.35 up to 0.62 wt% and An mol % ranging from 40 to 58, while in all the other stages plagioclases have FeO contents from 0.12 up to 0.28 wt% and An mol% ranging from 22 to 35.

Biotite is present in all eruptive units except Stage I. Machine learning thermobarometry based on biotite – silicate melt equilibrium (Li and Zhang 2022) yielded temperatures of 925-945 °C and pressures of 430-550 MPa in the Socapave unit. In all the other Stages, biotite-based pressure estimates are similar, but the estimated temperatures are lower (840 up to 870°C).

Thermobarometric calculations were performed on amphiboles from all the eruptions except the amphibole-free Stage I, using the calibration of Ridolfi (2021). Three discrete populations of amphiboles were identified: high-pressure amphiboles (600-850MPa) exclusive from Socapave unit; medium-pressure amphiboles (250-450 MPa) and low-pressure amphiboles (70-250 MPa) are present in all eruptive stages. Corresponding temperatures for these populations range from 1000-1050°C, 875-1000°C and 730-850°C respectively (Fig. 2). Compositionally, high and medium-pressure amphiboles were mainly classified as Mg-hastingsite, with few analyses identified as Tschermakitic pargasite, while low-pressure amphiboles are Mg-horblende.

Melt oxygen fugacity has been estimated at ΔQFM + 3.2 ±0.5 by spinel-olivine pairs (Ballhaus et al., 1991), at ΔQFM + 1.9 ±0.7 by the partitioning of V between olivine and melt (Shishkina et al., 2018) and using molar values of Al^{IV}, Al^{VI}, Ti, Fe^{3+}, Fe^{2+},Mn, Ca, Na^{A} and K in amphiboles, following the method of Ridolfi (2021). High-pressure amphiboles

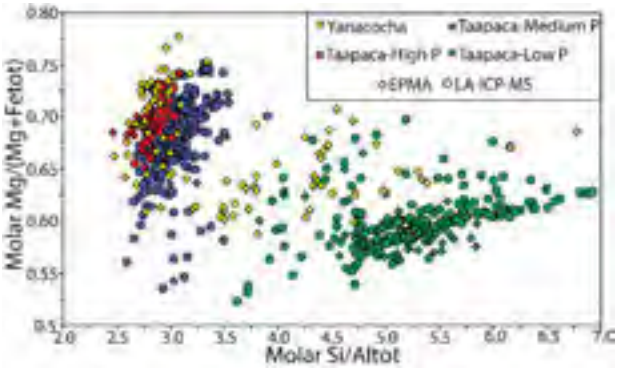


Figure 2. Molar Si/Al_{tot} vs Molar $Mg/(Mg+Fe_{tot})$ variations of Taapaca and Yanacocha amphiboles.

yielded a fO_2 of ΔQFM + 1.97 ±0.5, medium-pressure amphiboles yielded a fO_2 of ΔQFM + 1.71 ±0.6 and low-pressure amphiboles yielded a fO_2 of ΔQFM + 2.0 ±0.8 (Fig. 3).

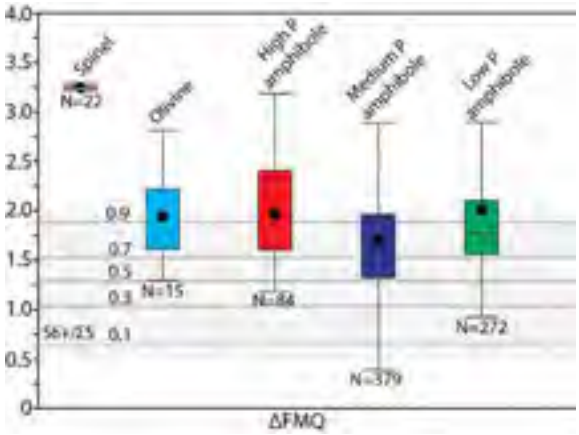


Figure 3. Oxygen fugacity in Taapaca magmas. Box and whisker diagrams showing the oxygen fugacity estimated using various methods. Dashed lines represent sulfur redox state based on Jugo (2009) with the S^{6+}/total S ratios in labels.

3.2. Silicate melt inclusion compositions

Silicate melt inclusions trapped in sanidine and plagioclase show rhyolitic compositions (>72 wt% SiO_2, and <0.08 MgO wt%), wheres those in olivine show a mafic composition (~54% wt SiO_2). There is no evidence for the presence of an intermediate melt. SMIs in olivine display sulfur concentrations up to 4000 µg/g, chlorine up to 2500 µg/g, copper ranging from 75 up to 175 µg/g, silver ranging from 0.05 up to 0.25 µg/g and notably an adakitic trace element signature with Sr/Y of 61 ± 14, La/Yb of 33 ± 8, Sr of 935 ± 268 µg/g and Y of 15.8 ± 4.0 µg/g (Fig. 4).

4. Magmatic evolution and ore-forming potential

We propose that the Taapaca dacites resulted from a mixing process between a basaltic andesitic melt and a rhyolitic melt. The mafic component was identified considering the whole rock geochemistry

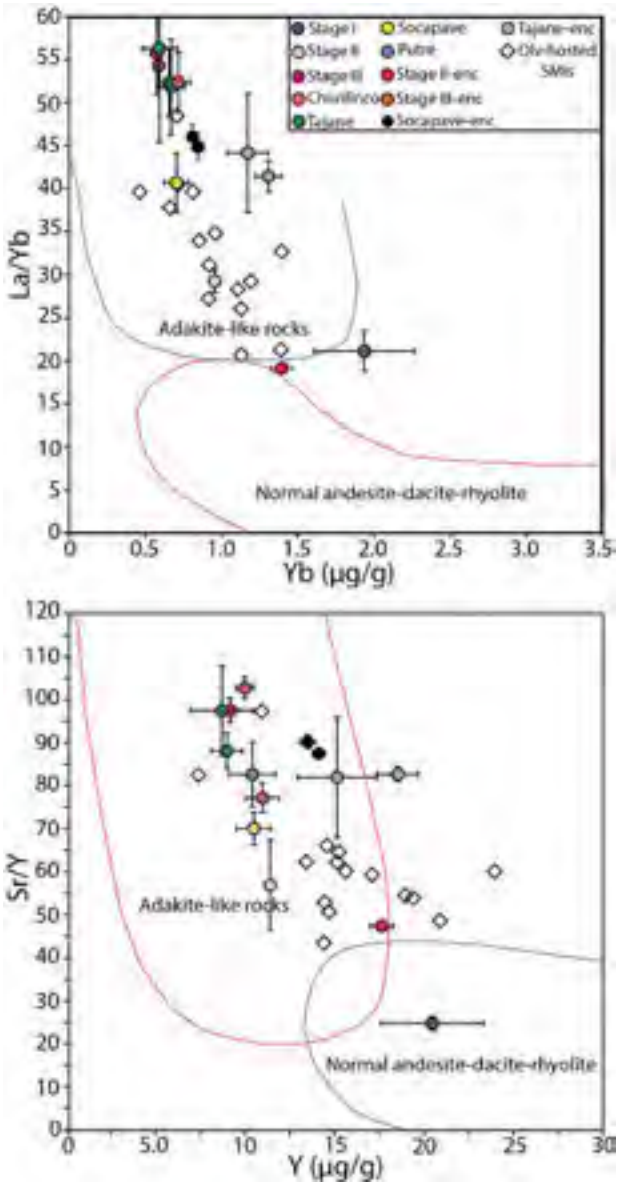


Figure 4. Whole rock geochemistry and composition of olivine hosted silicate melt inclusions from the Socapave unit on adakite geochemical discrimination diagrams.

of the mafic enclaves (~53 up to 58 SiO_2 wt%) that closely aligns with the primitive character of the SMIs hosted in olivine and the presence of Cr-rich spinel inclusions in the olivine. Furthermore, clinopyroxene found in Tajane enclaves with high Mg# (~80) and high Cr_2O_3 (up to 0.75 wt%), must have crystallized from near-primitive mantle melts (Pichavant and Macdonald 2007). Therefore, the fO_2 estimates suggest that oxidation does not occur during magma differentiation and that the oxidized nature of the Taapaca magmas is rather inherited from the mafic component which also donate significant amount of S and Cu to the mixed dacite magma (up to ~4000 µg/g and 175 µg/g S and Cu in the mafic component, respectively). Furthermore, these mafic melts exhibit adakitic signatures that cannot be the result of differentiation processes as suggested for other systems (Loucks 2014).

These mafic melts also donated amphibole phenocrysts to the mixed dacite magma, the composition of which resembles those found in the volcanics from the Yanacocha mining district in the Andes of northern Peru (Chambefort et al. 2013), as shown in Fig 2.

Notably, barometric data from biotite (430-550 MPa), which coexists with plagioclase as evidenced by the mineral inclusions of one within the other, contains silicate melt inclusions of rhyolitic composition and provides evidence of evolved melts in the middle crust that are physically segregated, as no phenocrysts or SMIs are recording intermediate melt compositions. This rhyolite contains primarily plagioclase phenocrysts with low An mol%, along with some quartz and biotite.

5. Conclusions

Voluminous dacites at Taapaca with compositions and textures resembling porphyry stocks in world-class porphyry systems were produced by mixing of rhyolitic melts stored at various crustal levels with mantle-derived, oxidized, S and Cu rich melts. The main site of magma storage, differentiation and hybridization appears to be the upper middle crust (250 – 450 MPa), and as opposed to the mainstream of current thinking, ore-fertility indicator trace element signatures are imposed by the mafic mantle derived component of the hybrid dacite, rather than by high-pressure amphibole and garnet fractionation.

Acknowledgements

This project has received funding from the European Research Council (ERC) under the European Union's Horizon 2020 research and innovation program (grant agreement no. 864792) granted to Zoltan Zajacz.

References

Ágreda-López M, Parodi V, Musu A, et al (2024) Enhancing machine learning thermobarometry for clinopyroxene-bearing magmas. Comput Geosci 193:. https://doi.org/10.1016/j.cageo.2024.105707

Audétat A (2010) Source and evolution of molybdenum in the porphyry Mo(-Nb) deposit at Cave Peak, Texas. Journal of Petrology 51:1739–1760. https://doi.org/10.1093/petrology/egq037

Audétat A (2015) Compositional evolution and formation conditions of magmas and fluids related to porphyry mo mineralization at Climax, Colorado. Journal of Petrology 56:1519–1546. https://doi.org/10.1093/petrology/egv044

Chambefort I, Dilles JH, Longo AA (2013) Amphibole geochemistry of the yanacocha volcanics, peru: Evidence for diverse sources of magmati Cvolatiles related to gold ores. Journal of Petrology 54:1017–1046. https://doi.org/10.1093/petrology/egt004

Chiaradia M (2022) Distinct magma evolution processes control the formation of porphyry Cu–Au deposits in thin and thick arcs. Earth Planet Sci Lett 599:. https://doi.org/10.1016/j.epsl.2022.117864

Chiaradia M, Caricchi L (2022) Supergiant porphyry copper deposits are failed large eruptions. Communications Earth & Environment 3:107. https://doi.org/10.1038/s43247-022-00440-7.

Chiaradia M, Ulianov A, Kouzmanov K, Beate B (2012) Why large porphyry Cu deposits like high Sr/Y magmas? Sci Rep 2:. https://doi.org/10.1038/srep00685

Clavero JE, Sparks RSJ, Pringle MS, et al (2004) Evolution and volcanic hazards of Taapaca Volcanic Complex, Central Andes of Northern Chile. J Geol Soc London 161:603–618

Grondahl C, Zajacz Z (2017) Magmatic controls on the genesis of porphyry Cu–Mo–Au deposits: The Bingham Canyon example. Earth Planet Sci Lett 480:53–65. https://doi.org/10.1016/j.epsl.2017.09.036

Grondahl C, Zajacz Z (2022) Sulfur and chlorine budgets control the ore fertility of arc magmas. Nat Commun 13:. https://doi.org/10.1038/s41467-022-31894-0

Halter WE, Pettke T, Heinrich CA, Rothen-rutishauser B (2002) Major to trace element analysis of melt inclusions by laser-ablation ICP-MS : methods of quantification. 183:63–86

Jugo PJ (2009) Sulfur content at sulfide saturation in oxidized magmas. Geology 37:415–418. https://doi.org/10.1130/G25527A.1

Li X, Zhang C (2022) Machine Learning Thermobarometry for Biotite-Bearing Magmas. J Geophys Res Solid Earth 127:. https://doi.org/10.1029/2022JB024137

Loucks RR (2014) Distinctive composition of copper-ore-forming arcmagmas. Australian Journal of Earth Sciences 61:5–16. https://doi.org/10.1080/08120099.2013.865676

Matjuschkin V, Blundy JD, Brooker RA (2016) The effect of pressure on sulphur speciation in mid- to deep-crustal arc magmas and implications for the formation of porphyry copper deposits. Contributions to Mineralogy and Petrology 171:. https://doi.org/10.1007/s00410-016-1274-4

Pichavant M, Macdonald R (2007) Crystallization of primitive basaltic magmas at crustal pressures and genesis of the calc-alkaline igneous suite: experimental evidence from St Vincent, Lesser Antilles arc. Contributions to Mineralogy and Petrology 154:. https://doi.org/10.1007/s00410-007-0208-6ï

Prezzi CB, Götze HJ, Schmidt S (2009) 3D density model of the Central Andes. Physics of the Earth and Planetary Interiors 177:217–234. https://doi.org/10.1016/j.pepi.2009.09.004

Ridolfi F (2021) Amp-tb2: An updated model for calcic amphibole thermobarometry. Minerals 11:1–9

Schirra M, Zajacz Z, Müller D (2024) The hidden link between dry ankaramitic melts and giant alkalic-type epithermal Au deposits: The Lihir Island example. Geochim Cosmochim Acta 378:82–98. https://doi.org/10.1016/j.gca.2024.06.024

Shishkina TA, Portnyagin M V., Botcharnikov RE, et al (2018) Experimental calibration and implications of olivine-melt vanadium oxybarometry for hydrous basaltic arc magmas. American Mineralogist 103:369–383. https://doi.org/10.2138/am-2018-6210

Venugopal S, Schiavi F, Moune S, et al (2020) Melt inclusion vapour bubbles: the hidden reservoir for major and volatile elements. Sci Rep 10:. https://doi.org/10.1038/s41598-020-65226-3

Copper Creek, Arizona: Laramide, Early Halo Style Porphyry, Cupola and Breccia Hosted Mineralization

Dante Padilla[1], Benedek Gal[1], Matias Sanchez[2], Thomas Bissig[1], Paul Harbidge[1]
[1]Faraday Copper Corp. 250-200 Burrard St. Vancouver, BC, Canada
[2]Faultrocks Inc. Victoria, BC, Canada

Abstract. Copper Creek is a Cu-Ag-Mo porphyry system, dated between 59 and 61.6 Ma, hosted within the Glory Hole volcanics (63 Ma) and the Copper Creek batholith (62 Ma). The intrusion of the host batholith, followed by subsequent porphyry and breccia emplacement is structurally controlled by a NW-trending Laramide thrust fault system and a NE-trending basement-involved normal fault set forming a cross graben. Late post-mineral deformation takes place mainly as fault reactivations associated with Basin and Range extension. The deposit exhibits a complex history of veinlet reopening with early halo (EH) and C veinlets as the main copper-bearing styles, extending outward from high-grade magmatic cupola zones, later overprinted by quartz-sericite-pyrite (D) veinlets and multiple high-grade hydrothermal breccias. Breccias range from 10 to > 250m across, vertically extend up to 1400 m, are predominantly clast-supported, and display minimal clast rounding. Hydrothermal cement consists of pyrite, chalcopyrite, ± quartz, tourmaline, and phyllosilicates. Unlike other porphyry Cu deposits in the region, supergene profiles at Copper Creek are poorly developed, suggesting a relatively late exhumation of the system.

1. Introduction

The Copper Creek district is situated at the intersection of two crustal scale NW and NE oriented metallogenic corridors in the prolific Cretaceous-Palaeocene Laramide porphyry copper province of the Southwest U.S. and Northern Mexico (Fig. 1). The district is approximately 20 km NE of the historic San Manuel mine in the Galiuro mountains.

Copper Creek is different from other porphyry systems in the region in that mineralization is largely hosted by early halo (EH) and C veinlets, as opposed to dense quartz vein stockworks (Riedell et al. 2013). EH and C veins are commonly overprinted by D veins, which also play an important role in grade re-distribution. Breccia bodies (382 mapped to date) host high-grade mineralization and are occasionally rooted in semi-massive sulphide feeders and/or magmatic cupola zones.

Recent exploration work led to the discovery of significant new near-surface mineralization and an improved understanding of the structural control, alteration and sulphide zonation of breccia and porphyry style mineralization.

2. Exploration and mining history

Small scale mining in the district occurred intermittently between 1861-1982, targeting near surface breccias, with approximately 300,000 tons of ore produced from the Old Reliable and Childs-Aldwinkle mines in the early 20th century. Subsequently, more than 200 km of drilling was carried out in the district, the bulk of it between the mid-1990s and 2015, delineating the main American Eagle porphyry ore shell and the high-grade Mammoth-Keel breccia system. Exploration activities resumed in late 2021 following Faraday Copper Corp.'s acquisition of the project. Since then, approximately 43 km of additional drilling has been completed (as of Q1 2025), alongside new studies to advance and optimize the project's technical profile. The current mineral resource estimate is 422 million tons at 0.48% Cu-eq (NI 43-101 report 2023). An updated technical study is planned for Q3-Q4 2025.



Figure 1. Location of Copper Creek, relative to other major porphyry copper deposits and prospects in Arizona, USA.

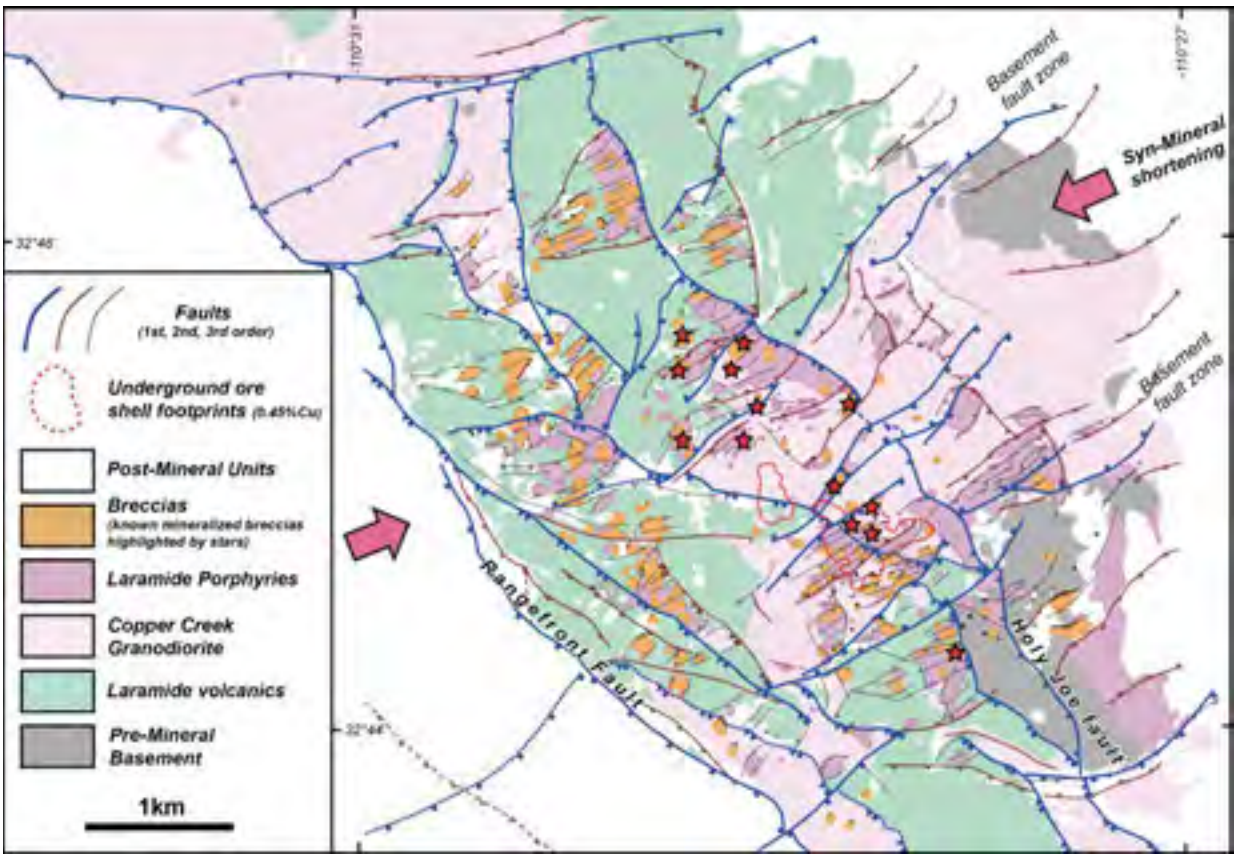


Figure 2. Schematic geology, structural architecture and breccia distribution in the Copper Creek district. Major mineralized breccias and outlines of underground ore shells indicated.

3. Geology of Copper Creek

Mineralization is largely hosted by the Palaeocene (~62 Ma) Copper Creek batholith which intruded Palaeocene-Cretaceous Glory Hole volcanics (~63 Ma) and Proterozoic to Palaeozoic sedimentary and metamorphic units (Figure 2). Four main types of porphyry phases were identified, interpreted to span pre-, syn-, and post-mineral times (Riedell et al.2013). Breccias crosscut all lithologies up to the post-mineralization porphyries. Oligocene Galiuro volcanics and Tertiary basin-fill sediments post-date mineralization and overlay older rock units.

The regional scale structural controls are an arc-parallel NW-trending thrust fault system, primarily mappable in exposed basement units (Favorito et al. 2018), and a NE-trending coeval normal fault set interpreted as a basement involved long-lived structural zone/corridor within the Proterozoic to Palaeozoic basement. Both major structural sets are obscured and/or covered by Laramide volcanism and later emplacement of the Copper Creek batholith (Figure 2).

At camp scale, porphyry and breccia emplacement are interpreted to be strongly preferentially emplaced in the hanging wall blocks along thrust-faults (Figure 3) and locally, following second- and third-order order structural planes.

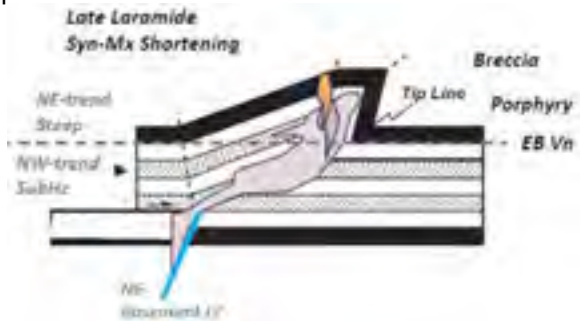


Figure 3. Regional scale batholith, porphyry and mineralization emplacement structural model

4. Alteration and mineralization

Mineralization can be subdivided into an earlier porphyry stage, overprinted by breccia-hosted mineralization. Supergene oxidation and secondary sulphide enrichment are relatively

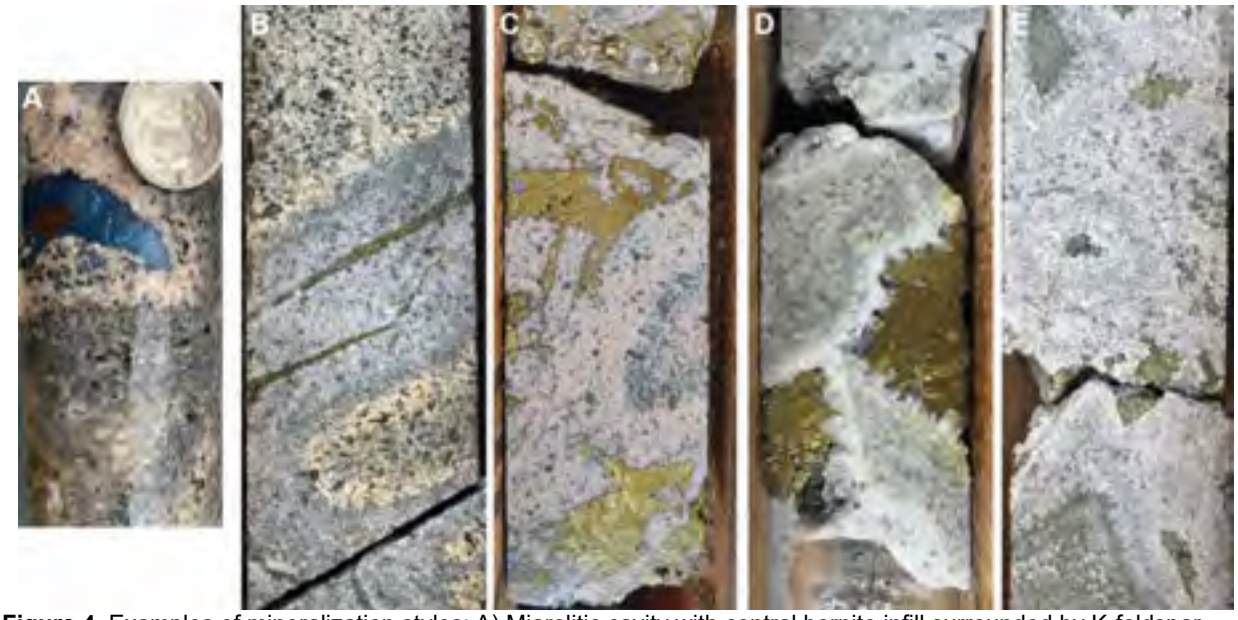


Figure 4. Examples of mineralization styles: A) Miarolitic cavity with central bornite infill surrounded by K-feldspar flooding, Keel cupola zone; coin for scale; B) Early halo vein with finely disseminated chalcopyrite in green-grey mica, re-opened by sulphide veinlet, chalcopyrite, American Eagle zone; C) Chalcopyrite cemented breccia on high-temperature phengitic to muscovitic mica partially overprinting former potassic alteration in cupola zone, Keel. D) Coarse chalcopyrite, quartz infill as breccia cement on muscovitic-sericite ± highly crystalline kaolinite altered clasts, Mammoth breccia; E) Chalcopyrite cemented breccia with pervasive paragonitic-sericite altered clasts, Banjo breccia. (B-E: width of core ~6cm)

minor but occurred within the uppermost 10-70 meters.

Porphyry-stage mineralization is primarily hosted by EH and C veins within the American Eagle and Mammoth-Keel zones (Figure 4B). Rather than forming stockworks, EH, C, and overprinting D veinlets occur as continuous, steeply dipping sheeted vein zones striking ENE. Below around 500m current depth, around the American Eagle and Mammoth-Keel centers, a sub-set of shallow (<45°), outward-dipping veins also contribute to the overall grade. Sulphides exhibit a vertical zoning from shallower pyrite, pyrite>chalcopyrite, chalcopyrite to bornite-chalcopyrite at depth (Figure 5), hosted by vein centers, halos and subordinate disseminations throughout the host rock. Miarolitic cavities and coarse quartz ± K-feldspar zones, interpreted as cupola style features, are important contributors of mineralization in some areas at depth, such as the Keel zone (Figure 4A, Figure 5).

Alteration related to early-stage porphyry style mineralization is subtle and mostly controlled by EH veinlets characterized by halos of K-feldspar-biotite, phengitic mica, ± specular hematite, as well as localized zones of K-feldspar, biotite, ±anhydrite replacement of the host rock and infills in open spaces (e.g. miarolitic cavities).

Breccia hosted mineralization is characterized by complete to partial infills of pyrite, chalcopyrite, ± bornite as breccia cement as well as disseminations in altered clasts. Breccia textures are predominantly crackle to jigsaw fit breccias with minor mosaic zones, accompanied by various degrees of clast corrosion and replacement by quartz and white mica (Figure 4D, E). Breccias have not experienced significant clast rounding, milling or rotation and incorporate lithologies from their immediate wall rocks. Open pore space was likely formed from post-explosive collapse as well as hydrothermal fluid-driven corrosion.

Breccias can be vertically extensive, e.g. with up to 1430 m of known vertical extent in the Keel-Mammoth zone (Anderson et al. 2009) but rarely exceed 100-150 m in width. Alteration associated with mineralized breccias is vertically zoned ranging from shallower, high sulphidation assemblages (quartz - pyrophyllite - alunite) to high crystallinity kaolinite - muscovitic mica ± quartz, to paragonitic/muscovitic mica zones, to deeper phengite/muscovite mica. K-feldspar, anhydrite, biotite ± molybdenite indicate an early, deep potassic assemblage, commonly overprinted by subsequent phyllic alteration (Figure 5).

The largest known breccia body in the district is the blind Mammoth breccia about 30 m from present surface. Recent relogging and evaluation suggests that it overprints earlier

cupola style mineralization in the Keel zone over 1000 m below surface (Figure 4C). Faraday Copper's recent drilling has confirmed and discovered additional high-grade breccia bodies within the American Eagle near surface zone (Figure 6). Simultaneously, additional target areas have been tested in the broader district with encouraging results.

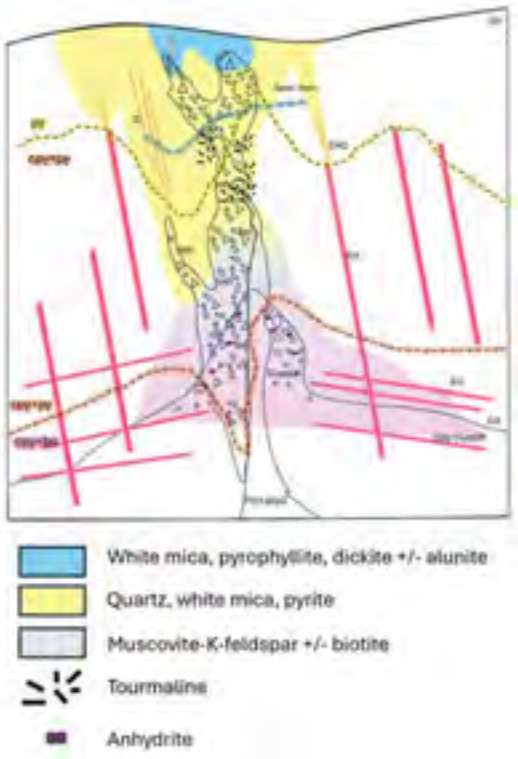


Figure 5. Geological conceptual model with alteration-sulphide zonation.

5. Mine plan

Approximately one third of the measured and indicated resource is hosted in high-grade breccias and occurs near the surface, whereas the remainder occurs as porphyry style, and magmatic cupola style mineralization 500-1100 m below surface. Spatial distribution of the mineralized resource lends itself to an initial open pit mine followed by an underground block caving operation (NI 43-101 report 2023).

6. Discussion and conclusions

Copper Creek is a porphyry copper deposit with dominantly EH and C-vein hosted porphyry style mineralization and high-grade breccias. Breccias generally show minimal clast movement or milling and likely never breached the surface. Batholith and subsequent porphyry and breccia emplacement is controlled by Laramide arc-parallel thrusts and cross-graben extensional structures. Alteration is characterized by early phyllic-K-spar overprinted by later QSP (D-veins). Multiple vein reopening events and overprinting alteration suggest an evolving system with some degree of telescoping and syn-mineral uplift.

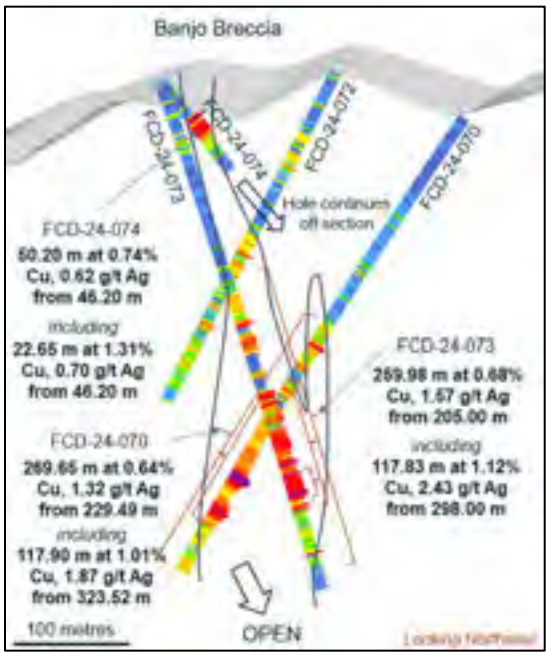


Figure 6. Recently discovered Banjo Breccia results from October 17th, 2024, press release (faradaycopper.com)

Acknowledgements

We thank all previous explorer's contributions and the ones of our team in the past four years.

References

Anderson ED, Atkinson WW, Marsh T, Iriondo A (2009) Geology and geochemistry of the Mammoth breccia pipe, Copper Creek mining district, southeastern Arizona: evidence for a magmatic–hydrothermal origin, Min Dep 44:151-170.

Faraday Copper NI 43-101 (2023) https://www.sedarplus.ca/csa-party/records/document.html?id=444a424db89ef6a6c6b87053e0fe02f2d1ca06a8ee405030b135bc3066fa2b9a

Favorito DA, Seedorff E (2018) Discovery of major basement-cored uplifts in the northern Galiuro Mountains, Southeastern Arizona: Implications for regional Laramide deformation style and structural evolution, Tectonics 37:3916-3940.

Riedell KB, Sandberg RJ, Guthrie JO, Gorecki AD, Lambiotte MJ, Reynolds SJ, Proffett JM, Ybarra SJ, Poulter JE (2013) Early Halo Type Porphyry and Breccia Cu-Mo Mineralization at Copper Creek, Pinal County, Arizona, Extended Abstract SEG 2013 conference, Whistler, BC, Canada, 9 p.

Ore deposits and prospects in the Bolnisi mining district: general overview and future exploration prospectivity, Lesser Caucasus, Georgia

Nino Popkhadze[1,2], Shota Tagviashvili[2], Malkhaz Natsvlishvili[2], Joni Shubitidze[2], Giorgi Ugrekhelidze[2], Badri Gogia[2], Şafak Utku Sönmez[3,4], Robert Moritz[3]

[1]Al.Janelidze Institute of Geology of Iv.Javakhishvili Tbilisi State University, Georgia
[2]RMG Rich Metals Group, Georgia
[3]Department of Earth Sciences, University of Geneva, Switzerland
[4]Present address: Department of Geology and Geological Engineering, Laval University, Quebec, Canada

Abstract. The Bolnisi mining district is located in the Late Cretaceous volcanic series of the Artvin – Bolnisi zone, Lesser Caucasus of the Tethys – Eurasian metallogenic belt. The generation of gold–copper epithermal mineralization of the Bolnisi ore district is related to the late subduction stage along the Eurasian active margin. Late Cretaceous voluminous silicic magmatism in the Bolnisi district is characterized by explosive bimodal volcanism, which is accompanied by metal-enriched fluids. There are numerous ongoing projects, major exploration and mining activities (including Sakdrisi, Madneuli, Kazreti, Beqtakari, Bnelikhevi, Mushevani, Tsitelisopeli, Dambludi) in the Bolnisi region. To better understand the controls of mineralization, 3D geological models of the ore deposits from the Bolnisi district were obtained based on detailed surface observations, mine mapping, and interpretation of drill core data. This paper summarizes the main characteristics of ore deposits from the Bolnisi district, their economic indicators, current status, potential and future development.

1 Introduction

The Late Cretaceous Bolnisi mining district (~87-71 Ma) of the northern Lesser Caucasus is the major metallogenic event before the South Armenian block was accreted within the Eurasian margin. It is a central segment of the Tethyan orogenic and metallogenic belt. The ore deposits and prospects associated with the Mesozoic subduction-related, magmatic evolution of the Eurasian margin hosted by the Kapan zone, the Somkheto-Karabagh belt, and its northern Georgian extension, named the Artvin-Bolnisi zone (Moritz et al. 2016). Different types of ore deposits and districts formed during this geodynamic evolution period. In this paper, we provide a general overview and new data on the main ore deposits and prospects of the Bolnisi district, which is a link between the Eastern Pontides and the Lesser Caucasus including its geodynamic evolution, volcanism type and ore deposit formation within the Tethyan metallogenic belt. Mining is currently active in the Bolnisi region, where RMG Rich Metals Group Company and CMG Caucasus Mining Group are successfully mining and exploring new projects.

2 Regional geology and stratigraphy

The Bolnisi district in southern Georgia represents the easternmost extension of the Eastern Pontides. The northeastern extremity of the Somkheto-Karabakh arc of Lesser Caucasus in Georgia is known as the Artvin-Bolnisi unit (Fig.1). The Late Cretaceous volcano-sedimentary units of the Bolnisi group were emplaced in a horst and graben setting (Moritz et al. 2020) between the Carboniferous Khrami and Locki massifs and Jurassic-Early Cretaceous intrusions and volcaniclastic rocks. According to previous data, the Bolnisi group includes Cenomanian to Campanian (89-71Ma) volcanogenic suites, overlain by Maastrichtian limestone marl (Popkhadze et al. 2014; Moritz et al. 2020). Eocene granodiorite and granite (52-53Ma) intruded the Late Late Cretaceous rocks (Hassig et al. 2020) (Fig 1b).

3 Ore deposits and prospects of the Bolnisi mining district

Georgia's first non-ferrous metal production facility is the Madneuli gold-copper-polymetallic mine in the Bolnisi district. Several epithermal deposits and prospects are located in this region, the study of which began in the 1940s at the Madneuli deposit. Nowadays the Bolnisi mining district includes the following ore deposits and prospects: Madneuli, Sakdrisi, Bectakari, Bneli Khevi, Kvemo Bolnisi, Tsiteli Sopeli, Mushevani 2, Mushevani 3, Kazreti, Zvareti, Dambludi, Darbazi, Tamarisi, Imedi, Samgereti, Balichi and Grma Khevi, Imedi, Dumanisi, Iraga, Ivanovka, Balichi, Kldeisi, Tsknari Abano, Madnisklde, Kakliani, Sofia (Fig.1a,b,c). Table 1 summarizes the main characteristics of the ore deposits and prospects of the Bolnisi district. The **Sakdrisi** epithermal deposit consists of a ~2 km long, NE-oriented system with five ore centers. A NE-oriented thrust fault zone separates the lower mineralized volcano-sedimentary complex (LVSC) and the upper barren (UCSC) complex (Popkhadze et al. 2023). New investigations allow us to define ore zones in the deeper part where

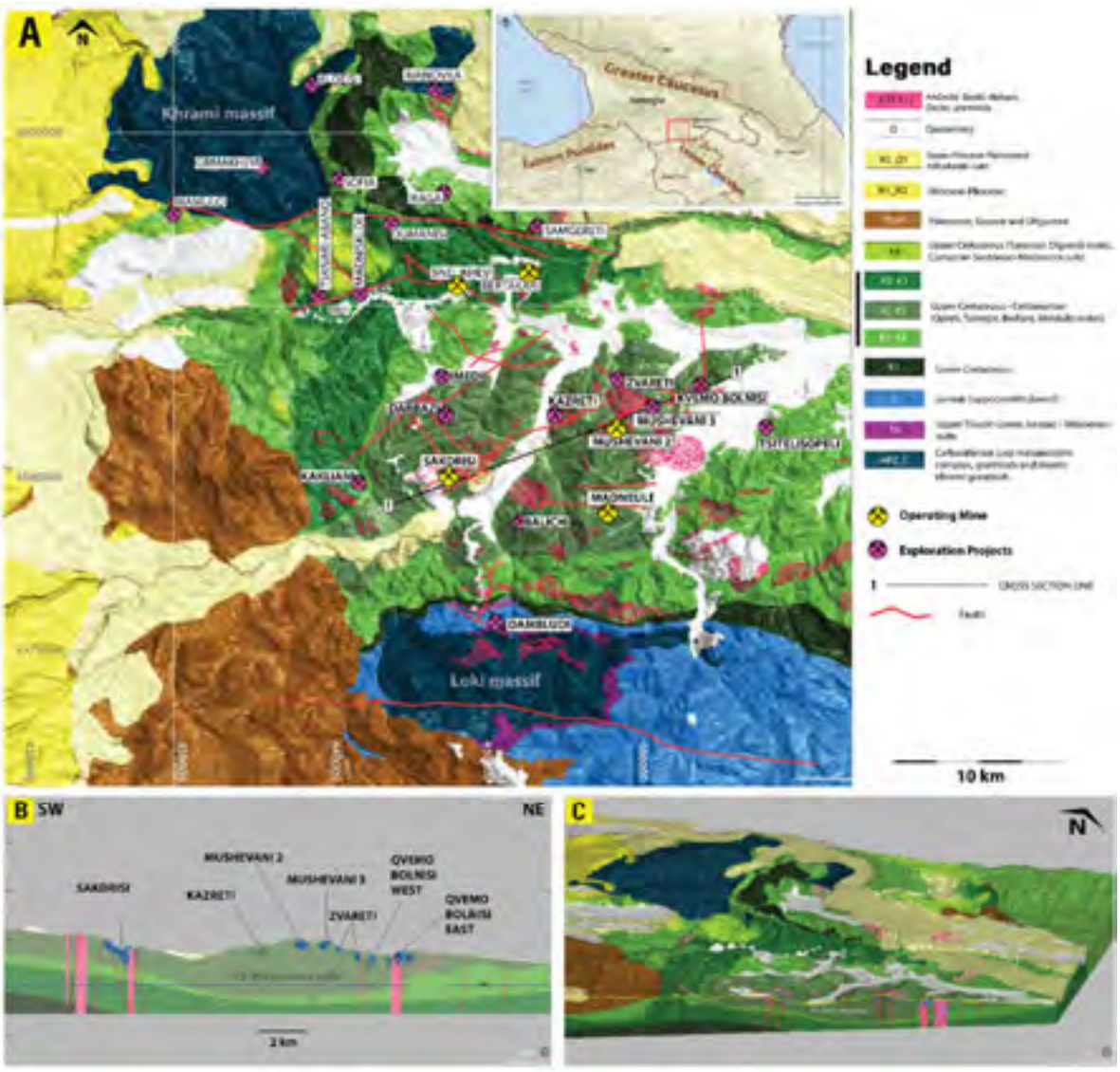


Figure 1. a) Geologic map of the Bolnisi district (adapted from CMG Caucasus Mining Group. 2016), b) cross section along the southwest to northeast direction regional fault with the locations of the major active mines (Madneuli, Sakdrisi, Mushevani2 and Beqtakari) and advanced exploration projects (Qvemo Bolnisi East and West, Kazreti, Zvareti and Mushevani3 with the ore bodies distribution (in blue color)) c) 3D geological model of the Bolnisi mining district.

Table 1 Main characteristics of the ore deposits and prospects of the Bolnisi mining district.

#	Deposit name and status	Deposit type	Mineral Resources	Ore Reserves	Age
1	**Sakdrisi** (Open pit mining/planned underground mining)	Epithermal/ medium sulfidation	(Indicated and measured) 36Mt @ Au 1.2 g/t; Cu 0.1% Inferred: 3 Mt @ Au 0.8 g/t; Cu 0.1 %	10 Mt @ Au1.6g/t; Cu 0.14%; (Proven and Probable)	Late Cretaceous (new data from Sönmez et al, submitted)
2	**Madneuli** (Open pit mining)	Transitional-VMS-porphyry-epithermal	(Indicated and measured) 11Mt @ Cu0.5%; Au 0.3 g/t (Inferred) 1.2 Mt @ Cu0.3%; Au 0.1 g/t	6.5 Mt @ Au 0.5 g/t; Cu 0.4%; (Proven and Probable)	Late Cretaceous-U-Pb zircon ages of dikes crosscutting Mashavera unit 86.6-87.1 Ma (Moritz et al., 2020)

3	**Beqtakari (**Underground mining)	Low sulfidation epithermal	(Indicated and measured) 1.8 Mt @ Au 2.5g/t; Ag 30 g/t; Cu 0.1%; Pb 0.6%; Zn 1.3%; (Inferred) 1.2 Mt @ Au 1.7 g/t; Ag 24 g/t; Cu 0.1%; Pb 0.4%; Zn 0.9%;	1.5 Mt @ Au 4 g/t; Cu 0.14%; Ag 15 g/t; Pb 1.14%; Zn 2.5 %; (Proven and Probable)	Late Cretaceous (new data from Sönmez et al, submitted)
4	**Mushevani 2 (**Open pit mining)	Epithermal	(Indicated) 4.5 Mt @ Au 1.8 g/t Cu 0.2% (Inferred) 0.05 Mt @ Au 0.3 g/t Cu 0.14 %	4 Mt @ Au 1.6 g/t; Cu 0.3%; (Probable)	Late Cretaceous (new data from Sönmez et al, submitted)
5	**Kazreti (**In development, is planning underground mining)	Epithermal	(Indicated) 6.6 Mt @ Au 1.8 g/t; Ag 0.6 g/t; Cu 0.1%; Pb 0.3%; Zn 0.5%; (Inferred) 6.7 Mt @ Au 1.6 g/t; Ag 0.7 g/t; Cu 0.1%; Pb 0.3%; Zn 0.5%;		Late Cretaceous (new data from Sönmez et al, submitted)
6	**Qvemo Bolnisi East (**In development)	Epithermal, low sulfidation	(Indicated) 1.8 Mt @ Cu 0.9%; (Inferred) 18 Mt @ Cu 1%;		Late Cretaceous (new data from Sönmez et al, submitted)
7	**Bnelikhevi (**Open pit mining)	Epithermal	(Indicated) 9 Mt @ Au 0.9 g/t (Inferred) 2 Mt @ Au 0.6 g/t	4 Mt @ Au 2.9 g/t; (Probable)	Late Cretaceous
8	**Tsiteli Sopeli (**In development)	Epithermal, Low sulfidation	(Indicated) 2.7 Mt @ Au 0.78 (Inferred) 33.7 Mt @ Au 0.7		Late Cretaceous Report (JCG Georgian Copper and Gold (2015))
9	**Dambludi (**In development)	Porphyry(?)	(Indicated) 24 Mt @ Au 0.5 g/t; Cu 0.1% (Inferred) 25 Mt @ Au 0.5 g/t; Cu 0.1 %		Late Jurassic (Oxfordian)159+1, 40 (Hässig et al, 2020)

#	Host rock geology	Alteration	Main mineralogy	Orebody geometry	References
1	Ignimbrite; Fine, massive, and Pumice tuff, layered volcano-sedimentary and sedimentary unit; explosive breccia; andesite-basaltic and rhyodacitic dikes	Silicification; oxidation; clay and Cl alteration	cp, py, sl, gn, Au, Cu, bar, qtz	Vein-dominant subvertical; stockworks; disseminated; breccia pipes	Popkhadze et al, 2023; Golay T 2019.
2	Ignimbrite; thin-layer, massive, and pumice tuff; breccia conglomerate, phreatomagmatic breccia; rhyoandesite dike	Silicification, oxidation, chlorination, sericite, argillic	cp, py, gn, sl, native Au, hm, cv, bn, enr, cc	Veins, breccia pipes, stockworks, disseminated, stratiform ore bodies, quartz-sulfide and sulfide ore zones and lenses	Popkhadze et al. (2014), Moritz et al. (2016), Migineishvili (2005), Gialli (2013).
3	Rhyodacite, andesite, andesite-basalt, tuff-breccia, fine tuff, hydrothermal breccia.	Silicification, oxidation, chlorination, argillic	py, cp, Au, sl, gn, tn, mrc, td	Disseminated precious metals in hydrothermal breccia, in cement and clasts	Lavoie (2015)
4	Rhyodacitic fine-grained tuff, litho-clastic tuff, Ignimbrite, Pumice tuff, rhyodacitic and andesitic dikes	Oxidation, silicification, chlorination, argillic	cp, py, sl, gn, melnic, cc, cv, bn, smid	Veins, stockworks, disseminated	Report (Caucasus Mining Group (2018))
5	Ignimbrite, pumice tuff, medium/fine-grained massive tuff, explosive breccia, tuff-breccia, mafic and felsic dikes	Silicification, Oxidation, clay alteration, chlorination.	py, cp, gn, sl, melnic, vurts, mr.	Veins, stockworks, disseminated, quartz-sulphide ore zones.	Report (Caucasus Mining Group (2020))
6	Welded and non-welded ignimbrite, explosive breccia, lithic/pumice-rich tuff, andesite and dacite dikes and domes	Argillic, oxidation, sericite	py, cp, sl, gn, cc,	Disseminated, explosive polymictic breccia, veins, stockworks	Report (Caucasus Mining Group (2020))

7	Fine-grained and lithic tuff, pumice tuff, tuff-breccia, rhyodacite and andesite dikes,	Sericite, clay, oxidation.	py, cp, gn, sl, mr, melnicovite.	Veins, vein-disseminated.	Report (Caucasus Mining Group (2016))
8	Pumice tuff, fine grained tuff, layered sedimentary rocks, rhyolite and andesite dacite dikes.	Silicification, clay:argillic/ kaolinite, chlorite, sericite.	py, cl, cc, sl, gn, mo, mal, az.	Subvertical quartz-gold-sulphide veins.	Report (JCG Georgian Copper and Gold (2015))
9	Granodiorite, fine grained tuff, andesite and basaltic dikes.	Silicification, propylitic, clay, chloritization, potassic.	py, native Au, gn, sl.	Vein-disseminated, stockworks.	Hässig et al, 2020; Report (CMG2016)

the underground development is taking place. Three main volcanic and volcano-sedimentary complexes of the Mashavera suite are defined at the **Madneuli** deposit: lower Madneuli (LVSC), upper Kazreti (UVSC) and Nabakrevi (VC). The mineralization is connected with the LVSC and intruding phreatomagmatic breccia (Popkhadze et al. 2017). The main mineralization at the **Beqtakari** deposit is connected with hydrothermal breccia. The **Kazreti** deposit is located at the junction of northwest, northeast and latitudinal fault structures. The **Dambludi** gold-polymetallic deposit itself is located on the northern flank of the Loki anticline and is controlled by the North Loki latitudinal fault. An intensive drilling program and exploration is in progress at the Dambludi deposit. It is interpreted as a porphyry type, but still, many questions are left which is a matter of future investigations.

Conclusions

In conclusion, the geological setting expressed by the extensional setting, the large-scale silicic magmatic evolution characterized by bimodal mainly explosive volcanism in the Bolnisi district accompanied with the voluminous ignimbrite and pumice-rich volcaniclastic rocks and different types of explosive breccias (including phreatomagmatic, phreatic, hydrothermal, polymictic) created the favorable structural environment for the movement of fluids and precipitation of metals. Based on detailed mapping of the ore districts, the interpretation of the historic and new drill holes, and finally the creation of geological and mineralized envelope 3D models of the ore deposits allow us to conclude that the structural control of ore deposits is related to regional faults. These are mainly northeast and marginal to the northwest directions and should be considered in conjunction with other local faults and fractures developed along them, which are visible on the geological map of the Bolnisi ore district. Future exploration of these structures is planned in the Bolnisi mineral district.

References

"Caucasus Mining Group" LLC (2016) Geological report on the estimation of the resources of the Bnelikhevi Gold-polymetallic deposit.

"Caucasus Mining Group" LLC (2018) Geological report on the Resource/Supply estimation of the Mushevani2 Gold-Copper deposit.

"Caucasus Mining Group" LLC (2020) Geological report on the estimation of resources/reserves of gold polymetallic ores of the Kazreti deposit.

Gialli S (2013) The Controversial Polymetallic Madneuli Deposit, Bolnisi District, Georgia: Hydrothermal Alteration and Ore Mineralogy. University of Geneva, Switzerland: M.Sc. thesis (unpublished).

Golay T (2019) The Sakdrisi Au-Cu deposit, Bolnisi mining district, Georgia: providing a genetic model based on petrographic, geochemical, structural and alteration studies. University of Geneva, Switzerland: MSc thesis.

Hässig M, Moritz R, Ulianov A, Chiaradia M, Popkhadze N, Galoyan G, Enukidze O (2020) Jurassic to Cenozoic magmatic and geodynamic evolution of the Eastern Pontides and Caucasus belts, and their relationship with the Eastern Black Sea Basin opening. Tectonics 39:e2020TC006336.

JCG "Georgian Copper and Gold" (2015) Geological report of reserves and resources calculated during preliminary exploration works of the Tsitelisopeli gold-copper deposit.

Lavoie J (2015) Genetic constraint of the Late-Cretaceous Epithermal Beqtakari prospect, Bolnisi Mining District, Lesser Caucasus, Georgia. University of Geneva, Faculty of Earth Science, Geneva, Switzerland: MSc thesis.

Migineishvili R (2005) Hybrid nature of the Madneuli Cu-Au deposit, Georgia: Geochemistry, mineralogy and petrology: Journal of the Bulgarian Academy of Sciences, v. 43:128–132.

Moritz R, Melkonyan R, Selby D, Popkhadze N, Gugushvili V, Tayan R, Ramazanov V (2016) Metallogeny of the Lesser Caucasus: From Arc Construction to Postcollision Evolution. Society of Economic Geologists, Special Publication 19, pp.157-192.

Moritz R, Popkhadze N, Hässig M, Golay T, Lavoie J, Gugushvili V, Ulianov A, Ovtcharova M, Grosjean M, Chiaradia M, Dumitrica P (2020) At the crossroads of the Lesser Caucasus and the Eastern Pontides: Late Cretaceous to early Eocene magmatic and geodynamic evolution of the Bolnisi district, Georgia. Lithos 378-379:105872.

Popkhadze N, Moritz R, Gugushvili V (2014) Architecture of Upper Cretaceous rhyodacitic hyaloclastite at the polymetallic Madneuli deposit, Lesser Caucasus, Georgia. Cent. Eur. J. Geosci 6(3):308-329.

Popkhadze N, Moritz R, Natsvlishvili M, Bitsadze N (2017) First evidence of phreatomagmatic breccia at the Madneuli Polymetallic Deposit, Bolnisi district, Lesser Caucasus, Georgia. In: Proceedings of the 14th SGA biennial meeting: Mineral resources to discovery, 20-23 August, Quebec City, Canada; 1:323-326.

Popkhadze n, Gogia B, Tagviashvili Sh, Ugrekhelidze G, Natsvlishvili M, Shubitidze J, Moritz R (2023) 3D lithological and structural model and prospectivity of the Late Cretaceous Sakdrisi Gold Copper Epithermal deposit, Bolnisi district, Lesser Caucasus, Georgia. 17th Biennial SGA Meeting ETH Zurich, Switzerland, August 28-Sep1, v1:184-188.

New lithological approach for the 3D geological modeling of the Upper Cretaceous Sakdrisi gold copper epithermal deposit, Bolnisi District, Georgia

Nino Popkhadze[1,2], Badri Gogia[2], Shota Tagviashvili[2], Giorgi Ugrekhelidze[2], Malkhaz Natsvlishvili[2], Joni Shubitidze[2], Safak Somenz[4], Robert Moritz[3]

[1]Al.Janelidze Institute of Geology of Iv.Javakhishvili Tbilisi State University&RMG Rich Metals Group
[2]RMG Rich metals Group
[3]Department of Earth Sciences, University of Geneva
[4]Present address: Department of Geology and Geological Engineering, Laval University, Quebec, Canada

Abstract. The Bolnisi mining district of Lesser Caucasus in southern Georgia hosts several high-grade and tonnage epithermal gold-copper deposits. To better understand what controls the mineralization and the distribution of ores on the deposit, a 3D geological model has been built considering the distribution of lithological unit boundaries and structures at the Sakdrisi epithermal deposit, based on outcrop observations, detailed mappings, and interpretations of drill core data. The ore types and their distribution in different levels on Sakdrisi deposit have always been questioned. Our new lithological approach, which is based on genetic naming of rocks, allowed us to perform correct paleovolcanological reconstructions with structures in context and obtain a complete representation in the 3D model of the stratigraphic unit and mineralized zones within them. The high-grade ore zones are mainly localized in massive tuffs, which are brittle and strongly silicified, which easily succumbed to fractures developed by faults and fissures together with the explosive breccias, and created a favorable environment or the movement of ore-forming fluids and, consequently, the precipitation of metals. Both lithological and structural control on mineralization was determined at the Sakdrisi deposit.

1 Introduction

Mining in Bolnisi district is very active and the Sakdrisi Gold Copper epithermal deposit is one of the main ore deposits in this area, where the exploration is going on. New ore zones are discovered in the dipper part of the Sakdrisi 4 deposit, where the underground mining is planned. Numerous ore deposits and prospects are known in Bolnisi district (~87-71 Ma), which is connected with Upper Cretaceous silicic volcanic event. Mineralization in Bolnisi district is staratigraphically controlled: the first is Turonian to early Santonian (Madneuli deposit; Tsiteli Sopeli, Kvemo Bolnisi and Kazreti prospects) ore deposit group and the second Campanian (Sakdrisi and Beqtakari deposits; Darbazi, Imedi, Bnelikhevi and Samgreti prospects) group (Gugushvili et al. 2014) (Fig.1).

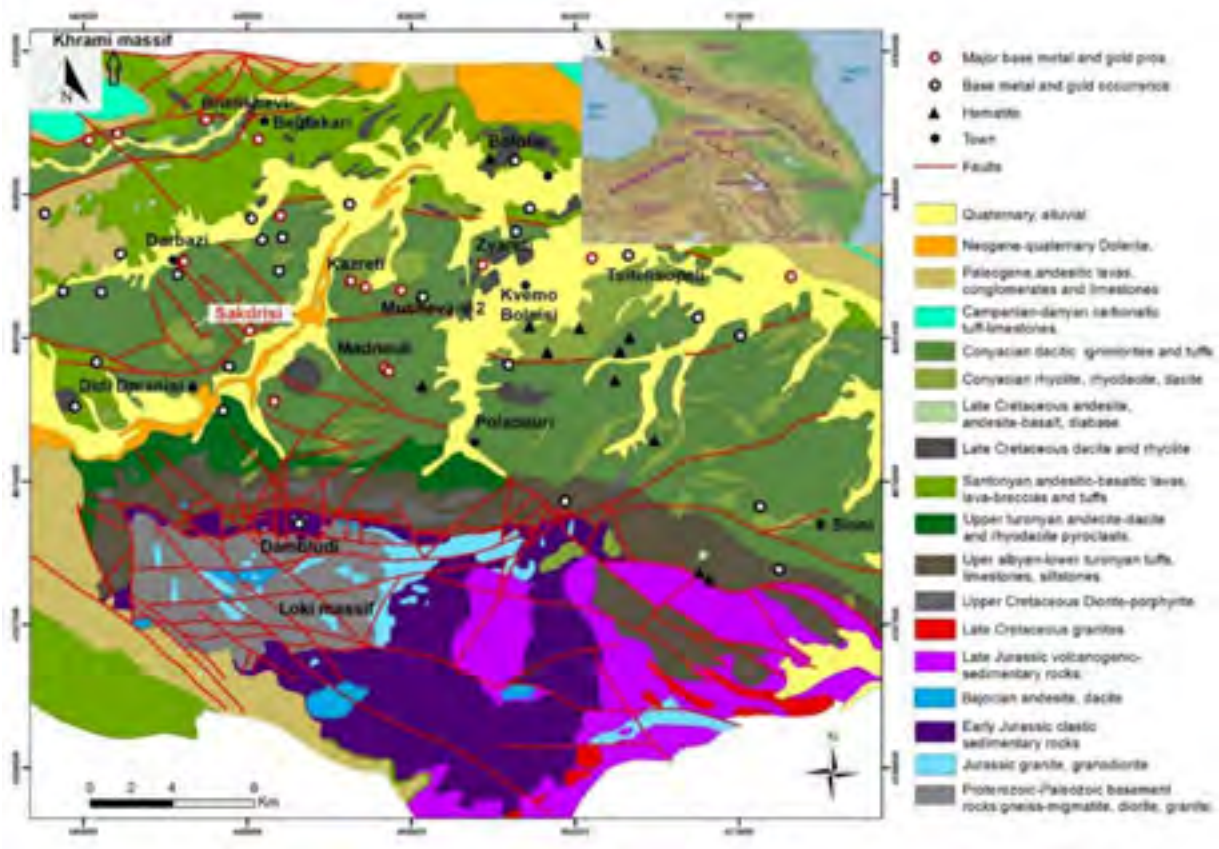


Figure 1. Geological map of the Bolnisi mining district with ore deposits and manifestations.

2 Regional and local geology

The Sakdrisi gold-copper polymetallic deposit is located in Artvin Bolnisi ore district, which continues to the west in the Eastern Pontides and from the east in the Lesser Caucasus (Moritz et al. 2016). The Lesser Caucasus is subdivided from SE to NW into three main domains **(**Sosson et al. 2010): the South Armenian Block (SAB), the ophiolitic Sevan-Akera suture zone (SASZ) and the Somkheto-Karabakh island arc (SKIA), the latter belonging to the Eurasian Plate. The northeastern extremity of the Somkheto-Karabakh arc in Georgia is known as the Artvin-Bolnisi unit (Yilmaz et al. 2000), which is located between the southeastern Black Sea – Adjara-Trialeti unit to the north which represents a Santonian-Campanian back-ark, and the Imbricated Baiburt-Karabakh unit to the South representing an Upper Cretaceous fore-arc. The Artvin-Bolnisi zone comprises a Hercynian basement, which consists of Precambrian and Paleozoic granite, gneiss and plagiogranite, cropping out in the Khrami and Loki massifs, overlain by Carboniferous volcano-sedimentary rocks. Within the Bolnisi zone, the Upper Cretaceous section is dominated by volcanic rocks consisting of calc-alkaline basalt, andesite, dacite and rhyolite (lavas, pyroclastics). Predominant Late Cretaceous volcanic and volcano-sedimentary rocks are in this region including rhyodacitic ignimbrites, ash fall and density current deposits with phreatomagmatic origin (Popkhadze et al. 2017; Popkhadze et al. 2014). Late Cretaceous sequences in this region are subdivided into six volcanogenic suites and correspond to Cenomanian and Maastrichtian in age. The bimodal character of Upper Cretaceous silicic volcanism is manifested by the alternation of mafic and felsic suites stratigraphically.

3 The geology of Sakdrisi deposit

The five mineralized blocks that comprise Sakdrisi (Sak-I to Sak-V) are aligned along an NE-oriented thrust fault zone (Fig.2). The five mineralized blocks of the Sakdrisi mine, some of which have undergone erosion and oxidation, are overlain by a thrust fault of barren ignimbrite (IGN) and are intersected by andesite basaltic (AN_BA) and rhyodacite (RHD) dikes, which represent the youngest rocks exposed at the Sakdrisi deposit. All of these rocks are described as the Upper Volcano-Sedimentary Complex (UVSC) (Jelev et al. 2020; Popkhadze et al. 2023). The lower volcano-sedimentary complex (LVSC) is composed of a thick (over 400m) sequence and separated from the upper complex by the sedimentary formation, formed along the thrust fault zone.

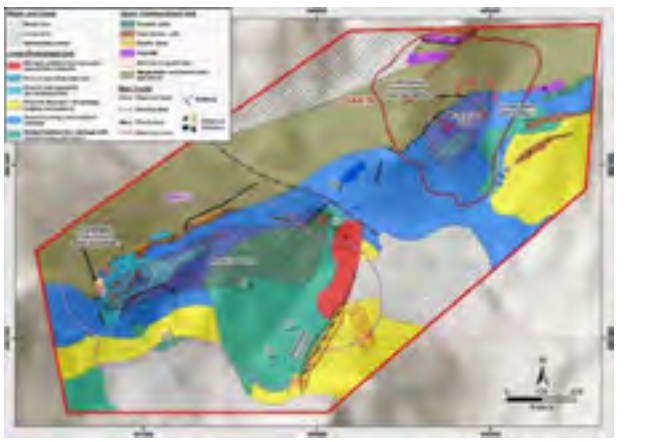


Figure 2. The geological map of Sakdrisi 4 and 5 deposit.

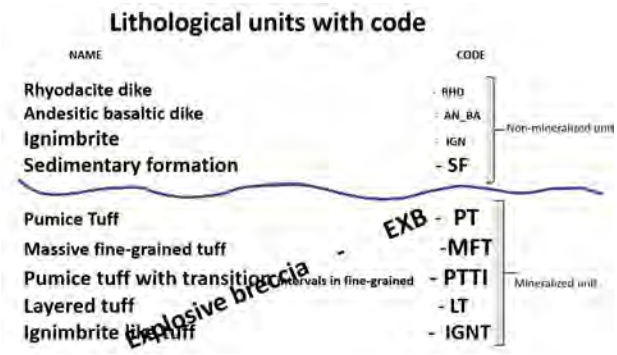


Figure 3. The lithological units with codes from Sakdrisi deposit

The lower complex is represented mostly by the volcaniclastic rocks: pumice tuff (PT) (part strongly oxidized and contains the gold monetarization), pumice tuff with transition intervals to fine-grained (PTTI), ignimbrite-like tuffs (IGNT) also the massive fine tuff (MFT) and layered tuff (LT) with gypsum veins. The lower complex is mineralized and cross-cutting by the explosive breccia pipes (EXB), which are also mineralized (Fig. 4).

4 3D Geological model of Sakdrisi deposit

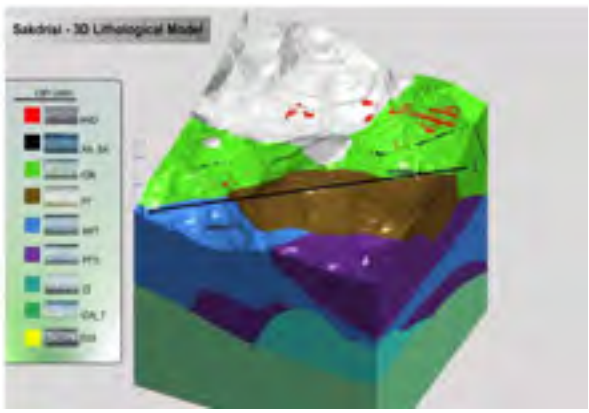


Figure 4. 3D Lithological-structural model of Sakdrisi 4 deposit.

Methodology: The geologic model of the Sakdrisi deposit was done using the Leapfrog Geo 2023 2.3 software package. The data set used for modeling includes surface topography, geologic map, drill core logs (about 350 new and historical drill core data was interpreted), and outcrop detailed mapping including the structural measurements. In the first stage, lithological units were separated and a stratigraphic scheme was developed for the host rocks of the Sakdrisi deposit. In the outcrops of the Sakdrisi deposit, where the mining is active, the contacts between units are not always obvious. Lithological codes from logging were grouped into the ten main units. The stratigraphic units identified during outcrop mapping and accordingly given lithological codes align effectively with the logged lithological codes, using the genetic names of rocks (Mc Phie et al. 1993). Figure 4 illustrates the 3D geological model of the Sakdrisi 4 deposit including all lithological units. Figure 5 represents the cross-section along the Sakdrisi 4 and partly the Sakdrisi 5 deposit with the distribution of ore bodies within the lithological units from the lower LVSC.

5 Ore bodies: distribution and types

The mineralization on Sak4 mostly is constrained by a stockwork, composed of polyphase and multi stage veins. The veins record multiple cycle fluid pulses connecting with different events: tectonic fracturing, hydraulic and hydrothermal filling (Golay et al. 2019). Vein size ranges from mm to tens of cm-s. The gangue minerals include mostly quartz, barite and less carbonates quartz-sulfide veins and stockworks (Popkhadze et al. 2022, Popkhadze et al. 2023). Disseminated ore connects mostly with explosive breccias (Fig 5) and the perrmable pyroclastic pumiceous rocks (pumice tuff PT). In some places the mineralized explosive breccia pipes are cross cut by the Q/Q-sulfide veins, which creates the high-grade zones inside the LVSC. The upper part of LVSC (pumice tuff PT) is affected by surface weathering and supergene overprinting in upper levels (consists primarily of gold) (Pic 5) on the cross-sections (Fig.6) The cross-section (Fig.6) clearly shows the distribution of the gold content in each lithological unit from LVSC.

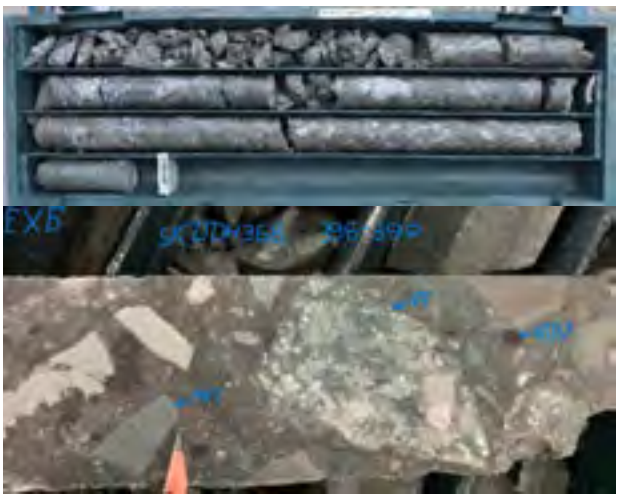


Figure 5. Explosive breccia with massive fine tuff, pumice tuff and breccia clasts.

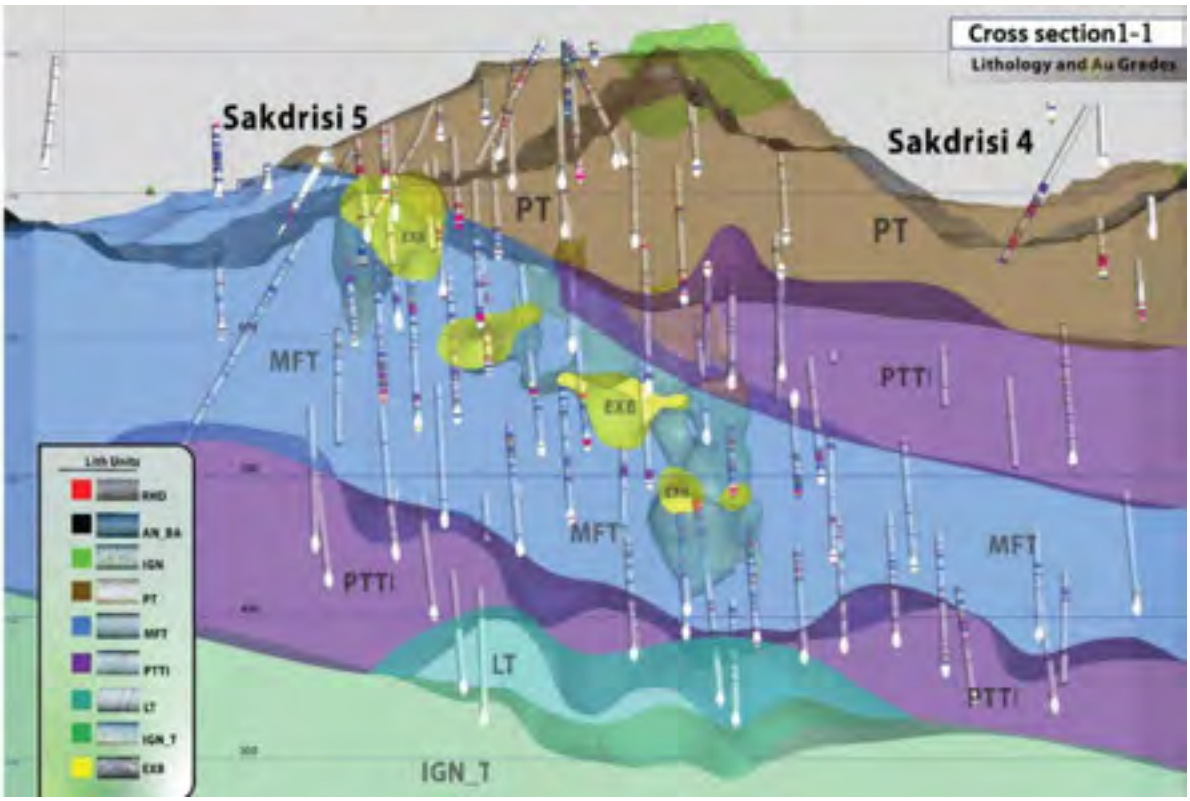


Figure 6. Cross section 1-1: ore bodies distribution by lithology on the Sakdrisi deposit.

Conclusions and recommendations

Our new approach for 3D geologic modeling based on genetic names and consequently the codes of lithological units was developed for the first time at the Sakdrisi deposit. The main ore-bearing lithological unit at the Sakdrisi deposit is massive tuffs (MFT). These are silicified and brittle and therefore they are easily fractured and associated with faults or energy release, such as the intrusion of explosive breccias. Explosive breccias (EXB) are also ore-bearing lithological units, but their areal distribution is less than that of massive tuffs. However, zones of high-grade mineralization are associated with explosive breccias. Other host rocks include pumice tuffs (PT), part of which have been eroded from the deposit and part have already been extracted, although it should be noted that the main gold content is related to the pumice tuffs (PT). Other lithological units from LVSC can be considered as relatively less mineralized, namely PTTI and LT, and finally IGNT. In conclusion, the MFT and EXB are good criteria for the discovery of new ore zones in this area and also for planning new drilling programs. The development of a new drilling program, which involved planning wells in the deeper part (approximately 800-900 m from the surface), led to the discovery of new high-grade ore zones. An underground project was subsequently planned and is currently being actively developed in the vicinity of Sakdriisi 4. Another discovery is the continuation of the high-grade zones in the north-west direction of Sakdriisi4, this project is successfully underway today.

The thrust fault is interpreted as a central fault on the Sakdrisi deposit, which separates the upper (UVSC) barren ignimbrites from the lower mineralized complex. The northwest-oriented transverse fault is identified between the Sakdrisi 5 and Sakdrisi 4 ore bodies, also Sakdrisi 4 and Sakdrisi 3 and Sakdrisi 3 and Sakdrisi 5 (Migineishvili et al 2009).

Two major trends of faults are recognized at the Sakdrisi deposit: NE and NW directions and dikes also are oriented mostly to the NE direction.

In Conclusion, the structural/lithological control is very obvious at the Sakdrisi deposit.

Acknowledgments

The authors would like to thank the RMG Rich Metal Group and CMG Caucasus Mining Group for access to open pits and prospects, and logistical support. The research would not have been possible without constant support provided by SGA, SEG and IAVCEI organizations for attending many international conferences, where the works from Bolnisi district was presented.

References

Golay T, Moritz R, Popkhadze N, Natsvlishvili M (2018) The Sakdrisi Au-Cu deposit, Bolnisi mining district, Georgia: providing a genetic model based on petrographic, geochemical, structural, and alteration studies. The 16th Swiss Geoscience Meeting, Bern, Switzerland, 30 November-1st December, pp. 104-105.

Gugushvili v, Bukia A, Goderdzishvili N, Javakhidze D, Zakaraia D, Muladze I, Shavishvili I, Shubitidze J, Tchokhonelidze M (2014) Bolnisi ore district: geological development and structure, genesis of mineralization, economic potential and perspectives. Caucasus Mining Group, Tbilisi. Ed. Natsvlishvili MP 55 p (in Russian)

Jelev V, Bitsadze N, Ananiashvili G, Aslanishvili G, Shavishvili I, Natsvlishvili M (2021) Litho-structural geological mapping of Sakdrisi and Madneuli deposits. Unpublished report for RMG. Tbilisi, Georgia. pp 0-31

Mc Phie J, Doyle M, Allen R (1993) Volcanic textures. A guide to the interpretation of textures in volcanic rocks. University of Tasmania. Book:1-178

Migineishvili R., Gaxaria D., Natsvlishvili M (2009) Geological map of Sakdrisi deposit. Unpublished enclosure report for RMG (In English)

Moritz R, Melkonyan R, Selby D, Popkhadze N, Gugushvili V, Tayan R, Ramazanov V (2016) Metallogeny of the Lesser Caucasus: From Arc Construction to Postcollision Evolution. Soc Econ Geol Special Pub 19:pp.157-192

Popkhadze n, Gogia B, Tagviashvili Sh, Ugrekhelidze G, Natsvlishvili M, Shubitidze J, Moritz R (2023) 3D lithological and structural model and prospectivity of the Late Cretaceous Sakdrisi Gold Copper Epithermal deposit, Bolnisi district, Lesser Caucasus, Georgia. 17th Biennial SGA Meeting ETH Zurich, Switzerland, August28-Sep1, v1:184-188

Popkhadze N, Moritz R, Gugushvili V (2014) Architecture of Upper Cretaceous rhyodacitic hyaloclastite at the polymetallic Madneuli deposit, Lesser Caucasus, Georgia. Cent. Eur. J. Geosci 6(3):308-329

Popkhadze N, Moritz R, Natsvlishvili M, Bitsadze N (2017) First evidence of phreatomagmatic breccia at the Madneuli Polymetallic Deposit, Bolnisi district, Lesser Caucasus, Georgia. In: proceedings of the 14th SGA biennial meeting: Mineral resources to discovery, 20-23 August, Quebec City, Canada; 1:323-326

Popkhadze N, Sonmez S, Moritz R, Natsvlishvili M, Bluashvili V, Gagnidze N (2022) The Late Cretaceous Sakdrisi epithermal deposit, Bolnisi district (Lesser Caucasus, Georgia): Geology and ore deposit setting. XXII International congress of the Carpathian-Balkan geological association (CBGA), 7-11 September,Plovdiv, Bulgaria, 2022, p.p. 362

Sosson M, Rolland Y, Muller C, Danelian T, Melkoyan R, Kekelia S, Adamia Sh, Babazadeh V, Kangarli T, Avagyan A, Galoyan G, Mosar (2010) Subductions, obduction and collision in the Lesser Caucasus (Armenia, Azerbaijan, Georgia) new insights. Geological Society, London, Special Publications, 329-352

Yilmaz A, Adamia Sh, Chabukiani A, Chkhotua T, Erdogan K, Tuzcu S, Karabiyikoglu M (2000) Structural correlation of the southern Transcaucasus (Georgia) – eastern Pontides (Turkey). Geol Soc London Special Pub173:171-182

Camp Creek Copper-Molybdenum-(Gold) Porphyry Alteration-Mineralogy and Intrusive Classification: Exploring for Blind Copper Mineralization in Northern British Columbia, Canada

Maxwell L. Porter[1], Shaun L. Barker[1], Farhad Bouzari[1], Maria A. Rodriguez-Mustafa[1], Robert G. Lee[2], K B. Riedell[3]
[1]Mineral Deposit Research Unit, The University of British Columbia, Vancouver, British Columbia, Canada
[2]BHP, Arizona, United States
[3]Riedell Exploration Ltd., Vancouver, British Columbia, Canada

Abstract. Camp Creek is a Late Cretaceous calc-alkalic Cu-Mo-(Au) porphyry prospect, located within the Stikine terrane in northern British Columbia, Canada. Multiple porphyry units have been previously classified and termed Porphyry X, Y, Z, and V. These units can be distinguished using 4-acid lithogeochemical data as they have different ratios of Zr, Ti, and Sc. However, these units are texturally and mineralogically challenging to differentiate in drillcore. This project characterizes lithology, alteration, mineralization, and timescales of magmatism at Camp Creek. Fifteen drillholes were studied along two cross-sections to capture information on mineralogy, alteration, veining and cross-cutting relationships. Disseminated and vein-hosted chalcopyrite mineralization is typically hosted within Porphyry X, a hornblende-quartz-biotite-plagioclase porphyry, cut by A-type quartz-vein stockwork, occurring together with K-feldspar and biotite alteration. Porphyry Z is a shallow, relatively unmineralized porphyry phase that transitions to Porphyry Y with increasing depth, correlating with increased grade and quartz vein density. Shortwave Infrared (SWIR) data shows multiple alteration zones, with mineralogy dominated by pyrophyllite at shallow levels, which transitions to illite and then muscovite with greater depths, and eventually K-feldspar in Porphyry X. Results of this study will identify key vectors to locate buried mineralization in porphyry copper deposits, enhancing regional exploration approaches.

1 Introduction

Porphyry Cu-Mo-(Au) deposits are a significant source of critical metals for technologies required to facilitate a transition toward electricity-based energy systems. Porphyry Cu deposits are the primary source of Cu globally, but the world-class discoveries needed to meet increasing demand are not being made. As most near-surface porphyries have likely been discovered, developing tools for exploring 'blind' subsurface porphyry deposits is vital to meet increasing global resource demand (Sillitoe 2010).

The Camp Creek prospect is a calc-alkalic porphyry Cu-Mo prospect located in the northwestern portion of the Canadian Cordillera of British Columbia (BC; Fig. 1) with other intermontane island-arc porphyry Cu deposits, including the Highland Valley Copper Mine, the Gibraltar Mine, and Schaft Creek (Mihalasky et al. 2010). In 2019, significant zones of porphyry-style veins with Cu and Mo mineralization were intersected at Camp Creek at depths of more than 300 m, with further drilling programs in 2021–2024 focused on discovering extensions of porphyry-style mineralization (Lemiski et al., 2023).

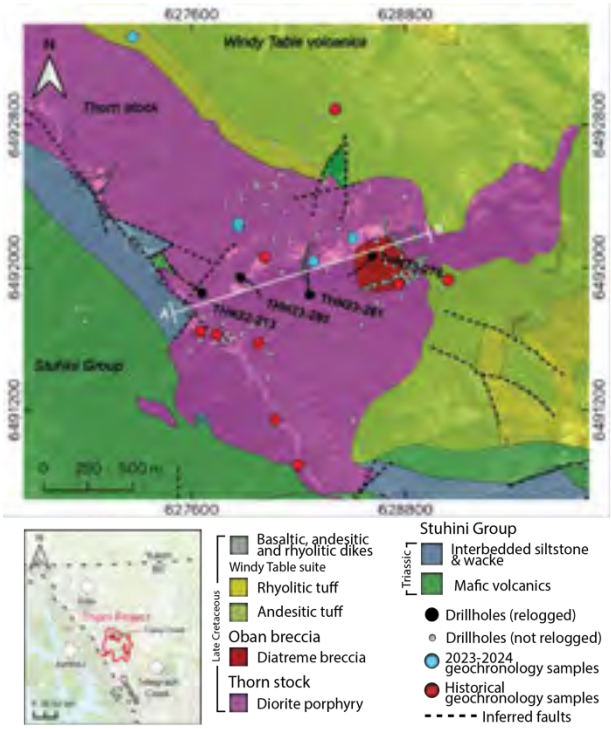


Figure 1. Simplified geology of the Camp Creek porphyry, part of the Thorn property in northwestern British Columbia. The location of the Thorn property is shown on the inset map, outlined in red. All coordinates are in UTM Zone 8N (NAD83).

This work is the first major geological review of the Late Cretaceous calc-alkalic Cu-Mo-(Au) Camp Creek porphyry prospect. It focuses on characterizing the alteration, mineralization, and timescales of magmatism. Ongoing research integrates petrography, micro X-Ray Fluorescence (microXRF) element mapping, Shortwave Infrared (SWIR), whole-rock geochemistry, and U-Pb geochronology. It will contribute insights into potential geochemical vectors for discovering blind porphyry Cu-Au-(Mo) mineralization.

2 Sampling and Analytical Work

Samples were selected and described over two summer field seasons in 2023 and 2024. Four drill holes were relogged to capture additional information on mineralogy, alteration, veins, and

crosscutting relationships. Detailed observations in drillcore have been recorded following logging advice from Williams (2022). As of February 2025, 40 samples have undergone whole-rock geochemical analysis. From this sample set, 20 were selected for petrographic analysis. MicroXRF analysis was completed on 14 samples to assess zircon content prior to U-Pb geochronology. SWIR data has been gathered every 25 m for 14 prioritized drillholes at Camp Creek, and further work will aim to constrain previously identified zones of alteration. MicroXRF is an effective tool to gauge modal abundances and review mineralogy by element mapping, mainly when phases are difficult to distinguish by eye.

3 Geology of the Camp Creek Property

Initial whole-rock geochemical analysis of core samples from Camp Creek by Bouzari and Barker (2021) revealed the occurrence of at least five porphyry units. These units are geochemically distinct from the Stuhini volcanosedimentary hostrocks, which are characterized by high Sc (>10 ppm). These porphyry units have been termed X, Y, Z, W and V, and are distinguished by low to high concentrations of several trace elements, including Zr, Ti and Sc (Fig. 2). Petrography by Bouzari and Barker (2021) provided an initial correlation between mineralogy and geochemistry, providing preliminary criteria for characterizing and distinguishing each porphyry unit. Examples are shown in Fig. 3, and field observations are summarized in the following section. The effective subdivision of the porphyry stocks is critical to refining Camp Creek's geological model.

3.1 Porphyry Characteristics

The dominant intersected lithologies at Camp Creek are porphyries Z, Y, and X, and characteristics of each phase have been summarised in Table 1. Porphyry Z typically occurs as the shallowest porphyry phase from the surface to 300-400 m depth, Porphyry Y from 400 to 600-800 m depth, and Porphyry X is typically found deeper from 800 to 1600m depth, commonly cross-cutting Stuhini volcano-sedimentary hostrocks. Porphyry V normally occurs as smaller dikes that crosscut porphyries Z, Y and X. A series of felsic, intermediate and mafic post-mineral dykes cross-cut all other observed porphyry phases. No clear crosscutting relationships were observed between porphyries Z, Y, and X.

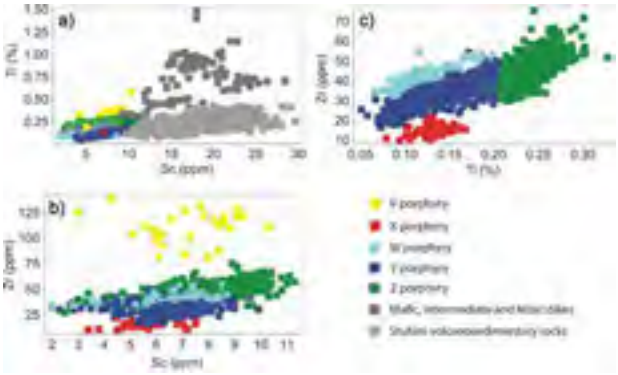


Figure 2. Classification of hostrocks at Camp Creek based on Zr, Ti, and Sc trace-element data from whole-rock geochemical analysis. Since 2023, Porphyry W has been grouped with porphyry Z due to near-identical mineralogy. **a)** Sc versus Ti; **(b)** Sc versus Zr; **(c)** Ti versus Zr (Bouzari and Barker, 2021; reproduced with permission).

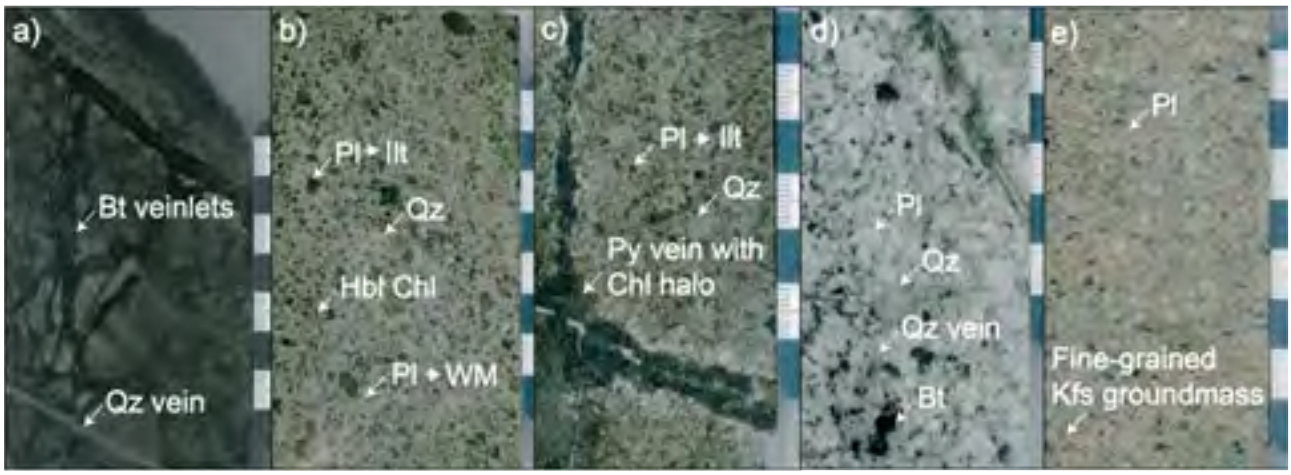


Figure 3. Examples of hostrocks observed at Camp Creek, with corresponding scale card shown to the right of each sample: **a)** siltstone with pervasive and veinlet-controlled biotite alteration overprinted by chlorite and white mica, THN23-261 841.20 m; **b)** quartz-biotite-hornblende-plagioclase porphyry (porphyry Z) with pervasive and phenocryst-replacement white mica alteration, THN23-277 348.60 m; **c)** hornblende-quartz-biotite-plagioclase porphyry (porphyry Y) with pervasive and phenocryst-replacement white mica alteration, overprinted by chlorite, THN23-276 875.25 m; **d)** hornblende-quartz-biotite-plagioclase-porphyry (porphyry X) with pervasive K-feldspar alteration and quartz-vein stockwork, THN23-276 1235.80 m; **e)** biotite-hornblende-plagioclase porphyry (porphyry V), THN22-201 845.97 m. Modified from Porter et al. (2024). Mineral abbreviations: Bt, biotite; Pl, plagioclase; Hbl, hornblende; Chl, chlorite; WM, white mica; Qz, quartz; Py, pyrite; Ilt, illite.

Porphyry Characteristics	Porphyry Z	Porphyry Y	Porphyry X	Porphyry V
Total Phenocrysts	35-45%	30-40%	45-50%	35-45%
Texture	Coarse	Fine	Coarse	Coarse
Groundmass	Aphanitic	Aphanitic	Apilitic	Aphanitic
Plagioclase	30-35%, 2-5mm	25-30%, 1-5mm	45-50%, 2-5mm	35-40%, 1-3mm
Quartz	2-5%. 1-5 mm	2-5%. 1-5 mm	2-5%, 3-5mm	<1%, <1 mm
Biotite	3-5%, 1-5 mm	2-3%, 1-3mm	3-5%, 1-5mm	1-2%, 1-3mm
Hornblende	5-8%, 1-2 mm	1-2%, 1-2mm	1-2%, 1-2 mm	3-5 %, 1-2 mm
Dominant Alteration	White mica, Pyrophyllite	White mica, Chlorite	K-feldspar	None
Quartz Vein Abundance	None	1-5%	5-10%	None
Sulphide Mineralization	1-10% py, trace cp	5-10% py, <0.1% cp	2-5% py, 0.1-1% cp	<1% py
Accessory Minerals	Rutile, Titanite, Apatite, Zircon			+ Magnetite

Table 1: Summary of Porphyry Z, Y, X, and V Characteristics.

Porphyry Z (dated at 85.46 ± 0.59 Ma) is the least altered and mineralized of the porphyry phases, dominantly pyrite (1–5%) with trace chalcopyrite (<0.1%). Porphyry Y (dated at 86.57 ± 0.54Ma) typically has stronger alteration and contains higher amounts of sulfide (5–10%) and Cu grades (>0.1%) when compared to porphyry Z. Diagnostic features of porphyry X (dated at 85.37 ± 0.45 Ma) include coarse biotite books, quartz-rich groundmass and intense K-feldspar alteration, dominantly within the groundmass. It is cut by a stockwork of A-type granular quartz veins and has the highest concentration of Cu mineralization among intrusive units (>0.2%). Porphyry V is weakly altered and contains trace pyrite but no Cu-bearing mineralization.

4 Alteration

Observations from drilling in the Camp Creek porphyry indicate multiple distinct types of alteration, which are evident in the classic porphyry-alteration model of Sillitoe (2010). The shallow-level alteration is characterized by abundant pyrophyllite with white mica, local diaspore, and rare high-sulfidation veins (Simmons 2005), suggesting a transition zone from Advanced Argillic to white mica above a porphyry system. A challenge to establishing alteration zoning is the subtle mineralogical changes across porphyritic units. Still, Shortwave infrared (SWIR) data has provided insight into various cryptic downhole alteration trends (Bouzari et al. 2022).

White mica alteration increases in intensity with depth, being weaker in porphyry Z and typically increasing in porphyry Y before transitioning to a dominantly K-silicate alteration in porphyry X (Fig. 4c and 5). White mica assemblages are usually classified by a quartz-white mica-pyrite assemblage, which transitions into zones of intense chlorite replacement of biotite and hornblende with depth. K-silicate alteration is classified by pervasive fine-grained K-feldspar alteration, common 1–3 mm K-feldspar haloes, and occasional biotite alteration. Propylitic alteration is characterized by abundant epidote and chlorite occurring distally to Camp Creek.

Regarding overprinting relationships, pyrophyllite appears to overprint zones of white mica alteration. A-type granular quartz veins are observed at a lower density in PY, occurring with strong white mica alteration, than the higher density quartz vein stockwork occurring with strong potassic alteration in PX, potentially indicating a significant degree of white mica alteration overprinting potassic alteration. Thin section petrography shows the increase in alteration intensity from PZ with partial replacement of plagioclase by white mica to near total replacement of plagioclase by white mica in PY (Fig. 4a and 4b).

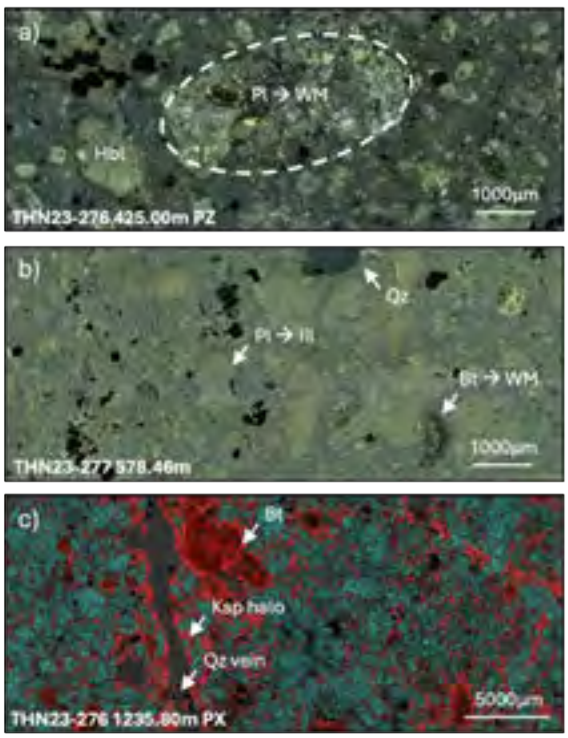


Figure 4. Thin-sections and microXRF element maps of hostrocks: a) Porphyry Z with moderate white mica alteration; b) Porphyry Y with strong white mica alteration; c) microXRF element map of potassic-altered porphyry X; Colours: Red, K; Green, Na.

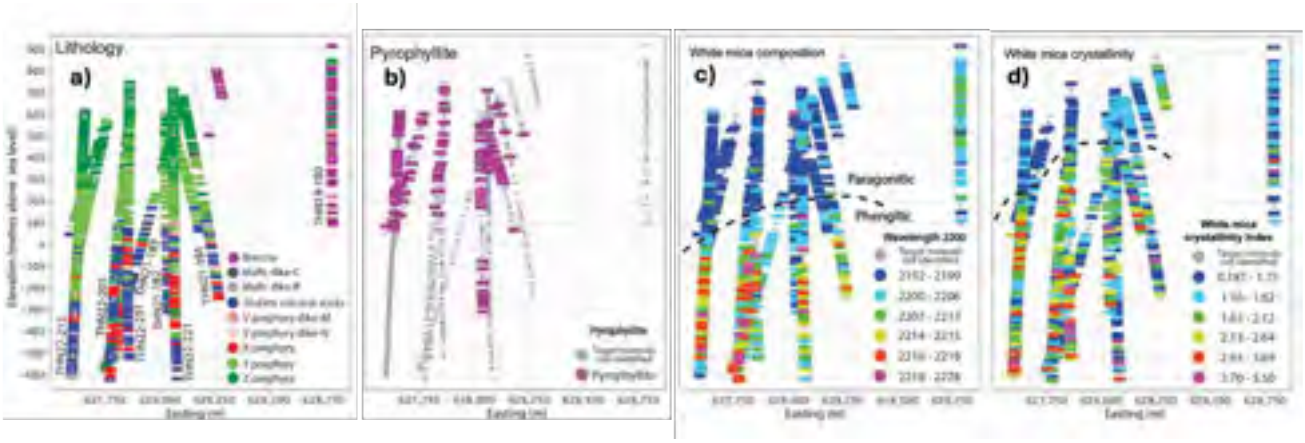


Figure 5. Downhole shortwave infrared data on drillcore samples collected in 2019–2022, plotted along northward-facing drillcore cross-sections (also shown is the corresponding location of the cross-section shown in Fig. 1 [modified from Bouzari et al., 2023]): **a)** lithology; **b)** pyrophyllite occurring at shallow levels with rare diaspore; **c)** white mica composition, dominated by paragonite illite near surface and transitioning to illite and then phengitic illite with depth; **d)** white mica crystallinity increasing with depth toward zones of K-silicate alteration.

5 Future Work

Additional samples have been selected for whole-rock geochemistry, and a complete geochemical analysis will be performed on the collected data. Further SWIR data will be processed to build an understanding of the alteration model. More microXRF scans will be collected from existing samples to gain insight into the modal abundance of mineralogy and textural relationships. Further U-Pb dating will be completed for intrusive phases to better constrain the timing and formation of the porphyry stocks at Camp Creek. Research outputs will focus on establishing the evolutionary model of the system, as well as developing an alteration model of the different porphyry phases.

6 Conclusions

Initial thin-section petrography and SWIR at Camp Creek have highlighted multiple alteration trends. Porphyry Z has weaker white mica alteration than Porphyry Y, but stronger pyrophyllite alteration that transitions to more intense white mica alteration and overprinting chlorite alteration near the porphyry X contact. These porphyry units overlap in time, based on U-Pb dating, and further analytical work will be needed to resolve uncertainties on timing. Additionally, crosscutting relationships do not provide information on the relative ages of porphyries Z, Y, and X through evidence gathered to date. Porphyry V postdates porphyries Z, Y, and X, with observed post-mineral dikes postdating all other intrusive phases. SWIR data show multiple alteration zones, with mineralogy dominated by pyrophyllite at shallow levels, transitioning to illite and then muscovite at greater depths, and eventually to K-feldspar in porphyry X. Future characterization work will aim to constrain field observations by detailed petrography, additional SWIR analysis, and geochemical analysis.

Acknowledgements

This study is being undertaken in collaboration with Brixton Metals and supported by the MDRU BC Porphyry Project sponsors. Thank you to Geoscience BC, the Society of Economic Geologists, and the International Association on the Genesis of Ore Deposits for providing financial support for M.P. M.P. thanks the team at Brixton Metals for supporting summer fieldwork, particularly D. Guestrin, C. James, and C. Anstey. M.P. thanks M. Manor and N. Moerhuis for providing continuous guidance in the field and lab.

References

Bouzari F, Lee RG, Hart CJR, van Straaten BI (2022) Porphyry Vectoring Techniques in Advanced Argillic Altered Rocks of British Columbia. Geoscience BC Report 2022-03, MDRU Publication 456.

Lemiski B, Stewart N, James C (2023) 2022 Geological, Geochemical, Geophysical and Diamond Drilling Report on the Thorn Property. Prepared for Brixton Metals Corporation

Mihalasky MJ, Bookstrom AA, Frost TP (2010) Porphyry Copper Assessment of British Columbia and Yukon Territory, Canada. US Geological Survey Scientific Investigations Report 2010-5090-C 1.1:128

Porter ML, Barker SLL, Bouzari F (2024) Camp Creek Copper-Molybdenum-(Gold) Porphyry-Alteration Mineralogy and Geochemistry: Exploring for Blind Copper Mineralization in Northern British Columbia (NTS 104K/10W). Geoscience BC Summary of Activities 2024, Report 2025-01, p 7-14.

Sillitoe RH (2010) Porphyry Copper Systems. Economic Geology 105:3–41. https://doi.org/10.2113/gsecongeo.105.1.3

Simmons AT (2005) Geological & Geochronological Framework and Mineralization Characterization of the Thorn Property, and Associated Volcanoplutonic Complexes of Northwestern British Columbia, Canada. Dissertation, University of British Columbia

Williams DK (2022) Capture Codes for Better Geology. SEG Discovery 15–23. https://doi.org/10.5382/SEGnews.2022-128.fea-01

Magmatic fluids in the Chuquicamata porphyry copper deposit, revealed by fluid inclusions analyses

Isaac Rodríguez[1], Ivan Farías[2], Kalin Kouzmanov[3], Alexandra Tsay[3], Zoltan Zajacz[3] and Eduardo Campos[2].
[1]Doctorado en Ciencias mención Geología, Universidad Católica del Norte, Antofagasta, Chile
[2]Departamento de Ciencias Geológicas, Universidad Católica del Norte, Antofagasta, Chile
[3]Department of Earth Sciences, University of Geneva, Switzerland

Abstract
Despite the numerous published studies on different aspects related to the genesis of the giant Chuquicamata porphyry copper deposit in Chile, no fluid inclusion data have yet been reported in the literature. In fact, the only information available on fluid inclusions for Chuquicamata is from an internal report to Codelco in 1987 and a BSc thesis in 1989. Both studies focused on the characterization of fluid inclusions hosted in quartz from stockwork veins. The reported data indicate trapped fluids of moderate to low temperature (< 400° C) and variable salinity (from 5 to ~40 wt. % NaCl equiv.)

We concentrate our efforts on the study of fluid inclusions mainly hosted in quartz phenocrysts and interstitial quartz from the Este porphyry at Chuquicamata. Our results demonstrate for the first time the presence of high-temperature fluid inclusions (homogenization temperatures of >500° C) with intermediate salinities (~ 10 wt. % NaCl equiv.), sharing characteristics with intermediate density fluid inclusions typical for many other porphyry copper systems. These fluids are considered as an analogue of pristine magmatic fluids and have not been previously reported for the Chuquicamata deposit.

1 Introduction

Porphyry copper deposits (PCDs) constitute the major source of copper in the world. In these magmatic-hydrothermal systems the parental magma constitutes the major source of the fluids, metals and other components that eventually will form a deposit (e.g. Hedenquist and Lowenstern 1994; Audétat and Simon 2012; Park et al. 2021; Heinrich 2024). Although the chemical and physical parameters of the magmatic fluids are variable and largely depend on the deposit that is being studied (e.g. Redmond et al. 2004; Campos et al. 2006; William-Jones and Heinrich 2005; Kouzmanov and Pokrovski 2012), in general mineralizing fluids are mainly composed of water, dissolved chlorides, metals, major and trace elements, and volatiles, such as CO_2, SO_2, and H_2S (e.g. Burnham 1979; Park et al. 2021; Bain et al. 2022).

Although Chuquicamata is one of the most studied porphyry copper deposits worldwide and represents a reference for the definition of porphyry copper systems, in the published literature there is no information regarding the characteristics of the hydrothermal fluids that were responsible for the mineralization and related hydrothermal alteration. In fact, the only information available on fluid inclusions has been reported in an internal report to Codelco in 1987 and the BSc thesis of Vega (1989). Considering that the information gathered from fluid inclusions can contribute significantly to improve our understanding on the evolution of mineralizing fluids in PCDs, we provide a new dataset helping to constrain the hydrothermal fluids evolution during the formation of the giant Chuquicamata porphyry copper system in northern Chile.

2 The Chuquicamata porphyry copper deposit

Chuquicamata, one of the largest porphyry copper deposits worldwide, is located in the Antofagasta Region of northern Chile, approximately 15 km north of Calama at an altitude of 2,800 m above sea level. The mine, operated since 1971 by the Corporación Nacional del Cobre de Chile, CODELCO, has been in production for more than 100 years. The open pit mining began in 1915, whereas on 2019 marks the start of underground mining by block caving. The deposit has estimated resources of 2,795 million metric tons (Mmt) with an average copper grade of 0.63 % and reserves of 1,152 Mmt with a Cu grade of 0.64 % (CODELCO 2023).

The Chuquicamata deposit is part of the Late Eocene-Early Oligocene porphyry copper belt that extends for about 1,400 km, from 18° to 31°S (Sillitoe and Perelló 2005). The belt is controlled by the Domeyko Fault System (DFS), a tectonic feature that has been described as a first order control on the emplacement of world class porphyry copper deposits in northern Chile such as Chuquicamata and Escondida (Mpodozis and Cornejo 2012).

The West Fault, related to the DFS, is the main structural feature observed along the belt and north of Calama it separates the Fortuna Granodiorite Complex to the west from the Chuquicamata Intrusive Complex (CIC; Tomlinson et al. 2018) to the east. The Fortuna Granodiorite Complex is a composite stock of hornblende-biotite granodiorite with phaneritic texture with reported zircon U-Pb ages of 39.1 ± 0.4 and 38.5 ± 0.4 Ma (Ballard et al. 2001). On the other hand, the CIC comprises the Este, Oeste and Banco porphyries whose composition varies between granodiorite and monzodiorite (Ossandón et al. 2001). According to Virmond et al. (2024), the ages obtained for the porphyries range between 34.402 ± 0.034 and 35.451 ± 0.096 Ma, for the Este porphyry; between 33.624 ± 0.070 and 33.860 ± 0.047 Ma, for the Oeste porphyry; and between 33.249 ± 0.050 and 34.133 ± 0.034 Ma, for the Banco porphyry. The

Triassic Elena Granodiorite (ca 233 Ma, Rivera et al. 2012) crops out along the southern margin of the deposit. The hydrothermal alteration and the Cu–Mo mineralization in the Chuquicamata deposit are mainly associated with the CIC.

3 Sampling and analytical methods

Samples were collected from drill cores from the potassic alteration zone in the Este, Oeste and Banco porphyries. Sampling was focused on quartz phenocrysts and interstitial quartz. Care was taken in collecting samples with no signs of deformation and with translucent quartz crystals. Double-polished thick sections of ~200 µm were prepared following the methodology proposed by Goldstein (2003). To determine the presence and types of fluid inclusions, petrography of the thick sections was carried out using an Olympus BX60 microscope, at ambient conditions. Under the microscope, some quartz crystals showed very large populations of fluid inclusions, making it difficult to differentiate potential primary from secondary fluid inclusions, or even to identify fluid inclusion assemblages (FIA). Where this problem occurred, special care was taken to determine if a FIA could be selected for later analyses. Microthermometry experiments were carried out using a Linkam THSM 600 freezing / heating stage. Parameters obtained were homogenization temperature and final ice/halite melting temperature. Calibration of the Linkam stage was done using freezing point of pure water, homogenization temperature of CO_2, and melting point of $NaNO_3$. Finally, LA-ICP-MS analyses of individual ID-type fluid inclusions were conducted to determine the composition of the fluid, considering the following elements: Li, B, Na, Al, Si, S, Cl, K, Ca, Ti, Mn, Fe, Cu, Zn, As, Br, Rb, Sr, Mo, Ag, Cd, Sb, Cs, Ba, Ay and Pb. The analyses were performed using an ESL 193 HE laser ablation system coupled with an Agilent 8900 Triple Quad ICP-MS at the University of Geneva. Data reduction was carried out using the SILLS software (Guillong et al. 2008), where the glass reference material NIST610 was used as an external standard, and the Na concentration determined by microthermometry experiment was used as an internal standard for data quantification.

4 Results and discussion

Petrography of the quartz phenocrysts revealed a great abundance of fluid inclusions in the samples. Five types of quartz-hosted fluid inclusions (FIs) were identified (Fig. 1A-E): 1) Intermediate density (ID-type) inclusions, characterized by vapor/liquid volume ratios between 0.5 and 0.7; 2) ID-opaque-type inclusions with an opaque daughter mineral; 3) Hypersaline liquid or “brine” (B-type) inclusions, characterized by the presence of vapor, liquid and halite as the main daughter mineral, occasionally accompanied by opaque minerals; 4) Aqueous liquid-vapor (LV-type) inclusions, characterized by the presence of a vapor bubble and a liquid, with bubble/liquid volume ratios below 0.4; and the less common 5) LV-Hm-type inclusions, characterized by the presence of vapor, liquid and a hematite crystal as a daughter mineral, with similar bubble/liquid volume ratio to LV-type inclusions. ID-, B- and LV-Hm-type inclusions are commonly found in groups and trails, while LV-type inclusions are found exclusively as secondary trails.

After optical petrography, SEM-CL was carried out on quartz phenocrysts. Most of the studied phenocrysts were homogeneous on the CL images, only in some from the Oeste porphyry a weak zonation was present.

After SEM-CL, fluid inclusion microthermometry was carried out. Homogenization temperatures ranged between 376° and >500°C, 332 – 423°C, 226 – 402°C, 328 – 388°C, and 185 – 381°C, for ID, ID-opaque, B, LV-Hm, and LV-type inclusions, respectively. Salinity was calculated based on ice melting temperature in ID and LV-type inclusions, and based on halite melting temperature in B-type inclusions, ranging between 0 and 19.29 wt% NaCl equiv. for ID-type inclusions, 8.35 – 21.73 wt% NaCl equiv. for ID-opaque-type inclusions, 31.93 – 38.76 wt% NaCl equiv. for B-type inclusions, 17.18 – 22 wt% NaCl equiv. for LV-Hm-type inclusions, and 5.91 – 13.06 wt% NaCl equiv. for LV-type inclusions. As shown in Figure 1F, the homogenization temperatures obtained from ID-type fluid inclusions hosted in quartz phenocrysts are consistently higher than those reported by Vega (1989). Together with these, the values obtained are consistent with other porphyry copper deposits (Redmon et al. 2004; Rusk et al. 2004; Klemm et al. 2007; Bodnar et al. 2014). LA-ICP-MS analyses on individual ID-type fluid inclusions were carried out to determine their composition (Fig. 2). Iron content varies from 372 to 5443 ppm, while Cu varies from 121 ppm to 913 ppm, Zn shows a broader range of concentrations, between 12 ppm and 561 ppm. Sulfur is mostly below the limits of detection, except for a few inclusions, some of them with opaque daughter minerals. Arsenic concentration ranges between 17 and 166 ppm, while Ag and Au are mostly below detection limits. Copper-Zn-Pb composition of ID-type fluid inclusions is similar to those reported in other porphyry copper deposits (Ulrich et al. 2001; Rusk et al. 2004; Kouzmanov and Pokrovski 2012).

5 Conclusions

Homogenization temperatures measured in early fluid inclusions hosted in quartz phenocryst and/or interstitial quartz from the Este porphyry from the Chuquicamata porphyry copper deposit vary between 376 and >500 °C, while the salinity is within the range of 0 – 19.29 wt% $NaCl_{equiv}$.

Elevated concentrations of Cu (121 – 913 ppm), Fe (372 – 5443 ppm), As (17 – 166 ppm) and Zn (12 – 561 ppm) were detected in the studied FIA. Sulfur is systematically below the detection limits, with a few exceptions. No CO_2 was detected in the studied

fluid inclusions. The fluid inclusions analyzed in this study are significantly different from those reported by Vega (1989) from hydrothermal quartz veins. While the former records early-stage of magmatic fluid exsolution, the latter are related to the main and late hydrothermal stages. Further studies will better constrain the fluid evolution during the formation of the Chuquicamata porphyry copper deposit.

Acknowledgements

Founding for this study was provided by the ANID (Chilean National Research of Development Agency) by means of the FONDECYT Regular project NO. 1230686. IRC was supported by ANID doctoral scholarship and, for this conference, by FCAC 2025-UCN. IFL was supported by FONDECYT project 1230686. We are grateful to the geologists of the Chuquicamata mine, especially Elizabeth Demane, Sergio Ahumada and Giorgio Realini for providing valuable insights into the geology of the deposit, and for providing access to the drill core samples.

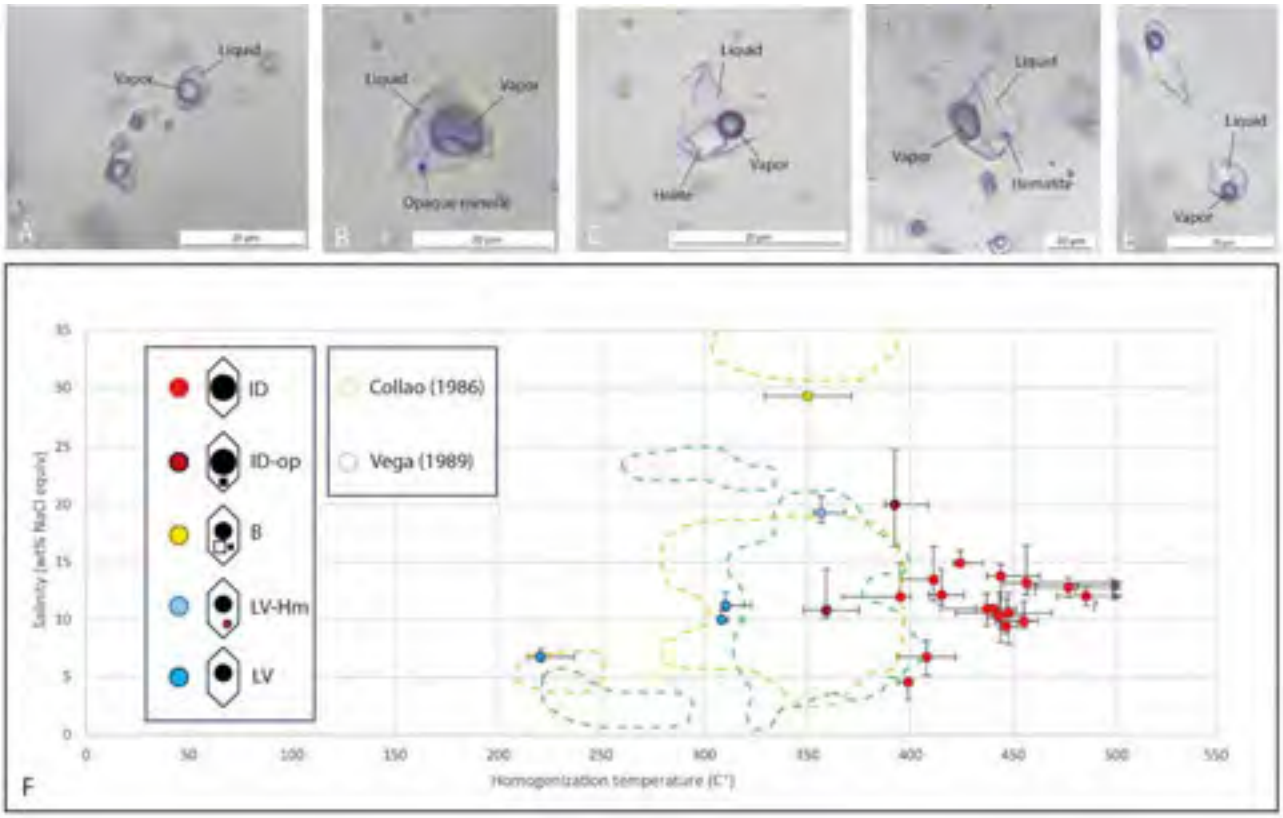


Figure 1. Petrography and microthermometry results. A: ID-type. B: ID-opaque-type. C: B-type. D: LV-Hm-type. E: LV-type trail. F: Salinity vs homogenization temperature diagram. Data are grouped by fluid inclusion assemblages (FIAs). In yellow and green are highlighted the data obtained by Collao (1986) and Vega (1989).

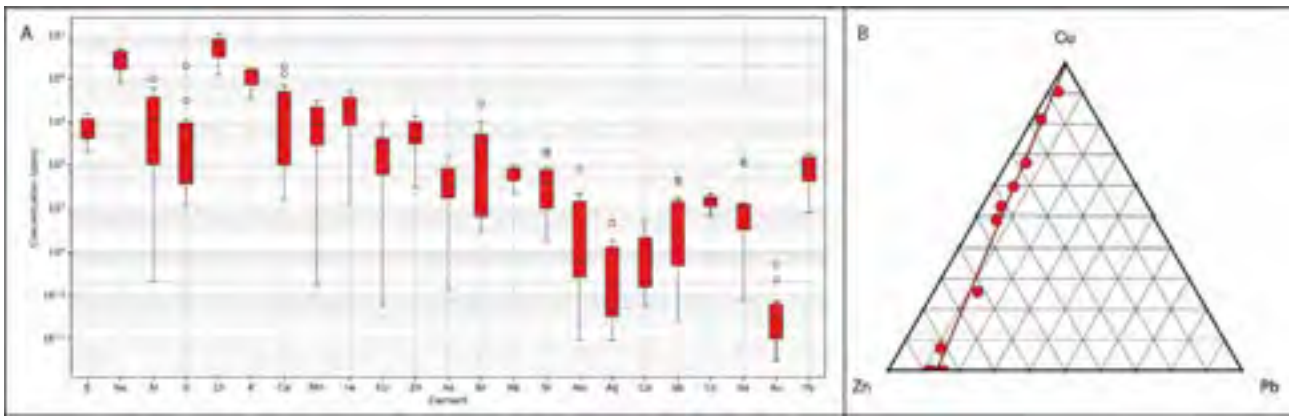


Figure 2. LA-ICP-MS data. A: Concentrations of major and trace elements in ID-type fluid inclusions. B: Ternary diagram showing the composition of ID-type fluid inclusions. The dark-red line corresponds to constant Zn/Pb ratio.

References

Audétat A, Simon AC (2012) Magmatic Controls on Porphyry Copper Genesis. In: Hedenquist JW, Harris M, Camus F (eds) Geology and Genesis of Major Copper Deposits and Districts of the World A Tribute to Richard H. Sillitoe. Soc Econ Geol:553–572

Bain WM, Lecumberri-Sanchez P, Marsh EE, Steele-MacInnis M (2022) Fluids and Melts at the Magmatic-Hydrothermal Transition, Recorded by Unidirectional Solidification Textures at Saginaw Hill, Arizona, USA. Econ Geol 117:1543–1571

Ballard JR, Palin JM, Williams IS, Campbell IH, Faunes A (2001) Two ages of porphyry intrusion resolved for the super-giant Chuquicamata copper deposit of northern Chile by ELA-ICP-MS and SHRIMP. Geology 29:383–386

Burnham CW (1979) Magmas and Hydrothermal Fluids. In: Barnes HL (ed) Geochemistry of Hydrothermal Ore. Wiley, pp 71–136

Campos E, Touret JLR, Nikogosian I, Delgado J (2002) Overheated, Cu-bearing magmas in the Zaldívar porphyry-Cu deposit, Northern Chile, Geodynamic consequences. Tectonophysics 345

CODELCO (2023) Memoria Anual 2023. https://www.codelco.com/prontus_codelco/site/docs/20240404/20240404191040/memoria_codelco_2023.pdf

Guillong M, Meier DL, Allan MM, Heinrich CA, Yardley BWD (2008) SILLS: A Matlab-based program for the reduction of laser ablation ICP-MS data of homogeneous materials and inclusions. *In* Sylvester P (ed.) Laser ablation-ICPMS in the earth sciences: Current practices and outstanding issues: Vancouver, British Columbia, Mineralogical Association of Canada: 328–333

Goldstein RH (2003) Petrographic analysis of fluid inclusions Hugoton Embayment View project. In: Samson I, Anderson A, Marshall D (eds) Fluid Inclusions: Analysis and Interpretation. Mineralogical Association of Canada, pp 9–53

Hedenquist JW, Lowenstern JB (1994) The role of magmas in the formation of hydrothermal ore deposits. Nature 370:519–527

Heinrich CA (2024) The Chain of Processes Forming Porphyry Copper Deposits — An Invited Paper*. Econ Geol 119:741–769

Klemm LM, Pettke T, Heinrich CA, Campos E (2007) Hydrothermal evolution of the El Teniente deposit, Chile: Porphyry Cu-Mo ore deposition from low-salinity magmatic fluids. Econ Geol 102

Kouzmanov K, Pokrovski GS (2012) Hydrothermal Controls on Metal Distribution in Porphyry Cu (-Mo-Au) Systems. In: Hedenquist JW, Harris M, Camus F (eds) Geology and Genesis of Major copper Deposits and Districts of the World: A Tribute to Richard H. Sillitoe. Soc Econ Geol, pp 573–618

Ossandón CG, Freraut CR, Gustafson LB, Lindsay DD, Zentilli M (2001) Geology of the Chuquicamata Mine: A Progress Report. Econ Geol 96:249–270

Park JW, Campbell IH, Chiaradia M, Hao H, Lee C-T (2021) Crustal magmatic controls on the formation of porphyry copper deposits. Nat Rev Earth Environ 2:542–557

Mpodozis C, Cornejo P (2012) Cenozoic Tectonics and Porphyry Copper Systems of the Chilean Andes. In: Geology and Genesis of Major Copper Deposits and Districts of the World A Tribute to Richard H. Sillitoe. Soc Econ Geol

Redmond PB, Einaudi MT, Inan EE, Landtwing MR, Heinrich CA (2004) Copper deposition by fluid cooling in intrusion-centered systems: New insights from the Bingham porphyry ore deposit, Utah. Geology 32:217–220

Rivera SL, Alcota H, Proffett J, Díaz J, Leiva G, Vergara M (2012) Update of the Geologic Setting and Porphyry Cu-Mo Deposits of the Chuquicamata District, Northern Chile. In: Hedenquist JW, Harris M, Camus F (eds) Geology and Genesis of Major Copper Deposits and Districts of the World A Tribute to Richard H. Sillitoe. Soc Econ Geol, pp 19–54

Rusk BG, Reed MH, Dilles JH, Klemm LM, Heinrich CA (2004) Compositions of magmatic hydrothermal fluids determined by LA-ICP-MS of fluid inclusions from the porphyry copper-molybdenum deposit at Butte, MT. Chem Geol 210:173–199

Sillitoe RH, Perelló J (2005) Andean Copper Province: Tectonomagmatic Settings, Deposit Types, Metallogeny, Exploration, and Discovery. In: One Hundredth Anniversary Volume. Soc Econ Geol

Tomlinson AJ, Blanco N, Dilles JH, Maksaev V, Ladino M (2018) Carta Calama, Región de Antofagasta. Servicio Nacional de Geología y Minería, Carta Geológica de Chile, Serie Geología Básica 199.

Ulrich T, Günther D, Heinrich CA (2002) The evolution of a porphyry Cu-Au deposit, based on LA-ICP-MS analysis of fluid inclusions: Bajo de la Alumbrera, Argentina. Econ Geol 97

Vega M (1989) Estudio y caracterización de vetas de cuarzo en un sector del yacimiento Chuquicamata. Bachelor Thesis, Universidad Católica del Norte

Virmond AL, Wotzlaw J-F, Rojas-Arancibia R, Selby D, Chelle-Michou C (2024) Multi-million-year magmatic and hydrothermal activity is key to the formation of supergiant to behemothian porphyry copper deposits. Contrib Mineral Petr 179:88

Williams-Jones AE, Heinrich CA (2005) 100th Anniversary Special Paper: Vapor Transport of Metals and the Formation of Magmatic-Hydrothermal Ore Deposits. Econ Geol 100:1287–1312

Aranzazu Skarn: Zoning Patterns and Geological Controls

Oscar Solis[1], Zhaoshan Chang[1]
[1]Department of Geology and Geological Engineering, Colorado School of Mines, Golden, CO 80401, USA

Abstract. The Aranzazu Cu skarn is in the Concepción del Oro mining district, northeast Zacatecas, Mexico. The regional geology consists of Jurassic and Cretaceous sedimentary rocks intruded by Eocene granodiorites. The structural setting is dominated by the La Caja anticline, a NW-SE fold modified by magma emplacement. The Aranzazu deposit is a skarn formed at the contact between an Eocene granodioritic intrusion complex and sedimentary rocks. The deposit has a typical calcic skarn paragenesis, progressing from contact metamorphism (Stage 1) to prograde (Stage 2) and retrograde stages (3-5), with the Cu mineralization mainly occurred in Stage 4 (sulfides and sulfosalts). A molybdenite sample is dated at 43.03 ± 0.19 Ma (Re-Os). Zoning patterns are evident in both endoskarn (four zones ranging from massive garnet-pyroxene to a transitional porphyry-skarn zone) and exoskarn (proximal dark/red garnet to distal yellow-green garnet then the far distal zone with fluid escape veins).

1 Introduction

The Aranzazu skarn (18.6 Mt @ 1.41% Cu, 0.89 g/t Au, 21 g/t Ag; Aura AIF 2024) is in the Concepcion del Oro mining district, northeastern Zacatecas, Mexico, between the coordinates 24° 05' - 24° 49' north latitude and 100° 59' - 101° 29' west longitude, WGS84 (Fig. 1). It was explored and mined before the 17th century. The district hosts various deposit types, including skarns, carbonate replacement deposits (CRDs), diatreme-hosted Zn-Pb-Au, and intermediate-sulfidation (IS) epithermal Ag-Au veins (Buseck 1966; Megaw et al. 1988; CRM 2003).

2 Regional Geology

2.1 Tectonic setting

Concepcion del Oro is in the Sierra Madre Oriental, where sedimentary and igneous rocks range from Jurassic to Cenozoic ages (CRM 2003). Tectonically, the NW-SE elongated Concepcion del Oro Block is bounded by high angle normal faults. The deformations in the block occurred during the Eocene-Oligocene, related to the Laramide Orogeny. The deformation created fold and faults that control the arrangement of mineral deposits (Ramírez-Peña et al. 2019).

2.2 Stratigraphy and intrusive rocks

The stratigraphy of the district includes, from old to young, Upper Jurassic Zuloaga formation (Fm) fossiliferous limestone and La Caja Fm thin-bedded calcareous siltstones and limestone, Lower

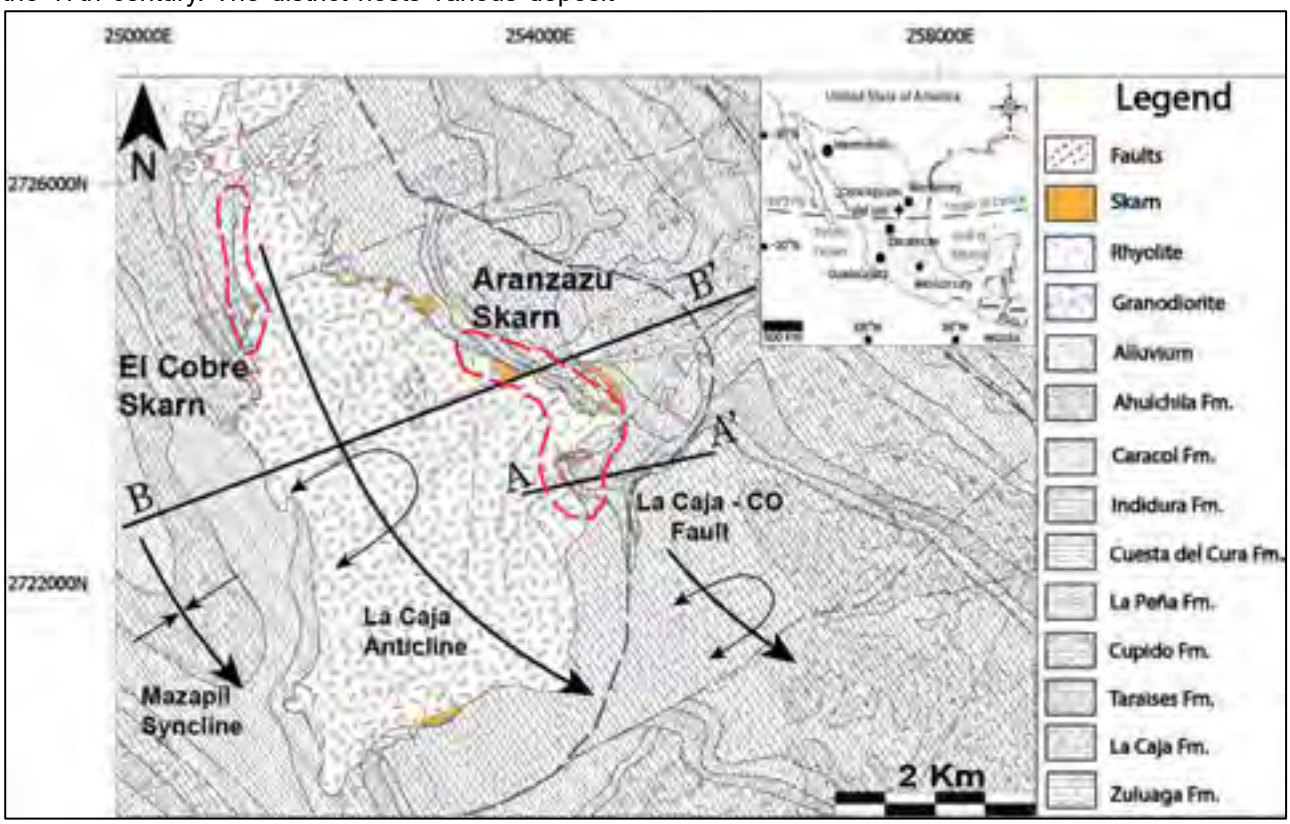


Figure 1. Surface map illustrating the regional geology of the Aranzazu deposit. CO=Concepción del oro. Modified from CRM (2003).

cretaceous Taraises Fm then Cupido Fm, both limestones interbedded with shales and pyrite nodules, La Peña and Cuesta del Cura Fms limestones with thin layers of calcareous shales and chert, and Cenozoic Ahuichila conglomerate and more recent alluvial deposits. The intrusive rocks include an intrusive complex composed of various Eocene granodioritic intrusions. The size is ~10 x 2 km (Fig. 1). There are also Oligocene hypabyssal rhyolitic porphyries (CRM 2003).

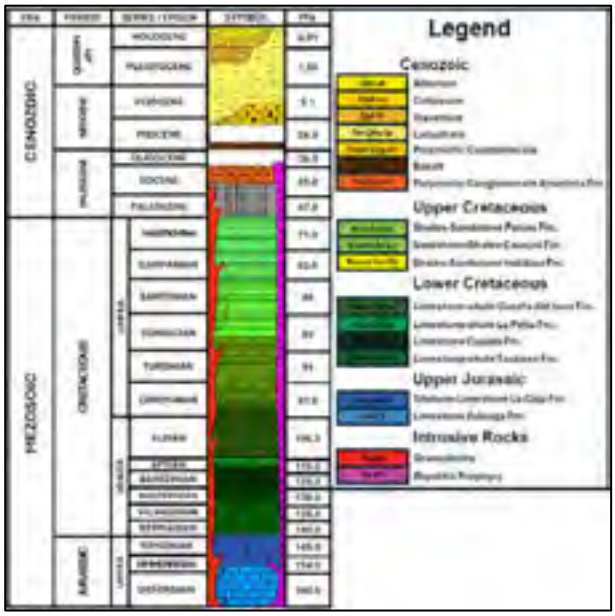


Figure 2. Stratigraphic column of the Concepcion del oro mining district. Modified from CRM (2003).

2.3 Regional deformation

The La Caja anticline is a regional structure which has Jurassic rocks in its core and Cretaceous sequences in its flanks (Fig. 1). It is an asymmetrical, overturned fold with an axial plane dip toward the SW (Fig. 3). Its axis trends NW-SE, dipping toward the SE. The flanks show dips of 50°-70° (SW) and 60°- 80° (NE), with the latter generally inverted. In the central area. The anticline is modified by magma emplacement, creating a deformation aureole that affected the pre-existing structures (Fig. 3).

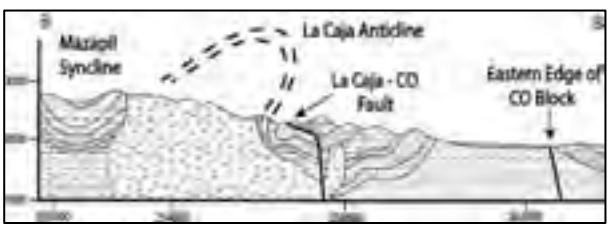


Figure 3. Regional deformation and structural model of Aranzazu. CO=Concepción del oro. Modified from Ramírez-Peña (2024).

3 Aranzazu Skarn

The Aranzazu skarn mainly occurs on the eastern side of the intrusion complex and the eastern flank of the La Caja anticline, where the stratigraphy generally strikes NW 40°- 45° SE and dips 60°-70° to NE (Figs. 2-3). The skarn includes, from north to south, the Los Zafiros-Conexion, BW, Mexicana, Glory Hole (GH), and Esperanza zones. The Zuloaga Fm, in direct contact with the intrusion is metamorphosed to marble and altered to 10-40 m wide massive exoskarn. Outwards, the 20-30 m thick La Caja calcareous siltstone is metamorphosed to a calc-silicate hornfels with 0.05-0.10 m thick discontinuous layers of skarn. Farther out, 30-100 m thick of the Taraises formation is now marble, locally with 10-25% of isolated garnet skarn patches (Fig. 4). Most of the skarn bodies have a stratabound, tabular shape, which may be because the generally impermeable layer of calc-silicate hornfels prevents the magmatic fluids from flowing outwards, and the slip faults along both sides of its boundary with limestones increase the permeability, making it the boundaries a favorable location for skarns. Locally, part of the Cupido Fm. is close enough to the intrusion to be metamorphosed to marble; no skarns occur in them. Some skarns also occur in the northwest (El Cobre zone) and south sides of the intrusion (Fig. 1).

Based on core logging and surface mapping, five stages of skarn paragenesis are recognized in the calcic skarns of Aranzazu. Stage 1 is the contact metamorphism that produced the marble and calc-silicate hornfels (Fig. 5A-B & D). Stages 2-5 produced both endo- and exoskarns. The Stage 2 prograde skarn consists of garnet, pyroxene, and wollastonite (Figs. 6A-B, 6C & 7A). Stage 3 is a higher temperature retrograde alteration composed of epidote, amphiboles, vesuvianite, quartz, specular hematite and mushketovite (Figs. 5A, 6C, 7A). Stage 4 is retrograde alteration at a lower temperature, consisting of chlorite, quartz, calcite, carbonates, sulfides and sulfosalts (Figs. 5A-B, 5D, 7A, & 7C). Copper-Au-Ag mineralization occurs in this stage. Stage 5 is the lowest temperature retrograde alteration consisting of barren veins of calcite and manganoan calcite, bright under UV light (Figs. 5A & 5D). The paragenesis is similar to other skarns worldwide (Meinert et al. 2005, Chang et al. 2019).

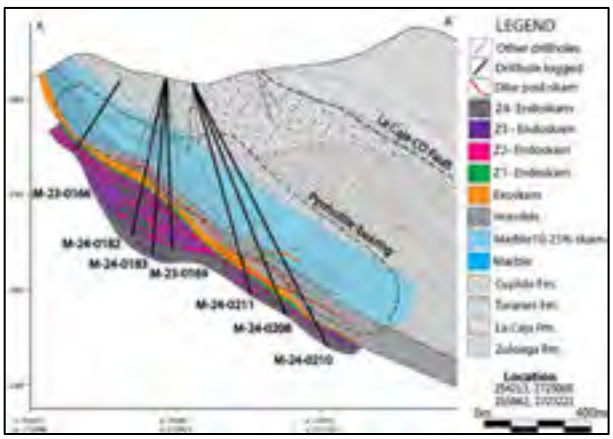


Figure 4. Cross section of the Esperanza zone showing the zoning patterns in both endo- and exoskarns. The pyrrhotite-bearing zone without any magnetite outside the massive exoskarn indicates a reduced condition in this part of Aranzazu.

The deposit has Cu, Au, and Ag mineralization. Oxides of Cu and Fe occur on the surface and shallow depths (Fig. 5C). Primary mineralization occurs meters below the surface (Figs. 5D, 6C & 7A). The sulfides cut across or replace prograde minerals (Stage 2), mainly in exoskarns (Figs. 5A-B & 6C). There is local molybdenite. One exoskarn sample has been dated at 43.03 ± 0.19 Ma using the molybdenite Re-Os method at University of Alberta.

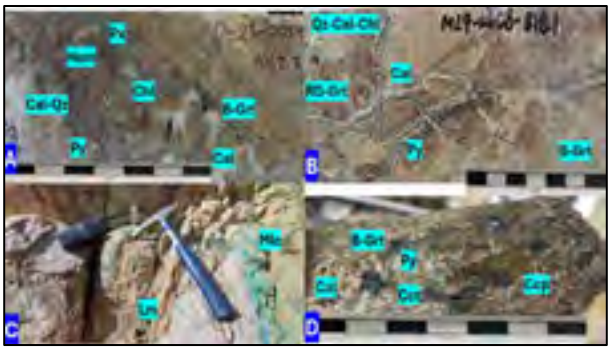


Figure 5. Aranzazu skarn paragenesis. **A**: Brown garnet and disseminated pyroxene exoskarn (Stage 2) with hematite veins (Stage 3), and interstitial chlorite, calcite, and quartz (Stage 4). **B**: Red/dark-brown garnet skarn (Stage 2) cut by quartz-calcite-chlorite-pyrite-chalcopyrite veins (Stage 4), and finally a calcite vein (Stage 5) cuts all preliminary veins. **C**: Oxidation outcrop with malachite and limonite. **D**: Sulfide-rich brown garnet exoskarn with calcite (Stage 5) filling vugs. Cal=calcite, Cct=chalcocite, Ccp=chalcopyrite, Chl=chlorite, B-Grt= brown garnet, RD-Grt=red/dark garnet, Hem=hematite, Lm=limonite, Mlc=malachite, Py=pyrite, Px=pyroxene, Qz=quartz.

4 Exoskarn Zoning Patterns

The Aranzazu skarn has zonation in both exoskarn and endoskarns (Figs. 5-7). The exoskarn replaces sedimentary rocks. The garnet color becomes lighter away from the main intrusion. Right next to the intrusive contact, red to brown garnet-dominant massive exoskarn occurs (Figs. 5B & 6C). Meters beyond the intrusive contact, the garnet color changes to mostly brown/yellow (Figs. 5A & D). Farther out, marble contains patches of light-colored (yellow/green) garnet skarn patches or veins (Figs. 6D). Tens to hundreds of meters away from the intrusive contact, there is only grey/dark marble (Stage 1) with local bleaching (Fig. 6E). At most distal locations, >500 m away from the intrusion contact, unmetamorphosed sedimentary rocks contain fluid scape veins of calcite (Fig. 8F). Pyroxene is lacking in the whole skarn and is only locally abundant.

5 Endoskarn Zoning Patterns

The endoskarn generally changes from massive at the intrusion margin to veins inside the intrusion, with four zones recognized, similar to endoskarns in other skarns (Chang and Meinert, 2004, 2008A; Lawrence et al. 2017; Chang et al. 2018). Zone 1 (Z1) endoskarn is massive or semi-massive, with no or only minor residual intrusive rocks (Fig. 7A). Skarn occupies >90 vol% of the rock. It is mainly

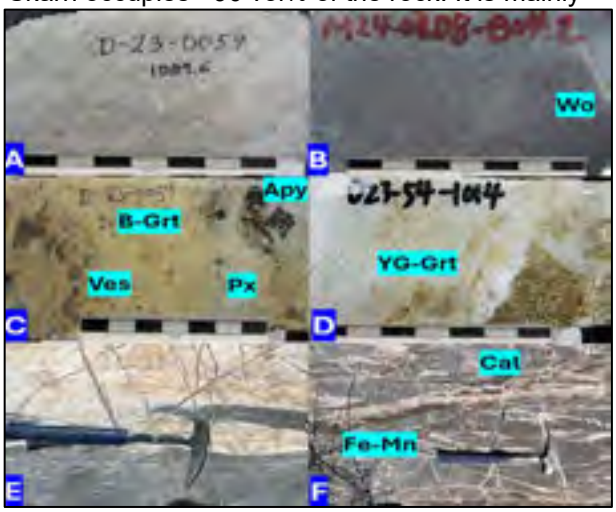


Figure 6. Aranzazu exoskarn zoning patterns. **A**: massive marble (Stage 1). **B**: Dark hornfels (Stage 1) cut by Stage 2 wollastonite vein. **C**: Massive brown garnet – light pyroxene exoskarn (Stage 2) with prismatic vesuvianite (Stage 3) replacing garnet. Interstitial sulfides (Stage 4) are later. **D**: White marble (Stage 1) with yellow-green garnet patch (Stage 2). **E**: Dark grey marble (Stage 1) with bleaching is cut by calcite-Fe oxide veins. **F**: Distal calcite and Fe-Mn oxide fluid scape structures in gray limestone. Apy=arsenopyrite, YG-Grt=yellow-green garnet, Ves= vesuvianite, Wo= wollastonite.

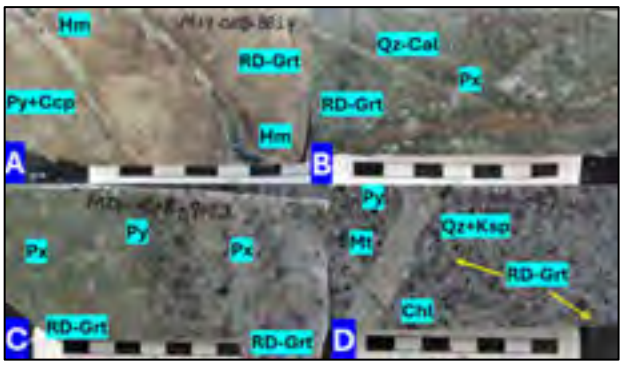


Figure 7. Aranzazu endoskarn zones. **A**: Z1 massive red garnet skarn (Stage 2) cut by a hematite vein (Stage 3) reused for pyrite-chalcopyrite precipitation (Stage 4). **B**: Z2 red/dark garnet vein with pyroxene halo (Stage 2) cut by late quartz-calcite vein (Stage 4). **C**: Z2-Z3 transition. Z2 (left) large pyroxene patch with some disseminated red garnet, without magmatic biotite and identifiable igneous texture. Z3 (right) disseminated pyroxenes (Stage 2), and pyrite (Stage 4), with magmatic biotite and igneous texture preserved. **D**: Z4 intrusive rock with quartz-feldspar vein with magnetite along its edges and disseminated pyrite (Stage 4), cuts by chlorite vein (Stage 4). Isolated red/dark garnet grains (Stage 2) disseminated in the igneous rock. Magmatic biotite preserved. Bt=biotite, Hm=hematite, Ksp=K-feldspars, Mt=magnetite.

composed of red/dark colored garnet with lesser pyroxene, locally with retrograde assemblages. Whole rock geochemistry is used to identify some of the massive endoskarn using the method proposed in Mrozek et al (2020). Zone 2 (Z2) features endoskarn veins (90-10 vol%) consisting of mainly red garnet with minor pyroxene and quartz. The halo

is mostly pyroxene. No residual magmatic mafic minerals (biotite, amphibole) are preserved, but there is local secondary biotite. The original igneous textures are identifiable (Fig. 7B & C). Zone 3 (Z3) contains minor endoskarn veins (< 10 vol%) that are red/dark garnet-dominant with pervasive disseminated pyroxene outside of the veins. Some magmatic biotite grains are preserved, with or without partial secondary biotite alteration. The original igneous textures are preserved (Fig. 7C). Zone 4 (Z4) is the endoskarn - porphyry transitional zone, with both endoskarn vein (garnet/pyroxene) and early-stage high temperature porphyry style veins (EDM, A, B, and AB veins with K-feldspar and/or secondary biotite halos). Some porphyry veins contain molybdenite. Magmatic biotite may be preserved between the veins, and the original igneous textures are preserved (Fig. 7D). There is an overall trend of Z1 to Z4 from the intrusion margin inwards. Domains of Z1 and Z2 zones also appear in Zone 3 a few times along an inward profile, but they become lesser inward (Fig. 4), similar to the situation at the Empire skarn, Idaho (Chang and Meinert, 2008A)

5 Discussions

The La Caja anticline has a weak zone in the axial plane, which probably facilitated the emplacement of granodioritic intrusion complex. The investigation of the intrusive sequence in the complex is on-going. Zuloaga Fm directly contacts the intrusion and is the most important host rock for the skarn. Its proximity to the intrusion is one reason. The impermeable calc-silicate hornfels layer converted from the La Caja calcareous siltstone during contact metamorphism, before hydrothermal activities, probably block the water from flowing outwards, which also helped confine the skarn and mineralization in the Zuloaga Fm, with higher grades (1.76% Cu) than many other skarns. Locally, Taraises Fm (“dirty” limestone) also hosts skarn (1.13% Cu), either because a fault cutting La Caja calc-silicate hornfels leaked the fluids, or there is another fertile subsurface intrusion located beyond La Caja.

The skarn lacks the pyroxene-dominant zone in exoskarns, probably because the magma and the derived hydrothermal fluids were very oxidized that the organic matters (the reason of the grey color of the host rocks; Figs. 6E-F) was not sufficient to reduce to fluids to generate sufficient Fe^{2+} to form pyroxene (Chang and Meinert, 2008B). The marble beyond the La Caja contains pyrrhotite rather than magnetite, which indicates a reduced environment (Fig. 4). It could have been caused by minor magmatic fluids passing through the impermeable calc-silicate hornfels along fractures and being reduced by the wallrocks due to low water/rock ratio, but by that time the fluid temperatures were too low to form skarns.

The endoskarn zones from Z1 to Z4 reflects the more availability of Ca to form more skarn minerals at the intrusion margin. The repetition of the endoskarn zoning might be caused by multiple fertile dykes emplaced along the intrusion margin, and each produces its own endoskarn zoning. Narrower dykes may not be thick enough to get to Z3 and Z4, therefore there are more Z1 and Z2 domains in the presently coalesced endoskarn.

Acknowledgements

We thank Aura Minerals for the sponsorship, and the Aranzazu Exploration Department for support.

References

Aura Minerals (2024) Annual information form (AIF) for the year ended December 31, 2023 (Dated as of April 1, 2024). https://auraminerals.com

Buseck PR (1966) Contact metasomatism and ore deposition: Concepcion del Oro, Mexico. Econ Geol 61:97-136

Chang Z, Meinert L, Lawrence D, Mrozek S, Zhang L (2018) Skarns replacing igneous rocks: Symposium Proceedings, 15th Quadrennial IAGOD International Association on the Genesis of Ore Deposits Symposium, Salta, Argentina. 28-31 August 2018:207-208

Chang Z, Meinert LD (2004) The magmatic-hydrothermal transition - Evidence from quartz phenocryst textures and endoskarn abundance in Cu-Zn skarns at the Empire Mine, Idaho, USA. Chem Geol 210:149-171

Chang Z, Meinert LD (2008A) The Empire Cu-Zn Mine, Idaho, USA: Exploration implications of unusual skarn features related to high fluorine activity. Econ Geol 103:909-938

Chang Z, Meinert LD (2008B) Zonation in skarns—complexities and controlling factors. PACRIM Congress 2008, Australasian Institute of Mining and Metallurgy (AusIMM), Gold Coast, Australia, November 24–26, 2008, Extended Abstracts:303–306

Chang Z, Shu Q, Meinert LD (2019) Skarn deposits of China. In: Chang Z, Golfarb RJ (Eds) Mineral Deposits of China, SEG Special Publications 22:189–234

Consejo de Recursos Minerales (2003) Informe de la carta geológico-minera Concepción del Oro G14-C62, escala 1:50,000. Subdirección de Operación, Gerencia de Geología:5-78

Instituto Nacional de Estadística y Geografía (INEGI) (2018) Marco Geoestadístico Nacional, febrero 2018. https://www.inegi.org.mx

Lawrence DM, Allibone AH, Chang Z, Meffre S, Lambert-Smith JS, Treloar PJ (2017) The Tongon Au deposit: Northern Cote d’Ivoire: An example of Paleoproterozoic Au skarn mineralization. Econ Geol 112:1571-1593

Megaw PKM, Ruiz J, Titley SR (1988) High-temperature, carbonate-hosted Ag-Pb-Zn (Cu) deposits of northern Mexico. Econ Geol 83:1856-1885

Meinert LD, Dipple GM, Nicolescu S (2005) World skarn deposits. Economic Geology 100th Anni Vol:299-336

Mrozek S, Chang Z, Spandler C, Windle S, Raraz C, Paz A (2020) Using whole rock geochemistry to optimize skarn classification and evaluate element mobility during skarn formation: An example from the Antamina deposit, Peru. Econ Geol 115:177-188

Ramírez-Peña CF (2024) Estudio estructural en Aranzazú, Concepción del Oro, Zacatecas. Technical report, Universidad Autónoma de Nuevo León, Facultad de Ciencias de la Tierra, prepared for Aura Minerals Inc.

Ramírez-Peña CF, Chávez-Cabello G, Fitz-Díaz E, Aranda-Gómez JJ, Sosa Valdés R (2019) Uplift and syn-orogenic magmatism in the Concepción del Oro block: A thick-skinned (Laramide style?) contractional structure in the Mexican fold-thrust belt. J South Am Earth Sci. Universidad Autónoma de Nuevo León, Facultad de Ciencias de la Tierra:241-251

Episodic Epithermal Ore Formation During Late Cretaceous Rifting and Felsic Magmatism in the Cu-Au Bolnisi Mining District, SW Georgia

Şafak Utku Sönmez[1,2], Robert Moritz[1], Nino Popkhadze[3,4], Alexey Ulianov[5], Malkhaz Natsvlishvili[4]
[1]*Department of Earth Sciences, University of Geneva, Switzerland*
[2]*Département de Géologie et de Génie Géologique, Université Laval, Québec City, Canada*
[3]*Al.Janelidze Institute of Geology of Iv. Javakhishvili Tbilisi State University, Georgia*
[4]*The RMG Rich metals Group, Georgia*
[5]*Institute of Earth Sciences, University of Lausanne, Switzerland*

Abstract. This study provides precise Late Cretaceous age constraints on the magmatic and mineralizing events within the Bolnisi mining district in Georgia. The Bolnisi district, located in the northern Lesser Caucasus, records a magmatic history characterized by Late Cretaceous subduction-related processes linked to the northern Neotethys Ocean, subsequently overprinted by early Eocene adakite-like magmatism driven by postcollisional tectonics. The mineral systems are predominantly epithermal and are hosted by volcano-magmatic rock successions, with lithofacies transitioning from submarine to subaerial environments. The Madneuli deposit, one of the major active mines, is a notable exception, preserving both submarine hydrothermal and epithermal mineralization styles. Comprehensive U-Pb zircon dating of host and post-mineralization rocks constrains Madneuli and Beqtakari as the earliest mineralization events, sequentially succeeded by Sakdrisi, Kazreti, Mushevani, and Qvemo Bolnisi. The juxtaposition of mineralized lithologies with crosscutting barren intrusions underscores the Late Cretaceous as the principal epoch of mineralization. Conversely, the extensive early Eocene magmatic phase is characterized by barren lithologies. These findings confirm the Late Cretaceous age of the magmatic-hydrothermal systems in the district, providing a temporal framework that enhances exploration targeting in the Bolnisi district.

1 Introduction

The Bolnisi district, situated within the northern Lesser Caucasus, is a key mining region in the Western Tethyan metallogenic belt (Fig. 1; Moritz et al., 2016). The geological evolution of the district is marked by Late Cretaceous silicic-dominant and bimodal magmatism during the waning subduction stages of the northern Neotethys Ocean, followed by early Eocene adakite-like magmatism in a postcollisional setting (Hässig et al. 2020; Moritz et al. 2020). This tectono-magmatic activity has profoundly influenced the metallogenic processes in the district, resulting in diverse mineralization styles and environments.

Mining activities in the Bolnisi district date back to the Bronze Age (Hauptmann and Klein 2009). The Sakdrisi deposit is regarded as the oldest gold mine in the world and underscores the district's metallogenic legacy (Fig. 1; Feresin 2007).

The metallogenic evolution of the Bolnisi district remains inadequately understood due to the paucity of temporal constraints on mineral systems and limited integration within the regional tectono-magmatic events.

This study addresses these topics by focusing on three major mines, including Madneuli, Beqtakari, and Sakdrisi, and three advanced exploration prospects, including Qvemo Bolnisi, Kazreti, and Mushevani. By combining U-Pb zircon dating with lithogeochemical analyses of host and post-mineralization volcanic rocks, the study establishes detailed temporal and genetic links between magmatic and mineralization events.

These findings provide a refined understanding regarding the metallogenic framework of the Bolnisi district, offering critical insights for both academic research and future mineral exploration.

2 Late Cretaceous Magmatic Activity in the Bolnisi Mining District

The Late Cretaceous magmatic arc rocks, defined as the Bolnisi Group, are predominantly composed of calc-alkaline rhyolitic to rhyodacitic volcanic and sub-volcanic rocks. They include subordinate dacitic, andesitic, and basaltic rocks, as well as lesser sedimentary rock formations (Fig. 1; Adamia et al. 2011; Hässig et al. 2020; Moritz et al. 2020). The older volcanic rocks in the group are primarily rhyolitic to rhyodacitic, with a predominant calc-alkaline affinity (Fig. 2). Recent geochemical studies of these felsic volcanic rocks have allowed us to distinguish high-HREE felsic rocks with an age range of ~87.1–80.9 Ma and low-HREE felsic rocks with an age range of ~85.7–82.5 Ma (Fig. 2; Hässig et al. 2020; Moritz et al. 2020; Sönmez et al. 2024; this study). These felsic units are generally associated with Late Cretaceous volcanoclastic rocks, which are mostly hosted or covered by them. The overlying Late Cretaceous volcanic coherent rocks are primarily composed of trachyandesitic rocks exhibiting a shoshonitic geochemical affinity and are mainly exposed in the western part of the district (Fig. 1; Moritz et al. 2020). Apatite U-Pb dating of this unit has provided an age of 80.4 ± 2.0 Ma (Sönmez et al. 2024). Shallow marine sedimentary rocks of the Campanian to Maastrichtian Tetritskaro suite rest conformably to unconformably atop the Bolnisi Group volcanic rocks (Adamia et al. 2011; Popkhadze et al. 2014).

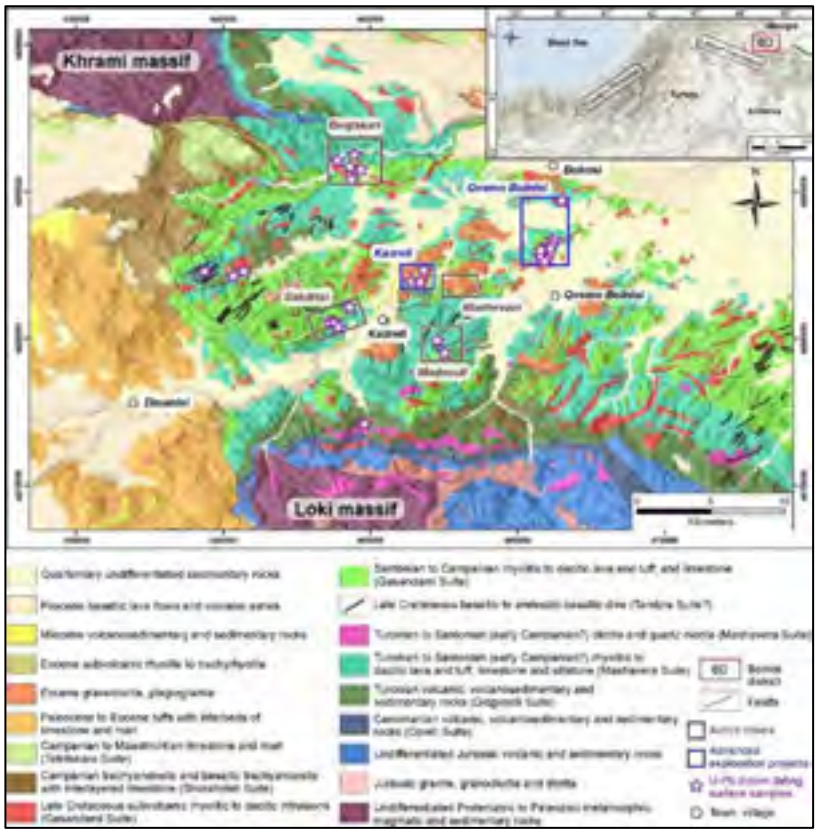


Figure 1. Geologic map of the Bolnisi district (adapted from Vashakidze and Gugushvili 2006; Moritz et al. 2020), with the locations of the major active mines (Madneuli, Sakdrisi, and Beqtakari) and advanced exploration projects (Qvemo Bolnisi, Kazreti, and Mushevani). The locations of samples dated by U-Pb zircon geochronology in this study are also indicated. The inset shows the location of the Bolnisi district within the Lesser Caucasus in southern Georgia.

3 Mineral Exploration and Mineral Systems in the Bolnisi Mining District

The Bolnisi mining district hosts abundant gold and base metal deposits, with present-day mining operations primarily led by the Rich Metal Group (RMG), focusing on the Madneuli, Beqtakari, Sakdrisi, and Mushevani deposits. Ongoing surface mineral exploration and drilling activities by the Caucasus Mining Group (CMG), a subsidiary of RMG, have unveiled new resources and reserves in the Bnelikhevi, Qvemo Bolnisi, and Kazreti prospects (Fig. 1). Previous studies concluded that the mineral systems in the Bolnisi district are epithermal in nature and are characterized by Au-bearing polymetallic crustiform and comb-textured quartz veins, as well as Au-base metal-bearing hydrothermal breccia (Gialli 2013; Lavoie 2015; Moritz et al. 2016; Golay 2019; Sönmez et al. 2022).

4 Geochemical Characteristics of the Volcanic Rocks of the Bolnisi District

Based on the Zr/TiO_2 vs. Nb/Y diagram, samples collected from the Late Cretaceous volcanic rocks plot in the rhyolite, rhyodacite, andesite and basaltic andesite fields (Fig. 2A). The felsic phases of the same samples plot in the calc-alkaline field in the Th/Yb vs. Zr/Y diagram except for some samples (Fig. 2B). Conversely, most of the samples from the intermediate to mafic phases plot in the transitional and subordinately in the calc-alkaline field (Fig. 2B).

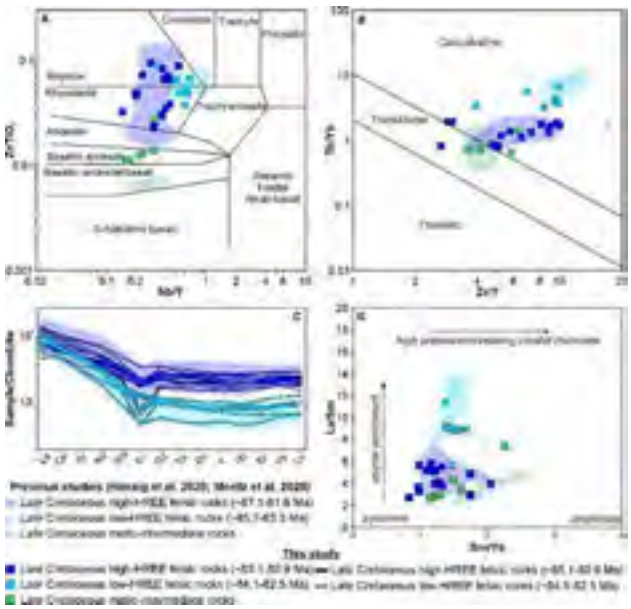


Figure 2. Geochemical diagrams for samples collected from Late Cretaceous volcanic rocks. A) Zr/TiO_2 vs. Nb/Y (fields from Lang et al. 2023, modified from Winchester and Floyd, 1977), B) Th/Yb vs. Zr/Y magmatic affinity diagram (Ross and Bédard 2009). C) chondrite-normalized REE diagrams (normalization values from Sun and McDonough 1989). D) La/Sm vs. Sm/Yb magmatic evolution and source characteristic diagrams showing magmatic processes (from Kay and Mpodozis 2001).

The felsic rocks exhibit distinct high and low concentration of HREEs patterns in the chondrite-normalized diagrams (Fig. 2C). In addition, weak to significant Eu depletion is observed in the felsic units (Fig. 2C).

5 Ore-Forming Events in the Bolnisi District: U-Pb Zircon LA-ICP-MS Dating

Dating alteration or gangue minerals using the $^{40}Ar/^{39}Ar$ method was not feasible due to the absence of suitable dating minerals and/or age resetting of post-mineralization magmatic and thermal events. Therefore, we used U-Pb zircon dating from pre- and post-ore magmatic events to bracket the lower and upper age limits of the mineralization events in the Bolnisi District (Fig. 3).

Uranium-lead zircon dating constrains the age of the host rocks at the Madneuli deposit between 87.1 ± 0.1 Ma and 87.0 ± 0.2 Ma, with unmineralized crosscutting volcanic units dated to 85.1 ± 0.4 Ma (Moritz et al., 2020, this study). Thus, Madneuli is the earliest mineralization event in Bolnisi. (Fig. 3).

At Beqtakari, ore formation is temporally constrained between 85.1 ± 0.4 Ma and 84.9 ± 0.6 Ma. Thus, our new geochronological data indicate that Beqtakari is the second oldest mineralized system of the Bolnisi District (Fig. 3).

In Sakdrisi, the Au-polymetallic veins are hosted by volcanosedimentary rocks dated at 83.9 ± 1.0 Ma, overlain by barren ignimbrite dated at 83.3 ± 0.4 Ma (Fig. 3).

Similarly, the Au-polymetallic veins in Kazreti are hosted by 83.3 ± 0.5 Ma volcanic and volcanoclastic rocks crosscut by unmineralized intrusions dated at 82.5 ± 0.5 Ma, indicating that ore formation is younger than at Sakdrisi. Comparable relationships are observed at Mushevani (Fig. 3).

The youngest mineralization system in the district is documented at Qvemo Bolnisi, where mineralization is hosted by volcanoclastic rocks dated at 82.2 ± 0.6 Ma. The upper boundary of this mineralization event remains unresolved, as the youngest rock dated so far are unmineralized Eocene subvolcanic rocks dated at 52.3 ± 0.4 Ma (Fig. 3).

6 Discussion and Conclusions

6.1 Mineral systems of the Bolnisi District in the context of Late Cretaceous geodynamic evolution

The Late Cretaceous volcanic and volcaniclastic rocks of the Bolnisi District were formed during multiphase magmatic episodes in an extensional tectonic regime linked to the waning subduction stages of the northern Neotethys Ocean (Fig. 4; Hässig et al., 2020; Moritz et al., 2020). Uranium-lead dating reveals that mineralization began at Madneuli (~87.0–85.1 Ma) and Beqtakari (~85 Ma) during this extensional phase (Fig. 4A; Moritz et al., 2020). Continued extension (~84–83 Ma) likely repositioned Madneuli southward and Beqtakari northward (Figs. 1 and 4A). This period aligns with regional explosive magmatism, producing breccia and ignimbrite with fiamme textures (e.g., Popkhadze et al., 2014; Moritz et al., 2020).

These volcanic successions host the Sakdrisi, Kazreti, Mushevani, and Qvemo Bolnisi deposits and prospects. New data reveal a SW to NE progression of magmatic activity during extension, forming epithermal deposits at ~83.5 Ma in Sakdrisi, ~83.0 Ma in Kazreti and Mushevani, and ~82 Ma or later in Qvemo Bolnisi (Figs. 3C-E and 4B). Moreover, the same ignimbrite unit overlies the Sakdrisi deposit, where it is barren and dated at 83.3 ± 0.4 Ma, but is the main host rock for Au and base metal veins at Kazreti and Mushevani, where it is dated at 83.3 ± 0.5 Ma. This supports the SW to NE younging trend of magmatic and ore forming activity in the Bolnisi District along the central corridor separating the older Beqtakari and Madneuli deposits (Fig. 3). These new insights into mineral system timing and magmatic evolution refine our understanding of the metallogenic history of the Bolnisi District during Late Cretaceous extensional tectonics.

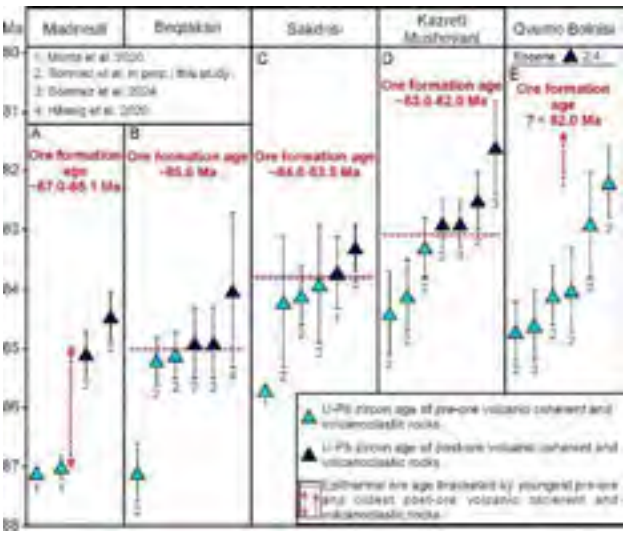


Figure 3. Late Cretaceous epithermal ages of mineral systems and prospects based on U-Pb zircon ages of altered pre-ore and unaltered post-pre volcanic rocks in each locality (Sönmez et al. in prep.).

6.2 Petrogenesis and source characteristics of magmatic rocks

The late Coniacian to early Campanian bimodal magmatism in the Bolnisi District is characterized by coeval felsic and mafic magmatic activity (Moritz et al., 2020). Felsic volcanic rocks exhibit two distinct geochemical signatures with overlapping ages (Fig. 2). For example, chondrite-normalized REE patterns reveal high- and low-HREE concentrations in the felsic volcanic coherent rocks. Similarly, on the La/Sm vs. Sm/Yb diagram, low-HREE rhyolite and rhyodacite demonstrate greater source enrichment compared to their high-HREE

counterparts, despite overlapping ages (Fig. 2D; e.g., Kay and Mpodozis, 2001).

These geochemical characteristics suggest that high-HREE felsic rocks were derived from deep-seated magma chambers, whereas low-HREE felsic rocks originated from shallower, upper crustal chambers (Figs. 3 and 4; e.g., Moritz et al., 2020). This dual geochemical behavior underscores the involvement of two distinct magmatic systems operating simultaneously. The coexistence of such diverse magma chambers provides compelling evidence for a polyphase magmatic history, highlighting their integral role in the generation and evolution of mineral systems in the Bolnisi district. Nevertheless, the role of these distinct felsic rock types in influencing ore formation processes within individual mineral systems remains unclear.

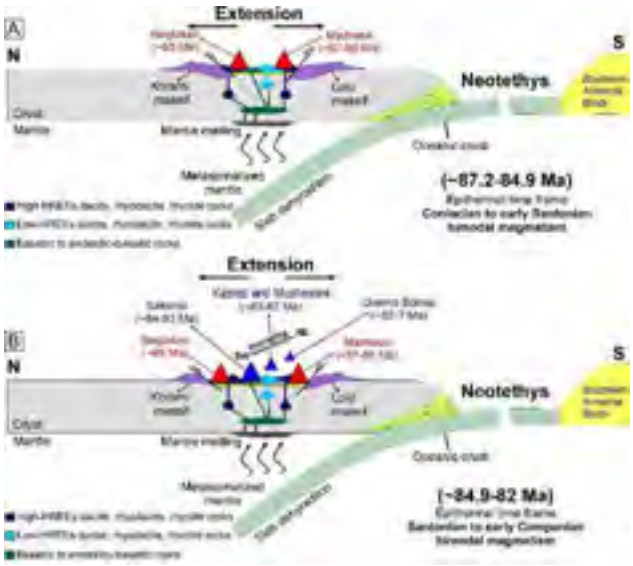


Figure 4. Late Cretaceous mineral systems with respect to the geodynamic evolution of the Bolnisi district (modified after Moritz et al. 2020).

Acknowledgements

The research was funded by the Swiss National Science Foundation grant 200021_188714. Şafak Utku Sönmez acknowledges the support from the student research grant program (Hugh McKistry Fund) of the SEG Foundation. We extend our appreciation to the Rich Metal Group (RMG) company for their support throughout the project. We are also grateful to the expert technical help provided by Jean-Marie Boccard and Antoine de Haller from the University of Geneva during sample preparation, and XRF analyses.

References

Adamia S, Zakariadze G, Chkhotua T, Sadradze N, Tsereteli N, Chabukiani A, Gventsadze A (2011) Geology of the Caucasus: A Review. Turk J Earth Sci 20: 489–544.

Feresin E (2007) Fleece myth hints at golden age for Georgia. Nature 448:846.

Gialli S (2013) The Controversial Polymetallic Madneuli Deposit, Bolnisi District, Georgia: Hydrothermal Alteration and Ore Mineralogy. University of Geneva, Faculty of Earth Science, Geneva, Switzerland: Unpubl MSc thesis.

Golay T (2019) The Sakdrisi Au-Cu deposit, Bolnisi mining district, Georgia: providing a genetic model based on petrographic, geochemical, structural and alteration studies. University of Geneva, Faculty of Earth Science, Geneva, Switzerland: Unpubl MSc thesis.

Hauptmann A, Klein S (2009) Bronze Age gold in Southern Georgia. Archeosciences 33:75-82.

Hässig M, Moritz R, Ulianov A, Chiaradia M, Popkhadze N, Galoyan G, Enukidze O (2020) Jurassic to Cenozoic magmatic and geodynamic evolution of the Eastern Pontides and Caucasus belts, and their relationship with the Eastern Black Sea Basin opening. Tectonics 39:e2020TC006336.

Kay S, Mpodozis C (2001) Central Andean ore deposits linked to evolving shallow subduction systems and thickening crust. Geol Soc Am Today 11:4-9

Lang M, Zhang Z, Chen Z, Cheng Z, Santosh M, Kusky T M (2023) Classification and nomenclature of volcanic rocks using immobile elements: A novel approach based on big data analysis. Lithos 454-455:107274

Lavoie J (2015) Genetic constraint of the Late-Cretaceous Epithermal Beqtakari prospect, Bolnisi Mining District, Lesser Caucasus, Georgia. University of Geneva, Faculty of Earth Science, Geneva, Switzerland: Unpubl MSc thesis.

Moritz R. Melkonyan R. Selby D. Popkhadze N. Gugushvili V. Tayan R. Ramazanov V (2016) Metallogeny of the Lesser Caucasus: From Arc Construction to Postcollision Evolution. Spec Pub Soc Econ Geol 19:157-192.

Moritz R, Popkhadze N, Hässig M, Golay T, Lavoie J, Gugushvili V, Ulianov A, Ovtcharova M, Grosjean M, Chiaradia M, Dumitrica P (2020) At the crossroads of the Lesser Caucasus and the Eastern Pontides: Late Cretaceous to early Eocene magmatic and geodynamic evolution of the Bolnisi district, Georgia. Lithos 378-379:105872

Popkhadze N, Moritz R, Gugushvili V (2014) Architecture of upper Cretaceous rhyodacitic hyaloclastite at the polymetallic Madneuli deposit Lesser Caucasus, Georgia. Central Eur J Geosci 6:308-329.

Ross PS, Bédard JH (2009) Magmatic affinity of modern and ancient subalkaline volcanic rocks determined from trace-element discriminant diagrams. Can J Earth Sci 46:823–839.

Sun SS, McDonough WF (1989) Chemical and isotopic systematics of oceanic basalts: implications for mantle composition and processes. Geol Soc Spec Publ 42:313-345

Sönmez ŞU, Paul AN, Popkhadze N, Ulianov A, Moritz R (2024) Screening Apatite for Potential Use as a U-Pb Geochronometer in Zircon-Poor Magmatic Rocks: Age of Late-Stage Alkaline Magmatism in the Bolnisi District, Georgia. CJMP 783-819.

Sönmez ŞU, Moritz R, Lavoie J, Ulianov A, Turlin F, Popkhadze N, Natsvlishvili M, Spangenberg J (2022) Magmatic and metallogenic evolution of the Late Cretaceous Beqtakari epithermal deposit, Bolnisi District, Lesser Caucasus, Georgia. XXII International Congress of the CBGA Plovdiv, Bulgaria (p. 363).

Vashakidze S. Gugushvili V (2006) Geological map of Bolnisi district (1: 50 000). Caucasian Institute of Mineral Resources, Tbilisi, Georgia.

Winchester JA, Floyd PA (1977) Geochemical discrimination of different magma series and their differentiation products using immobile elements. Chem Geol 20:325-343.

Revisiting the classic Tonopah Ag-Au district, Nevada

Cristy Stoian[1], Thomas Monecke[1], William Howald[2], Christopher Leslie[3], Peter Vikre[4], Mathias Burisch[1]
[1]*Department of Geology and Geological Engineering, Colorado School of Mines, Golden, Colorado, USA*
[2]*Blackrock Silver Corp., 200 Burrard Street, Vancouver, British Columbia, Canada*
[3]*Summa Silver Corp., 1030 West Georgia Street, Vancouver, British Columbia, Canada*
[4]*U.S. Geological Survey, Reno, Nevada, USA*

Abstract. New petrographic and geochemical data from the Tonopah Ag-Au intermediate-sulfidation epithermal district, Nevada, reveals systematic zoning of Ag/Au and Ag/base metals that reflect systematic physical and chemical changes along the fluid flow path. The geochemical database includes data from 164 recent drill holes, spread across the entire district. Preliminary petrographic observations recognize quartz, adularia, and sericite as the most abundant gangue minerals. Electrum and native silver occur as inclusions in sulfide minerals. Sulfide minerals include acanthite, polybasite, sphalerite, galena, and chalcopyrite. The district-scale preliminary analysis of geochemical data implies a systematic lateral decrease of Ag/Au away from the main Ag zones, suggesting decoupling of precious metals. The Ag/base metals ratio increase toward the center and decrease with paleodepth.

1 Introduction

Epithermal deposits have long been a valuable source of precious metals. Based on tectonic setting, origin and evolution of the hydrothermal fluids, and ore and gangue mineralogy, low-, intermediate-, and high sulfidation types are distinguished (Hedenquist 1987). Intermediate sulfidation (IS) epithermal deposits, introduced by Hedenquist et al. (2000), are characterized by quartz and adularia and may contain platy calcite or rhodochrosite. In contrast to low-sulfidation deposits, IS contain variable amounts of base metal sulfides such as tetrahedrite-tennantite, galena, sphalerite, chalcopyrite, and pyrite (Hedenquist and Sillitoe 2003; Simmons et al. 2005; Wang et al. 2020).

The historic Tonopah mining district, in west-central Nevada, is host to classical examples of IS epithermal deposits (Fig. 1; John et al. 1991; Hedenquist and Sillitoe 2003) with a total production of 174.2 Moz Ag and 1.9 Moz Au since its discovery in 1900 (Barker 1986). Gold and silver ores are confined to quartz veins, related to one of five stages of volcanism in the region (Silberman et al. 1978). Volcanism in the district occurred from 26 Ma to 10 Ma. John et al. (2022) provided a detailed study of volcanic rocks in the area and delineated the structure of the Tonopah caldera complex, which hosts the epithermal vein swarms.

Despite its long history of mining, the Ag-Au mineralization at Tonopah has not been studied in detail. Previous work suggested a systematic trend of decreasing Ag/Au away from the central Mizpah zone (Nolan 1935; John et al. 2022). Recent district-wide exploration efforts at Tonopah provide a unique opportunity to study new drill core and to better understand district-scale mineralogical and geochemical zoning and their underlying processes or fluid evolution.

2 Geologic Background

2.1 The Walker Lane Trend

Tonopah is located at the southeastern tip of the Walker Lane Trend, which parallels the Nevada and California border (Fig. 1). There are three major igneous suites within the Walker Lane Trend, namely the interior rhyolite-andesite assemblage, the western andesite assemblage, and the bimodal basalt-rhyolite assemblage (John 2001). Many compiled studies with various Ar^{40}/Ar^{39} analyses provided ranges of emplacement for each assemblage (McKee et al. 1970; John 2001). The interior rhyolite-andesite assemblage, which is comprised of rhyolitic to dacitic ash tuffs and rhyolitic to andesitic lava flow domes, was emplaced from 43 Ma to 19 Ma (Ar^{40}/Ar^{39} geochronology; Brooks et al. 1995). The western andesite assemblage is made up of high potassium calc-alkaline lava flows, breccias, and hypabyssal intrusions, and formed between 22 Ma to 4 Ma (McKee 1971). Both assemblages were formed by subduction-related volcanism. The bimodal basalt-rhyolite assemblage, which is associated with Basin and Range extension, began at 16.5 Ma and has continued since.

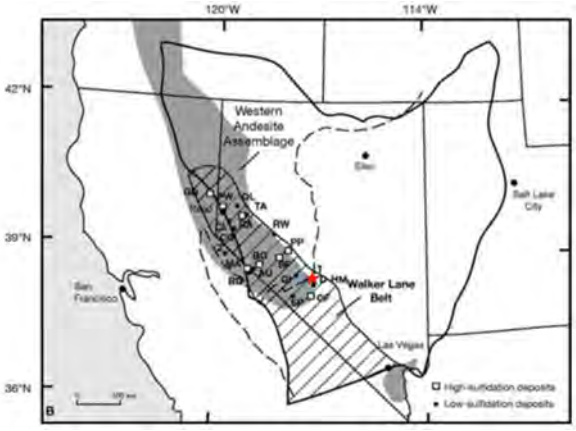


Figure 1. Map of the western United States highlighting the Walker Lane Trend, shown in stripes, the western andesite assemblage, shown in dark gray, and epithermal deposits (modified from John 2001). Tonopah is marked with a red star

2.2 The Tonopah Mining District

Lithologic units in the Tonopah district belong to the western andesite assemblage (John 2001). The main lithologic units in the district are a series of lava

flows and ash tuffs of andesitic to rhyolitic composition that overlay granodioritic basement rocks and older andesites (Fig. 2; John et al. 2022).

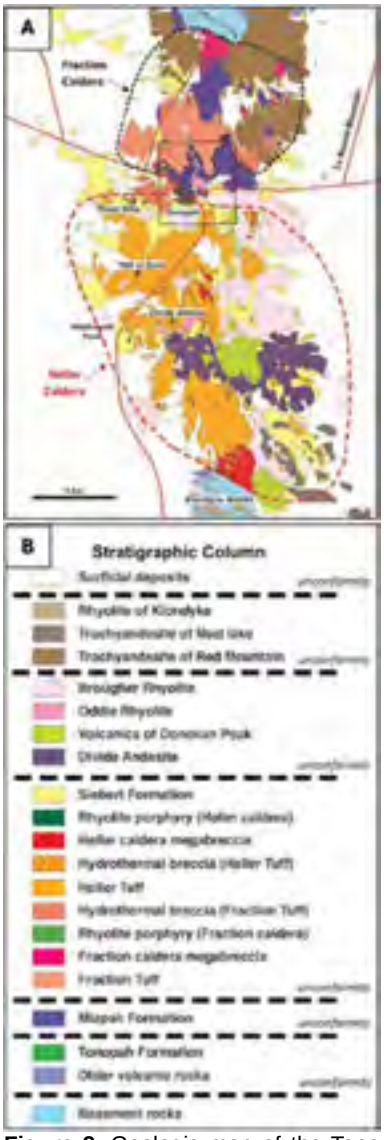


Figure 2. Geologic map of the Tonopah district and the surrounding area, from John et al. (2022)

Pre- and syn-ore volcanic units include the Tonopah Formation, West End Rhyolite, Extension Breccia, and Mizpah Andesite (Todd et al. 2024), which are the main host to Ag-Au veins. The volcanic units are comprised of silicic lava flows and tuffs, volcaniclastic breccias and flows, rhyolite tuffs, and andesitic to dacitic lavas, flow domes, and minor debris flows. These units range in age from ~22 Ma to ~21 Ma, according to Ar^{40}/Ar^{39} and U-Pb analyses by du Bray et al. (2019a). Vein formation, which has been dated via $^{40}Ar/^{39}Ar$ geochronology, occurred between 21 Ma and 20 Ma (du Bray et al. 2019b).

Post-ore volcanic units include the Siebert Formation, the Fraction Tuff, Heller Tuff, Oddie Rhyolite, and the Brougher Rhyolite. These units are comprised of rhyolitic to trachydacitic ash-flow tuffs and younger sedimentary rocks. The Oddie and Brougher rhyolites are intrusions, which date from ~17.29 Ma to ~16.55 Ma.

High-grade ore zones are mainly associated with quartz-adularia veins that have variable strike and dip. The veins generally dip northward towards the Fraction Caldera, with dip angles between 30º and 75º, though each individual vein may vary in dip up to 15º (Todd et al. 2024). Vein thickness varies from centimetres to tens of meters, with average thickness of 4 m. The strike length of the veins is also variable, but economically significant veins typically have strike lengths of several hundred meters. Ore may also occur as vein-related breccia zones. Common sulfide minerals are pyrite, chalcopyrite, sphalerite, galena, and acanthite. Historic mining records also include polybasite, pyrargyrite, and stephanite as principal silver minerals, while gold occurs as electrum (Spurr 1903).

Complex faulting is present throughout the district, however the Halifax Fault, which runs through the center of the district, seperates the Tonopah district into the Hughes Project, currently owned by Summa Silver Corp, and Tonopah West, currently owned by Blackrock Silver Corp. Both companies have completed recent drilling campaigns, yielding new diamond drill core which has been logged and assayed. This newly acquired information is used for this study to determine ore-forming processes within both sides of the district.

3 Methods and Results

3.1 Methods

Drill data from both sides of the district were compiled and used to create a 3D model of the Tonopah District. Geochemical data from assays were included to constrain geochemical zoning and related fluid flow pathways across the district. Samples were collected from 164 diamond drillholes spread across the district, covering a 3.3 by 10 km extent. Thin sections were prepared to determine mineral associations within the district. Petrographic analyses were completed on a Leica DM2700 P microscope. Tonopah West drill core was assayed for 50 elements by American Assay Laboratories. Gold was assayed using a fire assay method, and all other elements were assayed using a 5-acid digestion and either ICP-MS or -OES finish. Samples with Ag over the detection limit were quantified with gravimetric finish. Assay data were used for modelling in Leapfrog software with corresponding drillhole information and lithology.

3.2 Preliminary Results

Mineralized sulfide-quartz veins within the Tonopah district ranges from a few hundred to several thousand g/t of Ag. Preliminary evaluation of the geochemical data implies a systematic trend of decreasing Ag/Au away from the main ore zones (Fig. 3). The As/Sb ratio shows an opposite trend with higher

Sb concentration in Ag rich zones and As enriched more distally.

Geochemical zoning on both the western and eastern sides of the Tonopah district show higher precious metal concentrations in shallower zones and higher base metals in deeper zones. Silver and Au are decoupled, resulting in Ag/Au ratios decreasing laterally away from the main ore zones.

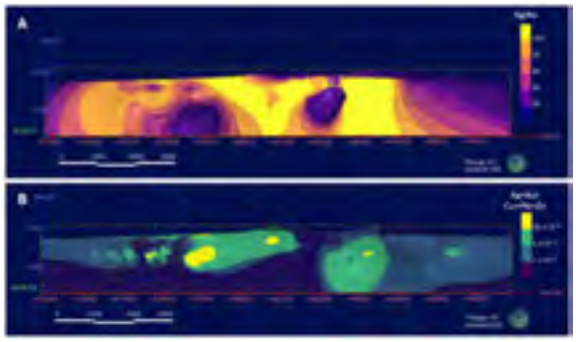


Figure 3. Cross-sections of the Tonopah district. A) Cross-section showing Ag/Au ratios across the district. B) Cross-section showing precious over base metals

Drill core from Tonopah West shows veins with varying sulfide and quartz textures (Fig. 4). Veins contain abundant colloform layers with varying quartz textures, sulfide associations, and grade. The main sulfides in Tonopah West are pyrite, chalcopyrite, galena, and sphalerite, and the main silver minerals are acanthite and polybasite-pearceite (Fig. 5). Electrum and rare native silver are present as well. Gold only occurs as electrum. Major gangue minerals in the deposit are quartz, adularia, and sericite.

The quartz, sericite, and adularia commonly form masses and bands at the vein selvages. Quartz is fine-grained, typically 50 µm in diameter. Sericite is generally disseminated with masses of quartz. Adularia forms grains 75 to 125 µm, typically concentrated at the rim of the veins.

A major sulfide mineral association seen in thin sections from the center high Ag/Au zone of the district consists of electrum and various sulfides, such as sphalerite, galena, acanthite, and pyrite. Electrum is also present and typically forms grains ≥25 µm and is frequently enclosed in pyrite and other sulfides (Fig. 5A). Pyrite is typically anhedral and may be encased by most of the other sulfides. Galena and sphalerite are commonly associated with each other (Fig. 5D). Sphalerite color may range from reddish tan to almost colorless in transmitted light, indicating higher to lower Fe concentrations, respectively. Sulfides generally range from 50 µm to 300 µm in grain size.

Silver-bearing sulfides and chalcopyrite concentrate in the center of the vein and in cavities and are intergrown with abundant quartz. They mainly comprise acanthite and polybasite, which is accompanied by chalcopyrite (Fig. 5E, F). Acanthite and polybasite are typically fine-grained, having grain sizes less than 20 µm. In this mineral association, quartz grains have commonly a lattice-like habit with ~150 µm in length. Quartz may also be present as comb quartz, typically lining the edge of veins, growing into empty space. These comb quartz crystals may reach up to 500 µm.

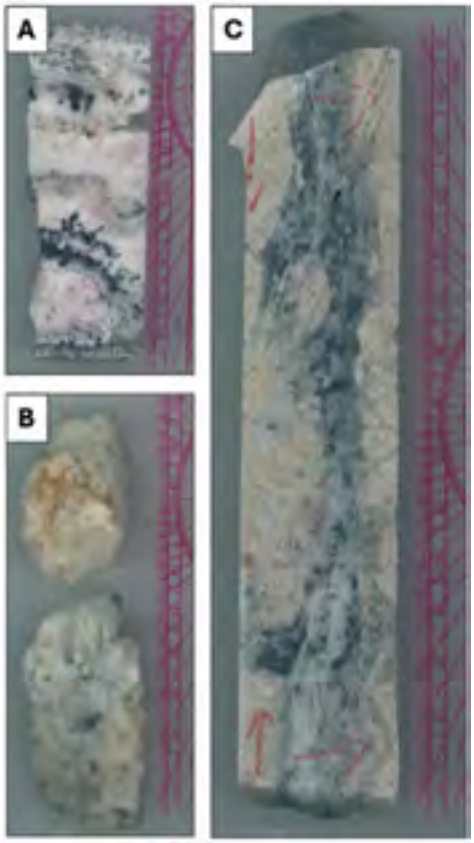


Figure 4. Scanned drill core from the western side of the Tonopah district. A) Drill core showing bands of sulfides followed by bands of coarse comb quartz. B) Lattice quartz with dispersed sulfides. C) A quartz-sulfide vein running through rhyolite

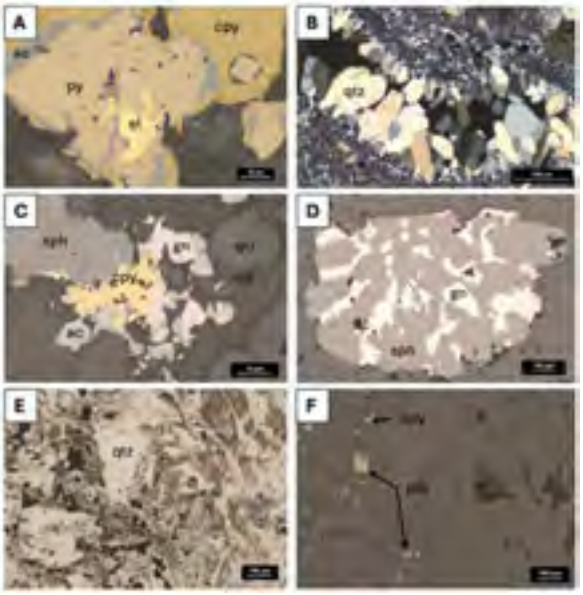


Figure 5. Thin section images from the western side of the Tonopah district. A) Electrum and sulfides mineral association with electrum contained by cubic pyrite, as well as

acanthite and chalcopyrite (reflected light). B) Comb quartz (crossed polarized transmitted light). C) Major ore mineral association showing the relationship between chalcopyrite, galena, acanthite, and sphalerite (reflected light). D) Sphalerite intergrown with galena (reflected light). E) Lattice-texture quartz (transmitted light). F) The same view as E in reflected light. Ore minerals shown in between lattice quartz are polybasite and chalcopyrite. Abbreviations: ac-acanthite, cpy-chalcopyrite, el-electrum, py-pyrite, qtz-quartz, gn-galena, and plb-polybasite

5 Discussion and Conclusions

The main silver minerals at Tonopah are acanthite and polybasite. Gold is present as electrum. Other minerals include sphalerite, galena, pyrite, and chalcopyrite, as well as minor digenite. Gangue minerals include quartz, sericite, and adularia. Lattice quartz textures provide evidence for boiling and/or flashing. Banded veins with varying ore mineralogy, however, may be evidence for silica recrystallization and flashing events in between crystallization of each band (Terry et al. 2021). Not only do mineral associations vary with bands, but with location within the district as well. Generally, the amount of base metal sulfides and sulfosalts is relatively low at Tonopah compared to other IS systems such as Fresnillo (Albinson et al. 2001).

District-scale evaluation of geochemical data reveals zoning patterns of Ag/Au and Ag/base metals that reflect systematic physical and chemical changes along the fluid flow path (Fig. 3). A better understanding of these geochemical gradients may provide important clues to better understand ore forming processes and may be useful for exploration targeting.

Acknowledgements

The authors thank Blackrock Silver Corp. and Summa Silver for allowing us to use their geochemical data, providing access to sample material, and support during field work. We also thank Paul Henderson for additional work on Tonopah East.

References

Albinson T, Norman DI, Cole D, Chomiak B (2001) Controls on Formation of Low-Sulfidation Epithermal Deposits in Mexico: Constraints from Fluid Inclusion and Stable Isotope Data. Society of Economic Geologists, pp 1–32

Barker WB (1986) The Tertiary Igenous Terrain in the Vicinity of the King Tonopah Mine, Tonopah, Nevada: An Exploration Case Study (ECONOMIC GEOLOGY, EXPLORATION) - ProQuest. University of Arizona

Brooks WE, Thorman CH, Snee LW (1995) The 40Ar/39Ar ages and tectonic setting of the middle Eocene northeast Nevada volcanic field. Journal of Geophysical Research: Solid Earth 100:10403–10416. https://doi.org/10.1029/94JB03389

du Bray EA, John D, Vikre PG, et al (2019a) Petrographic, geochemical, and geochronologic data for cenozoic volcanic rocks of the Tonopah, Divide, and Goldfield Mining Districts, Nevada. US Geological Survey

du Bray EA, John DA, Colgan JP, et al (2019b) Petrology of volcanic rocks associated with silver-gold (Ag-Au) epithermal deposits in the Tonopah, Divide, and Goldfield Mining Districts, Nevada

Hedenquist JW (1987) Volcanic-related hydrothermal systems in the Circum-Pacific Basin and their potential for mineralisation. Mining Geology 37:347–364

Hedenquist JW, Arribas A, Gonzalez-Urien E (2000) Exploration for epithermal gold deposits. In: Reviews in Economic Geology. pp 1–33

Hedenquist JW, Sillitoe RH (2003) Linkages between volcanotectonic settings, ore-fluid compositions, and epithermal precious metal deposits. Volcanic, geothermal, and ore-forming fluids 315–343

John D, Nash JT, Plouff D, Whitebread DH (1991) The Conterminous United States Mineral Appraisal Program; background information to accompany folio of geologic, geochemical, geophysical, and mineral resources maps of the Tonopah 1 by 2 degree Quadrangle, Nevada. US Geological Survey,

John DA (2001) Miocene and early Pliocene epithermal gold-silver deposits in the northern Great Basin, western United States: Characteristics, distribution, and relationship to magmatism. Economic Geology 96:1827–1853

John DA, Colgan JP, Vikre PG, et al (2022) Ancestral Cascade Arc Magmatism, Extensional Tectonics, and Miocene Epithermal Silver-Gold Deposits near Tonopah, Nevada: New Ideas About Old Districts: presentation to the Geol. In: Society of Nevada Symposium Program with Abstracts. p 88

McKee EH (1971) Tertiary Igneous Chronology of the Great Basin of Western United States–Implications for Tectonic Models. Geol Soc America Bull 82:3497. https://doi.org/10.1130/0016-7606(1971)82[3497:TICOTG]2.0.CO;2

McKee EH, Noble DC, Silberman ML (1970) Middle Miocene hiatus in volcanic activity in the Great Basin area of the Western United States. Earth and Planetary Science Letters 8:93–96. https://doi.org/10.1016/0012-821X(70)90156-1

Nolan TB (1935) The underground geology of the Tonopah mining district, Nevada. University of Nevada

Silberman ML, Bonham HF, Garside LJ, Ashley RP (1978) Radiometric ages of volcanic and plutonic rocks and hydrothermal alteration-mineralization in the Tonopah mining district and vicinity, Nye and Esmeralda counties, Nevada. US Geological Survey

Simmons SF, White NC, John DA (2005) Geological characteristics of epithermal precious and base metal deposits. In: Economic Geology 100th Anniversary Volume. Society of Economic Geologists, pp 485–522

Spurr JE (1903) The Ore deposits of Tonopah, Nevada. Washington: Government Printing Office

Terry LR, Monecke T, Reynolds TJ, et al (2021) Textural characteristics of barren and mineralized colloform quartz bands at the low-sulfidation epithermal deposits of the Omu camp in Hokkaido, Japan: Implications for processes resulting in bonanza-grade precious metal enrichment. Economic Geology 116:407–425

Todd R, Bickel J, Manning T, et al (2024) Preliminary Economic Assessment of Mineral Resources, Tonopah West Silver-Gold Project NYE AND ESMERALDA COUNTIES, NEVADA, USA. Blackrock Silver Corp

Wang L, Qin K, Song G, et al (2020) Geology and genesis of the Early Paleozoic Zhengguang intermediate-sulfidation epithermal Au-Zn deposit, northeast China. Ore Geology Reviews 124:103602

Igneous Amphibole and Apatite from the Grasberg Porphyry Cu-Au Deposit, Indonesia: Insights into the magmatic degassing of volatiles

Adi Sulaksono[1,2], Shogo Aoki[2], Takuya Echigo[2], Yasushi Watanabe[2], Antonio Arribas[3]
[1]PT Geo Fix Indonesia, South Jakarta, Indonesia
[2]Akita University, Akita, Japan
[3]University of Texas at El Paso, Texas, USA

Abstract. We explore how magma evolution and redox conditions affected the degassing of Cl- and S-bearing fluids from the source magma at Grasberg, based on the chemistries of amphibole and apatite obtained using electron microprobe (EPMA) and laser ablation inductively coupled plasma mass spectrometry (LA-ICP-MS). The combined physical and chemical data indicate that a less oxidized magma batch was injected into a strongly oxidized, Main Grasberg Intrusion (MGI)-related upper-crustal magma chamber, forming a hybrid magma from which the syn-mineral Early Kali Intrusion (EKI) porphyry was derived. The degassing of Cl from both the MGI and EKI magmas is likely related to the crystallization of phenocrysts in the upper crust. In contrast, the partitioning of S from the EKI magma into fluids may involve another process prior to the crystallization of phenocrysts in the upper-crustal magma chamber. We suggest that the mixing of magmas with distinct oxidation states could have generated SO_2 through the reduction of sulfate from the oxidized magma via oxidation of Fe^{2+} derived from the reduced or less oxidized magma.

1 Introduction

Chlorine and S are critical elements in porphyry-related fluids due to their role in complexing, transporting, and precipitating metals (Candela and Holland 1984; Tattitch and Blundy 2017). We present igneous mineral paragenesis and compositions of amphibole to establish the physicochemical conditions of the parent magmas. The available calibrated thermodynamic apatite/melt S and Cl partitioning models are applied to monitor fluctuations in volatile concentrations in the melt during magma evolution. The combined physical and chemical data are then used to discuss the evolution of the magma and the mechanisms that govern the separation of metalliferous fluids from the melt.

2 Geology

The Grasberg porphyry Cu-Au deposit is the world's largest Au-rich porphyry Cu deposit (Cooke et al. 2005) located in the Ertsberg-Grasberg mineral district in the Indonesian province of Papua, on the western half of the island of New Guinea. The district lies within the Central Range fold-and-thrust belt of the New Guinea island (Fig. 1a). This district contains deformed Cretaceous and Tertiary sedimentary rocks (Fig. 1b; Leys et al. 2012) that are cut by Pliocene intrusions.

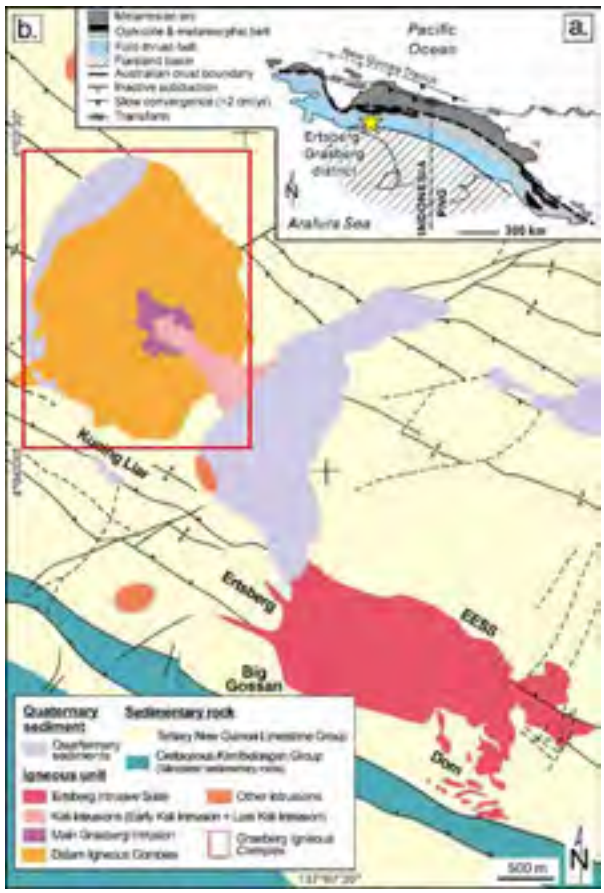


Figure 1. a. Lithotectonic map of the island of New Guinea (modified from Sapiie and Cloos 2004). **b.** Geological map of the Erstberg-Grasberg district modified from Leys et al. (2012). Also shown are locations of skarn ore bodies: Kucing Liar, Ertsberg, Ertsberg East skarn system (EESS), Big Gosan and Dom.

Most of the porphyry-style mineralization in the Grasberg-Ertsberg district is associated with Pliocene igneous breccias and intrusions of the Grasberg Igneous Complex (Peterson and Cloos 2005) that were emplaced into mainly siliciclastic Cretaceous Kembelangan Group and carbonate-dominated Tertiary New Guinea Limestone Group rocks (Fig. 1b; Leys et al. 2012). The Grasberg Igneous Complex consists of four igneous units (MacDonald and Arnold 1994; Wafforn 2017) such as 1) Pre-mineral Dalam Complex (Dalam) consisting by minor subaerial volcanics, near-surface breccias, and intrusions (3.60 and 3.30 Ma), 2) MGI (3.22 ± 0.04 Ma) immediately before the

mineralization, 3) the syn-mineral EKI (3.20 ± 0.04 Ma), and 4) the post-mineral Late Kali Intrusion (LKI; 3.09 ± 0.05 Ma). Field relationships indicate that porphyry Cu-Au mineralization closely post-dates the MGI, overlaps the EKI and predates the LKI (Leys et al. 2012).

3 Samples and analytical methods

Eight unaltered igneous rock samples from the MGI, EKI, and LKI were collected from below the Grasberg mineralization zone. Major and minor elements in amphibole and apatite were analyzed using a JEOL® JXA-8230 SuperProbe at Akita University with an accelerating voltage of 15 kV, a 20 nA beam current, and a 5 µm electron beam size. Astimex Inc. calibration standards for amphibole were fluorite (F), jadeite (Na), periclase (Mg), An65 plagioclase (Al and Ca), quartz (Si), tugtupite (Cl), orthoclase (K), rutile (Ti), rhodonite (Mn), and hematite (Fe). For apatite, the standards included fluorite (F), albite (Na), periclase (Mg), An65 plagioclase (Al and Ca), quartz (Si), apatite (P), celestite (S), tugtupite (Cl), rutile (Ti), and rhodonite (Mn). All analytical data were corrected using the ZAF matrix-correction program. For apatite, a pulse height analyzer (PHA) was used to avoid overlap between S and F.

Amphibole trace element analyses were conducted at Okayama University of Science using a Thermo Fisher Scientific iCAP-RQ single-collector quadrupole ICP-MS coupled to a Teledyne Cetac Technologies Analyte G2 ArF excimer laser ablation system equipped with a HelEx 2 volume sample chamber. NIST SRM-610 was used as the primary standard. The repetition rate, energy and laser diameter were 5 Hz, 7.92 mJ/cm2 and 35 µm, respectively.

4 Results

4.1 Amphibole composition

Homogeneous amphiboles of the MGI (Fig. 2a), EKI, and LKI are principally low-Al (Al^{tot} of 0.35–1.04 apfu) magnesiohornblende (hereafter referred to as “low-Al amphibole”). Heterogeneous amphiboles of the EKI (Fig. 2b) show a chemically distinct core and rim. The cores are magnesiohastingsite with Al^{tot} ranging from 1.53 to1.80 apfu (hereafter referred to as “high-Al amphibole”). In contrast, the rims are low-Al amphibole containing 0.93–1.03 apfu Al^{tot}.

The high-Al amphiboles of the EKI show higher total REE, Y, Cu, Li, V, Sr, Nb, Ba and Pb contents than the low-Al amphiboles. All high-Al amphiboles of the EKI have a narrow range in normalized values of REE (REE_N). They show a convex upward pattern (Fig. 3a) with maxima of approximately 130–220 and 120–210 times chondrite at Pr and Nd, respectively. The low-Al rims have a wider range of REE_N values than the high-Al core and show a convex downward pattern, similar to the associated homogeneous low-Al amphibole.

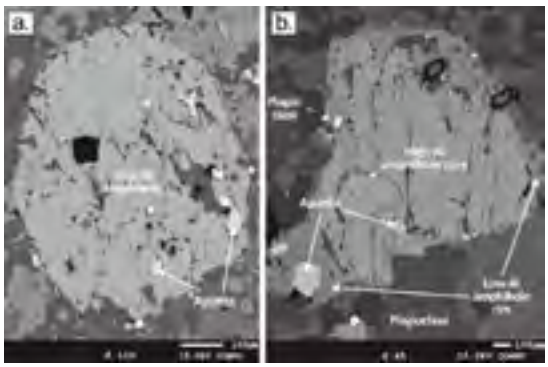


Figure 2. Back-scattered electron images of amphibole phenocrysts: **a.** Homogeneous amphibole from the MGI. **b.** Heterogeneous amphibole showing an Al-rich core and Al-poor rim in the EKI sample. Note the apatite inclusions in both the high-Al core and low-Al rim.

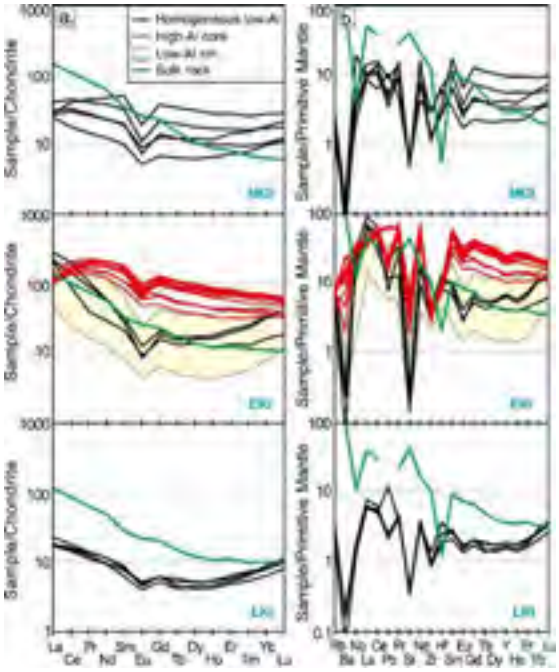


Figure 3. a. Chondrite-normalized REE patterns for amphibole and whole-rocks. **b.** Trace element patterns for whole-rock and amphibole normalized to primitive mantle values of Sun and McDonough (1989).

Trace element compositions of high-Al and low-Al amphiboles also differ on primitive mantle-normalized diagrams, where the low-Al amphiboles have large negative anomalies in large-ion lithophile elements such as Ba and Sr and low MREE and Y compared with the high-Al amphiboles (Fig. 3b).

4.2 Apatite composition

In the MGI sample, apatites associated with low-Al amphibole and plagioclase and apatites within the groundmass are all chemically similar based upon measured SO_3 and Cl concentrations (0.07–0.44 wt.% SO_3 and 0.79–1.09 wt.% Cl). In contrast, various apatites from the EKI fall into distinct populations in the SO_3 vs. Cl concentrations diagram. Apatite inclusions in high-Al amphiboles have highest Cl concentrations ranging from 0.68 to

1.01 wt.% with moderate SO_3 contents (0.19–0.39 wt.%), whereas apatite crystals associated with low-Al amphibole and plagioclase contain 0.15–0.34 wt.% SO_3 and 0.58–0.79 wt.% Cl. The groundmass apatites have SO_3 and Cl concentrations of 0.16–0.38 and 0.52–0.71 wt.%, respectively. In the LKI, groundmass apatites show a similar SO_3 and Cl concentrations (0.20–0.57 wt.% SO_3 and 0.68–0.96 wt.% Cl) with those associated with phenocrysts (0.20–0.52 wt.% SO_3 and 0.59–0.98 wt.% Cl).

5 Discussion

5.1 Amphibole and apatite crystallizations

The amphibole geothermobarometry (Ridolfi et al. 2010; Mutch et al. 2016) applied to the low-Al amphibole from the syn-mineral MGI showed approximate crystallization T and P of 730–700 (avg. 710) °C and 1.1–0.7 (avg. 1.0) kbar, respectively. Amphibole-plagioclase thermometry of Anderson (1996) indicates a remarkably similar crystallization T range of 720–700 °C. The syn-mineral EKI contains amphiboles with a chemically distinct disequilibrium texture of core and rim; the high-Al cores are estimated to have formed at approximately 900–850 (avg. 880) °C and 4.3–3.3 (avg. 4.0) kbar, whereas the low-Al rims and associated low-Al amphibole phenocrysts crystalized at 790–720 (avg. 760) °C and 1.9–1.0 (avg. 1.6) kbar. The low-Al amphiboles from the post-mineral LKI crystallized at 750–700 (avg. 720) °C and 1.4–0.9 (avg. 1.1) kbar.

Fractionation of high-Al amphibole may have reduced the middle REE (MREE) contents of residual melts because amphibole is the major host of MREE (Rohrlach & Loucks 2005; Watanabe et al. 2016). All EKI low-Al amphiboles are depleted in the MREE compared with the high-Al amphiboles, confirming that the low-Al amphibole was formed at lower T and P than those of high-Al amphibole.

The combined T-P estimates indicate that the low-Al amphiboles crystallized in an upper-crustal magma chamber at approximately 5 km depth, whereas the high-Al amphibole in the deeper zone at approximately 15 km depth (mid-crustal zone). These data lead to the following model of magma crystallization. A magma batch containing high-Al amphibole was injected into the bottom of the MGI upper-crustal magma chamber. The MGI porphyry magma rose soon after such an injection. The younger EKI was derived from the mixed magma, as evidenced by the disequilibrium texture of amphibole hosted by the porphyry.

Some apatite crystals appear to have equilibrated chemically with low-Al amphibole (Fig. 2). Apatite in the groundmass may have crystallized both in the upper-crustal magma chamber and from the residual melt after phenocryst crystallization, towards the end of magma solidification. In particular, EKI contains apatite that occurs as inclusions in high-Al amphibole (Fig. 2b). This occurrence suggests that the apatite formed at a depth of ~15 km prior to the mixing of the MGI upper-crustal magma and high-Al amphibole-bearing, deep-sourced magma.

5.2 Evolution of the oxidation state of magmas

The application of geothermobarometry equation by Ridolfi et al. (2010) shows that the low-Al amphiboles from the syn-mineral MGI record an oxidized condition of approximately FMQ+3.4. A less oxidized (FMQ+1), deep-sourced magma batch injected into such a strongly oxidized upper-crustal magma chamber as indicated by high-Al amphiboles contained in the syn-mineral EKI. This mixing produced a hybrid magma with fO_2 of approximately FMQ+2.7, from which the EKI porphyry was derived. This process is strongly evidenced by the EKI amphiboles that have a disequilibrium texture of high-Al core (FMQ+1) and low-Al rim (FMQ+2.7).

The amphibole fO_2 estimates agree with V concentration in both high-Al and low-Al amphiboles. Vanadium partitioning between amphibole and melt is related to magma fO_2, becoming more compatible in amphibole crystallized as V^{3+} from a more reduced magma (Iveson et al. 2018). The EKI high-Al amphiboles contain high V (280–392 ppm) compared with the low-Al amphiboles from all samples (139–241 ppm), confirming that the EKI high-Al amphibole crystallized at lower fO_2 than low-Al amphibole.

5.3 Magmatic degassing of volatiles

The melt S and Cl concentrations were computed based on their apatite/melt partitioning of Parat el al. (2011) and Li and Hermann (2017), respectively (Fig. 4). The changes in melt Cl and S concentrations calculated from apatite chemistry indicate a degassing sequence which can be divided into: 1) degassing of Cl from the MGI magma after low-Al amphibole and plagioclase phenocrysts crystallizations, 2) degassing of S from the EKI magma at ~800 °C and ~2 kbar, prior to the crystallizations of low-Al amphibole and plagioclase, and 3) degassing of Cl from the EKI magma after low-Al amphibole and plagioclase crystallizations.

During the syn-mineral magmatism, magmatic degassing of Cl occurs following the crystallization of phenocryst, whereas the partitioning of S from magma into fluids requires another process that occurs at higher P and T (e.g., at ~800 °C and ~2 kbar). We suggest that mixing of magmas of two distinct oxidation states could have generated SO_2 by the reduction of sulfate via oxidation of Fe^{2+}. The reaction occurred as the following equation: $CaSO_4 + 2FeO = CaO + SO_2 + 2FeO_{1.5}$ (Dilles et al. 2015), where in the case of Grasberg, the MGI upper-crustal magma chamber provided sulfate, whereas large amounts of Fe^{2+} were derived from the injected reduced or less oxidized magma (Fig. 5). Although the MGI upper-crustal magma is more oxidized than that of the EKI, anhydrite in the MGI is remarkably less abundant. This indicates that anhydrite was decomposed to generate SO_2.

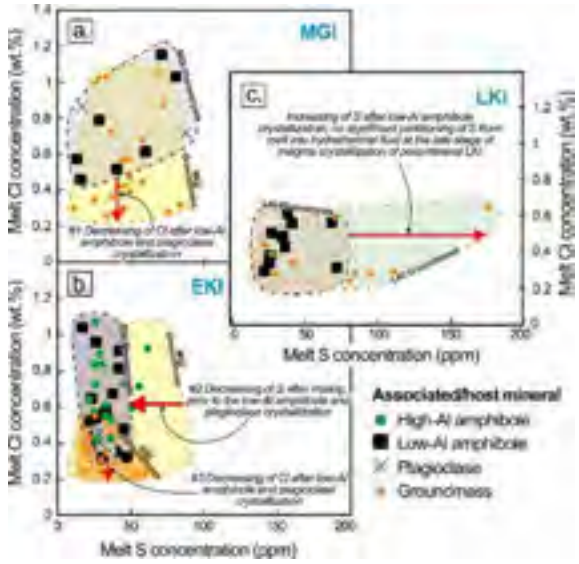


Figure 4. Plots of calculated melt S vs. Cl concentrations based on apatite composition for **a.** MGI, **b.** EKI, and **c.** LKI.

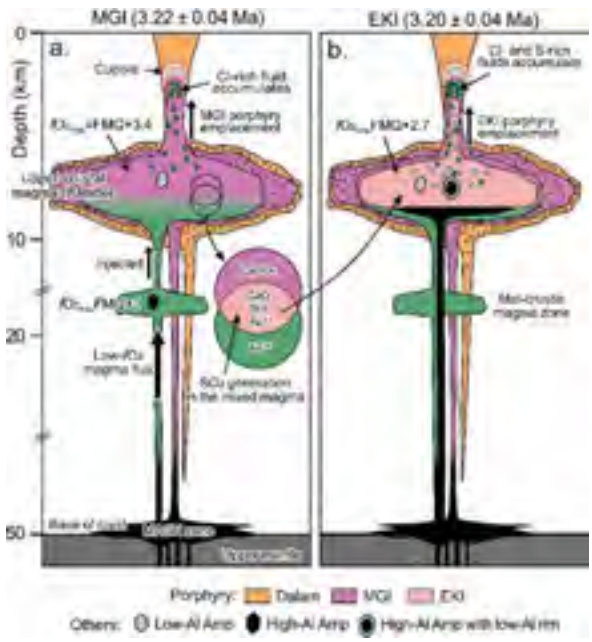


Figure 5. Conceptual model of syn-mineralization magmatic processes related to the degassing of volatiles and their accumulation in a pocket beneath the cupola. **a.** degassing of Cl from the MGI magma after phenocryst crystallizations. Mixing of magmas of two distinct oxidation states generate SO_2 via the oxidation of Fe^{2+}. **b**. SO_2-rich fluid degassed from the mixed magma prior to phenocryst crystallization, followed by Cl-rich volatiles after phenocrysts had already crystallized.

Magmatic degassing that occurred intermittently at Grasberg implies that localized accumulation of ore-forming fluids before a sudden discharge is required for an efficient hydrothermal system.

Acknowledgements

This project was financed by the Government of Japan and completed with the support of PT Freeport Indonesia and PT Eksplorasi Nusa Jaya.

References

Anderson JL (1996) Status of thermobarometry in granitic batholiths. Geological Society of America Special Paper 315:125–138.

Candela PA, and Holland HD (1984) The partitioning of copper and molybdenum between silicate melts and aqueous fluids. Geochim Cosmochim Acta 48:373–380.

Cooke DR, Hollings P, Walshe L (2005) Giant porphyry deposits: characteristics, distribution, and tectonic controls. Econ Geol 100:801–818.

Dilles JH, Kent AJR, Wooden JL, Tosdal RM, Kolezar A, Lee RG, Farmer LP (2015) Zircon compositional evidence for sulfur-degassing from ore-forming arc magmas. Econ Geol 110:241–251.

Iveson AA, Rowe MC, Webster JD, Neill, OK (2018) Amphibole-, clinopyroxene- and plagioclase- melt partitioning of trace and economic metals in halogen-bearing rhyodacitic melts. J Petrol 59:1579–1604.

Leys CA, Cloos M, New BTE, MacDonald GD (2012) Copper-gold±molybdenum deposits of the Ertsberg-Grasberg district, Papua, Indonesia. Soc Econ Geol Spec Pub 16:215–236.

Li H, Hermann J (2017) Chlorine and fluorine partitioning between apatite and sediment melt at 2.5 GPa, 800 °C: a new experimentally derived thermodynamic model. Am Min 102:580–594.

MacDonald GD, Arnold LC (1994) Geological and geochemical zoning of the Grasberg Igneous Complex, Irian Jaya, Indonesia. J Geochem Explor 50:143–178.

Mutch EJF, Blundy, JD, Tattitch BC, Cooper FJ, Brooker RA (2016) An experimental study of amphibole stability in low-P granitic magmas and a revised Al-in-hornblende geobarometer. Contrib Mineral Petrol 171:27p.

Parat F, Holtz F, Streck MJ (2011) Sulfur-bearing magmatic accessory minerals. Rev Mineral Geochem, 73:285–314.

Peterson JT, Cloos M (2005) Grasberg porphyry Cu-Au deposit, Papua, Indonesia: 1. Magmatic history, in Porter, T.M., eds., Super porphyry copper and gold deposits: a global perspective. PGC Publishing, Adelaide, 313–329.

Ridolfi F, Renzulli A, Puerini M (2010) Stability and chemical equi-librium of amphibole in calc-alkaline magmas: An overview, new thermo-barometric formulations, and application to subduction-related volcanoes. Contrib Mineral Petrol 160:45–66.

Rohrlach BD, Loucks RR (2005) Multi-million-year cyclic ramp-up of volatiles in a lower crustal magma reservoir trapped below the Tampakan Cu-Au deposit by Mio-Pliocene crustal compression in the southern Philippines, in Porter, T.M., ed., Super porphyry copper and gold deposits. Porter Geoconsultancy Publishing 2:369−407.

Sapiie B, Cloos M (2004) Strike-slip faulting in the core of the Central Range of west New Guinea: Ertsberg mining district, Indonesia. Geol Soc Am Bull 116:277–293.

Sun S, McDonough WF (1989) Chemical and isotopic systematics of oceanic basalts: implications for mantle composition and processes. In: Saunders, A.D., Norry, M.J. Eds., Magmatism in Ocean Basins. Geol Soc Spec Pub, London, 313–345.

Tattitch BC, Blundy JD (2017) Cu–Mo partitioning between felsic melts and saline-aqueous fluids as a function of XNaCleq, $fO2$, and $fS2$. Am Min 102:1987–2006.

Wafforn S (2017) Geo- and thermochronology of the Ertsberg-Grasberg Cu-Au mining district, west New Guinea, Indonesia, The University Texas at Austin, Ph.D. Dissertation, 357p.

Watanabe Y, Kon Y, Echigo T, Kamei, A (2017) Differential fractionation of rare earth elements in oxidized and reduced granitic rocks: Implication for heavy rare-earth enriched ion-adsorption mineralization. Resour Geol 67:35–52.

Paleosurfaces and hydrodynamics of a diatreme complex during formation of the Sunnyside porphyry Cu-Mo-Ag system, Arizona

Peter G. Vikre[1], Frederick T. Graybeal[2], Robert J. Kamilli[3], and Robert J. Fleck[4]
[1]*U.S. Geological Survey, Reno, NV*
[2]*Exploration Management LLC, Chatham, NJ*
[3]*U.S. Geological Survey, Tucson, AZ*
[4]*U.S. Geological Survey, Menlo Park, CA*

Abstract. The intact 60-58 Ma Sunnyside porphyry Cu-Mo-Ag system, Arizona, consists of stacked enargite-chalcocite-covellite (en-cc-cv) and chalcopyrite-molybdenite (cpy-mo) deposits (>2.3 Gt) in Mesozoic rocks and Laramide intrusions, and adjacent Zn-Pb-Cu-Ag-Mn carbonate replacement deposits (CRD; >200 Mt). Copper deposits are overlain by pyroclastic-epiclastic sequences representing three cycles of phreatomagmatic eruptions during emplacement of quartz feldspar porphyry intrusions. The sequences filled a ~2 km-wide crater of the initial eruption. Correlative paleosurfaces and paleo-potentiometric surfaces within sequences, and paleodepths constrained by critical fluid inclusions, place second cycle formation of the en-cc-cv deposit at ≥0.15 km and the cpy-mo and CRD at ≥1.16 km. Following the third cycle, paleodepths were ~0.5 km and ~1.5 km, respectively. Comparison of paleodepths and hydrodynamics of the Sunnyside system to the nearby higher grade (~0.6 wt% Cu) Red Mountain porphyry Cu-Mo-Ag system suggests that lower Cu grades at Sunnyside (~0.3 wt%) resulted from near-surface emplacement and rapid decompression of magmas, separation of critical fluids into large vapor/brine fluids, inefficient condensation of vapor with low Cu concentrations, and atmospheric dispersion of Cu. Large vapor/brine mass and transport of Cu in vapor in porphyry Cu systems that form at <3 km may lead to inefficient Cu retention and low Cu grades.

1 Introduction

The Sunnyside porphyry Cu-Mo-Ag deposits in southern Arizona, U.S.A., are part of a 61-58 Ma felsic magmatic-hydrothermal system that intruded and altered Mesozoic and Paleozoic rocks. The system includes a near-surface, hypogene enargite-chalcocite-covellite (en-cc-cv) deposit (ca 800 Mt @ 0.175% Cu, 0.2 opt Ag) that extends from 5100 ft (1554 m) to ~2700 ft (~818 m) elevation, a subjacent, hypogene chalcopyrite-molybdenite (cpy-mo) deposit (ca 1.5 Gt @ 0.33% Cu, 0.011% Mo, 0.16 opt Ag) at elevations below ~1900 ft (depths >~3000 ft (909 m)), and Zn-Pb-Ag-Mn vein and carbonate replacement deposits (CRD; >200 Mt) in Paleozoic and Mesozoic rocks east of the cpy-mo deposit at elevations below ~1000 ft (depths >4500 ft (>1364 m). Other epigenetic minerals in and adjacent to deposits include quartz, alunite, kaolinite, pyrophyllite, topaz, muscovite, anhydrite, K-feldspar, biotite, pyrite, and hematite (Fig. 1; 2). The Sunnyside system is distinguished from other porphyry Cu systems in western North America by undisplaced paleosurfaces that are coeval with three cycles of diatreme-forming phreato-magmatic eruptions (Fig. 3; Graybeal 1996; 2007; Vikre et al. 2014) and constrain paleodepths of en-cc-cv and cpy-mo deposits.

2 Paleosurfaces, Paleodepths, and Hydrodynamics of the Sunnyside System

At Sunnyside, subaerial paleosurfaces and paleo-potentiometric surfaces were recognized during field examinations. The Sunnyside system has not been displaced by faulting, and present elevations of these surfaces reflect relative paleo-elevations. Less precise critical fluid paleodepths and corresponding present elevations were independently estimated from fluid inclusion petrography of drill core samples.

Subaerial paleosurfaces are the tops of individual pyroclastic sequences that consist of coarse, relatively unsorted ejecta that grade upward into lapilli and ash beds that exhibit fluid sorting (air; water) in the form of graded and cross bedding. The oldest paleosurface is the unconformable contact of 60-59 Ma pyroclastic sequences of the first eruption cycle and ~73 Ma trachyandesite on the east side of the crater (present elevations 5160-5120 ft (1564-1552 m); Fig. 1). Numerous other largely conformable pyroclastic sequences of the second and third eruption cycles were delineated by concentric inward dips of lapilli and ash beds and have present elevations of ~5750, 5700, 5450, and 5430 ft (1742, 1727, 1652, and 1645 m), respectively. The pyroclastic-trachyandesite contact represents a ~13 m.y. erosion interval, whereas younger paleosurfaces were ephemeral and modified by little to no mass removal.

Paleo-potentiometric surfaces, or former water tables, are represented by stratiform masses of fine-grained gray quartz that mark the upper surfaces of water-saturation in pyroclastic sequences, and by the tops of near vertical quartz masses in Alum Gulch that cut those strata and subjacent feldspar porphyry (Fig. 1). The stratiform quartz mass (elevation 5575 ft) that has replaced permeable pyroclastic sequences of the second cycle of pyroclastic eruptions is coeval, or nearly so, with subjacent Cu-Mo-Ag deposits. A possible paleo-potentiometric surface at ~5100 ft elevation is represented by the sub-horizontal upper surface of the en-cc-cv deposit within quartz feldspar porphyry and adjacent pyroclastic sequences (Fig. 2). The similar elevation ranges of subaerial paleosurfaces

and paleo-potentiometric surfaces span ~700 ft (0.21 km; Fig. 2A).



Figure 1. Geologic map showing pre-Cenozoic and Laramide stratigraphy, three eruption cycles, stratiform and vertical quartz masses, strike and dips symbols, projection of the chalcopyrite-molybdenite (cpy-mo) deposit, 5000+ ft drill holes, and Fig. 2 section line.

Critical fluid inclusion populations are among numerous salt-saturated H_2O-NaCl-CO_2 and L-rich fluid inclusion populations that are broadly separated from predominantly V-rich populations by elevation (~2500 ft; Fig. 2A). The critical fluid populations occur in hydrothermal and igneous quartz in core intercepts within and above the cpy-mo deposit (Fig. 1; 2B). Critical fluid paleodepths were estimated from microthermometry of inclusions that exhibited critical fluid behavior (homogenization by meniscus fading rather than by vapor shrinkage or expansion), and comparison to experimentally determined temperature and pressure isochores of H_2O-NaCl-CO_2 fluids with similar compositions (Schmidt and Bodnar 2000). Pressures converted to depth, using an average pyroclastic sequence density (2.60 g/cm^3), correspond to present elevations of ~6775, 5920, 5760, 5570, 5035, 4975, 4840, and 4170 ft, which are similar to as well as higher and lower than elevations of paleosurfaces and paleo-potentiometric surfaces (Fig. 2A). However, paleo-elevations based on homogenization temperatures and compositions of critical fluid inclusions are minimum elevations because inclusion entrapment may have occurred at higher pressures and temperatures. Although within the elevation ranges of aerial paleosurfaces and paleo-potentiometric surfaces, the less precise minimum elevations of critical fluid paleosurfaces span ~1900 ft (~0.58 km; Fig. 2A).

At Sunnyside, confining pressures were episodically exceeded by fluid pressure, causing three cycles of catastrophic phreatomagmatic eruptions and deposition of pyroclastic sequences as recorded by paleosurfaces, paleo-potentiometric surfaces and critical fluid paleodepths. Variations among paleo-elevations during eruption cycles and critical fluid paleodepths suggest that (1) pressures in and above quartz feldspar porphyry intrusions fluctuated between lithostatic and hydrostatic, and (2) individual magmas decompressed and exsolved fluids over a range of paleodepths.

Some paleosurfaces, paleo-potentiometric surfaces, and paleodepths of the second cycle correspond spatially with the en-cc-cv and cpy-mo deposits (Fig. 1). Based on the highest elevation paleo-potentiometric surface of the second eruption cycle, and assuming a common elevation with the paleosurface, the paleodepths of the en-cc-cv and cpy-mo deposits were ~500 ft (~0.15 km) and ~3800 ft (~1.16 km), respectively.

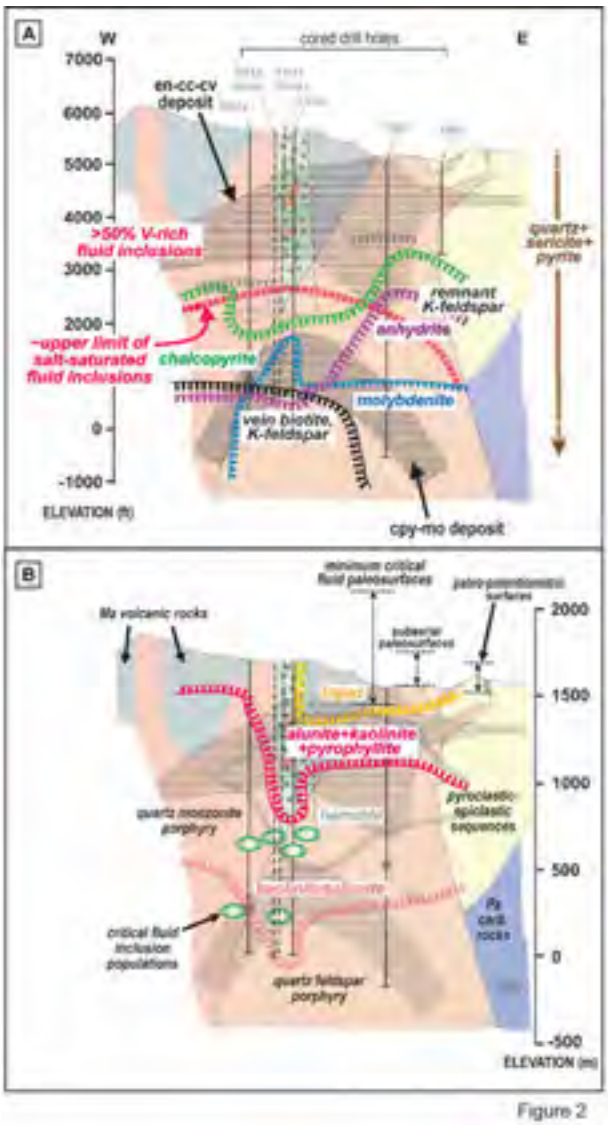


Figure 2

Figure 2. W-E section showing Cu-Mo-Ag resources and

A cored drill holes, distribution of quartz+sericite+pyrite, upper limits of chalcopyrite, anhydrite, molybdenite, remnant vein K-feldspar, and vein biotite and K-feldspar, and boundary between predominantly V-rich and salt-saturated fluid inclusion populations; B stratigraphy, paleosurface elevations, lower limits of topaz, alunite+kaolinite+ pyrophyllite, hematite, and kaolinite±alunite, and critical fluid inclusion populations.

3 Comparison of the Adjacent Red Mountain and Sunnyside Porphyry Systems

3.1 Tonnage and Grade Disparity

The ~62-60 Ma Red Mountain porphyry Cu-Mo-Ag system, ~5 km north of the Sunnyside system, is mostly in 73-68 Ma volcanic rocks, ~62 Ma small-volume granodiorite intrusions, and intrusive breccias (Bodnar and Beane 1980; Vikre et al. 2014). Similar to the Sunnyside system, the Red Mountain system includes a relatively deep chalcopyrite-bornite-molybdenite-Ag deposit (434 Mt @ 0.64 wt% Cu, 0.010 wt% Mo, and 0.12 opt Ag) ~3,000 to >5,000 ft (~0.9 to >1.5 km) below the present surface, and a partially exposed, sub-horizontal, enargite-supergene chalcocite deposit (100-150 Mt @ 0.31 wt% Cu) that extends to ~600 ft (~0.2 km) below the present surface. The Red Mountain deposits (combined: ~584 Mt @ 0.56 wt% Cu) contain ~75% fewer tons and 50% less Cu than the Sunnyside deposits (combined: ~2.3 Gt @ 0.28 wt% Cu), and the average copper grade of the Red Mountain deposits is twice that of the Sunnyside deposits.

3.2 Vapor/brine mass, Paleodepths, and SO_2 Disproportionation

Temporal relationships of fluid inclusion populations and hydrothermal minerals, including copper minerals, in porphyry copper deposits are often difficult to determine because of numerous populations present at the scale of a petrographic section. However, broad spatial association between Cu ore and saline fluid inclusions, and partitioning experiments, indicate that Cu in most deposits was transported in brine and vapor or both in some deposits (Audetat and Pettke 2006). Melt-brine-vapor partitioning of Cu may vary during evolution of porphyry Cu systems, and the mass of vapor could exceed the mass of brine in some systems, or parts of systems. Although Cu concentrations in vapor are usually much lower than in brine, vapor Cu concentrations in some deposits exceeds that of brine (Seo et al. 2009; Simon et al. 2006; Simon and Ripley 2011), and more Cu conceivably could be transported by vapor than brine in systems or parts of systems with high vapor/brine mass.

Spatial relationships of the Cu deposits at Red Mountain and Sunnyside and stratigraphy of epigenetic minerals and fluid inclusion populations imply fundamental differences in their evolution including (1) depths at which exsolved volatiles separated into brine and vapor, (2) brine/vapor mass, (3) mass of copper transported in brine and vapor, (4) efficiency of vapor retention, and (5) late SO_2 disproportionation.

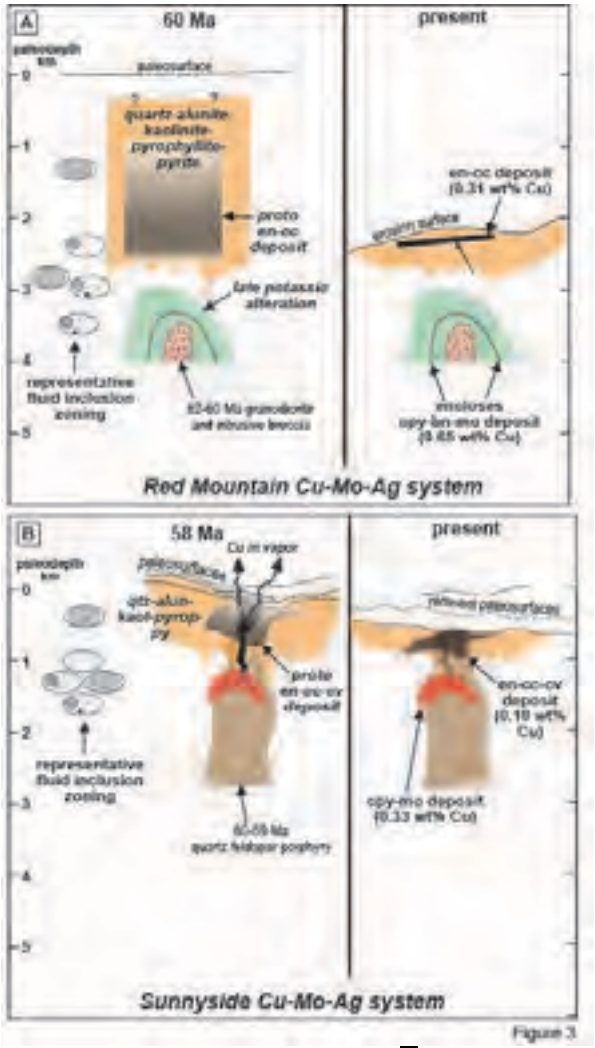


Figure 3. Schematic configuration of A Red Mountain at 60 Ma, B Sunnyside at 58 Ma and present, quartz-alunite-kaolinite-pyrophyllite-pyrite alteration zones, proto and present enargite-chalcocite-covellite (en-cc; en-cc-cv) and chalcopyrite-bornite-molybdenite (cpy-bn-mo; cpy-mo) deposits, associated intrusions, fluid inclusion types, paleosurfaces, and erosion surfaces. The lateral scale of the Sunnyside system is ~50% of that of the Red Mountain system. The Red Mountain system sections are based on simplified fluid inclusion and hydrothermal alteration mineral stratigraphy in Bodnar and Beane (1980) and Lecumberri-Sanchez et al. (2013), using a minimum erosion estimate based on hydrostatic pressure (evidence of fluid boiling), and on sections in Quinlan (1986), although fluid inclusion stratigraphy is somewhat simplified. Ages are based on geochronology in Vikre et al. (2014).

At Red Mountain, petrography and microthermometry of fluid inclusion populations (Bodnar and Beane 1980; Lecumberri-Sanchez et al. 2013), and undisrupted stratigraphy imply that phase separation of a critical fluid into vapor and brine occurred at ~3 km paleodepths (Fig. 3A), or

that magmatic brine was progressively diluted by meteoric water from those paleodepths toward the paleosurface. The relatively deep emplacement and devolatilization of magmas resulted in retention of most Cu in brine. A lesser mass of Cu in overlying vapor condensed with other volatiles in groundwater causing simultaneous advanced argillic alteration of 73-68 Ma volcanic and sedimentary host rocks and deposition of Cu minerals, forming the near-surface and supergene enriched en-cc deposit. During formation of the en-cc deposit little Cu in vapor was apparently dispersed into the troposphere.

At Sunnyside, the cpy-mo deposit is spatially associated with paleo-potentiometric surfaces of eruption cycle 2 and with fluid inclusions that entrapped critical fluids and brines at paleodepths below ~3,000 ft (~0.91 km), whereas fluid inclusions associated with the overlying en-cc-cv deposit are predominantly vapor-rich and occur in quartz-feldspar porphyry altered to alunite, kaolinite, pyrophyllite and topaz (Fig. 2A;B;3B. These spatial relationships suggest that (1) the cpy-mo deposit was predominantly deposited from brines, (2) some Cu in the en-cc-cv deposit was transported in vapor and condensed in near-surface water acidified by SO_2 disproportionation that altered quartz feldspar porphyry and pyroclastic sequences, and (3) some Cu in vapor may have vented to the troposphere, possibly as Cu-H-S complexes (Simon and Ripley 2011). If the mass of vapor generated during the second eruption cycle left a relatively small mass of residual brine at depth, then vapor separation and venting could have lowered the grades of both deposits.

In addition, the distribution of alunite implies that temporal differences in SO_2 disproportionation may also have affected Cu grades. The abundance of alunite and vapor dominant fluid inclusions at elevations >2,500 ft (Fig. 2A; Vikre et al, 2023) indicates that SO_2 disproportion to aqueous sulfide and sulfate caused intensive hydrolytic alteration in upper parts of the Sunnyside system, perhaps simultaneously with vapor separation. In deeper parts of the system anhydrite, chalcopyrite, and molybdenite were simultaneously deposited from brines. The downward extension of kaolinite and alunite into the cpy-mo deposit (Fig. 2B) suggests that later SO_2 disproportionation may have created acidic fluid that solubilized and dispersed Cu, lowering the grade of the cpy-mo deposit.

References

Audetat A, Pettke T (2006) Evolution of a porphyry-Cu mineralized magma system at Santa Rita, New Mexico (U.S.A.). Jour Petrol 47: 2021-2046

Bodnar RJ, Beane RE (1980) Temporal and spatial variations in hydrothermal fluid characteristics during vein filling in preore cover overlying deeply buried porphyry copper-type mineralization at Red Mountain, Arizona. Econ Geol 75: 876–893

Graybeal FT (1996) Sunnyside, a vertically-preserved porphyry copper system, Patagonia Mountains, Arizona: SEG Newsletter 26: 10–14

Graybeal, FT (2007) Geology of the Sunnyside Porphyry Copper System, Patagonia Mountains, AZ. Guidebook No. 8 for Arizona Geological Society Ores & Orogenesis Symposium, Tucson, Arizonia, Arizona Geological Society

Lecumberri-Sanchez P, Newton MC, Westman ED, Kamilli RJ, Canby VM, Bodnar RJ (2013) Temporal and spatial distribution of alteration, mineralization, and fluid inclusions in the transitional high-sulfidation epithermal-porphyry copper system at Red Mountain, AZ. Journ Geochem Explor 125: 80–93

Quinlan JL (1986) Geology and silicate-alteration zoning at the Red Mountain porphyry copper deposit, Santa Cruz County, Arizona. Arizona Geological Society Digest 16: 294–304

Schmidt C, Bodnar RJ (2000) Synthetic fluid inclusions: XVI. PVTX properties in the system H2O-NaCl-CO2 at elevated temperatures, pressures, and salinities. Geochim Cosmochim Acta 64: 3853–3869

Seo JH, Guillong M, Heinrich CA (2009) The role of sulfur in the formation of magmatic-hydrothermal copper-gold deposits. Earth Planet Sci Lett 282:323-328

Simon AC, Pettke T, Candela PA, Piccoli PM, Heinrich CA (2006) Copper partitioning in sulfur bearing magmatic systems. Geochim Cosmochim Acta 70: 5583-5600

Simon, AC, Ripley EM (2011) The role of magmatic sulfur in the formation of ore deposits. Rev Min Geochem 73: 513-578

Vikre PG, Graybeal FT, Fleck RJ, Barton MD, Seedorff E (2014) Succession of Laramide magmatic and magmatic-hydrothermal events in the Patagonia Mountains, Santa Cruz County, Arizona. Econ Geol 109: 1667-1704

Vikre PG, John DA, Wintzer NE, Koutz F, Graybeal F, Dail C, Annis DC (2023) Critical mineral in subduction-related magmatic-hydrothermal systems of the United States. USGS SIR 2023-5082: 110

Structural and Hydrothermal Controls on Mineralization of the Bronson Slope Porphyry Cu-Au-Mo Deposit, British Columbia: Implications for Exploration Targeting.

Luis Jacobo Yagual[1], Marcus Adam[2], William Threlkeld[2], Antonio Arribas[1]
[1]The University of Texas at El Paso, Department of Earth, Environmental and Resource Sciences, USA
[2]Seabridge Gold Inc.

Abstract. This study combines airborne magnetic and magnetotellurics data with geochemical information obtained through ICP-MS. It also incorporates structural and lithological data from drill holes and outcrops at the Bronson Slope Cu-Au-Mo porphyry deposit in the Iskut Region, British Columbia, Canada. This research aims to enhance exploration at the Bronson Slope. Lithology, alteration, mineralization, and structural models were constructed in Leapfrog Geo. The project comprises twenty-seven drill holes (25,246 meters) drilled between 2022 and 2023. The model defines the geometry, metal distribution, spatial orientation of ore zones, host stratigraphy, structural fabric, and magnetic and conductivity features. Airborne magnetic surveys and core magnetic susceptibility measurements define a northwest-southeast magnetic feature (~900 m long), suggesting a porphyry signature. Surface mapping and core logging confirm a porphyry copper deposit characterized by quartz-magnetite stockwork veining. Core logging shows mineralized shear veins rich in chalcopyrite and pyrite, representing a distinct, later-stage mineralization event. These overprint the high magnetic features and generate a low magnetic, high-conductivity northwest-southeast corridor. Our results indicate that a mineralization event rich in chalcopyrite-pyrite veins is not spatially associated with early quartz-magnetite stockwork, suggesting a complex overprinting history within the porphyry system.

.

1 Introduction

The Bronson Slope Deposit is situated in the Iskut River region of northwestern British Columbia, Canada. It is within the Intermontane Belt on the western portion of the Stikine terrain, bordered to the west by the Yukon-Tanana Terrain and the Coastal Pacific Pluton Complex and to the east by the Quesnellia Terrain (Alldrick et al., 2005) (Fig. 1). This deposit is part of the larger Golden Triangle mining district, primarily associated with porphyry copper-gold deposits, epithermal gold-silver systems, and volcanogenic massive sulfide (VMS) deposits (Nelson et al., 2018). It is near world-class porphyry copper type deposits, such as KSM and Red Chris, the Brucejack gold epithermal deposit, and the Eskay Creek polymetallic VMS deposit.Locally, the Stikine terrain is hosted by two volcano-sedimentary sequences separated by an angular unconformity: the folded turbiditic Triassic Stuhini Group and the felsic to intermediate lava flows and pyroclastic deposits of the Jurassic Hazelton Group (Rhys & Lewis, 2004). Several calc-alkaline intrusions have intruded this region from the Triassic to the Tertiary (McDonald et al., 1996).

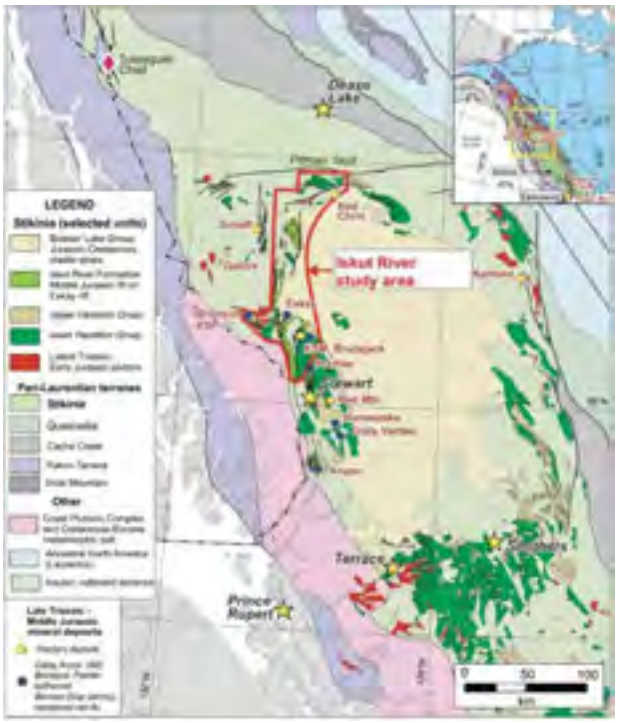


Figure 1. Regional geology map of the Iskut Region showing the late Triassic to mid-Jurassic metallogenic belt comprised of porphyry, epithermal, and volcanogenic mineral deposits (modified from Nelson et al., 2018).

Seabridge Gold explores three potential targets in the Iskut Project: the Bronson Slope deposit, the epithermal gold-silver Quartz Rise, and the porphyry copper-gold Snip North prospects (Fig. 2a). Bronson is a porphyry copper-gold style occurrence with current inferred resources totalling 517.3 million tons, with grades of 0.33 g/t Au and 0.09% Cu, for 5.4 Moz Au, 45 Moz Ag, and 1,057 Mlb Cu (Kim, 2024).

This deposit is hosted within multiphase quartz monzonite and quartz monzonite porphyry intrusions that intrude into the folded volcanic and volcanoclastic Stuhini and Hazelton Groups (Rhys, 1995). The deposit has an elongated tabular geometry, stretching 3,000 meters long and 250 to 450 meters wide, with a potential extension of 900 meters at depth (Fig. 2b).

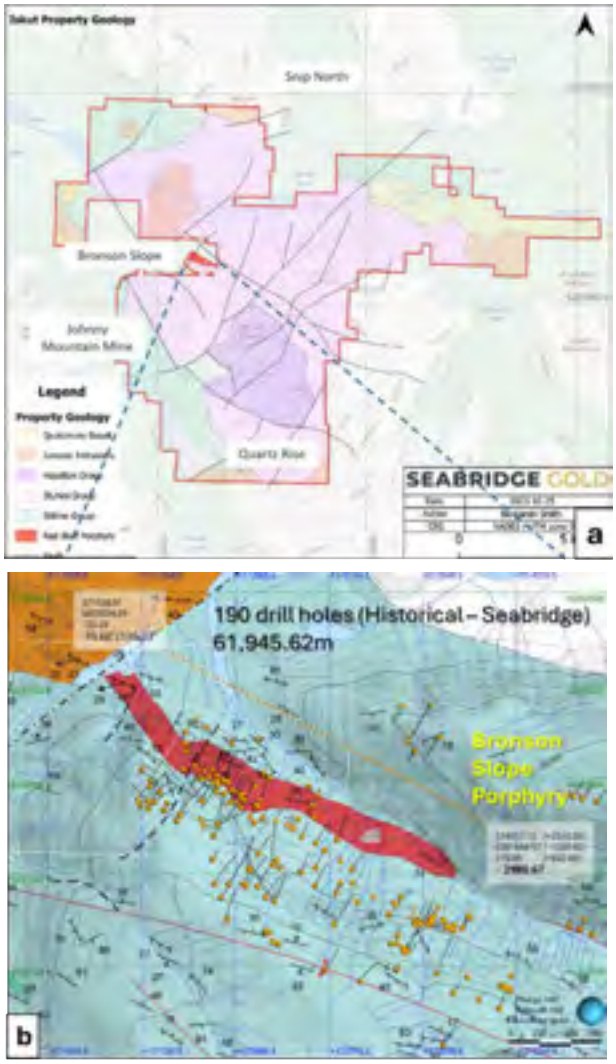


Figure 2. a) Regional geology map overlaps with the Seabridge Gold Claim and includes epithermal and porphyry targets: Quartz Rise, Bronson Slope, and Snip North. **b)** Local geology map at Bronson comprises a tabular, elongated quartz monzonite porphyry intrusion intruding the volcanic sedimentary Stuhini group.

2 Methods

In the summer of 2024, fieldwork research at the Iskut Project was conducted. In the fall of the same year, complementary software modelling and laboratory analyses at the University of Texas at El Paso were performed. The current study comprises the following stages:

a) Review of the historical database, including drill holes, regional and local models, maps, cross sections, and current onsite drilling.

b) Correlate lithology, alteration, and mineralization maps with the magnetic anomaly maps processed to the reduced magnetic intensity (RMI) and reduced to the pole (RTP) and resistivity – conductivity anomaly maps surveyed in an area of 201.25 km^2 conformed by 245 lines in a northeast-southwest direction, with a length of 14,000 m, 50 m spacing and 20 lines in a northwest-southeast direction, with a length of 16,000 m, 1,000 m spacing and resolution of 50 m x 50 m by helicopter in 2022 – 2023.

c) A detailed cross-section of the studied area, focusing on the deposit's geophysical signatures, geochemistry, structures, and mineralization.

d) Integrate and correlate magnetic susceptibility measurements taken every two meters across twenty-seven drill holes, totalling 25,246 m drilled from 2022 to 2023, within the detailed cross-section.

e) Create lithology, structural, alteration, and mineralization models.

f) Validate lithology, alteration, mineralization, and structural models.

3 Results and Discussion

Based on magnetic and resistivity-conductivity maps, magnetic susceptibility data, and a detailed log of the lithology, structures, alteration assemblages, and mineralization in drill holes SBS-22-09, 05, and 06, a cross-section labelled A-A' was proposed and created (Fig. 3).

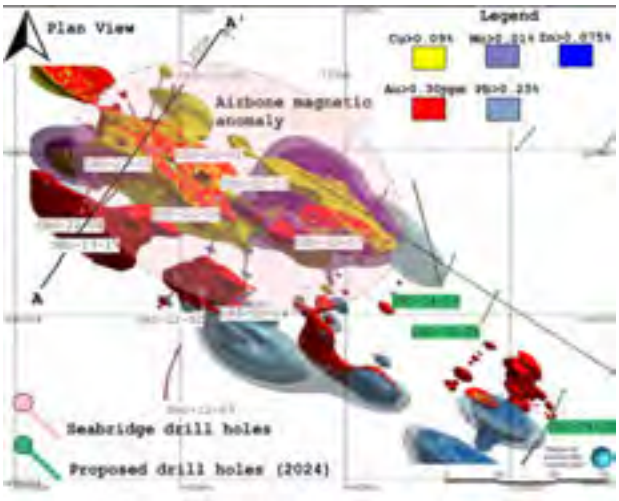


Figure 3. Plan view consists of high-grade Au-Cu-Mo-Pb and Zn shells and a significant magnetic anomaly detected through airborne surveying at Bronson Slope.

The Bronson Slope deposit is a porphyry copper-gold-molybdenum occurrence hosted within multiphase quartz monzonite and quartz monzonite porphyry intrusions. These intrusions crosscut the folded volcaniclastic formations of the Stuhini Group (Fig. 4).

The area is influenced by a network of two main fault systems: northwest-southeast faults that control north-south structures and east-west faults that control structures running from north to northeast and from south to southwest. These faults are associated with high conductivity anomalies, highlighting the structural corridor. These anomalies are linked to compressional deformation events that elongated and exhumed the deposit.

The alteration footprint is characterized by pervasive strong magnetite, tardimagmatic biotite, and potassic feldspar cut by milky quartz ± magnetite veins. This is intersected by intense multiphase quartz-magnetite stockwork veining, followed by quartz-molybdenite sheeted veins.

These features are associated with the high magnetic anomaly map and high magnetic susceptibility measurements at drill holes.

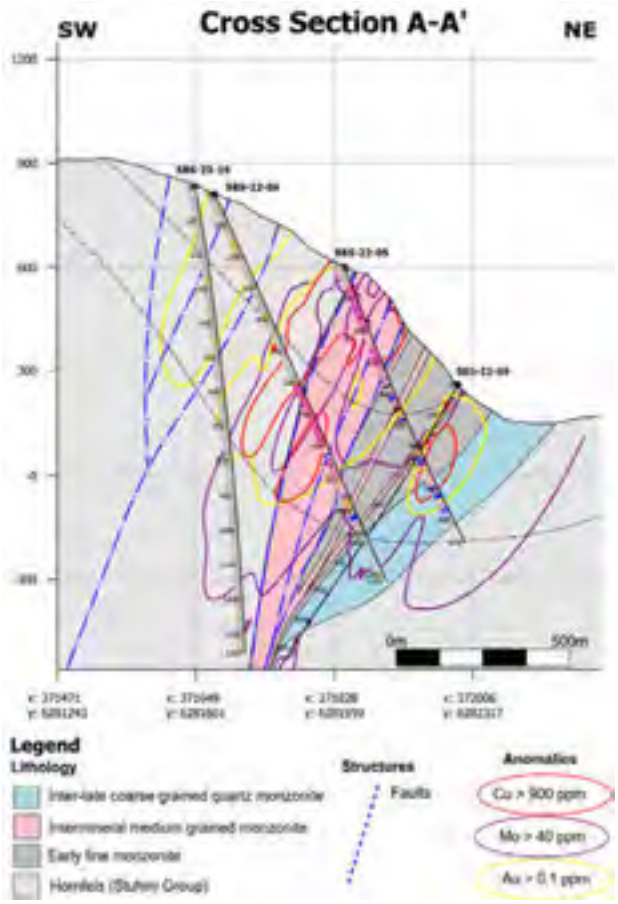


Figure 4. NE-SW Cross section (A-A'), looking northwest, with a minimum distance of 150 m to the section plane, displays the lithology, mineralization, and structures of the Bronson Slope Porphyry Cu-Au-Mo deposit.

Quartz-magnetite ± molybdenite stockwork veins were cross-cut by chalcopyrite veins with phengite-biotite halos developed in a syn-late stage, followed by pyrite veins bounded by chlorite-white mica halos in a late-stage event (Fig. 5). Sub-epithermal veins, dominated by sphalerite ± galena ± pyrrhotite ± chalcopyrite, developed along the margins of the porphyry system.

At least two shear events affected the porphyry-epithermal system, remobilizing sulfides and re-precipitating metal content. The first event is characterized by chalcopyrite-magnetite-hematite veins formed under a ductile-brittle regime, later overprinted by pyrite-bearing shear veins. A subsequent brittle-ductile phase formed calcite and quartz ± chalcopyrite ± specularite veins, crosscutting the earlier system (Fig. 6).

The low magnetic susceptibilities, which coincide with high gold and copper in chalcopyrite and pyrite veins, indicate that these structures overprint high magnetic features. This results in high conductivity and a low magnetic linear footprint (Fig. 7).

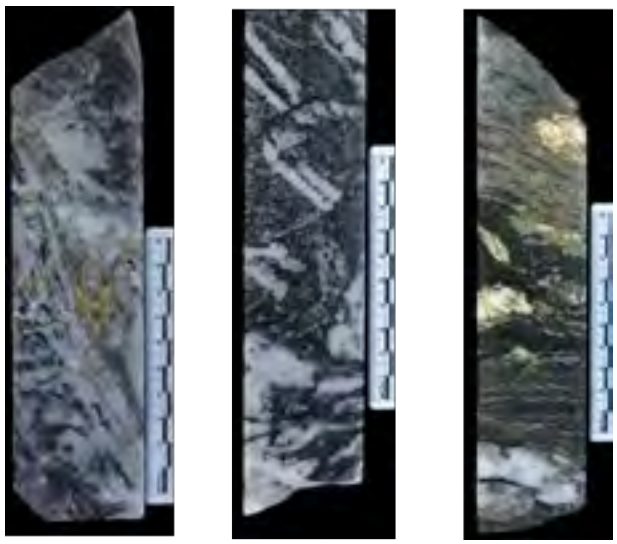


Figure 5. Quartz magnetite stockwork overprinted by chalcopyrite and pyrite veins.

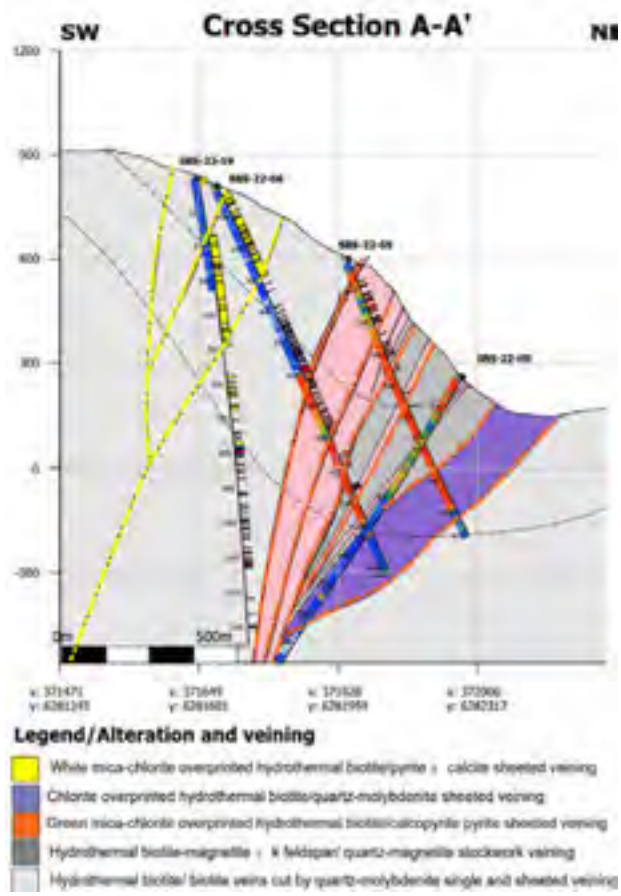


Figure 6. NE-SW Cross section, looking northwest, with a minimum distance of 150 m to the section plane, displays the alteration and high and low magnetic susceptibility recorded from drill holes SBS-22-05, 06, and SBS-23-19 of the Bronson Slope porphyry Cu-Au-Mo deposit.

High magnetic features characterize early non-economic mineralization events related to quartz-magnetite ± molybdenite stockwork veining. In contrast, the main and later mineralization events are rich in chalcopyrite and pyrite veins and correlate with low magnetic susceptibility and high conductivity features. The main mineralization event

is not linked to the quartz-magnetite stockwork veining associated with high magnetic features distinctive of porphyry copper deposits. This indicates that a late economic mineralization event has overprinted the original porphyry system.

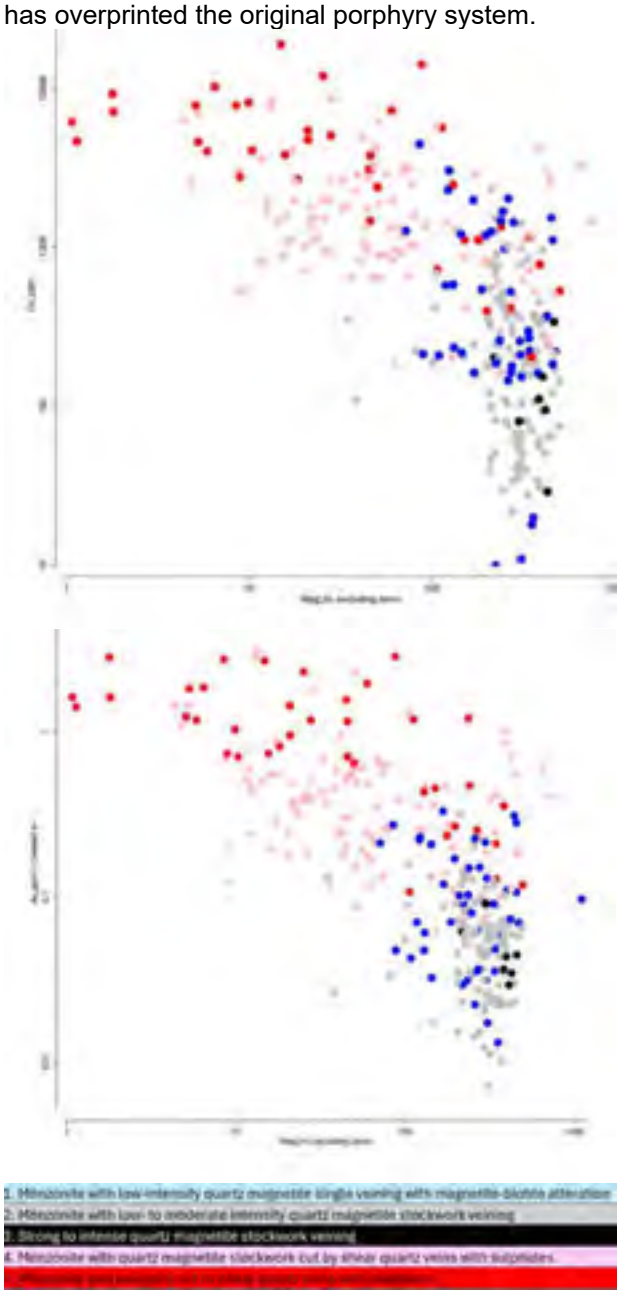


Figure 7. Scatter plots comparing Au/Cu contents vs. magnetic susceptibility from drill holes SBS-22-05, SBS-22-06, and SBS-23-19 at the Bronson Slope Porphyry Cu-Au-Mo deposit show distinct trends. High copper and gold grades are associated with low magnetic susceptibility, particularly in shear quartz veins containing chalcopyrite and pyrite. Conversely, areas displaying low copper and gold grades correlate with high magnetic susceptibility and are linked to quartz-magnetite stockwork.

4. Conclusions

High magnetic susceptibility features identified through airborne and susceptibility measurements are associated with early-stage quartz-magnetite stockwork veining. Chalcopyrite-pyrite veins formed during the syn-late stage exhibit high conductivity features with low magnetism. This change in magnetic susceptibility and conductivity allows for more precise targeting of copper mineralized zones.

The delineation of a NW-SE structural corridor, characterized by high conductivity features and shear-hosted mineralization, highlights the role of structural reactivation in influencing mineralization. Mineralized shear veins suggest that late-stage hydrothermal processes were critical in remobilizing and concentrating gold and copper as an overprint to early porphyry-type mineralization. The identification of these structural controls enhances the exploration model and provides a strategic plan for improving future drilling programs.

The hydrothermal evolution of Bronson Slope is defined by an early hydrothermal magnetite-biotite-potassic feldspar alteration, followed by later phengite and muscovite-chlorite haloes surrounding chalcopyrite-pyrite veins. This alteration pattern indicates a complex, multi-stage mineralization process, where later hydrothermal fluids overprinted and redistributed metals within the deposit. Results highlight the importance of multi-phase mineralization in structurally complex porphyry deposits, emphasizing the importance of incorporating overprinting events into exploration models. Ongoing geochronological studies will provide additional resolution to this sequence of intrusive and structural controls.

Acknowledgments

We express our gratitude to Seabridge Gold for strong support and financial assistance, as well as to Marisa de la Vega and Lewis Teal.

References

Alldrick D, Nelson J & Barresi T (2005) Geology and Mineral Occurrences of the Upper Iskut River Area: Tracking the Eskay Rift through Northern British Columbia. Telegraph Creek NTS 104G/1, 2, 30.

Kim H (2024) Seabridge Gold Reports Bronson Slope Resource Estimate at its Iskut Project in BC. Vancouver: Seabridge Gold.

Nelson J, Waldron J, Straaten B, Zagorevski A & Rees C (2018) Revised stratigraphy of the Hazelton Group in the Iskut River region, northwestern British Columbia. British Columbia Geological Survey, 15-38.

Rhys D (1995) The Red Bluff gold-copper porphyry and associated precious and base metal veins, northwestern British Columbia. CIM Special Volume 46, 838 - 850.

Rhys D & Lewis P (2004) The Snip and Stonehouse deposits: influences of shear zones, paleodepth and thermal zonation on of Au veins in a porphyry system. Gold Vein Deposits: Turning Geology into Discovery, 90-97.

Mafic underplating as a possible source for iron oxide-apatite deposits in Norrbotten, Sweden

Tobias E Bauer[1], Maxim Y Smirnov[1], Ervin Veress[1], Thorkild M Rasmussen[1], Oskar Rydman[1], Leslie A Logan[1], Joel BH Andersson[1], Jochen Kamm[2], Graham Hill[3], Fernando Tornos[1,4]
[1]Department of Civil, Environmental and Natural Resources Engineering, Luleå University of Technology, Luleå, Sweden
[2]GTK, Finland
[3]Institute of Geophysics, Prague, Czech Republic
[4]Instituto de Geociencias (IGEO, CSIC-UCM), Madrid, Spain

Abstract. The Norrbotten region in northern Sweden is a significant mining area, particularly known for its iron oxide-apatite (IOA) deposits, such as the Kiruna and Malmberget mines. These deposits have been studied for over a century, with various genetic models proposed, ranging from magmatic to hydrothermal origins. The IOA mineralization is linked to back-arc extension during the Svecokarelian orogeny (~1.88 Ga), forming chemically distinct syn-orogenic plutonic-volcanic rocks. Radiometric dating indicates a close temporal relationship between these rocks and the IOA deposits. Despite understanding the formation processes, the iron source remains debated, with ultramafic rocks from crustal thinning during back-arc extension being a potential source. Geophysical data, including magnetotelluric (MT) and potential field data, and petrophysical data were used to model the crustal structure and its relation to the mineral systems. The 3D electric conductivity model reveals enhanced conductivity structures in the middle and upper crust, suggesting a large volume of mafic-ultramafic rocks emplaced by underplating. These intrusions, interacting with crustal rocks, may have generated Si- and Fe-rich melts, forming the IOA deposits. This study supports a model where mafic-ultramafic intrusions and crustal assimilation play a crucial role in IOA deposit formation.

1 Introduction

The Norrbotten region in northern Sweden is a key mining area in Europe and a central hub for iron production. This region, particularly the northern Norrbotten ore province, is known for its unique cluster of iron oxide-apatite (IOA) deposits, with the Kiruna and Malmberget iron mines being the most notable examples (Fig. 1).

IOA deposits have been a subject of study for over a century. Geijer (1910) first described the deposit at Kiirunavaara, coining the term "Kiruna-type" deposit, which has since been applied to the Malmberget deposit and other similar deposits. The genetic models for these Kiruna-type IOA deposits remain controversial, with hypotheses ranging from a hydrothermal origin (Paràk 1973, Hildebrand 1986, Hitzman et al. 1992, Sillitoe and Burrows 2002 Smith et al. 2013, Dare et al. 2014) to magmatic models (Geijer 1910, Park 1961, Frietsch 1984, Nyström and Henríquez 1994, Troll et al. 2016) with either the ore forming from immiscible Fe-rich melts (Andersson 2013, Tornos et al. 2016) or by flotation of magnetite (Knipping et al. 2015). Martinsson (2004) and Martinsson et al. (2016) proposed a combination of both magmatic and hydrothermal processes for the Malmberget and Kiruna deposits.

The IOA mineralization processes in Norrbotten are linked to a phase of back-arc extension at the beginning of the Svecokarelian orogeny, around 1.88 Ga (e.g. Andersson et al. 2022). During this extensional phase, two types of chemically distinct but broadly coeval syn-orogenic plutonic-volcanic rocks were formed. The alkali-calcic Perthite Monzonite suite (PMS) - Kiirunavaara group (1.88-1.86 Ga: Bergman et al. 2001, Sarlus et al. 2018, Logan et al. 2022) predominate to the west of Norrbotten, whereas the calc-alkaline Haparanda suite - Porphyrite group (1.89-1.87 Ga: Bergman et al. 2001) predominate to the east (Fig. 1).

The timing of IOA formation in Kiruna has been determined through radiometric dating of both host rocks and associated alteration and ore minerals (Welin 1987, Cliff et al. 1990, Romer et al. 1994, Smith et al. 2009, Martinsson et al. 2016). This dating highlights the close temporal relationship between the PMS intrusive rocks, volcanic rocks of the Kiirunavaara group and the IOA deposits. The most precise age determination was conducted by Westhues et al. (2016) on zircon grains from the Kiirunavaara and Nukutus magnetite ores, yielding ages of 1874 ± 7 Ma and 1877 ± 4 Ma (U-Pb secondary ion mass spectrometry (SIMS), respectively. These ages overlap with a titanite age from a decimetre-wide calc-silicate alteration zone at the footwall contact to Kiirunavaara (1878 ± 4 Ma, U-Pb thermal ion mass spectrometry (TIMS; Martinsson et al. 2016).

Despite understanding the formation processes, the source of iron for these large systems remains a significant question. Potential sources include greenstone rocks, Svecofennian volcanic rocks, and mafic and ultramafic intrusions.

This study suggests mafic-ultramafic rocks emplaced due to crustal thinning during back arc extension as a possible source of iron for the formation of IOA deposits in northern Sweden.

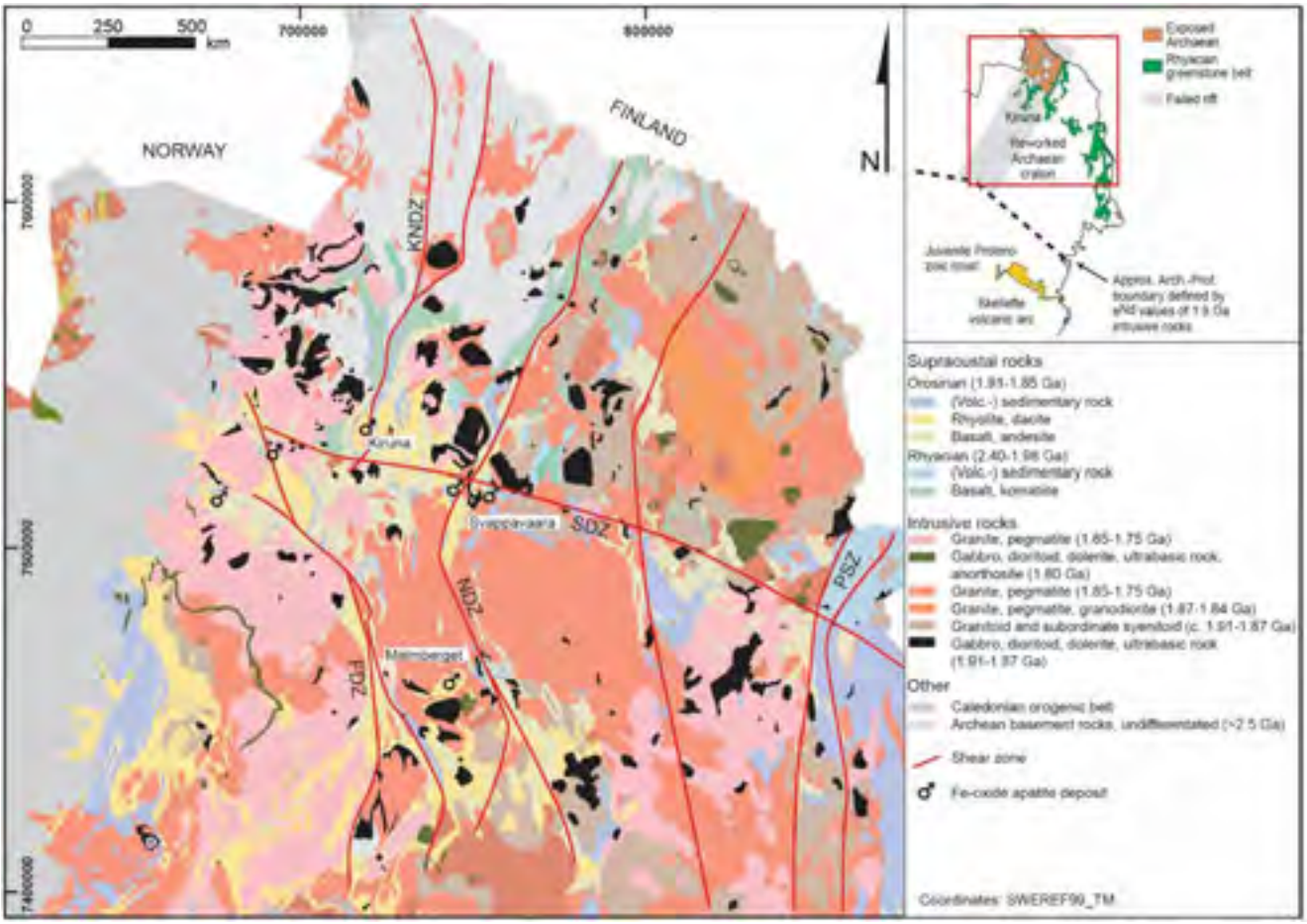


Figure 1. Geological overview of northern Norrbotten. Map source: Geological Survey of Sweden. Structures modified after Bauer and Andersson (2023).

2 Methods

2.1 Geophysical data and modelling

At a regional scale several geophysical data sets are available in the area. Magnetotelluric (MT) data were previously acquired in the area (Cherevatova et al. 2015), which provided a lithosphere scale 3D electrical conductivity model, which were later refined to better understand the crustal structures and their relation to mineral systems as a whole (Vadoodi et al. 2021). Potential field data are provided by the Geological Survey of Sweden (SGU), which were extensively used for building geophysical and geological models as well as joint interpretation with MT data (Vadoodi et al. 2022).

In order to better depict the crustal structures and relate them to known mineralisation, the DREX (Deposit to Regional scale Exploration) project recently acquired dense regional scale (~100^2 km^2) MT data consisting of roughly 400 sites distributed with about 5 km station spacing. Additionally, dense 3D MT arrays were measured around Malmberget and neighbouring Nautanen deposits with site spacing of about 1 km. Thus, all acquired data allow for both detailed and regional scale electrical conductivity modelling of the area and interpretation of their connection to deposit scale models. High quality MT data were inverted to obtain a 3D conductivity model of the entire crust (Fig. 2) and a detailed model of the Malmberget deposit.

The major rock units in Norrbotten have been sampled and characterized based on petrophysical properties encompassing density and magnetic susceptibility. Additionally potential field data were inverted to full 3D density and magnetic susceptibility models, allowing for a full integration of available data.

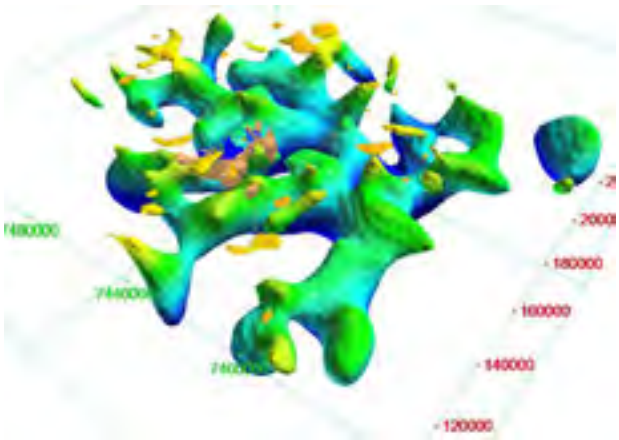


Figure 2. 100 Ωm iso-surface model showing the conductor ranging from 10-20 km depth. Color scheme refers to depth.

2.2 Geological information

The locations of ultramafic-mafic intrusive rocks are modelled in 3D based on the geological map presented in Fig. 1, and their spatial relationship with the inverted MT data are presented in Fig. 3. Two cross sections (A-A', B-B'; Fig. 3), highlight the relationship between ultramafic-mafic intrusive units and highly conductive pipe-like features, in mineralized terrains. Based on petrophysical laboratory measurements of magnetic susceptibility and density, ultramafic rocks, followed by mafic rocks have the highest density, while some intrusions or subparts of intrusions are characterised by high magnetic susceptibility.

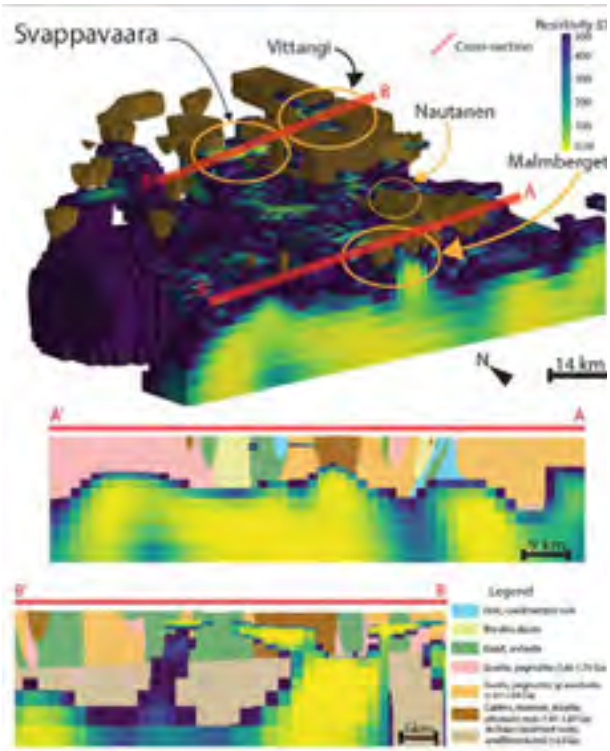


Figure 3. Regional MT model with superimposed 100 Ωm iso-surfaces (brown colour) for detailed model showing pipe-like conductors and their relationship to ultramafic-mafic intrusions of the 3D geological model. Geological model colour coding corresponds to map in Fig. 1.

3 Results and Discussion

A common feature that all IOA deposits in northern Norrbotten share is the existence of mafic-ultramafic and coeval felsic intrusions close by. The mafic intrusions are typically magnetite-rich and have a similar age as the related IOA deposits (Sarlus et al. 2018, Logan et al. 2022). The 3D conductivity model contains extensive enhanced conductivity structures in the upper, middle crust at depth range from about 10 to 30 km (Fig. 2). The resolution of the 3D model is sufficient to map pipe-like features that partly reach the surface in the close vicinity of known IOA deposits and magnetite-rich mafic-ultramafic intrusions (Fig. 3).

Those deep feeders are also mapped in more details with deposit scale MT arrays in Nautanen and Malmberget areas. The host rocks are generally highly resistive. Enhanced conductivities in the crust can be explained by the presence of small fractions of conductive material i.e. sulphides (interconnected structures or grain boundary conductivity), iron oxides (magnetite), graphite or iron-rich ultramafic rocks (e.g. Hill et al. 2021). Based on a combination of the 3D MT model with geological field observations, petrophysical measurements of density and susceptibility we suggest that the mid-crustal conductor connecting to the known IOA deposits represents a large volume of mafic-ultramafic rocks emplaced by underplating during the back-arc extension (Fig. 4). The complex 3D structure of the mid-crustal conductor is caused by the intrusion remobilising preexisting large scale weak zones in the crust. As such ultramafic rocks may not be sufficient to explain the observed high conductivities.

One possible model for the formation of the IOA deposits is generation of Si- and Fe-rich melts formed during complex processes involving melt immiscibility that subsequently produced the magnetite-rich magmas (Tornos et al. 2016).

Tornos et al. (2023) recently showed that assimilation of crustal rocks can promote immiscibility of an Fe-oxide melt and is interpreted as the formational process for IOA deposits. The data presented here suggests a comparable model where ultramafic intrusions intrude into the upper crust sourcing from a larger volume of ultramafic rocks caused by mafic underplating. Assimilation of crustal rocks (such as evaporites in the greenstone stratigraphy) during uprise of these intrusions can subsequently trigger separation and formation of Fe-rich melts.

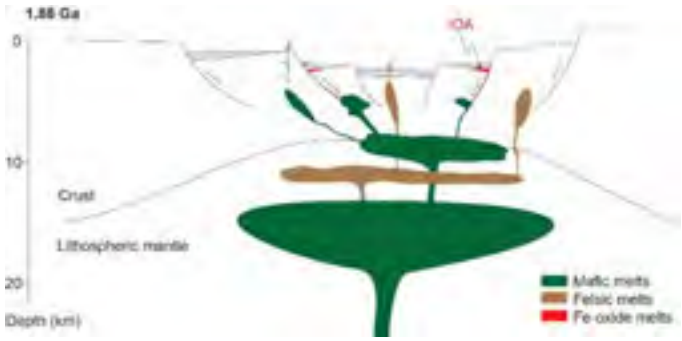


Figure 4. Conceptual cross section showing mafic underplating and the relation to Perthite Monzonite suite mafic and felsic intrusive rocks and IOA deposits.

Acknowledgements

This study is part of the DREX project, funded by ERAMIN and the project “Common Earth Modelling of the Kiruna mining district” funded by LKAB. M. Strand is thanked for reviewing.

References

Andersson UB (2013) Coeval iron oxide and silicate magmas; structural evidence for immiscibility and mingling at Kiirunavaara and Luossavaara, Sweden [ext. abs.]: Mineral Deposit research for a high-tech world, 12th biennial Meeting 2013. Proceedings 4: 1635–1638

Andersson JBH, Logan L, Martinsson O, Chew D, Kooijman E, Kielman-Schmitt M, Kampmann TC, Bauer TE (2022) U-Pb zircon-titanite-apatite age constraints on basin development and basin inversion in the Kiruna mining district, Sweden. Precambr Res 372: 106613

Bergman S, Kübler L, Martinsson O (2001) Description of regional geological and geophysical maps of northern Norrbotten County (east of the Caledonian orogen). Ba, Sveriges geologiska undersökning, 110 p

Cherevatova M, Smirnov MY, Jones AG, Pedersen LB, Becken M, Biolik M, Ebbing J, Gradmann S, Gurk M, Hübert J, Junge A, Kamm J, Korja T, Lahti I, Löwer A, Nittinger C, Savvaidis A (2015) Magnetotelluric array data analysis from north-west Fennoscandia. Tectonophysics 653:1–19

Cliff RA, Rickard D, Blake K (1990) Isotope systematics of the Kiruna magnetite ores, Sweden; Part 1, Age of the ore. Econ Geol 85(8):1770–1776

Dare SAS, Barnes SJ, Beaudoin G (2014) Did the massive magnetite “lava flows” of El Laco (Chile) form by magmatic or hydrothermal processes? New constraints from magnetite composition by LA-ICP-MS. Miner Dep 50:607–617

Frietsch R (1984) Petrochemistry of the iron ore-bearing metavolcanics in Norrbotten County, northern Sweden. Geol Surv Sweden, Serie C, 62 p

Geijer P (1910) Igneous rocks and iron ores of Kiirunavaara, Luosavaara and Tuolluvaara, Scientific and practical researches in Lapland arranged by Luossavaara-Kiirunavaara Aktiebolag. Stockholm, Norstedt & Söner, 278 p

Hildebrand RS (1986) Kiruna-type deposits: Their origin and relationship to intermediate subvolcanic plutons in the Great Bear Magmatic Zone, Northwest Canada. Econ Geol 81:640–659

Hill GJ, Roots EA, Frieman BM, Haugaard R, Craven JA, Smith RS, Snyder DB, Zhou X, Sherlock R (2021) On Archean craton growth and stabilisation: Insights from lithospheric resistivity structure of the Superior Province. Earth Planet Sci Let 562:116853

Hitzman MW, Oreskes N, Einaudi MT (1992) Geological characteristics and tectonic setting of Proterozoic iron oxide (Cu-U-Au-REE) deposits. Precambr Res 58:241–287

Knipping JL, Bilenker LD, Simon AC, Reich M, Barra F, Deditius AP, Lundstrom C, Bindeman I, Munizaga R (2015) Giant Kiruna-type deposits form by efficient flotation of magmatic magnetite suspensions. Geology 43:591–594.

Logan L, Andersson JBH, Whitehouse MJ, Martinsson O, Bauer TE (2022) Energy drive for the Kiruna Mining District mineral system(s): Insights from U-Pb zircon geochronology. Minerals 12(7):875–900

Martinsson O (2004) Geology and metallogeny of the Northern Norrbotten Fe-Cu-Au province. In: Allen RL, Martinsson O, Weihed P (eds) Svecofennian ore-forming environments of northern Sweden—volcanic associated Zn-Cu-Au-Ag, intrusion-related Cu-Au, sediment-hosted Pb-Zn, and magnetite-apatite deposits in northern Sweden. Soc Econ Geol Spec Publ 131–148

Martinsson O, Billström K, Broman C, Weihed P, Wanhainen C (2016) Metallogeny of the Northern Norrbotten Ore Province, northern Fennoscandian Shield, with emphasis on IOCG and apatite-iron ore deposits. Ore Geol Rev 78:447–492

Nyström JO, Henríquez F (1994) Magmatic features of iron ores of the Kiruna type in Chile and Sweden: Ore textures and magnetite geochemistry. Econ Geol 89:820–839

Parák T (1973) Rare earth in the apatite iron ores of Lappland together with some data about the Sr, Th, and U content of these ores. Econ Geol 68:210–221

Park CF Jr (1961) A magnetite “flow” in northern Chile. Econ Geol 56:431–441

Romer RL, Martinsson O, Perdahl JA (1994) Geochronology of the Kiruna iron ores and hydrothermal alterations. Econ Geol 89(6):1249–1261

Sarlus Z, Andersson UB, Bauer TE, Wanhainen C, Martinsson O, Nordin R, Andersson JBH (2018) Timing of plutonism in the Gällivare area: Implications for Proterozoic crustal development in the Northern Norrbotten Ore District, Sweden. Geol Mag 155(6):1351–1376

Sillitoe RH, Burrows DR (2002) New field evidence bearing on the origin of the El Laco magnetite deposit, northern Chile. Econ Geol 97:1101–1109

Smith MP, Storey CD, Jeffries TE, Ryan C (2009) In situ U-Pb and trace element analysis of accessory minerals in the Kiruna District, Norrbotten, Sweden: New constraints on the timing and origin of mineralization. J Petrol 50(11):2063–2094

Smith MP, Gleeson SA, Yardley BWD (2013) Hydrothermal fluid evolution and metal transport in the Kiruna District, Sweden: Contrasting metal behavior in aqueous and aqueous–carbonic brines. Geochim Cosmochim Acta 102:89–112

Tornos F, Velasco F, Hanchar J (2016) Iron oxide melts, magmatic magnetite, and superheated magmatic-hydrothermal systems: The El Laco deposit, Chile. Geology 44:427–430

Tornos F, Hanchar J, Steele-MacInnis M, Crespo E, Kamenetsky VS, Casquet C (2023) Formation of magnetite-(apatite) systems by crystallizing ultrabasic iron-rich melts and slag separation. Miner Dep 59(1):1–37

Troll VR, Weis F, Harris C, Jonsson E, Andersson UB, Majidi A, Högdahl K, Millet MA, Barker AK, Saravanan S, Kooijman E, Nilsson KP (2016) Magmatic origin of ‘Kiruna-type’ apatite-iron-oxide ores revealed by Fe-O isotope correlations. 35th Int Geol Congr, Cape Town

Vadoodi R, Rasmussen TM, Smirnov M, Bauer T (2021) Towards an understanding of mineral systems–Contributions from magnetotelluric data from the Fennoscandian Shield in northern Sweden. Tectonophysics 808:228816

Vadoodi R, Rasmussen T (2022) Joint interpretation of magnetotelluric and potential field data from north-eastern Norrbotten, Sweden. Pure Appl Geophys 179(3):1069–1088

Welin E (1987) The depositional evolution of the Svecofennian supracrustal sequence in Finland and Sweden. Precambr Res 35:95–113

Westhues A, Hanchar JM, Whitehouse MJ, Martinsson O (2016) New constraints on the timing of host-rock emplacement, hydrothermal alteration, and iron oxide-apatite mineralization in the Kiruna District, Norrbotten, Sweden. Econ Geol 111(7):1595–1618

New Perspectives on Fe-Ti±V Mineralization in the Ślęża-Kunów Area, SW Poland: Findings from the SEMACRET Project

Tomasz Bieńko[1], Olga Rosowiecka[1], Stanisław Mikulski[1], Marcin Olkowicz[1]
[1] Polish Geological Institute – National Research Institute, Warsaw, Poland

Abstract. The SEMACRET Horizon Europe project aimed to identify new mineralized zones through the application of innovative geophysical and geochemical methods. The northern part of the Central Sudetic Ophiolite, specifically the Ślęża Massif and its surroundings, was selected as the reference site. On the surface of Ślęża Mountain, four elongated, southwest-oriented lenses enriched in iron, titanium, and locally vanadium were delineated. Similar mineralized bodies were identified both at the surface and at depth on Kunów Hill. In both areas, the mineralized zones are composed of diallagic gabbros and ferro-gabbros with ophitic textures, indicating a magmatic origin of the Fe-Ti-V mineralization. Microscopic analyses reveal that the mineralization is predominantly monomineralic, consisting mainly of ilmenite with minor amounts of magnetite. Investigations of two boreholes suggest that the mineralized zones can be interpreted as south- or southwest-dipping lenses and dikes of oxide gabbros and ferro-gabbros. These oxide-rich zones were delineated using aeromagnetic surveys, electrical resistivity tomography (ERT), and gamma spectrometry. Future exploration efforts, particularly diamond drilling, should be concentrated in the eastern slopes of the Ślęża Mountain and Kunów area and guided by high-resolution geophysical surveys.

1 Introduction

The SEMACRET project aims to advance sustainable exploration of Critical Raw Materials (CRMs) essential for the green transition in the EU, ensuring a secure and continuous supply for its industries. The research focuses on orthomagmatic sulfide and oxide ore deposits, which host a variety of CRMs, including platinum-group metals (PGMs), copper, cobalt, nickel, vanadium, and titanium.

Currently, only one orthomagmatic sulfide deposit (Kevitsa Ni-Cu-PGE-Co, Finland) and one orthomagmatic oxide deposit (Kemi Cr, Finland) are in production within the EU. However, mafic and ultramafic complexes, which have the potential to host such deposits, are present in several European regions, including Portugal (e.g., Beja Igneous Complex), Spain (e.g., Aguablanca deposit), the Czech Republic (e.g., Staré Ransko deposit), Denmark (e.g., Skærgård deposit, Greenland), and Poland (Central Sudetic Ophiolite).

The primary objective of the SEMACRET project in southwestern Poland was to identify new concealed areas for CRM exploration by integrating advanced geophysical methods with geochemical and petrological investigations.

The Ślęża ophiolite was chosen as a reference site because it is the largest exposed section of the Central Sudetic ophiolite and retains a nearly complete, typical ophiolite pseudo-stratigraphic sequence (Kryza and Pin, 2010). From base to top (south to north), the sequence includes: (1) serpentinized peridotites – Gogołów-Jordanów, (2) pyroxene- and amphibole-rich rocks (ultramafic cumulates; Gogołów-Jordanów), (3) metagabbros (mainly mafic cumulates – Ślęża and Kunów), (4) diabases and metabasalts (likely representing sheeted dykes and lavas, including rare occurrences of pillowed basalts; Gozdnica), and (5) dark metacherts containing radiolaria. The Kunów massif (NE of the Ślęża mountain) is an example of the mafic plutonic sequence of the Ślęża ophiolite under sedimentary cover.

The Ślęża and Kunów regions are predominantly composed of gabbro, with occurrences of serpentinized peridotite. Within the plutonic section of the Ślęża ophiolite, the gabbros are generally medium- to coarse-grained and frequently display an igneous ophitic texture. These rocks exhibit a diverse range of textural features, including ophitic, subophitic, porphyritic, and glomeroporphyritic structures, along with significant variations in grain size and compositional layering (Wahed and Mierzejewski 1998). The primary mineral assemblage of the gabbro consists of partially uralitized clinopyroxene and saussuritized plagioclase, with original anorthite content varying between 50% and 70%, accompanied by minor amounts of opaque minerals. Additionally, secondary minerals formed through post-magmatic or metamorphic alteration are present, including uralitic green amphibole (ranging from Mg-hornblende to actinolite), albite, sphene, epidote (zoisite), calcite, and chlorite. Key accessory minerals include apatite, ilmenite, titanite, magnetite, pyrite, and pyrrhotite.

The presence of ilmenite-bearing rocks within the Ślęża ophiolite was initially documented prior to World War II (Finck, 1928). However, only preliminary geological exploration was conducted at that time, and the area was deemed economically unviable. Detailed geological and geochemical surveys in the 1980s identified three primary zones of ilmenite mineralization within the Ślęża mountain (Jamrozik et al., 1988). Later studies confirmed the presence of titanium- and vanadium-rich mineralized outcrops within the area, with concentrations reaching up to 6.35 wt.% TiO_2 and 0.164 wt.% V_2O_5 (Niśkiewicz and Siemiątkowski, 1993, Jamrozik, 1989). At the same time, geophysical surveys identified a SW-NE oriented magnetic anomaly

approximately 6 km long, extending from Strzegomiany village toward Kunów Hill, east of the Ślęża mountain. Analyses of gabbro samples from this area showed elevated levels of titanium and vanadium (4.92 wt.% and 0.154 wt.%, respectively) (Jamrozik, 1989). Later studies revealed multiple smaller, generally SW-NE- and W-E-oriented, lens-shaped outcrops of the ilmenite-bearing rocks on the Ślęża mountain (Wahed and Mierzejewski, 1998).

The mineralized zones are composed of diallagic gabbros with ophitic textures. Microscopic examinations indicate that it is essentially monomineralic—composed primarily of ilmenite with minor magnetite. Accessory minerals include rutile, pyrrhotite, pyrite, and chalcopyrite, with secondary minerals such as covellite and goethite also present. Ilmenite and magnetite occur in a dispersed form among rock-forming minerals, occasionally forming larger, intergranular aggregates. Grain size varies from very fine microscopic grains to 2–5 mm, with most grains ranging between 50–250 µm. The grains are typically xenomorphic to hypidiomorphic. Smaller grains often exhibit prismatic to needle-like shapes. Textural observations indicate that ilmenite-magnetite mineralization developed concurrently with the primary silicate minerals, clinopyroxene and plagioclase.

2 Methods

The primary objective of the field investigation was to characterize Fe-Ti±V mineralization within the plutonic assemblage of the Ślęża Massif, part of the Central-Sudetic ophiolite. To achieve this, geophysical surveys were conducted, including 12 geoelectrical tomography (ERT) profiles, three gamma-ray spectrometry profiles, and a magnetic survey, aimed at delineating the geophysical response associated with the mineralized rock basement. During the field tests, chemical composition analyss of the samples was conducted using portable X-ray fluorescence (pXRF). Based on the pXRF results, samples were selected for bulk-rock chemical testing and petrographic analysis. Samples of gabbro and metabasalt were collected from the Ślęża Massif, along with samples from Kunów Hill. A total of 20 samples from Mount Ślęża and 29 samples from Kunów Hill were analyzed to determine their bulk-rock chemical composition (Figure 1).

2.1 Geophysical surveys

The ERT surveys (12 profiles) were performed using 12-channel geoelectrical apparatus Terrameter LS, of Swedish company Abem Instrument AB. A gradient measurement system was used in the study with the 5 m and 10 m distance between measuring electrodes along 4 x 100 m and 4x200 m cables, giving 80 electrodes working simultaneously.

The UAV-based magnetic surveys were conducted to assess the feasibility of the method and optimize the methodology in accordance with the equipment and environmental conditions to enhance effectiveness. A total flight distance of 57.7 km was completed at the Kunów site. Three missions were executed over the same square grid with a 50 m line spacing, each covering a flight length of 5.4 km, at successive altitudes of 32 m, 52 m, and 77 m above ground level (a.g.l.). Additionally, ground-based gamma-ray spectrometry measurements were carried out along transects crossing Kunów Hill, with a sampling interval of 10 m (Figure 1, 2).

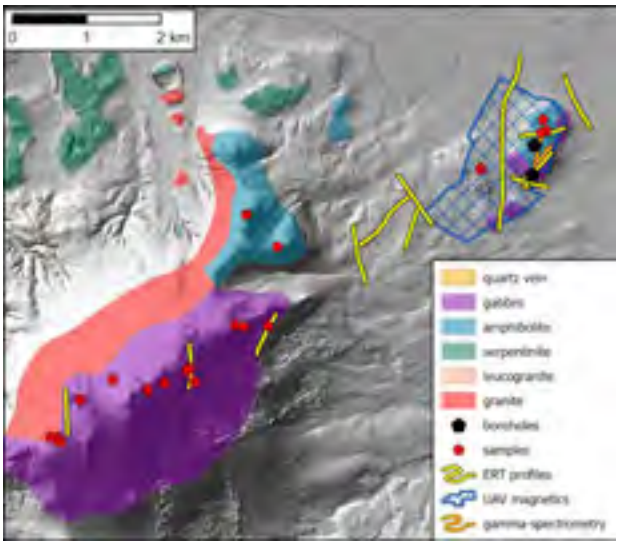


Figure 1. Location of samples, boreholes and geophysical surveys carried out in the reference site (geology after Gaździk 1957 and Trepka and Mierzejewski 1957)

2.2 Geochemical analysis

Olympus Vanta M Series XRF spectrometer was used to study composition of outcropping rocks in the field. Each sample was measured for 30 seconds per beam across three measurement beams, with multiple measurements taken per sample to ensure an accurate averaged composition due to the pinpoint nature of the method. The tests employed the "Soil Extra" mode to assess trace element content. The Olympus Vanta M Series XRF analyzed a broad set of elements, including Al, Si, P, S, Cl, K, Ca, Sc, Ti, V, Cr, Mn, Fe, Co, Ni, Cu, Zn, As, Se, Rb, Sr, Y, Zr, Nb, Mo, Pd, Ag, Cd, Sn, Sb, Cs, Ba, La, Ce, Pr, Hf, Ta, W, Pt, Au, Hg, Pb, Bi, Th, and U. Particular focus was placed on the concentrations of titanium, vanadium, and iron, along with critical and valuable metals related to orthomagmatic deposits, such as nickel, cobalt, chromium, gold, and platinum group elements. In total, over 1200 pXRF analysis were performed in the area of ca. 12 km^2.

Three analytical methods were applied to study chemical composition of sampled rocks – XRF for main elements (SiO_2, Al_2O_3, TiO_2, MnO, Fe_2O_3, K_2O, Na_2O, CaO, MgO, P_2O_5, SO_3, Cl, and F), XRF for trace elements (As, Ba, Bi, Br, Ce, Co, Cr, Cu, Ga, Hf, La, Mo, Nb, Ni, Pb, Rb, Sr, Th, U, V, Y, Zn, Zr, Cd, and Sn), and ICP-MS for rare earth elements (Ce,

Dy, Er, Eu, Gd, Ho, La, Lu, Nd, Pr, Sm, Tb, Tm, Yb, Sc, Y, and Th). Chemical analyses were performed in the Chemical Laboratory of the Polish Geological Institute – National Research Institute in Warsaw, Poland.

3 Results

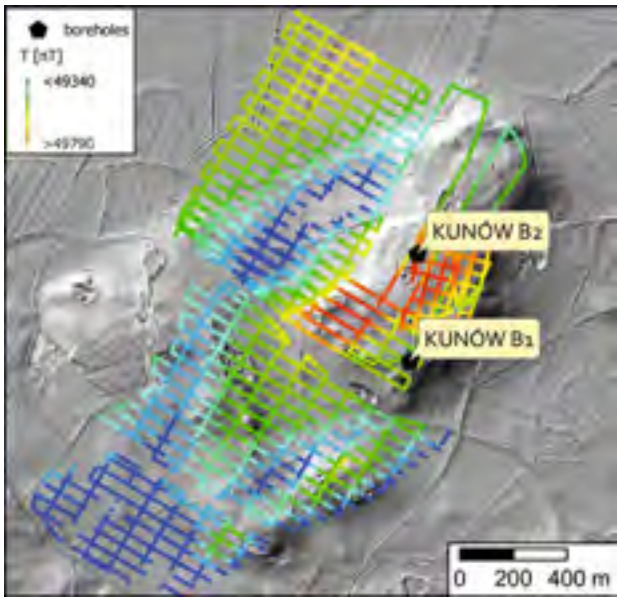


Figure 2. Map of Magnetic anomalies at Kunów hill.

Geochemical and geophysical investigations have identified multiple, small, ferro-gabbroic zones, each measuring a few tens of meters in length and a few meters in width, enriched in iron, titanium, and locally vanadium within the Ślęża Massif and the Kunów Hill. Magnetic survey showed set of strong, linear anomalies in the Kunów hill area (Figure 2). The B2 borehole is located at one of these anomalies. Magnetic image is confirmed with ERT results. Resistivity sections define the boundary between the basement rocks and the overlying Quaternary sedimentary cover while also revealing resistivity anomalies within the basement itself. This method demonstrated its effectiveness in determining approximate depth of the crystalline basement within the study area.

SEMACRET study showed that the mineralized ferro-gabbro from Ślęża contains as much as 5.6 wt. % TiO_2, 23.8 wt. % Fe_2O_3 and 1450 ppm vanadium. In the outcropping part of the Kunów area titanium contents are generally slightly lower (up to 5.5 wt. % TiO_2), whereas iron and vanadium contents are higher (27.8 wt. % Fe_2O_3 and 1600 ppm V). In both areas copper, nickel, cobalt and chromium concentration is generally very low, except one anomalous nickel-enriched sample from the eastern slope of the Ślęża Mountain.

Chemical analyses and portable X-ray fluorescence assays indicate that the highest concentrations of Fe-Ti±V mineralization occur in lens-shaped bodies with a southwest-northeast orientation. These bodies are spatially aligned in a linear pattern extending from the western slope of Mount Ślęża toward the gabbro outcrops at Kunów Hill. However, these mineralized zones are discontinuous, forming isolated lenses of gabbro with anomalously high Fe content rather than a continuous ore body. The results of the geophysical surveys suggest that these mineralized bodies may extend to greater depths within the investigated area.

Logging and sampling of two boreholes, Kunów B1 and Kunów B2, provided insights into the vertical extension of Fe-Ti±V mineralization down to a depth of ca. 100 meters below ground level. These boreholes intersected gabbro with varying textures, as well as multiple oxide-rich intervals ranging in thickness from less than 0.5 meters to nearly 2.0 meters. Portable X-ray fluorescence analysis of core samples identified elevated concentrations of iron, titanium, and vanadium in four oxide-rich intervals within the Kunów B1 borehole and six such intervals in the Kunów B2 borehole. Chemical analyses of three samples from the boreholes confirmed strong titanium and vanadium results (up to 4.77 wt. % TiO_2 and 1607 ppm V).

On the southeastern slope of Mount Ślęża, an ultramafic rock enriched in nickel has been identified. Geochemical analysis indicates that it contains 19.8 wt.% magnesium oxide (MgO), 14.3 wt.% ferric oxide (Fe_2O_3), and 0.19 wt.% nickel. The spatial distribution of this ultramafic body aligns closely with the results of an electrical resistivity tomography (ERT) survey, which reveals a diapir-like, very small (up to few meters in diameter) intrusion at shallow depths, characterized by a strong anomalous resistivity signal. To date, no petrographic studies have been carried out on rock samples from that location; however gabbro from adjacent area contain minor sulphide mineralization composed of pyrrhotite, chalcopyrite, pyrite and pentlandite.

3 Conclusions

The Ślęża area remains one of the most systematically studied and well-documented regions of the Central Sudetic Ophiolite. However, the application of advanced geophysical methods has demonstrated that further exploration could yield promising results, particularly in identifying deeper Fe-Ti±V mineralization and potential sulphide-bearing Ni-enriched zones. The most promising areas for future research include Kunów Hill, the eastern slopes of Mount Ślęża, and the region between Mount Ślęża and Kunów Hill, which may contain numerous small titanium-vanadium placer deposits. Future research should prioritize detailed field observations, a dense sampling grid, and the application of geophysical methods, including ERT, gamma and UAV magnetics. A critical raw materials perspective should also be incorporated, with ophiolitic sequences systematically analyzed for

their nickel, cobalt, vanadium, scandium and platinum group element potential.

Acknowledgements

The SEMACRET project is founded by Horizon Europe and UKRI during 6/2022-5/2025.

References

Finck L (1928) Erlauterungen zur geologischen Karte von Preussen. Lief. 210 Blatt Zobten. (In German).

Jamrozik L (1989) Strzegomiany-Kunów ilmenite mineralization zone in the Ślęża gabbro intrusion within Sobótka ophiolite (Lower Silesia). Przegląd Geologiczny 37: 477-485. (In Polish)

Jamrozik L, Niśkiewicz J, Cholewicka-Meysner D, Farbisz J, Jodłowski S (1988) Discovery of Fe-Ti mineralized zone in gabbros of the Ślęża massif (Fore-Sudetic). Geologia Sudetica 23: 122-127. (In Polish)

Kryza R, Pin C (2010) The Central-Sudetic ophiolites (SW Poland): Petrogenetic issues, geochronology and palaeotectonic implications. Gondwana Research 17: 292-305.

Niśkiewicz J, Siemiątkowski J (1993) Mineralizacja rudna metagabr strefy Strzegomiany-Kunów (masyw Ślęży, Dolny Śląsk). Acta Universitatis Wratislaviensis 1412. (In Polish)

Wahed MA, Mierzejewski MP (1998) A new discovery of ilmenite mineralization within the Sleza metagabbro, Lower Silesia (SW Poland). Przegląd Geologiczny 46(8): 684-688. (In Polish)

Mantle Oxidation and its impact in sulfur speciation: Insights from the Cretaceous Komatiites in Gorgona island

Camilo Andrés Conde Carvajal[1], Iván Mateo Espinel Pachón[1], Ana Elena Concha Perdomo[2]
[1]*University of Geneva, Switzerland*
[2]*Universidad Nacional de Colombia, Bogotá*

Abstract. Gorgona Island, located off the Pacific coast of Colombia, hosts the only known Mesozoic komatiites, formed as part of the Caribbean Large Igneous Province (CLIP) during the Late Cretaceous (~88 Ma). These ultramafic rocks, derived from a high-temperature, and high-degree of partial melting, provide a unique opportunity to investigate mantle conditions and metal transport in a Phanerozoic setting. This study examines the spinifex-textured komatiites of Gorgona to assess their petrological characteristics, comparing them with Archean counterparts to understand mantle oxidation state evolution. Oxygen fugacity (fO_2) estimates suggest an unusually oxidized mantle source (ΔQFM +2 to +3) significantly higher than typical ocean island basalts (OIB) and mid-ocean ridge basalts (MORB). These findings imply that mantle oxidation persisted beyond the Archean-Proterozoic transition, potentially driven by subduction-related inputs or long-term secular oxidation. This study provides new insights into mantle redox evolution and its implications for metal transport and magmatic sulfide mineralization in ultramafic systems.

1 Introduction

The Gorgona Island, located 50 km off the Pacific coast of Colombia, is a well-known locality for the only known Phanerozoic examples of komatiites. These ultramafic volcanic rocks are suggested to be formed as part of the Caribbean Large Igneous Province (CLIP) during the Late Cretaceous (~88 Ma) within a complex, compositionally and thermally heterogeneous mantle plume (Kerr, 2005), representing high-temperature (~1600 °C) and high-degree of partial melting (~30%) (Arndt et al., 1997; Kerr et al., 1996). This study aims to analyse the spinifex-textured komatiites on Gorgona Island to determine the mantle conditions during the Cretaceous evaluating whether there are any differences between these and the Archean komatiites. This comparison will provide insights into mantle dynamics, metal transport, and magmatic sulfide mineralization.

The relatively high MgO and FeO contents of the Gorgona komatiites suggest potential for Fe-Ni-Cu sulfide enrichment, but the extent of economic mineralization remains uncertain due to the lack of significant cumulate sequences and the open-system nature of oceanic plateau magmatism (Kerr et al., 1996). Komatiites are well known for hosting nickel (Ni), copper (Cu), and platinum-group element (PGE) sulfide deposits, which form through sulfide liquid segregation during magmatic differentiation. At Gorgona Island, geochemical studies reveal that while Ni and Cu concentrations are lower than in many Archean komatiites, these depletion patterns imply sulfide saturation may have occurred during magma evolution (Brügmann et al., 1987). However, PGE concentrations, while slightly reduced compared to komatiites of analogous composition, are not depleted to levels indicative of extensive sulfide segregation (Brügmann et al., 1987). This discrepancy highlights the need to integrate melt evolution processes and oxygen fugacity (fO_2) into predictive models, as sulfide segregation efficiency and metal transport dynamics depend on S^{2-} availability, a parameter depending on fO_2 (Jugo, 2009).

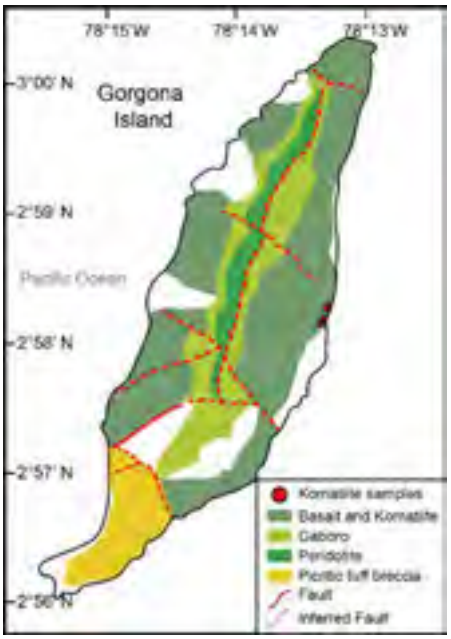


Figure 1. Simplified geological map of Gorgona island in western Colombia. Geology is shown as proposed by Serrano et al. (2011)

Trace element and isotopic compositions indicate a deep mantle plume source for Gorgona komatiites, with pressures estimated at 3–4 GPa (~90–120 km depth) (Herzberg, 1992). Mantle plumes, thermal upwellings interacting with the lithosphere (French & Romanowicz, 2015; Montelli et al., 2006), can generate rocks such as ocean island basalts (OIB). Studies of plume-related xenoliths in OIB reveal oxygen fugacity conditions ranging from ΔQFM −2 to ΔQFM +4, with a mean of ΔQFM +0.82 (±1.40) when calculated at 0.6 GPa, with recalculations at high pressures (~2.5 GPa) a

downward shift of *f*O2 by ~0.7 log units is observed (Cottrell et al., 2022). This agrees with the interpretation that plume-derived magmas typically exhibit low oxygen fugacity, a critical factor in sulfide stability and metal partitioning (Li and Audétat, 2015).

2 Methods

Automated mineral analysis and textural imaging of the studied samples were performed using an FEI QEMSCAN® Quanta 650F facility at the Department of Earth Sciences, University of Geneva. Major and minor element compositions of olivine and Cr-Spinel crystals were analyzed using a JEOL JXA-iHP200F hyperprobe electron probe micro analyser (EPMA), equipped with four Wavelength Dispersive X-ray Spectroscopy (WDS) detectors at the University of Geneva.

3 Results

Olivine showing spinifex texture and containing Cr-rich spinel inclusions is common within the suite of samples. It has a magnesium number (#Mg) of 89 and NiO concentrations ranging from 0.2 up to 0.35 %wt.

Chromium-rich spinel appear as skeletal and euhedral cubic and are present as inclusions in olivine crystals. It has high Cr# [100 × Cr/(Cr + Al)] values ranging from 55 to 75, moderate Mg# [100 × Mg/(Mg + Fe)] values between 35 and 53 and Cr_2O_3 ranging from 36 to 54 wt%.

Melt oxygen fugacity has been estimated at ΔQFM + 3.5 ± 1 by spinel-olivine pairs (Ballhaus et al., 1991), at ΔQFM + 2.1 ± 0.1 by the partitioning of V between olivine and melt (Shishkina et al., 2018) using published data from Kamenetsky et al (2010) and (Mobasheri et al., 2024).

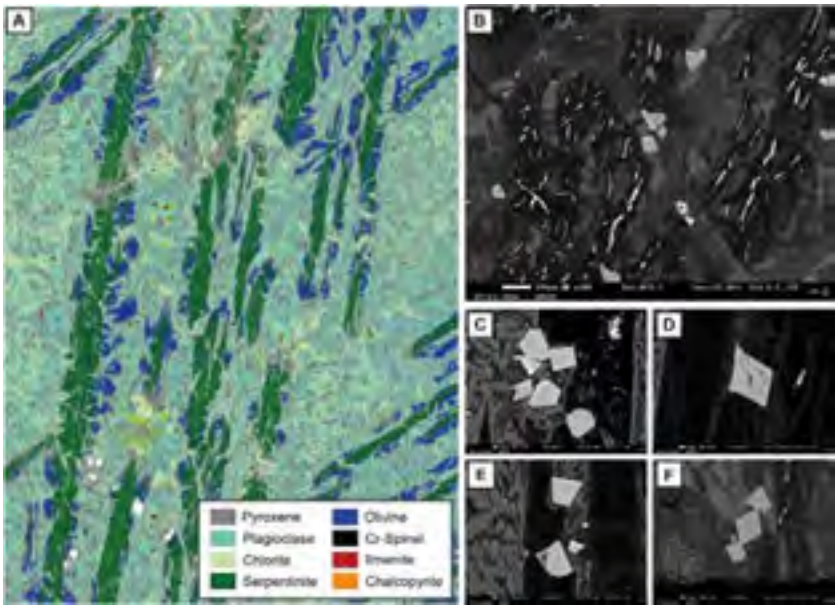


Figure 2. A) QEMSCAN mineral map of sample M1. B-F) BSE-images of Cr-rich spinels.

4 Magma source and oxidation state

The redox state of the mantle has undergone significant secular evolution through geological time. Nicklas et al. (2019) proposed that the Archean mantle was relatively reduced, with ΔQFM values near 0 at ~3.6 Ga, transitioning to ΔQFM ~ +1.3 by ~1.7 Ga based on data from the Winnipegosis komatiites. However, the discovery of oxidized conditions in the Cretaceous komatiites from Gorgona, the youngest known occurrence, extends this evolutionary record by nearly two billion years, raising new questions about the drivers of mantle oxidation in Phanerozoic time.

The elevated ΔQFM values obtained for the Gorgona komatiites (QFM+2 or higher) indicate that their parental melts were considerably more oxidized than typical modern mantle-derived melts. For comparison, mid-ocean ridge basalts (MORB) generally sit near QFM, while ocean island basalts (OIB) rarely exceed QFM+1 (Cottrell et al., 2022). The anomalously high fO_2 recorded in these komatiites suggests that the upper mantle in the Cretaceous may have been more oxidized than previously thought, potentially driven by large-scale geodynamic and surface evolution processes.

Several mechanisms could account for this oxidation. One plausible explanation is the extended influence of subduction, which introduced oxidized material into the mantle through altered oceanic crust and sedimentary inputs. The onset of modern-style subduction, widely considered to have intensified during the Proterozoic (Condie, 2018), could have progressively increased the mantle's redox state over time. An alternative but complementary mechanism involves the influence of Earth surface processes, particularly following the Great Oxidation Event (GOE). Prior to the GOE, the

atmosphere and oceans were largely reducing, limiting the extent to which oxidized materials could enter the mantle. However, after the GOE, oxidative weathering and sedimentary recycling may have delivered increasingly oxidized material into subduction zones, with long-term consequences for the mantle's redox state (Kasting & Catling, 2003; Evans, 2012). Our results suggest that this oxidative overprint persisted into the Cretaceous, influencing even deep mantle plumes.

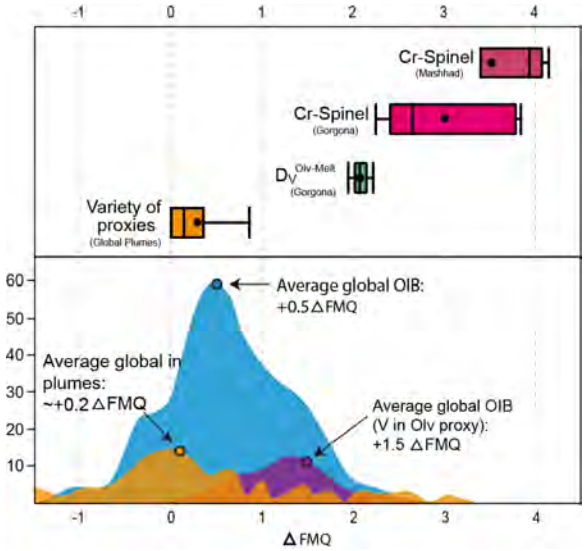


Figure 3. Oxygen fugacity of OIB, Global plumes, Gorgona and Mashhad komatiites. Willhite

To test whether this elevated oxidation is a localized anomaly tied to Gorgona's specific geodynamic setting (e.g., plume-lithosphere interaction near a subduction zone), we applied the same olivine-chromite oxybarometry to another suite of post-Archean komatiites, this time from the Permian. Using published data from (Mobasheri et al., 2024), we obtained similarly elevated fO_2 values for these samples, indicating that high oxidation states are not restricted to Gorgona. This suggests a broader trend, possibly reflecting the cumulative effects of mantle re-fertilization by oxidized subduction inputs, or a more fundamental secular oxidation process operating on a global scale.

Taken together, our results suggest that mantle oxidation continued well beyond the Archean-Proterozoic transition, with further enrichment in oxidized components persisting into the Phanerozoic. The Gorgona komatiites, with their primitive mineralogy (high-Mg olivine, Cr-rich spinels) coupled with unexpectedly high fO_2, capture a snapshot of this evolving mantle system. This discovery demands a re-evaluation of how we link mantle redox evolution to global tectonic processes, surface oxidation history, and the metallogenic potential of ultramafic magmas through time.

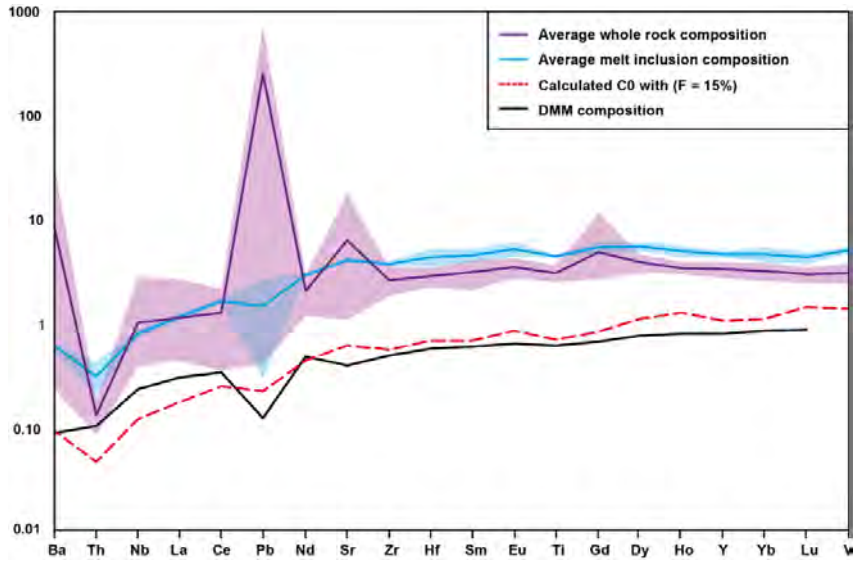


Figure 4. DMM normalized (Workman and Hart, 2004) trace element variation diagrams for whole-rock and silicate melt inclusions (SMIs) compositions.

To evaluate the compositional relationship between Gorgona komatiites and their parental melts, we plotted the average komatiite composition of Gorgona Island alongside silicate melt inclusion data from Kamenetsky et al. (2010) in a multi-elemental diagram normalized against Pyrolite. The two datasets exhibit similar trace and rare earth element (REE) patterns, supporting the interpretation that the melt inclusions represent the primitive melts that led to the origin of the komatittes with the minimum effect of mixing and or crustal contamination. To constrain the komatiite's primary source composition (C_0), we assumed the C_L is represented by the composition of the melt inclusions, and after testing a range of F values, the model with a partial melting degree of 15% yields a

calculated primary composition that exhibits minimal divergence from the depleted MORB mantle reservoir. This implies that the source, likely the depleted MORB mantle (DMM), was already oxidized QMF ~ +2, at the time of melt inclusion entrapment. In contrast, komatiite whole-rock compositions, with independent estimates of higher partial melting degrees (Arndt et al., 1997; Kerr et al., 1996), reflect later stages of magmatic evolution, recording higher oxygen fugacity values (QMF ~ +3), similar to typical arc magma values. The observed increase in QMF during magma evolution suggests the involvement of secondary processes (e.g., fractional crystallization, or crustal assimilation) that increase oxygen fugacity. This agrees with the oxygen fugacity calculated using olivine Cr-spinel pairs.

These findings carry deep implications not only for our understanding of mantle evolution, but also for the processes controlling metal transport and ore formation in ultramafic systems. In reduced melts, sulfur is dominantly present as sulfide (S^{2-}), saturating and forming immiscible sulfide liquids, key carriers of chalcophile metals such as Ni, Cu, and PGEs. In contrast, oxidized melts favour sulfur in its oxidized forms (SO_4^{2-}), which remain soluble in the silicate melt to much higher degrees (Farsang and Zajacz, 2025). This shift fundamentally alters the timing of sulfide saturation and the efficiency of metal transport, potentially explaining variations in metal fertility between Archean and younger komatiite-hosted systems.

Acknowledgements

We would like to thank Luca Caricchi for his support with the EPMA analyses, and Kalin Kouzmanov for the QEMSCAM mapping and processing.

References

Arndt NT, Kerr AC & Tarney J (1997) EPSL Dynamic melting in plume heads: the formation of Gorgona komatiites and basalts. In Earth Planet Sci Letters 146).

Ballhaus C, Berry R F & Green DH (1991) Contributions to Mineralogy and Petrology High pressure experimental calibration of the olivine-orthopyroxene-spinel oxygen geobarometer: implications for the oxidation state of the upper mantle. In Contrib Mineral Petrol 107.

Brügmann GE, Arndt NT, Hofmann AW & Tobschall WJ (1987) Noble metal abundances in koma~te suites from Alexo, Ontario, and Gorgona Island, Colombia.

Condie KC (2018) A planet in transition: The onset of plate tectonics on Earth between 3 and 2 Ga? Geoscience Frontiers, 9(1), 51–60. https://doi.org/10.1016/j.gsf.2016.09.001

Cottrell E, Birner SK, Brounce M, Davis FA, Waters LE & Kelly KA (2022) Oxygen Fugacity Across Tectonic Settings. In: Magma Redox Geochemistry (R. Moretti & D. R. Neuville, Eds.). Willey. https://doi.org/10.1002/9781119473206

Evans KA (2012) The redox budget of subduction zones. In Earth Sci Rev 113:1–32). https://doi.org/10.1016/j.earscirev.2012.03.003

Farsang S & Zajacz Z (2024) Sulfur species and gold transport in arc magmatic fluids. Nature Geoscience. https://doi.org/10.1038/s41561-024-01601-3

French SW & Romanowicz B (2015) Broad plumes rooted at the base of the Earth's mantle beneath major hotspots. Nature, 525(7567), 95–99. https://doi.org/10.1038/nature14876

Herzberg C (1992) Depth and degree of melting of komatiites. Journal of Geophysical Research, 97(B4), 4521–4540. https://doi.org/10.1029/91JB03066

Jugo PJ (2009) Sulfur content at sulfide saturation in oxidized magmas. Geology, 37(5), 415–418. https://doi.org/10.1130/G25527A.1

Kamenetsky VS, Gurenko AA & Kerr AC (2010) Composition and temperature of komatiite melts from Gorgona Island, Colombia, constrained from olivine-hosted melt inclusions. Geology, 38(11), 1003–1006. https://doi.org/10.1130/G31143.1

Kasting JF & Catling D (2003) Evolution of a Habitable Planet. Annual Review of Astronomy and Astrophysics, 41, 429–463. https://doi.org/10.1146/annurev.astro.41.071601.170049

Kerr AC (2005) La Isla de Gorgona, Colombia: A petrological enigma? Lithos, 84(1–2), 77–101. https://doi.org/10.1016/j.lithos.2005.02.006

Kerr AC, Marriner GF, Arndt NT, Tamey J, Nivia A, Saunders AD & Duncan RA (1996) The petrogenesis of Gorgona komatiites, picrites and basalts: new field, petrographic and geochemical constraints. In Lithos (Vol. 37).

Li Y & Audétat A (2015) Effects of temperature, silicate melt composition, and oxygen fugacity on the partitioning of V, Mn, Co, Ni, Cu, Zn, As, Mo, Ag, Sn, Sb, W, Au, Pb, and Bi between sulfide phases and silicate melt. Geochim Cosmochim Acta 162:25–45. https://doi.org/10.1016/j.gca.2015.04.036

Mobasheri M, Arndt N, Cordier C, Sobolev A, Ghasemi H & Garrido CJ (2024) Upper Paleozoic komatiites near Mashhad, NE Iran. Geology. https://doi.org/10.1130/g52289.1 Montelli, R., Nolet, G., Dahlen, F. A., & Masters, G. (2006). A catalogue of deep mantle plumes: New results from finitefrequency tomography. Geochemistry, Geophysics, Geosystems, 7(11). https://doi.org/10.1029/2006GC001248

Nicklas RW, Puchtel IS, Ash RD, Piccoli PM, Hanski E, Nisbet EG, Waterton P, Pearson DG & Anbar, A. D. (2019) Secular mantle oxidation across the Archean-Proterozoic boundary: Evidence from V partitioning in komatiites and picrites. Geochimica et Cosmochimica Acta, 250, 49–75. https://doi.org/10.1016/j.gca.2019.01.037

Shishkina TA, Portnyagin MV, Botcharnikov RE, Almeev RR, Simonyan AV, Garbe-Schönberg D, Schuth S, Oeser M & Holtz F (2018) Experimental calibration and implications of olivine-melt vanadium oxybarometry for hydrous basaltic arc magmas. American Mineralogist, 103(3), 369–383. https://doi.org/10.2138/am-2018-6210

Willhite LN, Arevalo R, Piccoli P, Lassiter JC, Rand D, Jackson MG, Day JMD, Nicklas RW, Locmelis M, Ireland TJ & Puchtel IS (2024) Oxygen Fugacity of Global Ocean Island Basalts. Geochemistry, Geophysics, Geosystems, 25(1). https://doi.org/10.1029/2023GC011249

Willhite LN, Arevalo R, Piccoli P, Lassiter JC, Rand D, Jackson MG, Day JMD, Nicklas RW, Locmelis M, Ireland TJ & Puchtel IS (2024) Oxygen Fugacity of Global Ocean Island Basalts. Geochemistry, Geophysics, Geosystems, 25(1). https://doi.org/10.1029/2023GC011249

Workman RK & Hart SR (2004) Major and trace element composition of the depleted MORB mantle (DMM). Geochemistry, Geophysics, Geosystems, 5(1). https://doi.org/10.1029/2003GC000568

Understanding lower crustal sulfide ore systems: Insights from ultramafic pipes in the Ivrea-Verbano Zone, Italy

Shelby Clark[1], Marek Locmelis[1,2], Marilena Moroni[3], Gianluca Sessa[3], Mattia Pistone[4], Sara Elliott[2]
[1]Department of Earth and Planetary Sciences, Jackson School of Geosciences, The University of Texas at Austin, Austin, Texas, USA
[2]Bureau of Economic Geology, Jackson School of Geosciences, The University of Texas at Austin, Austin, Texas, USA
[3]Department of Earth Sciences, University of Milan, Milan, Italy
[4]Department of Geology, Franklin College of Arts and Sciences, The University of Georgia, Athens, Georgia, USA

Abstract. The decline in discoveries of economically significant magmatic sulfide deposits in the uppermost crust requires extending the search space to deeper (exhumed) levels to meet future metal demands. One area that allows to study the genesis of deep lithospheric sulfide systems is the Ivrea-Verbano Zone (IVZ) in Italy, an exhumed cross section of lower continental crust and sub-continental lithospheric mantle. The IVZ hosts a strongly metasomatized and sulfide-mineralized ultramafic pipe system wherein sulfides are intergrown, or otherwise associated with, carbonates and hydrous silicates. We expand previous research of the 249 Ma Valmaggia pipe (intruded in Lower Permian gabbroic units) to the less-studied 277 Ma Fei di Doccio pipe (intruded at a higher level into Paleozoic amphibolite facies metapelites). We find that, similarly to Valmaggia, the Fei di Doccio pipe contains genetically associated sulfides, carbonates, and hydrous silicates with overall similar elemental patterns. Our results emphasize that the pipes are genetically linked and that sulfur- and carbon-rich mantle fluids played a critical role in mobilizing metals in the deep lithosphere and fertilizing the lower crust in metals. Future research will focus on understanding the fluid path architecture in the IVZ to help develop exploration models for Ni-Cu-PGE in exhumed lower crust.

1 Introduction

Magmatic sulfide deposits host the majority of the world's resources of Ni, Cu, and platinum-group elements (PGE; Naldrett, 1999). However, in recent years, discoveries of surface and near-surface economic ore deposits have declined (Schodde, 2023), suggesting that the majority of giant ore deposits near the surface have already been found. Consequently, exploration efforts need to shift to progressively deeper crustal deposits, including areas of exhumed deep crustal rocks that are often neglected. To guide exploration for such deposits, the physical and chemical mechanisms responsible for their metal-enrichment need to be understood. One exemplary area that allows to study exhumed deep crustal magmatic sulfide deposits is the Ivrea-Verbano Zone (IVZ) in northwest Italy (Fig. 1A), an exposed cross section of the sub-continental lithospheric mantle and overlying lower continental crust that was uplifted during the Alpine Orogeny (e.g., Mehnert, 1975; Garuti et al., 1980).

The IVZ hosts five known ~300-m-wide strongly metasomatized and sulfide-mineralized pipes (Fig. 1B). The pipes are harzburgites later percolated by

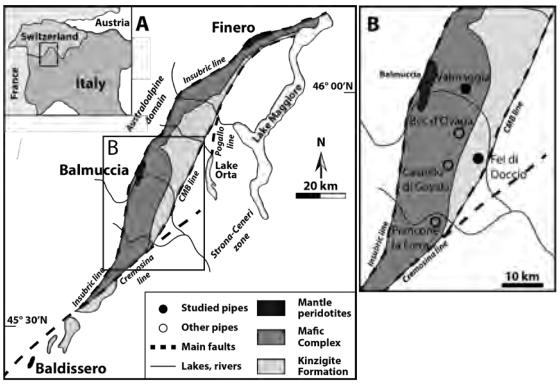


Figure 1. A) Simplified geologic map of the Ivrea-Verbano Zone. B) Locations of the ultramafic pipes, including Valmaggia and Fei di Doccio (filled circles). Modified after Fiorentini and Beresford (2008) and Locmelis et al. (2016).

metasomatic fluids that enriched the pipes in late-stage carbonates, phlogopite, and amphibole. Semi-massive sulfide mineralization is concentrated along the outer margins of the pipes and dominated by pyrrhotite, pentlandite, and chalcopyrite with ore tenors up to 11.9% Cu, 10.7% Ni, and 5 ppm PGE (Zaccarini et al., 2014). The sulfides are frequently intergrown with carbonates and hydrous silicates, suggesting a genetic link between the formation of the sulfide mineralization and the late-stage metasomatic event that enriched the pipes in volatiles. However, the relationship between carbon, sulfur, and metals as they are transferred from the mantle into the crust, and the importance for ore genesis, remains elusive.

Previous studies of the most accessible Valmaggia pipe suggested that sulfides were physically transported into the pipe via bubble-pair transport mechanisms (Blanks et al., 2020; Locmelis et al., 2021). In such a model, sulfides attached to gas/supercritical bubbles and were dragged upwards through a melt within a crystal mush. However, subsequent work focusing on the associations between sulfides and fluids indicated that metals were transported into the pipes via a mixed H_2O-CO_2-S and metal-rich metasomatic fluid percolating, co-precipitating sulfides, carbonates, and hydrous silicates (Clark, 2024). To further constrain the role of metasomatic fluids in the formation of the pipe-hosted sulfide ore in the IVZ, we expand the previous research on the Valmaggia pipe to the less-studied Fei di Doccio pipe that was

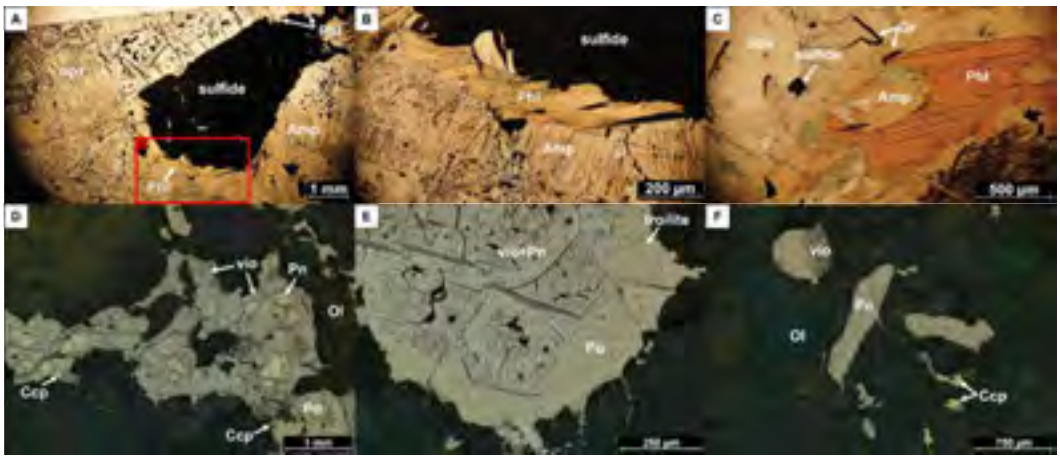


Figure 2. Representative thin section images of the Fei di Doccio pipe. Transmitted light images of: A) Sulfide bleb with peripheral symplectic sulfides, intergrown phlogopite laths, and surrounding amphibole; B) Detailed view of the phlogopite-sulfide intergrowths shown in A; C) Characteristic hydrous silicate assemblage. Reflected light images of: D) Interstitial sulfides consisting of pentlandite and violarite, with minor pyrrhotite; E) Pyrrhotite-pentlandite-violarite bleb with troilite exsolutions in Po; F) Irregular blebby sulfides in olivine cumulate. Amp=amphibole, Ccp=chalcopyrite, Gr=graphite, ol=olivine, opx=orthopyroxene, Phl=phlogopite, Pn=pentlandite, Po=pyrrhotite, sp=spinel, vio=violarite.

emplaced at a stratigraphically higher level, at least 1000 m above the Valmaggia pipe.

2 Geologic Setting

2.1 Ivrea-Verbano Zone

The Ivrea-Verbano Zone (IVZ) in the Alps of northwest Italy is an exhumed slice representing the boundary between the lower continental crust and subcontinental lithospheric mantle (Mehnert, 1975; Garuti et al. 1980). During the Alpine orogeny, the IVZ was exhumed ~15 km and emplaced into the upper crust where it is exposed at the surface today at a subvertical angle (Fig. 1A; Mehnert, 1975; Schmid et al., 1987; Quick et al., 1994). The IVZ is composed of three main lithological units: the Kinzigite Formation, the Mafic Complex, and the Mantle Peridotites. The Kinzigite Formation is a metasedimentary unit representing the basement of the continental crust of the Southern Alps (Bea and Montero, 1999). The Mafic Complex is an approximately 10-km-thick igneous unit that underplated the Kinzigite formation ca. 287 Ma ago (Fiorentini et al., 2018). The Mantle Peridotites consist of four obducted slices of mantle that crop out along the Insubric line at Baldissero, Balmuccia, Finero, and Premosello (Quick et al., 1994), and exhibit varying degrees of partial melting and decreasing degrees of metasomatism from north to south (Hartmann & Wedepohl, 1993).

2.2 Ultramafic pipes

The IVZ hosts five known ultramafic alkaline pipe-like bodies that exhibit varying degrees of metasomatism and Ni-Cu-PGE sulfide mineralization (Garuti et al., 2001; Fiorentini and Beresford, 2008; Zaccarini et al. 2014; Locmelis et al., 2016; Sessa et al., 2017). Four pipes intrude into the Mafic Complex at Bec d'Ovaga, Castello di Gavala, Piancone le Frera, and Valmaggia; one pipe intruded the metasedimentary Kinzigite Formation at Fei di Doccio (Fig. 1B).

Our current research focuses on the pipes at Valmaggia and Fei di Doccio that are metasomatized peridotite bodies enriched in a secondary assemblage of hydrous silicates (dominated by amphibole and phlogopite), with locally abundant carbonates, apatite, and disseminated to semi-massive Ni-Cu-PGE-sulfide mineralization. Previous geochronological zircon and baddeleyite studies have shown the Valmaggia pipe was emplaced 249 Ma ago (Locmelis et al., 2016) and the Fei di Doccio pipe 277 Ma ago (Fiorentini et al., 2018). Due to the subvertical tilting of the IVZ, the exposed portions of the Fei di Doccio pipe are interpreted to have been emplaced >1000 m stratigraphically higher than the Valmaggia pipe. Previous studies by Fiorentini et al. (2018) determined that pyrrhotite at Valmaggia showed a $\delta^{34}S$ mantle signature (-0.28 to -0.32‰), while pyrrhotite from Fei di Doccio showed heavier (but still mantle-like) signatures of +1.49 to 1.72‰, likely reflecting its emplacement into the Kinzigite Formation.

3 Samples and Methods

The Valmaggia and Fei di Doccio pipes were mined underground until the end of World War II. While the workings of the Valmaggia pipe remain accessible, the entrance to the Fei di Doccio is collapsed and sampling is restricted to tailings piles. Here, we present new data for Fei di Doccio integrated with previously published complementary data from both the Fei di Doccio and Valmaggia pipes (Locmelis et al., 2016; Fiorentini et al., 2018). Eight samples from the Fei di Doccio pipe (polished sections and mounts) were studied using transmitted and reflected light microscopy using a Zeiss Axioskop 40 in the Department of Earth and Planetary Sciences

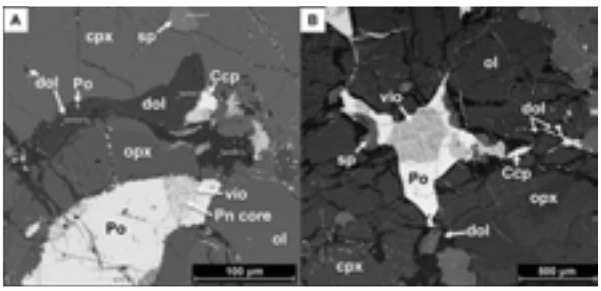


Figure 3. Backscattered electron images of sulfide-carbonate relationships in the Fei di Doccio pipe. A) Dolomite in contact with a chalcopyrite-pentlandite bleb; B) Interstitial polyphase sulfide composed of pyrrhotite, pentlandite and violarite with associated dolomite. Ccp=chalcopyrite, cpx=clinopyroxene, dol=dolomite, ol=olivine, opx=orthopyroxene, Pn=pentlandite, Po=pyrrhotite, sp=spinel, vio=violarite.

in the Jackson School of Geosciences at the University of Texas at Austin, Texas, USA. A subset of samples was further studied using a Zeiss Sigma high-vacuum (HV) field emission gun scanning electron microscope (FEG-SEM) in the Bureau of Economic Geology in the Jackson School of Geosciences at the University of Texas at Austin.

New bulk rock compositions of five samples from Fei di Doccio were analyzed at Activation Laboratories Ltd ("Actlabs"). Major and minor element compositions were determined via fusion X-Ray Fluorescence (XRF). Trace elements were determined via multi-acid partial digestion followed by sodium peroxide fusion inductively coupled plasma mass spectroscopy (ICP-MS) and optical emission spectroscopy (ICP-OES). Bulk rock data presented here was filtered to include only sulfide-poor samples (< 0.6 wt.% S) to determine the pipe composition rather than that of the sulfide ore.

4 Results

4.1 Petrographic observations

Similar to the Valmaggia pipe (*cf.* Fiorentini et al., 2002; Locmelis et al., 2016; Sessa et al., 2017), the silicate assemblage in the Fei di Doccio pipe is dominated by olivine, clinopyroxene, and orthopyroxene, with amphibole and phlogopite. Olivine, clinopyroxene, and orthopyroxene grains are commonly up to 3 mm in the longest direction. Amphibole ranges from < 25 µm to 3 mm in the longest direction. Phlogopite grains are < 25 µm to 1.5 mm, and are locally intergrown with amphibole and sulfides (Fig. 2A-C).

Sulfide mineralization in the Fei di Doccio pipe is dominated by pyrrhotite (40-50% modal), pentlandite and violarite (40-50% modal), and chalcopyrite (<10% modal) that occur as a semi-massive network, interstitial grains (Fig. 2D), and large disseminated blebs up to 5.5 mm across (Fig. 2E-F). Sulfides commonly show symplectic textures at the peripherals of large (< 1 mm) sulfide blebs (Fig. 2A). Similar to the Valmaggia pipe, sulfides are locally associated with carbonates and hydrous silicates. Carbonates in the Fei di Doccio pipe are present as sub- or anhedral grains ranging in size between < 25 µm to 500 µm in the longest direction and are spatially related to, or rimming, sulfide phases. Similar to the observations made for carbonates, sulfides are commonly intergrown with hydrous silicates, i.e., amphibole and phlogopite (Fig. 2B).

Semi-quantitative SEM studies show that carbonates in the Fei di Doccio samples have a dolomitic composition. The carbonates are commonly associated with sulfides (Fig. 3A), but are also found disseminated in the silicate assemblage with small sulfide blebs (< 25 µm) or alone (Fig. 3B). Fe-Ti-Al-oxides (magnetite, ilmenite, spinel) are commonly associated with sulfide mineralization, with ilmenite notably more abundant than magnetite. Graphite is found in association with sulfides and hydrous silicate mineralization as small flakes (< 50 µm) and lamellae within amphiboles and phlogopite (Fig. 2C).

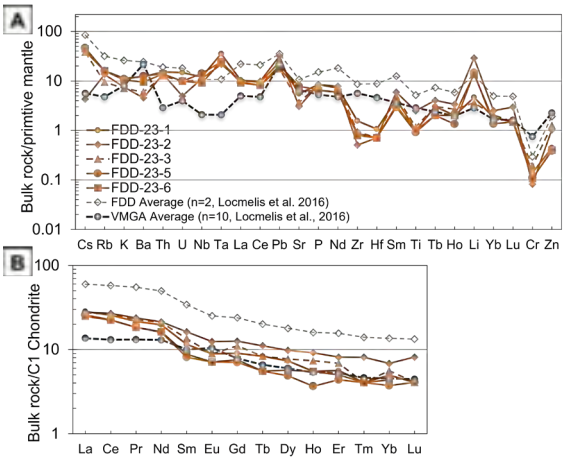


Figure 4. Normalized bulk-rock profiles for five samples from Fei di Doccio (FDD) compared to previously published data from Locmelis et al. (2016). A) Trace elements and B) rare earth elements. Primitive mantle and C1 chondrite values from McDonough and Sun (1995).

4.2 Bulk rock compositional data

Samples from Fei di Doccio are olivine hornblende pyroxenites enriched in all measured trace elements relative to the composition of the primitive mantle, with exception of Zr, Hf, and Cr (Fig. 4A). Notably, Ta, Pb, Sm, and Li display distinct positive anomalies, whereas Ba, Sr, Zr, Hf, Ti, and Cr exhibit mild to strong negative anomalies. Elemental abundances are relatively similar between all five studied samples, with the exception of FDD-23-2, which exhibits a negative Cs anomaly.

As illustrated in Figure 4B, all samples show an enrichment in REE relative to the composition of the C1 chondrite. Light rare-earth elements (La through Nd) display a shallow slope and are enriched relative to the heavy rare earth elements. All Fei di Doccio samples display a slightly negative Eu anomaly. Rare-earth element trends for all samples are similar, with the exception of Yb that displays variable concentrations ranging from negative to positive anomalies.

5 Discussion

The ultramafic pipes in the IVZ give critical insight into mass transport mechanisms between the subcontinental lithospheric mantle and continental crust along paleomargins. In order to determine the nature of the metasomatic fluids in the IVZ, we compare the previously published Valmaggia pipe to the new data from Fei di Doccio. There are notable differences in the sulfide and carbonate modal abundances between the pipes. Ni-sulfide phases (pentlandite, violarite) are more abundant in Fei di Doccio (Fig. 2D-E), exhibiting an abundance of 40-50 modal % compared to < 30 modal % in the Valmaggia pipe (Clark, 2024). Additionally, carbonates in the samples studied here are more abundant and are also much larger in size (up to 500 µm) compared to those observed at Valmaggia (< 200 µm).

Bulk rock analysis of sulfide-poor samples (< 0.6 wt.% S) in the Fei di Doccio pipe are plotted against previous pipe data from Locmelis et al. (2016) containing up to 15-20 wt.% S (Fig. 4). Without significant sulfide mineralization, the Fei di Doccio pipe is notably depleted in most trace metals and REE when compared to mineralized samples from the same pipe, however the poorly-mineralized samples are enriched in most trace metals and REE compared to the mineralized Valmaggia pipe (Locmelis et al., 2016; Fig. 4).

Our results indicate that while the metasomatizing fluids led to trace metal and REE enrichment throughout the entire pipe, the fluids associated with a higher S wt.% may contribute to higher trace element mobilization and metal fertilization of the lower crust. Our future research will utilize comprehensive (mineral) geochemical and geochronological studies to better constrain the evolution of H_2O-CO_2-S-rich fluids as they are transported from the subcontinental lithospheric mantle into the lower continental crust. The data will be interpreted within the framework of the geodynamic evolution of the IVZ to understand the mineralizing fluid path architecture, thereby aiding the development of exploration models for exhumed lower crustal rocks for Ni-Cu-PGE sulfide deposits.

Acknowledgements

S. C. acknowledges support from the Jackson School of Geosciences through a teaching fellowship. M. L. acknowledges support through the National Science Foundation (NSF) CAREER award #1944552 “Investigating the source, transport and deposition of economically important metals in the lower continental crust”. M.P. acknowledges support of the Swiss National Science Foundation (Ambizione Fellowship PZ00P2_168166). We thank Jeremiah Funke for his role in sample collection.

References

Bea F & Montero P (1999) Behavior of accessory phases and redistribution of Zr, REE, Y, Th, and U during metamorphism and partial melting of metapelites in the lower crust: An example from the Kinzigite Formation of Ivrea-Verbano, NW Italy. Geochim Cosmochim Acta 63:1133–1153.

Blanks DE, Holwell DA, Fiorentini ML, Moroni M, Giuliani A, Tassara S, González-Jiménez JM, Boyce A & Ferrari E (2020) Fluxing of mantle carbon as a physical agent for metallogenic fertilization of the crust. Nat Commun 11(1):4342.

Clark SL (2024) Fe-Ni-Cu-PGE Sulfide Transport Mechanisms and Carbon-Sulfur Interactions in Lower Crustal Magmatic Settings: A Study From the Valmaggia Ultramafic Pipe, Ivrea-Verbano Zone, Italy (Master's thesis, Missouri University of Science and Technology).

Fiorentini ML & Beresford SW (2008) Role of volatiles and metasomatized subcontinental lithospheric mantle in the genesis of magmatic Ni-Cu-PGE mineralization: Insights from in situ H, Li, B analyses of hydromagmatic phases from the Valmaggia ultramafic pipe, Ivrea-Verbano Zone (NW Italy). Terra Nova 20(5):333–340.

Fiorentini ML, LaFlamme C, Denyszyn S, Mole D, Maas R, Locmelis M, Caruso S & Bui TH (2018) Post-collisional alkaline magmatism as gateway for metal and sulfur enrichment of the continental lower crust. Geochim Cosmochim Acta 223:175–197.

Garuti G, Rivalenti G, Rossi A, Siena F, Sinigoi S (1980) The Ivrea–Verbano mafic ultramafic complex of the Italian western Alps: discussion of some petrologic problems and a summary. Rendiconti della Societa Italiana di Mineralogia e Petrografia 36:717-749.

Garuti G, Bea F, Zaccarini F & Montero P (2001) Age, geochemistry and petrogenesis of the ultramafic pipes in the Ivrea Zone, NW Italy. J Petrol 42(2):433–457.

Hartmann G & Wedepohl KH (1993) The composition of peridotite tectonites from the Ivrea Complex, northern Italy: Residues from melt extraction. Geochim Cosmochim Acta 57:1761–1782.

Locmelis M, Fiorentini ML, Rushmer T, Arevalo Jr R, Adam J and Denyszyn SW (2016) Sulfur and metal fertilization of the lower continental crust. Lithos 244:74-93.

Locmelis M, Moroni M, Denyszyn SW, Webb LE, Fiorentini ML, Sessa G, Caruso S, Mathur R and Nanzad B (2021) On the formation of magmatic sulphide systems in the lower crust by long-lived mass transfer through the lithosphere: Insights from the Valmaggia pipe, Ivrea Verbano Zone, Italy. Terra Nova 33(2):137-149.

McDonough WF & Sun SS (1995) The composition of the Earth. Chem Geol 120(3-4):223-253.

Mehnert KR (1975) The Ivrea Zone, a model of the deep crust. Neu Jb Mineral, Abh 125:156-199.

Quick JE, Sinigoi S & Mayer A (1994) Emplacement dynamics of a large mafic intrusion in the lower crust, Ivrea-Verbano Zone, northern Italy. J. Geophys. Res. 99(B11).

Schmid SM, Zingg A & Handy M (1987) The kinematics of movements along the Insubric Line and the emplacement of the Ivrea Zone. Tectonophysics 135(1–3):47–66.

Sessa G, Moroni M, Tumiati S, Caruso S & Fiorentini ML (2017) Ni-Fe-Cu-PGE ore deposition driven by metasomatic fluids and melt-rock reactions in the deep crust: the ultramafic pipe of Valmaggia, Ivrea-Verbano, Italy. Ore Geol Rev 90:485-509.

Schodde R (2023) Exploration: Australia vs The World. In International Mining and Resources Conference (IMARC)

Zaccarini F, Garuti G, Fiorentini ML, Locmelis M, Kollegger P & Thalhammer OA (2014) Mineralogical hosts of platinum group elements (PGE) and rhenium in the magmatic Ni-Fe-Cu sulfide deposits of the Ivrea Verbano Zone (Italy): an electron microprobe study. Neu Jb Mineral 191:169-187.

Preliminary LA-ICP-MS trace element data for ilmenite and apatite from Fedorivka, Stremyhorod and Nosachiv Ti-P deposits in the Ukrainian Shield

Krzysztof Foltyn[1], Władysław Zygo[1], Adam Piestrzyński[1], Leonid Shumlyanskyy[2,3,4]
[1]Faculty of Geology, Geophysics and Environmental Protection, AGH University of Kraków, Poland
[2]Institute of Geological Sciences, Polish Academy of Sciences, Kraków, Poland
[3]M.P. Semenenko Institute of Geochemistry, Mineralogy and Ore Formation, Kyiv, Ukraine
[4]School of Earth and Planetary Sciences, Curtin University, Australia

Abstract. Proterozoic massif-type anorthosite complexes in the Ukrainian Shield host a number of intrusions bearing economic ilmenite-apatite (Ti-P) ores. Among them are Fedorivka and Stremyhorodske deposits within the central part of the Korosten pluton and Nosachiv deposit in the Korsun-Novomyrhorod complex. LA-ICP-MS trace element analyses of apatite revealed similarities and differences between these deposits, partially attributed to fractional crystallization, such as strongly negative europium anomaly Eu/Eu* (0.09-0.11) in sample from the Nosachiv deposit. Application of trace elements in cumulus apatite as petrological indicators suggest potential crustal contamination by a silicic component in the case of Nosachiv and Stremyhorod ores, clearly distinct from more primitive melt composition revealed for the Fedorivka deposit. The sample from the Fedorivka has also the highest content of scandium (111 ppm on average) and lowest of REE which could indicate useful application of petrological data in mineral exploration focused on potential by-products such as scandium or REE.

1 Introduction

Ukraine holds the largest titanium reserves in Europe hosted in both primary and alluvial deposits and remains an important titanium producer, even though only placer ores are currently being mined. Proterozoic massif-type anorthosite complexes and related rocks contain economic concentrations of not only titanium and phosphorus but can be also considered as a potential source of other raw materials such as vanadium, scandium or REE occurring as substitutions in major ore minerals. The aim of this study was to analyse trace element content in ilmenite and apatite from three orthomagmatic Ti-P deposits in the Ukrainian Shield to gain a better insight into the ore forming processes and examine the potential for additional by-products.

2 Geological settings

The Ukrainian Shield hosts two Paleoproterozoic anorthosite-mangerite-charnockite-granite (AMCG) complexes: the Korosten and Korsun-Novomyrhorod plutons (Shumlyanskyy et al. 2017). The Korosten AMCG complex consists of a number of granitic rocks that belong to the rapakivi group, and a suite of basic rocks that includes predominantly anorthosite and leucogabbronorite, with subordinate gabbro-noritic rocks which host Fedorivka and Stremyhorod Ti-P deposits (Fig. 1).

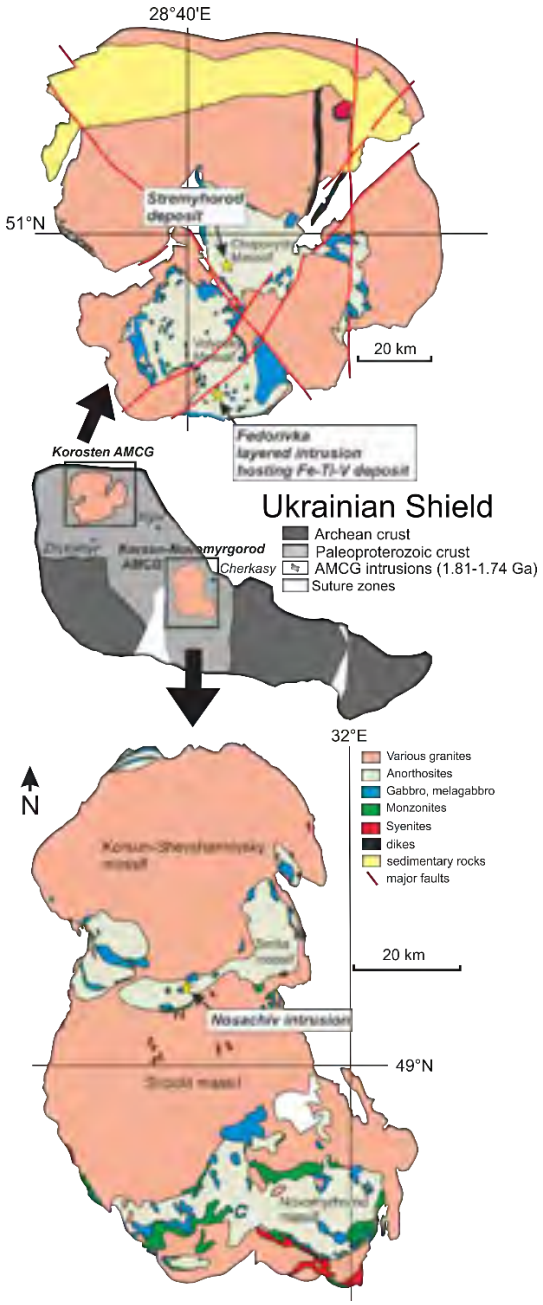


Figure 1. Geological map of the Korosten and Korsun-Novomyrhorod plutons in the Ukrainian Shield with the location of the studied Ti-P ore deposits (after Shumlyanskyy et al. 2017).

Similarly, the Korsun-Novomyrhorod AMCG complex (Fig.1) constituents are also mainly rapakivi granites, anorthosite, leuconorite, with less abundant mesocratic norite, gabbro-norite and gabbro (Shumlyanskyy et al. 2017).

The Fedorivka Ti-P deposit is located 30 km north of Zhytomyr and 125 km west of Kyiv. It is hosted by the Fedorivka Layered Intrusion (FLI), and consists of ilmenite, apatite and titanomagnetite accumulations within layers of oxide-rich olivine gabbro (Duchesne 2006). The gutter- or banana-shaped gabbroid intrusion, in the plan view, is 240-450 m wide and 3,5 km long in northeast direction with ore-bearing gabbro found at the depth up to 322 m (Gurskiy 2002). Available resource estimation amounts to 129.776 Mt of ore with 3 wt.% P_2O_5 (Syvyi et al. 2019) but the information about the reserves of titanium is limited. Average grade has been reported as 6.5 wt.% TiO_2, 2.9 wt.% P_2O_5 and 0.042 wt.% V_2O_5 (Scherbak and Bobrov 2005). Some ilmenite has been mentioned as carriers of isomorphic admixtures of Sc and V (Gurskiy 2002).

The Stremyhorod Ti-P deposit is located 20 km south-east of Korosten and 130 km north-west of Kyiv. Ore mineralization consists of ilmenite, apatite and minor titanomagnetite hosted by predominantly troctolites of the oval-shaped, 2.3 × 1 km in size, igneous body which appears conical in cross sections (Gursky et al. 2003). Resources are estimated as 886.344 Mt of ore with 2.4 wt.% P_2O_5 (Syvyi et al. 2019). Access to data on reserves of titanium and scandium ores is limited, but available sources report the average content of 6.91 wt.% TiO_2, 2.42 wt.% P_2O_5, 0.2 wt.% vanadium and 80 ppm of scandium (Scherbak and Bobrov 2005).

The Nosachiv Ti-P deposit is located 45 km south-west of Cherkasy, 160 km south-east of Kyiv. Hosted by a 2250 m long and 200-780 m wide gabbroid intrusion, the ilmenite-apatite deposit is drilled down to 600-650 m and open at depth (Kryvdik et al. 2009). The ore of Nosachiv deposit is related to two separate intrusive phases: the first stage is represented by fine- to medium-grained olivine and olivine-bearing, apatite-rich and ilmenite-poor gabbroids whereas the second one is the main ore stage characterized by an almost complete absence of olivine and apatite in ilmenite-rich, coarse to medium-grained norites (Gursky et al. 2003). Access to data on reserves of titanium and scandium ores is limited, but available sources report average grade to be 7.44% TiO_2 and 0.75% P_2O_5.

3 Samples and methods

One apatite-ilmenite bearing sample was chosen from each deposit based on overall abundance of ore minerals and bulk rock geochemical compositions (1.5-2.5 wt. % P_2O_5 and 4-5 % TiO_2). The sample from the Stremyhorod deposit (STR) is from the drillcore C80 (sample depth 66 m), Nosachiv material (NOS) is from the drillcore 2004 (depth 84 m) whereas sample from the Fedorivka deposit (FED) represents drillcore from the central part of deposit (no depth information available). Ilmenite and cumulus apatite are the main ore minerals in each sample; in the Stremyhorod deposit they are accompanied by minor magnetite (ca. 5%) with trellis ilmenite exsolutions whereas in the Fedorivka sample magnetite (ca. 5-10%) with very fine ulvöspinel exsolutions forming cloth texture is present.

After petrographic observations in reflected light, samples were analyzed using JEOL JXA-8230 electron microprobe as well as ESL213 Nd:YAG laser ablation system coupled to the Thermo Scientific iCAP TQe ICP-MS in the Laboratory of Critical Elements AGH-KGHM at AGH University of Krakow, Poland. For apatite, the laser was fired at a frequency of 20 Hz and fluence of 4 J/cm^2 with a 40 µm laser spot size. In case of ilmenite, a fluence of 5 J/cm^2 and a 50 µm laser spot size was used. Helium was used as a carrier gas with a flow rate of 0.70 L/min. Typical acquisition consisted of 20 s of gas blank measurement followed by 40 s of spot measurement and 10 second wash-out time between each analysis. For apatite, Ca concentrations determined by EPMA were used as internal standard while NIST 612 glass was used as the external standard for quantification of the trace element content whereas NIST 610 and Loliondo Arusha apatite nanopellet (myStandards GmbH) were also monitored for QAQC. In the case of ilmenite, Fe concentrations determined by EPMA were used as internal standard while Kennedy Ridge magnetite nanopellet (MAKR-NP, myStandards GmbH) was used for quantification of trace elements with BHVO-2-NP nano-pellet used for quality control of the analyses.

4 Results

4.1 Trace element composition of ilmenite

Ilmenite trace element composition is summarized in Table 1. Ilmenite from Nosachiv is enriched in vanadium which can be attributed to the lack of magnetite (typical host of vanadium) in comparison to that from the Fedorivka and Stremyhorod deposits. It is also characterized by higher content of Cr, Ni but also Nb, Ta and W. Ilmenite from Fedorivka contains the highest content of scandium (average 111 ppm of Sc), followed by Stremyhorod (average 91.7 ppm Sc) and Nosachiv (average 66.8 ppm of Sc).

4.1 Trace element composition of apatite

Among the analyzed samples, apatite from the Fedorivka deposit is clearly distinct from those from the Nosachiv and Stremyhorod deposits, which are more similar to each other and are characterized by higher contents of Y, REE, Th, U and lower Sr (Fig. 2).

	STR (n=7)	FED (n=9)	NOS (n=9)
	ppm		
Sc	**91.7** (79.7-105)	**111** (103-117)	**66.8** (64.2-70)
V	**620** (347-963)	**111** (84.3-129)	**1723** (1309-2028)
Cr	0.89 (0.75-1.12)	2.39 (1.84-2.7)	269 (210-297)
Mn	6372 (5962-7515)	5693 (5560-5946)	4654 (4488-4771)
Co	28.9 (20.7-38.6)	53.1 (47.9-56.5)	58.8 (47.1-67.7)
Ni	0.49 (0.28-0.85)	0.78 (0.57-1.11)	3.06 (1.8-3.79)
Cu	10.5 (9.6-11.2)	11.4 (9.99-17.7)	10.5 (10.1-10.8)
Zn	141 (61.9-210)	105 (79-205)	141 (118-189)
Nb	131 (39.6-173)	38.5 (36.4-40.3)	240 (233-251)
Mo	28.5 (22.7-33.5)	1.79 (1.29-2.74)	13.6 (13.2-14.4)
Sn	4.54 (3.37-8)	0.14 (0.11-0.18)	8.95 (8.22-9.72)
Hf	9.10 (2.18-21)	3.68 (3.54-3.76)	12.9 (0.95-21.1)
Ta	6.28 (1.17-8.88)	2.73 (2.49-2.96)	14.7 (14.18-15.3)
W	0.86 (0.46-1.02)	0.03 (0.02-0.04)	4.58 (3.99-5.37)

Table 1. Selected LA-ICP-MS trace element composition in ilmenite. Average content in ppm, minimum-maximum content in brackets, n=number of analytical spots.

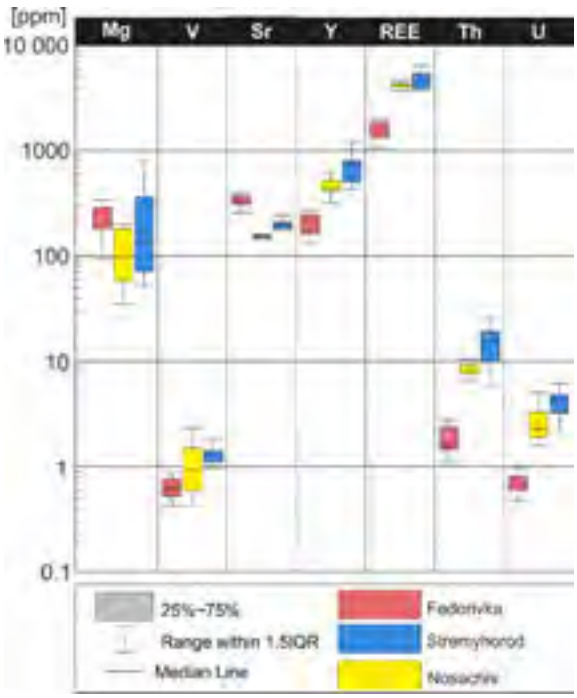


Figure 2. Box-and-whisker plot for selected trace elements from the analyzed apatites from Ti-P deposits of the Ukrainian Shield.

The total rare earth element (REE) content is the highest in the Stremyhorod sample (∑REE 3700-6411 ppm), followed by the Nosachiv (∑REE 3748-4800 ppm), and is distinctly lower in Fedorivka (∑REE 1058-2008 ppm); in all cases chondrite normalized REE patterns exhibit negative Eu anomalies (Fig. 3). Eu/Eu* (calculated as $Eu_N/(Sm_N \times Gd_N)^{0.5}$) range from 0.47-0.53 for Fedorivka, 0.24-0.27 for Stremyhorod to 0.09-0.11 for Nosachiv. A different degree of fractional crystallization is also suggested by ternary discrimination diagram (Kieffer et al. 2023, 2024a) where each deposit form separate field with the Fedorivka having crystallised from a more primitive melt composition, i.e. lower REE contents and smaller Eu/Eu* (Fig. 4), however a relatively wide spread of data collected within a single sample is noteworthy.

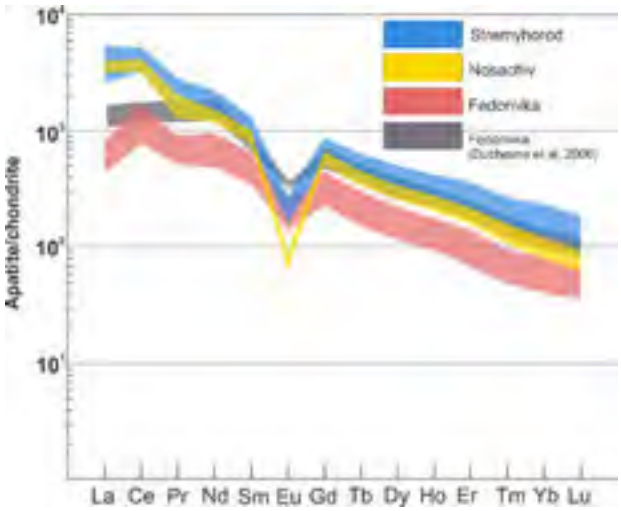


Figure 3. Chondrite normalized REE patterns for apatite from Ti-P deposits of the Ukrainian Shield.

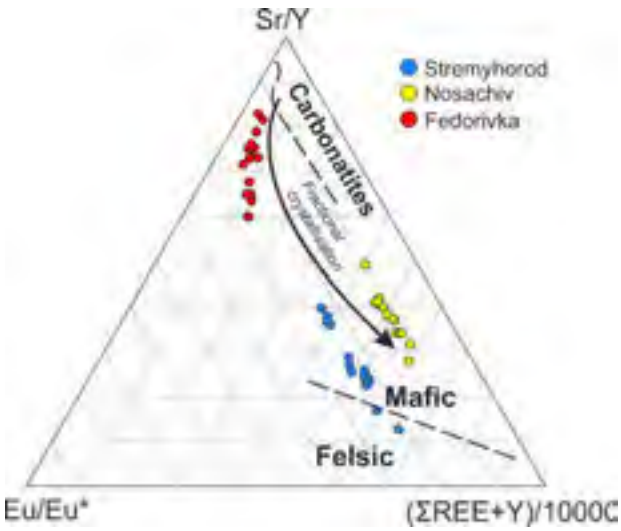


Figure 4. Ternary discrimination diagram for apatite (after Kieffer et al. 2023, Kieffer et al. 2024a).

Kieffer et al. (2024b) showed that trace element composition of cumulus apatite has a potential to be a tracer of crustal contamination and position of Nosachiv and Stremyhorod samples on the Th/Lu vs. $(La/Nd)_N$ diagram might be seen as a result of contamination by a silicic component (Fig. 5).

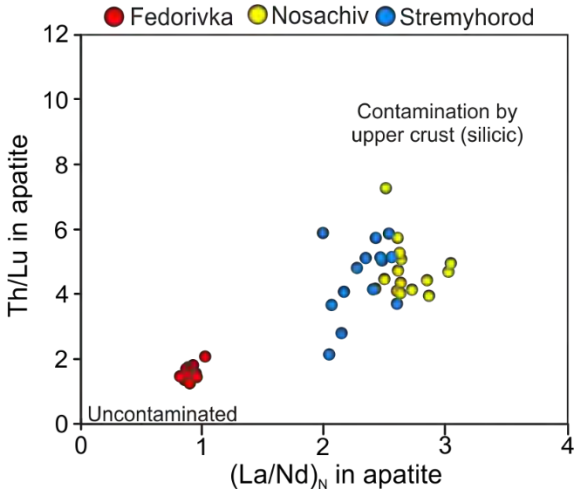


Figure 5. Th/Lu as a function of $(La/Nd)_N$ used as a tracker of crustal contamination (after Kieffer et al. 2024b).

5 Conclusions

The LA-ICP-MS trace element study of ilmenite and apatite revealed some similarities and differences between Ti-P deposits hosted by AMCG complexes of the Ukrainian Shield. Some of them can be attributed to fractional crystallization and potential crustal contamination by a silicic component but interestingly, these processes might be also linked to the enrichment in potential by-products such as scandium or REE. Samples from the Nosachiv and Stremyhorod deposits, exhibiting signatures of higher degree of fractional crystallization and crustal contamination compared to the more primitive melt composition of the Fedorivka deposit, exhibit both higher content of REE in apatite and lower content of Sc in ilmenite. Further studies will examine whether information obtained from petrological indicators can be applied to mineral exploration focused on potential by-products associated with Ti-P mineralization.

Acknowledgements

The authors would like to acknowledge the financial support of European Union in the frame of Horizon Europe AVANTIS project, Grant Agreement No. 101137552. The study was partially funded by statutory funds of the Faculty of Geology, Geophysics and Environmental Protection, AGH University of Kraków, Poland (No. 16.16.140.315).

References

Duchesne JC, Shumlyanskyy L, Charlier B (2006). The Fedorivka layered intrusion (Korosten Pluton, Ukraine): an example of highly differentiated ferrobasaltic evolution. Lithos 89: 353-376.

Gurskiy DS (ed.) (2002) Main types of rock complexes and mineral deposits in the Ukrainian Shield. Geological excursion guidebook. Geographica, Kyiv.

Gursky DS, Nechaev S, Bobrov A (2003). Titanium deposits in Ukraine focused on the Proterozoic anorthosite-hosted massifs. Norges Geologiske Undersøkelse, Special Publication 9: 21-26.

Kieffer MA, Dare SA, Namur O (2023). The use of trace elements in apatite to trace differentiation of a ferrobasaltic melt in the Sept-Iles Intrusive Suite, Quebec, Canada: Implications for provenance discrimination. Geochim. Cosmochim. Acta 342: 169-197.

Kieffer MA, Dare SA, Gendron M (2024a). Trace element discrimination diagrams to identify igneous apatite from I-, S-and A-type granites and mafic intrusions: Implications for provenance studies and mineral exploration. Chem. Geol. 649, 121965.

Kieffer MA, Dare SA, Namur O, Mansur ET (2024b). Apatite chemistry as a petrogenetic indicator for mafic layered intrusions. J Petrol 65(4): egae022.

Kryvdik SG, Guravsky TV, Dubyna OV, Bratchuk OM, Markhai OI, Nechaenko OM, Yakubenko PF (2009). Peculiarities of the material composition of the Nosachiv apatite-ilmenite deposit (Korsun-Novomyrhorod pluton, Ukrainian shield). Mineral. Journ. (Ukraine) 31(3): 55-57 (in Ukrainian).

Shcherbak MP, Bobrov OB (eds.) (2005) Mineral Deposits of Ukraine. Centre of Europe Publishing House, Kyiv-Lviv (in Russian).

Shumlyanskyy L, Hawkesworth C, Billström K, Bogdanova S, Mytrokhyn O, Romer R, Dhuime B, Claesson S, Ernst R, Whitehouse M, Bilan O (2017). The origin of the Palaeoproterozoic AMCG complexes in the Ukrainian shield: New U-Pb ages and Hf isotopes in zircon. Precambrian Res. 292: 216-239.

Syvyi M, Demyanchuk P, Havryshok B, Zablotskyi B (2019). Phosphates of Ukraine as raw materials for the production of mineral fertilizers and ameliorants. Miner. Resour. Manag. 35: 5-26.

Petrogenesis and ore-forming processes of the ultramafic Kylmäkoski Ni-Cu-(Co) magmatic sulfide deposit, SW Finland

Patrick Hehn[1], Karsten Haase[1], Manuel Keith[1], Reiner Klemd[1], Christoph Beier[2], Harald Strauss[3], Martin Kutzschbach[4]
[1]GeoZentrum Nordbayern, Friedrich-Alexander-Universität Erlangen-Nürnberg, Germany
[2]Department of Geosciences and Geography, University of Helsinki, Finland
[3]Institut für Geologie und Paläontologie, Westfälische Wilhelms-Universität, Münster, Germany
[4]Institute for Geology and Paleoenvironmental Research, Goethe-Universität, Frankfurt am Main, Germany

Abstract. The 1.89 Ga ultramafic Kylmäkoski intrusion, located in the Vammala Ni Belt in southwest Finland, is an example of a magmatic Ni-Cu-(Co) deposit that formed in a subduction zone setting. This study uses textural observations combined with mineral micro-analysis, whole-rock geochemistry, and $\delta^{34}S$ measurements to determine the petrogenetic history of the Kylmäkoski deposit. Mantle-like $\delta^{34}S$ isotope values (-0.91 ‰ to 0.08 ‰) of magmatic sulfides and intermediate Sb/Se and As/Se values in pentlandite suggest that assimilation of graphitic black schists was likely not the main mechanism causing sulfide saturation. By contrast, a wide range in forsterite contents of olivine (66 mol% to 78 mol%) is indicative of silicate melt fractionation. Consequently, the S contents of the silicate melt increased, followed by decreasing fO_2 of an initially oxidized alkaline melt (ΔFMQ +2.35±0.43) due to magnetite fractionation, which ultimately triggered sulfide segregation. The similar oxidized nature of the Paleoproterozoic Kylmäkoski and Phanerozoic arc magmas (ΔFMQ 1±1) provide first evidence that crustal assimilation is less critical for the formation of magmatic sulfide deposits in subduction zone settings than previously thought.

1 Introduction

Arc-related ultramafic Ni-Cu magmatic sulfide deposits form from magmas that are more oxidized than those of intra-plate settings (Evans 2012). The segregation of a sulfide liquid from a silicate melt is the main ore-forming mechanism in magmatic sulfide deposits and can be induced by the assimilation of crustal S (Keays et al. 2010) or fractional crystallization (Seat et al. 2009), thereby increasing the S content of the melt. The oxidized nature of arc magmas requires a reduction process to reach sulfide saturation, which can either be caused by magnetite fractionation (Jenner et al. 2010) or the assimilation of reducing components from crustal rocks (Peltonen 1995a).

Unlike world-class Ni-Cu deposits in intra-plate settings, the Kylmäkoski Ni-Cu-(Co) deposit was emplaced deep beneath a volcanic arc in a subduction setting (Peltonen 2005). The exposed lower crustal rocks of the Kylmäkoski deposit give a unique insight into old arc-related magmatic sulfide deposits. By retracing the evolution of the parental melt and estimating the physiochemical properties of the magma, this study focuses on understanding the ore-forming mechanisms in Proterozoic arc magmas and comparing them with younger subduction-related magmatic sulfide deposits.

2 Geological Setting

2.1 The Vammala Ni Belt

The Vammala Ni Belt is located south of the Central Finland Granitoid Complex (CFGC) and strikes approximately NW-SE. It hosts various mafic and ultramafic intrusions, many of them bearing magmatic Ni-Cu-(Co) sulfide deposits (Figure 1A; Peltonen 1995b). The intrusions form large boudins and lenses mainly consisting of olivine-chromite and olivine-clinopyroxene cumulates with clinopyroxene, hornblende, and phlogopite as intercumulus phases (Peltonen 1995b). All intrusions were emplaced between 1.89-1.87 Ga during peak deformation and metamorphism of the Svecofennian orogeny (Peltonen 2005). The country rocks are predominantly medium- to high grade paragneisses, granodiorites and granites (Figure 1B; Peltonen 2005).

2.2 The Kylmäkoski deposit

The Kylmäkoski magmatic sulfide ores are hosted by an ultramafic body consisting of regular and orbicular peridotite with minor proportions of pyroxenite, perknite, and hornblendite (Papunen 1980). These ultramafic rocks are in parts altered and recrystallized at amphibolite to granulite facies conditions to metaperidotite, serpentinite, and amphibolite (Papunen 1980).
Samples from three drill cores of the Kylmäkoski deposit were provided by the Geological Survey of Finland (GTK), which included mineralized regular and orbicular peridotite and amphibolite, as well as unmineralized granitoid country rock. Additionally, four field samples were recovered from the old mine site and the vicinity of the deposit (Figure 1B & C).

3. Methods

Major and minor element analyses in silicate (n=260) and sulfide (n=429) phases were performed using a JEOL JXA8200 Superprobe EPMA at GeoZentrum

Nordbayern. For the silicate and sulfide analysis, an acceleration voltage of 15 kV, a beam current of 15 nA, and a beam diameter of 3 µm were used.

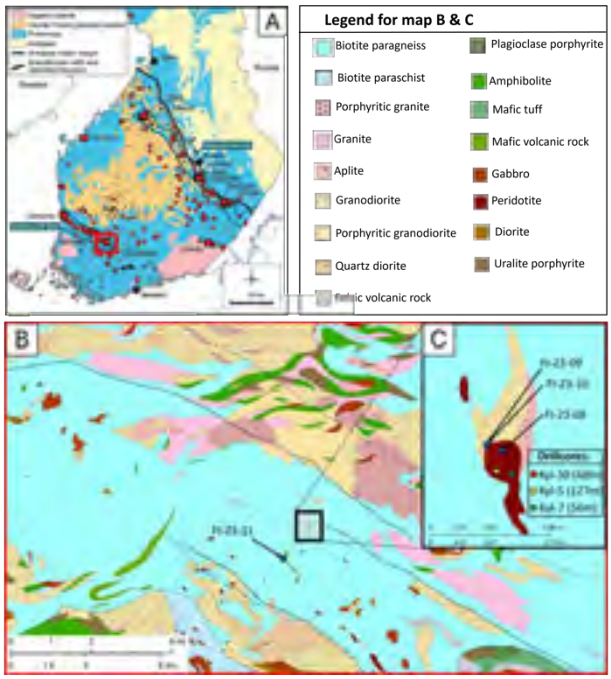


Figure 1. A) Simplified geological map of the 3.1-2.5 Ga Archean basement and the 1.9-1.8 Ga Proterozoic Svecofennian Domain. The red box represents the study area, as shown in (B). Map modified after Makkonen et al. (2020). **B)** Geological map of the study area with the Kylmäkoski Ni-Cu-(Co) deposit (black box). **C)** Geological map of the Kylmäkoski deposit with the location of the three studied drill cores and field samples. Map modified after the Geological Survey of Finland (GTK).

The trace element contents of silicate (n=45) and sulfide (n=100) minerals were determined at the TU Berlin, using an Agilent 8900 ICP-MS/MS coupled with an Analyte Excite 193 nm laser. For the silicate analyses the RSD was <5 % for all elements and for sulfide analyses the RSD was <14 % for all elements except Ni (18.19 %) and Cd (30.46 %). As primary standards for the silicates, we used NIST610 and NIST612 whereas BHVO and BCR were used as secondary standards to determine the accuracy. For sulfide measurements, the external standards MASS-1, Fe-$Ni_{(1-x)}S$, PO724, and FeS-1 were used, where the latter one served as a secondary standard.

Whole-rock compositions of peridotite (n=3), amphibolite (n=3) granitoid (n=4) samples were determined by an energy dispersive Spectro Xepos He X-ray fluorescence spectrometer at the GeoZentrum Nordbayern.

Sulfur isotope analyses were performed on pyrrhotite and mixed sulfide separates from peridotite (n=6) and amphibolite (n=3) samples at the University of Münster, using a Flash EA IsoLink elemental analyzer interfaced to a ThermoScientific Delta V Advantage IR-MS.

4. Results

4.1 Petrography

The mineralized peridotite of the Kylmäkoski Ni-Cu-(Co) deposit can be subdivided into regular and orbicular peridotite cumulates. The regular peridotite mainly consists of olivine, clinopyroxene, amphibole and small amounts of orthopyroxene. Olivine and pyroxene occur as rounded cumulate phases, whereas intercumulus minerals such as amphibole and magmatic sulfides show a poikilitic texture.

The orbicular peridotite is mineralogically similar to the regular peridotite, but shows textural differences. Olivine almost exclusively occurs as nodules embedded in an amphibolite groundmass. Magmatic sulfides can only be found in the amphibolite groundmass surrounding the nodules.

The sulfide-bearing amphibolite is characterized by magnesium-hornblende and pargasite, minor actinolite, tremolite, and clinopyroxene, as well as accessory orthopyroxene, and olivine. The medium grained granitoid country rocks mainly consist of plagioclase, K-feldspar, quartz, biotite, and chlorite.

4.2 Ore mineralogy and texture

The magmatic sulfides are dominated by pyrrhotite that is associated with chalcopyrite, pentlandite, and minor cubanite. They mostly occur as large agglomerates reaching several millimetres in size (Figure 2a) and occasionally show a poikilitic texture surrounding earlier formed silicate minerals. A transition between an agglomerate and net-like texture is often observed (Figure 2c). Magnetite was only found at shallow levels in the deposit (Figure 2a-b).

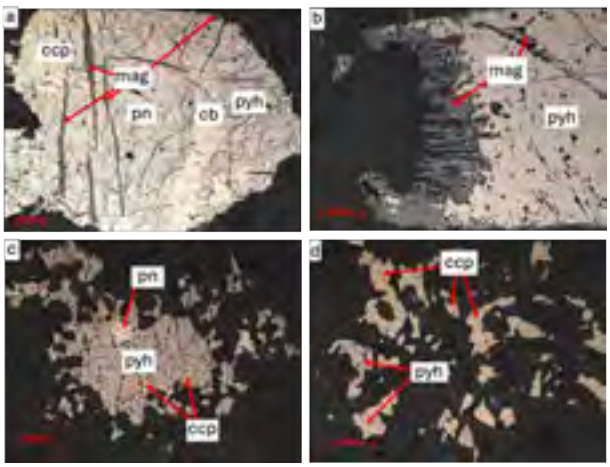


Figure 2. Photomicrographs of sulfide assemblages. Abbreviations: ccp, chalcopyrite; pyh, pyrrhotite; pn, pentlandite; cb, cubanite; mag, magnetite.

4.3 Mineral chemistry and S isotopes

Forsterite (Fo) contents in olivine range from 73 to 78 mol% in regular and orbicular peridotite (Kyl-5 & Kyl-7) and from 66 to 68 mol% in amphibolite (Kyl-

30). Olivine in orbicular peridotite always shows higher forsterite contents compared to olivine from regular peridotite. Nickel is enriched in olivine from the peridotite compared to that of the amphibolite (Figure 3). Olivine from Kylmäkoski shows a S-undersaturated trend in Ni vs. Fo, that is comparable to olivine data from the Central American Arc (Gavrilenko et al. 2016). By contrast, olivine that formed from S-saturated silicate melts, such as in the Kamchatka Arc, Russia (Gavrilenko et al. 2016; Kamenetsky et al. 2018), have noticeably lower Ni contents then that of the Kylmäkoski deposit (Fig. 3).

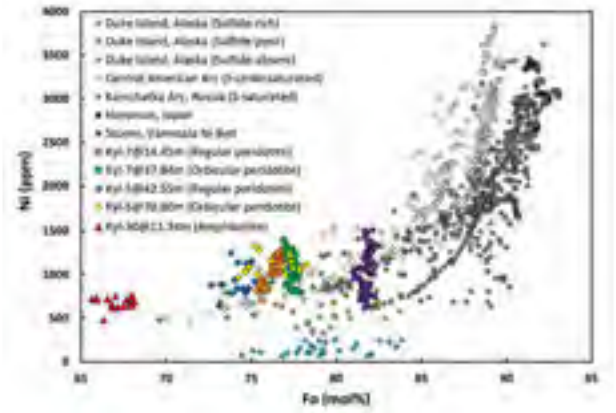


Figure 3. Nickel (ppm) vs. forsterite content (mol%) in olivine from the Kylmäkoski deposit and reference data from S-saturated and S-undersaturated magmas.

The trace element data of the parental melt displays very high Ba and elevated Th, U, and Pb values relative to N-MORB. Furthermore, high-field-strength elements (HFSE) are depleted compared to N-MORB, showing a dominant Nb-Ta and Zr trough. The samples also show a fractionated LREE/HREE pattern and no negative Eu anomaly in a chondrite-normalized spider diagram.

The $\delta^{34}S$ isotope composition of pyrrhotite and mixed sulfide compounds from Kylmäkoski show mantle-like values ranging from -0.91 ‰ to 0.08 ‰.

5. Discussion

5.1 Petrogenesis and melt evolution

The major element composition of the Kylmäkoski parental melt was calculated using the method by Cordier et al. (2020), which yielded 47.9 wt.% SiO_2, 10.85 wt.% FeO, and 6.45 wt.% MgO. The elevated Na_2O+K_2O concentrations (4.06 %) and high Th/Yb ratios (Th/Yb=2.61-26.32) suggest a high-K calc-alkaline to shoshonitic melt composition. The enriched signature of fluid-mobile elements (e.g. Ba, Th, U…) and depletion of fluid-immobile HFSE compared to N-MORB confirms that the Kylmäkoski deposit formed in an arc setting.

Fractional crystallization of the melt was indicated by the large range in forsterite contents of olivine (Figure 3). It is suggested that the most mafic orbicular peridotite crystallized at the bottom of the magma chamber, followed by the regular peridotite and ultimately the less mafic amphibolite. Temperature estimates based on clino- and orthopyroxenes thermometry (Putirka 2008) yielded ~1140°C. Mean values of pressure calculations (Neave and Putirka 2017) were ~5.7 kbar suggesting a pyroxene crystallization depth of ~20 km.

Sulfide saturation probably occurred relatively late, as the sulfide ore minerals infiltrate the intercumulus space between the already crystallized olivine and pyroxene grains. Since amphibole shows a similar poikilitic texture, we presume that sulfide saturation was attained during amphibolite crystallization.

5.2 Black schist assimilation as trigger for sulfide saturation?

The mantle-like S isotope values of the magmatic sulfides from Kylmäkoski rather exclude that assimilation of crustal material was a key process causing S saturation. Elements usually enriched in black schists, such as As, Sb, Bi, Mo, Sn, and Pb (Ketris et al. 2009), are not particularly enriched in magmatic sulfides from the Kylmäkoski deposit. This can be visualized by comparing for instance the As/Se and Sb/Se ratios in pentlandite, as suggested by Mansur et al. (2021). The As/Se and Sb/Se ratios in pentlandite from Kylmäkoski show a large spread mostly in the range of intermediate values (Figure 4). This suggests, in consideration of the mantle-like S isotope values, that minor black schist assimilation may have occurred, but that it was likely not the main mechanism causing S saturation.

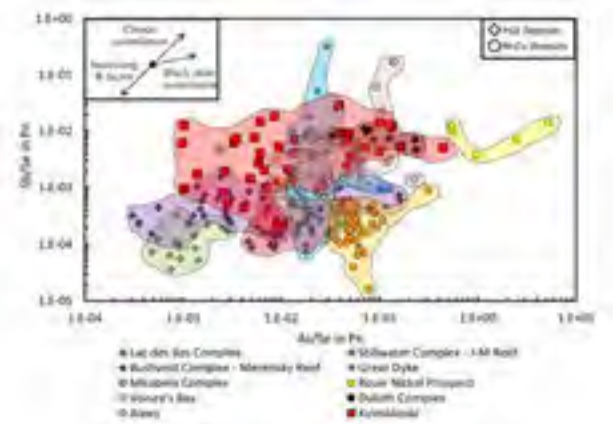


Figure 4. Logarithmic Sb/Se vs. As/Se in pentlandite plot with data from the Kylmäkoski Ni-Cu-(Co) deposit and several other Ni-Cu and PGE-dominated deposits. Figure modified after Mansur et al. (2021).

5.3 Silicate melt fractionation and magnetite crystallization as ore-forming mechanisms

Besides the addition of S by assimilation of crustal material, Ripley and Li (2013) and Seat et al. (2009) discussed the possibility of attaining saturation in a basaltic melt by silicate melt fractionation, which increases the S concentration due to its incompatible nature at S undersaturated conditions. Similarly, Jenner et al. (2010) argued that S saturation may be

caused by magnetite crystallization due to the reduction of SO_4^{2-} to S^{2-}.

These two processes might have had an effect on the Kylmäkoski deposit. When comparing the S content at sulfide saturation (SCSS = 572±156 ppm) and the fO_2 of the Kylmäkoski melts (ΔFMQ +2.4±0.4) (Figure 5), it becomes clear that melt reduction could not have been the only mechanism causing S saturation. However, our data also suggests that S assimilation also only played a minor role in reaching S saturation, as discussed above.

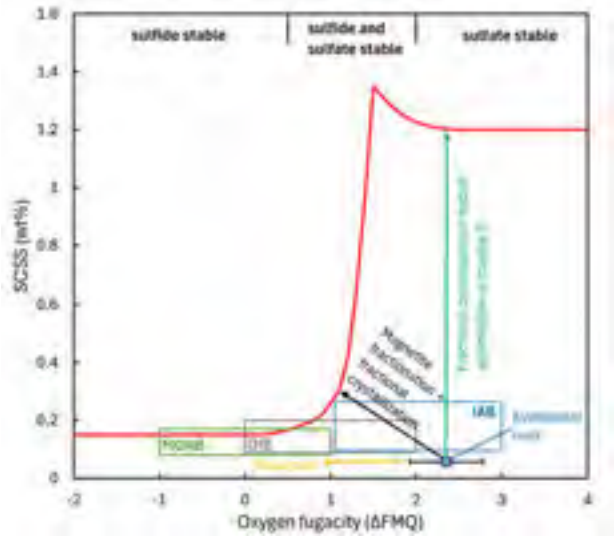


Figure 5. Sulfide concentration at sulfide saturation (SCSS) vs. fO_2. The red line describes the SCSS of basaltic melts at 1050°C (Jugo et al. 2010). Total figure modified after Cordier et al. (2020).

Consequently, a combination of moderately increasing the S concentration by fractional crystallization coupled with the reduction of the melt towards lower fO_2 values by magnetite crystallization is the most realistic scenario for the ore formation at Kylmäkoski. This ore-forming process might also find application in similarly oxidized Phanerozoic arc magmas (ΔFMQ 1±1) suggesting that arc-related magmatic sulfide deposits do not generally require the assimilation of crustal material for their formation.

6. Conclusions

The findings of this study suggest that sulfide segregation at Kylmäkoski occurred after the fractionation of olivine and pyroxene. Further, we propose that the assimilation of crustal rocks such as black schists had no major impact on the ore formation indicated by mantle-like $\delta^{34}S$ values and intermediate Sb/Se and As/Se ratios in pentlandite. The two main processes leading to the attainment of sulfide saturation are silicate mineral and magnetite fractionation accompanied by decreasing fO_2 conditions, which increased the S content of the silicate melt, but at the same time, the S saturation limit. This demonstrates that economic magmatic sulfide deposits at convergent plate boundaries can also form in the absence of crustal S assimilation.

References

Cordier C, Coin K, Arndt NT, Cartigny P (2020) The Älgliden Ni-Cu-Au deposit: magmatic sulfides in a subduction setting. Miner Deposita 55(6):1173-1196.

Evans KA (2012) The redox budget of subduction zones. Earth-Science Reviews 113(1-2):11-32.

Gavrilenko M, Herzberg C, Vidito C, Carr MJ, Tenner T, Ozerov A (2016) A calcium-in-olivine geohygrometer and its application to subduction zone magmatism. Jour Petrol 57(9):1811-1832.

Jenner FE, O'Neill HSC, Arculus RJ, Mavrogenes JA (2010) The magnetite crisis in the evolution of arc-related magmas and the initial concentration of Au, Ag and Cu. Jour Petrol 51(12):2445-2464.

Jugo PJ, Wilke M, Botcharnikov RE (2010) Sulfur K-edge XANES analysis of natural and synthetic basaltic glasses: Implications for S speciation and S content as function of oxygen fugacity. Geochim Cosmochim Acta 74(20):5926-5938.

Kamenetsky VS, Zelenski M, Gurenko, A et al. (2018) Reprint of Silicate-sulfide liquid immiscibility in modern arc basalt (Tolbachik volcano, Kamchatka): Part II. Composition, liquidus assemblage and fractionation of the silicate melt. Chem Geol 478:112-130.

Keays RR, Lightfoot PC (2010) Crustal sulfur is required to form magmatic Ni–Cu sulfide deposits: evidence from chalcophile element signatures of Siberian and Deccan Trap basalts. Miner Deposita 45:241-257.

Ketris MÁ, Yudovich YE (2009) Estimations of Clarkes for Carbonaceous biolithes: World averages for trace element contents in black shales and coals. International Journ Coal Geol 78(2):135-148.

Makkonen HV, Tuisku P (2020) Geology and crystallization conditions of the Särkiniemi intrusion and related nickel-copper ore, central Finland: implications for depth of emplacement of 1.88 Ga nickel-bearing intrusions. Bulletin of the Geological Society of Finland 92: 111-130.

Mansur ET, Barnes SJ, Duran CJ (2021) An overview of chalcophile element contents of pyrrhotite, pentlandite, chalcopyrite, and pyrite from magmatic Ni-Cu-PGE sulfide deposits. Miner Deposita 56(1):179-204.

Neave DA, Putirka KD (2017) A new clinopyroxene-liquid barometer, and implications for magma storage pressures under Icelandic rift zones. Amer Mineral 102(4):777-794.

Papunen H (1980) The Kylmäkoski nickel-copper deposit in southwestern Finland. Bulletin of the Geological Society of Finland 52(1): 129-145.

Peltonen P (1995a) Magma-country rock interaction and the genesis of Ni-Cu deposits in the Vammala Nickel Belt, SW Finland. Mineral Petrol 52:1-24.

Peltonen P (1995b) Petrogenesis of ultramafic rocks in the Vammala Nickel Belt: implications for crustal evolution of the early Proterozoic Svecofennian arc terrane. Lithos 34(4):253-274.

Peltonen P (2005) Svecofennian mafic-ultramafic intrusions. Developments in Precambrian Geology 14: 407-441.

Putirka KD (2008) Thermometers and barometers for volcanic systems. Rev Mineral Geoch 69(1):61-120.

Richards JP (2015) The oxidation state, and sulfur and Cu contents of arc magmas: implications for metallogeny. Lithos 233:27-45.

Ripley EM, Li C (2013) Sulfide saturation in mafic magmas: Is external sulfur required for magmatic Ni-Cu-(PGE) ore genesis? Econ Geol 108(1):45-58.

Seat Z, Beresford SW, Grguric BA, Gee MM, Grassineau NV (2009) Reevaluation of the role of external sulfur addition in the genesis of Ni-Cu-PGE deposits: Evidence from the Nebo-Babel Ni-Cu-PGE deposit, West Musgrave, Western Australia. Econ Geol 104(4):521-538.

The Mineral System Approach Applied to Magmatic Ni-Cu-PGE Sulfide Deposits: Sink Processes Revisited by Recent Experimental Studies

Giada IACONO-MARZIANO[1], Ville J. VIRTANEN[1,2], Shenghong YANG[3]
[1] Institut des Sciences de la Terre d'Orléans, UMR 7327, CNRS/Université d'Orléans/BRGM, Orléans, France
[2]Department of Geosciences and Geography, University of Helsinki, Helsinki, Finland
[3]Oulu Mining School, University of Oulu, Oulu, Finland

Abstract
Magmatic Ni–Cu–PGE sulfide deposits form by the segregation and accumulation of immiscible sulfide melts from mafic or ultramafic magmas. Here we use recent experimental studies to review magma-sediment interaction mechanisms that lead to the segregation of a sulfide melt at crustal levels. We then discuss physical processes favoring sulfide melt mobility and accumulation, and chemical processes leading to the metal enrichment of the sulfide melt. Several case studies are presented to illustrate how described processes affect ore genesis.

We conclude on the implications of the experimental studies in terms of ore exploration at the province, camp and deposit scales. At the province scale, magma emplacement within S-bearing sedimentary rocks favors magmatic sulfide ore formation and is facilitated by the preferential injection of the magma within carbonaceous and evaporitic sediments/rocks. The respective role of carbonaceous and evaporitic rocks in ore formation is discussed at the camp scale. We finally examine how magma-sediment interactions and the close association of the sulfide melt with the fluid phase affect ore distribution at the deposit scale.

1 The mineral system approach for magmatic sulfide deposits

The mineral system approach interprets the formation of ore deposits in terms of source, pathway, and sink processes, with the aim of improving ore exploration. For magmatic Ni–Cu–PGE sulfide deposits the mineral system approach mainly investigates (i) geodynamic settings, (ii) sources and compositions of ore-forming magmas, (iii) magma migration pathways at crustal scale, (iv) magma focusing and emplacement mechanisms at deposit scale, (v) chemical and physical mechanisms for ore precipitation (Barnes et al. 2016). Here we revisit points (iv) and (v) in the light of recent experimental studies, with a particular attention to chemical and physical mechanisms controlling the segregation of a sulfide melt at crustal levels, its accumulation and its metal enrichment.

2 Sulfur incorporation from external sources

A fundamental process in the formation of magmatic sulfide ores is sulfur incorporation into the magma from an external sedimentary source. This is generally necessary to produce Ni-Cu-(PGE) sulfide ores, as the sulfur content of most mafic-ultramafic magmas is not high enough to allow the formation of economically interesting deposits. Experimental studies reveal several possible mechanisms of magma-sediment interactions that allow early sulfide saturation and lead to sulfide melt segregation and accumulation.

2.1 Black shale devolatilization and assimilation

Black shale devolatilization within the contact aureole of magmatic intrusions leads to the formation of C-O-H-S-(Cu)-bearing fluids that can trigger sulfide saturation in the magma (Fig.1a; Virtanen et al. 2021).

Close to the intrusion, black shales may undergo partial melting and be assimilated by the magma in the form of Si-Ca-K-S-rich silicate melts and immiscible sulfide melts (Fig.1b; Virtanen et al. 2021; Deegan et al. 2022). Black shale devolatilization is likely to be at the origin of large volumes of disseminated sulfides like those observed in the troctolitic rocks of the Partridge River intrusion of the Duluth Complex (Virtanen et al. 2021, 2022). On the contrary, magmatic assimilation probably produces more localized but more massive sulfide deposits, similar to those described in the noritic rocks of the Duluth Complex at the footwall contact with the Virginia Formation black shales (Virtanen et al. 2021, 2022).

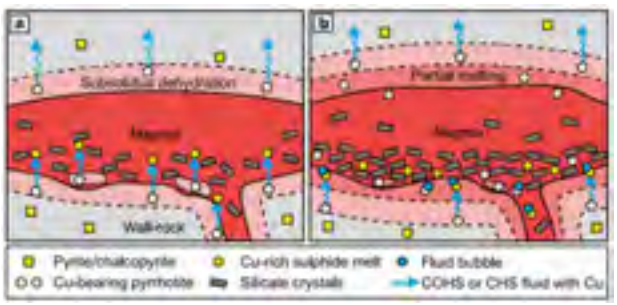


Figure 1. a) Devolatilization reactions in the wall-rock footwall and xenoliths form C-O-H-S-fluids that transport sulfur and copper to the magma causing sulfide saturation. b) As the heating of the wall-rock progresses, partial melting zones form close to the intrusion. At this stage, sulfides are suspended in silicate melt and can be assimilated by the magma. From Virtanen et al. (2021).

2.2 Anhydrite assimilation in the presence of a reducing agent

The mechanism that produces the largest sulfur oversaturation and therefore the largest amounts of sulfide melt is anhydrite assimilation in the presence of a reductant (Iacono-Marziano et al. 2017). Anhydrite dissolves into the magma enriching it in S, Ca and O; a reducing agent is therefore needed to transform the oxidized S dissolved in the silicate melt into a sulfide melt. Although the magma itself may have the capacity to partially reduce oxidized S, carbonaceous rocks are significantly more efficient reductants. Magma reduction is operated by the flushing of a C-dominated fluid phase through the magma. The sulfide melt preferentially segregates in contact with the fluid phase (Fig. 2a) and accumulates at the interface between magma and organic material (Fig. 2b).

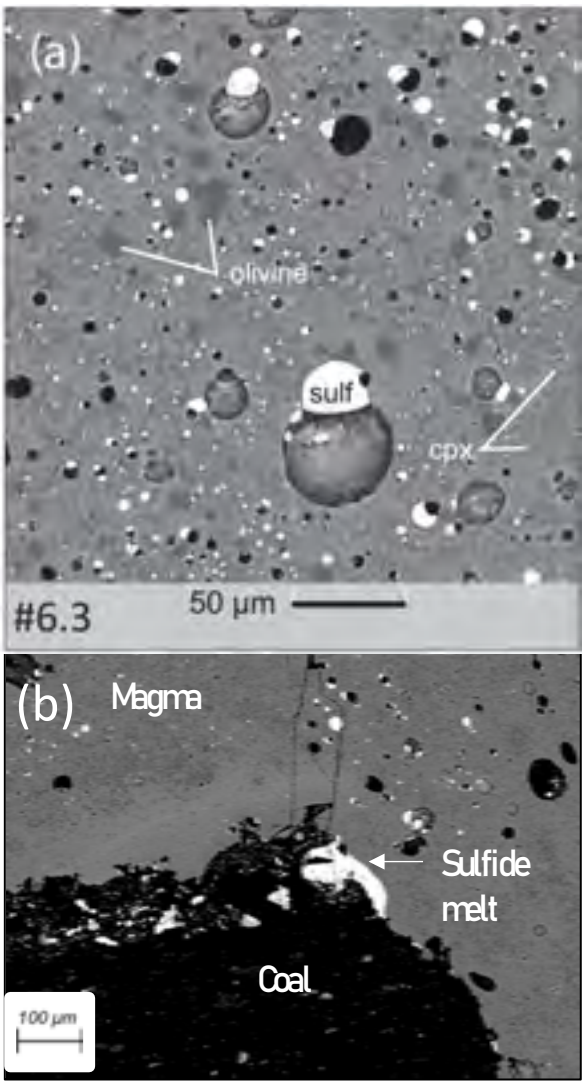


Figure 2. BSE images of experimental samples in which a sulfate-saturated magma interacted with coal at 1200°C and 75 ± 7 MPa. (a) The sample consists of glass, olivine, and clinopyroxene (cpx) crystals, sulfide globules (sulf), and generally round fluid bubbles. (b) Magma-coal interface with accumulated sulfide melt; the coal residue is most likely graphite. From Iacono-Marziano et al. (2017).

Carbonaceous components are often interlayered with anhydrite-bearing sedimentary rocks, however the interaction with carbonaceous rocks does not necessarily have to occur simultaneously to anhydrite assimilation, in order to produce sulfide ores. The assimilation of anhydrite-bearing rocks may occur during magma ascent as (i) it triggers only minor crystallization in the magma, and (ii) sulfur can easily be transported by the magma dissolved in its oxidized form, before reduction and sulfide segregation occur. On the contrary, the interaction with carbonaceous rocks is more likely to take place in the magma final position because it causes massive crystallization.

Extensive interaction of the ore-forming magmas with evaporitic and carbonaceous rocks is proposed to be at the origin of the Noril'sk-Talnakh world-class deposits in Siberia (Iacono-Marziano et al. 2017), and the Sakatti deposit in the Finnish Central Lapland Belt.

3 Role of the fluid phase

Magmatic assimilation of carbonaceous rocks supplies an abundant C-bearing fluid phase to the magma. Figure 2a shows the close association between sulfide droplets and fluid bubbles produced by coal devolatilization. More generally, the occurrence of a fluid phase in the magma has important consequences for sulfide melt mobility, due to the strong affinity of the sulfide melt for the fluid phase (Mungall et al. 2015; Virtanen et al. 2021; Iacono-Marziano et al. 2022). This is independent on the process originating the fluid phase: magmatic assimilation of sedimentary rocks is extremely efficient in providing mafic magmas with fluids, but first or second boiling processes (due to decompression or crystallization, respectively) can also contribute.

3.1 Sulfide melt mobility

The affinity of the sulfide melt for the fluid phase affects sulfide melt mobility via the formation of sulfide-fluid compound drops that (i) may float within the magma if their total density is lower than the density of the silicate melt (Mungall et al. 2015), and (ii) favor the accumulation of the sulfide melt (Iacono-Marziano et al. 2022). The accumulation of the sulfide melt is facilitated by the coalescence of sulfide droplets that are attached to the same fluid bubble (Fig.3). The coalescence is indeed more efficient in the presence of a fluid bubble that keeps the sulfide droplets in contact and allows the drainage of the melt film between them. This mechanism most likely accounts for ovoid or globular textures, with diameters ranging from hundreds of microns to several centimeters, observed in several sulfide deposits (Barnes et al. 2017), and may play an active role in the formation of massive sulfides.

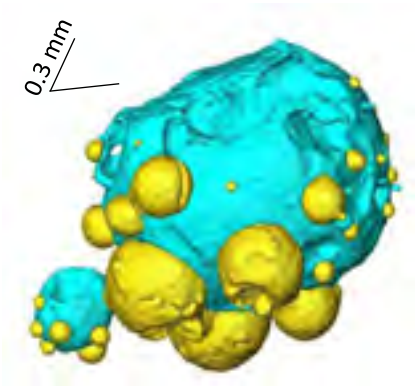


Figure 3. High-resolution X-ray computed tomography rendering of compound drops showing 3D distribution of sulfide droplets in yellow and fluid bubbles in blue.

3.2 Metal enrichment of the sulfide melt and PGM formation via desulfurization

The close association of the sulfide melt with the fluid phase can also favor the metal enrichment of the sulfide melt. This is due to the desulfurization of the sulfide melt and the concentration of chalcophile elements inside it. As sulfur is a volatile element, the higher the proportion of fluid phase in the magma, the higher the degassing of sulfur to the fluid phase. Experiments performed with a fixed amount of sulfur and variable amounts of fluid phase show an inverse relationship between the sulfide content and the fluid phase content (Iacono-Marziano et al. 2022). Consequently, experimental samples with increasing fluid contents present increasingly Ni and Cu-richer sulfide melts (Fig. 4). The trends depicted by experimental samples are in very good agreement with those calculated using the R-factor law (Campbell & Naldrett 1979), which only accounts for the equilibrium between the sulfide melt and the silicate melt. This suggests that Ni and Cu contents of the fluid phase are negligible with respect to those of the sulfide melt. Figure 4 illustrates how magma degassing increases the R-factor by decreasing the mass of the sulfide melt without modifying the mass of the silicate magma, therefore resulting in sulfide upgrading.

Experimental samples also illustrate how extreme desulfurization may lead to the crystallization of Pt alloys in the absence of sulfide minerals. This mechanism explains the textures observed in the low-sulfide PGE ores of Noril'sk-Talnakh intrusions. In these ores subspherical structures are described within the crystalline framework, and interpreted as fluid bubbles filled with late magmatic phases or hydrothermal minerals (Schoneveld et al. 2020). These subspherical structures generally contain low amounts of sulfides but abundant platinum group minerals. Similar subspherical structures are also observed in globular-disseminated sulfides inside picritic and taxitic rocks in the lower part of the intrusion, and contain higher sulfide and lower PGE proportions (Le Vaillant et al. 2017). Finally, massive sulfides are observed at the base of the intrusion and largely in the country rocks. This distribution of ore types implies a decrease in the sulfide content from the lower to the upper part of the intrusion, associated with an increase in the PGE contents. This suggests a strong involvement of fluids in ore formation and an increasing extent of desulfurization going from massive to low-sulfide PGE ores, through globular ores (Iacono-Marziano et al. 2022).

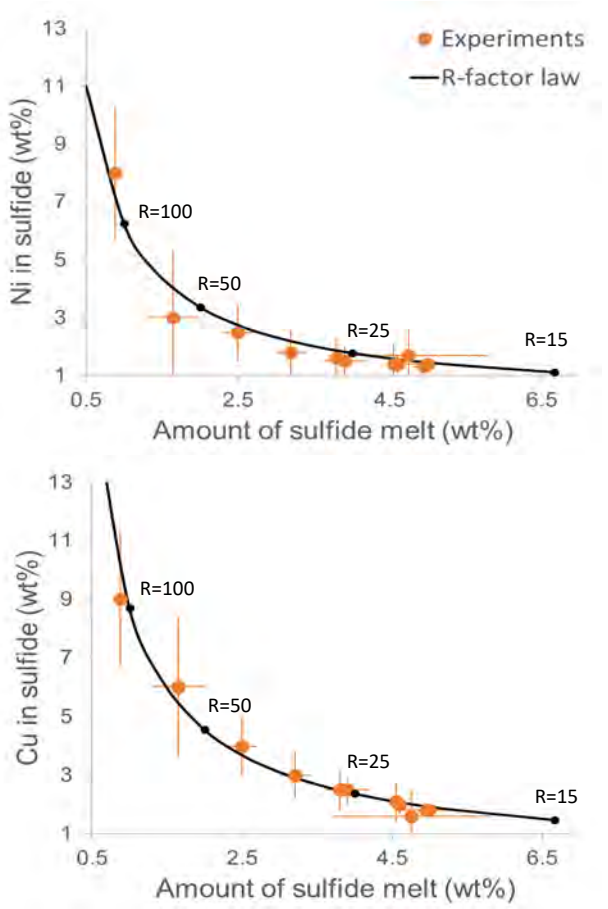


Figure 4. Ni and Cu contents of the sulfide melt versus its amount in experimental samples (orange dots) and in theoretical calculations (black line) using the R-factor law of Campbell & Naldrett (1979). Modified from Iacono-Marziano et al. (2022).

4 Implications for ore exploration

The results of the experimental studies presented above may provide predictive targeting criteria, if their validity is tested in the field. At the province scale, magma emplacement within sedimentary basins is often favorable to magmatic sulfide ore formation, if the sediments are S-rich. The nature of the sedimentary rocks is likely to play a role in the formation and propagation of sill-like structures, therefore controlling magma intrusion. Carbonaceous and evaporitic rocks are the most common rocks observed in the sill contact aureoles within volcanic basins (e.g. Svensen et al. 2015).

This suggests a preferential lateral propagation of the magma into these sediments, likely related to their chemical and physical properties. This preferential injection favors in turn the interaction of the magma with the S-rich sediments and consequently ore formation. The occurrence of anhydrite-bearing sedimentary rocks in the stratigraphic sequence may be an indicator of massive sulfide accumulations, provided the existence of a reducing agent (e.g. carbonaceous rocks) at the camp scale. Noril'sk-Talnakh ores, for instance, formed in the only part of the Siberian Traps in which the host sedimentary sequence includes Devonian anhydrite-bearing rocks (Iacono-Marziano et al. 2017). However, the ore bearing intrusions (only three out of more than 20 in the region) are emplaced within carbonaceous rocks, either coal or argillite-bearing. This highlights the critical role of the carbonaceous sediments/rocks in being both a preferential horizon of magma intrusion and a reducing agent.

At the deposit scale, the interaction of the magma with the carbonaceous rocks and the coexistence of the sulfide melt with a fluid phase may affect ore distribution within the intrusion. At the Duluth Complex, for instance, the transfer into the magma of S and Cu-rich fluids derived from the devolatilization of the host black shales formed disseminated ores within the intrusion, while the assimilation of the same rocks produced more localized and more massive ores at the intrusion border (Virtanen et al. 2021, 2022). In Noril'sk-Talnakh intrusions the assimilation of coal or argillitic rocks triggered early sulfide saturation and the generation of three main types of mineralization with decreasing sulfide content and increasing PGE content from the lower to the upper part of the intrusion (Iacono-Marziano et al. 2022).
Further studies on other contexts are needed to fully elucidate what are the main parameters that control ore distribution.

Acknowledgements

This study was supported by the SEMACRET project (101057741), co-funded by Horizon Europe program and UK Research Innovation, and by the programme TelluS of the Institut National des Sciences de l'Univers, CNRS.

References

Barnes SJ, Cruden AR, Arndt N, Saumur BM (2016) The mineral system approach applied to magmatic Ni-Cu-PGE sulphide deposits. Ore Geol Rev 76: 296-316.

Barnes SJ, Mungall JE, Le Vaillant M, Godel B, Lesher CM, Holwell D, Lightfoot PC, Krivolutskaya N, Wei B (2017) Sulfide-silicate textures in magmatic Ni-Cu-PGE sulphide ore deposits: disseminated and net-textured ores. Am Mineral 102: 473–506.

Campbell IH, Naldrett AJ (1979) The influence of silicate:sulfide ratios on the geochemistry of magmatic sulphides. Econ Geol 74: 1503-1506.

Deegan FM, Bédard JH, Grasby SE, Dewing K, Geiger H, Misiti V, Capriolo M, Callegaro S, Svensen HH, Yakymchuk C, Aradi LE, Freda C, Troll VR (2022) Magma-shale interaction in Large Igneous Provinces: Implications for climate warming and sulfide genesis. J Pet 63: 1-10.

Iacono-Marziano G, Ferraina C, Gaillard F, Di Carlo I, Arndt NT (2017) Assimilation of sulfate and carbonaceous rocks: experimental study, thermodynamic modeling and application to the Noril'sk-Talnakh region (Russia). Ore Geol Rev 90: 399–413.

Iacono-Marziano G, Le Vaillant M, Godel BM, Barnes SJ, Arbaret L (2022) The critical role of magma degassing in sulphide melt mobility and metal enrichment. Nat Comm 13: 2359.

Le Vaillant M, Barnes SJ, Mungall JE, Mungall EL (2017) Role of degassing of the Noril'sk nickel deposits in the Permian-Triassic mass extinction event. Proc Natl Acad Sci 114: 2485–2490.

Mungall JE, Brenan JM, Godel B, Barnes SJ, Gaillard F (2015) Transport of metals and sulphur in magmas by flotation of sulphide melt on vapor bubbles. Nat Geosci 8: 216–219.

Schoneveld L, Barnes SJ, Godel B, Le Vaillant M, Yudovskaya MA, Kamenetsky V, Sluzhenikin SF (2020) Oxide-sulphide-melt-bubble interactions in spinel-rich taxitic rocks of the Norilsk-Talnakh intrusions, polar Siberia. Econ Geol 115: 1305–1320.

Svensen H, Fristad KE, Polozov AG, Planke S (2015) Volatile generation and release from continental large igneous provinces. In A. Schmidt, K. Fristad, & L. Elkins-Tanton (Eds.), Volcanism and Global Environmental Change: 177-192. Cambridge University Press.

Virtanen VJ, Heinonen JS, Molnar F, Schmidt MW, Marxer F, Skyttä P, Kueter N, Moslova K (2021) Fluids as primary carriers of sulphur and copper in magmatic assimilation. Nat Comm 12: 6609.

Virtanen VJ, Heinonen JS, Barber ND, Molnar F (2022) Complex effect of assimilation on sulfide saturation revealed by modeling with the Magma Chamber Simulator: a case study on the Duluth Complex, Minnesota, USA. Econ Geol 117: 1881-1899.

Magmatic and Metasomatic Controls on PGE Mineralization in Chromitites of the Tróia-Pedra Branca Mafic-Ultramafic Complex, Borborema Province, Brazil

Adriana V Jacomini[1], Juliana C Marques[1,2], Rafael S Diniz[2.3], Thiago B Diniz[2.4]
[1]Universidade Federal do Rio Grande do Sul (UFRGS), Porto Alegre, BR
[2]ValOre Metals Corp, Pedra Branca Project, BR

Abstract. The Tróia-Pedra Branca Mafic-Ultramafic Complex (TPBC), in the Borborema Province of northeastern Brazil, hosts a PGE-Au deposit with an inferred resource of 2.2 Moz 2PGE+Au at 1.08 g/t in 63.3 Mt and a Pd/Pt ratio of ~2. This study investigates the metallogenetic processes controlling Pt–Pd + Au distribution in chromitites from the TPBC, integrating petrographic, mineralogical, and microanalytical data. Chromite displays igneous textures (e.g., chicken-wire structures) and pentlandite inclusions, suggesting early sulfide saturation and initial PGE incorporation, although limited Ni- and Au-bearing alloys inclusions indicate restricted sulfidation. Metamorphic and metasomatic overprinting, driven by serpentinization, caused Al–Mg depletion, Cr–Fe enrichment, and chromite alteration marked by compositional zoning and dissolution features along fractures and crystallographic axes. Platinum group minerals (PGM)—including michenerite, sperrylite, S-cherepanovite, and various tellurides, bismuthides, and arsenides—occur along foliation planes, Cr-clinochlore cleavage, and fractures, reflecting PGE remobilization. Enrichment in Pd, Te, As and Bi suggests metasomatic input from primary magmatic sulfides or hydrothermal fluids. These findings reveal the multistage evolution of chromitites in the TPBC and offer critical insights for understanding PGE-Au mineralization in metasomatized mafic-ultramafic systems, guiding future exploration in the area and analogous settings worldwide.

1 Introduction

The increasing demand for catalytic and superconducting metals is a key driver of the global energy transition. In this context, platinum group elements (PGE)—platinum (Pt), palladium (Pd), rhodium (Rh), ruthenium (Ru), iridium (Ir), and osmium (Os)—play a crucial role due to their catalytic efficiency, broad industrial applicability, and high stability in their natural metallic state, which minimizes environmental and biological impacts (Zientek et al. 2017). Given the necessity of expanding PGE exploration, advancing scientific and technical knowledge on their mineralization is essential, as these deposits are often associated with complex geological processes.

This study presents new insights into the metallogenetic processes controlling Pt–Pd + Au mineralization in chromitites of the Tróia-Pedra Branca Mafic-Ultramafic Complex (TPBC). Despite its economic potential, the TPBC remains largely unexplored from a metallogenetic perspective, with limited studies on its mineralization processes. By applying detailed petrographic, mineralogical, and microanalytical analyses, this research provides key data to enhance the understanding of PGE mineralization in the region, establishing the TPBC as an important reference for PGE studies in mafic-ultramafic systems. The study employs transmitted and reflected light microscopy, scanning electron microscopy (SEM) with energy-dispersive spectroscopy (EDS), and the Tescan Integrated Mineral Analyzer (TIMA).

2 Geological Setting and Exploration and Economic Significance

The study area is located within the TPBC, which is part of the Tróia Massif, an Archean/ Paleoproterozoic crustal block within the Ceará Central Domain of the Neoproterozoic Borborema Province, northeastern Brazil (Fig. 1). The TPBC represents the largest exposure of mafic-ultramafic rocks in the Borborema Province (Costa et al. 2015). It comprises an assemblage of serpentinites, hornblendites, metagabbros, and chromitites (Costa et al. 2018). Chromitites typically occur as semi-massive layers ranging from a few centimeters to 6 meters in thickness, as lenses associated with peridotites, or as discordant vein-like structures crosscutting peridotites (Angeli 2005, GE21 2022).

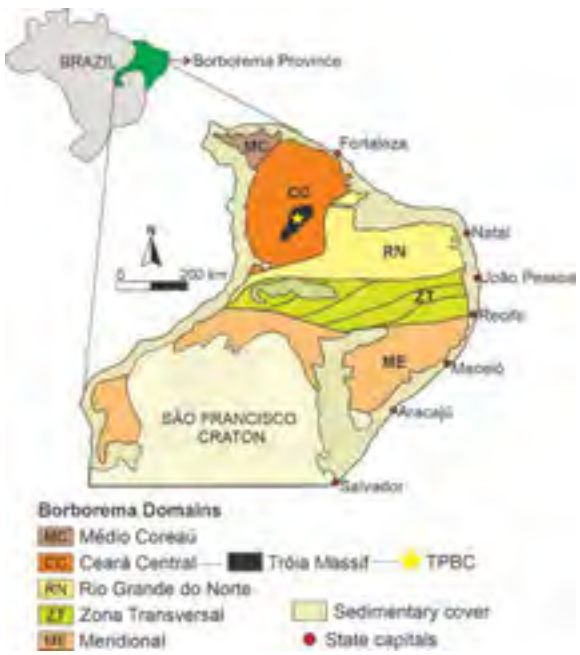


Figure 1. The location of the Borborema Province in the Northeast region of Brazil and its internal compartments (subprovinces). Highlighting the Troia-Pedra Branca

Mafic-Ultramafic Complex (TPBC) marked with a yellow star. Modified from Costa (2018).

The Pedra Branca Palladium-Platinum Project, owned by ValOre Metals, is the most advanced exploration initiative in the region. The project targets seven mineralized zones and reports an inferred resource estimate of 2,198 koz 2PGE+Au in 63.3 Mt grading 1.08 g/t, with Pd/Pt ratio of approximately 2 in fresh rock (GE21 2022) (Fig. 2). Despite this progress, the genetic and metallogenic aspects of these mineralized bodies remain poorly understood, highlighting the need for further research. Given its limited previous metallogenetic studies, the TPBC represents a unique and highly promising case study for understanding PGE mineralization in mafic-ultramafic systems. This study provides critical new data that can support future exploration strategies and refine metallogenic models for PGE mineralization in the Borborema Province.

2 Samples and Methods

2.1 Samples

Thirteen semi-massive chromitite samples were selected from seven drill holes across the Esbarro, Curiú, Cedro, and Trapiá mineralized bodies, which are part of ValOre's exploration project. Polished thin sections were then prepared from these drill core samples, serving as the basis for the petrographic and microanalytical analyses conducted in this study.

2.2 Methods

This study employed transmitted and reflected light optical microscopy, Scanning Electron Microscopy (SEM) with Energy Dispersive X-Ray Spectroscopy (EDS), and ongoing data acquisition using the Tescan Integrated Mineral Analyzer (TIMA). A total of 13 samples were analyzed via optical microscopy and five using SEM-EDS, while TIMA analyses are still in progress. These methods enabled the classification of microtextures and detailed features, the description of intergranular mineral relationships, imaging of compositional zoning in chromite, and the identification of associated PGE.

3 Results

The chromitites are semi-massive, containing approximately 50–55% fine- to medium-grained (50 µm to 2 mm) chromite crystals. Primary igneous silicates have undergone pervasive transformation into Cr-clinochlore, with rare serpentinized olivine relicts found within chromitite or preserved in dunite (Fig. 3). Cr-clinochlore crystals exhibit a complex intergrowth but are generally oriented, forming a fine- to medium-grained lepidoblastic texture (Fig. 3b).

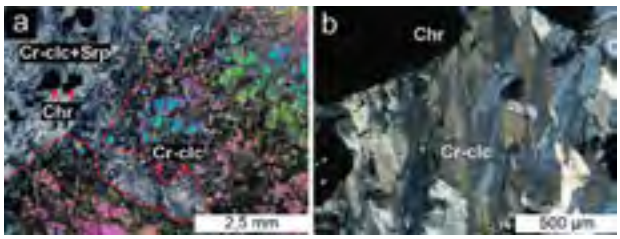


Figure 3. (a) Example of the contact zone between peridotites and chromitite, with emphasis on the interlobate texture (polarized light). (b) Lepidoblastic texture of the chromitite marked by the orientation of fibrous crystals of Cr-clinopyroxene (polarized light). Chr= chromite; Cr-Clc= Chromium-clinochlore; Srp= serpentine; Ol= olivine

Chromite crystals are often surrounded by Cr-clinochlore and, in some cases, included within olivine relicts, consistently displaying chemical disequilibrium features such as corroded or irregular edges (Fig. 4b, c, d). Chromite grains can be in direct contact or isolated, forming sinuous and parallel alignments, indicative of an igneous *chicken wire* texture (Barnes 1998) (Fig. 4a). Sulfide minerals (pyrrhotite, chalcopyrite, and pentlandite) occur locally, always in close proximity, either in rock interstices or as inclusions within chromite (Fig. 4c) and olivine, suggesting primary sulfide saturation followed by remobilization. Internally, chromite crystals exhibit corrosion patterns along crystallographic axes and textural zoning marked by rounded inclusions altered to Cr-clinochlore (Fig. 4b, c, d). The intensity of these textural features varies among samples (Fig. 4c, d).

Chromite also displays compositional zoning, with decreasing aluminium (Al) and magnesium (Mg) and enrichment in chromium (Cr) and iron (Fe) (Fig. 5a). The least altered portions are confined to fracture-free areas or the central regions of grains lacking Cr-clinochlore inclusions.

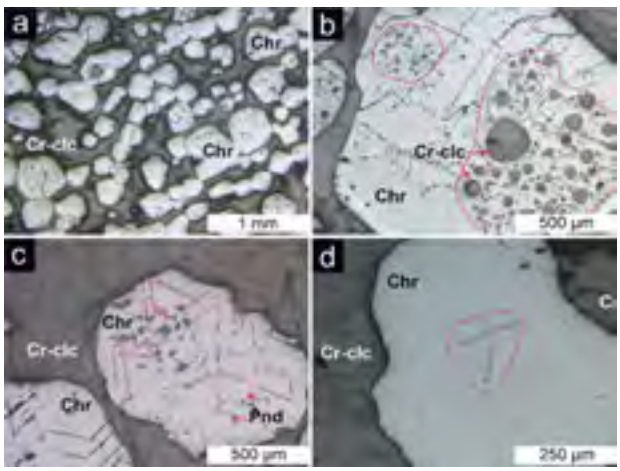


Figure 4. (a) Chromite crystals arranged in a chain-like structure forming "chicken wire" patterns (reflected light). (b) Chromite crystal in reflected light showing textural zoning marked by the presence of circular inclusions transformed into Cr-clinopyroxene (dashed in red) and massive portions. (c) Chromite with irregular edges, dissolution features across the crystal surface, and inclusions of pentlandite (reflected light). (d) Chromite

crystal with incipient dissolution features at the center of the grain (reflected light). Chr= chromite; Cr-Clc= Chromium-clinochlore; Pnd= pentlandite

The identified Platinum Group Minerals (PGM) include michenerite (Pd-Bi-Te), S-cherepanovite (Rh-As + S), Rh-telluride, sperrylite ($PtAs_2$), Pt-Ni and Pt-Au alloys, and Au-Fe alloy, as well as other Pd-Te-bismuthides, Rh-Te-sulfarsenides, Rh-arsenides, and Pt-arsenides (Fig. 5b, c, d). These minerals contain primarily palladium (Pd), platinum (Pt), and rhodium (Rh) from the palladium subgroup (PPGE), along with gold (Au). They occur along foliation planes, within Cr-clinochlore cleavage, and in fractures, indicating that post-magmatic processes played a critical role in PGE redistribution.

4 Discussion

The metallogenetic evolution of the chromitites in the Tróia-Pedra Branca Mafic-Ultramafic Complex (TPBC) reflects a complex interplay of igneous, metamorphic, and metasomatic processes that influenced the formation and redistribution of PGE+Au ore. The integration of petrographic and mineralogical data enables the recognition of key metallogenetic processes involved in the formation and transformation of chromite, as well as in the mobilization of PGE and Au. The textural and compositional heterogeneity in chromite grains, such as chemical disequilibrium features (corroded or irregular edges, dissolution patterns, and compositional zoning), indicates a dynamic evolution involving both primary magmatic crystallization and subsequent metamorphic/ hydrothermal modifications.

The chicken-wire texture observed in some chromite layers supports an igneous origin, in line with established magmatic chromitite formation models (Barnes, 1998; Prichard et al., 1994). The presence of pentlandite inclusions within chromite crystals suggests that early sulfide saturation occurred prior to or during chromite nucleation in the igneous stage. However, the occurrence of Ni and Au alloy inclusions indicates that this sulfidation process may not have been extensive. Given that initial sulfur saturation can act as a primary concentration mechanism for PGE due to their chemical affinity (e.g., Barnes and Maier, 1999), further investigation of primary inclusions in both chromite and magmatic silicates is essential.

During the metamorphic and metasomatic stages, pervasive serpentinization played a key role in chromite alteration and PGE redistribution. The release of MgO and SiO_2 from serpentinized olivine enriched the fluid phase, facilitating reactions with chromite that led to Al and Mg depletion and Cr and Fe enrichment, resulting in complex compositional zoning and the formation of ferrichromite. This transformation was accompanied by textural changes, including dissolution features along fractures and crystallographic axes. As metasomatic reactions continued, chromite–fluid interactions intensified, promoting additional Fe enrichment and ferrichromite homogenization. Similar chemical alteration in chromite has been reported by González-Jiménez et al. (2009) in podiform chromitites from the Dobromirtsi Ultramafic Massif, southeastern Bulgaria, within a progressive metamorphic context, and by Colás et al. (2017) in a retrograde setting in the Tapo Ultramafic Massif, Peru. Bach et al. (2006) demonstrated that chromite alteration requires prior serpentinization of primary silicates, occurring at temperatures of 200–300°C (greenschist facies).

This scenario is consisted with the regional metamorphic evolution of the TPBC, where amphibolite facies conditions have been reported (Pessoa et al. 1986). Moreover, the observed mineral paragenesis in this study further supports the influence of greenschist facies metamorphism and metasomatism on these rocks.

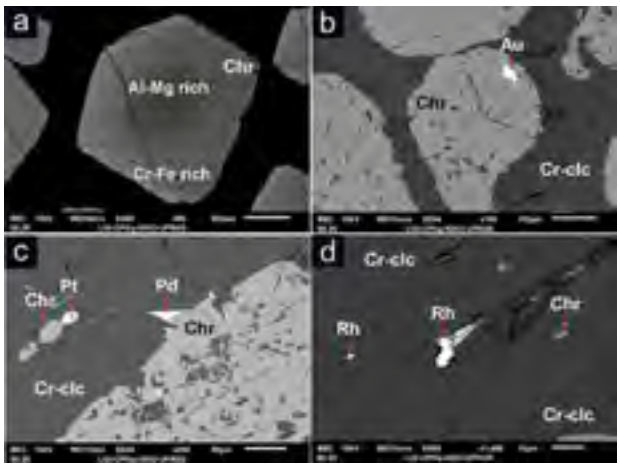


Figure 5. (a) Compositional zoning within the chromite crystal marked by a decrease in Al, Mg, and Cr towards the edges. (b) Gold-iron alloy inclusions within chromite. (c) Michenerite (Pd-Bi-Te) inclusions in chromite, filling fractures around it; Pt-Ni alloy associated with the anhedral and rounded chromite grains in the rock foliation. (d) S-Cherepanovite (Rh-As + S) and chromite crystals interlocked within the cleavage of Cr-clinopyroxene crystals. Chr= chromite; Cr-Clc= Chromium-clinochlore

Fluid-driven transformations affecting chromite and olivine in the TPBC significantly remobilized PGE, concentrating them into PGM that formed along rock foliation, Cr-clinochlore cleavage planes, and fractures. The spatial distribution of PGM, along with enrichment in PPGE (Pd/Pt = 2) and in Te, As, Bi, and Sb (TABS), indicates a metasomatic overprint (Escayola et al. 2011, Moreno et al. 1999, Prichard et al. 1994). The presence of secondary PGM enriched in PPGE and containing As, Bi, Te, and Au suggests that these TABS were either derived from primary magmatic sulfides or introduced later by hydrothermal fluids.

5 Conclusions

This study provides new insights into the metallogenetic evolution of chromitites in the TPBC through integration of petrographic and mineralogical data. It highlights the dynamic interplay of magmatic, metamorphic, and metasomatic processes in the formation and alteration of chromite and the redistribution of platinum-group and gold elements. The key conclusions are:

- Magmatic stage: Chromite formed in an igneous setting, evidenced by chicken-wire textures and pentlandite inclusions. Early sulfide saturation may have enabled initial PGE incorporation, although the presence of Ni- and Au-bearing alloys inclusions suggests that early sulfidation was limited.
- Metamorphic and metasomatic overprinting: Serpentinization released MgO and SiO_2 from olivine, enriching fluids that reacted with chromite, causing Al and Mg depletion and Cr and Fe enrichment. These changes were accompanied by dissolution features along fractures and crystallographic axes. Continued metasomatism intensified chromite–fluid interaction and led to ferrichromite homogenization.
- PGE remobilization and PGM formation: Metamorphic and metasomatic processes remobilized PGE, concentrating them along foliation planes, Cr-clinochlore cleavage, and fractures. The distribution and composition of PGM—enriched in PPGE and TABS—reflect a metasomatic overprint, with sources likely derived from either primary magmatic sulfides or later hydrothermal fluids.
- Implications for metallogeny and exploration: Recognizing the metallogenetic stages of chromitites in the TPBC enhances the understanding of PGE-Au systems and supports exploration in similarly overprinted ultramafic complexes.

Acknowledgements

The authors gratefully acknowledge the support provided by UFRGS and ValOre Metals Corp. JM also acknowledges CNPq (project 316460/2021-4) for additional funding that made this research possible.

References

Angeli N (2005) Platinum Group Minerals in Eastern Brazil: geology and occurrences in chromitite and placers. Platinum Metals Review 49(1):41-53. https://doi.org/10.1595/147106705X24391

Bach W, Paulick H, Garrido CJ, Ildefonse B, Meurer W, Humphris S (2006) Unraveling the sequence of serpentinization reactions: Petrography, mineral chemistry, and petrophysics of serpentinites from MAR 15°N (ODP Leg 209, Site 1274). Geophys Res Lett 33. L13306. 10.1029/2006GL025681.

Barnes SJ (1998) Chromite in komatiites, 1. Magmatic controls on crystallisation and composition. J of Petrol 39:1689-1720. https://doi.org/10.1093/petroj/39.10.1689

Barnes SJ, Maier WD (1999) The fractionation of Ni, Cu and the noble metals in silicate and sulphide liquids. In: Keays, R.R., Lesher, C.M., Lightfoot, P.C., Farrow, C.E.G. (Eds.), Dynamic Processes in Magmatic Ore Deposits and Their Application to Mineral Exploration, Short Course Notes, Geol Assoc Can 13:69–106.

Costa FG, Palheta ESM, Rodrigues JB, Gomes IP, Vasconcelos AM (2015) Geochemistry and U-Pb zircon ages of plutonic rocks from the Algodões granite–greenstone terrane, Troia Massif, northern Borborema Province, Brazil: implications for Paleoproterozoic subduction–accretion processes. J South Am Earth Sci 59:45–68.

Colás V, Padrón-Navarta JA, González-Jiménez JM, Fanlo I, Sánchez-Vizcaíno VL, Gervilla F, Ricardo Castroviejo (2017) The role of silica in the hydrous metamorphism of chromite. Ore Geol Rev 90:274-286. https://doi.org/10.1016/j.oregeorev.2017.02.025.

Costa FG (2018) Geologia e metalogênese do ouro do greenstone belt da Serra das Pipocas, Maciço de Troia, Província Borborema, NE-Brasil. Belém, 239p. Tese de Doutorado, Pós-graduação em Geologia e Geoquímica, Instituto de Geociências, Universidade Federal do Pará.

Escayola M, Garuti G, Zaccarini F, Proenza JA, Bédard JH, Van Staal C (2011) Chromitite and platinum-group-element mineralization at Middle Arm Brook, Central Advocate Ophiolite Complex, Baie Verte Peninsula, Newfoundland, Canada. Canadian Min 49(6):1523–1547. doi: https://doi.org/10.3749/canmin.49.6.1523

GE21 (2022) Independent Technical Report – Mineral Resource Update on the Pedra Branca PGE Project, Ceará State, Brazil.

González-Jiménez J, Kerestedjian T, Proenza J, Gervilla F (2009) Metamorphism on Chromite Ores from the Dobromirtsi Ultramafic Massif, Rhodope Mountains (SE Bulgaria). Geologica Acta 7:413-427. 10.1344/104.000001447.

Moreno T, Prichard HM, Lunar R, Monterrubio S, Fisher PC (1999) Formation of a secondary PGM assemblage in chromitites from the Herbeira ultramafic massif, Cabo Ortegal, NW, Spain. Eur J Mineral. 11:363-378.

Pessoa RR, Brito Neves BB, Kawashita K, Pessoa DR, Fuck RA (1986) Contribuição ao estudo da evolução geocronológica do Maciço de Tróia–CE. In: Simpósio de Geologia do Nordeste, 12:75-93.

Prichard HM, Ixer RA, Lord RA, Maynard J, Williams N (1994) Assemblages of platinum-group minerals and sulphides in silicate lithologies and chromite-rich rocks within the Shetland ophiolite. Can. Min. 32(2): 271-294.

Zientek ML, Loferski PJ, Parks HL, Schulte RF, Seal RR (2017) Platinum- group elements. In: Schulz, K.J., DeYoung, J.H., Jr., Seal, R.R., Bradley, D.C. (Ed). Critical mineral resources of the United States—Economic and environmental geology and prospects for future supply. U.S. Geol Survey Profes Paper 1802:1-91. https://doi.org/10.3133/pp1802N.

Origin of the high Pd/Pt ratio of the J-M Reef Stillwater Complex Montana USA

M. Christopher Jenkins[1] and William D. Smith[2]
[1]U.S. Geological Survey Geology Minerals Energy and Geophysics Science Center Spokane WA USA
[2]Commonwealth Scientific and Industrial Research Organisation Mineral Resources Kensington WA Australia

Abstract. The J-M Reef of the Stillwater Complex exhibits a high and consistent Pd/Pt ratio (~3.8). This ratio results from the equilibration of an immiscible sulfide liquid with a relatively high Pd/Pt silicate melt rather than an unusually Pd- and Pt-enriched parental melt. Numerical modeling suggests that the original silicate melt contained typical mantle-derived concentrations of Pd and Pt (~10–20 ppb Pd/Pt ~1). The partitioning of Pt and Pd between sulfide liquid and silicate melt alone cannot explain the consistently high Pd/Pt ratio across variable melt-to-sulfide mass ratios (R factors). Instead Pt-depletion caused by the early fractionation of Pt-alloy from S-undersaturated silicate magma likely established the high Pd/Pt signature. High Pd/Pt ratios can form through batch equilibration of sulfide liquid with silicate melt if partition coefficients are extremely high (>10^6). Alternatively Pd enrichment may result from sulfide upgrading within the resident footwall mush under smaller partition coefficients (10^4–10^6) in this model the instantaneous R factors remain low (R ≈ 100–700). This limits the impact of Pt and Pd partitioning on sulfide composition and helps explain the Pd-enriched character of the J-M Reef.

1 Introduction

The J-M Reef the world's highest-grade platinum-group element (PGE) deposit exhibits a remarkably consistent Pd/Pt ratio (~3.8; Fig. 1) over its 40 km strike length within the 2.7 Ga Stillwater Complex Montana USA (Jenkins et al. 2020; Wall and Scoates. 2016). This homogeneity contrasts with significant variations in ore grade and tenor. Understanding the origin of this high Pd/Pt ratio is key to unraveling PGE enrichment processes in magmatic systems as most PGE deposits have Pd/Pt ratios between 0.5 and 3 (Fig. 2; Barnes et al. 2015). Similar elevated Pd/Pt ratios (>3) are observed in deposits of other intrusions including Penikat Coldwell Complex Lac des Iles and Skaergaard.

Previous explanations for the J-M Reef's high Pd/Pt ratio include sulfide liquid equilibration with a fractionated silicate melt (Keays et al. 2012) post-magmatic fluid redistribution (Godel and Barnes (2008) or early Pt-alloy fractionation from sulfide-undersaturated magma (Jenkins et al. 2020). However most mantle-derived mafic and ultramafic magmas have Pd and Pt concentrations <20 ppb with Pd/Pt near unity (Barnes et al. 2015) making these models problematic.

In this contribution we apply Empirical Bayesan Kriging (EBK) to evaluate the homogeneity of J-M Reef Pd/Pt at the mine scale. Further Monte Carlo numerical simulations were used to test the effects of Pd and Pt partitioning between sulfide liquid and silicate melt at varying R factors. Finally, thermodynamic and mass balance modeling were used to show that infiltration of a contaminated komatiitic parental melt depleted in Pt compared to Pd into mushy cumulates can account for both the high sulfide tenors and the homogenous Pd/Pt ratios of the J-M Reef without requiring extreme partition coefficients or anomalously PGE-rich parental melts.

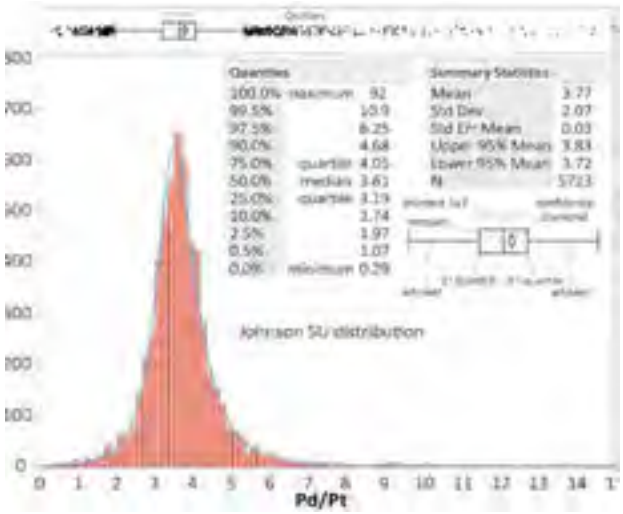


Figure 1. Tukey outlier box-and-whisker plot and histogram showing the Pd/Pt ratio of the J-M Reef in the Stillwater Mine area of the Stillwater Complex. Whole-rock Pd and Pt data are from Jenkins et al. (2020) and are composited width-weighted averages from each drill hole. Data population quantiles and summary statistics are shown in the inset tables in the figure.

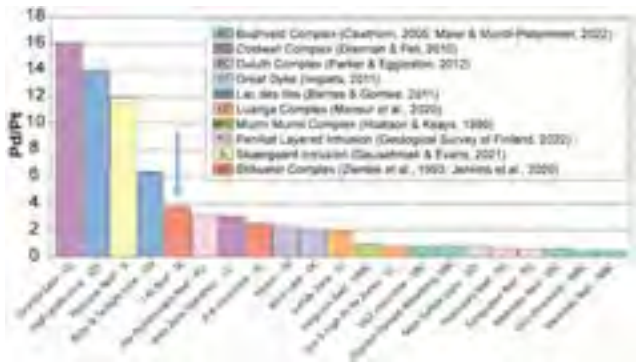


Figure 2. Bar plot showing the average Pd/Pt ratio for different global magmatic PGE deposits. The J-M Reef is indicated by the blue arrow. Data sources shown in the figure legend.

2 Methods

2.1 Empirical Bayesian Kriging

To assess the homogeneity of Pd/Pt ratios in the J-M Reef at the mine scale EBK was applied to a composite drill hole assay database (~5,000 drill

holes) from the Stillwater mine (Data are not available due to proprietary interest. Contact Sibanye-Stillwater for more information). EBK implemented in ArcGIS Pro v.3.0.2 iteratively simulates semivariograms to minimize user bias (Krivoruchko 2012). Due to confidentiality drill collar locations were projected onto a longitudinal vertical plane. Outliers (p=0.9; 591 of 5,730 drill holes) were removed to improve normality before interpolation. Kriging parameters included 1,000 simulations a subset size of 300 and an overlap factor of 5 using a linear semivariogram with 8–16 neighbors and a ~22 m spatial radius.

2.2 Monte Carlo

Monte Carlo simulations modeled silicate melt–sulfide liquid equilibration to evaluate the role of the R factor in Pd/Pt fractionation. Using Equation 1 from Campbell and Naldrett (1979),

$$C_{sulf} = \frac{C_0 * D * (R+1)}{R+D} \qquad (1)$$

Where C_{sulf} is the composition of the sulfide liquid C_0 is the initial composition of the silicate melt $D_X^{sul-sil}$ the partition coefficient for the element of interest (X) between the sulfide melt and the silicate liquid and R is the R factor. Simulations randomized R (1–10^6) and partition coefficients between sulfide liquid and silicate melt (D_{Pd} D_{Pt} = 10^4–10^7) over 10^5 iterations in Matlab R2022b. These values encompass experimental (e.g. Fleet et al. 1996 Mungall and Brenan 2014) and calculated (e.g. Fonseca et al. 2009) sulfide-silicate partitioning estimates. The model tested whether high Pd/Pt ratios could arise when D_{Pd} >> D_{Pt} consistent with observed J-M Reef sulfide tenors.

3 Results & Discussion

3.1 Pd/Pt Ratio Homogeneity in the J-M Reef

Kriging of ~5,000 drill hole assays from the Stillwater mine confirms that the Pd/Pt ratio remains highly consistent (~3.8) across the deposit (Fig. 3) with only minor local variations likely due to sampling effects (e.g. nugget effect; Stanley and Smee 2007). This homogeneity contrasts with variability in sulfur content sulfide tenor and PGE grade x thickness observed in prior studies (Jenkins et al. 2020) suggesting that although ore grades fluctuate the consistency of the Pd/Pt ratio is a fundamental characteristic of the J-M Reef mineralization.

3.2 Monte Carlo Simulations: Controls on Pd/Pt Ratios

Monte Carlo simulations of batch sulfide-silicate equilibration show that sulfide liquid compositions align well with observed J-M Reef tenors when assuming a silicate melt with an initial Pd/Pt ratio of ~3.8 (Fig. 4). At relatively low R factors the partition coefficients $D_X^{sul-sil}$ have minimal influence on sulfide composition reinforcing that the Pd/Pt ratio of the parental silicate melt is the primary control.



Figure 3. A) Cross section showing the predicted surface for Pd/Pt calculated using empirical Bayesian kriging (EBK) and Pd/Pt data from the composite database of whole-rock assays presented in Jenkins et al. (2020). Also shown are select geological features in the Stillwater mine such as the South Prairie thrust fault that truncates the J-M Reef at depth and the gabbro block offsets in the western part of the Stillwater Mine where the olivine-bearing package of rocks that host the J-M Reef cut down unconformably into layered gabbroic cumulates. Norite I on footwall (NI on FW) and Gabbronorite I on footwall (GNI on FW) correspond to areas where the J-M Reef is located above thin sections of the Norite I and Gabbronorite I zones. The Dow Meadow depression zone is an area in the western part of the Stillwater mine where the J-M Reef has an egg-carton geometry and the dip direction of the reef changes ~15 degrees on either side of the depression zone (Jenkins et al. 2020). B) Shows the distribution of drill hole collars used in the EBK as hollow circles. The size of the circle is relative to the measured composited Pd/Pt ratio from each drill hole intercept of the Reef.

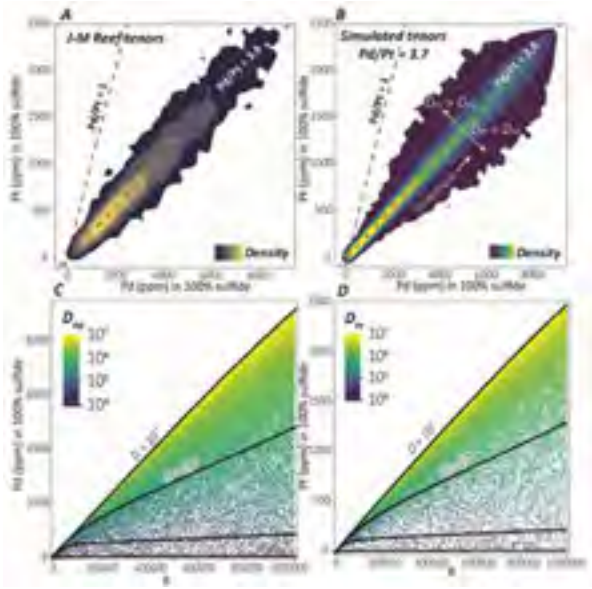


Figure 4. A) Bivariate plot showing calculated J-M Reef tenors as nonparametric density contours. B) Bivariate plot showing the results of Monte Carlo simulation of sulfide and silicate liquid equilibration for Pt and Pd using the closed system R factor model of Campbell & Naldrett (1979; Eq. 1) for a parental melt with Pd/Pt = 3.8. Simulated sulfide tenors are shown as nonparametric density contours. C) Bivariate plot showing simulated Pd tenors vs R factor. Simulated tenors are color-coded by the D_{Pd} for the given simulation. D) Bivariate plot showing simulated Pt tenors vs R factor. Simulated tenors are color-coded by the D_{Pt} for the given simulation.

3.3 Fractional Crystallization and Pd/Pt Ratios

Although some models propose that extensive fractional crystallization of silicate and oxide phases could elevate the Pd/Pt ratio in residual melts (Keays et al. 2012 Barnes et al 2020) available partitioning data do not support a strong preference for Pt incorporation into common cumulus phases in layered intrusions (e.g. Brenan et al. 2003; Zhang et al. 2022). Thermodynamic modeling of assimilation-fractional crystallization (AFC) shows that achieving a Pd/Pt ratio of 3.8 in a silicate melt without sulfide saturation would require implausibly high levels of crustal assimilation (>160%) indicating that fractional crystallization alone is unlikely to explain the Pd/Pt enrichment in the J-M Reef.

3.4 Pt-alloy Saturation and Sulfide Upgrading

A more plausible explanation for the high Pd/Pt ratio is early Pt-alloy fractionation from the parental silicate melt triggered by changes in temperature oxygen fugacity or crustal contamination (Mungall and Brenan 2014). Modeling shows that Pt solubility decreases dramatically under these conditions potentially leading to Pt depletion in the melt before sulfide saturation. This process could generate a Pd-dominant silicate melt which then equilibrates with sulfide liquid producing ores with high Pd/Pt ratios.

3.5 Implications for J-M Reef Formation

Mass balance and infiltration modeling suggest that the high Pd/Pt ratio of J-M Reef sulfides can be achieved either through batch equilibration with a Pt-depleted silicate melt or by incremental sulfide upgrading in a footwall mush via reaction with S-undersaturated Pt-depleted melt (e.g. Jenkins et al. 2021). Unlike previous models requiring extreme partition coefficients (D_{PGE}>10^6) or anomalously PGE-enriched parental melts sulfide upgrading via infiltration metasomatism operates effectively at experimentally supported values (D_{PGE} ~10^5–10^6) at low instantaneous R factors (R=100–700) in part because sulfide-silicate equilibration occurs with sulfide dissolution. Both mechanisms account for the observed tenors and homogeneity of the Pd/Pt ratio but distinguishing between them either geochemically or texturally may not be possible (Mungall et al. 2020).

4. Conclusions

The present study has shown that the Pd/Pt ratio of the J-M Reef can be modeled as the product of equilibration of a normal mantle-derived Pt-depleted silicate melt with ~10 ppb Pd. The main findings of this contribution are summarized below:

1. The Pd/Pt ratio of the J-M Reef is homogeneous as demonstrated by mine data and EBK.
2. AFC thermodynamic modeling demonstrates that based on the limited experimental data for Pd and Pt partitioning between silicate melts and the common rock-forming minerals in layered mafic-ultramafic intrusions it is highly unlikely that extensive fractional crystallization of silicate and oxide phases could produce silicate melts with high Pd/Pt ratios.
3. Monte Carlo simulations verify Pd/Pt ratios of the J-M Reef cannot be modeled by differences in the partitioning behavior ($D_{PGE}^{sul-sil}$) between Pd and Pt during batch equilibration of sulfide liquid and silicate melt particularly at R factors < 10^5.
4. Sulfide tenors and Pd/Pt ratios of the J-M Reef can be modeled by the infiltration of sulfide-undersaturated Pt-depleted silicate melt into resident sulfide liquid-bearing footwall mush causing an upgrading of footwall sulfides to very high tenors. This model is preferred because it does not require extremely large $D_{PGE}^{sul-sil}$ to produce Reef tenors. The mass ratio of silicate to sulfide liquid is small (R ~100-700) at each point in the model so $D_{PGE}^{sul-sil}$ ~ 10^5 are sufficient to model Reef tenors.
5. Early Pt-alloy saturation may be responsible for the relatively high Pd/Pt ratio of many magmatic sulfide deposits worldwide by producing parental melts with high Pd/Pt ratios prior to the onset of sulfide saturation.

Acknowledgements

Thoughtful reviews by Jake Poletti, Erin Benson, Mike Zientek (USGS), Steve Barnes (CSIRO) and Alan Boudreau (Duke University) greatly improved the quality of an early version of this work. Ville Virtanen (ISTO) Louise Schoneveld (CSIRO) and Wolf Maier (Cardiff) are thanked for reviewing this abstract. The Geology Departments at Sibanye-Stillwater's Stillwater and East Boulder mines are thanked for continuing to support the research of MCJ on the J-M Reef. Insightful discussions with Zhuo-sen Yao (China University of Geoscience) as well as Jim Mungall and Ying Li (Carleton University) helped develop the findings. This work was funded by the U.S. Geological Survey Mineral Resources Program.

Disclaimer

Any use of trade firm or product names is for descriptive purposes only and does not imply endorsement by the U.S. Government.

References

Barnes SJ, Mungall JE and Maier WD (2015) Platinum group elements in mantle melts and mantle samples: Lithos v. 232 p. 395–417.

Barnes SJ & Gomwe TS (2011) The Pd deposits of the Lac des Iles Complex Northern Ontario in Li C. and Ripley E.R. eds. Magmatic Ni-Cu and PGE deposits: Geology geochemistry and genesis. Econ Geol:351–370.

Barnes SJ, Pagé P, and Zientek M (2020) The Lower Banded series of the Stillwater Complex Montana: Whole-rock lithophile chalcophile and platinum-group element distributions: Min Depos 55:163–186.

Brenan JM, McDonough WF, and Dalpé C (2003) Experimental constraints on the partitioning of rhenium and some platinum-group elements between olivine and silicate melt: Earth Plan Sci. 212(1–2):135–150.

Campbell IH and Naldrett AJ (1979) The influence of silicate-sulphide ratios on the Geochemistry of Magmatic Sulphides: Econ Geol 74(6):1503–1506.

Cawthorn RG (2005) Stratiform platinum-group element deposits in layered intrusions in Mungall J.E. ed. Exploration for platinum-group element deposits: Min Assoc Can:57–74.

Drennan M, and Fell M, (2010) Technical report and resource estimate 2010 update for the Geordie Lake Property Northern Ontario: Python Mining Consultants Inc. prepared for Marathon PGM Corp. 250 p.

Fleet ME, Crocket JH and Stone WE (1996) Partitioning of platinum-group elements (Os Ir Ru Pt Pd) and gold between sulfide liquid and basalt melt: Geoch Cosmo Acta 60(13):2397–2412.

Fonseca ROC, Campbell IH, O'Neill HStC, and Allen CM (2009) Solubility of Pt in sulphide mattes: Implications for the genesis of PGE-rich horizons in layered intrusions: Geoch Cosmo Acta 73(19):5764–5777.

Geological Survey of Finland (2022) Mineral deposits of the Fennoscandian Shield Mineral deposits of the Fennoscandian Shield (http://gtkdata.gtk.fi/fmd/).

Geusebroek PA, and Evans L (2021) Technical report on the Skaergaard Project Southeastern Greenland Report for NI 43-101: SLR Consulting (Canada) Ltd for Major Precious Metals Corp. 120 p.

Godel B, and Barnes SJ (2008) Image analysis and composition of platinum-group minerals in the J-M Reef Stillwater Complex: Econ Geol 103(3):637–651.

Hoatson DM, and Keays RR (1989) Formation of platiniferous sulfide horizons by crystal fractionation and magma mixing in the Munni Munni layered intrusion West Pilbara Block Western Australia: Econ Geol 84(7):1775–1804.

Implats (2011) Mineral resource and mineral reserve statement as at 30 June 2011 Annual Reports (https://www.implats.co.za/pdf/annual-reports/mr-mr-statement/2011/implats-mrmr-2011.pdf).

Jenkins MC, Mungall JE, Zientek ML, Holick P, and Butak K (2020) The nature and composition of the J-M Reef Stillwater Complex Montana USA: Econ Geol 115(8): 1799–1826.

Jenkins MC, Mungall JE, Zientek ML Costin G, and Yao ZS (2021) Origin of the J-M Reef and Lower Banded series Stillwater Complex Montana USA: Precambrian Research 367:106457.

Keays RR, Lightfoot PC and Hamlyn PR (2012) Sulfide saturation history of the Stillwater Complex Montana: Chemostratigraphic variation in platinum group elements: Min Depos 47:151–173.

Krivoruchko K (2012) Empirical Bayesian Kriging implimented in ArcGIS geostatistical analyst: Esri.com v. Fall p. 10.

Maier WD and Mundl-Petermeier A (2022) Controls on Pt/Pd ratios in Bushveld magmas and cumulates: a review complemented by new W isotope data: Min Depos 58: 553–568

Mansur ET, Ferreira Filho CF and Oliveira DPL (2020) The Luanga deposit Carajás Mineral Province Brazil: Different styles of PGE mineralization hosted in a medium-size layered intrusion: Ore Geol Rev 118:103340.

Mungall J.E. and Brenan J.M. 2014 Partitioning of platinum-group elements and Au between sulfide liquid and basalt and the origins of mantle-crust fractionation of the chalcophile elements: Geochimica et Cosmochimica Acta v. 125 p. 265–289.

Mungall JE, Jenkins MC, Robb SJ, Yao ZS and Brenan JM (2020) Upgrading of magmatic sulfides revisited: Econ Geol 4(8): 1827–1833.

Parker H, and Eggleston T (2012) Maturi Birch Lake and Spruce Road Cu-Ni-PGE projects Ely Minnesota USA NI-43-101 technical report: AMEC prepared for Duluth Metals Ltd. 301 p.

Stanley CR & Smee BW (2007) Strategies for reducing sampling errors in exploration and resource definition drilling programmes for gold deposits: Geochemistry: Exploration Environment Analysis v. 7 no. 4 p. 329–340.

Wall CJ and Scoates JS (2016) High-precision U-Pb zircon-baddeleyite dating of the J-M Reef platinum group element deposit in the Stillwater Complex Montana (USA): Econ Geol. 111(3):771–782.

Zientek ML (1993) Mineral resource appraisal for locatable minerals--The Stillwater Complex in Hammarstrom J.M. Zientek M. and Elliott J.E. eds. Mineral resource assessment of the Absaroka-Beartooth study area Custer and Gallatin National Forests Montana: U.S. Geol Surv Open-file Report 93-207:F1–F83.

Zhang X, Maciag BJ, Brenan JM, and Mungall JE (2022) Experimental study of the partitioning of some platinum group elements (Pd and Ir) between orthopyroxene and silicate melt: Geoch Cosmo Acta 339:127–138.

Age and Isotopic Data from Mafic/Ultramafic Intrusions in the Karasjok Greenstone Belt, Northern Fennoscandia; Implications for Ni-Cu-PGE Prospectivity

Trond Slagstad[1], Alf Andre Orvik[1], Eduardo Mansur[1], Harald Hansen[2], Grace Howe[3], Peter Dodds[3]
[1]Geological Survey of Norway, Trondheim, Norway
[2]Dept. of Geology, University of Tromsø, Tromsø, Norway
[3]Kingsrose Mining Limited, Jersey, United Kingdom

Abstract. New age and Hf isotopic data from mafic/ultramafic intrusions in the early Paleoproterozoic Karasjok Greenstone Belt (KGB), northern Fennoscandia show that the intrusions form two main groups. The older group, dated at ca. 2.15 Ga, displays juvenile isotopic compositions indicating little interaction with the Archean substrate to the greenstone belt. In contrast, a younger group of intrusions, dated at ca. 2.05 Ga, yields highly variable isotopic compositions, consistent with parental melts derived from a depleted mantle source followed by variable and significant interaction with Archean crust. Although no economic deposits are known from the KGB, three mafic intrusions – Porsvann, Karenhaugen and Gállojávri– that belong to the younger group of intrusions, have minor sulphide occurrences and elevated Ni-Cu-PGE concentrations. Two major Ni-Cu-PGE deposits – Kevitsa and Sakatti – in the KGB-correlative Central Lapland Greenstone Belt (CLGB) in Finland yield similar ca. 2.05 Ga ages and have isotopic compositions consistent with interaction with Archean crust. These similarities along the ca. 300 km length of the KGB-CLGB suggest that the entire belt has a potential for economic deposits and that age and isotopic data may help identify prospective systems.

1 Introduction and Geological Background

Northern Fennoscandia is host to a range of mineral deposits, including mafic to ultramafic magmatic rocks rich in Ni-Cu-PGEs, hydrothermal systems rich in base and noble metals, and world-class apatite-iron-oxide ores (Jonsson et al., 2023). The region is likely to be a key for future mineral production in Europe. Nevertheless, large parts of northern Fennoscandia are underexplored, and the resource potential in some areas is only inferred from geological correlation.

The Karasjok Greenstone Belt (KGB) in northern Fennoscandia formed between ca. 2.45 and 2.05 Ga (Hansen et al., 2023; Orvik et al., 2022b), through several rifting events that terminated with the opening of the Kola Ocean, separating the Kola and Karelia Archean blocks. Protracted mafic and ultramafic magmatic activity peaked at ca. 2.22, 2.15 and 2.05 Ga with the emplacement of small to moderately sized intrusions that are the focus of this contribution. Closure of the Kola Ocean at ca. 1.90 Ga resulted in reamalgamation of the Kola and Karelia blocks and variable deformation of the KGB, which was also overridden by rock units formed within the Kola Ocean, including the Tanaelv Migmatite Belt and Lapland Granulite Belt.

Based on geochronological and stratigraphic/lithologic evidence, Hanski et al. (2001) and Hansen et al. (2023) argued that the KGB could be correlated with the Central Lapland Greenstone Belt (CLGB) in Finland, essentially on strike with the KGB, making up a ca. 300 km-long and several tens of kilometers wide greenstone belt (Fig. 1). The CLGB contains several economic deposits hosted within mafic/ultramafic intrusions and/or extrusives, including the Kevitsa and Sakatti Ni-Cu-PGE deposits, both dated at ca. 2.05 Ga (Höytiä et al., 2024; Mutanen and Huhma, 2001) and the existence of similarly aged mafic/ultramafic intrusions in the KGB could mean that the KGB is also prospective for magmatic sulphide deposits.

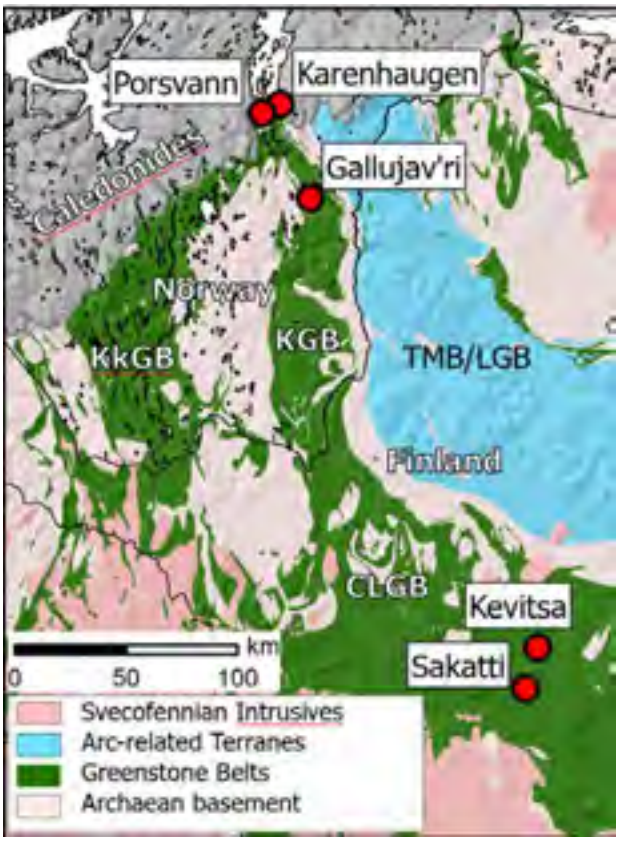


Figure 1. Simplified geologic map of northern Fennoscandia, highlighting the Karasjok and Central Lapland greenstone belts (KGB and CLGB, respectively). Abbreviations: KkGB: Kautokeino Greenstone Belt, KGB: Karasjok Greenstone Belt, CLGB: Central Lapland Greenstone Belt, TMB: Tanaelv Migmatite Belt, LGB: Lapland Granulite Belt.

Höytiä et al. (2024) noted that the ca. 2.05 Ga group of mafic magmatic rocks in the CLGB display a wide range of isotopic compositions indicating variable but significant interaction with continental crust. In contrast, a slightly older, ca. 2.15 Ga group of mafic rocks that is isotopically juvenile only contains minor mineralisations. They argued that these contrasts in age and isotopic composition could be used as a tool for further exploration. See also Guo (2024) for a recent summary of Fennoscandian mafic magmatism

Previously published isotopic data from mafic/ultramafic intrusions in the KGB are limited to the 2051 Ma Gállojávri intrusion, which displays a range of Hf and Nd compositions that are consistent with a primary melt derived from large-degree melting of depleted mantle followed by variable and significant interaction with continental crust during emplacement (Orvik et al., 2022a; Orvik et al., 2022b).This compositional variation is similar to coeval, ore-bearing mafic rocks in the CLGB and supports correlation between the KGB and CLGB.

Here, we present new age and Hf isotopic data from the KGB that establishes the KGB as a continuation of the CLGB with a similar potential for the discovery of large magmatic sulphide deposits.

2 Methods

Zircon U–Pb geochronology and Hf isotope measurements were carried out using laser-ablation multi-collector inductively coupled mass spectrometry (LA-MC-ICP-MS) at the Geological Survey of Norway (NGU). For both methods, the analytical setup consisted of a Photon Machines Analyte excite 193 nm excimer laser coupled to a Nu Plasma 3 MC-ICP-MS.

For U–Pb isotopic analyses, the laser was set to ablate with a frequency of 6 Hz, a fluence of 2 J/cm^2 and a spot size 15 µm. Ablations were carried out in a He atmosphere and sample aerosol was transported to the ICP-MS by a He carrier gas, with additional Ar added to the He-sample mixture bulb before the plasma torch. The masses 202, 204, 206-208 were measured on ion counters, and 232 and 238 were measured on Faraday cups. The GJ-1 zircon standard (608.5 ± 1.5 Ma; Jackson et al., 2004), was used as a calibration standard and analysed at the beginning and end of each run, and between every six to eight analyses.

For Hf isotopic analyses, a laser beam diameter of 40 µm was used to ablate the previously dated zircon domains, either covering the spots ablated for U–Pb determinations or placed in similar CL textural domains. A laser fluence of 4 J/cm^2 and a repetition rate of 9 Hz ablated the grains for 45 s. A He and Ar gas mixture transported the ablated aerosols to the MC–ICP–MS. Adjacent faraday cups with 10^{11} Ω resistors with an integration period of 0.1 s measured isotopes with masses between 171 and 180. To normalise the $^{176}Hf/^{177}Hf$ and calculate a scaling factor between Yb and Hf mass bias, the standards Plešovice (Sláma et al., 2008) and MUNZirc4 (Fisher et al., 2011) were used, respectively. These standards were analyzed at the beginning and end of each run and bracketing every 8–10 analyses of unknowns.

3 Results and Discussion

The dated intrusions from the KGB include three bodies yielding ages between 2157 and 2123 Ma assigned to the ‘ca. 2.15 Ga’ group, and four bodies yielding ages between 2056 and 2039 Ma assigned to the ‘ca. 2.05 Ga’ group. The locations of the dated intrusions are shown in Fig. 2. Analytical uncertainties for the age data are 0.5–1%.

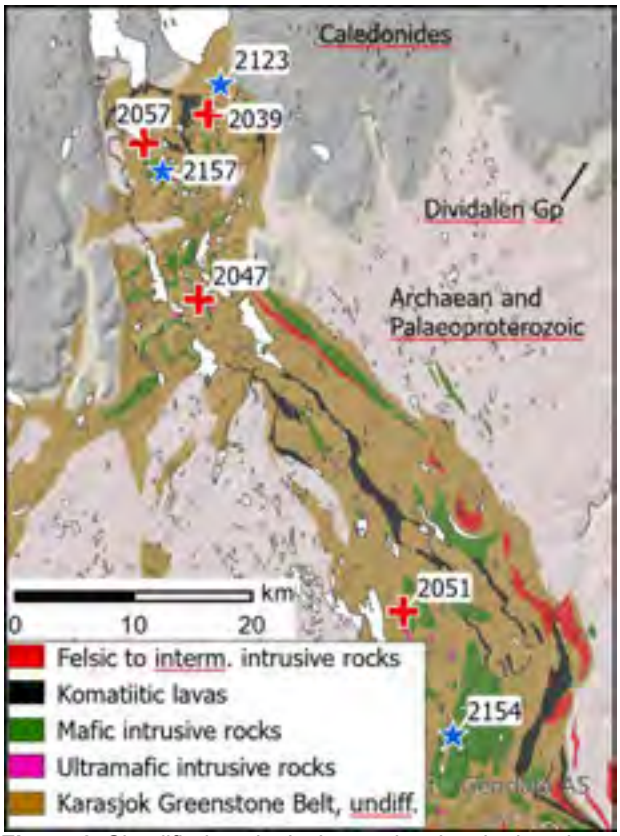


Figure 2. Simplified geological map showing the locations of the dated mafic/ultramafic intrusions. The ca. 2.15 Ga group is shown in blue crosses and the ca. 2.05 Ga group in red plus signs, with ages in Ma indicated.

Fig. 3 shows a plot of age vs εHf for the ca. 2.15 and 2.05 Ga groups of mafic/ultramafic intrusions in the KGB, and whole-rock εNd from the younger group. The ca. 2.15 Ga group has superchondritic εHf values averaging around +6, whereas the 2.05 Ga group yields a much greater spread in εHf values between ca. 0 and -12. Nd isotopic analyses from the ca. 2.05 Ga group yield a similarly wide range of εNd values, ranging from +4 to -18. These wide ranges of εHf and εNd values from the ca. 2.05 Ga group is consistent with earlier work from the 2051 Ma Gallojavri intrusion (Orvik et al., 2022b).

No Hf data have been reported from ca. 2.15 and 2.05 Ga intrusions in the CLGB, but numerous Nd whole-rock analyses were referenced by Höytiä et al. (2024). The older ca. 2.15 Ga group of intrusions

with only minor sulphide occurrences consistently yield superchondritic εNd values between +2 and +5, whereas the younger group of ca. 2.05 Ga intrusions and extrusives, including Kevitsa and Sakatti, yield a wide range of dominantly subchondritic compositions with εNd between +2 and -5 (Fig. 3).

The isotopic data from the two age groups of mafic/ultramafic rocks in the KGB and CLGB show that the younger, ca. 2.05 Ga magmas interacted much more strongly with Archean continental crust than the older magmas, and Höytiä et al. (2024) argued that this contrast could reflect the availability of external sulphur to the magmas, which in turn would have an effect on whether the magmas reached sulphur saturation. The similarities between the magmatic systems in the KGB and CLGB lead us to conclude that a similar model is applicable throughout the KGB-CLGB, and that while no economic deposits are currently known in the KGB, the potential for finding such deposits is similar to that of the CLGB.

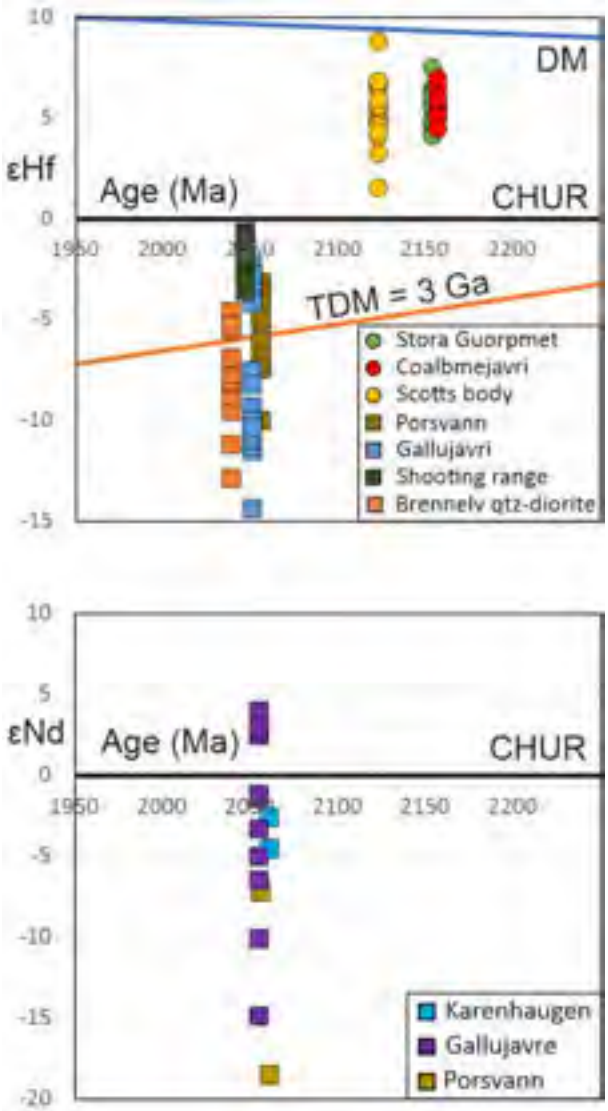


Figure 3. Age vs. εHf and εNd for ca. 2.15 and 2.05 Ga mafic/ultramafic intrusions in the KGB. The Hf isotopes were measured in zircon, whereas the Nd data represent whole-rock analyses.

4 Conclusions

Two groups of mafic/ultramafic intrusions have been identified in the Karasjok Greenstone Belt (KGB) based on age and isotopic composition. An older group consisting of rocks dated to ca. 2.15 Ga yields largely juvenile isotopic compositions, whereas a younger group dated to ca. 2.05 Ga yields highly variable, but dominantly subchondritic εHf and εNd values suggesting significant interaction with Archean continental crust. Three mafic/ultramafic intrusions belonging to the younger group (Porsvann, Karenhaugen and Gállojávri) are known to contain subeconomic concentrations of Ni, Cu and PGEs.

A similar relationship between age and isotopic composition is observed in the southern extension of the KGB into Finland, the Central Lapland Greenstone Belt (CLGB). The large Ni-Cu-PGE deposits at Kevitsa and Sakatti belong to the younger, ca. 2.05 Ga group of intrusions.

The available data from the KGB-CLGB suggests that a group of mafic/ultramafic intrusions found throughout the entire belt, may have a significant potential for future, new discoveries.

Acknowledgements

We thank NGU and Kingsrose for funding of this project. The Research Council of Norway is acknowledged for the support to the Norwegian Laboratory for Mineral and Materials Characterisation, MiMaC, project number 269842/F50.

References

Fisher, C.M., Hanchar, J.M., Samson, S.D., Dhuime, B., Blichert-Toft, J., Vervoort, J.D., Lam, R. (2011) Synthetic zircon doped with hafnium and rare earth elements: A reference material for in situ hafnium isotope analysis. Chemical Geology 286: 32-47.

Guo, F. (2024) Geochemistry of Archaean and Palaeoproterozoic mafic-ultramafic rocks in NE Fennoscandia and implications for their Ni-Cu-PGE prospectivity. PhD thesis, University of Oulo, 87 pp.

Hansen, H., Slagstad, T., Bergh, S.G., Bekker, A. (2023) Geochronology and chemostratigraphy of the 2.47–1.96 Ga rift-related volcano-sedimentary succession in the Karasjok Greenstone Belt, northern Norway, and its regional correlation within the Fennoscandian Shield. Precambrian Research 397: 107166.

Hanski, E., Huhma, H., Rastas, P., Kamenetsky, V.S. (2001) The Palaeoproterozoic Komatiite–Picrite Association of Finnish Lapland. Journal of Petrology 42: 855-876.

Höytiä, H.M.A., Jelsma, H.A., Armstrong, R.A., Dodds, P., Siikaluoma, J., Lamberg, P. (2024) SHRIMP U-Pb Geochronology of the Sakatti and Kaarrekumpu Cu-Ni-Platinum Group Element Deposits—Constraints on the Timing of Fertile Magmatism in the Central Lapland Greenstone Belt. Economic Geology 119: 1769-1790.

Jackson, S.E., Pearson, N.J., Griffin, W.L., Belousova, E.A. (2004) The application of laser ablation-inductively coupled plasma-mass spectrometry to in situ U-Pb zircon geochronology. Chemical Geology 211: 47-69.

Jonsson, E., Törmänen, T., Keiding, J.K., Bjerkgård, T., Eilu, P., Pokki, J., Gautneb, H., Reginiussen, H., Rosa, D., Sadeghi, M., Sandstad, J.S., Stendal, H. (2023) Critical

metals and minerals in the Nordic countries of Europe: diversity of mineralization and green energy potential. Geological Society, London, Special Publications 526: 95-152.
Mutanen, T., Huhma, H. (2001) U-Pb geochronology of the Koitelainen, Akanvaara and Keivitsa layered intrusions and related rocks. Geological Survey of Finland Special Paper 33: 229-246.
Orvik, A.A., Slagstad, T., Hansen, H., Nilsson, L.P., Sørensen, B.E. (2022a) The Palaeoproterozoic Gallujavri ultramafic intrusion, Karasjok Greenstone Belt; petrogenesis of a trans-crustal magma system. Journal of Petrology 63: 1-28.
Orvik, A.A., Slagstad, T., Sørensen, B.E., Millar, I., Hansen, H. (2022b) Evolution of the Gállojávri ultramafic intrusion from U-Pb zircon ages and Rb-Sr, Sm-Nd and Lu-Hf isotope systematics. Precambrian Research 379: 106813.
Sláma, J., Košler, J., Condon, D.J., Crowley, J.L., Gerdes, A., Hanchar, J.M., Horstwood, M.S.A., Morris, G.A., Nasdala, L., Norberg, N., Schaltegger, U., Schoene, B., Tubrett, M.N., Whitehouse, M.J. (2008) Plešovice zircon — A new natural reference material for U–Pb and Hf isotopic microanalysis. Chemical Geology 249: 1-35.

The role of alteration to Ni-Cu mineralization at the Great Dyke of Zimbabwe

Ema Vokic[1], Sibila Borojevic Sostaric[1]
[1] *University of Zagreb - Faculty of Mining, Geology and Petroleum Engineering, Zagreb, Croatia*

Abstract. The Great Dyke of Zimbabwe hosts large reserves of nickel, copper, chromium, and PGE within the Main Sulfide Zone. While various genetic models explain metal enrichment, the role of alteration in modifying ore distribution remains underexplored. In this study, petrography, X-ray diffraction (XRD), and X-ray florescence (XRF) analysis were conducted to assess the effects of alteration on ultramafic and mafic sequences. Four different stages of alteration were detected: (1) high-temperature hydrothermal overprint within the ultramafic sequence (390°C-500°C), (2) low-temperature overprint within mafic sequence (<115°C), (3) late-stage felsic overprint within ultramafic and mafic sequence (200 °C), and (4) surface weathering of ultramafic sequence. The results indicate that hydrothermal processes significantly influence mineralogy, altering primary magmatic minerals and decreasing base metal grades (low altered sample U-4b from the MSZ; Ni=6698 ppm, Cu=4019 ppm, compared to highly altered U-7 from the MSZ; Ni=449 ppm, Cu=100 ppm). However, surface weathering significantly increase nickel grades (low altered IMPG-3; Ni=3625 ppm, highly altered IMPG-4; Ni=12488 ppm), leading to the formation of supergene enrichment in nickel-bearing serpentine, spinel, and chlorite.

1 Introduction

The Great Dyke (GD) of Zimbabwe is a large, layered intrusion hosting significant reserves of nickel, copper, chromium, and platinum-group elements (PGE) within the Main Sulfide Zone (MSZ). While extensive research has been conducted on the GD's stratigraphy and mineralogy, less attention has been given to the effects of alteration processes on metal grade distribution. Understanding them is necessary to comprehend the genetic model and assess their impact on recoverability.

During the field campaign, a total of 20 samples of dunite, (un)mineralised pyroxenite, felsic and mafic pegmatite, and gabbronorite from outcrops, open pit, and underground mine were collected within the GD area to evaluate the influence of alteration overprinting on ultramafic and mafic rocks (Fig. 1A). The GD stratigraphically consists of two primary sequences: the Lower ultramafic sequence, comprising ultramafic dunite, harzburgite, and pyroxenite with chromitite seams at the base of cyclic units, and the Upper mafic sequence, dominated by gabbro and gabbronorite (Wilson 1996) (Fig. 1B). It is divided into five sub-chambers – Musengezi, Darwendale, Sebakwe, Shurugwi, and Wedza – based on variations in lithology and stratigraphic thickness (Wilson & Prendergast 1998). Some sub-chambers are influenced by the contact with the Archean greenstone belt, but the Shurugwi is of particular interest as it is bounded by the greenstone belt on its western margin zone (WMZ) and Archean granite on its eastern margin zone (EMZ) (Markwitz et al. 2009). The WMZ is characterized by high oxidation levels and abundant dolerite dykes, which led to the formation of serpentinite-magnetite assemblage and Fe-rich pegmatoids. The EMZ contains granite dykes, pyroxene-amphibole assemblages, and magnetite diorite (Wilson et al. 2000).

The MSZ forms a 3-10 m thick continuous layer, hosted by the uppermost orthopyroxenite sequence and situated 10-40 m below the ultramafic/mafic contact (Chaumba & Musa 2020). The MSZ exhibits vertical zonation of base metal sulfides (BMS) and PGE, dividing it into a lower PGE-rich subzone and an upper BMS-dominant subzone (Oberthür 2013). The MSZ contains 0.5–10 vol% pyrrhotite, pentlandite, and chalcopyrite in roughly equal proportions, with minor amounts of potential secondary pyrite (Oberthür 2011).



Figure 1. A Map of regional geology and sampling locations. Geology modified after Markwitz et al. (2009) and Chaumba (2017); **B** Road-cut near Unki mine.

2 Methods

The 20 samples were analysed using standard thin sections and polarized light microscopy to identify the mineral composition of the samples, classify the rocks and alteration processes. To determine the mineralogical composition of samples, an X-ray diffraction (XRD) analysis was conducted on the 20 samples, which were ground using an agate set to create a powdered fraction. XRD analysis was performed using a Malvern PanAnalytical vertical X-ray goniometer (X'Pert MPD model) equipped with a Cu tube and a graphite crystal monochromator at the Faculty of Mining, geology and Petroleum Engineering at University of Zagreb. An X-ray fluorescence (XRF) analysis of 20 powder samples was carried out using a portable energy-dispersive XRF analyser to determine the elemental composition of the rocks.

3 Results

3.1 Mineralogy and petrography

GD ultramafic unit
The yellowish to greenish dunite rocks are medium-grained with cumulus texture. A single heavily altered sample was crosscut by greenish (?garnierite) veinlets, having Mohs hardness <4. Dunite samples are composed of olivine (up to 60 vol%), and interstitial spinel (up to 30 vol%). A single sample (IMPG-8) comprises nodular, allotriomorphic opaque spinels within a serpentinised matrix. The degree of alteration varies from low (altered up to 10% of primary assemblage) to pervasively alteration (up to 60%) containing sporadically relict olivine grains. The alteration assemblage was determined by XRD. Predominant alteration minerals belong to serpentinite group (antigorite, lizardite, clinochrysotile, and pecoraite (Ni-bearing serpentine)), followed by hydrotalcite group (pyroaurite), carbonate group (calcite, dolomite, magnesite) and brucite. XRD analysis found several spinel types: chromite and magnesiochromite, likely related to primary magmatic crystallization whereas magnetite, and nichromite (Ni-bearing chromite) are found as fine-grained secondary minerals associated with serpentinite (Fig. 2A).

The orthopyroxenite samples are medium-grained with cumulus to poikilitic textures. The dominant mineral phase is hipidiomorphic orthopyroxene (enstatite-bronzite; up to 70 vol%), followed by allotriomorphic plagioclase (up to 10%), and clinopyroxene (augite, diopside; up to 5%; Fig. 2B). Underground samples of orthopyroxenite from the MSZ (U-7, U-4a, U-4b) contain fresh chalcopyrite and pyrrhotite, whereas an outcrop sample of orthopyroxenite from the MSZ (TRW-6) contain Ni-chlorite (nimite). The samples are altered to various degrees (5-60%). XRD analysis confirmed amphibole group (hornblende, actionilite), followed by pyrophyllite-talc group (willemseite), chlorite group (clinochlore), secondary quartz, cristobalite and magnetite (Fig. 2C). Optical microscopy additionally reveals secondary carbonate, clay minerals, and amorphous Fe-oxyhydroxide.
The greenish plagioclase clinopyroxenite is medium-grained with cumulus to poikilitic texture. It is primarily composed of allotriomorphic clinopyroxene (diopside, augite determined by XRD; up to 60 vol%), plagioclase (25 vol%), and orthopyroxene (enstatite; up to 10 vol%; Fig. 2D). The rocks are slightly altered, with a small portion of visible talc (<5%), determined as willemseite (pyrophyllite-talc group) via XRD analysis.

GD mafic unit
The dark grey gabbronorite sample is medium-grained and exhibits a granular texture. The predominant mineral is hipidiomorphic plagioclase (50%), followed by allotriomorphic clinopyroxene (15%), orthopyroxene (10%), and olivine (10%) (Fig. 2E right). Accessory opaque magnetite comprise less than 2% of the sample and are found interstitially among the pyroxene grains. The degree of alteration is low. Plagioclase alteration results in the formation of sericite and chlorite, which account for less than 10% of the rock, while chloritization of clinopyroxene accounts for less than 5%.

The pyroxenite pegmatite occurs within gabbronorite unit. They are coarse-grained rocks, with external zone composed of monomineralic orthopyroxene (enstatite), grading to plagioclase in intermediate zone, with a central part composed of quartz and clinopyroxene (augite). Whereas most of the idiomorphic plagioclase shows high degree of alteration (chlinoclore, kaolinite), a 5% of allotriomorphic plagioclase (albite) remains fresh and is interpreted as secondary. About 10% of pyroxene is altered to hornblende, and 5-10% to epidote, tremolite-actinolite and clinochlore (Fig. 2E left). A small portion of ilmenite is also present. XRD analysis additionally identified willemsite (pyrophyllite-talc group).

GD felsic dykes
The felsic, aplite rocks are medium-grained, greyish-white, and composed of K-feldspar (microcline, orthoclase; 50%), quartz (30%), and plagioclase (albite; 10%). Accessory opaque mineral (?magnetite) comprise 1-2% of the sample. Eutectic intergrowths of quartz and K-feldspar are common, as well as perthite and occasional antiperthite textures of K-Na feldspar (Fig. 2F). Feldspars are weakly altered (up to 10% of its primary assemblage) to kaolinite, sericite and clinoclore, detected by XRD analysis.

3.2 Whole rock geochemistry

GD ultramafic unit
Dunite is characterized by high MgO content (37.1-47.7 wt.%), variable FeO content (6.8–11.0 wt.%), increased Cr_2O_3 (1.0-2.2 wt.%). It also contains high concentrations of Ni and Co (Ni ≈ 3000 ppm; Co =increased Cr_2O_3 (1.0-2.2 wt.%). It also contains

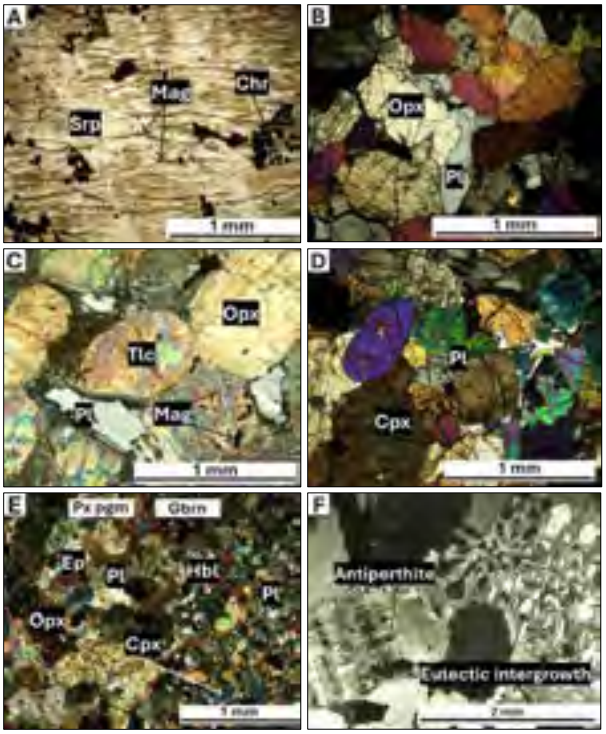


Figure 2. Microphotographs of: (A) serpentinite (Srp) and magnetite (Mag) within altered dunite containing accessory chromite (Chr); (B-C) different stages of orthopyroxenite alteration, from fresh cumulus orthopyroxene (Opx) (B) to highly altered orthopyroxene comprising talc (Tlc) and magnetite (Mag) (C); (D) fresh, cumulus clinopyroxene (Cpx) and interstitial plagioclase (Pl) within plagioclase clinopyroxenite; (E) contact of pyroxenite pegmatite (Px pgm) highly altered to hornblende (Hbl) and epidote (Ep), and gabbronorite (Gbrn) composed of fine-grained, granular pyroxenite and plagioclase; (F) felsic aplite showing antiperthite texture and eutectic intergrowth of K-feldspar and quartz.

high concentrations of Ni and Co (Ni ≈ 3000 ppm; Co =115–180 ppm). In heavily altered dunite, Ni content reaches anomalously high values of up to 12500 ppm. In contrast, SiO_2 content is very low (37.3–42.6 wt.%), and CaO is up to 0.2 wt.%, whereas Al_2O_3, K_2O, Cu, and S are below detection limits. Sample IMPG-8 has elevated Cr_2O_3 (33.6 wt.%), FeO (8.8 wt.%), and Al_2O_3 (2.9 wt.%), whereas SiO_2 and MgO are lower (20.2 wt.% and 27.5 wt.%) compared to fresh dunite. It also exhibits the highest Co (290 ppm) and the lowest Ni content (1.3 ppm).

Orthopyroxenite is characterized by higher contents of SiO_2 (48.3–51.2 wt.%), Al_2O_3 (2.4–5.7 wt.%), FeO (10.1–12.7 wt.%), and CaO (1.8–4.3 wt.%) compared to dunite. It also contains minor amounts of K_2O (up to 0.2 wt.%). MgO and Cr_2O_3 are significantly lower (23.6–25.6 wt.% and 0.4–0.5 wt.%, respectively). Ni and Co contents are slightly decreased (Ni up to 2650 ppm; Co up to 145 ppm), whereas Cu and S show notable enrichment (Cu up to 2150 ppm; S up to 2 wt.%). Underground samples from the MSZ are slightly depleted in SiO_2, exhibiting high Co, Ni, Cu and S values (Co up to 195 ppm; Ni up to 6700 ppm; Cu up to 4325 ppm and S up to 6.6 wt.%). An outcrop sample from the MSZ exhibits high Ni (1135 ppm) and Cu (3305 ppm), whereas S is below detection limit.

Plagioclase clinopyroxenite show increase of SiO_2, Al_2O_3, FeO and CaO and depletion of MgO and Cr_2O_3. Their S content is below detection limits, whereas Co, Ni and Cu are variable and high (Co up to 230 ppm; Ni up to 1135 ppm; Cu up to 3305 ppm).

GD mafic unit

Gabbronorite and pyroxenite pegmatite have higher SiO_2 to 52.4 wt.%, Al_2O_3 to 12.4 wt.% and CaO to 11.1 wt.%, compared to the GD ultramafic unit, whereas MgO (5.9 wt.%), Ni (180 ppm) and Cu (175 ppm) are much lower.

GD felsic aplite

Late-stage leucocratic aplite rocks have the highest SiO_2, Al_2O_3 and K_2O content (up to 76.5 wt.%; up to 11.9 wt.%, and up to 5.7 wt.%), their CaO drops down to 0.9 wt.%, whereas MgO, SO_2, Co, Ni and Cu values are below detection.

Table 1. Major oxides (%) and base metals (ppm) (L-low, M-medium, H-highly altered), and stages (presence of (1) high-T antigorite and amphibole (hornblende, tremolite-actinolite), chlorite (clinochlore), talc (willemseite); (2) low–T and clinochrysotile, pyroaurite, calcite, dolomite, magnesite, magnetite, brucite, secondary quartz; (3) late-stage felsic overprint (clinochlore, sericite, kaolinite); (4) weathering products (spinel (nichromite), serpentine (pecoraite), chlorite (nimite)).

Sample	Classification	Alteration degree /stage	[%]								[ppm]		
			SiO_2	Cr_2O_3	Al_2O_3	K_2O	FeO	MgO	CaO	SO_2	Co	Ni	Cu
IMPG-4	Dunite	H/(4)	42.6	1.8	<0.04	<0.002	11	37.1	0	<0.004	180	12488	<10
IMPG-2	Dunite	M/(1,2,4)	38.1	2.2	<0.04	<0.002	6.8	46.6	0	<0.004	175	3123	<10
IMPG-3	Dunite	M/(1,2,4)	38.8	1.3	<0.04	<0.002	7.9	45.5	0.1	<0.004	116	3625	<10
IMPG-7	Dunite	L/(2,4)	37.3	1	<0.04	<0.002	7.6	47.7	0.2	<0.004	166	2996	<10
IMPG-9	Dunite	L/(1,2)	37	2.2	0.3	<0.002	3	41.7	9.4	<0.004	116	1392	<10
IMPG-10	Dunite	L/(1,4)	21.4	5.7	0.2	0.002	3.2	39.2	23.5	<0.004	43	1355	<10
IMPG-8	Dunite	L/(2)	20.2	33.6	2.9	0.002	8.8	27.5	0.1	<0.004	289	1313	<10
TRW-6	Orthopyroxenite (MSZ)	H/(1,4)	50.9	0.3	5.8	0.2	12.7	19.1	4.4	<0.004	229	1135	3305
U-7	Orthopyroxenite (MSZ)	H/(1)	49.7	0.4	5.7	0.2	10.1	23.6	4.3	<0.004	140	449	100
U-4a	Orthopyroxenite (MSZ)	L/(1)	42.3	0.4	1.7	0.2	14.2	28.3	2.2	5.8	195	5805	4325
U-4b	Orthopyroxenite (MSZ)	L/(1)	45	0.4	2.7	<0.002	15.5	22.5	2.7	6.6	145	6698	4019
U-2	Orthopyroxenite	H/(1,2)	50.6	0.5	2.4	<0.002	12.5	24.9	1.8	0.8	145	2582	2149
N-2	Orthopyroxenite	L/(1)	49.6	0.5	3.6	<0.002	12.1	24.7	2.8	<0.004	140	1157	532
U-5	Orthopyroxenite	L/(1)	49.8	0.4	2.8	<0.002	12	25.5	2.5	0.4	107	1618	932
U-3	Orthopyroxenite	L/(1)	51.2	0.4	2.9	0.3	11.9	24	2.6	0.3	141	1470	682
U-6	Orthopyroxenite pgm	L/(1)	48.3	0.4	2.4	<0.002	12.7	25.6	2.5	2	<10	2662	1973
N-1	Plagioclase clinopyroxenite	L/(1)	50.1	0.6	3.2	<0.002	8.9	18.2	12.3	<0.004	185	784	413
RC-1	Gabbronorite + pyroxenite pgm	H(1,3)	52.4	<0.0007	12.4	0.3	11	5.9	11.1	<0.004	<10	178	172
TRW-3	Felsic aplite	L/(3)	75.3	<0.0007	11.2	5.7	1	0.0	0.9	<0.004	<10	<10	<10
TRW-1	Felsic aplite	L/(3)	76.5	<0.0007	11.9	4.6	0.5	0.0	0.5	<0.004	<10	<10	<10

4 Discussion and conclusions

4.1 Fractional crystallisation

The rocks show typical ultramafic to mafic to felsic trends increasing SiO_2, Al_2O_3, CaO and K_2O values and decreasing MgO and Cr_2O_3, indicating increasing degree of fractional crystallisation related to cooling of the magmatic system. The GD ultramafic unit also has high Co, Ni, Cu and Cr_2O_3 whereas the mafic and late-stage felsic rocks have very low base metals content.

4.2 The alteration stages

At least four different stages of alterations were recognised:
(1) High-temperature hydrothermal overprint is more extensive in GD ultramafic unit, compared to GD mafic units and presented by: (i) antigorite replacing olivine, (ii) secondary amphibole (hornblende, tremolite-actinolite), chlorite (clinochlore) and talc (willemseite) replacing pyroxene, and (iii) secondary cristobalite. Formation temperatures based on mineralogy were between 390°C and 500°C (Schwartz et al. 2013; Patterson et al. 2021).
(2) Low-temperature hydrothermal overprint within GD ultramafic to mafic rocks corresponds to classical serpentinization and carbonatization, forming lizardite and clinochrysotile, pyroaurite, calcite, dolomite, magnesite, magnetite and brucite (sensu Corre et al. 2023 and references therein) and likely formed at temperatures below 115°C (Warner and Taylor 1971).
(3) Mineral assemblage associated with autometasomatised pegmatite rocks (clinochlore, sericite, kaolinite) is like assemblage of surrounding rocks and should originate at temperatures around 200 °C (Anderson et al. 2019).
(4) Surface weathering in the GD ultramafic sequence is strong and leads to the formation of secondary spinel (nichromite), serpentine (pecoraite), and chlorite (nimite). High nickel values and low sulfur indicate that nickel is dominantly concentrated in spinel, serpentine, and chlorite rather than sulfide minerals.

4.3 Alteration vs. mineralization

Two important conclusions are drawn:
(1) With increasing degree of alteration, base metal concentrations decrease (as evidenced at fresh orthopyroxenite U-4b; Ni=6698 ppm, Cu=4019 ppm, compared to highly altered orthopyroxenite U-7; Ni=449 ppm, Cu=100 ppm).
(2) Surface weathering can increase the concentration of nickel to several orders of magnitude and lead to the formation of nickel supergene enrichment (highly altered dunite IMPG-4; Ni=12488 ppm, compared to normal dunite IMPG-3; Ni=3625 ppm).

Acknowledgements

This research has been supported by the "Young Researchers' Career Development Project" from the Croatian Science Foundation and the European Institute of Innovation and Technology (EIT), under the “NRE-ElectRA Project” (23024). We would like to thank Caston T. Musa, Jeff B. Chaumba, and Andrew Du Toit for their guidance during the SEG Great Dyke excursion.

References

Anderson MO, Hannington MD, McConachy T, Jamieson JW, Anders M, Wienkenjohann H, Strauss H, Hansteen T, Petersen S (2019) Mineralization and Alteration of a Modern Seafloor Massive Sulfide Deposit Hosted in Mafic Volcaniclastic Rocks. Econ Geol 114:857–896. doi: https://doi.org/10.5382/econgeo.4666

Barnes S-J, Campbell IH (1988) Role of crustal and mantle assimilation in the genesis of PGE deposits. Econ Geol 83:1100–1107.

Chaumba JB, Musa CT (2020) Formation of the main sulfide zone at Unki mine, Shurugwi subchamber of the Great Dyke, Zimbabwe: Constraints from petrography and sulfide compositions. Geosphere 16(2):685–710. https://doi.org/10.1130/GES02150.1

Corre M, Brunet F, Schwartz S, Gautheron C, Agranier A, Lesimple S (2023) Quaternary low-temperature serpentinization and carbonation in the New Caledonia ophiolite. Sci Rep 13, 19413 https://doi.org/10.1038/s41598-023-46691-y

Markwitz V, Gonzalez-Alvarez I, Maier WD, Maier W, McCuaig TC, Porwal A (2009) Nickel Sulfide Deposits in Archaean Greenstone Belts in Zimbabwe: Review and Prospectivity Analysis. https://www.researchgate.net/publication/260792212

Oberthür T, Locmelis M (2013) The oxidized ores of the Main Sulfide Zone, Great Dyke, Zimbabwe: Turning resources into minable reserves-mineralogy is the key. In Article in Journal of the Southern African Institute of Mining and Metallurgy. https://www.researchgate.net/publication/283089747

Oberthür T (2011) Platinum-Group Element Mineralization of the Main Sulfide Zone, Great Dyke, Zimbabwe. SEG, 17: 329–349, DOI: 10.5382/Rev.17.12

Patterson SN, Lynn KJ, Prigent C, Warren JM (2021) High temperature hydrothermal alteration and amphibole formation in Gakkel Ridge abyssal peridotites. Lithos, 392–393, 106107, https://doi.org/10.1016/j.lithos.2021.106107

Schwartz S, Guillot S, Reynard B, Lafay R, Debret B, Nicollet C, Lanari P, Auzende AL (2013) Pressure–temperature estimates of the lizardite/antigorite transition in high pressure serpentinites, Lithos, 178, 197-210, https://doi.org/10.1016/j.lithos.2012.11.023

Wennerd B, Taylorh P Jr (1973) Oxygen and hydrogen isotope studies of the serpentinization of ultramafic rocks in oceanic environments and continental ophiolite complexes. Am. J. Sci. 273, 207-239.

Wilson AH (1996) The Great Dyke of Zimbabwe. Elsevier, 15, 365-402, https://doi.org/10.1016/S0167-2894(96)80013-3

Wilson A, Prendergast M (1998) The Great Dyke of Zimbabwe: Guidebook for the Pre-Symposium Excursion 23-28 June 1998, 1–94.

Wilson AH, Murahwi CZ, Coghill BM (2000) Stratigraphy, geochemistry and PGE mineralization of the central zone of the Selukwe Subchamber, Great Dyke. J. Afr. Earth Sci, 30, 633–653.

Petrogenesis and mineralization potential of the Bradley Peak komatiitic basalts, Wyoming Province

Lisa Zieman[1], M. Christopher Jenkins[1], Michael Zientek[1], Jacob Poletti[1], Alan D. Rooney[2]
[1]U.S. Geological Survey, Geology, Minerals, Energy, and Geophysics Science Center, Spokane, WA, USA
[2]Department of Earth and Planetary Sciences, Yale University, New Haven, CT, USA

Abstract. The ca. 2.72 Ga Bradley Peak greenstone terrane in the Wyoming Province contains spinifex- and cumulate-textured komatiitic volcanic rocks that may host Ni-Cu-PGE sulfide mineralization. New whole rock geochemistry classifies these rocks as Al-undepleted komatiitic basalts derived from a parental melt with ~17 wt. % MgO. Isotopic data (Sm-Nd, Re-Os) and REE profiles suggest a plume source and possible assimilation of juvenile footwall volcanic rocks. Calculated sulfur concentrations at sulfide saturation and low-detection PGE geochemistry indicate these magmas did not saturate a sulfide liquid resulting in sulfide mineralization. Although the Bradley Peak komatiitic basalt flows are unlikely to host magmatic sulfide mineralization, they are likely the source of Au for regional orogenic gold deposits.

1 Introduction

Archean komatiitic greenstone belts are important hosts of Ni-Cu-platinum-group element (PGE) sulfide ore deposits (e.g., Barnes et al. 2016) and are fundamental to understanding Precambrian tectonics, magmatism, and secular changes in the chemistry and thermal state of the mantle (e.g., Arndt 2008). The ca. 2.72 Ga Bradley Peak greenstone terrane in the Wyoming Province, United States is currently a target for mineral exploration and a focus area for critical mineral investigations by the U.S. Geological Survey. This komatiitic greenstone terrane is speculated to be genetically related to the Abitibi greenstone terrane in the Superior Province (Killian et al. 2016), which contains komatiite-hosted Ni-Cu-PGE mineralization as well as orogenic gold deposits. Despite this possible connection and its implications for the presence of Abitibi-scale mineral deposits in the Bradley Peak greenstone terrane, the petrology and geochemistry of the Bradley Peak komatiitic volcanic rocks remains poorly understood. In this study, new field and textural observations, bulk rock geochemistry, Sm-Nd and Re-Os isotopic data, and olivine mineral chemistry are presented for the Bradley Peak ultramafic volcanic rocks to investigate their petrogenesis and eruption history, assess their potential to host magmatic sulfide mineralization, and evaluate their relationship with regional orogenic gold deposits.

2 Samples and Methods

Thirty-six samples were collected from the Bradley Peak ultramafic rocks in the Seminoe Mountains, central Wyoming in 2023 and 2024. Sampling targeted both spinifex- and cumulate-textured rocks from six discrete volcanic flows. Three banded iron formation interbedded with the ultramafic unit and underlying mafic metavolcanic rocks were also sampled.

2.1 MicroXRF mapping

X-ray fluorescence (XRF) chemical maps of spinifex- and cumulate-textured ultramafic rocks were produced using a bench-top Atlas M microXRF spectrometer (iXRF Systems, Austin, TX) at the U.S. Geological Survey in Spokane, Washington.

2.2 Whole rock platinum-group element and isotope geochemistry

Whole rock major and trace element geochemical data were collected for 36 ultramafic volcanic rocks and three banded iron formation samples. For a subset of the ultramafic volcanic rocks (n = 12), low-detection whole-rock PGE geochemical data were measured by NiS fire assay at the Université du Québec à Chicoutimi. Whole-rock ultramafic volcanic samples were also analyzed for Sm-Nd isotopes (n = 16) at Washington State University and Re-Os isotopes (n = 6) at Yale University.

2.3 Olivine compositions

Olivine compositions were obtained by electron microprobe for the three olivine cumulate samples that contained relict olivine. For each sample, 5–6 points were analyzed on 7–8 grains, avoiding serpentinized rims and cracks.

3 Results and Discussion

3.1 Mineralogy and textures

The stratigraphy of four discrete volcanic flows, with individual thicknesses up to 37 m, were mapped in the field. The flows show reccurring patterns of fine-grained random spinifex textures transitioning to coarse-grained random (Fig. 1a) and oriented (string-beef) spinifex (Fig. 1b). Only (pseudomorphed) pyroxene spinifex, opposed to olivine spinifex, was observed. All spinifex-textured rocks contain acicular needles of pyroxene replaced by pseudomorphs of actinolite within a groundmass of talc ± tremolite ± chlorite, indicating these units were affected by amphibolite facies metamorphism. Each flow unit contains a basal layer of variably serpentinized olivine cumulates with minor chromite (Fig. 1c).

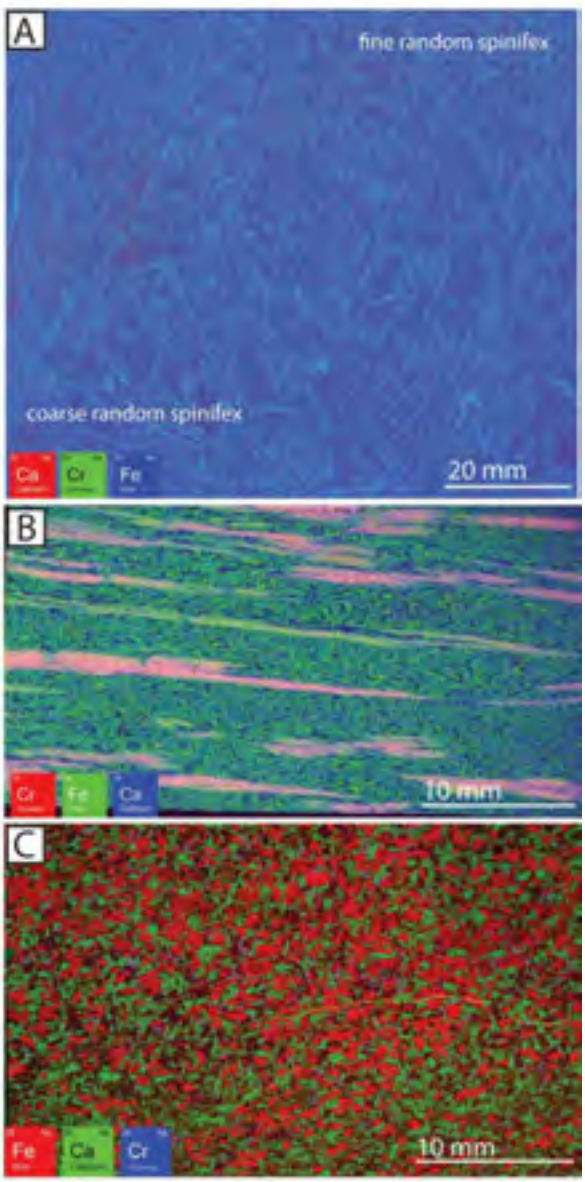


Figure 1. Representative false-color microXRF maps of textures observed in the Bradley Peak komatiitic basalt volcanic sequences. A) Fine-grained random pyroxene spinifex (top) transitioning to coarse-grained random spinifex (bottom). B) Oriented pyroxene spinifex in the form of hollow acicular needles within a tremolite-chlorite matrix. C) Serpentinized olivine cumulate hosting preserved olivine cores (red), including the most magnesian olivine measured in this study, and minor chromite (blue).

3.2 Whole rock major, trace, and chalcophile element geochemistry

Based on the whole-rock major element geochemistry of the Bradley Peak ultramafic rocks and the Al-Mg-(Fe+Ti) classification diagram (Jensen 1976), the spinifex-textured volcanic rocks are komatiitic basalts. Compared to global komatiitic affinity rocks, these samples are categorized as Al-undepleted komatiites (AUK), or "Munro-type", characterized by chondritic Al_2O_3/TiO_2 and Gd/Yb. All 36 samples included here successfully pass the geochemical filter for AUK described by Barnes et al. (2004), indicating their major immobile elements can be explained by olivine fractionation and/or accumulation and have not been significantly modified by post-magmatic processes.

All spinifex-textured rocks are higher SiO_2 (49-54 wt. %) and lower MgO (8-17 wt. %) than komatiites *sensu stricto* (MgO > 18 wt. %). Such high-Mg and high-Si spinifex volcanic rocks can be produced by differentiation of true komatiites, low degrees of partial mantle melting, or mixtures of komatiite magma with evolved silicic crust. The Bradley Peak komatiitic basalts have rare earth element (REE) profiles depleted in light REE relative to heavy REE and similar profiles to a typical Munro-type parental melt (Sossi et al. 2016; Fig. 2a), indicating they have not assimilated silicic crust. The slight REE enrichments of these komatiitic basalts relative to the typical Munro-type parental melt cannot be explained by a simple mixture of komatiite magma and interbedded banded iron formation, which have lower heavy REE contents than the komatiitic basalts. Thus, the Bradley Peak komatiitic basalts do not represent komatiite-silicic crust mixtures, which are most commonly associated with sulfide mineralization. Instead, they are interpreted as primitive melts from low degrees of partial melting or derivative melts from differentiation of a true komatiites.

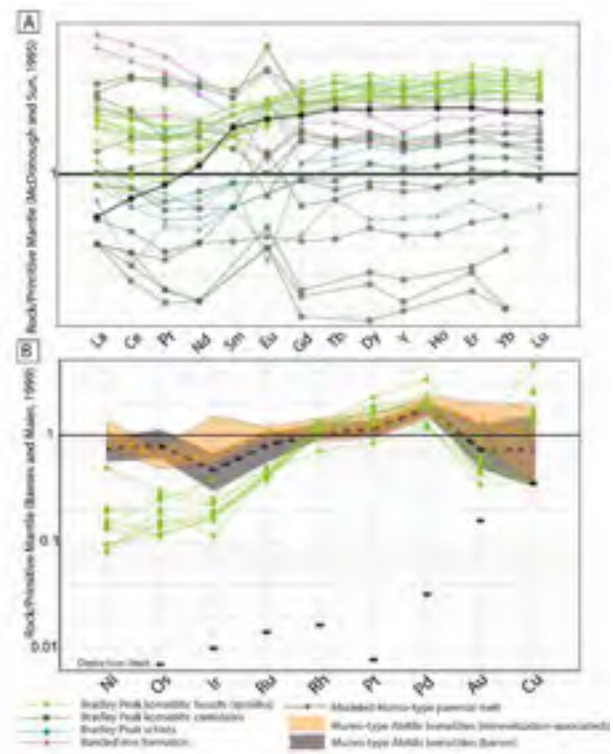


Figure 2. A) Primitive-mantle normalized diagram of bulk rock REEs showing the komatiitic basalts and interbedded banded iron formation samples, as well as a typical Munro-type komatiite parental melt (Sossi et al. 2016). B) Primitive-mantle normalized diagram of bulk rock PGE geochemistry. Polygons for Munro-type Abitibi komatiites show the 25th to 75th percentile fields and medians (dashed lines) from the compilation by Fiorentini et al. (2011).

The Bradley Peak komatiitic basalts have similar concentrations of PGEs and chalcophile

elements as global Munro-type (Fig. 2b). Most samples are enriched in Pd-group PGEs and depleted in Ir-group PGEs relative to 75 % of Munro-type komatiites from the compilation by Fiorentini et al. (2011). The Bradley Peak samples are depleted in Au relative to Munro-type komatiites, suggesting that the Bradley Peak komatiitic basalts may be the source of nearby orogenic gold deposits, which are current exploration targets (Relevant Gold 2024). Dehydration reactions associated with komatiites undergoing greenschist to amphibolite facies metamorphism (~700 °C) are estimated to release ~3–6 ppb Au cumulatively (Yu et al. 2023). If the Bradley Peak komatiitic basalts originally contained 3–7.5 ppb Au, a typical range for Archean komatiites (Yu et al. 2023 and references therein), release of 3–6 ppb Au would explain the depleted Au concentrations in these samples (0.3–1 ppb).

3.3 Sm-Nd and Re-Os isotopes

Initial εNd values at 2.72 Ga range from -0.53 to +4.70 and are predominately positive, indicating a depleted mantle or plume source. All 16 samples overlap with the Abitibi greenstone terrane komatiites and tholeiitic basalts (Fig. 3a), suggesting they may be genetically linked to the same plume event as plate reconstructions suggest (Killian et al. 2016). Initial γOs values, on the other hand, vary substantially, ranging from +11 to +99.

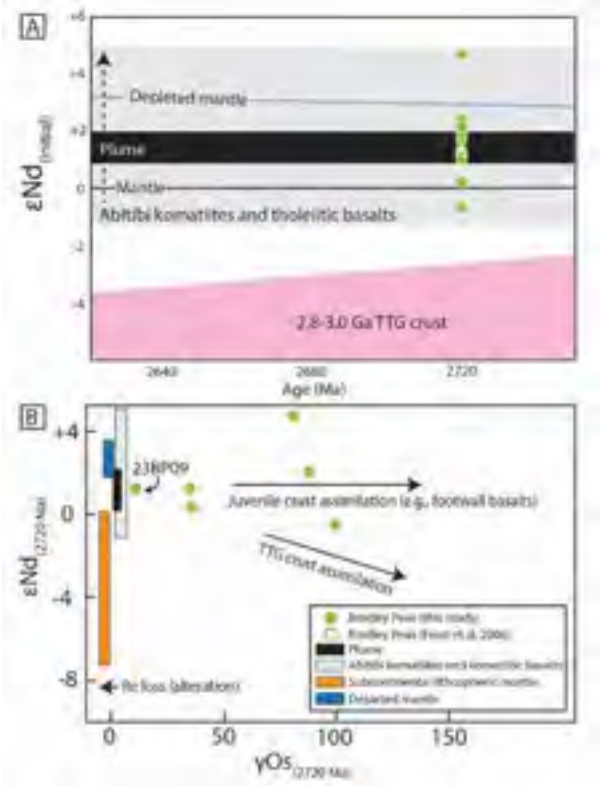


Figure 3. A) Initial εNd of Bradley Peak komatiitic basalts. Compilation of Abitibi (ultra)mafic volcanic rocks is from Ashwal et al. (1985) and the tonalite-trondhjemite-granodiorite (TTG) field from Frost et al. (2006). B) Initial εNd-γOs of Bradley Peak komatiitic basalts compared with plume, subcontinental lithospheric mantle, and depleted mantle fields after Lambert et al. (1994). Osmium data for synchronous (2.72 Ga) Abitibi komatiites and komatiitic basalts are from Gangopadhyay et al. (2005).

These γOs values and variability cannot be explained by mantle heterogeneities, Re loss via degassing or alteration, Re/Os increase during magmatic differentiation, or mixtures with pre-existing tonalite-trondhjemite-granodiorite (TTG) crust. The γOs values, which are high relative to the Abitibi komatiites and mantle sources (Fig. 3b), may be attributed to the komatiitic parental magma mixing with variable amounts of a juvenile crust component, expected to have positive εNd and positive γOs. Another important observation from the isotopic data is that the most primitive spinifex-textured sample from the Bradley Peak komatiitic basalts (23BP09) has an initial εNd-γOs composition similar to an uncontaminated plume source, suggesting this sample is most representative of the parental magma of this ultramafic volcanic suite (Fig. 3b).

3.3 Olivine compositions and parental melt conditions

The forsterite (Fo) content of the cumulus olivine grains is relatively consistent for all individual spot measurements from the three cumulates, ranging from Fo_{81} to Fo_{85}. Using the highest Fo composition, Fo_{85} from the olivine cumulate in Fig. 1c, and the whole-rock FeO-MgO contents of the volcanic suite (e.g., Arndt 2008), the parental magma in equilibrium with this olivine is estimated to have 11 wt. % MgO, far lower than the highest MgO spinifex-textured rock (23BP09, MgO = 17 wt. %). This sample, which stands out for its uncontaminated plume-like Nd-Os isotopic composition (Fig. 3b), is estimated to have an eruption temperature of 1354 °C (Nisbet 1982). A melt with the composition of this spinifex sample was determined (using MELTS software; Ghiorso and Sack 1995, Smith and Asimow 2005) to be in equilibrium with Fo_{89} olivine, which is more magnesian than all measured olivine. Thus, this sample is interpreted to be the closest in composition to parental magma of the Bradley Peak volcanic suite. The relatively low MgO of this parental magma composition requires either derivation from low degree partial mantle melting or differentiation from higher MgO komatiite magmas. Both petrogenetic scenarios are unfavorable for sulfide mineralization (Barnes et al. 2016).

3.4 Magmatic sulfide mineralization potential

The sulfur content at sulfide saturation ($[S]_{SCSS}$) was determined for the komatiitic basalt suite using the method of Smythe et al. (2017). A minimum of 1357 ± 371 ppm S is required to achieve sulfide saturation given the bulk rock compositions of the spinifex-textured rocks. The measured S concentrations in these samples are typically an order of magnitude lower (60-740 ppm, median = 200 ppm S) than the minimum $[S]_{SCSS}$. This result, along with the observation that the PGE and chalcophile element

contents of these samples do not overlap with the majority of Ni-Cu-PGE mineralization-associated Abitibi komatiites (Fig. 2b), indicates that these melts have not reached sulfide saturation and are unlikely to be prospective for magmatic sulfide mineralization. Furthermore, these ultramafic volcanic rocks have REE profiles and positive initial εNd values indicating that they have not incorporated pre-existing evolved crust (i.e., a Si or S source), which is considered a general requirement for komatiitic magmas to reach sulfide saturation (e.g., Barnes et al. 2016).

4 Conclusions

New geochemical and petrological data for the Bradley Peak ultramafic volcanic rocks in the Archean Wyoming Province classify these samples as Al-undepleted komatiitic basalts. The relatively low MgO contents determined for their parental melt as well as their trace element signatures suggest that these komatiitic basalts represent differentiated komatiites or low-degree partial mantle melts that may have incorporated variable amounts of footwall juvenile basalts. New Nd and Os isotopic results demonstrate a possible link with synchronous Abitibi greenstone belt komatiites and identify one sample from the Bradley Peak suite as the most plume-like uncontaminated parental melt composition.

Despite the inferred connection between the Bradley Peak komatiitic basalts and the magmatic sulfide deposit-hosting Abitibi komatiitic greenstone terrane, evidence from this study suggests that the Bradley Peak komatiitic volcanic rocks are not prospective for Ni-Cu-PGE sulfide mineralization. Whole-rock and isotope geochemistry indicate minimal contamination of the komatiitic magmas with evolved crustal components, potential sulfur sources. Platinum-group element geochemistry and $[S]_{SCSS}$ estimates suggest that sulfide liquid saturation was not achieved in the studied flows. Although the Bradley Peak volcanic rocks do not appear to be promising for magmatic sulfide mineralization, depletions in Au suggest they are the source of Au to nearby orogenic gold prospects.

Disclaimer

Any use of trade, firm, or product names is for descriptive purposes only and does not imply endorsement by the U.S. Government.

References

Arndt N (2008) Komatiite. Cambridge University Press, Cambridge.

Ashwal LD, Wooden JL, Phinney WC, Morrison DA (1985) Sm−Nd and Rb−Sr isotope systematics of an Archean anorthosite and related rocks from the Superior Province of the Canadian Shield. Earth and Planetary Science Letters 74:338–346.

Barnes SJ, Cruden AR, Arndt N, Saumur BM (2016) The mineral system approach applied to magmatic Ni–Cu–PGE sulphide deposits. Ore Geology Reviews 76:296–316.

Barnes, S-J, Maier, WD (1999) The fractionation of Ni, Cu and the noble metals in silicate and sulfide liquids. Geological Association of Canada, Short Course 13:69–106.

Barnes SJ, Hill RET, Perring CS, Dowling SE (2004) Lithogeochemical exploration for komatiite-associated Ni-sulfide deposits: strategies and limitations. Mineralogy and Petrology 82:259–293.

Fiorentini ML, Barnes SJ, Maier WD, Burnham OM, Heggie G (2011) Global variability in the platinum-group element contents of komatiites. Journal of Petrology 52: 83–113.

Frost CD, Fruchey BL, Chamberlain KR, Frost BR (2006) Archean crustal growth by lateral accretion of juvenile supracrustal belts in the south-central Wyoming Province. Can J Earth Sci 43:1533–1555.

Gangopadhyay A, Sproule RA, Walker RJ, Lesher CM (2005) Re-Os systematics of komatiites and komatiitic basalts at Dundonald Beach, Ontario, Canada: Evidence for a complex alteration history and implications of a late-Archean chondritic mantle source. Geochimica et Cosmochimica Acta 69:5087–5098.

Ghiorso MS, Sack RO (1995) Chemical mass transfer in magmatic processes IV. A revised and internally consistent thermodynamic model for the interpolation and extrapolation of liquid-solid equilibria in magmatic systems at elevated temperatures and pressures. Contributions to Mineralogy and Petrology 119: 197–212.

Jensen LS (1976) A new cation plot for classifying subalkalic volcanic rocks. Ontario Geological Survey Miscellaneous Papers 66:22.

Kilian TM, Bleeker W, Chamberlain K (2016) Palaeomagnetism, geochronology and geochemistry of the Palaeoproterozoic Rabbit Creek and Powder River dyke swarms: implications for Wyoming in supercraton Superia. SP 424:15–45.

Lambert DD, Walker RJ, Morgan JW, Shirey SB, Carlson RW, Zientek ML, Lipin BR, Koski MS, Cooper RL (1994) Re-Os and Sm-Nd isotope geochemistry of the Stillwater Complex, Montana: Implications for the petrogenesis of the J-M Reef. Journal of Petrology 35: 1717–1753.

McDonough WF, Sun S-S (1995) The composition of the Earth. Chemical Geology 120:223–253.

Nisbet EG (1982) The tectonic setting and petrogenesis of komatiites. In: N. T. Arndt and E. G. Nisbet (eds.) Komatiites. London: George Allen and Unwin. 501–520.

Relevant Gold (2024) Relevant Gold Defines Large-Scale Drilling Target at Bradley Peak Sampling 46.8 g/t Au, 7.8% Cu and 2% Zn in Apex Zone. https://relevantgoldcorp.com/news/. Accessed April 11, 2025.

Smith PM, Asimow PD (2005) Adiabat-1ph: A new public front-end to the MELTS, pMELTS, and pHMELTS models. Geochemistry Geophysics Geosystems 6: 1–8.

Smythe DJ, Wood BJ, Kiseeva ES (2017) The S content of silicate melts at sulfide saturation: New experiments and a model incorporating the effects of sulfide composition. American Mineralogist 102:795–803.

Sossi PA, Eggins SM, Nesbitt RW, Nebel O, Hergt JM, Campbell IH, O'Neill HSC, Van Kranendonk M, Davie DR (2016) Petrogenesis and geochemistry of Archean komatiites. Journal of Petrology 57:147–184.

Yu C, Zhong R, Tomkins AG, et al (2024) Expanding the metamorphic devolatilization model: Komatiites as a source for orogenic gold deposits in high-grade metamorphic rocks. Geology 52:67–71.

The Role of Alkali Bicarbonate-sulfate Brines in the Genesis of Carbonatite REE Resources at the Bear Lodge Alkaline Complex, Wyoming

Allen K. Andersen[1], Danielle A. Olinger[2], Mitchell M. Bennett[2]
[1]U.S. Geological Survey, Spokane, WA 99201
[2]U.S. Geological Survey, Denver, CO 80225

Abstract. Rare-earth element (REE) resources in the Bear Lodge Alkaline Complex, Wyoming, are hosted in a variably leached carbonatite dike swarm spatially related to bodies of diatreme breccia. This study examines fluid inclusions in carbonatite dikes, peripheral fluorite breccias, and smoky quartz veins to reconstruct the physiochemical conditions of REE mineralization. Results reveal a multi-stage evolution of carbonatitic fluids: 1) high-temperature (330–432°C), CO_2-rich magmatic fluids, 2) REE-enriched alkali bicarbonate-sulfate brines, and 3) low-temperature meteoric (117–182°C) or diluted magmatic fluids. Multiphase inclusions (stage-2) contain burbankite, nahcolite, and alkali sulfate daughter crystals, linking the brines to early burbankite [$(Na,Ca)_3(Sr,Ba,REE)_3(CO_3)_5$] mineralization in carbonatite. REE mobility has been linked to the stability of aqueous complexes with ligands such as Cl^-, SO_4^{2-}, and HCO_3^-. However, light REEs were not initially transported significant distances, rather they crystallized as burbankite from brines or brine-melts associated with the carbonatite magma. Crystallization of burbankite removed Na from the system, leaving residual fluids with high K/Na ratios and promoting potassic fenitization throughout the complex. Fractionation of light and heavy REEs and involvement of low temperature (<300°C), high K/Na bicarbonate brines may have facilitated transport and formation of peripheral occurrences that are more enriched in heavy REEs at Bear Lodge.

1 Geology and Mineral Resources

The Bear Lodge Alkaline Complex (BLAC), located in the northern Black Hills region of Wyoming, comprises Eocene alkaline intrusions dominantly of phonolitic composition. Notable dome-topped pipes of heterolithic diatreme breccia occur near the center of the complex at Bull Hill, Carbon Hill, and Whitetail Ridge. A carbonatite dike swarm and vein stockwork adjacent to the diatreme bodies hosts a combined measured and indicated REE resource of 6.02 million tonnes averaging 4.08 wt.% total rare earth oxide, using a cut-off grade of 2.18 wt.% (Noble et al. 2024).

Carbonatite emplacement depth is inferred from studies of the Black Hills uplift and the known thickness of overlying strata. The present erosional surface reveals, at roughly equal elevation, the carbonatite dike swarm, breccia pipes, and phonolitic sills along the Precambrian nonconformity (Fig. 1). An emplacement depth of 1.0 to 1.5 km is estimated based on these factors.

Occurrences of fluorite-matrix breccia and smoky quartz veins are known at Smith Ridge, approximately 1.5 km southeast of the central carbonatite dike swarm. The fluorite-mineralized matrix overprints a pseudoleucite porphyry breccia that hosts a gold resource of 408,000 ounces (Rare Element Resources Ltd. 2011). Nearby smoky quartz veins represent silica remobilization related to emplacement of the silica-undersaturated alkaline melts or fenitizing fluids.

The aim of this study was to determine the physiochemical conditions of REE proto-ore formation in this moderate-size, carbonatite-hosted deposit through the study of fluid inclusions. We examine the importance of alkalis (Na, K), anions (SO_4^{2-}, CO_3^{2-}, F^-, Cl^-), and relationships with explosive diatremes that have possible importance to the fate and transport of light REE (LREE) and heavy REE (HREE) in alkaline-carbonatite complexes. Carbonatitic fluids are compared with those responsible for peripheral fluorite and smoky quartz occurrences to assess changes in temperature and element mobility with distance.

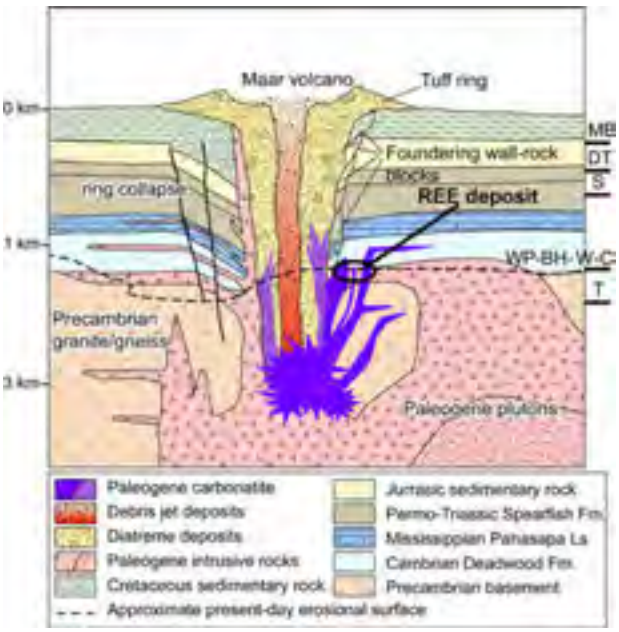


Figure 1. Schematic cross-section of a diatreme in the northern Black Hills region (modified from Paterson et al. 1989; Lisenbee and Roggenthen 1990; and Závada et al. 2015). Erosion levels are shown for respective diatremes at Missouri Buttes (MB), Devils Tower (DT), Sugarloaf (S), Warren Peaks-Bull Hill-Whitetail-Carbon (WP-BH-W-C), and Tomahawk (T). Position of carbonatite intrusion and REE deposit is approximated relative to diatreme and other units exposed at the present-day erosional surface.

2 Sampling and Methods

Three key mineralized zones of the BLAC were sampled, including the central REE-bearing carbonatite dikes at Bull Hill and Whitetail Ridge, gold-bearing breccias and smoky quartz veins at Smith Ridge, and fluorspar replacement deposits at the Peterson Claims. Our sampling of carbonatite focused on rocks that escaped the near-surface fluid alteration responsible for ore-grade enrichment and instead contain evidence of early-stage REE mineralization (e.g., presence of burbankite and primary igneous carbonate $\delta^{13}C$ and $\delta^{18}O$ values; Andersen et al. 2019).

Samples were analyzed using multiple techniques. Petrography and cathodoluminescence imaging were used to identify growth zoning in host minerals and distinguish fluid inclusion populations as primary, secondary, and pseudosecondary. Raman spectroscopy was used to identify daughter minerals and ligands in the aqueous phase. The presence of CO_2 was determined by crushing mineral wafers immersed in kerosene and observing bubble formation. Homogenization and ice melt temperatures were recorded using classic microthermometry techniques. Qualitative compositional information was acquired using decrepitate mount analysis by SEM-EDS and LA-ICP-MS. Noble gas isotopes were determined by bulk leachate analysis to differentiate mantle and crustal contributions to fluids. Together, these methods offered a comprehensive view of the physical and chemical conditions under which mineralization developed.

3 Results

3.1 Fluid Inclusion Populations

Four main types of aqueous inclusions were found in calcite, fluorite, and smoky quartz: 1) liquid-vapor (LV) inclusions where vapor bubbles commonly constitute 60-95 vol.% of the inclusion, 2) liquid-vapor-solid (LVS) inclusions commonly containing multiple daughter crystals, 3) fluorite-hosted “double bubble” inclusions containing large CO_2 vapor bubbles with outer rinds of liquid CO_2 (LVC), and 4) liquid-dominant $L_{90}V_{10}$ inclusions.

In calcite and fluorite from the central carbonatite dikes, secondary and pseudosecondary inclusions revealed three fluid stages: 1) orthomagmatic fluids containing CO_2 and SO_4^{2-}, captured as LV inclusions with high homogenization temperatures (320–450°C), 2) alkali bicarbonate-sulfate brine represented by LVS inclusions (~270°C to >556°C) with associated LVC inclusions, and 3) dilute, low-temperature (117–182°C) meteoric or neutralized magmatic fluids in coarse-grained or rhombic calcite.

In Smith Ridge fluorite and smoky quartz, primary inclusions found in relation to primary crystal growth zones have lower homogenization temperatures (100-300°C) relative to stage 1 and 2 carbonatite-hosted inclusions.

3.2 Fluid Compositions

Inclusion compositions were investigated by Raman spectroscopy, decrepitate mound analysis, and LA-ICP-MS. The presence of SO_4^{2-} was confirmed by Raman spectroscopy in high-temperature calcite-hosted inclusions. Intermediate, stage 2 inclusions contain burbankite, nahcolite, and alkali sulfate daughter crystals (Fig. 2). Sulfate was commonly present in the aqueous phase.

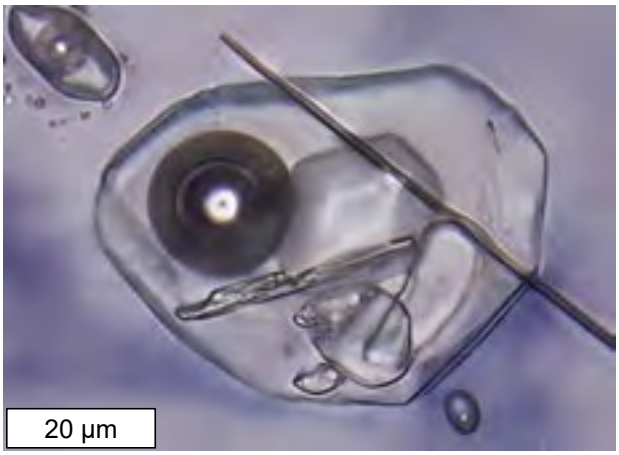


Figure 2. Magnified image of typical multi-phase LVS inclusion in late, inclusion-poor fluorite. The largest crystal is typically nahcolite, rod-shaped crystals are commonly burbankite, and equant high-relief solids are alkali sulfates.

Halite was notably absent in all examined inclusions; however, the presence of Cl was confirmed based on depressed ice melt temperatures (-1.2 to -13.4°C) and the formation of halite in decrepitate mounds. When LVS inclusions are heated, solids like nahcolite and alkali sulfate are dissolved, and the carbonate previously bound in carbonates (nahcolite) is released as CO_2 vapor upon decrepitation. The alkali cations, Ca, and Sr recombine with SO_4^{2-} and Cl^- from solids and the aqueous phase to form gypsum/anhydrite, thenardite/mirabilite, celestine, and halite in the decrepitate mounds. The presence of burbankite was confirmed by Raman spectroscopy and LA-ICP-MS that showed LREE are present in the fluid inclusions (Fig. 3).

Smoky quartz and fluorite samples from the peripheral Smith Ridge locality contain primary inclusions with similar alkali bicarbonate-sulfate compositions but lack REE-bearing daughter minerals. Helium isotope ratios of Smith Ridge samples display crustal He source signatures with $^3He/^4He$ R/RA of <0.1, whereas the central carbonatite dikes display mantle source signatures with R/RA of >1.0.

In the central carbonatite bodies, late-stage rhombic calcite and some re-equilibrated coarse-grained calcite host inclusions with the lowest trapping temperatures (117–182°C), consistent with

heated meteoric or diluted magmatic waters. Similar solute-poor inclusions were observed at the peripheral Peterson Claims fluorspar deposits.

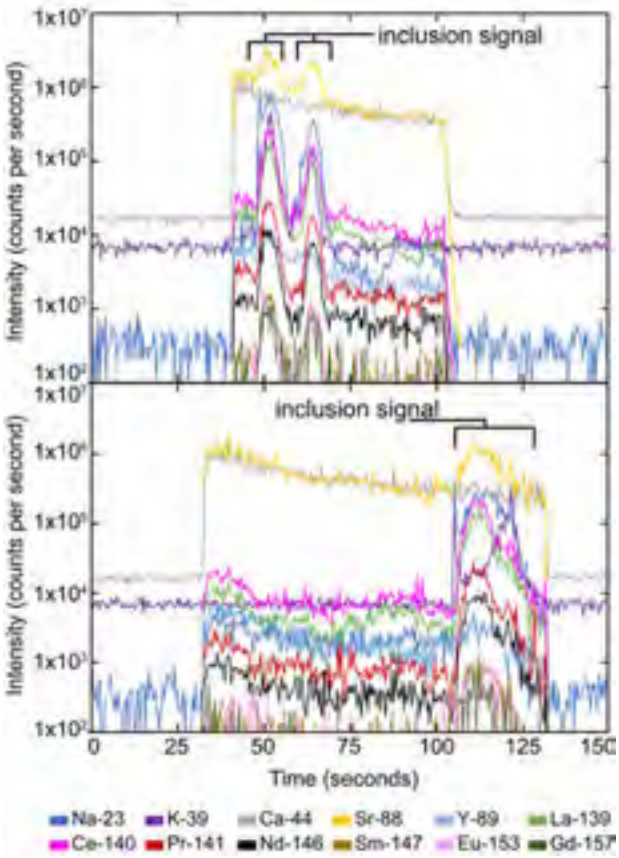


Figure 3. Time-resolved LA-ICP-MS spectra for LVS inclusions in calcite. Profiles show consistent downhole decrease of Ca and Sr and spike of Na, K, Sr, and LREE through the inclusion intercepts.

4 Discussion

4.1 Pressure estimates and phase separation

Homogenization pressures between 225 and 334 bars calculated for LVC inclusions in the H_2O-CO_2-NaCl system equate to an uncorrected paleodepth of 0.9–1.3 km at lithostatic pressure, in good agreement with the depth estimated from the thickness of overlying strata in the BLAC during the Eocene (Fig. 1). Such shallow depths for the lithostatic regime may be possible if fluid temperatures exceeded the typical brittle-ductile transition temperature for a carbonatite host rock, which may be lower than the typical transition (350-400°C) for volcanic rocks. LVC inclusions had higher homogenization pressures (600–846 bars), greatly exceeding the depth predicted by stratigraphic reconstructions. Pressures exceeding the lithostatic load are generated in plutonic environments as large volumes of exsolved fluid migrate through ductile host rocks as overpressure-permeability waves (Weis et al. 2012). Large changes in volume due to fluid immiscibility during ascent may further enhance this effect.

The co-existence of a Na-Sr-K-REE bicarbonate-sulfate brine represented by LVS inclusions (Fig. 2) and LVC inclusions containing $CO_{2(aq)}$ suggests that fluid immiscibility occurred during or after the formation of fluorite. Spatially associated diatremes could be linked to episodic pressure buildup, rapid release of volatiles, followed by re-sealing of the system. Phase separation could also be linked to decarbonation reactions as ascending carbonatite magma reacts with alkali silicate wall-rock to form fenite aureoles. The somewhat restricted width of fenites (typically < 1 meter) may indicate limited reaction, thus allowing retention of volatile-rich fluids and formation of early apatite-barite/celestine-burbankite mineralization confined to the carbonatite bodies.

4.2 Spatiotemporal fluid evolution

If fluids responsible for the Smith Ridge fluorite matrix breccias and remobilized smoky quartz veins were derived directly from carbonatitic magmas, they appear to have cooled, lost some CO_2, lost REE while forming the central Bull Hill and Whitetail resources, and interacted with groundwater or older granitic wall-rock acquiring low $^3He/^4He$ R/RA.

Alternatively, mineralization at Smith Ridge may be related to volatiles released during emplacement of a pseudoleucite porphyry breccia pipe. Regardless of the source, the inclusion characteristics show that mineralizing fluids were enriched in F, CO_2, SO_4, Ca, Na, and K, yet Cl-poor in comparison to most intrusion-related fluids. Further diluted fluid inclusions in the fluorite-filled replacement deposits at the Peterson Claims suggest that these distal fluids had lost much of their alkali, REE, Sr, SO_4, and CO_2 content before reaching the Mississippian Pahasapa Limestone which surrounds much of the complex's igneous core.

4.3 Role of alkali bicarbonate-sulfate brines in REE resource formation

LVS inclusions containing nahcolite+burbankite +alkali sulfates suggest that alkali bicarbonate-sulfate brines provided the necessary conditions for early-stage REE precipitation. Anenburg et al. (2021) suggest that these types of brines are capable of mobilizing REE because of their elevated Na and K content, whereas SO_4^{2-}, CO_3^{2-}, F^-, or Cl^-, acting individually as transport ligands do not satisfactorily explain REE mobility and LREE-HREE fractionation. Additionally, the lack of significant Cl^- indicates a departure from most magmatic-hydrothermal fluids, including the orthomagmatic or brine-like fluids reported in many carbonatites (cf., Walter et al., 2021).

The presence of nahcolite and burbankite show that early inclusion-trapped carbonatitic fluids were Na-rich. These fluids might be expected to produce sodic fenitization surrounding a carbonatite. However, fenitization along carbonatite dike

margins and throughout the BLAC is dominantly potassic. We suggest that this zonation results from alkali fractionation whereby Na is retained during crystallization of early burbankite leaving residual outward-emanating fluids with higher K/Na, to promote crystallization of K-feldspar and biotite-phlogopite. Sodium is lost from the carbonatite intrusions as fluids back-react causing replacement of burbankite by Ca+REE±Sr (fluoro)carbonates—a process aided by the high solubility of burbankite (Broom-Fendley 2024).

Although mineralization in the central carbonatites is demonstrably LREE-enriched, some peripheral REE occurrences in the BLAC are HREE-enriched or HREE-dominant (Andersen et al. 2016). Experiments by Louvel et al. (2022) showed that in low temperature (<300°C) (F, CO_3^{2-})-rich alkaline carbonate fluids, F does not act as a precipitating ligand, and HREE may remain in solution. Anenburg et al. (2020) showed LREE-HREE decoupling to be more extreme in K-bearing experiments indicating higher HREE solubility in the potassic system. Fluids of this composition may satisfactorily explain the areas of HREE-enrichment in the BLAC.

5 Conclusions

This study demonstrates the importance of alkali bicarbonate-sulfate brines in the formation of early carbonatite-hosted proto-ore REE mineralization at the BLAC. Recent experimental studies show how these fluids may result in alkali fractionation that in-turn promotes LREE:HREE fractionation. Such changes in fluid chemistry may manifest as complex-wide patterns in alkali alteration (potassic versus sodic) and spatial zonation of light and heavy REE. These findings present a testable exploration strategy: Can the mineralogy and K/Na ratio of fenite aureoles help predict whether a carbonatite crystallized early burbankite or different primary REE minerals (e.g., monazite/apatite or bastnäsite)? More sodic fenites may be predicted to have reduced the requisite Na to form burbankite, thus favoring monazite/apatite in a high-phosphorus environment and bastnäsite in a low-phosphorus environment.

At Bear Lodge, explosive venting of diatremes at Bull Hill, Whitetail Ridge, and Carbon Hill likely led to a net loss of volatiles from the system, but a genetic link between diatremes and carbonatites remains unclear. Peripheral mineralization at Smith Ridge and the Peterson Claims appears to reflect an evolving system with fluids becoming progressively depleted in REE, Sr, CO_2, SO_4, and Na outward from the carbonatite-hosted resources.

Acknowledgements

This study was funded by the U.S. Geological Survey, Mineral Resources Program. We thank Eric Ellison for help with Raman spectroscopy, Andrew Hunt for performing noble gas isotope analyses, John Wallis for figure drafting, and Erin Marsh for help with LA-ICP-MS analyses. This study benefited from discussions with Philip Verplanck, Al Hofstra, James Reynolds, Matthew Steele-MacInnis, and Heather Lowers. Erin Benson and Adrian Van Rythoven are thanked for their constructive reviews.

References

Andersen AK, Clark JG, Larson PB, Neill OK (2016) Mineral chemistry and petrogenesis of a HFSE(+HREE) occurrence, peripheral to carbonatites of the Bear Lodge alkaline complex, Wyoming. Am Mineral 101:1604–1623. https://doi.org/10.2138/am-2016-5532

Andersen AK, Larson PB, Cosca MA (2019) C–O stable isotope geochemistry and $^{40}Ar/^{39}Ar$ geochronology of the Bear Lodge carbonatite stockwork, Wyoming, USA. Lithos 324–325:640–660. https://doi.org/10.1016/j.lithos.2018.11.030

Anenburg M, Broom-Fendley S, Chen W (2021) Formation of rare earth deposits in carbonatites. Elements 17:327–332. https://doi.org/10.2138/gselements.17.5.327

Anenburg M, Mavrogenes JA, Frigo C, Wall F (2020) Rare earth element mobility in and around carbonatites controlled by sodium, potassium, and silica. Sci Adv 6:eabb6570. https://doi.org/10.1126/sciadv.abb6570

Broom-Fendley S (2024) Out of sight burbankite. Nat Geosci 17:284. https://doi.org/10.1038/s41561-024-01410-8

Lisenbee AL, Roggenthen W (1990) Diatremes and breccia pipes of the northern Black Hills, Wyoming. In: Paterson CJ, Lisenbee AL (eds) Metallogeny of gold in the Black Hills, South Dakota. Soc Econ Geol Guideb Ser 7:175–181.

Louvel M, Etschmann B, Guan Q, Testemale D, Brugger J (2022) Carbonate complexation enhances hydrothermal transport of rare earth elements in alkaline fluids. Nat Commun 13:1456. https://doi.org/10.1038/s41467-022-28943-z

Noble AC, Bouza MB, Pickarts J (2024) Technical report summary on the Bear Lodge REE Project located in Crook County, Wyoming. Prepared for Rare Element Resources, Inc., February 29, 2024, 179 p. Accessed 22 Jan 2025. https://rareelementresources.com/docs/default-source/pdfs/rer-trs-march-2024.pdf?sfvrsn=2

Paterson CJ, Uzunlar N, Groff J, Longstaffe FJ (1989) A view through an epithermal-mesothermal precious metal system in the northern Black Hills, South Dakota: A magmatic origin for the ore-forming fluids. In: Keays RR, Ramsay WRH, Skinner BJ (eds) The geology of gold deposits: The perspective in 1988. Econ Geol Monogr 6:564–570.

Rare Element Resources Ltd (2011) Rare Element reports inferred mineral resource estimate for Sundance Gold Project. Exhibit 99.2 - News Release, March 15, 2011, Securities and Exchange Commission Form 6-K, SEC File No. 000-53834. Accessed 11 Feb 2025. https://www.sec.gov/Archives/edgar/data/1419806/000105291811000107/rareelement6kmar22-11.pdf

Walter BF, Giebel RJ, Steele-MacInnis M, Marks MAW, Kolb J, Markl G (2021) Fluids associated with carbonatite magmatism: A critical review and implications for carbonatite magma ascent. Earth Sci Rev 215:103509. https://doi.org/10.1016/j.earscirev.2021.103509

Weis P, Driesner T, Heinrich CA (2012) Porphyry-copper ore shells form at stable pressure-temperature fronts within dynamic fluid plumes. Science 338:1613–1616. https://doi.org/10.1126/science.1225009

Závada P, Dědeček P, Lexa J, Keller GR (2015) Devils Tower (Wyoming, USA): A lava coulée emplaced into a maar-diatreme volcano? Geosphere 11:354–375. https://doi.org/10.1130/GES01166.1

Stable Isotope Composition and Geochemistry of Calcite and Dolomite in the Mountain Pass carbonatite: A lens into petrogenesis

Erin K. Benson[1], Kathryn E. Watts[1], Jay M. Thompson[2], Heather A. Lowers[2]
[1]U.S. Geological Survey, Spokane, Washington, USA
[2]U.S. Geological Survey, Denver, Colorado, USA

Abstract. Carbonatites host most of the global rare earth element (REE) deposits. The petrogenesis of these rocks, including magmatic and post-magmatic processes, are poorly understood but critical in forming and upgrading these deposits. The Mountain Pass carbonatite, which hosts the only active REE mine in North America, is lithologically variable but consistently contains >50% calcite and/or dolomite. Multiple generations of carbonates are evident, suggesting bulk analysis of carbonate minerals would generate a mixed isotopic and geochemical signature. *In-situ* stable carbon and oxygen isotopes, combined with geochemical analysis and petrography, distinguish carbonate generations, trace the source region of the carbonatite magma, and link carbonate genesis to REE mineralization throughout the intrusion. Primary carbon and oxygen isotope values outside the accepted mantle range may suggest a subduction-related carbon and oxygen source in the mantle. Deformation textures in primary calcite indicate syn- or post-crystallization ductile flow. Carbonates with secondary textures and heavy $\delta^{13}C$ and $\delta^{18}O$ values are associated with ore mineralization, suggesting fluid mobilization was important in concentrating REE and upgrading of the Mountain Pass deposit.

1 Introduction

Carbonatites, which host the majority of the world's rare earth element (REE) deposits, are classified as igneous rocks, in part because their carbon and oxygen isotopes indicate a primary mantle origin (Taylor et al. 1967). Carbonate minerals are the principal constituent of these rocks. Calcite and dolomite tend to be the dominant gangue minerals, while REE fluorocarbonates, such as bastnäsite, are the dominant rare earth minerals. Textural and chemical variations of calcite and dolomite in intrusive carbonatites record magmatic evolution, syn- and post-magmatic fluid interaction, and deformation events (Chakhmouradian et al. 2016).

Bulk carbon and oxygen analyses of carbonate minerals can constrain sources for primary carbonatite melts and the fluids with which carbonate minerals so easily re-equilibrate. Castillo-Oliver et al. (2020) observed that bulk isotope analysis of carbonate minerals in kimberlites can produce a mixed signature between two isotopically distinct endmembers, which may be identified by *in-situ* analysis. Given the textural complexity and range of fluid inputs possible in carbonatite systems, *in-situ* isotopic analysis is a powerful tool to parse carbonate generations and constrain intrusion petrogenesis.

The Mountain Pass carbonatite in California, known as the Sulphide Queen stock, hosts a world-class REE deposit. Although the deposit was traditionally considered a magmatic carbonatite, recent work has shown that both magmatic and metasomatic processes were central to its genesis (Benson and Watts 2024). Modally abundant calcite and dolomite in the Sulphide Queen stock have not been investigated in detail. Examination of these minerals provides an opportunity to evaluate the disparate roles of primary source enrichment and post-magmatic upgrading in forming the deposit.

2 Geological Setting and Methods

Within the Mountain Pass Intrusive Suite (ca. 1.45-1.37 Ga), the Sulphide Queen stock is the only known carbonatite intrusion and represents the last stage of magmatism following the emplacement of alkaline silicate stocks. The Sulphide Queen is a composite stock ranging from calcite to dolomite carbonatite. Lithologies are complexly distributed, occurring in stacked lenses and dikes interspersed with breccia and host rock (Castor 2008).

This study utilized 15 drill core samples from the historic Mountain Pass drill core collection. After detailed petrographic examination, 4-mm circles were drilled from doubly polished thin sections. Samples were mounted in epoxy with NIST-610 glass and UNMC calcite standards. Mounts were coated with a 2 nm layer of Ir and carbonates were imaged by backscattered electrons (BSE) and major and minor element data were collected at the U.S. Geological Survey Denver Microbeam Laboratory using a JEOL JXA-8530FPlus electron microprobe. Oxygen and carbon isotopes in carbonate were collected using a CAMECA ims-1290 ion microprobe at the University of California Los Angeles SIMS facility. Analyses of dolomite were corrected for iron content (Śliwiński et al. 2016a, b). Replicate analyses of in-mount calcite standard UNMC were used to correct for instrument drift and inter-mount variability. Average $\delta^{18}O$ uncertainty (1σ) is 0.3‰ for calcite and 0.5‰ for dolomite, and average $\delta^{13}C$ uncertainty is 0.5‰ for calcite and 0.8‰ for dolomite. Trace element concentrations were measured at the USGS Denver LTRACE laboratory with an Applied Spectra Resolution S155 laser ablation system with an ATL excimer ArF laser source. For these analyses, a spot size of 20 µm with a 30 second ablation duration was used. Data

were processed using the LADR software (Norris and Danyushevsky 2018). Small inclusion-induced signals were removed from the analytical signal.

3 Results

Petrographic and geochemical analysis indicates three major populations of calcite. Primary magmatic Cal-1 calcites (Fig. 1A) are coarse, typically euhedral grains, sometimes with a poikilitic texture enclosing dolomite or barite. Cal-1 grains exhibit deformation twinning. Carbon and oxygen isotope signatures in Cal-1 are remarkably homogeneous (Fig. 2). Primary calcite is HREE-enriched relative to other calcite generations (Fig. 3A, 4). Primary calcite samples typically lack dolomite or any other magnesian phases.

Secondary calcites are separated into two textural groups: Cal-2, which occurs with fine-grained bastnäsite (Fig. 1B), and Cal-3, which does not. The first group often occurs interstitially with secondary dolomite, where it consists of equant grain aggregates lacking any deformation features (Fig. 1B). In one sample, the secondary calcite is associated with fine-grained barite intergrowths as well as rare earth minerals (REM) and occurs along the boundaries of primary calcite grains. Carbon and oxygen isotopes in these samples define two clusters (Fig. 2): one with substantially heavier $\delta^{13}C$ compared to primary calcite, but similar $\delta^{18}O$ (Cal-2a), and another with substantially heavier $\delta^{18}O$ but only slightly heavier $\delta^{13}C$ (Cal-2b). Cal-2a typically exhibits no or a slight positive Ce anomaly, whereas Cal-2b generally exhibits strongly negative but sometimes positive Ce anomalies (Fig. 3B). Cal-2 is generally enriched in LREE over HREE (Fig. 4). Cal-3 is generally represented by late calcite veinlets cross-cutting the samples, some of which may postdate the intrusion, based on differences in texture and composition.

Primary dolomites (Dol-1) are identified in BSE imaging as BSE-bright regions and have carbon and oxygen isotope compositions that overlap primary calcite or the primary mantle box (Figs. 1D, 2). Primary dolomite is Sr-rich and contains similar REE concentrations to primary calcite. Samples with primary dolomite lack primary calcite. Secondary dolomite (Dol-2) occurs either as euhedral rhombohedral grains with secondary calcite (Fig. 1C) (Chakhmouradian et al. 2016) or as BSE-dark altered regions alongside primary dolomite (Fig. 1D). Secondary dolomite exhibits similar carbon isotope compositions, but moderately heavier oxygen isotope compositions. It is LREE-depleted relative to primary dolomite (Fig. 3A).

4 Discussion

While analyses of primary dolomite from two samples fall within the primary mantle field of Taylor et al. (1967), many primary dolomite and all primary calcite analyses fall outside this field. Two possible explanations for this shift in isotopic composition

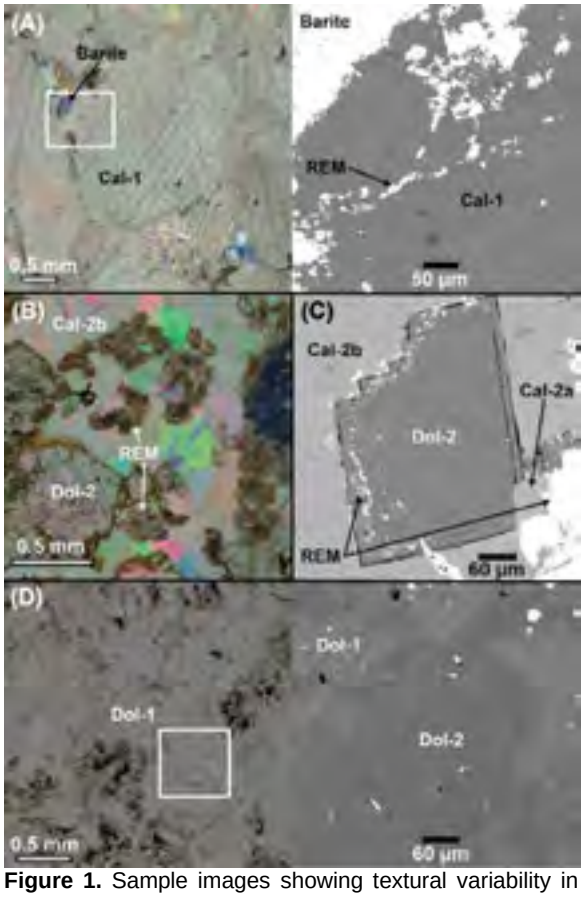


Figure 1. Sample images showing textural variability in carbonates. (A) Cal-1 associated with minor rare earth minerals (REM) and barite. Many grains show deformation twinning. White box indicates the location of BSE image to the right. (B) Cal-2 associated with REM precipitation. (C) Rhombohedral Dol-2 with REM precipitation in Fe-rich rim. (D) Fluid alteration within pre-existing Dol-1. White box indicates the location of BSE image to the right.

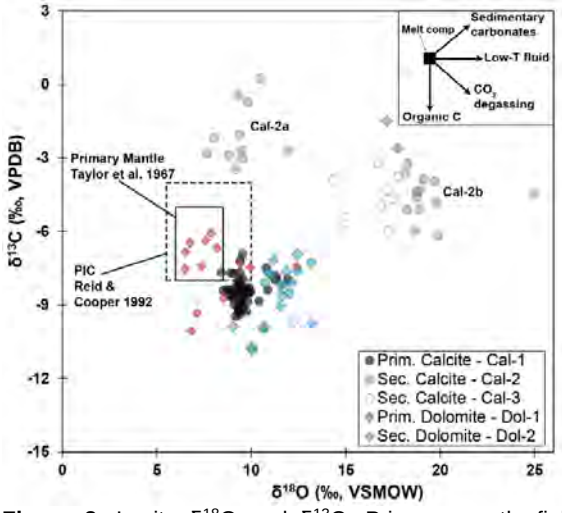


Figure 2. In-situ $\delta^{18}O$ and $\delta^{13}C$. Primary mantle field (Taylor et al. 1967) and primary igneous carbonatite (PIC) field (Reid and Cooper 1992) are indicated. Inset box at the top indicates direction of alteration or contamination of a starting melt composition by incorporation of organic C or sedimentary carbonates, CO_2 degassing, and low-T fluid alteration.

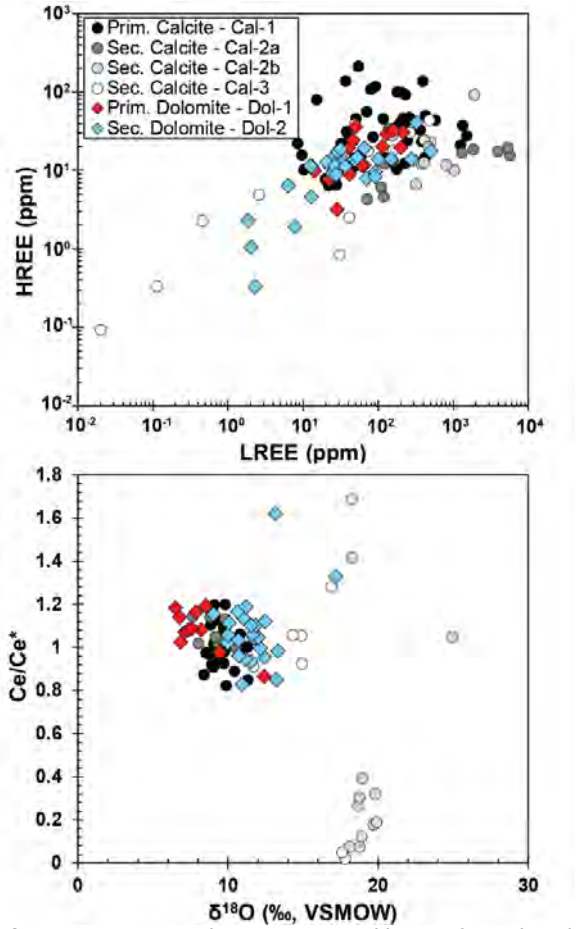


Figure 3. Trace element compositions of analyzed carbonate minerals. (A) LREE (La-Eu) plotted against HREE (Gd-Lu). (B) Oxygen isotope composition against Ce anomaly ($Ce/Ce^* = Ce_{CN}/(La_{CN}*Pr_{CN})^{1/2}$).

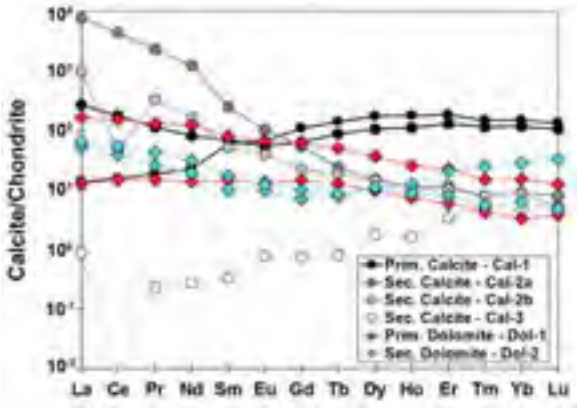


Figure 4. Representative chondrite-normalized REE abundances of the carbonate groups. Chondrite values of McDonough and Sun (1995) are used for normalization.

from "primary mantle" carbon and oxygen to isotopically heavier oxygen and lighter carbon are considered. First, the shift in oxygen and carbon may be consistent with a CO_2 degassing signature (Demény et al. 2004). In the degassing model, dolomite with the primary mantle signature represents the isotopic signature of the carbonatite melt. This model is consistent with the composition of calcite, which is near-endmember calcite lacking substantial Sr or Mg (Chakhmouradian et al. 2016).

Combined, this could suggest C and O isotope signatures of primary calcite do not reflect the composition of the melt and were altered during a degassing event. However, the dolomite degassing reaction requires that dolomite disassociate to calcite, CO_2 gas, and periclase (alternatively Mg-rich magnetite or Mg silicates). No such magnesian phases have been observed in the Sulphide Queen carbonatite, which is notoriously magnetite-poor (Denton and Ponce 2016) and lacks silicate phases. Further, degassing is a local process and would not result in homogeneous isotopic signatures, particularly in a complex composite stock, which likely intruded as a series of sills at variable depths. If the calcite records the isotopic signature of the intruding melt, then carbon was generally lighter and oxygen heavier than typical mantle. This may indicate subducted slab contributions to the source region (Chakhmouradian et al. 2008).

Samples with primary, coarse-grained calcite often exhibit low-degree deformation twinning (some of which are bent) consistent with ductile deformation (Chakhmouradian et al. 2008). The cause and timing of this strain, and the potential effect on carbon and oxygen isotopes in these calcite grains, remains under investigation.

Primary calcite and dolomite are HREE-enriched compared to their secondary counterparts. The resultant REE profiles for primary carbonates (Fig. 4) reflect the relationship between melt composition and carbonate/melt partition coefficients for REEs. The whole-rock data (e.g., Benson and Watts 2024) demonstrate that the carbonatite melt was substantially LREE-enriched over HREE – with an average $(La/Yb)_{CN}$ of 6200. However, HREE are more compatible in carbonate minerals than LREE (Chebotarev et al. 2019). Flat REE profiles thus reflect greater partitioning into carbonates of HREE compared to LREE, but in the presence of significant LREE enrichment in the melt.

The presence of two isotopically distinct secondary calcite populations, both associated with REE mineralization, emphasizes the role of fluids in upgrading the deposit. Fluids moving through the stock remobilize LREE from disseminated REE mineralization or non-REM hosts, and redeposit them in more concentrated forms, such as high-grade bastnäsite mineralization. One population of REM-associated secondary calcite (Cal-2a) lacks a Ce anomaly and is only identified by texture and a heavy carbon isotope signature. This suggests interaction with a fluid rich in carbon but unable to alter the oxygen isotope signature of the calcite. The source of such a fluid remains under investigation. However, this fluid event was clearly distinct from the fluid that formed the Cal-2b population. The other population of secondary REM-related calcite (Cal-2b) possess isotopically heavy carbon and oxygen compared to typical mantle values. This may be an indication of carbonate-rich fluids sourced from sedimentary carbonate occurrences.

However, the lack of known sedimentary carbonates in the region pre-dating the intrusion of the Mountain Pass carbonatite poses a challenge to this model. The carbonatite intruded primarily metaigneous rocks (leucocratic and augen gneisses and amphibolites) which do not contain sedimentary carbonate. However, presence of sedimentary or metasedimentary carbonates at depth remains a possibility. The Cal-2b fluid was oxidized, as most calcites record a negative Ce anomaly consistent with oxidation of Ce^{3+} to Ce^{4+}.

Primary dolomite broadly overlaps the isotopic and REE composition of primary calcite but is more heterogeneous. No textural evidence for dolomite exsolution from calcite has been observed. Mountain Pass is a composite stock which intruded in compositionally distinct pulses, resulting in dolomite or calcite dominance (Castor 2008).

Secondary dolomite generally forms rhombohedral crystals, with Fe enrichment toward the rims associated with rare earth mineralization (Fig. 1C) and with secondary calcite precipitation. It lacks substantial Ce anomalies, aside from two Dol-2 analyses associated with possible supergene alteration. In contrast to both secondary calcite generations, the carbon isotope signature of dolomite is similar between primary and secondary occurrences, whereas the oxygen isotopes are systematically heavier in the secondary dolomites. Secondary dolomite occurs in association with both Cal-2a and Cal-2b. Thus, despite both lacking Ce anomalies, Dol-2 may be unrelated to Cal-2a. This further supports a model in which primary magmatic crystallization of the Mountain Pass carbonatite was followed by multiple metasomatic events, often associated with REE mineralization.

Acknowledgements

Robby Ruesch, Lin Xia, and Nicole Franco of MP Materials and Steve Castor (formerly of Molycorp) are thanked for providing access to their archival drill core collection. Beth Ann Bell (UCLA SIMS lab) assisted with stable isotope data. This research was supported by the U.S. Geological Survey Mineral Resources Program. Any use of trade, firm, or product names is for descriptive purposes only and does not imply endorsement by the U.S. Government.

References

Benson EK, Watts KE (2024) Apatite and Monazite Geochemistry Record Magmatic and Metasomatic Processes in Rare Earth Element Mineralization at Mountain Pass, California. Economic Geology 119:1611–1642. https://doi.org/10.5382/econgeo.5108

Castillo-Oliver M, Giuliani A, Griffin WL, et al (2020) New constraints on the source, composition, and post-emplacement modification of kimberlites from in situ C–O–Sr-isotope analyses of carbonates from the Benfontein sills (South Africa). Contrib Mineral Petrol 175:33. https://doi.org/10.1007/s00410-020-1662-7

Castor SB (2008) The Mountain Pass rare-earth carbonatite and associated ultrapotassic rocks, California. The Canadian Mineralogist 46:779–806. https://doi.org/10.3749/canmin.46.4.779

Chakhmouradian AR, Mumin AH, Demény A, Elliott B (2008) Postorogenic carbonatites at Eden Lake, Trans-Hudson Orogen (northern Manitoba, Canada): Geological setting, mineralogy and geochemistry. Lithos 103:503–526. https://doi.org/10.1016/j.lithos.2007.11.004

Chakhmouradian AR, Reguir EP, Zaitsev AN (2016) Calcite and dolomite in intrusive carbonatites. I. Textural variations. Miner Petrol 110:333–360. https://doi.org/10.1007/s00710-015-0390-6

Chebotarev DA, Veksler IV, Wohlgemuth-Ueberwasser C, et al (2019) Experimental study of trace element distribution between calcite, fluorite and carbonatitic melt in the system $CaCO_3 + CaF_2 + Na_2CO_3 \pm Ca_3(PO_4)_2$ at 100 MPa. Contrib Mineral Petrol 174:4. https://doi.org/10.1007/s00410-018-1530-x

Demény A, Sitnikova MA, Karchevsky PI (2004) Stable C and O isotope compositions of carbonatite complexes of the Kola Alkaline Province: phoscorite-carbonatite relationships and source compositions. In: Wall F, Zaitsev AN, Treloar PJ (eds) Phoscorites and carbonatites from mantle to mine. Mineralogical Society of Great Britain and Ireland, pp 407–431

Denton KM, Ponce DA (2016) Gravity and Magnetic Studies of the Eastern Mojave Desert, California and Nevada. U.S. Geological Survey

McDonough WF, Sun S -s. (1995) The composition of the Earth. Chemical Geology 120:223–253

Norris A, Danyushevsky L (2018) Towards estimating the complete uncertainty budget of quantified results measured by LA-ICP-MS [Conference Abstract]. In: Goldschmidt Abstracts. Goldschmidt, Boston, MA

Reid DL, Cooper AF (1992) Oxygen and carbon isotope patterns in the Dicker Willem carbonatite complex, southern Namibia. Chemical Geology: Isotope Geoscience section 94:293–305. https://doi.org/10.1016/0168-9622(92)90004-T

Śliwiński MG, Kitajima K, Kozdon R, et al (2016a) Secondary Ion Mass Spectrometry Bias on Isotope Ratios in Dolomite–Ankerite, Part II: $\delta^{13}C$ Matrix Effects. Geostandard Geoanalytic Res 40:173–184. https://doi.org/10.1111/j.1751-908X.2015.00380.x

Śliwiński MG, Kitajima K, Kozdon R, et al (2016b) Secondary Ion Mass Spectrometry Bias on Isotope Ratios in Dolomite–Ankerite, Part I: $\delta^{18}O$ Matrix Effects. Geostandard Geoanalytic Res 40:157–172. https://doi.org/10.1111/j.1751-908X.2015.00364.x

Taylor HP, Frechen J, Degens ET (1967) Oxygen and carbon isotope studies of carbonatites from the Laacher See District, West Germany and the Alnö District, Sweden. Geochimica et Cosmochimica Acta 31:407–430. https://doi.org/10.1016/0016-7037(67)90051-8

The 3D structure and evolution of a REE-rich carbonatite: insights from the Chilwa Alkaline Province

Sam Broom-Fendley[1], Kathryn Goodenough[2], Michael Marks[3], Paul Armitage[4], and the REEDRILL Science Team.
[1] *Camborne School of Mines, University of Exeter, Penryn Campus, Cornwall, United Kingdom*
[2] *British Geological Survey, The Lyell Centre, Edinburgh, United Kingdom*
[3] *Department of Geosciences, Eberhard Karls Universität Tübingen, Germany*
[4] *Mkango Resources Ltd., Vancouver, BC, Canada*

Abstract. Carbonatite complexes form via some of the most extreme petrological conditions on Earth and can culminate in the formation of the large and high grade rare earth element (REE) deposits needed for the transition to a low-carbon society. However, the evolution and structure of carbonatites, and their importance for forming REE deposits, especially in relatively shallow examples, is poorly constrained. Here we outline the results of new geophysical data from two carbonatite complexes in the Chilwa Alkaline Province, Malawi, and link these data to petrological models to infer the presence of calcite carbonatite at depth in REE-rich carbonatites. We outline the need for research-focussed drilling to ground truth the inferred structures and to resolve the challenges of sampling REE-rich carbonatites which are extremely out-of-equilibrium with the surface environment, resulting in the rapid oxidation and breakdown of surface material.

1 Background

As society moves to low-carbon energy, demand for the 'critical raw materials' needed for this energy transition is rapidly increasing. Among those, the REE are particularly important as they are essential ingredients in high-strength permanent magnets used in wind turbines and most electric vehicles. Demand for the REE is forecast to grow, requiring further extraction of REE minerals (Goodenough et al. 2018). The largest and highest grade REE deposits are in carbonatites, which are consequently the focus of most global REE mining and exploration. However, the details of how carbonatites are emplaced and evolve to form critical raw material deposits remain poorly understood. Individual complexes are known to be both laterally and vertically zoned (Frolov 1971) but it has thus far proven challenging to understand variations on a 3D scale. This contribution explores new data from the Chilwa Alkaline Province, Malawi, where exploration over the last ~15 years has encouraged investigation of the deeper structure and evolution of these complexes. We summarise the geological and geophysical characteristics of carbonatites from these localities, and outline plans for future research drilling in order to build up a holistic 3D carbonatite model.

2 Carbonatite structure and evolution

Carbonatite complexes are envisaged as vertically and laterally zoned pipe-like structures and major rock types, textures, and associated mineralisation show broad changes with depth (Fig. 1; Garson 1965; Frolov 1971; Le Bas 1977). The deeper parts of these systems (emplaced at ~>5 km) often comprise carbonatites, phoscorites and (mostly) ultramafic silicate rocks which can contain high concentrations of P, Ti, Zr, Nb, and Fe resulting from cumulate processes; these occurrences can be large enough and sufficiently high grade to become ore deposits. However, REE mineralization typically occurs in carbonatites associated with evolved silicate rocks at sub-volcanic levels, resulting from protracted magmatic and hydrothermal processes.

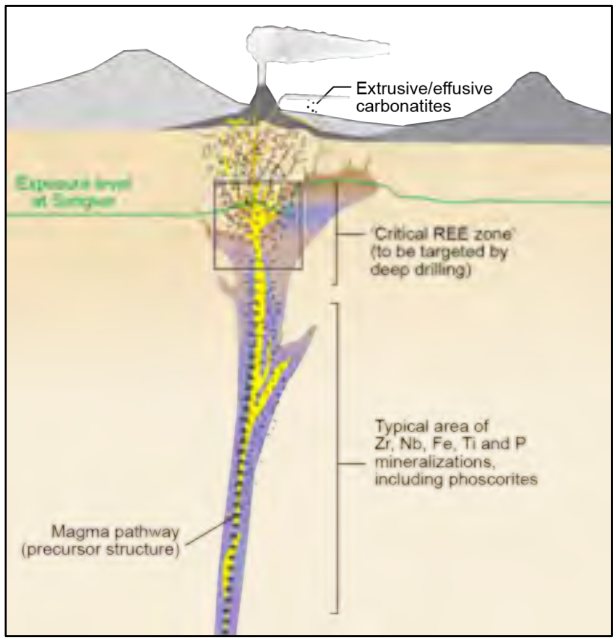


Figure 1. Schematic section of an alkaline-carbonatite complex showing a magma pathway and the typical vertical zonation in terms of rock types and commodities. Vertical depth, c. 15 km.

The formation and evolution of REE mineralization in shallow carbonatites is typically a multi-stage process. While the 3D structure is poorly constrained, many REE-rich carbonatites follow a common 2D structure which comprises an alkaline silicate rock (commonly nepheline syenite and/or ijolite), penetrated by one or more 'vents' of breccia. Carbonatite generally occurs as a later phase intruding the breccia vents and it, in turn, can be differentiated as a series of rings with calcite carbonatite occurring as the outermost ring and Fe content progressively increasing towards the center. A good example is Chilwa Island, Malawi, where a central breccia vent is intruded by calcite carbonatite, followed by ankerite-bearing

carbonatite and finally a central cone of sideritic carbonatite, which is REE rich (Garson 1965). Commonly, the central Fe-rich carbonatite comprises a stockwork of dykes and veins, rather than a single plug, and is also typically the locus for hydrothermal alteration.

Different carbonatite types are commonly interpreted as evidence for different degrees of carbonatite fractionation, with calcite interpreted as an early fractionation product followed by later dolomite and ferroan dolomite. The REE are incompatible in these phases (Chebotarev et al. 2019; 2022) and, consequently, fractionation of carbonates can result in sufficient magmatic REE enrichment to form primary mineralization in an evolved carbonatitic magma (Anenburg et al. 2021). However, many models for carbonatites conceptualise carbonatite structures as vertically continuous, with little to no variation in the proportion of the different carbonatite types over shallow depths. Where the fractionated carbonatite resides in the general structure of a carbonatite complex remains unclear.

Experimental results (Beckett 1987; Anenburg et al. 2020), and melt inclusion data (Prokopyev et al. 2016), indicate that evolved carbonatite magmas have elevated Na contents. Any early phases crystallising from such a magma, such as alkali carbonate minerals, are likely to be highly soluble and modified by post-emplacement hydrothermal processes and weathering. As REE-rich parts of a carbonatite are the most evolved and Na-rich, they are also the most susceptible to weathering and alteration, hindering the petrological efficacy of surface sampling and masking the evolution of the complex as a whole. Weathering is prominent even where thick regolith profiles are not developed, and dissolution of carbonates (and other phases), re-precipitation of calcite, and the oxidation of sulfide minerals can occur to 200 m depth. Lithological contacts are commonly a plane of weakness for fluid ingress, promoting weathering and obscuring surface relationships in the places where such observations are the most critical. In most cases, only fresh drillcore can allow sampling of relatively fresh REE-rich carbonatite.

3. Insights from carbonatites of the Chilwa Alkaline Province.

The Chilwa Alkaline Province extends across southern Malawi and Mozambique and comprises over 20 alkaline syenite, granite, and carbonatite intrusive complexes, as well as volumetrically minor alkaline dykes, plugs and breccia vents (Garson 1965; Woolley 2001; Fig. 2). While alkaline syenites and granites comprise the majority of the rocks of the province by volume, the most prospective for new mineral deposits are the carbonatites. The largest carbonatites in the province are Chilwa Island, Monte Muambe, Tundulu, Songwe Hill and Kangankunde (Fig. 2), but carbonatite occurs and is prospective at numerous other localities as well, such as Nkalonje and Namangali. The eponymous and largest example in the Province, Chilwa Island, is in an ecological reserve and consequently has had little investigation as a potential resource.

Here, we focus on results from the Songwe Hill and Nkalonje carbonatites following extensive collaborative research with Mkango Resources, who are the licence holders for both localities. We present new Natural Source Audio-Magnetotelluric (NSAMT) data and inverted magnetic and Bouguer gravity surveys to help elucidate on the structure of each complex. These data were collected and processed by Gregory Symons Geophysics.

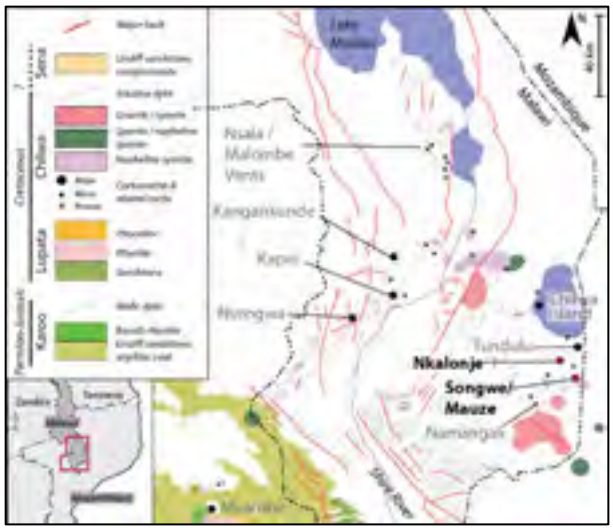


Figure 2. Map of the Chilwa Alkaline Province highlighting the location of the Songwe and Nkalonje carbonatites. Modified and updated from Garson (1965), Woolley (2001) and Broom-Fendley et al. (2017).

3.1 The Songwe Hill carbonatite complex

The Songwe Hill carbonatite forms a steep-sided hill, approximately 800 m in diameter abutting the north-western flank of the 6 x 4 km Mauze nepheline syenite intrusion. The geology of the complex comprises multiple intrusion phases, consisting of nepheline syenite and phonolite cut by at least three different carbonatite stages, late-stage Fe- and Mn-rich veins and apatite-fluorite veins, as well as extensive brecciation and hydrothermal alteration (Broom-Fendley et al. 2017). The carbonatite is surrounded by a fenite halo, forming a distinct carbonated nepheline syenite across the contact zone with the Mauze nepheline syenite, and characteristic fenitised basement rock to the north and west. The different carbonatite stages consist of a typical carbonatite evolution sequence from coarse-grained calcite carbonatite occurring as clasts in younger lithologies, through fine-grained calcite carbonatite, to Sr- and REE-rich ferrocarbonatite. Phonolite dykes are entrained within and cross-cut carbonatite and represent either continuous or pulsed silicate melt activity during carbonatite emplacement.

The new geophysical data allows the interpretation of four distinct but simplified groups

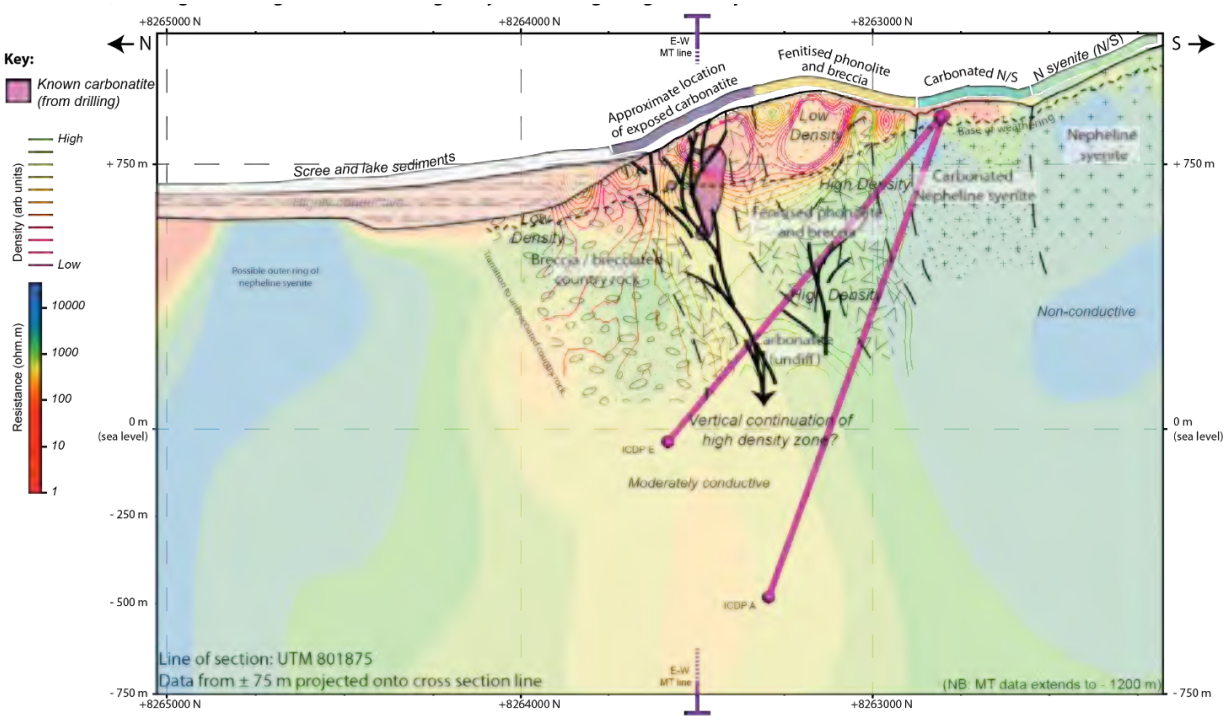


Figure 3. North-south cross-section of Songwe Hill illustrating (A) magnetotelluric (colour) and gravity (contour) data, overlain by an interpretation of the geology of the body and two planned drill paths for research drilling.

which make up the deeper structure at Songwe: (1) A low density, high conductivity area within a few hundred metres of the surface, interpreted to correspond to an area of weathered carbonatite. (2) An area of relatively high density, high magnetic susceptibility and medium conductivity, roughly corresponding to the locations of known carbonatite from drill core. (3) A low density, low magnetic susceptibility, low conductivity zone, which fits the expected geophysical properties of a breccia. (4) Low conductivity areas fitting nepheline syenite. Based on these interpretations, the current geological interpretation of Songwe Hill follows the conceptual structure of a REE-mineralized carbonatite and phonolite neck, emplaced between 1–5 km depth, enveloped by carbonatite-rich breccias and altered phonolite and passing outwards through a halo of carbonated nepheline syenite into fresh nepheline syenite (Fig. 3). The carbonatite has steeply-dipping but irregular contacts. The exact structure of the complex at depth remains unclear, but a large, high-density area occurs approximately 400 m below the centre of the hill and a second, smaller carbonatite neck is interpreted to offshoot from this deeper body, narrowly reaching the surface. These features may indicate the presence of a magnetite and calcite rich cumulate body, fitting the occurrence of similar rocks found as xenoliths in surface samples. Magnetic and MT data both suggest that the carbonatite tapers to a narrower body beneath ~750 m depth.

3.2 The Nkalonje carbonatite complex

The Nkalonje carbonatite complex is approximately 14 km NW of Songwe Hill. It consists of a series of low hills predominantly composed of fenitised basement rocks. These are intruded by a partly exposed plug of nepheline syenite, a highly altered fenite breccia and a series of small anastomosing carbonatite dykes. Owing to the large amount of cover in the area, the total size of the complex is hard to estimate but exposed alkaline rocks cover an area of about 1.7 km in diameter. Recent mapping and sampling by Mkango Resources has shown that the dykes consist of calcite carbonatite and darker Fe-bearing carbonatite, the latter containing up to ~5.5% rare earth oxides. Considering these dykes as the product of protracted fractional crystallisation, it follows that the complex must be much larger at depth than the extent of carbonatite at the surface and that the high REE contents in the dykes indicates potential for further REE mineralization in the hill.

Based on its potential to host a larger deposit, Mkango Resources commissioned additional geophysical data to understand the broad structure and size of the complex (Fig. 4). Regions of high density, mid–high magnetic susceptibility, and low conductivity correlate well with nepheline syenite outcrops at surface, and form a ring around the hill marking the outermost part of the intrusion. The nepheline syenite is cross-cut by one or more breccia vents which correspond to a circular low-density and high-conductivity structure to at least 650 m depth. A bowl-like structure with high magnetic susceptibility and conductivity occurs from approximately 350 m to 750 m, fitting a conceptual model of a central cumulate of magnetite-rich calcite carbonatite. The low density of this area is somewhat contrasting when compared to ‘pure’ carbonatite, but this may be a result of a mixed lithology, incorporating fragments of lower density

breccia, as occurs at Songwe Hill. A high-density anomaly occurs in the center of the breccia pipe from the surface to approximately 350 m depth. This anomaly may correspond with Fe-rich carbonatite in breccia, owing to the higher density of this carbonatite type. Moreover, the area at the surface where this anomaly occurs corresponds to a poorly exposed part of the breccia vent, with high Th contents, in a relatively eroded part of the hill. The high Th content can be indicative of REE mineralization, while the increased erosion and poor exposure can be common for Fe-rich carbonatite, which is easier to weather than other rock types associated with carbonatites.

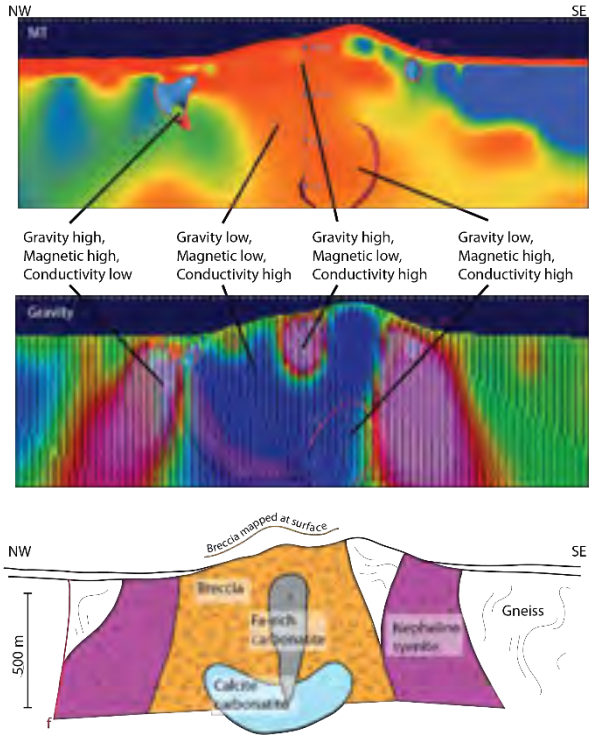


Figure 4. An interpreted NW–SE cross section of Nkalonje Hill, comprising NSAMT data (top panel), inverted gravity data (middle panel) and magnetic data (shells on top and middle panels).

4. Outlook and future drilling

Considerable variations in density, magnetic susceptibility and conductivity evidently occur with changes in depth in the cases of the two examples above. These features indicate considerable heterogeneity and complexity in the structure of a carbonatite, even on relatively shallow scales of 1-5 km. While variations in the geophysical properties of the complexes can be broadly ascribed to existing conceptual models of carbonatite evolution, they do not provide unequivocal evidence for the presence of calcite carbonatite cumulates, and geophysical data need to be ground-truthed by drilling. The authors of this paper are leading a bid for research-focused drilling at the Songwe Hill carbonatite to further resolve the structure of the complex and to also address the challenges of sampling REE-rich lithologies from these complexes, the effect of carbonatites on groundwater composition, and investigate for the possible presence of carbonatite-consuming microbiota. We are happy to welcome additional members to the REEDRILL science team.

Acknowledgements

The data presented here would not have been possible without Greg Symons, who supported REEDRILL from the start and was always happy to puzzle over geophysical data from carbonatites. We also thank the team from Mkango Resources for data access and support. Funding from the UoE Sub-Saharan African Development Fund, NERC project NE/X015114/1 and ICDP is acknowledged.

References

Anenburg M, Broom-Fendley S, Chen, W (2021) Formation of rare earth deposits in carbonatites. Elements 17:327–332. doi.org/10.2138/gselements.17.5.327.

Anenburg M, Mavrogenes JA, Frigo C, Wall F (2020) Rare earth element mobility in and around carbonatites controlled by sodium, potassium, and silica. Sci Adv 6:eabb6570. doi.org/10.1126/sciadv.abb6570.

Beckett MF (1987) Phase relations in synthetic alkali-bearing dolomite carbonatites and the effect of alkalinity and fluorine content on the solubility of pyrochlore and the formation of niobium deposits in carbonatites. MSc thesis, University of Toronto.

Broom-Fendley S, Brady AE, Horstwood MSA, Woolley AR, Mtegha J, Wall F, Dawes W, Gunn G (2017) Geology, geochemistry and geochronology of the Songwe Hill carbonatite, Malawi. J Afr Earth Sci 134:10-23. doi.org/10.1016/j.jafrearsci.2017.05.020.

Chebotarev DA, Veksler IV, Wohlgemuth-Ueberwasser C, Doroshkevich AG, Koch-Müller M (2019) Experimental study of trace element distribution between calcite, fluorite and carbonatitic melt in the system $CaCO_3$ + CaF_2 + $Na_2CO_3 \pm Ca_3(PO_4)_2$ at 100 MPa. Contrib Mineral Pet 174:4. doi.org/10.1007/s00410-018-1530-x.

Chebotarev DA, Wohlgemuth-Ueberwasser C, Hou T (2022) Partitioning of REE between calcite and carbonatitic melt containing P, S, Si at 650–900 °C and 100 MPa. Sci Rep 12:3320. doi.org/10.1038/s41598-022-07330-0.

Frolov A (1971) Vertical zonation in deposition of ore, as in ultrabasic alkaline rocks and carbonatites. Int Geol Rev 13:685-695. doi.org/10.1080/00206817109475486.

Garson MS (1965) Carbonatites in southern Malawi. Bulletin of the Geological Survey of Malawi 15.

Goodenough KM, Wall F, Merriman D (2018) The rare earth elements: demand, global resources, and challenges for resourcing future generations. Nat Res Research 27:201–216.

Le Bas MJ (1977) Carbonatite-Nephelinite Volcanism, John Wiley & Sons, 347 pp, ISBN 9780471994220.

Prokopyev IR, Borisenko AS, Borovikov AA, Pavlova GG (2016) Origin of REE-rich ferrocarbonatites in southern Siberia (Russia): implications based on melt and fluid inclusions. Mineralogy and Petrology 110:845–859.

Woolley A (2001) Alkaline Rocks and Carbonatites of the World Part 3: Africa. The Geological Society, London.

The rare earth element and fluorite deposit at Monte Muambe, Northwest Mozambique

A. Jamie Church[1], Sam Broom-Fendley[1], Cédric Simonet[2], Frances Wall[1]
[1]Camborne School of Mines, University of Exeter, Penryn Campus, Cornwall, TR10 9FE United Kingdom
[2]Altona Rare Earths Plc, 25 Eccleston Place, Eccleston Yard, London, SW1W 9NF, United Kingdom

Abstract. Increasing demand for the rare earth elements (REE) has increased focus on the formation of REE deposits. Carbonatites, alongside alkaline-silicate rocks, form the primary ore type worldwide. However, carbonatite formation remains debated, and the mechanisms of REE mineralisation are not fully understood. In this study, we present our observations and work undertaken to date at the Monte Muambe Carbonatite-hosted REE-deposit, Mozambique. The complex hosts a variety of lithologies, including multiple generations of carbonatite. These lithologies have both relatively unevolved, REE-poor calcitic compositions and more evolved REE-rich ferroan compositions with an evolutionary trend within the deposit. In addition to REE mineralisation, fluorite-rich dykes are also present, alongside fenites and breccias which are strongly associated with the more evolved carbonatites. Other rock types recognised include pyroclastic deposits, which appear to pre-date the carbonatites, and mafic dykes, which appear to post-date the rocks within the crater. We describe the lithologies present at Monte Muambe, and the ongoing exploration being undertaken by Altona Rare Earths.

1 Introduction

The REE are increasingly important as we transition away from fossil fuels. They are critical in industrial applications, particularly in high strength permanent magnets used in wind turbines and electric cars (BGS 2024). Global mining production is dominated by China, as is processing and manufacturing. As such, a variety of countries (UK, US, EU) consider the REE as a critical mineral owing to its supply risk and their economic importance (BGS 2024; Burton 2022; European Commission et al. 2023). Consequently, many countries are endeavouring to diversify primary sources and processing as a national security priority. REE are sourced from a variety of different deposit types but principally from carbonatites and alkaline-silicate deposits (BGS 2024). One such locality being evaluated as a new potential REE deposit is the Monte Muambe carbonatite, Tete Province, NW Mozambique. This locality is being developed by Altona Rare Earths, who are looking at the REE and fluorite potential of the carbonatite. Here, we outline some of the findings from the exploration by Altona, as well as ongoing research into the characterisation of the REE mineralisation.

2 Regional and local geology

Monte Muambe is situated approximately 50 km SSE of the city of Tete, NW Mozambique. The carbonatite intrudes Karoo sediments and volcanic rocks of the Zambezi basin, which range from Early Jurassic to Late Carboniferous in age (GTK 2006). Monte Muambe is considered as part of the Chilwa Alkaline Province of Malawi and Mozambique, which comprises over 20 alkaline syenite, granite, and carbonatite intrusive complexes, as well as volumetrically minor alkaline dykes, plugs, and breccia vents (Woolley 2001; Fig. 1).

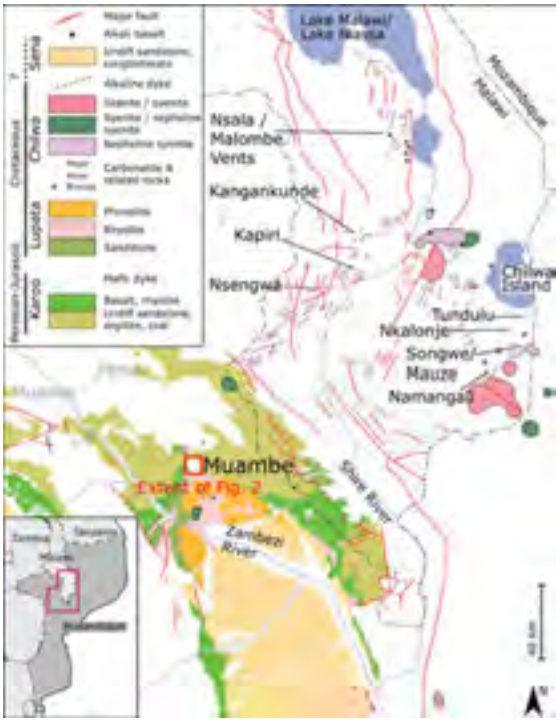


Figure 1. The Chilwa Alkaline Province of Malawi and Mozambique. Modified and updated from Garson (1965); Woolley (2001); and Broom-Fendley et al. (2017)

Monte Muambe intrudes the Karoo Moatize-Minjova coal basin at the eastern part of the Zambezi Graben. Around Monte Muambe, Karoo sediments are bound to the SW by a normal fault marking the edge of the graben, and to the north by an unconformity between the Lower Karoo Matinde Formation (sandstones and conglomerates), and the underlying Mesoproterozoic Tete gabbro suite. To the north of Monte Muambe there are a series of small syenite hills, which are also likely part of the Chilwa Province (GTK, 2006). To the south, Karoo sediments are overlain by the Cretaceous age Lupata series volcanics and sediments, which consist primarily of sandstones and conglomerates, rhyolites, and phonolites. The Lupata series and the carbonatites of Monte Muambe are loosely considered to be coeval, with the Lupata phonolites and rhyolites considered as an extrusive component of Chilwa Alkaline Province rocks (Eby et al. 1995). Monte Muambe is currently undated but is inferred to be Cretaceous based on the relationships exhibited with the hosting country rocks.

3 The Monte Muambe Carbonatite complex

The Monte Muambe Carbonatite complex was first described by Dixey (1930), who compared it to the carbonatites of Malawi. It consists of a 5 km diameter circular caldera-like structure with an outer ridge of sandstone and an inner basin composed of carbonatites and related rocks (Fig. 2). Most of the interest in the locality has been for its REE content and its fluorite potential (e.g. Cilek 1989; GTK 2006). The first attempt at commercial development was undertaken by Globe Metals and Mining, from 2009-2012, who explored the fluorite deposits at the western edge of the crater and released an inferred resource of 1.6 Mt @ 19% CaF_2 (Journeaux 2012). As part of this study, they also documented the REE potential of the carbonatites at Muambe.

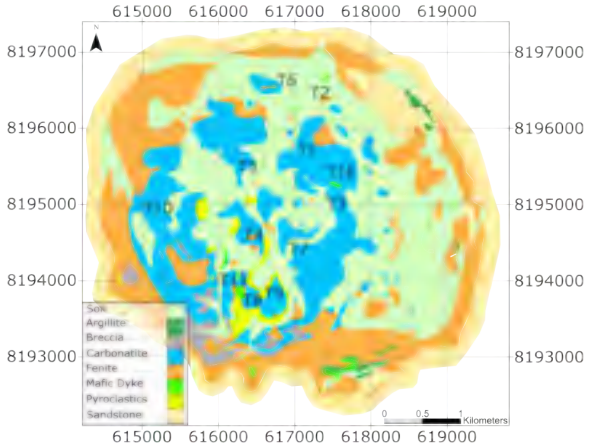


Figure 2. Geological map of Monte Muambe, showing exploration targets. Adapted from Dias (1960).

A variety of rock types outcrop in the complex. The main lithologies are as follows: (1) multiple generations of carbonatite; (2) fenites; (3) breccias; (4) fluorite veins; (5) pyroclastics; (6) mafic dykes; and (7) Karoo sandstones. Based on field observations, and further supported by detailed geochemistry, the carbonatites within the crater can be split into four generations, CC1-CC4.

The geochemical data presented is from intervals of 1 m length quarter and half core commercial assays provided by Altona Rare Earths. The samples were crushed and pulverized to <75 µm by Intertek Genalysis before being prepared as lithium metaborate fusions and analysed for major elements using ICP-OES and trace elements as ICP-MS. Validity of the results were confirmed by submission of duplicates, OREAS certified reference materials, and blanks at fixed intervals (Scogings et al. 2024). For the data analysis, mixed samples were screened for contamination from fenite by omitting any data with Al_2O_3 greater than 2 wt%, <20 wt.% SiO_2, and <10 wt.% LOI so that only relatively pure carbonatite data are considered.

CC1 consists of coarse-grained calcite carbonatite clasts occurring only within pyroclastics. CC2 consists of finer-grained calcite carbonatite with accessory magnetite and apatite, forming grey coloured outcrops with an elephant skin weathering texture. CC3 consists of fine-grained iron-rich carbonatite veins, which crosscut CC2, and are typically associated with breccias. The last carbonatite generation identified is CC4, which crosscuts all the earlier carbonatites. It has a medium-crystalline ferroan dolomite mineralogy, Mn-oxide veining, and strong REE-enrichment (1-4 wt.% total REE). All carbonatite types show REE profiles typical of carbonatites in the Chilwa Alkaline Province and Rufunsa district (Zambia) (Fig. 3).

The different carbonatite generations can be

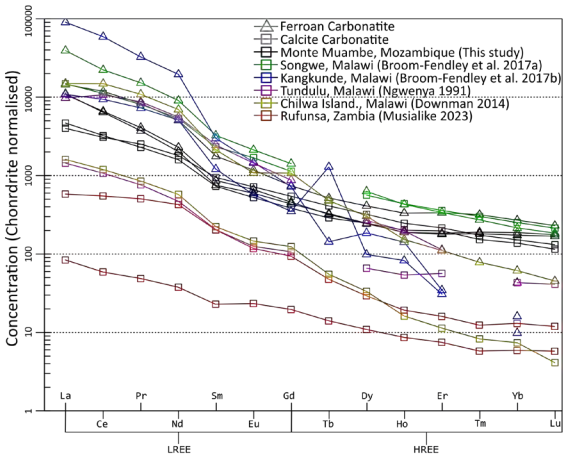


Figure 3. Chondrite normalised REE-profile of selected carbonatites within the Chilwa, and Rufunsa District, Zambia, compared to Monte Muambe.

broadly considered as belonging to one of two groups. Group A consists of CC1 and CC2 carbonatite. These carbonatites outcrop extensively throughout the crater over an approximate area of 3.3 km in diameter (Scogings et al. 2024). They typically have elevated Nb (435.1 ppm average), depleted F (0.28 wt.% average), and REE (0.47 wt.% average) concentrations, with an elevated HREE profile (LREE/HREE ratio, 31.92). They show conformable sub-horizontal relationships with the underlying pyroclastic rocks (Fig. 4), which have not experienced brecciation following deposition. In addition to this, these carbonatites lack a strong fenite aureole, except where material is entrained. These features are inferred to represent extrusive emplacement of relatively unevolved, calcite carbonatite.

Group B consists of CC3 and CC4 carbonatite generations. These carbonatites cross-cut earlier group A carbonatites and have discordant relationships with host-rocks accompanied by brecciation and an intense potassic fenite aureole. These carbonatites form distinct plugs in the crater, consisting of evolved, more iron-rich end-members. The carbonatites are generally Fe- and Mn-rich, with relatively depleted Nb (156.5 ppm average), elevated F (7.37 wt.% average) and REE (1.76 wt.% average) concentrations, with an elevated LREE profile (LREE/HREE ratio, 100.11). The REE mineralisation in these carbonatites is hosted in

bastnäsite, florencite, and synchysite (Scogings et al. 2024).

In addition to the carbonatites, extensive pyroclastic deposits have been identified both at outcrop and in core. These pyroclastic deposits



Figure 4. Conformable contact between the CC2 Carbonatite and Pyroclastics.

consist of earlier pyroclastic material, phonolite and carbonatite clasts, Karoo sandstones, and mafic inclusions. They do not contain fiamme. They are largely fresh, with little to no fenitisation, except where group B carbonatites crosscut. The pyroclastic units show cyclic fining upwards sequences in core and at outcrop, suggesting a sustained period of volcanism occurred prior to carbonatite emplacement (Fig. 5). They have conformable relationships with CC2 carbonatites.

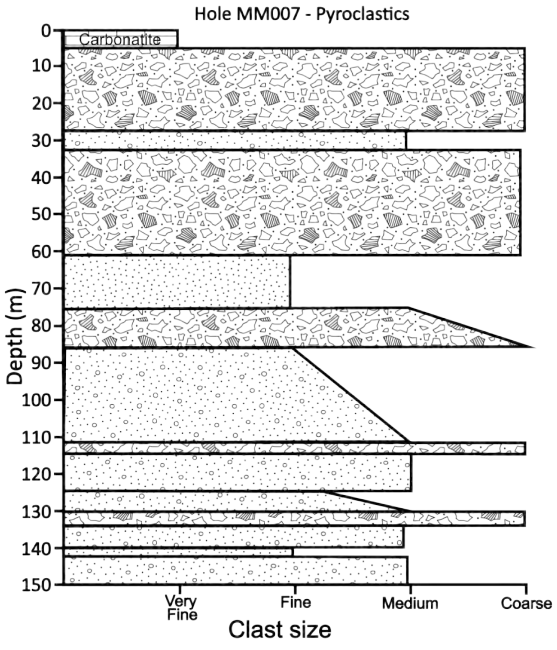


Figure 5. Pyroclastic deposits at Target 2.

Fluorite is locally abundant at Monte Muambe and is present both in a fine grained, disseminated blue form within carbonatites and associated fenites, and a coarse yellow type forming large fluorite veins in the west side of the crater. Breccias formed of clasts of Karoo sandstones, pyroclastic deposits and earlier carbonatites, occur near group B carbonatites and in a small locality to the E of the crater. These are typically associated with strong fenitisation. Outside of the intensely fenitised breccia, fenites formed of Karoo sandstones occur throughout the crater, including the crater rim, which is formed of hardened silica-rich Cádzi formation sandstones.

4 Ongoing exploration work

Altona Rare Earths started exploration for REE and fluorite at Monte Muambe in August 2021. As part of this, they have undertaken a drilling campaign over three seasons (2021, 2022, and 2023), comprising 7800 m of diamond drill and reverse circulation drilling over 11 targets. This drilling campaign was done with the aim of constraining the geometry and style of mineralisation, as well as determining the resource of the REE-enriched bodies within the crater (Scogings et al. 2024). These targets were determined through a mix of historical exploration data, geophysical surveying, and a soil sampling survey. As a result of this campaign, Targets 1 and 4 (Fig. 2) were identified as potentially economic for REE mining, with a total combined resource of 13.6Mt, at 2.42% TREO, using a 1.5% TREO cut off (Scogings et al. 2024). Further drilling on the other targets is expected to lead to an increase of the mineral resource.

In addition to targeting the REE mineralisation, focus has been placed upon the historically explored fluorite deposit within the crater for small scale CaF_2 mining. In September 2024, Altona began a scoping study to produce metallurgical grade fluorite from high-grade veins found along the western side of the crater. The results of this study suggest the possibility of a product with an average CaF_2 grade of 88.03% (Altona Rare Earths 2025). Further work is currently being undertaken to determine the style and geometry of the mineralisation of this deposit, with the aim of producing 15,000-20,000 tons of fluorite per year (Altona Rare Earths 2025). Altona Rare Earths have recently (January 2025) been granted a mining licence for REE and associated minerals, which would allow the company to begin high-grade fluorite production, following the completion of the fluorite mining scoping study (Altona Rare Earths 2025).

REE production at Monte Muambe is currently subject to the development of the pre-feasibility study. To this end, work is currently being undertaken on metallurgical testing and processing of the REE ore to produce a high-grade REE product. Following this, geotechnical studies will be undertaken to determine the pit geometry suitable for extraction. The metallurgy result will be integrated to determine the optimal extraction method (Scogins et al. 2024).

5 Conclusions and next steps

The Monte Muambe carbonatite complex hosts significant deposits of both the REE and fluorite. With the increasing demand for the REE, understanding of the formation of these carbonatite-hosted deposits is becoming essential to further exploration, and will aid in the exploitation of this deposit. Within the complex, multiple lithologies have been identified, with evidence for both intrusive and extrusive volcanism. Multiple generations of carbonatite occur, with contrasting compositions and REE mineralisation, which are similar to other carbonatites in the Chilwa Alkaline Province. Altona has identified two main mineralised targets with a combined resource of 13.6 Mt at 2.42% TREO, contained within CC3 and CC4 generation carbonatites and associated rocks. In addition, Altona Rare Earths have identified high grade fluorite, which they aim to extract in the near future. Further research at Monte Muambe will include:

- Additional characterisation of the lithologies at Monte Muambe to study the links between, and evolution of, the intrusive and extrusive volcanism in the complex.
- Further study on the type and structure of the REE mineralisation at Monte Muambe, focussing on mineralisation within the carbonatites and associated rocks, and undertaking further work on exploration indicators that may be used for further target identification.
- Study of the broader regional structure, with geochronology and isotopic work on the previously undated carbonatites at Monte Muambe. This will be combined with comparison to local syenite intrusions, and the Lupata volcanics, to understand whether Monte Muambe and Lupata are part of the Chilwa Alkaline Province, or part of a different magmatic province, with the aim of better understanding the regional controls on carbonatite formation, and REE mineralisation.

Acknowledgements

We thank Altona Rare Earths for facilitating field work to Monte Muambe, and for assistance in sample collection. AJC acknowledges support of a UK-NERC GW4+ studentship (NE/S007504/1), SBF and FW acknowledge support from the University of Exeter Sub-Saharan African Development Fund and NERC project NE/X015114/1.

References

Altona Rare Earths (2025) LSE:REE - Altona Rare Earths - Monte Muambe Fluorite Results. Altonare.com. https://investors.altonare.com/announcements/6785768. Accessed 12 February 2025

BGS (2024) UK 2024 Criticality Assessment. Open Report OR/24/047. British Geological Survey, Nottingham. https://www.ukcmic.org/downloads/reports/ukcmic-2024-criticality-assessment.pdf Accessed 20 February 2025

Broom-Fendley S, Brady AE, Horstwood MSA, Woolley AR, Mtegha J, Wall F, Dawes W, Gunn G (2017a) Geology, geochemistry and geochronology of the Songwe Hill carbonatite, Malawi. J Afr Earth Sci 134:10-23. doi.org/10.1016/j.jafrearsci.2017.05.020

Broom-Fendley S, Wall F, Spiro B, Ullmann V. (2017b) Deducing the source and composition of rare earth mineralising fluids in carbonatites: insights from isotopic (C, O, $^{87}Sr/^{86}Sr$) data from Kangankunde, Malawi. Contrib Mineral Petrol 172:96 https://doi.org/10.1007/s00410-017-1412-7

Burton J (2022) U.S. Geological Survey Releases 2022 List of Critical Minerals | U.S. Geological Survey. www.usgs.gov. https://www.usgs.gov/news/national-news-release/us-geological-survey-releases-2022-list-critical-minerals. Accessed 12 February 2025

Cílek V G (1989) Industrial Minerals of Mozambique. Czech Geological Office, Prague.

Dias, M.B. (1961). Geologia do Monte Muambe. Boletim, Serviços de Geologia e Minas, 27, pp.37–64.

Dixey F (1930) The Geology of the Lower Shire–Zambezi Area. Geological Magazine 67:49–60.

Downman E (2014) Mineralisation and fluid processes in the alteration zone around the Chilwa Island and Kangankunde carbonatite complexes, Malawi. Dissertation, Natural History Museum, United Kingdom

Eby G N, Woolley A R, Din V, and Platt G (1998) Geochemistry and Petrogenesis of Nepheline Syenites: Kasungu-Chipala, Ilomba, and Ulindi Nepheline Syenite Intrusions, North Nyasa Alkaline Province, Malawi. J. of Petrolog, 39(8), pp.1405–1424. https://doi.org/10.1093/petroj/39.8.1405

European Commission Directorate-General for Internal market, Industry, Entrepreneurship and SMEs, Grohol M, and Veeh C (2023) Study on the critical raw materials for the EU 2023: final report. Publications Office of the European Union. https://data.europa.eu/doi/10.2873/725585 Accessed 12 February 2025

Garson MS (1965) Carbonatites in southern Malawi. Bulletin of the Geological Survey of Malawi 15.

GTK (2006). Map Explanation; Volume 2: Sheets 1630 – 1934. Geology of Degree Sheets Mecumbura, Chioco, Tete, Tambara, Guro, Chemba, Manica, Catandica, Gorongosa, Rotanda, Chimoio and Beira, Mozambique. Ministério dos Recursos Minerais, Direcção Nacional de Geologia, Maputo.

Journeaux T (2012) Mt Muambe Resource Report. Globe Metals & Mining, Perth. https://announcements.asx.com.au/asxpdf/20120430/pdf/425wy08n6d7bzd.pdf Accessed 20 February 2025

Musialike M (2023) New Geomodels for Zambian Carbonatites. Dissertation, University of Exeter.

Ngwenya BT (1991) Magmatic and post-magmatic geochemistry of phosphorus and rare earth elements in carbonatites. Dissertation, Reading University

Scogings A, Cervoj K, Barnett R, et al (2024) Report for Altona Rare Earths Plc Monte Muambe Competent Person's Report and Scoping Study. Snowden Optiro, Perth. https://res.cloudinary.com/investorhub/raw/upload/v1727236637/leaf-prod/200/documents/JB207282_Altona_Monte_Muambe_CPR_SS_UPDATE_APR24_FINAL_opt_pzzj2l.pdf

Woolley AR (2001) Alkaline Rocks and Carbonatites of the World: Part 3 Africa. Geological Society of London, London. https://doi.org/10.2113/gscanmin.40.3.996-a

Crystallization Age and Evolution of Calcite Melteigite-Calcium Carbonatite: a Study of Zircon Systematics from the Fen Complex, Southern Norway

Nolwenn Coint[1], Trond Slagstad[1], Magdalena Huyskens[1], Kristian Drivenes[1] and Ana Carolina Rodrigues Miranda[1]

[1]Geological Survey of Norway, Trondheim, Norway

Abstract. The Fen alkaline and carbonatite complex in southern Norway is a 2.2 km-diameter pipe-like intrusion emplaced in Proterozoic granitic gneisses. The Fe-dolomite carbonatite unit hosts the largest rare earth element resource in Europe, making the Fen complex an important strategic resource. Zircon is locally found in mafic silicate-rich schlieren in the calcium carbonatite and displays complex U-Pb systematics influenced by a combination of recent Pb-loss and non-radiogenic Pb in U-poor zircon. The $^{207}Pb/^{206}Pb$ weighted average age of four combined samples is 585 ± 5 Ma (MSWD=1.1). The median εHf value is 1.9 (n=54) with an associated depleted-mantle model age (TDM) of 1380 Ma, indicating non-negligeable crustal contribution, a feature not seen in the Nd isotopes (median εNd_{580} =6.6, TDM = 650 Ma). This difference most likely reflects buffering from high Nd concentrations. The trace element in zircon, combined with textural relationships indicate a complex history. Zircon cores show evidence of disturbance, associated with a metasomatic alteration front growing from the primary zircon rims towards the cores. Brighter oscillatory zoned rims, depleted in Sr, Nb, REE and U, around some of the grains, stem from a metasomatic event or interaction with late carbonatitic melt.

1 Introduction

Carbonatite is the main source of critical metals including Nb and REE, and a significant contributor to the production of high-quality apatite separates used in fertilizer (Liu et al. 2023).

Although still highly debated, the formation of carbonatite likely involves one or several processes, including partial melting of metasomatized mantle, fractionation of alkaline magmas, liquid immiscibility, and subsequent metasomatic events related to the emplacement of the alkaline silicate and carbonatitic magmas. These events can be recorded in the minerals that grew throughout the evolution of the complex.

Zircon is considered one of the most reliable accessory minerals for U-Pb geochronology due to its high closure temperature, slow diffusion rates and robustness against alteration. In addition, it incorporates a range of High Field Strength Elements (HFSE) such as Nb, Th and Hf, and REE in its crystal structure which, when coupled with textural relationships, provide a powerful tool to track the evolution of the chemical composition of the melt(s) or fluid(s) in equilibrium with the mineral (Yang et al. 2023).

Here we investigate zircon texture and U-Pb/Hf isotopes systematics from the Fen carbonatite complex in southern Norway and show how they elucidate some of the complex petrogenetic processes involve in its formation.

2 The Fen Alkaline and Carbonatite Complex

2.1 Geological Context

The Fen alkaline and carbonatite complex, located in Telemark, southern Norway, is a circular 2.2 km-diameter pipe-like body, composed of numerous carbonatite dikes, breccias, alkaline rocks and late damtjernitic plugs emplaced in Sveconorwegian 1100-1400 Ma granitic gneisses (Fig. 1). The Fen complex was mined successively for Fe in the hematized carbonatite and Nb hosted by the calcium carbonatite.

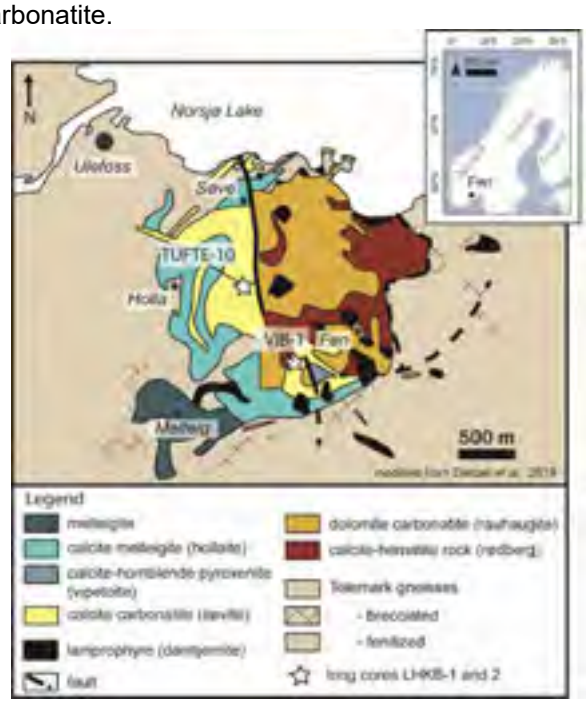


Figure 1. Geologic map of the Fen alkaline and carbonatite complex.

A non-negligible amount of apatite is associated with the latter and nearby lithologies; however, its economic potential remains unknown. A recent drilling campaign in the Fe-dolomite carbonatite provided an inferred JORC-compliant resource estimate of 559 Mt at 1.57 wt% TREO making Fen the largest REE deposit in Europe and an important strategic resource.

2.2 Sample Description

Zircon growing from carbonatite melts record a complex history which can help shed light on the evolution of alkaline and carbonatite complexes (Yang et al. 2023).

Four of five samples in this study are calcium carbonatites with variable modal proportions of mafic silicates predominantly biotite variably altered into chlorite, and apatite (samples FEN117906, FEN197967, FEN197973 and FEN197974 TUFTE-10 core; Fig.1). Zircon is associated with mafic silicates- or apatite-rich schlieren. Sample FEN118164, is a hematized apatite-rich carbonatite with zircon in the apatite-rich layers (VIB-1 core, Fig.1). Zircon occurs as single crystal or clusters of crystals which vary between a few tens of microns to 0.7 mm (Fig. 2) in all samples.

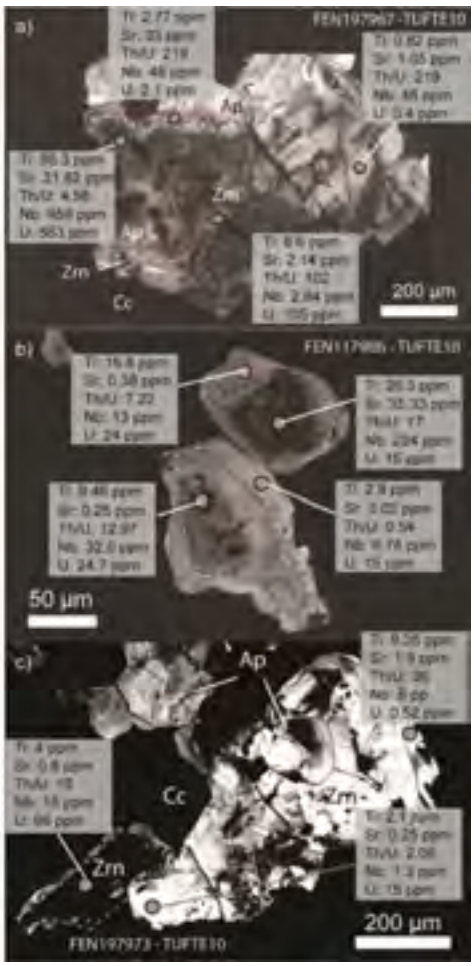


Figure 2. a-c) Representative textures (CL images) of zircon from the calcium carbonatite in Fen.

Zircon with complex core zoning containing inclusions of baddeleyite and apatite (Fig.2b) are found in all samples. Some cores display a dark homogeneous response in CL imaging (Fig. 2c) outlined by a thin brighter rim which locally can be oscillatory zoned. One zircon core displays replacement texture of a former unknown tabular mineral which now consists of Fe-dolomite, accessory monazite and baddeleyite (Fig. 2a). The rims are characterized by a higher CL intensity and are oscillatory zoned (Fig. 2a-c).

3 Results

3.1 Trace Elements in Zircon

Trace elements in zircon record the chemical variation of the magma or fluid it crystallized from and can be used to unravel their petrogenesis.

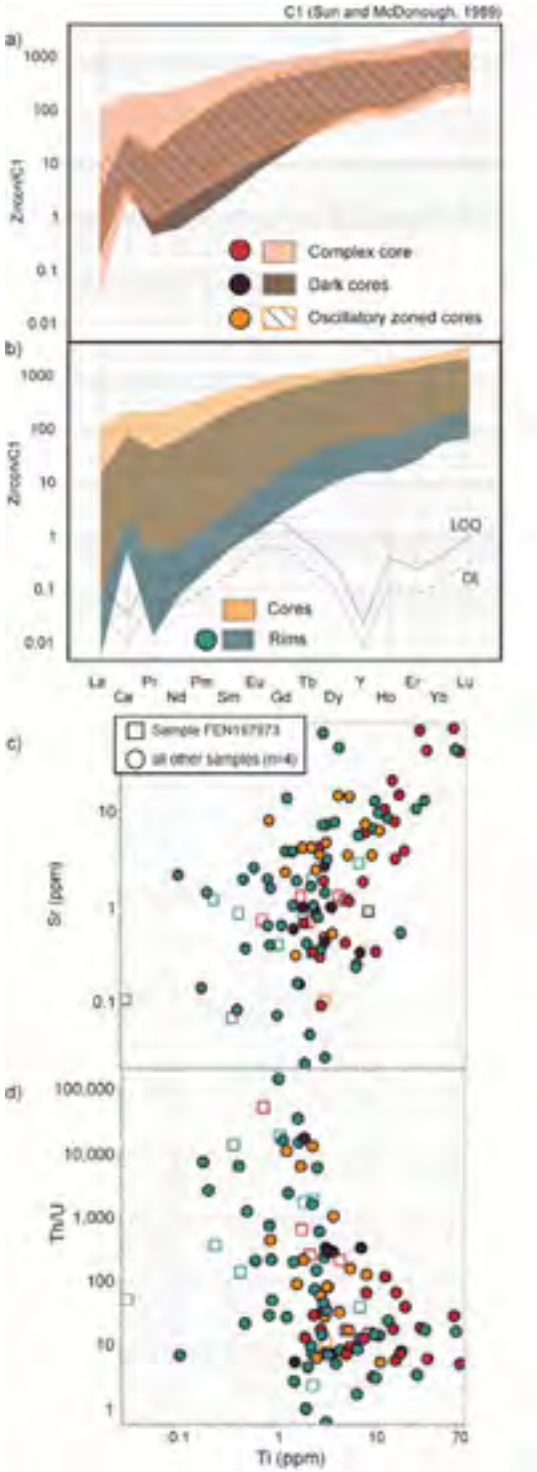


Figure 3. Zircon trace element composition. a-b) Zircon REE pattern normalized to chondrite. LOQ Lower limit of quantification, DL: Detection limit c-d) binary diagrams.

Zircon from individual samples can vary significantly in composition, leading to large compositional overlap between groups distinguished by CL imaging. Nevertheless, general trends are identified.

Zircon cores showing complex zoning (Fig.2) are enriched in most trace elements including Ti, Nb, Sr, REE, U and Th (Fig.3a-d). They also have the lowest Th/U ratios (4.5-108) despite high concentration of Th (49-2500 ppm), with the exception of sample FEN197973 which contains zircon with U-poor cores (0.015-1.27 ppm), leading to extreme Th/U values (200-52000) (Fig. 3d). Oscillatory zoned cores and dark cores overlap in composition and plot in between complex cores and oscillatory zoned rims (Fig. 3a, c and d). Zircon from the hematized carbonatite overlaps in most trace element concentrations with zircon from other samples, except for U which is systematically low (<10 ppm).

3.2 U-Pb geochronology

In-situ U-Pb isotopic analysis were acquired in the MiMaC lab at the Geological Survey of Norway in Trondheim, using a Laser ablation (193 nm) multi-collector ICP-MS (nu Plasma 3) system.

Most of the zircon analyzed have high to extreme Th/U ratio. Analyses with U> 1ppm were discarded. In all the samples, the majority of the analyses are discordant and plot along two trends. The first one is related to the low U-content of some of the grains, especially in rims, where the non-radiogenic Pb composition dominates. In all samples it is possible to draw a discordia line, anchored at $^{207}Pb/^{206}Pb$=0.85 (average Pb composition at 580 Ma according to the Stacey and Kramer (1975) two-steps model and obtain a rough age with a large uncertainty. The second trend can be explained by recent Pb loss and observed in all of the samples, dragging the analyses towards higher $^{238}U/^{206}Pb$ values (Fig. 4a). Sparse older concordant analysis shown in Figure 4a, possibly attributed to either inheritance or more complex system disturbance were discarded. Concordia ages are systematically discordant related to the influence of minor recent Pb loss in most analyses (Fig. 4b), therefore the $^{207}Pb/^{206}Pb$ weighted average ages are retained as the final ages (Fig. 4c).

We used the same approach summarized in figure 4 to calculate the age of the other three samples. Sample FEN117906 gives a weighted average $^{207}Pb/^{206}Pb$ age of 585 ± 7 Ma (MSWD: 0.58), which overlaps within uncertainty with the 3 other ages (Sample FEN197967: 582 ± 8 Ma (MSWD: 1.5); FEN197973: 599 ±13 Ma (MSWD: 3.1) and FEN197974: 593±10 Ma (MSWD: 0.28).

Large uncertainties associated with the ages are due to low U content and recent Pb loss, introducing scattering in the dataset. In the Ediacaran, Norway was in a stable geodynamic setting. Ages obtained for the crystallization of the carbonatite likely represent a single crystallization event. We therefore combined the selected U-Pb ages for the four samples and obtained a $^{207}Pb/^{206}Pb$ weighted average age of 585 ± 5 Ma (MSWD=1.1).

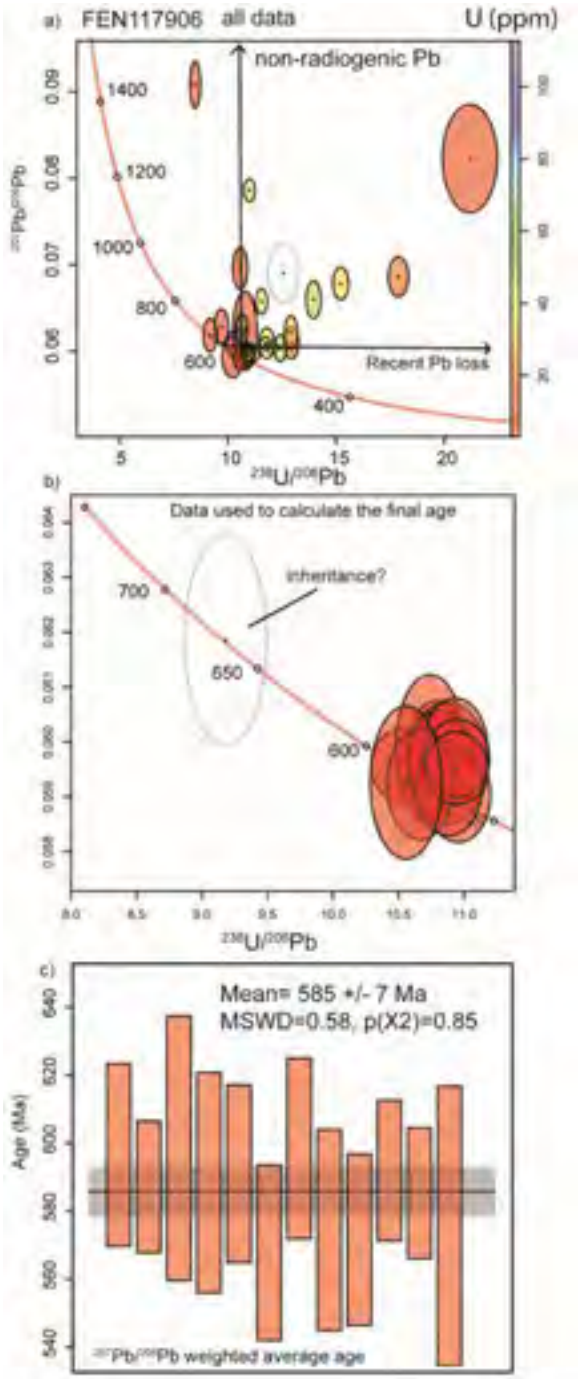


Figure 4. U-Pb analyses for FEN117906 illustrating the steps followed to calculate the final ages.

Zircon from sample FEN118164 contains too little U to retrieve a precise age.

3.3 Hf Isotopes

In-situ Hf isotopes were measured using the same instrumentation as U-Pb isotopes on zircons in two calcium carbonatite samples (FEN197967, n=18; FEN197974, n=18) and the hematized carbonatite (FEN118164, n=19). The median εHf values are overall positive and range between 1.1±2.9,

1.1±2.9, and 3.4 ±2.1 εHf units for each sample respectively. Associated average TMD model ages for each sample is 1430 ± 193 Ma, 1431 ± 190 Ma and 1286 ± 139 Ma respectively.

4 Discussion

Zircon from Fen records extreme Th/U ratios, indicative of zircon growing from a carbonatitic melt (e.g. Yang et al. 2023). This is supported by the core-to-rim decreasing concentrations of Nb, Sr (Fig. 3c), REE reflecting the fractionation of abundant apatite, carbonates, pyrochlore, and ferrocolumbite, principal minerals in the calcium carbonatite.

The final $^{207}Pb/^{206}Pb$ weighted average age of 585 ± 5 Ma obtained combining data from the four samples corresponds to crystallization of the calcium-carbonatite.

Individual final ages, and the final single combined age agree with previously published Ediacaran ages (Meert et al. 1998). The Ar/Ar age on a phlogopite separate from a damtjernite dike, (583 +/10 Ma) is similar within uncertainty to our final age.

Discarded older concordant analyses can be interpreted as inheritance, although these ages are virtually absent in this part of Norway which at the time was situated in stable geodynamic setting. We therefore argue that these ages results from the disturbance of the U-Pb system, possibly related to incorporation of excess ^{230}Th (Rodionov et al. 2012), resulting in excess ^{206}Pb, superposed to effect of non-radiogenic Pb composition in U-poor zircon.

Hafnium isotopes values (εHf 1.1-3.4; TMT modal Mesoproterozoic ages) are relatively juvenile but necessitate the intervention of crustal interaction to explain the results. Neodymium isotopes obtained on REE-fluorocarbonates, on the other hand, have median εNd composition of 6.6 ± 0.5 and an associated TDM model age of 652 Ma (Liu et al. 2024), suggesting a much more juvenile source, close to depleted mantle values. Neodynium isotopes were measured on REE-F-carbonates, the principal minerals hosting REE in the deposit. The Sm-Nd isotopic signature is therefore likely buffered by the signature from the source of the magma and not the contaminant which contains much lower concentrations of these elements. The Lu-Hf isotopic system, however, is more sensitive to crustal interactions, explaining the hybrid signature between the depleted mantle and the crust.

Textural relationships reveal an intricate history. Zircon cores with complex textures display evidence of alteration. Thin light-colored rims with internal lobate contact towards the complex zoned cores (Fig. 2b) hint at a high-temperature metasomatic event (Harlov et al. 2023) by alkali-bearing and F-rich fluids, resulting in alteration of zircons. This event is followed by the growth of oscillatory zoned brighter rims (Fig.2b) depleted in most trace elements which likely crystallized from a hydrothermal fluid.

Conclusions

Despite the unusually large Th/U ratio, typical of zircon crystallizing from carbonatites and and extensive recent Pb loss resulting in complex U-Pb datasets, we obtained a robust crystallization age for Fen 585 ± 5 Ma.

Isotopic systems are not all sensitive to crustal contamination. The Lu-Hf system is more likely to record crustal interaction, since these two elements are not particularly enriched in the host-rock nor in the carbonatite. The Sm-Nd isotopic signature however is dominated by signature from the source, which is close to depleted mantle composition.

Zircon systematics in carbonatites, while complex because of the high Th/U ratio, can shed light on the evolution of the melt / fluid through time. Although the transition between magmatic and hydrothermal processes remains difficult to identify with certainty, zircon can record evidence of metasomatic events potentially responsible for reconcentration and remobilization of key elements.

Acknowledgements

Analyses for this study were performed in the MiMaC laboratory, supported by the Research Council of Norway project number 269842/F50.

References

Harlov DE, Anczkiewicz R, Dunkley DJ (2023) Metasomatic alteration of zircon at lower crustal P-T conditions utilizing alkali- and F-bearing fluids: Trace element incorporation, depletion, and resetting the zircon geochronometer. Geochim Cosmochim Ac 352:222-235. doi: https://doi.org/10.1016/j.gca.2023.05.011.

Liu S-L, Fan H-R, Liu X, Meng J, Butcher AR, Yann L, Yang K-F, Li X-C (2023) Global rare earth elements projects: New developments and supply chains. Ore Geology Reviews 157:105428. doi: https://doi.org/10.1016/j.oregeorev.2023.105428.

Liu X, Keiding JK, Coint N, Jonsson E, Stendal H, Þórðarson Þ, Sadeghi M, Keulen N, Heredia B, Eerola T, Huyskens M, Clausen RJ, Gautason B, Yang J, Höskuldsson Á, Þórhallsson ER, Fransson H, Lahaye Y (2024) Mineral to Metal Traceability: A Proof-Of-Concept Study of Rare Earth Elements in the Nordic Region In: Report NI (ed). pp 90.

Meert JG, Torsvik TH, Eide EA, Dahlgren S (1998) Tectonic Significance of the Fen Province, S. Norway: Constraints from Geochronology and Paleomagnetism. The Journal of Geology 106:553-564. doi: 10.1086/516041.

Rodionov NV, Belyatsky BV, Antonov AV, Kapitonov IN, Sergeev SA (2012) Comparative in-situ U–Th–Pb geochronology and trace element composition of baddeleyite and low-U zircon from carbonatites of the Palaeozoic Kovdor alkaline–ultramafic complex, Kola Peninsula, Russia. Gondwana Research 21:728-744. doi: https://doi.org/10.1016/j.gr.2011.10.005.

Stacey JS, Kramers JD (1975) Approximation of terrestrial lead isotope evolution by a two-stage model. Earth and Planetary Science Letters 26:207-221. doi: https://doi.org/10.1016/0012-821X(75)90088-6.

Yang D-M, Hou T, Song W, Qin J, Luo D, Wang M, Veksler IV (2023) Tracking carbonatitic melt infiltration in the Miaoya carbonatite–syenite complex (central China) from zircon textures and geochemistry. Ore Geology Reviews 163:105741. doi: https://doi.org/10.1016/j.oregeorev.2023.105741.

Niobium-rich Minerals from the Sheep Creek Carbonatite-Related Deposits, Montana, USA

Christopher H. Gammons[1], Heather A. Lowers[2], Jay M. Thompson[2]
[1]Department of Geological Engineering, Montana Technological University, Butte, MT, USA
[2]U.S. Geological Survey, Denver, CO, USA

Abstract. The Sheep Creek area in southwest Montana contains a number of small, tabular, carbonatite-related deposits that are rich in Nb- and REE-minerals. The most abundant Nb-bearing minerals are columbite-(Fe), nioboaeschynite-(Ce), baotite, and two varieties of Ti-Nb-Fe-oxide. An early oxide with Ti/Nb (atomic) near unity later broke down to a mixture of columbite + TiO_2 with distinctly lower Nb content. Zircon intergrown with the Nb-REE minerals was dated by U-Pb methods to 116 ± 2 Ma. This age is in agreement with previous dating, and indicates that the Sheep Creek deposits are early Cretaceous in age.

1 Introduction

The Nb-REE-rich, carbonatite-related "vein-dikes" of southern Ravalli County, Montana, have been known since the late 1950s, when the area was prospected and mined at a small scale for columbite (Crowley 1960; Heinrich and Levinson 1961). Most of the occurrences are in the vicinity of Sheep Creek, and nearby Woods Creek (Fig. 1). The carbonate bodies are tabular, steeply dipping, < 2m wide, and difficult to follow on strike for more than about 50 m. Host rocks consist of amphibolite, granite/augen gneiss, and diabase/gabbro, dated to ~ 1.37 Ga (Doughty and Chamberlain 1996). These rocks represent a bimodal, igneous flareup near the end of faulting and sedimentation in the Mesoproterozoic Belt Basin. The carbonatite bodies, however, are thought to be much younger, as explained below.

REE minerals include monazite, allanite, and ancylite, as well as a number of late carbonate and silicate phases (Heinrich and Levinson 1961; Gammons et al. 2024). The deposits as a whole are strongly enriched in LREE and depleted in HREE, and have bulk Nb/Ta mass ratios between 100 and 1000 (Risedorf 2023).

The main focus of the present study is to revisit the mineralogy of niobium in the Sheep Creek and Woods Creek carbonatites. A secondary objective is to obtain new radiometric dates on zircon that coexists with the Nb-REE mineralization.

2 Methodology

Samples of Nb-rich carbonatite were collected from dumps at the Adit 3 location at Sheep Creek, and the Rocky Point #5 occurrence at Woods Creek (Fig. 1). Polished 1"-round mounts (n = 5) were examined by scanning electron microscopy-energy dispersive spectroscopy (SEM-EDS) at Montana Tech, using a Tescan MIRA 3-TIMA GMU field emission scanning electron microscope (FE-SEM) and Tescan Integrated Mineral Analysis (TIMA) software. The same samples were sent to the U.S. Geological Survey Denver Microbeam Laboratory in Colorado for electron probe microanalysis (EPMA). Carbon coated sections were analyzed on a JEOL 8530F Plus operated at 20 kv, 20 nA, 1 µm defocused spot, peak count times ranging from 20-60 seconds depending on predicted concentrations and mean atomic number backgrounds. Natural and synthetic minerals, and oxides were used as primary standards. X-ray intensity maps were collected at 20 kV, 100 nA, 1 µm step, and 20 msec dwell.

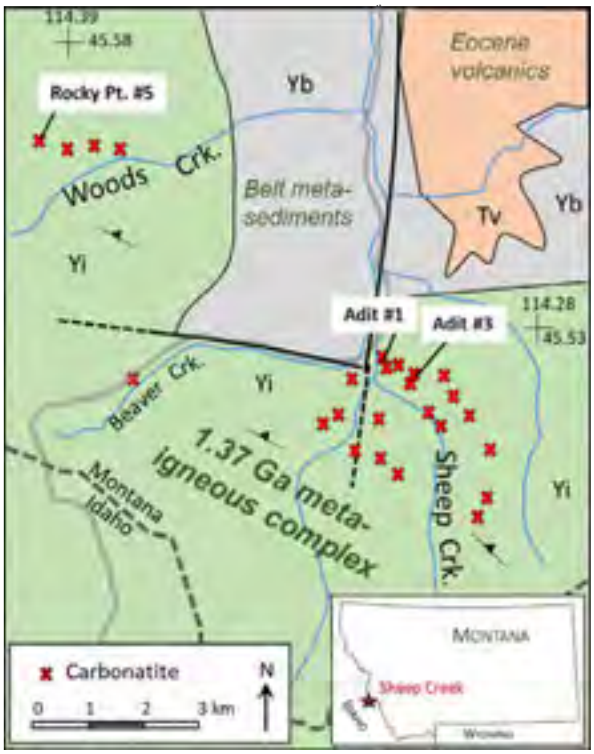


Figure 1. Simplified geologic map of the Sheep Creek area, showing the location of the deposits discussed in the text. Geology modified from Berg and Lonn, 1996. Yb = Clastic sedimentary rocks of the Belt Supergroup; Yi = Bimodal meta-igneous complex; Tv = Eocene volcanics.

One large (200 µm) zircon crystal intergrown with Nb-REE minerals was dated by U-Pb methods using LA-ICP-MS at the USGS LTRACE lab. A Resolution SE 155 ablation system (193 nm) was coupled to an Agilent 8900 ICP-MS and 3.5 ml/min N_2 was added to the Ar to increase sensitivity. A 20 µm spot was used to ablate zircon at 5 Hz and 2.2 J/cm^2 for 30 seconds. The 91500 zircon was used to calibrate U/Pb ratios for age calculation.

3 Results and Discussion

The following Nb-rich minerals were identified from the Sheep Creek and Woods Creek samples: columbite-(Fe), nioboaeschynite-(Ce), baotite, niobobaotite, Nb-bearing chevkinite-(Ce), fergusonite-(Nd), and two varieties of TiO_2 rich in Nb and Fe, herein labelled rutile-I and rutile-II. Representative chemical formulae (based on EPMA data) for each phase are summarized in Table 1. Other minerals closely associated with the Nb-rich assemblages include ferroan dolomite, calcite, baryte, apatite, phlogopite, actinolite, quartz, celsian, allanite-(Ce), and monazite-(Ce), with lesser ilmenite, Fe-oxide, and zircon. Although fersmite was previously reported from Sheep Creek (Hess and Trumpour 1959), this mineral was not found in our study.

Table 1. Representative chemical formulae for Nb-rich minerals examined in this study.

Mineral	Formula
columbite	$(Fe^{II}_{0.86}Mg_{0.11}Mn_{0.04})(Nb_{1.83}Ti_{0.19})O_6$
aeschynite	$(Ce_{0.85}La_{0.20}Nd_{0.18}Pr_{0.04}Sm_{0.03}Gd_{0.01}Ca_{0.31}Th_{0.03}Fe_{0.04})(Nb_{1.23}Ti_{0.77})O_6$
baotite	$(Ba_{3.8}Sr_{0.1})(Ti_{3.3}Nb_{3.0}Fe_{1.5}V_{0.1})O_{16}(SiO_3)_4Cl$
chevkinite	$(Ce_{2.0}La_{1.2}Pr_{0.5}Nd_{0.2})(Ti_{1.9}Fe^{III}_{1.7}Fe^{II}_{0.3}Nb_{0.4}Ca_{0.2}Mg_{0.2})O_8(Si_2O_7)_2$
fergusonite	$(Nd_{0.31}Ce_{0.22}Y_{0.08}Sm_{0.07}Pr_{0.07}La_{0.05}Gd_{0.04}Ca_{0.13})(Nb_{0.96}W_{0.07})O_4$
rutile-I	$Ti_{0.37}Nb_{0.34}Fe^{III}_{0.22}Fe^{II}_{0.05}O_2$
rutile-II	$Ti_{0.71}Nb_{0.16}Fe^{III}_{0.11}Fe^{II}_{0.03}O_2$

Sample “SC-18-21a” from the Adit #3 location at Sheep Creek serves as a good example to illustrate textural relationships between the Nb-rich minerals, the REE-minerals, and the matrix minerals (Fig. 2).

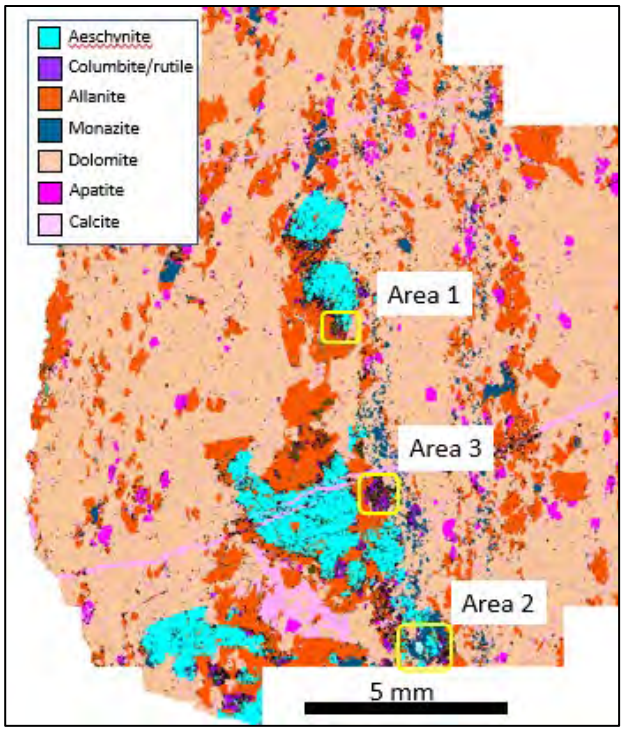


Figure 2. Automated SEM-EDS phase map (false-color) of the SC-18-21a sample. Areas outlined in yellow are shown in more detail below.

Figure 3A shows detail at the edge of one of the nioboaeschynite grains in Figure 2. The aeschynite is replaced around the edges by columbite + monazite + allanite + rutile-II. The zircon crystal used for U-Pb dating (Fig. 3B) is surrounded by coarse monazite and aeschynite, as well as a fine-grained intergrowth of columbite + allanite + rutile-I + rutile-II. We hypothesize that this intergrowth was originally a single phase – rutile-I – which subsequently broke down (partially) to rutile-II + columbite, with excess REE fixed as allanite and/or monazite. A similar fine-grained intergrowth is shown in more detail in Figure 4. We hypothesize that the region outlined in Figure 4 was originally a single grain of rutile-I. Some of this phase remains, while some has broken down to columbite + rutile II.

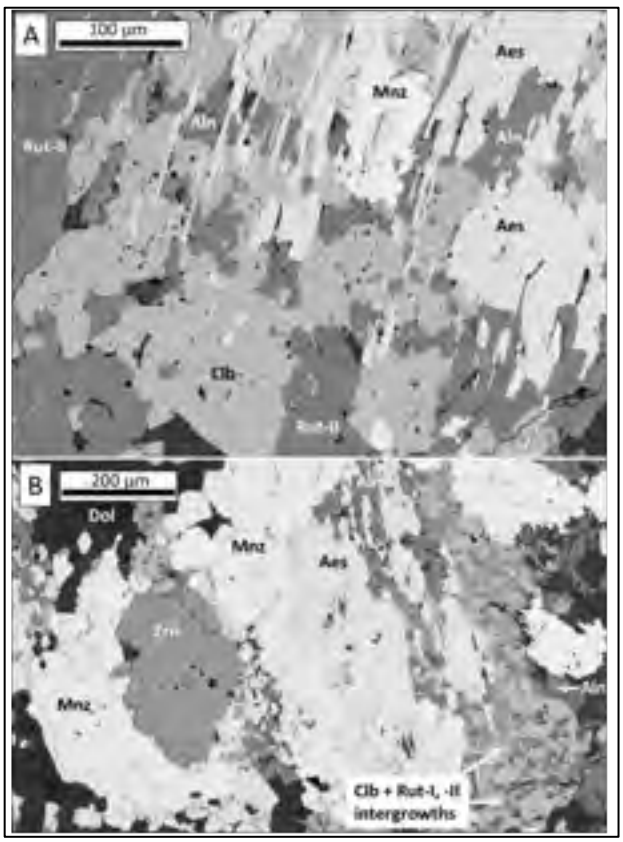


Figure 3. SEM-BSE images of Area 1 (A), and Area 2 (B) marked on Figure 2. Abbreviations: Aln = allanite; Mnz = monazite; Aes = nioboaeschynite; Rut-I = rutile phase I; Rut-2 = rutile phase 2; Clb = columbite; Dol = dolomite.

Phase relationships between the Nb-rich minerals are explored further with the help of a ternary Ti-Nb-Fe diagram (Fig. 5). Rutile analyses from this study (n = 80) define two linear arrays – i.e., rutile-I and rutile-II - separated by a compositional gap. The same gap exists for samples collected from Sheep Creek and from Woods Creek. We propose that the Nb-Fe-rich Rutile I phase was an early mineral that subsequently broke down to the ternary assemblage columbite + rutile-II + Fe-oxide (± ilmenite). Indeed, small grains of Fe-oxide and ilmenite are shown in Figure 4.

Figure 5 can also help to understand the textures shown in Figure 3A. If we assume for the moment

that nioboaeschynite co-existed with rutile-I in the original assemblage, then the intergrowth of columbite + rutile-II could have been the result of a tie-line switch. In fact, the reaction is not this simple, since nioboaeschynite contains REE, and therefore plots off the ternary diagram.

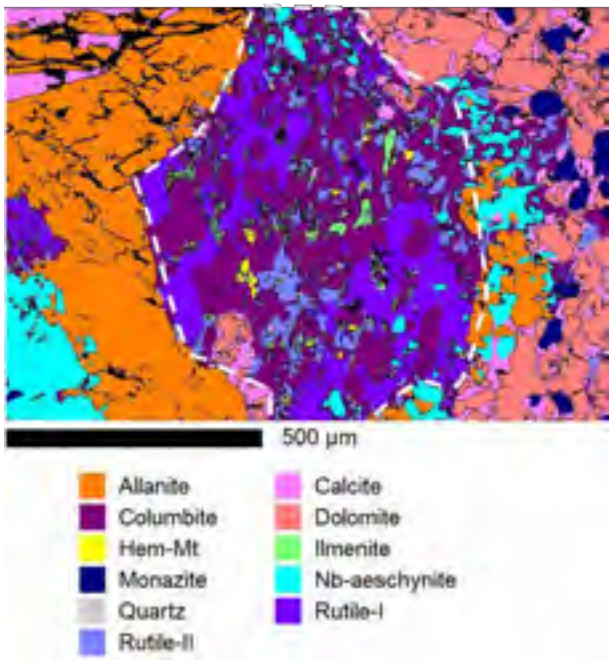


Figure 4. EPMA phase map for Area 3 of Figure 2. The inferred original shape of a single "rutile I" grain is shown by white dashes.

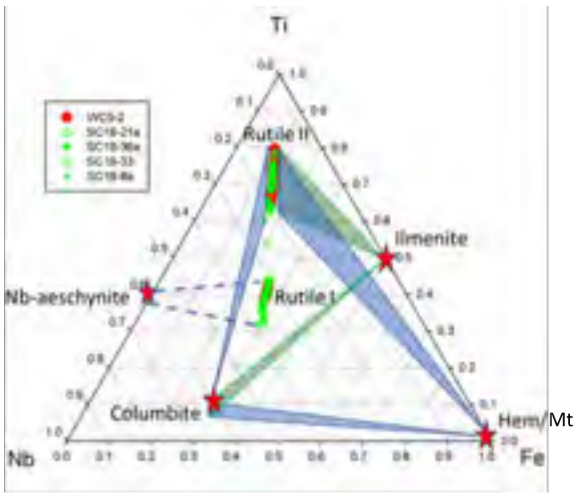


Figure 5. EPMA analyses of Nb-rich minerals from Sheep Creek projected onto a Ti-Nb-Fe ternary (atomic %). Green symbols are analyses from the Adit #3 location (Sheep Creek), whereas red samples are from Woods Creek. Shaded regions represent two-phase fields. The dashed lines show a possible early assemblage of rutile 1 + nioboaeschynite.

A plot of X_{Nb} vs. X_{Ti} (Figure 6; X = mole fraction) emphasizes the linear compositional trends for both rutile-I and rutile-II, as well as the compositional gap that separates them. Five of the rutile-1 analyses have $X_{Nb} > X_{Ti}$, which indicates the possible existence of a new mineral, following current IMA conventions. Although Nb-bearing rutile is relatively common, only one other occurrence of rutile with $X_{Nb} > X_{Ti}$ could be found in the literature (Černý et al. 1981).

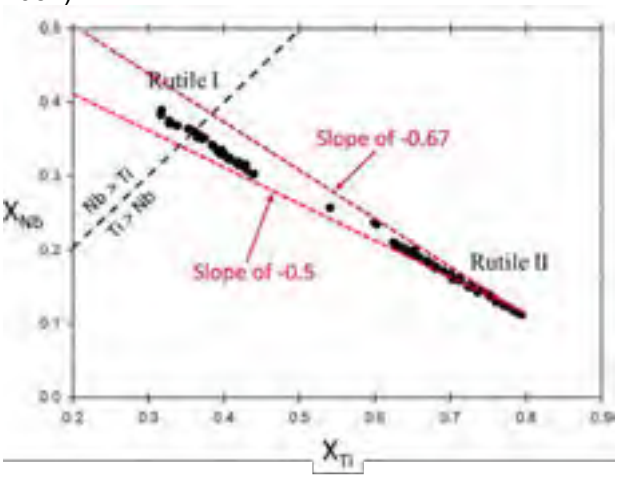


Figure 6. Mole fraction of Nb vs. Ti for all types of rutile analyzed by EPMA. Grains with $X_{Nb} > X_{Ti}$ could be classified as a new mineral following IMA conventions.

Niobium can enter the TiO_2 structure by coupled substitution with Fe^{3+} or Fe^{2+}, as shown by the following reactions (Werner and Cook 2001):

$2Ti^{4+} \leftrightarrow Nb^{5+} + Fe^{3+}$ (i)
$3Ti^{4+} \leftrightarrow 2Nb^{5+} + Fe^{2+}$ (ii)

A host of other ions could also be involved, e.g., Ta^{5+}, Al^{3+}, V^{3+}, $YREE^{3+}$, Mn^{2+}, Mg^{2+}, Sr^{2+}, or Ba^{2+}. Although all of these elements were detected by EPMA, only Ti, Nb, and Fe are present at mole % levels. Based on reactions (i) and (ii), the data in Figure 6 should have slopes of -1/2 or -2/3, respectively. The data plot between these slopes, indicating that a mix of Fe^{3+} and Fe^{2+} is present. Both Fe^{2+} and Fe^{3+} were needed to achieve overall charge balance for the EPMA analyses (Table 1).

Baotite was first described from Sheep Creek by Heinrich et al. (1962), although no chemical analysis was given. In the samples examined in this study, baotite most commonly occurs as rounded inclusions or small patches in columbite, or as irregular grains in baryte-rich segregations. Of the 27 EPMA analyses performed, 14 (roughly half) satisfy the condition $X_{Nb} > X_{Ti}$, which would indicate the presence of the extremely rare mineral, niobobaotite (only 2 localities worldwide are listed on the Mindat database as of Feb. 2025). The average formula we obtained for this phase has Ti slightly exceeding Nb on an atomic basis (Table 1).

Chevkinite-(Ce) was found in one sample (SC-18-22) where it is intergrown with allanite and minor nioboaeschynite-(Ce) (Fig. 7). Although chevkinite is not typically a Nb-rich mineral, the grains in this sample contained up to 6.5 wt% Nb_2O_5 (average 4.0 wt% Nb_2O_5, n = 8). Dudás and Chatterjee (2022) reported a sample of chevkinite from Sheep Creek that contained 10 wt% Nb_2O_5 (EPMA -WDS analyses), and concluded that Sheep Creek has some of the most Nb-rich chevkinite specimens, worldwide.

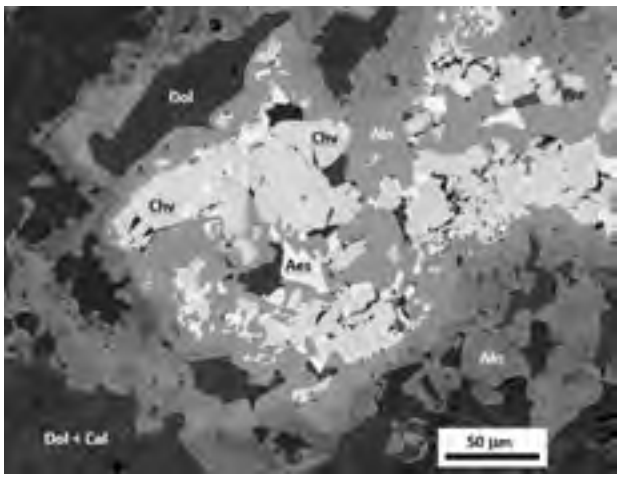


Figure 7. EPMA-BSE image of a chevkinite (Chv)-rich zone in SC-18-22. Aes = nioboaeschynite; aln = allanite; Dol = dolomite; Cal = calcite. Zonation in Aln is due to varying REE content.

The zircon crystal (Fig. 3B) was analyzed via 11 laser points from which a ^{207}Pb-corrected $^{206}Pb/^{238}U$ age of 116 ± 2.0 Ma (95% conf.) was obtained. This age is within the range of Th-Pb dates obtained from LA-ICP-MS analyses of monazite grains from the Adit #1 and Adit #3 carbonatite veins (~ 150 to ~ 70 Ma) previously reported by Gammons et al. (2023), as well as Re-Os dates (109 Ma and 149 Ma) of molybdenite samples from two separate carbonatite bodies reported by Risedorf (2023). Although details are yet to be worked out, the new zircon data corroborate our earlier findings that the carbonatites of Sheep Creek are most likely of early Cretaceous age. This age does not correlate with any known episode of alkaline magmatism in southwest Montana. This part of Montana and neighbouring Idaho was experiencing regional metamorphism and deformation associated with the Sevier/Laramide orogenies at this time. Thus, the Sheep Creek deposits do not fit standard models of carbonatite emplacement associated with crustal extension. It is possible that localized zones of extension or transtension developed during the protracted orogenic period. Another possibility is that the Sheep Creek "vein-dike" deposits were derived by remelting of buried carbonatite bodies during regional metamorphism. These and other questions provide fertile ground for future research.

4 Conclusions

The REE-Nb deposits of the Sheep Creek area have a rich mineralogy that includes many rare phases such as niobobaotite and Nb-rich TiO_2 (this study), as well as several uncommon REE-rich minerals (Heinrich and Levinson 1961; Gammons et al. 2024). The deposits have yet to be drilled, so it is premature to speculate as to whether they could be of economic importance. More geochronological and isotopic work is needed to place the Sheep Creek district (and its neighbour to the south, the Mineral Hill district of Idaho) within the broader context of plate tectonic and magmatic events that took place during the Mesozoic Era in the northern U.S. Cordillera.

Acknowledgements and Disclaimers

This research was supported by a grant from the Army Research Laboratory (ARL) to Montana Tech. The views and conclusions contained in this document are those of the authors, and should not be interpreted as representing the official policies, either expressed or implied, of the ARL. We thank Gary Wyss at Montana Tech for his help with the SEM-EDS work, and the late Francis Dudás for his friendship and encouragement to delve deeply into the mineralogy of the Sheep Creek deposits. We also thank U.S. Critical Materials for allowing access to the deposits.

Any use of trade, firm, or product names is for descriptive purposes only and does not imply endorsement by the U.S. Government. These data are preliminary or provisional and are subject to revision. They are being provided to meet the need for timely best science. The data have not received final approval by the U.S. Geological Survey (USGS) and are provided on the condition that neither the USGS nor the U.S. Government shall be held liable for any damages resulting from the authorized or unauthorized use of the data.

References

Berg RB, Lonn JD (1996) Preliminary geologic map of the Nez Perce Pass 30' x 60' quadrangle, Montana. Mont Bur Mines Geol Open-File Report 339.

Černý P, Paul BJ, Hawthorne FC, Chapman R (1981) A niobian rutile — disordered columbite intergrowth from the Huron Claim pegmatite, southeastern Manitoba. Can Mineral 19:541–548.

Crowley FA (1960) Columbium-rare-earth deposits, southern Ravalli County, Montana. Mont Bur Mines Geol Bull 18.

Doughty PT, Chamberlain KR (1996) Salmon River Arch revisited: new evidence for 1370 Ma rifting near the end of deposition in the Middle Proterozoic Belt basin. Can J Earth Sci 33:1037-1052.

Dudás F, Chatterjee N (2022) Niobian chevkinite and other niobium minerals from Sheep Creek, Montana. Mineral News, March, 2022, 5-11.

Gammons CH, Risedorf S, Gary M, Stein H, Thompson JA (2023) Age of carbonatite-related REE-Nb mineralization in the Sheep Creek district, southern Ravalli County, Montana. Northwest Geol 52:83-88.

Gammons CH, Risedorf S, Wyss G, Lowers H (2024) Occurrences of the rare, REE minerals daqingshanite, törnebohmite, biraite, sahamalite, and ferriperbøeite from the Sheep Creek area, Montana, USA. Minerals 14(10): 1047.

Heinrich EW, Levinson AA (1961) Carbonatic niobium-rare earth deposits, Ravalli County, Montana. Am Mineral 46: 1424-1447.

Heinrich EW, Boyer WH, Crowley FA (1962) Baotite (Pao-t'ou-k'uang) from Ravalli County, Montana. Am Mineral 47: 987-993.

Hess HD, Trumpour HJ (1959) Second occurrence of fersmite. Am Mineral 44:1-8.

Risedorf S (2023) Investigation of the Sheep Creek carbonatites, Ravalli County, Montana. M.S. thesis, Montana Tech, Butte, MT.

Werner M, Cook NJ (2001) Nb-rich brookite from Gross Brukkaros, Namibia: substitution mechanisms and Fe^{2+}/Fe^{3+} ratios. Mineral Mag 65:437-440.

New Perspectives on Hydrothermal Mobilization of Rare Earth Elements (REE) in Carbonatites − Alkaline Systems in New Mexico, USA

Alexander Gysi[1,2], Nicole Hurtig[2], Daniel Harlov[3], Jay M. Thompson[4], Katharina Pfaff[5]
[1]New Mexico Bureau of Geology and Mineral Resources, New Mexico Institute of Mining and Technology, Socorro, NM 87801, USA
[2]Dpt of Earth and Environmental Science, New Mexico Institute of Mining and Technology, Socorro, NM 87801, USA
[3]GeoForschungsZentrum, Telegrafenberg, 14473 Potsdam, Germany
[4]U.S. Geological Survey; Denver Federal Center, Denver, CO 80225, USA
[5]Center to Advance the Science of Exploration to Reclamation in Mining, Dpt of Geology and Geological Engineering, Colorado School of Mines, Golden, Colorado 80401, USA

Abstract. Carbonatites and alkaline-igneous related deposits are among the most important sources of rare earth elements (REE) worldwide. New Mexico contains a series of Cambrian-Ordovician carbonatites, including those in the Lemitar Mountains, and younger Eocene-Oligocene alkaline-igneous related deposits, such as those in the Gallinas Mountains. Most of these deposits have been overprinted by hydrothermal fluid-rock interaction processes during their final evolution stages, and in many instances, these fluids were able to transport, fractionate and enrich the REE in veins and alteration zones. Calcite and/or fluorite are ubiquitous in veins containing REE-bearing minerals such as bastnäsite-(Ce) and apatite. However, the nature of the fluids that transport REE and their overall partitioning behavior in carbonatite and alkaline mineral deposits is unclear. This is why we need to develop new models capable of interpreting the REE signatures in calcite and fluorite, which commonly have multiple generations and form at different stages within a deposit. This study presents a combination of petrographic observations (SEM-based mineralogy and cathodoluminescence), LA-ICP-MS trace element analysis, combined with observations from hydrothermal laboratory experiments. Geochemical modeling of fluid-rock interaction is used to constrain REE mobility in veins and alteration zones in carbonatites and alkaline complexes.

1 Introduction

The REE are classified as critical because of their essential uses in the high-tech and green energy industries (wind turbines, cell phones, batteries, lights, catalysts, etc.). The light REE are essentially produced from carbonatites from the mineral bastnäsite, such as Mountain Pass in CA and Bayan Obo in China, whereas alkaline systems are considered exploration targets for the heavy REE (Smith et al. 2016; Van Gosen et al. 2017).

In REE mineral deposits, hydrothermal calcite, quartz, barite, and fluorite veins are commonly found together with REE minerals such as fluorocarbonates (i.e. bastnäsite, parisite, synchysite) and REE phosphates (i.e., apatite, monazite, xenotime). The hydrothermal alteration zones within and surrounding carbonatites and alkaline igneous complexes include alkali metasomatism, such as the formation of sodic/potassic feldspars (i.e. fenites in carbonatites), and later stage Ca-F metasomatism with the formation of hydrothermal REE-bearing fluorocarbonates or the formation of phosphates such as apatite and monazite/xenotime (Gysi and Williams-Jones 2013; Gysi et al. 2016; Elliott et al. 2018; Verplanck et al. 2014, 2022).

New Mexico hosts a series of magmatic-hydrothermal REE-bearing occurrences spanning Proterozoic to Eocene-Oligocene rock formations; mainly carbonatites and alkaline igneous systems (McLemore 2015, 2018). The Lemitar Mountains carbonatite displays fenitization, chloritization, hematization, silicification, and a series of hydrothermal veins that include several generations of apatite, calcite and fluorite (McLemore 1987, Ruggles 2024). The Gallinas Mountains REE-fluorite hydrothermal vein/breccia deposit is associated with syenite/trachyte intrusives and displays a complex history of barite, fluorite, bastnäsite and calcite veining, and the formation of volcanic and hydrothermal breccia pipes mineralized with bastnäsite (McLemore et al. 2021, Owen 2024, Velmani et al. 2024).

In this study, we explore the role of these hydrothermal fluids in controlling the mobility of REE. Gallinas and Lemitar Mountains veins and alteration zones are studied using automated mineralogy and geochemical modeling of fluid-rock interaction. Hydrothermal laboratory experiments are further used to constrain the controls of fluid-mineral interaction on REE partitioning, fractionation and enrichment in hydrothermal veins.

2 Methods

Automated mineralogy was conducted at the department of Geology and Geological Engineering, Colorado School of Mines (CSM), using a TESCAN Integrated Mineral Analyzer on selected thin sections from the Gallinas and Lemitar Mountains. The instrument is a TESCAN-VEGA-3 variable pressure SEM equipped with two EDDAX spectrometers operated at an accelerating voltage of 25 kV, a beam intensity of 14 and a step distance of 25 µm.

Hydrothermal low temperature fluorite-fluid REE partitioning experiments were carried out in the Ore Deposits and Critical Minerals experimental laboratory at New Mexico Tech (NMT). The experiments were carried out in Teflon-lined batch-

type reactors (Parr 4744) between 100−250 °C at saturated water vapor pressure. Natural fluorite crystals from the Surprise mine (Cooke's Peak, NM) were reacted with aqueous solutions of variable starting pH (2–10, HCl/NaOH), salinities (0 and 15 wt.% NaCl), and initial REE concentrations (undoped to 0.5 ppm). More details of the experimental method is given in Payne et al. (2023). High temperature and pressure fluorite-fluid experiments were conducted at GeoForschungsZentrum Potsdam using cold-seal pressure vessels. The experiments were conducted in gold capsules between 100-200 MPa and at 400−600 °C using similar starting solutions as the low temperature experiments but with varying initial Ce-Y concentrations (undoped to 1 ppm).

Crystal zoning and reaction textures were studied in the reacted fluorite crystals using a TESCAN MIRA3 LMH Schottky field-emission SEM at the department of Geology and Geological Engineering (CSM). LA-ICP-MS analyses were performed on fluorite crystals at the U.S. Geological Survey LTRACE laboratory at the Denver Federal Center. The analytical instrument consists of a Photon Machines Analyte G2 laser ablation system (193 nm and 4 ns excimer) coupled to an Agilent 8900 ICP-MS. Ablation was carried out using a 20 µm diameter spot size, a laser energy density of 1.3 J/cm^2 and a pulse frequency of 5 pulses per second. Additional backscattered electron images and WDS element maps were produces using a Cameca 4-spectrometer SX-100 electron microprobe at the New Mexico Bureau of Geology and Mineral Resources (NMT).

Geochemical modeling was conducted using GEM-Selektor (https://gems.web.psi.ch) and the MINES thermodynamic database (Gysi et al. 2023) to simulate the alteration styles (e.g. alkali metasomatism, hematization, chloritization, etc.) and the replacement reactions in calcite-fluorite and REE fluorocarbonate veins associated with Ca-F metasomatism. The simulations were carried out in the Ca-Na-REE-F-Cl-C-H-O system at 400−600 ºC and 0.5−2 kbar with an acidic REE-F-Cl-bearing (0.5 mol/kg HCl/HF) and an alkaline Na-F-Cl-OH-bearing starting fluids (0.5 mol/kg NaOH/NaF/NaCl). Two types of simulations were conducted including a multipass leaching model and a 1-D reactive mass transport model.

3 Results

3.1 Field vein petrography and metasomatism

The Gallinas Mountains hydrothermal REE-fluorite vein/breccia deposit displays three fluorite vein types with complex fluorite microtextures and CL signatures (Owen 2024, Velmani et al. 2024). These include: Type I barite-fluorite (±hematite, quartz) veins overprinted by dissolution texture, microbreccias, and infills of later fluorite and/or calcite; Type II bastnäsite-fluorite (±quartz, calcite) veins occurring as infills in breccias, fine grained disseminated veinlets, and large bastnäsite crystals; Type III fluorite-calcite veins crosscut or occur as interstitial infills to Type I-II veins and in fractured host rocks. Automated mineralogy thin section maps (Fig. 1) indicate that some of the fluorite veins result in the formation of K-feldspar alteration halos at the contact to the host rocks, with dissolution of barite crystals, and an overall progression of fluorite veins ± barite > bastnäsite > calcite. The alteration zones observed in Gallinas Mountains, suggest that aqueous fluids transport the following components that need to be incorporated in geochemical models: Ca, REE, Si, NaCl/KCl, SO_4^{2-}, F^-, CO_3^{2-}.

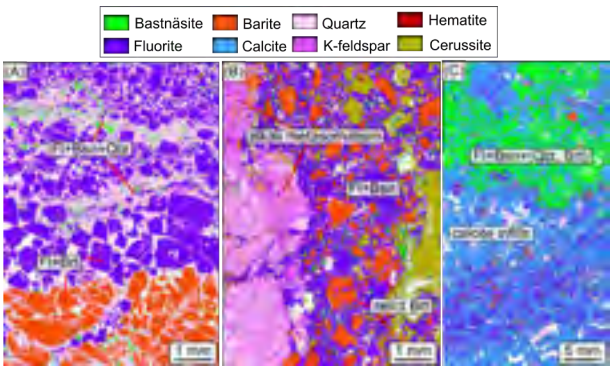


Figure 1. Automated mineralogy maps of bastnäsite-fluorite veins and breccias from the Gallinas Mountains fluorite-REE deposits in NM. The earliest veins/breccia consist of Brt-Fl veins (type I) followed by Bsn-Fl (type II) and Fl-Cal veins (type III). Interaction of these fluids with the host rocks (sandstones and trachyte) results in alkali metasomatism. Brt: barite, Bsn: bastnäsite, Fl: fluorite, Qtz: quartz, Cal: calcite.

The Lemitar Mountains carbonatite comprises calcio- and magnesio-carbonatites with silicate and oxide xenoliths (McLemore 1987, Ackerman et al. 2021, Ruggles 2024). The calcio-carbonatite (i.e. sövite) studied here consists of calcite with xenocrysts of phlogopite, magnetite, baddeleyite, columbite-Fe and apatite, and hydrothermal hematite, chlorite, calcite, quartz veinlets. Veins rimming and/or crosscutting the carbonatites and the host metadiorite include three major types (Ruggles, 2024): Type I Qtz-Fsp veins (i.e., Qtz-Ab and Qtz-Kfs-Chl veins); Type II (hematite)-chlorite-quartz-calcite veins; Type III (barite)-fluorite-quartz-calcite veins. Figure 2 shows the vein types and alteration features of the host rocks surrounding the carbonatites. Type II (hematite)-chlorite-quartz-calcite veins crosscut the metadiorite and result in the formation of potassic fenitization, silicification, and chloritization of the host rocks. Hydrothermal REE-bearing apatite occurs close to these veins, for example in chloritized host rocks (Fig. 2B) and as Ap+Qtz assemblages in association with potassic fenitization (Fig. 2C). The REE are mainly hosted in the apatite and hydrothermal fluorocarbonates. The presence of hydrothermal zircon and pyrochlore has also been observed in veins and alteration zones (Ruggle, 2024). The alteration assemblages observed in Lemitar Mountains suggest that the

fluids transport the following components: Ca, REE, Zr, Si, NaCl/KCl, Fe, PO_4^{3-}, SO_4^{2-} and CO_3^{2-}. These components are similar to those from the Gallinas Mountains veins but at much lower abundance of F and higher amounts of alkalis, Fe, Si, PO_4^{3-} and CO_3^{2-}. This is reflected by the more pervasive mineralization of chlorite, hematite, quartz, and calcite associated with the carbonatites in the Lemitar Mountains.

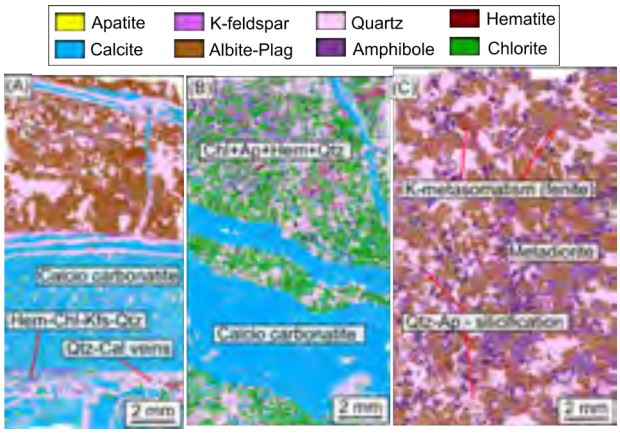


Figure 2. Automated mineralogy maps of carbonatites, hydrothermal veins, and host rock alteration from the Lemitar Mountains carbonatite deposit in NM. Hem: hematite, Chl: chlorite, Kfs: K-feldspar, Qtz: quartz, Cal: calcite, Ap: apatite.

3.3 Experimental results

Fluorite crystals reacted with both acidic and alkaline solutions are used to better understand the mobility of REE in hydrothermal solutions. Fluorite reacted at 400 and 600 °C displays metasomatized reaction rims with variable enrichment/depletion of the REE. Backscattered images and element maps (Fig. 3) reveal that fluorite reacted with a 1 ppm Ce-Y-doped solution displays a surface dissolution texture and reprecipitation of Y-enriched channels or veinlets. Fluorite crystals reacted with alkaline fluids in the non-doped experiments display a leaching texture with a REE-depletion at the rims and enrichment in the core of the crystals (Fig. 4). These results suggest that both acidic and alkaline fluids are capable of dissolving fluorite crystal surfaces, which is in line with our previous low temperature experiments (Payne et al. 2023).

Our interpretation is that the REE-doped fluids form REE-enriched fluorite crystal growth zones due to the low solubility of fluorite. This indicates that metasomatism of fluorite can potentially further concentrate the REE. This contrasts with the behavior of the REE in the undoped experiments, where the REE are leached from the fluorite crystal surfaces. The latter indicates a potential mechanism of REE remobilization despite the low solubility of fluorite (Payne et al. 2023). Further investigations are needed to quantify how much of the REE can be transported and concentrated from such coupled fluorite dissolution-reprecipitation processes. Similar mechanisms apply to other minerals (e.g. apatite, calcite) which can either host the REE and/or release anions (PO_4^{3-} and CO_3^{2-}) that can contribute to the precipitation of insoluble REE minerals (e.g. bastnäsite and monazite/xenotime).

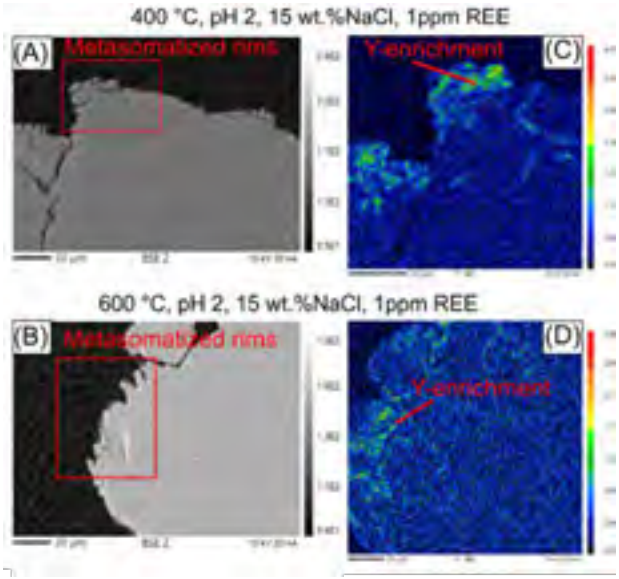


Figure 3. (A-B) EPMA backscattered images and (C-D) WDS Y element maps of fluorite reacted experimentally in acidic fluids at 400 and 600 °C, in a starting HCl fluid with pH 2, 15 wt.% NaCl, and doped with 1 ppm Y and Ce. The overall element distribution suggests the formation of rims on the fluorite crystal surface enriched in Y due to fluid-mineral metasomatism.

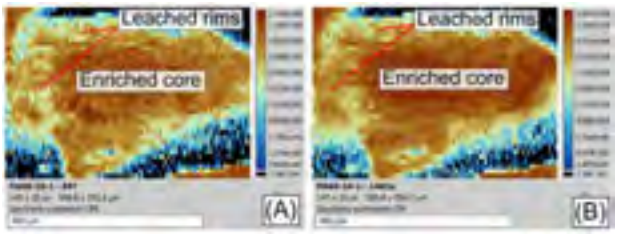


Figure 4. LA-ICP-MS trace element maps of (A) Y and (B) Ce of a fluorite crystal reacted experimentally in an undoped alkaline fluid at 600 °C, in a starting NaOH fluid with pH 10. The overall element distribution suggests REE leaching on the fluorite crystal rims.

3.2 Geochemical modeling

Geochemical modeling was used to determine the controls on REE transport in hydrothermal fluids reacted with a carbonate vein. Figure 5 shows an example of a 1-D reactive transport simulation at 400 °C for an acidic HF-HCl-REE-bearing fluid interacting with calcite. The simulated mineral distribution is shown as a function of distance and increased fluid-vein interaction. The simulations indicate that acidic fluids provide F and REE^{3+} whereas the existing vein provides Ca and CO_3^{2-} to form both fluorite and bastnäsite. Three different vein zones develop in these models including a fluorite, a bastnäsite-fluorite and a bastnäsite-calcite vein, respectively. These results approximate some of the textures observed in the Gallinas Mountains fluorite veins (Fig. 1). In addition, sulfate complexes (SO_4^{2-}) can be considered for REE transport, because barite is present throughout this deposit.

Remobilization of sulfate is evident by an increase in barite dissolution textures in veins containing bastnäsite.

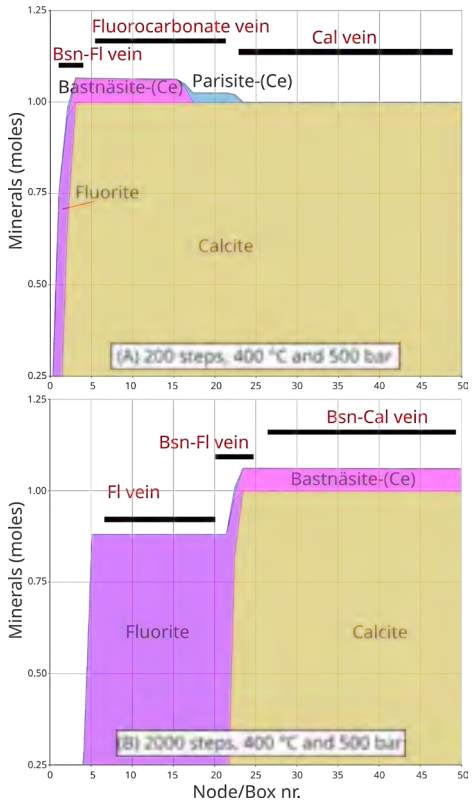


Figure 5. 1-D reactive transport simulations showing the mineralogy in 50 nodes of rock after (a) 200 steps and (b) 2000 steps, representing the number of fluid "waves" flushed through all the calcite boxes.

3 Conclusions

There is strong evidence for the importance of fluid-rock interaction for REE transport in critical mineral deposits. Examples from the Gallinas and Lemitar Mountains in NM, indicate that the components that are transported in hydrothermal fluids include: Ca, REE, Si, NaCl/KCl, Fe, PO_4^{3-}, F^-, SO_4^{2-} and CO_3^{2-}. A major difference between alkaline and carbonatite systems is the higher concentrations of alkalis, Si, and P in carbonatite-related fluids, and the predominance of Ca-F metasomatism in alkaline deposits. Fluorite metasomatism experiments indicate that despite its low solubility, dissolution-reprecipitation of fluorite can lead to either depleted or enriched REE-bearing fluorite veins. Geochemical modeling yields crucial insights on the controls (temperature, pH, ligand activity) of hydrothermal REE mobilization, and permits simulating the formation of alteration zones and veins in natural deposits.

Acknowledgments

The research presented here was supported through a National Science Foundation grant, NSF CAREER EAR-2039674 to APG.

References

Elliott HA, Wall F, Chakhmouradian AR, Siegfried PR, Dahlgren S, Weatherley S, Finch AA, Marks MA, Dowman E, Deady E. (2018) Fenites associated with carbonatite complexes: A review. Ore Geol Rev 93: 38−59. https://doi.org/10.1016/j.oregeorev.2017.12.003

Gysi AP, Hurtig NC., Pan R, Miron GD., Kulik DA (2023) MINES thermodynamic database, NM Bur Geol Miner Res, version 23. https://doi.org/10.58799/mines-tdb

Gysi AP, Williams-Jones AE, Collins P. (2016) Lithogeochemical vectors for hydrothermal processes in the Strange Lake peralkaline granitic REE-Zr-Nb deposit. Econ Geol 111: 1241−76. https://doi.org/10.2113/econgeo.111.5.1241

Gysi AP, Williams-Jones AE (2013) Hydrothermal mobilization of pegmatite-hosted REE and Zr at Strange Lake, Canada: A reaction path model. Geochim Cosmochim Acta 122: 324-352. https://doi.org/10.1016/j.gca.2013.08.031

McLemore V, Kelley S, Zimmerer M, Owen E, Haft EB, Cantrell T, Gysi A, Dietz H, Cherotich S, Trivitt A (2021) Geology and mineral deposits of the Gallinas Mountains, Lincoln and Torrance counties, New Mexico. NM Bur Geol Miner Res, Open-file Report 617: 164 p.

Mclemore VT (2015) Rare Earth Elements (REE) Deposits in New Mexico: Update. NM Geol 37: 59–69. https://doi.org/10.58799/NMG-v37n3.59

McLemore VT (1987) Geology and regional implications of carbonatites in the Lemitar Mountains, central New Mexico. J Geol 95, 255-270.

McLemore VT (2018) Rare earth elements (REE) deposits associated with great plain margin deposits (alkaline-related), southwestern united states and eastern Mexico. Res 7: 1–44. https://doi.org/10.3390/resources7010008

Owen E (2024) Mineral paragenesis and geochemistry of hydrothermal REE-F bearing veins and breccias in the Gallinas Mountains, New Mexico. M.Sc. Thesis, NMT.

Payne MR, Gysi AP, Hurtig NC. (2023) Hydrothermal fluorite solubility experiments and mobility of REE in acidic to alkaline solutions from 100 to 250 °C. Chem Geol 617:121256. https://doi.org/10.1016/j.chemgeo.2022.121256

Ruggles EL (2024) Mineral paragenesis, mineral chemistry, and rare earth element mobility related to the magmatic-hydrothermal transition of the Lemitar Mountains Carbonatites, New Mexico. M.Sc. thesis, NMT.

Smith MP, Moore K, Kavecsánszki D, Finch AA, Kynicky J, Wall F. (2016) From mantle to critical zone: A review of large and giant sized deposits of the rare earth elements. Geosci Front 7: 315−334. https://doi.org/10.1016/j.gsf.2015.12.006

Van Gosen BS, Verplanck PL, Seal RR, Long KR, Gambogi J, (2017) Rare-earth elements, chap. O of Schulz, K.J., DeYoung JH., Seal RR, Bradley DC, eds., Critical mineral resources of the United States − Economic and environmental geology and prospects for future supply: USGS Prof Pap 1802, p. O1–O31, https://doi.org/10.3133/pp1802O.

Velmani A., Gysi AP, Hurtig NC (2024) Hydrothermal rare earth element partitioning into fluorite: A fluid inclusion study from the Gallinas Mountains REE-bearing fluorite deposit in New Mexico. ThermoCon 2024, Socorro, NM. NM Bur Geol Miner Res Bull 166: 65–66. https://doi.org/10.58799/B-166

Verplanck PL, Van Gosen BS, Seal RR, McCafferty AE (2014) A deposit model for carbonatite and peralkaline intrusion-related rare earth element deposits: USGS Sci Inv Rep 2010–5070-J, 58 p., http://dx.doi.org/10.3133/sir20105070J.

Verplanck PL, Farmer GL, Kettler RM, Lowers HA, Johnson CA, Koenig AE, Blessington MJ. Petrogenesis and rare earth element mineralization of the Elk Creek carbonatite, Nebraska, USA (2022) Ore Geol Rev 146:104953. https://doi.org/10.1016/j.oregeorev.2022.104953

Fingerprinting magmatic REE deposit sources with zircon petrochronology

Ian W. Hillenbrand[1], Erin K. Benson[2], Kathryn Watts[2], and Jay Thompson[3]
[1] U.S. Geological Survey, Geosciences and Environmental Change Science Center, Denver, CO 80225, USA
[2]U.S. Geological Survey, Geology, Minerals, Energy, and Geophysics Science Center, Spokane, WA 99201, USA
[3]U.S. Geological Survey, Geology, Geophysics, and Geochemistry Science Center, Denver, CO 80225, USA

Abstract. Carbonatites and associated alkaline silicate rocks are of considerable economic interest due to their enrichments in rare earth elements. The petrogenesis and source(s) of these complexes, however, are poorly understood. Models propose either mantle plume-derived carbon-rich melts or a mantle source enriched by subduction-related metasomatism. We use zircon trace elements to fingerprint carbonatite-alkaline complex sources, focusing on the economically significant 1.4 Ga Mountain Pass intrusive suite (MPIS). Autocrystic zircon from MPIS alkaline silicate rocks are enriched in Th and U relative to Nb suggesting a subduction influenced, oxidized source region. Lower Sc/Yb, higher Ti concentrations, and the absence of Eu anomalies in autocrystic zircon suggest derivation from a less hydrous, hotter, and deeper mantle source relative to arc-related 1.8–1.6 Ga inherited zircon. These data are best explained by syn- to post-collisional Mesoproterozoic reactivation of a subduction-metasomatized mantle source. The source and tectonic setting of the MPIS contrasts with Mesoproterozoic Gifford Creek and Bayan Obo carbonatites which exhibit plume-like compositions and are associated with rifts, suggesting different sources and tectonic settings for these economically significant deposits. We demonstrate that zircon petrochronology is a robust method for distinguishing carbonatite sources and can inform more targeted exploration strategies for critical mineral resources.

1 Introduction

The majority of primary rare earth element (REE) deposits are hosted by carbonatites and their associated alkaline silicate complexes (Castor 2008; Chakhmouradian and Wall 2012; Gibson et al. 2024).These relatively rare igneous rocks are commonly highly enriched in critical minerals such as REE and host Earth's largest REE ore deposits such as Mountain Pass (USA) and Bayan Obo (China) (Castor 2008; Gibson et al. 2024). Commonly applied petrogenetic models for carbonatites and associated alkaline silicate magmas involve derivation from a carbon-enriched, ocean-island basalt-like mantle, possibly associated with mantle plumes, or from a mantle source region that was enriched by subduction (Mitchell 2005). Differentiating between the sources of these magmatic REE deposits is challenging due to difficulties with alteration which obscures their primary whole-rock compositions (Yaxley et al. 2022).

Zircon is a widely used geochronometer and retains an archive of geochemical and magmatic processes and sources. Zircon trace elements (TE), particularly Th, U, Nb, Sc, and Yb can discriminate between zircon derived from depleted mantle-type, ocean-island-like enriched mantle, and arc-type sources in modern plate-tectonic regimes (Grimes et al. 2015). Zircon can also constrain intensive parameters such as crystallization temperature (Ferry and Watson 2007), oxidation state (Zou et al. 2024), and pressure (Moreira et al. 2023). Zircon is commonly resistant to alteration by weathering, hydrothermal processes, and diffusive exchange making zircon petrochronology a particularly attractive tool for investigating magmatic sources in deep time or highly altered systems.

With the goal of investigating the sources and petrogenesis of carbonatites and their associated alkaline silicate complexes, we apply a novel approach involving zircon petrochronology. We demonstrate the utility of this approach with detailed investigation of the Mesoproterozoic Mountain Pass intrusive suite (MPIS), the most economically important REE deposit in the United States. Then, we apply this methodology to a global zircon TE dataset to further demonstrate the utility of this method as an exploration tool for fingerprinting magmatic REE deposits and their sources.

2 Materials and Methods

The MPIS includes seven ultrapotassic alkaline silicate stocks, one carbonatite stock, and compositionally diverse dikes (Castor 2008; Watts et al. 2022).These genetically related ca. 1.4 Ga rocks intrude a complex assemblage of 1.8–1.6 Ga basement gneisses of the Mojave Province.

We examined inherited and autocrystic zircon grains from alkaline silicate rocks in the MPIS, primarily from shonkinite and syenite. These units have been shown to have the strongest mantle affinity of the alkaline magmas in the MPIS and may have been contemporaneous with carbonatite magmatism (Poletti et al. 2016; Watts et al. 2022). U-Pb ages and some TEs were obtained by sensitive high resolution ion microprobe-reverse geometry (SHRIMP-RG) as well as measuring stable O isotopic compositions by secondary ion mass spectrometry (Watts et al. 2022). Benson et al. (2025) then determined Lu-Hf isotopic compositions by laser ablation inductively coupled plasma mass spectrometry (LA-ICP-MS).

We analyzed autocrystic (1.4 Ga) zircon grains (n=57) and inherited (1.8–1.5 Ga) zircon grains (n=72) by LA-ICP-MS at the U.S. Geological Survey in Denver, CO for TE and U-Pb dates. LA-ICP-MS

spots were placed as close as possible to previous SHRIMP-RG U-Pb and LA-ICP-MS Lu-Hf isotopic analyses. Zircon analyses were filtered for inclusions and open system behavior by (1) using only grains with concordant dates and (2) culling analyses with greater than 1 ppm La.

Oxygen fugacity was estimated using the machine learning oxybarometer of Zou et al (2024) which has a propagated error of ±0.10 log units. Data are reported relative to the ΔFMQ buffer. The $^{176}Lu/^{177}Hf$ ratio was used to estimate zircon source and/or crystallization pressure using the calibration of Moreira et al. (2023).

3 Results

Inherited zircon yield values of -0.5 to +2 relative to ΔFMQ with most falling between +0.5 and +1.5 (Fig. 1A). These grains are also dominantly elevated in Sc/Yb (>0.1) and U/Nb (>30) and plot within the arc-type fields (Fig. 1B-C). Pressure estimates from the Lu/Hf proxy are variable (Fig. 1D). A running average of the calculated pressures indicates a gradual increase from 1.0 to 1.3 GPa between 1.80 and 1.72 Ga. At ca 1.72–1.68 Ga pressures increase markedly to 1.8 GPa and show a tighter range of values (1.3–1.8 GPa). This is consistent with crustal thickening associated with the 1.72–1.68 Ga Ivanpah (Yavapai) orogeny (Wooden and Miller 1990; Hillenbrand et al. 2023).

Autocrystic zircon (1.4 Ga) from the MPIS yield a median of $+1.6^{+0.4}/_{-0.8}$ relative to ΔFMQ (Fig. 1A). Sc/Yb values span the mantle- to arc-type fields while U/Nb values are between 100 and 1000 and fall within the arc field (Fig. 1B-C). Estimated pressures range from 0.5 to 1.6 GPa (Fig. 1D).

Both inherited and autocrystic zircon predominantly plot above the mantle array and within arc-type fields on the U-Nb-Sc-Yb bivariate discrimination diagrams of Grimes et al. (2015) (Fig. 2). Only a few zircons fall within the fields for either depleted or enriched mantle (Fig. 2).

Figure 3A shows that autocrystic MPIS zircon domains have generally higher Ti concentrations and lower Sc/Yb ratios relative to inherited grains. Autocrystic grains largely fall within the amphibole-poor, less hydrous field whereas inherited zircon dominantly plot in the amphibole-saturated, more hydrous field. Similarly, inherited grains yield lower Sc/Yb and an absence of Eu* anomalies (Eu/Eu*≈1) for whereas inherited zircon trend towards higher Sc/Yb and yield negative Eu* (Fig. 3B).

4 Discussion

4.1 Sources and Petrogenesis of the MPIS

Inherited zircon from the MPIS are oxidized (Fig. 1A), plot within arc-type fields (Fig. 1B-C; Fig. 2), and have hydrous sources (Fig. 3) consistent with long-lived Paleoproterozoic subduction in the Mojave Province (Wooden and Miller 1990).

Autocrystic zircon yield higher Ti concentrations, lack an Eu anomaly, and have lower Sc/Yb ratios. This suggests the Mesoproterozoic MPIS was derived from a hotter (Ferry and Watson 2007), deeper (Tang et al. 2021), and less hydrous source than that of the inherited Paleoproterozoic zircon grains. Ti-in-zircon temperatures greater than >800°C, a plagioclase-free (>50 km depth) source, and less hydrous compositions indicate that these zircon grains are unlikely to be derived from arc-related melts. This accords with zircon Lu-Hf isotopic evidence that suggest autocrystic zircon largely record the signature of their mantle source (Benson et al. 2025).

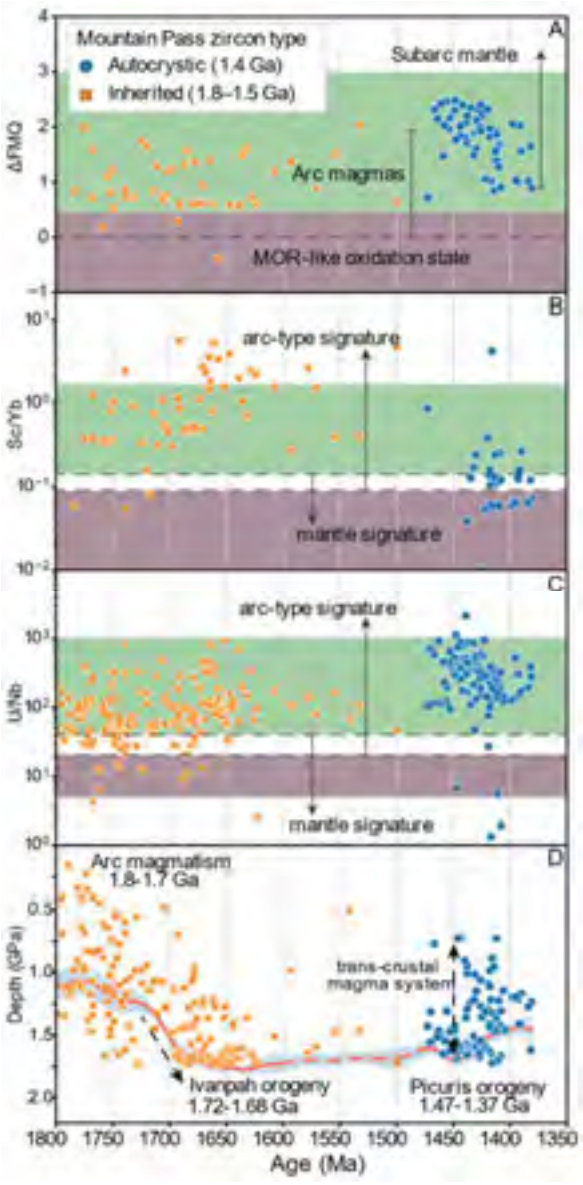


Figure 1. Time series of Mountain Pass zircon TE data. (A) Zircon oxybarometry calculated after Zou et al. (2024) with reference fO_2 values from Cottrell et al (2021). (B) Zircon Sc/Yb. (C) Zircon U/Nb. Mantle and arc fields are after Drabon et al. (2024), (D) Zircon crystallization depth with running mean and 95% uncertainty calculated after Moreira et al. (2023). MOR – Mid ocean ridge.

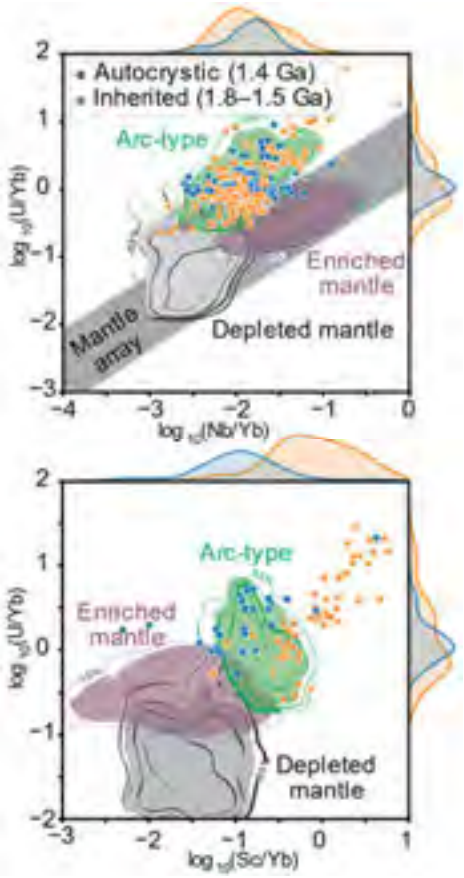


Figure 2. MPIS zircon TE bivariate plots and kernel density estimates after Grimes et al. (2015).

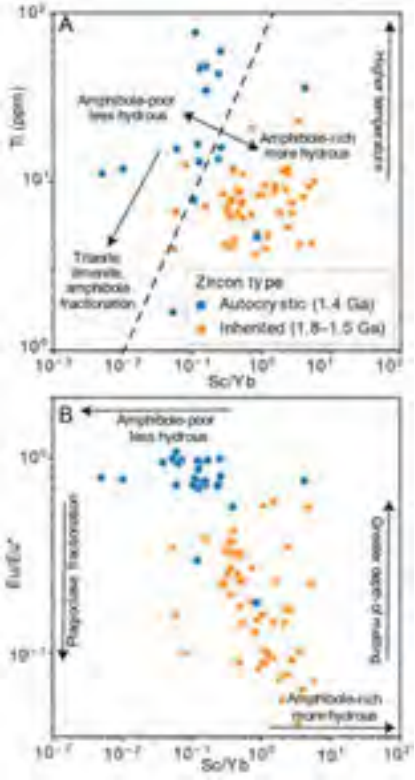


Figure 3. Petrogenetic diagrams of MPIS zircon TE data.

4.2 Global synthesis and analysis of carbonatite-alkaline silicate complex zircon TE

To test this approach more broadly, we compiled a global compilation of zircon TE compositions from carbonatites and associated alkaline silicate complexes (Fig. 4). The compiled dataset contains 270 zircon analyses from 13 complexes ranging in age from 2.6 to 0.1 Ga (Fig 4A).

Figure 4B shows two distinct trends on the Th-Nb-Yb discrimination diagram (Grimes et al. 2015). Several complexes including MPIS, Phalaborwa, Miaoya, and Yangyugou plot within the subduction-related field. Independent isotopic evidence supports a subduction component at Phalaborwa (Bolhar et al. 2020) and Miaoya (Çimen et al. 2018), validating this analysis. Most other complexes plot along the mantle array in or above the enriched mantle field including the 1.3 Ga Gifford Creek and Bayan Obo carbonatite and the 0.1 Ga Zomba-Malosa complex in the East African rift.

The subduction signature and syn- to post-collisional setting of the MPIS contrasts with the mantle array-compositions and rift association of Gifford Creek and Bayan Obo. Differences in source composition and tectonic setting suggests a distinct petrogenesis for the MPIS.

The successful discrimination of carbonatite source signatures and application to Mesoproterozoic carbonatite complexes demonstrates the robust nature of this approach. Zircon is a refractory phase that can distinguish source compositions as well as quantifying intensive parameters including temperature, oxidation state, and depth in addition to U-Th-Pb geochronology. Zircon TE data provide a promising approach to identifying and characterizing carbonatite and detrital zircon, especially in detrital mineral studies. We suggest that zircon petrochronology represents a promising tool for petrogenetic studies and exploration strategies for critical mineral resources.

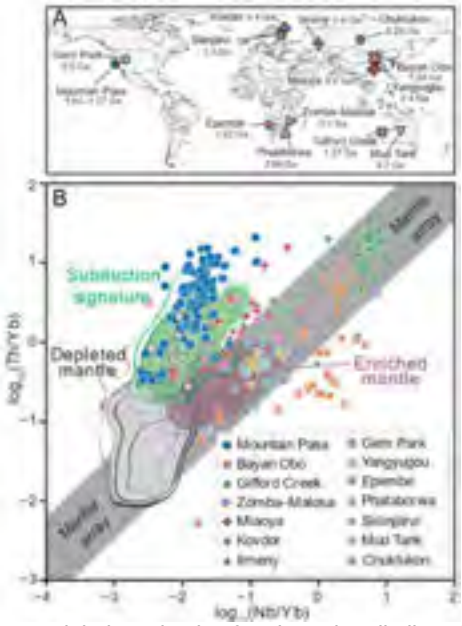


Figure 4. Global synthesis of carbonatite-alkaline silicate complexes zircon TE compositions. (A) Map of the localities included in the compilation. (B) Bivariate plot.

Acknowledgements

This research was funded and supported by the U.S. Geological Survey Mineral Resources Program. Any use of trade, firm, or product names is for descriptive purposes only and does not imply endorsement by the U.S. government. We appreciate reviews by Amy Gilmer, Ben Magnin, Danielle Olinger, and Sophia Ducrée.

References

Benson EK, Watts KE, Hillenbrand IW (2025) Geochemistry and radiogenic isotopes constrain the mantle source region of the Mountain Pass Intrusive Suite, California. Lithos.

Bolhar R, Whitehouse MJ, Milani L, et al (2020) Atmospheric S and lithospheric Pb in sulphides from the 2.06 Ga Phalaborwa phoscorite-carbonatite Complex, South Africa. Earth and Planetary Science Letters 530:115939. https://doi.org/10.1016/j.epsl.2019.115939

Bowman EE, Mallik A, Ducea MN (2024) Partial melting of arclogite and petrogenesis of alkaline-silicate complexes. Earth and Planetary Science Letters 645:118952. https://doi.org/10.1016/j.epsl.2024.118952

Castor SB (2008) The Mountain Pass Rare Earth Element Carbonatite and Associated Ultrapotassic Rocks, California. The Canadian Mineralogist 46:779–806. https://doi.org/10.3749/canmin.46.4.779

Chakhmouradian AR, Wall F (2012) Rare Earth Elements: Minerals, Mines, Magnets (and More). Elements 8:333–340. https://doi.org/10.2113/gselements.8.5.333

Çimen O, Kuebler C, Monaco B, et al (2018) Boron, carbon, oxygen and radiogenic isotope investigation of carbonatite from the Miaoya complex, central China: Evidences for late-stage REE hydrothermal event and mantle source heterogeneity. Lithos 322:225–237. https://doi.org/10.1016/j.lithos.2018.10.018

Cottrell E, Birner SK, Brounce M, et al (2021) Oxygen Fugacity Across Tectonic Settings. In: Magma Redox Geochemistry. pp 33–61

Drabon N, Kirkpatrick HM, Byerly GR, Wooden JL (2024) Trace elements in zircon record changing magmatic processes and the multi-stage build-up of Archean proto-continental crust. Geochimica et Cosmochimica Acta 373:136–150. https://doi.org/10.1016/j.gca.2024.03.014

Ferry JM, Watson EB (2007) New thermodynamic models and revised calibrations for the Ti-in-zircon and Zr-in-rutile thermometers. Contributions to Mineralogy and Petrology 154:429–437. https://doi.org/10.1007/s00410-007-0201-0

Gibson S, McKenzie D, Lebedev S (2024) The distribution and generation of carbonatites. Geology 52:667–671. https://doi.org/10.1130/G52141.1

Grimes CB, Wooden JL, Cheadle MJ, John BE (2015) “Fingerprinting” tectono-magmatic provenance using trace elements in igneous zircon. Contributions to Mineralogy and Petrology 170:46. https://doi.org/10.1007/s00410-015-1199-3

Hillenbrand IW, Karlstrom KE, Williams ML, et al (2023) Geochemical evidence for evolving Proterozoic crustal thickness and orogenic styles in southwestern Laurentia. Earth and Planetary Science Letters 622:118417. https://doi.org/10.1016/j.epsl.2023.118417

Mitchell RH (2005) Carbonatites and carbonatites and carbonatites. The Canadian Mineralogist 43:2049–2068. https://doi.org/10.2113/gscanmin.43.6.2049

Moreira H, Buzenchi A, Hawkesworth CJ, Dhuime B (2023) Plumbing the depths of magma crystallization using 176Lu/177Hf in zircon as a pressure proxy. Geology 51:233–237. https://doi.org/10.1130/G50659.1

Poletti JE, Cottle JM, Hagen-Peter GA, Lackey JS (2016) Petrochronological Constraints on the Origin of the Mountain Pass Ultrapotassic and Carbonatite Intrusive Suite, California. Journal of Petrology egw050. https://doi.org/10.1093/petrology/egw050

Tang M, Ji WQ, Chu X, et al (2021) Reconstructing crustal thickness evolution from europium anomalies in detrital zircons. Geology 49:76–80. https://doi.org/10.1130/G47745.1

Wall CJ, Hanson RE, Schmitz M, et al (2020) Integrating zircon trace-element geochemistry and high-precision U-Pb zircon geochronology to resolve the timing and petrogenesis of the late Ediacaran–Cambrian Wichita igneous province, Southern Oklahoma Aulacogen, USA. Geology 49:268–272. https://doi.org/10.1130/G48140.1

Watts KE, Haxel GB, Miller DM (2022) Temporal and Petrogenetic Links Between Mesoproterozoic Alkaline and Carbonatite Magmas at Mountain Pass, California. Economic Geology 117:1–23. https://doi.org/10.5382/econgeo.4848

Wooden JL, Miller DM (1990) Chronologic and isotopic framework for Early Proterozoic crustal evolution in the eastern Mojave Desert Region, SE California. Journal of Geophysical Research: Solid Earth 95:20133–20146. https://doi.org/10.1029/JB095iB12p20133

Yaxley GM, Anenburg M, Tappe S, et al (2022) Carbonatites: Classification, Sources, Evolution, and Emplacement. Annual Review of Earth and Planetary Sciences 50:261–293

Zou S, Brzozowski MJ, Chen X, Xu D (2024) Machine-learning oxybarometer developed using zircon trace-element chemistry and its applications. American Mineralogist 109:1181–1192. https://doi.org/10.2138/am-2023-8978

Scandium-rich Mineralization at the Crystal Mountain Fluorspar Mine, Montana, USA

Natalie Kilanowski-Doroh[1], Gary Wyss[2], and Christopher H. Gammons[1]
[1]Department of Geological Engineering, Montana Technological University, Butte, MT, USA
[2]Center for Advanced Minerals and Materials Processing, Montana Technological University, Butte, MT, USA

Abstract
The Crystal Mountain Mine (CMM) was a significant US producer of high-purity fluorspar between 1952 and 1972. The ore occurred as lodes of massive fluorite up to 10m thick and 100m long, with few other associated minerals. The deposit is unusually rich in scandium (Sc), in the form of the rare Sc-silicate, thortveitite, as well as Sc-rich pyroxene and amphibole in metasomatized gneiss. New U-Pb dates based on LA-ICP-MS spot analysis of titanite and thortveitite indicate a late Cretaceous age for the mineralization at CMM, although some resetting of U-Th-Pb systematics during regional metamorphism and magmatism is possible (details will be presented elsewhere).

1 Introduction

The Crystal Mountain Mine (CMM) is located in the in the southern Sapphire Mountains of western Montana (lat. 46.00583N, long. 113.88667W). The CMM is one of a band of deposits enriched in REE and other metals that has been informally named the Montana-Idaho Alkalic Belt (MIAB) (Figure 1). The REE-Nb-rich carbonatite deposits of Sheep Creek and Mineral Hill are in the MIAB, as are the REE-rich deposits of Diamond Creek, Lemhi Pass, and the Idaho Cobalt Belt. The MIAB connects to the north with the British Columbia Alkaline Province, a > 1000 km trend that contains a number of mineralized carbonatites and other rare metal occurrences (Simandl et al. 2013).

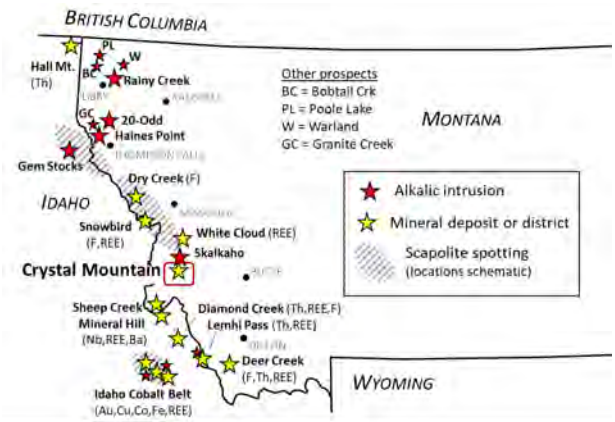


Figure 1. Selected mineral deposits of the Montana-Idaho Alkalic Belt showing the location of Crystal Mountain (after Gammons, 2020).

The CMM operated between 1952 and 1972, during which time it was a significant producer of high-purity fluorspar (Taber 1952). Foord et al. (1993) documented the occurrence of thortveitite ($Sc_2Si_2O_7$) at the CMM deposit. Tailings from an ore processing plant at the nearby town of Darby were cited as a possible domestic source of scandium by the U.S. Geological Survey (e.g., Gambogi 2014).

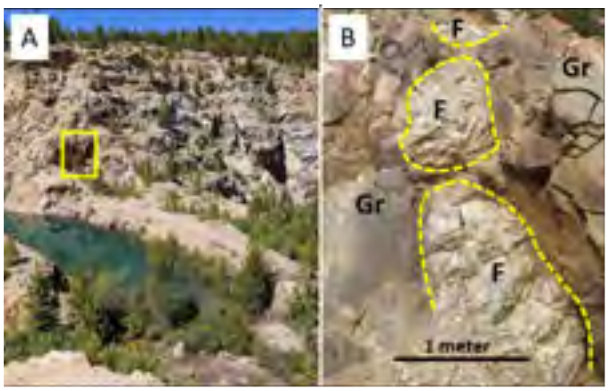


Figure 2. A) Photo of the main open pit at the CMM. Most of the rock in view is unmineralized granite. B) Ovoid masses of sun-bleached fluorite (F) surrounded by fine-grained granite (Gr) (hammer for scale). This photo was taken near the area outlined in panel A.

The geology of the area consists of amphibolite-grade metasedimentary rock of the Meso-proterozoic Belt Supergroup intruded by multiple generations of late Cretaceous to Paleocene granitoid bodies (Lonn et al. 2003). Amphibolites interfoliated with the metasediments may have been sills that intruded into the Belt Basin during late Precambrian time. Regionally, the CMM is located in the Sapphire Tectonic Block (Hyndman 1980), an allochthonous terrain that slid eastward up to 60 km along the east-dipping Bitterroot detachment fault shortly after consolidation of the late Cretaceous Idaho Batholith (Hyndman 1980; Foster and Fanning 1997).

The geometry of the fluorite ore bodies at CMM consists of elongate masses of nearly pure fluorite up to 10 m thick and 100 m long, surrounded by fine-grained granite (Figure 2B, Figure 3). Although bleached on the outcrop, most of the fluorite is deep purple on a fresh surface, more rarely apple green or bluish. The fluorite has a coarse, granoblastic texture suggesting regional metamorphism or perhaps an igneous origin. Granite next to the fluorite is unaltered and lacks chill margins (Figure 2B). Some of the more common mineral impurities in the fluorite ore include plagioclase feldspar, phlogopite, actinolite, titanite, magnetite, and trace Nb-Th-REE minerals such as fergusonite, aeschynite, and thorite (Foord et al. 1993; Grondin, 2019; Kilanowski-Doroh, 2025).

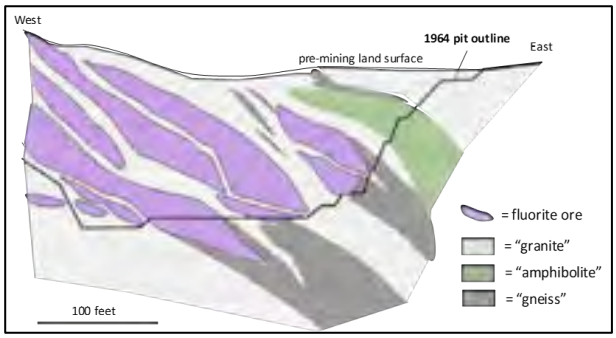


Figure 3. Geologic cross section through the fluorite deposit showing the outline of the 1964 open pit. The image was redrawn by Grondin (2019) from company files.

The focus of the present study is to re-examine the mineralogy and geochemistry of scandium and REE within the fluorspar deposits of the CMM. A second objective is to conduct preliminary geochronological studies.

2 Methodology

Representative samples of fluorite and metasomatized amphibolite were collected on multiple trips between 2019 and 2024 from the main open pit at CMM, as well as the Retirement Claims (a second deposit located on a ridge 1.5 km east of the open pit). Polished thick sections and 1"-diameter epoxy plugs were prepared for optical and microanalytical work. Each sample of interest was examined by scanning electron microscopy-energy dispersive spectroscopy (SEM-EDS) at Montana Tech, using a Tescan MIRA 3-TIMA GMU field emission scanning electron microscope (FE-SEM) and Tescan Integrated Mineral Analysis (TIMA) software. A subset of samples was sent to the U.S. Geological Survey Denver Microbeam Lab in Colorado for laser ablation inductively coupled plasma mass spectrometry (LA-ICP-MS) and electron probe microanalysis (EPMA). The LA-ICP-MS employed an SE 155 ablation system (193 nm) coupled to an Agilent 8900 ICP-MS instrument.

3 Results and Discussion

Thortveitite was found to be exceedingly rare in specimens of massive fluorite. Instead, it occurs as crystals up to 2 mm long in a mafic gneiss rich in diopside (X_{Mg} = 0.61), actinolite (X_{Mg} = 0.66), hornblende (X_{Mg} = 0.59), phlogopite (X_{Mg} = 0.78), smoky quartz, fluorite, fluorapatite, and titanite (Figures 4A, 4C). The origin of the mafic gneiss is unclear. It could represent metasomatized amphibolite country rock, or perhaps an igneous rock with highly unusual composition. In outcrop, the mafic gneiss occurs as isolated patches (xenoliths?) surrounded by granite, in a matter that resembles the fluorite masses themselves (Figure 5).

Thortveitite most typically occurs as subhedral grains intergrown with diopside (Figure 6A) and/or amphibole (actinolite, hornblende) (Figure 6B). Thortveitite is zoned under BSE imagery due to varying YREE content. A total of 80 LA-ICP-MS spot analyses gave a range in Y content from 0.5 to 11.1 wt% (average 2.6%). Y-rich growth zones are also rich in heavy REE, including Yb (up to 1.96 wt%) and Er (up to 1.1 wt%). The thortveitite locally has a "dusty" appearance due to an abundance of minute, micron-sized fluid and mineral inclusions, the latter consisting of thorite, titanite, and one or more REE-rich phases (Figure 6B).

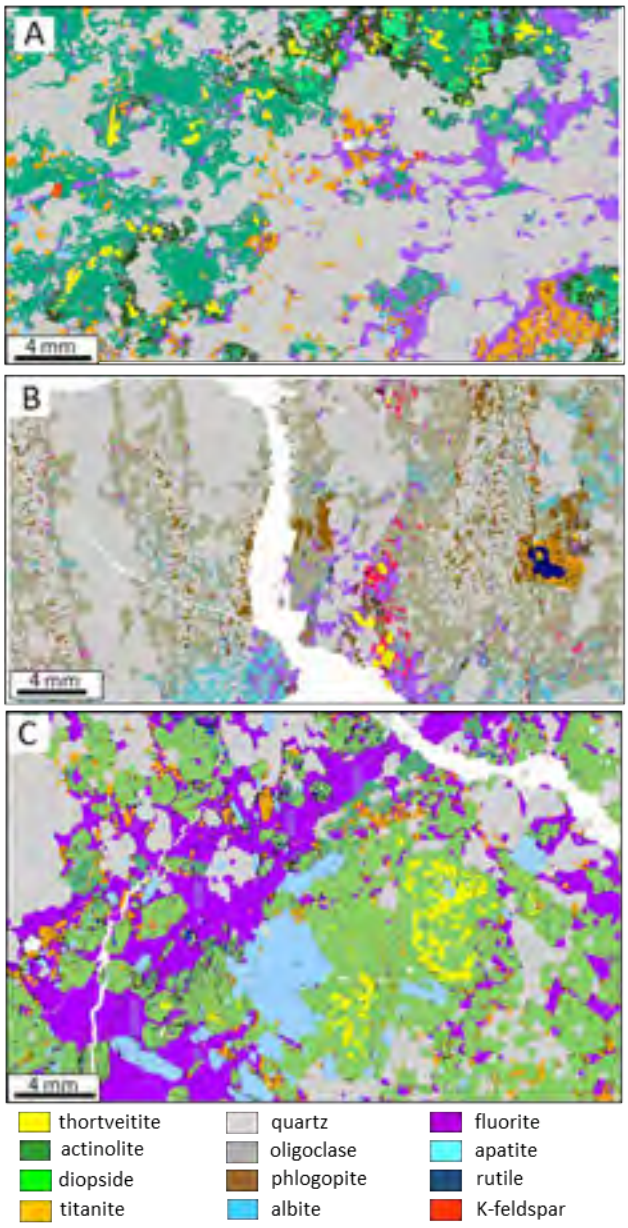


Figure 4. False color SEM-TIMA mineral maps of three polished sections from Crystal Mountain.

Figure 7 summarizes the content of scandium in the minerals shown in Figures 4A, 4B, and 4C. As expected, thortveitite has an extremely high scandium content (avg. of 29.6 wt% Sc). Unexpectedly, the mafic silicate minerals are also highly enriched in Sc, with up to 3.1, 1.6, and 1.0 wt% Sc in diopside, hornblende, and actinolite, respectively. Titanite contains 1000s of ppm of Sc, with much lower concentrations in biotite and the feldspars. Scandium is virtually absent in fluorite. All

of the hydrous silicate phases have high F-content. Fluorapatite in the mafic gneiss is Y-rich (up to 1.4 wt% Y), and locally contains many tiny inclusions, such as magnesio-rowlandite-(Y), synchysite, parisite, and thorite, amongst others.



Figure 5. Photograph of a large xenolith (1.5 m across) of mafic gneiss infused with fluorite and cut by granite. This photo was taken at the Retirement Claims.

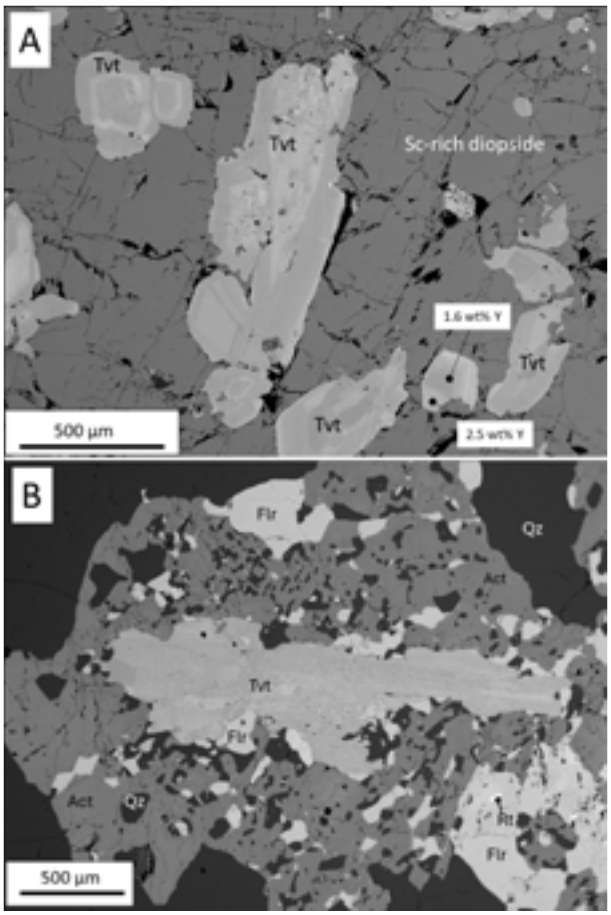


Figure 6. SEM-BSE images of thortveitite (Tvt) associated with Sc-rich diopside (A) and Sc-rich actinolite (B). Abbreviations: Flr = fluorite; Qz = quartz; Rt = rutile; Act= actinolite.

Figure 8 gives REE profiles for the same minerals in Figure 7. All phases show a strong negative Eu anomaly, and a lack of any Ce anomaly. This is consistent with an igneous origin in which a reduced magma crystallized Ca-rich plagioclase early in its fractionation history. It also suggests a common heritage for the thortveitite, fluorite, apatite, and the rock-forming silicate minerals (diopside, amphibole) in the mafic gneiss rock. Fluorite shows a sharp (+) anomaly at Y, which suggests preferential incorporation of this element into fluorite compared to the coexisting phases. Thortveitite is strongly enriched in Y and heavy REE.

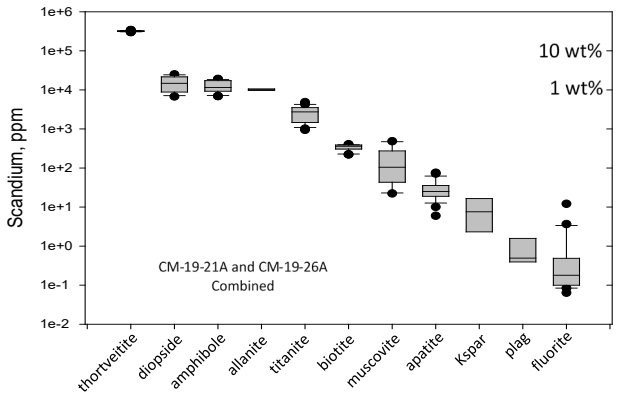


Figure 7. Concentrations of scandium (LA-ICP-MS data) in co-existing minerals from the Crystal Mountain mine.

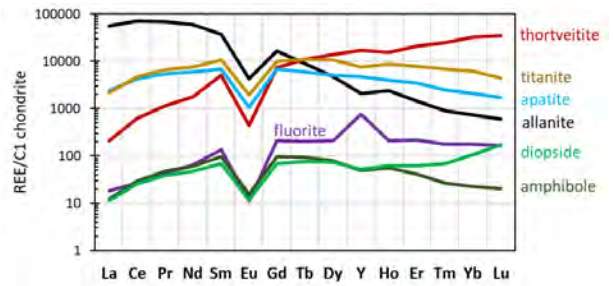


Figure 8. Chondrite-normalized REE profiles (LA-ICP-MS data) for co-existing minerals from the Crystal Mountain mine. Each curve is the average of 10 or more spot analyses.

Another distinctive rock type in the main open pit and the Retirement Claims is herein termed a “fluorite migmatite” (Figure 9). This rock resembles a partially melted metasediment, with quartz + plagioclase leucosomes, biotite-rich melanosomes, and monomineralic fluorite segregations. Figure 4B (above) is an automated mineral map of the same rock. Near the bottom of the Figure 4B, fluorite appears to replace the Ca-component in pre-existing oligoclase, leading to an abundance of pure albite. Significantly, several grains of thortveitite exist, intergrown with fluorite and late K-feldspar.

The origin of the fluorite migmatite is obscure. It could represent a large xenolith or roof pendant of partly melted Belt metasedimentary rock. An influx of F-rich fluids may have acted as a flux to lower the melting temperature of the system, promoting anatexis.

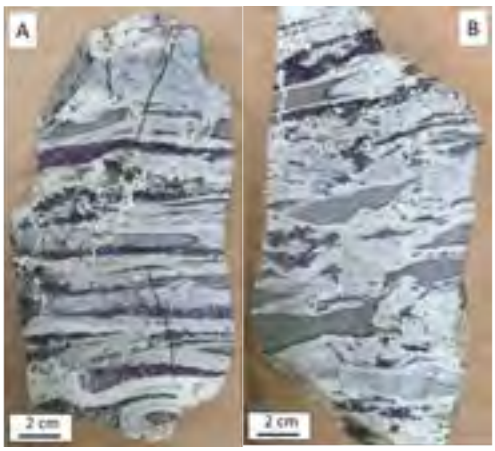


Figure 9. Two sawn slabs of the "fluorite migmatite" that outcrops at the north end of the main CMM pit. Fluorite is dark purple. Other minerals include phlogopite (black), plagioclase (white), and quartz.

Grondin (2019) performed microthermometric work on fluid inclusions in fluorite at the CMM, and concluded that the fluorite formed at very high temperature (up to and exceeding 500°C) and pressure (> 2.5 kbar), from hyper-saline fluids of unknown origin. Grondin speculated that the fluorite bodies at CMM may represent immiscible Ca-F and granite melts, as was shown experimentally (e.g., Yang and van Hinsberg, 2019).

In situ LA-ICP-MS analysis of titanite in the samples shown in Figure 4 gave $^{238}U/^{206}Pb$ isochron ages of 72.6±0.6, 73.6±0.7 and 71.2±1.1 Ma. These results fall within the range of ages published for the Idaho Batholith and satellite plutons (e.g. Gaschnig et al. 2010). Given that the "mafic gneiss" likely experienced high temperatures associated with regional and contact metamorphism, it is possible that the U-Th-Pb systematics in titanite were isotopically reset. If so, then the dates obtained could have little bearing on the age of fluorite and associated thortveitite mineralization at CMM.

4 Conclusions

The fluorspar deposits of Crystal Mountain, Montana, are highly unusual for their size, their geometry, and their lack of associated mineral impurities. A mafic gneiss, containing clinopyroxene, actinolite ± hornblende, fluorapatite, titanite, fluorite, and smoky quartz, crops out at CMM as large xenoliths or pendants surrounded by fine-grained granite. This gneiss is enriched in scandium and contains the rare mineral thortveitite, as well as Sc-rich pyroxene and amphibole. Thortveitite is intimately intergrown with pyroxene and amphibole, and rarely occurs as isolated grains in massive fluorite. Thortveitite, fluorite, apatite, and the mafic silicates all show a similar negative Eu anomaly, suggesting a common heritage. Thortveitite is enriched in heavy REE, and contains up to 1 wt% of Yb and Er. The fluorspar and associated Sc mineralization at Crystal Mountain took place at near magmatic temperatures (up to 500°C) and pressures (up to 3 kbar), and involved hypersaline fluids. These fluids may have induced localized partial melting of the surrounding country rock. Crystal Mountain is a unique example of the deposition of large masses of nearly pure fluorite from magmatic-hydrothermal, or "brine-melt" fluids. The possible role of fluid immiscibility between fluorite melt and silicate melt cannot be discounted.

Acknowledgements and Disclaimers

This research was supported by a grant from the Army Research Laboratory (ARL) to Montana Tech. The views and conclusions contained in this document are those of the authors, and should not be interpreted as representing the official policies, either expressed or implied, of the ARL or the U.S. Government.

We thank Jay Thompson and Heather Lowers of the USGS for the LA-ICP-MS and EPMA data, respectively. These data are preliminary or provisional and are subject to revision. They are being provided to meet the need for timely best science. The data have not received final approval by the U.S. Geological Survey (USGS) and are provided on the condition that neither the USGS nor the U.S. Government shall be held liable for any damages resulting from the authorized or unauthorized use of the data. Any use of trade, firm, or product names is for descriptive purposes only and does not imply endorsement by the U.S. Government.

References

Foord EE, Birmingham SD, Demartin F, Pilati T, Gramaccioli CM, Lichte FE (1993) Thortveitite and associated Sc-bearing minerals from Ravalli County, Montana: Can Mineral 31: 337-346.

Foster DA, Fanning CM (1997) Geochronology of the northern Idaho batholith and the Bitterroot metamorphic core complex: Magmatism preceding and contemporaneous with extension. Geol Soc Am Bull 109: 379-394.

Gambogi J (2014) Scandium: US Geol Surv, Mineral Commodities Summaries, February, 2014, 140-141.

Gammons CH (2020) The Montana-Idaho alkalic belt: An exploration target for critical metals. Mont Bur Mines Geol Special Publ 121:151-157.

Gaschnig RM, Vervoort JD, Lewis RS, McClelland WC (2010) Migrating magmatism in the northern US Cordillera: in situ U–Pb geochronology of the Idaho batholith: Contr Mineral Petrol 159: 863–883.

Grondin F (2019) Mineralogy and fluid inclusion study of the Crystal Mountain fluorite mine, Ravalli County, Montana: MS Thesis, Montana Tech, Butte, MT.

Hyndman DW (1980) Bitterroot dome-Sapphire tectonic block, an example of a plutonic-core gneiss-dome complex with its detached suprastructure: Cordilleran metamorphic core complexes. Geol Soc Am Memoir 153:427-443.

Lonn JD, McDonald C, Lewis RS, Kalakay TJ, O'Neill JM, Berg RB, Hargrave P (2003) Preliminary geologic map of the Philipsburg 30'× 60'quadrangle, Montana. Mont Bur Mines Geol Open File Report, MBMG 483.

Simandl GJ, Reid HM, Ferri F (2013) Geological setting of the Lonnie niobium deposit, British Columbia, Canada. BC Geol Surv Paper 2013-1: 127-138.

Taber JW (1952) Crystal Mountain fluorite deposits, Ravalli County, Montana. US Bur Mines, Rept Invest 4916.

Yang L, van Hinsberg VJ (2019) Liquid immiscibility in the CaF_2-granite system and trace element partitioning between the immiscible liquids: Chem Geol 511:28-41.

Zr-U-Th-Phases in Clinohumite-Spinel-Bearing Marbles as Potential Tracers of HFSE-Fertile Granitic Rocks

Šárka Kučerová[1], Martin Kubeš[1,2], Milan Novák[1], Michal Poňavič[2], Anna Vymazalová[2], Jaromír Leichmann[1]
[1]Masaryk University, Brno, Czech Republic
[2]Czech Geological Survey, Prague, Czech Republic

Abstract. Abundant clinohumite-spinel-bearing marbles in the eastern part of the Moldanubian Zone of the Bohemian Massif (Czech Republic) typically host Zr-U-Th phase assemblages involving zirconolite, baddeleyite, zircon, uranothorite and thorianite. Although the provenance of the HFSE source is generally considered inside the marbles, usually of detrital and/or metamorphic origin, our current observations suggest the import of Zr, U and Th from an external source. The textural features and chemical composition of the Zr-U-Th phases point towards the influx of late-magmatic hydrothermal fluids most likely generated during the emplacement of the HFSE-fertile durbachite plutons from the Moldanubian Zone, in line with previous EMP chemical dating of zirconolite from the marbles. Accordingly, common occurrences of F-rich clinohumite, phlogopite and fluorapatite in the studied marbles possibly reflect infiltration of F-, K- and P-rich fluids that may represent crucial complexing ligands for fluid-driven HFSE mobilization. Taken together, this case study suggests that hydrothermally-derived Zr-U-Th minerals in metacarbonates can be used as potential tracers of HFSE-fertile granitic rocks, which can play a crucial role in the future exploration of economically important ore deposits worldwide.

1 Introduction

The Moldanubian Zone of the Bohemian Massif in Czech Republic (central Europe) is characterized by abundant occurrences of intercalations of marbles within the high-grade metamorphic basement predominantly composed of anatectic gneisses to migmatites (e.g. Lardeaux et al. 2014). These metacarbonate rocks usually have different lithological compositions with distinct mineral assemblages. For instance, within the southern part of the Moldanubian Zone in the Bohemian Massif, there were distinguished six lithological types of marbles (Houzar et al. 2017; references therein), based on their characteristic mineral associations: 1) Silicate-calcite marbles (Cal + Di + Ttn ± Tr ± Qz ± Pl ± Kfs ± Wo; (2) pure calcite marbles, locally with dolomite (Cal + Phl ± Di ± Qz ± Dol and Tr + Cal + Phl); (3) graphite-calcite marbles, locally with silicates (Cal + Phl + Gr + Di + Py ± Dol); (4) calcite-dolomite marbles (Fo + Cal + Dol ± Chl (Spl) ± Chu ± Chn and Di + Cal + Dol); and (5) dolomite marbles (Dol + Tr ± Cal ± Phl ± Fo).

Accordingly, the described type no. 4 “calcite-dolomite marble” also occurs in the eastern part of the Moldanubicum in the Bohemian Massif (e.g. Houzar et al. 2010) (Figure 1a, b). In contrast to other classified lithological types of marbles, the calcite-dolomite marbles are generally characterized by presence of Ti-rich clinohumite (± chondrodite), spinel and rare accessory phases such as geikielite, zirconolite, baddeleyite and U-Th-Nb-Ta-rich oxides (Čopjaková et al. 2009; Houzar and Gadas 2019). However, despite abundant occurrences of clinohumite-spinel-bearing metacarbonates typically containing the accessory Zr-U-Th phases, the possible source of HFSE for the marbles in the Moldanubicum remains a matter of debate for several decades.

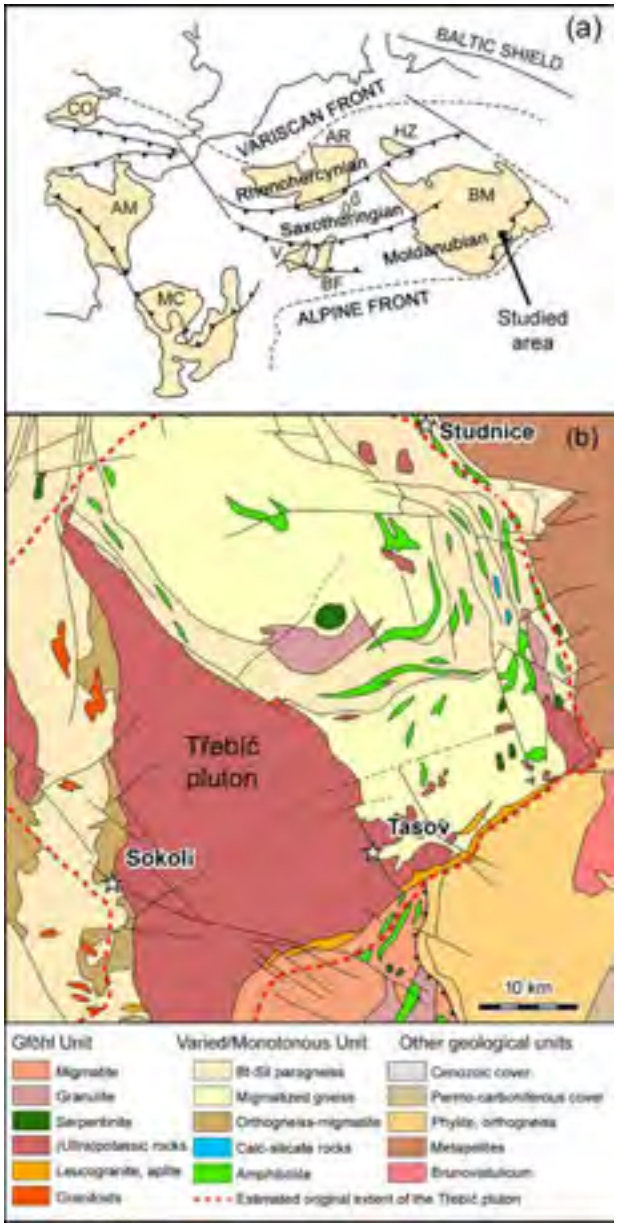


Figure 1. a Position of the investigated area in the eastern part of the Moldanubicum in the regional frame of western-central Europe. **b** Locations of the studied clinohumite-spinel-bearing marbles from the Moldanubian Zone. Geological map modified after Kubeš et al. (2022).

The potential HFSE source is currently considered as either detrital and metamorphogenic material in metacarbonates or external hydrothermal fluids (Houzar et al. 2010, 2017). This contribution presents a detailed mineralogical study of Zr-U-Th-phases from clinohumite-spinel-bearing marbles, which in combination with our previously published work (Kubeš et al. 2024) provides important implications for exploration and targeting HFSE-fertile granitic systems linked to the metallogenesis of significant hydrothermal ore deposits without apparent spatial relation to fertile granitic rocks. Accordingly, our observations suggest an external HFSE source for the formation of Zr-U-Th phases in marbles, likely represented by HFSE-rich durbachite intrusions, implying the potential utilization of these phases as tracers of HFSE-fertile granitic rocks.

2 Sampling and analytical techniques

The studied samples of clinohumite-spinel marbles with accessory Zr-U-Th phases come from three different localities near Tasov, Sokolí and Studnice villages in the eastern part of the Moldanubicum (Figure 1b). The Tasov and Sokolí localities are situated within the Třebíč durbachite pluton and its contact aureole, respectively. These two sampling sites represent deep boreholes previously described in detail by Leichmann et al. (2017). The depth of the clinohumite-spinel marbles within the boreholes corresponds to ca. 520–540 m below the surface. The third sampling site Studnice is located 20 km north of the Třebíč durbachite pluton (Figure 1b). At this locality, the marbles usually form lenses several tents meters long in host migmatitized gneisses.

Backscattered electron (BSE) images along with mineral chemistry were obtained by electron microprobe (EMP) Cameca SX 100 at the Department of Geological Sciences, Masaryk University, Brno, Czech Republic. Operating conditions for spot analyses were as follows: wavelength-dispersive mode, accelerating voltage of 15 kV, beam current of 10–40 nA, and beam size of 2–7 μm for Zr-U-Th-rich phases involving zirconolite, baddeleyite, zircon, uranothorianite and thorianite. The following natural and synthetic standards were used: almandine (Fe, Al), zircon (Zr), ThO_2 (Th), UO_2 (U), columbite (Nb), $CrTa_2O_6$ (Ta), $REEPO_4$ (REE), YAG (Y), $ScVO_4$ (Sc, V), topaz (F), fluorapatite (P), alamosite (Si, Pb), wollastonite (Ca), Mn_2SiO_4 (Mn), titanite (Ti).

3 Results

3.1 Mineral assemblages and textures

A detailed description of main mineral assemblages of the clinohumite-spinel-bearing calcite-dolomite marbles from the Moldanubicum has been previously provided by Houzar et al. (2010, 2017), and thus only a brief description of their mineral composition is given here. The studied samples of calcite-dolomite marbles are typically composed of forsterite, calcite, dolomite, phlogopite, chlorite and their characteristic feature is the presence of spinel and clinohumite. Accessories include abundant fluorapatite, minor sulphides, titanite and cassiterite. This study primarily focuses on assemblages, textures and chemistry of accessory Zr-U-Th minerals from the clinohumite-spinel marbles.

Zircon represents the most common Zr-phase in marbles and usually forms anhedral to subhedral isometric crystals (50–100 μm) chiefly intergrown with clinohumite, spinel and phlogopite. It is ordinarily associated with other Zr-U-Th-rich phases such as baddeleyite, uranothorianite and thorianite. Occasionally, zircon replaces baddeleyite or is rimmed by zirconolite (Figure 2a, b). Most zircon grains display no evidence of primary zoning, only a few grains have preserved a weak sectoral zonation. Zircon shows effects of self-induced radiation damage and subsequent late fluid-driven alteration, as reflected by abundant intra-grain microfractures and variable BSE intensity (Figure 2c, d).

Baddeleyite occurs as anhedral to subhedral grains with relatively variable sizes ranging from 20 to 150 μm. It is associated with spinel a clinohumite. Also, it forms mineral clusters (40–120 μm) or is commonly intergrown with zircon, uranothorianite or thorianite (Figure 3a, b). Besides, baddeleyite forms at the expense of abundant zircon (Figure 2d). Rare baddeleyite inclusions (≤10 μm) in zirconolite were also observed in the studied samples (Figure 3c).

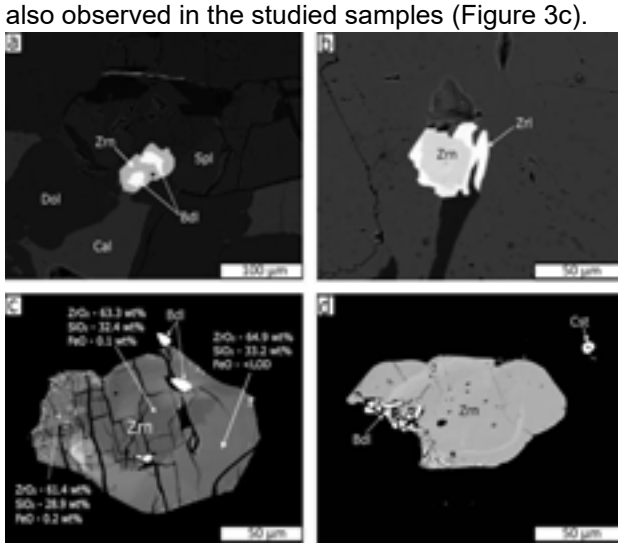


Figure 2. BSE images of Zr-U-Th-rich phases in clinohumite-spinel marbles. **a** Baddeleyite overgrown by zircon. **b** Zirconolite overgrowths around zircon. **c** Altered metamict zircon showing different chemistry between BSE brighter and darker domains. **d** Baddeleyite forming at the expense of zircon. Abbreviations: Zrn = zircon; Zrl = zirconolite; Bdl = baddeleyite; Spl = spinel; Dol = dolomite; Cal = calcite; Uth = uranothorite; Cst = cassiterite.

Zirconolite shows slightly different textural morphologies, mineralogical associations, and zonation patterns (Figure 3c–e). Zirconolite forms irregular grains (50–80 μm) associated with spinel and clinohumite. It is characterized by two different zonation patterns with respect to a degree of hydrothermal alteration: 1) patchy zonation is typical of extensively altered grains, and 2) sectoral

zonation prevails in slightly altered to pristine crystals (Figure 3d, e). In addition, zirconolite forms overgrowths (≤8 µm) surrounding zircon (Figure 2b).

Uranothorianite and thorianite usually form similar, rounded or subhedral to euhedral grains with variable sizes varying between 15–90 µm. Their characteristic feature is a close spatial association to Zr-phases (Figure 3a). Often, they form radiation-damaged halos in surrounding spinel and irregular inclusions (≤10 µm) in zircon crystals (Figure 3f).

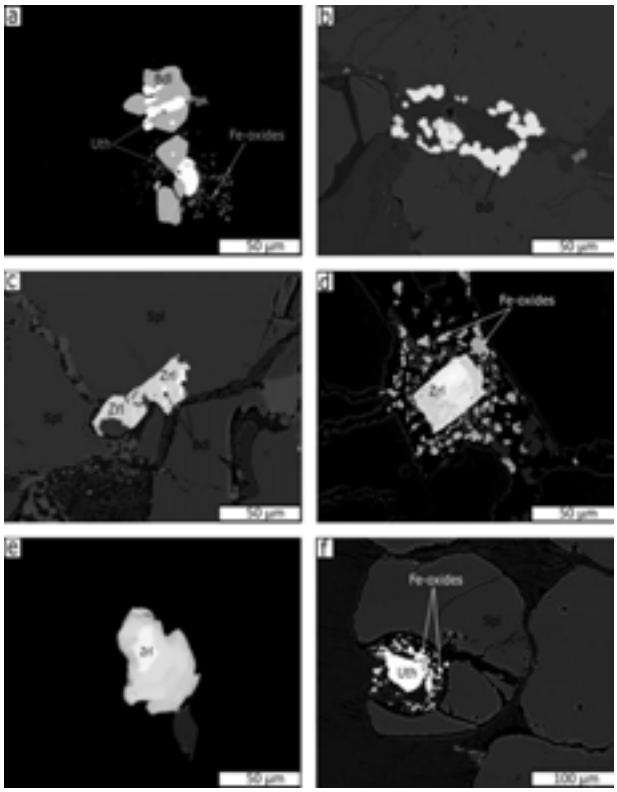


Figure 3. BSE images of Zr-U-Th phases. **a** Baddeleyite and uranothorite intergrowths. **b** Clusters of baddeleyite. **c** Zirconolite associated with spinel. **d** Altered zirconolite. **e** Sectoral zonation of pristine zirconolite. **f** Uranothorianite surrounded by a radiation-damaged halo in spinel. Mineral abbreviations are same as in Figure 2.

3.2 Chemical composition

Pristine zircon has homogenous chemical composition, reflected by high ZrO_2 (~64–66 wt%) and SiO_2 (~31–33 wt%) contents and EMP analytical totals (99.5–100 wt%) along with low contents of non-formula elements (e.g. Ca, Al, Fe) below EMP detection limits. By contrast, altered zircon shows low ZrO_2 (~61–63 wt%), SiO_2 (~28–31 wt%), EMP analytical totals (93–98 wt%) and elevated contents of non-formula elements (CaO ≤0.21 wt%, Al_2O_3 ≤0.95 wt%, FeO ≤0.25 wt%) (Figure 2d).

Baddeleyite exhibits a rather uniform chemical composition in all analysed samples, with ZrO_2 and HfO_2 contents varying between 94.48–97.28 wt% and 1.45–3.36 wt%, respectively.

Unaltered zirconolite domains ordinarily show low BSE intensity due to low content of actinides (UO_2 0.30–5.66 wt%, ThO_2 0.21–3.00 wt%), except for Th-rich zirconolite (ThO_2 11.40–16.50 wt%) with well-marked sectoral zonation or thin overgrowths around zircon. Pristine zirconolite exhibits the highest contents of ∑REE (1.21–3.91 wt%) and chemically resembles zirconolite from metasomatic rocks (Figure 4). Altered zirconolite domains and/or grains show higher BSE intensity reflecting high contents of actinides (UO_2 2.24–12.78 wt%, ThO_2 3.58–7.09 wt%) and low ∑REE (0.14–1.54 wt%).

Uranothorianite typically shows highly variable UO_2 (40.08–60.44 wt%) and ThO_2 (34.32–51.91 wt%) contents along with high PbO (up to 3.30 wt%). Thorianite has relatively uniform UO_2 (8.58–15.71 wt%) and ThO_2 (81.32–88.97 wt%) contents and lower PbO (up to 1.84 wt%).

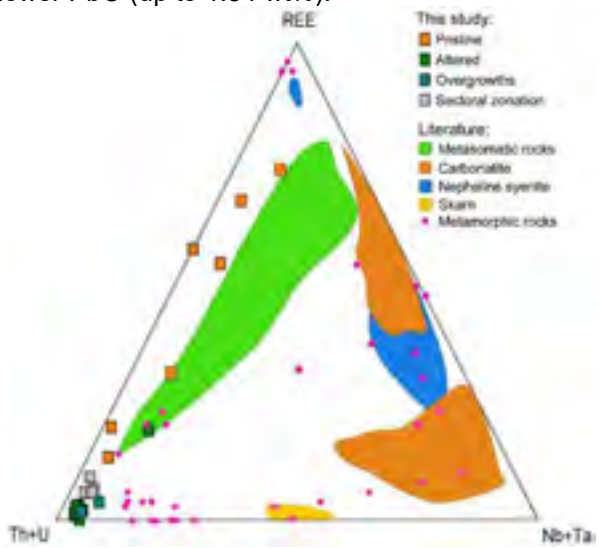


Figure 4. REE–(Th + U)–(Nb + Ta) diagram for zirconolite. Compositional fields are from Hurai et al. (2018).

4 Discussion and conclusions

4.1 Potential source of HFSE

Zircon and zirconolite occasionally form overgrowths around other accessory minerals (Figure 2a, b), suggesting that zircon and zirconolite in this textural position do not represent residual detrital material that originally comes from protolithic sedimentary rock. Besides, the chemical composition of pristine zirconolite resembles those of zirconolite from metasomatic rocks (Figure 4), such as skarnoids in the contact aureole of granitic intrusions from Bergell (Gieré 1986) and Adamello in Italy (Gieré 1990) and Koberg Bergslagen in Sweden (Zakrzewski et al. 1992). Accordingly, the Zr-U-Th-rich phases were identified exclusively in clinohumite-spinel-bearing marbles in the Moldanubicum (Houzar et al. 2017). Within our studied marble samples, Zr-U-Th-rich minerals are usually associated with clinohumite and spinel (Figure 3c, d, e), both of which represent important constituents of metasomatic mineral assemblages of the skarnoids linked to Bergell and Adamello granitic massifs (Gieré 1986, 1990).

These observations suggest the metasomatic origin of Zr-U-Th phases, likely related to vigorous ultrapotassic magmatism in the Moldanubian Zone, as indicated by a close spatial link of some clinohumite-spinel marbles to durbachite plutons

(Figure 1b; Houzar and Gadas 2019). The influx of HFSE-bearing fluids was most likely linked to the emplacement of durbachites, in line with previous EMP U–Pb age of 339 ± 10 Ma for zirconolite in marbles near the Třebíč durbachite pluton (Čopjaková et al. 2009). This agrees with U–Pb zircon date of 335 ± 0.061 Ma for the Třebíč pluton (Schaltegger et al. 2021). Indeed, the marbles from the Moldanubicum recorded a significant heat flow generated by the Třebíč pluton (Novák and Houzar 1996) and thus allowed to constraint an original extent of the durbachite intrusion (Leichman et al. 2017), as illustrated in Figure 1b.

Considering the presence of F-rich clinohumite (2.08–5.11 wt%), phlogopite and fluorapatite in the studied samples, the late-magmatic hydrothermal fluids derived from the durbachites must have been enriched in F-, K- and P-bearing ligands able to transport HFSE (Kubeš et al. 2021, 2024).

The fluid-driven dissolution of metamict zircon and zirconolite implies time span up to several 10 Ma between their crystallization and late alteration, necessary for metamictization enabling subsequent hydrothermal decomposition. The dissolution is usually accompanied by release of HFSE and REE, as evidenced by low ZrO_2 content of altered zircon and decreased ∑REE in altered zirconolite with high content of actinides (Figure 4). Considering high chemical stability of zircon and zirconolite in hydrothermal systems, the influence of F-bearing fluids related to a Permian hydrothermal event responsible for the formation of vein-type U-mineralization appears to be the most likely explanation (Kubeš et al. 2024).

4.2 Possible implications for targeting HFSE-fertile granitic systems

The recognition of the metasomatic origin of Zr-U-Th phases in clinohumite-spinel marbles linked to the release of late-magmatic fluids during emplacement of durbachite plutons in Moldanubicum provides possible implications for exploration and targeting of HFSE-fertile granitic rocks responsible for the metallogenesis of hydrothermal ore deposits.

The durbachite plutons represent an ideal source of U and other HFSE for formation of hydrothermal ore deposits (Kubeš et al. 2024). Although some occurrences of clinohumite-spinel marbles in Moldanubicum show no evidence of spatial link to durbachite intrusions (e.g. Houzar et al. 2017), these metacarbonate rocks are typically highly sensitive to interaction with mineralized hydrothermal solutions expelled from HFSE-rich granitic rocks such as durbachites. The fluid-rock interaction may lead to the precipitation of Zr-U-Th-phases in marbles, which makes them potential tracers of HFSE-fertile granitic systems genetically linked to hydrothermal ore deposits. This case study thus demonstrates importance of Zr-U-Th-rich phases in marbles for future exploration of significant ore deposits and clarification of original extent of source granitic rocks in metallogenetic province worldwide.

Acknowledgements

The research was primarily conducted under the OP VVV project [**CZ.02.1.01/0.0/0.0/16_026/0008459**] (Geobarr) from the European Regional Development Fund, and was also supported by the project RENS [**SS02030023**] of the Technological Agency of the Czech Republic (TACR).

References

Čopjaková R, Houzar S (2009) Zirconolite in marble near Krahulov and the HT/LP metamorphism age of the Moldanubicum in the contact aureole of the Třebíč pluton. Acta Mus Morav Sci Geol 94:67–76.

Gieré R (1986) Zirconolite, allanite and hoegbomite in a marble skarn from the Bergell contact aureole: implications for mobility of Ti, Zr and REE. Contrib Mineral Petr 93:459–470.

Gieré R (1990) Hydrothermal mobility of Ti, Zr and REE: examples from the Bergell and Adamello contact aureoles (Italy). Terra Nova 2:60–67.

Houzar S, Gadas P, Čopjaková R (2010) Geikielite-baddeleyite mineral association in dolomitic marbles of the Moravian Moldanubicum in the contact aureole of the Třebíč pluton. Acta Mus Morav Sci Geol 95:71–82.

Houzar S, Novák M, Cícha J (2017) Overview of mineral associations and lithology of marbles of the Czech part of the Moldanubicum (Bohemian Massif). Bull Mineral Petrol 25:113–140.

Houzar S, Gadas P (2019) A unique mineral association with chondrodite in marble from the Bílá mountain near Čechočovic (West Moravia). Acta Mus Morav Sci Geol 104:73–85.

Hurai V, Huraiová M, Gajdošová M, Konečný P, Slobodník M, Siegfried PR (2018) Compositional variations of zirconolite from the Evate apatite deposit (Mozambique) as an indicator of magmatic-hydrothermal conditions during post-orogenic collapse of Gondwana. Miner Petrol 112:279–296.

Kubeš M, Leichmann J, Wertich V, Mozola J, Holá M, Kanický V, Škoda R (2021) Metamictization and fluid-driven alteration triggering massive HFSE and REE mobilization from zircon and titanite: Direct evidence from EMPA imaging and LA-ICP-MS analyses. Chem Geol 586, 120593.

Kubeš M, Leichmann J, Buriánek D, Holá M, Navrátil P, Scaillet S, O'Sullivan P (2022) Highly evolved miaskitic syenites deciphering the origin and nature of enriched mantle source of ultrapotassic magmatism in the Variscan orogenic root (Bohemian Massif, Moldanubian Zone). Lithos 432, 106890.

Kubeš M, Leichmann J, Wertich V, Čopjaková R, Holá M, Škoda R, Kříbek B, Mercadier J, Cuney M, Deloule E, Lecomte A, Krzemińska E (2024) Ultrapotassic plutons as a source of uranium of vein-type U-deposits (Moldanubian Zone, Bohemian Massif): insights from SIMS uraninite U–Pb dating and trace element geochemistry. Miner Dep 59:1325–1362.

Lardeaux JM, Schulmann K, Faure M, Janoušek V, Lexa O, Skrzypek E, Edel JB, Štípská P (2014) The Moldanubian zone in the French Massif Central, Vosges/Schwarzwald and Bohemian Massif revisited: differences and similarities. Geol Soc London, Spec Publ 405:7–44.

Leichmann J, Gnojek I, Novák M, Sedlák J, Houzar S (2017) Durbachites from the Eastern Moldanubicum (Bohemian Massif): erosional relics of large, flat tabular intrusions of ultrapotassic melts–geophysical and petrological record. Int J Earth Sci 106:59–77.

Novák M, Houzar S (1996) The HT/LP metamorphism of dolomite marbles in the eastern part of the Moldanubicum; A manifestation of heat flow related to the Třebíč Durbachite Massif. J Geosci 41:139–146.

Schaltegger U, Gaynor SP, Widmann P, Kotková J (2021) Comment on “Ultrapotassic magmatism in the heyday of the Variscan Orogeny: the story of the Třebíč Pluton, the largest durbachitic body in the Bohemian Massif” by Janoušek et al. Int J Earth Sci 110:1127–1132.

Zakrzewski MA, Lustenhouwer WJ, Nugteren HJ (1992) Rare-earth minerals yttrian zirconolite and allanite-(Ce) and associated minerals from Koberg mine, Bergslagen, Sweden. Mineral Mag 56:27–35

Mineralogical and Geochemical Variation of Porphyritic Dikes within the North Stock Gold Prospect, Rattlesnake Hills Alkaline Complex, Central Wyoming, USA

Brandi Lawler[1]
[1] *Department of Geology and Geophysics, University of Wyoming, USA.*

Abstract. The discovery of large gold deposits within alkaline magmatic suites at sites such as Cripple Creek, Colorado, USA and Porgera, Papua New Guinea suggests that alkaline volcanics can be worthwhile exploration targets. The presence of elevated gold anomalies found during early drilling at the North Stock site within the Rattlesnake Hills Alkaline Complex of Central Wyoming, USA led to a desire to better understand the nature of the alkaline volcanism and associated hydrothermal alteration of the site. Drill core samples of the main phonolite diatreme that comprises North Stock and the porphyritic dikes that crosscut the diatreme were examined during this study using petrographic analysis, automated mineralogy modal analysis, and geochemical analyses. Patterns uncovered during petrographic and geochemical analyses allowed for the grouping of core samples into four subsets, each sharing certain common characteristics. Detection of elevated Au concentrations in samples from three of the four subgroups indicates that Au mineralization is not confined to a single host-rock type at North Stock.

1 Introduction

The Rattlesnake Hills Alkaline Complex (RHAC) is an area of Eocene calc-alkaline to alkalic volcanism (Pekarek et al. 1974) located within a 325 square-kilometre region of central Wyoming, U.S.A. (Shive et al. 1977) (Fig. 1).



Figure 1. Plan view map of the state of Wyoming, USA with the location of the RHAC outlined in red.

The RHAC is comprised of approximately 50 volcanic vents and intrusions which are believed to have been emplaced during rollback of the Farallon slab following the end of the Laramide orogeny (Pekarek et al. 1974; Shive et al. 1977; Hoch and Frost 1993). The compositions of the intrusive and extrusive rocks of the RHAC include phonolite, trachyte, alkali-melatrachyte, sodic trachyte, latite, quartz latite, and rhyolite (Pekarek 1977; Stupak 1984; Hoch 1991; Hoch and Frost 1993).

The RHAC is subdivided into three volcanic groups based on petrographic characteristics: the Eastern Felsic Group, the Central Alkaline Group, and the Western Felsic Group (Hoch 1991). The North Stock site is located with the Central Alkaline Group of the RHAC and represents the remnants of a phonolite diatreme that was heavily brecciated upon emplacement (Ripple 2012). Sanidine from the North Stock phonolite diatreme returned an age of 44.65+/-0.19 Ma (Autenrieth 2012) which is consistent with the Eocene ages from the RHAC determined by Pekarek et al. (1974).

Exploration drilling at the North Stock site has revealed the presence of gold mineralization. This study was conducted to gain a better understanding of the mineralogical and geochemical variability of the altered volcanics at North Stock and to determine which alteration assemblages were most often associated with elevated gold concentrations.

2 Samples and Methods

2.1 Samples

Access to the North Stock drill core repository was provided in early 2020 to facilitate the collection core samples representing multiple porphyritic dikes and phonolite breccias intersected during recent drilling programs at the North Stock site. Samples were taken from both minimally altered and heavily altered dikes and phonolite breccias in an effort provide a sample set that would be representative of the variation in the mineralogy and geochemistry of the altered dikes and breccias.

A total of 52 core samples were collected, each representing less than six inches or 15.26 centimetres of half-core or quarter-core (Fig. 2). From the 52 core samples collected, a subset of 32 samples were selected for further analysis by grouping the total sample set by visual similarities based on phenocryst size and type as well as visible groundmass mineralogy and alteration patterns. The samples chosen for further analysis were

representative of each of the groupings made during the visual comparison process and multiple samples from certain groupings were chosen to test whether macroscale observations of similarities held at the microscopic scale. From the narrowed subset of 32 samples, 15 samples were chosen for further investigation using geochemical analysis and are the focus of this study.



Figure 2. Fifty-two drill core samples taken from the North Stock core repository displaying the variation in the altered volcanics.

2.2 Methods

Each of the 32 sections of core chosen for the first phase of analysis were slabbed lengthwise into three parts. The top portion of the half-core or quarter-core was kept as a hand sample, the middle and bottom portions were used to create billets for thin sections and geochemical analysis. Thin sections were created by Wagner Petrographic in Lindon, Utah.

Hand sample and thin section analysis was conducted by the author at the University of Wyoming. Visible characteristics of each hand sample were recorded. Mineralogy of each thin section was examined using a petrographic microscope under both plain and polarized light.

Automated mineralogy modal analysis was performed on thin sections from each of the 32 samples by staff at the Colorado School of Mines Automated Mineralogy Laboratory using a TESCAN Integrated Mineral Analyzer.

Portions of each of the 15 samples chosen for geochemical analysis were sent to ALS Geochemistry in Tucson, Arizona. Samples were analysed for major and trace elements, as well as Au and certain platinum group elements.

3 Results and Discussion

Using the 15 samples on which both the automated mineralogy modal analysis and the geochemical analyses were obtained, it was possible to further group the samples into four distinct subgroups based on inferred pre-alteration mineralogy and alteration geochemistry. The six samples shown in Figure 3 represent a single subgroup of similar volcanic products that have albite and biotite as the primary phenocrysts or contain alteration assemblages that suggest such minerals were originally present. The samples have undergone varying amounts of albitization or potassic alteration.

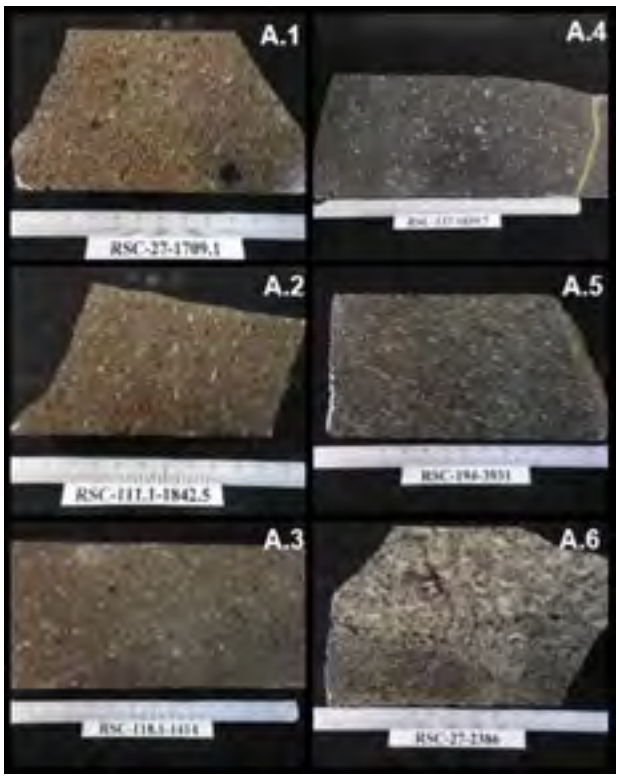


Figure 3. Subset of six samples having similar primary mineralogy and varying degrees of alkali alteration.

Samples A.1-A.3 and B.1-B.3, shown in Figure 4 below, represent two of the additional subgroups identified during this study. Samples A.1-A.3 represent the most primitive samples studied based on major and trace element geochemical patterns. These samples have the lowest wt % SiO_2 ranging from 50.6-51.4 wt % while all other samples have greater than 54 wt % SiO_2.

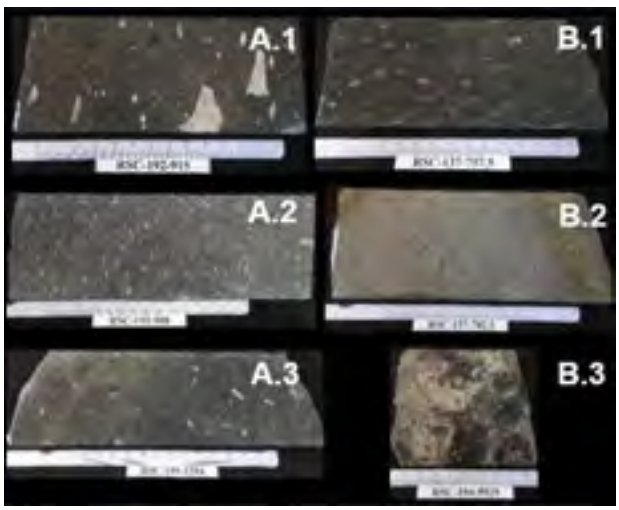


Figure 4. Two subsets of petrographically and geochemically similar samples. A.1-A.3) the three most primitive samples examined, all of which underwent extensive calcite replacement. B.1-B.3) Phonolites exhibiting varying levels of alteration.

Samples A.1-A.3 also have the highest wt % CaO_3 with the elevated CaO_3 values resulting from the addition of calcite. While all three samples from column A of Figure 4 have elevated mantle compatible elements compared to the rest of the sample set, sample RSC-191-1294 has anomalously high Co, Cr, Cs, and Ni at 19 ppm, 250 ppm, 42.3 ppm, and 62 ppm, respectively, which is likely attributable to the presence of minor xenoliths that were observed in sections of core surrounding the sample during sample collection.

Samples RSC-137-757.5 and RSC-137-782.5, shown as B.1 and B.2 in Figure 4, represent porphyritic phonolites that have undergone varying levels of hydrothermal alteration. Sample RSC-194-5929, shown as B.3 in Figure 4, was obtained at the greatest drill depth below surface of any of the studied samples. This sample has undergone a much greater degree of alteration compared to samples RSC-137-757.5 and RSC-137-782.5 but has been grouped together with those samples based on rare earth element geochemistry.

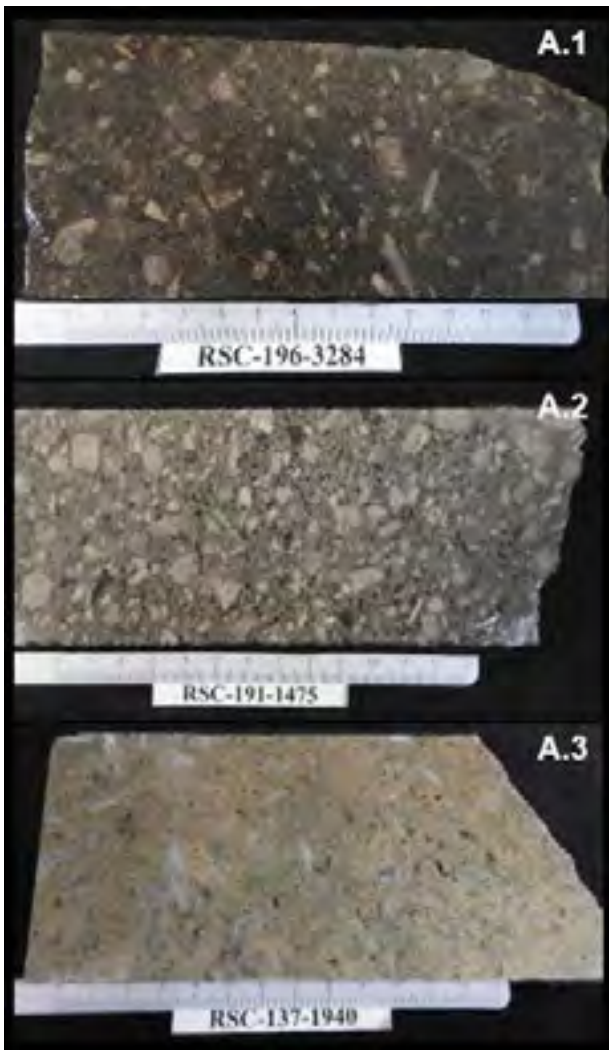


Figure 5. Samples sharing similar pre-alteration macro-phenocryst assemblages but significant variation in geochemistry due to alteration.

The samples shown in Figure 5 share similar pre-alteration phenocryst assemblages of zoned alkali feldspars but exhibit a level of variation in trace element geochemistry that is unlikely to be a result of alteration alone. As shown below in Table 1, the measured concentration of certain relatively immobile trace elements from the samples of Figure 5 suggests that the samples may represent mixing between a common feldspar phenocryst-rich magma and other less evolved magmas.

Sample	Y	Ni	Cr	V
3284	*34.1*	*49*	*130*	*342*
1475	*31.7*	*18*	*50*	*190*
1940	*26.1*	*8*	*10*	*102*

Table 1. Selected trace element geochemical data in parts per million (ppm) for samples shown in Figure 5.

Four of the fifteen samples contained elevated concentrations of Au (Fig 6). Gold values ranged from a high of 0.528 ppm to a low of 0.017 ppm. The depth of the mineralized samples ranged from approximately 1,940 feet to 5929 feet below surface. While only a small group of the samples chosen for this study had elevated Au concentrations, three out of the four subgroups identified during this study are represented by the mineralized samples. Only the subgroup that had undergone extensive calcite replacement lacked at least one sample with elevated Au.

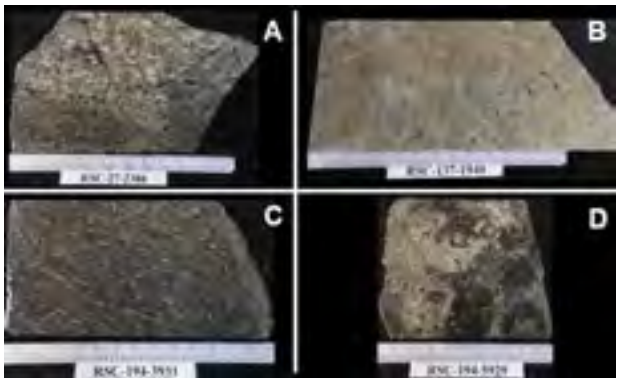


Figure 6. Samples containing elevated gold concentrations. A) 0.528 ppm Au. B) 0.035 ppm Au. C) 0.021 ppm Au. D) 0.017 ppm Au.

4 Conclusions

The small sample size used in this study prevents extrapolation of results to the entire North Stock site, but the presence of elevated gold concentrations in three of the four petrologically similar subgroups indicates that mineralization at North Stock was not limited to a certain pre-alteration rock type. Mineralized samples also represent significantly different depth profiles suggesting that gold mineralization is not limited across a short vertical horizon, but additional analysis of samples from various locations in and around the diatreme is

needed to determine the approximate geometry of the mineralization zone.

Acknowledgements

The author thanks the previous field site operator, GFG Resources Inc., and the current field site operator, Patriot Gold Vault, for access to drill core and conversations regarding the geology of the site. The author also thanks Dr. Simone Runyon, former University of Wyoming Assistant Professor of Economic Geology, for providing guidance and valuable insights during the early stages of this project and Dr. Ken Sims for sharing his vast knowledge of volcanic processes. Financial support for this research was provided by the University of Wyoming, the Geological Society of America Graduate Student Research Grant Program, and the National Science Foundation.

References

Autenrieth KD (2012) Geologic Setting of Gold Mineralization in the Rattlesnake Hills, Wyoming: M.S. Thesis, Idaho State University.

Hausel WD (1996) Geology and Gold Mineralization of the Rattlesnake Hills, Granite Mountains, Wyoming: Wyoming State Geological Survey Report of Investigations 52, 25 p.

Hoch AR (1991) Petrological and Geochemical Evolution of the Rattlesnake Hills Alkaline-Intrusive Complex, Natrona County, Wyoming: M.S. Thesis, University of Wyoming.

Hoch AR, Frost CD (1993) Petrographic and geochemical characteristics of mid-Tertiary igneous rocks in the Rattlesnake Hills, central Wyoming, with a comparison to the Bear Lodge intrusive suite of northeastern Wyoming, in Snoke, A.W., Steidtmann, J.R., and Roberts, S.M., editors, Geology of Wyoming: Wyoming State Geological Survey Memoir 5, p. 508-528.

Pekarek AH, Marvin RF, Mehnert HH (1974) K-Ar Ages of the Volcanics in the Rattlesnake Hills, Central Wyoming: Geology, v. 2, p. 283-285.

Ripple A (2012) Hydrothermal Fluid and Ore Paragenesis of the Gold-Bearing Rattlesnake Hills Alkaline Complex, Wyoming: M.S. Thesis, Colorado State University.

Shive PN, Pekarek AK, Zawislak RL (1977) Volcanism in the Rattlesnake Hills of central Wyoming: A paleomagnetic study: Geology, v. 5, p. 563-566.

Stupak WA (1984) The Petrography and Petrochemistry of the Eocene Volcanics, Rattlesnake Hills, Central Wyoming: MS Thesis, University of Wyoming.

Rare Earth Element Redistribution in Ultramafic Lamprophyres of Western Kentucky: Insights from Petrography and Geochemistry

Georgina Lukoczki[1], Kyle Dayton[2], Zachary Walton[1], Esteban Gazel[2]
[1]*University of Kentucky, Kentucky Geological Survey, USA*
[2]*Cornell University, Department of Earth and Atmospheric Sciences, USA*

Abstract. Ultramafic lamprophyre (UML) intrusions in western Kentucky and southern Illinois are spatially associated with the Coefield Magnetic Anomaly and Hicks Dome in the Illinois-Kentucky Fluorspar District. While Hicks Dome has been a focus of rare earth element (REE) studies, the Coefield Magnetic Anomaly remains less explored. This study investigates the origin and alteration history of these UML intrusions, with a focus on REE distribution. Samples from legacy drill cores were analyzed using thin section petrography as well as whole-rock and in-situ geochemistry. The UML intrusions exhibit intense alteration, with primary mafic minerals largely replaced by serpentine and carbonates. Despite low bulk-rock REE concentrations (64–620 ppm), anatase and apatite host significant REE enrichment, with anatase containing up to 95,620 ppm REEs. Elemental mapping suggests REE enrichment in anatase results from micron- to sub-micron-sized Ce-phosphate (monazite) inclusions. The restriction of REE minerals to the vicinity of anatase suggests perovskite alteration by magmatic-hydrothermal fluids led to REE redistribution.

1 Introduction

Ultramafic lamprophyre (UML) intrusions occur in western Kentucky and southern Illinois and are spatially associated with the Coefield Magnetic Anomaly and Hicks Dome (also referred to as the Hicks Dome Igneous Complex) and fluorite mineralization in the Illinois-Kentucky Fluorspar District (IKFD). While Hicks Dome has been the focus of renewed research interest in recent years due to high rare earth element (REE) concentrations in igneous breccias there (e.g., Trela et al. 2024), the Coefield Magnetic Anomaly (also referred to as Coefield Igneous Complex; Anderson 2019) is a lesser-known feature prominent in geophysical maps (Fig. 1, Lukoczki et al. 2022).

The lamprophyre intrusions and fluorite mineralization are associated with a structurally and geochemically complex area situated at the intersection of the Reelfoot Rift and the Rough Creek Graben (e.g., Trace and Amos 1984). This failed rift system is interpreted to have originated during the breakup of Rodinia, with the emplacement of dikes, derived from near-primary melts of a metasomatized lithospheric mantle, occurring during the Permian, amid a regional tectonic reorganization (Maria et al. 2019).The close association of fluorite deposits and igneous dikes in the IKFD has long been invoked to support a magmatic origin of fluorine (e.g., Plumlee et al. 1995); however, the exact role of the igneous intrusions in fluorite mineralization is still debated. The prevailing hypothesis suggests that the introduction of HF-rich gases from alkaline igneous sources into basin brines transformed them into highly acidic, fluorine-rich fluids capable of precipitating the extensive fluorite deposits observed in the IKFD (Plumlee et al. 1995).

The focus of this research is to explain the origin and alteration history of the igneous dikes in western Kentucky, with special emphasis on characterizing the REE distribution in these rocks.

2 Samples and methods

2.1 Samples

Samples were collected from legacy mineral exploration drill cores archived at the Earth Analysis Research Library of the Kentucky Geological Survey. A total of 46 drill cores were sampled for whole-rock geochemistry and thin section petrography, and a subset of eight samples were selected from six historic mining and exploration areas in Crittenden and Livingston counties of Kentucky: Columbia Mine, Crystal-Holly, Hutson, Lady Farmer, Maple Lake, and Minner (Fig. 1).

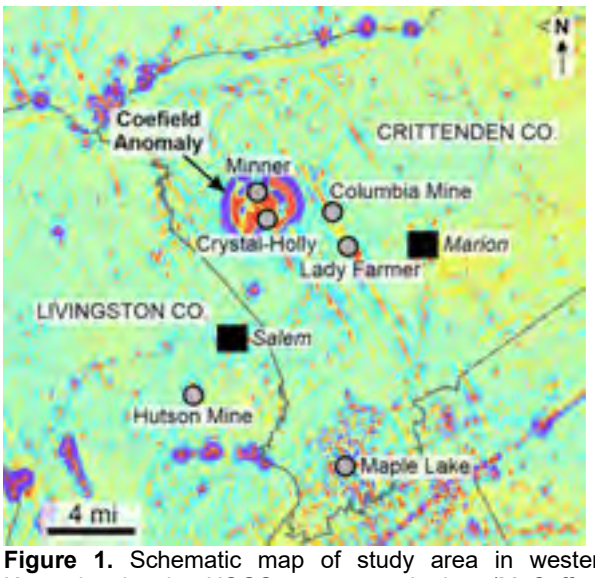


Figure 1. Schematic map of study area in western Kentucky showing USGS aeromagnetic data (McCafferty and Brown 2020) and sampling locations. Gray lines mark county borders. Red magnetic highs trending NW-SE indicate igneous intrusions.

2.1 Methods

Whole-rock geochemical data from 162 dike samples were obtained through wavelength dispersive X-ray fluorescence (XRF) spectrometry and inductively coupled plasma mass spectrometry (ICP-MS) by the U.S. Geological Survey contract laboratories. These data, combined with thin section petrography, guided the selection of a representative subset of samples for detailed geochemical characterization. In-situ geochemical data on apatite and anatase, as well as other minerals, were collected from eight thin sections via laser ablation (LA) ICP-MS at Cornell University, with precision better than 5% for all elements except Cs (5.5%) and Pb (10.8%) and accuracy better than 5% for all elements except Ni (6.8%), Hf (5.5%), Ta (5.4%) and U (6.2%) from secondary standard values across all analytical sessions. Laser ablation spot analysis (n=319) of individual mineral phases were selected based on energy dispersive X-ray spectroscopy (EDS) element maps. EDS elemental composition data were used as internal standards for the laser ablation ICP-MS data.

3 Results and discussion

Petrographic observations indicate intense alteration of the UML intrusions, with most primary mafic minerals (olivine and pyroxene) completely replaced by serpentine and carbonate minerals. Carbonate pseudomorphs after olivine and pyroxenes contain serpentine inclusions and abundant magnetite, suggesting carbonate replacement followed serpentinization.

The studied samples can be divided into two groups based on relatively Si-rich (ca. 25–50 wt.% SiO_2) and Si-poor composition (<25 wt.% SiO_2). The mineralogy of the Si-rich samples is dominated by phlogopite and serpentine, whereas the mineralogy of the Si-poor samples is dominated by carbonates. Carbonates are abundant in both types of rocks and are mostly represented by dolomite, ferroan dolomite, and calcite. Ferroan calcite, siderite, and magnesite also occur but with lower abundances. The pseudomorphic fabric of all carbonate-rich (Si-poor) samples suggests secondary carbonation. The Si-rich rocks have been tentatively classified as aillikites (Tappe et al. 2005) due to their mostly melilite-free mineralogical composition.

Apatite is a common but not abundant mineral phase that occurs mostly as small (<10 μm) crystals in the matrix of both Si-rich and Si-poor samples. Less typically, larger (up to 500 μm) lath-shaped apatite crystals enclosing abundant inclusions also occur, suggesting prolonged or secondary apatite crystallization. Opaque phases are also abundant in both Si-rich and Si-poor samples and are dominated by spinel group minerals, mostly magnetite, and lower amounts of chromite. Ti-rich opaque minerals were identified as anatase.

Whole-rock geochemical data show relatively low total (Σ) REE content in these rocks (51–569 ppm, average 303 ppm). Laser ablation ICP-MS data revealed that the highest amounts of ΣREE are found in anatase (highest measured ΣREE 95,620 ppm, average 11,982 ppm) and apatite (highest measured ΣREE 3,729 ppm, average 1,181 ppm). Chondrite-normalized plots of REE distribution show light REE (LREE) enrichment (Fig. 2) characteristic of mantle-derived materials. Sc and Y contents of both minerals are relatively low; however, a few instances of high (>3,000 ppm) Sc were found in a few anatase and ilmenite data points. The relatively high Nb content of anatase (1,926–12,547 ppm, average 5,245 ppm) and ilmenite (300–2,593 ppm, average 1,816 ppm) also sets these minerals apart from the others. In the carbonates, the total REE content of dolomite ranges from 9 ppm to 1,098 ppm (average 321 ppm), and the total REE content of calcite ranges from 1 ppm to 1,576 ppm (average 509 ppm).

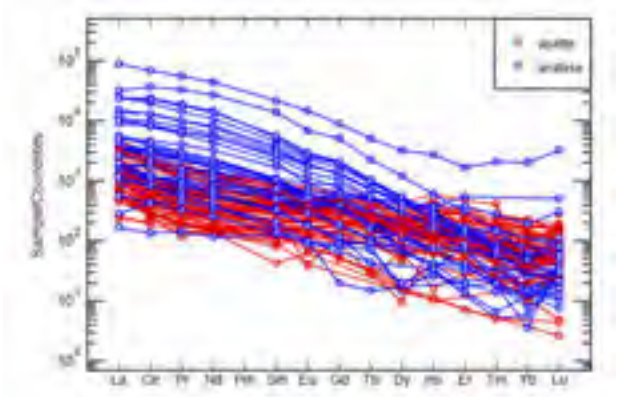


Figure 2. Chondrite-normalized (McDonough and Sun 1995) rare earth element distribution in apatite and anatase in lamprophyre dikes of western Kentucky.

Given the remarkably high REE content in anatase, these minerals were further analyzed using EDS. Observations indicate that the elevated REE concentrations result from micron- to sub-micron-sized Ce-phosphate (likely monazite) inclusions (Fig. 3).

Elemental mapping revealed a complex texture, where cryptocrystalline phases—tentatively identified as anatase and monazite—are intimately intergrown, suggesting that the observed mineral assemblage formed through alteration processes. Further detailed analyses are planned to confirm the mineralogical composition. These preliminary observations fit well with observations elsewhere (e.g., Kola Peninsula, Russia; Iron Mountain, USA; Prairie Lake, Canada; Benfontein, South Africa), where Ti-oxide minerals, such as rutile and anatase, are known to occur together with REE minerals and are interpreted to have formed as alteration products after perovskite (e.g., Mitchell and Chakhmouradian 1998, Chakhmouradian and Mitchell 2000, Martins et al. 2014). Perovskite, which forms a complete solid solution with LREE-

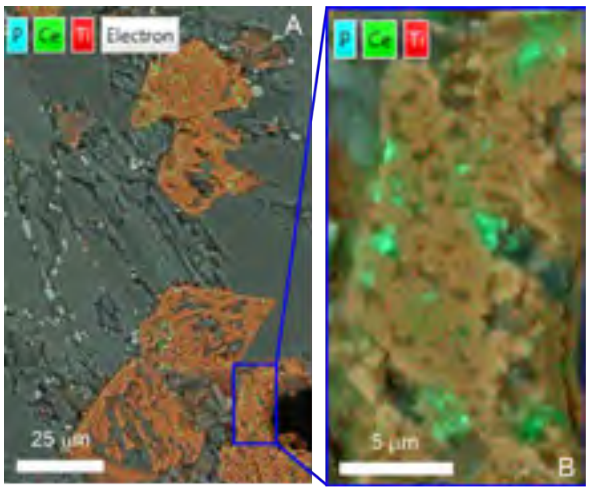


Figure 3. Element maps overlain on back-scattered electron images showing the distribution of P, Ce, and Ti in a lamprophyre dike sample from western Kentucky. (A) Altered anatase pseudomorphs likely after perovskite. Green speckles within orange-red anatase indicate Ce-rich inclusions. Blue rectangle next to ablation pit highlights the location of zoomed-in image in B. (B) Higher-magnification element map detail of A, clearly showing Ce-rich inclusions (green) within anatase (orange).

dominant end member loparite, is a chief host for LREEs in undersaturated ultramafic and alkaline rocks (Mitchell and Chakhmouradian 1998) similar to those in western Kentucky. The REE content of perovskite varies widely and may contain as much as 4–5 wt.% REE oxide (e.g., Jones and Wyllie 1984). As a result of deuteric alteration due to interaction with CO_2-rich fluids, LREEs are released from perovskite and are incorporated into secondary REE minerals. This process is interpreted to be a result of the same alteration event responsible for serpentinization and phlogopitization of the primary mafic minerals (olivine and pyroxene) in alkaline ultramafic rocks (Mitchell and Chakhmouradian 1998). While these studies report ancylite and lucasite as LREE-bearing phases (hydrated REE carbonate and REE-Ti hydroxide-oxide, respectively) and not REE-phosphates (e.g., monazite), the overall similar paragenesis in the UMLs of western Kentucky suggests similar processes were at play. Our preliminary observations suggest REE minerals are limited to the immediate vicinity of anatase, hence we suggest that these REE-bearing phases formed as a result of perovskite alteration by a phosphate-bearing magmatic-hydrothermal fluid.

4 Conclusions

Petrographic and geochemical analyses of the UML intrusions in western Kentucky indicate extensive alteration, with primary mafic minerals largely replaced by serpentine and carbonate minerals. The studied samples can be categorized into Si-rich and Si-poor groups. Geochemical data revealed low overall REE concentrations in bulk rocks but significantly elevated REE contents in anatase and apatite, with anatase hosting the highest REE concentrations. Elemental mapping indicates that the REE enrichment in anatase results from micron- to sub-micron-sized Ce-phosphate (likely monazite) inclusions. The intimate intergrowth of anatase and monazite suggests REE redistribution through alteration processes.

These findings align with previous studies on Ti-oxide-associated REE mineralization, where alteration of perovskite in ultramafic and alkaline systems leads to the formation of secondary REE minerals. The paragenesis observed in the UMLs of western Kentucky is consistent with REE mobilization and mineralization during the magmatic-hydrothermal transitional stage. The restriction of REE minerals to the vicinity of anatase supports the interpretation that perovskite alteration by hydrothermal fluids played a key role in REE concentration in these rocks. Further studies are required to confirm the mineralogical assemblages and better constrain the mechanisms of REE enrichment.

Acknowledgements

This project was funded by the USGS Earth Mapping Resources Initiative Program. Discussions with Craig Dietsch and core sampling work by Tom Uhl are much appreciated.

References

Anderson WH (2019) Mineralogy and chemistry of rare earth elements in alkaline ultramafic rocks and fluorite in the Western Kentucky Fluorspar District: Kentucky Geological Survey, ser. 8, Report of Investigations RI-8, 49p. doi.org/10.13023/kgs.ri08.13.

Chakhmouradian AR, Mitchell RH (2000) Occurrence, alteration patterns and compositional variation of perovskite in kimberlites. Canadian Mineralogist, 38(4): 975-994.

Jones AP, Wyllie PJ (1984) Minor elements in perovskite from kimberlites and distribution of rare earth elements: an electron probe study. Earth and Planetary Science Letters, 69: 128-140.

Lukoczki G, Dietsch C, Hickman JB, Morris E, Curl DC, Pulliam C, Vicroy S, Andrews WM (2022) Phase I activities of the Earth Mapping Resources Initiative (Earth MRI) in the Western Kentucky Fluorspar District: Kentucky Geological Survey, ser. 13, Report of Investigations 12, 22p. doi.org/10.13023/kgs.ri55.13.2022

Maria AH, Denny FB, DiPietro JA, Howard KF, King MD (2019) Geochemistry and Sr-Nd isotopic compositions of Permian ultramafic lamprophyres in the Reelfoot Rift–Rough Creek Graben, southern Illinois and northwestern Kentucky. Lithos, 340-341: 191-208.

Martins T, Chakhmouradian AR, Medici L (2014) Perovskite alteration in kimberlites and carbonatites: the role of kassite, $CaTi_2O_4(OH)_2$. Physics and Chemistry of Minerals, 41: 473-484.

McCafferty AE, Brown PJ (2020) Airborne magnetic and radiometric survey, southeastern Illinois, western Kentucky, and southern Indiana, 2019: U.S. Geological Survey data release.

McDonough WF, Sun SS (1995) The composition of the Earth. Chemical Geology, 120(3-4): 223-253.

Mitchell RH, Chakhmouradian AR (1998) Instability of perovskite in a CO_2-rich environment: examples from carbonatite and kimberlite. Canadian Mineralogist, 36: 939-952.
Plumlee GS, Goldhaber MB, Rowan EL (1995) The potential role of magmatic gases in the genesis of Illinois-Kentucky Fluorspar deposits: Implications from chemical reaction path modeling: Economic Geology, 90(5): 999–1011.
Tappe S, Foley SF, Jenner GA, Kjarsgaard BA (2005) Integrating ultramafic lamprophyres into the IUGS classification of igneous rocks: rationale and implications. Journal of Petrology, 46(9): 1893-1900.
Trace RD, Amos DH (1984) Stratigraphy and structure of the Western Kentucky Fluorspar District: U.S. Geological Survey, Professional Paper 1151-D, 41p.
Trela J, Freiburg JT, Gazel E, Nuelle L, Maria AH, Malone DH, Molinarolo JM (2024) Petrologic relationship between lamprophyres, carbonatites, and heavy rare-earth element enriched breccias at Hicks Dome. Terra Nova, 36(4): 298-305.

Characterization of REE-bearing Syenites in the Semarule Igneous Complex (SIC), Southeast Botswana

Rita Ngwanaotsile[1], Akira Imai[1], Kotaro Yonezu[1], Akane Ito[1], Zibisani Bagai[2]
[1]Department of Earth Resources Engineering, Faculty of Engineering, Kyushu University, Japan
[2]Department of Geology, University of Botswana, Gaborone, Botswana

Abstract.
The Semarule Igneous Complex (SIC) is a small 3 km wide intrusion that occurs within the Neoarchean Gaborone Granite of the Kaapvaal craton. This study focuses on discussing petrographic and geochemical characteristics of the REE-bearing syenites in the (SIC) to understand their nature based on SEM-EDX and whole rock geochemistry data. The syenite samples predominantly consist of orthoclase feldspar as the main felsic phase and amphibole as the primary mafic phase. Accessory phases are mainly represented by zircon, magnetite and titanite. Allanite and apatite are commonly identified as the primary REE-bearing minerals, characterized by elevated concentrations of light REEs such as La, Ce, and Nd. All samples fall within the syenite field on the total alkali silica (TAS) diagram, while the amphibole syenites straddle the boundary between the monzonite and monzo-syenite fields. Generally, these syenites are characterized by relatively high contents of SiO_2, Na_2O, K_2O, and Al_2O_3, along with lower levels of MgO, Fe_2O_3, and CaO. They are classified as metaluminous, peralkaline, high-K calc-alkaline, and have shoshonitic affinity.

1 Introduction

The recent emergence of REEs as essential metals for modern technology has fuelled global efforts to discover new REE orebodies. China currently dominates REE production, accounting for almost 95% of global production (European Commission 2017). As a result, the price of REEs has increased, and industrial countries are concerned about supply shortages. According to Roskill (2015), the demand for REOs was reported at 118 thousand tonnes in 2014, with projections estimating it to rise to approximately 170 thousand tonnes by 2020. Prominent deposits associated with alkaline rocks include Ilimaussaq (Greenland), Lovozero and Khibiny (Russia), Thor Lake (Canada), Strange Lake (Canada), Bokan Mountain (USA), Toongi and Brockman (Australia), and Pilanesberg (South Africa) (Dostal 2017; Elburg and Cawthorn 2017). REE deposits have captured the interest of both the exploration industry and the geological literature, especially in areas that might have been initially overlooked.

Alkaline igneous rocks are classified as either silica-oversaturated, such as granites and rhyolites with quartz and alkali amphiboles or pyroxenes, or silica-undersaturated, such as syenites, trachytes, and phonolites with normative feldspathoids (Le Maitre et al. 2004). The term "alkaline" refers to the high alkali (Na_2O + K_2O) content in these rocks (Winter 2010). Alkaline igneous complexes are typically enriched in incompatible REE elements, which is commonly attributed to magmatic evolution (Vasyukova and Williams-Jones 2020).

The Botswana Geological Institute (BGI) investigated the textural, mineralogical composition as well as the emplacement sequence of the syenites, dolerite and zoned dykes within the complex based on field relations. According to the report by BGI (2017), the complex is a result of continuous emplacement of magmatic intrusions with contrasting composition intruding the Gaborone granite. Lusty et al. (2012) investigated the petrogenesis and REE enrichment in the SIC, revealing that the complex formed through several phases of magma emplacement. Geochemical results depicted a maximum total rare earth oxide (TREO) concentration in the syenite approach 3000 ppm, particularly in the more mafic syenites. Therefore, this study aims to provide a comprehensive petrographical and geochemical characterization of the REE-bearing phases in the syenites in the SIC.

2 Background geology

2.1 Regional Geology

The Kaapvaal Craton in Southern Africa is one of the largest Archaean fragments found in the region (Poujol et al. 2003). A large area in the southern part of Botswana is underlain by the Kaapvaal Craton (Aldiss et al. 1994). The craton hosts a rich and pristine geological history and has undergone a long and complex history of magmatic events, starting as early as in the Paleoarchean. It is suggested to have formed from the accretion of individual crustal blocks namely the Eastern, Central, Northern and Western terranes (Poujol et al. 2003). According to de Witt et al. (1992) welding of continental fragments to produce the current Kaapvaal Craton occurred sometime between ~3100 and 2900 Ma. Following the assembly of the blocks that make up the Kaapvaal Craton, which was relatively unstable, a period of Mesoarchean magmatism occurred around 3100 Ma (Poujol et al. 2003). This is evident through the emplacement of voluminous, extensive sheetlike, potassic granitoid batholiths. These granitoids were mostly found in all crustal blocks and were thought to be responsible for the crustal thickening, stabilization, and consolidation of the blocks into what is now known as the Kaapvaal Craton. The Archaean basement of the Kaapvaal craton is primarily composed of high-grade metamorphic igneous and metasedimentary rocks.

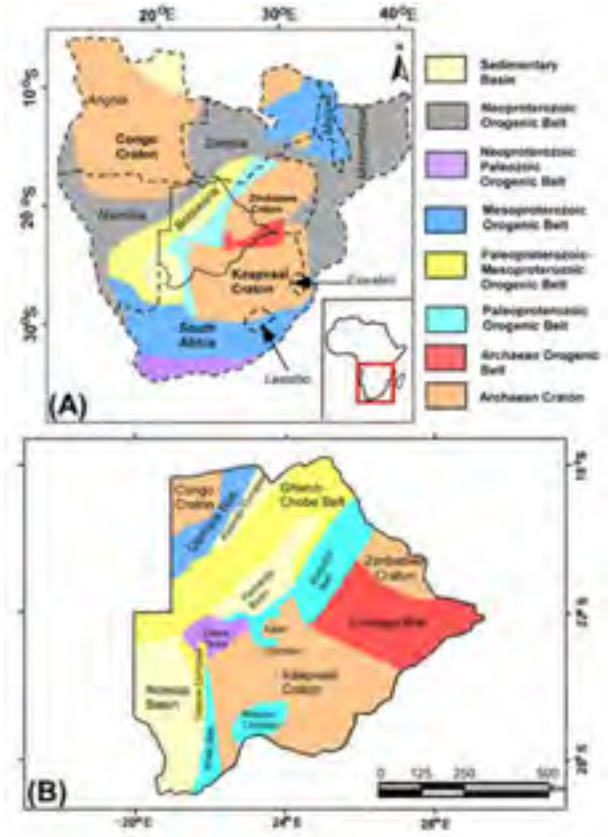


Figure 1. The Map of (A) Southern Africa Archaean cratons and its orogenic belts and (B) Geology of Botswana (modified after Singletary et al.2003).

2. 2 Local geology

The Gaborone granite complex forms part of the Kaapvaal craton basement rocks, extending at least 140km east-west and 100km north-south, although the western part is obscured by the Kalahari beds it continues to outcrop in some areas. The granite series is a Precambrian complex comprising of volcanic, granophyric, and granitic rocks (Grobler and Walraren 1993).

The SIC is a 3-km-wide alkaline intrusive suite emplaced within Neoarchean Gaborone Granite in the southern part of the Kaapvaal craton (Lusty et al. 2012). It forms a small range of hills around the south of Molepolole, namely the Semarule, Deritshane, Hamongwane and Mmamolo hills. The age of the Semarule is otherwise uncertain (Carney et al. 1994). It has an overall elongated WNW–ESE-trending shape, suggesting that a preexisting fracture in the host Gaborone Granite controlled its emplacement, although the main exposure forms a crescent-shaped body The inner part of the intrusion is more complex and compositionally varied, consisting of grained syenite, coarse to pegmatitic syenite and zoned syenite veins. A thick (~50-meter), sub-horizontal dolerite intrudes the eastern part of the complex (Lusty et al, 2012).

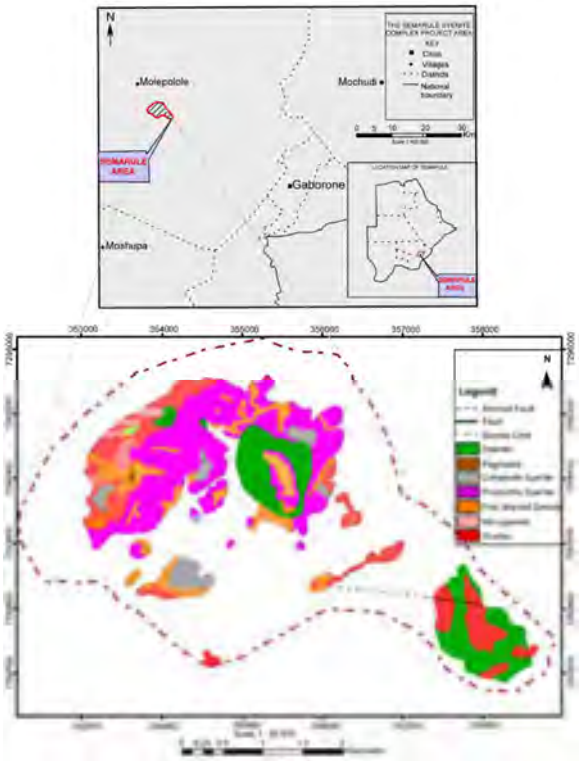


Figure 2. Local geology of the Semarule Igneous Complex (Botswana Geological Institute, 2020).

3 Samples and Methods

Thirty representative samples were collected and processed into thin sections and polished blocks at the Department of Earth Resources Engineering, Kyushu University. Thinsections were examined with the Hitachi SU 3500 High Tech scanning electron microscope with energy-dispersive X-ray Spectroscopy (SEM-EDX) at the Center of Advanced Instrumental Analysis, Kyushu University. Whole rock geochemistry of the representative compressed powder pellets for major and trace elements was determined by X-ray fluorescence spectrometer (XRF) analysis using Rigaku ZSX Primus IV at Kyushu University. loss on ignition (LOI) was determined by weight difference after oven to 105 ˚C for 1.5 hrs. and ignition at 500 ˚C for 1 hour, followed by 1000 ˚C for 2 hrs for each sample. The precision and accuracy of the XRF analysis were evaluated using duplicate measurements of the JA-2 standard material provided by the Geological Society of Japan (Imai et al., 1995).

4 Results and Discussion

4.1 Sample observations

The predominant rock type in the Semarule Igneous Complex is syenite, primarily composed of alkaline feldspars, and amphiboles. These rocks are predominantly pinkish and exhibit a range of textures, from fine-grained to coarse-grained, as well as porphyritic and pegmatitic textures (Fig. 3).

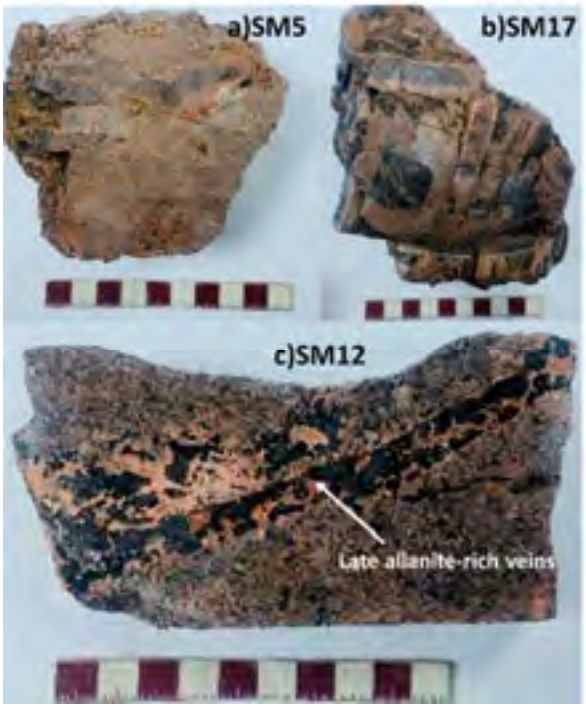


Figure 3. Photographs of representative hand specimens of syenitic rocks from the study area (a) alkaline syenite (b) pegmatitic syenite and (c) amphibole syenite.

Amphibole syenites, characterized by prismatic amphiboles and over 50% mafic minerals, display greyish pink to pinkish-grey color with fine to coarse porphyritic textures. In some cases, these samples are cut across by the late allanite-rich veins.

4.2 Mineralogical characteristics

The syenites are characterized by the presence of alkaline feldspar, particularly orthoclase, which serves as the primary rock-forming mineral (Fig. 4). Amphibole-rich syenites are commonly abundant in allanite, which typically appears as large, euhedral to subhedral blebs with a coarse texture. Allanite porphyroblasts often contain orthoclase inclusions (Fig. 4a-c). Apatite minerals within these syenites are identified as fluorapatite, characterized by a high fluorine content, suggesting that the associated fluids were likely fluorine-rich (Walters et al. 2013). Fluorapatite generally forms as euhedral to subhedral crystals and is frequently found in association with allanite (Fig 3.d-f) The samples indicate the presence of typical accessory minerals such as monazite, magnetite, and zircon (Fig. 3g-i). Notable replacement textures and mineral inclusions are visible in monazite and apatite although monazite shows no REE concentration through SEM spot analysis. Monazite is altered and often replaced by an assemblage of allanite, apatite, thorite, and occasionally zircon (Sato et al. 2014).

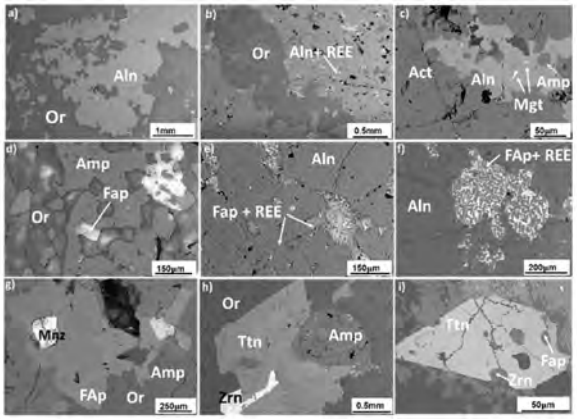


Figure 4. Backscattered Electron (BSE) images of mineral assemblages in syenites from the SIC (a) allanite occurs as large blebs within an orthoclase groundmass (b) allanite, a major REE-bearing mineral, is associated with fine-grained REE-rich patchy grains (c) allanite is associated with amphibole and magnetite, forming a distinct mineral assemblage (d) REE-enriched fluorapatite occurs as euhedral to subhedral grains within an orthoclase groundmass (e) fluorapatite is associated with allanite, which displays noticeable fractures and irregular grain boundaries (f) subhedral fluorapatite bleb with a patchy texture (g) monazite occurs as a subhedral commonly associated with fluorapatite, feldspar, and amphibole (h) titanite-zircon-amphibole rich mineral assemblage occur within an orthoclase matrix (i) zircon and fluorapatite are enclosed within the wedge-shaped titanite grain.

4.3 Whole Rock geochemistry

The analyzed geochemical data from alkaline syenites, amphibole syenites and pegmatitic syenites samples depict a high total alkali content (9.75–14.36 wt.%). Most samples plot within the syenite while the amphibole syenite staddle between the monzonite and monzo-syenite fields on the TAS diagram (Fig 5a). The low aluminum saturation index values of A/CNK (0.5–0.8) and A/NK (0.9–1) indicate that these rocks fall within the peralkaline and peraluminous series (Fig 5b). Peralkaline rocks have an ASI of less than 1, suggesting they are enriched in alkali elements relative to aluminum. In contrast, peraluminous samples are suggestive of an excess of aluminum relative to alkali elements. The high K_2O/Na_2O ratios and elevated K_2O concentrations indicate that these rocks in the SIC exhibit affinities for high -K calcic-alkaline and shoshonite series (Fig.4c). The shoshonite series is characterized by low iron enrichment, elevated $Na_2O + K_2O$ levels, a high concentration of light ion lithophile elements (LILE), a high but variable Al_2O_3 content, a high Fe_2O_3/FeO ratio, and low TiO_2 content (Morrison, 1980).

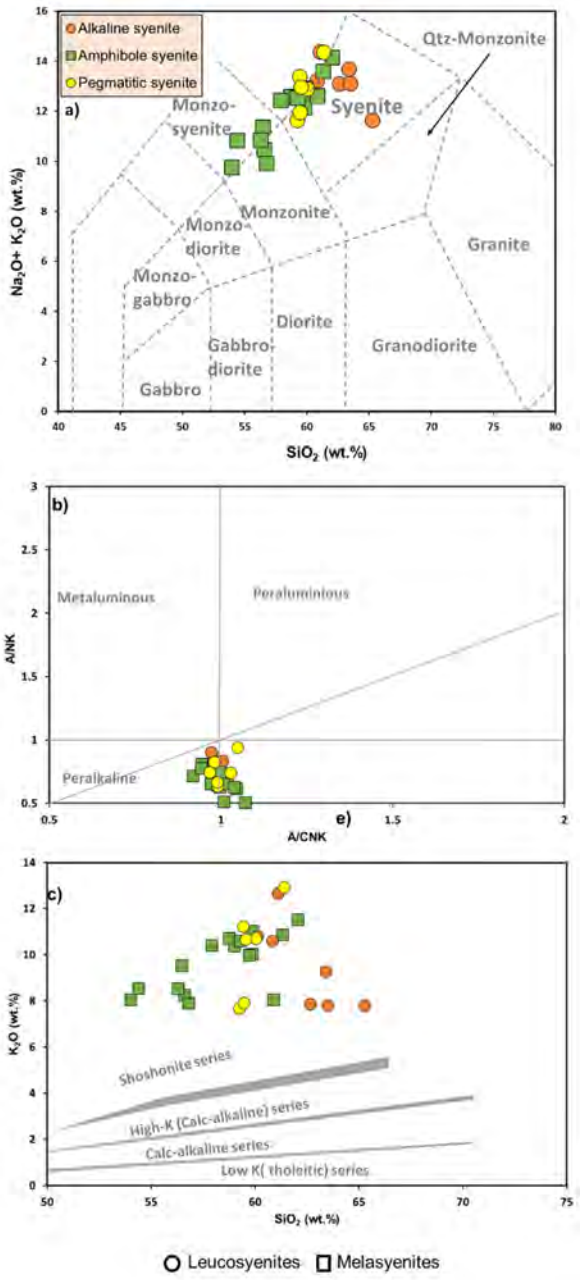


Figure 5. Geochemical bivariate plots of the alkaline complex in the SIC a) TAS diagram modified after (Middlemost, 1994) (b) A/CNK versus A/NK plot. (c) SiO2 versus K2O, modified after (Peccerillo et al. 1976).

5 Conclusions

Based on SEM EDX analysis, accessory minerals, including titanite, magnetite zircon were identified. The main minerals hosting REEs are apatite and allanite, with monazite occurring less frequently. These minerals concentrate significant amounts of incompatible elements such as La, Ce and Nd. The samples plot in the field of syenite in the TAS classification except few amphibole-rich syenites that straddle between the monzo-syenite and monzonite fields. The geochemistry confirms the alkaline nature of the igneous suite, with a calc-alkaline and shoshonitic affinity.

Acknowledgments

We sincerely appreciate the financial support from the Society of Resource Geologists (SRG), which finance the fieldwork of this research.

References

Botswana Geoscience Institute Report (2020) Detailed geological mapping of the Semarule Igneous Complex (SIC) Southeast Molepolole Botswana.

de Witt M, Armstrong R, Hart R, de Ronde C, Green R, Tredoux M, Perberdy E, Roering C (1992) Formation of Archean continent. Nature 357(6379):553–562.

Dostal J (2017) Rare earth element deposits of alkaline igneous rocks. Resources 6(3):34.

Elburg MA, Cawthorn RG (2017) Source and evolution of the alkaline Pilanesberg Complex South Africa. Chemical Geology 455:148-165.

European Commission (2017) Study on the review of the list of critical raw materials industrial policy Trade Competition EU 1–93 https://doi.org/10.2873/876644 978-92-79-47937-3.

Grobler DF, Walraven F (1993) Geochronology of Gaborone Granite Complex extensions in the area north of Mafikeng South Africa. Chemical Geology 105:319–337.

Imai N (1995) Compilation of analytical data for minor and trace elements in seventeen GSJ geochemical reference samples "igneous rock series" Geostandards Newsletter 19(2):135–213

Lusty PA, Walters AS, Key RM, Gunn AG, Kewame G (2012) Petrogenesis and REE enrichment of the Semarule Syenite, south-eastern Botswana. European Mineralogical Conference British Geological Survey United Kingdom Geological Survey of Botswana.

Morrison GW (1980) Characteristics and tectonic setting of the shoshonite rock association. Lithos 13(1):97-108.

Poujol M, Robb LJ, Anhaeusser CR, Gericke B (2003) A review of the geochronological constraints on the evolution of the Kaapvaal Craton South Africa. Precambrian Research 127(1–3):181–213.

Roskill (2015) Rare Earths Market Outlook to 2020.Roskill Information Services Ltd London, UK .15th edition.

Sato K, Minakawa T, Kato T, Maki K, Iwano H, Hirata T, Suzuki K (2013) Behavior of rare elements in Late Cretaceous pegmatites from the Setouchi Province Inner Zone of southwest Japan. Journal of Mineralogical and Petrological Sciences 109(1):28-33.

Singletary SJ, Hanson RE, Martin MW, Crowley JL, Bowring SA, Key RM, Krol MA (2003) Geochronology of basement rocks in the Kalahari Desert Botswana and implications for regional Proterozoic tectonics. Precambrian Research 121(1-2):47-71.

Vasyukova O, Williams-Jones A (2020) Partial melting fractional crystallization liquid immiscibility and hydrothermal mobilization, A recipe for the formation of economic A-type granite-hosted HFSE deposits. Lithos 356:105300.

Walters AS, Goodenough KM, Hughes HS, Roberts NM, Gunn AG, Rushton J, Lacinska A (2013) Enrichment of Rare Earth Elements during magmatic and post-magmatic processes a case study from the Loch Loyal Syenite Complex northern Scotland Contributions to Mineralogy and Petrology 166:1177-1202.

Winter JD (2001) An introduction to igneous and metamorphic petrology. New Jersey Prentice Hall 697 p.

Hydrothermal Veining and Fenitization as Vectors for Hydrothermal REE Mobilization in the Lemitar Mountains Carbonatite, New Mexico

Willa Obringer[1,2], Alexander Gysi[1,2], Nicole Hurtig[2]
[1]New Mexico Bureau of Geology and Mineral Resources, New Mexico Institute of Mining and Technology, Socorro, NM 87801, USA
[2] Department of Earth and Environmental Science, New Mexico Institute of Mining and Technology, Socorro, NM 87801, USA

Abstract. Rare earth elements (REE) are critical elements essential to high-tech and green energy industries. Carbonatites are the primary global source of light REE, yet the processes controlling their formation remain unclear. While magmatic processes contribute to REE enrichment during carbonatite emplacement, hydrothermal alteration can further mobilize and concentrate the REE. This study examines hydrothermal veins and fenitization associated with Cambrian carbonatite dikes in New Mexico's Lemitar Mountains. Three hydrothermal vein types are identified: (I) quartz-albite, (II) quartz-calcite with chlorite and hematite, and (III) (barite)-fluorite-quartz-calcite. Type II and III veins contain REE fluorocarbonate minerals. Fenitization of the surrounding Proterozoic metadiorites is marked by sodic and potassic feldspar alteration and hydrothermal REE-bearing phases like apatite that display features different from primary apatite in the carbonatite. Petrographic observations include optical microscopy, SEM-BSE, and cathodoluminescence that were used to characterize a mineral paragenesis, alteration styles in the surrounding host rocks, and hydrothermal vs. magmatic REE-bearing minerals. These observations yield insights into REE mobilization mechanisms in carbonatites and assess fenitization zones as an exploration tool for carbonatite-hosted REE deposits.

1 Introduction

Rare earth elements are essential for the global shift to high-tech and green energy (Verplanck et al. 2014). Economic REE deposits are primarily hosted in carbonatite and alkaline/peralkaline igneous systems within intraplate tectonic settings (Smith et al. 2015). Carbonatites are the most significant global source of global light (L)REE production. These igneous rocks are mantle-derived and contain >50% carbonate minerals and minor phosphates, oxides, and silicates (Yaxley et al. 2022). Along with LREE, carbonatites are economical sources of iron, niobium, phosphorus, fluorine, and uranium (Verplanck et al. 2014).

Magmatic processes initially enrich carbonatites in the LREE, but hydrothermal alteration redistributes the REE into secondary minerals in alteration zones and veins, and therefore plays a significant role in the final evolution of these deposits (Elliott et al. 2018; Wang et al. 2020). Major REE deposits such as Bayan Obo (China) and Bear Lodge (US) show that late- to post-magmatic fluids introduce or remobilize REE, yet uncertainties remain about fluid evolution and REE transport in these deposits (Moore et al. 2015; Liu et al. 2018).

The Lemitar Mountains in New Mexico host REE-enriched carbonatite dikes with extensive hydrothermal overprinting and fenitization of the surrounding host rocks and multiple generations of hydrothermal veins (McLemore 1987; Ruggles 2024). Well-preserved outcrops and clear field relationships offer insights into hydrothermal REE transport, precipitation, and controls on fenitization. The properties of fenites can reflect fluid composition, metasomatic conditions, and fluid/rock ratios, unveiling important details regarding carbonatite formation and secondary enrichment (Elliott et al. 2018; Yaxley et al. 2022).

This study examines hydrothermal veins and alteration in the Lemitar Mountains carbonatites, focusing on quartz-albite, (hematite)-chlorite-quartz-calcite, and (barite)-fluorite-quartz-calcite assemblages. Optical microscopy evaluates mineralogy, alteration sequences, and vein paragenesis. Cathodoluminescence imaging is used to delineate apatite and calcite generations and feldspar alteration. SEM-BSE imaging provides REE analysis and microtextural insights. In this study, we assess the potential of using hydrothermal vein sequences and fenitization as geochemical exploration tools for carbonatite-hosted REE deposits.

2 Geological background

The Lemitar Mountains are located 10 km north of Socorro, NM and host to a series of calcio- and magnesio-carbonatites with xenocrysts of apatite, phlogopite, and magnetite; some of the carbonatites are also iron-rich and contain ankerite (McLemore 1987; Ackerman et al. 2021; Ruggles 2024). The carbonatites occur as complex stockworks, dikes, and micro-dikelets ranging from 1 cm to over a meter in thickness, intruding exposed Proterozoic country rocks, including the Lemitar metadiorite and metagabbro, the Polvadera granitoid, and the Corkscrew Canyon metasediments (McLemore 1987; Haft et al. 2022). These carbonatites were emplaced during Cambrian magmatism, with Ar-Ar and U-Pb dating yielding ages of 516.7 ± 0.7 Ma and 514.1 ± 2.7 Ma, respectively (Haft et al. 2022).

The deposit is considered low-grade and small tonnage with an estimated REE grade of ~1.1 wt% (McLemore 1987; Haft et al. 2022). The carbonatites most enriched in REE in the Lemitar Mountains are pervasively altered and overprinted

by hematization, chloritization, silicification, and patchy Ca-F metasomatism, and crosscut by multiple generations of hydrothermal veins (McLemore 1987; Ruggles 2024). The REE fluorocarbonates identified include bastnäsite, synchysite, and/or parisite (Ruggles 2024). Preliminary fluid inclusion studies in apatite, quartz, calcite, and fluorite indicate homogenization temperatures of >400 °C down to ~180 °C with reported salinities ranging between ~5 wt.% and ~20 wt.% NaCl (Ruggles 2024). Fenitization is present in the surrounding Lemitar diorite and gabbro in proximity to the carbonatites (McLemore 1987) but the extent of fenitization and detailed relationships to veining is yet still unclear.

3 Methods

Samples selected in this study are from the main Lemitar Mountains carbonatite in the southern area and include carbonatite dikes, hydrothermal veins described in Ruggles (2024), and the fenitized surrounding metadiorite. The hydrothermal veins studied include: (Type I) quartz-albite, (Type II) quartz-calcite with chlorite and hematite, and (Type III) barite-fluorite-quartz-calcite veins. Petrographic observations are conducted using an Olympus BX petrographic microscope equipped with an Olympus SC100 camera under transmitted and reflected light. Cathodoluminescence (CL) imaging is carried out with an ELM-3R Luminoscope attached to an Olympus BX2 petrographic microscope, operating under 100 mTorr vacuum pressure and a 12 kV accelerating voltage. Photomicrographs are captured with a Canon Rebel T7 camera.

Scanning electron microscopy (SEM) is performed using a JSM-IT700HR JEOL Field Emission SEM, with backscattered electron (BSE) images acquired at a 9–10 mm working distance and 15 kV accelerating voltage. Semi-quantitative compositional data is acquired through SEM-EDS using an Oxford X-MaxN silicon drift detector, with data processed in Aztec 6.1 software.

4 Petrography results

4.1 Carbonatite mineralogy/textures

The Lemitar Mountains carbonatite exhibits a diverse range of mineralogy and textures. Least altered calcio- and magnesiocarbonatites are characterized by phenocrysts of calcite and dolomite and xenocrysts of apatite, magnetite, phlogopite, and hornblende embedded in a fine-grained calcite matrix (Fig. 1a). Hydrothermal alteration styles include sodic and potassic fenitization, silicification, chloritization, hematization, carbonatization and Ca-F metasomatism.

Phlogopite xenocrysts commonly display alteration features, which include irregular replacement textures by quartz, apatite, and fluorite (Fig. 1b), replacement along cleavage planes, and in many instances, rim replacement by hematite and chlorite (Fig. 1c). Additional secondary minerals within carbonatites include hydrothermal REE-fluorocarbonates, calcite, apatite, zircon, Nb-rutile, and pyrite. Within the host metadiorite, primary plagioclase is replaced by albite and K-feldspar (Fig. 1d). Hydrothermal quartz overprints the metadiorite, growing within the fractures of pervasively altered feldspar, and hornblende and biotite are heavily chloritized.

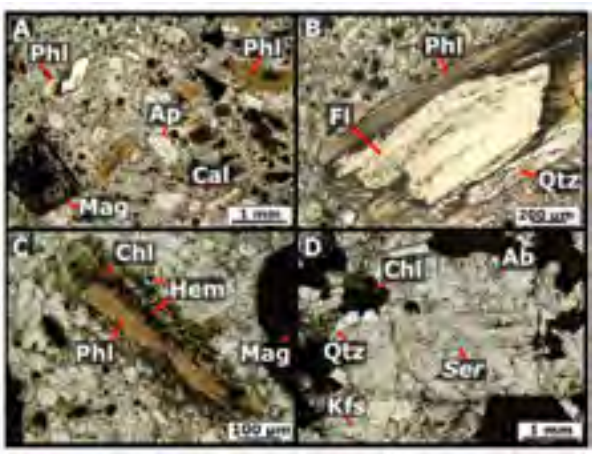


Figure 1. a) Mineralogy of primary carbonatites shows phenocrysts of magnetite, apatite, and phlogopite within the matrix of a primary carbonatite (LMC 3001). b) Phlogopite dissolution texture and replacement by fluorite and quartz (LMC 3001). c) Chloritization and hematization of phlogopite grain in primary carbonatite (LMC 3001). d) Alkali metasomatism, silicification, and chloritization in metadiorite (LMC 3010). Ab= Albite, Ap= Apatite, Cal= Calcite, Chl= Chlorite, Fl= Fluorite, Hem= Hematite, Kfs= K-Feldspar, Phl= phlogopite, Mag= Magnetite, Qtz= Quartz, Ser= Sericitization.

4.2 Hydrothermal veining and alteration styles

Three types of hydrothermal veins crosscut the carbonatites (Fig. 2). Type I quartz-albite veins represent the earliest hydrothermal veins, occurring as 1–2 cm wide veins composed of large, subhedral albite grains and quartz (Fig. 2a). Albite exhibits replacement by K-feldspar along grain boundaries and dissolution textures with K-feldspar veinlets and infills of sericite and quartz, where small (~25 μm) needle-like apatite crystals are occasionally observed in association with silicification, likely associated with Type II veins.

Type II (hematite)-chlorite-quartz-calcite veins crosscut Type I veins (Fig. 2a). Euhedral quartz grows inward, with large-grained, blocky calcite filling the center of the vein. Chlorite, followed by hematite, sequentially infill the vein, overprinting both calcite and quartz. Chloritization and hematization are extensive surrounding these veins, overprinting the carbonatite matrix. Pervasive silicification, carbonatization, and minor sulfidation are also associated with Type II veins. Carbonatization is evident through the presence of secondary calcite, distinguishable from magmatic

calcite by a bright orange CL signature, observed within Type II veins, and secondary calcite growing along vein margins as well as very fine-grained calcite dispersed throughout the carbonatite matrix. Silicification extends beyond Type II veins as quartz veinlets crosscutting Type I veins and primary carbonatites (Fig. 2a,b). Minor sulfidation is marked by pyrite growth along magnetite grain boundaries and as small amounts of disseminated pyrite adjacent to Type II veins. The presence of these veins also marks the onset of secondary REE fluorocarbonate mineralization. Parisite displays an acicular habit ranging in size from 10–100 µm and can be found inside, along vein margins, and in alteration selvages of type II or III veins crosscutting the carbonatite (Fig. 3a).

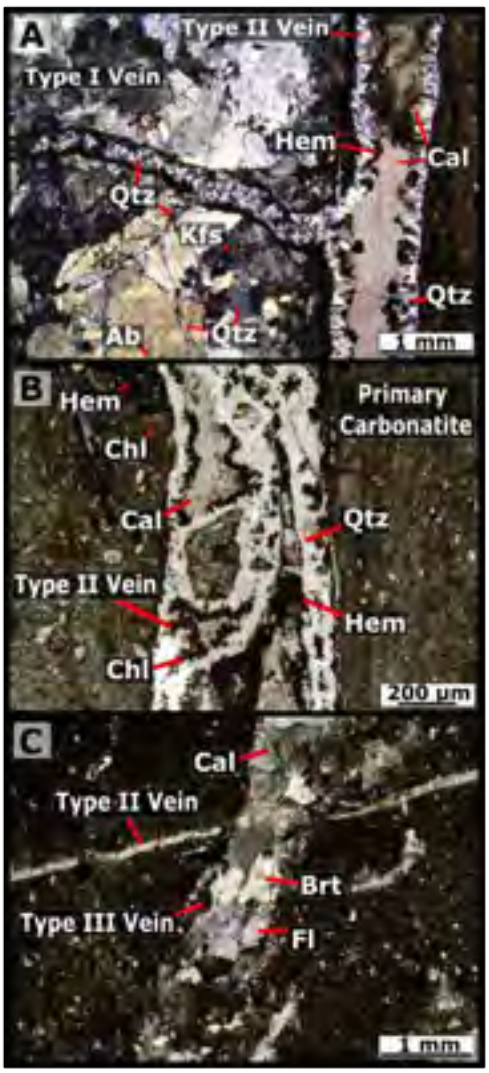


Figure 2. Optical microscopy images of the three different hydrothermal vein types. a) Primary carbonatite crosscut by type I albite and K-feldspar veins, subsequently crosscut by Type II quartz-calcite vein (LMC 8004). b) Type II hematite-chlorite-quartz-calcite vein crosscutting primary carbonatite, resulting in localized chloritization and hematization within the carbonatite matrix (LMC 8004). c) Type III barite-calcite-fluorite vein crosscutting an earlier Type II vein and the host carbonatite (LMC 3012). Ab= Albite, Brt= Barite, Cal = Calcite, Chl= Chlorite, Fl= Fluorite, Hem= Hematite, Kfs= K-feldspar, Qtz= Quartz

Type III (barite)-fluorite-quartz-calcite veins (Fig. 2c) crosscut Type II veins. Large subhedral quartz and blocky calcite grow along the vein margins with calcite, fluorite, and barite found toward the vein center. Disseminated, patchy Ca-F metasomatism and silicification, and pervasive carbonatization are observed within the carbonatite matrix adjacent to Type III veins. Carbonatization and Ca-F metasomatism related to Type III veins are important for REE-fluorocarbonate mineralization.

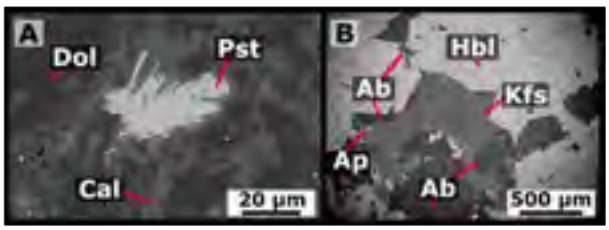


Figure 3. SEM images of a) hydrothermal parisite within primary carbonatite (LMC 3001) and b) the internal replacement of albite by K-feldspar in fenitized metadiorite (LMC 3010). Ab= Albite, Ap= Apatite, Cal= Calcite, Dol= Dolomite, Hbl= Hornblende, Kfs= K-feldspar, Pst= Parisite

4.3 Fenitization

Fenitization is observed as pervasive alteration of the Proterozoic metadiorite in proximity to the carbonatite dikes, and characterized by sodic and potassic metasomatism, silicification, and later chloritization and hematization. Sodic fenitization is marked by the replacement of primary plagioclase with large euhedral hydrothermal albite which exhibits a light pink CL signature with red-orange reaction rims along grain boundaries (Fig. 4a). Inclusions of K-feldspar with a light blue CL signature are present in albite. Albite replacement by K-feldspar forms either discrete patchy overgrowths or gradational rims. K-feldspar also occurs as large, separate grains with a similar light blue-white CL signature. These K-feldspar grains display strong dissolution textures and are overprinted by hydrothermal quartz and later chloritized. Highly acicular apatite is intergrown with quartz and K-feldspar. This apatite has a bright orange CL signature and occurs as euhedral, 5–200 µm needle-like and prismatic crystals (Fig. 4b). This bright orange apatite is different from magmatic apatite 1 and 2, which show a yellow CL signature and hydrothermal apatite 3 associated with potassic fenitization and chloritization, which show a purple-yellow CL signature (Ruggles 2024).

Silicification is observed throughout the fenitized metadiorite, particularly affecting K-feldspar and to a lesser extent albite. Hornblende and biotite are overprinted by chlorite followed by hematization.

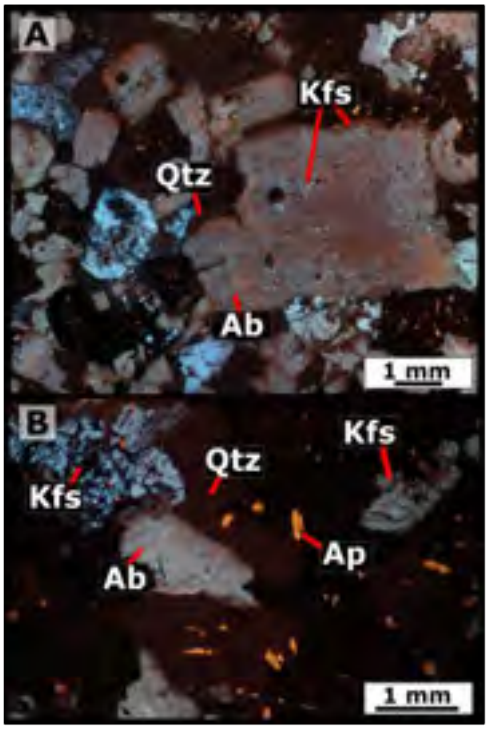


Figure 4. CL of fenitized metadiorite showing a) the light pink CL signature of hydrothermal albite grains in metadiorite rimmed by and containing K-feldspar inclusions with a light blue-white signature and b) feldspar dissolution textures and interstitial hydrothermal quartz and apatite, represented by dark red and bright orange respectively (LMC 3010). Ab= Albite, Ap= Apatite, Kfs= K-feldspar, Qtz= Quartz

5 Conclusions

The Lemitar Mountains carbonatite preserves a complex history of hydrothermal alteration, recorded in extensive veining and pervasive alteration affecting both carbonatite dikes and surrounding metadiorite. Hydrothermal alteration coincides with three distinct vein types each linked to different alteration mineralogies. The earliest alteration stage is characterized by sodic and potassic fenitization in surrounding rocks, where primary plagioclase in the metadiorite is replaced by albite, followed by partial overprinting by K-feldspar and silification. Type I quartz-albite veins are associated with this stage, and the presence of interstitial apatite+quartz in the metadiorite suggests that fenitization and hydrothermal apatite precipitation occurred simultaneously. Subsequent alteration is marked by hematization and chloritization, affecting both the carbonatites and the surrounding rock, shown as extensive replacement of mafic minerals such as phlogopite and hornblende in the carbonatites and hornblende and biotite in the metadiorite. This alteration is linked to Type II (hematite-)chlorite-quartz-calcite veins. These alteration sequences result from the release and transport of essential cations such as Ca, Si, K, Na, and Fe from either the carbonatite or the surrounding mafic host rocks. REE mobilization and Ca-F metasomatism are associated with Type III (barite)-fluorite-quartz-calcite veins. REE-bearing fluorocarbonates such as parisite and bastnäsite are found in these veins and altered vein selvages in the carbonatite. The presence of fluorite mostly in veins, suggests that F^- is possibly sourced from the breakdown of F-bearing minerals such as magmatic fluorapatite. The observed alteration sequences indicate significant hydrothermal overprinting in the Lemitar Mountains carbonatite and hydrothermal REE mobilization associated with late-stage alteration.

Acknowledgments

The research presented here was supported through a National Science Foundation grant, NSF CAREER EAR-2039674 to APG.

References

Ackerman L, Rapprich V, Polák L, et al (2021) Petrogenesis of silica-rich carbonatites from continental rift settings: a missing link between carbonatites and carbonated silicate melts? J Geosci 71–87. http://doi.org/10.3190/jgeosci.320

Elliott HAL, Wall F, Chakhmouradian AR, et al (2018) Fenites associated with carbonatite complexes: A review. Ore Geol Rev 93:38–59. https://doi.org/10.1016/j.oregeorev.2017.12.003

Haft EB, McLemore VT, Ramo OT, Kaare-Rasmussen J (2022) Geology of the Cambrian Lemitar carbonatites, Socorro County, New Mexico: Revisited. In: Socorro Region III. NMGS. https://doi.org/10.56577/FFC-72.365

Liu Y-L, Ling M-X, Williams IS, et al (2018) The formation of the giant Bayan Obo REE-Nb-Fe deposit, North China, Mesoproterozoic carbonatite and overprinted Paleozoic dolomitization. Ore Geol Rev 92:73–83. https://doi.org/10.1016/j.oregeorev.2017.11.011

McLemore VT (1987) Geology and regional implications of carbonatites in the Lemitar mountains, central New Mexico. J Geol 95:255–270. https://doi.org/10.1086/629123

Moore M, Chakhmouradian AR, Mariano AN, Sidhu R (2015) Evolution of rare-earth mineralization in the Bear Lodge carbonatite, Wyoming: Mineralogical and isotopic evidence. Ore Geol Rev 64:499–521

Ruggles EL (2024) Mineral paragenesis, mineral chemistry, and rare earth element mobility related to the magmatic-hydrothermal transition of the Lemitar Mountains Carbonatites, New Mexico. M.Sc. thesis, New Mexico Tech.

Smith MP, Moore K, Kavecsánszki D, et al (2016) From mantle to critical zone: A review of large and giant sized deposits of the rare earth elements. Geosci Front 7:315–334. https://doi.org/10.1016/j.gsf.2015.12.006

Verplanck PL, Van Gosen BS, Seal RR II, McCafferty AE (2014) A deposit model for carbonatite and peralkaline intrusion-related rare earth element deposits. Scientific Investigations Report. https://doi.org/10.3133/sir20105070J

Wang Z, Fan H, Zhou L, et al (2020) Carbonatite-related REE deposits: An overview. Minerals 10:965. https://doi.org/10.3390/min10110965

Yaxley GM, Anenburg M, Tappe S, et al (2022) Carbonatites: Classification, sources, evolution, and emplacement. Annu Rev Earth Planet Sci 50:261–293. https://doi.org/10.1146/annurev-earth-032320-104243

Distribution and Genesis of REE-Nb-Ta Deposits Associated with Carbonatites and Alkaline Complexes in Canada

Anne-Aurélie Sappin[1], Michel G. Houlé[1], Wouter Bleeker[2]
[1]Geological Survey of Canada, Lands and Mineral Sector, Natural Resources Canada, Québec City
[2]Geological Survey of Canada, Lands and Mineral Sector, Natural Resources Canada, Ottawa

Abstract. Canada hosts many carbonatites and alkaline complexes, prospective for economic REE, Nb, and Ta mineralization. They range in age from Neoarchean to Mesozoic and mainly occur within the Canadian Shield and Cordillera. They were emplaced into intracratonic anorogenic or post-orogenic extensional settings, spatially related to major crustal-scale weakness zones or along terrane/craton margins. A comprehensive compilation of the main REE, Nb, and Ta ore deposits associated with Canadian carbonatites and alkaline complexes identifies four groups based on their lithological association: 1) carbonatites, 2) peralkaline intrusions, 3) peralkaline volcanic rocks, and 4) other igneous rocks. Preliminary results reveal a discrepancy between the number of deposits and the total occurrences of carbonatites and alkaline units in Canada, suggesting significant untapped potential. In addition, this exercise highlighted the need to improve our understanding of the primary and secondary processes controlling the formation of the REE-HFSE deposits associated with peralkaline volcanic rocks and metamorphosed peralkaline intrusions, as well as the deformation mechanisms influencing the emplacement of the host units in deformed terranes. These insights could improve metallogenic models and highlight the potential for new discoveries within Canada's largely underexplored carbonatites and alkaline complexes.

1 Introduction

Although carbonatites and alkaline complexes are relatively uncommon on the Earth's surface, accounting for less than 1% of all the igneous rocks (e.g., Woolley and Kjarsgaard 2008; Wall 2021), Canada hosts a significant number of such complexes (e.g., Currie 1976; Sinclair et al. 1992; Woolley and Kjarsgaard 2008; Fig. 1). They range in age from Neoarchean to Mesozoic and occur within the Canadian Shield, the Cordillera and various rift zones (e.g., Currie 1976; Woolley and Kjarsgaard 2008). They are emplaced into intracratonic anorogenic (e.g., Boily and Williams-Jones 1994; Kerr and Rafuse 2011; Néron et al. 2018; Easton 2020; Matte et al. 2022) or post-orogenic extensional settings (e.g., Millonig et al. 2012; Millonig and Groat 2013).

Carbonatites and alkaline complexes are prospective host units for economic rare earth element (REE), Nb, Ta, P, Fe, and Zr mineral resources and most of the world's REE, Nb, and Ta production comes from these igneous rocks. Previous compilations of REE, Nb, and Ta deposits and occurrences associated with carbonatites and alkaline complexes across Canada (e.g., Sinclair et al. 1992; Simandl et al. 2012) include an inventory of the deposits and occurrences, as well as a general description of their main host rock units. However, the genetic information relative to these various deposits and occurrences remains limited. As a result, evaluating the progress made in recent years toward understanding mineralized carbonatite and alkaline magmatic systems in Canada remains challenging. A comprehensive compilation of the main Canadian REE, Nb, and Ta deposits associated with carbonatites and alkaline complexes has therefore been undertaken to provide an update on the current state of knowledge, to recognize critical processes responsible for the formation of these deposits, and to identify gaps in our current knowledge. The compilation will include information such as the geographical location of the deposits, their mineral commodities, and their deposit type, but also additional information on geological characteristics (e.g., host unit size, host unit composition, and age), ore production, geological resources, and genetic characteristics (e.g., tectonic setting, structural control, nature of the mantle/crustal source, and parental magma).

2 Compilation methodology

The present compilation is based on several sources, such as provincial/territorial mineral occurrence databases; geological reports of provincial/territorial geological surveys; technical reports of exploration and mining companies; and peer-reviewed literature. REE, Nb, and Ta deposits included in this compilation consist primarily of deposits that have associated NI 43-101 compliant geological resources/production. Historical resources/production are also included to provide a better representation of the distribution of these ore systems across the country.

3 Canadian REE, Nb, and Ta deposits associated with carbonatites and alkaline complexes

3.1 Classification

Canadian REE, Nb, and Ta deposits associated with carbonatites and alkaline igneous rocks were grouped into four main types based on their lithological association (Fig. 2): 1) carbonatite-

associated deposits, including those hosted by or in close spatial association with carbonatites and allied alkaline rocks; 2) peralkaline intrusion-associated deposits, hosted by peralkaline oversaturated to undersaturated intrusive rocks (e.g., granite, syenite); 3) peralkaline volcanic rocks-associated deposits, hosted by peralkaline trachyte and rhyolite; and 4) other igneous rock-associated deposits, including deposits related to a magmatic source of unknown carbonatitic or alkaline origin.

3.2 Spatial and temporal distribution

Canadian REE, Nb, and Ta deposits associated with carbonatites and alkaline complexes mainly occur within the Canadian Shield, the Cordilleran Orogen, and various rift zones (Fig. 2), and range in age from Paleoproterozoic to Cretaceous. They are commonly spatially related to major crustal structures (e.g., Ottawa-Bonnechère structural corridor in Quebec and Ontario and Kapuskasing Structural Zone in Ontario; Sappin and Beaudoin 2015; Easton 2020) or occur along terrane/craton margins (e.g., carbonatite-associated deposits in British Columbia; Fig. 2). Twenty-two carbonatite-associated REE, Nb, Ta deposits were compiled as part of the current effort. These deposits are distributed across several geological provinces, including the Cordilleran Orogen, where host carbonatites range from Devonian to Carboniferous in age; the Superior Province, with Paleoproterozoic to Mesoproterozoic carbonatites; the Churchill Province, characterized by Paleoproterozoic occurrences; the Grenville Province, hosting Neoproterozoic carbonatites; and the St. Lawrence Platform, where carbonatites are Cretaceous in age. Seven REE-high field strength elements (HFSE) deposits belong to the peralkaline intrusion-associated deposit type. They were emplaced in the Slave Province during the Paleoproterozoic, as well as the Churchill and Grenville provinces during the Mesoproterozoic. Two REE-HFSE deposits are associated with peralkaline volcanic rocks. They are located in the Grenville Province and are Mesoproterozoic in age. Finally, the deposit type associated with other igneous rocks includes the Paleoproterozoic Hoidas Lake deposit located in the Churchill Province. This deposit consists of a REE-enriched vein system derived from a magmatic source at depth (Halpin 2010). However, the carbonatitic or alkaline affiliation of this magmatic source is still unknown.

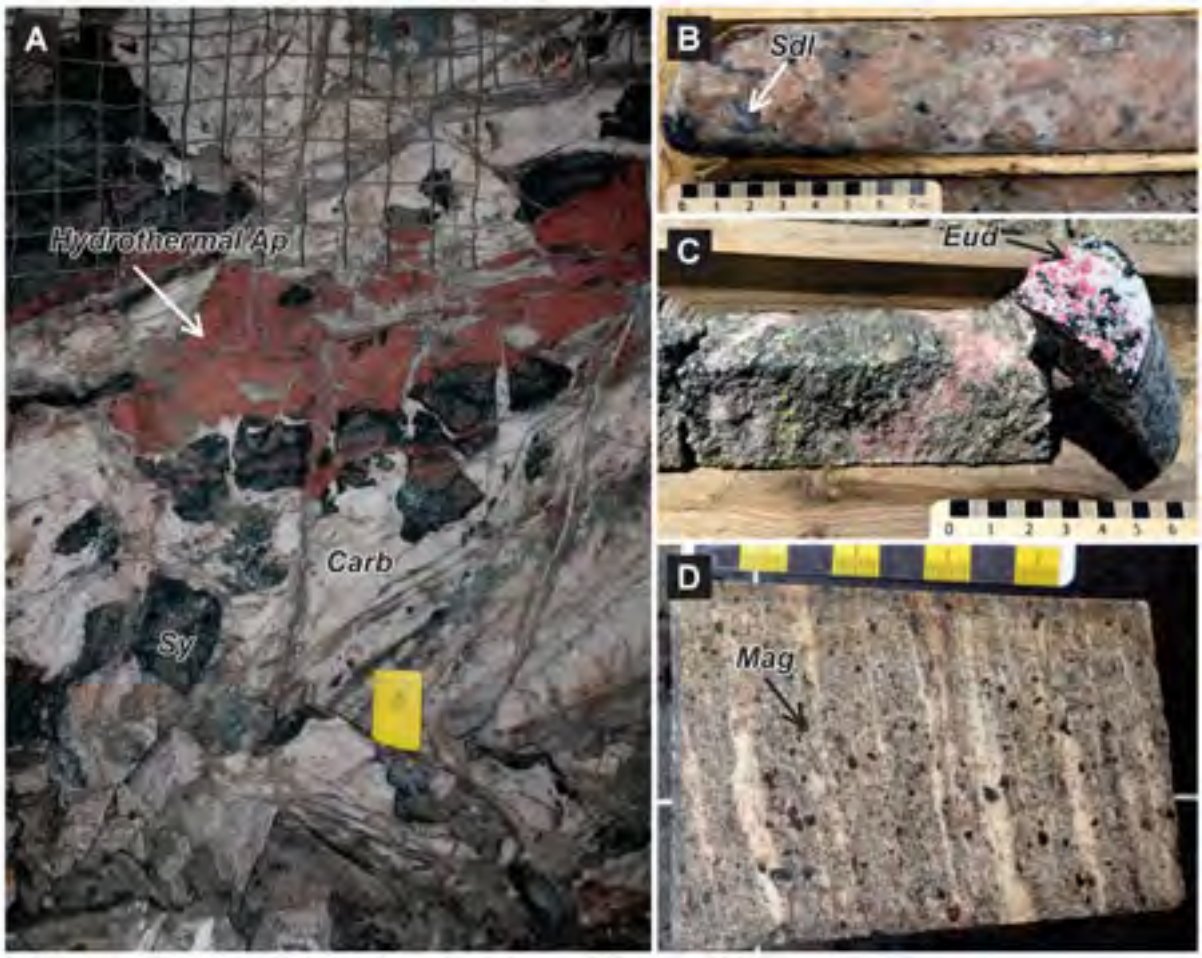


Figure 1. Example of carbonatites and alkaline units in Canada. A) Syenite (Sy) enclaves and hydrothermal apatite (Ap) within Nb mineralized Mg-carbonatite (Carb) from the Saint-Honoré carbonatite complex; field notebook is 18 cm tall. B) Pegmatitic syenite with sodalite (Sdl) from the Crevier alkaline complex C) Mesocratic syenite rich in eudialyte (Eud) from the Kipawa alkaline complex. D) Pantellerite with magnetite (Mag) phenocrysts from the Fox Harbour belt (photo from Magyarosi 2022).



Figure 2. Spatial distribution of REE, Nb, and Ta deposits with estimated resources and/or reserves, and past and active producers associated with carbonatites and alkaline complexes across Canada, as well as known occurrences of carbonatites and/or alkaline rocks (data are from Woolley and Kjarsgaard, 2008; Easton et al., 2021; https://alkcarb.myrocks.info/map; and Bleeker personal communication). Geological provinces modified after Wheeler et al. (1996).

4 Results and implications

4.1 Key genetic processes

The compilation of the Canadian REE, Nb, and Ta deposits associated with carbonatites and alkaline complexes and their genetic features highlights some common and key factors controlling the formation of these deposits. First, their carbonatite and/or alkaline host rocks appear to be generated by low degrees of partial melting of an enriched lithospheric mantle, a depleted asthenospheric mantle, or a metasomatized crustal source and to crystallize from volatile-bearing carbonatite and alkaline magmas. Secondly, they are generally spatially related to major crustal structures or terrane/craton margins that served as magmatic pathways allowing magmas to rise to the surface. Finally, Nb and Ta mineralization in these magmatic mineral systems is mainly formed by magmatic processes (e.g., fractional crystallization, magmatic immiscibility) and rarely by chemical weathering and mechanical erosion, whereas REE mineralization is generated either by hydrothermal or igneous processes, and locally by metamorphic remobilization.

4.2 Potential for REE, Nb, Ta carbonatite-alkaline mineral systems in Canada

As part of this compilation effort, 32 Canadian REE, Nb, and Ta deposits associated with carbonatites and alkaline complexes were identified (Fig. 2). However, previous compilations of known occurrences of carbonatites and alkaline rocks worldwide (https://alkcarb.myrocks.info/map; Woolley and Kjarsgaard 2008) identified more than 200 of these prospective units for REE, Nb, and Ta mineralization in Canada (Fig. 2). This significant difference between the number of known Nb, Ta, and REE mineral deposits and the number of prospective units for this type of mineralization highlights the potential for additional discoveries of REE, Nb, and Ta deposits within the large number of apparently barren, poorly mineralized, and/or lesser-known carbonatites and alkaline complexes across Canada.

4.3 Remaining knowledge gaps

This updated inventory of the Canadian REE-Nb-Ta deposits associated with carbonatites and alkaline complexes and their main geological and genetic

characteristics has enabled us to identify a few knowledge gaps relative to these magmatic mineral systems in Canada:

- Detailed genetic information on most of the carbonatite-associated deposits of the Canadian Shield, particularly for those in Ontario, remains limited.
- The magmatic and hydrothermal processes responsible for REE-HFSE mineralization in peralkaline volcanic rock are poorly constrained.
- The secondary processes driving rare metal remobilization and enrichment in metamorphosed peralkaline mineral systems require further investigation to clarify their role in mineralization processes.
- The structural evolution and deformation mechanisms influencing the emplacement of the host intrusions or volcanic belts in structurally complex terranes need to be better understood.

Filling these knowledge gaps will allow us to enhance our understanding of the large-scale processes controlling deposit formation at the craton-scale and to refine the current ore genesis models for carbonatite and alkaline magmatic systems, especially in metamorphosed and deformed terranes. This will be useful in identifying the areas with highest potential for these critical mineral systems, thus increasing the likelihood of discovering additional mineral resources.

Acknowledgements

Support for this study was provided through the Magmatic Ore Systems Sub-Activity: 'Critical minerals within carbonatite, syenite, and allied peralkaline-alkaline rocks in the central and eastern parts of the Canadian Shield: where, when and how were they formed' of the NRCan's Targeted Geoscience Initiative Program. We would like to thank A. Morin and F. Aucoin from the Geological Survey of Canada (GSC) for generating maps. We also would like to express our appreciation to Z. Magyarosi (Geological Survey of Newfoundland and Labrador), N. Rayner (GSC), P.L. Bédard and N. Van Weelderen (Université du Québec à Chicoutimi), M. Grégoire (Centre National de la Recherche Scientifique – Université Toulouse III), M. Constantin and S. Matte (Université Laval), F. Gervais and J. Carabin (Polytechnique Montréal), and E. Thiessen and N. Prieto (Memorial University of Newfoundland) for their valuable inputs into this project by generating in parallel new geological data.

References

Boily M, Williams-Jones AE (1994) The role of magmatic and hydrothermal processes in the chemical evolution of the Strange Lake plutonic complex, Québec-Labrador. Contrib Mineral Petrol 118: 33-47. doi.org/10.1007/BF00310609.

Currie KL (1976) The alkaline rocks of Canada. Geol Surv Can, Bulletin 239, 228 p.

Easton RM (2020) Exploration guidelines for carbonatites in Ontario. In: Summary of Field Work 2020. Ont Geol Surv, Open File Report 6370, 9-1 to 9-10.

Easton RM, Kamo SL, Robichaud L (2021) Evidence for Geon 12 carbonatitic magmatism in the Wawa area: A distal manifestation of the Sudbury dike swarm mantle plume? In: Summary of Field Work and Other Activities 2021. Ont Geol Surv, Open File Report 6380, 10-1 to 10-11.

Halpin KM (2010) The characteristics and origin of the Hoidas Lake REE deposit. MSc thesis, University of Saskatchewan, Saskatoon, Saskatchewan.

Kerr A, Rafuse H (2011) Mineral commodities of Newfoundland and Labrador, rare-earth elements (including Y, Zr, Nb, Be). NL Dept Nat Res, Geol Surv, Mineral Commodities Series, Number 6, 12 p.

Magyarosi Z (2022) Preliminary investigation of rare-earth-element mineralization, Fox Harbour Volcanic Belt, southeastern Labrador. NL Dept Ind Energy Technol, Geol Surv, Current Research, Report 22-1, 57-83

Matte S, Constantin M, Stevenson R (2022) Mineralogical and geochemical characterization of the Kipawa syenite complex, Quebec: Implications for rare-earth element deposits. Geol Surv Can, Scientific Presentation 129, 36 p. doi.org/10.4095/329212.

Millonig LJ, Groat LA (2013) Carbonatites in Western North America—Occurrences and metallogeny. In: Colpron M, Bissig T, Rusk BG, Thompson JFH (eds) Tectonics, Metallogeny, and Discovery: The North American Cordillera and Similar Accretionary Settings. Soc Econ Geol, Special Publication 17, pp. 245-264. doi.org/10.5382/SP.17.07.

Millonig LJ, Gerdes A, Groat LA (2012) U–Th–Pb geochronology of meta-carbonatites and meta-alkaline rocks in the southern Canadian Cordillera: A geodynamic perspective. Lithos 152: 202-217. doi:10.1016/j.lithos.2012.06.016.

Néron A, Bédard LP, Gaboury D (2018) The Saint-Honoré carbonatite REE zone, Québec, Canada: Combined magmatic and hydrothermal processes. Minerals 8: 397. doi:10.3390/min8090397.

Sappin A-A, Beaudoin G (2015) Rare earth elements in Québec, Canada: Main deposit types and their economic potential. In: Simandl GJ, Neetz M (eds) Symposium on Strategic and Critical Materials Proceedings, November 13-14, 2015, Victoria, British Columbia. BC Min Energy Mines, BC Geol Surv, Paper 2015-3, pp. 265-273.

Simandl GJ, Prussin EA, Brown N (2012) Specialty metals in Canada. BC Geol Surv, Open File 2012-7, 48 p.

Sinclair WD, Jambor JL, Birkett TC (1992) Rare earths and the potential for rare-earth deposits in Canada. Explor Min Geol 1: 265-281.

Wall F (2021) Rare earth elements. In: Alderton D, Elias SA (eds) Encyclopedia of Geology (Second Edition). Academic Press, pp. 680-693. doi.org/10.1016/B978-0-08-102908-4.00101-6.

Wheeler JO, Hoffman PF, Card KD, Davidson A, Sanford BV, Okulitch AV, Roest WR (1996) Geological map of Canada. Geol Surv Can, "A" Series Map 1860A, 3 sheets, 1 .zip file, scale 1:5 000 000.

Woolley AR, Kjarsgaard BA (2008) Carbonatite occurrences of the world: Map and database. Geol Surv Can, Open File 5796, 1 CD-ROM + 1 map.

The early magmatic history of the Cripple Creek complex, Colorado, USA: Insights from olivine-hosted melt inclusions and implications for ore formation

Michael Schirra[1,2], Zoltan Zajacz[1]
[1]University of Geneva, Department of Earth Sciences, Switzerland
[2]University of Nevada, Las Vegas, Department of Geoscience, USA

Abstract. The genetic relationship between the formation of giant epithermal Au deposits and specific alkaline magmatic centres is an open research question with vast economic implications. Silicate melt inclusions (SMIs), the most direct method of accessing the parental melts of mineralized alkalic intrusions, can provide novel insights into magma generation with implications for ore fertility. Here, we present a preliminary dataset of olivine-hosted SMIs from two lamprophyre dikes that are assumed to be genetically related to Au mineralization in the Cripple Creek district, Colorado, USA. Our results indicate that primitive melts are nepheline-normative, sodic and ankaramitic in composition with elevated concentrations of incompatible fluid-mobile and -immobile elements, indicating a metasomatized mantle source. Metasomatism appears to be linked to upwelling asthenospheric mantle during rifting of the overlying lithosphere. Carbonatitic melts are a potential metasomatizing agent, explaining the high CaO/Al_2O_3 ratio, the low silica content and high incompatible element concentrations of the Cripple Creek magmas. Exceedingly high S concentrations (3000 to 6000 μg/g), which significantly affect the transport of Au, seem to be also linked to this metasomatic event, indicating that ore formation at Cripple Creek might be linked to cryptic metasomatic events in the melting source.

1 Introduction

Giant alkalic-type epithermal Au deposits are characterized by their association with alkaline igneous rocks. Despite numerous investigations (Richards 1990; Kelley et al. 1998; Jensen & Barton 2000; Müller et al. 2001), the genetic relationship between alkaline magmatism and Au deposits remains an open research question. The Cripple Creek district in Colorado, USA, is a prime example of this deposit type, having produced more than 821 tons of Au so far (Kelley et al. 2020).

The exotic nature of alkaline igneous rocks associated to alkalic-type epithermal Au deposits like Cripple Creek suggests a potential magmatic control on ore formation. This ore-deposit type appears to be genetically linked to small stocks or clusters of intrusions with high alkali-element contents varying in composition from ultramafic lamprophyres to highly evolved phonolites (Jensen & Barton 2000). Ore-fertile alkaline magmas are believed to originate from low-degree partial melting of volatile-rich, metasomatized mantle wedges modified during previous subduction (Richards 1990; Müller et al. 2001). As these magmas ascend, they evolve and interact with the crust, creating conditions favorable for Au deposition.

This paper examines the magmatic history of the Cripple Creek deposit, focusing on new SMI LA-ICP-MS data from lamprophyre dikes, which are supposed to be closely related to Au mineralization (Kelley et al. 1998, 2020). These preliminary data offer valuable information on the composition and origin of the most primitive magmas at Cripple Creek and their implications for gold mineralization.

2 Geological background

The Cripple Creek district in central Colorado is a breccia-dominated diatreme complex situated at the junction of four Proterozoic lithologies (Fig. 1). The district's geological history is marked by a series of magmatic events during the Oligocene, following a shift in the regional stress regime likely induced by slab break-off or rollback after the Laramide orogeny (Humphreys 1995).

The initial magmatic activity (around 32.5 Ma) involved the shallow emplacement of phonolite intrusions, followed by progressively more mafic melts (Kelley et al. 1998). This progression from felsic to mafic compositions suggests a multi-stage magma evolution characterized by fractional crystallization within a subjacent crustal magma reservoir, periodically replenished by less evolved melts (Kelley et al. 1998, 2020).

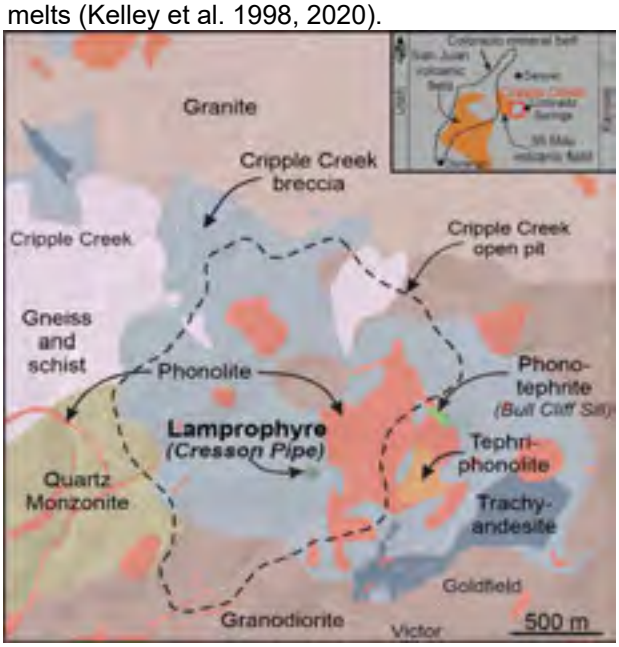


Figure 1. Geological overview of the Cripple Creek complex showing the location of the lamprophyre dikes (modified from Kelley et al. 1998).

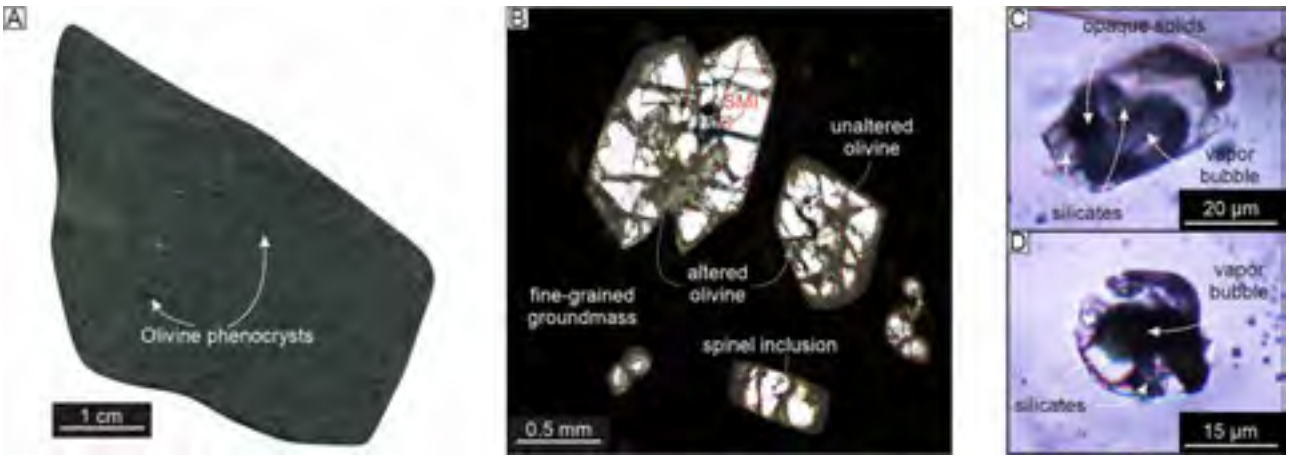


Figure 2. Sample petrography of lamprophyres at various scales, from A) altered olivine-phyric lamprophyre hand specimen, over B) transmitted light image of partially replaced olivine phenocrysts hosting spinel and melt inclusions to C) and D) transmitted light images of relatively large olivine-hosted SMIs.

The final phase of magmatism is marked by the emplacement of ultramafic lamprophyre dikes and pipes, such as the Cresson pipe, around 28.4 million years ago. These intrusions are significant as they are spatially and temporally associated with Au-Te mineralization (Kelley et al. 1998, 2020).

3 Methods

Two lamprophyre samples from the Cresson pipe containing olivine phenocrysts that show only minor hydrothermal overprinting have been selected for melt inclusion screening. Unexposed silicate melt inclusions exceeding a size of 10 µm in at least two dimensions have been selected for laser ablation ICP-MS analysis, which was conducted at the University of Geneva using a Coherent 193 nm excimer laser system coupled to an Agilent 8900 QQQ ICP-MS. Adjustable rectangular ablation patterns have been used to minimize the host contribution during inclusion ablation and signals were quantified following the method outlined by Halter et al. (2002), applying a constant Fe-Mg exchange coefficient between olivine and melt of 0.3 to deconvolute mixed LA-ICP-MS signals.

4 Results

4.1 Silicate melt inclusion petrography

Olivine is the dominant phenocrystic phase in the lamprophyre dikes from Cripple Creek (Fig. 2A), although phlogopite and clinopyroxene phenocrysts also exist (Kelley et al. 1998). Olivine crystals exhibit euhedral, rounded and angular shapes and are typically replaced by a fine-grained mixture of talc, biotite and chlorite along grain boundaries and cracks but preserve unaltered cores (Fig. 2B). Spinel inclusions are abundant in most unaltered olivine phenocrysts whereas well-preserved SMIs, especially those exceeding 10 µm in diameter, are infrequent. Olivine-hosted SMIs typically contain a relatively large bubble, occupying approximately 30 to 50% of the total inclusion volume, and multiple opaque and transparent solids (Fig. 2C, D). Besides SMIs, tiny (typically <5 µm) vapor fluid inclusions occur as clusters and trails in some olivine crystals.

4.2 Melt composition

Successfully quantified olivine-hosted SMIs (n=25) unravel a primitive (MgO >10 wt.%, SiO_2 ≤50 wt.%), ankaramitic (CaO/Al_2O_3 >1), sodic (Na_2O/K_2O >2), nepheline-normative magma composition (Fig. 3) that produced the ultramafic dikes in the Cripple Creek district. The SMIs display adakite-like trace element features, like high Sr/Y and La/Yb ratios (Fig. 3C, D), and contain exceptionally high S concentrations (>3000 µg/g) that correlate positively with Sr (Fig. 3F) as well as with other incompatible elements like Y, Ba, La, Pb, Th and U (not shown). There is no apparent correlation between S and Cu concentrations, which range from 25 to 100 µg/g. Chlorine concentrations vary between 1000 and 2500 µg/g and do not show any apparent correlation with other trace elements. Incompatible trace element ratios point towards a highly enriched mantle source (Fig. 3E). Trace element signatures resemble those of ocean-island basalts (OIB) and are clearly distinct from typical subduction-zone patterns, for which pronounced HFSE depletions are characteristic (Fig. 4). However, compared to typical OIBs, Cripple Creek magmas show elevated LILE (e.g., Sr, Ba, Pb, Th, U) and LREE (e.g., La, Ce, Nd) concentrations (Fig. 4), which result in high LILE/HFSE ratios (e.g., Th/Ta >4, Ba/Zr >2).

5 Discussion

The small, preliminary dataset of olivine-hosted SMIs from Cripple Creek provides novel insights into the early magmatic history of the Au-fertile magmas. In contrast to most other Au mineralization related to alkaline magmatism (e.g., Ladolam, Galore Creek, and Vatukoula), a genetic link between subduction processes and ore-fertile magma generation is not apparent at Cripple Creek due to the absence of a HFSE depletion pattern (e.g., Nb and Ta), which is characteristic for arc magmas (Fig. 4A). Whole rock compositions and

isotope systematics support the absence of subduction-related processes during magma generation (Kelley et al. 1998). The selective enrichment of incompatible elements relative to Rb, K, Zr, and Hf (Fig. 4A) cannot be explained by low melting degrees but require a metasomatized mantle source. Melting of this mantle source occurred under garnet-stable conditions as suggested by the high LREE/HREE ratios of the primitive SMIs (Fig. 3D, 4B). The igneous affiliation of the Cripple Creek magmas is comparable to those associated with the Porgera deposit in Papua New Guinea (Richards 1990).

The primitive, silica-undersaturated and ultra-calcic composition of the Cripple Creek melts is comparable to SMIs from Lihir Island (Schirra et al. 2024), although their distinct trace element signatures dictate fundamentally different magma generation processes. High-degree partial melting of a subduction-modified clinopyroxene-dominated source has been invoked to explain the composition of primitive melts on Lihir Island (Schirra et al. 2024), which produced the giant Ladolam epithermal Au deposit. The ultra-calcic character of SMIs from both locations is clearly distinct from typical arc magmas (e.g., San José, Fig. 3A), which form porphyry Cu deposits. The high concentrations of incompatible elements of the Cripple Creek magmas (Fig. 3E, 4) however preclude high degrees of partial melting. Instead, the positive correlation between CaO/Al_2O_3 ratios and incompatible element concentrations such as Sr and La indicates that the source exercises a major influence on melt composition.

Carbonatitic melts, characterized by elevated concentrations of Ba, Th, Sr and LREE relative to Rb, K, Zr, Hf, Ti and HREE (Walter et al., 2008), are commonly associated with alkaline magmatism, although they rarely reach the surface unmodified (Yaxley et al., 1998). Reaction of such melts with mantle lithologies could introduce high La/K and Ba/K and low Hf/Sm, Zr/Sm, and Ti/Eu ratios (Walter et al., 2008) as well as high CaO/Al_2O_3 ratios due to the replacement of orthopyroxene with Al-poor clinopyroxene (Rudnick et al., 1993; Yaxley et al., 1998); characteristics that are transferred to the primitive melts at Cripple Creek. Direct evidence for carbonatitic metasomatism of the mantle beneath the Rio Grande Rift are calcite-bearing clinopyroxenite xenoliths (Porreca et al. 2006).

The positive correlation of S with the presumably metasomatically enriched incompatible trace elements such as Sr (Fig. 3F), suggests that the high S concentrations of primitive Cripple Creek magmas, which significantly exceed the range of

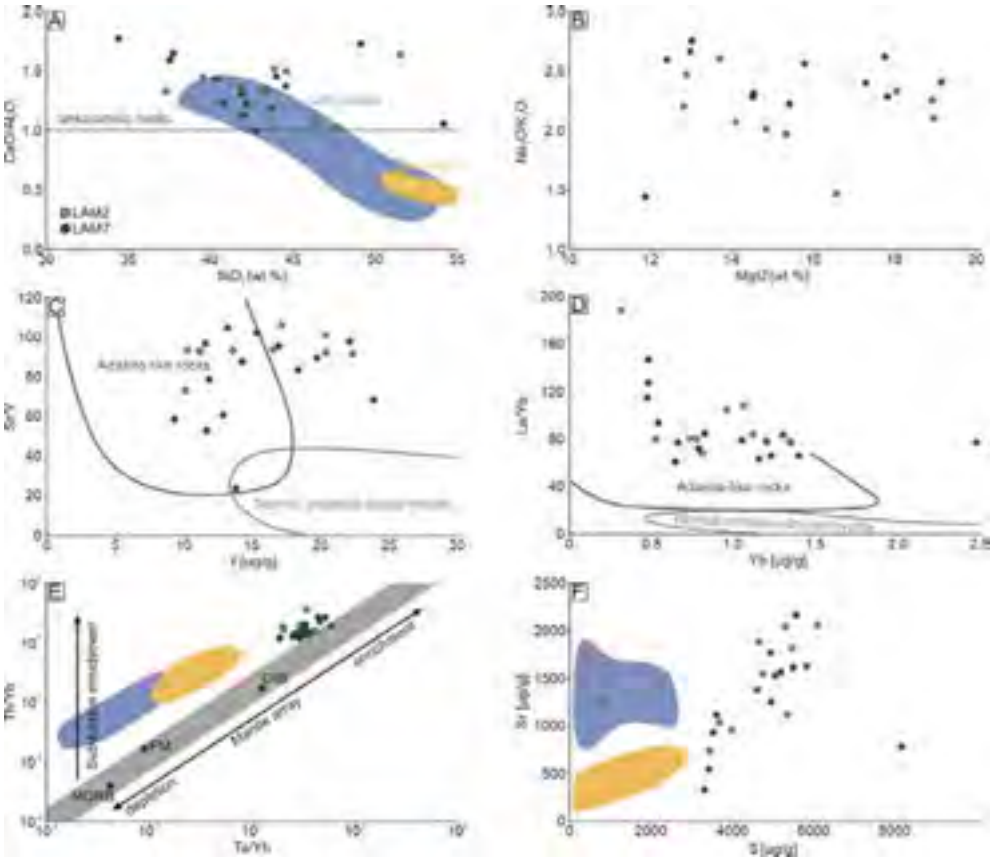
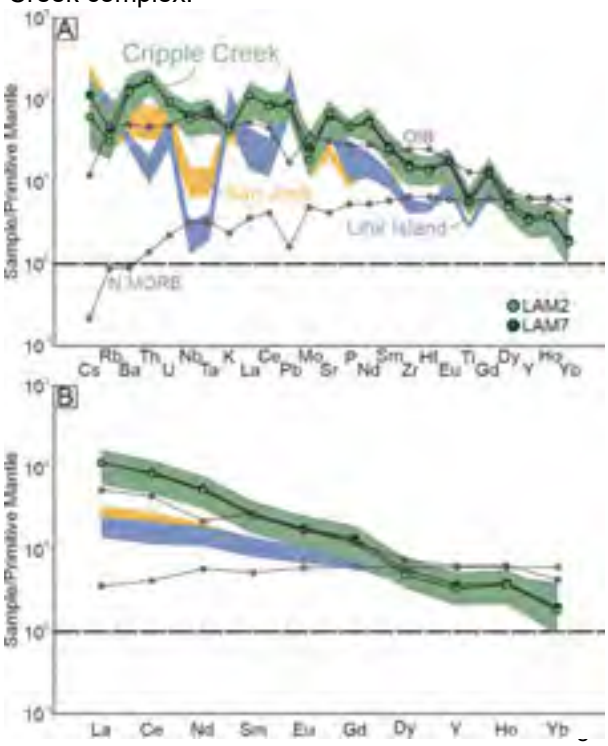


Figure 3. Major and trace element composition of olivine-hosted SMIs. A) Ankaramitic (CaO/Al_2O_3 > 1) and silica deficient nature of entrapped melts. B) Sodic character of primitive (MgO >12 wt.%) SMIs. C) and D) Adakite-like trace element systematics of the entrapped melts. E) Th/Yb vs Ta/Yb diagram after Pearce (1983) showing the enrichment of the Cripple Creek melts in incompatible elements. F) Positive relationship between S and incompatible elements exemplified at the example of Sr. Blue and yellow shades represent the compositional ranges of olivine-hosted SMIs from Lihir Island (Schirra et al. 2024) and the arc volcano San José in Chile (unpublished) for comparison. Trace element ratios for MORB, PM (primitive mantle) and OIB are taken from Sun & McDonough (1989).

typical arc magmas (1000 to 3000 µg/g, Muth & Wallace 2022) and MORB magmas (≤1000 µg/g, Ding & Dasgupta 2017), could be inherited from the metasomatizing agent. The crucial impact of S on Au transport in the magmatic and hydrothermal environment might play a crucial role for ore formation (Zajacz et al. 2012; Farsang & Zajacz 2025). Additionally, carbonatitic melts might be enriched in Au, a hypothesis yet to be tested. Accordingly, the cryptic involvement of carbonatitic melts in the generation of alkaline magmas, facilitated by the complex geodynamic context, might be a prerequisite for subsequent ore formation at Cripple Creek.

6 Conclusions and outlook

Olivine-hosted primitive SMIs from the lamprophyric dikes from Cripple Creek exhibit an exotic composition marked by high CaO/Al_2O_3 ratios, high MgO and low SiO_2 contents and an enrichment of incompatible elements. This exotic melt composition is not genetically related to previous subduction processes, in contrast to other alkalic-type epithermal Au deposits. Instead, the SMI compositions hint at the involvement of carbonatitic melts in the generation of Au-fertile magmas, a genetic relation not reported before for Cripple Creek. The small SMI dataset presented here will be expanded in the future to obtain a more complete picture of the evolution of the Cripple Creek complex.



(1989) are shown.

Acknowledgements

We would like to thank Dr. Karen Kelley for sharing sample material from Cripple Creek, without which this study would not have been possible.

References

Ding S, Dasgupta R (2017) The fate of sulphide during decompression melting of peridotite – implications for the sulfur inventory of the MORB-source depleted upper mantle. Earth Planet Sci Lett 459: 183-195.

Farsang S, Zajacz Z (2025) Sulfur species and gold transport in arc magmatic fluids. Nat Geo 18: 98-104.

Halter WE, Pettke T, Heinrich CA, Rothen-Rutishauser B (2002) Major and trace element analysis of melt inclusions by laser-ablation ICP-MS: methods of quantification. Chem Geol 183: 63-86.

Humphreys E (1995) Post-Laramide removal of the Farallon slab, western United States. Geology 23: 987-990.

Jensen EP, Barton MD (2000) Gold deposits related to alkaline magmatism. SEG Reviews 13: 279-314.

Kelley KD, Romberger SB, Beaty DW, Pontius JA, Snee LW, Stein HJ, Thompson TB (1998) Geochemical and geochronological constraints on the genesis of Au-Te deposits at Cripple Creek. Econ Geol 93: 981-1021.

Kelley KD, Jensen EP, Rampe JS, White D (2020) Epithermal gold deposits related to alkaline igneous rocks in the Cripple Creek district, Colorado, United States. SEG special publications 23: 355-373.

Müller D, Franz L, Herzig PM, Hunt S (2001) Potassic igneous rocks from the vicinity of epithermal gold mineralization, Lihjir Island, Papua New Guinea. Lithos 57: 163-186.

Muth MJ, Wallace PJ (2022) Sulfur recycling in subduction zones and the oxygen fugacity of mafic arc magmas. Earth Planet Sci Lett 599: 117836.

Pearce JA (1983) Role of the subcontinental lithosphere in magma genesis at active continental margins. – In: Hawkesworth CJ, Norry MJ (eds) Continental basalts and mantle xenoliths: 230-249.

Porreca C, Selverstone J, Samuels K (2006) Pyroxenite xenoliths from the Rio Puerco volcanic field, New Mexico: Melt metasomatism at the margin of the Rio Grande rift. Geosphere 2: 333-351.

Richards JP (1990) Petrology and geochemistry of alkalic intrusives at the Porgera gold deposit, Papua New Guinea. J Geochem Explo 35: 141-199.

Rudnick RL, McDonough WF, Chappell BW (1993) Carbonatite metasomatism in the northern Tanzanian mantle: petrographic and geochemical characteristics. Earth Planet Sci Lett 114: 463-475.

Schirra M, Zajacz Z, Müller D (2024) The hidden link between dry ankaramitic melts and giant alkalic-type epithermal Au deposits: the Lihir Island example. Geochim et Cosmochim Acta 378: 82-98.

Sun SS, McDonough WF (1989) Chemical and isotopic systematics of oceanic basalts: implications for mantle composition and processes. Geol Soc London Spec Pub 42: 313-345.

Walter MJ, Bulanova GP, Armstrong LS, Keshav S, Blundy JD, Lord OT, Lennie AR, Clark SM, Smith CB, Gobbo L. (2008) Primary carbonatite melt from deeply subducted oceanic crust. Nature 454: 622-626.

Yaxley GM, Green DH, Kamenetsky V (1998) Carbonatite metasomatism in the Southeastern Australian lithosphere. J Pet 39: 1817-1930.

Zajacz Z, Candela PA, Piccoli PM, Wälle M, Sanchez-Valle C (2012) Gold and copper in volatile saturated mafic to intermediate magmas: Solubilities, partitioning, and implications for ore formation. Geochim et Cosmochim Acta 91: 140-159.

Hyperspectral Cathodoluminescence of Bastnäsite at the Mountain Pass Mine, USA: Implications for REE Mineralisation and Mining

Paul Slezak[1], Siri L. Simonsen[2], Chloe L. Tolbert[3], Travis McLing[1]
[1]Idaho National Lab, Center for Advanced Energy Studies, 995 MK Simpson Blvd, Idaho Falls, ID, 83401, USA
[2]Department of Geosciences, University of Oslo, P.O. Box 1047, Blindern, N-0316 Oslo, Norway
[3]Idaho National Lab, Energy Innovation Laboratory, 755 MK Simpson Blvd, Idaho Falls, ID, 83401, USA

Abstract. This study uses micro-analyses including hyperspectral cathodoluminescence to image and obtain mineral spectral to help evaluate REE deportment via from Mountain Pass Mine in California. It presents the first known CL-based spectra for bastnäsite, new information regarding baryte CL spectra, providing insights on the coeval and spatial relationship between REE, Ba, and S in carbonatite systems. Bastnäsite, baryte, and monazite are often intergrown in both brecciated, "blue ore" samples, and these minerals occur as an apparent intercumulus texture in the dolomite-rich, "white ore" samples. Bastnäsite luminescence is present, but very low compared to baryte in the visible spectrum. Bastnäsite illustrates some textural variability related to its main luminescent peak ~1.4 eV, which is indicative of Nd^{3+}. It also exhibits several other small peaks comprised of multiple activators related to various REE, including Ce^{3+}, Sm^{3+}, Eu^{3+}, and potentially Eu^{2+}. Baryte displays textures of variable complexity but often with darker rims near crystal margins. It luminesces mainly at 1.4-1.52 eV, 2.05 eV, and 3.59-4.08 eV. The 2.05 eV peak is likely attributed to Ag^{+}, but the other peaks are more enigmatic.

1 Introduction

Carbonatites are rare alkaline igneous rocks and one of the most important sources of rare earth elements (REE), which are critical materials for energy security, defence technologies, and high technology items such as smartphones and electric motors. Carbonatites are particularly abundant in light rare earth elements (LREE), typically having higher REE grades and more favourable mineralogies for processing, resulting in better metallurgical recoveries (Wall 2014).

The Sulphide Queen Carbonatite (Fig. 1) hosts the world-class Mountain Pass Mine (operated by MP Materials) in California (USA), which was the most productive rare earth element (REE) mine in the world until the mid-1990s. It is currently the largest REE mine in the United States. The main REE ore mineral is bastnäsite [$(REE)CO_3(OH,F)$], which is typically associated with monazite [$(REE,Th),PO_4$] and baryte ($BaSO_4$) as well as other minor REE-bearing phases (Castor 2008; Watts et al. 2022; Bensen and Watts 2024).

Many carbonatite-hosted, REE-bearing minerals (e.g. apatite) are easily distinguishable in hyperspectral cathodoluminescence (HyCL), which can identify and map luminescent activators in regions beyond the visible spectrum (e.g. UV and IR; MacRae et al., 2012). Several studies (e.g. Slezak et al. 2018; Bensen and Watts 2024) have examined the cathodoluminescence (CL) of carbonatite-hosted monazite and apatite, but few studies have examined the CL nature of other REE-bearing phases, like bastnäsite.

This work builds on previous REE HyCL studies by examining the spectra of bastnäsite as well as baryte and monazite from various samples from the Mountain Pass Mine. Here we combine multiple petrographic techniques (see Methods) and *in situ* data to elucidate on the origins of bastnäsite mineralisation and the REE deportment within the Mountain Pass Mine's ore minerals. Since some REE are more desirable (e.g. Nd and Pr) than others (e.g. La and Ce), identifying the location of specific elements at the mineral scale is important for the development of advanced mining, processing, and separations techniques.

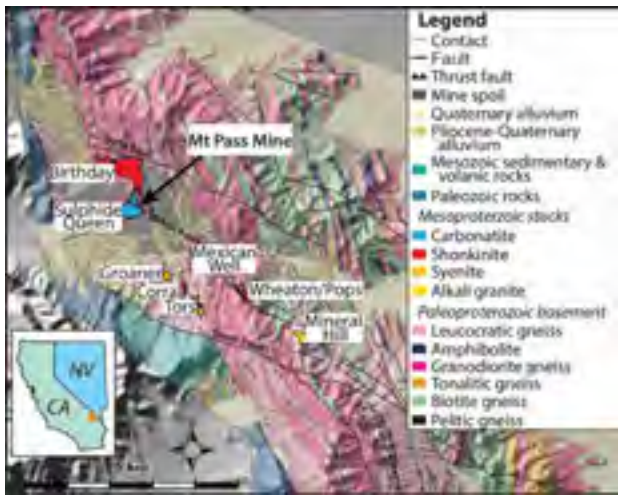


Figure 1. Location of the Sulphide Queen carbonatite and Mountain Pass Mine, CA. Map is from Watts et al. (2022) and is available in the public domain courtesy of the USGS Geology, Minerals, Energy, and Geophysics Science Center (2022) at https://www.usgs.gov/media/images/mountain-pass-regional-geologic-map-draped-over-topography.

2 Geologic Background

The Mountain Pass Mine (Fig. 1) is hosted by the Sulphide Queen carbonatite, which is part of the Mountain Pass Intrusive Suite (MPIS). In addition to carbonatites, which occur as plugs (e.g. Sulphide Queen) and dykes, much of the MPIS is comprised of ultrapotassic, alkaline silicate rocks including shonkinites, syenites, and alkali granites (Fig. 1) (Castor 2008; Poletti et al. 2016; Watts et al. 2022).

The MPIS is Mesoproterozoic in age, with dates ranging from ~1.45 to 1.37 Ga (Poletti et al. 2016; Watts et al. 2022).

The Sulphide Queen is predominantly a dolomite carbonatite with lesser zones of calcite carbonatite also present. Baryte is also a major rock-forming mineral, either intergrown with the carbonate minerals and presenting as large phenocrysts up to a centimeter in size. Bastnäsite is the most common REE-bearing phase, followed by monazite with minor amounts of secondary REE-carbonates such as parasite [$Ca(REE)_2(CO_3)_3F_3$], synchysite [$Ca(REE)(CO_3)F$] and sahamalite [$(Mg,Fe)(REE)_2(CO_3)_4$] (Castor 2008; Bensen and Watts 2024).

3 Methods

Whole rock samples from Mountain Pass, CA (USA) were cut and prepared as 30 µm polished thin sections, which were then analysed and scanned at the University College Dublin (Ireland) and Idaho National Laboratory (USA) using Nikon Eclipse LV100NPol optical microscopes.

Backscatter electron images (BSE), electron dispersive spectroscopy (EDS), and chemical mapping images were completed using a Hitachi Su5000 field emission scanning electron microscope (FE-SEM) with a Dual Bruker Quantax XFlash 30 EDS system at the University of Oslo. Variable accelerating voltages of 7 kV, 10 kV, and 15 kV were used with lower voltages being preferred for baryte and higher voltages preferred for bastnäsite and monazite.

A Delmic Sparc hyperspectral cathodoluminescence (HyCL) unit coupled to the Hitachi Su5000 FE-SEM was used to take HyCL images. Images were captured using 7 to 10 kV with 30-60 µs dwell times, 600-900 mv gain, and a blue filter to mask blurring related to abundant calcite luminescence. Small raster scans (e.g. ~15 x 15 µm) on crystal zones were used to mimic "spot" analyses. These were obtained using a 10 kV spot with 100-200 ms exposures and an input slit of 200 µm with a constant diffraction grating of 150 l/mm (500 nm blaze). Large Areas Spectra (LAS) scans were obtained using the same energy potential and diffraction grating as the spot analyses but with a 60 ms dwell time and 400 µm input slit. Spectral data are contained within the images as square spots and as rasters. These images/spectra were optimised and exported using Delmic's Odemis Viewer. Spectra were plotted and deconvoluted using CSIRO's OpticalFit 21.x (Torpy and Wilson 2008).

BSE images (Fig. 2a), spot EDS, and chemistry maps were acquired to better identify minerals to expediate CL imaging. High-resolution spectra were collected from nearby zone equivalents in the CL images to obtain stronger spectral signals since minerals like baryte (Fig. 2b) lost luminescence quickly. LAS maps of multiple minerals (Fig. 2c) were also acquired as panchromatic images. Some of these images were overlain with false colour red-green-blue (RGB) maps (50 nm in width) on specific spectral peaks. These were made to highlight luminescence outside the visible spectrum for minerals with lower CL in intensities such as bastnäsite.

4 Petrography

Several ore samples from Phase 9 were obtained from the Mountain Pass Mine, including "blue ore" (BUO) and "white ore" (WO) samples as termed by MP Materials.

4.1 Blue ore

The BUO sample consists of a dolomite carbonatite brecciating potassium feldspar-rich silicate wall rock. The feldspar crystals, when present, are up to 500 µm in size and have a patchy texture. Arfvedsonite/riebeckite is also present as larger (100 µm) anhedral to subhedral crystals (Fig. 2a). The rims of clasts are altered to platy anhedral to subhedral phlogopite, which ranges in size from 50 µm up to 250 µm (Fig. 2a). Phlogopite is also found inside and outside of the clasts. The matrix is comprised mainly of anhedral to subhedral dolomite crystals approximately 200 µm to 300 µm in size. Interspersed among the dolomite crystals are anhedral baryte crystals of similar size (Fig. 2a). Anhedral to subhedral bastnäsite (up to 400 µm) is also present, often adjacent to baryte (Fig. 2a,b). Monazite presents as small, 10 to 50 µm subhedral to euhedral laths that form larger splays and clusters within the baryte proximal to bastnäsite (Fig. 2a). Trace galena is also present filling voids and fractures (Fig. 2a).

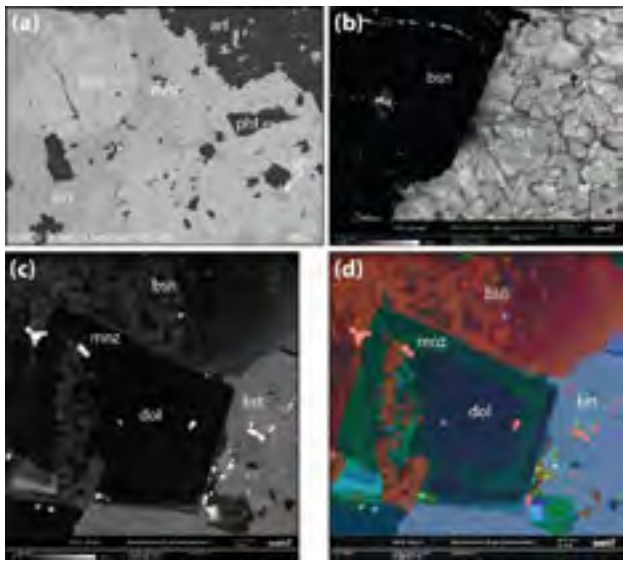


Figure 2. a BSE image of sample BUO-4 showing compositional similarity of baryte (brt), monazite (mnz), and bastnäsite (bsn). **b** CL image of BUO-3a illustrating complex zonation in baryte. **c** CL image of Sample WO-2. **d** False colour overlay of 'c' with 330 nm (blue), 665 nm (green), and 880 nm (red).

4.2 White ore

The WO samples are dolomite carbonatites that form a mesocumulate texture. Dolomite is the main cumulus phase. It is subhedral to euhedral and ranges in size from 50 µm to 400 µm (Fig. 2c,d). Calcite is present as occasional, subhedral patches (up to 50 µm in size) within dolomite and as rare, 20 µm, euhedral rhombohedrons in the intercumulus zones. Baryte occurs as both a cumulus and intercumulus phase. Cumulus baryte is rare, but may present as large megacrysts up to 1 cm long. Intercumulus baryte is more common and occurs up to 150 µm long. It predominantly exists along with bastnäsite (Fig. 2c,d), which is up to 100 µm long and occasionally is altered to parisite/synchysite. Monazite is also present with baryte and bastnäsite, but it is much smaller, appearing as 10 µm laths (Fig. 2c,d) that may form larger ~50 µm splays. Monazite also occurs on its own, typically in between and along dolomite crystal margins, and creating long chains along these margins.

5 Hyperspectral cathodoluminescence results and discussion

Within the visible spectrum of CL (i.e. ~380–700 nm), bastnäsite is typically dark (Fig. 2b) whereas baryte is often very bright, showing irregular and patchy textures of very bright and slightly darker zones (Fig. 2b). However, 50 nm wide colour bands were placed at 330 nm (blue), 665 nm (green), and 880 nm (red) to highlight that minerals like bastnäsite and monazite are luminescent, just outside of the visible spectrum.

5.1 Dolomite and baryte spectra

Dolomite is dark under panchromatic CL imaging in the visible range, and its luminescence is restricted mainly to growth bands in the crystals (see the green bands in Fig. 2d). The main luminescent activator is likely caused by Mn^{2+} (Gorobets and Rogojine, 2002; Richter et al. 2003). It occurs at a single peat at 1.89 eV and typically has lower count rates (Fig. 3a,b).

5.2 Baryte spectra

In some samples, baryte exhibits complex textures only observable under CL (Fig. 2b), whereas in others it was less complicated (e.g. Fig. 2c,d). Baryte luminesces primarily at 1.4 to 1.52 eV, 2.05 eV, and 3.59 to 4.08 eV (Fig. 3a). The 1.4 to 1.52 eV peak is not well-documented in baryte but may be partially attributed to Cu^{+} (Gaft et al 2001). However, this does not explain the shoulder that extends down to 1.41 eV. This shoulder may partly represent Nd^{3+} as it often luminesces in this region, though more work is needed to confirm this observation. The peak near 2.05 eV is known to be caused by the presence of Ag^{+} (Gaft et al., 2005) whereas the wide peak from 3.59 to 4.08 eV has been shown to be related to Ce^{3+}. Baryte also displayed high counts between 2.45 and 3.3 eV, which may be related to activators such as Eu^{2+}, Bi^{2+}, and/or Yb^{2+} (Dorenbos, 2003; Gaft et al 2001; Gaft et al. 2005).

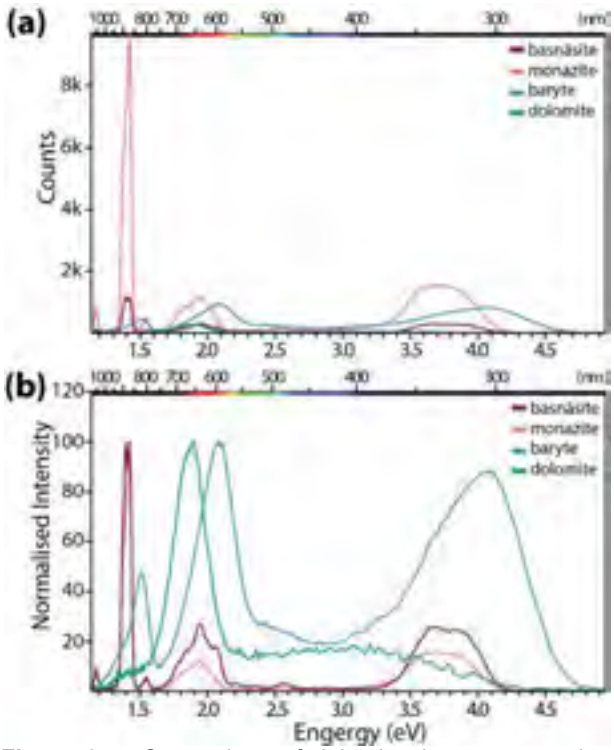


Figure 3. a Comparison of dolomite, baryte, monazite, and bastnäsite spectra obtained the minerals in Fig. 2d. **b** Normalised spectra for the same minerals and zones in 'a'. Note that baryte and dolomite, though having lower total counts, luminesce in the visible range, whereas monazite and bastnäsite do not.

5.2 Monazite spectra

Monazite is very bright in both the panchromatic and false colour CL images. It has some of the highest count rates (Fig. 3a) with peaks centered at approximately 1.40 eV. 1.95 eV and 3.75 eV, which are likely attributed to Nd^{3+} with the higher energies potentially associated with Sm^{3+} and Dy^{3+} (Richter et al. 2008; Lenz et al. 2013). Monazite also has smaller peaks at 1.18 eV, which also may be attributed to Nd^{3+} (Lenz et al. 2015) as well as 1.54 eV and 2.56 eV (Fig. 3a,b). When normalised, it shows a very similar spectral pattern to bastnäsite (Fig. 3b).

5.3 Bastnäsite spectra

Bastnäsite luminescence is present but very low compared to baryte (Fig. 1b). This is caused by baryte's stronger luminescence in the visible spectrum (Fig. 3a) compared to bastnäsite, which mainly luminesces in the infrared at ~1.4 eV (i.e. 880-900 nm; Fig. 4). This large peak is most likely related to Nd^{3+}. Bastnäsite also has several other small peaks comprised of multiple luminescent activators (Fig. 4) at 1.18 eV, 1.54 eV, 1.85 to 2.06 eV, 2.56 eV, and 3.66 to 3.93 eV related to various

REE^{3+}, including but not limited to Ce^{3+}, Sm^{3+}, Eu^{3+} (see Richter et al. 2008; Lenz et al. 2013; 2015). This is similar to monazite since many REE are matrix-independent in relation to their energy/wavelength location (Lenz et al. 2013). The very small peak at 2.56 eV may be related to Eu^{2+} but more investigation is needed as many REE luminesce in this range (Fig. 4) (MacRae and Wilson 2008; Lenz et al. 2013).

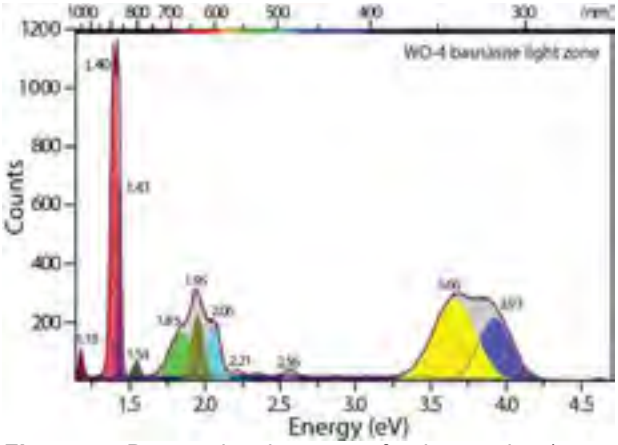


Figure 4. Deconvoluted spectra for bastnäsite (same spectra as in Fig. 2

6 Conclusions

The minerals from the Sulphide Queen carbonatite display strong evidence of similar REE activators, with monazite and bastnäsite having similar profiles distinguished mainly by differences in count rates (Fig. 3). Other minerals such as baryte also display some potential REE activators, though this needs to be investigated further. The HyCL textures in baryte and bastnäsite as well as intercumulus character of these minerals in the WO samples suggests that at least some of the carbonatite-hosted REE mineralization at Mountain Pass may be of late magmatic origin.

Acknowledgements

This project is supported by United States Department of Energy Lab Directed Research Fund (25P1098-002FP) awarded to P. Slezak. It has also received funding from the European Union's Horizon 2020 research and innovation program under grant agreement No. 101005611 for Transnational Access (award code EXCITE_TNA_C3_2023_019) conducted at the SEM lab of the Department of Geosciences, University Oslo. Additionally, we thank N. Coint for their time and review, which greatly improved this manuscript.

References

Benson EK, Watts KE (2024) Apatite and monazite geochemistry record magmatic and metasomatic processes in rare earth element mineralization at Mountain Pass, California. Econ Geol, 119: 1611–1642. https://10.5382/econgeo.5108

Castor, SB (2008) The Mountain Pass rare-earth carbonatite and associated ultrapotassic rocks, California. Can Min, 46: 779–806. https://doi.org/10.3749/canmin.46.4.779

Dorenbos P (2003) Anomalous luminescence of Eu^{2+} and Yb^{2+} in inorganic compounds. Journal of Phys Cond Mat, 15: 2645–2665. https://doi.org/10.1088/0953-8984/15/17/318

Gaft ML, Bershov LV., Krasnaya AR, Yaskolko VY (1985) Luminescence centers in anhydrite, barite, celestite and their synthesized analogues. Phys Chem Min, 11: 255–260. https://doi.org/10.1007/bf00307403

Gaft M, Reisfeld R, Panczer G, Boulon G, Saraidarov T, Erlish S (2001). The luminescence of Bi, Ag and Cu in natural and synthetic barite $BaSO_4$. Optic Mat, 16: 279–290. https://doi.org/10.1016/s0925-3467(00)00088-4

Gaft, M, Reisfield, R, Panczer G (2005) Modern luminescence spectroscopy of minerals and materials. Berlin Heidelberg. Springer.

Gorobets BS, Rogojine AA (2002) Luminescent spectra of minerals. Institute of Mineral Resources. Moscow.

Lenz C, Talla D, Ruschel K, Škoda R, Götze J, Nasdala L (2013) Factors affecting the Nd^{3+} (REE^{3+}) luminescence of minerals. Miner Petrol 107:415–428. https://10.1007/s00710-013-0286-2

Lenz C, Nasdala L, Talla D, Hauzenberger C, Seitz R, Kolitsch U (2015). Laser-induced REE^{3+} photoluminescence of selected accessory minerals — An "advantageous artefact" in Raman spectroscopy. Chem Geol, 415, 1-16. https://doi.org/10.1016/j.chemgeo.2015.09.001

MacRae CM, Wilson NC (2008) Luminescence database I - minerals and materials. Microsc Microanal. Cambridge University Press, Cambridge, U.K., pp 184–204. http://dx.doi.org/10.1017/S143192760808029X

MacRae C, Wilson NC, Torpy A, Davidson CJ (2012) Hyperspectral cathodoluminescence imaging and analysis extending from ultraviolet to near infrared. Microsc Microanal 18:1239–1245. https://10.1017/S1431927612013505

Poletti JE, Cottle JM, Hagen-Peter GA, Lackey JS (2016) Petrochronological constraints on the origin of the Mountain Pass ultrapotassic and carbonatite intrusive suite, California: J Pet, 57: 1555–1598. https://doi.org/10.1093/petrology/egw050

Richter D, Götte T, Götze J, Neuser RD (2003) Progress in application of cathodoluminescence (CL) in sedimentary petrology. Min Pet 79: 127–166. https://doi.org/10.1007/s00710-003-0237-4

Richter DK, Görgen P, Götte T (2008) Monazite cathodoluminescence – a new tool for heavy mineral analysis of siliciclastic rocks. Sediment Geol 209:36–41. https://doi.org/10.1016/j.sedgeo.2008.06.008

Slezak P, Spandler C, Blake K (2018) Ghosts of apatite past: Using hyperspectral cathodoluminescence and micro-geochemical data to reveal multi-generational apatite in the Gifford Creek Carbonatite Complex, Australia. Can Min, 56:773–797. https://doi.org/10.3749/canmin.1800021

Torpy A, Wilson NC (2008) OpticalFit Software by CSIRO Australia. http://www.csiro.au/luminescence/opticalfit/

Wall F (2014) Rare earth elements In: Gunn AG (ed) Critical Metals Handbook. John Wiley & Sons, pp 312–339

Watts KE, Haxel GB, Miller DM (2022) Temporal and petrogenetic links between Mesoproterozoic alkaline and carbonatite magmas at Mountain Pass, California: Econ Geol,117: 1–23. https://10.5382/econgeo.4848

Cambro-Ordovician Alkaline Intrusions in Idaho: Examining a Segment of North America's Western Interior Alkaline REE belt

Cody J. Steven[1], Reed S. Lewis[1], Liam Knudsen[1]
[1]Idaho Geological Survey, University of Idaho, Moscow, ID.

Abstract. The western interior of North America contains a lineament of rift-related Cambro-Ordovician intrusions. Many of the intrusions are low in silica, making up a diverse suite of syenites, carbonatites, gabbros, and granites. Throughout the Cambro-Ordovician magmatic belt, intrusions have elevated REE, Nb, Th, and Zr contents. Cambro-Ordovician intrusions in Idaho are no exception to this trend and contain some of the greatest enrichments of incompatible elements among magmatic rocks in the state. Mafic rocks within this suite are nearly as REE-rich as adjoining syenites, and may represent metasomatized mantle partial melts. Syenites, though not significantly more enriched in REE's than their mafic counterparts, demonstrate significant spikes in Zr and Nb content.

1 Introduction

East-central Idaho encapsulates a large band of cratonic rocks of ancestral western Laurentia. Hosted within these rocks are three packages of alkaline intrusive rocks 1) the ~1380 Ma bimodal magmatic suite (Evans, 1981; Evans and Zartman, 1990; Doughty and Chamberlain, 1996); 2) the ~651 Ma Cryogenian alkaline suite (Lund et al., 2010); and 3) the 530 to 486 Ma Cambro-Ordovician alkaline and ultrapotassic suite (Evans and Zartman, 1988; Lund et al., 2010; Link et al., 2017). The Cambro-Ordovician suite is a part of an extensive belt of small alkaline intrusions that span from Mexico into Canada within the deformed craton zone of western North America (Figure 1). This alkaline suite is notable for its elevated incompatible element concentrations, which includes REE's, Nb, Zr, and Ti among others. The goal of this research is to establish the basic petrologic characteristics of the Idaho Cambro-Ordovician suite with an emphasis on the genesis and emplacement conditions of the Deep Creek complex. Here we report the anomalously high REE, Nb, and Zr contents of several intrusions, which may be parent bodies to other incompatible element anomalies in the region.

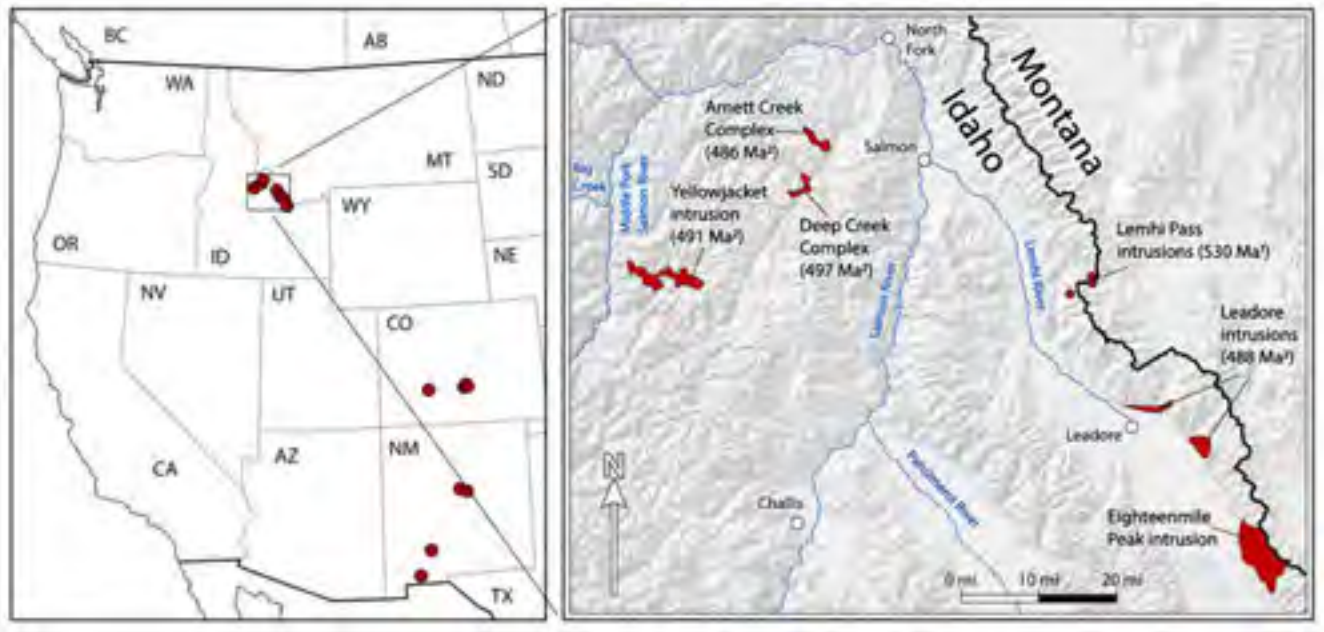


Figure 1. Index map depicting a selection of Cambro-Ordovician intrusions in western North America in red (left) and shaded relief map outlining the locations of major Cambro-Ordovician intrusions of Idaho and their ages (right). Ages by Lund et al. (2010)[1] and Gillerman et al. (2008)[2]. Cambro-Ordovician intrusion locations by McMillan and McLemore (2004), Lewis et al. (2012), Burmester et al. (2018a), and Burmester et al. (2018b)

2 Methods

Whole-rock geochemistry was obtained using inductively-coupled plasma optical emission spectroscopy (ICP-OES) and X-ray fluorescence (XRF) by AGAT Laboratories. Mineral chemistry was collected using wavelength dispersive electron probe microanalysis (EPMA) with a JEOL JXA8500F field-emission electron microprobe at Washington State University's Peter Hooper Geoanalytical Lab.

3 Results and Discussion

3.1 Petrologic Overview

Cambro-Ordovician intrusions are characterized by their distinct alkaline composition, and typically low silica content. Lithologically, the Cambro-Ordovician suite in Idaho varies from leucocratic granites to ultramafic cumulates (Figure 2). Despite the range of compositions, all lithologies appear to be enriched in incompatible elements relative to primitive mantle for the sample set in Figure 3.

3.2 Lemhi Pass Intrusions

The Lemhi Pass area contains multiple small stocks of Cambrian gabbro and alkali syenite. Lemhi Pass is recognized for its Th-rich quartz veins, which share similarities with Th veins in the Wet Mountains area of Colorado (Staatz et al., 1979; Armbrustmacher, 1988). The Lemhi Pass intrusions have some of the highest concentrations of LREE, Zr, and Nb among the Cambro-Ordovician suite (Figure 3).

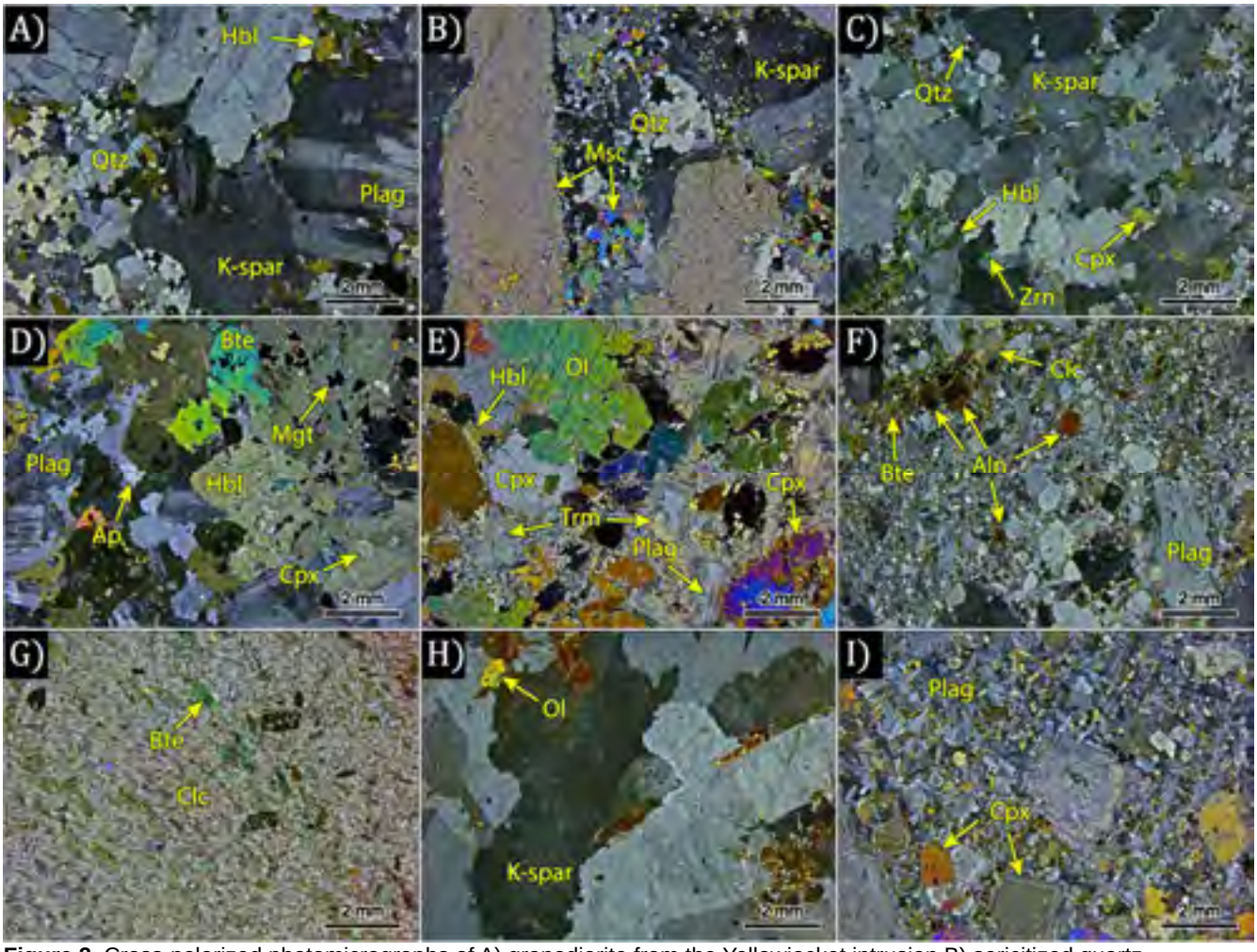


Figure 2. Cross-polarized photomicrographs of A) granodiorite from the Yellowjacket intrusion B) sericitized quartz monzogranite from Arnett Creek C) alkali syenite from Arnett Creek D) hornblende gabbro from Deep Creek E) ultramafic cumulate from Deep Creek F) allanite-rich brecciated diorite from Deep Creek G) carbonatite from Deep Creek H) alkali syenite from the Leadore area and I) gabbro from Lemhi Pass. Symbols are as follows: Qtz = quartz; Hbl = hornblende; Plag = plagioclase; K-spar = potassium feldspar; Msc = muscovite; Cpx = clinopyroxene; Zrn = zircon; Bte = biotite; Ap = apatite; Ol = olivine; Trm = tremolite; Aln = allanite; Clc = calcite.

3.3 Leadore Intrusions

The Leadore area intrusions include three, compositionally similar, Cambrian alkali granites. Proximal to the intrusions are a series of historic producers of Ag, Pb, Zn, Cu, and Au, the most significant of which is the Leadville mine. Ore minerals are principally argentiferous galena and sphalerite that are hosted in carboniferous limestones surrounding the Cambrian intrusions (Ruppel and Lopez, 1989). In global occurrences of Ag, Pb, Zn deposits, many deposits are associated with a magmatic intrusion (Beaudoin and Sangster, 1992). These intrusions are suspected to be heat source for circulating hydrothermal fluids, which scour Ag, Pb, and Zn (Beaudoin and Sangster, 1992). However, the fact that the ores are hosted in rocks that are younger than the Cambrian intrusions discredits this as a possibility in this case.

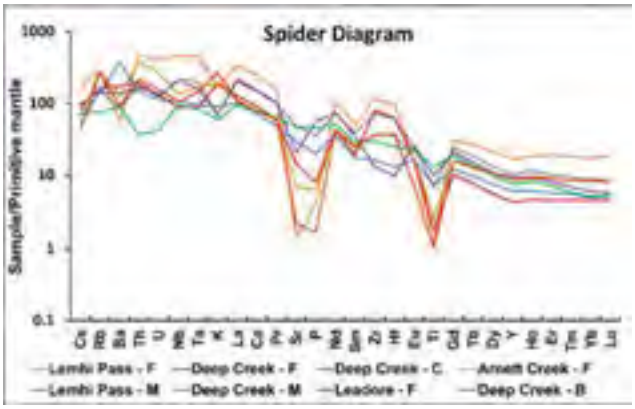


Figure 3. Spider diagram normalized to primitive mantle (Sun and McDonough, 1989) of the average compositions of felsic and mafic Cambro-Ordovician rocks. F, M, C, and B stand for felsic, mafic, carbonatite, and breccia respectively.

3.4 Deep Creek Complex

The Deep Creek intrusive suite is approximately four miles south of another Cambro-Ordovician alkaline complex, the Arnett Creek intrusive suite. The primary rock type at Deep Creek is alkali syenite, which is accompanied by carbonatite, theralite, alkali gabbro, and diorite. The northern portion of the Deep Creek suite contains a stock of intermediate and mafic rocks, which are candidates for the edenite + albite = richterite + anorthite exchange thermobarometry (Holland and Blundy, 1994). Applying the calibration by Holland and Blundy (1994), preliminary data from these rocks yield a crystallization pressure of 3.28 to 3.38 kilobars (EPMA data in Table 1), equating to a crystallization depth of approximately 12.3 kilometers.

Table 1. Representative EPMA data of hornblende and plagioclase for crystallization barometry.

Hornblende EPMA (WT% oxide)		
Sample	23CS056_A_rim	23CS061_B_rim
SiO2	40.71	40.94
TiO2	3.04	2.86
Al2O3	12.95	11.44
FeO*	14.28	15.99
MgO	11.22	10.71
MnO	0.17	0.24
CaO	11.60	11.23
Na2O	2.09	1.79
K2O	1.36	1.30

Plagioclase mole fractions		
XAb	0.47	0.58
X An	0.53	0.42

The intermediate to mafic stock at Deep Creek is cut by syenite dikes, suggesting it is an earlier magmatic phase to the primary syenite (Figure 4). Furthermore, xenoliths of hornblende gabbro are also found in the syenite stock surrounding the lobe of hornblende gabbro.



Figure 4. Outcrop of hornblende gabbro crosscut by an alkali syenite dike.

3.5 Arnett Creek Complex

The Arnett Creek intrusions include a complex of at least three distinct intrusive units 1) Cambrian syenite 2) Cambrian quartz monzonite porphyry and 3) Ordovician leucogranite. Historically, the Arnett Creek area is recognized for its extensive Au mineralization. Lode and placer operations have extracted Au in the area since its initial discovery on Napias Creek in 1866 (Umpleby, 1913). Today, the Beartrack mine is

actively exploring for Au, and is situated approximately two miles northeast from the Arnett Cambrian syenite intrusion (Figure 1). There, Au mineralization is associated with the Panther Creek shear zone, which is along a segment of the Coiner fault (Bissonnette and Kim, 2022).

4 Conclusions

Mafic rocks that are associated with syenites at Deep Creek and Lemhi Pass may represent the incompatible element-rich plagioclase melts that the syenites were extracted from. They contain abundant LREE's, and are characterized by flat sample normalized to primitive mantle trace element patterns, as illustrated in Figure 3.

Syenites, including those that crosscut the mafic rocks, are not significantly more enriched in REE's than the adjoining mafic rocks. In the case of Deep Creek, if the syenites are melt extracts of the mafic stocks, differentiation from the parent melt only moderately impacts REE concentration. In contrast, Zr, Nb, and Ta demonstrate significantly greater enrichment in the syenites. This characteristic indicates that REE enrichment is more controlled by the initial introduction of REE's to mafic partial melts, than subsequent magmatic differentiation.

Acknowledgements

We thank Revival Gold Inc. for sampling and mapping permission in the Arnett Creek area. We also thank the USGS Earth MRI program for geochemical analyses of samples in this research.

References

Armbrustmacher TJ (1988) Geology and resources of thorium and associated elements in the Wet Mountains Area, Fremont and Custer Counties, Colorado (Vol. 1049). US Government Printing Office.

Beaudoin G and Sangster DF (1992) A descriptive model for silver-lead-zinc veins in clastic metasedimentary terranes. Econ Geol 87(4):1005-1021.

Bissonnette B and Kim H (2022) NI 43-101 Technical Report on the Mineral Resource Update of the Beartrack-Arnett Gold Project Lemhi County, Idaho, USA. Revival Gold Inc.

Burmester RF, Othberg KL, Stanford LR, Lewis RS, Lonn JD (2018a) Geologic Map of the Agency Creek Quadrangle, Lemhi County, Idaho.

Burmester RF, Mosolf J, Stanford LR, Lewis RS, Othberg KL, Lonn JD (2018b) Geologic Map of the Lemhi Pass Quadrangle, Lemhi County, Idaho, and Beaverhead County, Montana.

Evans KV (1981) Geology and geochronology of the eastern Salmon River Mountains, Idaho, and implications for regional Precambrian tectonics. The Pennsylvania State University.

Evans KV and Zartman RE (1988) Early Paleozoic alkalic plutonism in east-central Idaho. Geological Society of America Bulletin, 100(12), 1981-1987.

Evans KV and Zartman RE (1990) U-Th-Pb and Rb-Sr geochronology of middle Proterozoic granite and augen gneiss, Salmon River Mountains, east-central Idaho. Geological Society of America Bulletin, 102(1), 63-73.

Gillerman VS, Fanning CM, Link PK, Layer P and Burmester RF (2008) Newly discovered intrusives at the Lemhi Pass thorium-REE iron oxide district, Idaho: Cambrian syenite and mystery ultramafics: Signatures of a buried alkaline complex or two systems?: Geological Society of America Abstracts with Programs, v. 40, no. 1, p. 51.

Holland T and Blundy J (1994) Non-ideal interactions in calcic amphiboles and their bearing on amphibole-plagioclase thermometry. Contributions to mineralogy and petrology, 116, 433-447.

Lewis RS, Link PK, Stanford LR and Long SP (2012) Geologic Map of Idaho: Idaho Geological Survey Map 9, scale 1:750,000.

Lewis RS, Stewart DE, Burmester RF, Tkach MK, Canada AS (2022) Geologic Map of the Jureano Mountain and Leesburg Quadrangles, Lemhi County, Idaho.

Link PK, Todt MK, Pearson DM, and Thomas RC (2017) 500–490 Ma detrital zircons in Upper Cambrian Worm Creek and correlative sandstones, Idaho, Montana, and Wyoming: Magmatism and tectonism within the passive margin. Lithosphere, 9(6), 910-926.

Lund K, Aleinikoff JN, Evans KV, DuBray EA, Dewitt EH, and Unruh DM (2010) SHRIMP U-Pb dating of recurrent Cryogenian and Late Cambrian–Early Ordovician alkalic magmatism in central Idaho: Implications for Rodinian rift tectonics. Bulletin, 122(3-4), 430-453.

McMillan NJ and McLemore VT (2004) Cambrian–Ordovician magmatism and extension in New Mexico and Colorado. New Mexico Bureau of Geology and Mineral Resources Bulletin, 160, 1-11.

Ruppel ET and Lopez DA (1989) Regional geology and mineral deposits in and near the central part of the Lemhi Range, Lemhi County, Idaho (No. 1480). US Government Printing Office.

Staatz MH, Sharp BJ, and Hetland DL (1979) Geology and mineral resources of the Lemhi Pass thorium district, Idaho and Montana (pp. A1-90). US Government Printing Office.

Sun SS and McDonough WF (1989) Chemical and isotopic systematics of oceanic basalts: implications for mantle composition and processes. Geological Society, London, Special Publications, 42(1), 313-345.

Umpleby JB (1913) Geology and ore deposits of Lemhi County, Idaho (No. 528). US Government Printing Office.

Fluorite as a vector for hydrothermal REE mineralization in the Gallinas Mountains deposit, New Mexico

Aadish Velmani[1,2], Alexander Gysi[1,2], Nicole Hurtig[2]

[1]New Mexico Bureau of Geology and Mineral Resources, New Mexico Institute of Mining and Technology, 801 Leroy Place, Socorro, NM 87801, USA
[2] Department of Earth and Environmental Science, New Mexico Institute of Mining and Technology, 801 Leroy Place, Socorro, NM 87801, USA

Abstract: Rare earth elements (REE) are increasingly important due to their use in the green energy and high-tech industries. Understanding the mechanisms behind REE mineralization in geological systems is vital for mineral exploration. Hydrothermal fluids are known to play an important role in the enrichment and transport of REE in critical mineral deposits. Fluorite is a key mineral that occurs with bastnäsite, a light REE fluorocarbonate mineral, in hydrothermal veins found in many alkaline complexes and carbonatites. However, its capacity to vector the hydrothermal evolution and REE mineralization stages of these systems still needs to be better constrained. The Gallinas Mountains hydrothermal REE-fluorite deposit in New Mexico (NM) contains multiple generations of hydrothermal fluorite and bastnäsite-(Ce) in veins and breccias associated with a series of trachytic to syenitic dikes and sills. These minerals also host fluid inclusions. Here, we focus on fluorite vein petrography and textures using optical microscopy, cathodoluminescence, and SEM-BSE imaging to identify different vein generations and fluorite types, and their relationship to bastnäsite mineralization in the deposit. Fluid inclusion petrography is used to distinguish inclusion types based on their size, shape, and proportions of vapor, liquid, and solid phases.

1 Introduction

Rare earth elements (REE) are critical in modern society due to their applications in the green energy and high-tech sectors (Chakhmouradian and Wall 2012). Carbonatites are the major light REE deposits mined today such as Mountain Pass in California and Bayan Obo in China, where the main ore mineral is bastnäsite-(Ce) (Smith and Henderson 2000). Other important deposits include alkaline igneous complexes (Smith et al. 2016). While igneous processes control the initial emplacement of these deposits, many studies have shown that hydrothermal processes can significantly impact the mobilization and enrichment of REE in these deposits (e.g. Williams-Jones et al. 2000; Gysi et al. 2016).

In this study, we use the Gallinas Mountains REE-fluorite deposit in NM (Williams-Jones et al. 2000; McLemore et al. 2021) as a natural laboratory to vector hydrothermal REE mobilization processes, with a focus on bastnäsite-fluorite veins. This research combines optical microscopy, SEM and cathodoluminescence to study microtextures and vein petrography to establish a mineral paragenesis. Different fluorite vein generations and their fluid inclusions are used to vector bastnäsite mineralization in the Gallinas Mountains.

2 Geological background

The Gallinas Mountains is an alkaline-igneous related hydrothermal REE-fluorite deposit located in Lincoln and Torrance Counties in New Mexico. It has been related to the North American Cordilleran alkaline-igneous belt which runs from Alaska and British Columbia through the western United States and into eastern Mexico (McLemore et al. 2018). The Gallinas Mountains district consists of a series of hydrothermal fluorite and bastnäsite-(Ce) veins and breccias hosted in Permian sedimentary rocks and is associated to ~30 My old trachyte/syenite intrusive sills and dikes (Perhac and Heinrich 1964; McLemore 2010, 2015; McLemore et al. 2021). A series of historic prospects are located in the southern-central portion of the district, some of which have been mined for Fe, Pb, Cu, Ag, fluorite, and notably bastnäsite-(Ce); the deposit has been inferred to contain 537,000 short tons with a grade of 2.95% total REE (McLemore et al. 2021). The major deposits in the Gallinas Mountains include the M&E No. 13 mine, Red Cloud fluorite mine, Park prospect, Sky High prospect, and Rough Mountain area (see McLemore et al. 2021 and Owen 2024 for geologic maps). Many of these fluorite deposits occur in proximity to E-W, NW-SE, and NE-SW trending fault systems or volcanic/hydrothermal breccia pipes intruded in the Permian sedimentary units.

McLemore et al. (2010) discusses the mineralized structures and divides them into four types of deposits: epithermal REE-F veins, Cu-REE-F veins, REE-F breccia pipes and iron skarn deposits. Cherotich et al. (2023) characterized the breccia pipes, which include magmatic intrusive breccia pipes, tectonic fault breccia, brecciated country rocks, and brecciated hydrothermal vein deposits. The fluorite veins were also subdivided by geochemistry into F, F-Ba, F-Ba-Cu, F-Cu, REE-F, REE-F-Ba, REE-F-Ba-Cu and REE-F-Cu veins (McLemore et al. 2021). Owen (2024) further refined the vein classification based on textures, cathodoluminescence, and mineral association. Three fluorite vein types were recognized: Type I barite-fluorite veins; Type II bastnäsite-fluorite veins; and Type III calcite-fluorite veins. Each of these

veins contain different generations of fluorite, however, the exact nature of the fluids responsible for mineralization and REE transport in the district needs to be further determined.

Previous work by Williams-Jones et al. (2000) indicates the presence of fluorite (Fl), quartz, and bastnäsite (Bsn) hosted fluid inclusions (Fi). Microthermometry shows homogenization temperatures up to ~400 °C in quartz and bastnäsite-hosted Fi. Salinity ranges from 12-18 wt% $NaCl_{eq.}$ with the presence of sulfate-rich NaCl-KCl brines in early-stage Fi and lower salinity NaCl brines in later stage Fi. Williams-Jones et al. (2000) describe an early, subhedral to euhedral, green-blue fluorite (P1) with sparse inclusions. Fluorite (P1) commonly displays replacement textures by a clear-purple fluorite (P2) with a large quantity of fluid inclusions. A fine-grained matrix fluorite (P3) commonly surrounds and alters earlier formed minerals including P1-P2 fluorite and barite (Brt).

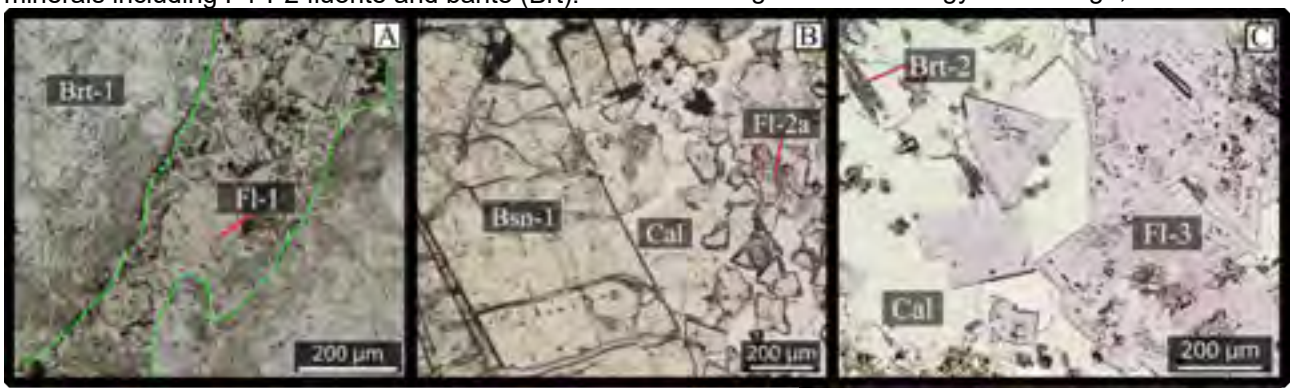


Figure 1. Optical photomicrographs of fluorite-bearing veins. A) Type I, Brt-Fl vein consists of Fl-1 and Brt, both crosscut by Qtz veinlets (GAL370, M&E No.13 prospect). B) Type IIa, Bsn-Fl veins showing large tabular Bsn crystals and Fl-2a crosscut by calcite veins (GAL3044A, M&E No.13 prospect). C) Type III Fl-Cal veins containing barren subtype Fl-3 and Cal, intergrown with fine-grained Brt (GAL3018, Rough Mountain). Fl: fluorite; Brt: barite; Bsn: bastnäsite; Cal: calcite; Qtz: quartz.

3 Methods

Vein samples were selected based on the presence of barite, fluorite, calcite, bastnäsite and the main vein types categorized by Owen (2024). Locations sampled and sample numbers include: Rough Mountain (GAL2022, GAL3015B, GAL3018A, GAL3018B, GAL3024, GAL7a), Red Cloud (GAL 3041A), and M&E No.13 prospects (GAL3044A, GAL3044AH11, GAL3044C, GAL3046, GAL370). The fluorite veins were cut into billets and prepared into 30 µm thin sections for petrography and 70-120 µm thick sections for fluid inclusion work. Transmitted light microscopy was done using an Olympus-BX petrographic microscope to study the vein petrography. Cathodoluminescence (CL) was analysed in fluorite using an ELM-3R Luminoscope to identify growth and replacement textures. Microtextural relationships and mineral identification was further investigated using a JSM-IT700HR JEOL scanning electron microscope equipped with an Oxford Ultim Max X-ray energy-dispersive spectrometer (EDS). Raman spectroscopy on solids in FIA was conducted using a Horiba HR Evolution confocal microscope.

4 Results

4.1 Fluorite vein classification

Three main different fluorite (Fl) vein types were distinguished based on mineralogy, textural relationships, and fluorite CL signature (Figs. 1-3). Vein naming is based on the least abundant mineral to the most abundant and is in line with Owen (2024): Type I barite-fluorite veins (Brt-Fl ± Qtz, Hem), Type II bastnäsite-fluorite veins (Bsn-Fl ± Hem, Str), and Type III calcite-fluorite veins (Fl-Cal ± Brt). Therefore, the different fluorite vein types show a clear progression from barite > bastnäsite > calcite bearing vein mineralogy. Late stage, calcite veins and metal sulfide veins crosscut these veins in certain areas of the deposit.

4.2 Vein petrography

Type I Brt-Fl veins (Fig. 1A) consist of fluorite and coarse-grained, cm-sized, tabular micro-fractured barite relicts; some veins also contain hematite after pyrite and quartz. Barite is less altered and retains a subhedral habit in comparison to other vein types. Fluorite occurs as fragmented cubes that are in some instances heavily fractured and crosscut by calcite and/or quartz veins. In many Type I veins, fluorite occurs as later infills in fractured barite together with calcite. Type I veins are rarely preserved and more commonly occur as brecciated barite in veins and fluorite breccia with infills of Type II Bsn-Fl veins.

Type II Bsn-Fl veins (Fig. 1B) represent the main hydrothermal REE mineralization stage. Type II veins occur in breccia and infills, and as replacement of Type I veins. Type II veins are further divided in this study based on bastnäsite and fluorite textures. Figure 2 shows SEM-BSE images of the different bastnäsite types. Subtype IIa veins contain >200 µm sized bastnäsite crystals (Fig. 1B, 2A). Subtype IIb veins are characterized by euhedral fluorite cubes with bastnäsite occurring as small acicular/needle-like inclusions (Fig. 2B). This fluorite occurs in veins that crosscut subtype IIa vein. Subtype IIc veins

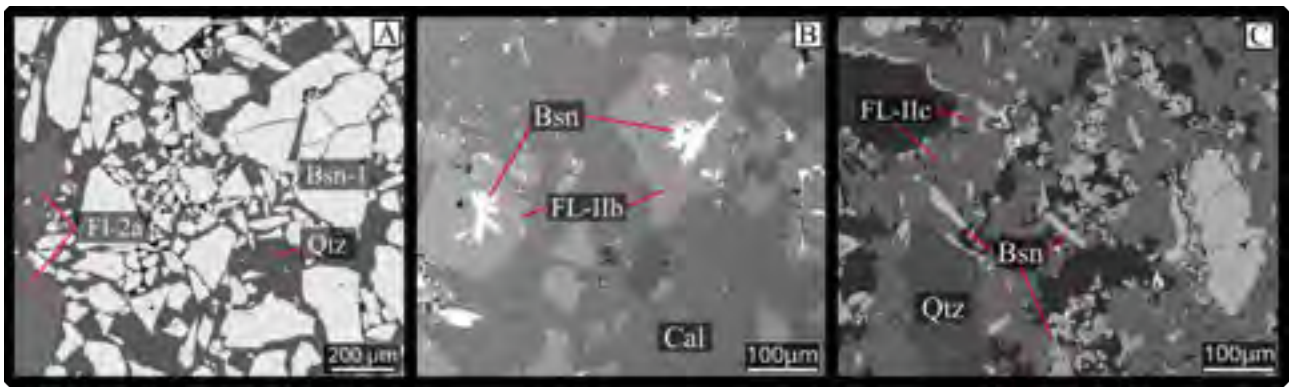


Figure 2. SEM-BSE images of Bsn-bearing Type II veins. A) Subtype IIa veins showing large tabular Bsn crystals alongside barren Fl crystals with infills of Cal (GAL3044AH11, M&E No.13 prospect). B) Subtype IIb veins with euhedral Fl cubes and needle-like Bsn inclusions (GAL3044A M&E No.13 prospect). C) Subtype IIc vein with fine grained Fl matrix with bladed bastnäsite crystals crosscutting a Type I vein (GAL3041, Red cloud).

commonly occur as breccia infills, with barite relicts from Type I veins and are characterized by fine-grained fluorite intergrown with elongated ~50-100 µm bladed bastnäsite crystals (Fig. 2C). Type III Fl-Cal veins are mostly barren, and crosscut former Type I and II veins, and may contain sparse amounts of fine-grained barite (Fig. 1C, 3C).

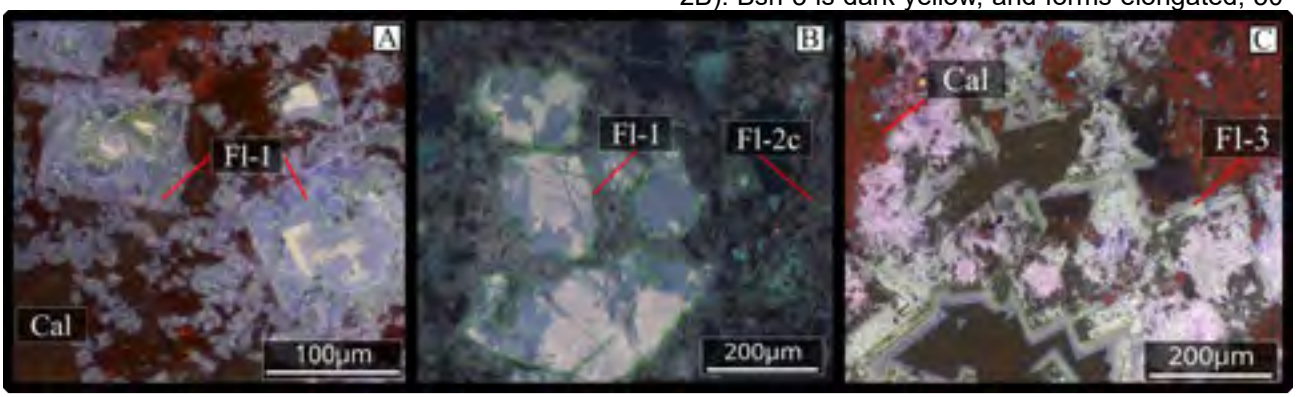


Figure 3. CL images of Fl types. A) Type I vein with Fl-1 and barite fragments cut by calcite veins. Fl-1 shows a pale blue-white CL signature (GAL2022, M&E No.13 prospect). B) Subtype IIc vein with fine-grained Fl-2c cutting and altering relict Fl-1. Fl-2c has a blue-gray signature, in contrast with the blue-white signature of Fl-1 (GAL3041, Red cloud district). C) Type III vein showing well zoned, Fl-3 with lavender-green CL signature, along with calcite (GAL3018, Rough Mountain)

4.3 Mineral generations and CL signatures

Fluorite can be categorized into three types (Fl-1, Fl-2, Fl-3) based on their occurrence in each vein type, their microtextures and CL signature. Fl-1 in Type I veins typically occurs as well zoned and fragmented to individual euhedral cubes, ranging from <50 up to ~100 µm. Fl-1 displays a clear to purple color in transmitted light, and a pale blue CL signature with complex, compositional zoning and dissolution-precipitation textures (Fig. 1A, 3A,B). Fl-2 is subdivided based on bastnäsite microtextures (Fig. 2). Fl-2a and Fl-2b both form pale purple, euhedral cubes and have blue-green CL signatures; Fl-2b contains small bladed Bsn crystals (Fig. 1B, 2B). Fl-2c is a fine-grained, purple matrix fluorite with a gray-blue CL signature (Fig. 2C, 3B). Fl-3 forms zoned, euhedral purple fluorite with a green-lavender CL signature and displays compositional growth zones and core dissolution and fluorite replacement textures (Fig. 1C, 3C). Multiple bastnäsite types have been recognized and are subdivided into Bsn-1, Bsn-2, and Bsn-3. Bsn-1 presents as large, elongate, euhedral, yellow-brown crystals on the mm scale (Fig 1B, Fig 2A). This type is commonly found in Type IIa veins and forms adjacent to Fl-2a. Bsn-2 is associated with Type IIb veins and occurs as small dark brown, 1-5 µm crystals that form blade like inclusions/replacements within or near Fl-2b (Fig. 2B). Bsn-3 is dark yellow, and forms elongated, 50-100 µm bladed crystals that are hosted within a matrix of Fl-2c, and rarely in barite (Fig. 2C). Two types of barite are also identified, Brt-1 and Brt-2. Brt-1 is found in Type I veins and forms euhedral to subhedral, tabular, cm-sized crystals. Brt-2 is a fine-grained barite that forms alongside calcite in Fl-3 veins (Fig. 2C).

4.4 Fluid inclusion petrography

Several primary fluid inclusion (Fi) types have been identified based on size, shape, and phase constituents including vapor (V), V plus liquid (VL), and VL plus solid (VLS). V type inclusions are found within Fl-1 and Brt-1 in Type I veins, and Bsn-1 in Type IIa veins and rarely in Fl-2. V type inclusions range from sub-micron to ~5-10 µm in width. VL type inclusions can be subdivided based on the proportions of L to V. VL1 are typically found in Fl-1

and Brt-1 in Type 1 veins and in Fl-2a, and Fl-2b, and Bsn-1 in Type 2a veins. VL1 inclusions consist of >50 vol% of vapor and are round to boxy, with sizes commonly ranging from ~5 to 20 µm. VL2 inclusions contain 20-45 vol% vapor, and are more common than VL1, found mainly in Fl-2a and Fl-2b and Bsn-1 in Type IIa veins. VL2 inclusions are elongate and boxy but can also be round or irregular shaped. Inclusion sizes range from sub-micron to 20 µm. VL3 inclusions occur in Fl-2c in Type IIc veins, and also in Fl-3 in Type-III veins, and contain <10 % vapor. These are round to irregular in shape, with sizes ranging between 5-10 µm.

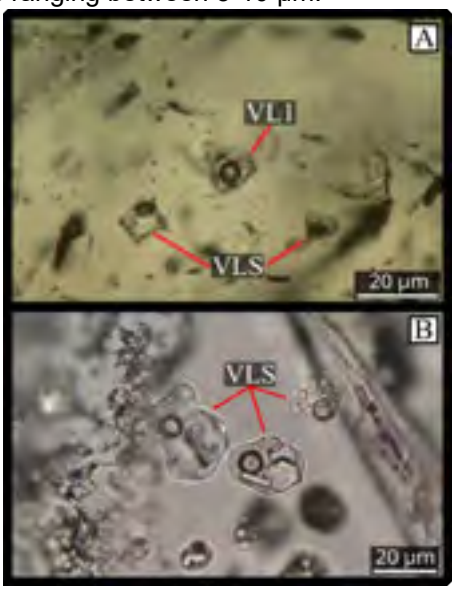


Figure 4. Optical photomicrographs of fluid inclusions. A) VL1 and VLS inclusions hosted in Bsn-1 in a Type 2a vein (GAL3044H11, M&E No.13). B) VLS inclusions hosted in Fl-2b in Type 2b vein (GAL7a, M&E No.13 prospect)

VLS inclusions are hosted in Brt-1 in Type I veins and in Fl-2b and Bsn-1 (Fig. 4A,B) in Type II veins. They contain multi-phase solids with proportions of ~20 vol% V, ~40-50 vol% L, and ~30-40 vol% S. VLS inclusions are generally irregular but can also present as elongate and round, with sizes ranging from ~5-20 µm. Solids include barite and celestite, which occurs as prismatic ~10µm crystals, identified with Raman spectroscopy. VLH inclusions are a subtype of VLS inclusions and are distinguished by containing halite as a solid phase. These inclusions are found in Fl-2b in Type 2 veins. These inclusions also contain barite and celestite.

Looking at Fi assemblages (FIA), V inclusions are found together in Fl-1 in Type-I veins. In Type IIb veins, Fl-2b can host assemblages of V and VL1 inclusions. Type IIa veins contain assemblages of VLS and VL1 inclusions hosted in Bsn-1. Type IIb veins can contain assemblages of purely VLS inclusions in Fl-2b (Fig. 4B). Type IIc and Type III veins both contain assemblages of VL2 and VL3 inclusions hosted in Fl-2c and Fl-3 respectively. Williams-Jones et al. (2000) describe LVS inclusions hosted in P1-Fl and Bsn, which is similar to VLS inclusions described in this study.

5 Conclusions

There are multiple progressive generations of fluorite within the Gallinas deposit. The successive nature of fluorite types, CL signature, and bastnäsite mineralization shows clear trends in the ore fluids. The main REE mineral bastnäsite is absent from the earliest vein types and is abundant in the “middle” stage, indicating a clear evolution of the hydrothermal fluids. This stage is then proceeded by another stage of barren fluorite-calcite veins. Fluid inclusions show a progression from vapor-rich Fi transitioning to liquid-dominant fluid inclusions, which indicates cooling. Therefore, the ore forming stage is clearly delineated at Bsn-fluorite veins showing precipitation of REE during cooling of hydrothermal fluids.

Acknowledgements

This project was supported by the National Science Foundation to APG (NSF CAREER grant EAR-2039674) and through the Frank E. Kottlowski scholarship awarded to AV, and supported through the New Mexico Bureau of Geology and Mineral Resources

References

Chakhmouradian AR, Wall F (2012) Rare Earth Elements: Minerals, Mines, Magnets (and More). Elements 8:333–340 https://doi.org/10.2113/gselements.8.5.333

Cherotich S, McLemore VT (2023) Characterization and origin of the ree-bearing magmatic-hydrothermal breccia pipes. New Mexico Geological Society Annual Spring Meeting https://doi.org/10.56577/sm-2023.2918

Gysi AP, Williams-Jones AE, Collins P (2016). Lithogeochemical Vectors for Hydrothermal Processes in the Strange Lake Deposit. Econ Geol 111:1241–1276. https://doi.org/10.2113/econgeo.111.5.1241

McLemore VT (2010) Geology and mineral deposits of the Gallinas Mountains. New Mexico Bureau of Geology and Mineral Resources Open-file report 532. https://doi.org/10.58799/OFR-532

Mclemore VT (2015) Rare Earth Elements (REE) Deposits in New Mexico: Update. New Mexico Geology 37:59-69. https://doi.org/10.58799/NMG-v37n3.59

McLemore VT (2018) Rare earth elements (REE) deposits associated with great plain margin deposits (alkaline-related), southwestern united states and eastern Mexico. Resources 7: 1–44. https://doi.org/10.3390/resources7010008

McLemore VT, Kelley S, Zimmerer MJ, Owen E, Haft E, Cantrell T, Trivett A (2021) Geology and mineral resources of the Gallinas Mountains. New Mexico Bureau of Geology and Minerals Resources Open-file Report 617: 164. https://doi.org/10.58799/OFR-617

Owen, EJ (2024) Mineral Paragenesis and Geochemistry of Hydrothermal REE-F Bearing Veins and Breccias in the Gallinas Mountains. Master’s Thesis New Mexico Institute of Mining and Technology

Perhac RM, Heinrich EW (1964) Fluorite-bastnaesite deposits of the Gallinas Mountains. Econ Geol 59:226–239. https://doi.org/10.2113/gsecongeo.59.2.226

Smith MP, Henderson P (2000) Preliminary fluid inclusion constraints on fluid evolution in the Bayan Obo Fe-REE-Nb deposit. Econ Geol 95:1371-1388. https://doi.org/10.2113/gsecongeo.95.7.1371

Williams-Jones AE, Samson IM, Olivo GR (2000) The genesis of hydrothermal fluorite-REE deposits in the Gallinas Mountains, New Mexico. Econ Geol 95: 327-341. https://doi.org/10.2113/gsecongeo.95.2.327

Formation of the Mount Weld rare earth deposit, Western Australia: geochronology constraints

Philip L. Verplanck[1], Cameron M. Mercer[1], Jay M. Thompson[1], Martin Danišík[2], Ganesh Bhat[3], and Heather A. Lowers[1]
[1]US Geological Survey, Denver, Colorado, USA
[2]John de Laeter Centre, Curtin University, Perth, Australia
[3]Lynas Rare Earths Ltd., Laverton, Australia

Abstract. Constraining the age of protracted chemical weathering in stable cratonic areas that may form thick regoliths and the potential enrichment of various elements is challenging. Economic deposits of aluminium, iron, copper, nickel, cobalt, niobium, and rare earth elements (REEs) form in this manner. Determining the age of formation can provide key information for exploration of similar deposits as well as to better constrain paleoclimatic conditions. This study describes our effort to constrain the age of formation of the Mount Weld deposit, a world-class carbonatite-derived REE laterite deposit. We utilize multiple geochronological techniques on different minerals. The oldest dates, ranging from ca. 100 to 50 Ma, were from laser ablation ICPMS, Lu-Hf dating of churchite, a heavy REE phosphate mineral formed by mineral saturation in groundwater. Growth bands on individual minerals show a younging outwards. $^{40}Ar/^{39}Ar$ geochronology of cryptomelane, a potassium-bearing manganese oxide mineral, yielded ages ranging from ca. 40 to 26 Ma. Similarly, (U–Th)/He geochronology of goethite yielded ages from ca. 45 to 19 Ma.

1 Introduction

With the increasing reliance on high technology and green energy products, demand for critical metals has become an important driver in economic geology. The REEs are a family of elements that have been defined as critical on most lists because of their unique magnetic and optical properties and their geographical-limited supply locations. Carbonatite-hosted REE deposits are the primary source of the world's light REEs (LREEs) and have the potential to be a source of heavy REEs (HREEs). Carbonatites are defined by the International Union of Geological Sciences (IUGS) as igneous rocks composed of greater than 50 volume percent primary carbonate minerals, primarily calcite and/or dolomite, and containing less than 20 wt.% SiO_2 (Le Maître 2002). The Mount Weld REE deposit (Figures 1 and 2) in Western Australia is hosted in a lateritic sequence above an underlying carbonatite. It is one of four giant, active REE mines associated with carbonatites, the largest producer of separated REE outside of China, and the only one of the four that is laterite hosted. Lynas Rare Earths Ltd. (2024) reported a total mineral resource (measured, indicated, and inferred) of 106.6 million tonnes at an average grade of 4.12% Total Rare Earth Oxide (TREO) for a total of 4.39 million tonnes of contained TREO.

The Mount Weld carbonatite occurs within Eastern Goldfields province of the Yilgarn craton, near Laverton, Western Australia. The laterite is covered by 20 to 40 m of lacustrine and alluvial sedimentary rocks, so there is no surface expression of the mineralization. The deposit was discovered by drilling a large, circular magnetic anomaly identified in a 1966 regional airborne geophysical survey undertaken by the Australian Bureau of Mineral Resources. Magnetite from the carbonatite was dated at 2025 ± 10 Ma by the Re-Os method (Graham et al. 2004). The age of laterization is poorly constrained. Due to of active mining and extensive exploration drilling, this is an ideal setting to evaluate REE enrichment associated with lateritically-weathered carbonatites.

The objective of this study is to constrain the age of formation of the Mount Weld deposit. Because of the complexity of the deposit, four dating methods were utilized (with three discussed here) using secondary minerals formed during weathering: (U-Th)/He dating of goethite [FeO(OH)], $^{40}Ar/^{39}Ar$ dating of cryptomelane [$K(Mn^{4+},Mn^{2+})_8O_{16}$], Lu-Hf and U-Pb dating of churchite [$HREE(PO)_4(H_2O)$], and U-Pb dating of rhabdophane [$LREE(PO)_4$ (H_2O)].



Figure 1. Location of Mount Weld deposit



Figure 2. Photograph of the Mount Weld mine.

2 Methods

Samples were collected in October 2018 from archived drill core stored at the Mount Weld deposit and from the active pit (18MW0X). A second set of samples from the active pit was collected in November 2022 (22MW0X).

All samples were air dried. Cryptomelane and goethite samples were processed in a similar fashion. Polished thin sections were made to help with mineral identification and evaluate textural characteristics using binocular microscope, reflected light microscopy, and scanning electron microscope (SEM). Grains of interest were either plucked from hand samples or handpicked using a binocular microscope from samples lightly crushed with a mortar and pestle. Crushed samples were washed in deionized water and ultrasonic bath for 3-minute intervals. Representative grains of cryptomelane and goethite from each sample were analyzed by X-ray diffractometry (XRD), SEM, and electron probe microanalysis (EPMA) to check for impurities.

Laser ablation inductively coupled plasma mass spectrometry (LA-ICPMS) analysis was utilized to determine Lu-Hf ages and REE concentrations of churchite at the U.S. Geological Survey Denver LTRACE laboratory. (U-Th)/He analyses of goethite were carried out at the Western Australia Thermochronology Hub (WATCH) facility of the John de Laeter Centre (Curtin University, Perth) following the analytical procedures of Danišík et al. (2013). Cryptomelane $^{40}Ar/^{39}Ar$ age determinations were determined at the USGS Denver Argon Geochronology Laboratory.

3 Results

The Mount Weld carbonatite is approximately 4 km in diameter and is buried under approximately 20-40 m of surficial sediment and up to 120 m of weathered material. Carbonatite samples from older drill core are either calcite- or dolomite-rich, with minor minerals including apatite, magnetite, olivine, biotite, pyrite, monazite, and pyrochlore. Carbonatite samples from core from recent drilling at the base of the active pit are primarily ankerite/dolomite carbonatite and contain REE fluorocarbonate minerals, bastnäsite and parisite, as well as apatite and monazite (Figure 3). Chondrite-normalized REE diagrams of the Mount Weld carbonatite are LREE enriched, and samples with REE fluorocarbonate minerals are more LREE enriched and have a steeper negative slope (Figure 4).

The laterite sequence, up to approximately 90 m thick, lies above a residual zone that overlays the carbonatite. Overall, the composition of the laterite samples is variable, most samples are iron rich with goethite, the dominant mineral phase. Other minerals include hematite, calcite, dolomite, apatite, hollandite, kaolinite, nacrite, illite, maghemite, montmorillonite, magnetite, pyrochlore, ilmenite, and rutile, and traces of quartz, barite, anatase, cryptomelane, and vermiculite. Calcite and barite appear to be secondary phases while dolomite, magnetite, and pyrochlore are residual phases from the carbonatite. The transition to the underlying carbonatite is termed the “residual zone” and is composed of apatite, magnetite, pyrochlore, and dolomite with secondary goethite, kaolinite, and hematite. The REE mineralogy in the laterite is variable and complex (Figure 5). Within the active pit, medium-grained primary monazite is observed. Secondary phosphate minerals include monazite, rhabdophane, crandallite subgroup minerals (goyazite and gorceixite, florencite, and churchite. Cerianite is also observed. Mineral textures are complex, displaying variable zoning and overprinting.

The chondrite-normalized REE patterns of samples from the laterite display LREE enrichment (Figure 4). The LREEs are moderately enriched compared to the ankerite carbonatite, and more substantially enriched compared to the calcite carbonatite.

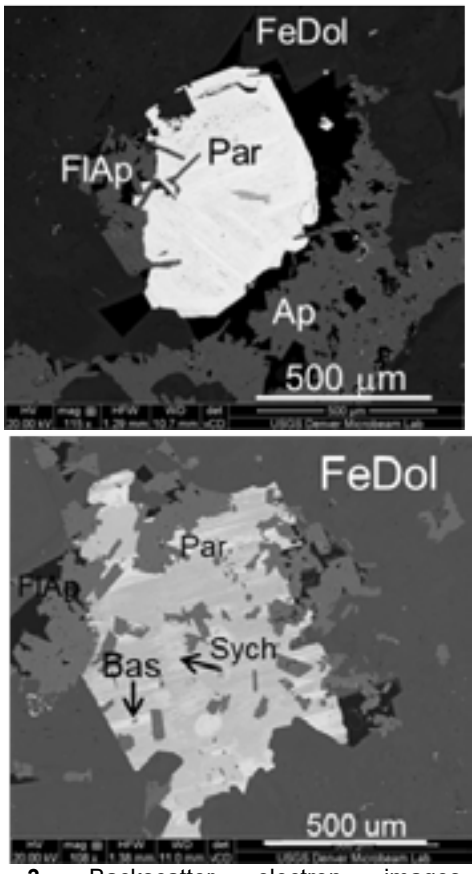


Figure 3. Backscatter electron images of ankerite/dolomite (FeDol) carbonatite. Par (parisite), Sych (synchysite), Ap (apatite), (Bas) bastnäsite, and FlAp (fluorapatite).

To constrain the age of formation and provide insight into landscape evolution of the Mount Weld deposit, multiple geochronological techniques on different minerals were utilized. Lu-Hf dating of the mineral churchite yielded the oldest ages. The two oldest Lu-Hf dates (88.1 ± 11.9 and 98.4 ± 13.4 Ma) occur in the cores of grains 4 and 10. Both spots

have nearly identical REE patterns. The outer material on grain 10 has an age of 51.3 ± 8.2 Ma. Three zones on grain 4 were analysed with the core at 88.1 ± 11.9 Ma, the next outer zones at 65.8 ± 10.4 and 58.7 ± 12.0 Ma and the outermost zone at 54.7 ± 10.3 and 56.2 ± 10.7 Ma. These two grains display younger ages outward. Lu-Hf ages of grains 7A and B (4 spots) yield results similar to the middle zone of grain 4 with ages ranging from 69.5 ± 8.7 Ma to 57.8 ± 9.3 Ma. Overall, the ages for churchite formation range from approximately 98 to 51 Ma.

Three samples were utilized for $^{40}Ar/^{39}Ar$ geochronology using cryptomelane with five to seven individual grains per sample. Cryptomelane is a secondary MnK oxide mineral in the hollandite mineral group and has been used to date supergene deposits in Central Africa, China, Australia, South America, and India. Two grains from one sample yielded indistinguishable dates that both round to 38.0 ± 1.4 Ma. The range in integrated ages for all seven grains of this sample was 39.2 ± 1.5 and 33.8 ± 1.5 Ma, and the range in ages for all seven isochron ages was between 40.4 ± 1.6 and 35.3 ± 2.3 Ma. Two grains from a second sample yielded plateau ages of 29.2 ± 1.1 and 27.6 ± 1.0 Ma, and the range in integrated ages for all six grains of this sample was from 29.1 ± 1.1 and 26.8 ± 1.0 Ma. No statistically meaningful isochron ages were determined. The third sample did not yield any plateau ages. Integrated age spectra for 5 grains of this sample ranged between 34.8 ± 1.3 and 31.9 ± 1.2 Ma, and the range in the isochron ages was between 37.4 ± 1.4 and 34.8 ± 1.3 Ma. In summary, for the three samples, the overall range in integrated ages ranged from 39.2 to 26.8 Ma, and the isochron ages ranged from 40.4 to 34.8 Ma. Four grains from two samples yielded plateau ages of 38.0 Ma and 28.4 Ma (average of the two grains in each sample).

From the Mount Weld laterite, three samples of goethite, with 8 individual grains per sample, were analysed by the (U-Th)/He dating technique. The mean ages for the samples were 44.88±3.32, 37.63 ±2.72, and 19.34 ±1.49 Ma.

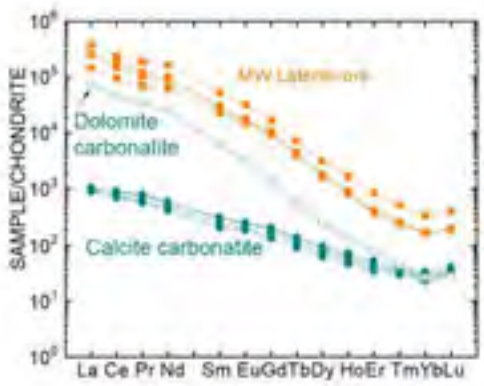


Figure 4. Chondrite-normalized REE diagram displaying the Mount Weld calcite carbonatite, dolomite carbonatite, and laterite ore. Chondrite values from Anders and Ebihara (1982).

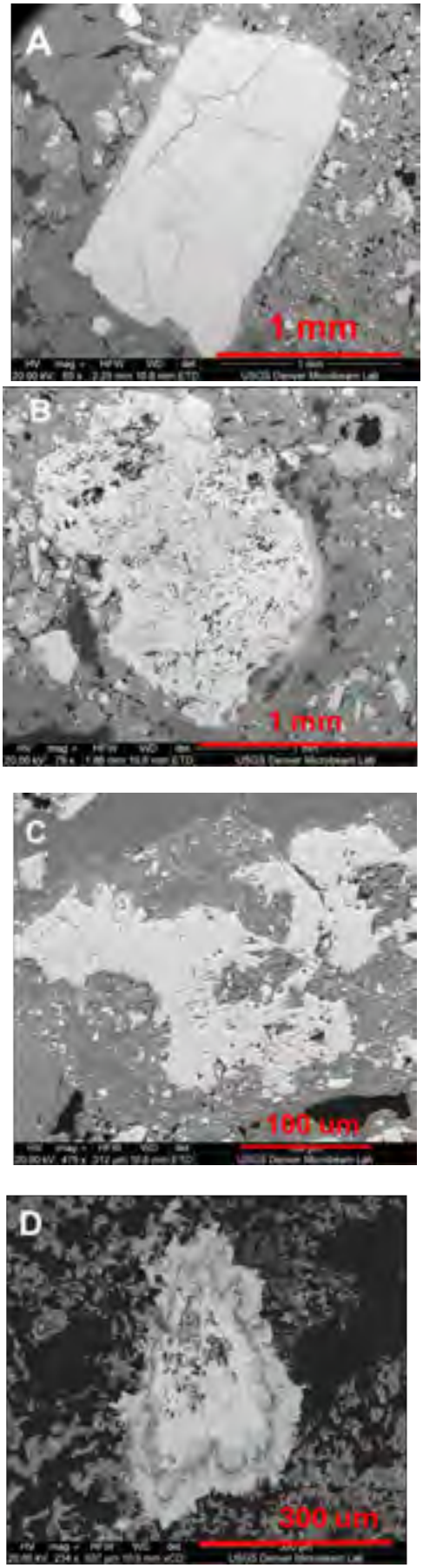


Figure 5. Backscatter electron images of A) primary monazite, B) secondary monazite, C) rhabdophane, and D) churchite within the laterite ore material.

4 Discussion

Utilization of multiple mineral phases that form under different conditions provides constraints on the formation of the Mount Weld deposit. The secondary hydrated REE phosphate mineral, churchite, forms in the weathering environment by precipitation when groundwater becomes supersaturated in REEs and PO_4 and this process is not redox dependent. Cryptomelane is observed in supergene manganese deposits and some weathering profiles. Dissolved manganese occurs in groundwater and upon oxidation may form cryptomelane if potassium is present. This occurs at or near the paleo-water table. Similarly, goethite in weathering profiles forms when groundwater and oxygen mix, commonly at or near the paleo-water table.

The oldest ages were generated from Lu-Hf geochronology of churchite. These ages range from ~ 98 to 51 Ma. Because churchite forms by mineral saturation in ground water, these ages likely reflect the onset of weathering in a karst-like environment. Cryptomelane and goethite form near the water table because oxygen is needed. When comparing results from these two different dating techniques, a general complimentary picture emerges. The majority of dates from both techniques fall between ~42 and 20 Ma, with a few older and younger ages from individual grains or steps. This suggests that the redox front was active within the section during this period and after ~15 Ma weathering had slowed or ceased. During this time period, Western Australia experienced minimal uplift and a wet, warm climate enabling extensive chemical weathering of the carbonatite.

5 Conclusions

Utilization of multiple geochronological techniques on different minerals provides insight into the age of laterization and the evolution of the weathering profile. The new age dates show that weathering within the laterite at Mount Weld had been at work for ~80 million years (~100 Ma to ~20 Ma). Protractive weathering of the underlying carbonatite, telescoping of the weathering profile, supergene enrichment, and a stable tectonic framework can account for the ore-grade REE enrichment in the laterite. These characteristics can be used to guide future exploration for REE deposits in weathering environments.

Acknowledgements

This work was supported by the U.S. Geological Survey Mineral Resources Program. Any use of trade, firm, or product names is for descriptive purposes only and does not imply endorsement by the U.S. Government.

References

Anders E, Ebihara M (1982) Solar-system abundances of the elements. Geochimica et Cosmochimica Acta. 46:2363-2280

Danišík M, Evans NJ, Ramanaidou ER, McDonald BJ, Mayers C, McInnes BIA (2013) (U–Th)/He chronology of the Robe River channel iron deposits, Hamersley Province, Western Australia. Chemical Geology 354:150-162

Graham S, Lambert D, Shee S (2004) The petrogenesis of carbonatite, melnoite and kimberlite from the Eastern Goldfields Province, Yilgarn Craton. Lithos 76:519–533

Le Maître RW, ed. (2002) Igneous Rocks: A Classification and Glossary of Terms. Cambridge University Press, Cambridge, U.K. 193 p

Lynas Rare Earths Ltd. (2024) Annual Report. 116 p

The Geochemistry of Magnetite from Bayan Obo Fe-REE-Nb Deposit, China: Implications for Ore Genesis

Lan Yang[1,2], Yang Li[3], Yan Yu[1,2], Xian-Hua Li[1,2]
[1]State Key Laboratory of Lithospheric and Environmental Coevolution, Institute of Geology and Geophysics, Chinese Academy of Sciences, China
[2]College of Earth and Planetary Science, University of Chinese Academy of Sciences, China
[3]Ministry of Education Key Laboratory of Orogenic Belts and Crustal Evolution, School of Earth and Space Sciences, Peking University, China

Abstract. Despite ~30 carbonatite-related rare earth elements (REE) deposits, only a few contain established iron (Fe) resources, and Bayan Obo deposit, the world's largest REE deposit, is a premier example and provides an opportunity to investigate how Fe can be enriched within carbonatitic systems. The REE and Fe ores are mainly hosted in the 1320 Ma H8 unit at Bayan Obo, with most REE being sourced from the 430 Ma carbonatites. The age and genesis of Fe mineralization remain debated, hindering a coherent genetic understanding. Here we show that most magnetites have low Ti contents and Ni/Cr ratios with estimated crystallization temperatures of ~350–550 ℃, indicating a hydrothermal origin. Monazite intergrown with magnetite from the massive ores yields U-Th-Pb ages of ~430 Ma, being coeval with the REE-bearing Paleozoic carbonatite. We suggested that the progressively elevated concentration of F and increasing oxygen fugacity during brine/fluid evolution played a significant role in Fe and REE mineralization at Bayan Obo, highlighting the essential role of highly evolved carbonatitic systems in forming Fe-rich REE deposits.

1 Introduction

Carbonatites are typically enriched in light rare earth elements (LREE), while iron (Fe)-rich carbonatites are relatively rare (Chakhmouradian and Zaitsev, 2012). Among ~30 global carbonatite-related REE deposits, only a few, including Bayan Obo in China, Kovdor in Russia, and Phalaborwa in South Africa, report significant Fe resources. Understanding whether Fe was derived from the same carbonatitic system as REE, or from a different source is key to understanding mineralization processes within carbonatitic systems. Moreover, Fe-rich carbonatites often host abundant magnetite, enhancing geophysical signatures that can aid in exploration.

Bayan Obo is now the world's largest REE producer, with over 100 Mt of REO at 5.6% grade (Li et al. 2015). It was first discovered as a Fe-bearing deposit in 1927, with 2033 Mt of Fe ore at 32% grade, providing an opportunity to explore Fe mineralization within carbonatite systems. The premier role of Bayan Obo in the global REE market is partially reached by recovering REE and fluorine as byproducts during Fe mining.

The REE orebodies at Bayan Obo, predominantly hosted in the H8 unit (Fig. 1A), exhibit a close spatial relationship with Fe mineralization (Chao et al. 1997). The stratiform textures and the presence of detrital quartz and clastic rocks, are used to argue for a Mesoproterozoic sedimentary origin, later modified by hydrothermal activity (Chao et al. 1997). It is supported by banded Fe ores with near-zero $\delta^{18}O$ values and depleted trace elements (Wei and Shang-Guan, 1983). Conversely, a carbonatitic origin for the H8 unit has been proposed, supported by fenitization in surrounding rocks and geochemical similarities with nearby carbonatite dikes (Zhou et al. 1980). The cogenetic hematite and carbonate inclusions in dolomite phenocrysts is used to proposed liquid immiscibility between Fe-rich and carbonatitic melts at 1.3 Ga (Yang et al. 2019). Further support for a magmatic model includes near-zero $\delta^{56}Fe$ values in iron oxides (Sun et al. 2013). However, magnetites mainly distributed at shallow levels, associated with hydrothermal minerals argues against a dominant magmatic origin, favoring hydrothermal origin.

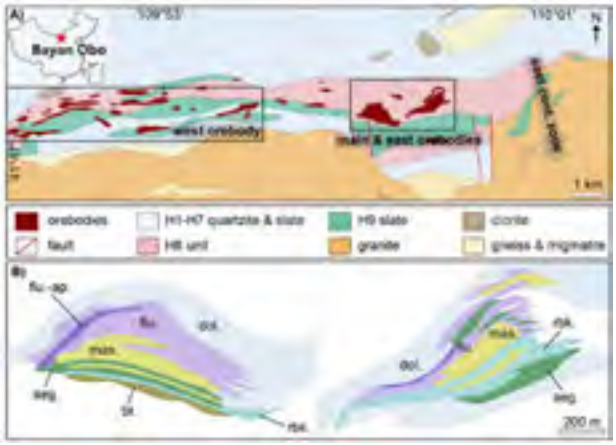


Figure 1. (A) Geological map of Bayan Obo deposit near the north border of China, showing the locations of west, main and east orebodies and the east contact (cont.) zone. (B) Geological map of typical mineralization zone of main and east orebodies. Revised from Chao et al. (1997).

Although most studies prefer a Mesoproterozoic model, the –1~4 ‰ $\delta^{26}Mg$ values for carbonatite dikes, and a dominancy of Th-Pb ages at 430 Ma, are used to argue that Paleozoic subduction dehydration-derived fluids leached Fe from the mantle wedge, with REE being sourced from mid-crustal hypothetical carbonatites (Ling et al. 2013). Field mapping reveals widespread Paleozoic carbonatites contributing >70% of REE at Bayan Obo (Li et al. 2025). Given the close spatial association between REE and Fe mineralization, it is reasonable to assume that Fe may also have a

genetic linkage with the Paleozoic carbonatites, which can be tested by constraining the age of Fe mineralization.

Magnetite, the dominant Fe oxide at Bayan Obo, accounts for over 90% of Fe output (Li et al. 2015). Its textural and chemical features can reveal ore-forming conditions, while cogenetic monazite enables age dating.

In this study, we combined petrographic and geochemical to characterize magnetite, and used U-Th-Pb geochronology of magnetite-associated monazite to constrain the age of Fe mineralization. Our results indicate magnetite formed from hydrothermal fluids (~350–550 °C) with a potential linkage to the 430 Ma REE-bearing carbonatites.

2 Alteration and Fe mineralization

Massive ores (mas.), primarily found in the central parts of the main and east orebodies (Fig. 1B), are the predominant Fe ores in the mining area. These ores are dark, dense, and magnetic, with Fe content >55 wt.%, and are composed mainly of magnetite, hematite, martite, fluorite, biotite, calcite, and monazite. Magnetite in massive ores forms coarse-grained (200 μm) aggregates, sometimes partially replaced by hematite along cleavage planes and microfractures (Fig. 2A).

Fluorite-type banded ores (flu.) occur mostly in the northern parts of the main and east orebodies (Fig. 1B), consisting of millimeter- to centimeter-thick bands of fine-grained minerals. Magnetite and hematite are the major Fe minerals, while bastnäsite is the primary REE mineral. Fluorite is the most abundant gangue mineral, with minor apatite, aegirine, barite, and calcite. Magnetite forms subhedral to anhedral granular aggregates, while hematite appears as granular aggregates or is intergrown with magnetite (Fig. 2B).

Aegirine-type ores (aeg.) are found in the southern parts of the main and east orebodies (Fig. 1B), which are dark green and have a disseminated or vein texture. Magnetite is the main Fe mineral, with monazite and bastnäsite as the main REE minerals. Aegirine is the most abundant gangue mineral, with apatite, fluorite, barite, and calcite present. Magnetite forms subhedral to anhedral granular aggregates (100–200 μm), often associated with ilmenite and monazite inclusions (Fig. 2C).

Dolomite-type ores (dol.), predominantly found in the outermost parts of the main and east orebodies and in the west orebody (Fig. 1B), are dark to grey with a disseminated texture. Magnetite and monazite are the main Fe and REE minerals, respectively, with dolomite as the most abundant gangue mineral. Magnetite forms anhedral granular aggregates (50–200 μm) along coarse-grained carbonate boundaries (Fig. 2D).

Biotite-type ores (bt.) are common in the west orebody (Fig. 1B), with a lamellar structure and a mineral assemblage similar to dolomite- and riebeckite-type ores. Magnetite and monazite are the main Fe and REE minerals, with biotite as the primary gangue. Magnetite forms euhedral to anhedral granular crystals (50–400 μm), often in sheeted aggregates with biotite, and contains inclusions of calcite, biotite, bastnäsite, and pyrochlore (Fig. 2D).

Riebeckite-type ores (rbk.) are found in the south of the main and east orebodies and extensively in the west, often adjacent to biotite-type ores (Fig. 1B). They are characterized by dark blue, disseminated textures, and contain magnetite, monazite, and bastnäsite. Riebeckite is the main gangue, with minor dolomite, biotite, fluorite, and pyrite. Magnetite is euhedral to subhedral granular (> 200 μm), often associated with riebeckite, and contains ilmenite prisms (Fig. 2E).

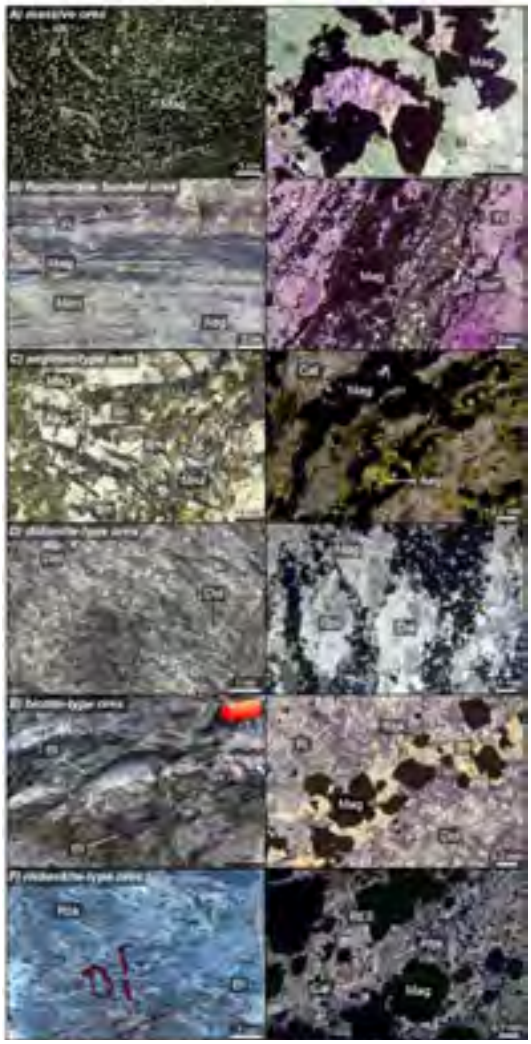


Figure 2. Representative field photography and photomicrograph of main type of ores.

3 Samples and Methods

Fifteen representative samples from six types including Fe ores and breccia and carbonatite dikes from Bayan Obo were selected for this study. We made detailed petrographic observations prior to further analysis. To obtain a representative dataset of Fe mineralization at Bayan Obo, we also sampled

a concentrated Fe ore from large-scale mining (produced in 2020).

We analysed the major elements of magnetite using a JEOL JXA-iHP200F instrument equipped with five wavelength-dispersive spectrometers. Next, the trace element compositions of magnetite were determined using an Agilent 7900 inductively coupled plasma mass spectrometer coupled to a 193-nm ArF excimer laser-ablation system. In addition, we measured the age of monazite intergrown with magnetite with a CAMECA IMS 1280HR secondary ion mass spectrometry.

4 Results and Discussion

Iron mineralization at Bayan Obo exhibits a circular zoning pattern, with massive ores centralized and lower-grade banded and disseminated ores distributed peripherally (Fig. 1B). This zoning, along with the common intergrowth of magnetite with hydrothermal minerals such as fluorite, barite, and apatite (Fig. 2), supports a hydrothermal origin.

The incompatible elements such as Ti and HFSEs are preferentially partitioned into magnetite at high temperatures (Nadoll et al. 2014), and are a useful indicator to differentiate magmatic magnetites from hydrothermal ones. Magmatic magnetites from Fe-Ti-V and Oka carbonatite deposits show high Ti contents (up to 10000 ppm). Similarly, magnetites from Bayan Obo carbonatite dikes are euhedral, Ti-rich (>1000 ppm), and exhibit low Ni/Cr ratios—consistent with a magmatic origin (Chen et al. 2019).

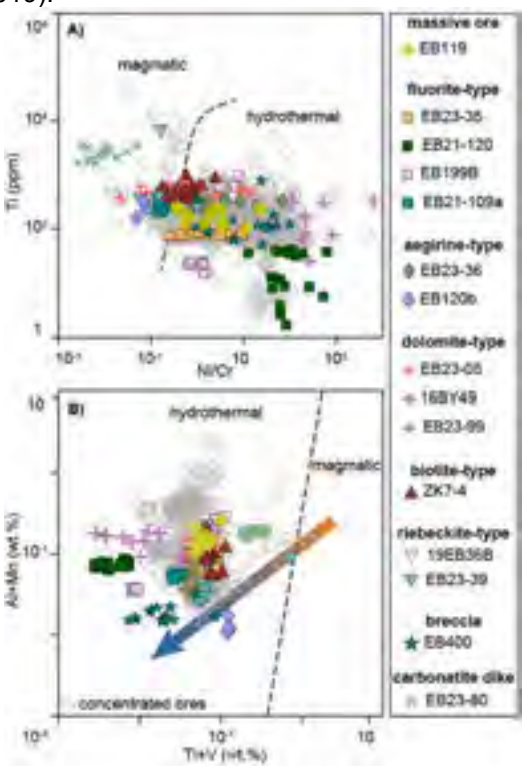


Figure 3. Composition of (A) Ti vs. Nr/Cr and (B) [Ti+V] vs. [Al+Mn] in magnetite at Bayan Obo. Modified after Nadoll et al. (2014).

In contrast, the majority of Bayan Obo magnetites are Ti-poor (<500 ppm) with high Ni/Cr ratios, indicating hydrothermal formation (Fig. 3). We estimated the crystallization temperatures for magnetites range from 350–550 °C (Fig. 4) using the Mg-in magnetite geothermometer, and coexisting magnetite-ilmenite pairs yield 380–540 °C. These are also consistent with temperatures from fluid inclusions (420–480 °C) and carbonate geothermometry (431–485 °C). These are significantly lower than magmatic crystallization temperatures (~800 °C), confirming a hydrothermal origin for most Fe mineralization at Bayan Obo.

There is a decreasing trend in temperature from 560–550 °C of dolomite- and biotite-type ores, to ~500 °C of riebeckite-type ores, and finally to 400–380 °C of aegirine-type, fluorite-type banded and massive ores (Fig. 4). This decreasing trend is broadly consistent with alkaline alteration assemblage (biotite, riebeckite, and aegirine) occurring near calcite and dolomite, and these early phases commonly replaced by hydrothermal minerals such as fluorite and apatite (Fig. 2).

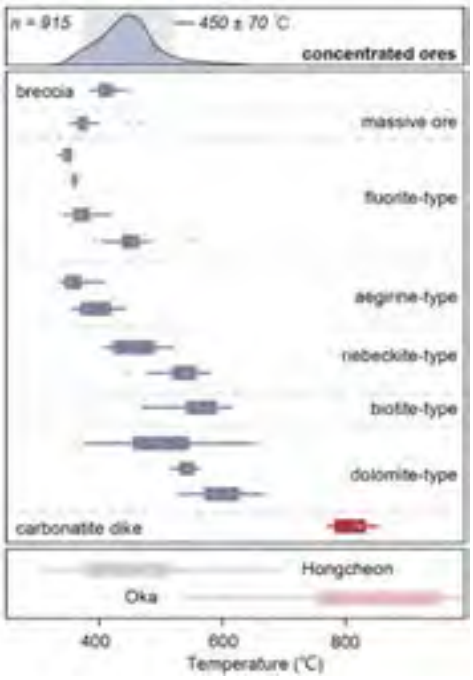


Figure 4. Calculated temperature for magnetite from Bayan Obo using the $T_{Mg\text{-}Mag}$ (Canil and Lacourse 2020). Magnetite data from Oka and Hongcheon carbonatites are taken from Chen et al. (2019).

Determining the age of Fe mineralization is a prerequisite for understanding the genesis of Bayan Obo, but directly dating magnetite using the U-Pb chronometer is difficult due to low U contents in these samples. Abundant anhedral monazites occur as inclusions within and/or closely associate with magnetites in massive ore, suggesting their simultaneous crystallization with magnetite, and providing an opportunity to constrain the timing of Fe mineralization. While the low U and high common-lead nature of monazites prohibit precise

dating, they faithfully demonstrate that monazite, and by inference Fe mineralization occurred at ~430 Ma (Fig. 5). Our monazite U-Th-Pb dates (~430 Ma) are consistent with monazite isochron Th-Pb age (421 ± 3.3 Ma, Wang et al. 1994) and carbonatite zircon U-Pb ages (~430 Ma, Li et al. 2025), suggesting a potential genetic linkage between Fe mineralization and the 430 Ma REE-bearing carbonatite.

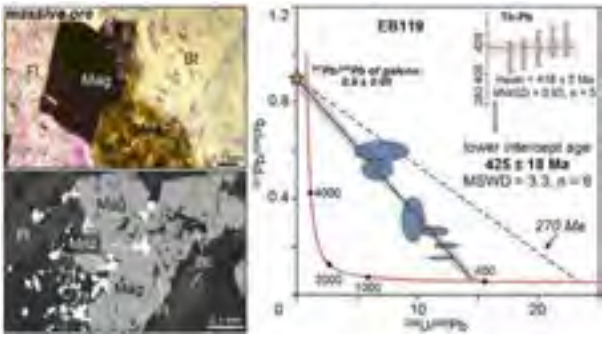


Figure 5. Dated monazite intergrown with magnetite and corresponding Tere-Wasserburg U-Pb plot with weighted average $^{208}Pb/^{232}Th$ age from massive ore.

Previous studies proposed that the ore-forming fluids were derived from Paleozoic subduction plate, with Fe being leached from the mantle wedge (Ling et al. 2013). Based on the widespread distribution of Paleozoic carbonatite dikes at Bayan Obo (Fig. 1), and the close association between magnetite and typical carbonatite-derived hydrothermal minerals such as fluorite and aegirine, we suggest that fluids for Fe mineralization originated from Paleozoic carbonatites.

5 Conclusions and Implications

Carbonatitic magmas typically evolve from calcic to magnesian and ferroan compositions, with iron becoming enriched in residual melts. During crystallization of calcite and dolomite, incompatible elements such as HFSEs and REEs are partitioned into evolved melts and/or fluids (Anenburg et al. 2021). At Bayan Obo, magnetite, monazite, and bastnäsite commonly occur with late-stage minerals like fluorite, supporting transport by brine/ fluids. These brine/fluids rich in CO_3^{2-}, SO_4^{2-}, and Na^+, efficiently mobilize REEs at 300–500 °C (Yuan et al. 2024), as evidenced by abundant calcite and barite. Fluorine likely acts as a precipitation agent rather than a transporter under low-pH conditions (Xing et al. 2019). Additionally, the cogenetic magnetite and hematite from the main stage fluorite-type banded ores (Chao et al. 1997) indicate a more oxidized condition.

In conclusion, Fe mineralization at Bayan Obo is dominated by a ~350 – 550 °C hydrothermal process associated with ~430 Ma REE-bearing carbonatite. Our study highlights that the crystallization of Fe- and REE-rich minerals was also driven by fluid evolution within a carbonatitic system under high oxygen fugacity conditions.

Acknowledgements

This work was supported by the National Natural Science Foundation of China grants 42325303 and 92262303.

References

Anenburg M, Mavrogenes JA, Frigo C, Wall F (2020) Rare earth element mobility in and around carbonatites controlled by sodium, potassium, and silica. Sci Adv 6:eabb6570

Canil D, Lacourse T (2020) Geothermometry using minor and trace elements in igneous and hydrothermal magnetite. Chem Geol 541:119576

Chakhmouradian AR, Zaitsev AN (2012) Rare Earth Mineralization in Igneous Rocks: Sources and Processes. Elements 8:347-353

Chao ECT, Black JM, Minkin JA, Tatsumoto M, Wang JW, Conrad JE, McKee EH, Hou ZL, Meng QR (1997) The sedimentary Carbonate-Hosted Giant Bayan Obo REE-Fe-Nb Ore Deposit of Inner Mongolia, China: A Cornerstone Example for Giant Polymetallic Ore Deposits of Hydrothermal Origin. U.S. Geological Survey Bulletin

Chen W, Ying YC, Bai T, Zhang JJ, Jiang SY, Zhao KD, Shin D, Kynicky J (2019) In situ major and trace element analysis of magnetite from carbonatite-related complexes: Implications for petrogenesis and ore genesis. Ore Geol Rev 107:30-40

Li CL, Li XG, Xu GY (2015) Technology Development and Industrialization of Resources Comprehensive Utilization of Intergrowth and Associated Ore in Baiyun Obo. Chinese Rare Earths 36:151-158

Li Y, Wu LG, Yu Y, Yang L, Selby D, Li, XH (2025) Paleozoic carbonatite controlled rare-earth-elements mineralization at Bayan Obo. Sci Adv 11: ads9481

Ling M-X, Liu Y-L, Williams IS, Teng F-Z, Yang X-Y, Ding X, Wei G-J, Xie L-H, Deng W-F, Sun W-D (2013) Formation of the world's largest REE deposit through protracted fluxing of carbonatite by subduction-derived fluids. Sci Rep 3: 1776

Nadoll P, Angerer T, Mauk JL, French D, Walshe J (2014) The chemistry of hydrothermal magnetite: A review. Ore Geol Rev 61:1-32

Sun J, Zhu XK, Chen YL, Fang N (2013) Iron isotopic constraints on the genesis of Bayan Obo ore deposit, Inner Mongolia, China. Precambrian Res 235:88-106

Wang JW, Tatsumoto M, Li XB, Premo WR, Chao ECT (1994) A precise 232Th-208Pb chronology of fine-grained monazite: Age of the Bayn Obo REE-Fe-Nb ore deposit, China. Geochim Cosmochim Acta 58:3155-3169

Wei JY, Shang-Guan ZG (1983) Oxygen isotope composition of magnetite and hematite in Baiyun ebo iron deposit, inner mongolia. Chinese Journal of Geology 18:217-224

Xing Y, Etschmann B, Liu W, Mei Y, Shvarov Y, Testemale D, Tomkins A, Brugger J (2019) The role of fluorine in hydrothermal mobilization and transportation of Fe, U and REE and the formation of IOCG deposits. Chem Geol 504:158-176

Yang KF, Fan HR, Pirajno F, Li XC (2019) The Bayan Obo (China) giant REE accumulation conundrum elucidated by intense magmatic differentiation of carbonatite. Geology 47:1198-1202

Yuan X, Yang Z, Mayanovic RA, Hou Z (2024) Experimental evidence reveals the mobilization and mineralization processes of rare earth elements in carbonatites. Sci Adv 10:eadm9118

Zhou ZL, Li GY, Song TY, Liu YG (1980) Geological characteristics of dolomite carbonatite and discussion on its genesis, Bayan Obo Inner Mongolia. Geol Rev 26:35-44

Hydrothermal Metasomatism Controlled REE Mineralization at Bayan Obo Revealed by Zircon Petrochronology

Yan Yu[1], Yang Li[2]*, Lan Yang[1], Li-Guang Wu[3], Xian-Hua Li[1] *

[1]State Key Laboratory of Lithospheric and Environmental Coevolution, Institute of Geology and Geophysics, Chinese Academy of Sciences, Beijing 100029, China
[2]Ministry of Education Key Laboratory of Orogenic Belts and Crustal Evolution, School of Earth and Space Sciences, Peking University, Beijing 100871, China
[3]State Key Laboratory of Geological Processes and Mineral Resources, China University of Geosciences (Beijing), Beijing 100083, China

Abstract. Genesis of the Bayan Obo REE deposit remains debated after a century of exploration and study, mainly due to an apparent conflict between Mesoproterozoic carbonatites dated at 1320 Ma and a dominant Paleozoic REE mineralization age peaking at 430 Ma. Here we apply zircon petrochronology to resolve this paradox under the robust geological framework. Zircons from Mesoproterozoic carbonatites (1320 Ma) are characterized by weakly zoned texture and sub-mantle like $\delta^{18}O$ (4.9 ± 0.4‰, 2SD), while zircons from a coeval carbonatite dike were intensively altered with chaotic texture and elevated $\delta^{18}O$ of 6.9 ± 1.2‰ (2SD). Zircon from Paleozoic carbonatites exhibit extreme $\delta^{18}O$ variability ranging from 5‰ to 11‰. Such isotopic spread is best explained by zircon crystalized from mantle derived, highly fractionated carbonatitic melts/brines, as further supported by the coeval increase in HfO_2 contents (2–5 wt.%) and $\delta^{18}O$ values when host rocks composition changes from Ca-rich to Mg-rich. Notably, some Paleozoic zircons exhibit rims containing dense inclusions of riebeckite and monazite, indicating the presences of alkali- and REE-rich brines/fluids, which were derived from Paleozoic carbonatites after extensive fractionation, and played a critical role in REE mineralization at Bayan Obo.

1 Introduction

Carbonatites and their associated alkaline systems host ~80% of global REE resources (Weng et al. 2015). Despite carbonatites are rare with only 676 known occurrences globally, about 9% of them contain REE resource (Li et al. 2025), and all major REE deposits are linked to carbonatites. Additionally, growing petrological and experimental evidence demonstrates that alkaline fluids derived from carbonatitic systems are crucial for the enrichment and mobilization of REE (Anenburg et al. 2020).

The REE mineralization at Bayan Obo is hosted by the H8 unit, which is a ~1320 Ma carbonatite (Le Bas et al. 1992; Smith et al. 2015). However, monazite and bastnäsite, the primary REE minerals, show a spread in Th-Pb dates from 1.4 Ga to 0.27 Ga peaking at ~430Ma (Wang et al. 1994; Ling et al. 2013; Li et al. 2021). This contradiction has been explained by: (1) REE ores were primarily sourced from the Mesoproterozoic carbonatite (Zhu et al. 2015; Yang et al. 2019), but was reworked by metamorphic fluids (Song et al. 2018; Li et al. 2021), or Paleozoic subduction derived fluids (Liu et al. 2018); or (2) REE ores were formed around ~430 Ma through hydrothermal processes by subduction derived, REE-rich fluids (Wang et al. 1994; Chao et al. 1992). However, both models contradict the widely accepted view that only carbonatitic alkali-rich fluids can effectively remobilize and transport REE (Yuan et al. 2024; Anenburg et al. 2020). This raises two fundamental questions: (a) Could there be a previously unrecognized ~0.43 Ga carbonatite magmatism which provided both REE and requisite alkaline fluids? (b) If not, does this challenge the general understanding that alkaline fluids are essential for REE mineralization?

The recent identification of ~0.43 Ga carbonatites (Li et al. 2025) provide a solution for the paradox at Bayan Obo if this Paleozoic carbonatite can provide abundant REE-bearing alkaline fluids. Globally, carbonatites are known to evolve from Ca- to Mg- and ultimately Fe-rich compositions (Anenburg et al. 2020; Buckley and Woolley 1990), with incompatible elements such as REE, Hf, and Zr progressively enriched in the residual melt and then bines/fluids.

Carbonatite evolution from calcite to dolomite to siderite-rich is accompanied by progressively depletion in the $\delta^{18}O$ of residual melt. When non-carbonate minerals such as magnetite, apatite, and biotite are crystallized, which prefer light oxygen isotopes, $\delta^{18}O$ of the residual melt will markedly increase. This unique signature can be recorded by zircons, which crystalized after advanced fractional crystallization given the low zirconium and silicon concentrations in carbonatite magma.

Using carbonatite zircon trace element compositions and $\delta^{18}O$, we propose that alkali- and REE-rich brines/fluids derived from Paleozoic carbonatites are critical for REE mineralization at Bayan Obo.

2 Samples and Methods

Representative rock samples were collected from carbonatite outcrops both inside and outside the mining area (Fig. 1). Zircons from six dated carbonatites dikes/cliffs (Li et al. 2025) were further analysed for Laser Raman spectroscopic analysis, major element analysis via electron probe

microanalyzer (EPMA), and SIMS oxygen isotope analysis.

Sample EB130 was from the H8 unit Ca-rich carbonatite outcrop on the East open pit, with zircons constraining a concordia U-Pb age of 1321 ± 9 Ma (2SD, n=23). Sample EB170 was collected from the Ca-rich carbonatite dike (Wu dike) located on the East contact zone, with zircons defines a U-Pb age of 1293 ± 26 Ma (2SD, n=9).

Sample EB21-06 and EB21-36 were collected from a Mg-rich carbonatite dike in the west open pit. Zircon from both samples yield a concordia U-Pb age of 430 ± 4 Ma (2SD, n=15). Sample EB21-14 was collected from a Ca-rich carbonatite cliff in the west open pit, and zircons from this sample yielded a concordia U-Pb age of 436 ± 5 Ma (2SD, n=13). Sample EB 103B was acquired from a V shape Mg-rich carbonatite dike in the Main open pit. Zircons from this sample defined a concordia U-Pb age of 431 ± 3 Ma (2SD, n=34).



Figure 1. Geological map of the Bayan Obo deposit. The sample locations are marked by stars**.**

3 Results and Discussion

3.1 Zircon $\delta^{18}O$ records magma fractionation

Zircons from 6 carbonatite samples were classified as 5 types according to their age, morphology, and inclusion hosted (Fig. 2). Type 1a, 1b, 2, 3, 4 zircons are of carbonatitic origin, as indicated by their association with carbonatite host rocks and their tetragonal bipyramidal morphology lacking prismatic faces (Fig. 2), typical for zircon found in carbonatite melts (Corfu et al. 2003; Chakhmouradian and Williams 2004).

Mesoproterozoic Zircons from the East open pit (Type 1a) preserve primary magmatic features such as euhedral bipyramidal morphology, faint oscillatory zoning, and non-metamict Raman spectra. Their δ18O values (4.9 ± 0.4‰, Fig. 3) are slightly lither than the mantle value (5.3 ± 0.3‰, 2SD, Valley et al. 1998). The gentle decrease in δ18O can arise from fractional crystallization of high-δ18O minerals, assimilation of low-δ18O materials or high-T alteration with water. In carbonatites, zircon crystallization commonly occurs late due to low Zr and Si concentration. For carbonatites evolve from Ca-, through Mg-, to Fe-rich melts, δ18O of melts progressively decrease (Fig. 4a). Zircons crystalized after 95% dolomite can reduce crystallization at 600℃ have a δ18O of 4.9‰ (Fig. 4b), suggesting that melt evolution alone can account for the sub-mantle δ18O signatures, without invoking external factors.

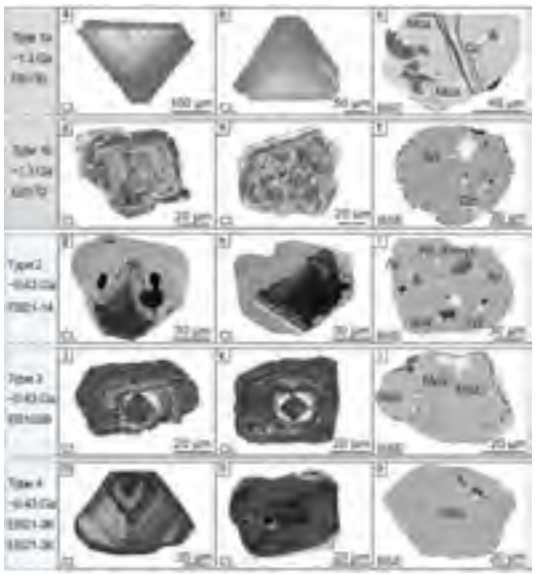


Figure 2. Morphology, textures, and mineral inclusions of zircons. (a–c) Type 1a zircons (EB130): Mica and quartz occur as veins and irregular grains. (d–h) Type 1b zircons (EB170): Anhedral inclusions of quartz, columbite and barite. (g–i) Type 2 zircons (EB21-14): Apatite, ankerite, quartz and euhedral apatite and xenotime-Y inclusions in the rim. (j–l) Type 3 zircons (EB103B): Fine grain euhedral riebeckite and anhedral monazite and mica inclusions. (m–o) Type 4 zircons (EB21-06 & 36): Dolomite and riebeckite inclusion. Qz-Quartz, Mca-Mica, Brt-Barite, Ap-Apatite, Ank-Ankerite, Xtm-Y: Xenotime-Y, Zrn-Zircon, Rbk-Riebeckite, Mnz-Monazite.

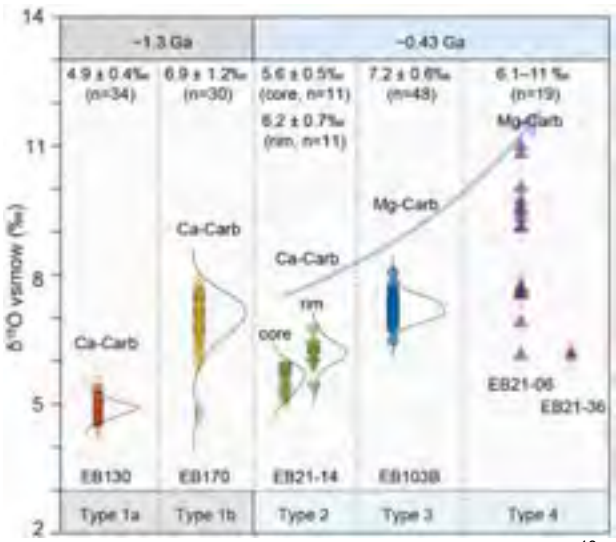


Figure 3. Zircon oxygen isotope composition. The $\delta^{18}O$ values are given as ± 2SD. “Ca-Carb” and “Mg-Carb” denote zircons hosted in Ca-rich and Mg-rich carbonatite, respectively.

Type 1b zircons from the Wu dike show patchy zoning, secondary quartz-barite inclusions, indicating hydrothermal overprinting (Figs. 2d–f). Their U-Pb discordance (Li et al. 2025) and associated monazite Paleozoic Th-Pb ages (0.4–0.5 Ga, Zi Jianwei 2024) suggest alteration by Paleozoic carbonatites. Their elevated $\delta^{18}O$ values (6.9 ± 1.2‰, Fig. 3) likely reflect metasomatism by Si-Sr-rich

fluids, as evidenced by barite and quartz inclusions (Fig. 2f).

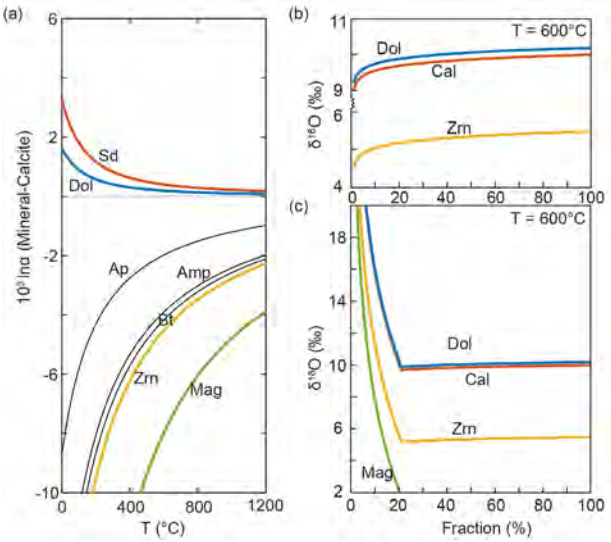


Figure 4. Oxygen isotope fractionation in carbonatites. (a) Mineral oxygen isotope fractionation in carbonatites, fractionation factors are from Zheng (1999). (b, c) Modelled mineral $\delta^{18}O$ as a function of fractionation. Magnetite crystallization after 80% crystallization of calcite/dolomite leads to significant increase in melt $\delta^{18}O$.

Paleozoic zircons (Type 2–4) exhibit magmatic features include oscillatory or sector zoning with subrounded apatite-ankerite inclusions (Figs. 2g–o). The spongy-textured rims (Figs. 2j and k) with riebeckite-monazite and dolomite-riebeckite inclusions (Figs. 2l and o) indicate their crystallization from an evolved brine-melt. Such features align with the cauliflower-like zircon rims hosting REE and alkaline mineral inclusions from Campbell et al (2014), collectively reflecting alkali- and REE-rich brine-melt composition during the final stages of carbonatite evolution at 430 Ma.

Zircon core and rim from the Ca-rich carbonatite cliff (Type 2) yield $\delta^{18}O$ of 5.6 ± 0.5‰ and 6.2 ± 0.7‰ (Fig. 3). Zircons from Mg-rich dikes (Type 3 and 4) show significantly elevated $\delta^{18}O$ (6–11‰, Fig. 3). While assimilation and fluids alteration cannot be ruled out, advanced melt differentiation is the most likely cause. As discussed above, crystallization of Fe-Mg silicates, apatite and magnetite preferentially removes light oxygen isotopes (Fig. 4a), enriching residue melts in ^{18}O. Magnetite, in particular, has a high $\Delta^{18}O_{calcite\text{-}magnetite}$ (6–11‰ at 800–400℃, Fig. 4a). With the melt evolves, increasing Fe enrichment allows magnetite to saturate easily, particularly in the late stages of melt evolution. Modeling results (Fig. 4c) show that the crystallization of just 50% of magnetite from the remaining 20% melt could drive zircon $\delta^{18}O$ values increase dramatically from 5.6‰ to 11.3‰.

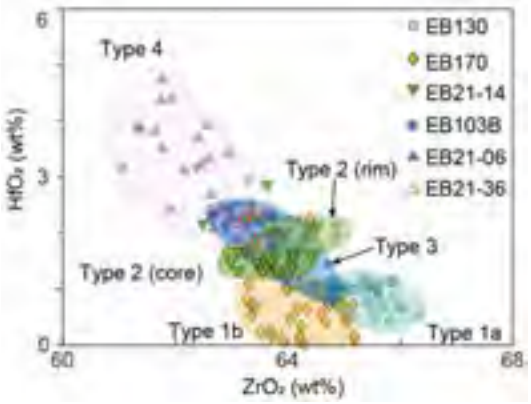


Figure 5. Zircon HfO_2 Vs. ZrO_2 binary plot.

The HfO_2 content in zircons increases (Fig. 5) from Type 2 cores (1.6 wt.%) to rims (2.1 wt.%), and further in Type 3 (2.5 wt.%) and Type 4 (2–5wt.%). This is accompanied by their host carbonatites' evolution from Ca-rich to Mg-rich compositions (Fig. 3), and an increase in their zircon $\delta^{18}O$ from 6.2 ± 0.7‰, 7.2 ± 0.6‰ and to 6–11‰. These features collectively point to zircon crystallization from highly evolved melt which extensive fractionation of low-$\delta^{18}O$ minerals such as magnetite.

3.2 Evidence of hydrothermal brines/fluids related to 430 Ma carbonatite

Paleozoic hydrothermal overprinting in the Bayan Obo deposit is well documented, notably though REE-rich veins cutting banded/massive ores. These veins contain mineral assemblages like aegirine-apatite, aegirine-calcite, and alkali amphibole-fluorite-apatite, which typical in massive and banded ores (Hu et al. 2009). Fluid inclusion studies reveal hypersaline brines rich in REE, with bastnäsite and cebaite as daughter minerals (Fan et al. 2006). Altogether, the mineralogical and fluid inclusion evidence indicate alkaline, REE-rich fluids derived from the Paleozioc carbonatites.

The abundant Paleozoic carbonatite outcrops both as dikes and pit walls at Bayan Obo, have induced strong alkali metasomatism, forming assemblages like riebeckite, albite, phlogopite, and barite with REE mineralization. Zircon from these dikes, especially Type 3 from the Main open pit, bearing magmatic ores and rims bearing sponge-texture with alkaline and REE inclusions (riebeckite & monazite, Figs. 2j–l), marking a transition from magmatic to brine-dominated stages. Dense monazite aggregates in alteration zones and REE rich inclusions in Type 3 zircon rims (Fig. 2l) suggest REE precipitation followed alkali metasomatism. This aligns with models where K-Na carbonatitic fluids react with silicate country rocks, destabilizing REE complexes and triggering precipitation (Anenburg et al. 2020).

In summary, our zircon petrochronology offer direct evidence for ~430 Ma carbonatitic magmatism, which are associated with alkali-and REE-rich brins/fluids, being critical for REE mineralization at

Bayan Obo. The contrasting REE contribution from the ~1.3 Ga and ~430 Ma carbonatitic magmatism—where the younger accounts for >70% of total REE resources (Li et al. 2025)—can be attributed to differences in magmatic differentiation. The younger carbonatites underwent extensive differentiation, leading to an enrichment of REE and potentially Fe in late-stage brine-melt/fluids. In contrast, the older carbonatites experienced limited fractionation, hence REE enrichment and mineralization are prohibited. This highlights the importance of highly evolved carbonatitic systems in forming giant REE deposit like Bayan Obo.

Acknowledgements

We appreciate the assistance of Prof. Deng-Feng Li and Dr. Qiao-Fen Liu with CL and BSE imaging at Sun Yat-sen University. We are grateful to Shen He and Ze-Long Shi for their help with zircon analysis. This study is supported by National Natural Science Foundation of China (42325303 and 92262303), Baotou Iron and Steel (Group) LTD (GZ-2023-1LH-001/002), and the Institute of Geology and Geophysics, Chinese Academy of Sciences (IGGCAS-201901).

References

Anenburg M, Mavrogenes JA, Frigo C, Wall F (2020) Rare earth element mobility in and around carbonatites controlled by sodium, potassium, and silica. Science Advances 6:eabb6570. doi: doi:10.1126/sciadv.abb6570.

Buckley HA, Woolley AR (1990) Carbonates of the magnesite–siderite series from four carbonatite complexes. Mineralogical Magazine 54:413-418. doi: 10.1180/minmag.1990.054.376.06.

Campbell LS, Compston W, Sircombe KN, Wilkinson CC (2014) Zircon from the East Orebody of the Bayan Obo Fe–Nb–REE deposit, China, and SHRIMP ages for carbonatite-related magmatism and REE mineralization events. Contributions to Mineralogy and Petrology 168. doi: 10.1007/s00410-014-1041-3.

Chakhmouradian AR, Williams CT (2004) Mineralogy of high-field-strength elements (Ti, Nb, Zr, Ta, Hf) in phoscoritic and carbonatitic rocks of the Kola Peninsula, Russia In: Wall F, Zaitsev AN (eds) Phoscorites and carbonatites from mantle to mine: the key example of the Kola alkaline province. Mineralogical Society of Great Britain and Ireland.

Chao ECT, Back JM, Minkin JA, Chen RY (1992) Host-rock controlled epigenetic, hydrothermal metasomatic origin of the Bayan Obo REE-Fe-Nb ore deposit, Inner Mongolia, P.R.C. . Applied Geochemistry 7:443–458. doi: 10.1016/0883-2927(92)90005-n

Corfu F, Hanchar JM, Hoskin PWO, Kinny P (2003) Atlas of Zircon Textures. Reviews in Mineralogy and Geochemistry 53:469-500. doi: 10.2113/0530469.

Fan HR, Hu FF, Yang F, Wang KY (2006) Fluid unmixing/immiscibility as an ore-forming process in the giant REE–Nb–Fe deposit, Inner Mongolian, China: Evidence from fluid inclusions. Journal of Geochemical Exploration 89:104-107. doi: 10.1016/j.gexplo.2005.11.039.

Hu FF, Fan HR, Liu S, Yang KF, Chen FK (2009) Samarium-Neodymium and Rubidium-Strontium Isotopic Dating of Veined REE Mineralization for the Bayan Obo REE-Nb-Fe Deposit, Northern China. Resource Geology 59:407-414. doi: 10.1111/j.1751-3928.2009.00107.x.

Le Bas MJ, Keller J, Kejie T, Wall F, William CT, Peishan Z (1992) Carbonatite dykes at bayan Obo, inner Mongolia, China. Mineralogy and Petrology 46:195-228. doi: 10.1007/bf01164647.

Li XC, Yang KF, Spandler C, Fan HR, Zhou MF, Hao JL, Yang YH (2021) The effect of fluid-aided modification on the Sm-Nd and Th-Pb geochronology of monazite and bastnäsite: Implication for resolving complex isotopic age data in REE ore systems. Geochimica et Cosmochimica Acta 300:1-24. doi: 10.1016/j.gca.2021.02.028.

Li Y, Wu L-G, Yu Y, Yang L, Selby D, Li X-H (2025) Paleozoic carbonatites controled rare-earth-elements mineralization at Bayan Obo. Science Advances 11:1-14. doi: 10.1126/sciadv. Ads9481.

Ling MX, Liu YL, Williams IS, Teng FZ, Yang XY, Ding X, Wei GJ, Xie LH, Deng WF, Sun WD (2013) Formation of the world's largest REE deposit through protracted fluxing of carbonatite by subduction-derived fluids. Scientific Reports 3. doi: 10.1038/srep01776.

Liu S, Fan H-R, Yang K-F, Hu F-F, Wang K-Y, Chen F-K, Yang Y-H, Yang Z-F, Wang Q-W (2018) Mesoproterozoic and Paleozoic hydrothermal metasomatism in the giant Bayan Obo REE-Nb-Fe deposit: Constrains from trace elements and Sr-Nd isotope of fluorite and preliminary thermodynamic calculation. Precambrian Research 311:228-246. doi: 10.1016/j.precamres.2018.04.021.

Smith MP, Campbell LS, Kynicky J (2015) A review of the genesis of the world class Bayan Obo Fe–REE–Nb deposits, Inner Mongolia, China: Multistage processes and outstanding questions. Ore Geology Reviews 64:459-476. doi: 10.1016/j.oregeorev.2014.03.007.

Song WL, Xu C, Smith MP, Chakhmouradian AR, Brenna M, Kynický J, Chen W, Yang Y, Deng M, Tang H (2018) Genesis of the world's largest rare earth element deposit, Bayan Obo, China: Protracted mineralization evolution over ~1 b.y. Geology 46:323-326. doi: 10.1130/g39801.1.

Valley JW, Kinny PD, Schulze DJ, Spicuzza MJ (1998) Zircon megacrysts from kimberlite: oxygen isotope variability among mantle melts. Contributions to Mineralogy and Petrology 133:1-11. doi: 10.1007/s004100050432.

Wang JW, Tatsumoto M, Li XB, Premo W, Chao ECT (1994) A precise 232Th-208Pb chronology of fine-grained monazite: Age of the Bayan Obo REE-Fe-Nb ore deposit, China. Geochimica et Cosmochimica Acta 58:3155-3169.

Weng Z, Jowitt SM, Mudd GM, Haque N (2015) A Detailed Assessment of Global Rare Earth Element Resources: Opportunities and Challenges*. Economic Geology 110:1925-1952. doi: 10.2113/econgeo.110.8.1925.

Yang K, Fan H, Pirajno F, Li X (2019) The Bayan Obo (China) giant REE accumulation conundrum elucidated by intense magmatic differentiation of carbonatite. Geology 47:1198-1202. doi: 10.1130/g46674.1.

Yuan X, Yang Z, Mayanovic RA, Hou Z (2024) Experimental evidence reveals the mobilization and mineralization processes of rare earth elements in carbonatites. Science Advances 10:eadm9118. doi: doi:10.1126/sciadv.adm9118.

Zheng YF (1999) Oxygen isotope fractionation in carbonate and sulfate minerals. Geochemical Journal 33:109-126.

Zhu XK, Sun J, Pan CX (2015) Sm-Nd isotopic constraints on rare-earth mineralization in the Bayan Obo ore deposit, Inner Mongolia, China. Ore Geology Reviews 64:543-553. doi: 10.1016/j.oregeorev.2014.05.015.

Zi Jianwei LL, Li Yike, Rasmussen Birger, Ke Changhui (2024) Magmatic-Hydrothermal History of Bayan Obo REE-Rich Carbonatites Revealed by Monazite Th-Pb Geochronology of the Wu Dyke Earth Science 49. doi: 10.3799/dqkx.2023.027.

Multi-scale hydrothermal mobilization of Ca, Al and Cu during serpentinization: new insights from the Ronda Massif (Spain)

Bastien Audran[1,4], Marc Ulrich[2], Yannick Branquet[1], Guillaume Barré[3], Georges Beaudoin[3], Philippe Boulvais[1]
[1] Géosciences Rennes, UMR 6118, Université de Rennes, France
[2] ITES-EOST, UMR 7063 University of Strasbourg, France
[3] Département de géologie et de génie géologique, Centre de recherche sur la géologie et le génie des ressources minérales (E4m), Université Laval, Canada
[4] GeoRessources, UMR 7359, Faculté des Sciences et Technologies, Université de Lorraine, France

Abstract. Serpentinization of mantle rocks is a key vector for chemical exchange between reservoirs involved at mid-ocean ridges and subduction zones. Metal mobilization during serpentinization could also play an important role in ore deposit formation. This study was conducted in the Ronda Massif to elucidate the elemental mobility during serpentinization. The study found that the trace element composition of serpentines, such as Al, Ti, V, Cr, Ni and Co, is controlled by the primary mineral composition (i.e., olivine and pyroxenes). Conversely, bastites exhibit a systematic depletion in Al and Ca when compared to preserved primary pyroxene, suggesting an associated liberation of these elements. Furthermore, the copper concentration in serpentines is significantly higher than in primary minerals, indicating that Cu is being mobilized at least at the mineral scale. Loss on ignition (LOI) serves as a proxy for serpentinization intensity in whole rock analyses, a crucial aspect in understanding mobility during the evolution of serpentinization. Consequently, a comparison of LOI with CaO, Al_2O_3, and Cu documents their progressive losses as the serpentinization rate increases. It has been proposed that serpentinization may facilitate the leaching of copper, thereby establishing a potential source within the ultramafic-hosted seafloor massive sulfide metallogenic systems.

1 Introduction

Serpentinization is defined as a hydrothermal process involving the hydration of ultramafic rocks that are exhumed in a variety of geological contexts. While earlier studies have suggested an isochemical nature of this transformation, recent research has challenged this hypothesis, particularly with respect to Ca, "fluid mobile elements" and even Al (Jöns et al. 2010; Deschamps et al. 2013). Numerous studies have identified serpentinization as a vector for chemical exchange between oceans and the mantle (Deschamps et al. 2013). However, there is a paucity of research focusing on metal mobility during serpentinization (Debret et al. 2024). Substantial metal mobilization has been observed through hydrothermal processes leading to the formation of ultramafic-hosted seafloor massive sulfide (UM-SMS) deposits analogous to black smokers found along mid-oceanic ridges (Patten et al. 2022). The most common fluid-rock interaction in such deposits is serpentinization, which may be responsible for the mobility of Cu and other elements (Debret et al. 2024). The objective of this study is to ascertain the mobility of Ca, Al, and Cu. It is noteworthy that these elements, in principle, are predicted to demonstrate divergent behaviour during metasomatism.

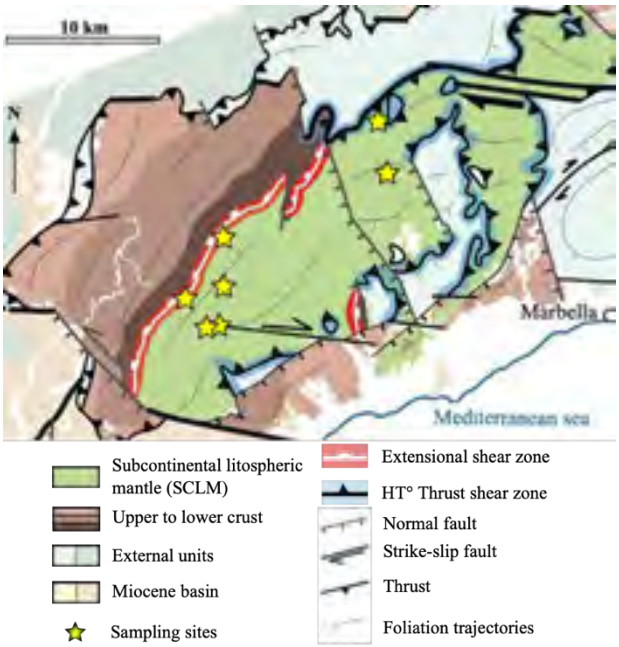


Figure 1. Simplified geologic map of the Ronda Massif and the location of the sampling sites (modified after Audran et al. 2024).

The Ronda Massif has been selected to address this issue due to its unique characteristics. The massif is distinguished by a substantial area of outcrops and peridotites that have undergone serpentinization at varying rates (Audran et al. 2024).

2 Geological setting and serpentinization in the Ronda Massif

The Ronda Massif, situated within the alpine Betic chain in Spain, is a well-known segment of subcontinental lithospheric mantle (SCLM). It is the largest segment of exhumed SCLM, spanning approximately 300 km^2. The Ronda mantle rocks are overlain by a sequence of metamorphic crustal rocks, and together they correspond to a section of thinned paleolithosphere (Frasca et al. 2017; Fig. 1). This tectonic segment was thrust over the Iberian margin ca. 21 Ma ago (i.e., the external unit) during

the African-Eurasian convergence (Frasca et al., 2017 and references therein).

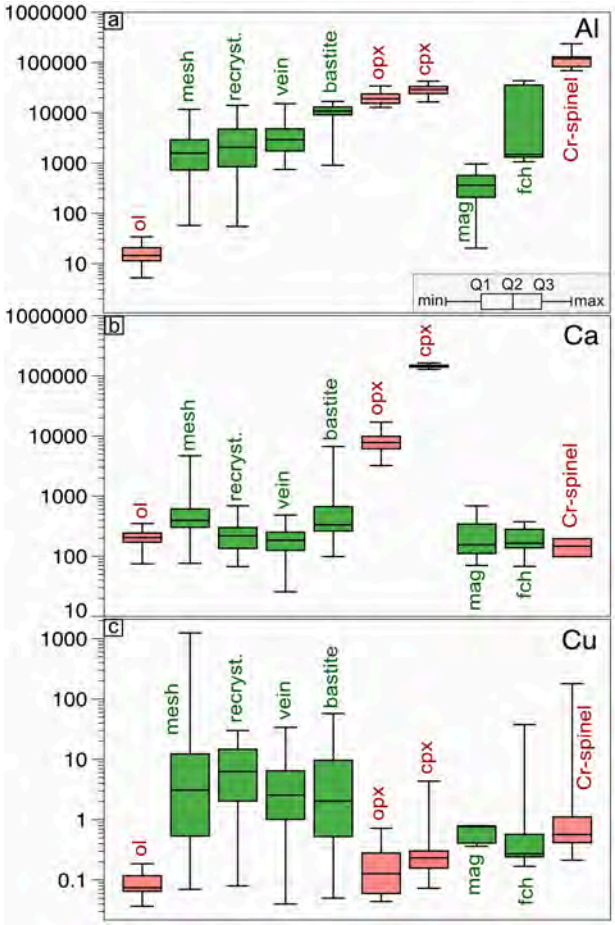


Figure 2. Box plot of trace element composition (ppm) of the various minerals contained within serpentinized peridotites from the Ronda Massif. Boxes filled with red color correspond to primary minerals such as olivine (ol), orthopyroxene (opx), clinopyroxene (cpx), and Cr-spinel of peridotite. Green boxes represent secondary minerals during serpentinization, including various serpentine textures (mesh, recrystallized, vein, bastite), magnetite (mag), and ferritchromite (fch).

This exhumation occurred concurrently with the hydration of peridotite, which was likely due to metamorphic fluids (Audran et al. 2024). Serpentinization is characterized by three successive, overprinting stages, from pervasively and variably serpentinized peridotites S1 to localized S2 and S3 serpentinites. The third stage of serpentinization is synchronous with cataclastic deformation, resulting in the formation of a meter-scale shear zone and a discrete extensional hybrid shear vein. Audran et al. (2024) detailed the mineralogy and texture of serpentine across serpentinization the various stages of serpentinization. S1 exhibits remnants of olivine, pyroxenes, and Cr-spinels, accompanied by variable amounts of mesh texture. S2 corresponds to fully serpentinized corridors, which are characterized by the presence of recrystallized texture, bastite, and chrysotile veins, along with crystallized magnetite and ferritchromite. S3 is distinguished by the presence of veins comprising serpentine and magnetite, leading to the formation of a metasomatic halo featuring bastite, chrysotile tension gashes, recrystallized serpentine and magnetite.

3 Sampling strategy and methods

Samples of the Ronda peridotite exhibit a range of serpentinization rates from 30 to 95%, thus serving as a reliable indicator for assessing element mobility through increasing serpentinization. A complementary approach was employed to collect six pairs of poorly (S1) and highly serpentinized peridotites (S2 and S3) located within a minimum distance from each other (i.e., less than a meter).

Whole rock analyses were performed on 20 samples shown in Figure 1. Rock powders were dehydrated for a period of four hours at a temperature of approximately 1015°C to obtain the loss on ignition (LOI). Concentrations of major elements were measured on pressed pellets of powder using a micro-X-ray fluorescence Bruker M4 Tornado. Concentrations of trace elements were determined using an Inductively Coupled Plasma Mass Spectrometry (ICP-MS) Thermo Scientific X series II instrument and ICAP RQ Thermo Scientific instrument. Both major and trace element analyses were carried out at the ITES laboratory in Strasbourg, France.

In situ trace element measurements on diverse minerals were conducted using an Applied Spectra RESOlution-SE 193 nm ArF excimer laser ablation system, which was coupled to an Agilent 8900 ICP-QQQ-MS at Université Laval, Canada. The analysis was conducted on serpentine minerals exhibiting variable textures, including mesh, bastite, and vein, as well as magnetite, ferritchromite, olivine, clinopyroxene, orthopyroxene, and Cr-spinel.

4 Results

4.1 Trace element mineral composition

A significant range of trace element contents is exhibited by serpentine, which is more variable than in primary minerals (i.e., olivine, pyroxenes) (Fig. 2). The distinctive serpentine chemistry exhibits no discernible correlation with the various stages of serpentinization, in contrast to serpentine texture. Mesh texture displays a low content of Al ~ 2000 ppm (i.e., Q2), whereas bastite displays a high content of ~ 11000 ppm (i.e., Q2) (Fig. 2a). Despite this variability, all serpentine textures fall within the composition of primary minerals. A similar observation is applies to Ti, V, Cr, Ni and Co. Magnetite displays a very low Al content, with concentrations below 1000 ppm. The variability of Ca in secondary minerals is considerably lower than that of Al, exhibiting a Q2 range of 185 to 396 ppm, which is significantly lower than the composition of pyroxenes (Fig. 2b). The distribution of Cu differs with serpentine minerals exhibiting a pronounced enrichment compared to primary minerals, with concentrations exceeding 1 ppm. Conversely,

magnetite and ferritchromite exhibit low Cu concentrations, with a median value of less than 1 ppm, which is similar to those observed in primary minerals such as olivine, pyroxene, and Cr-spinel.

4.2 Whole rock composition

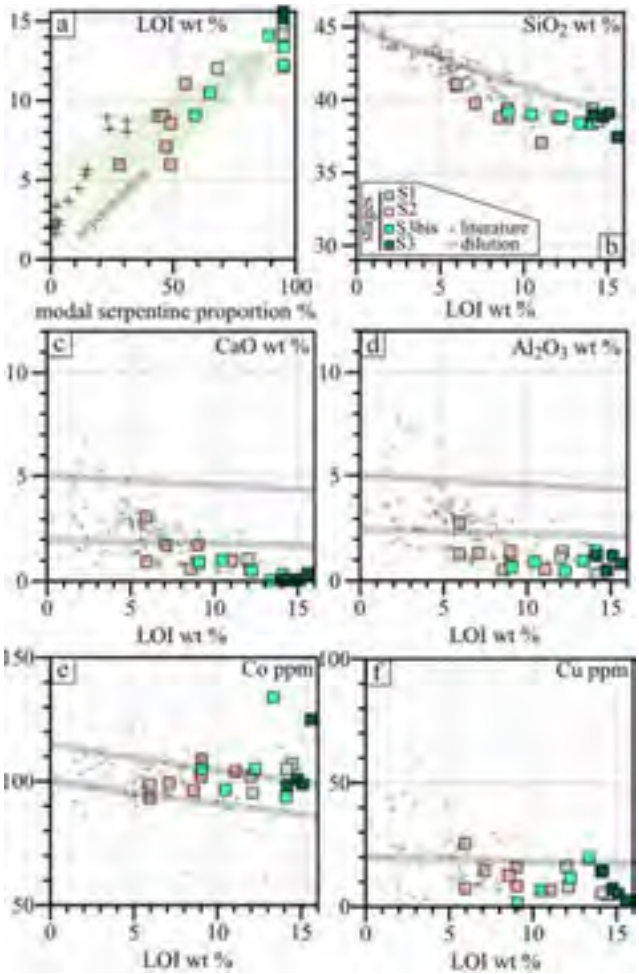


Figure 3. a) Correlation between LOI and the modal proportion of serpentine in our samples compared with data from Frey et al. (1985); b) to f) Major and trace element concentration of variably serpentinized peridotite in the Ronda Massif as a function of LOI. Literature data are from Frey et al. 1985, Gueddari et al. 1996, Van der Wal and Bodinier 1996, Lorand et al. 2000, Lenoir et al. 2001, Pereira et al. 2003, Bodinier et al. 2008, Marchesi et al. 2013 and Hidas et al. 2015. The grey lines correspond to the theoretical distribution of elements if solely controlled by dilution due to hydration.

Consequently, plotting different major or trace elements against LOI provides insight into element behaviour during progressive serpentinization. Figure 3b illustrates the strong correlation between SiO_2 and LOI, with SiO_2 ranging from 45 to 38 wt. %. A similar pattern is exhibited by the concentrations of Ni and Zn. However, this correlation is not uniformly applicable to all elements (Fig. 3c, d, e, f). For instance, the variation in CaO is significant at low LOI contents for poorly serpentinized peridotite, ranging from 7 to approximately 1 wt. %. Conversely, the amplitude of CaO diminishes in proportion to an augmentation in LOI, attaining a negligible level of ~0 wt. % in the context of fully serpentinized peridotite. A similar pattern is observed for Al_2O_3 and Cu against LOI (Fig. 3d, f). Conversely, Co exhibits a divergent behaviour, with the exception of two outliers, Co remains essentially constant with LOI values (Fig. 3e).

4.3 Grant isocon of peridote-serpentinite pairs

The rate of serpentinization in our samples ranges from ~50% to ~100% (Fig. 3a). The experimental results of Klein and Leroux (2020) provide a ~45% increase in volume during full serpentinization from 0 to 100%. Consequently, the predicted volume change in our serpentinite samples (S2 and S3) would be + 22.5%, thereby enabling the establishment of the isocon by considering pure dilution (i.e., constant mass). Isocon analysis facilitates the identification of elemental gains or losses during metasomatic transformation (Grant, 1986). Figure 4 illustrates this approach by highlighting element mobility through S1-S2 and S1-S3 pairs, where S1 represents the protolith and S2 and S3 correspond to the product of serpentinization. Figure 4a displays the loss of CaO, Al_2O_3, and Cu, while LOI exhibits a gain. The SiO_2, Fe_2O_3, and MgO elements are close to the isocon. The S1-S3 pairs exhibit a similar pattern in figure 4b, with exception for Al_2O_3, which plots within the gain area. Cu is also close to the isocon for two pairs, which could be attributed to the nugget effect of Cu-sulfides in the whole rock powder. A preliminary calculation of the S1-S2 transformation suggests that the leaching of Cu reaches approximately 39% on average.

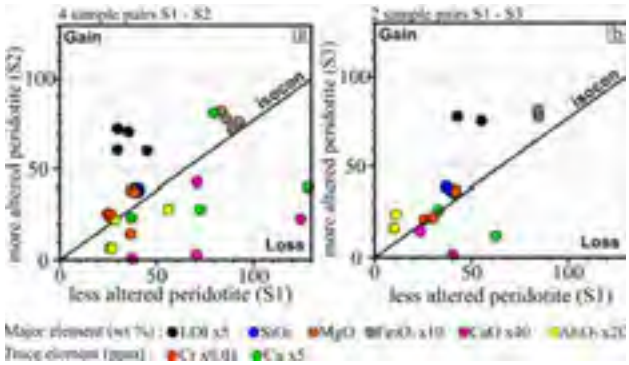


Figure 4. Grant isocon diagrams of a) 4 pairs of S1-S2 and b) 2 pairs of S1-S3, showing element mobility during serpentinization at different stages; as specified in the legend, some elements have been multiplied by 0.01, 5, 10, 20, or 40 to align with the dimensions of the diagram.

5 Discussion

5.1 Element mobility at mineral to outcrop scales

The *in situ* trace element chemistry of pseudomorphic serpentine (i.e., mesh and bastite) and primary minerals (i.e., olivine, pyroxenes) facilitates the deciphering of potential element gains or losses. This analysis is based on a comparison of

olivine with mesh texture and pyroxenes with bastite. The systematic depletion of bastite in Ca and Al relative to primary pyroxenes suggests that the process of pyroxene serpentinization is responsible for Al and Ca liberation (Fig. 2a, b). The Cu enrichment of serpentine underscores the potential for Cu mobility at the mineral scale, which may be attributed to precipitation from a relatively Cu-rich fluid resulting from the dissolution of Cu-rich sulfides (Fig. 2a, b). It is noteworthy that the whole rock serpentinite data reflect Cu depletion, whilst the serpentine mineral itself is rich in Cu. This paradox can be explained by the assumption that during the process of serpentinization, only a portion of the Cu is retained in the serpentine mineral, with the rest being released into the fluid. To further advance our understanding of the mobility of Cu, further exploration is required into the destabilization of Cu-sulfides during serpentinization and upscaling at the whole rock level.

The diagram depicting the composition of whole rocks against LOI and the isocon diagrams facilitate discussion of element mobility on a greater scale, ranging from sample to outcrop size. The SiO_2-LOI correlation aligns with the calculated dilution line and SiO_2 plots along the isocon (Fig. 3, 4), suggesting negligible SiO_2 mobility during serpentinization. This outcome is noteworthy given the established mobility of Si during hydrothermal processes. A similar distribution is also observed for Ni and Zn, suggesting minimal mobility during the process of serpentinization. However, the triangular distribution of CaO, Al_2O_3 and Cu in figure 3 indicates element leaching during progressive serpentinization. The location of these elements within the loss field of the Grant diagram (Fig. 4) supports this leaching, which can be almost complete (Ca) or partial (Cu), regardless the stage of serpentinization. A distinctive case is observed with Al_2O_3 exclusively during S3 serpentinization, which may be either introduced into the system or remain immobile (Fig. 4b).

5.2 Metallogenic implication

In oceanic settings, Debret et al. (2024) proposed, based on the analysis of Cu isotopes, that Cu is released during serpentinization. Patten et al. (2022) documented a notable occurrence of UM-SMS deposits in these settings, with Cu identified as the most prevalent metal in these deposits. The findings of this study underscore the mobility of Cu at various scales during the process of serpentinization and aim to quantify such mobility. Specifically, the serpentinization of 1 m^3 of peridotite (approximately 3 tons, containing 20 ppm of Cu) may release 23 g of copper, assuming a 39% leaching rate. At the UM-SMS Eastern Metals deposit in Quebec, the estimated copper resource is approximately 1.32 million tonnes. To deposit this amount of copper would require an estimated volume of fully serpentinized peridotite of around 50 million m^3 (1 km^2 x 50 m). This suggests that serpentinized peridotite could serve as a viable source of copper, under conditions of complete serpentinization and similar fluid-rock interactions.

6 Conclusion

This study investigates the mobility of elements at both the grain scale and the macroscopic scale using the Ronda partially serpentinized peridotites as a study case. The study meticulously documents three distinct stages of serpentinization within the massif, which were deliberately targeted to elucidate the dynamics of element mobility. At the mineral scale, bastite shows a depletion of Al and Ca. Furthermore, both mesh and bastite textures are found to be enriched in Cu. With the exception of Cu, other trace elements in the serpentine texture indicate a compositional evolution between those of pyroxenes and olivine. At the macroscopic scale, it has been demonstrated that LOI values serve as an effective proxy for serpentinization, and complete leaching of Ca has been observed during the three stages of serpentinization. The initial stage of serpentinization exhibits a substantial decrease in Al and Cu, consistent with an increase in serpentinization intensity. When considering mass change, S2 serpentinization leads to leaching of Ca, Al, and Cu, while S3 serpentinization shows Ca and Cu leaching. The mobility of Cu offers novel insights into the metallogenic role of serpentinization as a source of metals for UM-SMS deposits worldwide.

References

Audran B, Boulvais P, Branquet Y, Gautier P, Ulrich M, Raymond G, Beaudoin G, Layton-Matthews D, Leduc E, Bévan M, Coltat R (2024) Serpentinization of the Ronda Massif (Spain): Structural controls and fluid origin. Lithos 488:107817.

Debret B, Andreani M, Godard M (2024) A review of abyssal serpentinite geochemistry and geodynamics. Earth-Science Reviews 258:104910.

Deschamps F, Godard M, Guillot S, Hattori K (2013) Geochemistry of subduction zone serpentinites: A review. Lithos 178:96-127.

Frasca G, Gueydan F, Poujol M, Brun JP, Parat F, Monié P, Pichat A, Mazier S (2017) Fast switch from extensional exhumation to thrusting of the Ronda Peridotites (South Spain). Terra Nova 29(2):117-126.

Grant JA, (1986) The isocon diagram; a simple solution to Gresens' equation for metasomatic alteration. Economic Geology.

Jöns N, Bach W, Klein F (2010) Magmatic influence on reaction paths and element transport during serpentinization. Chemical Geology 274(3-4):196-211.

Klein F, Le Roux V (2020) Quantifying the volume increase and chemical exchange during serpentinization. Geology, 48(6):552-556.

Patten CG, Coltat R, Junge M, Peillod A, Ulrich M, Manatschal G, Kolb J (2022) Ultramafic-hosted volcanogenic massive sulfide deposits: an overlooked sub-class of VMS deposit forming in complex tectonic environments. Earth-Science Reviews 224:103891.

The Hambok volcanic-associated massive sulfide deposit, Bisha VMS District, Eritrea: discovery, geology and mineralogy

C. Tucker Barrie[1], Ingrid Kjarsgaard[2], and Demetrius Pohl[3] *1 CTBA Geoconsultants, Ottawa, Canada*
2 Mineralogist, Ottawa, Canada
3 Carlson-Pohl Associates, Los Angeles, California

Abstract. The Hambok volcanic-associated massive sulfide (VMS) deposit was discovered in 2005, shortly after the discovery of the nearby Bisha VMS mine, in the Neoproterozoic Nakfa Terrane of western Eritrea. Hambok mineralization was discovered during field mapping of a large license area, as gossanous horizons up to 30 m long and 1-3m thick, with anomalous gold and base metal values in rock chip and soil samples. It has clear magnetic, electromagnetic and gravity signatures that correspond to massive sulfide at depth. The deposit is within a mafic - siliciclastic stratigraphic sequence with lesser felsic tuff, at mid-greenschist facies, with a variable-strength penetrative fabric sub-parallel to bedding. The deposit is enveloped by moderate to strong talc-chlorite magnetite alteration, with lesser epidote, siderite, sericite, and relict staurolite and andalusite. In the hanging wall, disseminated magnetite is abundant within tuffaceous strata, and as magnetite-rich conformable layers up to 30 cm thick which may represent paleo-seafloor iron-rich precipitates. The sulfide and sulfosalt mineralogy is generally medium- to coarse-grained and subhedral to euhedral, and is comprised of pyrite, chalcopyrite, and sphalerite; with minor galena, tennantite, and digenite; and trace altaite (PbTe), rucklidgeite ($(Bi,Pb)_3Te_4$), tellurobismuthite (Bi_2Te_3) and volynskite ($AgBiTe_2$); accompanied by abundant magnetite, and minor hematite locally.

1 Discovery, and Setting within the Bisha VMS District, Western Eritrea

Hambok mineralization was discovered during field mapping of a large license area in 2005, soon after the discovery of the Bisha VMS mine 14 km to the NE. At surface, it presented as gossanous horizons up to 30 m long and 1-3m thick, with anomalous gold and base metal values in rock chip and soil samples. Deposit-scale mapping and detailed soil surveys (100 m line spacing, 25 m stations) led to several drill targets along the Hambok - Ankereit NNE trend. The main deposit was detected by ground EM and gravity surveys before initial drilling in 2006. The deposit has clear magnetic, electromagnetic (EM and IP), and gravity signatures that correspond to massive sulfide at depth.

The Hambok VMS deposit is one of several significant Cu-Zn-Au-Ag deposits currently under development in the Bisha VMS district (Fig. 1), including the Bisha mine (total resources >60 million tonnes (MT), Harena mine (>29 MT), Bisha Northwest (>4 MT) and Asheli mine (>2.4 MT: Jankowski et al 2017). Hambok resources are: 16.1 MT @ 1.61% Zn, 0.84% Cu, 5.48 g/t Ag and 0.18 g/t Au (Indicated), plus 24.8 MT @ 1.3% Zn, 0.75 % Cu, 4.66 g/t Ag and 0.17 g/t Au (Inferred: Giroux and Barrie, 2009).

The deposit is within a Neoproterozoic mafic - siliciclastic stratigraphic sequence with lesser felsic tuff, at mid-greenschist facies, with a variable-strength penetrative fabric sub-parallel to bedding. It comprises several stacked lenses, each with thicknesses up to tens of meters and strike lengths up to 1 km, within strata that dip 60^O-70^O to the ESE (Fig. 2). Footwall sulfide stringer mineralization is consistently on the WSW side, indicating a facing direction to the ESE. The deposit does not have the significant near-surface oxidation, gossan and supergene sulfide development as seen at Bisha, 14 km to the NW (Barrie et al 2007).

Limited whole rock geochemistry of less-altered volcanic strata indicate a tholeiitic affinity for host basalts, and tholeiitic to transitional calc-alkalic affinity for nearby dacite and rhyolite tuffs.

2 Sulfide, sulfosalt and gangue mineralogy

Petrography was conducted on a limited set of ore samples and supported by WDS and EDS analyses using a microprobe at the Carleton University, Ottawa, Canada. The sulfide and sulfosalt mineralogy is generally medium- to coarse-grained and subhedral to euhedral, and is comprised of pyrite, chalcopyrite, and sphalerite; with minor galena, tennantite, and digenite; and trace altaite (PbTe), rucklidgeite ($(Bi,Pb)_3Te_4$), tellurobismuthite (Bi_2Te_3) and volynskite ($AgBiTe_2$); accompanied by abundant magnetite, and minor hematite locally. Gangue minerals associated with massive and semi-massive sulfide include quartz, sericite, Mg-chlorite, siderite and feldspar; with minor and accessory Zn-siderite, manganoan ferroan dolomite, clinozoisite, biotite, anhydrite (or gypsum) talc and barite; and trace rutile and an unidentified Fe-Zn phosphate (platy or fibrous). Also of note: 1) pyrrhotite and arsenopyrite, two minerals commonly found in VMS deposits, are absent in these sections and by inference in the deposit; 2) pyrite and chalcopyrite analyses (n = 11, 6 respectively) are near end member compositions, with little or no solid solution. Chalcopyrite has minor Zn up to 0.28 wt. % in one analysis. Most of the pyrite and chalcopyrite analyses have measurable bismuth at 0.1-0.3 wt. % Bi; 3) sphalerite analyses (n=9) also have near end member composition, with only minor iron contents of 0.4-2.6 wt. % Fe. The low iron content is consistent with low temperature seafloor deposition; 4) galena analyses (n=3) have selenium at 0.5-1.0 wt. % Se, silver at 0.18-0.26 wt. % Ag, and 0.32 - 0.88 Bi. Samples that have galena generally have BiTe minerals, and elevated Ag contents; 5) no primary gold- or silver-bearing phases have been observed; 6) gold is present in one tellurobismuthite WDA analysis (HAM 040 297 (1): 0.34 wt. % Au); and one digenite analysis (diamond drill hole (DDH) HAM 09 152.5 (6): 0.11 wt. % Au). Silver is present at values of 0.2-0.55 wt. % Ag in lead-bearing and most BiTe-bearing minerals, including galena, altaite, rucklidgeite and volynskite. One volynskite analysis has 13.05 wt. % Ag (DDH HAM-09 133 m.

In figure 3, petrographic and backscatter images are given of Hambok massive sulfide material.

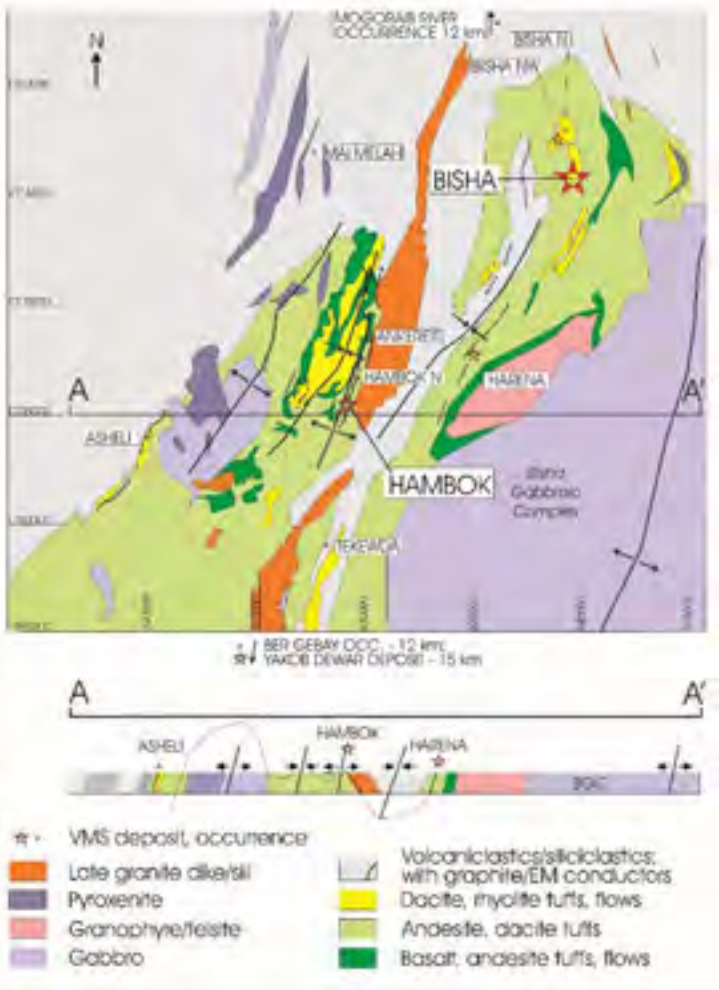


Figure 1. Simplified geology of Bisha VMS District with locations for Hambok and other VMS deposits. Modified after Barrie et al 2017.

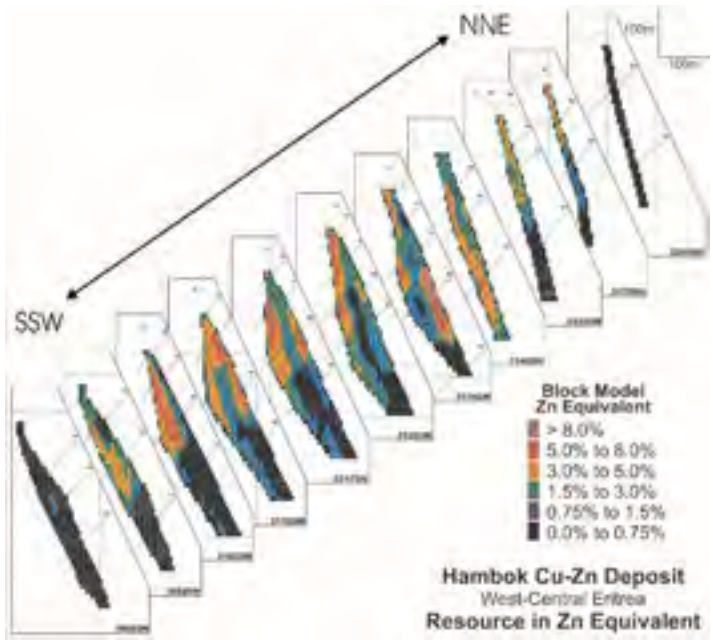


Figure 2. Drill sections showing Hambok massive and semi-massive sulfide as zinc equivalent values. Zn equivalent calculated using Zn = $0.79/lb, Cu = $1.3/lb, Au = $675/oz Ag = $10/oz, assumed recoveries of Zn=84%, Cu=85%, Au=36%, Ag=29%. Values based on initial metallurgical studies and using metal prices in 2009. Source: Sanu Resources website 2009.



Figure 3a. Typical medium-grained massive sulfide (DDH HAM-021 268.5m): Pyrite - light yellow; chalcopyrite - yellow, sphalerite - intermediate gray, and tennantite - light gray, and gangue - quartz and carbonate - dark gray to black. Reflected light, scale - 1 mm across image horizontally. The fine-grained, euhedral to subhedral pyrite is relatively inclusion-free. The other minerals are sub- to anhedral and infill between more competent pyrite. Microprobe analyses of the tennantite indicate that it is nearly end member, containing 18-19 wt. % As, 0.5 wt. % Sb, and very low silver contents (0 - 0.03 wt. % Ag; n=3.

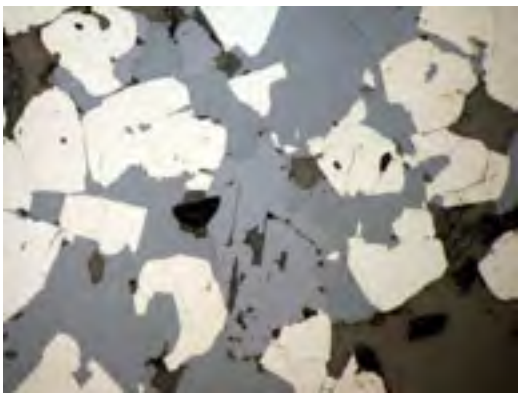


Figure 3b. DDH HAM-09 152.5 m: Magnetite-rich massive sulfide. Euhedral pyrite, magnetite (intermediate gray), and sphalerite (lighter gray and with prominent cleavage and gangue along crystallographic planes), and gangue minerals including barite (dark gray) and carbonate; reflected light, 1.2 mm across. Magnetite has equilibrium textures with both pyrite and sphalerite, consistent with co-precipitation of all three minerals. It contains low vanadium, manganese and cobalt; titanium was not measured but may be up to ~5 wt. % Ti.

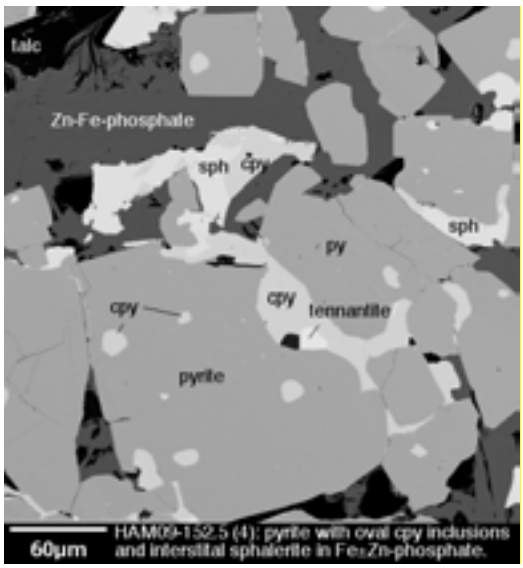


Figure 3c. DDH HAM-09 152.5m: Backscatter image showing rounded chalcopyrite (cpy) inclusions within euhedral pyrite, interstitial chalcopyrite, sphalerite (sph) and tennantite, and an unknown interstitial Zn-Fe phosphate mineral.



Figure 3d. DDH HAM-040 297m: Banded pyrite-magnetite ore. Euhedral magnetite and subhedral to rounded pyrite, reflected light, 1 mm across. Some of the pyrite occurs as rounded inclusions in magnetite, indicating probable replacement of pyrite by magnetite in a desulfidation reaction. As with the magnetite in DDH HAM-09-152.5, this magnetite is nearly end member composition, with very low concentrations of V, Mn and Co. This comes from bedded or layered, magnetite-rich massive sulfide.

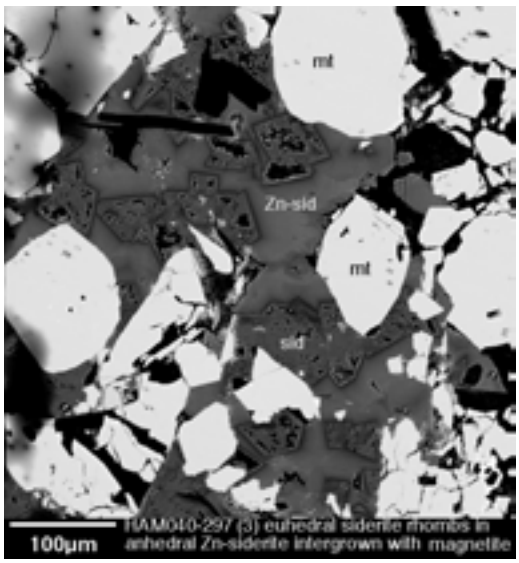


Figure 3e. DDH HAM-040 297m: Banded pyrite-magnetite ore. Backscatter image showing abundant rhombic euhedral siderite (sid) and anhedral Zn siderite (Zn sid) interstitial to, and partly replacing magnetite (mt).

Acknowledgements

We acknowledge Steve Olson of Sanu Resources Eritrea who oversaw much of the Mogoraib license exploration from 2005-2008; and Daniel Weldeyohannes of Bisha Shares Mining Company for permission to publish. CTB is indebted to the late Jim Franklin for his support and enthusiasm while at the Geological Survey of Canada in Ottawa in the 1990s.

References

Barrie CT, Nielson FW, Aussant CH (2007) The Bisha Volcanic-Associated Massive Sulfide Deposit, Wstern Nakfa Terrane, Eritrea: Econ. Geol. V. 102, p. 717-728.

Barrie CT, Abu Fatima M, Hamer D (2017) Volcanogenic Massive Sulfide – Oxide Gold Deposits of the Nubian Shield, NE Africa, In Bouabdellah, M., and Slack, J., eds., Geology and Mineral Deposits of North Africa, Mineral Resource Reviews, doi: 10.1007/978-3-319-31733-5_17 , Springer, p. 417- 435.

Giroux GH, Barrie CT (2009) Hambok Deposit, Mogoraib Exploration License, Gash-Barka District, Western Eritrea - 43-101 Technical Report and Preliminary Resource Assessment: 130 p.

Jankowski P, Ebrahim A, Dance A, Elliott C, Winkelmann N, Scott C, Whelan T (2017) Independent Technical Report 2016 Resources and Reserves Update, Bisha Mine, Eritrea: for Nevsun Resources Ltd., 313 p.

Polymetallic quartz veins at the Hod Maden Cu-Au deposit, Turkey

Bader Bilgin[1] , Thomas Monecke[1] , T. James Reynolds[1]
[1]Center to Advance the Science of Exploration to Reclamation in Mining, Department of Geology and Geological Engineering, Colorado School of Mines, 1516 Illinois Street, Golden, 80401 Colorado, USA

Abstract: The Hod Maden Au-Cu deposit in the Eastern Pontides of Turkey comprises semi-massive sulfide and massive sulfide ore bodies hosted by a Cretaceous submarine succession. The volcanic host rocks are crosscut by polymetallic quartz veins that commonly show crustiform textures and contain abundant pyrite, sphalerite, or chalcopyrite. The quartz occurs as fine-grained mosaic quartz, flamboyant quartz grains showing inclusion-rich cores and arrays of radiating inclusions, and prismatic quartz grains having feathery domains. The quartz microtextures are consistent with the quartz having formed through recrystallization from a non-crystalline silica precursor. The quartz is crosscut by secondary fluid inclusions having a wispy appearance that have been affected by post-entrapment modification. The fluid inclusion evidence suggests that the quartz formed prior to Paleocene to Eocene fold-and-thrust belt development and regional metamorphism. The polymetallic quartz veins are not associated with a post-collisional hydrothermal overprint associated with a porphyritic intrusion.

1 Introduction

The Hod Maden Au-Cu deposit in the Eastern Pontides in Turkey comprises a measured and indicated mineral resource of 8.1 Mt of ore grading 1.8 % Cu and 10.6 g/t Au. High-grade ores occur as multiphase quartz-pyrite-chalcopyrite and hematite/jasper breccia bodies and semi-massive to massive sulfides, within a Cretaceous succession of volcanic rocks deposited in a submarine depositional environment. In terms of the host rock succession, Hod Maden shares many similarities with the volcanogenic massive sulfide (VMS) deposits of the Eastern Pontides (Revan and Göç 2016).

However, classification of Hod Maden as a VMS deposit remains contentious. In part, this is because polymetallic quartz veins recognized in exploration drill core are distinctly different from stringer veins encountered in VMS deposits. These veins are composed of crustiform quartz and contain abundant sulfide minerals, including pyrite, sphalerite, and chalcopyrite. High precious metal grades have been reported in drill intercepts.

Determining the relative timing and genetic origin of the polymetallic quartz veins at Hod Maden is crucial for exploration. If these veins are related to a Cretaceous hydrothermal system, recording their abundances in exploration drill core could potentially be used as a vector to massive Cu-Au ores. Alternatively, it appears feasible that these polymetallic quartz veins were formed during a Tertiary overprint and could, therefore, indicate the nearby presence of an unidentified post-collisional porphyry intrusion.

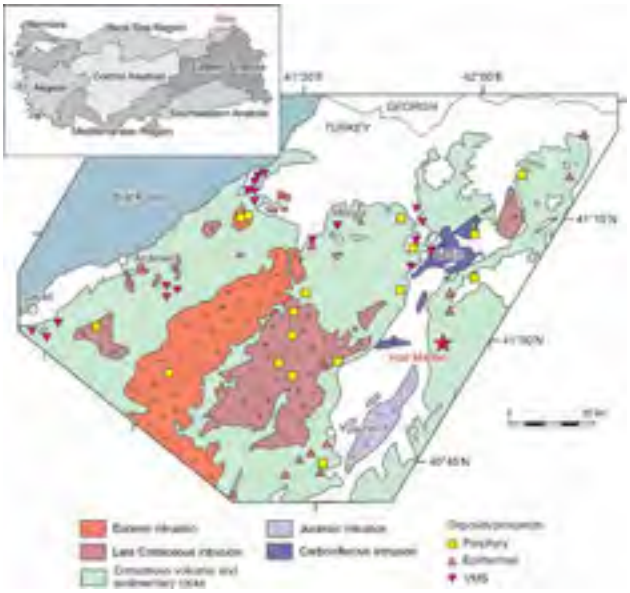


Figure 1. Geologic map of the Artvin area in Turkey showing the locations of major ore deposits, including the Hod Maden Cu-Au deposit (modified from Rabayrol et al. 2023).

This study reports on a preliminary petrographic study on the polymetallic quartz veins that aimed at clarifying the relative timing of formation of these unusual veins. The study has regional significance as similar veins have been described in other massive sulfide deposits in the Eastern Pontides, including the world-class Murgul deposit (Abdioğlu et al. 2015).

2 Geological Background

The Hod Maden Cu-Au deposit is located within the Eastern Pontides in Turkey. The Eastern Pontides are part of the Alpine-Himalayan orogenic belt and extend for ~500 km along the coast of the Black Sea from central Turkey to Georgia (Yilmaz et al. 1997). The geological evolution of the region was shaped by subduction of the Neotethyan oceanic lithosphere under the Eurasian margin during the late Mesozoic and Cenozoic (Şengör and Yılmaz 1981). The main episode of

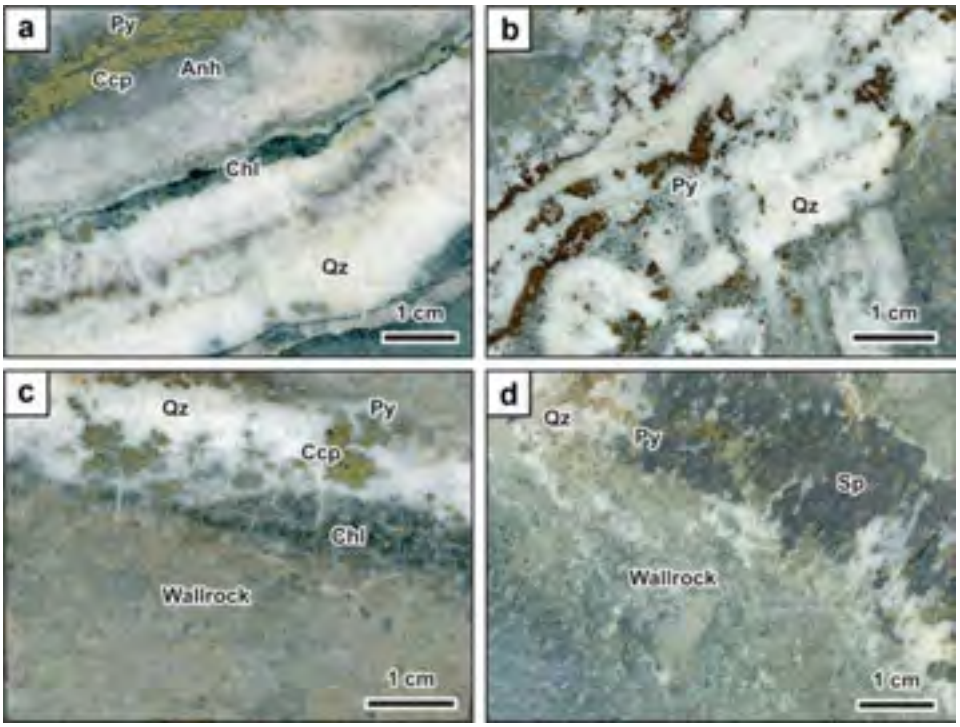


Figure 2. Hand specimen images of polymetallic quartz veins from Hod Maden, Turkey. **a** Crustiform vein with distinct bands containing large quartz crystals, anhydrite, pyrite, and chalcopyrite. Sample from drillhole HTD-099 at 356.85 m. **b** Banded vein containing pyrite (some pyrite has been affected by oxidation and shows a dark red tarnish). Sample from drillhole HTD248A at 309.65 m. **c** Quartz vein hosting large pyrite aggregates. Sample from drill hole HTD029 at 185.5 m. **d** Quartz vein consisting of grayish-brown sphalerite and minor pyrite. Sample from drill hole HTD152 at 200.7 m. Anh = anhydrite, Ccp = chalcopyrite, Chl = chlorite, Py = pyrite, Qz = quartz, Sp = sphalerite.

arc magmatism resulted in the formation of a ~5.5-km- thick submarine arc volcanic succession in the Turonian to late Campanian (~94–75 Ma; Kandemir et al. 2019; Aydin et al. 2020). Basin closure and fold-and- thrust-belt development occurred during the Paleocene to Eocene. The volcanic succession was metamorphosed due to convergence and collision between the Pontides and Eurasia (Kandemir et al. 2019). Post-collisional magmatism and associated porphyry and epithermal Cu-Au deposits in the Eastern Pontides are Eocene in age (~51–47 Ma; Delibaş et al. 2019; Rabayrol et al. 2023).

The Hod Maden Cu-Au deposit is hosted by a steeply east-dipping Late Cretaceous volcanic succession. The footwall succession consists of predominantly andesitic and dacitic rocks. Coherent units, along with associated autobreccia, are primarily distributed across the western and central parts of the deposit. Andesite is characterized by chlorite alteration while dacite shows zones of chloritization, silicification, and assemblages of quartz-hematite, jasper-hematite, and illite+smectite±sericite. The hanging-wall succession at Hod Maden comprises stratified redeposited volcaniclastic and volcanogenic sedimentary units, tuffaceous deposits, basaltic to andesitic lava flows, as well as rhyodacite sills and dikes. The volcanic rocks at Hod Maden have U-Pb zircon ages of 84.78 ± 0.43 Ma to 84.00 ± 0.44 Ma (Bilir 2023).

3 Materials and Methods

Fieldwork at Hod Maden involved logging of diamond drill core and the construction of geological sections. During logging, the occurrence of polymetallic quartz veins was registered along with their textures and mineral compositions. Polished thick (~60 μm) sections were prepared from representative vein samples and used for petrographic analysis in transmitted and reflected light. Optical cathodoluminescence (CL) microscopy was conducted using an HC5-LM microscope by Lumic Special Microscopes, Germany.

4 Results

Relogging of exploration drill core and the construction of representative cross-sections shows that the frequency of polymetallic quartz veins is highest in the stratigraphic footwall of the Cu-Au zones where chlor ite alteration predominates. The veins also occur in the favorable stratigraphic interval characterized by quartz-hematite and jasper-hematite alteration. In

general, the abundance of veins is higher in the southern part of the deposit within the so-called South and Old Working zones. The vein abundance decreases in the stratigraphic hanging-wall of the ore zones, where the host rocks have been affected by illite-smectite±sericite alteration.

The polymetallic quartz veins can be up to 5 cm wide. They commonly exhibit banded and comb textures (Fig. 2a,b). Individual bands are quartz-rich or consist of late anhydrite (Fig. 2a,b). Sulfide minerals include pyrite and grayish-brown sphalerite. Chalcopyrite is present in some veins (Fig. 2a, c).

Different quartz textures are observed in thin sections, including fine-grained mosaic quartz that is characterized by interpenetrating grain boundaries and flamboyant quartz grains showing inclusion-rich cores and arrays of radiating inclusions (Fig. 3a). In addition, large prismatic quartz grains characterized by domains of feathery quartz having a splintery appearance in cross-polarized light are common. Some prismatic quartz grains also show recrystallization fronts characterized by pseudoprimary inclusions (Fig. 3b). Recrystallization fronts have distinct short-lived bright yellow CL colors (Fig. 3c).

The quartz grains are crosscut by myriads of secondary fluid inclusions resulting in a wispy texture (Fig. 4a). Most secondary fluid inclusion assemblages show inconsistent liquid-to-vapor volumetric proportions. The secondary inclusions can be black and filled by vapor only (Fig. 4b). These large black inclusions can be surrounded by smaller neonate inclusions filled by liquid.

5 Discussion and Conclusions

The field evidence demonstrates that there is a strong stratigraphic control on the distribution of the polymetallic quartz veins at Hod Maden. The vein density correlates with the asymmetric distribution of mappable alteration facies around the Cu-Au ore zones. The drill core observations argue against the polymetallic veins being related to a late hydrothermal overprint of the volcanic succession hosting the massive sulfides.

The microscopic observations are consistent with this interpretation. The quartz textures observed in thin sections suggest that the polymetallic quartz veins originally consisted largely of non-crystalline silica. Mosaic quartz, flamboyant quartz, and prismatic quartz with remnant recrystallization fronts and feathery domains are characteristic microtextures formed as a result of recrystallization of non-crystalline silica (cf. Dong et al. 1995; Gissler et al. 2024). The recrystallized quartz is crosscut by abundant secondary fluid inclusions forming dense, wispy arrays. The secondary fluid inclusions show evidence for post-entrapment modification. Post-entrapment modification is known to occur due to differential under- or over-

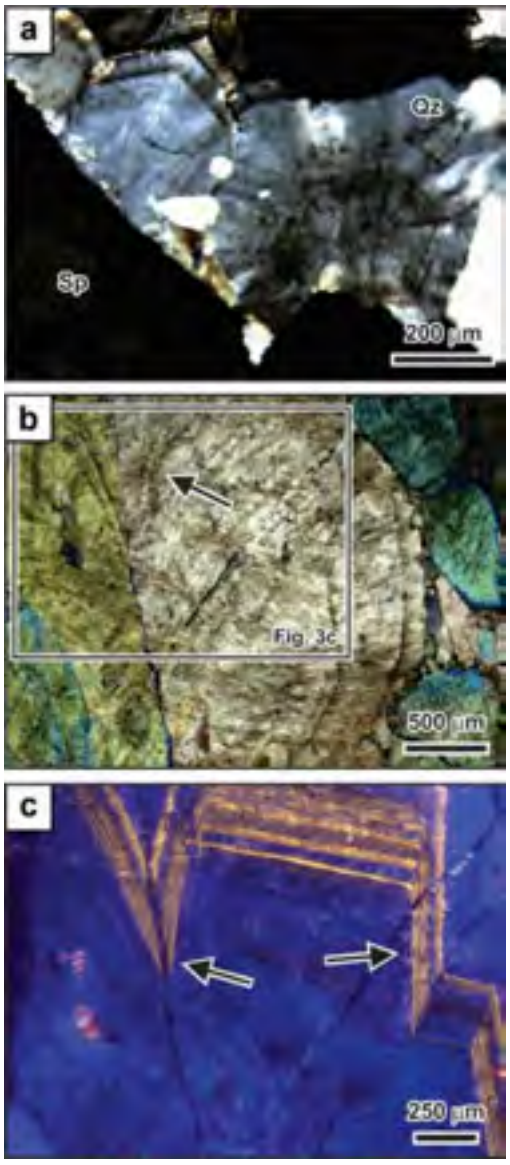


Figure 3. Petrographic characteristics of quartz in polymetallic veins at Hod Maden, Turkey. **a** Flamboyant quartz crystals showing radiating arrays of pseudoprimary inclusions. Sample from drill hole HTD152 at 200.70 m. **b** Remnant recrystallization fronts in prismatic quartz. Some fronts are curved and cross grain boundaries of neighboring prismatic grains (arrow) and some are more linear , having become crystallographically controlled. The recrystallization fronts are characterized by abundant pseudoprimary inclusions. Sample from drill hole HTD248A at 321.70 m. **c** Cathodoluminescence image of the highlighted area. The recrystallization front is located immediately adjacent to bands having a short-lived yellow emission during electron bombardment. The irregular shape of the bands (arrows) suggests that they formed during recrystallization from a non-crystalline precursor and are not primary growth zones.

pressuring between fluid inclusions and their surroundings (Sterner and Bodnar 1989). Post-entrapment modification explains the irregular shapes of the

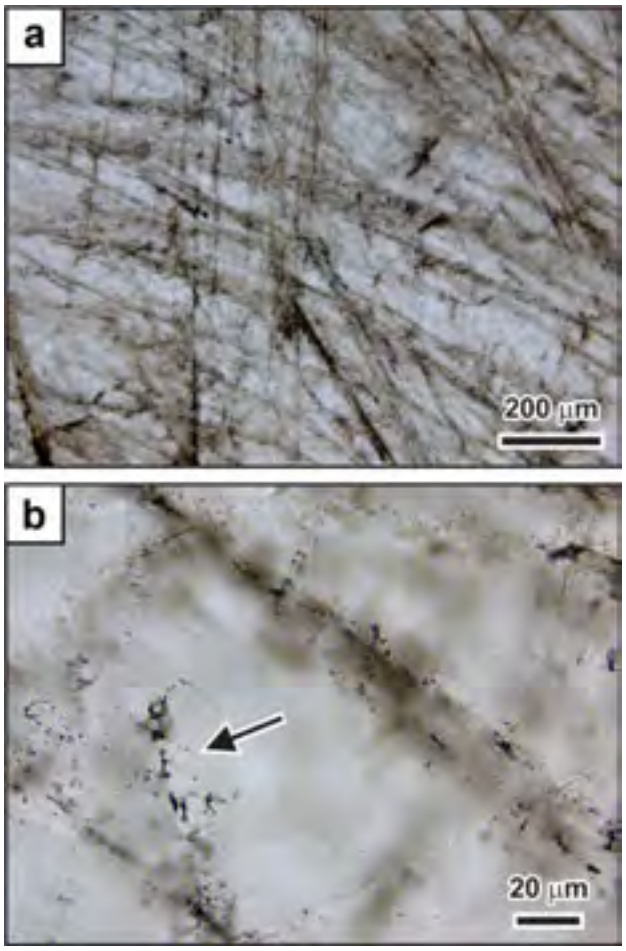


Figure 4. Fluid inclusion characteristics of quartz in polymetallic veins at Hod Maden, Turkey. **a** Secondary fluid inclusions forming wispy arrays in quartz. The textural characteristics suggest that entrapment occurred under metamorphic conditions. **b** Large black inclusions (arrow) showing highly irregular shapes indicating that they were affected by post-entrapment modification. The post-entrapment modification likely occurred in response to pressure and temperature changes during exhumation and uplift. Sample from drill hole HTD152 at 149.60 m.

secondary fluid inclusions and the inconsistent liquid-to-vapor volumetric proportions observed in the inclusion assemblages. Post-entrapment modification is characteristic of inclusions that have undergone metamorphic reequilibration (Sterner and Bodnar 1989).

The observations of this study suggest that the polymetallic quartz veins at Hod Maden formed prior to fold-and-thrust belt development and regional metamorphism in the Paleocene to Eocene. The veins are either related to the formation of the submarine VMS deposits or, alternatively, are part of a currently unrecognized Cretaceous metallogenic event. It can be ruled out that the polymetallic quartz veins at Hod Maden are genetically associated with a post-collisional hydrothermal system such as those that formed porphyry or epithermal deposits in the region.

Acknowledgments

We acknowledge the Hod Maden project geology and technical team for their support during the fieldwork. We are indebted to Rex Brommecker and Osman Uludağ for their insights and support discussion of the results. We thank SSR Mining for supporting this study. The research was conducted within the Center to Advance the Science of Exploration to Reclamation in Mining, a joint industry-university collaborative research center between the Colorado School of Mines and Virginia Tech under National Science Foundation award numbers 2310920 and 2310948.

References

Abdioğlu E, Arslan M, Kadir S, Temizel İ (2015) Alteration mineralogy, lithochemistry and stable isotope geochemistry of the Murgul (Artvin, NE Turkey) volcanic hosted massive sulfide deposit: Implications for the alteration age and ore forming fluids. Ore Geol Rev 66:219–242

Aydin F, Saka SO, Şen C, Dokuz A, Aiglsperger T, Uysal İ, Kandemir R, Karslı O, Sarı B, Başer R (2020) Temporal, geochemical and geodynamic evolution of the Late Cretaceous subduction zone volcanism in the eastern Sakarya Zone, NE Turkey: Implications for mantle-crust interaction in an arc setting. J Asian Earth Sci 192:104217

Bilir ME (2023) Characteristics, genesis and triggers for the formation of Hod Maden Au-Cu mineralization system, NE Turkey. PhD thesis, Muğla Sıtkı Koçman University

Delibaş O, Moritz R, Selby D, Göç D, Revan MK (2019) Multiple porphyry Cu-Mo events in the Eastern Pontides metallogenic belt, Turkey: From Early Cretaceous subduction to Eocene postcollision evolution. Econ Geol 114:1285–1300

Dong G, Morrison G, Jaireth S (1995) Quartz textures in epithermal veins, Queensland – Classification, origin, and implication. Econ Geol 90:1841–1856

Gissler GD, Monecke T, Reynolds TJ, Guzman MA, Ellison ET, Sherlock R (2024) Microtextural evidence for recrystallization of opal-A to quartz in epithermal veins: A case study from the McLaughlin deposit, California. Ore Geol Rev 169:106105

Kandemir Ö, Akbayram K, Çobankaya M, Kanar F, Pehlivan S, Tok T, Hakyemez A, Ekmekçi E, Danacı F, Temiz U (2019) From arc evolution to arc-continent collision: Late Cretaceous–middle Eocene geology of the Eastern Pontides, northeastern Turkey. GSA Bull 131:1889-1906

Rabayrol F, Wainwright AJ, Lee RG, Hart CJR, Creaser RA, Camacho A (2023) District-scale VMS to porphyry-epithermal transitions in subduction to postcollisional tectonic environments: The Artvin Au-Cu district and the Hod gold corridor, Eastern Pontides belt, Turkey. Econ Geol 118: 801–822

Revan MK, Göç D (2016) The Upper-Cretaceous volcanogenic massive sulfide (VMS) deposits of the Eastern Pontide orogenic belt (NE Turkey). SEG Guideb Ser 53, p 56

Şengör AMC, Yılmaz Y (1981) Tethyan evolution of Turkey: A plate tectonic approach. Tectonophysics 75:181–241

Sterner SM, Bodnar RJ (1989) Synthetic fluid inclusions – VII. Re-equilibration of fluid inclusions in quartz during laboratory-simulated metamorphic burial and uplift. J Metamorph Geol 7:243–260

Yılmaz Y, Tüysüz O, Yiğitbaş E, Genç ŞC, Şengör AMC (1997) Geology and tectonic evolution of the Pontides. AAPG Mem 68:183–226

James Franklin and ore deposits in the 1970s

Lawrence M. Cathles[1]
[1]*Emeritus Professor, Cornell University, Ithaca, New York 14853*

Abstract. The 1970s and the decade or so that followed was a period of particularly rapid change in our understanding of geological processes and ore deposits, and a time when particularly talented individuals like James Franklin engaged to make contributions of enduring value. I was fortunate to live through these times. I will try to describe the ideas that were circulating, and the contributions Canadian geological giants like Franklin made. Of necessity, this will be a personal perspective from one struggling to learn and understand geology and ore deposits himself. I will close with some questions that might remain for future Franklin's to resolve.

1 Background

Harry Hess was Chair of the Princeton Geology Department in 1966. Jason Morgan had just been hired. Hess recruited Fred Vine, and assigned Jason and Fred Vine to a common lab-sized office. Plate tectonics was about to be born. Ed Sampson, Joe Kalliokoski, and Heinrich Holland were the economic geologists. Minerals were a matter of cold war competition and important. Geophysics was a brand new subject, as was Geochemistry. I entered in the second Geophysics class with a pure physics background and no knowledge or background whatsoever in geology or economic geology. One could not hope for a less biased reporter.

The academic environment was rich. Hess had profiled the seafloor as an Admiral in the navy during the war. He published his paper on sea floor spreading in 1962. All kinds of interesting speakers passed though the Department. Warren Carey suggested the issue of what to do with the spreading ocean crust could be resolved if the earth was expanding like a balloon. Bob Dicke, my undergraduate advisor (and Jason's Ph.D advisor) was interested in whether the gravitational constant G might change with time. Jason was tasked with investigating whether the pattern of earthquakes suggested Earth expansion. I investigated the viscosity of the Earth's mantle. Geological instruction was conventional. It took me two years to begin to understand why geologists had so many words for rocks, and the distinction between a miogeosyncline and a eugeosyncline remain a mystery. But the setting was rich, and things were about to change rapidly.

In 1968 Jason delivered his AGU talk on plate tectonics. There was great discussion, but adoption was remarkably rapid. Isacks, Oliver and Sykes imaged the subduction of the ocean crust at the trenches that outlined the Pacific rim of fire. The home of the beautifully zoned porphyry deposits of Lowell and Gilbert was explained. Papers abounded on how geology was related to plate tectonics, and how ore deposits fit into the new paradigm.

The discovery of black smokers, a missing piece that came as a great surprise but shouldn't have, was yet to occur. In fact, the lack of hydrothermal circulation at ocean ridges was cited in a commentary in the Proceedings of the Royal Academy as evidence that sea floor spreading was unlikely. If magmas were upwelling at ridges, hydrothermal activity should have been observed and it had not. Solomon and Walsh predicted just what black smokers should look like, and Ballard discovered one in 1978. A VMS deposit was alive!

2 The dash to discovery

All of a sudden Canadian geologists like Jim Franklin, Steve Scott, and Lloyd Clark were in great demand. They knew about volcanogenic massive sulphide deposits on land, and were the ones to say if the seafloor massive sulphide deposits were the same or different. I was at Kennecott's Ledgemont Laboratory at the time, and suddenly my knowledge of plate tectonics was of interest and relevance. We began to consider all kinds of ways plate tectonics and convective processes might help find ore deposits.

A seminal event for Steve Scott, Mike Mottle, an engineer named Kurt Schusterick and me was a summer at Woods Hole with Bob Ballard. Steve had sold a group of copper companies on the idea that they should understand the connection between VMS and their seafloor cousins, and raised the money, payable upon delivery and acceptance of our final report, to rent a summer house on the Cape for us and our families. Times were good! − for one weekend. Then it was nonstop science. Ballard delivered papers and discussion each morning. We read and calculated. It was a tremendously stimulating experience that launched Steve on his ocean exploration adventures and gave me a lifelong interest in seafloor processes.

3 Franklin's contribution

As this special session in Jim's honour demonstrates so well, everyone knew Jim Franklin. He was incredibly welcoming, enthusiastic, and willing to share his insights. One interaction I do clearly remember was a discussion we had at a meeting about how basement metal signatures were transmitted through glacial overburden. This is evidently a matter of firm observation, but as far as I know it is not well understood, at least not by me. Robert Zartman documented a remarkably regional variation of lead isotopes in the Tri-State MVT

district, which is a pattern possibly related by similar processes. Jim's investigations of seafloor massive sulphides surrounded by sediment was of interest in indicating how convection might scavenge metals in convecting systems.

But Jim's most important contributions possibly came from his leadership skills − his ability to talk to legislators and communicate the importance of geology and geological studies, and his ability to inspire and bring new geologists into the exploration community. He showed how to benefit from competition. He and Steve Scott were great competitors in the same seafloor area of investigation. They often had different views, but their competition was always courteous, professional, and constructive. This gave those of us at a distance confidence that, if there were uncertainties, we were likely to hear of them. Jim's was a class act, and a continuing example to all of us.

4 Work remaining

Like the mythical tree that grows two chips from each one chopped, there is a great deal more to learn. An ongoing debate involves the degree to which ore metals are scavenged from the ocean crust or delivered by magmatic volatiles that mix into the hydrothermal system. How metals are extracted from the sub-crustal lithosphere, and even the asthenosphere, seems to me a particularly interesting subject for future cogitation.

Acknowledgements

I thank Mark Hannington and Jorge Manuel Rodrigues de Sancho Relvas for encouragement to submit this personal perspective. I apologize for its brevity and incompleteness. The extended abstract deadline caught me by surprise. I will try to cover more details in the presentation.

Insights on the formation of tin ores in the Neves Corvo Cu-Zn-Pb(-Sn) deposit, from in situ trace element analysis and O-isotopes of cassiterite

Marta S. Codeço[1,2], Sarah A. Gleeson[2,3], Jorge M.R.S. Relvas[4], Vitor Barrote[2,5], Maria R. Scicchitano[2], Franziska D.H. Wilke[2]
[1]Lowell Institute for Mineral Resources, Department of Geosciences, USA
[2]GFZ Helmholtz Centre for Geosciences, Germany
[3]iCRAG and University College Dublin, Ireland
[4]Instituto Dom Luiz, Faculdade de Ciências, Universidade de Lisboa, Portugal
[5]Paul Scherrer Institut (PSI), Switzerland

Abstract. The Neves Corvo Cu-Zn-Pb(-Sn) deposit (Portugal) is a world-class volcanic-hosted massive sulfide deposit that originally contained an early, structurally controlled high-grade tin mineralization (stockwork and massive cassiterite), which has now been mined out. We present a high-resolution multi-analytical study using a combination of petrography, high-resolution imaging and cathodoluminescence, mineral chemistry, and oxygen isotopes to understand the ore-forming processes and evolution of the tin mineralization at Neves Corvo. Our preliminary results show cassiterite has very complex micro-textures and zoning patterns that, combined with mineral chemistry and oxygen-isotope signatures, can provide unique insights into the evolution of the ore-forming system.

1 Introduction

Cassiterite (SnO_2), the most important tin ore mineral, can incorporate up to a few weight percent of Fe, Ti, Nb, Ta, and W and significant trace elements such as Al, Si, V, Co, Zr, Hf, U, and Pb (e.g., Gemmrich et al. 2021; Wang et al. 2022; Bennett et al. 2024). In addition, cassiterite has considerable internal heterogeneity, often displaying chemical and optical zoning suggestive of precipitation in an evolving and dynamic physicochemical environment (Bennett et al. 2024). Oxygen isotopes in cassiterite have also been used to track the source of mineralizing fluids and the thermal history of mineralization (e.g., Li et al. 2021). Cassiterite is thus a versatile mineral phase with great potential to decipher the nature and evolution of ore-forming systems (Hagemann et al. 2016).

Even though cassiterite is commonly associated with deposits linked to S-type, peraluminous granites in post-collisional settings, it has been described in a number of other settings, including sediment-hosted massive sulfides (Sullivan - Slack et al. 2020) and volcanic-hosted massive sulfides (VHMS) (e.g., Kidd Creek - Hennigh and Hutchinson 1999; and Neves Corvo - Relvas et al. 2006a).

Despite decades of investigation on cassiterite mineralization at Neves Corvo, its genesis remains enigmatic, with some authors proposing a magmatic-hydrothermal origin (e.g., Relvas et al. 2006b; Huston et al. 2011; Li et al. 2019) and others suggesting a hydrothermal origin from the leaching of underlying basement and host rocks (Tornos 2006).

In this study, we report new in-situ geochemistry and O-isotopes of cassiterite to understand the trace element distribution patterns, variations, zoning, and the sources of components. We combine O-isotopic composition data of cassiterite with co-coexisting quartz and apatite to constrain the thermal evolution of the tin mineralization at Neves Corvo.

2 Neves Corvo Deposit

Neves Corvo is a world-class VHMS deposit well known for its size, Cu-Zn grades, tonnages, and the occurrence of high-grade Sn mineralization. Its orebodies lie on the SW termination of the NW-SE trending-SW plunging Rosário-Neves Corvo anticline in the western part of the Iberian Pyrite Belt (Fig. 1).

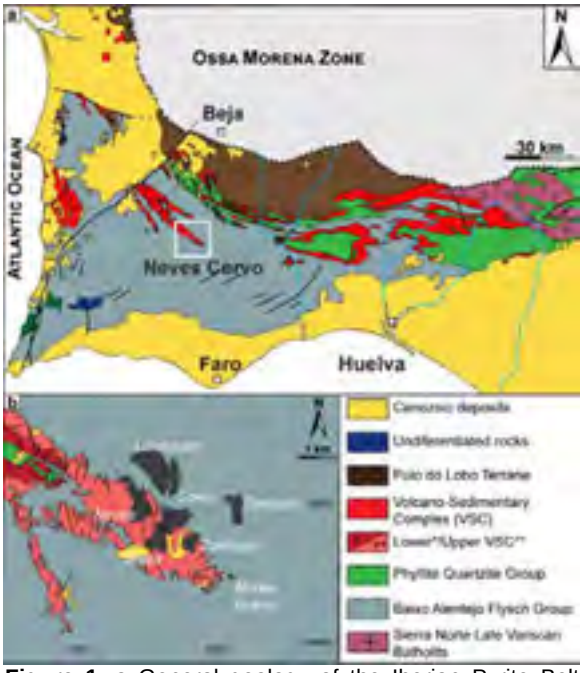


Figure 1. a General geology of the Iberian Pyrite Belt showing the location of Neves Corvo (white box) and other massive sulfide deposits. **b** Geological map of the Rosário-Neves Corvo anticline. Modified from Codeço et al. (2025) and references therein.

At Neves Corvo, two main types of mineralization are recognized: (1) stringer and massive tin mineralization and (2) stringer and massive sulfide mineralization (Relvas et al. 2006a). Tin ores are mostly primarily confined to an N-S-oriented, graben-bounding, syn-volcanic fault system in the western part of the Corvo orebody ("tin-corridor"). Tin and sulfide mineralization are associated with two spatially and temporally independent feeder systems and mineralizing episodes, with tin deposition predating [363–366 Ma, Li et al. (2019)] sulfide mineralization [ca. 358–363 Ma, Pereira et al (2004)].

Published stable isotope data (O- and H-isotopes) and radiogenic isotopes (Pb, Rb-Sr, Sm-Nd, and Re-Os systems) of host rocks and sulfide mineralization indicate signatures of multiple metal sources, with contributions from deep "external" source(s), possibly magmatic, in addition to the typical seawater-derived hydrothermal fluids (Marcoux 1997; Relvas et al. 2001; Munhá et al. 2005). The origin of this "external" source is still highly debated.

3 Analytical Methods

Chemical analyses of cassiterite were carried out using a JEOL Hyperprobe JXA-8530F+ electron microprobe at GFZ Potsdam. Trace elements were analyzed at the EleMap LA-ICP-MS Lab (GFZ Potsdam) using a Teledyne Analyte Excite, 193 nm ArF excimer laser coupled to a quadrupole-ICP-MS iCAP-RQ from Thermo Scientific. Oxygen isotopes of cassiterite, apatite, and quartz were acquired by SIMS using the CAMECA 1280-HR instrument at GFZ Potsdam. Cathodoluminescence (CL) images were acquired at the University of Arizona using a Gatan MonoCL4 panchromatic cathodoluminescence spectrometer on a JEOL 6010LA benchtop scanning electron microscope.

4 Petrography and CL imaging

Cassiterite is strongly zoned in both stockwork and massive tin ores, often showing irregular complex, concentric, and sector zoning. Under transmitted light, zoning varies between a pale yellow and an ash brown. Cassiterite crystals typically form subhedral to euhedral grains up to 3 mm, often displaying fine-scale growth features such as optically continuous lamellae, discordant embayment, and other discordant features. Due to the complexity of zoning and crystal growth, it is difficult to establish a clear pattern for zoning of the cassiterite grains from the tin stockwork, which display a range of internal textures, as revealed by CL. The most common texture is oscillatory zoning (Fig. 2a, b), which exhibits bands ranging in intensity from a bright CL response to black. Several grains show concentric zoning and secondary dissolution/reabsorption features (Fig. 2c, d). Some complex grains also show CL patches and sector zoning. In contrast, cassiterite crystals from the massive ores have no CL response.

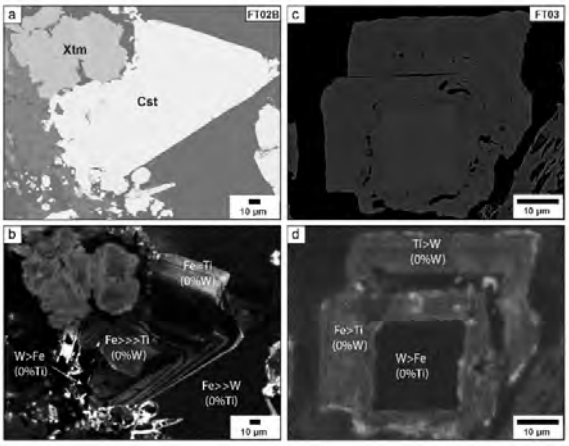


Figure 2. a and b Backscatter Electron (BSE) and CL image (respectively) of cassiterite showing fine scale oscillatory CL zoning. **c and d** BSE and CL images showing concentric zoning, as well as evidence for dissolution along zone boundaries.

5 Geochemistry

5.1 Mineral chemistry and trace element composition and variations

Cassiterite shows a relatively large compositional range for Sn (75-79 at.%) (Fig. 3), and minor W, Fe, and Ti have maximum concentrations of 1.8, 2.0, and 1.9 at.%, respectively (Fig. 3b, c). Tantalum and Nb concentrations are below the detection limit for EPMA. Thus, the main compositional variations are in Fe, W, and Ti contents; the massive cassiterite ores lack Ti (Fig. 3c). As shown in Fig. 3b, Fe and W concentrations are not correlated in half of the samples, suggesting that $(Fe^{2+} + Ti^{4+})_2 Sn^{4+}_{-3}$ exchange alone does not account for the observed variability, and therefore, $(Fe^{2+} + W^{6+})_2 Sn^{4+}_{-2}$ exchange may play an important role in cassiterite composition. Moreover, the absence of correlation between Fe and W may indicate that Fe enters the structure both as Fe^{2+} and Fe^{3+}. By plotting the log Fe/Sn vs. log W/Sn (Fig. 3d), it can be observed that some data plots along the W/Fe ratio of 0.5 indicating some excess of Fe and incorporation as Fe^{3+} into cassiterite (Möller et al. 1988).

Box plots of selected results from LA-ICP-MS are presented in Fig. 4. Cassiterite contains variable but relatively high Fe, Ti, and W (>100 to >1000 µg/g), moderate contents (10-100s µg/g) of Sc, V, Co, Ni, Ga, Sb, and In and low REEs, Y, and Hf (<1 µg/g). Particularly interesting are the relatively higher concentrations of Ga, In, and Sb in cassiterites from the massive ores compared to the stockwork ores. In contrast, stockwork tin ores have higher Sc, V, Zr, Nb, and Ta than massive ores.

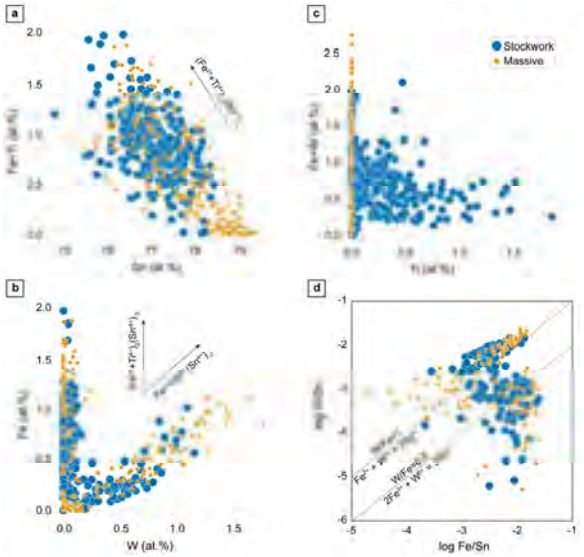


Figure 3. Binary plots for EPMA data showing: **a** Sn vs. Fe+Ti, **b** W vs. Fe, **c** Ti vs. Fe+W, (in atomic %) and **d** log Fe/Sn vs. log W/Sn (Möller et al. 1988). Exchange vectors are indicated by arrows.

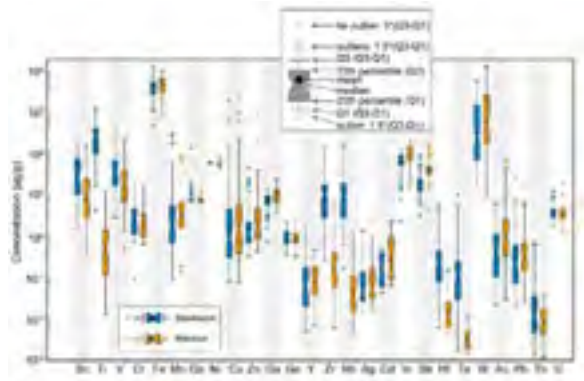


Figure 4. Box and whisker plot of selected cassiterite minor and trace element LA-ICP-MS analyses.

Variations in CL response are due essentially to variations on the amount of Ti and W, which act as activators, and Fe, which acts as a quencher, but it may also reflect, although less clearly, the trace contents of Sb, Nb, Ta, Ga, U, V and Al (Bennett et al. 2020). In grains displaying concentric or oscillatory zoning within the stockwork, there is a tendency for the dark CL zone to be enriched in Fe, V, Sc, Ga, Sb, and In, whereas lighter zones tend to be enriched in Ti. Tungsten contents are variable, and no pattern has been observed. Our preliminary results suggest that higher Fe, Ga, and Sb contents typically correlate with the darker zones, thus suggesting that these elements may act as quenchers. This is also consistent with the fact that cassiterite from the massive ores has no CL response and yields the highest Ga and Sb.

5.2 Oxygen Isotopic composition and thermal evolution

The $\delta^{18}O$ values of cassiterite from the stringer and massive ores range from -5.8 to +0.7‰ (n=103) and -7.7 to +2.0 (n=102), respectively. Quartz coexisting with cassiterite within the stockwork yielded $\delta^{18}O$ values between 12.2 and 15.2‰ (n=25), whereas quartz from massive ores had a narrow range from 14.8 to 15.4‰ (n=6). In contrast, apatite, which only occurs within the tin stockwork, varies between 5.9 and 8.9‰ (n=36).

Using the cassiterite-quartz O-isotope exchange geothermometer of Li et al. (2022) we estimated the temperature of cassiterite and quartz formation within the stockwork and massive ores and calculated the fluid composition (Fig. 5). The results show that stockwork mineralization formed in the interval of 225-300°C, whereas the massive cassiterite formed at 150-200°C, which indicates temperature ranges very close to, but slightly higher, than the ones previously obtained by (Relvas et al. 2006b) from cassiterite-quartz separates.

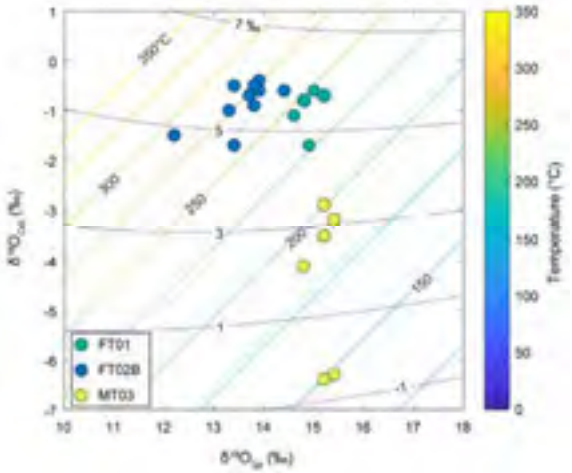


Figure 5. Temperature and $\delta^{18}O_{fluid}$ values were calculated from cassiterite-quartz pairs using the fractionation factors of Li et al. (2022 and references therein). Samples FT01 and FT02B are from stockwork and sample MT03 is from massive cassiterite ores. Solid blue lines are isotherms, and dashed lines are isopleths of $\delta^{18}O_{fluid}$ values.

Calculated $\delta^{18}O_{fluid}$ compositions yielded by pairs formed within the massive mineralization vary between -1 and 3‰, similar to the results of Relvas et al. (2006b), whereas the $\delta^{18}O_{fluid}$ values estimated from cassiterite-quartz pairs from the stockwork mineralization are moderately higher, between 5 to 6‰. The latter may be compatible with the circulation of a seawater-dominated fluid equilibrated with the footwall sequence under rock-dominated conditions. However, independently of the origin of the tin-bearing fluid – either magmatic or leached by a much-evolved seawater-derived fluid, given the extreme insolubility of tin – the expected $\delta^{18}O$ composition of the tin-bearing fluid would be significantly heavier, close to 10‰, or higher. Therefore, the moderate $\delta^{18}O_{fluid}$ compositions obtained from stringer cassiterite in the upper part of the sequence and the increasingly lower compositions yielded by massive cassiterite formed by direct venting on the seafloor likely reflect

progressive mixing between a hotter heavy tin-bearing fluid and cooler unmodified seawater.

6 Final Remarks

Our results show that cassiterite microtextures at Neves Corvo are complex and provide important information about its formation conditions. Mineral chemistry, particularly redox-sensitive elements like Fe, suggests tin ores formed under changing redox conditions.

Further geochemical modelling is needed to fully understand the evolution of the system. As pointed out by Relvas et al. (2006a, b), the unique mode of occurrence of the Neves Corvo cassiterite ores – minable blocks with hundreds of tons of almost pure, very fine-grained cassiterite - requires a remarkably efficient precipitation mechanism associated with huge and brusque thermal and chemical gradients. This is consistent with our data, which argues for a massive cassiterite precipitating mechanism dominated by the disproportional mixing of the tin-bearing fluid with unmodified seawater through direct venting onto or near the seafloor. Concerning the tin source, the oxygen-isotopic composition of cassiterite may thereby be of limited significance. However, the inferences allowed by its signatures revealed to be of prime importance to understanding the tin ore-forming processes in Neves Corvo.

Acknowledgements

This study was financed by the Dynamics of Ore Metal Enrichment (DOME) SPP, German Research Foundation (DFG, GL945/1–1), and the Portuguese *Fundação para a Ciência e Tecnologia* (FCT)*, I.P./MCTES* through national funds (PIDDAC): UID/50019/2025 and LA/P/0068/2020 (https://doi.org/10.54499/LA/P/0068/2020).

References

Bennett JM, Kemp AIS, Hagemann SG, et al (2024) Systematic trends in the substitution mechanisms of minor elements in cassiterite. Australian Journal of Earth Sciences

Bennett JM, Kemp AIS, Roberts MP (2020) Microstructural controls on the chemical heterogeneity of cassiterite revealed by cathodoluminescence and elemental X-ray mapping. American Mineralogist 105:58–76. https://doi.org/10.2138/am-2020-6964

Codeço MS, Gleeson SA, Barrote V, et al (2025) Textural, mineralogical, and geochemical evidence for apatite metasomatism and REE mobility within the Corvo orebody at the Neves Corvo Cu-Zn-Pb(-Sn) deposit (Iberian Pyrite Belt). Miner Deposita. https://doi.org/10.1007/s00126-025-01348-w

Gemmrich L, Torró L, Melgarejo JC, et al (2021) Trace element composition and U-Pb ages of cassiterite from the Bolivian tin belt. Mineralium Deposita 56:1491–1520. https://doi.org/10.1007/s00126-020-01030-3

Hagemann SG, Lisitsin VA, Huston DL (2016) Mineral system analysis: Quo vadis. Ore Geology Reviews 76:504–522. https://doi.org/10.1016/j.oregeorev.2015.12.012

Hennigh Q, Hutchinson RW (1999) Cassiterite at Kidd Creek: An Example of Volcanogenic Massive Sulfide-Hosted Tin Mineralization. In: Hannington MD, Barrie CT (eds) The Giant Kidd Creek Volcanogenic Massive Sulfide Deposit, Western Abitibi Subprovince, Canada. Society of Economic Geologists, p 0

Huston DL, Relvas JMRS, Gemmell JB, Drieberg S (2011) The role of granites in volcanic-hosted massive sulphide ore-forming systems: An assessment of magmatic-hydrothermal contributions. Mineralium Deposita 46:473–507. https://doi.org/10.1007/s00126-010-0322-7

Li X, Zhao K-D, Jiang S-Y, Palmer MR (2019) In-situ U-Pb geochronology and sulfur isotopes constrain the metallogenesis of the giant Neves Corvo deposit, Iberian Pyrite Belt. Ore Geology Reviews 105:223–235. https://doi.org/10.1016/j.oregeorev.2018.12.023

Li Y, He S, Zhang R-Q, et al (2022) Cassiterite oxygen isotopes in magmatic-hydrothermal systems: in situ microanalysis, fractionation factor, and applications. Miner Deposita 57:643–661. https://doi.org/10.1007/s00126-021-01068-x

Li Y, Tang GQ, Liu Y, et al (2021) Revisiting apatite SIMS oxygen isotope analysis and Qinghu-AP reference material. Chemical Geology 582:120445. https://doi.org/10.1016/j.chemgeo.2021.120445

Marcoux E (1997) Lead isotope systematics of the giant massive sulphide deposits in the Iberian Pyrite Belt. Mineralium Deposita 33:45–58. https://doi.org/10.1007/s001260050132

Möller P, Dulski P, Szacki W, et al (1988) Substitution of tin in cassiterite by tantalum, niobium, tungsten, iron and manganese. Geochimica et Cosmochimica Acta 52:1497–1503. https://doi.org/10.1016/0016-7037(88)90220-7

Munhá J, Relvas JMRS, Barriga FJAS, et al (2005) Osmium isotope systematics in the Iberian Pyrite Belt. Mineral Deposit Research: Meeting the Global Challenge 663–666. https://doi.org/10.1007/3-540-27946-6_169

Pereira, Z., Pacheco N, Oliveira, J. T. (2004) A case applied palynology: dating the lithological succession of the Neves Corvo mine, Iberian Pyrite Belt, Portugal. In: Proceedings of the XVth ICCP Stratigraphy. Academy Arts and Sciences, pp 345–354

Relvas JMRS, Barriga FJAS, Ferreira A, et al (2006a) Hydrothermal Alteration and Mineralization in the Neves-Corvo Volcanic-Hosted Massive Sulfide Deposit, Portugal. I. Geology, Mineralogy, and Geochemistry. Economic Geology 101:753–790. https://doi.org/10.2113/gsecongeo.101.4.753

Relvas JMRS, Barriga FJAS, Longstaffe FJ (2006b) Hydrothermal Alteration and Mineralization in the Neves-Corvo Volcanic-Hosted Massive Sulfide Deposit, Portugal. II. Oxygen, Hydrogen, and Carbon Isotopes. Economic Geology 101:791–804. https://doi.org/10.2113/gsecongeo.101.4.791

Relvas JMRS, Tassinari CC, Munhá J, Barriga FJ (2001) Multiple sources for ore-forming fluids in the Neves Corvo VHMS deposit of the Iberian Pyrite Belt (Portugal): Strontium, neodymium and lead isotope evidence. Mineralium Deposita 36:416–427. https://doi.org/10.1007/s001260100168

Slack JF, Neymark LA, Moscati RJ, et al (2020) Origin of tin mineralization in the Sullivan Pb-Zn-Ag deposit, British Columbia: Constraints from textures, geochemistry, and LA-ICP-MS U-pb geochronology of cassiterite. Economic Geology 115:1699–1724. https://doi.org/10.5382/ECONGEO.4761

Tornos F (2006) Environment of formation and styles of volcanogenic massive sulfides: The Iberian Pyrite Belt. Ore Geology Reviews 28:259–307. https://doi.org/10.1016/j.oregeorev.2004.12.005

Wang C, Zhao K-D, Chen J, Ma X (2022) Examining fingerprint trace elements in cassiterite: Implications for primary tin deposit exploration. Ore Geology Reviews 149:105082. https://doi.org/10.1016/j.oregeorev.2022.105082

New geochemical and Sr-Nd data from Lower Cryogenian arc volcanic rocks of Tichibanine Ben-Lagrad Group (Bou-Azzer, Central Anti-Atlas, Morocco): Constraints on petrogenesis and geodynamic context

Ali El-masoudy[1], Abdeslam Toummite[1], Moha Ikenne[2], Said Ilmen[3], Yassine Lmahfoudi[4], Laurent Sapor[4], Lhou Maacha[4], Mohamed Zouhair[4], Yassine Lmahfoudi[4], Marieme Jabbour[2], Stanislav Zverev[5].

[1] Research team: Applied Geology and Remote Sensing, Moulay Ismail University of Meknes, Faculty of Sciences and Techniques, BP 509, Errachidia Boutalamine, 52000, Morocco
[2] Laboratory of Applied Geology and Geo-Environment (LAGAGE) Department of Geology, Faculty of Sciences. B.P 8106, Dakhla city, 80 000 Agadir, Morocco.
[3] Polydisciplinary Faculty of Ouarzazatate, Ibn Zohr University, Ouarzazate, Morocco.
[4] MANAGEM Group, Twin Center, Tour A, BP 5199, Casablanca. Morocco.
[5] Sobolev institute of Geology and Mineralogy, Siberian Branch of the Russian Academy of Science, Russia

Abstract. In this study, we present new whole-rock chemistry and isotopic data (Sr-Nd) for Neoproterozoic volcanic rocks from the Bou-Azzer inlier (Anti-Atlas, Morocco), aiming to understand their petrogenesis and geodynamic context in relation to the Anti-Atlas Pan-African orogeny. The volcanic rocks, aged at 767 Ma, range from basalt to rhyolite and show varying degrees of differentiation, including volcanoclastic components. These rocks display tholeiitic characteristics with low to medium K, LREE, and LILE enrichment, and Nb-Ta depletion. The low (87Sr/86Sr) ratios (~0.703) and positive εNd(t) values (+4) suggest a depleted mantle source, while negative εNd(t) values in two samples indicate moderate continental crust influence. The TDM model ages, although imprecise, fall into two ranges: 1400-1000 Ma (Mesoproterozoic mantle dynamics) and 1900-1600 Ma (Paleoproterozoic activity), with the latter corresponding to granite intrusions in the western Anti-Atlas. Evidence for this activity is also seen in the eastern Anti-Atlas through inherited zircons and isotopic compositions of granitoids. Geochemical analyses show that fractional crystallization primarily controls the volcanic series evolution, with minor crustal contamination in an arc context. These magmatic events, dated to 761 ± 7 Ma and 767 ± 7 Ma, align with major episodes across various cratons during the Rodinia breakup, linked to continental rifting and large igneous province formation.

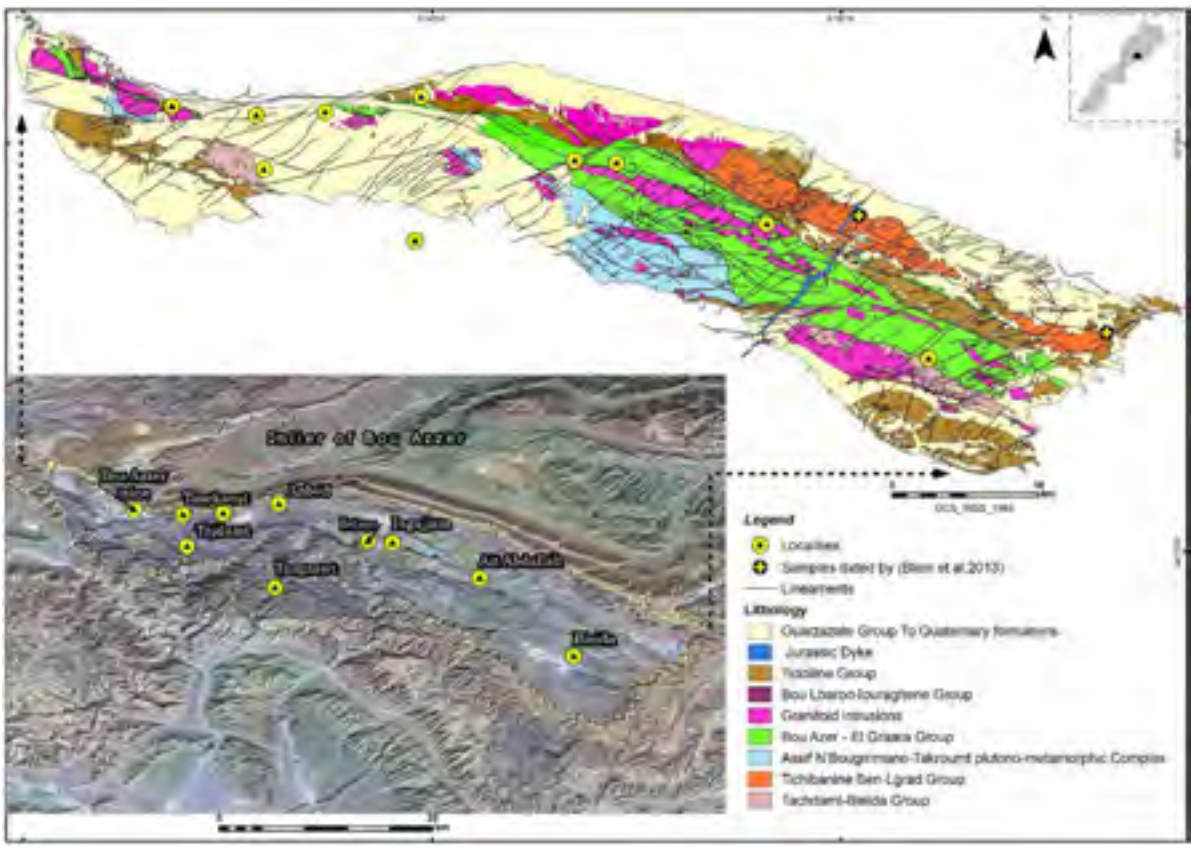


Figure. 1 Geological map of the Bou-Azzer inlier, showing the location of the studied volcanic group of TBL. Constructed from the geological maps (1/50.000) of Bou-Azzer, Alougoum, Ait Semgane, Ait Hmane, Al Gloa (Admou et al. 2013; Soulaimani et al. 2013a, b; Blein et al. 2013, 2013b, 2013c; Yazidi et al. 2007). At the bottom left, the localities are projected on image Landsat multispectral composition.

1. Geologic Context

The Bou-Azzer inlier, located in the eastern part of the central Anti-Atlas, is known for its well-exposed ophiolitic complex and significant mineralization in cobalt and nickel linked to serpentinized ultramafic rocks, as well as copper and gold deposits. The Proterozoic terrains in the inlier range from the Early Cryogenian to the Late Ediacaran (Choubert 1963, Leblanc 1981) (Fig. 1)

The oldest terrains are found in the southern part of the inlier and include the Tachdamt-Bleida formation, the Tazegzaout-Assif N'Bougmane unit, and the Oumlil granite, with recent U/Pb geochronological ages of 883 Ma for the Tachdamt formation and 697.1 ± 2.2 Ma for the Bleida formation (Blein et al. 2014, Ikenne et al. 2023). The Bou-Azzer ophiolitic complex, including serpentinized peridotites and stratified gabbros, was dated to 759 ± 2 Ma (Hodel et al. 2020).

Geochemical links between the Bou-Azzer and Siroua ophiolites suggest contemporaneous formation under a back-arc spreading regime (Ikenne et al. 2023).

The Ediacaran period in the Bou-Azzer inlier is represented by the Tiddiline Group (dated to 606 ± 5 Ma) and the Ouarzazate Group (567 ± 5 Ma) (Blein et al. 2014). A geotectonic model proposes three main stages: 1) formation of back-arc basins (770-760 Ma), 2) subduction and restoration of back-arc lithosphere (755-695 Ma), and 3) collision with the Tasriwine-Tichibanine Arc (770-760 Ma) (Blein et al. 2014).

2. Results

2.1 Field and petrographic data

The Tichibanine Ben-Lagrad Group (TBL), located on the northeastern flank of the Bou-Azzer inlier, consists of volcanic and detrital components, ranging from mafic to felsic rocks, with lava flows varying in thickness. The series is interrupted by dolerite dyke swarms and quartz and carbonate veins containing iron oxides and copper. It is divided into three formations: the Ousdrate formation (deep turbidites), the Ait Abdellah-Tichibanine formation (volcano-sedimentary deposits), and the Tanaldat-Ben-Lagrad formation (submarine eruptions). Tectonic evolution involved basin collapses and the formation of normal faults.

Petrographic analysis of 38 thin sections reveals basalts, andesites, rhyolites, dacites, and dacitic tuffs, many affected by hydrothermal alteration and low-grade metamorphism, but preserving primary igneous textures in some cases (Fig. 2). The rocks are microlitic or porphyritic with phenocrysts of feldspar, quartz, and plagioclase, often replaced by secondary minerals like epidote, chlorite, and iron oxides.

Basalts and basaltic andesites exhibit massive or pillow-shaped lavas, andesites show porphyritic textures with plagioclase and pyroxene relics, while dacitic to rhyolitic units have porphyritic textures with mylonitized structures, and pyroclastic levels contain tuffs and ash-tuffs with lithic clasts (Fig. 2).

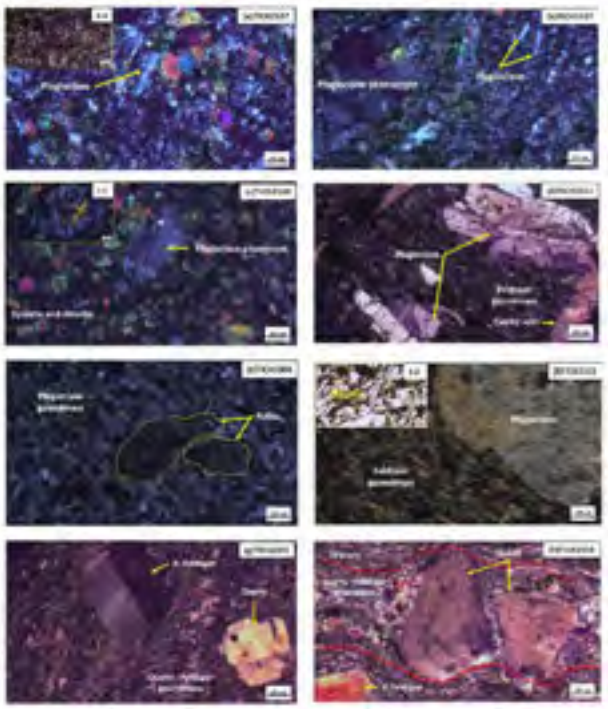


Figure 2. Representative photomicrographs of the TBL volcanic rocks. (a) Aphanitic porphyry-microlitic texture in basalt (a-a): Development of epidotization and chloritization in basalt; (b) porphyry-microlitic texture in basalt;(c) porphyritic texture in basalt (c-c): Alteration of plagioclase to epidote); (d) porphyritic andesite; (e) microlitic porphyritic andesite; (f) fluidal trachytic texture in trachy-andesite (f-f): chlorite inter microlites of feldspar; (g) porphytic texture in rhyodacite; (h) Effect of schistosity S1 in rhyodacite; (i) andesitic tuff; (j) Dacitic tuff.

2.2 Major, trace element and Sr-Nd compositions

Whole-rock major, trace element and Sr-Nd compositions were determined for twenty-one representative samples from different volcanic units, which were prepared and analyzed at the Analytical Center of the SB RAS Institute of Geology and Mineralogy (Novosibirsk, Russia).

The volcanic rocks of the TBL Group show Loss on Ignition (LOI) values ranging from 1.03% to 5.64%, indicating the presence of minerals like chlorite, serpentinite, clays, and carbonates, with no primary hydrous phases identified. The chemical compositions were recalculated by subtracting the LOI values. Based on the (Na_2O + K_2O) vs SiO_2 classification diagram (LeBas et al. 1986), the rocks range from basalts to rhyolites, with SiO_2 contents between 46.10 and 82.38 wt% (Fig. 3a). The variation in compositions is consistent with previous studies (Admou et al. 2012; Tekiout et al. 1991).

Elemental contents include Al_2O_3 (8.59-19.66 wt%), Fe_2O_3T (1.49-14.08 wt%), MgO (0.29-5.27 wt%), CaO (0.53-14.70 wt%), and TiO_2 (0.26-1.24 wt%), with negative correlations between these elements and SiO_2. This pattern suggests fractional crystallization involving minerals such as olivine and clinopyroxene, with Cr and Ni contents decreasing from basalts to rhyolites.

In terms of trace elements, basalts and basaltic andesites show low rare earth element (REE) content but are enriched in light rare earth elements (LREE), with moderate Eu anomalies. The $(La/Sm)_{CN}$, $(La/Yb)_{CN}$, and $(Gd/Yb)_{CN}$ values indicate slight LREE enrichment and flat trends for heavy rare earth elements (HREE).

The mantle-normalized trace element diagram reveals enrichments in Pb and Sr, and depletions in Nb, Ta, Zr, Hf, and Ti. Dacitic tuffs show similar REE trends, with one sample displaying pronounced LREE/HREE fractionation.

In the spider diagram, the samples show slight Pb enrichment and depletion in high-field-strength elements (HFSE) like Nb, Ta, and Hf, with variable Sr anomalies. The K_2O vs SiO_2 diagram classifies the rocks as a low-to-medium K series, exhibiting a tholeiitic signature (Fig. 3b). The REE patterns are nearly flat, further supporting this classification.

Most of initial ratios ($^{87}Sr/^{86}Sr$)i are close to 0.703, excluding those with elevated Rb concentrations, and the εNd(t) values predominantly show positive values around +4 (Fig. 4).

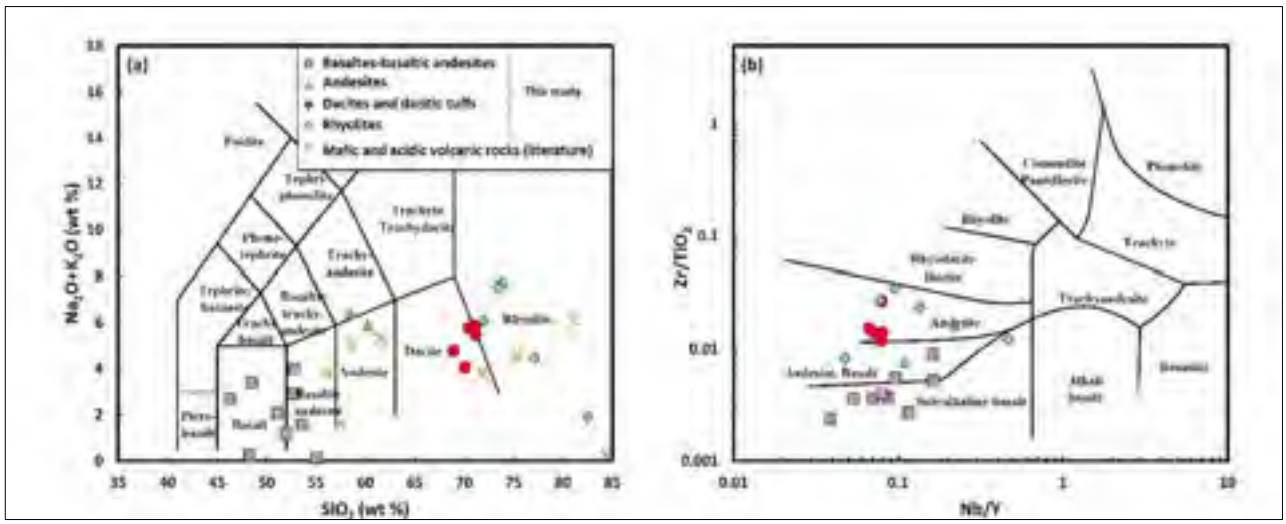


Figure 3. (a) SiO_2 versus Na_2O + K_2O (TAS) classification diagram (LeBas. 1986); (b) K_2O vs. SiO_2 diagram; All major elements are re-calculated on a volatile-free basis. Data sources: basic to felsic volcanic rocks (literature) from Tichibanine Ben-Lagrad Group (Admou et al. 2013)

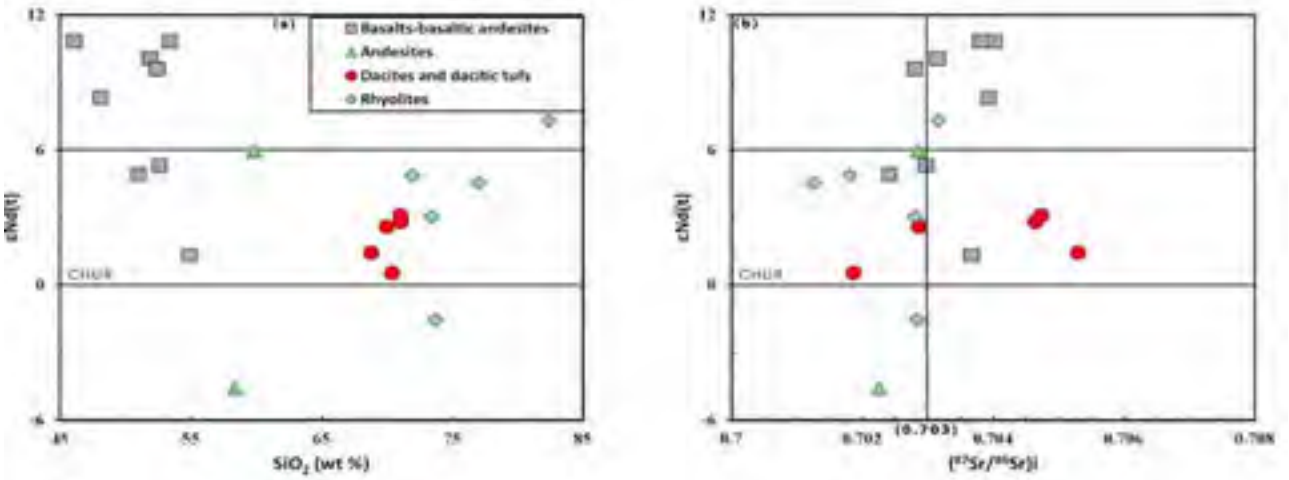


Figure 4. εNd vs SiO_2 diagram for the volcanic rocks of the TBL. (b). εNd vs $^{87}Sr/^{86}Sr$ at 762 Ma diagram for the volcanic rocks of the TBL.

3. Conclusions

The key conclusions for this study are as follows:

The TBL Group volcanic rocks range from basalt to rhyolite, are predominantly pyroclastic, and are crosscut by dolerite dykes linked to Ouarzazate volcanic activity. Greenschist facies metamorphism has significantly altered their chemical compositions, affecting the mobility of major elements, LILEs, and some REEs.

These volcanic rocks formed around 767 Ma in an intra-oceanic volcanic arc setting, characterized by a low-K tholeiitic affinity, LREE and LILE enrichment, and Nb-Ta depletion. Their ages (761–767 Ma) align with those of the Bou-Azzer and Tasriwine ophiolitic complexes, indicating magmatic activity in a supra-subduction zone. This was followed by intense plutonism between 660–640 Ma, shaping the regional tectonic evolution.

Sr and Nd isotopic data show a juvenile mantle source with positive εNd values (~+4) and low Sr isotopic ratios (~0.703).

TDM model ages fall into two main ranges: 1400–1000 Ma, associated with Mesoproterozoic mantle dynamics, and 1900–1600 Ma, linked to Paleoproterozoic activity. The latter coincides with granite intrusions in the western Anti-Atlas and inherited zircons in the Eastern Anti-Atlas.

The magmatic activity of the TBL Group aligns with significant magmatic episodes in the Greater Congo, Tarim, and Arabian-Nubian Shields. These events, occurring during the Rodinia breakup, indicate widespread magmatism related to continental rifting and the formation of Large Igneous Provinces (LIPs).

References

Admou H, Fekkak A, Razin P, Egal E, Youbi N, Soulaimani A, Blein O, Baudin T, Chevremont P (2012) Carte géologique Maroc (1/50 000), feuille d'Aït Ahmane – Notes et Mémoires Service Géologique Maroc, no. 533.

Ait Lahna A, Youbi N, Tassinari CCG, Basei MAS, Ernst RE, Chaib L, Barzouk A, Mata J, Gärtner A, Admou H, Boumehdi MA, Söderlund U, Bensalah MK, Bodinier JL, Maacha L, Bekker A (2020) Revised stratigraphic framework for the lower Anti-Atlas Supergroup based on U–Pb geochronology of magmatic and detrital zircons (Zenaga and Bou-Azzer-El Graara inliers, Anti-Atlas Belt, Morocco). Jour African Earth Sci 171:103946. https://doi.org/10.1016/j.jafrearsci.2020.103946.

Blein O, Baudin T, Chèvremont P, Soulaimani A, Admou H, Gasquet P, Cocherie A, Egal E, Youbi N, Razin P, Bouabdelli M, Gombert P (2014b) Geochronological constraints on the polycyclic magmatism in the Bou-Azzer-El Graara inlier (Central Anti-Atlas Morocco). Jour African Earth Sci 99:287–306. https://doi.org/10.1016/j.jafrearsci.2014.04.021.

Choubert G (1963) Histoire géologique du Précambrien de l'anti-Atlas de l'Archéen à l'aurore des temps primaires. Notes et Mémoires du Service Géologique du Maroc 162:352.

D'Lemos RS, Inglis JD, Samson SD (2006a) A newly discovered orogenic event in Morocco : Neoproterozoic ages for supposed Eburnean basement of the Bou-Azzer inlier, Anti-Atlas Mountains. Precambrian Research 147: 65–78. https://doi.org/10.1016/j.precamres.2006.02.003.

El Bahat A, Ikenne M, Söderlund U, Cousens B, Youbi N, Ernst R, Soulaimani A, El Janati M, Hafid A (2013) U–Pb baddeleyite ages and geochemistry of dolerite dykes in the Bas Drâa Inlier of the Anti-Atlas of Morocco: Newly identified 1380 Ma event in the West African Craton. Lithos:174:85–98. https://doi.org/10.1016/j.lithos.2012.07.022.

El Hadi H, Simancas JF, Martínez-Poyatos D, Azor A, Tahiri A, Montero P, Fanning CM, Bea F, González-Lodeiro F (2010a) Structural and geochronological constraints on the evolution of the Bou-Azzer Neoproterozoic ophiolite (Anti-Atlas, Morocco). Precambrian Res 182:1–14. https://doi.org/10.1016/j.precamres.2010.06.011.

Hodel F, Triantafyllou A, Berger J, Macouin M, Baele JM, Mattielli N, Monnier C, Trindade RIF, Ducea MN, Chatir A, Ennih N, Langlade J, Poujol M (2020) The Moroccan Anti-Atlas ophiolites: Timing and melting processes in an intra-oceanic arc-back-arc environment. Gondwana Res 86:182–202. https://doi.org/10.1016/j.gr.2020.05.014.

Ikenne M (1997) La boutonnière précambrienne de Bas Drâa (Anti-Atlas Occidental, Maroc): caractérisation pétrologique et géochimique des roches magmatiques et métamorphiques et leur relation avec la déformation. Univ. Ibn Zohr University, Agadir, Morocco, p. 259. Unpub thesis (Thèse d'état).

Ikenne M, Souhassou M, Arai S, Soulaimani A (2017) A historical overview of Moroccan magmatic events along northwest edge of the West African Craton. Jour of Afr Earth Sci 127:3–15. https://doi.org/10.1016/j.jafrearsci.2016.10.002.

Le Bas MJ, Le Maitre RW, Streckeisen A, Zanettin B (1986) A chemical classification of volcanic rocks based on the total alkali-silica diagram. J Petrol 27:745–750.

Leblanc M (1976) Proterozoic oceanic crust at Bou-Azzer. Nature 261:34–35.

Leblanc M (1981) The late Proterozoic ophiolites of Bou-Azzer (Morocco): evidence for Panafrican plate tectonics. In: Kroner, A. (Ed.), Precambrian Plate Tectonics. Elsevier, Amsterdam, pp. 435–451.

Saquaque A, Admou H, Cisse A, Benyoussef A, Reuber I (1989) Les intrusions calco-alcalines de la boutonnière de Bou Azzer-El Graara (Anti-Atlas) : marqueurs de la déformation panafricaine majeure dans un contexte de collision d'arc. Comptes Rendus de l'Académie des Sciences Paris 308:1279–1283.

Tekioute B (1991) Stratigraphie, pétrographie, géochimie et structure arc/avant-arc de la boutonnière de Bou-Azzer El Graara (Unité Nord), Anti-Atlas, Maroc. Unpublished Thesis, Marrakech, Morocco, p. 151p.

Youbi N, Söderlund U, Ernst RE, Ait Malek M, Barzouk A, Ait Lahna A, Palassia M, Gong Z, Evans D, Wen B, Jing XQ, Boumehdi MA, Ikenne M, Bensalah MK, Admou H, Bajddi A, Maacha L (2019) Ca. 1.65 Ga mafic sills emplaced into the quartzite of Jbel Lkest from Kerdous Inlier, Anti-Atlas, West African craton, Morocco: additional evidence that the basal part of Taghdout group is nearly 1 Ga older than previously thought. In: The 7 International Science Conference Abstracts, p. 165. Tomsk.

The mid-Cretaceous VMS belt in the Peruvian coast.

Lluís Fontboté[1], Massimo Chiaradia[1], Jorge E. Spangenberg[2], Irena Peytcheva[3]
[1]Department of Earth Sciences, University of Geneva, Switzerland
[2]Institute of Earth Surface Dynamics, University of Lausanne, Lausanne, Switzerland
[3]Geological Institute, Bulgarian Academy of Sciences, 1113 Sofia, Bulgaria

Abstract. A VMS belt linked to submarine volcanism of calc-alkaline affinity, suggesting a subduction-related arc setting, occurs in the northern and central Peruvian coastal region. Recent U-Pb zircon ages from deposits of this belt indicate that all the known deposits in the belt have a mid-Cretaceous age. The location of the main mineralization centers is structurally controlled, probably by oblique subduction. Pb, Nd, and Sr isotope signatures of ore and volcanic host rocks, suggest a mantle source with contributions from old continental crustal material during subduction. Ages of inherited zircons support the presence of old continental crust beneath the belt. Available data indicate that the deposits formed mainly below the seafloor through the mixing of hydrothermal fluids of magmatic origin with ocean water.

1 Introduction

A VMS belt hosted in volcano-sedimentary sequences of mid-Cretaceous age stretches between Tambogrande, located in the northernmost part of the Peruvian Coast, to 170 km south of Lima. From north to south, it includes (i) the Tambogrande Cu-Zn-Au VMS deposit in the Lancones basin and (ii) the deposits of Maria Teresa (Zn-Pb-Ag-Cu-Ba), Aurora Augusta (Ba-Zn-Pb-Cu), Perubar (Zn-Pb-Ba, Palma (Zn-Pb-Ba), Balducho (Zn-Pb-Ag) and Cerro Lindo (Cu-Zn-Pb) in the Cretaceous Casma Group in Central Perú (León, 2023). Numerous other VMS occurrences occur in the belt. Recent exploration successes (e.g., Farfán et al. 2019, Pichardo et al. 2019) suggest that the belt is underexplored. Table 1 summarizes the key characteristics of selected deposits with references to relevant publications.

The deposits of the belt show strong similarities. They occur mainly in submarine sequences dominated by bimodal (sub-)volcanic rocks with calc-alkaline affinity (at Tambogrande, tholeiitic basalts are also identified) with variable participation of pelitic and less abundant carbonate rocks. Two host rock end members are distinguished. The Maria Teresa and Cerro Lindo deposits are emplaced exclusively in (sub-)volcanic rocks whereas at Palma and Perubar sedimentary rocks are predominant. This disparity in the host rock lithology correlates with differences in ore body morphology and hydrothermal alteration. At Perubar and Palma, mineralization replaces favorable sedimentary beds, forming "mantos" extending for several hundreds of meters, and weak sericitic alteration is only identified near feeders. In contrast, at Maria Teresa and Cerro Lindo, the ore bodies show elongated, partly upright irregular shapes and are either accompanied by or lying on top of intense sericitic alteration (Ishikava et al. 1976; AI index up to over 90). In the latter deposits, smaller "mantos" also occur, mainly replacing volcaniclastic horizons, including autobreccias and hyaloclastites.

In this contribution we focus on (i) the age of the deposits, which necessitates a reassessment of previously published ages and interpretations (Fontboté, 2019) using new data; (ii) the geometry of ore bodies and feeders that suggests a strong structural control, and (iii) evidence pointing to an essentially magmatic origin of the hydrothermal fluids forming the VMS deposits of the belt.

2 Age of the VMS deposits

Zircon U-Pb ages of the host rock are now available for the deposits of Tambo Grande (104.8±1.3 to 100.2±0.5 Ma on lavas directly underlying the massive sulfides, Winter et al., 2010), Maria Teresa (101.7±1.6 Ma on a dacitic dike affected by intense sericitic alteration, i.e., most likely syn-mineralization, Fig. 2), Palma (108±2.8 Ma and 101±5.3 Ma in crosscutting dikes, Choquehuanca 2020), and Cerro Lindo (105.7 and 106.9 Ma±0.2 in host rhyolite, Bueno, 2019). These ages indicate that the four deposits were formed between approximately 111 and 100 Ma. According to K-Ar ages in sericite (116±18, 106±17Ma, Vidal 1987), Aurora Augusta would also be of mid-Cretaceous age.

The only zircon U-Pb ages outside this time range are those for the Perubar deposit. There, Polliand et al. (2005) obtained high-resolution zircon U-Pb ages of 69.71±0.18 Ma, and 68.92±0.16 for a "felsic volcanic tuff" and a "rhyolitic lava", respectively, interpreted to be syn-mineralization. Considering that the same host volcano-sedimentary sequence has been dated by Choquehuanca (2020) as older than 101 ± 5.3 Ma (zircon U-Pb) at the Palma deposit, located 16 km to the south, the uppermost Cretaceous ages obtained at Perubar can be questioned. It is unlikely that the host rock of the two VMS deposits located at such a short distance and occurring basically in the same sequence, would have a 30 My age difference. It is more likely that the "felsic volcanic tuff" and "rhyolitic lava" dated at Perubar were misinterpreted and were not effusive rocks but fine-grained facies of felsic sills and dikes. This hypothesis is also supported by the occurrence at Perubar of crosscutting, post-mineralization rhyodacitic dikes dated (zircon U-Pb) by Polliand et al. (2005) at 67.91±0.17 Ma, an age indistinguishable from that of a large quartz monzonitic (67.89±18 Ma) intrusion cutting the volcano-sedimentary sequence and only slightly younger than the age of the supposed effusive

Table 1. Key characteristics of selected deposits of the "mid" Cretaceous VMS belt in the Peruvian coastal region

Deposits N to S	Resource	Main host rock	Acidic alteration in footwall	Age	References[1]
Tambogrande	109 Mt 1.6% Cu, 1.0% Zn, 0.5 g/t Au, 22 g/t Ag; 16.7 Mt 3.5 g/t Au and 64 g/t Ag in oxide ore; TG3 deposit: 82 Mt 1.0% Cu, 1.4% Zn, 0.8 g/t Au, and 25 g/t Ag	Submarine mafic and felsic volcanic rocks, partly volcaniclastic. Calcalkaline and tholeiitic affinity	Moderate sericitic alteration	104.8 ± 1.3 to 100.2 ± 0.5, zircon U-Pb zircon, felsic volcaniclastic rocks directly underlying the massive sulfides	Winter (2008), Winter et al. (2010)*
Maria Teresa	>18 Mt including 9.5 Mt with 7.4% Zn, 0.5% Cu, 1.4% Pb, 4.0 oz Ag/t and 8.7 Mt with 6.2% Zn, 1.1% Cu, 0.7% Pb, 24 g/t Ag. Operation started in massive barite	Submarine mafic and subordinated felsic volcanic rocks, partly volcaniclastic. Mafic and felsic sills and dykes. Calcalkaline affinity	Strong sericitic alteration Al>90 affects also some ductile dykes	101.7±1.6 Ma zircon U-Pb in syn-mineralization dyke affected by intense sericitic alteration	Pichardo et al. (2019) Torró et al. (2022) This paper*
Aurora Augusta	150000 t barite were exploited. Zn-Pb-Cu sulfides under exploration	Mainly mafic lavas	Sericite in places	116±18, 106±17 K/Ar in hydroth. sericite (likely reworked K/Ar age: 68.3±2, 63±2 Ma)	Vidal (1987)*
Perubar	>6 Mt 11.4% Zn and 1.4% Pb Operation started in massive barite	Submarine volcanic (mainly mafic) sedimentary sequence. Mafic and felsic sills and dykes. Calcalkaline affinity	Weak sericitic alteration in feeder vicinity	Quartzmonzonite age: 69.71±0.18 Ma (68.92±0.16, zircon U-Pb. Probable mis-interpretation. Possibly fine-grained post mineralization dykes and not rhyolite flows were dated.	Vidal (1987) Polliand et al. (2005)* Polliand (2016)
Palma	>14.5 Mt including 9.6 Mt indicated at 5% Zn, 0.7% Pb, and 22 g Ag/t and 4.9 Mt inferred at 6% Zn, 1% Pb, and 21 g/t Ag	Submarine volcano (mainly mafic) - sedimentary sequence. Calcalkaline affinity	Weak sericitic alteration only in parts	>108 ±2.8 Ma and 101±5.3 zircon U-Pb in dykes crosscutting host	Farfán et al. (2019) Choquehuanca (2019)*
Balsaita (Cacua)	In exploration. Legacy underground workings (Ba, Zn, Cu) in several levels	Submarine volcano-sedimentary sequence. Mafic and felsic sills and dykes.	Strong sericitic alteration Al>90 in mafic rocks.	No dating available. Attributed to a mid Cretaceous age based on similarities with the deposits	Fontboté and Pichardo (2019) Mons et al. (this vol)
Cerro Lindo	>95 Mt . Typical grade: 1.5 %Zn, 0.8 Cu, 62% Pb, 0.21 g/t Ag, 0.05 g/t Au	Submarine, mainly felsic calcalkaline volcanic rocks, partly volcaniclastic.	Strong sericitic alteration Al>90	105.7 Ma 106.9 Ma ±0.3 zircon U-Pb in host rhyolite	Bueno (2019*), Villacorta (2017), Inaluz et al. (2019)

1) Mainly recent references owing space limitations.

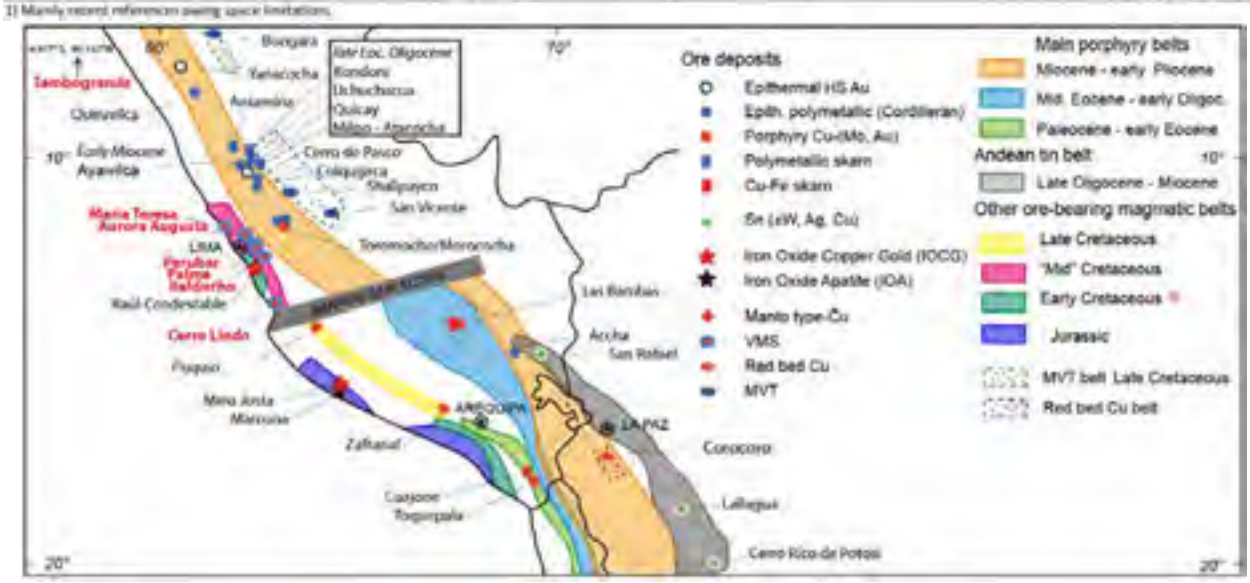


Figure. 1. Location of the central part of "mid" Cretaceous VMS belt in central Perú. Modified from Fontboté (2019, in particular several ages have been updated.

rocks dated at Perubar (69.71±0.18 and 68.92±0.16 Ma, respectively).

Thus, the alleged latest Cretaceous age of Perubar is strongly doubtful, also taking in account recent zircon U-Pb ages on the Casma Group (León et al. 2023). The most logical conclusion is that Perubar also has a "mid" Cretaceous age like the nearby Palma deposit with which it shares large similarities in terms of mineral assemblage, alteration, ore body geometry, and host sequence.

Based on the above discussion, it appears that all reliably dated VMS deposits in the 1000 km long belt along the Peruvian coast have mid Cretaceous ages, ranging from 116±18 to 101.7±1.6 Ma. The hypothesized uppermost Cretaceous ages for the VMS deposits of Perubar (although based on the high-resolution data of Polliand et al., 2005), Palma (based on proximity to Perubar, Farfán et al. 2019, Fontboté 2019), and Maria Teresa (Pichardo et al., 2019, based on a possibly reset Rb-Sr age in hydrothermal sericite of 68 ± 6 Ma, Romero et al., 2008) should be dismissed.

3 Structural control of dikes and feeders

A striking feature identified through recent surface mapping both at the Palma and Maria Teresa VMS deposits (Farfán et al., 2019, Pichardo et al., 2019), is the occurrence at regional scale of sets of roughly parallel mafic and felsic dikes, oriented approximately perpendicular to bedding and trending from north to south at N160E (Palma) and N150E (Maria Teresa). At Perubar, although mapped with less detail, these dikes also show a similar pattern (Polliand, 2016). In the three deposits, mafic dikes are crosscut by pyrite±pyrrhotite and Zn-Pb±Cu mineralization, while at Colquisiri, dacitic dikes are also affected by the sericitic alteration accompanying mineralization (samples 10401E and 2806 in Table 1 of Pichardo et al., 2019). This suggests that the hydrothermal system responsible for ore formation was at least partly active during the emplacement of the dikes.

At Maria Teresa, where no sedimentary rocks buffer the fluid and favor bed-parallel replacement, the ore bodies show a distinct N150E elongation

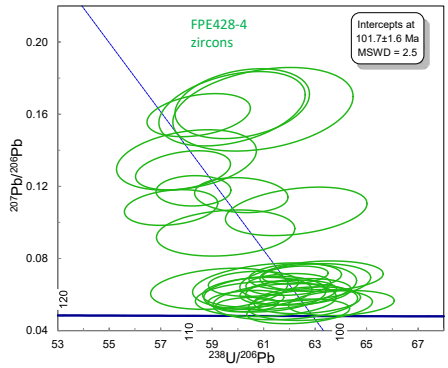


Figure 2. LA-ICP-MS dating of syn-mineralization (affected by intense sericitization) dacitic dike at Maria Teresa.

parallel to the main dikes (Fig. 1 in Pichardo et al. 2019). The intense sericitic alteration typical of this deposit also aligns with this orientation. These observations, together with the highest copper grades at the contact and along andesitic dikes (Sofia D body, Minera Colquisiri, unpublished reports), strongly suggest that the channels for the ore-forming fluids used the same pathways as the N150E dikes. In Perubar, Polliand et al. (2005) proposed that ore emplacement occurred within a pull-apart basin triggered by strike-slip dextral faulting. The elongated shape of the ore bodies in Cerro Lindo (Votorantim, 2017; Fig. 1 of Bueno and Mendoza, 2019) strongly resembles those at Colquisiri.

At Palma, as mentioned above, mafic and felsic dikes display a similar configuration. Specific elongations of the ore bodies have not yet been documented, possibly due to insufficient data and because the sedimentary host rock favors bed-parallel replacement. The swarms of parallel dikes, which, at least at Maria Teresa, appear roughly coeval with mineralization, may indicate emplacement in a predominantly transpressional environment initiated by oblique subduction. Intersection with crosscutting NE and NW-trending structures likely controls the location of the main mineralization centers and the pull-apart basins where the VMS deposits have formed.

3 Ore source

The published sulfur isotope composition of ore sulfides (Fontboté, 2019 and references therein) and new data of Maria Teresa ($\delta^{34}S$ = –2.2 to +1.6‰) are both compatible with direct magmatic contribution or sulfur derived from the leaching of magmatic sulfur contained in the footwall volcanic rocks. The sulfur isotope composition of barite, including new data from Maria Teresa ($\delta^{34}S$ = 20–21.4‰), is typical of mid-Cretaceous marine sulfate in all studied deposits.

The lead isotope composition of Pb-rich ore samples from both published sources and our new data in central Perú (Maria Teresa, Perubar, Palma, Balducho and Cerro Lindo) is plotted in Fig. 3. The deposits from central Peru show similar compositions and uniform values within each deposit, indicating a good homogenization of the lead source. Overall, the "mid" Cretaceous Peruvian deposits, similarly to the Early Tertiary VMS deposits in Ecuador La Plata, Macuchi, and Patiño (Chiaradia and Fontboté, 2001), plot between the upper crust and orogen evolution curves of Zartman and Doe (1981). These signatures suggest mixing between mantle and crustal sources.

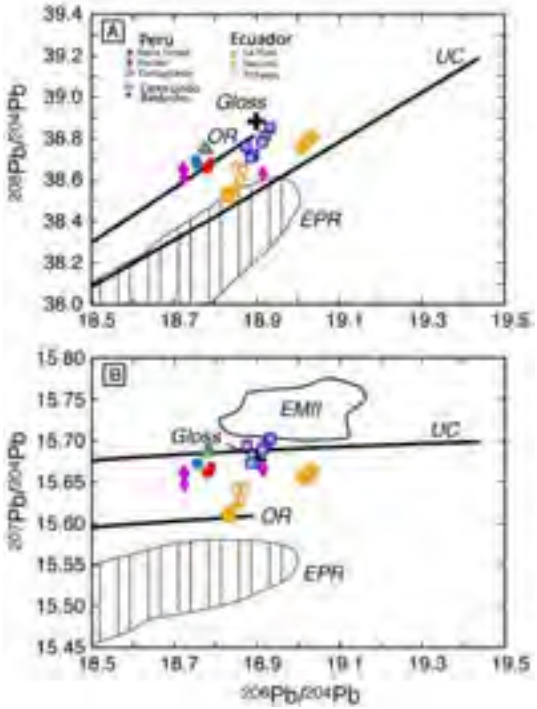


Figure 3. Lead isotope composition of Pb-rich ore samples. Data for Tambogrande are from Winter (2010) for Ecuador deposits from Chiaradia and Fontboté (2001).

The crustal contribution could result, as suggested for the Ecuadorian VMS deposits, from a mixing of radiogenic lead derived from pelagic sediments with a residual mantle, depleted in incompatible elements such as low radiogenic, MORB-type lead (Chiaradia and Fontboté, 2001; Chiaradia et al., 2008). Alternatively, as suggested by Winter (2008), the radiogenic lead isotope signature might reflect the assimilation of old continental crustal material during subduction (Winter, 2008). This latter possibility is supported by the identification of large crustal domains in the Peruvian offshore basement, attributed in its northern part to a southern continuation of the Amotape-Tahuin block and, in the central offshore part of Peru, to Grenville basement (Romero et al., 2013). Recently acquired Pb, Sr, and Nd isotope data on host volcanic rocks of the VMS deposits in central Peru support this hypothesis. Proterozoic to Mesozoic ages of inherited zircons in Palma (Cochehuanca, 2020) and Maria Teresa support the presence of old continental crust beneath the VMS belt.

4 Magmatic-hydrothermal fluids

As discussed by Fontboté (2019), mixing and cooling of uprising hydrothermal fluids with ocean

water percolating into aquifers within the host-sequence appears to be the main mechanism for ore mineral precipitation. This process explains the overall bed-parallel morphology, mineral zoning of the ore bodies, and alteration patterns, along with radiogenic and stable isotopic data.

The reviewed deposits in Peru exhibit similarities in geological setting, mineral assemblages, zoning, and alteration to active submarine arc-related hydrothermal systems in the Kermadec and Aeolian arcs, as well as at the SuSu Knolls site in the Manus basin where mineralization by magmatic-hydrothermal fluids has been proposed based on extensive evidence (de Ronde et al., 2023 and references therein). Mineralization by hydrothermal fluids of magmatic origin appears to be the most likely hypothesis for the Peruvian deposits. This is supported by: (i) the predominant calc-alkaline affinity of the host volcanic rocks, which is typical of subduction-related arcs; (ii) the involvement of acidic-oxidizing fluids as indicated by the intense sericitic alteration; and (iii) the tetrahedrite-tennantite rich mineral assemblages in deposits devoid of the buffering capacity of sedimentary rocks (e.g., Maria Teresa, where the presence of enargite has been reported by Díaz, 2015). A magmatic fluid origin was already proposed in the Andes for the intermediate to high sulfidation assemblages of the Au-rich La Plata VMS deposit in Ecuador (Chiaradia and Fontboté, 2001; Chiaradia et al., 2008).

Acknowledgements

We thank the geological staffs of Maria Teresa, Palma, and Cerro Lindo for their support. Careful review by Jorge Relvas is acknowledged.

References

Bueno Carreón JP, Mendoza Mondragón M (2019) Caracterización litogeoquímica en el yacimiento VMS - Cerro Lindo y su relación con la mineralización para determinar vectores guías en exploración. Propexplo, Lima, extended abstracts, 6 p

Choquehuanca (2020) Petrology, geochronology and geochemistry of the Lower Cretaceous in Palma volcanogenic massive sulfide (VMS) deposit, Central Peru. Master Thesis. China University of Geosciences, Wuhan, 79 p

De Ronde CEJ., Humphris SE, Höfig TW (2023),Time series studies and drilling results from IODP Expedition 376 to Brothers Volcano, New Zealand: Insights into petrology, hydrothermal processes, and mineralization—Introduction: Econ Geol 118:1537–1547

Chiaradia M, Fontboté (2001) Radiogenic lead signatures in Au-rich volcanic-hosted massive sulfide ores and associated volcanic rocks of the Early Tertiary Macuchi island arc (Western Cordillera of Ecuador). Econ Geol 96: 1361–1378.

Chiaradia M, Tripodi D, Fontboté L, Reza B (2008) Geologic setting, mineralogy, and geochemistry of the Early Tertiary Au-rich volcanic-hosted massive sulfide deposit La Plata, Western Cordillera, Ecuador: Econ Geol v 103:161-183.

Díaz M (2015) Estudio microscópico de 41 muestras de roca. Informe privado APT para Minera Colquisiri, 100 p

Farfán C, Monge R, Fontboté L. (2019) Palma, yacimiento de Zn-Pb tipo VMS en una cuenca intra-arco del Cretácico Superior en Perú central, nuevos avances en exploración para un gran potencial. Proexplo 2019, Lima, Abstracts

Fontboté L (2018) Ore deposits of the central Andes: Elements 14: 257-261

Fontboté L (2019) Volcanogenic Zn-Pb±Cu massive sulfide deposits in the Upper Cretaceous plutono-volcanic arc in central Peru. In: Proceedings of Proexplo 2019, Peru, Extended Abstracts 45–52

Fontboté L, Pichardo E (2024) Visitas a Cuculí (Balducho). Private report of 26-1-2024 to Colquisiri Minera, Lima 42p

Fontboté L, Pichardo E (2025) Private report of 7-2-2025 to Colquisiri Minera, Lima, 48 p

Imaña M, Aspajo H, Bueno JP, Mota J (2019) The Cerro Lindo VMS deposit: volcanic architecture, stratigraphy and hydrothermal alteration of a world class sulphide deposit, Central Peru. Field Guide, Proexplo 2019, Lima, 6 p

Ishikawa Y, Sawaguchi T, Ywaya S, Horiuchi M (1976) Delineation of prospecting targets for Kuroko deposits based on modes of volcanism underlying dacite and alteration haloes. Mining Geology 26:105-117

León Lecaros WR, Ramírez, AMA, Gómez Cahuaya EH (2023) Stratigraphy and new U-Pb ages of the Quilmana Formation rocks in South Lima, XXI Congreso Peruano de Geología, extended abstracts 102-108

Mora E, Fontboté, L, Rosas Lizárraga S, García V, Mena T, Pichardo E (this volume) Hydrothermal alteration overprinted by contact metamorphism: Balducho VMS prospect, central Peru

Pichardo E, Fontboté L, Mena T, Chirinos O, and Halter W 2019) El yacimiento de Zn-Pb-Cu-Ag tipo VMS María Teresa, Perú: geología y exploración. Proexplo 2019, extended abstracts, 7 p

Polliand M (2006) Genesis, evolution, and tectonic setting of the Upper Cretaceous Perubar Ba-Pb–Zn volcanic-hosted massive sulfide deposit, central Peru. Ph.D. Thesis University of Geneva, Terre and Environement 60, 141 p

Polliand M, Schaltegger U, Frank M, Fontboté L (2005) Formation of intra-arc volcanosedimentary basins in the western flank of the central Peruvian Andes during Late Cretaceous oblique subduction: field evidence and constraints from U-Pb ages and Hf isotopes. International Journal of Earth Sciences, 94:231-242

Romero D, Quispe J, Carlotto V, Tassinari C (2008). Los depósitos de la cuenca Maastrichtiano - Daniano: relación con los yacimientos tipo sulfuros masivos volcanogénicos de Pb - Zn - Cu; Perú central. 14 Congreso Peruano de Geología, Lima, 2008. Sociedad Geológica del Perú 6 p

Romero D, Valencia K, Alarcón P, Peña D, Ramos VA (2013) The offshore basement of Peru: Evidence for different igneous and metamorphic domains in the forearc. Journal of South American Earth Sciences, 42:47-60

Torró L, Benites D, Vallance J, Laurent O, Ortiz-Benavente BA, Chelle-Michou C, Proenza JA, Fontboté, L (2022) Trace element geochemistry of sphalerite and chalcopyrite in arc-hosted VMS deposits: Journal of Geochemical Exploration, 232: 106882, 21 p

Vidal, CCE (1987) Kuroko-type deposits in the Middle-Cretaceous marginal basin of central Peru. Econ Geol 82: 1409-1430

Votorantim (2017) Cerro Lindo polymetallic mine, NI 43-101 Technical Report on Operations, 315 p

Winter LS (2008) The genesis of “giant” copper-zinc-gold-silver volcanogenicmassive sulphide deposits at Tambogrande, Peru: Age, tectonicsetting, paleomorphology, lithogeochemistry and radiogenic isotopes: Unpublished Ph.D. thesis, Vancouver, Canada, University of British Columbia, 260 p: p. 1–274.

Winter LS, Tosdal RM, Mortensen JK, Franklin JM (2010) Volcanic stratigraphy and geochronology of the Cretaceous Lancones Basin, northwestern Peru: position and timing of giant VMS deposits. Econ Geol 115:715-742.

Lithogeochemistry of the La Mina VMS deposit in the Macuchi Unit (Western Cordillera, Ecuador): metalogenetic implications

Darío Fuentes[1], Fabián Villares[2], Luis López[3], Joaquín A Proenza[1], Álvaro Perez[3], Santiago Almagor[3], Xandé López[2]
[1]Departament de Mineralogia, Petrologia i Geologia Aplicada, Facultat de Ciències de la Terra, Universitat de Barcelona
[2]Departamento de Geología, Facultad de Geología y Petróleos, Escuela Politécnica Nacional
[3]Compañía Minera La Plata, Cumbayá-Ecuador

Abstract. The lithogeochemistry of the Macuchi Unit hosting the La Mina VMS deposit is reviewed, classified, and updated based on new whole-rock major and trace element geochemical data. The rocks of the Macuchi Unit are composed of basalts, basaltic andesites, and andesites characterizing a mafic bimodal magmatism. The basalts show a tholeiitic arc affinity and are classified into two groups. LOTI basalts are associated with a forearc setting where VMS mineralization was probably emplaced through an extensional regime. Normal IAT basalts exhibit higher REE enrichment and tend to evolve towards calc-alkaline compositions.

1 Introduction

The Macuchi block located in the Western Cordillera of Ecuador is characterized by hosting VMS-type mineralization (Fig. 1). Three VMS deposits of economic importance are known: La Mina (formerly known as La Plata), Macuchi, and El Domo (Vallejo et al. 2016; Chiaradia et al. 2009). The La Mina deposit is located approximately 100 km to the west-south-west of Quito, in the Cotopaxi province; it is a high-grade gold-rich VMS discovered around 1946 to 1947 by Cotopaxi Exploration company. The project benefits from a modern drilling and exploration database and is currently operated by Atico Mining Corporation through its subsidiary Compañía Minera La Plata. Initial probable mineral reserves total 2.51 Mt of sulfide ore averaging 1.59% Cu, 2.28 g/t Au, 30.41 g/t Ag, and 2.18% Zn, indicated mineral resources over 2.34 Mt, averaging 2.13% Cu, 2.98 g/t Au, 40 g/t Ag, and 3.05% Zn (NI 43-101 report).

Most VMS deposits have been formed in extensional geodynamic settings, spatially, temporally, and genetically related with volcanic and rift environments in ancient and modern ocean floors (Franklin et al. 2005; Piercey 2011; Schulz 2012). The use of immobile element geochemistry is a reliable tool for the study of igneous rocks protoliths, magmatic affinities and mineralogical changes in hydrothermally altered sequences (Hokka 2020). Hence, lithogeochemical signatures provide important information about the petrogenetic history, tectonic setting and hydrothermal alteration of volcanic rocks associated with VMS deposits (Piercey 2011).

This research aims to address the petrochemical characteristics of volcanic rocks of the Macuchi Unit in north-central Ecuador, based on new drilling surveys and whole-rock geochemistry, in order to understand the tectonic environment for these VMS deposits.

2 Geological setting

The Macuchi block is located on the west side of the Western Cordillera of Ecuador and extends approximately 300 km in an NNE to SSW direction (Fig. 1).



Figure 1. Regional geology showing the Macuchi block and VMS deposits. Geological map modified from Vallejo et al. (2019).

This block comprises a lithotectonic unit limited by the Chimbo-Toachi fault, and is composed mainly of mafic lithologies, including volcaniclastic rocks and massive lavas of basaltic and andesite composition (Vallejo et al. 2016). Several authors

suggest that the Macuchi block is allochthonous, having been accreted to the continental margin during the late Eocene (e.g., Kerr et al. 2002; Hughes and Pilatasig 2002; Spikings et al. 2005). Vallejo et al. (2009) proposed an autochthonous origin due to the presence of detrital zircons from the Cambrian, assuming that the Macuchi arc was located close to older basement rocks of the Eastern Cordillera of Ecuador.

The Macuchi Unit, located within the Macuchi block, is composed of volcaniclastic and primary volcanic rocks, including andesites, pillow lavas, hyaloclastites and breccias, deposited in a submarine volcanic arc sequence, with a thickness of, at least 2000 m (Aguirre and Atherton 1987; Vallejo et al. 2019). This unit is characterized by hosting the gold-rich VMS deposits, whose mineral emplacement is still debated. Chiaradia et al. (2008) suggested that La Mina deposit is formed during the Eocene in an active volcanic environment on, or below, the sea floor, associated with an island arc, or immature back-arc setting. On the other hand, Vallejo et al. (2016) proposed to the El Domo deposit a submarine arc setting, where the mineralization formed coevally with the deposition of immature volcaniclastic rocks.

3 Sampling and analytical methods

Representative drilling cores were analysed to determine the lithological characteristics of the La Mina project. Drill hole CMLP-16-01 was selected, approximately 500 m deep, which intersects all the volcanic lithologies, and the main mineralization as well.

Whole-rock geochemistry was determined for a total of 56 samples for major and trace elements by means of XRF and ICP-MS at the ALS labs. The extensive hydrothermal alteration of rocks from the Macuchi Unit is evident in the Alteration Box Plot of Large et al. (2001), mainly sericitization, chloritization, and sulfide mineralization (pyrite) related to VMS ore formation. Therefore, immobile elements were used for the classification of igneous rocks (HFSE, REE, transition elements and Th).

4 Results and Discussion

According to the Pearce (1996) diagram, the studied rocks are classified as basalts, basaltic andesites, and less abundant andesites, indicating a bimodal suite.

4.1 Geochemistry of mafic rocks

Mafic rocks were classified according to the guidelines proposed by Pearce (2014), based on their TiO2 and Cr (used as immobile proxy for MgO) contents into three types: type I or boninites (TiO2<0.5 wt%, Cr>275 ppm), type II or low-Ti island-arc tholeiites (LOTI IAT; 0.4<TiO2<0.8 wt%, Cr<275 ppm), and type III or normal island arc tholeiites (IAT; TiO2 > 0.8 wt%).

Type I (boninites) rocks exhibit a slight negative slope up to MREE in the chondrite-normalized REE spider diagram, followed by a flat slope from MREE to HREE, with values below 10. In a multi-element NMORB-normalized diagram, boninites have high Th/Nb ratios, which are characteristic of rocks from subduction zones. According to the formal classification of boninites using the criteria of Si8>52 and Ti8<0.5 (Pearce and Reagan 2019), the rocks are classified as low-Ti basalts.

Type II (LOTI) shows geochemical trends like those found in type I (Fig. 2A), but a higher enrichment in LREE is evident in the chondrite normalized REE spider diagram, and a nearly flat pattern from MREE to HREE. This trend is consistent with the high MgO basalts from the Caribbean plateau reported by Kerr (2014). LOTI also exhibit high Th/Nb ratios, typical fingerprint of subduction-related magmas (Fig. 2B). Most of the mafic rocks of the Macuchi Unit reported by Hughes and Pilatasig (2002) correspond to LOTI basalts.

Type III (normal IAT) represents the most evolved basalts, showing chondrite-normalized values above 10 with negative slopes from LREE up to MREE (i.e. LREE enriched with respect to MREE and HREE) and nearly flat patterns from MREE to HREE (Fig. 2A). Thorium values are enriched relative to NMORB, while Nb exhibits a varying negative anomaly in the NMORB-normalized spider diagram (Fig. 2B).

4.2 Geochemistry of felsic rocks

The rocks of felsic composition in the chondrite-normalized REE spider diagram shows a significant LREE enrichment relative to MREE and HREE, typical of calc-alkaline rocks (Fig. 2C). Most rocks exhibit a negative Eu anomaly, showing fractionation. Multi-element compositions in the NMORB-normalized diagram show general negative anomalies in Nb and Ti (Fig. 2D), indicating subduction-related signatures. In the rhyolite discrimination diagram, the rocks plot predominantly in the FIV field, indicating tholeiitic and boninitic affinities with low Zr/Yb and La/Yb_{CN} ratios (Fig. 2E, Hart et al. 2004).

4.3 Geodynamic setting

Basaltic rocks of the Macuchi Unit are enriched in the Th/Yb ratios and displaced above the MORB-OIB array defined in the Th/Yb vs. Nb/Yb diagram of Pearce (2014), with most samples plotted within the oceanic arc field. The Ti/V ratios for most of the basalts analysed are in the range of 10 to 20, corresponding to IAT compositions, including slab-proximal fore-arc and back-arc basalts. Some basalts plotted in the FAB field of the Izu-Bonin-Mariana system. On the other hand, few basalts with Ti/V between 20 to 50 correspond to MORB.

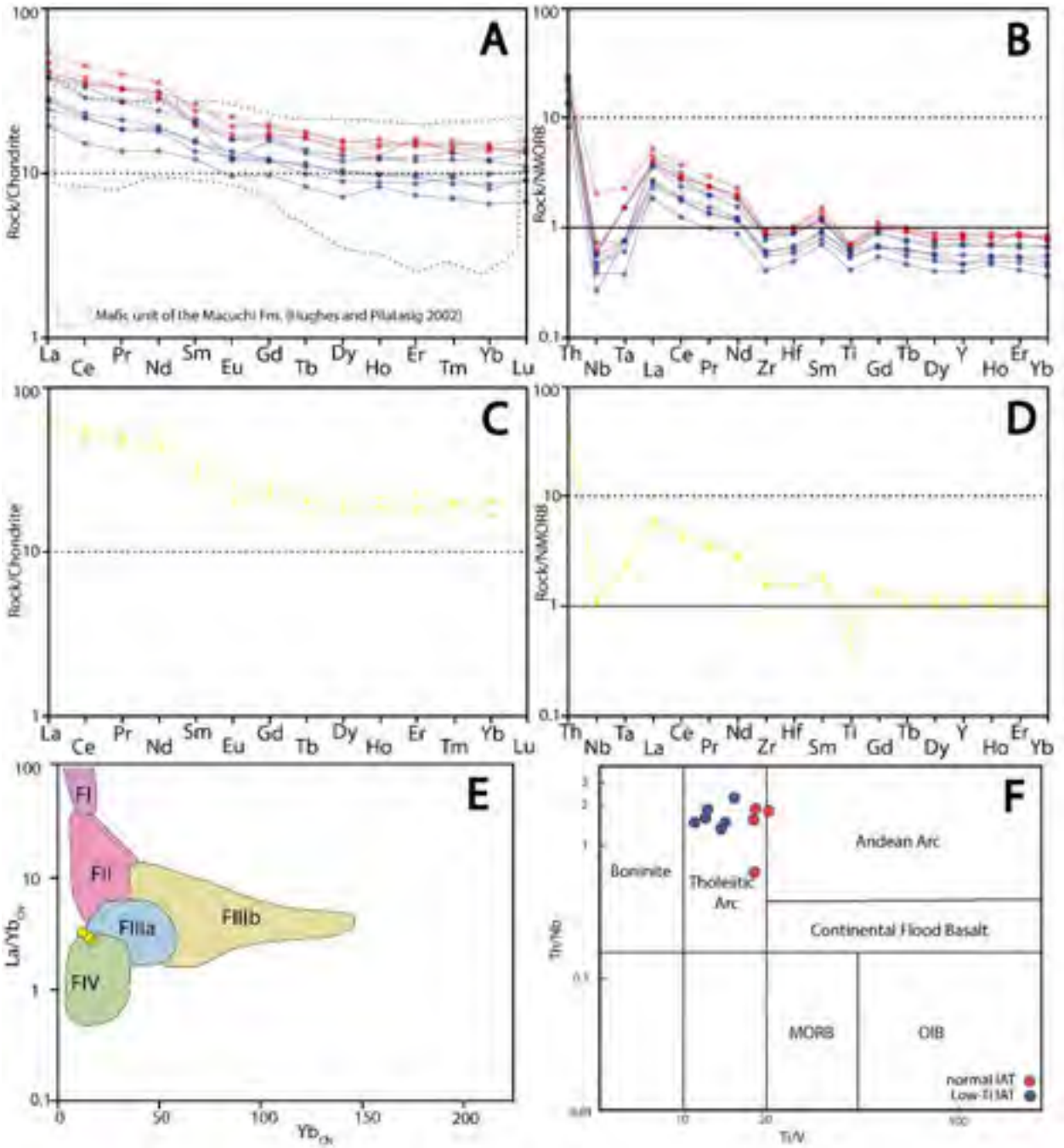


Figure 2. A, C. Chondrite-normalized REE diagrams for LOTI and normal-IAT (A) and felsic (C) rocks. **B, D.** Multielement NMORB-normalized diagram for LOTI and normal IAT (B) and felsic (D) rocks. **E.** La/Yb_{CN} – Yb_{CN} discrimination diagram for felsic rocks (Hart et al. 2004). **F.** Ti/V vs Nb/Th diagram (Shervais 2022).

In the Ti/ V vs. Th/Nb diagram (Fig. 2F), the basalts of the Macuchi Unit plot in the arc tholeiites field, which are characteristic of juvenile island arc. These geochemical signatures indicate the formation of oceanic lithosphere in a fore-arc setting of an intra-oceanic arc (Shervais 2022).

4.4 Metallogenetic evolution of the Macuchi Unit

Based on the host volcanic rocks of the Macuchi Unit classified as LOTI and normal IAT, the VMS mineralization must have formed in an Eocene intra-oceanic arc, probably associated with a fore-arc setting. Felsic rocks of the Macuchi Unit are depleted in trace elements, commonly with very low HFSE and HREE contents, and FIV signatures (indicative of M-type tholeiitic affinities). The VMS deposits associated with juvenile terrains have similar characteristics for their felsic rocks (Piercey 2011).

Chiaradia et al. (2008) suggest an island arc or immature back-arc tectonic setting based on the first-order factors controlling the gold-rich nature of the La Mina VMS deposit. In addition, Vallejo et al. (2016) proposed that the El Domo VMS deposit formed in a fault-bounded pull-apart basin, with magmatic and hydrothermal activity controlled by local extensional faults in the fore-arc.

The rocks of the Macuchi Unit show a broad compositional range, defining trends that originate in the tholeiitic field and evolve into the calc-alkaline field (Chiaradia 2009). The world-class Cu-Au-(Ag) porphyry Cascabel deposit is considered to be hosted by the Macuchi Unit, characterized by basalts with similar geochemical affinities and dated to approximately 35 Ma (Díaz 2020). A space-time relationship is suggested for the formation of mineral deposits during the evolution of the Macuchi intra-oceanic arc: 1) VMS-type mineralization related to LOTI basalts in a fore-arc setting (38 – 42 Ma) and 2) porphyry-type mineralization associated to normal IAT magmatism (35 – 39 Ma) during the establishment of the volcanic front.

5 Conclusions

The La Mina Cu-Zn-Ag-Au deposit is hosted by volcanic rocks of the Macuchi Formation, including basalts, basaltic andesites, and andesites. Tectonic setting discrimination geochemical diagrams, together with REE and NMORB-normalized multi-element spider diagrams, indicate that the Macuchi Unit was formed in an intra-oceanic island arc on the Caribbean plateau during the Eocene to Oligocene. In addition, the mafic rocks were classified into the two types of basaltic affinities. Type I, or low-Ti basalts, are the most abundant type and we propose that they led to the formation of VMS mineralization in an extensional regime, probably related to the fore-arc setting. Type II, or normal IAT basalts, show a greater REE enrichment and are associated with a transition field between tholeiitic and calc-alkaline affinities, reflecting the beginning of a mature arc.

The basalts, mostly associated with LOTI affinities and with FIV-type felsic volcanism, must be taken into account as prospective for VMS deposits in the Macuchi Unit.

Acknowledgements

This research has been financially supported by the EPN project PIS-22-03. The help and hospitality extended by the staff at CMLP mine are also gratefully acknowledged.

References

Aguirre L, Atherton MP (1987) Low-grade metamorphism and geotectonic setting of the Macuchi formation, western cordillera of Ecuador. J Metamorph Geol 5:473–494

Chiaradia M (2009) Adakite-like magmas from fractional crystallization and melting-assimilation of mafic lower crust (Eocene macuchi arc, western cordillera, Ecuador). Chem Geol 265:468–487

Chiaradia M, Tripodi D, Fontboté L (2008) Geologic setting, mineralogy, and geochemistry of the early tertiary Au rich volcanic-hosted massive sulfide deposit of La Plata, western cordillera, Ecuador. Econ Geol 103:161–183

Díaz C (2020) The Cascabel Cu-Au-Ag porphyry cluster in northern Ecuador. Master in Economic Geology thesis. University of Tasmania

Franklin JM, Gibson HL, Jonasson IR, Galley AG (2005) Volcanogenic massive sulfide deposits. Econ Geol 100th Anniversary volume:523-560

Hart T, Gibson HL, Lesher CM (2004) Trace element geochemistry and petrogenesis of felsic volcanic rocks associated with volcanogenic Cu-Zn-Pb massive sulphide deposits. Econ Geol 99:1003-1013

Hokka J (2020) Geology, alteration and lithogeochemistry of the Paleoproterozoic Korpela VMS occurrence in Eastern Finland. Miner Deposita 55, 1581–1604. https://doi.org/10.1007/s00126-020-00954-0

Hughes RA, Pilatasig LF (2002) Cretaceous and tertiary terrane accretion in the cordillera occidental of the Andes of Ecuador. Tectonophysics 345:29–48

Kerr AC (2014) Oceanic Plateaus. In: Holland H.D. and Turekian K.K. (eds.) Treatise on Geochemistry, Second Edition, vol. 4, pp. 631-667. Oxford: Elsevier

Kerr AC, Aspden JA, Tarney J, Pilatasig LF (2002) The nature and provenance of accreted terranes in western Ecuador: geochemical and tectonic constraints. J Geol Soc Lond 159:577–594

Large R, Allen R, Blake M, Herrmann W (2001) Hydrothermal alteration and volatile element halos for the rosebery K lens volcanic-hosted massive sulfide deposit, western Tasmania. Econ Geol 96:1055–1072

Pearce JA (1996) A user's guide to basalt discrimination diagrams. Geological Association of Canada Special Publication 12, pp. 79–113

Pearce JA (2014) Immobile elements fingerprinting of ophiolites. Elements 10:101-108

Pearce JA, Reagan MK (2019) Identification, classification, and interpretation of boninites from Anthropocene to Eoarchean using Si-Mg-Ti systematics. Geosphere 15 (4), 1008–1037.Shanks

Piercey SJ (2011) The setting, style, and role of magmatism in the formation of volcanogenic massive sulfide deposits. Miner Deposita 46:449-471

Schulz KJ (2012) Regional environment in volcanogenic massive sulfide occurrence model. In: Shanks III, W.C., Thurston, R. (Eds.), Volcanogenic massive sulfide occurrence model, U.S. Geological Survey Scientific Investigation Report 2010–5070-C, Reston, pp. 5–8

Shervais JW (2022) The petrogenesis of modern and ophiolitic lavas reconsidered: Ti-V and Nb-Th. Geosci. Front. 13, 101319 https://doi.org/10.1016/j.gsf.2021.101319

Spikings RA, Winkler W, Hughes RA, Handler R (2005) Thermochronology of allochthonous terranes in Ecuador: unraveling the accretionary and post-accretionary history of the northern Andes. Tectonophysics 399:195–220

Vallejo C, Soria F, Tornos F, Naranjo G, Rosero B, Salazar F, Cochrane R (2016) Geology of El domo deposit in Central Ecuador: a VMS formed on top of an accreted margin. Mineral. Deposita 51, 389–409

Vallejo C, Spikings RA, Horton BK, Luzieux L, Romero C, Winkler W, Thomsen T (2019) Late Cretaceous to Miocene stratigraphy and provenance of the coastal forearc and Western Cordillera of Ecuador: Evidence for accretion of a single oceanic plateau fragment, in Horton, B.K., and Folguera, A., eds., Andean Tectonics: Amsterdam, Elsevier, p. 209–236, https://doi.org/10.1016/B978-0-12-816009-1.00010-1.

Vallejo C, Winkler W, Spikings RA, Luzieux L, Heller F, Bussy F (2009) Mode and timing of terrane accretion in the forearc of the Andes in Ecuador. In: Kay, S.M., Ramos, V.A., Dickinson, W.R. (Eds.), Backbone of the Americas: Shallow Subduction, Plateau Uplift, and Ridge and Terrane Collision. GeolSoc of Am Mem 204:197–216

Mineralization Processes at Escanaba Trough

Amy Gartman[1], Jaycee Favela[1], Katlin Adamczyk[1], John Jamieson[2], Rob Zierenberg[3], Isobel Yeo[4]
[1]U.S. Geological Survey, Pacific Coastal and Marine Science Center
[2]Memorial University, Newfoundland
[3]Department of Earth and Planetary Sciences, University of California Davis
[4]National Oceanography Center, Southampton

Abstract. Escanaba Trough off northern California is the southernmost and only sediment covered segment of the Gorda Ridge. Hydrothermal mineralization was first discovered in Escanaba Trough in 1985, and subsequent investigations included the delineation of the NESCA (northern Escanaba) and SESCA (southern Escanaba) sections of Escanaba Trough, as well as drilling by Ocean Drilling Program (ODP) Leg 169 in 1996. Preliminary research conducted in the 1980s distinguished two classes of sulfide mineral assemblages within the Escanaba Trough: one dominated by pyrrhotite ($Fe_{1-x}S$) and one containing 'mixed sulfides' including chalcopyrite ($CuFeS_2$) and sphalerite (ZnS). In 2022, we conducted a research expedition to the Escanaba Trough to more thoroughly characterize mineralization processes and consider preservation of precipitated minerals throughout hydrothermally active and inactive sections of Escanaba Trough, with the specific objective of characterizing the host minerals, and processes of enrichment for specific elements which are currently listed as critical elements and can also be toxic under certain conditions (Sb, As, Ba, Co, Ga, Ge, Te). The following will include initial results from that work.

1 Characterization of Escanaba Trough minerals

Hydrothermal sulfide minerals were discovered in Escanaba Trough in 1985 (Morton et al., 1987). The initial characterization of hydrothermal sulfides at Escanaba Trough included a pyrrhotite ($Fe_{1-x}S$) dominated class and a 'mixed sulfide' class composed mainly of chalcopyrite ($CuFeS_2$) and sphalerite (ZnS), although these two classes were not bimodally distributed (Koski et al., 1994). Metal sulfide minerals at Escanaba Trough have been observed to occur in inactive mounds, chimneys, cement and aggregates, and Escanaba Trough also contains regions of active venting. In a 2022 research expedition, we used the autonomous underwater vehicle (AUV) Sentry to expand currently existing high-resolution bathymetric maps (Clague et al., 2022) and the remotely operated vehicle (ROV) Jason to collect rock and sediment samples throughout the Escanaba Trough, including previously unsampled regions. Given current interest in delineating and understanding active and inactive seafloor massive sulfide deposits (Jamieson and Gartman, 2020), which are the modern analogue of ancient volcanogenic massive sulfide deposits (Franklin et al., 2005), our work aims to better understand the geochemical changes that occur in hydrothermal chimneys and mounds after the cessation of hydrothermal venting.

Although prior work had suggested that Central Hill, NESCA region was the only active venting occurring at Escanaba Trough (Morton et al., 1994), we additionally found hot fluids emitted from Hill S3A, SESCA region. A comparison of several trace elements from active regions (Central Hill, Hill S3A) and inactive regions (all other regions sampled) is presented in Figure 1 and indicates that active and inactive regions have comparable results for these elements. Additionally, we compared subsamples of bulk sulfide minerals to oxidized "rind" material which coated inactive chimneys and talus. Initial results suggest that the oxidized material has significantly lower copper, zinc and higher barium than corresponding bulk samples; interestingly, cobalt was the only trace mineral with significantly different concentrations; cobalt concentrations were significantly lower in rind material (Figure 2).

Major primary sulfide minerals observed during initial x-ray diffraction analyses include pyrrhotite, sphalerite, galena, and chalcopyrite. Barite is also a major primary mineral, and abundant marcasite was observed to occur as a replacement mineral. The "rinds" are composed of several different oxyhydroxide and hydroxysulfate minerals including goethite, akaganeite, and jarosite. These results will provide valuable insights into the preservation potential for seafloor massive sulfide deposits and the mineralogical and geochemical controls on mobility of critical metal distributions within these deposits during oxidation processes.

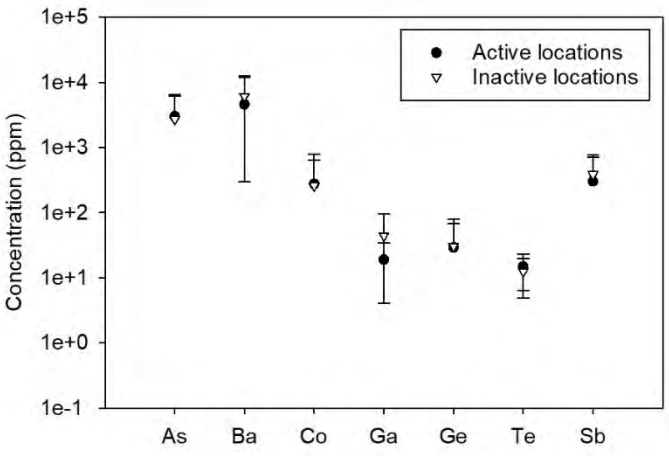


Figure 1. The concentration of several elements in bulk sulfide minerals from Escanaba Trough, separated by whether the location where the minerals occurred was active or inactive. Error bars indicate a standard deviation. Gallium is significantly different between the active and inactive sites t(42), p=0.005), no other elements exhibited a significant difference

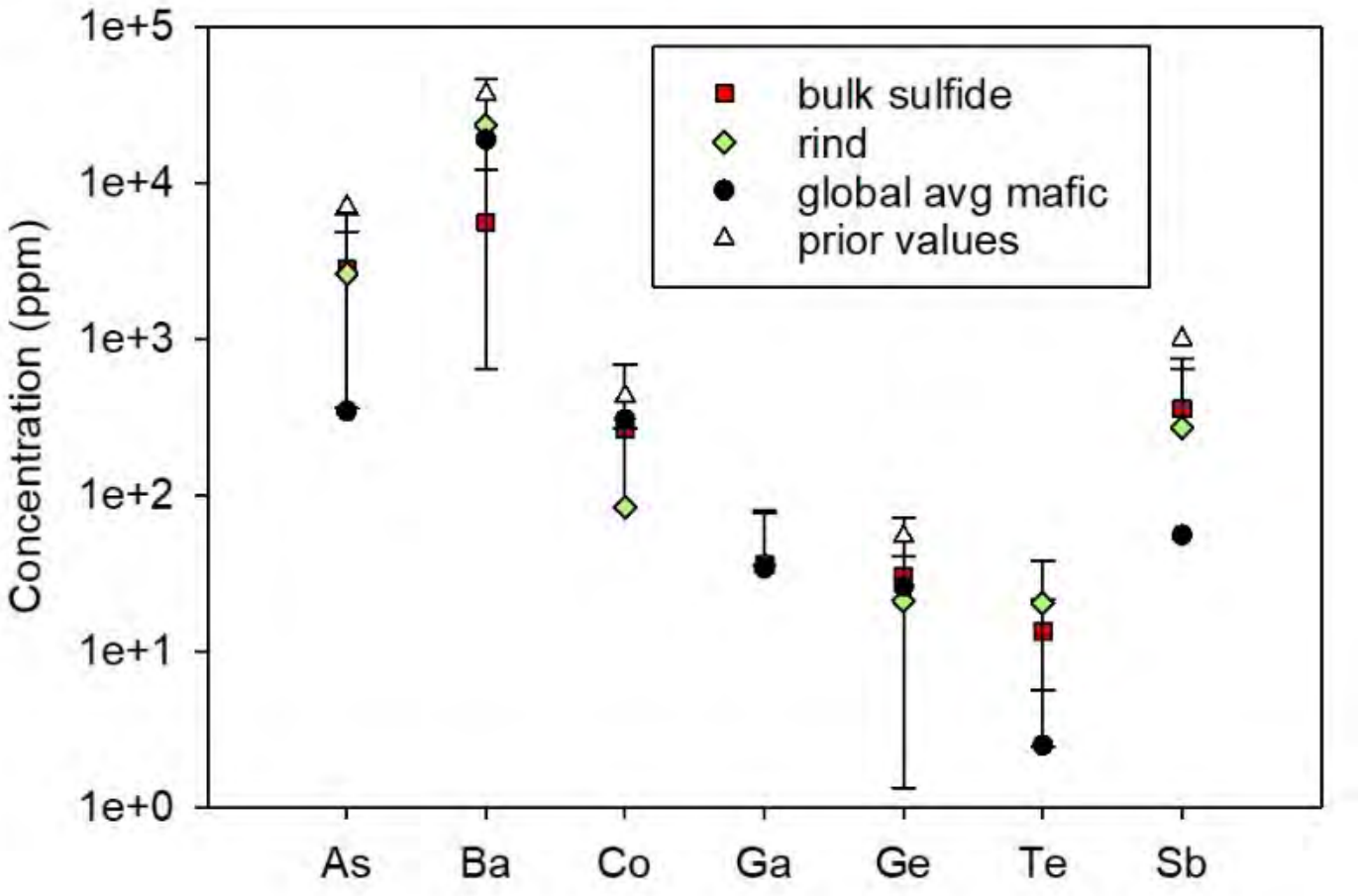


Figure 2. The concentration of several elements in different fractions of sulfide minerals from Escanaba Trough, including bulk minerals and the oxidized material coating the exterior of chimneys and talus, which is, labeled "rind". Also included are values from previous work, where available. Error bars indicate a standard deviation. Cobalt is significantly different between the bulk sulfide and rind samples t(69), p=0.006), as is barium t(20), p=0.001)

Acknowledgements

We thank the Captain and crew of the R/V Thomas G. Thompson, the ROV Jason, and the AUV Sentry. Escanba Trough, Exploring the Seafloor and Oceanic Footprints is an interagency effort involving the National Oceanic and Atmospheric Administration (NOAA), the U.S. Geological Survey, and the Bureau of Ocean Energy Management. Funding is acknowledged from NOAA Ocean Exploration via its Ocean Exploration Fiscal Year 2019 Funding Opportunity and through the National Oceanographic Partnership Program (NOPP), the USGS Coastal and Marine Hazards and Resources Enhanced Funding Opportunities, the Bureau of Ocean Energy Management through Interagency Agreement M19PG00021 with the United States Geological Survey, the USGS Coastal and Marine Hazards Program, Mineral Resources Program, and Mendenhall Research Fellowship Program. These data are preliminary or provisional and are subject to revision. They are being provided to meet the need for timely best science. The data have not received final approval by the U.S. Geological Survey (USGS) and are provided on the condition that neither the USGS nor the U.S. Government shall be held liable for any damages resulting from the authorized or unauthorized use of the data. Any use of trade, firm, or product names is for descriptive purposes only and does not imply endorsement by the U.S. Government.

References

Clague DA, Zierenberg RA, Paduan JB, Caress DW, Cousens BL, Dreyer BM, Davis AS, McClain J, Ross SL (2022) Emplacement and impacts of lava flows and intrusions on the sediment-buried Escanaba Segment of the Gorda mid-ocean ridge. Journal of Volcanology and Geothermal Research 432:107701.

Franklin JM, Gibson HL, Jonasson IR, Galley, AG (2005) Volcanogenic Massive Sulfide Deposits. Economic Geology 100th Anniversary Volume; Society of Economic Geologists: Littleton, CO, USA.

Jamieson, JW, Gartman, A (2020) Defining active, inactive, and extinct seafloor massive sulfide deposits. Marine Policy, 117:103926

Koski RA, Benninger LM, Zierenberg RA, Jonasson IR (1994) Composition and growth history of hydrothermal deposits in Escanaba Trough, southern Gorda Ridge. *In* USGS Bulletin 2022 Geologic, hydrothermal, and biologic studies at Escanaba Trough, Gorda Ridge, Offshore Northern California Eds. Morton, J.L., Zierenberg, R.A., and Reiss, C.A.

Morton JL, Holmes ML, Koski RA (1987) Volcanism and massive sulfide formation at a sedimented spreading center, Escanaba trough, Gorda ridge. Geophys Res Lett 14:769-772

Morton JL, Zierenberg RA, Reiss CA (1994) Geologic, hydrothermal, and biologic studies at Escanaba Trough, Gorda Ridge, offshore northern California. U.S. Geological Survey bulletin 2022 10.3133/b2022

.

The volcanic-hosted massive sulfide mineral system in space and in time – a tribute to Jim Franklin

David L Huston[1]
[1]*CODES, University of Tasmania*

Abstract. Preserved volcanic-hosted massive sulfide (VHMS) deposits, the ancient analogues of black smokers, formed mostly in back-arc basins and rifted arcs along convergent margins since ~3500 Ma. The VHMS mineral system commonly forms above subvolcanic multiphase intrusions that provide heat, drive ore fluid convection and, in some cases, contribute magmatic-hydrothermal fluids and metals to the system.

VHMS deposits form at or just below the seafloor when upwelling 200-400°C ore fluids mix with ambient seawater and rapidly cool. One of the more important recent insights into ore formation is recognition of the importance of sub-seafloor replacement of the upper levels of the volcanic pile in both modern and ancient systems. Mineralization involves zone refining as hotter mineral assemblages replace cooler mineral assemblages from bottom to top as the ore fluids cool and mix with seawater. Secular changes in ocean chemistry also can influence ore mineralogy.

1 Introduction

In a career that spanned six decades, Jim Franklin established himself as a world expert on the geology and genesis of volcanogenic (or volcanic-hosted) massive sulfide (VHMS) deposits. Although he contributed many important papers on individual deposits and districts (Franklin et al. 1975, 1977), his main contribution was a series of synthesis papers on these deposit types, most notably those in the 75th and 100th Anniversary Volumes of Economic Geology (Franklin et al. 1981, 2005). These papers are excellent examples of synergy, where the total is greater than the sum of the parts. Franklin et al. (2005) was one of the first to publish a comprehensive data set of global VHMS deposits.

In his role at the Geological Survey of Canada, Franklin also studied seafloor massive sulfide (SMS) deposits (aka black smokers), modern analogues of VHMS deposits. The combination of his (and other's) knowledge of VHMS and SMS deposits has led to a better understanding of VHMS mineral system processes. Although confirming many concepts developed from VHMS research prior to the discovery of black smokers in the late 1970s (e.g., Franklin et al. 1981; Ohmoto and Skinner 1983), SMS research has provided new insights into the tectonic setting of the VHMS mineral system (Hannington et al. 2005) and, particularly, the importance of sub-seafloor mineralizing processes (Hannington et al. 1999).

Based on the syntheses of Franklin et al. (1981, 2005) and more recent compilations (Huston et al. 2022, 2023), below I provide an overview of the VHMS/SMS mineral system (Fig. 1), from the global to deposit scales and how this system has changed over time.

2 Tectonic setting and secular distribution

According to Hannington et al. (2005), SMS deposits occur in two broad tectonic settings – along convergent margins in back-arc basins or rifted arcs, and along divergent margins in mid-oceanic rifts. As mid-oceanic rifts are typically consumed by subduction, ancient VHMS deposits mostly include those formed along convergent margins. Franklin et al. (2005) noted that ancient VHMS deposits formed during supercontinent assembly (Fig. 2a). When subdivided according to Barrie and Hannington (1999), deposits from bimodal (both felsic- and mafic-dominated) volcanic successions occur across geological time, but deposits from mafic, mafic-siliciclastic and siliciclastic-felsic successions are mostly restricted to the Phanerozoic, after modern-style subduction began.

Mercier-Langevin et al. (2007) suggested that the position of a deposit relative to the convergent margin influences the metallogenic characteristics of that deposit. In this model, deposits closer to the arc are more likely to have a magmatic contribution, including the development of Cu-Au-rich high sulfidation-type deposits (Fig. 1).

Richards (2009) suggested that although most porphyry copper deposits formed during arc construction, a proportion of deposits – those associated with alkalic magmatism – formed during post-collisional extension. The association of some VHMS districts with alkalic (high-K to boninitic) volcanism, most notably the Mount Read Volcanics in Tasmania, Australia (Crawford et al. 1992), raises the possibility of a similar, post-collisional setting for some VHMS districts.

3 District-scale architecture, fluid flow and alteration

Early in his career, Franklin undertook deposit- and regional-scale studies of the Sturgeon Lake district in western Ontario, Canada (Franklin et al. 1975, 1977). These and later studies (Gibson 1990; Galley 1993, 2003; Brauhart et al. 1998, 2001; Huston et al. 2001) enabled development of a regional model for a "typical" VHMS mineral system (left inset of Fig. 1) in which conformable, polyphase subvolcanic granites drive convection of seawater through the volcanic pile, producing semi-conformable alteration zones that have been leached of metals and sulfur. An important question, addressed later in this abstract, is the role of magmatic hydrothermal fluids in the VHMS mineral system.

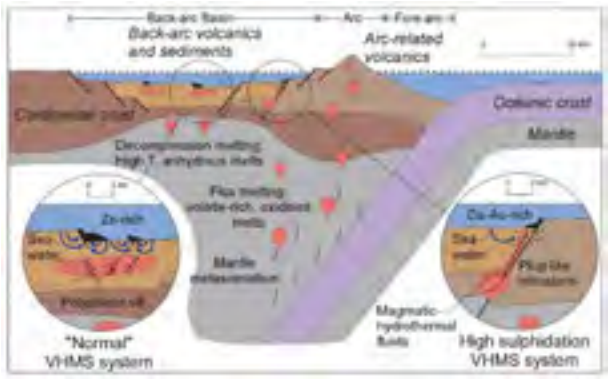


Figure 1. Schematic diagram showing the volcanic-hosted massive sulfide mineral system (after Huston et al. 2011; © Geoscience Australia)

4 Alteration and mineralization at the deposit-scale

As shown in many districts (Franklin et al 1981, 2005; Galley 1993; Brauhart et al. 1998), regional, semi-conformable alteration zones pass upwards into crosscutting zones near individual deposits or occurrences. Proximal to the deposits the alteration assemblages are commonly zoned, in many (though not all) cases with proximal chlorite-rich and distal sericite-rich zones. Large et al. (2001) used bulk chemistry of altered rocks to indicate zonation and as an exploration vector in VHMS systems.

In addition to silicate minerals, VHMS alteration and mineralized zones also contain variable carbonate, sulfide and sulfate minerals (Mosier et al. 2009). Figure 2b shows that the proportion of VHMS deposits that contain sulfate minerals (mainly barite) changes with geological time. During the Paleoarchean (> 3200 Ma), most VHMS contained sulfate minerals, but in the Meso- to Neoarchean (3200-2500 Ma) sulfate minerals are virtually unknown. During the Paleoproterozoic (2500-1800 Ma), the proportion of VHMS deposit increases, although at a lower proportion than during the Phanerozoic (< 540 Ma). This change reflects the changes in the redox state (and sulfate abundance) in Earth's oceans through time.

Although most VHMS deposits are characterized by chlorite-, silica- and/or sericite-dominated assemblages, a sub-set of deposits, high-sulfidation deposits (Sillitoe et al. 1996), contain high-sulfidation minerals such as bornite. These deposits, which tend to be Au-Cu-rich, are also characterised by advanced argillic (i.e., alumino-silicate dominated) alteration zones (Fig. 1). Huston et al. (2021) indicates that these deposits constitute approximately 5% of global VHMS deposits. Although constituting only a small proportion of deposits, this sub-class includes some of the largest VHMS Au resources, such as Bousquet in the Abitibi Subprovince of Québec (Dubé et al. 2007).

5 Fluid, metal and sulfur sources

Because of the existence of modern analogues and extensive studies of ancient systems, the fluid, metal and sulfur sources in VHMS systems are well, though not totally, understood. This understanding derives from fluid inclusion, stable isotope and mineral chemistry data in modern and ancient deposits (Franklin et al. 1981, 2005; Ohmoto et al. 1983) and fluid geochemistry in modern systems (Von Damm 1990; Hannington et al. 2005). Moreover, data from ancient, well-dated systems indicates that the composition and sources of VHMS ore fluids have changed significantly over geological time in response to changes in geodynamic drivers and tectonics and in ocean chemistry.

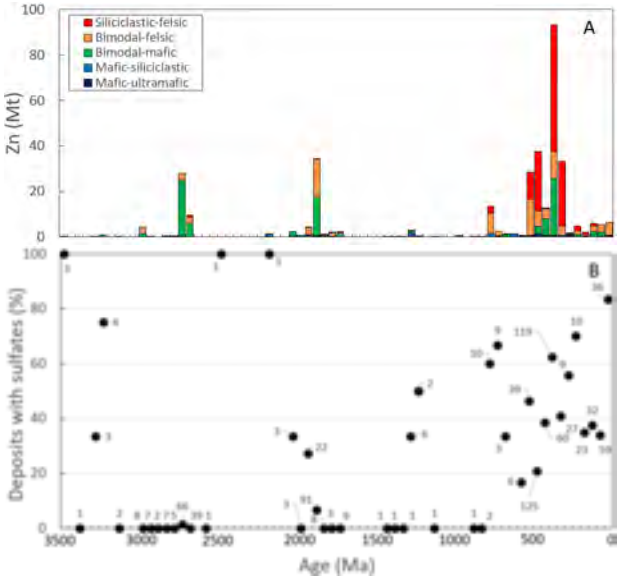


Figure 2. Secular variations in (A) contained Zn by deposit type, and (B) percentage of deposits containing sulfates. Part (B) is binned to 50 Myr intervals; numbers beside symbols indicate the number of deposits in each bin.

5.1 Fluid characteristics and sources

From measurements of SMS fluids (Von Damm 1990; Hannington et al. 2005) and fluid inclusion data (e.g. Pisutha-Arnond and Ohmoto 1983), VHMS ore fluids had temperatures of 200–400˚C, and salinities near seawater with dispersion to lower and higher salinity. This dispersion is interpreted as the consequence of phase separation in the underlying volcanic pile, or the inclusion of magmatic-hydrothermal fluids (Franklin et al. 1981, 2005; Von Damm 1990; Hannington et al. 2005). As Knauth (2005) has argued that ancient seawater was more saline than modern seawater (by up to 1.8×), some of the enhanced salinity may have been due to secular variations in seawater salinity.

Important, additional evidence from fluid source stems from O-H isotope data, which can be a powerful discriminator of fluid source as the isotopic composition of seawater (δD ~ 0‰; δ^{18}O ~ 0‰) differs from that of magmatic hydrothermal fluids (δD ~ -80 – -40‰; δ^{18}O ~ 6-9‰) (Sheppard 1986). Compilation of ore fluid O-H isotopic data by Huston et al. (2023) indicates most data cluster around the seawater value, some data indicating a magmatic-hydrothermal contribution (e.g., Neves Corvo:

Relvas et al. 2006). Hence, most VHMS ore fluids are evolved seawater although some deposits have a significant magmatic-hydrothermal component.

5.2 Metal sources

As summarized by Franklin et al. (1981, 2005), ore metals have commonly been leached from semi-conformable alteration zones. For example, in the Paleoarchean Panorama district, well over 50% of Cu, Zn, Pb and S have been leached from a semi-conformable zone 1.5 km below the ore horizon that can be traced for 10 km (Brauhart et al. 2001; Huston et al. 2001). These studies indicate that metal leaching is an important source of ore metals in many VHMS systems, but others have argued for a significant magmatic-hydrothermal metal source. Citing metal associations (e.g., Cu-Au or Cu-Sn) and unusual alteration assemblages, Relvas et al. (2006) and Sillitoe et al. (1996) have argued for a magmatic-hydrothermal contribution to some deposits. However, it must be noted that Mo, a metal commonly considered indicative of a magmatic-hydrothermal contribution, has been leached in the Panorama district (Huston et al. 2001).

5.3 Sulfur sources

Like fluid sources, sulfur sources in VHMS systems have long been debated, with three possibilities – seawater sulfur, sulfur leached from semi-conformable alteration zones and magmatic-hydrothermal sulfur – inferred. Evidence for a leached source derives from geochemistry of the semi-conformable alteration zones (e.g. Brauhart et al 2001; Huston et al. 2001). The importance of the other sources is based on sulfur isotope and mineralogical data.

As originally documented by Sangster (1968), $\delta^{34}S$ values of sulfides from Phanerozoic VHMS deposits are consistently lower than those of coeval seawater sulfate. Huston et al. (2023) found that $\Delta^{34}S_{\text{seawater sulfate – sphalerite}}$ was typically 15-20‰. This pattern has been interpreted to indicate mixing between reduced seawater sulfate (Sangster 1968; Sasaki 1970; Solomon et al 1988), and deep sulfide (Ishihara and Sasaki 1978). Based on mass balance calculations using $\delta^{34}S$ values of 0‰ for deep sulfur and $\delta^{34}S$ values of coeval seawater sulfate from the curve of Crockford et al. (2019), Huston et al (2023) estimated a median contribution of seawater sulfur of 23%, 9%, and 7% for Phanerozoic, Paleoproterozoic and Archean deposits. Although there is a large amount of variability between individual deposits, overall “deep” sulfur dominates, especially in Paleoproterozoic and Archean deposits. The results from the older deposits are consistent with estimates derived from Paleoproterozoic and Neoarchean deposits based on multiple sulfur isotope data (Jamieson et al. 2013; LaFlamme et al. 2021).

Sulfur isotope data do not differentiate “deep” sulfur into that leached from underlying volcanics or that evolved from crystalizing magmas. Both sources are important in some deposits, and other data, such as detailed $\delta^{34}S$ data, O-H isotope data, alteration assemblages and ore mineralogy, can provide additional constraints (Huston et al. 2011).

6 Ore-forming processes

The main depositional mechanism in VHMS mineral systems is rapid cooling as ore fluids mix with seawater (Franklin et al. 1981; Ohmoto et al. 1983), a mechanism confirmed by studies of SMS deposits ((Von Damm 1990; Hannington et al. 2005). In detail the process is complex, involving “zone refining” where changes in thermal gradients result in the bottom-up replacement of lower by higher temperature mineral assemblages. This produces the typical VHMS metal zonation of Fe (base) → Cu-Fe → Cu-Zn(Pb) → Zn-Pb(Cu) → Zn-Pb → Pb-barite (top) (Franklin et al. 1981; Eldridge et al. 1983). Based initially on SMS deposits (Hannington et al. 2005), ore deposition can occur below the seafloor, with sub-seafloor replacement now recognized as an important process in VHMS systems. Studies of SMS deposits indicate that these small to medium-sized deposits form by multiple mineralizing pulses over periods of 1000s to 100,000s of years (Hannington et al., 2005). An important unanswered question is the duration required to form giant VHMS deposits such as Kidd Creek. Finally, magmatic SO_2 disproportionation may be an important process producing high-sulfidation VHMS systems (Huston et al 2011).

7 Further work

Over the six decades that Jim Franklin has studied VHMS mineral systems, the mineral system model has evolved so that it is one of the best understood. Despite this, many outstanding questions remain. A better understanding of anomalous districts such as the Mount Read Volcanics may lead to a better understanding of tectonic controls on VHMS deposits. New data on secular variations in the characteristics of VHMS deposits can provide new understandings of the mineral system and new insights on Earth evolution with time. More studies on stable isotopes, especially using microanalytical techniques, multiple isotope systems and metallic isotopes have and will continue to provide knowledge of ore formation. Finally, VHMS deposits have the potential to host many critical minerals – In, Ge, Se, Sn to name a few. A better understanding of the distribution of these elements will enable recovery of these minor, but important, elements.

Acknowledgements

Jonathan Cloutier and Mike Baker are thanked for comments on early versions of this abstract.

References

Barrie CT, Hannington MD (1999) Classification of VMS deposits based on host rock composition. Rev Econ Geol 8:1–12

Brauhart CW, Groves DI, Morant P (1998) Regional alteration systems associated with volcanogenic massive sulfide mineralization at Panorama, Pilbara, Western Australia. Econ Geol 93:292–302

Brauhart CW, Huston DL, Groves DI, Mikucki EJ, Gardoll SJ (2001) Geochemical mass transfer patterns as indicators of the architecture of a complete volcanic-hosted massive sulfide hydrothermal alteration system in the Panorama district, Pilbara, Western Australia. Econ Geol 96:1263–1278

Crawford, AJ, Corbett KD, Everard JL (1992) Geochemistry of the Cambrian volcanic-hosted massive sulfide-rich Mount Read volcanics, Tasmania, and some tectonic implications. Econ. Geol. 87:587–619.

Crockford PW, Kunzmann M, Bekker A, Hayles J, Bao H, Halverson GP, Peng Y, Bui TH, Cox GM, Gibson TM, Wörndle S, Rainbird R, Lepland, A, Swanson-Hysell NL, Master S, Sreenivas B, Kuznetsov A, Krupenik V, Wing BA (2019) Claypool continued: extending the isotopic record of sedimentary sulfate. Chem Geol 513:200–225

Dubé B, Mercier-Langevin P, Hannington MD, Gosselin G, Gosselin P (2007) The LaRonde Penna world-class Au-rich volcanogenic massive sulfide deposit, Abitibi, Quebéc: mineralogy and geochemistry of alteration and implications for genesis and exploration. Econ Geol 102:633–666

Eldridge CS, Barton PB, Ohmoto H, (1983) Mineral textures and their bearing on the formation of Kuroko orebodies. Econ Geol Mon 5:570–604

Franklin JM, Kasarda J, Poulsen KH (1975) Petrology and geochemistry of the alteration zone of the Mattabi massive sulfide. Econ Geol 70:63–69

Franklin JM, Gibb W, Poulsen KH, Severin P (1977) Archean metallogeny and stratigraphy of the South Sturgeon Lake area. Thunder Bay, Canada, Institute of Lake Superior Geology, 73 pp

Franklin JM, Lydon JW, Sangster DF (1981) Volcanic-associated massive sulfide deposits. Econ Geol 75th Anniversary Volume, pp 485–627

Franklin JM, Gibson HL, Jonasson IR, Galley AG (2005) Volcanogenic massive sulfide deposits. Econ Geol 100th Anniversary Volume, pp 523–560

Galley AG (1993) Characteristics of semi-conformable alteration zones associated with volcanogenic massive sulphide districts. J Geochem Explor 48:175–200

Galley AG (2003) Composite synvolcanic intrusions associated with Precambrian VMS-related hydrothermal systems. Miner Depos 38:443–473

Gibson HL (1990) The mine sequence of the central Noranda Volcanic Complex: geology, alteration, massive sulphide deposits and volcanological reconstruction. Unpublished PhD thesis, Carleton University, 715 pp

Hannington MD, Bleeker W, Kjarsgaard I (1999) Sulfide mineralogy, geochemistry, and ore genesis of the Kidd Creek deposit: Part I. North, Central, and South orebodies. Econ Geol Mon 10: 163–224

Hannington MD, de Ronde CEJ, Petersen S (2005) Sea-floor tectonics and submarine hydrothermal systems. Econ Geol 100th Anniversary Volume, pp 111–141

Huston DL, Brauhat CW, Drieberg SL, Davidson GJ, Groves DI (2001) Metal leaching and inorganic sulfate reduction in volcanic-hosted massive sulfide mineral systems: evidence from the paleo-Archean Panorama district, Western Australia. Geology 29:687–690

Huston DL, Relvas JMRS, Gemmell JB, Drieberg S (2011) The role of granites in volcanic-hosted massive sulphide ore-forming systems: an assessment of magmatic–hydrothermal contributions. Miner Deposita (2011) 46:473–507

Huston DL, Eglington B, Pehrsson S, Piercey SJ (2022) Global database of zinc-lead-bearing mineral deposits. Geosci Austr Rec 2022/10

Huston DL, LaFlamme C, Beaudoin G, Piercey S (2023) Light stable isotopes in volcanic-hosted massive sulfide ore systems. In: Huston DL, Gutzmer J (eds) Isotopes in economic geology, metallogenesis and exploration. Mineral Resources Reviews, Springer-Nature, pp 245–282

Ishihara S, Sasaki A (1978) Sulfur of kuroko deposits—a deep seated origin. Mining Geol 28:361–367

Jamieson JW, Wing BA, Farquhar J, Hannington MD (2013) Neoarchaean seawater sulphate concentrations from sulphur isotopes in massive sulfide ore. Nature Geosci 6:61–64

Knauth LP (2005) Temperature and salinity history of the Precambrian ocean: implications for the course of microbial evolution. Palaeogeogr Palaeoclimatol Palaeoecol 219:53–69

LaFlamme C, Barré G, Fiorentini ML, Beaudoin G, Occhipinti S, Bell J (2021) A significant seawater sulfate reservoir at 2.0 Ga determined from multiple sulfur isotope analyses of the Paleoproterozoic Degrussa Cu-Au volcanogenic massive sulfide deposit. Geochim Cosmochim Acta 295:178–193

Large RR, Gemmel JB, Paulick H, Huston DL (2001) The alteration box plot: a simple approach to understanding the relationship between alteration mineralogy and lithogeochemistry associated with volcanic-hosted massive sulfide deposits. Econ Geol 96:957–971

Mercier-Langevin P, Dubé B, Hannington MD, Richer-Laflèche M, Gosselin G (2007b) The LaRonde Penna Au-rich volcanogenic massive sulphide deposit, Abitibi greenstone belt, Quebec: part II. Lithogeochemistry and paleotectonic setting. Econ Geol 102:611–631

Mosier DL, Berger VI, Singer DI (2009) Volcanogenic massive sulfide deposits of the world: Database and grade and tonnage models. US Geol Surv Open-File Rep 2009-1034

Ohmoto H, Skinner BJ (eds) (1983) The Kuroko and related volcanogenic massive sulphide deposits. Econ Geol Mon 5, 604 pp

Ohmoto H, Mizukami M, Drummond SE, Eldridge CS, Pisutha-Arnond V, Lenagh TC (1983) Chemical processes in Kuroko formation. Econ Geol Mon 5:570–604

Pisutha-Arnond V, Ohmoto H (1983) Thermal history, and chemical and isotopic compositions of the ore-forming fluids responsible for the kuroko massive sulfide deposits in the Hokuroku district of Japan. Econ Geol Mon 5:523–558

Relvas JMRS, Barriga FJAS, Longstaffe F (2006) Hydrothermal alteration and mineralization in the Neves-Corvo volcanic-hosted massive sulfide deposit, Portugal: II. Oxygen, hydrogen and carbon isotopes. Econ Geol 101:791–804

Richards JP (2009) Postsubduction porphyry Cu-Au and epithermal Au deposits: products of remelting of subduction-modified lithosphere. Geology 37:247–250

Sangster DF (1968) Relative sulphur isotope abundances of ancient seas and strata-bound sulphide deposits. Proc Geol Assoc Can 19:79–91

Sasaki A (1970) Seawater sulfate as a possible determinant for sulfur isotopic compositions of some strata-bound sulfide ores. Geochem J 4:41–51

Sillitoe RH, Hannington MD, Thompson JFH (1996) High sulfidation deposits in the volcanogenic massive sulfide environment. Econ Geol 91: 204–212

Solomon M, Rafter TA, Jensen ML (1969) Isotope studies on the Rosebery, Mount Farrell and Mount Lyell ores, Tasmania. Mineral Deposita 4:172–199

Sheppard SMF (1986) Characterization and isotopic variations in natural waters. Rev Mineral 16:165–183

Von Damm LK (1990) Seafloor hydrothermal activity; black smoker chemistry and chimneys. Ann Rev Earth Planet Sci 18:173–204

Relationship between Fe-Cu and polyelement Co-Ni-Pb-Bi-Sb-As-S mineralization at the Tisová deposit (Bohemian Massif)

Jan Kamenský[1,2], Jan Pašava[1], Anna Vymazalová[1], Irina Andronikova[1], Petr Rojík[3]
[1]Czech Geological Survey, Prague, Czech Republic
[2]Institute of Geochemistry, Mineralogy and Mineral Resources, Faculty of Science, Charles University, Prague, Czech Republic
[3]Příbramská 381, 357 01 Rotava, Czech Republic

Abstract. We studied relationship between massive sulfide Fe-Cu and polyelement Co-Ni-Pb-Bi-Sb-As-S mineralization at the Tisová deposit (Bohemian Massif). Main base metal sulfides (BMS) are predominantly represented by chalcopyrite, pyrrhotite and pyrite, accompanied by arsenopyrite, native Bi, breithauptite, cobaltite, Fe-oxides, galena, sphalerite and ullmanite-willyamite phase. We propose the following mineral succession: (1) pyrite I, chalcopyrite, pyrrhotite, sphalerite, pyrite II; (2) Co-Ni-Sb-As-S mineralization (3) galena and Bi-minerals. The presence of Co-Ni-Pb-Bi-Sb-As-S phases associated with BMS at Tisová and dominant Pb-Cu-Fe-Sb-As mineralization at the nearby Skalka occurrence can indicate late hydrothermal processes likely associated with intrusion of Variscan granitoids. Subsequent laser ablation (LA-ICP-MS) study resulted in the determination of elevated amounts of several critical metals (Co, Ni, Ga, Ge, As, Sb and Bi) and the deposit can be considered prosperous resource of critical metals (CRMs).

1 Introduction

The Tisová deposit (2.5 km north of Kraslice, Czech Republic) was one of the most important deposits of Cu (Au, Ag) ores in Bohemia. It was mined from the 13th century but reached its peak between the 15th and 17th centuries. The deposit was then mined in the period 1899-1908 and 1959-1973 (Beran 1997, Chrt et al. 1972, Pertold et al. 1994).

Several genetic models have been suggested on the genesis of the deposit (from a purely sedimentary to volcano-sedimentary and/or epigenetic hydrothermal) and Pertold et al. (1994) based on geological environment, host rock association and relatively high contents of As, Co and Au in the ores classified the Tisová deposit as a Besshi-type deposit.

Anomalous concentrations of platinum group elements (PGE) and selected critical metals were reported by Pašava et al. (2011) and Pašava et al. (2022), respectively.

The mineralogy of the Tisová deposit was studied by many authors, e.g. Beran (1997), Chrt et al. (1972), Pertold et al. (1994) and others. The ore bodies are dominantly composed of chalcopyrite, pyrite and pyrrhotite. Furthermore Beran (1997) reports that 86 minerals are known from the Tisová deposit, including Bi (native Bi, bismuthinite, bismutoferrite) and Co-Ni-As-S mineralization (cobaltite, ullmanite-willyamite phase).

Our study focuses on the common Fe-Cu ores and its relationship between Co-Ni-Pb-Bi-Sb-As-S mineralization, which is described in more detail.

2 Geological settings

The deposit is formed by a number of concordant ore lenses within a sequence of phyllitic metasediments, with interbedded metabasic layers of the Paleozoic age between the Karlovy Vary and the Smrčiny granite plutons. The whole sequence is crosscut by a porphyry granodiorite veins (Fig. 1; Pertold et al. 1994) but also by neovolcanites and pegmatites (Beran 1997). The footwall of the deposit is characteristic of brecciated fragments of the host rocks. The ore bodies can be generally divided into three horizons - lower, middle and upper (Beran 1997, Chrt et al. 1972, Pertold et al. 1994). Of these described horizons, the middle horizon is the most economically important. The average Cu-grade at the Tisová deposit is approximately 1 %. The thickness of individual ore bodies usually varies between 1-2 metres, but exceptionally reaches up to 10-30 metres. The ore bodies are concordant in relation to the host rocks and have a sharp contact with them (Pertold et al. 1994).

3 Material and analytical methods

3.1 Ore samples

The studied ore samples were collected in 1950's by Dr. V. Škvor (**†)** at the Tisová deposit (Helena schaft) and were obtained from the most economically middle horizon of the deposit.

3.2 Electron microscopy techniques

The study of the ore mineralization from the Tisová deposit were performed using electron microscope Tescan Mira3 GMU equipped with a field emission gun (FEG; Tescan, Czech Republic) using energy-dispersive spectroscopy (EDS) and wave-dispersive spectroscopy (WDS) at the Czech Geological Survey. The chemical analyses were performed using WDS mode. Analytical conditions were: accelerating voltage 15 kV, beam current 35 nA, beam size 1-3 μm. The standards and wavelengths used were: Bi (Mα), Cu (Kα), Fe (Kα),

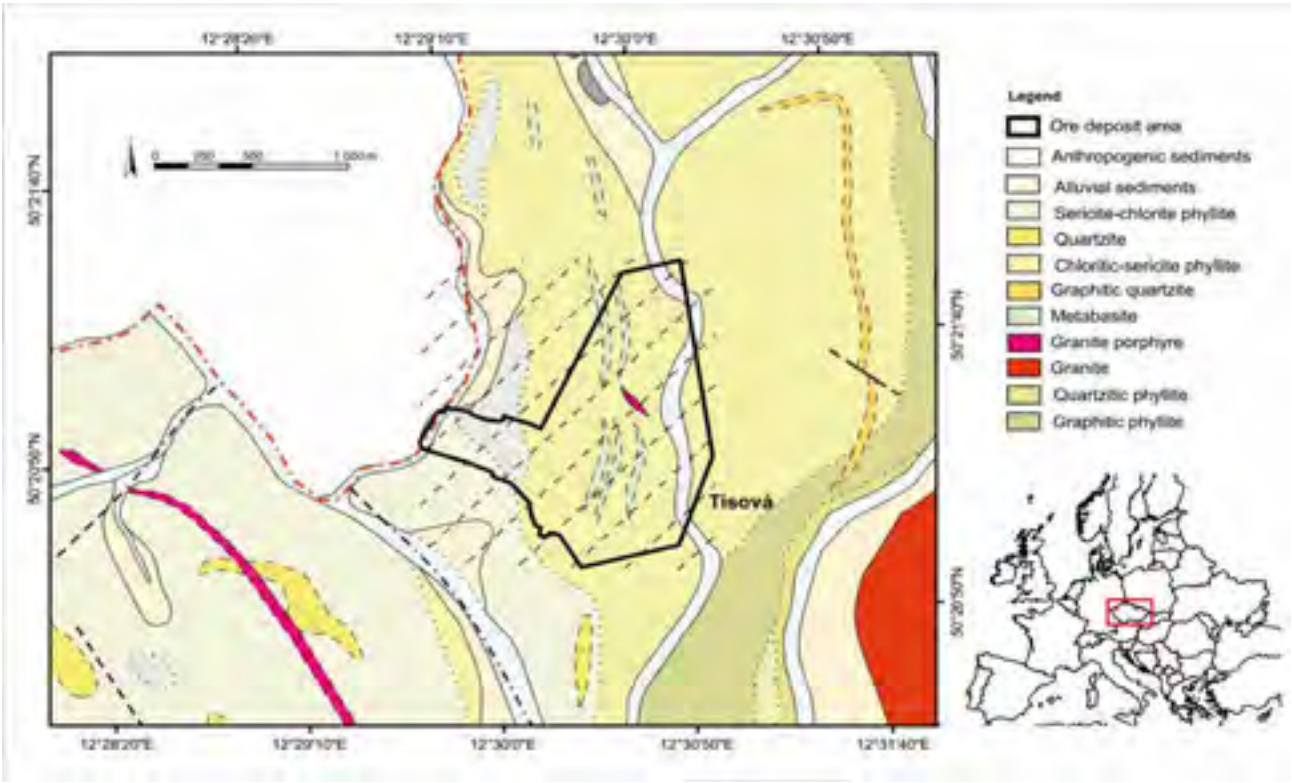


Figure 1. Geological map of the Tisová deposit (modified from Chrt et al. 1972 and Pertold et al. 1994).

Ni (Kα), Pb (Mα), S (Kα) and Sb (Lα). Count times were 5/10s for Sb, 10/20s for Fe and 10s for Bi, Cu, Ni, Pb and S. Count time for background was 5/10s.

3.3 LA-ICP-MS

Trace elements analyses in selected sulfides were performed at the LA-ICP-MS (Czech Geological Survey) using an Agilent 7900 quadrupole ICP-MS (Agilent Technologies Inc., Santa Clara, USA) coupled to an Analyte Excite Excimer 193 nm LA system (PhotonMachines, USA) equipped with a two-volume HelEx ablation cell. Two reference materials were used for external calibration: USGS MASS-1 standard Fe-Cu-Zn-S pressed powder pellet (Willson et al. 2002) and UQAC-FeS-1 synthetic versatile reference material from the LabMaTer (University of Quebec in Chicoutimi, Canada; Duran et al. 2019). A synthetic basalt material (GSE-2g) was used as a control standard.

4 Results and discussion

The main mineralization at the Tisová deposit is represented by massive Fe-Cu sulfides (chalcopyrite, pyrite and pyrrhotite). Pyrite from our samples can be divided into three generations: *Pyrite 1* (synmetamorphic) forms layers/impregnations of euhedral and/or fractured grains in phyllite
Pyrite I (epigenetic/hydrothermal and/or recrystallized) forms larger anhedral/rounded grains which resulted from fracturing and replacement/corrosion of pyrite by younger pyrrhotite, chalcopyrite, pyrite II, quartz and carbonate
Pyrite II (epigenetic/hydrothermal and/or recrystallized) is fine grained, forming tiny veinlets intruding ore sulfides and also a product of transformation of pyrrhotite.

Major BMS are accompanied by accessory polyelement Co-Ni-Pb-Bi-Sb-As-S mineralization (bismuthinite, native Bi, breithauptite, cobaltite, galena and ullmanite-willyamite phase) which has been studied in more detail.

Bismuthinite forms an aggregates up to 15 μm in massive sulphide ores (chalcopyrite, pyrite I, pyrrhotite and sphalerite) and it is associated with, native bismuth, cobaltite, Bi-S phase, galena and ullmanite-willyamite phase (Fig. 2a,d). It is likely that the decomposition of bismuthinite results in the formation of native Bi (Trdlička and Kupka 1957).

Native Bi (Fig. 2b,c,d) is in our samples relatively common and forms irregular aggregates up to 10 μm in massive sulfides (chalcopyrite, pyrite I, pyrrhotite and sphalerite). It occurs in association with bismuthinite, breithauptite, cobaltite, galena and ullmanite-willyamite. It also fills cracks in the massive sulfides. According to Trdlička and Kupka (1957), native Bi may be formed by the decomposition of bismuthinite. Beran (1997) considers that native Bi and Bi-minerals are the youngest phases of mineralogical succession of the ore fill at the deposit.

Breithauptite is rare and occurs as a tiny inclusions (up to 7 μm) in aggregates of ullmanite-willyamite phase. These phases are in assemblage with native Bi and galena and occur in sphalerite and chalcopyrite (Fig. 2b).

Cobaltite forms euhedral and subhedral grains in association with Bi-minerals and ullmanite-willyamite phase (2d). It also occurs as automorphic grains in BMS (e.g. pyrite I.)

Galena is present as a common accessory mineral and occurs together with bismuthinite, native Bi, breithauptite, cobaltite, ullmanite-willyamite phase in BMS (e.g. chalcopyrite, pyrite I, pyrrhotite and sphalerite; Fig. 2a,b,c).

Ullmanite-willyamite phase in our samples forms irregular aggregates up to 15 μm and occur in common sulfides (pyrrhotite, pyrite) and it is associated with bismuthinite, native Bi, breithauptite, cobaltite, and galena (Fig. 2b,c). The empirical formula of ullmanite-willyamite phase with minor amount of Fe (up to 0.18 apfu) corresponds to $(Co_{0.49-0.60}Ni_{0.35-0.47}Fe_{0.11-0.18})_{\sum 1.05-1.11}Sb_{0.89-0.96}S_{1.00}$ and the Co/Co+Ni ratio is between 0.51 to 0.64.

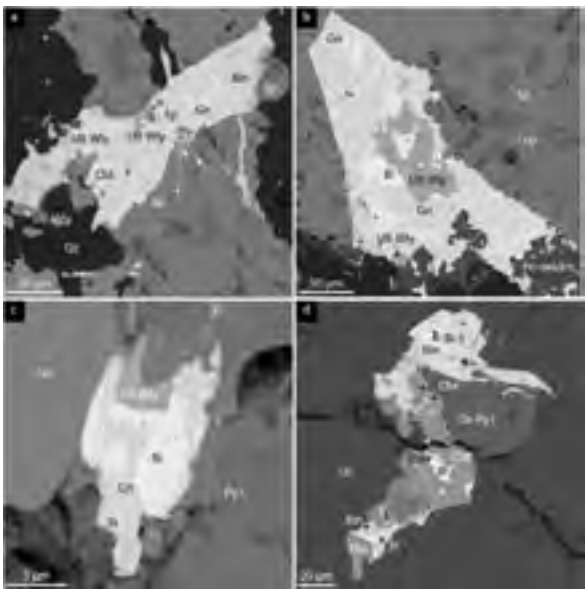


Figure 2. Representative back-scattered electron images (BSEI) of Fe-Cu and polyelement Co-Ni-Pb-Bi-Sb-As-S mineralization. a) Association of bismuthinite (Bin), native (Bi), cobaltite (Cbt), ullmanite-willyamite (Ull-Wly) phase in sphalerite (Sp). b) An aggregate of native bismuth, galena and ullmanite-willyamite phase in sphalerite and chalcopyrite (ccp). Inclusions of breithauptite (Bhp) occur in aggregates of the ullmanite-willyamite phase. c) Assemblage of native bismuth, galena and ullmanite-willyamite phase in sphalerite and pyrite I. d) An aggregate of bismuthinite, Bi-S phase, native bismuth, cobaltite in quartz and pyrite I.

It was found that some of BMS contain elevated amounts of critical metals (Tab. 1); the highest values follows: ^{59}Co (median = 432 ppm; pyrite 1), ^{60}Ni (median = 59 ppm; pyrite II), ^{71}Ga (median = 2.73 ppm; pyrite 1), ^{72}Ge (median = 2.7 ppm; chalcopyrite), ^{75}As (median = 244 ppm; pyrite I), ^{121}Sb (median = 37 ppm; pyrite II), ^{209}Bi (median = 3.6 ppm; chalcopyrite).

Table 1. Content of critical metals in selected BMS from the Tisová deposit.

	^{59}Co	^{60}Ni	^{71}Ga	^{72}Ge	^{75}As	^{121}Sb	^{209}Bi
Pyrite 1 (n=60)							
min	99	3	0.01	1.2	2.0	3	0.01
max	1781	166	35.09	4.6	29.2	87	24
median	432	30	2.73	2.2	4.3	12	0.6
Pyrite I (n=580)							
min	0.01	0.2	0.001	0.0	0.1	0.01	0.001
max	43603	2748	53.05	7.9	27047	1009	620.5
median	143	24	0.02	0.1	244	2	0.3
Pyrite II (n=411)							
min	0.01	2	0.004	0.02	0.2	0.1	0.014
max	33776	3282	8.27	5.6	382579	1490	4290
median	411	59	0.07	0.3	1.6	37	2.5
Chalcopyrite (n=417)							
min	0.02	0.4	0.04	1.8	0.2	0.1	0.1
max	46840	1950	36.81	5.0	184405	7377	55338
median	3	3	0.4	2.7	2.3	3	3.6

Sejkora et al. (2016) described dominant jamesonite accompanied by boulangerite, Ag-rich tetrahedrite, Fe-rich sphalerite and ullmanite with minor content of As and Fe from ore mineralization from the Skalka adit (western part of Kraslice city, about 3 m SSE of the Tisová deposit). The mineralization is bound to quartz veinlets hosted in volcano-sedimentary complex (mainly in chlorite-muscovite schist) accompanied by numerous porphyry dykes and lamprophyres. It is quite different from the typical massive ores from the Tisová deposit, where chalcopyrite, pyrite and pyrrhotite predominate, but in a way close to less frequent and apparently younger Pb-Cu-Zn-Ag-Bi-Sb-S mineralization described from Tisová (Beran 1997, Pašava et al. 2011).

5 Conclusions

The results of our study can be summarized as follows:

Main BMS represented by chalcopyrite, pyrite, pyrrhotite and sphalerite are enriched in selected critical metals. The presence of discrete Co phases and anomalous Co concentrations in synmetamorphic and epigenetic/hydrothermal pyrite make this deposit a promising source of CRM (especially Co).

It is likely that main BMS were followed by Co-Ni-Sb-As-S mineralization represented mainly by cobaltite and ullmanite-willyamite phase and that the Pb-Bi-S mineralization is associated with the youngest hydrothermal processes.

Acknowledgements

We would like to thank Dr. Š. Křížová and Mgr. O. Pour (Czech Geological Survey) for electron microscopy analysis. We thank Dr. F. Veselovský (Czech Geological Survey) for stimulating discussions. The project Rock Environment and Natural Resource (RENS), No SS02030023 from

the Technological Agency of the Czech Republic (Environment for Life Programme) is gratefully acknowledged. This is also a contribution to the Strategic Research Plan of the Czech Geological Survey (DKRVO 2023-2027). We sincerely appreciate Jim Franklin´s extraordinary contribution to economic geology and especially genesis and classification of Volcanogenic Massive Sulfide (VMS) deposits worldwide.

References

Beran P (1997) Mineralogie ložiska Cu (Ag, Au, Co) rud Tisová u Kraslic. Bull mineral-petrolog Odd Nár Muz (Praha) 4(1): 65–77 (in Czech).

Duran CJ, Dube´-Loubert H, Page´ P, Barnes SJ, Roy M, Savard D, Cave B, Arguin JP, Mansur ET (2019) Applications of trace element chemistry of pyrite and chalcopyrite in glacial sediments to mineral exploration targeting: Example from the Churchill Province, northern Quebec, Canada. J Geochem Explor 196: 105–130.

Chrt J, Neumann J, Hoffman V, Trdlicka Z (1972) Copper-sulfide deposit of Tisová (Krušné hory Mts.). Sbor geol Věd R LG 15: 7–52 (in Czech).

Pašava J, Vymazalová A, Malec J, Rojík P (2011) Anomalous PGE in Fe-Cu-As ores from the Tisová Besshi-type deposit (Bohemian Massif). In: Campos E (ed) Proc 11th SGA Bienn Meet 26–29.

Pašava J, Andronikova I, Veselovský F, Vymazalová A, Pour O (2022) Critical metals in sulfides of the Tisová Cu (Fe-As) deposit (Bohemian Massif, Czech Republic): results from LA-ICPMS study. In: Christie AB (ed) Proc 16th SGA Bienn Meet 2:136.

Pertold Z, Chrt J, Budil V, Burda J, Burdova P, Kříbek B, Pertoldová J, Gaskarth B (1994) The Tisová Cu deposit: a Besshi-type mineralization in the Krušné hory Mts., Bohemian Massif, Czech Republic. Monogr Ser Mineral Depos 31: 71–95.

Sejkora J, Krištůfek M, Pauliš P, Jakobec K (2016) Sulfidická mineralizace ze Skalky u Kraslic (Česká republika). Bull mineral-petrolog Odd Nár Muz (Praha) 24(2): 278–284 (in Czech).

Trdlička Z, Kupka F (1957) Bismutin a ryzí vizmut z Tisové u Kraslic. Čas Mineral Geol 2: 331–337 (in Czech).

Wilson SA, Ridley WI, Koenig AE (2002) Development of sulfide calibration standards for the laser ablation inductively-coupled plasma mass spectrometry technique. J Anal At Spectrom 17: 406-409.

Zircon petrochronology of Paleoproterozoic VMS deposits in the Penokean Orogen, Wisconsin, USA

Robert Lodge[1], Aidan Kwiatkowski[1], and Evan Weber[1,2]
[1]Department of Geology and Environmental Science, University of Wisconsin-Eau Claire, Eau Claire, Wisconsin, USA
[2]Current Affiliation: Intertek PSI, Chippewa Falls, Wisconsin, USA

Abstract. The Paleoproterozoic Penokean Orogen in Northern Wisconsin is known to host multiple volcanogenic massive sulfide (VMS) deposits, which are important sources of Cu, Zn, Pb, Ag, and Au. Despite known large and potentially economic VMS deposits, limited outcrop exposure and lack of continuous exploration efforts has hindered detailed reconstructions of the VMS-hosting environment. This study utilizes zircon petrochronology (U/Pb, Lu-Hf, trace elements) from several VMS deposits (Lynne, Flambeau, Eisenbrey) to provide a more complete understanding of the timing of magmatism and magmatic environment in which they formed. Zircons were imaged and analyzed at the Mineral Exploration Research Center, Laurentian University, Canada via split stream multicollector LA-ICPMS. Results have indicated two distinct VMS-forming magmatic events at ca. 1835 Ma and inherited 1875 Ma zircon population present in each sample. The ca. 1835 Ma VMS-forming event supports widespread submarine extension when historic tectonic reconstructions have Penokean orogenesis ending. Epsilon-Hf and trace element discrimination reveal both magmatic events are petrogenetically identical and are produced in similar peri-continental arc environments that are producing hydrated, variably oxidized magmas contaminated with Archean basement.

1 Introduction

The Paleoproterozoic Penokean orogen in the Great Lakes region of northern USA **(Fig. 1)** represents one of the classic Precambrian orogenic belts in North America (e.g., Schulz and Cannon 2007). The Pembine-Wausau terrane within the orogen is best known for its extensive mineral endowment, comprising at least 150 million metric tons of polymetallic volcanogenic massive sulfide (VMS) deposits (DeMatties 1994, 2018). Despite decades of successful greenfields exploration and rapid discovery of VMS showings, the extensive mineral endowment of this terrane, the only mining operation in the mineral belt was the supergene-enriched zone of the Flambeau Cu-Au deposit near Ladysmith, Wisconsin. The Penokean Orogen and its VMS deposits remains one of the more poorly understood and underexplored mineral districts in North America.

The volcanic terranes in the Penokean orogen are comprised of dominantly submarine volcanic rocks formed in a suprasubduction setting at the southern edge of the Archean Superior craton during the formation of the Columbia supercontinent (LaBerge and Myers 1984; Schulz and Cannon 2007; Sims et al. 1989). The VMS deposits are almost entirely contained within the Ladysmith-

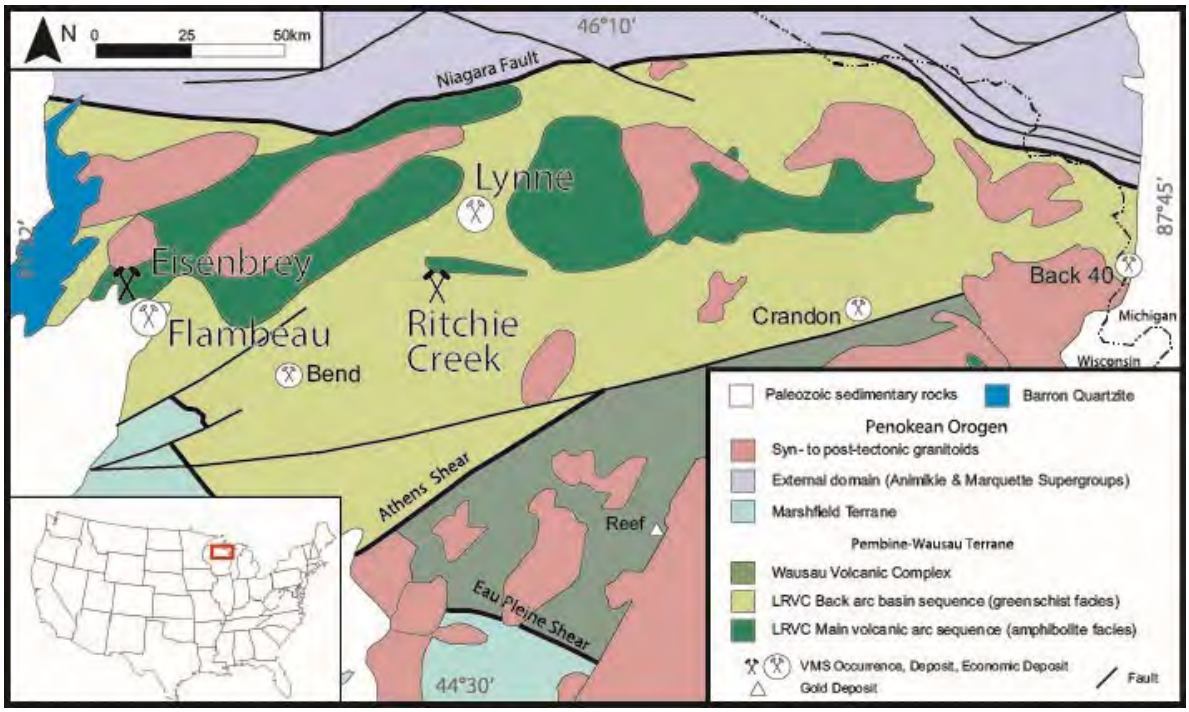


Figure 1. Generalized geologic map of the Penokean Orogen illustrating major tectonostratigraphic subdivisions and the location of sampled and major VMS occurrences. See inset map for location. Figure modified from Schulz and Cannon (2007) and DeMatties (1994). Subdivisions of Pembine-Wausau terrane from DeMatties (1994, 2018). LRVC = Ladysmith-Rhinelander volcanic complex.

Rhinelander Volcanic Complex in the Pembine-Wausau terrane (Fig. 1). Historic U-Pb geochronology indicates that volcanism occurred between 1889–1835 Ma (Sims et al. 1989) and most VMS-hosting strata is constrained between 1875–1873 Ma (Quigley 2016). The Penokean orogen has been interpreted to have ended ca. 1835 Ma with the intrusion of local unfoliated "stitching" plutons (Schulz and Cannon 2007), but ca. 1835 Ma U/Pb ages from the Back Forty Zn-Cu deposit (Quigley 2016) and several intrusion and gneissic complexes in the eastern part of the terrane (Zi et al. 2021) questions when orogenic activity ended.

The discovery of the 18.2 Mt Back Forty VMS deposit in Michigan, changes in Wisconsin's mining legislation easing the sulfide mining moratorium in 2018, and a recent national push for securing domestic critical mineral resources have reinvigorated exploration interests in the Penokean orogen. This study represents one of the first datasets that attempts to constrain the timing, geodynamic setting, and crustal architecture of VMS deposits in the region to further our knowledge of the mineral-forming systems in the belt.

2 Samples and Methods

2.1 Sample Descriptions

The sample obtained from the 5.8 Mt Flambeau Cu-Zn-Au deposit was from the quartz-chlorite unit that is interpreted to be a chlorite-altered felsic volcaniclastic rock representative of the felsic units in both hanging wall and footwall strata (Lodge et al. 2024). The unit is a quartz augen chlorite schist unit characterized by 1-3 mm grayish-blue quartz porphyroclasts in a variably altered, chlorite- and quartz-rich matrix.

The volcanic strata of the 7.3 Mt Lynne Zn-Pb-Cu deposit has been previously dated at ca. 1875 Ma (Quigley 2016). The sample obtained from the Lynne deposit for this study is from a granodiorite pluton that was previously interpreted to be synvolcanic based on similar rift-like geochemistry to overlying felsic volcanic strata (Glodowski and Lodge 2023).

A sample from the 1.8 Mt Eisenbrey Zn-Cu deposit was obtained from a bedrock exposure of an intermediate schist that is 400 ft along strike from the sulfide mineralization. The homogeneous composition, crude layering, and faint lapilli suggest that this rock is volcanic in origin. The sample is fine-grained, grey to yellow in color, and has 5% biotite in a chlorite and quartz-feldspathic matrix.

2.2 Analytical Methods

Samples from each deposit were pulverized prior to processing on a Gemini shaking table to separate heavy mineral fractions. Zircons were further concentrated by magnetitic separation, heavy liquid separation, and pyrite flotation prior to mounting on epoxy disks. Polished disks were imaged by cathodoluminescence and backscattered electron microscopy at the Mineral Exploration Research Centre's Isotope Geochemistry Lab, Laurentian University, Canada. Zircon isotopic (U-Pb, Lu-Hf) and trace element data were analyzed simultaneously using a laser ablation split-stream system including a 193 nm Photon Machines Analyte G2 laser, a Neptune Plus multicollector–inductively coupled plasma–mass spectrometer (ICP-MS), and an iCap-TQ quadrupole ICP-MS. Analyses with discordant $^{207}Pb/^{206}Pb$ and $^{206}Pb/^{238}U$ ages, Sr > 10 ppm, or detected ^{204}Pb were excluded from the U-Pb and Lu-Hf datasets. Those of La > 10 ppm or detected Ca were also omitted from the zircon trace element data to avoid hydrothermal or inclusion contamination.

3 Results

3.1 U/Pb Ages

Following geochemical filtering and screening, final interpreted U/Pb ages were determined using Isoplot. All samples showed a similar bimodal distribution of U/Pb ages centred on ca. 1830-1835 Ma and 1870-1875 Ma (Fig. 2). Low U/Th abundances and magmatic zoning observed in cathodoluminescence indicate all ages are of magmatic origin, and the youngest peak of ages represent the crystallization age of each sample. The footwall granodiorite at the Lynne Deposit is 1827.4 ± 1.9 Ma. The altered felsic volcanic rock at the Flambeau Deposit is 1834.1 ± 2.9 Ma. The intermediate volcaniclastic rock at the Lynne Eisenbrey Deposit is 1831.4 ± 2.0 Ma.

The second, older peak of ages from each deposit at ca. 1875 Ma are interpreted to be inherited grains from an older Penokean magmatic event. The Flambeau also included some inherited Archean-aged zircons.

3.2 Zircon Trace Element Geochemistry

Since two similar clusters of U/Pb ages at ca. 1835 Ma and 1875 Ma are present in each sample, zircon trace element data allowed for petrogenetic interpretations of both magmatic events. After filtering of dataset, a total of 269 zircons were analysed. There is little difference between the magmatic events (Fig.3). Rare earth element concentrations are typical of magmatic zircons with strongly depleted LREE (chondrite-normalized $La/Yb < 0.1$) and high Th/U ($Th/U > 0.3$). All zircons have positive Ce anomalies ($Ce/Ce^* > 1$) and negative Eu anomalies ($Eu/Eu^* < 1$). Most zircons also have high U/Yb (< 0.2) and Nb/Yb (< 0.01) ratios.

3.3 Lu-Hf Isotopes

The purpose of Lu-Hf isotopic analyses in zircons was to test the role and extent of Archean basement

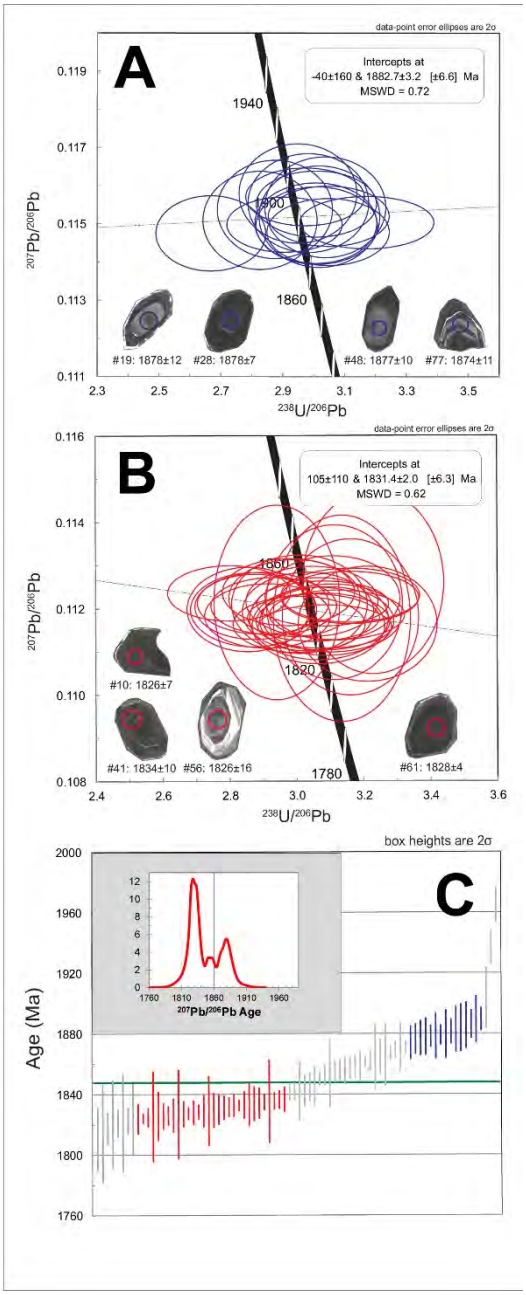


Figure 2. U/Pb data from the Eisenbrey deposit illustrating trends in ages present in all samples. A) U/Pb concordia diagram of older magmatic zircons. (B) U/Pb concordia diagram of younger magmatic zircons interpreted to be crystallization age of sample. (C) Weighted mean diagram distribution of ages and analysed grains. Inset image shows frequency distribution of ages in sample.

involvement in the petrogenesis of Penokean VMS. A total of 189 individual Lu-Hf analyses were completed across all samples. Data obtained from each deposit shows variable Hf isotopic compositions with initial ƐHf ($ƐHf_{(i)}$) values ranging from -22 to +25, with most values being above the CHUR line (Fig. 3). Analyses from individual deposits all broadly show the same trends with a mix of both positive and negative $ƐHf_{(i)}$ values and have no obvious correlation with either magmatic pulse.

4 Discussion

4.1 Timing of Penokean VMS formation

The interpreted ages of the VMS deposits in this study are generally coeval with Back Forty deposit (Quigley 2016), and represent a better constrained VMS-forming event at ca. 1835 Ma in the Penokean Orogen at a time when accretionary events were historically considered complete in the orogen. This prompts a new evaluation of the VMS metallogeny of the region and the different tectonic components of the Penokean Orogen.

Magmatic zoning observed in cathodoluminescence and careful geochemical filtering of the datasets suggest the analysed zircons are of magmatic origin and not a ca. 1835 metamorphic resetting of U/Pb systematics. Additionally, there is no correlation between $^{207}Pb/^{206}Pb$ age and metamorphic geochemical proxies (Th/U, U/Ce), which suggests younger ages are metamorphic. Both volcaniclastic rocks and intrusive rocks from these VMS deposits show the sample bimodal distribution regardless of metamorphic grade: younger ca. 1835 Ma VMS-hosting strata are inheriting zircons from older ca. 1875 VMS-forming magmatism.

4.2 Tectonic and Magmatic Environment

Despite the significance of discovering two magmatic episodes forming VMS deposits in the Penokean Orogen, the petrogenetic similarities between the events are strikingly similar. Trace element discrimination plots reveal all zircons from Penokean VMS deposits have arc-like affinities (Grimes et al. 2015) producing hydrated, variably oxidized magmas (Mole et al. 2021). Sub-chondritic $ƐHf_{(i)}$ and inherited Archean zircons indicate both magmatic pulses have isotopic inheritance from Archean basement. This is consistent with a peri-continental arc environment, in accordance with interpretations from Van Wyck and Johnson (1997).

The episodic nature of rift magmatism suggests that the tectonic conditions were variable. Tectonic models from Zi et al. (2021) suggest episodic rifting punctuated by a period of compression, possibly from ridge or plateau subduction, that will account for uplift and erosion present in ca. 1850 Penokean basins (Schulz and Cannon 2007). Our dataset confirms a wide-spread second rifting event that forms VMS deposits. However, the remarkable similarity between rift magmatism suggests little modification to the magmatic environment or crustal architecture as might be expected during compressional events. Our data suggests a 40-million-year volcanic hiatus. More data is needed to understand the mechanism of this hiatus and its significance to the metallogeny of the region.

5 Conclusions

This study presents the one of the first known zircon petrochronological datasets from the any part of the Penokean orogen and the first attempt to apply it to

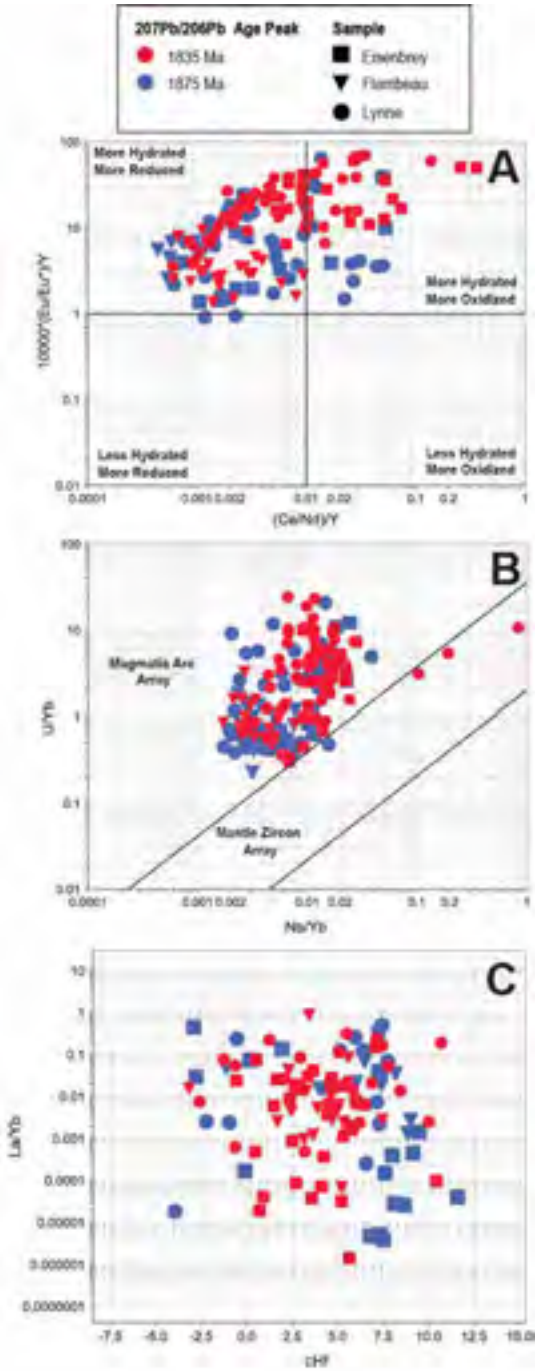


Figure 3. Zircon trace element and Hf-isotope discrimination diagrams. (A) Magmatic discrimination diagram from Mole et al. (2021). (B) Tectonic discrimination diagram from Grimes et al. (2015). (C) Chondrite-normalized La/Yb versus $\varepsilon Hf_{(i)}$.

the petrogenesis of Penokean VMS deposits. Data from the Flambeau, Lynne, and Eisenbrey VMS-hosting strata reveal a widespread ca. 1835 Ma magmatic pulse that requires a re-examination of the tectonic model for the Penokean Orogen and the geodynamic setting of VMS mineralization. Additionally, both magmatic pulses of have similar trace element and Hf-isotopic systematics, requiring a 40-million-year hiatus in volcanism without significant change in petrogenetic characteristics. More information on the magmatic and tectonic setting of the Penokean VMS deposits is required to properly guide future exploration efforts.

Acknowledgements

The authors would like to acknowledge the Wisconsin Geological and Natural History Survey and the Natural Resources Research Institute (Duluth, Minnesota) for providing access to drill core. Funding for the project has been provided by the WiSys Ignite Applied Research Grant, USGS Data Preservation Grant, and grants through the University of Wisconsin-Eau Claire Office of Research and Sponsored Programs.

References

DeMatties TA (1994) Early Proterozoic volcanogenic massive sulfide deposits in Wisconsin: An overview. Econ Geol 89: 1122-1151.

DeMatties TA (2018) Effects of paleoweathering and supergene activity on volcanogenic massive sulfide (VMS) mineralization in the Penokean Volcanic Belt, northern Wisconsin, Michigan and east-central Minnesota, USA: Implications for future exploration. Ore Geol Rev 95: 216-237.

Grimes CB, Wooden JL, Cheadle, MJ, John, BE (2015) "Fingerprinting" tectono-magmatic provenance using trace elements in igneous zircon. Contrib Mineral Petrol 170, 46.

Glodowski, LN, Lodge RWD (2023) Characterizing volcanic host stratigraphy and syn-volcanic intrusions at the Lynne, Zn-Pb-Cu deposit, Oneida Co., Wisconsin. Institute on Lake Superior Geology Proceedings, 69th Annual Meeting, Eau Claire, Wisconsin, Part 1-Program and Abstracts, p. 34-35.

LaBerge GL, Myers PE (1984) Two early Proterozoic successions in central Wisconsin and their tectonic significance. Geol Soc Am Bull 95: 246-253.

Lodge RWD, Zens ZA, Jacobson RE, Leybourne M (2024) Geology and lithogeochemistry of the Paleoproterozoic Flambeau Cu-Zn-Au volcanogenic massive sulfide deposit, Wisconsin, USA. Econ Geol, v. 119: 23-44.

Mole DR, Thurston PC, Marsh JH, Stern RA, Ayer JA, Martin LAJ, Lu YJ (2021) The formation of Neoarchean continental crust in the south-east Superior Craton by two distinct geodynamic processes. Precambrian Res 356, 106104.

Quigley A (2016) Setting of the volcanogenic massive sulfide deposits in the Penokean Volcanic belt, Great Lakes region, USA. Colorado School of Mines, Masters Thesis. 95 p.

Schulz KJ, Cannon WF (2007) The Penokean orogeny in the Lake Superior region. Precambrian Res 157: 4-25.

Sims PK, Van Schmus WR, Schulz KJ, Peterman ZE (1989) Tectonostratigraphic evolution of the Early Proterozoic Wisconsin magmatic terranes of the Penokean orogen. Can J of Earth Sci 26: 2145-2158.

Zi J-W, Sheppard S, Muhling JR, Rasmussen B (2021) Refining the Paleoproterozoic tectonothermal history of the Penokean Orogen: New U/Pb age constraints from the Pembine-Wausau terrane, Wisconsin, USA. Geol Soc Am Bull 134: 776-790.

Van Wyck N, Johnson CM (1997) Common Lead, Sm-Nd, and U-Pb constraints on petrogenesis, crustal architecture, and tectonic setting of the Penokean orogeny (Paleoproterozoic) in Wisconsin. Geol Soc Am Bull 109: 799-808.

Hydrothermal alteration overprinted by contact metamorphism: Balducho VMS prospect, central Peru

Emily Mora[1], Lluís Fontboté[2], Silvia Rosas Lizárraga[1], Victor García[1], Thed Mena[3], Edgar Pichardo[3]
[1] Geological Engineering Program, Pontifical Catholic University of Peru (PUCP), Peru
[2] Department of Earth Sciences, University of Geneva, Switzerland
[3] Minera Colquisiri S.A., Parque Norte 724, Lima, Perú

Abstract. The host rock of the Balducho prospect shows typical features for a submarine VMS deposit that has been affected by contact metamorphism. Acidic hydrothermal alteration and ocean floor mineral assemblages on mafic flows and sills have been largely obliterated by metamorphic reactions while preserving the overall chemical composition. Whereas felsic sills are partly affected by acidic hydrothermal alteration, the studied felsic sills occurring at the footwall are not. At this point, it is not possible to elucidate if the latter are post alteration or they just occur in areas devoid of hydrothermal alteration, leaving its relative timing as an open question.

1 Introduction

The Balducho VMS prospect in central Peru (-12.339 ºS, -76.479º W, 4.7 km SE of the Cuculí village), is emplaced within a steeply dipping and partly inverted submarine volcano-sedimentary sequence affected by contact metamorphism caused by the surrounding Coastal Batholith (Figs. 1, 2). Small scale underground workings exploited in the past a "manto" bearing massive barite, sphalerite, and chalcopyrite outcropping at surface for 500 m in N160 direction and dipping between 75 and 85° NE and recognized at surface between 1900 and 2150 m.a.s.l. Drilling performed in 2006-2007 identified the "manto" until 100-150 m below the surface (Fig. 2). The best intersection was 6.7 m thick with 6.4 % Zn and 0.18% Cu (Minera Huallanca 2007). The footwall of the "manto" is intensely altered and includes stockwork areas (Fig. 3). Vidal (1987) recognized the VMS character of Balducho. Recent lead isotope data show a strong similarity with signatures of mid Cretaceous VMS deposits in central Peru (Fontboté et al. 2025).

In the frame of the "Cuculí exploration project" of Minera Colquisiri, S.A., we present new observations on the host rock of the Balducho prospect, in particular on the effects of contact metamorphism on (i) mafic rocks previously intensely sericitized at the footwall of the "manto", and (ii) on rocks previously affected by sea-floor alteration in the rest of the sequence. Also, the question of which sills are overprinted or not by alteration is examined.

2 Methods

In addition to field work and microscopic observations, this contribution is based on extensive use of a portable XRF analyzer (pXRF) Niton® XL5 in rock powder aliquots. Despite their semiquantitative nature, the obtained analyses have helped to discriminate fine-grained magmatic rocks using Zr/TiO_2 ratios and to determinate Al and CCPI values of the alteration box plot of Large et al. (2001). For this, the Na value has been estimated using the method proposed by Fontboté (2018), estimation that has proved to be useful for VMS exploration projects.

3 Host rock

Two main rock types conform the geology of the Balducho area (Fig. 1). (i) The submarine volcano-sedimentary sequence hosting the VMS deposit that is dominated by mainly mafic and subordinate felsic rocks that were attributed to the Casma Group by Vidal (1987), and which may be tentatively correlated with basalts occurring 50 km NNW of Balducho, mapped as Quilmaná Formation, the lower unit of the Casma Group (León et al. 2023). There, 135.1 Ma ±1.6 and 136.7 ±1.6 Ma U-Pb zircon ages of samples from its lower levels and the fact that the formation is overlaid by the Late Cretaceous Chilca Formation allow to propose an Early Cretaceous age for the Quilmaná Formation (León et al. 2023). (ii) Intrusive rocks ascribed to the Cretaceous Peruvian Coastal Batholith. They include large granodiorite and tonalite bodies and decimetric to metric aplitic dykes. According to Santisteban Angeldonis et al. (2021), they belong to the Late Cretaceous Super Tiabaya unit that includes also monzogranitic and dioritic intrusions.

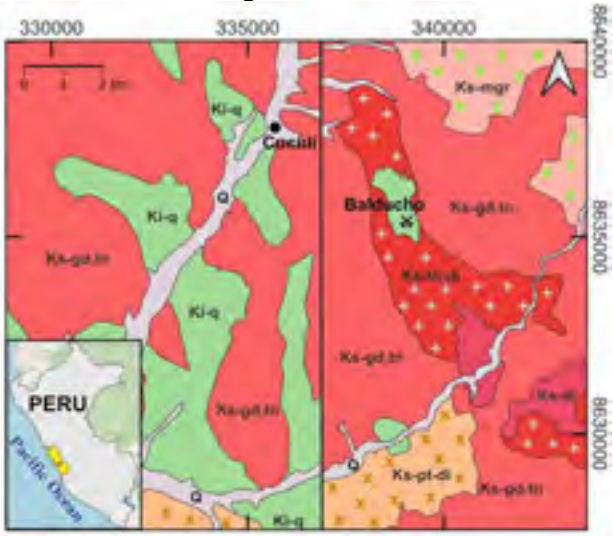


Figure 1. The occurrence area of the Quilmaná Formation (K-q) in the study area has been inserted in the geological sketch drawn with data of Palacios (1998, western part) and Santisteban Angeldonis (2021, eastern part). Diorite

(Ks-di), granodiorite-tonalite (Ks-gd,tn), tonalite-diorite (Ks-tn, di), monzogranite (Ks-mgr) units of the Tiabaya Super Unit and diorite of the Patap Super Unit (Ks pt-di) of the Coastal Batholith as well as Quaternary alluvial deposits (Q) are also shown.

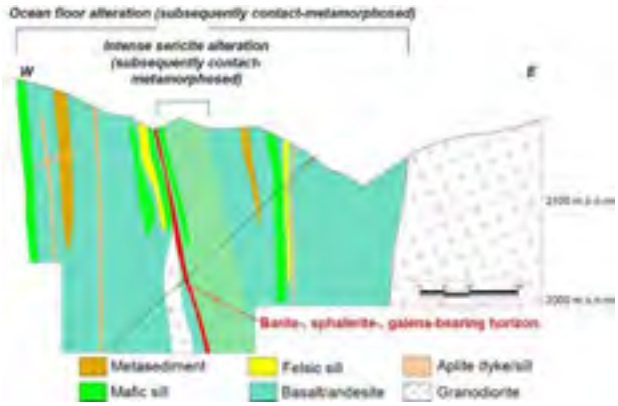


Figure 2 Schematic cross section of the Balducho deposit. Note the hydrothermal alteration on the footwall of the ore-bearing horizon (the sequence is slightly inverted).



Figure 3 Intensely altered (AI>85) stockwork beneath the ore-bearing horizon. Picture looking N.

2.1 Rocks attributed to the Quilmaná Formation

Volumetrically, the main rocks of the volcano-sedimentary sequence are basaltic and andesitic flows and sills (Zr/TiO2 <0.03). The flows have fine-grained matrix consisting mainly of plagioclase, partly fluidal. In places, they contain phantoms of plagioclase and amphibole phenocrysts. Small amounts of pyrite and magnetite grains occur too.

Only two of the studied mafic flows fall in the field of least altered samples of Large et al. (2001, Fig. 4). The rest show one of the following two alteration patterns.

1) Flows yielding AI values between 6 and 25 and CCPI larger than 65, i.e., values typical for ocean floor alteration (Fig. 4). The mineral associations consist mainly of plagioclase, quartz, biotite and subordinate chlorite and amphibole. Biotite replaces amphibole and chlorite and occurs in veinlets. Note that epidote and other minerals typical of ocean floor alteration are lacking as well as that chlorite is not abundant. The quartz biotite±amphibole mineral association is interpreted as a result of contact metamorphism. In mafic rocks, biotite crystallization requires temperatures above 400°C (Bucher 2023).

2) Flows with AI values between 70 and 98, i.e. values typical of acidic hydrothermal alteration with formation of sericite ± chlorite (Fig. 4). However, although a few samples show abundant muscovite, most of them have mineral associations largely dominated by quartz and biotite ± amphibole ± chlorite, being sericite or muscovite scarce or absent (Fig. 5). Again, this mineral association is interpreted as the result of contact metamorphism, in this case of rocks rich in hydrothermal sericite. The observed mineral assemblages dominated by quartz and biotite ± amphibole may be explained by metamorphic reactions such as the following proposed by Bucher (2023):

1 Chl + 4 Cel = 3 Phl + 1 Ms + 7 Qtz + 4 H_2O
4 Tr + 6 Chl + 25 Cel = 25 Phl + 4 Czo + 63 Qtz + 26 H_2O.

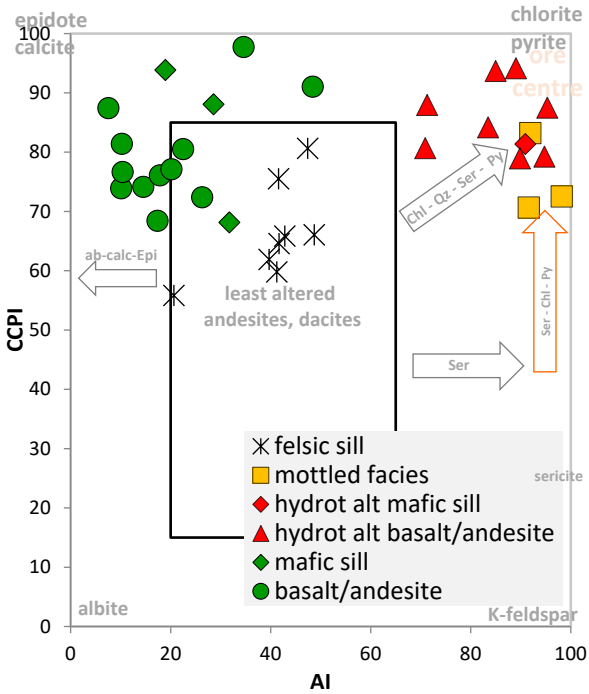


Figure 4. CCPI and AI values of basalt/andesitic flows and mafic and felsic sills plotted on the alteration box plot of Large et al. (2001)

In places, a mottled or spotted facies texture is present (Fig. 6), similar to that described in María Teresa and Cerro Lindo in altered rocks subsequently affected by contact metamorphism. (Fontboté 1999; Imaña et al. 1999). Neither cordierite nor garnet have been recognized in Balducho so far.

All the analyzed samples showing acidic hydrothermal alteration were collected in the first 50 meters beneath the mineralized horizon (Fig. 3). In contrast, ocean floor alteration is identified on top of and further below the mineralized horizon. In both types of altered rocks, metamorphic biotite, amphibole, and quartz grains are up to 50 to 500 µm in size and overprint the matrix or crystallize in veinlets. In a few cases (Fig. 5), biotite is planar-

oriented suggesting that the contact metamorphism took place under tectonic stress.

Coarser-grained and porphyritic basaltic/andesitic (Zr/TiO_2 =0.01- 0.04) planar bodies roughly parallel to the flows are interpreted as sills. They show millimetric amphibole and plagioclase phenocrysts and, in general, they are less altered than the lavas (Fig. 7), but some of them show ocean floor alteration or are affected by intense acidic hydrothermal alteration (Fig. 4).

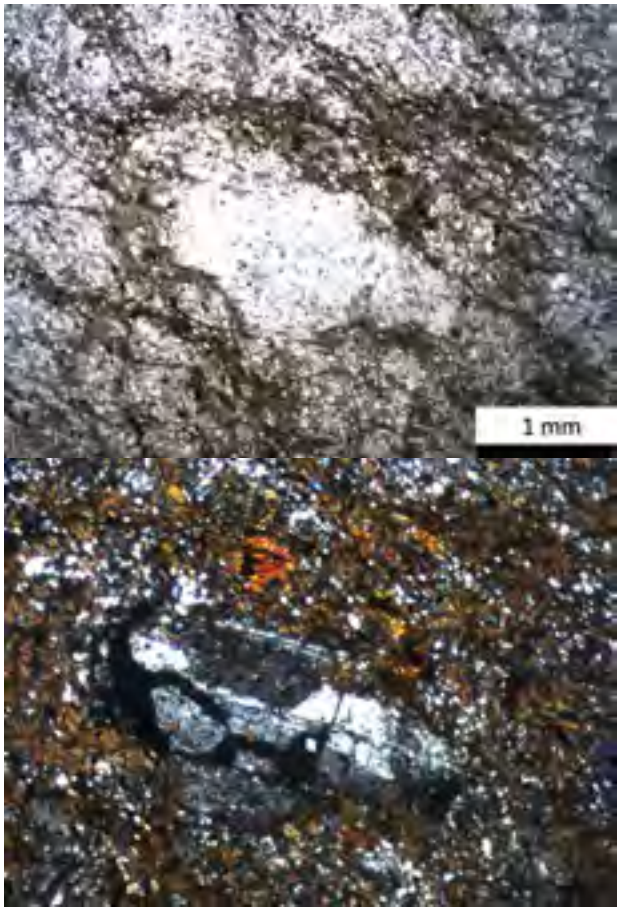


Figure 5. Microphotograph (parallel and crossed nicols) of biotite-quartz hornfels interpreted to have been formed at the expenses of a mafic flow affected by intense sericitic alteration (AI= 95). Note the biotite banding suggesting tectonic stress during conmtact metamorphism. (Sample 173).

Porphyritic felsic bodies interpreted as sills occur, both in the hanging, and in the footwall of the ore-bearing horizon. They show subhedral plagioclase and amphibole phenocrysts, with minor anhedral quartz. The matrix contains tabular plagioclase, quartz and minor amphibole grains (Zr/TiO_2 ratios from 0.036 to 0.47 suggesting dacitic to rhyodacitic compositions. All analyzed samples fall in the "least altered" field (Fig. 4). In places, amphibole and plagioclase phenocrysts are replaced by biotite, muscovite, and sericite suggesting that these sills have also been affected by metamorphism. The identified felsic sills do not occur in areas affected by hydrothermal acidic alteration; therefore, it cannot be elucidated if they were emplaced before or after hydrothermal alteration.

Biotite schists to biotite-bearing quartzites occur in the project area as cm- to dm-wide layers consisting mainly of (sub)rounded quartz (~100 µm in size), biotite, and scarce amphibole and muscovite. They show a notorious foliation caused by the mica orientation. The occurrence of ilmenite suggests reduced conditions reflecting possibly presence of organic matter in the protolith. In places, two schistosity planes are identified (Fig. 8).

Rocks of sedimentary origin or volcaniclastic facies that could favor replacement have not been identified at the ore-bearing horizon so far.



Figure 6. Mottled texture in mafic flow intensely altered (AI>90) subsequently contact metamorphosed.

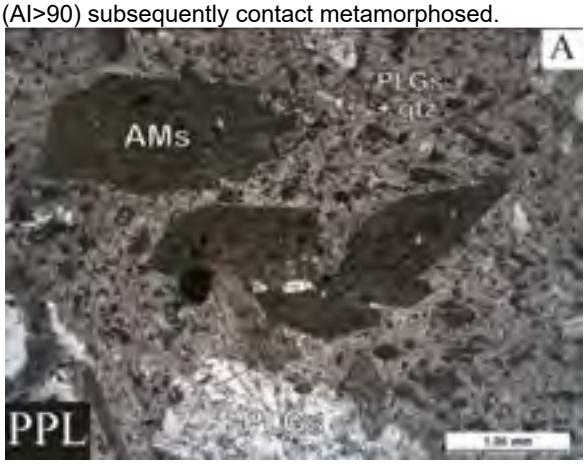


Figure 7. Porphyritic mafic sill plotting in the least altered box of Fig. 4 (sample EMC-3).

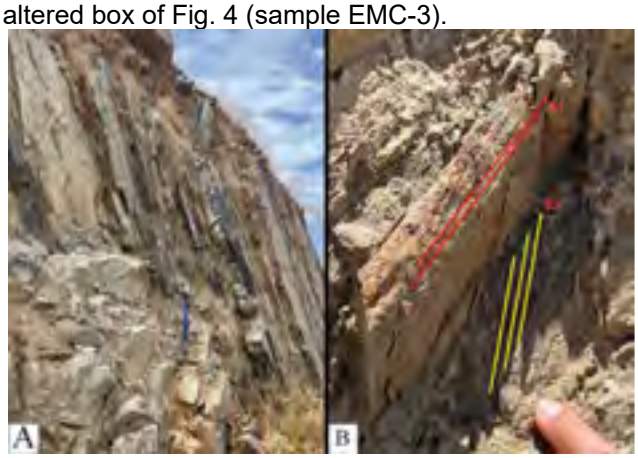


Figure 8. Biotite schist showing two schistosity planes.

2.2 Rocks attributed to the Coastal Batholith

In addition to the granodiorite and tonalite bodies identified in the SE and N parts of the study area, respectively, subvertical and sub-horizontal aplite dykes intrude the volcano-sedimentary sequence (Fig. 9). They have phaneritic texture, and consist of coarse-grained quartz, tabular plagioclase, scarce K-feldspar and amphibole (mostly altered) and fine-grained biotite. Some plagioclase and K-feldspar grains are weakly altered to sericite.



Figure 9. Aplite dyke crosscutting andesite sill and biotite schists.

3 Discussion and conclusion

The host rock of the Balducho prospect shows typical features of a VMS deposit that has been affected by contact metamorphism. Acidic hydrothermal alteration is identified in the mafic rocks of the ore-bearing horizon and at its footwall. There, the former sericite-chlorite assemblages, to which AI values up to 95 should have corresponded, have been largely transformed in metamorphic assemblages dominated by quartz and biotite. The rest of the studied basalts/andesites and sills of the same composition show mostly AI and CPPI values typical of sea-floor alteration. These rocks have been also affected by contact metamorphism as also the felsic dykes and schists and mica-rich quartzites. The fact that the studied dacitic samples are devoid of alteration does not allow to constrain their age relative to both types of alteration. However, the hypothesis that felsic sills belong also to the Early Cretaceous Quilmaná Formation is supported by the frequent bimodal character of the volcanism linked to the VMS deposits in the mid-Cretaceous belt of the Peruvian coast (Fontboté et al. 2025).

The occurrence of cleavage and schistosity in the interlayered metasediments is not typical for Cretaceous rocks in Peru and would open the possibility that the sequence is much older. However, according to W. León (written comm. 2024), similar foliations have been found in basalts occurring in the mid-Cretaceous Junco Formation in the Casma valley. Ongoing age determinations should shed light on this issue.

Acknowledgements

We thank Colquisiri Minera S.A. for the financial and logistical support. The contribution has benefited of review by Jorge Relvas.

References

Bucher K (2023) Petrogenesis of metamorphic rocks, Springer, 476 p

Fontboté L (2018) An empiric method to estimate Na contents for altered andesitic rocks based on pXRF analysis. Private report to Minera Colquisiri, S.A., Lima, 1 p.

Fontboté L (2019) Volcanogenic Zn-Pb±Cu massive sulfide deposits in the Upper Cretaceous plutono-volcanic arc in central Peru. In: Proceedings of Proexplo 2019, Peru, Extended Abstracts 45–52

Fontboté L, Chiaradia M, Spangenberg JE, Peytcheva I (2025) The mid Cretaceous VMS belt in the Peruvian coast. This volume.

Imaña M, Aspajo H, Bueno JP, Mota J (2019) The Cerro Lindo VMS deposit: volcanic architecture, stratigraphy and hydrothermal alteration of a world class sulphide deposit, Central Peru. Field Guide, Proexplo 2019, Lima, 6 p

Large RR, Gemmell JB, Paulick H, Huston DL (2001) The Alteration Box Plot: A simple approach to understanding the relationship between alteration mineralogy and lithogeochemistry associated with volcanic-hosted massive sulfide deposits Deposits. Econ Geol 96:957–971

León Lecaros WR, Ramírez AMA, Gómez Cahuaya EH (2023) Stratigraphy and new U-Pb ages of the Quilmana Formation rocks in South Lima, XXI Congreso Peruano de Geología, extended abstracts 102-108

Minera Huallanca (2007) Informe Técnico Cuculí, Abril 2007: 20 p

Palacios O (1998) Mapa geológico del Cuadrángulo del Lurin. Hoja 25-j 1:100 000. INGEMMET, Lima

Santisteban Angeldonis A, Trinidad Aranciaga I, Huanca Calla W, Alarcón A (2021). Mapa geológico del Cuadrángulo de Huarochirí (1:50000) - Hoja 25k3. INGEMMET. Lima

Vidal CCE (1987) Kuroko-type deposits in the middle-Cretaceous marginal basin of central Peru. Econ Geol 82: 1409-1430

Geologic setting of the Pueblo Viejo Au-Ag-(Cu-Zn) mining district, Dominican Republic – links to volcanogenic massive sulphide (VMS) mineralization

Carl Nelson[1], Hugo Dominguez[2], Rene Leonardo A.[3], Jose Polanco[2], Carlos Carrasco C.[4]
[1]Recursos del Caribe, S.A., Boulder, Colorado, USA
[2]SIGeomaticas EIRL, Santo Domingo, Dominican Republic
[3]Independent Consulting Geologist, Maimón, Dominican Republic
[4]Independent Consulting Geologist, La Chorrera, Panamá

Abstract. Ore deposits at the Pueblo Viejo Au-Ag-(Cu-Zn) mine, Dominican Republic, and across the surrounding Pueblo Viejo district, formed (~112 Ma) in a tholeiitic volcanic dome field during a period of extension across an emergent, intraoceanic island arc. Geologic maps reveal links between volcanic domes, high-angle structure, hydrothermal alteration, and mineralization. The largest ore deposits formed in a subsiding, marginal marine, volcano-sedimentary basin. Stacked intervals of bedded volcanogenic massive sulphide (VMS) mineralization indicate that the basin was actively subsiding while mineralization was underway. Calc-alkaline dikes and plutons intruded at ~88 Ma, well after mineralization had ended. Low-angle reverse faulting, greenschist facies metamorphic recrystallization, and milky quartz veining and replacement were also Late Cretaceous (post-mineral) events. Ore deposits in the Pueblo Viejo district are best described as hybrid epithermal – VMS deposits, formed during a period of Early Cretaceous extension, tholeiitic volcanism, and volcanic dome emplacement in a marginal-marine volcano-sedimentary basin. Exploration for similar deposits should focus on tholeiitic volcanic dome fields, extensional volcano-sedimentary basins and VMS mineral occurrences.

1 Introduction

The Pueblo Viejo Au-Ag-(Cu-Zn) mine, Dominican Republic, consistently ranks among the top ten gold producers in the world. Production through 2023 of 26 Moz gold and 157 Moz silver plus 400,000,000 tonnes of known resources reported (Yuhasz et al. 2023) combine for a total mineral endowment of 41 Moz Au and 213 Moz Ag. Copper and zinc are currently not recovered.

The age and geologic setting of mineralization has long been a subject of controversy. Kesler et al. (1981) published the first detailed description of the ore deposits and concluded that they formed in a hot spring environment, “during sedimentation in a small basin in the upper part of the Los Ranchos Formation.” Sillitoe and Bonham (1984) proposed that the basin was the product of a maar-diatreme eruption, a geologic setting subsequently embraced by Russell and Kesler (1991). Sillitoe et al (1996) described the deposits as having formed in “an environment that is transitional between those of terrestrial epithermal and deep-water volcanogenic massive sulphide systems,” a model endorsed by Hannington et al. (1999). Nelson (2000) presented evidence for a volcanic dome field at Pueblo Viejo; Nelson et al. (2020, 2023) described VMS-related mineralization in a shallow-water, marginal marine setting. Re/Os dating by Kirk et al. (2014) and by Nelson et al. (2015) fixed the age of mineralization at ~112 Ma. For all of these authors, mineralization at Pueblo Viejo was an Early Cretaceous event, coeval with volcanism and epiclastic sedimentation within the Los Ranchos Formation.

A porphyry-copper model has been advocated by Sillitoe et al. (2006) who concluded that “there is no genetic relationship between the gold-silver ore bodies and either a maar-diatreme system or volcanic dome complex.” Instead, “this new model for Pueblo Viejo assigns the deposit to a well-defined Late Cretaceous to Early Tertiary calc-alkaline magmatic arc.” Torro et al. (2017) advocated for distinct, early Cretaceous, VMS- and porphyry-related mineralization events.

2 Geologic Setting

The Pueblo Viejo district is part of an intra-oceanic island arc that stretches for 2000 km across the northern margin of the Caribbean plate. According to (most) tectonic models (e.g., Mann et al. 2007; Pindell et al. 2011) the arc emerged in the Early Cretaceous off the western coast of the Americas and was later incorporated into the proto-Caribbean basin as North and South America drifted apart. Late Cretaceous to Paleogene oblique collision of the volcanic arc with the southern margin of North America put an end to island arc volcanism (e.g., Garcia-Casco et al. 2006 and references therein).

This paper compiles geologic mapping of the open pits (1:2000 scale), the mine area (1:5000 scale), and the district (1:15,000 scale). Figure 1 shows the location of the Pueblo Viejo district and the regional geology of the Los Ranchos Fm. Figure 2 shows the distribution of rock units and structure. Figure 3 shows the extent of hydrothermal alteration and mineralization. Figure 4 shows the distribution of post-mineral structure and metamorphic recrystallization. Larger versions of these maps can be reviewed at www.pvgoldmap.net. Detailed descriptions (of rock units, structure, hydrothermal alteration, mineralization, isotopic dating, and metamorphic recrystallization) can be found in Nelson et al. (2015, 2020, 2023) and references therein.

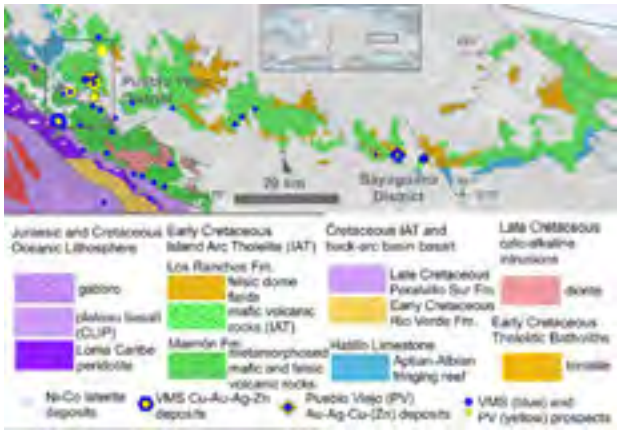


Figure 1. Regional geologic map of the Los Ranchos Formation, modified from Escuder-Viruete et al. (2007) and Nelson et al. (2015). Index map shows the location of Figure 1 on the island of Hispaniola. Gray box indicates the location of the Pueblo Viejo district (Figs. 2, 3, 4).

3 Rock Units and Structure

Several distinct rock units are well exposed across the Pueblo Viejo district (Fig. 2). Amygdaloidal and locally pillowed basalt flows underlie the northern portion of the district. The basalt package is overlain by interfingering volcanic andesite and basaltic andesite (andesite), quartz-plagioclase-pyroxene phyric dacite with distinctive embayed quartz phenocrysts (dacite porphyry), and carbonaceous volcano-sedimentary rocks.

The volcano-sedimentary section along the eastern margin of the Moore pit contains dacite porphyry clasts, quartz phenocrysts as clasts, and interbedded lenses of epiclastic dacite porphyry. Massive dacite porphyry intruded, breached the paleosurface, was locally eroded into and, later, was buried by younger volcano-sedimentary rocks as the basin continued to subside. Contacts between exogenous volcanic domes, coarsely-fragmental epiclastic volcanic dome aprons, and overlying carbonaceous volcano-sedimentary rocks are conformable (sedimentary).

Massive andesite in the Monte Negro pit is homogenous and without stratification over vertical distances of several tens of meters. The roots of these mushroom-shaped bodies clearly cut (intrude) the sub-horizontal, volcano-stratigraphic section. However, as with massive dacite porphyry, the upper contacts of massive andesite bodies with overlying volcano-sedimentary beds are sedimentary rather than intrusive.

The volcano-sedimentary basin at the Pueblo Viejo mine measures close to 2 km in width and over 400 meters in thickness. It includes thinly-bedded, carbonaceous, volcaniclastic siltstone, sandstone and limey siltstone. Terrestrial plant fossils are present as first reported by Russell and Kesler (1991). Within the basin, volcano-sedimentary rocks underlie, overlie, and interfinger with volcanic rocks (including volcanic domes) of andesite and dacite porphyry composition (Fig. 2). Soft-sediment deformation structures include convolute bedding, rip-up clasts, and sedimentary dikes.

A conformable contact between the volcano-sedimentary section and the overlying Hatillo Limestone was described by Bowin (1966), Bonilla-Rodriguez et al. (2014), and Nelson et al. (2020). Interbedded carbonaceous sandstones, siltstones and minor calcareous volcano-sedimentary rocks assigned to the Los Ranchos Fm. are overlain by near-shore to shallow-water marine sedimentary rocks of the Hatillo Limestone. The contact marks the Aptian-Albian transition from an emergent, intraoceanic island arc and marginal-marine volcano-sedimentary basin (Los Ranchos Fm.) to near-shore marine sediments and overlying deeper-water limey mudstones (Hatillo Limestone).

Northerly-striking, high-angle, normal faults occur within and along the margins of the volcano-sedimentary basin. Many are growth faults, recognized by increasing displacement with increasing depth and by volcano-sedimentary rock units that are thicker on the footwall side than on the hanging wall side. High-angle normal faults also controlled the emplacement of phreatomagmatic vent breccias and volcanic domes and acted as conduits for hydrothermal fluids.



Figure 2. Pueblo Viejo district geology showing rock units and structure after Nelson et al. (2023). The Maimón and Los Ranchos Formations are shown as a single rock unit.

4 Hydrothermal Alteration & Mineralization

VMS mineralization is well established in the Pueblo Viejo district and gossans are widely distributed (Fig. 3). Kesler et al. (1991) described Loma la Mina as a VMS deposit; Lewis (2000) and Torró et al. (2016) described the Cerro de Maimón mine as a VMS deposit.

Ore-grade volcanogenic massive sulfide beds have been observed in the Moore pit (Fig. 3) at two (stacked) levels in the volcano-sedimentary section (Nelson et al. 2020, 2023). Although VMS beds do not contribute significantly to the Au-Ag-(Cu-Zn) resource, they do provide a firm marker of the paleosurface at the time of mineralization. The presence of eroded clasts of bedded massive sulfide mineralization are clear evidence that VMS beds were exposed to erosion during basin sedimentation. Growth faults and stacked VMS beds indicate that the basin was subsiding while volcano-sedimentary rock units were being deposited and while mineralization was underway.

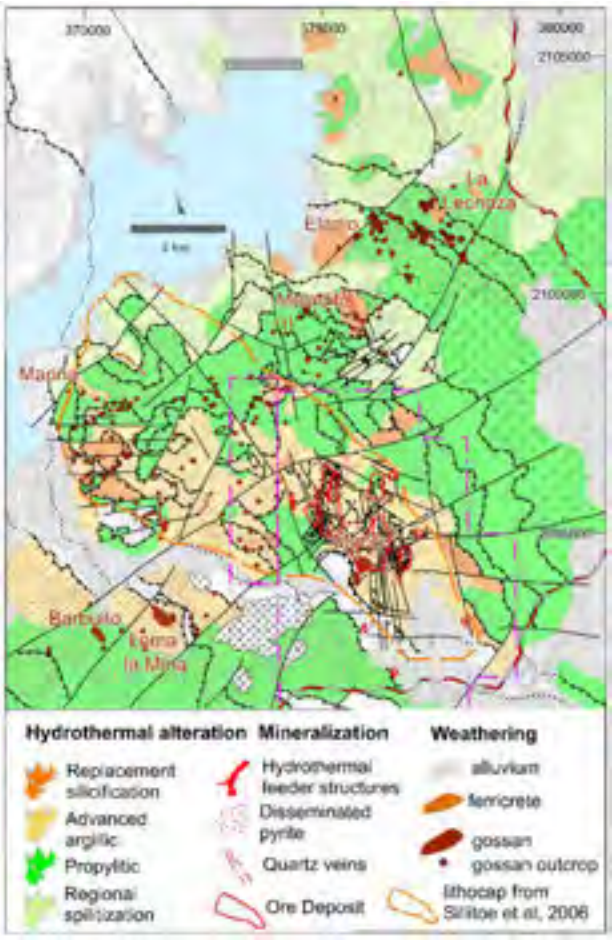


Figure 3. Geologic map showing the distribution of hydrothermal alteration, mineralization, and gossans across the Pueblo Viejo district, after Nelson et al. 2023.

4 Post-mineral metamorphism

Low-angle reverse faults mark the boundaries of metamorphic rock packages and are well exposed in the Pueblo Viejo district (Fig. 4). The faults generally strike parallel to the Hatillo thrust and dip and flatten to the southwest. They consistently offset hydrothermal alteration and mineralization.



Figure 4. Map showing the distribution of metamorphic rocks in the Pueblo Viejo district. The Hatillo thrust marks the boundary between greenschist facies schists formerly assigned to the Maimón Fm. (south of the thrust) and the Los Ranchos Fm. (north of the thrust).

5 Conclusions

Geologic mapping at the Pueblo Viejo mine and across the surrounding district reveals massive andesite and dacite porphyry bodies that are homogeneous with a crystalline texture and no stratification, are mushroom-shaped in cross section, and narrow with depth into intrusive feeders. These intrusions breached the paleosurface thereby qualifying as volcanic domes. Volcanic domes occur throughout the Pueblo Viejo district and are well exposed in the pits.

Ore deposits in the Pueblo Viejo district formed in a volcanic dome field during a period of extension across an intraoceanic island arc. Volcanogenic massive sulfide beds were deposited on the paleosurface and became stacked, along with volcanic domes, as a subsiding basin filled with epiclastic volcano-sedimentary rocks. High-angle faults controlled the growth of the basin, the location of phreatomagmatic vents, and the emplacement of volcanic domes. These same high-angle faults provided feeders for mineralizing hydrothermal

solutions. A shallow, marginal marine environment of deposition resulted in ore bodies with characteristics that are transitional between terrestrial epithermal and traditional (deep water) volcanogenic massive sulfide deposits.

Geologic mapping of the Pueblo Viejo district links tholeiitic island arc volcanism, extension, volcanic dome emplacement, and marginal-marine VMS mineralization. This new geologic model for a 41 Moz precious metal district focuses attention on tholeiitic volcanic dome fields and marginal marine VMS mineralization and away from calc-alkaline intrusions and their associated porphyry deposits.

Acknowledgements

Detailed mapping in the pits took place from 1994 to 1997 and from 2004 to 2008. District-scale mapping continued from 2012 through 2021. Field work by Dominguez, Carrasco, and Leonardo was supported by Everton Resources Inc. during the period 2005 to 2014. Hugo Dominguez, whose guidance and support as the country manager for the Everton Resources program of geologic mapping and diamond drilling, sadly passed away after a long illness in January of 2024. The observations and conclusions presented here do not imply endorsement by Barrick Gold Corporation, operator of the Pueblo Viejo mine.

References

Bonilla-Rodríguez AJ, González LA, Walker JD, Santos H (2014) Strontium isotope ($^{87}Sr/^{86}Sr$) stratigraphy from the *Coalcomana* - *Caprinuloidea* rudist assemblage in the Greater Antilles (Puerto Rico, Dominican Republic and Jamaica). Cretac Res 50: 97-109.

Bowin CO (1966) Geology of the Central Dominican Republic (a case history of part of an island arc). In Hess HH (ed) Caribbean Geological Investigations. Geol Soc Amer Mem 98: 11-84.

Escuder-Viruete J, Díaz de Neira A, Hernaiz Huerta PP, García-Senz J, Monthel J, Joubert M, Lopera E, Ullrich T, Friedman R, Weis D, Pérez-Estaún A (2007) Implicaciones tectonomagmáticas y edad de las toleítas de arco-isla, boninitas y rocas ácidas relacionadas de la formación Los Ranchos, Cordillera Oriental, República Dominicana. Bol Geol Min 118: 195-220.

García-Casco A, Torres-Roldan RL, Iturralde-Vinent MA, Millan G, Nunez Cambra K, Lasaro C, Rodriguez Vega A (2006) High pressure metamorphism of ophiolites in Cuba. Geol Acta 4: 63-88.

Hannington MD, Poulson KH, Thompson JFH and Sillitoe RH (1999) Volcanogenic gold in the massive sulfide environment. Reviews in Econ Geol 8: 319-350.

Kesler SE, Russell N, Seaward M, Rivera J, McCurdy K, Cumming GL, Sutter JF (1981) Geology and geochemistry of sulfide mineralization underlying the Pueblo Viejo gold-silver oxide deposit, Dominican Republic. Econ Geol 76: 1096-1117.

Kesler SE, Russell N, Reyes C, Santos L, Rodriguez A, Fondeur L (1991) Geology of the Maimón Formation, Dominican Republic. In Mann P, Draper G, Lewis JF (eds) Geologic and tectonic development of the North American – Caribbean plate boundary in Hispaniola. Boulder, Colorado, Geol Soc Amer Spec Pap 262: 173-187.

Kirk JD, Ruiz J, Kesler SE, Simon A, Muntean JL (2014) Re-Os age of the Pueblo Viejo epithermal deposit, Dominican Republic. Econ Geol 109: 503-512.

Lewis JF, Astacio V., Espaillat J, Jimenez J (2000) The occurrence of volcanogenic massive sulfide deposits in the Maimón Formation, Dominican Republic: the Cerro de Maimón, Loma Pesada and Loma Barbuito deposits. In Sherlock R, Barsch R, and Logan A (eds) VMS deposits of Latin America. Geol Soc of Can Spec Publ 2: 213-239.

Mann P, Rogers RD, Gahagan L (2007) Overview of plate tectonic history and its unresolved tectonic problems. In Bundschuh J and Alvarado GE (eds) Central America: Geology, Resources and Hazards. A.A. Balkema, Francis and Taylor Group London 1: 201-237.

Nelson CE (2000) Volcanic domes and gold mineralization in the Pueblo Viejo District, Dominican Republic. Miner Deposita 35: 511-525.

Nelson CE, Stein HJ, Dominguez H, Carrasco C, Barrie T, Torró L, Proenza J (2015) Re-Os dating of molybdenite from the Pueblo Viejo Au-Ag-Cu and Douvray Cu-Au districts, Hispaniola. Econ Geol 110: 1101-1110.

Nelson C, Polanco J, Macassi A, Dominguez H, Proenza J, Torró L, Rhys D, Iturralde M (2020) The Hatillo Limestone, Pueblo Viejo district, Dominican Republic: Marginal reef or impermeable cap? Bol Soc Geol Mex 72 (3): doi.org/10.18268/BSGM2020v72n3a011119.

Nelson CE, Dominguez H, Leonardo R, Polanco J, Carrasco, C (2023) Geologic setting of the Pueblo Viejo Au-Ag-Cu-(Zn) mining district, Dominican Republic: Links to volcanic domes and volcanogenic massive sulfide mineralization: Jour S Am Earth Sci 123: doi.org/10.1016/j.jsames.2022.104158

Pindell J, Maresch WV, Martens U, Stanek K (2011) The Greater Antillean Arc: Early Cretaceous origin and proposed relationship to Central American subduction mélanges: implications for models of Caribbean evolution: Inter Geol Rev: DOI:10.1080/00206814.2010.510008.

Russell N and Kesler SE (1991) Geology of the maar-diatreme complex hosting precious metal mineralization at Pueblo Viejo, Dominican Republic. In: Mann P, Draper G and Lewis JF (eds.) Geologic and tectonic development of the North America-Caribbean plate boundary in Hispaniola: Boulder, Colorado, Geol Soc Amer Spec Pap 262: p. 203-215.

Sillitoe RH and Bonham HF Jr (1984) Volcanic landforms and ore deposits. Econ Geol 79: 1286-1298.

Sillitoe RH, Hannington MD and Thompson JFH (1996) High sulfidation deposits in the volcanogenic massive sulfide environment. Econ Geol 91: 204-212.

Sillitoe RH, Hall DJ, Redwood SD, Waddell AH (2006) Pueblo Viejo high-sulfidation epithermal gold-silver deposit, Dominican Republic. a new model of formation beneath barren limestone cover. Econ Geol 101: 1427-1434.

Torró L, Proenza JA, Melgarejo JC, Alfonso P, Farré de Pablo J, Colomer JM, García-Casco A, Gubern A, Gallardo E, Cazañas X, Chávez C, Del Carpio R, León P, Nelson CE, Lewis J (2016) Mineralogy, geochemistry and sulfur isotope characterization of Cerro de Maimón (Dominican Republic), San Fernando and Antonio (Cuba) lower Cretaceous VMS deposits: Formation during subduction initiation of the proto-Caribbean lithosphere within a fore-arc. Ore Geol Rev 72: 794-817.

Torró L, Proenza JA, Camprubí A, Nelson CE, Dominguez H, Carrasco C, Reynoso R, Melgarejo JC (2017) Towards a unified genetic model for the Au-Ag-Cu Pueblo Viejo District, central Dominican Republic. Ore Geol Rev 89: 463-494.

Yuhasz C, Quarmby R, Saarelainen M, Bar N, Burton B (2023) Technical report on the Pueblo Viejo mine, Dominican Republic. prepared for the Barrick Pueblo Viejo joint venture, March 17, 2023, 277 p.

Mineral and geochemical zonation at the Åkulla Au-Te deposit, Skellefte VMS district, Sweden

Paulina Nordfeldt[1,2,3], Iain K. Pitcairn[1], Scott Halley[4], Rodney L. Allen[5] and Harold L. Gibson[3]
Department of Geological Sciences, Stockholm University, Sweden
Boliden Mines AB, Sweden
MERC, Harquail School of Earth Sciences, Laurentian University
Mineral Mapping Pty Ltd., Australia
Volcanic Resources AB, Sweden

Abstract. The Åkulla Au-Te deposit exhibits a distinct alteration pattern and ore style in the VMS-dominated Skellefte District, Northern Sweden. Hosted by a volcanic and hydrothermal breccia complex, the deposit has a zoned quartz-topaz-aluminosilicate-rich alteration. The alteration zonation in the deposit show an intensely leached quartz±topaz-dominated core that is depleted in most major cations including Al, is sulfide-poor and enriched in Si, Au, Ag, Te, Bi, Sb and Mo. Outer zones are dominated by a chlorite-muscovite-andalusite alteration mineralogy and enriched in sulfide and base metals, similarly to nearby VMS deposits. The zoned distribution of alteration minerals and chemical elements are interpreted to be controlled by progressively increasing pH and decreasing temperatures of the hydrothermal fluid outwards from the core of the deposit. We argue that the Åkulla Au-Te deposit is a syn-volcanic magmatic-hydrothermal deposit that formed at the sub-seafloor and represents a high-temperature magmatic end-member VMS deposit in the Skellefte District.

1 Introduction

The Åkulla Au-Te deposit is a newly recognized, mineral deposit style in the Paleoproterozoic (1.9-1.8 Ga) Skellefte District (SD), Northern Sweden (Fig. 1), which is mainly known as a volcanogenic massive sulfide (VMS) district (Allen et al.1996). From production start in 2012 to the end of 2024, total mineral reserves and resources (including inferred) of the Åkulla Au-Te deposit sums up to 11.8 Mt of ore, grading 4.1 g/t Au, 7.7 g/t Ag, 150.0 g/t Te, 89.7 g/t Bi and 1.0 wt% S (Boliden 2024 and internal reports). The host rocks consist of coherent dacitic to andesitic intrusions, lavas and volcaniclastic rocks, with the core of the deposit hosted by a volcanic and hydrothermal breccia complex (Fig. 2A). The alteration mineral association in the core is dominated by quartz, topaz, sericite, andalusite and corundum (Fig. 2B). The ore is composed by native Au and a range of tellurides, having a lower proportion of sulfides (0-3 %) when compared with typical VMS deposits in the SD.

Using an extensive geochemical dataset of more than 100,000 assays and lithogeochemical data we (i) describe the geochemical distribution relative to the mineral association at the Åkulla Au-Te deposit, (ii) we investigate the nature and conditions of the Åkulla ore-forming system, and (iii) we present a genetic model for the deposit. We argue that the Åkulla Au-Te deposit is a syn-volcanic, relatively high-temperature, magmatic-hydrothermal deposit that may represent a magmatic sub-seafloor end-member of the mineralization spectrum in the Skellefte VMS District.

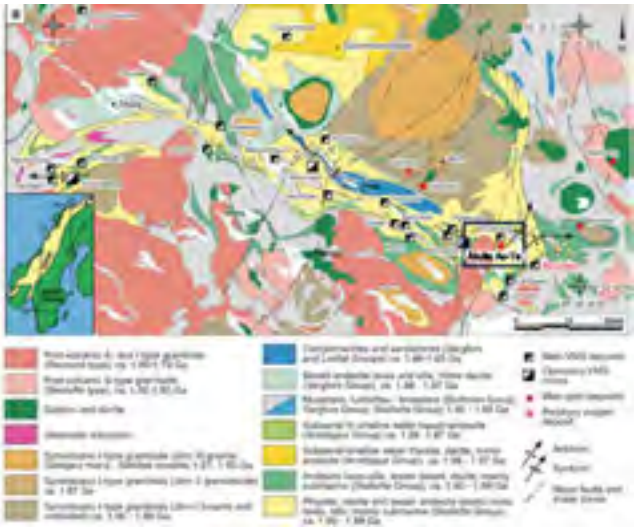


Figure 1. Simplified geological map over SD, modified after Allen et al. 1996. The Åkulla Au-Te deposit is located in the Kankberg area, visualized by the black box.

2 Geological setting

The Skellefte District formed during the Svecokarelian orogeny 1.90-1.80 Ga (Kathol & Weihed 2005 and references therein; Fig. 1) and is interpreted to be the remnant of a ca 1.9 Ga volcanic arc that was accreted to an Archean continental margin located to the north. The SD comprises metamorphosed (locally to amphibolite facies) and deformed volcanic, sedimentary and intrusive rocks. The district has undergone polyphase deformation that resulted in a strong structural control of the distribution and shape of the VMS deposits in the district (Bauer et al. 2014). Regional metamorphism has modified the alteration mineral assemblages and caused remobilization, within mineral deposits, of base- and precious metals (Mercier-Langevin et al. 2013; Bauer et al. 2014). The VMS deposits are related to a period of extensional volcanism. Some of the deposits are interpreted to have formed on the sea floor, whereas others formed meters below the sea floor (Allen et al. 1996).

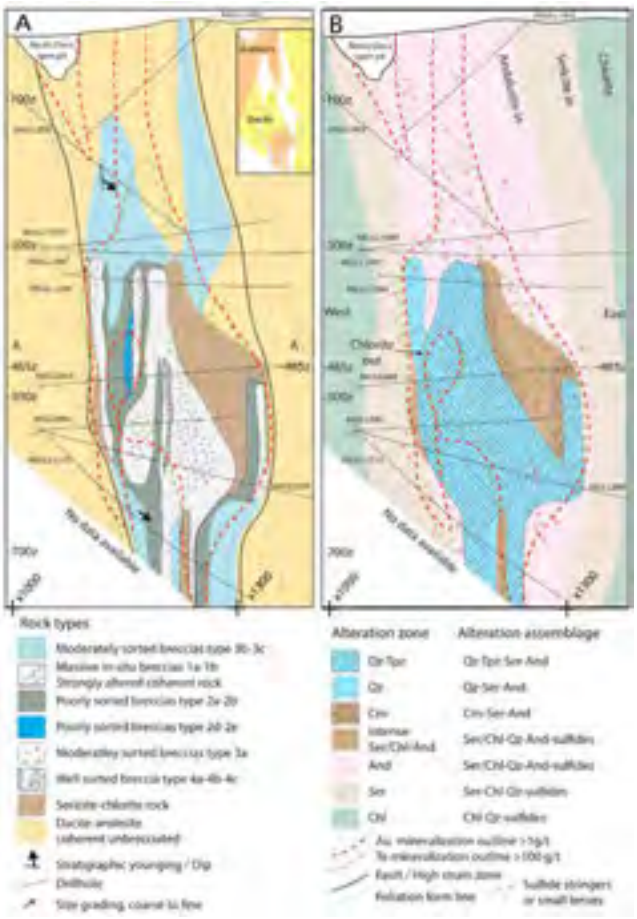


Figure 2. Cross-section y4200 of Kankberg Au-Te deposit looking south, showing geology and alteration associations, position of Au-Te mineralization, and sulfide occurrences. Åkulla Östra open pit sits at surface. Small insert shows the dacite and andesite rock unit distribution. Note that the core lacks chlorite. Modified from Nordfeldt et al. (submitted). Coordinates are in SWEREF99. Mineral abbreviations: And- andalusite, Chl- chlorite, Crn- corundum, Qz- quartz, Ser- sericite.

The Åkulla deposit is located in the Kankberg area (Figs. 1) where three previously mined massive sulfide ore bodies occur within 1km^2 (Kankberg, Åkulla Västra and Åkulla Östra). The Åkulla Au-Te host rocks and mineralization are flattened and elongated subparallel to the main D2 tectonic foliation and lineation and metamorphosed to upper greenschist facies (Nordfeldt et al. submitted). The deposit is centered on a strongly altered breccia complex with four main breccia facies that are described in detail in Nordfeldt et al. (submitted). Alteration at the deposits shows an almost concentrically zoned pattern with a quartz-topaz rich core progressing outwards to a sericite-chlorite-andalusite zone with local corundum, followed by sericite and chlorite zones (Fig. 2). The core is sulfide poor but stringer veins and small semi-massive to massive base metal sulfide lenses occur in the outer alteration zones and continue ~300m up-dip to the Åkulla Östra massive sulfide deposit (Fig. 2).

3 Element distributions

Element distribution maps for cross section y4200 are shown in figure 3. The figures represent groups of selected elements, i.e., major (Figs. 3A-D), high field strength (Fig. 3E), chalcophile (Fig. 3F) ore related elements (Figs. 3G-I). For comparison with the alteration mineral association, two alteration association boundaries are shown: the quartz-sericite-andalusite±topaz association (dashed line), and the sericite/chlorite-quartz-andalusite-sulfide association (dotted line).

The color gradients in the elemental distribution maps are based on the complete value range for each element. Continuous color gradients were generated in Leapfrog Geo. The colors are set based on minimum (blue), maximum (red) and median (green) values and the upper and lower quartiles represent the inflection or break points between the color changes. For most elements the green color corresponds to the least altered sample compositions. For Au and Te, the blue color corresponds to the least altered rocks; green, yellow and red correspond to increasingly elevated concentrations relative to background.

The core of the deposit contains the highest SiO_2 concentrations with mass change evaluations indicating silica addition to these rocks. The core of the deposit is strongly depleted in all other major elements including Al, Na and Mn, as well as S and chalcophile elements including Cu, Zn, Pb, As and Ni (Figs 3 and 4). A zone of SiO_2 depletion just outside the quartz-topaz zone contour in the upper and eastern parts of the deposit correlates with high Al concentrations and the occurrence of corundum-bearing alteration assemblages. The other major elements including Al and HFSE, such as Zr, show patchy enrichment associated to the zone of SiO_2 depletion (Fig. 3). Sulfur and the base metals show patchy enrichment in the outer alteration zones, tracing up towards the surface. The ore associated elements Au and Te together with Mo show similar distribution patterns with elevated concentrations (green to red colors, Fig.3) occurring throughout the core of the deposit and the inner sericite alteration zone. The highest Au concentrations occur on and around the quartz-topaz zone margins.

5 Discussion

Alteration zonation of the Åkulla Au-Te deposit trends from the intensely leached, quartz±topaz-dominated core, to intense sericite±andalusite alteration with local corundum, to sericite and chlorite zones. The formation of corundum is most likely due to both residual Al enrichment due to leaching of silica and possibly addition of Al remobilized from the core of the deposit. The alteration and element zonation could be indicative of gradual neutralization of a highly acidic F-rich hydrothermal fluid generated through input of magmatic volatile species (Seedorf et al. 2005). A pH front is emphasized by the sharp transition in Mn concentrations (Fig. 3E); similar trends have been observed in the transition from advanced argillic to sericitic and phyllic alteration at the top of some porphyry Cu systems (Halley et al. 2015).

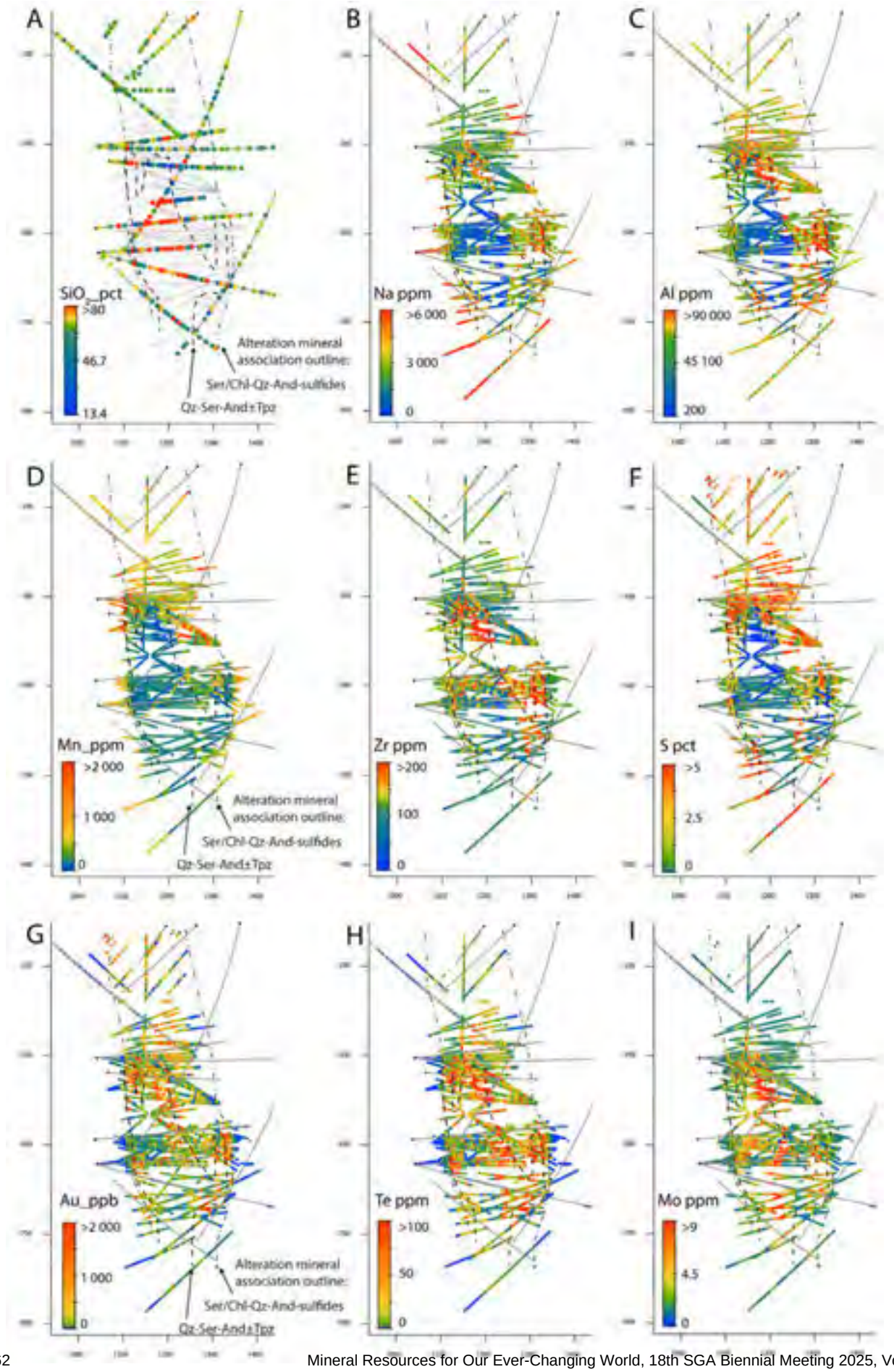

A
SiO2_pct
>80
46.7
13.4
Alteration mineral association outline:
Ser/Chl-Qz-And-sulfides
Qz-Ser-And±Tpz
B
Na ppm
>6 000
3 000
0
C
Al ppm
>90 000
45 100
200
D
Mn_ppm
>2 000
1 000
0
Alteration mineral association outline:
Ser/Chl-Qz-And-sulfides
Qz-Ser-And±Tpz
E
Zr ppm
>200
100
0
F
S pct
>5
2.5
0
G
Au_ppb
>2 000
1 000
0
Alteration mineral association outline:
Ser/Chl-Qz-And-sulfides
Qz-Ser-And±Tpz
H
Te ppm
>100
50
0
I
Mo ppm
>9
4.5
0

Figure 3. Profile y4200 with selected element distributions and mineral assemblage contours; dotted line sericite/chlorite-andalusite-sulfides and dashed line quartz-sericite-andalusite±topaz. A) SiO_2 % distribution as points for lithogeochemical samples, assay samples in grey. B-E) Major elements Al, Na, Mn (ppm) and S (%) distributions from assay data. F) HFSE Zr in ppm from assay data. G-H) Ore elements Au (ppb) and Te (ppm) distributions from assay data. I) Mo element distributions in ppm from assay data.

Several other elements follow this pattern emphasizing the major boundary between a high temperature, highly acidic core to more neutral pH and lower temperatures on the margins. The sequence of metal distribution with Mo, Te-Bi and Ag-Sb-As showing progressive enrichment towards the periphery of the deposit and base metals S, Fe and Cu being enriched in the outer alteration zones can be explained by decreasing solubility of metal chlorides in ore fluids during cooling (Reed and Spycher 1984). Elevated Mo and Te-Bi in the core of the deposit is a feature also observed in porphyry copper systems where these elements are precipitated at high temperature and low pH (Halley et al. 2015).

The mineralogical and chemical zoning discussed above indicates that temperatures ≥400°C occurred in the core of the deposit (Hemley et al. 1980), decreasing to around 375°C in the corundum zone (Hemley et al. 1980) and ≤250°C in the sericite and chlorite zones that surround the core of the deposit (Hedenquist and Arribas 2022). The extreme acidity in the core of the deposit is most likely controlled by HF rather than H_2SO_4. We interpret that the high temperature, F-bearing hydrothermal fluid is most likely of magmatic-hydrothermal origin.

The breccia complex is interpreted to have formed during crustal extension in a subaqueous and subsurface environment (Nordfeldt et al. submitted). Formation of the breccia complex, hydrothermal system and mineralization are interpreted to be coeval, followed by regional deformation, metamorphism and tilting to current orientation (Fig. 4a). The results strongly suggest that the Åkulla Au-Te deposit is a syn-volcanic, relatively high-temperature, magmatic-hydrothermal deposit that formed at the sub-seafloor, representing a high-temperature magmatic end-member within the mineralization spectrum of the Skellefte VMS District.

Acknowledgements

This research is part of a PhD project funded by Boliden Mines, organized via a co-supervision agreement between Laurentian and Stockholm Universities.

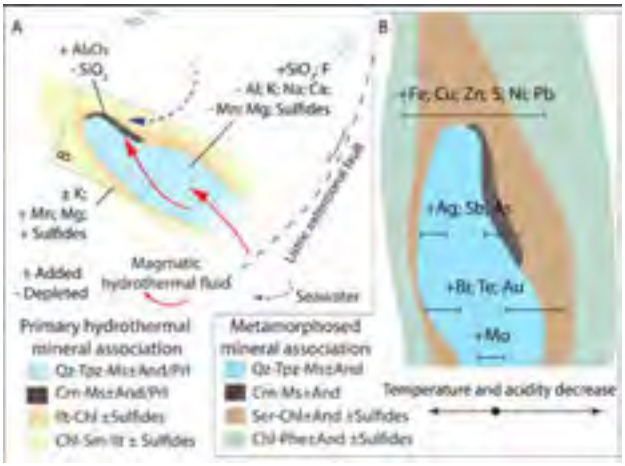


Figure 4. Schematic diagram showing the development of the hydrothermal system. A) during the hydrothermal peak and B) after subsequent regional deformation metamorphism and tilting. Mineral abbreviations: illite, ms- muscovite, sm-smectite phe-phengite, pyr-pyrophyllite, see figure 2 caption.

References

Allen RL, Weihed P, Svenson SÅ (1996) Setting of Zn-Cu-Au-Ag massive sulphide deposits in the evolution and facies architecture of a 1.9 Ga marine volcanic arc, Skellefte district, Sweden. Econ Geol 91: 1022–1053.

Bauer TE, Skyttä P, Hermansson T, Allen RL, Weihed P (2014) Correlation between distribution and shape of VMS deposits and regional deformation patterns, Skellefte district, northern Sweden. Miner Deposita 49: 1–19.

Boliden (2024) Mineral resources and mineral reserves, Summary Report, Boliden Group, 27p.

Corbett GJ, Leach TM (1998) Southwest Pacific Rim Gold-Copper Systems: Structure, Alteration, and Mineralization. Soc Econ Geol, Special Publication 6, 238p.

Halley S, Dilles JD, Tosdal RM (2015) Footprints: Hydrothermal alteration and geochemical dispersion around porphyry copper deposits. Soc Econ Geol Newsl 100: 1–17.

Hedenquist JW, Arribas A (2022) Exploration implications of multiple formation environments of advanced argillic minerals. Econ Geol 117: 609–643.

Hemley JJ, Montoya JW, Marinenko JW, Luce RW (1980) Equilibria in the system Al_2O_3-SiO_2-H_2O and some general implications for alteration/mineralization processes. Econ Geol 75: 10–28.

Kathol B, Weihed P (2005) Description of regional geological and geophysical maps of the Skellefte district and surrounding areas. Geol Surv Sweden Ba 57.

Mercier-Langevin P, McNicoll V, Allen RL, Blight JHS, Dubé B (2013) The Boliden gold-rich volcanogenic massive sulfide deposit, Skellefte district, Sweden: new U–Pb age constraints and implications at deposit and district scale. Miner Deposita 48: 485–504.

Nordfeldt P, Allen RL, Pitcairn IK, Gibson HL, Albrecht L (2025) The origin of topaz-rich breccias at the Åkulla Au-Te deposit, Paleoproterozoic Skellefte district, Sweden. In review at Econ Geol.

Reed M, Spycher N (1984) Calculation of pH and mineral equilibria in hydrothermal waters with application to geothermometry and studies of boiling and dilution. Geochim Cosmochim Acta 48: 1479–1492.

Seedorf E, Dilles JH, Proffett JM, Einaudi MT, Zurcher L, Stavast WJA, Johnson DA, Barton MD (2005) Porphyry deposits: characteristics and origin of hypogene features. Econ Geol 100th Anniv Vol 251–298.

Definition of Besshi-type VMS deposits based on their geological, geochronological features and tectonic settings

Tatsuo Nozaki[1,2], Ken Nakayama[3] and Yasuhiro Kato[2,4]
[1]Faculty of Science and Engineering, Waseda University, Tokyo, Japan
[2]School of Engineering, The University of Tokyo, Tokyo, Japan
[3]Marine Core Research Institute, Kochi University, Nankoku, Japan
[4]Ocean Resources Research Center for Next Generation, Chiba Institute of Technology, Narashino, Japan

Abstract. The Re-Os dating method has revealed the exact timing of the volcanogenic massive sulfide (VMS) deposition on a paleo-seafloor and its tectonic setting. Based on the geological and geochronological features, the Besshi-type VMS distributed in the Japanese Islands can be classified into following three groups. (1) VMS formed on a pelagic mid-ocean ridge (MOR) with constituent sulfide minerals preserved from the oxic seawater owing to Late Jurassic Ocean Anoxic Event, now observed in the Sanbagawa metamorphic belt. (2) VMS formed on a MOR close to the continental shelf crust associated with ridge subduction that was taking place from Late Cretaceous beneath the Japanese Islands. In this case, constituent sulfide minerals were preserved from oxic seawater by coverage of sedimentary rock, now found in Northern Shimanto Belt and its northern extension (Hidaka Belt). (3) Small-scale VMS formed on a pelagic MOR, now found in Northern / Southern Shimanto and Chichibu (Mino-Tamba) Belts. The preservation mechanism for these deposits is still unclear. Thus, the Besshi-type VMS deposit is derived from paleo-seafloor hydrothermal deposit on a MOR *sensu stricto*.

1 Introduction

Besshi-type deposit is one of the classifications for volcanogenic massive sulfide (VMS) and is defined as a “pelitic-mafic type” or “mafic-siliciclastic type” based on its associated lithology and wallrock (e.g., Franklin et al., 2005, Piercey, 2011). The type locality of Besshi-type VMS deposit is Besshi Deposit hosted in the Sanbagawa high-P/T metamorphic belt, Ehime Prefecture, Japan (Figs. 1 and 2). Here, regional metamorphism destroyed original / primary geological, mineralogical and geochemical features. Moreover, geological, petrographical and mineralogical descriptions of several Besshi-type VMS deposits in Japan, that are essential for the classification of each ore deposit, are often written only in Japanese. These points have hampered the understanding of the true meaning and definition of the Besshi-type VMS deposits and this scientific term is often used incorrectly. And finally, these sentences could be slightly modified for clarity, as follows: Because Hitachi VMS Deposit can be classified into two groups of (1) basic-rock associated (Fudotaki group) and (2) acidic-rock associated (Fujimi group), and Hitachi Deposit has several different geological and mineralogical features, their details are reported elsewhere (Sato and Kase, 1996; Nozaki et al., 2014). Besshi-type VMS originated from paleo-seafloor hydrothermal deposition on a mid-ocean ridge (MOR) *sensu stricto*.

The authors have conducted the geochronological studies using a Re-Os isotope method to understand the timing and tectonic setting of the Besshi-type VMS deposition on a paleo-seafloor (Nozaki et al., 2010, 2013, 2014, 2018, 2024). In the present study, we review the geological and geochronological features and try to redefine the scientific meaning of the term of the Besshi-type VMS deposit.

2 Samples and Methods

2.1 Samples

The Besshi-type VMS deposits are the most extensively distributed in Sanbagawa Belt, including

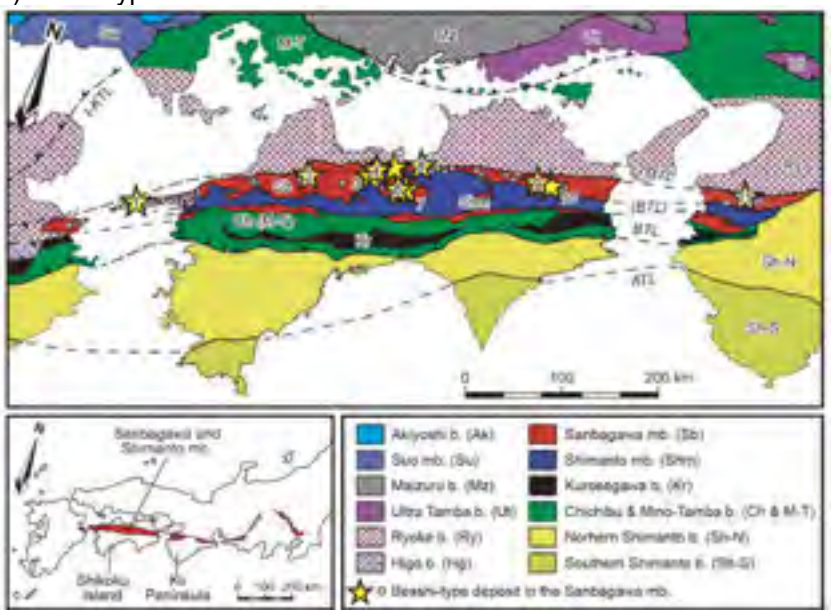


Figure 1. Locality map of 11 Besshi-type VMS deposits in Sanbagawa Belt, southwest Japan, targeted in this study. After Nozaki et al. (2013).

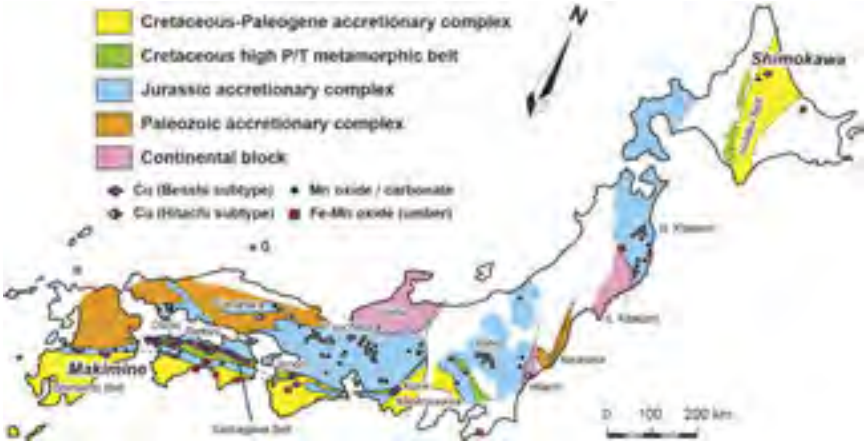


Figure 2. Locality map of Makimine and Shimokawa Deposits in Northern Shimanto Belt and its northern extension (Hidaka Belt). After Nozaki et al. (2024).

the type locality of Besshi Deposit, and then Northern Shimanto Belt and its northern extension in Hokkaido District (Hidaka Belt) together with Hitachi Deposit in the Hitachi metamorphic belt (Sato and Kase, 1996). We used 118 ore samples from 11 deposits in Sanbagawa Belt, southwest Japan (Takaura, Kuki, Nii, Besshi, Iyo, Shirataki, Shimokawa, Sazare, Kotsu, Higashiyama and Iimori Deposits) (Fig. 1), 12 and 10 ore samples from Makimine and Shimokawa Deposits in Northern Shimanto Belt and its northern extension (Fig. 2) as well as 20 ore samples from Hitachi Deposit (Fudotaki and Fujimi orebodies). Because Hitachi Deposit can be classified into two groups of (1) basic rock associated one (Fudotaki group) and (2) acidic rock associated one (Fujimi group), and Hitachi Deposit has several different geological and mineralogical features with other Besshi-type VMS deposits in the Japanese Islands and will skip from this mini-review (details are reported by Sato and Kase, 1996 and Nozaki et al., 2014).

2.2 Methods

Re and Os concentrations and Os isotope ratios were determined by the isotope dilution method after Carius tube digestion. Approximately 50–500 mg of powdered sample of sulfide mineral aggregate obtained by CH_2I_2 heavy liquid separation (i.e., bulk sulfide samples after removing silicate minerals) was spiked with ^{185}Re and ^{190}Os and digested in 10 mL of inverse aqua regia in a sealed Carius tube at 220 °C for 24 h, followed by solvent extraction of Os using the CCl_4 solution, back extraction of Os to the HBr solution, purification of Os by microdistillation. From the aqueous phase remaining after the CCl_4 extraction of Os, Re was separated in an anion exchange resin.

The Re and Os isotope compositions were measured in static multiple Faraday collector mode and pulse-counting electron multiplier mode of a thermal ionization mass spectrometer (TIMS, Thermo Fisher Scientific TRITON) at Japan Agency for Marine-Earth Science and Technology (JAMSTEC), respectively. For precise analysis of the Re isotope composition, a total evaporation method was used to eliminate the effect of instrumental mass fractionation during the measurement. The total procedural blank was ca. 7 pg for Re and 2 pg for Os with a $^{187}Os/^{188}Os$ ratio of 0.15. Our Re-Os analytical procedures have been fully described elsewhere Kato et al. (2005) and Nozaki et al. (2010, 2013).

3 Results and Discussion

3.1 Tectonic Setting of the Besshi-type VMS Deposits in Sanbagawa Belt

Geological features: Surrounding rocks of the Besshi-type VMS deposits in Sanbagawa Belt are strongly deformed due to high-P/T regional metamorphism. Taking into consideration of the existence of folds, an original stratigraphic sequence of surrounding rocks is basic schist (basalt-origin), VMS, quartz schist (quartz-origin) and psammitic / pelitic schist (sandstone / mudstone-origin) in ascending order (Isozaki and Nakayama, 2003). This stratigraphic sequence corresponds to the oceanic plate stratigraphy (OPS) observed in the accretionary complex and whole-rock geochemical composition of footwall basic schist is like that of normal mid-ocean ridge basalt (N-MORB) (Nozaki et al., 2006), indicating that the VMS was formed on a pelagic MOR, which is supported by occurrence of hangingwall quartz schist.



Figure 3. Re-Os isochrons of the Besshi-type VMS deposits in Sanbagawa Belt. After Nozaki et al. (2013).

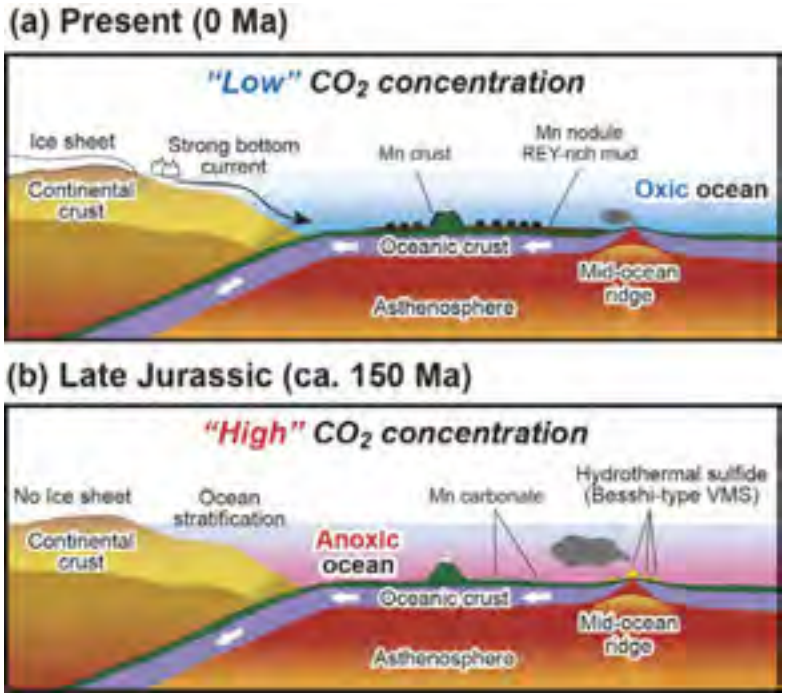


Figure 4. Formation model and depositional environment of the Besshi-type VMS deposits in Sanbagawa Belt. VMSs were formed on a pelagic MOR under the reducing condition (Modified from Nozaki et al., 2018).

Re-Os age: Depositional ages of eleven Besshi-type VMS deposits in Sanbagawa Belt, southwest Japan determined by the Re-Os isotope method are all centered in ca. 150 Ma of Late Jurassic (Figs. 1 and 3), including the Besshi Deposit of 152.4 ± 2.9 Ma which is the type locality of the Besshi-type VMS deposit. The timing of the peak metamorphism is estimated to be 120–110 Ma or 90 Ma. Since the timing of accretion is estimated to be 130–120 Ma or 95–65 Ma, the travel time of VMS on a paleo-seafloor to the subduction zone is for at least 20 Myr. Based on the relative motion of Pacific Plate to Eurasia Plate at that time, the tectonic setting of the Besshi-type VMS deposits in Sanbagawa Belt was a pelagic MOR several thousand km away from the continental crust. However, sulfide mineral is unstable under the oxic condition like as the present ocean and we proposed that the Late Jurassic Ocean Anoxic Event (OAE) functioned to preserve the constituent sulfide mineral until coverage by chert that is now observed as hangingwall quartz schist (Fig. 4) (see details in Nozaki et al., 2013).

3.2 Tectonic Setting of the Besshi-type VMS Deposits in Northern Shimanto Belt and its Extension (Hidaka Belt)

Geological features: Northern Shimanto Belt is mainly composed of the Cretaceous accretionary complexes and their typical metamorphic degree is from prehnite-pumpellyite facies to pumpellyite-actinolite facies. Due to the much lower metamorphic degree than that of Sanbagawa Belt, it still preserves the original stratigraphic sequence of greenstone (basalt origin), VMS and sandstone / phyllite (turbidite origin) in ascending order. The VMS occurs (1) between greenstone and sandstone / phyllite, (2) within sandstone / phyllite and (3) within greenstone. This greenstone often intrudes to sandstone / phyllite and whole-rock geochemical composition is analogous to that of N-MORB, not island-arc basalt (IAB). Thus, such a greenstone is referred to as "*in-situ* greenstone" (Kiminami and Miyashita, 1992; Kiminami et al., 1994; Kiminami and Ikeda, 2019). Because chert is absent around the VMSs, a depositional setting of VMS is on a MOR in the shelf sea closed to the continental crust.

Re-Os age: The Re-Os age of Makimine Deposit that is the largest VMS deposit in Northern Shimanto Belt was dated to be 89.4 ± 1.2 Ma using the Re-Os isotope method. Sedimentary age of sandstone / phyllite is estimated to be from Santonian to middle Coniacian (86.3–77.9 Ma) by microfossil (radiolarian) occurrences (Teraoka et al., 1990). Thus, the timings of VMS deposition and sandstone / phyllite sedimentation are almost equivalent within their uncertainties. Based on the radiogenic Pb isotopic composition of the Makimine VMS, wide and high $\delta^{34}S$ values (+4 to +7‰), higher thermal gradient estimated by the metamorphic mineral assemblage than that of surrounding area and coherent occurrence of VMS and sandstone / phyllite confirmed by the same deformation direction of pyrite grains, the tectonic setting of VMS was on a MOR in a shelf sea close to the continental crust along with the ridge subduction beneath the paleo-Japanese Islands in Late Cretaceous. Geological and geochronological lines of evidence strongly suggest that Shimokawa VMS in Hidaka Belt was also formed on the similar tectonic setting with that of Makimine Deposit when the ridge subduction passed through the paleo-Japanese Islands from southwest to northeast in Late Cretaceous and Paleogene. In such tectonic settings, the constituent sulfide mineral was preserved from oxic seawater due to the coverage of sedimentary rock. See the detailed discussion of Nakayama et al. (2022) and Nozaki et al. (2024).

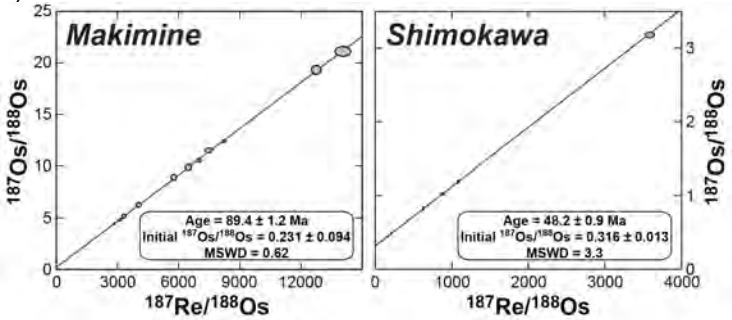


Figure 5. Re-Os isochrons of the Besshi-type VMS deposits in Northern Shimanto Belt and its northern extension (Hidaka Belt). Modified from Nozaki et al. (2024).

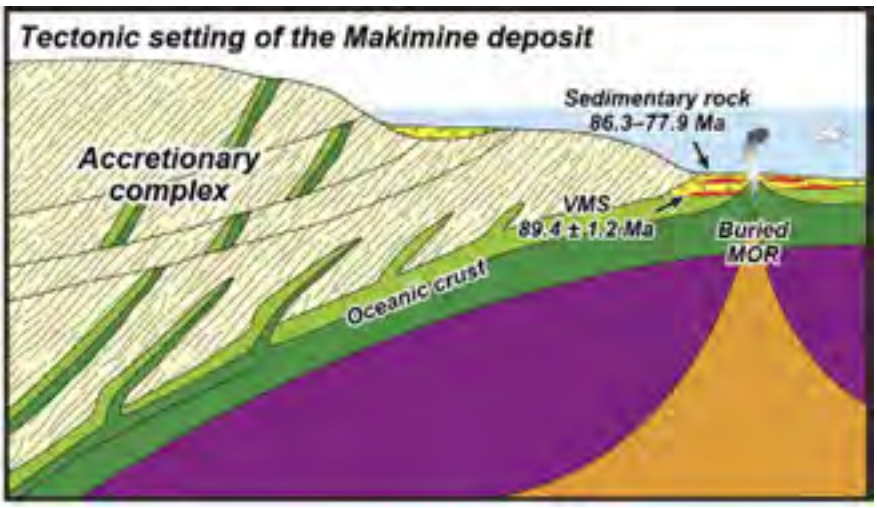


Figure 6. Tectonic setting of Makimine Deposit. VMS was formed on a MOR closed to the continental crust covered by terrigenous sediment. After Nozaki et al. (2024).

3.3 Tectonic Setting of the Besshi-type VMS Deposits in Northern / Southern Shimanto and Chichibu (Mino-Tamba) Belts

Geological features: There are more than ten small-scale Besshi-type VMS deposits in Northern / Southern Shimanto and Chichibu (Mino-Tamba) Belts. These Besshi-type VMS deposits are associated with hangingwall chert and footwall greenstone (basalt-origin), hosted in the melange structure of the accretionary complexes. Thus, depositional setting would be on a pelagic MOR.

Re-Os age: No data so far. Thus, the preservation mechanism of constituent sulfide mineral is still unclear. This point should be addressed in the future.

4 Conclusions

Besshi-type VMS deposit is originated from the paleo-seafloor hydrothermal deposit on a mid-ocean ridge (MOR) *sensu stricto*. Based on the geological, mineralogical and geochronological features, tectonic setting of the Besshi-type VMS deposits in the Japanese Islands can be mainly classified into following three groups; (1) VMS formed on a pelagic MOR in Late Jurassic and constituent sulfide mineral was preserved due to the OAE, now hosted in Sanbawa Belt, (2) VMS formed along with the ridge subduction from Late Cretaceous, which is occurring in Nothern Shimanto Belt and its northern extension (Hidaka Belt) and (3) Small-scale VMS hosted in the melange structure of the accretionary complexes whose preservation mechanism of constituent sulfide mineral on a pelagic MOR is still unclear.

Acknowledgements

Some Besshi-type VMS samples were kindly provided by The University Museum, The University of Tokyo. Discussion with late Prof. Kosei Komuro of University of Toyama and Kazunori Hatsuya of Japan Organization for Metals and Energy Security (JOGMEC) was fruitful. Field investigation and heavy liquid separation were supported by Yutaro Takaya of The University of Tokyo. This research was supported by JSPS KAKENHI nos. 07J02740, 23H03812 and 23K26607 to TN and nos. 15H05771 and 20H05658 to YK.

References

Franklin JM, Gibson HL, Jonasson IR, Galley AG (2005) Volcanogenic Massive Sulfide Deposits. Soc Econ Geol 100th Anniv Vol: 523-560.

Isozaki Y, Nakayama K (2003 Tectonic setting of Besshi-type deposits. *in* Resource and Environmental Geology (ed. The Society of Resource Geology) 95-100 (Tokyo, Japan).

Kato Y, Fujinaga K, Suzuki K (2005) Major and trace element geochemistry and Os isotopic composition of metalliferous umbers from the Late Cretaceous Japanese accretionary complex. Geochem Geophys Geosyst 6: Q07004.

Kiminami K, Miyashita S (1992) Occurrence and geochemistry of greenstones from the Makimine Formation in the Upper Cretaceous Shimanto Supergroup in Kyushu. Japan. J Geol Soc Jpn 98: 391-400.

Kiminami K, Miyashita S, Kawabata K (1994) Ridge collision and in situ greenstones in accretionary complexes: An example from the Late Cretaceous Ryukyu Islands and southwest Japan margin. Isl Arc 3; 103-111.

Kiminami K, Ikeda Y (2019) Was the Eocene magmatism in Hokkaido-Sakhalin caused by ridge subduction? General Geol 3: 10-30.

Nakayama K, Nakamura K, Fujinaga K, Takaya Y, Haraguchi S, Nagaishi K, Kawai T, Ishikawa T, Kato Y (2022) Genesis of the argillite-hosted cupriferous iron sulfide deposits of the Shimokawa mine in the Hidaka Belt, northern Hokkaido, Japan. Shigen-Chishitsu 72; 21-55.

Nozaki T, Fujinaga K, Kato Y (2018) Ore deposit formed on a paleo-seafloor in the Japanese accretionary complex. J Geol Soc Jpn 124: 995-1020.

Nozaki T, Kato Y, Suzuki K (2010) Re-Os geochronology of the Iimori Besshi-type massive sulfide deposit in the Sanbagawa metamorphic belt, Japan. Geochim Cosmochim Acta 74: 4322-4331.

Nozaki T, Kato Y, Suzuki K (2013) Late Jurassic ocean anoxic event: evidence from voluminous sulphide deposition and preservation in the Panthalassa. Sci Rep 3: 1889.

Nozaki T, Kato Y, Suzuki K (2014) Re-Os geochronology of the Hitachi volcanogenic massive sulfide deposit: The oldest ore deposit in Japan. Econ Geol 109: 2023-2034.

Nozaki T, Nakamura K, Awaji S, Kato Y (2006) Whole-rock geochemistry of basic schists from the Besshi area, central Shikoku: Implications for the tectonic setting of the Besshi sulfide deposit. Resour Geol 56: 423-432.

Nozaki T, Takaya Y, Nakayama K., Kato Y (2024) Re–Os dating of the Makimine and Shimokawa VMS deposits for new age constraints on ridge subduction beneath Japanese Islands. Sci Rep 14: 30094.

Piercey SJ (2011) The setting, style, and role of magmatism in the formation of volcanogenic massive sulfide deposits. Mineral Deposita 46:449-471.

Sato K, Kase, K (1996) Pre-accretionary mineralization of Japan. Isl Arc 5: 216-228.

Teraoka Y, Okumura K, Murata A, Hoshizumi H (1990) Geology of the Saiki district with geological sheet map, scale 1:50,000. Geological Survey of Japan, 78 p.

In-situ sulfur isotope analysis of pyrite in the c. 1.88Ga Rävliden North VMS deposit, Skellefte district, Sweden

Jonathan Rincon[1], Nils F. Jansson[1], Helen Thomas[2], Majka C. Kaiser[2], Mac F. Persson[2], Heejin Jeon[3], and Christina Wanhainen[1]

[1] Division of Geosciences and Environmental Engineering, SBN department, Luleå University of Technology, Sweden
[2] Exploration department, Boliden Mineral AB, Sweden
[3] NordSIMS laboratory, Swedish Museum of Natural History, Sweden

Abstract. Sulfur isotopes are a key tool for deciphering fluid and metal sources in volcanogenic massive sulphide (VMS) deposits. Despite their extensive use globally, sulfur isotopic data remain scarce in the world-class, VMS-rich Skellefte district (SkD). This study presents the first texturally resolved sulfur isotope ($\delta^{34}S$) data for pyrite in the greenschist- to amphibolite-facies metamorphosed Rävliden North (RvN) Zn, Pb, Cu, Ag VMS deposit. Results indicate a mantle-derived sulfur source for the c. 1.88 Ga VMS mineralisation, likely leached from the hosting volcano-sedimentary rocks. In contrast, pyrite occurrences and remobilised mineralisation in the stratigraphic hanging wall exhibit a mixed signature, with contributions from both mantle-derived and heavier sedimentary sulfur. This heavier component likely originated from Paleoproterozoic sedimentary rocks deposited under euxinic conditions and was later mobilised during metamorphism. Progressive sulfur incorporation in remobilised mineralisation is evidenced by pyrite growth zonation, with near-zero $\delta^{34}S$ values at the core and ~5‰ in metamorphic overgrowths. These findings support well-established models of VMS formation in the SkD and globally while contributing to the growing body of research on sulfur cycling during the Paleoproterozoic.

1 Introduction

VMS deposits are an important source of base and precious metals essential for modern society. These deposits have formed throughout Earth's history, and their detailed characterisation provides valuable insights into their formation and subsequent modifications. Metamorphism and deformation can re-distribute metals, produce new rocks from alteration products, and have a re-equilibration effect on isotopic signatures in VMS deposits (Cook and Hoefs 1997).

Despite isotopic re-equilibration during metamorphism, sulfur isotopes retain most of their initial signatures (Cook and Hoefs 1997). They offer critical insights into fluid and metal sources, temperature, and the physicochemical processes that have influenced VMS mineralisation (Ohmoto and Goldhaber 1997; Seal 2006). Identification of sulfur sources and their potential mixing is valuable for guiding exploration efforts towards areas with relative enrichment of target commodities.

The SkD in northern Sweden, hosts numerous VMS deposits, and in the west of this district lies the RvN Zn, Cu, Pb, and Ag VMS deposit, one of Sweden's most recent mining developments, located adjacent to the Kristineberg mine (Fig. 1A). This deposit is an excellent example of a typical SkD VMS deposit with well-preserved textural features and alteration distribution despite greenschist to lower amphibolite facies metamorphism and polyphase deformation (Rincon et al. 2024; Simán

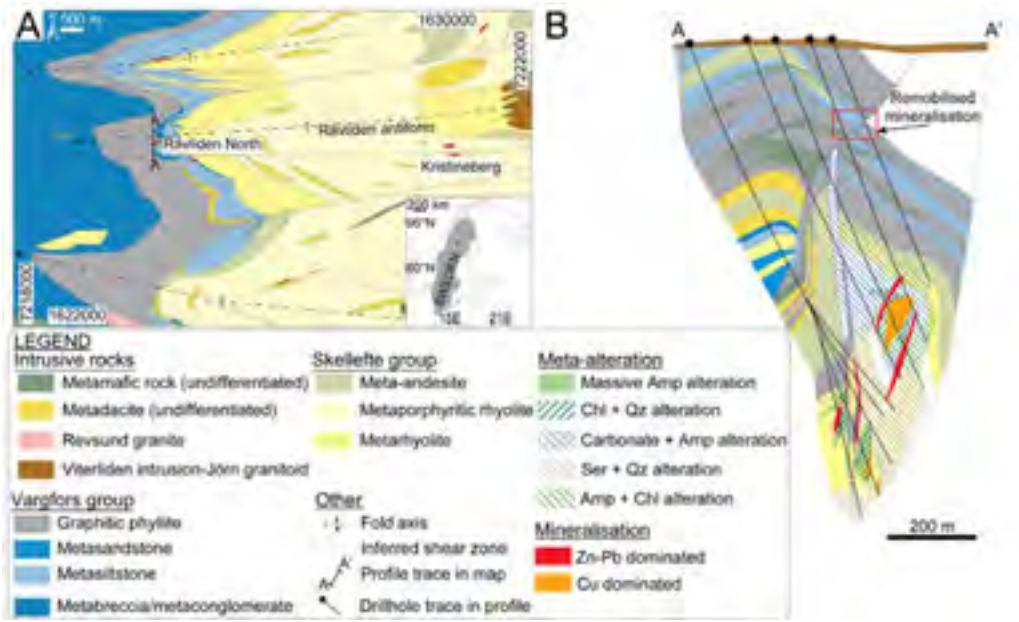


Figure 1. A. Geological map of the Kristineberg area. B. Geological cross-section of the Rävliden North deposit looking west. Map and cross-section were modified after Jansson and Persson (Unpublished report) and Rincon et al. (2024). Abbreviations after Warr (2021): Amp: Amphibole, Chl: Chlorite, Ser: Sericite, Qz: Quartz.

et al. 2025). Rincon et al. (2024) performed a detailed documentation of the main mineralisation types, texture, and subsequent modifications during the 1.88-1.86 Ga (D1 and D2) (Lundström et al. 1997; Rutland et al. 2001; Skyttä et al. 2020), and 1.80 Ga D3 (Bergman Weihed 2001) events of the Svecokarelian orogeny. However, sulfur isotope studies are limited (Rickard et al. 1979; Wagner et al. 2004).

The RvN deposit lies at the transition between the Skellefte (SG) and Vargfors (VG) groups, hosted in the west-plunging Rävliden antiform (Fig. 1B). The SG comprises (meta-) andesites, rhyolites, and porphyritic rhyolites, while the VG consists of graphitic phyllites, (meta-)sandstone, siltstone, breccia, and conglomerate. Intrusions in the Kristineberg area include the 1.89–1.88 Ga Viterliden intrusion (Skyttä et al. 2011), the 1.82–1.78 Ga Revsund granite (Kathol and Weihed 2005), and undifferentiated rocks of mafic and dacitic composition (Fig. 1A). The deposit is hosted in metamorphosed hydrothermally altered rocks: tremolite- and calcite-bearing marble, chlorite-quartz schist, and graphitic phyllite. Mineralisation occurs as massive to semi-massive Zn-Pb mineralisation composed of sphalerite, pyrrhotite, galena, and pyrite, and as Cu stringer-type composed of chalcopyrite, pyrrhotite, and pyrite. In the stratigraphic hanging wall, uneconomic mineralisation includes sphalerite, galena, and minor sulphosalts in quartz veinlets and sulphide-cemented breccia, along with barren pyrrhotite, pyrite, and arsenopyrite. For a more detailed description, see Rincon et al. (2024).

Pyrite occurs in all mineralisations, exhibiting both primary and metamorphic textures. Early pyrite helps determine the sulfur source at the time of precipitation, complemented by isotopic data from sub- to euhedral pyrite overgrowths, which can be metamorphic in origin (Rincon et al. 2024).

This study aims to identify sulfur sources and subsequent isotopic processes during VMS mineralisation at RvN, and the impact of metamorphism on sulfur isotopic signatures.

2 Materials and methods

Samples were collected from the mineralisation types described above. Pyrite from the Zn-Pb- and Cu- dominated mineralisations are hosted in massive to semi-massive sulphide, and ball ore. Pyrite from the stratigraphic hanging wall is associated with sphalerite, galena and sulphosalts in quartz veinlets, and breccia. Additionally, pyrite is associated with pyrrhotite and minor arsenopyrite in syn-tectonic (relative to D2) pyrite porphyroblasts and is hosted in quartz veins that crosscuts S2 foliation defined by graphite in graphitic phyllites of the hanging wall.

Microscale sulfur isotope analyses were conducted using a CAMECA IMS1280 ion microprobe at the Swedish Museum of Natural History (NordSIMS). The instrument operated in multi-collector mode, with magnetic field stability maintained via an NMR sensor. $\delta^{34}S$ measurements in pyrite followed Whitehouse (2013). A $^{133}Cs^{+}$ ion beam (20 kV impact energy, ~1 nA) was Gaussian-focused, with a 10 µm raster for beam homogenisation. Secondary ions ^{32}S and ^{34}S were detected with Faraday cups (10^{10}–10^{11} Ω resistors). After a 60s pre-sputter and beam centring, data were acquired in 12 cycles (4s integrations). Pyrite reference material (RM) S0302A was analysed every five sample runs. External precision was ~0.06‰. Internal repeatability was ~0.06‰ for ^{32}S at 1×10^{9} cps. Data were corrected for instrumental mass fractionation and session drift using RM and reported in $\delta^{34}S$ (‰) relative to V-CDT (Ding et al. 2001).

3 Results and discussion

Figure 2 shows the sulfur isotopic signature for pyrite grains in the RvN deposit, with selected grains showing spot results in centre and overgrowth zones in Fig. 3A-C. Overgrowth zones are only noticeable under microscopy in the pyrite grains from the hanging wall mineralisations (Fig. 3B-C). The Zn-Pb- and Cu-dominated mineralisations (Fig. 2A) have a range of $\delta^{34}S$ values from -2.2 to 1.2‰ with median of -1.7‰. Pyrite grains of the hanging wall mineralisations (Fig. 2B) have a wider range of values than the main ore and span from -0.8 to 5.2‰ with median of 3.7‰.

Within the deposit, variation of $\delta^{34}S$ values between pyrite cores and overgrowths has a more restricted range compared to pyrite grains in the hanging wall (Fig. 3A). For the Zn-Pb- and Cu-dominated mineralisations the sulfur isotopic signature is consistent with mantle-derived $\delta^{34}S$, typically reported in the literature as approximately 0 ± 2‰ (Thode et al. 1961; Seal 2006; Shanks 2014). Seal (2006) notes that this range should not be considered a strict boundary, as mantle-derived rocks can exhibit broader values, though they generally cluster around 0‰. In RvN, the $\delta^{34}S$ values suggest that mantle-derived sulfur was introduced into the system through hydrothermal fluids leaching sulfur from the volcanic pile that hosts the mineralisation. These fluids likely percolated through the volcanic rocks, acquiring a mantle-derived isotopic signature in the process.

Allen et al. (1996) argued for a deep-marine environment during the formation of VMS mineralisation in the SkD. The RvN deposit presents a stratigraphy that agrees with a similar environment (Simán et al. 2025). In this environment, during the Paleoproterozoic, seawater sulphate concentrations were likely lower than in younger geological periods due to lower levels of oxygen in the atmosphere (Canfield and Farquhar 2009). The restricted nature of the horst-graben structure in the SkD (Allen et al. 1996; Skyttä et al. 2013) may have further limited external seawater sulfur, potentially preserving a mantle-like sulfur isotopic signature. This signature, combined with stratigraphic and

alteration observations documented in detail by Simán et al. (2025) suggests that ore deposition at RvN occurred through the interaction of hot, hydrothermal metal-rich fluids with cooler, reduced, water-saturated volcanic and volcano-sedimentary rocks, leading to sulphide precipitation.

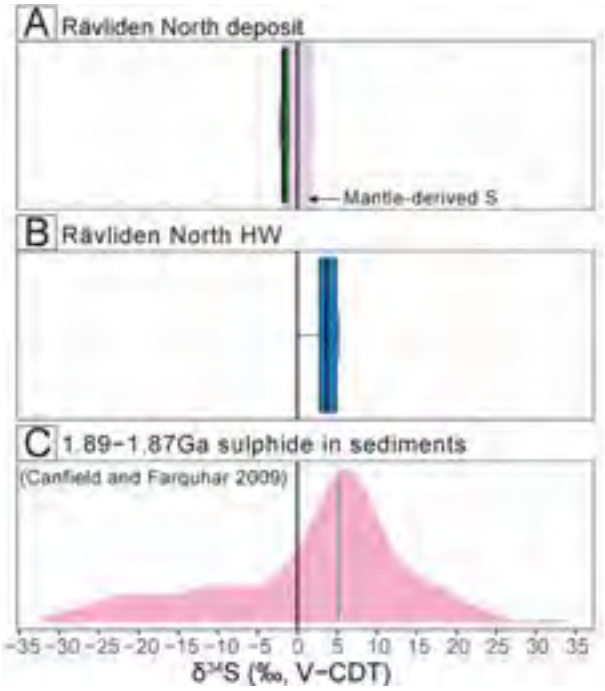


Figure 2. $\delta^{34}S$ data for analysed pyrite. (A) Zn-Pb- and Cu-dominated mineralisations within the RvN deposit. (B) Remobilised pyrite associated with sphalerite, galena and sulphosalts, and pyrite associated with pyrrhotite, and minor arsenopyrite in the stratigraphic hanging wall (HW) of the RvN deposit. (C) $\delta^{34}S$ data compiled by Canfield and Farquhar (2009) for sulphides in 1.89-1.87 Ga sediments. Green line shows median $\delta^{34}S$ = 5.1‰.

In the hanging wall, the more positive $\delta^{34}S$ values suggest a complex interplay of geological processes, including metamorphic mobilisation and potential contributions from sedimentary sulfur sources. Sulfur could have been derived from ^{34}S-enriched reservoirs, such as graphitic phyllites and associated sedimentary rocks. A comparison between $\delta^{34}S$ values for RvN hanging wall pyrite and pyrite in 1.89-1.87 Ga sedimentary rocks (Fig. 2C) (Canfield and Farquhar 2009), shows overlap around 4-5‰. Positive $\delta^{34}S$ values in pyrite associated with euxinic environments where bacterial sulphate reduction (BSR) occurs under sulphate-limited conditions have been reported in Paleoproterozoic sedimentary rocks (Canfield and Farquhar 2009), notably in black shales (Scott et al. 2014). In such environments, the rate of bacterial reduction exceeds sulphate diffusion, leading to sulphides that retain $\delta^{34}S$ values similar to the initial seawater reservoir (Scott et al. 2014). If the seawater originally had a positive $\delta^{34}S$ signature, the resulting sulphides would inherit this signature.

The SG and VG may also have introduced a mantle-derived sulfur component, further mixing the isotopic signal. This suggests that the metamorphic syntectonic pyrite grains from barren mineralisation (Fig. 3B) at RvN, hosted in graphitic phyllites, which exhibit $\delta^{34}S$ values with a median of 5.1‰, likely reflect a mixed signature from the host volcano-sedimentary rocks of the VG. A comparable process was described by Bark et al. (2021) for syn-metamorphic arsenopyrite at the neighbouring Fäboliden orogenic gold deposit (west of RvN), where $\delta^{34}S$ values (ranging from −1.5‰ to +3.6‰) were assigned to sulfur leached from the hosting carbonaceous meta-sedimentary rocks.

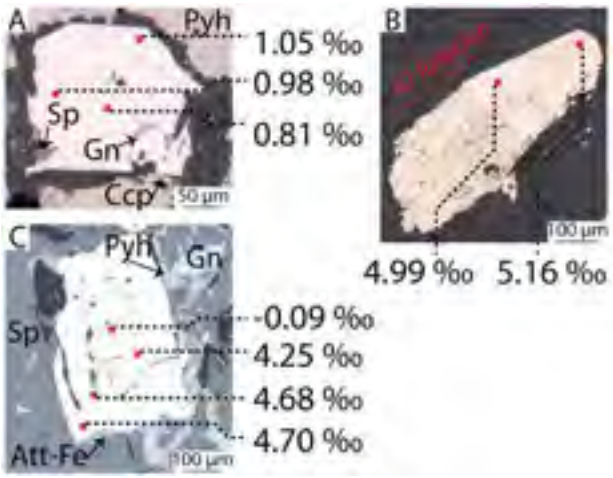


Figure 3. Pyrite grains with in-situ SIMS $\delta^{34}S$ results overlain, highlighting textural variations in sulfur isotope compositions. (A) Pyrite from Zn-Pb dominated mineralisation hosted in tremolite-calcite marble. (B) Pyrite hosted in a quartz vein that crosscuts graphitic phyllites in the hanging wall. (C) Pyrite hosted in sulphide-cemented breccia within the stratigraphic hanging wall. Abbreviations after Warr (2021): Att-Fe: Argentotetrahedrite-(Fe), Ccp: Chalcopyrite, Gn: Galena, Py: Pyrite, Pyh: Pyrrhotite, Sp: Sphalerite.

The identification of the sulfur sources in the RvN main ore and the stratigraphic hanging wall allows for interpretation of complex $\delta^{34}S$ values displayed in remobilised mineralisation. The progressive $\delta^{34}S$ enrichment observed in pyrite grains hosted in sulphide-cemented breccia from the remobilised mineralisation (Fig. 3C) provides evidence for a ^{34}S-enriched signature incorporation during metamorphic growth. These grains show a core-to-overgrowth increase in $\delta^{34}S$ values, from near-zero at the core to 4.7‰ at the outermost overgrowth. Rincon et al. (2024) interpreted the origin of this mineralisation as a result of remobilisation from deeper Zn-Pb dominated mineralisation, likely during the D3 deformation event. The increase in $\delta^{34}S$ suggests that pyrite incorporated ^{34}S from the volcanic and volcano-sedimentary host rocks, during recrystallisation and growth under metamorphism. Such process happened earlier or in conjunction with remobilisation from mineralisation at depth.

4 Conclusions

Sulfur isotope data collected via SIMS from pyrite grains in the RvN deposit suggest multiple processes occurring during its formation, metamorphism, and deformation. The main Zn-Pb dominated and Cu-dominated mineralisations exhibit mantle-derived $\delta^{34}S$ values of 0 ± 2‰, consistent with extensively reported values in the literature. These values align with classic Paleoproterozoic VMS deposits, where metals and sulfur were sourced from fluids leaching the volcano-sedimentary pile hosting the mineralisation.

In contrast, pyrite grains in mineralisations hosted within the stratigraphic hanging wall display significantly more positive $\delta^{34}S$ values, suggesting a more mixed origin. This likely reflects the mixing of a positive $\delta^{34}S$ syn-sedimentary sulfur source with near zero $\delta^{34}S$, mantle-derived sulfur. Such mixing likely occurred during metamorphism, as evidenced by syn-tectonic pyrite grains and a gradual core-to-edge increase from 0 to ~5‰ in remobilised pyrite grains.

Acknowledgements

We thank SGU and Boliden Mineral AB for funding, and Martin Whitehouse for sulfur isotopes analyses.

References

Allen RL, Weihed P, Svenson S-A (1996) Setting of Zn-Cu-Au-Ag massive sulfide deposits in the evolution and facies architecture of a 1.9 Ga marine volcanic arc, Skellefte District, Sweden. Econ Geol 91:1022–1053. https://doi.org/10.2113/gsecongeo.91.6.1022

Bark G, Boyce AJ, Fallick AE, Weihed P (2021) Fluid and metal sources in the Fäboliden hypozonal orogenic gold deposit, Sweden. Miner Depos 56:425–440. https://doi.org/10.1007/S00126-020-00977-7/FIGURES/6

Bergman Weihed J (2001) Palaeoproterozoic deformation zones in the Skellefte and Arvidsjaur areas, northern Sweden. In: Weihed P (ed) Economic geology research, C 833. Sveriges geologiska undersökning, Uppsala, pp 46–68

Canfield DE, Farquhar J (2009) Animal evolution, bioturbation, and the sulfate concentration of the oceans. Proc Natl Acad Sci 106:8123–8127. https://doi.org/10.1073/pnas.0902037106

Cook NJ, Hoefs J (1997) Sulphur isotope characteristics of metamorphosed Cu□(Zn) volcanogenic massive sulphide deposits in the Norwegian Caledonides. Chem Geol 135:307–324. https://doi.org/10.1016/S0009-2541(96)00119-2

Ding T, Valkiers S, Kipphardt H, et al (2001) Calibrated sulfur isotope abundance ratios of three IAEA sulfur isotope reference materials and V-CDT with a reassessment of the atomic weight of sulfur. Geochim Cosmochim Acta 65:2433–2437. https://doi.org/10.1016/S0016-7037(01)00611-1

Kathol B, Weihed P (2005) Description of regional geological and geophysical maps of the Skellefte District and surrounding areas. Sveriges Geol Undersökning 57:202

Lundström I, Vaasjoki M, Bergström U, et al (1997) Radiometric age determinations of plutonic rocks in the Boliden area: the Hobergsliden granite and the Stavaträsk diorite. In: Lundqvist T (ed) Radiometric Dating Results 3. Sveriges geologiska undersökning, pp 20–30

Ohmoto H, Goldhaber MB (1997) Sulfur and carbon isotope. In: Barnes HL (ed) Geochemistry of Hydrothermal Ore Deposits, 3rd edn. John Wiley \& Sons, pp 511–611

Rickard DT, Zweifel H, Donnelly TH (1979) Sulfur isotope systematics in the Aasen pyrite-barite deposits, Skellefte District, Sweden. Econ Geol 74:1060–1068. https://doi.org/10.2113/gsecongeo.74.5.1060

Rincon J, Jansson NF, Thomas H, et al (2024) Ore Remobilization History of the Metamorphosed Rävliden North Volcanogenic Massive Sulfide Deposit, Skellefte District, Sweden. Econ Geol 119:907–934. https://doi.org/10.5382/econgeo.5083

Rutland RWR, Kero L, Nilsson G, Stølen LK (2001) Nature of a major tectonic discontinuity in the Svecofennian province of northern Sweden. Precambrian Res 112:211–237. https://doi.org/10.1016/S0301-9268(01)00165-6

Scott C, Wing BA, Bekker A, et al (2014) Pyrite multiple-sulfur isotope evidence for rapid expansion and contraction of the early Paleoproterozoic seawater sulfate reservoir. Earth Planet Sci Lett 389:95–104. https://doi.org/10.1016/j.epsl.2013.12.010

Seal RR (2006) Sulfur Isotope Geochemistry of Sulfide Minerals. Rev Mineral Geochemistry 61:633–677. https://doi.org/10.2138/rmg.2006.61.12

Shanks WCP (2014) Stable Isotope Geochemistry of Mineral Deposits. Treatise Geochemistry Second Ed 13:59–85. https://doi.org/10.1016/B978-0-08-095975-7.01103-7

Simán F, Jansson N, Liwicki F, et al (2025) Stratigraphy, facies, and chemostratigraphy at the Palaeoproterozoic Rävliden North Zn-Pb-Ag-Cu VMS deposit, Skellefte district, Sweden. Ore Geol Rev 106489. https://doi.org/10.1016/j.oregeorev.2025.106489

Skyttä P, Bauer T, Hermansson T, et al (2013) Crustal 3-D geometry of the Kristineberg area (Sweden) with implications on VMS deposits. Solid Earth 4:387–404. https://doi.org/10.5194/se-4-387-2013

Skyttä P, Hermansson T, Andersson J, et al (2011) New zircon data supporting models of short-lived igneous activity at 1.89 Ga in the western Skellefte District, central Fennoscandian Shield. Solid Earth 2:205–217. https://doi.org/10.5194/se-2-205-2011

Skyttä P, Weihed P, Högdahl K, et al (2020) Chapter 4 Paleoproterozoic (2.0–1.8 Ga) syn-orogenic sedimentation, magmatism and mineralization in the Bothnia–Skellefteå lithotectonic unit, Svecokarelian orogen. Geol Soc London, Mem 50:83–130. https://doi.org/10.1144/M50-2017-10

Thode H., Monster J, Dunford H. (1961) Sulphur isotope geochemistry. Geochim Cosmochim Acta 25:159–174. https://doi.org/10.1016/0016-7037(61)90074-6

Wagner T, Boyce drian J, Jonsson E, Fallick AE (2004) Laser microprobe sulphur isotope analysis of arsenopyrite: experimental calibration and application to the Boliden Au–Cu–As massive sulphide deposit. Ore Geol Rev 25:311–325. https://doi.org/10.1016/J.OREGEOREV.2004.05.002

Warr LN (2021) IMA–CNMNC approved mineral symbols. Mineral Mag 85:291–320. https://doi.org/10.1180/mgm.2021.43

Whitehouse MJ (2013) Multiple Sulfur Isotope Determination by SIMS: Evaluation of Reference Sulfides for Δ33S with Observations and a Case Study on the Determination of Δ36S. Geostand Geoanalytical Res 37:19–33. https://doi.org/10.1111/J.1751-908X.2012.00188.X

Petrogenesis and VMS Prospectivity of 1.8 Ga Magmatism within the Archean Marshfield Terrane, Penokean Orogen, USA

Lyndsie Vickers[1], Robert Lodge[1], and Evan Weber[1,2]
[1]Department of Geology and Environmental Science, University of Wisconsin-Eau Claire, Eau Claire, Wisconsin, USA
[2]Current Affiliation: Intertek PSI, Chippewa Falls, Wisconsin, USA

Abstract. This study presents new zircon petrochronological data from an understudied region east of Eau Claire, Wisconsin, providing critical insights into its geological history and economic potential. The results indicate that what was previously interpreted as Paleoproterozoic volcanic rocks is instead an Archean greenstone belt, fundamentally altering the understanding of the region's stratigraphy. Lu-Hf isotopic data further show that the Paleoproterozoic magmatic unit did not interact with the Archean basement, consistent with the characteristics of the Marshfield terrane. These findings have important economic implications, as similar units are associated with the Pembine-Wausau terrane, which hosts world-class VMS deposits. While extensive Paleozoic sedimentary cover has historically limited exploration, it may have preserved potential mineralization, increasing the area's viability for future resource assessment. This study demonstrates that the region is more geologically complex than previously thought and highlights the need for further research into its tectonic and economic significance.

1 Introduction

The Paleoproterozoic Penokean orogen in the Great Lakes region of the northern United States represents one of the major Precambrian orogenic belts in North America. This 1.9-1.8 Ga orogen represents an accretionary event on the southern margin of the Superior Craton. The most widely cited tectonic model for the orogen describes the collision of oceanic arcs (Pembine-Wausau terrane) and Archean crustal fragments (Marshfield terrane) with the Superior Craton (Shultz and Cannon, 2007). One of the intriguing parts of this model is a "double" subduction zone that overprinted the Archean Marshfield terrane with Penokean-aged volcanic and intrusive rocks. Little is known about the nature of volcanism except for ages and physical descriptions of outcrops and its mineral potential is poorly constrained. This is partly due to the fact that many of the Marshfield terrane outcrops are only exposed as outliers in river valleys and little mineral exploration in these rocks has taken place.

The Eau Claire Volcanic Complex (ECVC) is the type locality for Penokean-age magmatism within the Marshfield terrane and has played a significant role in shaping tectonic models and terrane-boundary interpretations. Traditionally, the ECVC has been considered a continental volcanic arc built upon Archean crust (Shultz and Cannon, 2007), distinct from the oceanic-affinity Pembine-Wausau terrane, which hosts approximately 150 million metric tons of volcanogenic massive sulfide (VMS) deposits (e.g. DeMatties, 1994). However,

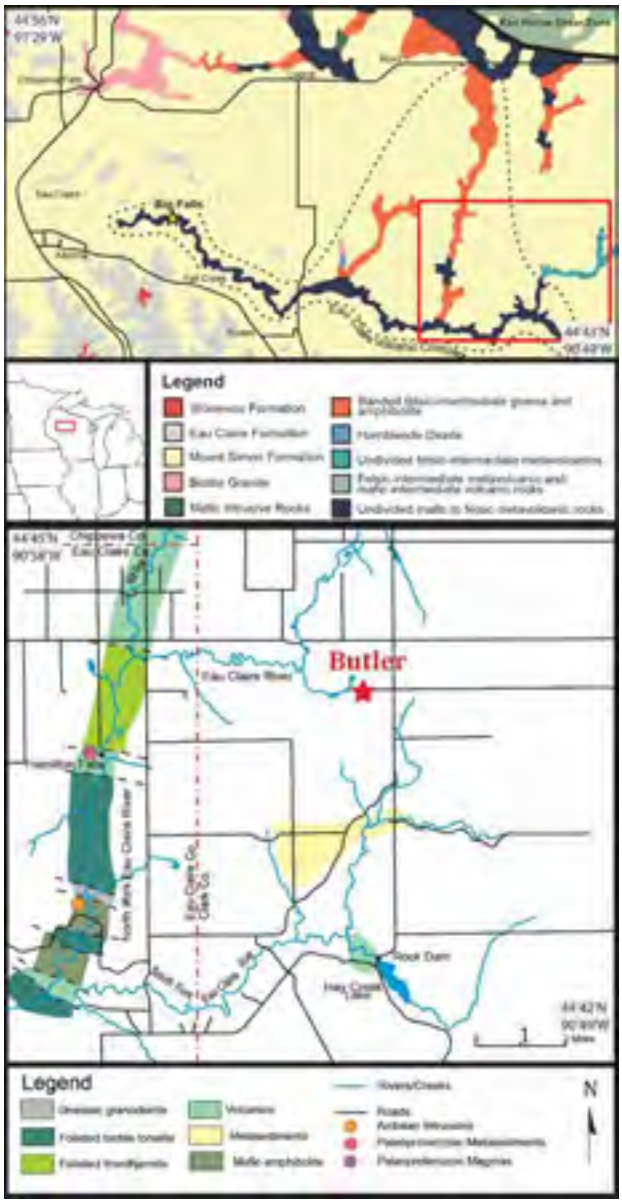


Figure 1. The top image of the figure displays a regional map of the Eau Claire Volcanic Complex, located east of Eau Claire, Wisconsin. The lower image highlights the North Fork of the Eau Claire River adapted from Brown 1988. The map includes the location of the Butler VMS prospect, as well as sites where U/Pb age data was collected.

recent U-Pb geochronology and geochemical data (Weber et al., 2023) challenge this model, suggesting that gneissic portions of the ECVC near Big Falls (Fig. 1) were mantle-derived and lacked Archean crustal contamination.

The discovery of the Butler Zn-Cu prospect within the Marshfield terrane further complicates this understanding. Historically, the Marshfield terrane was thought to be largely barren of significant VMS deposits compared to the adjacent Pembine-Wausau terrane. New geochemical and lithostratigraphic evidence suggests that portions of the ECVC, including volcanic strata hosting the Butler prospect, may share characteristics with VMS-hosting terranes globally (Lawrence et al, 2024; Vickers and Lodge, 2024). Despite its importance in regional tectonic reconstructions, the ECVC remains one of the least understood volcanic sequences within the Penokean orogen.

This study aims to refine the tectonic setting and metallogenetic potential of the ECVC by integrating new zircon U-Pb geochronology, trace element geochemistry, and petrographic analysis. Samples collected from scattered outcrops along the Eau Claire River and adjacent areas provide new constraints on the timing, magmatic evolution, and metallogeny within the complex.

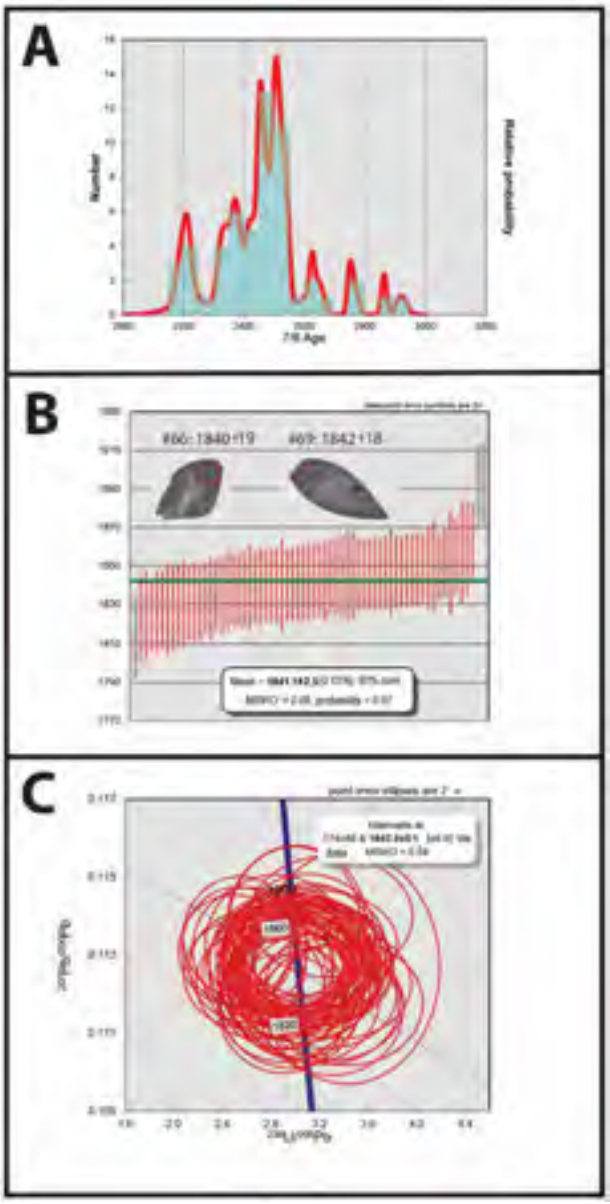


Figure 2. U/Pb geochronology results from samples Paleoproterozoic samples. (A) Histogram displaying the distribution of zircon ages from a metasedimentary sample (B) Weighted mean diagram for intrusive sample showing a uniform range of zircon $^{207}Pb/^{206}Pb$ ages. Grey bars represent outliers and were excluded from age calculation. Representative analysed and zircon grains under cathodoluminescence are displayed within figure. (C) U/Pb concordia plot for intrusive sample.

2 Samples and Methods

2.1 Sample Descriptions

Samples from the ECVC were obtained through transect-style mapping along sections of the Eau Claire River accessible only by kayak. Isolated outcrops were mostly felsic to intermediate gneiss, intrusions, amphibolites, and metasedimentary units interpreted to be supracrustal. Samples were further categorized based on U/Pb ages from this study.

The Archean intrusions are foliated and medium-grained hornblende-biotite tonalites that are moderately heterogeneous with more mafic enclaves. Overall exposure of these rocks was obstructed due to heavy lichen growth.

The Paleoproterozoic metasedimentary unit sampled is a strongly banded, fine- to medium-grained felsic gneiss with isoclinal folds. Banding alternates with wispy discontinuous quartz-feldspar leucosomes and quartz-feldspar-biotite melanosomes at the cm-scale. These are interlayered with quartz-pebble conglomerate layers up to 10-20 cm thick and with minor felsic dikes.

The Paleoproterozoic magmatic rocks include a massive fine- to medium-grained, equigranular biotite tonalite. No contact relationships in the field were observed.

Samples of metarhyolites exposed near Rock Dam (Fig. 1) were also analyzed and results are pending.

2.2 Analytical Methods

Samples from each outcrop were pulverized then processed on a Gemini shaking table to separate heavy mineral fractions. Zircon grains were further concentrated through magnetic separation and heavy liquid separation before being mounted in epoxy disks. These mounts were polished and imaged using cathodoluminescence and backscattered electron microscopy at the Mineral Exploration Research Centre's Isotope Geochemistry Lab, Laurentian University, Canada. Zircon U-Pb and trace element analyses were conducted simultaneously using a laser ablation split-stream system, which included a 193 nm

Photon Machines Analyte G2 laser, a Neptune Plus multicollector inductively coupled plasma mass spectrometer (MC-ICP-MS), and an iCap-TQ quadrupole ICP-MS. Lu-Hf isotope measurements were performed on the same zircon spots in a subsequent session using the same laser and MC-ICP-MS. Raw spectral ablation data were processed with Iolite v4 (Paton et al., 2011). To ensure data integrity, zircon grains with discordant $^{207}Pb/^{206}Pb$ and $^{206}Pb/^{238}U$ ages, Sr concentrations exceeding 10 ppm, or detectable ^{204}Pb were excluded from the U-Pb and Lu-Hf datasets, as these characteristics are commonly associated with zircons that have lost their closed isotopic system. Additionally, grains with La concentrations above 10 ppm or detectable Ca were omitted from the trace element dataset to minimize the influence of hydrothermal alteration or mineral inclusions.

3 Results

3.1 U/Pb Ages

This study presents some of the first U-Pb age constraints on Marshfield terrane rocks from this region. The Archean intrusive rocks have a broad but single peak of ages that provide a weighted mean $^{207}Pb/^{206}Pb$ age of 2570.7 ± 4.0 Ma and they are the first Archean rocks discovered in the Eau Claire River region. Paleoproterozoic metasediments have a wide range of U-Pb ages with notable peaks at ca. 1850 Ma, 2200 Ma, and 2500 Ma (Fig. 2A). Zircons from Paleoproterozoic intrusions have relatively uniform $^{207}Pb/^{206}Pb$ ages (Fig. 2B) resulting in a mean concordant $^{207}Pb/^{206}Pb$ crystallization age of 1842 ±3.1 Ma.

3.2 Zircon Trace Element Geochemistry and Lu-Hf Isotopes

After geochemical filtering of data, a total of 72 grains from the Paleoproterozoic intrusions in the ECVC were analyzed for trace element and Lu-Hf compositions. Rare earth element concentrations are typical of magmatic zircons with strongly depleted LREE (chondrite normalized La/Yb < 0.1) +and high Th/U (Th/U > 0.3). All zircons have positive Ce anomalies (Ce/Ce* > 1) and negative Eu anomalies (Eu/Eu* < 1). Most zircons also have high U/Yb (< 0.2) and Nb/Yb (< 0.01) ratios (Fig. 3).

The purpose of Lu-Hf isotopic analyses in zircons was to test the role and extent of Archean basement involvement in the petrogenesis of Paleoproterozoic magmatism in the ECVC. Initial ƐHf ($ƐHf_{(i)}$) values all plotted above the CHUR line ranging from +3 to +7 (Fig. 3C).

4 Discussion

This study presents one of the first petrochronological datasets collected for this Penokean orogen and is the first known attempt to constrain the volcanic and tectonic setting of

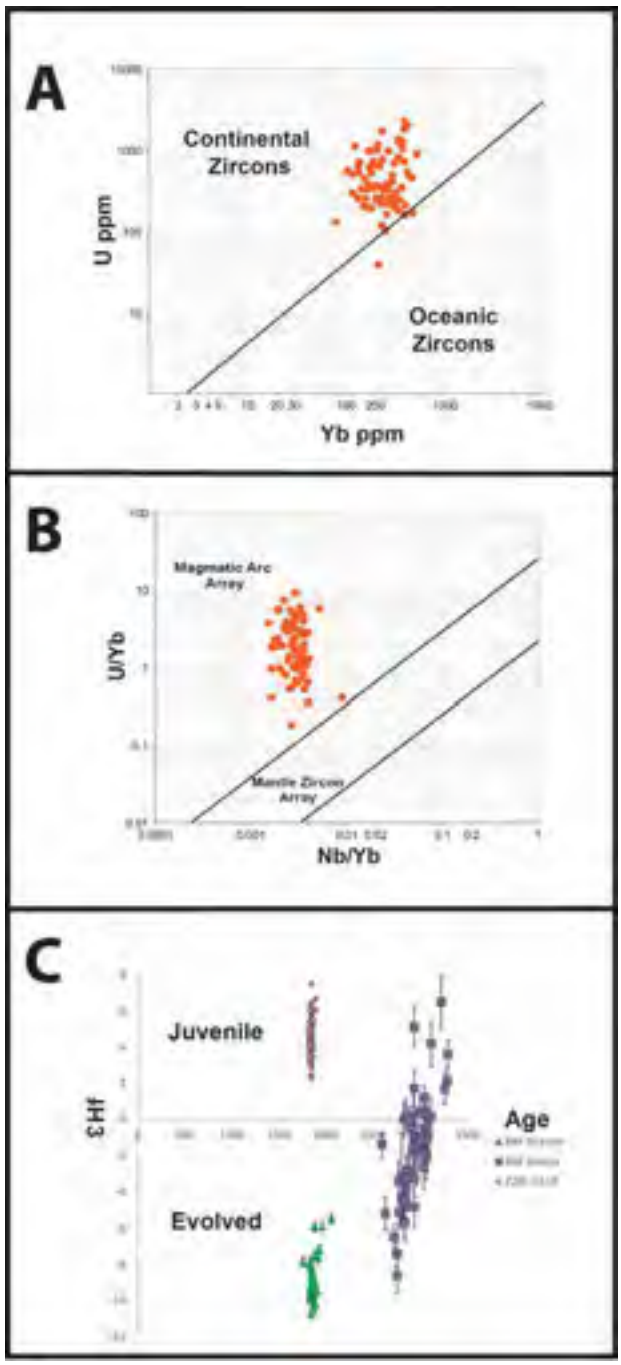


Figure 3. Geochemical discrimination (Grimes et al. 2015) and isotopic analysis from the study suit. (A) U versus Yb discrimination plot suggesting a zircon population in a continental setting or evolved magmatic systems. (B) U/Yb vs. Nb/Y plot is used to distinguish between magmatic arc zircon arrays and mantle-derived zircon arrays. Zircons show a consistent arc-like chemistry. (C) $ƐHf_{(i)}$ versus $^{207}Pb/^{206}Pb$ age comparing ECVC intrusion to other Penokean intrusions in the Marshfield Terrane (Weber et al., 2023).

Paleoproterozoic magmatism in the Marshfield terrane. However, data from this study discovered more Archean basement outcrops than was previously known in Wisconsin. Many classic outcrops in the region that was assumed to be Paleoproterozoic in age (Myers et al. 1980) are redefined as Archean supracrustal rocks.

While Paleoproterozoic units were still found to be present, their characteristics deviated from previous interpretations, indicating a more complex tectonic and magmatic history. These results suggest the need for a reassessment of the stratigraphy and evolution of this portion of the Marshfield terrane. The Paleoproterozoic metasedimentary samples show a wide range of sedimentary sources suggesting they are deriving detritus from Penokean, Marshfield, and a 2 Ga source. The Chocolay and Huronian groups north of the Penokean orogen share similar ages and represent a continental rift assemblage formed during the breakup of an Archean supercontinent (e.g. Schulz and Cannon, 2007). If the source of the 2 Ga zircons in our samples share a similar provenance as the sediments from the Chocolay or Huronian groups, then the Marshfield terrane may represent a fragment of the southernmost Superior Craton. More data will be needed to fully explore this hypothesis.

Perhaps the most significant interpretations of data from the ECVC come from the Paleoproterozoic intrusions. Lu-Hf isotopic analysis from these Paleoproterozoic intrusions indicate they did not inherit evolved isotopic compositions and they have positive $\varepsilon Hf_{(i)}$ values. This suggests that Penokean magmas in the ECVC region have not interacted with Marshfield basement unlike they have in other locations (e.g. Weber et al. 2023). This finding has significant economic implications, as units with similar geochemical signatures are known to be associated with VMS-hosting strata within the Pembine-Wausau terrane. The presence of the Butler VMS prospect and juvenile, arc-like petrochronologic data from the ECVC suggest a grossly underexplored volcanic arc region prospective for VMS mineralization. Additionally, while the presence of Paleozoic sedimentary cover has historically posed challenges for exploration in this region, it could also serve as a protective layer preserving easily weathered supergene-enriched mineralization during Quaternary glaciations (DeMatties, 2018). These findings emphasize the need for further exploration and reassessment of the region's metallogenic potential. Additional petrochronologic data from Paleoproterozoic supracrustal rocks at the Butler prospect and Rock Dam could potentially provide more clarity on these interpretations.

Magmatic zoning observed in cathodoluminescence study and careful geochemical filtering of the datasets suggest the analyzed zircons are of magmatic origin. Additionally, there is no correlation between $^{207}Pb/^{206}Pb$ age and metamorphic geochemical proxies (Th/U, U/Ce) that suggest younger ages are metamorphic.

5. Conclusions

This study provides some of the first U-Pb isotopic data for the region, revealing a more complex geological history than previously recognized. The identification of an Archean greenstone belt, rather than the expected Paleoproterozoic volcanic units, challenges existing interpretations of the area's stratigraphy. Additionally, Lu-Hf isotopic data indicate that the Paleoproterozoic magmatic unit did not interact with the Archean basement, aligning with characteristics of the Marshfield terrane. These findings have significant economic implications, as similar units are associated with the VMS-bearing Pembine-Wausau terrane. Furthermore, while Paleozoic sedimentary cover has hindered past exploration, it may have preserved potential mineralization, increasing the area's economic viability. Overall, this study highlights the need for further investigation, as the region may hold greater metallogenic potential than previously assumed. These data, when compared to known VMS-hosting terranes, can offer new insights into the metallogenic significance of the ECVC and its potential relationship to the broader Penokean Orogen.

Acknowledgements

Funding for the project has been provided by the WiSys Ignite Applied Research Grant and grants through the University of Wisconsin-Eau Claire Office of Research and Sponsored Programs. Additionally, the authors would like to acknowledge Matt Leahy, Bekah Thompson, and Aidan Kwaitowkoski for their assistance during field work.

References

Brown BA (1988) Bedrock Geology Map of Wisconsin (Regional Map Series: West-Central Sheet), University of Wisconsin-Extension Geological and Natural History Survey, Scale: 1:250,000.

DeMatties TA (1994) Early Proterozoic volcanogenic massive sulfide deposits in Wisconsin: An overview. Economic Geology 89:1122-1151.

DeMatties TA (2018) Effects of paleoweathering and supergene activity on volcanogenic massive sulfide (VMS) mineralization in the Penokean Volcanic Belt, northern Wisconsin, Michigan and east-central Minnesota, USA: Implications for future exploration. Ore Geol Rev 95:216-237.

Lawrence AC, Vanderkin A, Lodge RWD (2024) Volcanic and Hydrothermal Reconstruction of the Paleoproterozoic Butler Zn-Cu occurrence, Clark County, Wisconsin. Institute on Lake Superior Geology Proceedings, 70th Annual Meeting, Houghton, Michigan, Part 1-Program and Abstracts, p. 50-51

Schulz KJ, Cannon WF (2007) The Penokean orogeny in the Lake Superior region. Precambrian Research 157:4-25.

Vickers LA, Lodge RWD (2024) Petrology and Geochemistry of Felsic Magmatism in the Paleoproterzoic Eau Claire Volcanic Complex, Northcentral Wisconsin. Institute on Lake Superior Geology Proceedings, 70th Annual Meeting, Houghton, Michigan, Part 1-Program and Abstracts, p. 105-106

Weber EM, Lodge RWD, Marsh JH (2023) U/Pb geochronology and zircon petrochronology of Paleoproterozoic magmas from the Marshfield terrane, Penokean Orogen, Wisconsin. Institute on Lake Superior Geology Proceedings, 69th Annual Meeting, Eau Claire, Wisconsin, Part 1-Program and Abstracts, p. 97-98.

Unraveling the genesis of critical minerals: Petrogenetic and hydrothermal controls on cassiterite mineralization in the Mayo-Darlé region, Cameroon

Jonas Didero Takodjou Wambo[1*], Sylvestre Ganno[2], Kumbong Terence Chiandeh[2], Jean Paul Nzenti[2], Paul D. Asimow[3]

[1]Department of Earth and Space Sciences, Lamar University, Beaumont, TX, USA
[2]Department of Earth Sciences, University of Yaoundé I, Yaoundé, Cameroon
[3]Division of Geological and Planetary Sciences. California Institute of Technology, Pasadena, CA, USA

Abstract. The global supply of tin, and tungsten, comes primarily from tin-tungsten (Sn-W) vein and greisen deposits. These deposits form through magmatic-hydrothermal systems, a result of interactions between magmatic activity and hydrothermal processes that effectively mobilize and concentrate mineralizing fluids, often enriched in REEs. This research aims to understand the geological and hydrothermal processes driving metal accumulation and deposit formation, particularly focusing on the associated REE mineralization. We employ a multidisciplinary approach, integrating: (1) detailed field investigations; (2) optical petrography; (3) whole-rock geochemistry; (4) micro-Raman spectroscopy; (5) laser-ablation ICP-MS; and (6) cassiterite U-Pb geochronology. This provides a comprehensive understanding of texture, mineralogy, major and trace element chemistry (including REEs), and mineral ages. Our study focuses on the Lower Eocene Sn deposit in Mayo-Darlé, northwest Cameroon. The deposit is linked to Late Cenozoic intraplate calc-alkaline felsic magmatism and associated greisenization, originating from metal-rich magmatic-hydrothermal or hydrogenic systems. Tin mineralization occurs as massive bodies, veins, stockworks, and disseminations within highly fractionated granites, alongside REE-bearing minerals like bastnaesite (Ce-rich), columbite (Fe-rich), and fluorite. Petrographic analysis reveals cassiterite-rich and cassiterite-barren greisens, while stockworks and veins show consistent mineralization. This study highlights the crucial interplay between magmatism, evolving permeability, and hydrothermal alteration.

1 INTRODUCTION

Large-scale magmatic-hydrothermal tin deposits are typically associated with evolved granite systems, which play a crucial role in the formation of these economically significant resources. These granite belts are often located in regions that have undergone post-orogenic tectonic activity, particularly along active continental margins. Both peraluminous (S-type) and metaluminous (I-type) granites are known to host these tin deposits, highlighting the diversity of geological settings in which tin mineralization can occur.

In Cameroon, the Mayo Darlé region is particularly renowned for its Lower Eocene tin-rich younger granites, dated at approximately 54.99±0.35 Ma and 56.08±0.46 Ma (Takodjou Wambo et al. 2024, Bineli Betsi et al. 2024). Here, primary tin mineralization has been primarily linked to quartz veins and greisen formations located near the granite-gneiss contact, as well as to disseminated occurrences within highly fractionated granite (Takodjou Wambo et al. 2024, Bineli Betsi et al. 2024).

Previous research in this area has only focused on characterizing cassiterite, the main tin ore mineral, limiting our understanding of the associated rare earth elements and their relationships to magmatic processes, greisenization, and the broader hydrothermal systems at play. This study seeks to address this gap by providing a comprehensive petrogenetic analysis of the Mayo Darlé rare metal granite by integrating field observations, mineral chemistry, whole-rock geochemistry, and U-Pb geochronology of cassiterite.

The Cameroon Volcanic Line (CVL), a 1700 km long Cenozoic tectonic feature, is thought to have formed by the reactivation of pre-existing faults (Fig. 1). This line of volcanic and plutonic activity stretches from Pagalu Island to Lake Chad, encompassing both oceanic islands (Pagalu, Sao Tome, Principe, Bioko) and continental massifs (Etindé, Cameroon, Manenguba, etc.). These continental massifs are built on horsts and grabens within the Pan-African fold belts, composed of metamorphic and igneous rocks (660-480 Ma). The Mayo-Darlé pluton, a Tertiary anorogenic complex within the CVL, is the focus of this study. Located within the Banyo shear zone, it intrudes Pan-African metasedimentary and metavolcanic rocks (dated to 614 ± 20 Ma). The Mayo-Darlé complex itself consists of various alkaline rocks (rhyolite, syenite, granite), including tin-bearing granites (around 55 ± 1 Ma) known for cassiterite mineralization within quartz/greisen veins and disseminated in fractionated granite (Takodjou Wambo et al. 2024; Bineli Betsi et al. 2024; Nyemb Sayom et al. 2024; Bih Tantoh et al. 2024; Ndema Mbongue et al. 2023; Njiganga Nwamba et al. 2023). These diverse rock types are believed to have originated through fractional crystallization of lower crustal magmas.

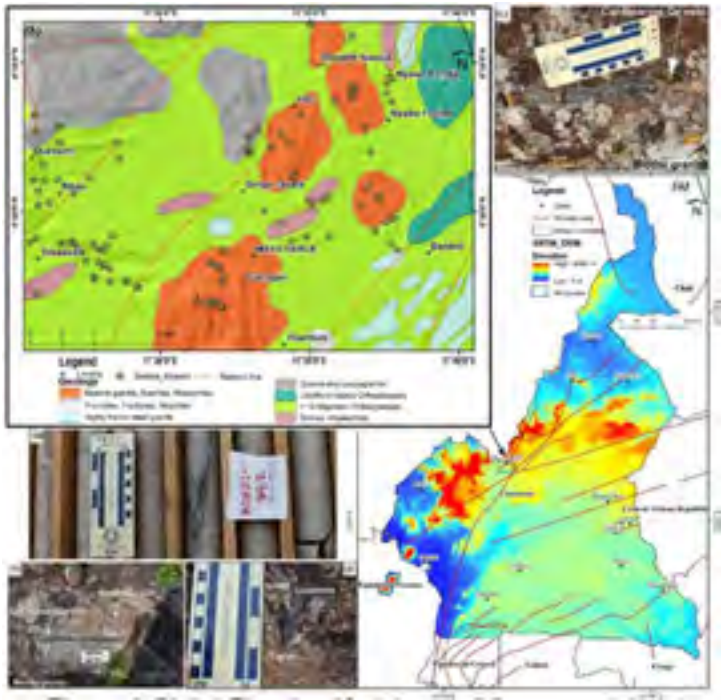


Figure 1. Digital Elevation Model map of Cameroon (a) and Mayo-Darlé geological map (b) showing the major formations and tectonic features, and field view of cassiterite hosting in hydrothermal quartz veins and topaz-rich greisen (c, d, e and f).

2 Samples and Analytical Methods

Sixty-three representative rock samples from surface outcrops and drill cores were collected to characterize the study area's geology. For each sample, polished thin sections and powdered aliquots were prepared. Powdered samples underwent XRF and ICP-MS at Caltech for bulk major and trace element analysis. Thin sections were analyzed at Caltech using optical petrography, SEM, mapping XRF, EPMA, and micro-Raman spectroscopy for detailed textural, mineralogical, and chemical characterization at a fine scale. Cassiterite U-Pb geochronology was performed on select samples at CAGS in Beijing using LA-ICP-MS to determine the timing of mineralization. This multi-technique approach enabled comprehensive analysis from bulk chemistry to mineral-level characteristics and dating.

3 Results and Discussion

3. 1 Petrography

Fieldwork in the study area revealed a significant, cassiterite-bearing magmatic unit characterized by numerous mafic enclaves. This unit exhibits a diverse range of granitic rock types, including medium-grained biotite granite, amphibole-biotite granite, biotite granodiorite, porphyritic granite rich in alkali feldspar, quartzolite, two-mica granite, and miarolitic granite. Importantly, this entire suite of granitic rocks is cut by hydrothermal quartz veins that also contain cassiterite, suggesting a close genetic relationship between the veins and the host granites.

This main, earlier phase of granitic rocks is subsequently intruded by later, finer-grained, porphyritic, and microgranitic intrusions, all of which are notably enriched in alkali feldspar. The most prominent alteration associated with these intrusions is a quartz-muscovite greisenization, a process that involves the alteration of feldspars to quartz and muscovite (Fig. 2). In some zones, this greisenization is particularly intense, leading to the formation of topaz-rich greisen containing exceptionally high topaz concentrations, reaching up to 56% granoblastic topaz. The cassiterite mineralization within these greisen zones typically occurs as millimeter-sized aggregates, often displaying distinct zoning, indicating multiple stages of crystal growth.

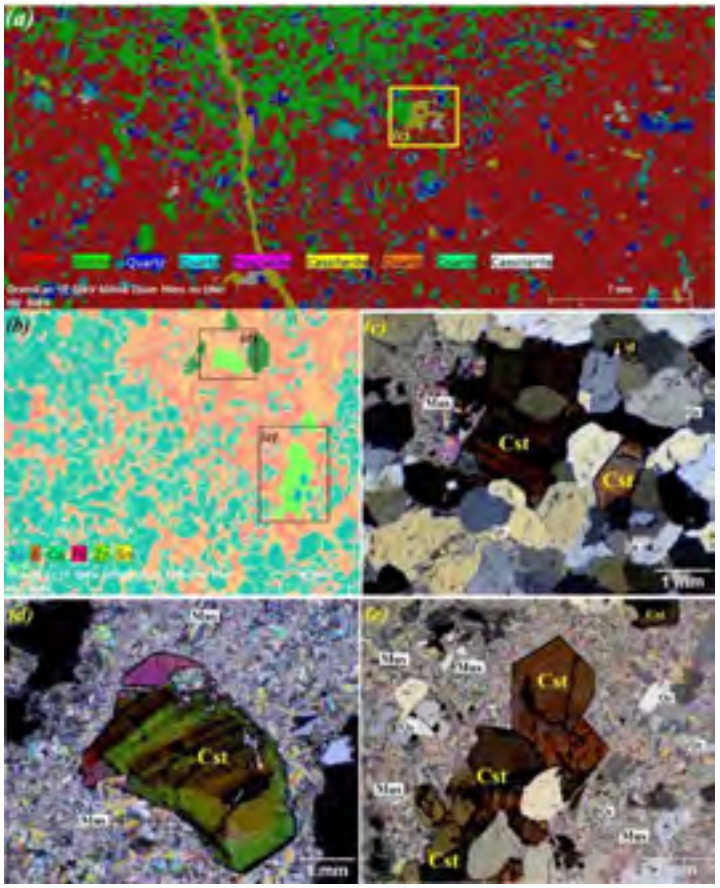


Figure 2. (a and b) XRF maps on thin sections, (c, d, e) Details cross-polarized light microphotographs showing Cst-Mus rich greisen. Note the (c and e) cassiterite crystals exhibiting a typical zoning and (d and e) partial fracturing.

3.2 Mineral Chemistry (EPMA)

The tin mineralization at Mayo-Darlé occurs in two primary forms: within quartz veins and disseminated throughout highly fractionated portions of the granite.

Importantly, the tin is accompanied by a suite of rare earth elements (REEs) and other critical minerals, including bastnaesite (a cerium-rich REE mineral), columbite (an iron-bearing niobium-tantalum oxide), fluorite (a calcium fluoride mineral), and tantalum-bearing minerals (Fig. 3). This association of tin with REEs and other critical elements suggests a complex magmatic-hydrothermal origin for the mineralization. The mineralogical composition recorded is:

- Qtz+Cst+Mus+Bt+Fl+Rt+Pl for the cassiterite-bearing greisen;
- Qtz+Mus+Tour+Chl for the barren greisen,
- Qtz+Mus+Cst+Tour+Chl for the veins and stockworks and
- Qtz+Kfs+Bt+Fl+Bsn-(Ce)+Ccp+Mus+Mag, Qtz+Cst+Kfs+Pl+Fl+Rt+Mag+Ilm and Qtz+Bt+Clb-(Fe)+Kfs+Pl+Fl+Mus in granite samples.

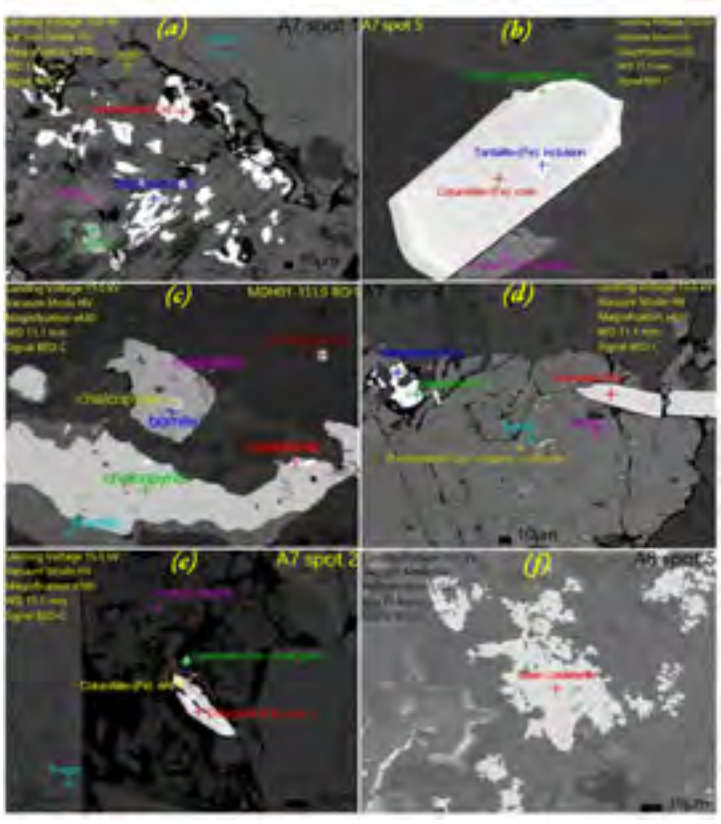


Figure 3. Electron microprobe analysis (EPMA)

3. 3 Whole-Rock Geochemistry

Petrographic analysis and geochemical classification show a range of granitoid types in the study area, including tin-rich greisen (quartzolite), quartz-rich granitoid, alkali feldspar granite, syenogranite, monzogranite, rhyolite, and two isolated samples of granodiorite and monzonite (Fig. 4). All samples are sub-alkaline (with one exception) and highly siliceous (averaging 83 wt.% SiO_2 in quartzolite/quartz-rich granitoids and 76.8 wt.% in the other samples). They are characterized by low CaO (0-3.03 wt.%) and P_2O_5 (0-0.14 wt.%) contents. Total alkalis ($Na_2O + K_2O$) vary from very low (0.02-3.58 wt.%) in quartzolite to high (up to 10.13 wt.%) in other samples. Based on K_2O vs. SiO_2, the granitoids range from calc-alkaline to shoshonitic.

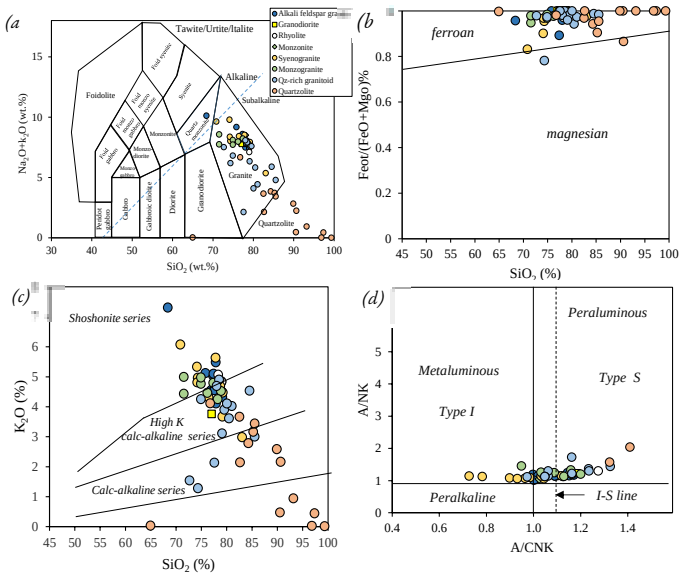


Figure 4. Major element classification plots of the granitoids from the Mayo-Darle massifs.

On the A/NK vs. A/CNK diagram, the granitoid samples range from metaluminous to peraluminous compositions, indicating a spectrum from I-type to S-type granites (A/CNK values 0.72-1.27). Most samples are ferroan, as shown on the FeOt/(FeOt + MgO) vs. SiO_2 diagram, with only two samples plotting as magnesian.

3.4 Cassiterite U-Pb Geochronology

Cassiterite is well-suited for U-Pb dating due to its favorable geochemical properties: it incorporates measurable uranium, has low initial lead, and maintains a high temperature for U-Pb isotopic closure. This makes it ideal for precise age determination (Fig. 5). U-Pb analyses of cassiterite from two greisen granite samples in Mayo-Darlé yielded crystallization ages of 55.34 ± 0.84 Ma and 56.39 ± 0.73 Ma. These ages are consistent with previously published ages of 56.7 ± 0.6 Ma (Bih Tantoh et al. 2024), 54.99 ± 0.35 Ma, and 56.08 ± 0.46 Ma (Bineli Betsi et al. 2024). This strong concordance confirms the reliability of our results and firmly establishes the Mayo-Darlé tin mineralization as having occurred in the Cenozoic Era. This is crucial for understanding the broader geological context of the ore deposit formation and its relationship to regional tectonic and magmatic events.

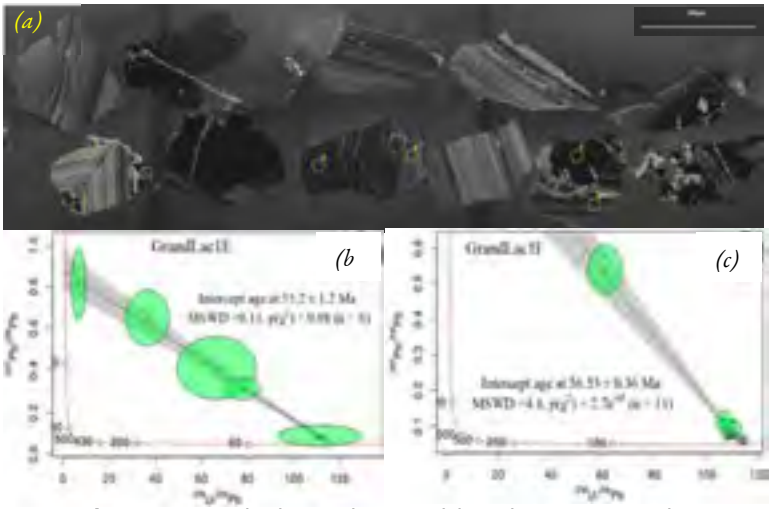


Figure 5. Cassiterite CL images (a) and Terra-Wasserburg U-Pb concordia diagrams of tin ore samples GrandLac 1E (b) and GrandLac 1F (c).

4. Conclusions

Our findings indicate that the Mayo-Darlé tin deposit formed from metal-rich magmatic-hydrothermal (or hydrogenic) fluids during Early Cenozoic intraplate calc-alkaline felsic magmatism, with greisenization of the granitic intrusions playing a key role. The tin mineralization occurs in various forms (massive, vein, stockwork, and disseminated) within highly fractionated granite, and is associated with REEs and other critical minerals such as bastnaesite (Ce-rich), columbite (Fe-rich), fluorite, and tantalum-bearing minerals. While the REE, niobium, and tantalum concentrations are likely too low for economically viable standalone mining, the area is already heavily mined for cassiterite. This suggests that significant quantities of these other valuable critical minerals are probably being discarded in waste rock by operations solely focused on tin extraction.

Acknowledgements

JDTW was supported by the geochemistry option postdoctoral fellowship from the Division of Geological and Planetary Sciences at Caltech.

References

Takodjou Wambo JD, Ganno S, Kumbong Chiandeh T, Nzenti JP, Asimow PD (2024) Geological Context of a Typical cassiterite deposit: Mayo-Darlé, Cameroon. In: Clark S, Locmelis M, Moats M, Awuah-Offei K, Alagha L, Fitch M, Fikru M, & Krolikowski A (2024) Proceedings of the 4th Annual Workshop on Resilient Supply of Critical Minerals, 7-8 August 2024, Missouri University of Science and Technology, Rolla, Missouri, USA, 45 pages.

Bineli Betsi T, Binam Mandeng EP, Beranaoguirre L, Njee EJ, Mvondo H, Kolb J (2024) In-situ zircon and cassiterite LA-ICP-MS geochronology and implications for granite hosted Sn deposit models and exploration: insights from the Cameroon Line, Am. Mineral 109: 1960-1972

Nyemb Sayom P, Mbang Bonda BM, Bayiga EC, Mbai SJ, Ngon Ngon GF, Nono Foudje RN, Essono E, Etame J, (2024) Petrogenesis of cassiterite-rich greisens from Guengue hill, Mayo Darlé, Northwestern Cameroon, Ore Energy Resour. Geol 17 ,100050, https://doi.org/10.1016/j.oreoa.2024.100050.

Bih Tantoh S, Lehmann B, Suh CE, Ngatcha RB, Zhang R, Cottle J, Njiganga Nwamba M, Belyatsky BV, Goldmann S (2024) Zircon and cassiterite U-Pb geochronology and petrochemical characteristics of early Tertiary tin mineralization at Mayo Darlé, Cameroon Volcanic Line, *J. Geochem. Explor* 257: 1-21

Njiganga Nwamba M, Tebogo K, Ngatcha RB, Suh CE, Isidore Ilouga CD, Mutum Shemang E, Tantoh BS, Tata E, Agyingi CM, (2023) Compositional provenance study of alluvial cassiterite at Bambol and Mayo Seni localities of the Mayo Darlé massif, northern Cameroon. J. *Sediment. Environ* 8:311–338

Ndema Mbongue JL, Ndongfong EF, Eseya Mengu EJ (2023) Petrogenesis of the Mayo-Darley tin formations, anorogenic complex of the Cameroon Line: implication for tin deposit. Acta Geochim 42: 704–725

Ore minerals on the flanks of the Deputatskiy Sn-Ag cluster – Bulatskoye, Jubileyniy and Kaleo Ag-Au-Zn-Pb ore occurrences, Republic of Sakha (Yakutia), Russia

Polina N. Leibham[1], Nikolay V. Bondarenko[1], Valentina N. Gerasimova[2], Mikhail V. Bereznev[3]
[1]Central Research Institute of Geological Prospecting for Base and Precious Metals, Moscow, Russia
[2]AO Yakutskgeologiya
[3]OOO Geotekhkonsalting

Abstract. We have studied the host rocks and ores of the Bulatskoye, Kaleo and Jubileyniy ore occurrences located on the flanks of the Deputatskiy ore cluster. This paper details ore minerals and ore mineral composition as determined from optical microscopy and EMPA studies. Results show that the ore-forming process can be divided into arsenopyrite-quartz, pyrrhotite-chalcopyrite-sphalerite, arsenopyrite-pyrrhotite, carbonate-pyrite, bournonite-fahlore, boulangerite-galena and pyrite-calcite stages. The main silver-bearing minerals are fahlores, pyrargyrite and hypergene minerals (acanthite and silver-bearing covellite).

1 Introduction

The Deputatskiy ore cluster is located in the north-east of the Republic of Sakha (Yakutia) within the Ust-Yansky District of Russia (Fig. 1). The area has been known since 1947 and most subsequent research has focused on the study of tin placers and its indigenous sources. In 1987–1994, research was carried out with emphasis not only on tin but also on silver, gold, lead and zinc. As a result of this work, new occurrences of silver mineralization have been identified and continue to be explored at present.

Here we report the first results of the study of the mineralization of the ores, which is ongoing.

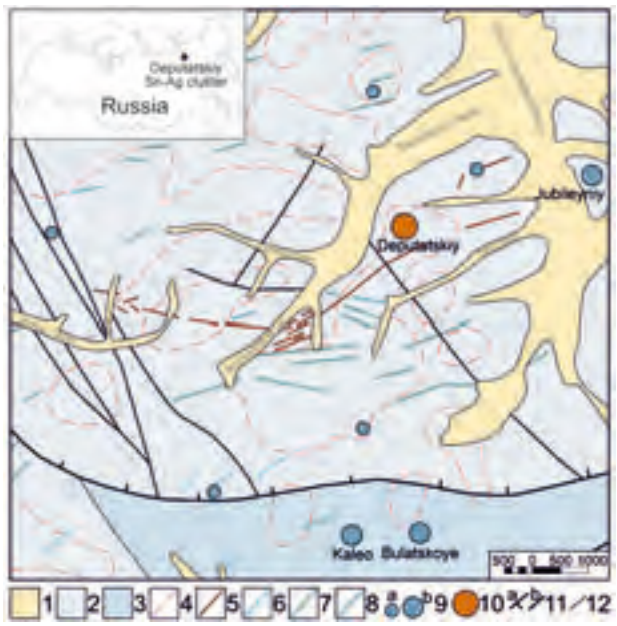


Figure 1. Simplified geological map showing location of the Deputatskiy ore cluster. (1) Quaternary alluvium, (2) Oxfordian stage, (3) Bajocian–Bathonian stage, Igneous complex (Lower Cretaceous): (4) unexposed Deputatskiy granite pluton (geophysical data), (5) granite-porphyry and rhyolite-porphyry dikes, (6) trachydolerite, trachybasalt and monzonite dikes, (7) lamprophyre dikes, (8) andesite-basalt, andesite and diorite dikes, (9) Ag-Au-Zn-Pb ore occurrences: a – known and b – studied, (10) tin deposit, (11) a – thrust with fall direction of thrust plane and b – faults, (12) geological boundaries

2 Geological settings

The geological structure of the Deputatskiy ore cluster includes Middle–Upper Jurassic terrigenous and marine sedimentary rocks of the Mokhoroi and Mirny formations (Oxfordian stage) underlain by the Elbuk Formation (Bajocian–Bathonian stage) of mudstone and siltstone composition (Fig. 1). The Mokhoroi and Mirny formations mainly consist of polymictic sandstone alternating with interbedded argillaceous and sandy-argillaceous shale. Less frequently there are layers of calcareous sandstone, lenses of conglomerate and coal shale.

The sedimentary strata accumulated in a passive continental margin setting and form the sloping northern flank of the asymmetric, W–E trending, Deputatskaya brachysyncline, which is displaced by longitudinal and transverse faults.

The Deputatskiy ore cluster is located on the southern side of this brachysyncline, which is situated in the area of the junction of two large structures: the Polousny synclinorium and the Tuostakhsky anticlinorium (Parfenov and Kuzmin 2001). The Deputatskaya brachysyncline outside the area is bounded by two regional faults: the Irigchan fault to the north and the Byllat fault to the south (Ivanov 1991). Such an intermediate position of the cluster between two first-order structures predetermined its complex differentiated mosaic structure.

In the central part of the area, the main Deputatskiy block, which contains the Deputatskiy deposit, stands out. The block is characterized by gently (5–20º) monoclinal bedding of strata, complicated by local brachysyncline and anticlinal folds. The rocks underwent contact-metamorphism and metasomatism of varying intensity during the formation of the unexposed Deputatskiy granite pluton of Early Cretaceous age. In the subsequent stages of Cretaceous magmatism, dikes of acid, intermediate and basic composition were formed.

For the Deputatskiy ore field, four stages of formation of tin mineralization were previously identified (Borisenko et al. 1997), whereas other researchers distinguished 5–6 stages (Nekrasov

1960; Flerov et al. 1971). The products of the first stage are greisen of the apical parts of the granitic pluton. At the second stage, cassiterite-tourmaline-sulfide-quartz veins were formed, localized in the underlying zone of the pluton among the contact-metamorphosed rocks. The third stage includes cassiterite-chlorite-sulfide and cassiterite-arsenopyrite-quartz veins, and the fourth stage includes sulfide and sulfide-carbonate veins.

The zonality of altered rocks and hydrothermal formations in relation to the Deputatskiy pluton is asymmetric horizontal-concentric, mainly due to the depth of the pluton and the morphology of its roof. In the central, most eroded part of the ore cluster there are mainly quartz-tourmaline ore bodies; in the intermediate zone – quartz-chlorite and quartz-sulfide (with pyrrhotite), and in the peripheral zone – quartz-carbonate-sulfide (with galena and sphalerite), quartz-manganosiderite and quartz-calcite. The Jubileyniy ore occurrence is located on the eastern flank of the ore cluster, while the Kaleo and Bulatskoye ore occurrences are located on the southern flank (Fig. 1).

The host rocks of the ore occurrences are flat-lying formations of oligomictic feldspar-quartz sandstone and quartz sandstone that have been weakly sericitized and contain disseminated mineralization. The host rock formations contain sublatitudinal, steeply dipping, brecciation zones cemented by massive aggregates of ore minerals.

3 Material and research methods

Studies were carried out on surface samples collected on geological traverses during fieldwork by AO Yakutskgeologiya.

The mineral composition of ores and host rocks were studied using an optical microscope in the laboratory of precious metals in TsNIGRI. The elemental composition of ore minerals was determined using an EMPA (JEOL JXA-8200, JEOL, Ltd, Tokyo, Japan) at IGEM RAS (analyst E.V. Kovalchuk) and an EMPA (JCXA-733 Superprobe Jeol, INCA Energy 450) at Fersman Mineralogical Museum (analyst A.A. Agahanov). All analyses were conducted using the standard manufacturer user guide recommendations and suggestions for mineral analyses.

4 Ore minerals

Gangue minerals are generally subordinate to ore minerals in the veins and are represented at all ore occurrences by quartz, ankerite, siderite, manganosiderite and most recently calcite and dolomite. It is important to note that at the Kaleo ore occurrence the opposite situation is true – vein gangue minerals are significantly more common than ore minerals.

For all veins of ore occurrences, the main ore minerals are galena and sphalerite, the ratio of which varies. Chalcopyrite, fahlores, boulangerite and bournonite were identified as the predominant minor minerals. At the Bulatskoye ore field, minor minerals – pyrrhotite, pyrite and arsenopyrite and trace minerals – stannite, pyrargyrite, diaphorite and native gold, were also noted. Hypergene minerals identified are: acanthite, cerussite, anglesite, hematite, malachite and covellite. They comprise concentrically zonal aggregates along the border of crystals and clusters of ore minerals. In these aggregates, the minerals, which are difficult to identify because of their small size, are often observed in the form of thin accretions (Fig. 2D).

Galena is predominantly allotriomorphic, which is expressed in the repetition of the outlines of quartz and carbonate crystals. Inclusions of boulangerite and fragments of pyrite and sphalerite crystals are present (Fig. 2E). Elemental analysis of galena returned 0.1-1.8 wt.% Ag and 0.1–2.6 wt.% Sb, with a positive correlation between them.

Fahlores and bournonite are observed in the form of irregularly shaped crystals with tortuous boundaries in carbonate veins, in cracks in sphalerite (Fig. 2F) and in the form of highly altered fragments in galena. Elemental analysis of fahlores returned 10.8-33.3 wt.% Ag. Fahlores occur as tetrahedrite-(Zn) and tetrahedrite-(Fe) and their Ag-bearing types as well as argentotetrahedrite-(Fe) (Table 1). Most notable among hypergenic minerals, covelline has up to 9.2 wt.% Ag in EPMA analyses.

Native gold was observed in one polished section in an aggregate of hypergene minerals that formed over siderite and galena (Fig. 2C).

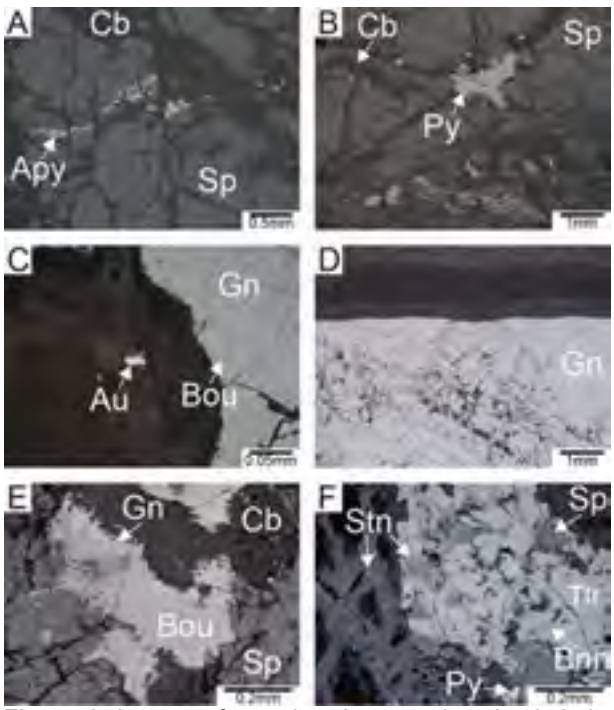


Figure 2. Images of samples. A – cataclazed sphalerite (Sp) with arsenopyrite (Apy) veinlet cemented by carbonate (Cb); B – cataclazed sphalerite cemented carbonate and pyrite (Py); C – native gold (Au) an aggregate of hypergene minerals; D – concentrically zonal aggregate of hypergene minerals along the border of galena (Gn); E – intergrowth of galena and boulangerite (Bou); F – stannite (Stn) and bournonite (Bnn), sphalerite and pyrite fragments in tetrahedrite (Ttr)

Table 1. Maximum and minimum values of the elements in EPMA analyses of fahlores. Formula units based on 29 atoms

		Ag	Cu	Hg	Zn	Fe	Pb	Cd	Sb	As	Bi	Sn	S	Se	Te	Total
Tetrahedrite-(Zn) and tetrahedrite-(Fe)																
wt. %	Maximum	17.3	29.9	1.2	5.7	5.2	0.2	0.9	28.3	3.3	2.0	0.5	24.1	0.2	0.6	100.8
	Minimum	10.8	22.7		1.0	2.7	0.1		22.6				21.2			93.9
apfu	Maximum	3.0	8.1	0.1	1.6	1.7		0.1	4.3	0.8	0.2	0.1	13.1		0.1	
	Minimum	1.8	6.6		0.3	0.9			3.2				12.7			
Ag-bearing tetrahedrite-(Zn) and tetrahedrite-(Fe)																
		Ag	Cu	Hg	Zn	Fe	Pb	Cd	Sb	As	Bi	Sn	S	Se	Te	Total
wt. %	Maximum	30.7	23.7		4.0	4.9	0.7	0.9	27.5		1.0		22.4			100.0
	Minimum	17.5	14.9		1.0	2.3	0.6	0.3	25.2		0.3		20.0			93.4
apfu	Maximum	5.5	6.9		1.2	1.7	0.1	0.1	4.3		0.1		13.1			
	Minimum	3.0	4.7		0.3	0.8			3.9				12.5			
Argentotetrahedrite-(Fe) (the place of analysis is shown by an arrow in Fig. 3)																
		Ag	Cu	Hg	Zn	Fe	Pb	Cd	Sb	As	Bi	Sn	S	Se	Te	Total
	wt. %	33.3	14.0		1.1	4.5			25.6				19.8			98.3
	apfu	6.2	4.4		0.3	1.6			4.2				12.3			29.0

Boulangerite occurs in the form of needle crystals generally intergrowth with galena between carbonate fragments (Fig. 2E) and as inclusions in late-generation carbonate. The mineral is often observed in the form of idiomorphic inclusions located along the crystallographic directions of galena crystals.

Pyrargyrite and diaphorite were observed in association with galena, Ag-bearing tetrahedrite-(Fe) and argentotetrahedrite-(Fe) in EMPA images and analyses (Fig. 3). Irregularly shaped minerals are located along the border and fractures of the fahlores. The chemical composition of pyrargyrite and diaphorite is shown in Table 2.

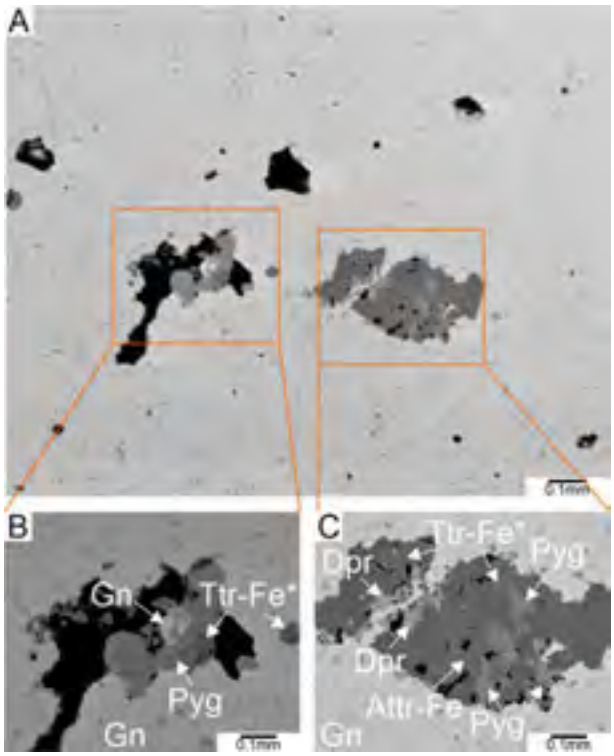


Figure 3. A – observed BSE-image; B – pyrargyrite (Pyg) in void in galena (Gn); C – pyrargyrite and diaphorite (Dpr) in voids and cracks in intergrowth Ag-bearing tetrahedrite-(Fe) (Ttr-Fe*) and argentotetrahedrite-(Fe) (Attr-Fe)

Table 2. Chemical composition of pyrargyrite (Pyg) and diaphorite (Dpr). Formula units (apfu) based on 7 atoms for pyrargyrite and on 16 atoms for diaphorite

	S	Cu	Ag	Cd	Sb	Pb	Total
Pyg Fig. C	16.5		58.7		21.8		97.0
	16.9		58.5		21.5		96.8
	16.1		58.6		21.4		96.1
	16.8		58.7		22.0		97.5
	16.9		58.1		22.0		96.9
	16.6		58.5		21.6		96.6
	17.1		57.7		22.4		97.2
	17.0		57.9		21.5		96.4
apfu	2.9-3		3-3.1		1		
Pyg Fig. B	16.6		56.4	0.7	22.5	0.5	96.7
	16.4	0.3	57.1	0.6	21.3	0.6	96.2
	16.8		56.4		22.0	0.9	96.0
apfu	2.9-3		3		1-1.1		

	S	Ag	Sb	Pb	Total
Dpr Fig. C	18.5	24.2	27.2	24.9	94.8
	18.0	24.2	27.7	25.8	95.7
	17.9	24.1	26.3	24.6	92.8
apfu	7.9-8.1	3.1-3.2	3.1-3.2	1.7-1.8	

Sphalerite forms massive vein aggregates with fractured structure, where the fractures are filled with later minerals such as galena, fahlores, stannite and others (Fig. 2 A, B, E). Sphalerite is also characterized by the presence of panidiomorphic arsenopyrite fragments, pyrrhotite and chalcopyrite inclusions. Rare pyrrhotite and chalcopyrite inclusions are present in the central parts of crystals. The rims of crystals are saturated with chalcopyrite inclusions to such an extent that sphalerite has a yellow tint in reflected light. In some places, the inclusions form a lattice texture that repeats the crystallographic outlines of sphalerite crystals. Elemental analysis of sphalerite returned 0.1 to 11.6 wt.% Fe and up to 1 wt.% Cd.

Pyrite occurs in aggregates with irregular shape (Fig. 2B) and fine sieve-like texture, where idiomorphic crystals are arranged along the border, probably due to pseudomorphosis of pyrite by pyrrhotite.

Pyrite occurs in the host rocks as an accessory mineral of cubic morphology. In addition, in one of the polished sections, pyrite filled thin cleavage

cracks in galena and, probably, is the most recent generation.

5 Results

Based on the results of the study of host rocks and ore minerals, a general scheme of mineral formation sequence was constructed for Bulatskoye, Kaleo and Jubileyniy ore occurrences localized on the periphery of the Deputatskiy ore cluster (Fig. 4).

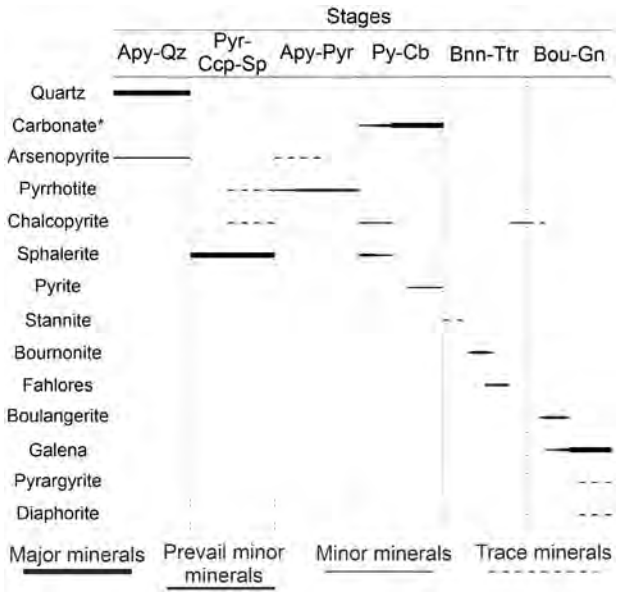


Figure 4. The general scheme of mineral formation sequence for Bulatskoye, Kaleo and Jubileyniy. *carbonate minerals include siderite, manganosiderite and ankerite

At the initial stage there was transformation of sedimentary rocks by diagenesis with the formation of early generation pyrite.

After the intrusion of the Deputatskiy granite pluton, the sedimentary rocks were subjected to contact metamorphism, but this did not affect the studied areas. The only observed transformations of the host rocks are near-surface hydrothermal alteration shown by sericitization of sandstones and mudstones. Such weak rock alteration can be explained by the fact that the studied areas are located at a distance from the source of heat and ore-forming fluids. The described changes in the host rocks occurred before the ore hydrothermal stage and, it should be noted, may not coincide with contact metamorphism.

At the early stage of the hydrothermal process, the formation of arsenopyrite and quartz of the first generation proceeded. The morphology of the bodies that composed these minerals is not clear, as they occur only as fragments or panidiomorphic crystals in later minerals.

Thereafter, following weak cataclasis of the host rocks and previously formed ore mineral associations, sphalerite with rare inclusions of pyrrhotite 1 and chalcopyrite 1 was formed.

After weak cataclasis of sphalerite, arsenopyrite 2 and probably pyrrhotite 2 were formed, which were observed in one polished section from the Bulatskoye ore occurrence.

Cataclasis of the previously formed mineral associations resulted in the formation of fractures that were filled with pyrite and carbonate 1. At this stage, sphalerite 2 with numerous chalcopyrite inclusions formed along the rim of sphalerite 1 fragments. Supposedly later than this stage, stannite, bournonite and fahlores were formed without cataclasis of the earlier minerals.

After cataclasis of earlier minerals, boulangerite, chalcopyrite and galena were formed.

The latest mineral association, not reflected in the scheme of mineral formation sequence, is represented by pyrite, dolomite and calcite. Pyrite was observed in one polished section and filled the cleavage cracks in galena. Calcite was encountered during fieldwork and its veins cut gangue aggregates of manganosiderite and siderite. It is important to note that no contact of pyrite, calcite and dolomite was found.

The last stage, not reflected in the scheme of mineral formation sequence, is represented by hypergenic alteration of previously formed ores.

The described sequence of ore formation for the Bulatskoye, Kaleo and Jubileyniy ore occurrences can be correlated with the already known data on the stages of mineralization of the Deputatskiy deposit.

Comparing the obtained data and the data of predecessors, we can conclude that the ore occurrences were formed at the final fourth stage, and minerals of the third stage were also found in them.

It is not completely clear in what stage the native gold was formed. Work is currently in progress to clarify mineral relations, the mineral composition of the ores and the elemental composition of the minerals, and to study fluid inclusions in quartz and carbonate.

Acknowledgements

We are grateful to analysts E.V. Kovalchuk (IGEM RAS), V.M. Gekimyanez and A.A. Agahanov (Fersman Mineralogical Museum) for production of the analytical data.

References

Borisenko AS, Kholmogorov AI, Borovikov AA, Schebanin AP, Babich VV (1997) Composition and metallization of ore-forming fluids at the Deputatskoe tin-ore deposit (Yakutia). Russian Geology and Geophysics 38(11):1860-1871

Flerov BL, Indolev LN, Yakovlev YaV, Bichus BYa (1971) Geology and genesis of tin deposits of Yakutia. Nauka, Moscow

Ivanov OP (1991) Typomineralogical analysis of ore deposits. Nauka, Leningrad

Nekrasov IYa (1960) Main features of mineralization of Deputatskoye tin deposit. Trudi YaF SO AN USSR Seriya Geologiya 7:58-72

Parfenov LM, Kuzmin MI (2001) Tectonics, geodynamics and metallogeny of the Sakha Republic (Yakutia). MAIK NaukaAnterperiodica, Moscow

Precipitation mechanisms of wolframite and scheelite from hydrothermal fluids

Xiang-Chong Liu[1,2]
[1]*Institute of Geomechanics, Chinese Academy of Geological Sciences, China*
[2]*Key Laboratory of Paleomagnetism and Tectonic Reconstruction, Ministry of Natural Resources, China*

Abstract. Wolframite ([Fe,Mn]WO_4) and scheelite ($CaWO_4$) are the predominant ore minerals of tungsten. Whether their existence in tungsten deposits is singly caused by the Ca content of host rocks is poorly constrained. The solubility differences and precipitation mechanisms of wolframite and scheelite from hydrothermal fluids were examined using thermodynamic modeling programmed in the open-source R language. The updated model parameters can well reproduce the available experimental data for these two tungstates. The modeling results suggest that scheelite is more soluble than hübnerite ($MnWO_4$) in NaCl-H_2O fluids, and hübnerite more soluble than ferberite ($FeWO_4$). Two mechanisms can cause scheelite to replace ferberite (hübnerite): cooling plus a rise in the Ca/Fe (Ca/Mn) molality ratio in fluids and a decrease in fluid pressure. The second mechanism is identified for the first time. These two mechanisms are independent of the existence of CO_2 in the fluids. The combined influence of temperature, pressure, and cation supply (e.g., Ca^{2+}) from host rocks would produce a zonation where wolframite is more likely precipitated in the inner parts, while scheelite easily occurs in the outer parts of the same ore system.

1 Introduction

Wolframite and scheelite are the predominant ore minerals of tungsten (Černý et al. 2005; Kwak 1987). Scheelite generally occurs in skarn-type tungsten deposits hosted by carbonate rocks (Kwak 1987), while wolframite, a solid-solution series between hübnerite ($MnWO_4$) and ferberite ($FeWO_4$), often occurs in vein-type tungsten deposits hosted by clastic sedimentary rocks (e.g., Ni et al. 2020). This difference in tungsten ore minerals in various types of tungsten deposits is commonly interpreted to be caused by the Ca content of the host rocks (Kwak 1987; Paterson and Rankin 1979). This view highlights the geochemical influence of the Ca supply from host rocks, but whether this phenomenon is also affected by the solubility and precipitation mechanisms of these two tungstates is poorly understood. Furthermore, by singly using Ca supply from host rocks it is difficult to explain why great amounts of wolframite and scheelite can coexist in many large-scale vein-type or skarn-type deposits, such as Shizhuyuan (Lu et al. 2003), Xingluokeng, China (Wang et al. 2021), and the Stanne tungsten-molybdenum deposit, South Korea (Shelton et al. 1986).

The pioneering modeling work of Wood and Samson (2000) placed quantitative constraints on the relative solubilities of ferberite and scheelite in hydrothermal fluids. Their models, however, only consider ferberite and lack hübnerite. Some of the major tungsten-bearing species and thermodynamic parameters in their models should also be revised given that many experimental progress have been made since the work of Wood and Samson (2000).

This study is organized as follows: (1) we propose the standard and model parameters of the revised Helgeson-Kirkham-Flowers (HKF) equations for $H_2WO_4^0$ for the first time and update the heat capacity equations of scheelite and hübnerite; (2) these updated model parameters are tested by experimental solubility data for scheelite, ferberite, and hübnerite available in the literature; (3) four chemical systems, scheelite-ferberite and scheelite-hübnerite in NaCl-H_2O and NaCl-H_2O-CO_2 are modeled to examine the relative solubilities of scheelite-hübnerite and scheelite-ferberite in hydrothermal fluids; and (4) the implications for the formation of wolframite and scheelite under W-mineralizing conditions are discussed.

2 Thermodynamic modeling

2.1 Methods

W-mineralizing fluids belong to the NaCl-H_2O±CO_2 system (Naumov et al. 2011; Ni et al. 2020; Wood and Samson 2000). The main tungsten species in these fluids are monomeric tungstates $H_2WO_4^0$, HWO_4^-, and WO_4^{2-} (Liu and Xiao 2020; Wang et al. 2020, 2019; Wood and Samson 2000). Compared to HWO_4^- and WO_4^{2-}, the thermodynamic parameters of $H_2WO_4^0$ are poorly constrained. We propose, for the first time to our knowledge, the standard molar Gibbs free energy $\Delta_f G^0_{P_rT_r}$ (P_r = 1 bar, T_r = 298.15 K), the standard molar entropy $S^0_{P_rT_r}$, the standard heat capacity C^0_P, and six model parameters of the revised Helgeson-Kirkham-Flowers (HKF) equations for $H_2WO_4^0$ using the experimental Gibbs free energies of Wood (1992) and Wang et al. (2019). We also fitted the heat capacity function of temperature for $CaWO_4$ and $MnWO_4$ using the published experimental data. More details of these updated parameters are shown in Liu et al. (2021) and Liu and Xiao (2020).

For other major species of the solutes NaCl, KCl, and $CaCl_2$, we use the thermodynamic data updated by Miron et al. (2017) in the models. The equilibrium constants of reactions and activity coefficients of electrically charged species (an extended Debye-Hückel equation) were calculated using the CHNOSZ package (Dick 2019), which is written by the open-source R language. The nonlinear

equations in each model are solved using another R language package called rootSolve (cf. Soetaert and Herman 2008), and the solving process was similar to that in our previous paper (Liu and Xiao 2020). Molality (mol/kg) was used for the concentrations of species.

2.2 Comparisons with experimental data

We tested the updated thermodynamic parameters by modeling the chemical systems of available solubility experiments. The experimental solubility data we considered include scheelite (Derrey et al. 2017; Foster 1977; Malinin and Kurovskaya 1996), ferberite (Redkin and Cygan 2020), scheelite-ferberite (Korzhinskaya and Zaraisky 1998; Uchida et al. 1989), and scheelite-hübnerite (Korzhinskaya and Zaraisky 1998; Uchida et al. 1989). The updated thermodynamic parameters could well reproduce these available experimental data at 250–800 °C and 20–200 MPa (Fig. 1). More detailed comparisons are shown in Liu et al. (2021) and Liu et al. (2024).

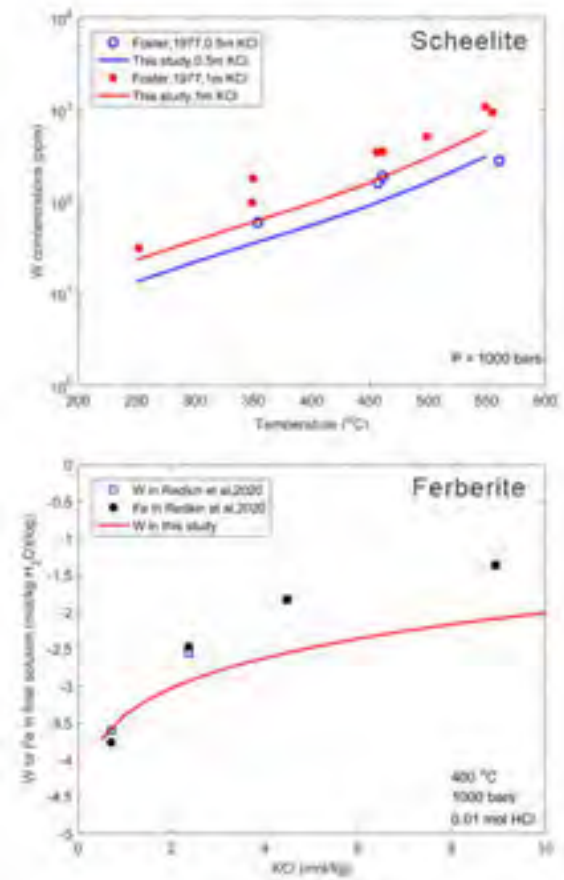


Figure 1. Comparisons between calculated and experimentally determined scheelite and ferberite solubility

2.3 Modeling results for NaCl-H_2O fluids

Two chemical systems, W-Ca-Fe-Na-Cl-O-H and W-Ca-Mn-Na-Cl-O-H, were modeled to examine how temperature, pressure, salinity, and pH affect the relative solubilities of scheelite and wolframite under the following conditions: 300–400 °C, 500–1500 bars, 1–3 mol/kg NaCl, and pH=3–8 (Naumov et al. 2011; Wood and Samson 2000). Neutral pH levels at these temperature and pressure conditions range from 5–6.

The contour plot of the Ca/Fe log-ratios of fluids in equilibrium with scheelite and ferberite at acidic pH levels shows that scheelite is more soluble (logCa/Fe>0) than ferberite at most temperature and pressure conditions investigated except at the corner of high temperatures and low pressures (Fig. 2). Additionally, the Ca/Fe log-ratios increase with decreasing temperature and decrease with decreasing pressure.

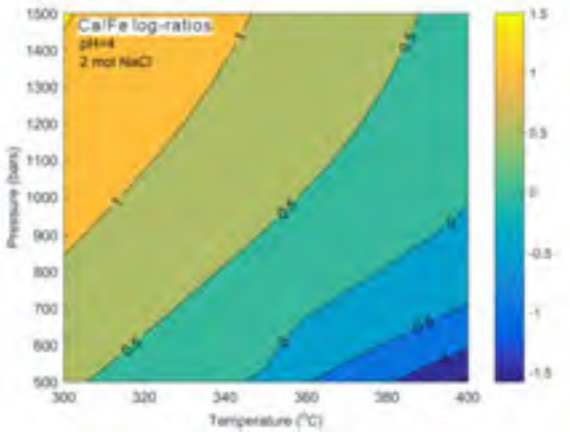


Figure 2. Contour plots of the Ca/Fe log-ratios in fluids in equilibrium with scheelite and ferberite against temperature and pressure at a fixed pH and salinity

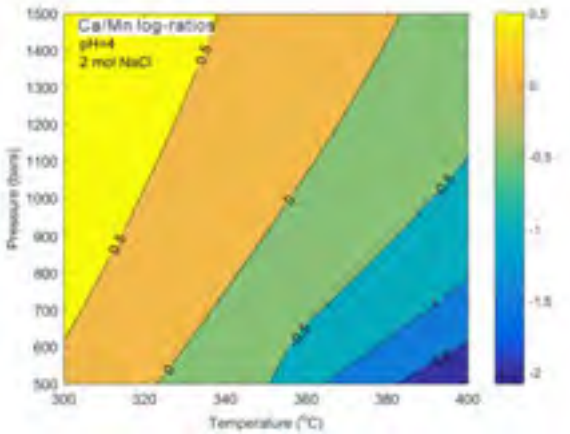


Figure 3. Contour plots of the Ca/Mn log-ratios in fluids in equilibrium with scheelite and hübnerite against temperature and pressure at a fixed pH and salinity

From the contour plot of the Ca/Mn log-ratios of fluids in equilibrium with scheelite and hübnerite at acidic pH levels (Fig. 3), scheelite is more soluble than hübnerite under more than half of the temperature and pressure conditions investigated, but this area is smaller than that in the case of scheelite/ferberite. Similar to the Ca/Fe ratios, the Ca/Mn ratios also increase with decreasing temperature and decrease with decreasing pressure.

2.4 Modeling results for NaCl-H_2O-CO_2 fluids

CO_2 acts only as a pH−buffering agent in the tungsten-bearing fluids. In the models, CO_2 was assumed to be saturated in H_2O−NaCl solutions, and CO_2 solubility was calculated from the solubility model developed by Mao et al. (2013). The solubilities of scheelite under 250–450°C, 50–150MPa, and 1 molal NaCl were calculated.

From the contour lines of Fig. 4, the scheelite solubility in fluids varies from 13.5 to 123 ppm, mainly depending on pressure. In contrast, scheelite solubility is insensitive to temperature when the pressure is high (>100 MPa). At lower pressure, scheelite solubility is a U-shape function of temperature.

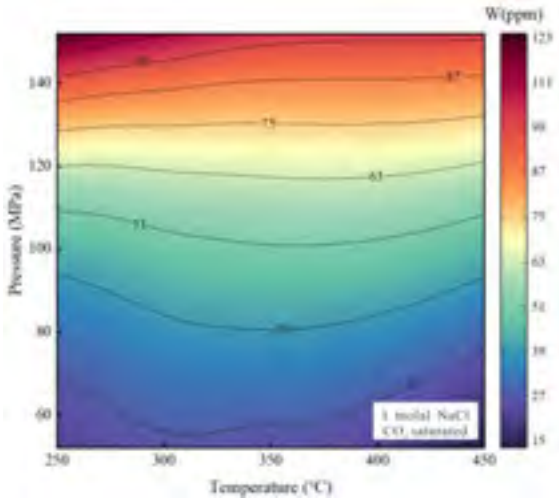


Figure 4. Solubility of scheelite in CO_2-saturated fluids with 1 molal NaCl

The contour plot in Fig. 5 shows that the Ca/Fe log-ratios are over zero under most conditions except at the high-temperature and low-pressure corner. Similar to the cases without CO_2, the Ca/Fe and Ca/Mn log-ratios increase with decreasing temperature and decreasing pressure.

3 Implications for tungsten deposits

Wood and Samson (2000) found that simple cooling with a fixed Ca/Fe ratio cannot lead to the replacement of ferberite by scheelite and that a correlation between the temperature decrease and Ca/Fe increase (adding Ca or removing Fe) is required to do so. This mechanism is supported by our modeling results and also applicable to the replacement of hübnerite by scheelite. Our modeling results also show that a single decrease in fluid pressure is an alternative mechanism for the replacement of ferberite (hübnerite) by scheelite. In this mechanism, neither the addition of Ca from Ca-rich wallrocks nor the removal of Fe (Mn) from hydrothermal fluids is required, so the replacement of wolframite by scheelite is not as difficult as previously thought. These two mechanisms also act independent of the existence of CO_2 in hydrothermal fluids.

The combined influence of temperature and pressure would produce a zonation if wolframite and scheelite coexist in the same hydrothermal system. Wolframite easily occurs in the inner parts of a hydrothermal system because it has lower solubility than scheelite and is easily saturated in the fluids. As the hydrothermal fluids move away from their sources, both temperature and pressure would inevitably decrease. Under these conditions, the fluids still have a relatively high solubility of scheelite and can form a great amount of scheelite in the outer parts. The zonation of inner wolframite and outer scheelite is identified in a few tungsten deposits, such as the Richardson's Kop, Rhodesia (Foster 1975). Therefore, the solubility differences between wolframite and scheelite, together with cation supply (e.g., Ca^{2+}) from host rocks, affect the occurrence of these two tungstates in hydrothermal systems.

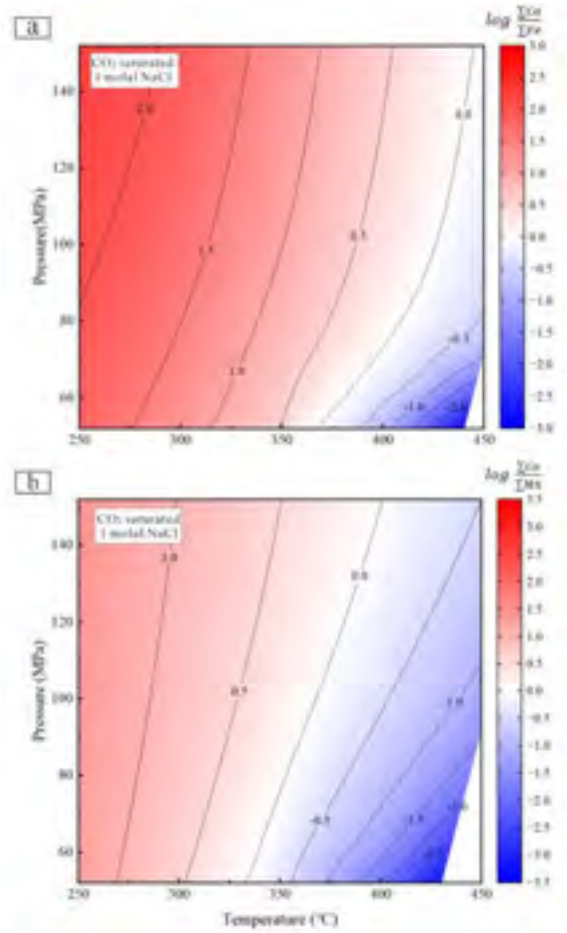


Figure 5. Contour plots of the Ca/Fe of CO_2-saturated fluids in equilibrium with scheelite and ferberite (a) and Ca/Mn log-ratios in fluids in equilibrium with scheelite and hübnerite (b) at a fixed salinity

4 Conclusions

The formation of wolframite and scheelite is strongly affected by the solubility differences between wolframite and scheelite and cation supply (e.g., Ca^{2+}) from host rocks. These internal and external factors would produce a zonation where wolframite and scheelite easily occurs in the inner and outer parts of the same ore system, respectively. Such a

zonation can aid in prospectinng for tungsten deposits. This study also shows that reliable thermodynamic modeling has the capability to decipher the genesis of hydrothermal ore deposits.

Acknowledgements

The authors appreciate Prof. Mao Shide for offering the code for calculating CO_2 solubility and thank Prof. Jeffrey Dick for his generous help in using CHNOSZ. The work is financially supported by the National Natural Science Foundation of China (No. 42473079), the Chinese Academy of Geological Sciences Basal Research Fund (No. JKYQN202339), and China Metallurgical Geology Bureau (No. CMGBKYS202403).

References

Černý P, Blevin PL, Cuney M, London D (2005) Granite-related ore deposits. Econ Geol, 100th Anniversary Volume: 337-370.

Derrey IT, Albrecht M, Dupliy E, Botcharnikov RE, Horn I, Junge M, Weyer S, Holtz F, (2017) Experimental tests on achieving equilibrium in synthetic fluid inclusions: results for scheelite, molybdenite, and gold solubility at 800 °C and 200 MPa. Am Mineral 102(2): 275-283.

Dick JM (2019) CHNOSZ: thermodynamic calculations and diagrams for geochemistry. Front Earth Sci 7(180): 1-18.

Foster RP, Mann AG, Armin T, Burmeister BB (1975) Richardson's Kop wolframite deposit, Rhodesia: a geochemical model for the hydrothermal behaviour of tungsten. In: Verwoerd, W.J. (Ed.), Mineralization in Metamorphic Terranes. Geological Society of African Special Publication, pp 107-128.

Foster RP (1977) Solubility of scheelite in hydrothermal chloride solutions. Chem Geol 20: 27-43.

Korzhinskaya VS, Zaraisky GP (1998) Calcium-to-manganese ratio in a chloride fluid in equilibrium with sheelite-hubnerite association at T=300-600 ºC, P=1 kbar. Experiment in GeoSciences 7(2): 31-32.

Kwak TAP (1987) W-Sn Skarn Deposits and Related Metamorphic Skarns and Granitoids. Dev Econ Geol, 24. Elsevier, Amsterdam, pp 451

Liu H, Liu X-C, Zhang D-H, Zhou Z-J, Han F-B (2024) The precipitation mechanisms of scheelite from CO2-rich hydrothermal fluids: Insight from thermodynamic modeling. Appl Geochem 175: 106187.

Liu XC, Xiao CH (2020) Wolframite solubility and precipitation in hydrothermal fluids: Insight from thermodynamic modeling. Ore Geol Rev 117: 103289.

Liu XC, Xiao CH, Wang Y, (2021) The relative solubilities of wolframite and scheelite in hydrothermal fluids: Insights from thermodynamic modeling. Chem Geol 584(4): 120488.

Lu HZ, Liu Y, Wang C, Xu Y, Li H (2003) Mineralization and fluid inclusion study of the Shizhuyuan W-Sn-Bi-Mo-F skarn deposit, Hunan province, China. Econ Geol 98(5): 955-974.

Malinin SD, Kurovskaya NA (1996) The effect of pressure on mineral solubility in aqueous chloride solutions under supercritical conditions. Geokhimiya(1): 51-58.

Mao S, Zhang D, Li Y, Liu N (2013) An improved model for calculating CO_2 solubility in aqueous NaCl solutions and the application to CO_2–H_2O–NaCl fluid inclusions. Chem Geol 347: 43-58.

Miron GD, Wagner T, Kulik DA, Lothenbach B (2017) An internally consistent thermodynamic dataset for aqueous species in the system Ca-Mg-Na-K-Al-Si-O-H-C-Cl to 800 °C and 5 kbar. Am J Sci 317(7): 755-806.

Naumov VB, Dorofeev VA, Mironova OF (2011) Physicochemical parameters of the formation of hydrothermal deposits: a fluid inclusion study. I. tin and tungsten deposits. Geochem Int 49(10): 1002-1021.

Ni P, Li W, Pan J (2020) Ore-forming fluid and metallogenic mechanism of wolframite–quartz vein-type tungsten deposits in south China. Acta Geologica Sinica - English Edition 94(6): 1774-1796.

Paterson CJ, Rankin PC (1979) Trace element distribution in the schist surrounding a quartz-scheelite lode, Glenorchy, New Zealand. New Zeal J Geol. Geophys 22(3): 329-338.

Redkin AF, Cygan GL (2020) Experimental determination of ferberite solubility in the KCl–HCl–H_2O system at 400–500 °C and 20–100 MPa. In: Litvin Y, Safonov O (Eds), Advances in Experimental and Genetic Mineralogy: Special Publication to 50th Anniversary of DS Korzhinskii Institute of Experimental Mineralogy of the Russian Academy of Sciences. Springer International Publishing, Cham, pp 137-162

Shelton KL, So C-S, Rye DM, Park M-E (1986) Geologic, sulfur isotope, and fluid inclusion studies of the Sannae W-Mo Mine, Republic of Korea; comparison of sulfur isotope systematics in Korean W deposits. Econ Geol 81(2): 430-446.

Soetaert K, Herman PMJ (2008) A Practical Guide to Ecological Modelling - Using R as a Simulation Platform. Springer, Dordrecht, pp 372

Uchida E, Gima M, Imai N (1989) Experimental studies on ion exchange equilibria between minerals and aqueous chloride solution in the system $CaWO_4$-$FeWO_4$-$MnWO_4$ under supercritical condition. Geochem J 23(6): 339-347.

Wang H, Feng CY, Li RX, Zhao C, Liu P, Wang G, Hao Y (2021) Petrogenesis of the Xingluokeng W-bearing granitic stock, western Fujian Province, SE China and its genetic link to W mineralization. Ore Geol Rev: 103987.

Wang XL, Qiu Y, Lu JJ, Chou IM, Zhang WL, Li GL, Hu WX, Li Z, Zhong RC (2020) In situ Raman spectroscopic investigation of the hydrothermal speciation of tungsten: Implications for the ore-forming process. Chem Geol 532: 119299.

Wang XS, Timofeev A, Williams-Jones AE, Shang LB, Bi XW (2019) An experimental study of the solubility and speciation of tungsten in NaCl-bearing aqueous solutions at 250, 300, and 350 °C. Geochim. Cosmochim Acta 265: 313-329.

Wood SA (1992) Experimental determination of the solubility of WO_3(s) and the thermodynamic properties of H_2WO_4(aq) in the range 300–600°C at 1 kbar: Calculation of scheelite solubility. Geochim Cosmochim Acta 56(5): 1827-1836.

Wood SA, Samson IM (2000) The hydrothermal geochemistry of tungsten in granitoid environments: I. relative solubilities of ferberite and scheelite as a function of T, P, pH, and m_{NaCl}. Econ Geol 95: 143-182.

Magmatic Hydrothermal vs. Metamorphic Hydrothermal Fluids: Scheelite Trace Element Signatures

Kairan Liu[1,2], Zhaoshan Chang[1], Shiqiang Huang[1]
[1] Department of Geology and Geological Engineering, Colorado School of Mines, Golden, CO 80401, USA.
[2] Wildsky Resources Inc., Vancouver, BC V6C 1G8, Canada.

Abstract. Gold and/or W-bearing quartz veins, and in rare cases skarns, in areas consisting of meta-siliciclastic and intrusive rocks, are frequently debated on whether they are metamorphic-hydrothermal (e.g., orogenic gold deposits) or magmatic-hydrothermal. This study develops a discrimination method using scheelite trace elements. Laser ablation-inductively coupled plasma-mass spectrometry (LA-ICP-MS) analyses were conducted on scheelite from six magmatic-hydrothermal deposits and seven metamorphic-hydrothermal deposits from multiple regions. The data are combined with carefully validated data from the literature to form a database of 2,763 analyses from 83 deposits. Based on the data, a discrimination diagram of Mo×(Nb+Ta) vs. $Sr \times Eu_A$ is designed. This diagram has a success rate of ~90% in discriminating between deposits in this database, and a test using recent data yields a success rate of ~99%. Minor misclassifications may have resulted from fluid mixing or wall-rock interaction. By focusing on early-stage scheelite and sampling a large area, these inconsistencies can be minimized.

1 Introduction

Scheelite is a common W ore mineral in skarn (Meinert et al. 2005; Chang et al. 2019), greisen (e.g., Chang et al. 2017; Mao et al., 2019), pegmatite (e.g., Liu et al. 2018), porphyry (e.g., Liu et al. 2020), intrusion-related gold systems (IRGS, Thompson et al. 1999), and orogenic Au types of deposits (Goldfarb et al. 2005). Although magmatic and metamorphic-hydrothermal deposits can be geologically distinct, their classification becomes challenging when Au and/or W quartz veins—and, in rare cases, skarns—occur in areas consisting of both metamorphic and intrusive rocks (e.g., Watershed skarn, Australia; Poblete et al. 2021, 2024; Zaozigou, China; Qiu et al. 2020). They are frequently in hot debate on whether the mineralization fluids were magmatic or metamorphic (e.g., Goldfarb and Groves 2015, and references therein). This study explores scheelite trace elements as a new tool to help distinguish magmatic and metamorphic-hydrothermal deposits. Previous studies include Poulin et al. (2018) and Sciuba et al. (2020) proposed Sr, Mo, As, and Eu anomalies as indicators, and Miranda et al. (2022) suggested Nb and Ta. No definitive classification criteria have been proposed.

This study analyzes scheelite from six magmatic-hydrothermal deposits (four skarns: Dachang, China; King Island and Mt Lindsay, Australia; Sangdong, Korea; one greisen-pegmatite: Wolfram Camp, Australia; one greisen-quartz vein: Dajishan, China) and seven orogenic deposits with an exclusively metamorphic fluid origin (El Nido, Kensington, Port Wells, and Valdez, USA; Woxi, Zaozigou, and Zhazixi, China). The results are integrated with published data into a comprehensive dataset, from which we propose a discrimination diagram to distinguish magmatic and metamorphic hydrothermal deposits.

2 Methodology

Trace element analysis of scheelite was conducted at the LA-ICP-MS Lab, Colorado School of Mines, USA. Samples were prepared as 90 μm thick sections and examined petrographically before analysis. The instruments are an Applied Spectra RESOlution-SE 193 nm ArF excimer laser system with an S155 sample cell, coupled to an Agilent 8900 ICP-MS QQQ via a signal smoothing device SQUID. Ablation was performed with a laser beam of 18–50 μm, 5 J/cm^2 fluence, and a 5 Hz repetition rate. Helium carried the ablated material, which was mixed with Ar before introduction to the ICP-MS. Each analytical spot was pre-cleaned with a laser shot, followed by a 15-second washout, 30-second gas blank collection, and 60-second sample signal acquisition. External standards were NIST 610 and 612 glasses, with a bracketed sequence of reference material (RM)-unknown-RM. Data reduction was performed using Iolite v4, with Ca (13.93 wt.%) as the internal standard. A total of 382 spots on 35 samples were analyzed, with at least 10 spots per sample to cover compositional variations. After filtering out 27 analyses affected by inclusions, 353 valid analyses were obtained.

3 Data Compilation

This study compiled scheelite trace element data from the literature up to October 2020. Out of 92 deposits reported in 48 publications, data from only 70 deposits (33 publications) were included after quality assessment. Data were excluded based on the following criteria: deposits with debated origins; analyses performed by bulk dissolution methods potentially contaminated by inclusions; deposits represented by less than 5 analyses, considered unrepresentative; and data containing conflicting Mo values, misidentified minerals, or implausible elemental compositions.

After filtering, 2,410 analyses from the literature were added to the database. Combined with 353 new analyses from this study, the final database includes 2,763 analyses from 83 deposits: 1,888

from 46 magmatic-hydrothermal deposits and 875 from 37 metamorphic-hydrothermal deposits. In addition, 429 recent analyses (de Vazelhes et al. 2021; Miranda et al. 2022; Li et al. 2022) were collected to test the discrimination diagram.

4 Results and Discrimination Diagram

The database shows that magmatic-hydrothermal scheelite has higher concentrations of Mo (Q1-Q3: 113-6,370 ppm), Nb (Q1-Q3: 7.85-109 ppm), and Ta (Q1-Q3: 0.16-9.04 ppm), less Sr (Q1-Q3: 62.1-245 ppm), and lower calculated Eu anomaly values (Q1-Q3: 0.34-1.47). By contrast, metamorphic-hydrothermal scheelite has lower concentrations of Mo (Q1-Q3: 0.08-4.03 ppm), Nb (Q1-Q3: 0.64-4.59 ppm), and Ta (Q1-Q3: 0.03-2.68 ppm), more Sr (Q1-Q3: 546-2,967 ppm), and higher Eu anomaly values (Q1-Q3: 1.39-7.39).

Although Mo, Nb, Ta, Sr, and Eu_A show differences between magmatic and metamorphic-hydrothermal deposits, overlaps exist at the individual deposit level, limiting their discrimination effectiveness. Binary plots (e.g., Sr vs. Mo, Eu_A vs. Nb+Ta) also show significant overlaps (Fig. 1).

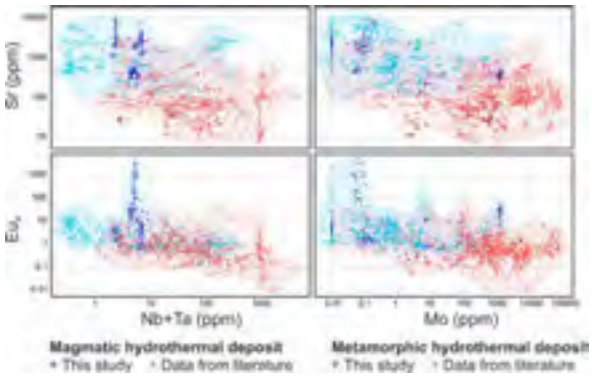


Figure 1. Binary plots of trace elements in scheelite.

To improve the discrimination success rate, we developed a Mo×(Nb+Ta) vs. Sr×Eu_A diagram (Fig. 2). In this plot, scheelite from all 31 orogenic deposits falls in the upper left domain (low Mo×(Nb+Ta), high Sr×Eu_A), whereas 22 of 28 skarns and greisens plot in the lower right domain (high Mo×(Nb+Ta), low Sr×Eu_A). The discrimination line consists of two parts: the upper segment follows Mo×(Nb+Ta) = Sr×Eu_A; and the lower, horizontal segment is set at Sr×EuA = 200. Most of the magmatic-hydrothermal scheelite has a higher Mo×(Nb+Ta) value than Sr×Eu_A, whereas most of the metamorphic-hydrothermal scheelite has a lower Mo×(Nb+Ta) value than Sr×Eu_A value. Overall, 53 of 59 deposits (90%) are effectively classified, while others lack Nb/Ta data to plot.

Six magmatic-hydrothermal deposits (Xiangdong, Shimensi, Tongshankou, Dabaoshan, Muguayuan, and Dajishan, China) show multiple scheelite stages. The early scheelite plots in the magmatic domain, while the late scheelite shifts toward the metamorphic domain and causes overlaps (Fig. 3).

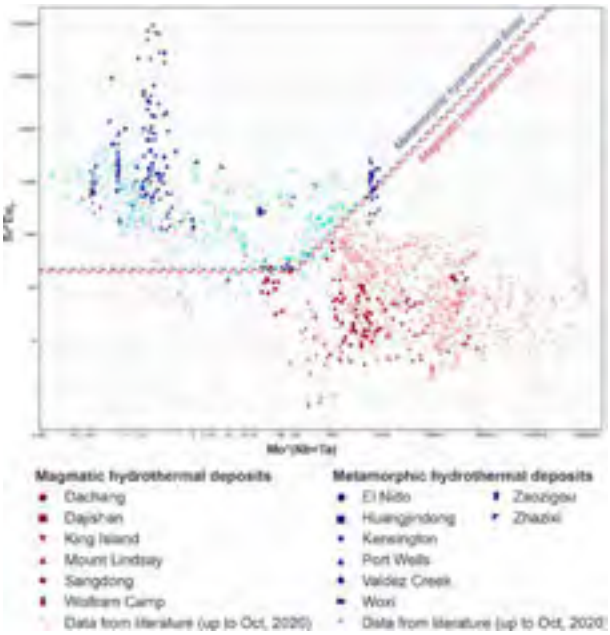


Figure 2. Mo×(Nb+Ta) vs. Sr×Eu_A plot to discriminate magmatic-hydrothermal vs. metamorphic-hydrothermal scheelite.

5 Discussions

5.1 Geochemical features of scheelite of different fluid origins

Magmatic-hydrothermal scheelite is enriched in molybdenum due to the oxidized nature of its source fluids, which causes Mo^{6+} substitution for W^{6+}. In contrast, metamorphic-hydrothermal fluids are typically reduced (Goldfarb and Groves 2015), which limits Mo incorporation.

Magmatic-hydrothermal scheelite contains higher Nb and Ta due to their enrichment in fractionated granitic magmas that W deposits are typically associated with, and high-temperature (>700°C), F-bearing magmatic fluids that enhance HFSE solubility (Blevin and Chappell 1995; Lang and Baker 2001). Metamorphic systems, being lower in temperatures (<350°C) and F-deficient, contain little Nb and Ta.

Metamorphic-hydrothermal scheelite has significantly higher Sr than magmatic scheelite, as the W-rich magmatic fluids are from fractionated granitic magmas and, therefore, are Sr-depleted due to plagioclase fractionation. In contrast, metamorphic fluids derive Sr from altered sedimentary and mafic rocks that typically contain more Sr-bearing plagioclase.

Eu can exist as Eu^{2+} and Eu^{3+}, and both Eu^{2+} and Eu^{3+} can substitute for Ca^{2+} in scheelite, but Eu^{2+} is more compatible due to charge balance constraints (Blundy and Wood 1994). In metamorphic fluids that are typically reduced due to the commonly carbonaceous host rocks, Eu^{2+} is more abundant, leading to positive Eu anomalies in scheelite (Bau 1991). In contrast, magmatic-hydrothermal fluids from fractionated magmas are Eu-depleted due to plagioclase crystallization,

resulting in lower Eu anomaly values in magmatic-hydrothermal scheelite.

Previous studies suggested lower As in orogenic scheelite due to reduced conditions (Poulin et al. 2018; Sciuba et al. 2020). However, this study finds no clear trend in As, likely due to low As compatibility in scheelite, regardless of redox conditions.

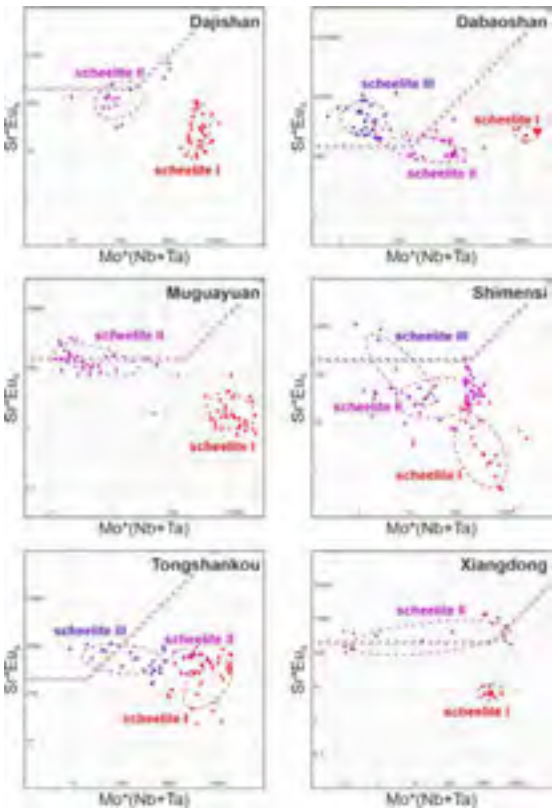


Figure 3. The compositional comparison of multiple types of scheelite from Dajishan, Baoshan, Shimensi, Xiangdong, Dabaoshan and Muguayuan.

5.2 Discrimination diagram: why does it work?

Although Mo, Nb, Ta, Sr, and Eu_A differ between metamorphic and magmatic-hydrothermal scheelite, single elements and binary plots (Fig. 1) are ineffective for fluid discrimination due to local geological influences. For example, metamorphic scheelite in deposits hosted in felsic rocks (e.g., Kensington and Kochkar deposit, USA; Sciuba et al. 2020) can have high Mo (>100 ppm), overlapping with magmatic scheelite (Fig. 2). However, all five elements are unlikely to be affected simultaneously. The Mo×(Nb+Ta) vs. Sr×Eu_A diagram provides a more reliable classification method, achieving ~90% accuracy.

5.3 Potential reasons for the overlap in the discrimination diagram

Six magmatic-hydrothermal deposits in China, including Dajishan (this study), Xiangdong (Liu et al. 2019), Shimensi (Sun and Chen 2017), Tongshankou (Han et al. 2020), Dabaoshan (Su et al. 2019), and Muguayuan (Li et al. 2018) have some data plotting in the metamorphic-hydrothermal domain. These deposits feature multiple scheelite generations with distinct compositions, and the overlap occurs only in late-stage and/or distal scheelite (Fig. 3).

The overlap likely results from fluid-rock interaction, particularly the alteration of Sr-rich carbonate rocks or the sericite alteration of Ca-plagioclase in wall rocks, which can increase Sr in fluids at distal locations (Turekian and Wedepohl 1961; Blevin et al., 1996; Thompson et al., 1999). A minor overlap in Kensington scheelite (Fig. 2) may also stem from fluid interaction with fractionated intrusion host rocks (Miller et al. 1994, 1995).

To increase the success rate of discrimination using the Mo×(Nb+Ta) vs. Sr×Eu_A diagram, earlier stage scheelite should be prioritized, and sampling should be conducted over a broad area to avoid misclassification.

5.4 Test with Recent Data

Data from recent papers (de Vazelhes et al. 2021; Miranda et al. 2022; Li et al. 2022) are plotted in the Mo×(Nb+Ta) vs. Sr×Eu_A diagram (Fig. 4) to test its effectiveness. Miranda et al. (2022) analyzed 19 skarn deposits (magmatic-hydrothermal), while the other papers reported scheelite data from orogenic gold deposits (metamorphic-hydrothermal).

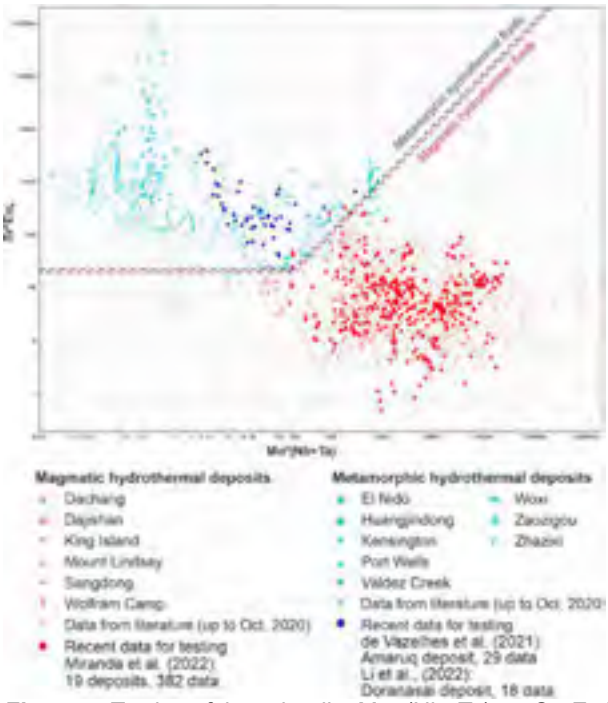


Figure 4. Testing of the scheelite Mo×(Nb+Ta) vs. Sr×EuA discrimination diagram using data from recent literature

As shown in Fig. 4, only 5 out of 429 data points cross the boundary, which indicates a success rate of 99%. The testing confirms that the diagram is effective for fluid nature discrimination.

Acknowledgments

We appreciate colleagues and mining companies for providing samples for this study: Thomas Monecke, Richard Goldfarb, Philip Persson, Duncan McIntire, Mario Guzman, Bo Zhu, Liang Zhang, Dexian Zhang, Yinchao Liu, Xueke Liu, Jiangxi Tungsten Holdings Group Co., Ltd., and Hunan Gold Group Co., Ltd.

References

Bau M (1991) Rare-earth element mobility during hydrothermal and metamorphic fluid-rock interaction and the significance of the oxidation state of europium. Chem Geol 93:219–230

Blevin PL, Chappell BW (1995) Chemistry, origin, and evolution of mineralized granites in the Lachlan fold belt, Australia; the metallogeny of I- and S-type granites. Econ Geol 90:1604–1619

Blevin PL, Chappell BW, Allen CM (1996) Intrusive metallogenic provinces in eastern Australia based on granite source and composition. Trans R Soc Edinb Earth Sci 87:281–290

Chang Z, Clarke G, Cheng Y, Poblete J, Liu K (2017) Sn–W–Mo mineralization in north-east Queensland. In: Phillips GN (ed) Australian Ore Deposits. The Australasian Institute of Mining and Metallurgy, Melbourne, pp 681–688

Chang Z, Shu Q, Meinert LD (2019) Skarn deposits of China. In: Chang Z, Goldfarb RJ (Eds) Mineral Deposits of China, Society of Economic Geologists Special Pub 22:189–234

De Roo JA (1988) Structural controls on the emplacement of the vein-type tungsten-tin ore at Mount Carbine, Queensland, Australia. Econ Geol 83:1170–1180

de Vazelhes VDB, Beaudoin G, McMartin I, Côté-Mantha O, Boulianne-Verschelden N (2021) Assessment of the Amaruq gold deposit signature in glacial sediments using multivariate geochemical data analysis and indicator minerals. J Geochem Explor 228:106800

Goldfarb RJ, Baker T, Dubé B, Groves DI, Hart CJ, Gosselin P (2005) Distribution, character and genesis of gold deposits in metamorphic terranes. Econ Geol 100th Anniv Vol:407–450

Goldfarb RJ, Groves DI (2015) Orogenic gold: Common or evolving fluid and metal sources through time. Lithos 233:2–26

Goldfarb RJ, Pitcairn I (2023) Orogenic gold: is a genetic association with magmatism realistic? Miner Depos 58:5–35

Han J, Chen H, Hong W, Hollings P, Chu G, Zhang L, Sun S (2020) Texture and geochemistry of multi-stage hydrothermal scheelite in the Tongshankou porphyry-skarn Cu-Mo (-W) deposit, eastern China: Implications for ore-forming process and fluid metasomatism. Am Mineral 105:945–954

Lang JR, Baker T (2001) Intrusion-related gold systems: the present level of understanding. Miner Depos 36:477–489

Li X, Aibai A, He X, Tang R, Chen Y (2022) Chemical composition and strontium isotope characteristics of scheelite from the Doranasai gold deposit, NW China: Implications for ore genesis. Minerals 12:637

Li XY, Gao JF, Zhang RQ, Lu JJ, Chen WH, Wu JW (2018) Origin of the Muguayuan veinlet-disseminated tungsten deposit, South China: Constraints from in-situ trace element analyses of scheelite. Ore Geol Rev 99:180–194

Liu B, Li H, Wu QH, Evans NJ, Cao JY, Jiang JB, Wu JH (2019) Fluid evolution of Triassic and Jurassic W mineralization in the Xitian ore field, South China: Constraints from scheelite geochemistry and microthermometry. Lithos 330:1–15.

Liu J, Li W, Zhu X, Zhou JX, Yu H (2020) Ore genesis of the Late Cretaceous Larong porphyry W-Mo deposit, eastern Tibet: Evidence from in-situ trace elemental and S-Pb isotopic compositions. J Asian Earth Sci 190:104199

Liu K, Chang Z, Cheng Y (2018) The geology and genesis of the Wolfram Camp Mine W-Mo deposit, Queensland, Australia: Fluid inclusion and stable isotope studies. Metals, Minerals, and Society, Proceedings, the Society of Economic Geologists 2018 conference: Keystone, CO, USA. 22-25 September 2018. 1 p.

Mao J, Ouyang H, Song S, Santosh M, Yuan S, Zhou Z, Zheng W, Liu H, Liu P, Cheng Y, Chen M (2019) Geology and metallogeny of tungsten and tin deposits in China. Soc Econ Geol Spec Publ 22:411–482

Meinert LD (2005) World skarn deposits. Econ Geol 100th Anniv Vol:299–336

Miller LD, Goldfarb RJ, Gehrels GE, Snee LW (1994) Genetic links among fluid cycling, vein formation, regional deformation, and plutonism in the Juneau gold belt, southeastern Alaska. Geology 22:203–206

Miller LJ, Goldfarb RJ, Snee LW, Gent CA, Kirkham RA (1995) Structural geology, age, and mechanisms of gold vein formation at the Kensington and Jualin deposits, Berners Bay district, southeast Alaska. Econ Geol 90:343–368

Miranda ACR, Beaudoin G, Rottier B (2022) Scheelite chemistry from skarn systems: implications for ore-forming processes and mineral exploration. Miner Depos 57:1469–1497

Poblete JA, Dirks PH, Chang Z, Huizenga JM, Griessmann M, Hall C (2021) The watershed tungsten deposit, Northeast Queensland, Australia: permian metamorphic tungsten mineralization overprinting carboniferous magmatic tungsten. Econ Geol 116:427–451

Poblete JA, Huizenga JM, Chang Z, Dirks P (2024) The Permian Watershed tungsten deposit (northeast Queensland, Australia): Fluid inclusion and stable isotope constraints. Aust J Earth Sci 71:1183–1202

Poulin RS, Kontak DJ, McDonald A, McClenaghan MB (2018) Assessing scheelite as an ore-deposit discriminator using its trace-element and REE chemistry. Can Mineral 56:265–302

Qiu K, Yu H, Deng J, McIntire D, Gou Z, Geng J, Chang, Z, Zhu R, Li K, Goldfarb R (2020) The giant Zaozigou Au-Sb deposit in West Qinling, China: magmatic- or metamorphic-hydrothermal origin? Miner Depos 55: 345-362.

Sciuba M, Beaudoin G, Grzela D, Makvandi S (2020) Trace element composition of scheelite in orogenic gold deposits. Miner Depos 55:1149–1172

Su SQ, Qin KZ, Li GM, Olin P, Thompson J (2019) Cathodoluminescence and trace elements of scheelite: Constraints on ore-forming processes of the Dabaoshan porphyry Mo-W deposit, South China. Ore Geol Rev 115:103183

Sun K, Chen B (2017) Trace elements and Sr-Nd isotopes of scheelite: Implications for the W-Cu-Mo polymetallic mineralization of the Shimensi deposit, South China. Am Mineral 102:1114–1128

Thompson JFH, Sillitoe RH, Baker T, Lang JR, Mortensen JK (1999) Intrusion-related gold deposits associated with tungsten-tin provinces. Miner Depos 34:197–217

Turekian KK, Wedepohl KH (1961) Distribution of the elements in some major units of the earth's crust. Geol Soc Am Bull 72:175–192

Timing of meteoric-water incursion controls tin mineralization scale

Peng Liu[1*], Bernd Lehmann[2], Francois Holtz[3], Stefan Weyer[3], Nigel J. Cook[4], Maria Rosa Scicchitano[5], Christopher L. Kirkland[6], Xiaoyan Li[1], Zhian Bao[1], Zexian Cui[7], Franziska D.H. Wilke[5], Honglin Yuan[1], Jingwen Mao[1,2]

[1] State Key Laboratory of Continental Evolution and Early Life, Department of Geology, Northwest University, Xi'an 710069, China

[2] Mineral Resources, Clausthal University of Technology, Clausthal-Zellerfeld 38678, Germany

[3] Institute of Earth System Sciences, Section Mineralogy, Leibniz University Hannover, Hannover 30167, Germany

[4] School of Chemical Engineering, The University of Adelaide, Adelaide, South Australia 5005, Australia

[5] GFZ Helmholtz Centre for Geosciences, Potsdam 14473, Germany

[6] Timescales of Mineral Systems Group, School of Earth and Planetary Sciences, Curtin University, Perth 6102, Australia

[7] State Key Laboratory of Isotope Geochemistry, Guangzhou Institute of Geochemistry, Chinese Academy of Sciences, Wushan, Guangzhou 510460, China

[8] Institute of Mineral Resources, Chinese Academy of Geological Sciences, Beijing 100037, China

Abstract. Here we combine *in-situ* Sn and O isotope analysis of cassiterite from the multiphase granites of the Cretaceous Mikengshan Sn district, South China, to better constrain the key factors for tin ore genesis. Petrological imaging and trace-element compositions of distinct cassiterite types indicate that they crystallized from distinct pulses of exsolved magmatic fluids. Cassiterite oxygen isotope compositions imply that these fluids had variable contributions of meteoric water, up to 50 %. Corresponding Sn isotopes define a trend in which δ^{124}Sn decreases from early to late cassiterite, indicating a redox-controlled mechanism for cassiterite formation. Furthermore, the variable but relatively elevated δ^{124}Sn values in cassiterite are explained through a combination of vapor- and redox-controlled isotope fractionation. These findings suggest that post-magmatic meteoric-water incursion during progressive cooling of shallow granitic intrusions leads to oxidation. This process plays a key role in the redistribution of Sn and formation of large-scale deposits, indicating the timing of meteoric-water incursion as a key control on the scale of Sn mineralization.

1 Introduction

The key controlling factors that govern the scale of magmatic-hydrothermal Sn mineralization has, hitherto, remained elusive. Here we use a novel combination of *in-situ* cassiterite Sn and O isotope analysis to explore the role of oxidation by meteoric water in the formation of magmatic-hydrothermal Sn mineralization. We find that variable contributions of meteoric water (up to 50 %) already occur at a late magmatic stage of the crystallization, which increases oxidation state with cooling of the shallow granitic intrusion and thus controls Sn redistribution and large-scale Sn ore formation. This study evidences that the timing of meteoric-water incursion is a critical factor defining the scale of magmatic-hydrothermal Sn mineralization.

2 Geology and samples

The Mikengshan Sn district, with a total resource of about 250,000 t Sn, is hosted in the Lower Cretaceous Mikengshan volcanic basin, South China There are several Sn deposits of disseminated, stockwork, greisen, and vein style associated with an intrusive center of the 135–140 Ma Mikengshan volcano-plutonic complex. Cassiterite U-Pb ages for disseminated, vein, and greisen mineralization are identical within uncertainty (ca. 135 ± 2 Ma, Liu et al. 2021), suggesting that all Sn deposits around the Mikengshan complex belong to a single magmatic-hydrothermal system. The lithological package within a circular host basin comprises tuff, tuffaceous lava, rhyolite, and rhyolite porphyry. The central part of the intrusive complex is a fluorine-rich, highly-fractionated, and relatively reduced composite porphyry/granite (Liu et al. 1999), comprising granite porphyry, K-feldspar megacrystic fine-grained biotite granite, porphyritic K-feldspar biotite granite, and late-phase fine-grained biotite granite. The main minerals in this multiphase granitic system consist of quartz, albite, orthoclase, biotite, muscovite, topaz, fluorite, and minor columbite, rutile, and zircon. Notably, cassiterite grains were identified in the granite porphyry, K-feldspar megacrystic fine-grained biotite granite, and late-phase fine-grained biotite granite.

Cassiterite-1 (Cst-1) in the granite porphyry mostly occurs as anhedral crystals, smaller than 80 μm across and intergrown with albite, orthoclase, and biotite. Cassiterite-2 (Cst-2) in the K-feldspar megacrystic fine-grained biotite granite occurs as 80–120 μm euhedral to subhedral crystals intergrown with muscovite, albite, biotite, quartz, and rutile. Cassiterite-3 (Cst-3) occurs in the late-stage fine-grained biotite granite as stubby prismatic and euhedral to subhedral crystals, mostly >100 μm across and intergrown with columbite, rutile, K-feldspar, albite, quartz, and topaz.

3 Methodology

Cassiterite samples for cathodoluminescence (CL) imaging, trace element, and Sn isotope analyses were handpicked under a binocular microscope, mounted in an epoxy resin disc, and polished. Cassiterite grains were then drilled from the mount

using a microdrill, mounted along with grains of the Yongde cassiterite reference material in the center of two 25.4 mm-diameter epoxy discs (> 5 mm from the edges to avoid X-Y effects), and repolished for CL imaging and SIMS O isotope analysis. Each trace element and Sn-O isotope analysis was performed on the same domain of the same cassiterite grain.

4 Results and interpretation

Based on CL images, Cst-1 and Cst-3 can each be separated into two distinct types of cassiterite (Cst-1a and Cst-1b, and Cst-3a and Cst-3b, respectively). Cst-1a has low CL intensity, and is homogenously dark in CL images, whereas Cst-1b has higher CL intensity, and displays regular bright zoning in CL, partly forming rims on, or replacing Cst-1a. Cst-2 has low CL intensity, and locally displays regular zoning and bright domains in CL images. Cst-3a is characterized by regular zoning with locally homogeneous domains with bright or dark color in CL images. Cst-3b has high CL intensity, and locally displays growth zones, which are overprinted, fractured, and refilled by cassiterite and columbite, partly forming rims on, or replacing Cst-3a. Both Cst-1a and Cst-1b display wide ranges of $\delta^{18}O$ values, varying from –4.6 to +2.6 ‰ (n= 11) and –6.5 to +2.9 ‰ (n= 21), respectively, and variable $\delta^{124}Sn$ values, ranging from –0.38 to +1.1 ‰ (n= 11) and –0.86 to +0.61 ‰ (n= 21), respectively. By contrast, Cst-2 displays significantly higher $\delta^{124}Sn$ values ranging from +0.39 to +2.11 ‰ (n= 15) with a wide range of $\delta^{18}O$ values from –5.2 to +3.9 ‰ (n = 21), similar to that observed in Cst-1. Cst-3a and Cst-3b grains have distinct $\delta^{124}Sn$ and $\delta^{18}O$ values; Cst-3a displays relatively high $\delta^{124}Sn$ values with a large variation from –0.04 to +2.25 ‰ (n= 11), while Cst-3b displays lower $\delta^{124}Sn$ values with a relatively narrow range (–0.35 to +0.16 ‰; n= 9). Both Cst-3a and Cst-3b display moderately high $\delta^{18}O$ values, ranging from –0.5 to +3.7 ‰ (n= 11) and –1.7 to +3.2 ‰ (n= 9), respectively, i.e., lacking the distinctly negative $\delta^{18}O$ values shown by some Cst-1a and Cst-1b grains.

Assuming a temperature of about 600 °C for primary magmatic fluids exsolved from highly fractionated granitic melts (Fonseca Teixeira et al., 2022), the $\delta^{18}O_{water}$ values in equilibrium with Cst-1a, Cst-1b, Cst-2, Cst-3a, and Cst-3b were calculated to be in the ranges from –0.1 to +7.2 ‰, –2.0 to +7.5 ‰, –0.7 to +8.5 ‰, +4.1 to +8.3 ‰, and +2.4 to +7.8 ‰, respectively. The calculated $\delta^{18}O_{water}$ values are in most cases significantly lower than those of their magmatic source (average 7.65 ‰), which are derived from measured $\delta^{18}O$ values in zircon from the granite porphyry ($\delta^{18}O_{zircon}$ = 7.28 ± 0.18 ‰), and calculated $\delta^{18}O_{water}$ values in equilibrium with igneous quartz in the Mikengshan multiphase granites ($\delta^{18}O_{water}$ = 7.4–7.9 ‰) (Liu et al., 1999). The shift towards low $\delta^{18}O_{water}$ in cassiterite is interpreted to indicate an influx of meteoric water in the late- to post-magmatic evolution of the system. Assuming a typical $\delta^{18}O$ value for Mesozoic meteoric water of about –9 ‰ (Zhang 1989), isotopic mass balance calculations for binary mixing allow estimation of the contribution of meteoric water (Burrows et al. 1986). Such calculations indicate that the mean contributions of meteoric water are 16 % (up to 46 %) for Cst-1a, 18 % (up to 58 %) for Cst-1b, 8 % (up to 50 %) for Cst-2, 6 % (up to 22 %) for Cst-3a, and 14 % (up to 29 %) for Cst-3b, respectively.

Previous experimental work has indicated that redox reactions alone, without fractional crystallization along the fluid path, produce only minor Sn isotope fractionation in cassiterite with a $\delta^{124}Sn$ range of ~0.8 ‰. In contrast, cassiterite formed by Sn oxidation in the presence of a fractionating vapor phase results in a much larger variation in $\delta^{124}Sn$ values of ~2 ‰ (Wang et al. 2019). As such, the large variation in $\delta^{124}Sn$ values that we observe for Cst-1a (~1.5 ‰), Cst-2 (~1.7 ‰), and Cst-3a (~2.3 ‰) cannot be caused, alone, by Sn oxidation from a fluid phase. Rather, the experimental and theoretical data for Sn reduction indicate that cassiterite with heavy Sn isotope composition precipitated from a $SnCl_2$ vapor phase (Wang et al. 2019; She et al. 2020; Wang et al. 2021). Vapor separation and redox reactions during the post-magmatic stage most likely contributed to formation of Cst-1a, Cst-2, and Cst-3a with a relatively elevated and broad range of $\delta^{124}Sn$ values.

5 Implications

Sn^{4+} (r= 0.69 Å) is compatible with biotite, ilmenite, rutile, and titanite due to its substitution for Ti^{4+} (r= 0.605 Å) in these minerals (Badullovich et al. 2017). Sn^{4+} would be incorporated into these Ti^{4+}-bearing minerals and even crystallize as cassiterite in a highly fractionated granite under relatively oxidizing conditions (Linnen et al. 1995). The involvement of meteoric water during the late-magmatic stage would oxidize and cool the magmatic-hydrothermal system. In particular, progressively decreasing temperature and increasing f_{O2} (> FMQ + 0.7) can dramatically lower SnO_2 solubility in silicate melts, resulting in cassiterite precipitation within the intrusive body at a fluid-present magmatic stage of the crystallization. This oxidizing and cooling process can therefore lead to cassiterite precipitation in the granitic magma and the scavenging of Sn before it massively partitions into exsolved brine or vapor (Lehmann 2021). Taking into account that Sn can also be transported in fluids as Sn^{4+} (Schmidt 2018), ongoing incursion of meteoric water at high temperatures can reactivate part of this Sn reservoir and remobilize Sn to eventually form Sn mineralization in domains of focused fluid ascent with large physicochemical gradients. Thus, the oxidation of the magmatic/hydrothermal system by meteoric water would prevent the formation of large-scale hydrothermal Sn mineralization and result in high Sn concentrations in the surrounding granites, as was

likely the case for the investigated Mikengshan granites.

In contrast, under reducing conditions, with Sn^{2+} dominant, Sn could remain concentrated in residual liquids in the intergranular pore space for most of the magmatic stage, preventing magmatic cassiterite crystallization, with Sn then transported by exsolved magmatic fluids (brine or vapor). Meteoric-water incursions leading to interaction with magmatic fluids would trigger massive Sn precipitation and formation of large-scale Sn mineralization. This process may well explain why giant Sn deposits are associated with evolved granites which often have low Sn contents and only rare accessory cassiterite. Examples include the world-class deposits of Gejiu (China, 3.2 Mt Sn), Dachang (China, 1.5 Mt Sn), and San Rafael (Peru, 1 Mt Sn). Therefore, our results elucidate the importance of the timing of meteoric-water incursion for the redistribution of Sn and the formation of large-scale Sn mineralization.

Acknowledgements

This research was jointly funded by the National Natural Science Foundation of China (42130102, 42102080 and 42272070), and the Young Star of Science and Technology Plan Projects in Shaanxi Province, China (2023KJXX-037), and the Outstanding Young Talents of Special Support Program in Shaanxi Province, China (Peng Liu). F.H. and S.W. acknowledge the German Science Foundation (project HO 1337-49).

References

Badullovich N, Moynier F, Creech J, Teng FZ, Sossi PA (2017) Tin isotopic fractionation during igneous differentiation and Earth's mantle composition. Geochem Perspect Lett 5: 24–28.

Burrows DR, Wood PC, Spooner ETC (1986) Carbon isotope evidence for a magmatic origin for Archean gold quartz vein ore deposits. Nature 321: 851–854.

Lehmann B (2021) Formation of tin ore deposits: A reassessment. Lithos 402–403: 105756.

Linnen RL, Pichavant M, Holtz F, Burgess S (1995) The effect of f_{O2} on the solubility, diffusion, and speciation of tin in haplogranitic melt at 850 °C and 2 kbar. Geochim Cosmochim Acta 59: 1579–1588.

Liu P, Mao JW, Lehmann B, Peng LL, Zhang RQ, Wang FY, Lu GA, Jiang CY (2021) Cassiterite U-Pb dating of the lower Cretaceous Yanbei tin porphyry district in the Mikengshan volcanic basin, SE China. Ore Geol Rev 134: 104151.

Liu CS, Ling HF, Xiong XL, Shen WZ, Wang DZ, Huang XL, Wang RC (1999) An F-rich, Sn-bearing volcanic-intrusive complex in Yanbei, South China. Econ Geol 94: 325–342.

Schmidt C (2018) Formation of hydrothermal tin deposits: Raman spectroscopic evidence for an important role of aqueous Sn (IV) species. Geochim Cosmochim Acta 220: 499–511.

She JX, Wang TH, Liang HD, Muhtar MN, Li WQ, Liu XD (2020) Sn isotope fractionation during volatilization of Sn (IV) chloride: Laboratory experiments and quantum mechanism calculations. Geochim Cosmochim Acta 269: 184–202.

Wang D, Mathur R, Powell W, Godfrey L, Zheng YY (2019) Experimental evidence for fractionation of tin chlorides by redox and vapor mechanisms. Geochim Cosmochim Acta 250: 209–218.

Wang TH, She JX, Yin K, Wang K, Zhang Y, Lu XC, Liu XD, Li WQ (2021) Sn (II) chloride speciation and equilibrium Sn isotope fractionation under hydrothermal conditions: A first principles study. Geochim Cosmochim Acta 300: 25–43.

Zhang LG (1989) Petrogenetic and Minerogenetic Theories and Prospecting. Press of Beijing University of Technology, Beijing (in Chinese).

Metal source evolution of Carboniferous molybdenum-tungsten (Mo-W) mineralization during incremental growth of a granite batholith (Late Variscan Aar Massif, Switzerland)

N.J. Saintilan[1,2], N.D. Greber[3,4,5], R.A. Creaser[6], M. Ovtcharova[4], D. Selby[7], M. Wiederkehr[8], U. Schaltegger[4]
[1]Department of Geological Sciences, University of Alabama, Tuscaloosa, Alabama, 35487, USA
[2]Department of Earth and Planetary Sciences, ETH Zürich, 8092 Zürich, Switzerland
[3]Muséum d'histoire naturelle de Genève, 1208 Geneva, Switzerland
[4]Department of Earth Sciences, University of Geneva, 1205 Geneva, Switzerland
[5]Institute of Geological Sciences, University of Bern, 3012 Bern, Switzerland
[6]Department of Earth and Atmospheric Sciences, University of Alberta, Edmonton, Alberta, T6G 2E3, Canada
[7]Durham Geochemistry Centre, Durham University, DH1 3LE, Durham, United Kingdom
[8]Swiss Geological Survey, Federal Office of Topography Swisstopo, 3084 Wabern, Switzerland

Abstract. We report high-precision rhenium-osmium model ages and molybdenum isotope values (δ^{98}Mo) for molybdenite mineralization found in aplitic quartz veins or as impregnation in the Baltschieder granodiorite, Alpjuhorn molybdenum-tungsten (Mo ± W) deposit, Late Variscan Aar Massif. Three discrete events of molybdenite mineralization (ca. 333 Ma, ca. 323 Ma, ca. 315–303 Ma) span ~30 million years and match with three pulses of late-orogenic extensional to transtensional magmatism during incremental growth of the Aar Massif batholith between ca. 335–295 Ma. These distinct phases of molybdenite mineralization reflect changes in the source of Mo (and, by corollary W) in a geodynamic scenario of increasing proportion of juvenile mantle and decreasing proportion of crustal contamination in the granitic magmas. In light of this case study in the Late Variscan Aar Massif, we anticipate that Mo isotopes could be used to track heavy crustal Mo isotope signatures that may signal intrusions that were prone to scavenge Mo, and by corollary W, from pre-enriched crustal sources: heavy δ^{98}Mo values of granite-hosted molybdenite could be used as proxy for syn-orogenic/late-orogenic extensional to transtensional granitic magmas contaminated by (meta-)sedimentary protoliths pre-enriched in W and Mo (including hematite, rutile, titanite) with noticeable heavy δ^{98}Mo values.

1 Rationale of the work

Post-collisional granite magmatism is prone to be the heat engine at the root of major tungsten (W) mineral deposits, e.g., the crustally-derived Tungsten Plutonic Suite (TPS) in NW Canada (Rasmussen et al. 2023). Orogenic heating of sediment protoliths pre-enriched in W and deposited in passive margin settings (Romer & Kroner 2015, 2016), produces reduced melts that efficiently scavenge W (Romer & Kroner, 2016; Elongo et al. 2022).

The Variscan belt of Western and Central Europe is comprised of several metallogenic provinces that host some significant tungsten-tin (W-Sn) deposits and are underlain by the Armorican Spur of the Gondwana plate (e.g., NW Iberia, Brittany, French Massif Central, Bohemian Massif; Romer & Kroner 2015; their Fig. 1). Tungsten mineralization was shown to be polyphase with three distinct magmatic-hydrothermal events reflecting changes in the tectono-metamorphic evolution of the Variscan belt over ~40 Ma (Tornos et al 2000; Melleton et al. 2012, 2015; Neiva et al. 2012; Romer & Kroner 2015; Harlaux et al. 2018). Thus, considering the work carried out in the TPS to identify the origin of magmas and source of metals in some of the economically most significant W deposits in the world (Elongo et al. 2022; Rasmussen et al. 2023), constraints on the source of W-associated magmas in the Variscan are critically needed. To address these questions, the present study focuses on the historical molybdenum-tungsten (Mo ± W) deposit of the Alpjuhorn in the Baltschiedertal, SW Aar Massif, Switzerland (30,000 metric tons MoS_2; Kenngott 1866; Ledermann 1955; Engel 1988). To this end, we used molybdenite Mo isotope geochemistry and high-precision molybdenite Re-Os geochronology to (1) identify three discrete events of magmatic-hydrothermal Mo ± W mineralization, and (2) specify the source(s) of metals over ~30 million years of Mo ± W mineralization constrained by the new molybdenite Re-Os ages.

2 Samples and methods

2.1 Molybdenite samples and the host Baltschieder granodiorite

The Alpjuhorn molybdenite mineralization is found in aplitic quartz veins or as impregnations in the Baltschieder granodiorite. Due to physical erosion and the steep cliffs of the Alpjuhorn, many molybdenite-bearing blocks fell down the north face of the Alpjuhorn. Molybdenite is associated with scheelite ($CaWO_4$) that replaced (now rare) ferberite ($Fe_{0.77}Mn_{0.23}WO_4$) whereas ilmenite ($FeTiO_3$) was replaced by titanite ($CaTiSiO_5$) and rutile (TiO_2). Galena with inclusions of bismuth sulfides ends the paragenetic sequence (Greber & Hoffmann 2013).

All molybdenite samples except BLST-1 are from this boulder field beneath the Alpjuhorn cliffs. Four hand samples with molybdenite (AJ-007, -009, -010, -011) were taken from the sample set used by Greber et al. (2011) when addressing the fractionation of Mo isotopes in high-temperature and low-temperature hydrothermal systems from the Swiss Alps. A fifth sample (AJ-012) was added in the

present set from N. Greber's sample collection. In contrast, sample BLST-1 originates from the Lötschberg Basis tunnel, which is located about 16 km in the 304 Ma Gastern granite (Schaltegger 1993) to the northwest of the Alpjuhorn. In addition, new sampling of the Baltschieder granodiorite was conducted in 2023 with the aim of dating accurately autocrystic zircons for this intrusion using uranium-lead (U-Pb) chemical-abrasion isotope dilution thermal ionization mass spectrometry (CA-ID-TIMS).

2.2 Molybdenite Re-Os isotope geochemistry & geochronology

Molybdenite Re-Os isotope geochemistry and geochronology was conducted at both the Institute of Geochemistry and Petrology, ETH Zürich (ETHZ), Switzerland, and the Canadian Centre for Isotopic Microanalysis, University of Alberta (UofA), Canada. A blind sample was sent to Durham University, Durham Geochemistry Centre. Molybdenite mineral separates were produced by adapting the protocol of sulfide mineral separation for Re-Os geochronology. For each analysis, between 43 and 114 mg of molybdenite mineral separates were weighed and transferred into thick-walled borosilicate Carius tubes. Each sulfide aliquot was dissolved in inverse Aqua Regia (~3 mL of 11N HCl and ~6 mL 16N HNO_3) with a known amount of "^{185}Re+^{188}Os+^{190}Os spike" solution at 220ºC for 24 h. The laboratory protocol used in the present work to produce purified aliquots of Re and Os is described in full details in Selby and Creaser (2001). The Re and Os isotopic compositions were determined by negative thermal ionization mass spectrometry (N-TIMS) using a Thermo Scientific Triton Plus mass spectrometer (Creaser et al. 1991; Völkening et al. 1991). Measurement quality was monitored by repeated measurements of in-house standard solution for Re (125 pg aliquot – $^{185}Re/^{187}Re$ = 0.5986 ± 0.0005, 2σ, *n* = 22) and Os (Durham Romil Os Standard, DROsS; Nowell et al., 2008; 50 pg aliquot – $^{187}Os/^{188}Os$ = 0.16092 ± 0.00069, 2σ, *n* = 12 at ETH Zürich & Durham; AB-2 Os Standard, $^{187}Os/^{188}Os$ = 0.10696 ± 0.00032, 2σ, *n* = 9 at UofA). Total procedural blank using inverse Aqua Regia was: (i) 2 ± 1 pg Re and 0.5 ± 0.2 pg Os with a blank $^{187}Os/^{188}Os$ isotope composition of 0.30 ± 0.10 (2σ, *n* = 2). The analytical uncertainties result from full error propagation of weighing errors, standard measurements, mass spectrometry analyzes and blanks. Individual model dates are calculated as follows:

$$T = 1/\lambda \times \ln(^{187}Os^*/^{187}Re + 1);$$

Total uncertainty on the Re-Os dates is presented without and with including the decay constant of ^{187}Re as determined by Smoliar et al. (1996; $\lambda = 1.666e^{-11} \pm 5.165e^{-14}$ a^{-1}, 2σ). The accuracy of the whole analytical protocol was checked by analyses of the Henderson mine molybdenite reference material (NIST RM 8599) in the same batches as the unknowns, yielding ages at 27.67 ± 0.06 Ma (*n = 1*, ETHZ) and 27.78 ± 0.06 Ma (*n = 1*, UofA), similar to the reference value (27.66 ± 0.10 Ma, 2σ; Markey et al. 2007).

2.3 Molybdenite Mo isotope geochemistry

The Mo isotope composition (relative to $NIST_{SRM-3134}$) of molybdenite in sample AJ-012 was determined using the same protocol as Greber et al. (2011) used for molybdenite in samples AJ007, -009, -010, -011 & BLST-1. Molybdenum isotope measurements were conducted at the University of Bern using a Neptune Plus MC-ICP-MS.

2.4 Zircon CA-ID-TIMS U-Pb geochronology

For U-Pb geochronology, a sample was taken in the Bietschtal, some 8 km to the west of the Alpjuhorn locality. Zircon was separated with standard techniques, and a selection of euhedral, prismatic zircon crystals were chemically abraded and analyzed for U and Pb isotope composition according to the techniques outlined in Condon et al. (2024). The EARTHTIME ^{202}Pb-^{205}Pb-^{233}U-^{235}U tracer solution was used. Isotope compositions were measured on a Triton TIMS at University of Geneva: Pb isotopes were analysed sequentially on a MasCom secondary electron multiplier, whereas U was measured using 10^{13} Ω resistance Faraday cups. Accuracy in this lab is constantly monitored by measurement of ET100 synthetic solution (Schaltegger et al. 2021).

3 Results

The molybdenite samples have low to moderate Re and radiogenic $^{187}Os^*$ contents (0.650 to 22.174 µg g^{-1} Re; 2.264 to 72.084 ng g^{-1} $^{187}Os^*$). Model ages range between 302.95 ± 0.94 [1.33] million years ago [Ma] and 331.75 ± 1.68 [1.97] Ma (Fig. 1).

Sample AJ-012 has a $\delta^{98}Mo$ value of +0.55 ± 0.05 ‰ (2SD). The $\delta^{98}Mo$ values of all other molybdenite samples (Greber et al. 2011) were recalculated v-$NIST_{SRM-3134}$ following Nägler et al. (2014) and the arithmetic mean value is reported for the *n* number of aliquots for each sample (Fig. 1).

The CA-ID-TIMS dating of four prismatic zircons from the Baltschieder granodiorite yields a weighted mean $^{206}Pb/^{238}U$ age of 313.15 ± 0.36 Ma (including all external systematic errors plus decay constant error, MSWD = 2.4).

4 Discussion & conclusions

4.1 Molybdenum source evolution during incremental growth of the Aar Massif batholith

Given that the Re-Os geochronometer in molybdenite is not disturbed by Alpine-type lower

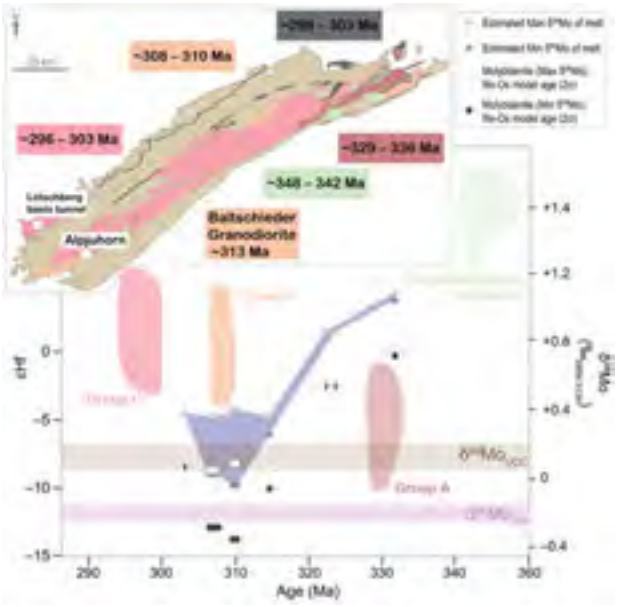


Figure 1. Temporal evolution of δ^{98}Mo in molybdenite during incremental growth of the Aar Massif Batholith (inset – Groups A to C after Schaltegger & Corfu 1992; Ruiz et al. 2022). The minimum and maximum δ^{98}Mo values for the melts at the root of each molybdenite mineralization are shown (modelling based on the fractionation trend between melt and magmatic-hydrothermal fluids after Bezard & Guo 2023). The blue field shows the range of possible $\delta^{98}Mo_{melt}$ values through the incremental growth of the Aar Massif (see text for details; $\delta^{98}Mo_{UCC}$ after Yang et al. 2017; $\delta^{98}Mo_{DM}$ after Hibbert et al. 2013; Freymuth et al. 2015).

grade amphibolite metamorphic overprint (Langthaler et al. 2004), the new Re-Os model dates in the Carboniferous are pristine and geologically meaningful ages. The Aar Massif is comprised of three groups of Carboniferous granite intrusions that define a clear temporal trend of decreasing U/Yb ratios at constant Nb/Yb ratio and increasing εHf values in zircon (Fig. 1, Gr. A, B, C). This temporal and geochemical evolution of the Aar granite batholith results from three pulses of late-orogenic extensional to transtensional magmatism between ca. 335–295 Ma (Schaltegger & Corfu 1992; Ruiz et al. 2022). Within this period of incremental growth, we identify three distinct molybdenite mineralizing events in the Alpjuhorn area (Fig. 1):

(I) ca. 331.75 Ma (n = 1) consequent to granitic intrusions of the ca. 336–333 Ma "A group". The latter is part of a high-K-Mg magmatic suite present in most of the Variscan orogen that resulted from large-scale partial melting of metasomatically enriched lithospheric mantle that was contaminated by crustal melts (von Raumer et al. 2014). The low εHf values [−9.7 ; −2.4] and elevated U/Yb ratios are compatible with this interpretation (Ruiz et al. 2022);

(II) ca. 322.89 Ma (n = 2) that is not matching any known granitic intrusion of this age in the Aar Massif;

(III) ca. 314.63 to 302.96 Ma (n = 7) overlapping with the two known pulses of granitic melts ("B & C groups") at c. 310 and 300 Ma. At their older end, the Re-Os dates coincide with the new CA-ID-TIMS U-Pb age of 313.15 Ma for the Baltschieder granodiorite, which situates this intrusion in between the recognized pulses (Schaltegger & Corfu 1992; Ruiz et al. 2022).

The increase in εHf values from [−9.7 ; −2.4] at ca. 336–333 Ma in group A to [−3.6 ; +4.7] at ca. 313–298 Ma in groups B & C confirms a geodynamic scenario of increasing relative proportion of juvenile mantle and decreasing relative proportion of crustal contamination in the granitic melts (Schaltegger & Corfu 1992; Ruiz et al. 2022). However, the ca. 313 Ma Baltschieder granodiorite features abundant inherited cores, pointing rather to a formation through anatexis of metasedimentary basement. This basement is comprised of Neoproterozoic metasedimentary rocks sourced from detrital input from Gondwanan cratonic sources, lithologies from a Neoproterozoic-Cambrian active margin at the edge of Gondwana, and a Cambrian-Ordovician extensional period (von Raumer et al. 2013). Therefore, a crustal isotopic signal may be anticipated. The molybdenite δ^{98}Mo values decrease from [+0.73; +0.77]‰ at ca. 332 Ma, to [−0.29; +0.07]‰ at ca. 314.63 to 302.96 Ma. As Mo isotopes fractionate with around –0.32‰ between fluid and melt (Bezard and Guo 2023), the $\delta^{98}Mo_{melt}$ values of the melts could have been between that of molybdenite up to [+1.05; +1.09]‰ at ca. 332 Ma, and up to [+0.03; +0.39]‰ at ca. 314.63 to 302.96 Ma, depending on the fraction of Mo that is incorporated into the fluid phase. Overall, a remarkable picture stands out with a decrease of the δ^{98}Mo values of the modelled melts mirroring the increase of the εHf values of the granitic melts between ca. 336–333 Ma and ca. 309–298 Ma (Fig. 1). In other words, as the granitic melts incorporated less crustal components through time but record an increasing influence of juvenile mantle sources ($\delta^{98}Mo_{depleted\ mantle\ -\ DM}$ = –0.20 ± 0.05 ‰; Hibbert et al. 2013; Freymuth et al. 2015), the source of Mo (and, by corollary, W) evolved from a dominant crustal source to a more mantle-like signature during the late-orogenic thinning and decompression of the lithosphere (Schaltegger 1997; Schaltegger & Corfu 1992). This trend is then not disturbed by the crustal nature of the Baltschieder magma since the metasediments in the basement have a very mixed origin.

4.2 Future work: testing the δ^{98}Mo molybdenite proxy to track W sources in major W deposits?

With our study in the Aar Massif on sub-economical Mo(±W) mineralization, we speculate that molybdenite δ^{98}Mo values may be used to track granitic bodies that could be prone to host economical W mineralization. Indeed, considering that orogenic heating of sediment protoliths pre-enriched in W produces melts that efficiently scavenge W (Romer & Kroner, 2016; Rasmussen et al. 2023), heavy δ^{98}Mo values of granite-hosted

molybdenite could be used as proxy for syn-orogenic/late-orogenic extensional to transtensional granitic melts contaminated by sedimentary protoliths with noticeable heavy δ^{98}Mo values (Willbold & Eliott 2017). A type locality where to test this hypothesis would be the major Mactung deposit in the TPS, Canada where molybdenite (97.2 ± 0.3 Ma, average over *n* = 6, Re-Os model ages; Selby et al. 2003) is coeval with the Cretaceous, porphyitic biotite granite from the main Mactung Pluton (97.6 ± 0.2 Ma, zircon CA-ID-TIMS U-Pb age; Gebru 2017).

References

Bezard R & Guo H (2023) Fluid-melt Mo isotope fractionation: implications for the δ^{98}Mo of the upper crust. Geochem Pers Lett 26:25-30.

Condon D, Schoene B et al. Recommendations for the Reporting and Interpretation of Isotope Dilution U-Pb Geochronological Information. *GSA Bulletin, 136:4233–4251*

Creaser RA, Papanastassiou DA, Wasserburg GJ (1991) Negative thermal ion mass spectrometry of Os, Re, Ir. Geochim Cosmochim Acta 55:397-401.

Elongo V, Falck H et al. (2023) Ancient roots of tungsten in western North America. Geology 50:791-795.

Engel (1988) Petrographische und Geochemische Untersuchungen der Molybdan-Lagerstatte am Alpjuhorn, Wallis, Schweiz. Doktorarbeit, Universitat Heidelberg.

Freymuth H, Vils F et al. (2015) Molybdenum mobility and isotopic fractionation during subduction at the Mariana arc. Earth Planet Sci Lett 432:176-186.

Gebru AL (2017) Petrogenesis of Granitoids in the Vicinity of the Mactung Tungsten Skarn Deposit, NE Yukon Northwest Territories: Characterization of Skarn Mineralization and Causative Plutons through Geological, Petrochemical, Mineralogical, and Geochronological Analysis. UnPub PhD Thesis University of New Brunswick, New Brunswick, Canada.

Greber ND & Hoffmann BA (2013) Minerale der Molybdänitlagerstätte am Alpjuhorn im Baltschiedertal (VS). Schweizer Strahler 1/2013.

Greber ND, Hofmann BA et al. (2011) Mo isotope composition in Mo-rich high- and low-T hydrothermal systems from the Swiss Alps. Geochim Cosmochim Acta 75:6600-6609.

Harlaux M, Romer RL et al. (2018) 40 Ma of hydrothermal W mineralization during the Variscan orogenic evolution of the French Massif Central by U-Pb dating of wolframite. Miner Deposita 53:21-51.

Hibbert K, Willbold M et al. (2013) Searching for evidence for Mo isotope fractionation in the mantle. Mineral Mag 77:1296.

Kenngott A (1866) Die Minerale der Schweiz. S. 365/366

Langthaler KJ, Raith JG, Cornell DH, et al. (2004) Molybdenum mineralization at Alpeiner Scharte, Tyrol (Austria): results of in-situ U–Pb zircon and Re–Os molybdenite dating. Mineral Petro 82:33-64.

Ledermann H (1955) Zur Kenntnis der Molybdanglanzlagerstatte im Baltschiedertal (Wallis). Beitrage zur Geologie der Schweiz.

Markey R, Stein HJ, Hannah JL et al. (2007) Standardizing Re–Os geochronology: a new molybdenite reference material (Henderson, USA) and the stoichiometry of Os salts. Chem Geol 244:74-87.

Melleton J, Gloaguen E et al. (2012) How are the emplacement of rare-element pegmatites, regional metamorphism and magmatism interrelated in the Moldanubian domain of the Variscan Bohemian Massif, Czech Republic? Can Mineral 50: 1751–1773

Melleton J, Gloaguen E, Frei D (2015) Rare-elements (Li-Be-Ta Sn-Nb) magmatism in the European Variscan Belt, a review. In Proceedings of the 13th Biennial SGA Meeting, 24–27 August 2015, Nancy, France

Nägler TF, Anbar AD, Archer C et al. (2014) Proposal for an international molybdenum isotope measurement standard and data representation. Geostandards Geoanal Res. 38:149-151.

Neiva AMR, Williams IS et al. (2012) U-Pb and ^{40}Ar/^{39}Ar data constraining the age of the Variscan Gouvaiea area, Portugal. Lithos 153:72-83.

Nowell GM, Pearson DG et al. (2008) Precise and accurate ^{186}Os/^{188}Os and ^{187}Os/^{188}Os measurements by Multi-collector Plasma Ionisation Mass Spectrometry, part II: Laser ablation and its application to single-grain Pt–Os and Re–Os geochronology. Chem Geol 248:394–426.

Rasmussen KL, Falck H et al (2023) The source of tungsten-associated magmas in the northern Canadian Cordillera and implications for the basement. Geology 51:657-662.

Romer RL, Kroner U (2015) Sediment and weathering control on the distribution of Paleozoic magmatic tin-tungsten mineralization. Mineral Deposita 50:327–338

Romer RL, Kroner U (2016) Phanerozoic tin and tungsten mineralization – tectonic controls on the distribution of enriched protoliths and heat sources for crustal melting. Gondwana Res 31:60–95

Ruiz M, Schaltegger U et al. (2022) Reassessing the intrusive tempo and magma genesis of the late Variscan Aar Batholith: U-Pb geochronology, trace element, and initial Hf isotope composition of zircon. Swiss J Geosci 115:20.

Schaltegger U (1993) The evolution of the polymetamorphic basement of the Central Alps unravelled by precise U–Pb zircon dating. Cont. Mineral Petro. 113:466–478.

Schaltegger U (1997) Magma pulses in the Central Variscan Belt: Episodic melt generation and emplacement during lithospheric thinning. Terra Nova 9:242-245.

Schaltegger U & Corfu F (1992) The age and source of late Hercynian magmatism in the central Alps: evidence from precise U-Pb ages and initial Hf isotope ratios. Cont Miner Pet 111:329-344.

Schaltegger U, Ovtcharova M et al. (2021) Long-term repeatability and interlaboratory reproducibility of high-precision ID-TIMS U-Pb geochronology. J. Anal. Atom. Spectrom., 36, 1466-1477

Selby D, Creaser RA (2001) Re-Os geochronology and systematics in molybdenite from the Endako porphyry molybdenum deposit, British Columbia, Canada. Econ Geol 96:197-204.

Selby D, Creaser RA, Heaman LM, Hart CJ (2003) Re-Os and U-Pb geochronology of the Clear Creek, Dublin Gulch, and Mactung deposits, Tombstone Gold Belt, Yukon, Canada: absolute timing relationships between plutonism and mineralization. Can. J. Earth Sci. 40:1839–1852.

Smoliar MI, Walker RJ, Morgan JW (1996) Re-Os ages of group IIA, IIIA, IVA, and IVB iron meteorites. Science 271:1099-1102.

Tornos F, Delgado A, Casquet C, Galindo C (2000) 300 million years of episodic hydrothermal activity: stable isotope evidence from hydrothermal rocks of the eastern Iberian central system. Mineral Deposita 35:551–569

Völkening J, Walczyk T, Heumann KG (1991) Osmium isotope ratio determinations by negative thermal ionization mass spectrometry. Int J Mass Spectrom Ion Process 105:147–159

Von Raumer JF, Bussy, F et al. (2013) Pre-Mesozoic Alpine basements – Their place in the Euopean Paleozoic framework. Geol Soc Amer Bull 125:89-108.

Von Raumer JF, Finger F et al. (2014) Durbachites-Vaugnerites – a geodynamic marker in the central Europea Variscan orogen. Terra Nova 26:85-95.

Willbold M & Eliott T (2017) Molybdenum isotope variations in magmatic rocks. Chem Geol 449:253-268.

Yang J, Barling J et al. (2017) The molybdenum isotopic compositions of I-, S-, and A-type granitic suites. Geochim Cosmochim Acta 205:168-186.

Zircon and cassiterite U-Pb dating of the Taucane Project: New horizons for tin exploration in Peru

Pablo Valverde[1], Lisard Torró[1], Daniel Alayza[2], Diego Benites[1], Sava Markovic[3], Lorenzo Tavazzani[3], Dawid Szymanowski[3], Cyril Chelle-Michou[3], Matthieu Harlaux[4], Miroslav Kalinaj[2]
[1]Geological Engineering Program, Pontifical Catholic University of Peru (PUCP), Peru
[2]Minsur S.A., Peru
[3]Department of Earth and Planetary Sciences, ETH Zurich, Switzerland
[4]BRGM – French Geological Survey, Orléans, France

Abstract. The discovery of the Taucane Sn-polymetallic deposit within the Central Andean Backthrust Belt of southern Peru represents an exploration breakthrough as it indicates potentially more extensive tin prospective zones in the region than previously thought. The Sn-polymetallic mineralization in Taucane occurs as 'mantos' and veins hosted by Mesozoic sedimentary rocks. It is mostly comprised of sulfides, with lesser amounts of sulfosalts and cassiterite. Our *in situ* U-Pb isotope analysis of cassiterite yielded an age of 23.0 ± 2.4 Ma, which overlaps with a zircon age of 24.16 ± 0.37 Ma for quartz monzodiorite in the study area. These dates clearly contextualize the mineralization at Taucane within the Oligocene-Miocene metallogenic event of the Central Andean tin belt.

1 Introduction

The only currently active Sn mine in Peru is the world-class San Rafael deposit, the largest Sn producer in the Western hemisphere accounting for ~12 % of the yearly mined Sn globally (Minsur S.A. 2024). Exploration in the Peruvian segment of the Central Andean tin belt (Fig. 1A) has led to the discovery of dozens of Sn(-W-polymetallic) deposits and occurrences such as Nazareth, Santo Domingo, Jesica, San Jose, Ocuara, Condoriquiña, Quenamari, Sarita, and Palca 11. One of the most recent discoveries, Taucane, has sparked special interest due to a number of distinctive characteristics. Unlike the other known Sn deposits and occurrences in the region, which are found in the Macusani Structural Zone (Perez et al. 2016), also known as the pre-Cordillera de Carabaya (Clark et al. 1983, 1990; Kontak et al. 1990), and hosted by Paleozoic rocks, Taucane is hosted in Mesozoic sequences of the adjacent Central Andean Backthrust Belt morphostructural domain (Fig. 1B). This domain had been previously disregarded as prospective for Sn deposits. Highlighted drill core intersections at Taucane include 7.5 m @ 2.59 % Sn (Lorena system) and 4.5 m @ 2.33 % Sn, 13.55 g/t Ag, 1.36 % Pb, 0.51 % Zn, and 0.11 % Cu (Kelly system). The discovery of Taucane ushers in a significant extension of the exploration boundaries to Mesozoic rocks located south of the Macusani Structural Zone. In this work, we present a general description and first U-Pb cassiterite and zircon dating of Taucane.

2 Geological setting

The Taucane project is located in the Puno Department in southeastern Peru, ~35 km to the southeast of the San Rafael mine (Fig. 1B). The project covers two distinct lithostratigraphic domains separated by the Taucane fault, which is part of the Pre-cordillera de Carabaya Fault System. Paleozoic and Triassic (meta)sedimentary and volcanic basement units crop out north of the fault system, and Mesozoic basement rocks south of it.

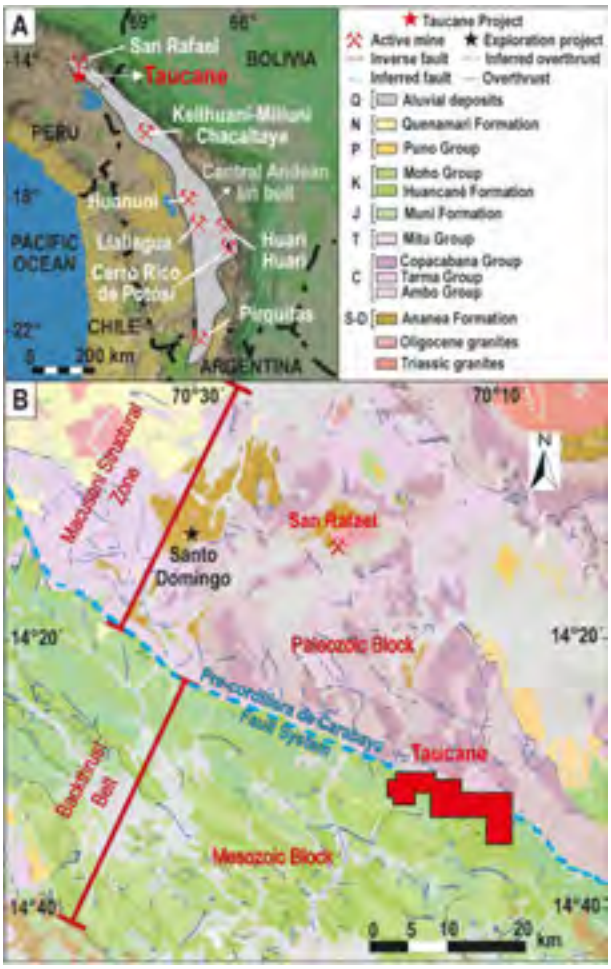


Figure 1. A) Location of the Taucane Sn-polymetallic project and major active mines within the Central Andean tin belt. **B)** Location of Taucane concessions in regional geologic map with morphostructural domains in the Eastern Cordillera of the Andes in southeastern Peru.

The rocks exposed in the main prospects in Taucane (i.e., Lorena and Kelly) are mostly of Jurassic and Cretaceous age. The Liassic-Lower Dogger Quilcapunco Formation, which is composed of whitish sandstone and thin levels of red pelite, discordantly overlies the Triassic Mitu Group. Overlying the Quilcapunco Formation are arkosic sandstone, calcareous sandstone, and siltstone of the Muni Formation (Upper Dogger), followed by a sequence of whitish sandstone intercalated with microconglomerate of the Neocomian Huancané Formation (De la Cruz 1995, Sempere et al. 2004). The Mesozoic sequence is capped by Lower Cenomanian sandstone with limestone intercalations of the Moho Group (De la Cruz et al. 1995). The sequence is cut by a series of intrusive rocks, which mostly crop out along the Pre-cordillera de Carabaya Fault System just north of the main mineralized areas (Alayza 2016).

3 Intrusive rocks

Intrusive rocks at Taucane include the main stock with an ~7 x 2 km^2 area and a series of dikes, all belonging to the Yurac Apacheta intrusive suite (De la Cruz 1995). The intrusive facies include a suite of peraluminous monzogranite, quartz monzodiorite, and monzodiorite, as well as restricted exposures of lamprophyre (Vallance 2015). The volumetrically dominant intrusive rocks composing the stock are the monzogranite and the quartz monzodiorite. The monzogranite shows a porphyritic texture with quartz, K-feldspar, plagioclase, and biotite phenocrysts embedded in a coarse- to medium-grained groundmass of the same composition. This facies is easily distinguished by the occurrence of K-feldspar megacrysts (up to 1.32 cm). The quartz-monzodiorite is characterized by its medium grained, phaneritic, porphyritic texture and a mineralogy dominated by plagioclase, K-feldspar, quartz, biotite, and tourmaline. The monzodiorite forms dikes that cut the quartz-monzodioritic stock and has a distinctive equigranular texture defined by plagioclase, K-feldspar, quartz, hornblende, and biotite. Lamprophyres form 0.3–1 m-thick dikes that cut the granitic rocks and are classified as minette.

4 Mineralization

The mineralization at Taucane is mostly associated with stratiform replacement ore-bodies (mantos) along calcareous horizons of the Muni Formation and Moho Group, and to a lesser extent, to vein systems that cut across the Mesozoic sedimentary sequence (Fig. 2; Alayza 2016). The mantos have thicknesses that vary between 1 and 24 m and have been observed in both the Kelly and Lorena areas (Fig. 2). The main vein systems, Lorena and Kelly, have azimuths between 110° and 170°, dips between 60° and 80°, and exhibit along-strike extensions exceeding 1 km. Their thicknesses range from 0.1 to 1.5 m. Some of the veins cut the monzogranite dikes (Alayza 2016).

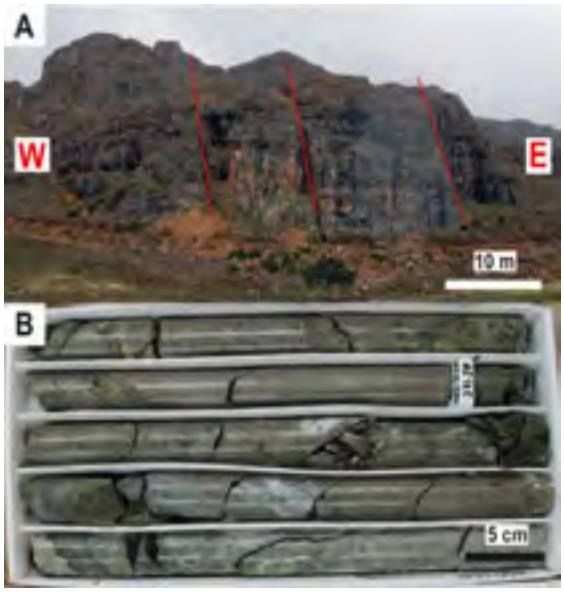


Figure 2. A) Narrow, subvertical structures (red lines) of the Kelly Vein system hosted by sandstone of the Huancané Formation. **B)** General aspect of the manto-type sulfide mineralization, dominated by pyrrhotite (60%), followed by chalcopyrite (10%) and pyrite (7%) in rocks with pervasive alteration to quartz and chlorite (Kelly area).

In order of abundance, the identified minerals in both mantos and veins are Fe sulfides (pyrrhotite and pyrite), sphalerite, cassiterite, chalcopyrite, stannite, galena, marcasite, Ag-tetrahedrite-(Fe), franckeite, boulangerite, arsenopyrite, acanthite, and native Bi (Fig. 3). While pyrrhotite is more abundant in mantos from the Kelly area, pyrite is dominant in mantos from the Lorena area and in veins from both areas. In the subsurface, an oxidation zone includes anglesite, goethite, and hematite.

Three main hypogene paragenetic stages have been identified (Fig. 4). Stage 0 is only observed in mantos and is characterized by a skarn-like alteration assemblage of green garnet (grossular-andradite), pyroxene (hedenbergite), and lesser amounts of quartz. Stage I is composed of a low-sulfidation assemblage comprising needle tin cassiterite aggregates and pyrrhotite, arsenopyrite, chalcopyrite (1st and 2nd generations), Fe-rich sphalerite (1st generation; 7.5-12 wt.% Fe), and stannite. In mantos from the Kelly area, pyrrhotite forms irregular grains partially replaced by 1st-generation chalcopyrite and sphalerite (Fig. 3B-C). First-generation sphalerite hosts fine chalcopyrite disseminations (2nd generation) and has been partly replaced by stannite. Stage I assemblages are overprinted by Stage II minerals defining an intermediate-sulfidation assemblage. During Stage IIa, subhedral to coarse anhedral pyrite ± marcasite formed mostly as replacements of pyrrhotite. While this replacement was partial in mantos from the Kelly area, it was more pervasive in mantos from the Lorena area and in veins, in which only rare and minute relicts of pyrrhotite remain within pyrite.

Stage IIb is primarily composed of Fe-poor sphalerite (2nd generation; < 1 wt.% Fe) and galena (Fig. 3D), with smaller amounts of Ag-tetrahedrite-(Fe), franckeite, boulangerite, acanthite, and native bismuth. The Fe-poor sphalerite, which presents clean surfaces and yellow-orange internal reflections, is partially replaced by galena and, occasionally, coated with acanthite. Laminar aggregates of franckeite and boulangerite occur mainly filling fractures in and interstices between pyrite, Fe-poor sphalerite, and galena. Native bismuth appears as minute inclusions within galena and boulangerite.

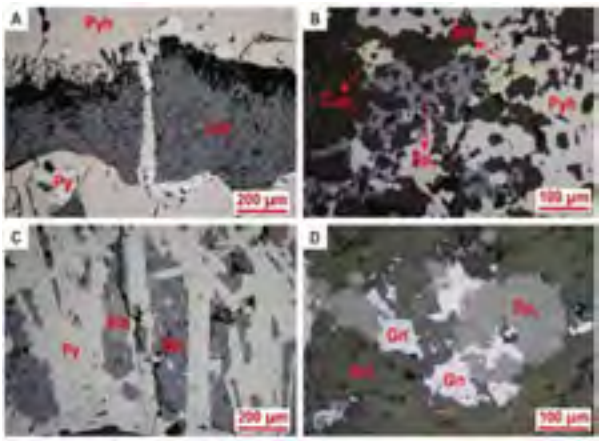


Figure 3. Textures of metallic mineralization at Taucane observed by reflected-light microscopy. A) Fine-grained cassiterite aggregates (*var.* needle-tin) cut by a thin veinlet of pyrrhotite, which in turn, has been partially replaced by pyrite (manto, Kelly area). B) Pyrrhotite replaced by Fe-rich sphalerite (1st), chalcopyrite (1st), and stannite along borders (manto, Kelly area). C) Sphalerite (1st) replaced by stannite and these in turn, by pyrite (vein, Kelly area). D) Anhedral aggregates of Fe-poor sphalerite (2nd) replaced by galena in a baryte matrix (vein, Lorena area). Brt—Baryte, Ccp—Chalcopyrite, Cst—Cassiterite, Gn—Galena, Py—Pyrite, Pyh—Pyrrhotite, Sp—Sphalerite, Stn—Stannite.

5 Geochronology

5.1 *In situ* U-Pb zircon geochronology

In situ U-Pb isotope analyses were carried out on zircon grains from the main quartz-monzodiorite intrusion (sample TC-23-02). Zircon grains exhibit oscillatory growth zoning observed by cathodoluminescence imaging on a scanning electron microscope. Eighty-six U-Pb isotope analyses from core and rim pairs of 45 grains were performed by laser ablation–inductively coupled plasma mass spectrometry (LA-ICP-MS) at ETH Zurich. All the analyses cluster tightly on the concordia curve, yielding a weighted mean $^{206}Pb/^{238}U$ date at 24.16 ± 0.37 Ma (Fig. 5A).

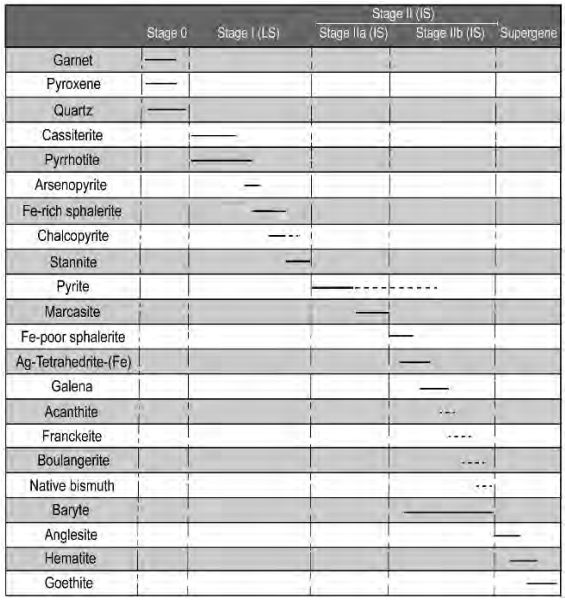


Figure 4. Generalized paragenetic sequence for mantos and veins in the Kelly and Lorena areas. Bars indicate greater abundances and dashed lines, lesser abundances.

5.2 *In situ* U-Pb cassiterite geochronology

A total of 143 *in situ* U-Pb analyses were performed on cassiterite grains from a manto sample from the Kelly area (2024-TAU-21) by LA-ICP-MS at ETH Zurich. From the measured $^{207}Pb/^{206}Pb$ and $^{238}U/^{206}Pb$ ratios, we calculated a lower intercept age of 23.0 ± 2.4 Ma on the U-Pb Tera-Wasserburg concordia diagram (Fig. 5B).

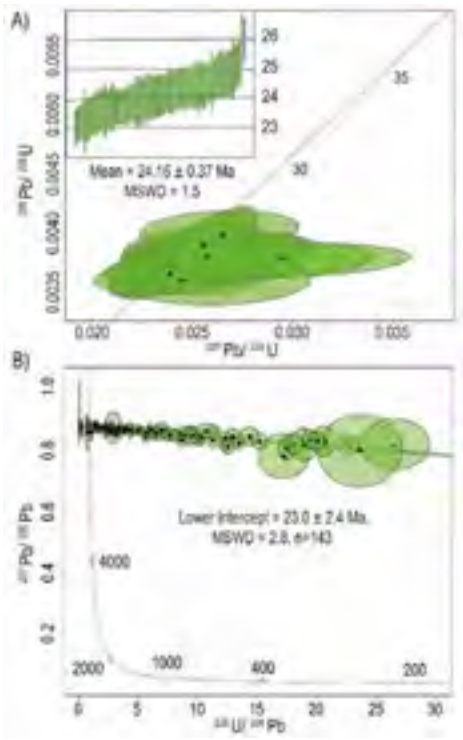


Figure. 5 Results of in situ U-Pb isotope analyses of (**A**) zircon from the quartz-monzodiorite intrusion and (**B**) cassiterite from manto-type mineralization in the Kelly area from Taucane.

Due to the high closure temperature for the U-Pb isotope system in cassiterite (~850 °C; Zhang et al. 2011), this age likely corresponds to the formation age of the Sn mineralization.

6 Discussion

Tin deposits along the Central Andes tin belt are genetically associated with peraluminous magmatism, which includes granitic plutons and stocks emplaced during two main events in the Triassic and latest Oligocene-Early Miocene (Clark et al. 1983, 1990; Farrar et al. 1990; Gemmrich et al. 2021, Harlaux et al. 2021). The U-Pb cassiterite age for Taucane clearly contextualizes its emplacement during the latest Oligocene-Early Miocene metallogenic event. The obtained age overlaps with that of cassiterite from other deposits in the Bolivian (Viloco: 24.4 ± 0.4 Ma; Huanuni: 24.0 ± 2.4 Ma; Llallagua: 24.0 ± 5.1 Ma; Gemmrich et al. 2021) and Peruvian segments of the Central Andean tin belt. In Peru, Harlaux et al. (2023) obtained U-Pb cassiterite dates for the nearby San Rafael deposit within the range of 24.10 ± 0.37 to 23.47 ± 0.53 Ma.

More precise is the obtained U-Pb zircon date on a quartz-monzodiorite intrusion in Taucane, of 24.16 ± 0.37 Ma. This date overlaps with the dates obtained in intrusive rocks in nearby deposits. In San Rafael, U-Pb zircon dates yield average values of 24.02 ± 0.25 Ma (Harlaux et al. 2021). In Santo Domingo, magmatic biotite K-Ar dating yielded 24.3 ± 0.6 Ma (Clark et al. 1983). This indicates synchronicity in magmatism and hydrothermal activity not only within the Macusani Structural Zone but also along its boundary with the Central Andean Backthrust Belt.

7 Final remarks

The discovery of Taucane marks a paradigm shift in Sn exploration in southern Peru and addresses the historical uncertainty raised by Petersen (1972) regarding the northward extension of the Central Andean tin belt. On the one hand, its volumetrically dominant manto-type mineralization contrasts with the region's typical vein and lode-type deposits (e.g., Harlaux et al. 2023), resembling Bolivian examples in Cretaceous sedimentary rocks such as the Sn ± Ag Catavi deposit near Potosí (Ahlfeld and Schneider-Scherbina 1964). On the one hand, while the San Rafael deposit previously demonstrated the economic potential of the region, Taucane's location outside the traditionally prospective Paleozoic block marks a critical departure from established exploration models and expands the known boundaries of the Central Andean tin belt southwestward.

Robust U-Pb geochronology (~24 Ma) confirms Taucane's formation during the latest Oligocene-Early Miocene metallogenic event, demonstrating temporal synchronicity with major tin deposits across the Central Andean tin belt.

Acknowledgements

This research was funded by the project PI1117 granted by PUCP. We appreciate the constructive review by Prof. Bernd Lehmann.

References

Alayza D (2016) Generación de un modelo exploratorio local mediante la caracterización de la ocurrencia polimetálica del prospecto Taucane en la pre cordillera de Carabaya-Puno. Universidad Nacional de Ingeniería, Lima, 324 p.

Ahlfeld F, Schneider-Scherbina A (1964) Los yacimientos minerales y de hidrocarburos de Bolivia. Bolivia Departamento Nac Geol 5:1–388.

Clark A, Palma V, Archibald D, Farrar E, Arenas F, Robertson R (1983) Ocurrence and age of tin mineralization in the Cordillera Oriental, southern Peru. Econ Geol 78:514–520.

Clark A, Farrar E, Kontak D, Langridge R, Arenas M, France L, Mcbride S, Woodman P, Wasteneys H, Sandeman H (1990) Geologic and Geochronological Constraints on the Metallogenic Evolution. Econ Geol Bull Soc 85:1520–1583.

De La Cruz N (1995) Estudio geológico de los cuadrángulos de Velille, Yauri y Azángaro. INGEMMET, v. 58 (A), 150 p.

Gemmrich L, Torró L, Melgarejo J, Laurent O, Vallance J, Chelle-Michou C, Sempere T (2021) Trace element composition and U-Pb ages of cassiterite from the Bolivian tin belt. Miner Depos 56:1491–1520.

Harlaux M, Kouzmanov K, Gialli S, Laurent O, Rielli A, Dini A, Chauvet A, Menzies A, Kalinaj M, Fontboté L (2020) Tourmaline as a tracer of late-magmatic to hydrothermal fluid evolution: the world-class San Rafael tin (-copper) deposit. Econ Geol 115:1665–1697.

Harlaux M, Kouzmanov K, Gialli S, Clark A, Laurent O, Corthay G, Flores E, Dini A, Chauvet A, Ulianov A, Chiaradia M, Menzies A, Durand G, Kalinaj M, Fontboté L (2021) The upper Oligocene San Rafael intrusive complex (Eastern Cordillera, southeast Peru), host of the largest-known high-grade tin deposit. Lithos 400:106409.

Harlaux M, Kontak D, Clark A, Kouzmanov K, Holm-Denoma C, Gialli S, Fontboté L (2023) Depositing >1.5 Mt of tin within <1 my of initial granitic intrusion in the San Rafael tin (-copper) Deposit, Southeastern Peru. Econ Geol 118(6):1371-1396.

Kontak D, Farrar E, Clark A, Archibald D (1990) Eocene tectono-thermal rejuvenation of an upper Paleozoic-lower Mesozoic terrane in the Cordillera de Carabaya, Puno, southeastern Peru, revealed by K–Ar and 40Ar/39Ar dating. J South Am Earth Sci 3:231–246.

Minsur S.A. (2024) Annual report: December 31, 2023, 86 p.

Perez N, Horton B, Carlotto V (2016) Structural inheritance and selective reactivation in the central Andes: Cenozoic deformation guided by pre-Andean structures in southern Peru. Tectonophysics 671:264–280.

Petersen U (1972) Geochemical and tectonic implications of South American metallogenie provinces. New York Acad Sci Ann 196:3-38.

Sempere T, Acosta H, Carlotto V (2004) Estratigrafía del Mesozoico y Paleógeno al norte del Lago Titicaca. Publicación Especial Sociedad Geológica del Perú 5: 81-103.

Vallance J (2015) Informe de estudio petrográfico y mineragráfico de 19 láminas delgadas y 12 secciones pulidas del proyecto Taucane. Reporte Interno para Minsur S.A., 7p.

Zhang D, Peng J, Hu R, Yuan S, Zheng D (2011) The closure of U-Pb system in cassiterite and its reliability for dating. Geol Rev 57:549–554 (in Chinese with English abstract).

Quantitative Prediction Methods and Applications of Digital Ore Deposit Models

Keyan Xiao[1]
[1]*SinoProbe Laboratory, Institute of Mineral Resources, Chinese Academy of Geological Sciences, Beijing 100037, China*

Abstract. As surface mineral deposits are depleted, focus has shifted to deep mineral exploration. The development of three-dimensional digital ore deposit models, driven by advances in computer technology, has transformed traditional geological models into computer-recognizable digital formats. This enables the quantitative expression of geological concepts, improving the accuracy of deep mineral exploration. This paper discusses the transition from traditional to digital ore deposit models, highlighting their ability to incorporate a wide range of geological information, such as mineralogy, ore types, structural geology, geochemistry, and geophysics. Building on these models, a three-dimensional geological model is created, integrating regional metallogenic patterns and conducting quantitative extraction. A comprehensive prospecting model is developed, utilizing deep learning for deep mineral exploration. This approach forms a unified system for quantitative prospecting of concealed mineral deposits, integrating geological models, three-dimensional geological modeling, and quantitative exploration. The method is demonstrated using the Zaozigou gold deposit in Gansu Province, providing valuable insights for future exploration efforts.

1 Instruction

As surface mineral deposits become depleted, there is a growing emphasis on the detection and exploitation of deep-seated concealed mineral resources. Prospecting endeavors have shifted focus from surface and shallow mineral deposits, which are easily identifiable, towards uncovering concealed and more challenging-to-detect deposits (Salama et al. 2016). In comparison to surface deposits, concealed mineral resources are more difficult to identify due to their greater depth and the associated complexities in detection. Given this scenario, two-dimensional (2D) prospecting methods are evidently inadequate to meet the requirements of national or corporate mineral exploration efforts, thereby making the imperative development of three-dimensional (3D) mineral resource prediction methods urgent (Nielsen et al. 2015, Payne et al. 2015).

Due to the inherent three-dimensional nature of geological information and phenomena, accurately grasping the overall geological situation using only two-dimensional representations is challenging. Transitioning from 2D to 3D is not just about adding depth, but is essential for visualizing and understanding mining operations and geological contexts. While the shift from 2D to 3D adds only one dimension, the complexity increases qualitatively. Three-dimensional ore prospecting requires an understanding of metallogenic regularities, constructing accurate digital ore deposit models, selecting appropriate prospecting indicators, and using predictive models.

Ore deposit models mark a breakthrough in mineral exploration by integrating empirical data and metallogenic regularities, serving as a theoretical guide for exploration (Cox and Singer 1986). Scholars such as Chen and Zhu (1993) developed geological models for key ore deposits in China, which significantly advanced metallogenic theory. With the rapid advancement of exploration and computer technologies, mineral data has grown exponentially. Traditional qualitative descriptions struggle to convey detailed ore deposit information, especially with the rise of Geographic Information Systems (GIS), which now allows for the vectorization of geological maps. Digital ore deposit models have emerged to meet these needs.

These models digitize descriptive ore deposit models, transforming them into data, knowledge rules, and symbolic representations recognizable by computers (Wang et al. 2003). This allows for the visual representation of ore body distributions and trends, providing the foundation for three-dimensional spatial quantitative analysis (Chen et al. 2012b). Digital ore deposit models are essential for predicting concealed mineral deposits and conducting quantitative predictions (Chen et al. 2012a).

Spatial analysis based on digital ore deposit models enables the quantitative extraction of mineralization elements, enhancing three-dimensional mineralization predictions. This approach integrates multi-disciplinary geological information and uses methods like Comprehensive Information Assessment, which establishes relationships between ore deposits and various geological factors. This results in the identification of mineralization-favorable zones. The use of multi-element statistical methods and GIS technologies supports the extraction of mineralization data, leading to the development of quantitative resource prediction models.

Machine learning and deep learning can also be integrated with ore deposit models to improve intelligent ore prospecting predictions. For instance, Deng (2022) proposed a method using Convolutional Neural Networks (CNNs) for three-dimensional ore prospecting, enhancing deep ore body prediction while reducing risks. Li et al. (2023) demonstrated that CNNs outperform other models like logit, SVM, and RF in predicting mineralized areas. Qin (2021) found RF models more effective than evidence-weighted models for three-dimensional mineralization prediction.

These studies indicate that mineral resource prediction is moving toward three-dimensional forecasting, integrating quantification, intelligence, and machine learning. While machine learning serves as a tool for handling diverse data, the foundation remains in ore deposit models. These models, built on interdisciplinary knowledge, offer a comprehensive understanding of mineral deposits' formation, distribution, and potential. Integrating ore deposit models with machine learning improves exploration accuracy and provides a reliable basis for resource development.

2 Ore deposit model

2.1 Traditional Ore Deposit Models

The traditional ore deposit model is a descriptive geological conceptual model of mineral deposits expressed in natural language. It is derived from the analysis and comparison of similar deposits and is often depicted through cross-sectional slices. This model summarizes geological characteristics, including metallogenic environment, ore-controlling factors, physical-chemical indicators, and mineralogical features (Wang 2003). In modern assessments, it serves as a reference for evaluation, aiding in understanding mineralization processes and improving exploration efficiency.

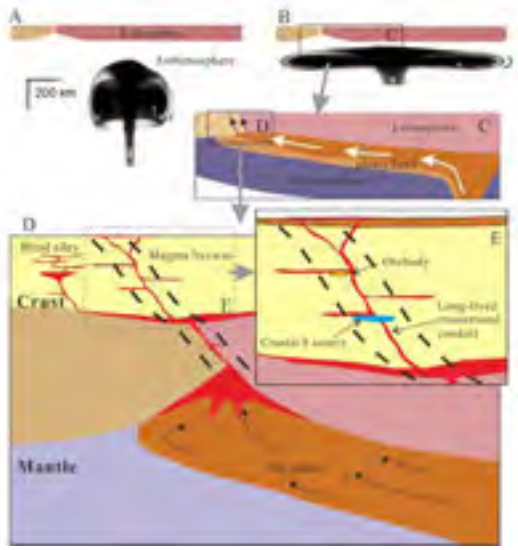


Figure 1. (A) Starting plume ascending beneath an Archaean craton, within a few hundred kilometers of an original craton boundary. Plume head is mixture of high temperature tail and entrained ambient mantle. (B) Impingement and flattening of plume head beneath lithosphere. (C) Channeling of plume head and tail to thinnest lithosphere at craton margin, generation of continental rifting cantered on original suture, and onset of high-Mg, low-Ti melts production. Maximum melt production occurs beneath the craton margin, controlled by flow of plume along sloping base of cratonic lithosphere, focusing of predominant flux of komatiite plume-tail melt at craton margin. (D) Development of favorable and unfavorable environments for mineralization above the melting zone, showing the combination of long-lived mantle-tapping structure and high magma production giving rise to high flux “magma freeways” with potential for assimilation of crustal S, transport and deposition of magmatic sulfide ores (Barnes et al., 2016).

Research on ore deposit models dates back to the early 20th century, with key contributions from W.H. Emmons on geothermal zoning in granite ore deposits and C.C. Smirnov on the oxidation zone of sulfide deposits. Over time, the study of primary and regional zoning led to the development of models like the porphyry copper ore deposit model. The U.S. Geological Survey's D.P. Cox and D.A. Singer also contributed to classifying ore deposit models globally (Figure 1).

In China, research on metallogenic models began in 1966 with the descriptive model of black tungsten ore. By 1979, new theories integrating geophysical, geochemical, and mathematical geological methods were proposed. Digital technology and GIS now offer new opportunities for ore deposit model evolution, transforming them into more intuitive, comprehensive, and efficient tools for mineral exploration and resource evaluation.

2.2 Digital Ore Deposit Models

The digital ore deposit model, introduced by the U.S. Geological Survey (Cox and Singer 1986), and similarly proposed by China's Professor Zhao, converts traditional descriptive models into digital, computer-recognizable forms, enabling automated reasoning and decision-making for ore deposit types.

A digital ore deposit is a virtual, geographically referenced, three-dimensional model of a mineral deposit. Built from geological data such as maps, cross-sections, and drillhole data, it incorporates mineralogy, ore deposit types, structural information, and geophysics. This model visually represents geological bodies and their spatial relationships within the study area.

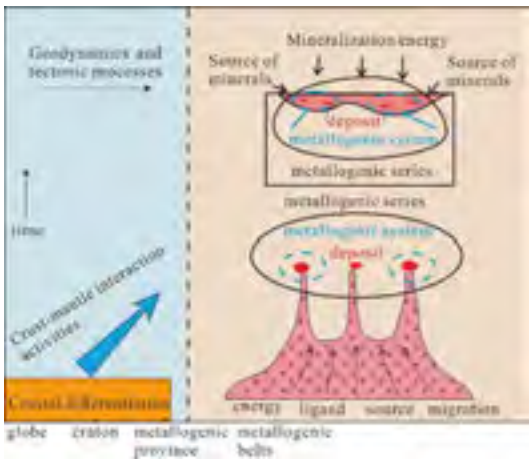


Figure 2. Relationship between metallogenic system and metallogenic series (Xiao et al. 2023).

The digital ore deposit model is grounded in regional metallogenic regularities and guided by ore-forming system theory. It combines with the "trinity" theory to establish a prospecting model,

which aids in identifying prospective target areas through three-dimensional geological modeling.

In conclusion, the scope of digital ore deposit models includes three-dimensional geological, geochemical, and geophysical models, as well as geological prospecting models for metallogenic systems, which guide the construction of these models.

Metallogenic patterns encapsulate comprehensive descriptions and explanations of ore genesis, ore-forming mechanisms, and characteristic features of mineral deposits, guided by metallogenic series and metallogenic systems. These descriptions summarize the universal characteristics and laws governing mineral deposits, aiding in analyzing the ore-forming/control factors (as Figure 2).

3 Ore Prediction Applied to the Zaozigou Gold Deposit, Gansu Province

3.1 Geological Setting

The Zaozigou gold deposit is situated in the Xiahe–Hezuo area within the Western Qinling Orogenic Belt, which lies in the transitional zone between the Yangtze Block and the North China Block. As an extension of the Western segment of the Qinling Orogenic Belt, the Western Qinling Orogenic Belt has undergone multiple phases of geological movements. It possesses exceptionally favorable mineralization conditions with large-scale magmatic rocks. Granite syenite and quartz syenite bodies are found as either basement or stocks, with intrusive rocks concentrated in the age range of 230 to 250 million years ago (Ma).

3.2 3D geological model

Three-dimensional geological modeling encompasses solid models such as borehole models, stratigraphic models, ore body models, rock mass models, and fault models. It involves visualizing the three-dimensional spatial morphology of geological bodies by integrating various data sources like borehole data, cross-sectional data, geological maps, and employing visualization software. Given the relatively small study area, an explicit modeling approach with stronger human-computer interaction is adopted to construct a comprehensive three-dimensional model by connecting geological bodies using drilling and cross-sectional data (Figure 3).

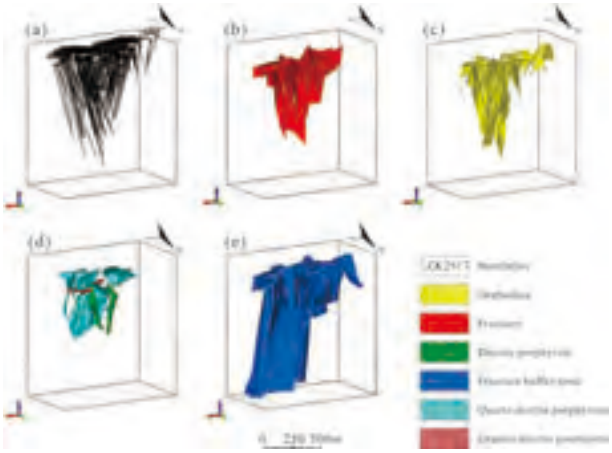


Figure 3. The 3D geological model of the Zaozigou gold deposit. (**a**) 3D borehole model. (**b**) 3D fracture model. (**c**) 3D orebody model. (**d**) 3D Intrusive model. (**e**) 3D fracture surface model.

3.3 3D Quantitative Prediction

Based on the mineralization laws and the distribution of ore bodies in the three-dimensional model, it is considered that faults and rock masses exhibit significant correlation with the occurrence of gold deposits. Therefore, these two elements are selected as predictive factors. Additionally, previous studies have demonstrated the indicative role of As-Sb-Au element combinations in mineral exploration within this region. Furthermore, Li also suggested that the primary halos of gold deposits display vertical zonation characteristics, generally categorized into three types based on element combinations: the front halo, near-ore halo, and tail halo. Among these, the characteristics of the front halo indicate a gradual decrease in the ratio of indicative elements' contents or the ratio between the indicative elements' contents of the front halo (As-Sb-Hg) to the tail halo (W-Bi-Co-Mo) from the front halo of the ore body → middle part of the ore body → tail halo. Consequently, this combination is considered as one of the predictive factors used in constructing the quantitative prediction model.

The visual representation of three-dimensional ore body prediction in Figure 4 distinctly illustrates a high likelihood of deep-seated mineralization, thereby indicating the extension of ore bodies into deeper strata and delineating two potential target areas for exploration.

Target area I is located at an altitude of 1700-2000m in the southeast direction. This area exhibits excellent continuity with the Au1 ore body above, indicating a likely extension of Au1 downwards. It is closely associated with extending faults, showing strong anomalous Au element occurrences; however, there are limited indications of additional rock body features, requiring further verification.

Target area II is situated at an altitude of 2200-2400m in the northwest direction. This zone displays high structural complexity with intricate fault systems, presenting a favorable setting for mineralization. Compared to target area I, the mineralized bodies discovered in the northwest

direction are shallower in depth, thus categorizing it as target area II.

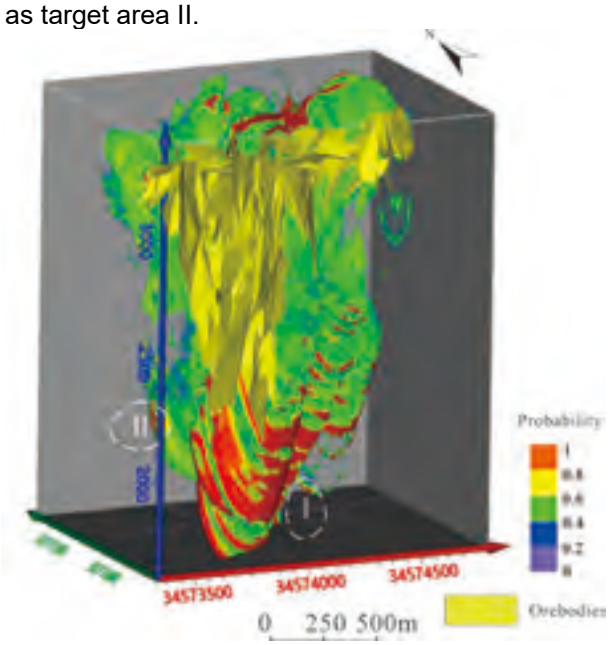


Figure 4. Deep mineral prediction map based on CNN.

4 Results

This paper primarily delineates the disparities between conventional ore deposit models and digital ore deposit models, while also exploring the associated methodological processes for constructing digital ore deposit models and conducting three-dimensional hidden ore deposit mineralization predictions. The key insights include:

(1) Digital ore deposit models have evolved from conventional ore deposit models and can more intuitively display the characteristics of ore deposits while inheriting their traits. They not only integrate exploration models guided by metallogenic system theories and metallogenic series theories more clearly, proposing exploration indicators, but also visually display various 3D models including 3D geological models, 3D geochemical models, and 3D geophysical models within the study area, thus better depicting the underground distribution of ore deposits. This aids exploration personnel in better understanding the distribution of deep-seated mineral resources.

(2) Achieving three-dimensional quantitative predictions of mineral resources requires an understanding of ore-forming regularities and the use of digital ore deposit models to accurately express various ore-controlling elements. This is achieved by constructing comprehensive information mineral prediction models and integrating multi-source data. Finally, deep learning technology is used to extract and integrate multi-source data related to mineralization, thus achieving a more comprehensive and accurate quantitative prediction of mineral resources.

(3) The demonstration application of the Zaozigou Gold Deposit in Gansu Province combines the digital ore deposit model with three-dimensional quantitative prediction using a convolutional neural network model. This has identified two favorable prospecting areas, providing practical guidance and methodological exploration for three-dimensional quantitative prediction of mineral resources based on digital ore deposit models. This approach not only enhances prediction accuracy and efficiency but also provides new ideas and technical support for mineral exploration efforts.

Acknowledgements

Thanks to all team members for their support of the work.

References

Barnes SJ, Cruden AR, Arndt N, Saumur BM (2016) The mineral system approach applied to magmatic Ni-Cu-PGE sulphide deposits. Ore Geol Rev 76:296-316.

Chen G, Zhang S, Li Y (2012a) 3D Geological modeling and assessment of site suitability based on orthogonal polynomials and Markov matrix. Information-an International Interdisciplinary Journal 15 (11B), 4755-4761.

Chen J, Shi R, Chen Z, Wang L, Sun Y (2012b) 3D Positional and quantitative prediction of the Xiaoqinling Gold Ore Belt in Tongguan, Shaanxi, China. Acta Geologica Sinica-English Edition 86 (3):653-660.

Chen Y, Zhu Y (1993) Metallogenic model of ore deposits in China: Geology Press, Beijing; 1993.

Cox DP, Singer DA (1986) Mineral deposit models: US Government Printing Office Bulletin; 1986.

Deng H, Zheng Y, Chen J, Yu S, Xiao K, Mao X (2022) Learning 3D mineral prospectivity from 3D geological models using convolutional neural networks: Application to a structure-controlled hydrothermal gold deposit. Computers & Geosciences 161, 105074.

Li C, Liu B, Xiao K, Kong Y, Wang L, Tang R, Xie M, Wu Y, (2023) Metallogenic prediction of the Zaozigou Gold Deposit using 3D geological and geochemical modeling. Minerals 13 (9), 1205.

Nielsen SHH, Cunningham F, Hay R, Partington G, Stokes M (2015) 3D prospectivity modelling of orogenic gold in the Marymia Inlier, Western Australia. Ore Geology Reviews 71, 578-591.

Payne CE, Cunningham F, Peters KJ, Nielsen S, Puccioni E, Wildman C, Partington GA (2015) From 2D to 3D: Prospectivity modelling in the Taupo Volcanic Zone, New Zealand. Ore Geol Rev 71:558-577.

Qin Y, Liu L, Wu W (2021) Machine learning-based 3D modeling of mineral prospectivity mapping in the Anqing Orefield, Eastern China. Natural Resources Research 30 (5):3099-3120.

Salama W, Anand RR, Verrall M (2016) Mineral exploration and basement mapping in areas of deep transported cover using indicator heavy minerals and paleoredox fronts, Yilgarn Craton, Western Australia. Ore Geol Rev 72:485-509.

Wang Y, Xiao K, Zhu Y, Zhang S, Chen Z, Xue Q (2003) A preliminary view on digital mineral deposit model for copper in china. Geology and Prospecting 39 (3), 20-24.

Xiao K, Fan M, Sun L, Zhu Y, Xu Y (2023) Theoretical method of integrated geological information prediction of metallogenic series for mineral resource potential assessment. Acta Geoscientica Sinica 44 (05), 769-780.

Zhu YS (1997) Metallogenic prediction methods: Geology Press, Beijing; 1997.

Can Sn^{4+} be transported in hydrothermal fluids?

Shun-Da Yuan[1,2], Jia-Xin Wang[1,3], Xue-Ni Zhang[1,3], Ying Yang[1,2], Liu-Lin Xu[1,2], Pan-Lao Zhao[1,2]

[1]MNR Key Laboratory for Exploration Theory & Technology of Critical Mineral Resources, China University of Geosciences, Beijing, China
[2]Mineralization Process Simulation and Experimental Research Center, China University of Geosciences, Beijing, China
[3]MNR Key Laboratory of Metallogeny and Mineral Assessment, Institute of Mineral Resources, Chinese Academy of Geological Sciences, Beijing, China

Abstract. This study investigates tin speciation and transport mechanisms in fluoride-rich hydrothermal systems through integrated experimental and computational approaches. Tin solubility experiments (170-350°C) combined with ab initio molecular dynamics simulations reveal four dominant complexes, including SnF_4, SnF_3OH, $SnF_2(OH)_2$, and $SnF(OH)_3$. First-principles calculations demonstrate temperature-dependent Sn-F bond contraction between 170–350 °C, enhancing Sn-F bonding strength. Thermodynamic modeling shows F bearing oxidized fluids achieve Sn concentrations (~100 ppm) comparable to ore-forming fluids and cooling effectively induces precipitation as speciation shifts from SnF_4/SnF_3OH above 350°C to $SnF_2(OH)_2$/$SnF(OH)_3$ below, decreasing solubility by 99.8% with little remobilization below 350°C. The results offer precise quantitative insights into tin mobilization and deposition, enhancing predictive models for tin mineralization within magmatic-hydrothermal systems.

1 Introduction

Over 95% of primary tin deposits are genetically associated with magmatic-hydrothermal systems (Mao et al. 2019; Lehmann 2021). Enrichment of Sn in hydrothermal fluids is crucial for the formation of Sn deposits (Heinrich 1990; Lehmann 1990; Webster et al. 2004; Yuan et al. 2019; Romer et al. 2022; Zhao et al. 2022; Chi et al. 2024). Traditionally, tin is seen to be primarily transported as Sn(II) in hydrothermal fluids, stabilized by chloride complexes. (Jackson and Helgeson 1985; Heinrich 1990; Müller and Seward 2001; Lehmann 2021). Nevertheless, under elevated oxygen fugacity, Sn(II) is oxidized to Sn(IV), which exhibits significantly lower solubility in hydrothermal fluids, leading to tin precipitation and ore formation (Heinrich 1990; Halter et al. 1998; Müller and Seward 2001). However, recent studies increasingly note the contribution of aqueous Sn(IV) to cassiterite mineralization. Stable Sn(IV)-chloride complexes have been reported in aqueous solutions under conditions of fO_2 ≥ HM (Wilson and Eugster 1990). In situ Raman spectroscopic analyses of chloride fluids have further indicated that Sn(IV) remains stable under fO_2≥NNO (Schmidt 2018; Chou et al. 2021), and it may become the predominant aqueous tin species in intermediate oxidizing environments with high HCl content (Wang et al. 2021; Liu et al. 2023). Accordingly, some scholars propose that Sn(IV) may prevail over Sn(II) in some Sn-ore forming hydrothermal fluids (Schmidt 2018; Schmidt et al. 2021; Wang et al. 2021).

Given that Sn^{4+} is a hard acid, it exhibits limited affinity toward the borderline base Cl^-, as predicted by the Hard and Soft Acids and Bases (HSAB) principle. Experimental data indicate that the solubility of Sn(IV)-Cl complexes is approximately 1 ppm at 400°C (Pabalan 1986), significantly lower than the Sn concentrations found in fluid inclusions from typical Sn deposits (average of ~100 ppm, Naumov et al. 2016; Chi et al. 2024). Conversely, F^-, a hard base, exhibits a stronger affinity for Sn^{4+} compared to Cl^- (Pearson 1963; Aksyuk 2000). Crucially, fluorine is closely associated with Sn mineralization. Sn-mineralized granites are often enriched in F, with some granites displaying extremely high F concentrations (>5 wt%, Webster 2004). Fluorine can effectively dissolve into hydrothermal fluids from these high F granitic magmas (Carroll & Webster 1994; Thomas et al. 2005). Fluids exsolving from these magmas have been computed to contain elevated F concentrations (4 wt% or more, Webster 2004), often surpassing their chloride contents (Webster 2004; Liao et al. 2014; Naitza et al. 2016; Lu et al. 2003; Thomas et al. 2005).

In addition, Sn and F concentrations in solution show a positive correlation, with Sn levels generally rising alongside F concentrations (Duc-tin et al. 2007). Fluorine-bearing minerals such as fluorite, topaz, and some lithium micas are frequent associates of cassiterite (Sato 1980; Thomas 1982; Aksyuk 2000; Johan and Johan 2001; Lenharo et al. 2002; Webster 2004; Liao et al. 2014; Xie et al. 2014). High Sn contents (~1000 ppm) have been detected in fluorite inclusions formed during tin mineralization periods (Korges et al. 2020; Rizvanova et al. 2021). Notably, oxidized granitoids related Sn deposits typically exhibit very high F contents (Li et al. 2024; Xie et al. 2013; Lu et al. 2003; Wang et al. 2012), and some of these deposits, such as the Shizhuyuan oxidized tin deposit, have developed into substantial fluorite reserves (reaching 76 Mt), making it one of the largest fluorite deposits in China (Liu et al. 1995; Lu et al. 2003). In summary, F demonstrates significant potential to mobilize Sn^{4+} in hydrothermal fluids. However, the effectiveness remains uncertain due to the current lack of experimental evidence on the solubility of Sn in these fluids.

Our study conducts an experimental investigation into the solubility and speciation of tin in fluoride-bearing solutions at temperatures from 100 to 350 °C. We provide thermodynamic data for the dominant tin fluoride species to predict the probable concentration of tin in acidic fluoride-bearing hydrothermal fluids. This research aims to enhance our understanding of the geochemical processes that facilitate tin mobilization and deposition, contributing valuable insights into mineral exploration and sustainable resource management.

2 EXPERIMENTAL TECHNIQUES

2.1 Solubility experiment

The experiments involved investigating the solubility of synthetic SnO_2 (solid) in acidic solutions (with a pH_T of 3) with varying HF concentration (0.001 to 0.3 mol/kg) at temperatures from 170 to 350 °C under vapor-saturated water pressure. Solutions were prepared employing

nano-pure de-ionized water, along with precise quantities of NaF, $HClO_4$, and $NaClO_4$/NaCl. The oxygen fugacity of the solutions was regulated by the introduction of MoO_3 and MoO_2.

The experimental equipment adopted in this study involved Teflon and Monel reactors at temperatures of 100-260℃ and 290-350℃, respectively. The method is similar to that employed in our previous studies (e.g., Wang et al. 2022; Wang et al. 2023).

2.2 Ab initio molecular dynamics simulations

The AIMD simulations were conducted with the CP2K/QUICKSTEP software package (Kühne et al. 2020) to determine the geometry of the Sn-F complexes. The CP2K software employs Kohn-Sham (Kohn and Sham 1965) density functional theory (DFT) with mixed Gaussian basis sets. Time-averaged stoichiometric and geometric information was obtained with VMD (Humphrey, et al. 1996), and bond distances were retrieved from the radial distribution function. The method is similar to that employed in our previous studies (e.g., Wang et al. 2025).

2.3 Method used in calculating ion activity

The ion activity was calculated using the extended Debye-Hückel equation (Helgeson et al. 1981):

$$\log \gamma_n = \frac{-A \cdot [z_n]^2 \cdot \sqrt{I}}{1 + B \cdot \mathring{a} \cdot \sqrt{I}} + b_\gamma \cdot I$$

where A and B stand for the solvent parameters of the Debye-Hückel equation that, in turn, depend on the thermodynamic properties and dielectric constant of H_2O. The Haar–Gallagher–Kell (Kestin et al. 1984) and Marshall and Franck models (Marshall and Franck 1981) were used to determine the values of A and B under our experimental conditions. The term å is an ion size parameter for the electrolyte, z stands for the charge of the ion, and *I* represents the ionic strength of the solution when all dissolved components are considered. The term bγ is the extended parameter.

3 Results and Discussion

Based on experimental results obtained at temperatures ranging from 170 to 350 ºC under conditions of MMO-buffered oxygen fugacity and saturated water vapor pressure, we identified the Sn-F species and determined cassiterite solubility in fluoride-bearing aqueous solutions. Four major complexes dominate tin speciation in fluoride-bearing aqueous solutions, including SnF_4, SnF_3OH, $SnF_2(OH)_2$, and $SnF(OH)_3$. Through first-principles molecular dynamics simulations, we have determined the spatial geometries of these complexes (Fig. 1). The first-principles calculation results demonstrate that the Sn-F bond length decreases from 2.03 Å to 1.98 Å as the temperature increases from 170 °C to 350 ºC, indicating enhanced bonding strength between F^- and Sn^{4+} ions at elevated temperatures. Furthermore, through comprehensive thermodynamic calculations, we have determined the standard Gibbs free energies, formation constants, and MRB parameters for these complexes.

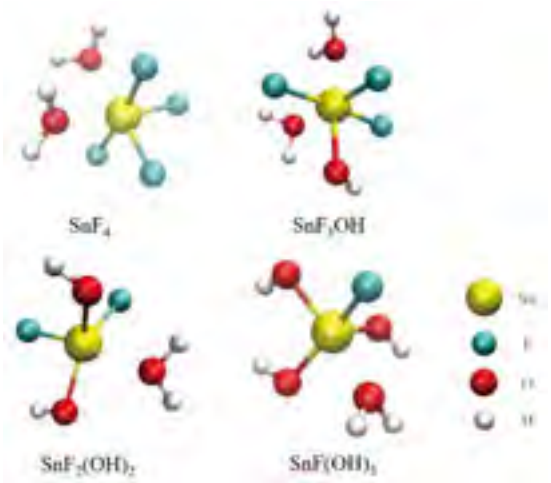


Figure 1. Snapshots of the configurations of Sn-F complexes during the AIMD simulations.

We conducted numerical simulations to investigate the relationship between F concentration and Sn solubility in fluoride-bearing oxidized hydrothermal fluids. Under simulated hydrothermal conditions of 400 ºC, 500 bar, and pH 5, our results demonstrate a positive correlation between F concentration and Sn solubility. The model predicts that at F concentration of 0.2 mol/L, the Sn concentration in the fluid reaches levels comparable to those observed in tin-mineralizing hydrothermal fluids (~100 ppm; Naumov et al. 2016). This finding is consistent with Kovalenko's (1989) observation that topaz crystallization requires a minimum F^- concentration of 0.3 mol/kg in the fluid, our model indicates Sn solubility can exceed 1000 ppm. These results demonstrate the capacity of F-rich oxidized hydrothermal fluids for Sn transport and ore formation.

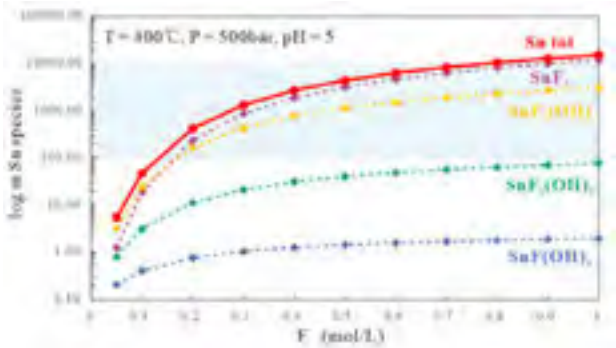


Figure 2. Tin solubility as a function of fluoride concentration in oxidized hydrothermal fluids at 400 ºC and 500 bar.

To investigate the dominant mechanisms controlling tin precipitation, we performed systematic simulations examining temperature-dependent tin solubility evolution. The simulations were constrained at pH 5 with initial concentrations of 0.2 mol/kg F and 1 mol/kg Sn, modeling progressive cooling from 450 to 300 ºC.

As shown in Figure 3, tin concentration exhibits a two-stage evolutionary pattern: (1) a rapid decline from ~6000 ppm at 450 ºC to ~10 ppm at 350 ºC, followed by (2) a stabilization phase where further cooling to 300 ºC causes negligible concentration changes (<2% variation). This thermal threshold signifies a pivotal transition in the predominant tin complexes: SnF_4 and $SnF_3(OH)$ species dominate at temperatures >350 ºC, whereas $SnF_2(OH)_2$ and $SnF(OH)_3$ complexes prevail at <350 ºC. The

dramatic 99.8% solubility reduction observed between 450-350 °C underscores the remarkable efficiency of temperature-controlled precipitation, while the subsequent stabilization at lower temperatures indicates minimal remobilization capacity below 350 °C.

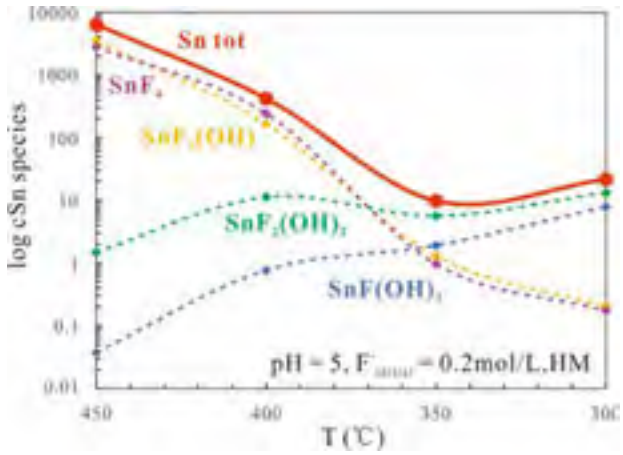


Figure 3. Diagram illustrating the solubility of tin in fluoride-bearing oxidizing hydrothermal fluids as a function of temperature.

5 Conclusions

Tin speciation in fluoride-bearing aqueous systems is dominated by four complexes (SnF_4, SnF_3OH, $SnF_2(OH)_2$, $SnF(OH)_3$). First-principles calculations show Sn-F bond contraction (2.03 → 1.98 Å) from 170–350°C, indicating enhanced F^-–Sn^{4+} bonding at higher temperatures. Fluoride-rich oxidized hydrothermal fluids exhibit strong tin transport capacity, while the 99.8% solubility drop between 450–350 °C demonstrates thermally driven precipitation efficiency.

References

Aksyuk AM (2000) Estimation of fluorine concentrations in fluids of mineralized skarn systems. Econ Geol 91:1339–1347. https://doi.org/10.2113/gsecongeo.95.6.1339

Chi Z, Pan JY, Ni P, (2024) Magmatic–hydrothermal evolution at the barren Wushan Pluton, Southeast China: Insight into controls on mineralization potential. J Petrol 65:p.egae047. https://doi.org/10.1093/petrology/egae047

Chou I, Wang R, Fang J (2021) In situ redox control and Raman spectroscopic characterization of solutions below 300 ℃. Geochem Perspect Lett 20:1–5.https://doi.org/10.7185/geochemlet.2135

Duc-Tin Q, Audétat A, Keppler H (2007) Solubility of tin in (Cl, F)-bearing aqueous fluids at 700 degrees C, 140 MPa: a LA-ICP-MS study on synthetic fluid inclusions. Geochim Cosmochim Acta 71:3323–3335. https://doi.org/10.1016/j.gca.2007.04.022

Halter WE, Williams-Jones AE, Kontak DJ (1998) Modeling fluid-rock interaction during greisenization at the East Kemptville tin deposit: implications for mineralization. Chem Geol 150:1–17. https://doi.org/10.1016/S0009-2541(98)00050-3

Heinrich CA (1990) The chemistry of hydrothermal tin (-tungsten) ore deposition. Econ Geol 85:457–481.https://doi.org/10.2113/gsecongeo.85.3.457

Helgeson HC, Kirkham DH, Flowers GC (1981) Theoretical prediction of the thermodynamic behavior of aqueous electrolytes by high pressures and temperatures; IV, Calculation of activity coefficients, osmotic coefficients, and apparent molal and standard and relative partial molal properties to 600℃ and 5kbar. Am J Sci 281:1249–1516. https://doi.org/10.2475/ajs.281.10.1249

Humphrey W, Dalke A, Schulten K (1996) VMD: visual molecular dynamics. J Mol Graph 14:33–38. https://doi.org/10.1016/0263-7855(96)00018-5

Jackson KJ, Helgeson HC (1985) Chemical and thermodynamic constraints on the hydrothermal transport and deposition of tin: I. Calculation of the solubility of cassiterite at high pressures and temperatures. Geochim Cosmochim Acta 49:1-22. https://doi.org/10.1016/0016-7037(85)90187-5

Johan Z, Johan V (2001) Les micas de la coupole granitique de Cinovec (Zinnwald), République tchèque: un nouvel aspect sur la métallogenèse de l'étain et du tungstène. Earth and Planetary Science 332:307–313.https://doi.org/10.1016/S1251-8050(01)01541-5

Kestin J, Sengers JV, Kamgar-Parsi B, Sengers JL (1984) Thermophysical properties of fluid H_2O. J Phys Chem Ref Data 13:175–183. https://doi.org/10.1063/1.555707

Kohn W, Sham LJ (1965) Self-consistent equations including exchange and correlation effects. Phys Rev 140:A1133. https://doi.org/10.1103/PhysRev.140.A1133

Korges M, Weis P, Lüders V, Laurent O (2020) Sequential evolution of Sn–Zn–In mineralization at the skarn-hosted Hmmerlein deposit, Erzgebirge, Germany, from fluid inclusions in ore and gangue minerals. Miner Deposita 55:937–952.https://doi.org/10.1007/s00126-019-00905-4

Kovalenko NI, Dorofeeva VA, Velyukhanova TR (1989) Thermodynamic properties of Sn(II) complexes in supercritical acidic fluoride solutions. Sci Géol Bull Mémoires 42:343–350.

Kühne TD, Iannuzzi M, Del Ben M, Rybkin VV, Seewald P, Stein F, Hutter J (2020) CP2K: an electronic structure and molecular dynamics software package Quickstep: efficient and accurate electronic structure calculations. J Chem Phys 152 (19). https://doi.org/10.1063/5.0007045

Lehmann B (1990) Metallogeny of tin. Springer-Verlag, Berlin.https://doi.org/10.1007/BFb0010922

Lehmann B (2021) Formation of tin ore deposits: A reassessment. Lithos 105756.https://doi.org/10.1016/j.lithos.2020.105756

Lenharo SL, Moura MA, Botelho NF (2002) Petrogenetic and mineralization processes in Paleo- to Mesoproterozoic rapakivi granites: examples from Pitinga and Goiás, Brazil. Precambr Res 119:277–299.https://doi.org/10.1016/S0301-9268(02)00126-2

Li JX, Ding L, Evans NJ et al (2024) Garnet geochemistry reveals late-stage oxidation of tin-bearing fractionated granite. Lithos 107449. https://doi.org/10.1016/j.lithos.2023.107449

Liao SL, Chen SY, Deng XH, Li P, Zhao JN, Liao RYZ (2014) Fluid inclusion characteristics and geological significance of the Xi'ao copper–tin polymetallic deposit in Gejiu, Yunnan Province. J Asian Earth Sci 79:455–467. https://doi.org/10.1016/j.jseaes.2013.10.023

Liu Y, Wang C, Xu Y, Lu HZ (1995) The ore-forming conditions of the superlarge multimetal deposit in Shizhuyuan. Hunan Geology 14:211–219 (in Chinese).

Lu HZ, Liu YM, Wang CL, Xu YZ, Li HQ (2003) Mineralization and fluid inclusion study of the Shizhuyuan W-Sn-Bi-Mo-F skarn deposit, Hunan Province. China. Econ Geol 98:955–974.https://doi.org/10.2113/gsecongeo.98.5.955

Mao JW, Ouyang H, Song S, Santosh M, Yuan S, Zhou Z, Zheng W, Liu H, Liu P, Cheng Y, Cheng M (2019) Geology and metallogeny of tungsten and tin deposits in China. Soc Econ Geol Spec Publ 22:411–482.https://doi.org/10.5382/SP.22

Marshall WL, Franck EU (1981) Ion product of water substance, 0-1000℃, 1-10,000 bars. New international formulation and its background. J Phys Chem Ref Data 10:295–304. https://doi.org/10.1063/1.555643

Müller B, Seward TM (2001) Spectrophotometric determination of the stability of tin(II) chloride complexes in aqueous solution up to 300℃. Geochim Cosmochim Acta 65:4187e4. https://doi.org/10.1016/S0016-7037(01)00690-1

Naumov VB, Girnis AV, Dorofeeva VA, Kovalenker VA (2016) Concentration of ore elements in magmatic melts and natural fluids as deduced from data on inclusions in minerals. Geol Ore Dep 58:327–343. https://doi.org/10.1134/S1075701516040048

Pabalan R (1986) Solubility of cassiterite tin(iv)dioxide in sodium-chloride solutions from 200 degrees c - 350 degrees c, with geologic applications (complexes, deposits, stannous complex, stannic, equilibrium constants). PhD thesis, Pennsylvania State University.

Pearson, R.G., 1963. Hard and soft acids and bases. J Am Chem Soc 85:3533–3539.

Romer RL, Kroner U, Schmidt C, Legler C (2022) Mobilization of tin during continental subduction-accretion processes. Geology 50:1361–1365.https://doi.org/10.1130/G50466.1

Sato K (1980) Tungsten skarn deposit of the Fujigatani Mine, Southwest Japan. Econ Geol 75:1066–1082.https://doi.org/10.2113/gsecongeo.75.7.1066

Schmidt C (2018) Formation of hydrothermal tin deposits: Raman spectroscopic evidence for an important role of aqueous Sn(IV) species. Geochim Cosmochim Acta 220:499-511.https://doi.org/10.1016/j.gca.2017.10.011

Schmidt C, Gottschalk M, Zhang R, Lu J (2021) Oxygen fugacity during tin ore deposition from primary fluid inclusions in cassiterite. Ore Geol Rev 139:104451.https://doi.org/10.1016/j.oregeorev.2021.104451

Thomas R (1982) Ergebnisse der thermobarogeohemischen Untersuchungen an Flüssigkeitseinschlüssen in Mineralen der postmagmatischen Zinn-Wolfram-Mineralisation des Erzgebirges. Freiberger Forschungshefte 370:1–85.

Thomas R, Förster HJ, Rickers K, Webster JD (2005) Formation of extremely F-rich hydrous melt fractions and hydrothermal fluids during differentiation of highly evolved tin-granite magmas: a melt/fluid-inclusion study. Contrib Miner Petrol 148:582–601.https://doi.org/10.1007/s00410-004-0624-9

Wang JX, Williams-Jones AE, Timofeev A, Liu J, Yuan S (2022) An experimental investigation of the solubility and speciation of scandium in fluoride-bearing aqueous liquids at temperatures up to 250℃. Geochim Cosmochim Acta 330:67–79. https://doi.org/10.1016/j.gca.2022.01.032

Wang JX, Williams-Jones AE, Timofeev A, Zhang X, Liu J, Yuan, S (2023) The role of scandium chloride and hydroxide complexes in the formation of scandium deposits: insights from experiments and modeling. Econ Geol 118:1995–2004. https://doi.org/10.5382/econgeo.5026

Wang JX, Williams-Jones AE, Zhang X, Yuan S (2025) Are scandium sulfate complexes effective in mobilizing scandium? Geochim Cosmochim Acta (In Press). https://doi.org/10.1016/j.gca.2025.01.038

Wang R, Yu AP, Chen J, Xie L, Lu JJ, Zhu JC (2012) Cassiterite exsolution with ilmenite lamellae in magnetite from the Huashan metaluminous tin granite in southern China. Miner Petrol 105:71–84. https://doi.org/10.1007/s00710-012-0194-x

Wang TH, She JX, Yin K, Wang K, Zhang YJ, Lu XC, Liu XD, Li WQ (2021) Sn(II) chloride speciation and equilibrium Sn isotope fractionation under hydrothermal conditions: A first principles study. Geochim Cosmochim Acta 300:25–43.https://doi.org/10.1016/j.gca.2021.02.023

Webster J, Thomas R, Förster HJ, Seltmann R, Tappen C (2004) Geochemical evolution of halogen-enriched granite magmas and mineralizing fluids of the Zinnwald tin–tungsten mining district, Erzgebirge, Germany. Miner Deposita 39:452–472.https://doi.org/10.1007/s00126-004-0423-2

Webster JD (2004) The exsolution of magmatic hydrosaline chloride liquids. Chem Geol 210:1-4.https://doi.org/10.1016/j.chemgeo.2004.06.003

Wilson GA, Eugster HP (1990) Cassiterite solubility and tin speciation in supercritical chloride solutions. Geochem Soc Special Publ 2:179–195.

Xie LW, Yin QZ, Yang JH, Wu FY, Yang YH (2013) A tin-mineralized topaz rhyolite dike with coeval topaz granite enclaves at Qiguling in the Qitianling tin district, southern China. Lithos 170:252–268. https://doi.org/10.1016/j.lithos.2013.03.001

Yuan SD, Williams-Jones AE, Romer RL, Zhao PL, Mao JW (2019) Protolith-related thermal controls on the decoupling of Sn and W in Sn-W metallogenic provinces: Insights from the Nanling region, China. Econ Geol 144:1005-1012.https://doi.org/10.5382/econgeo.4669

Zhao PL, Zajacz Z, Tsay A, Yuan,SD (2022) Magmatic hydrothermal tin deposits form in response to efficient tin extraction upon magma degassing. Geochim Cosmochim Acta 316:331–346.https://doi.org/10.1016/j.gca.2021.09.011.





COLORADO SCHOOL OF
MINES